Transactions of the ASME

Technical Editor, L. B. FREUND

Division of Engineering
Brown University
Providence, R.I. 02912

APPLIED MECHANICS DIVISION

Chairman, J. D. ACHENBACH
Secretary, M. M. CARROLL
Associate Editors,
T. BELYTSCHKO
D. B. BOGY
R. M. CHRISTENSEN
R. J. CLIFTON
MAURICE HOLT
W. D. IWAN
W. G. KNAUSS
F. A. LECKIE
L. E. MALVERN
FRANCIS C. MOON
R. P. NORDGREN
R. H. PLAUT
J. R. RICE
R. T. SHIELD
C. T. SUN
J. S. WALKER
G. A. WEMPNER
S. E. WIDNALL

BOARD ON COMMUNICATIONS
Chairman and Vice-President
K. N. REID, JR.

Members-at-Large
W. BEGELL
J. T. COKONIS
W. G. GOTTENBERG
H. C. REEDER
D. KOENIG
M. KUTZ
F. LANDIS
R. E. NICKELL
J. E. ORTLOFF
C. PHILLIPS

President, G. KOTNICK
Exec. Dir.
PAUL ALLMENDINGER
Treasurer, ROBERT A. BENNETT

PUBLISHING STAFF
Mng. Dir., Pub., J. J. FREY
Dep. Mng. Dir., Pub.
JOS. SANSONE
Managing Editor,
CORNELIA MONAHAN
Production Editor, SUZANNE MAGIDA
Prod. Asst., MARISOL ANDINO

The Journal of Applied Mechanics (ISSN 0021-8936) is published quarterly for $100 per year by The American Society of Mechanical Engineers, 345 East 47th Street, New York, NY 10017. Second class postage paid at New York, NY and additional mailing offices. POSTMASTER: Send address changes to The Journal of Applied Mechanics, c/o THE AMERICAN SOCIETY OF MECHANICAL ENGINEERS, 22 Law Drive, Box 2300, Fairfield, NJ 07007-2300. **CHANGES OF ADDRESS** must be received at Society headquarters seven weeks before they are to be effective. Please send old label and new address.

PRICES: To members, $24.00, annually; to nonmembers, $100.00. Add $6.00 for postage to countries outside the United States and Canada.

STATEMENT from By-Laws. The Society shall not be responsible for statements or opinions advanced in papers or . . . printed in its publications (B7.1, Par. 3).

COPYRIGHT © 1985 by the American Society of Mechanical Engineers. Reprints from this publication may be made on condition that full credit be given the TRANSACTIONS OF THE ASME, JOURNAL OF APPLIED MECHANICS, and the author, and date of publication be stated.

INDEXED by the Engineering Index, Inc.

Journal of Applied Mechanics

Published Quarterly by The American Society of Mechanical Engineers

VOLUME 52 • NUMBER 2 • JUNE 1985

TECHNICAL PAPERS

247 The Generation of Internal Gravity Waves in a Multilayered Moving Fluid by a Flap-Type Wave Maker
M. R. Müller and P. C. Shang

253 A Finite Element Study of Low Reynolds Number Two-Phase Flow in Cylindrical Tubes
E. I. Shen and K. S. Udell

257 Nonuniqueness in Steady-State Heat Transfer in Prestressed Duplex Tubes – Analysis and Case History
M. G. Srinivasan and D. M. France

263 Hydrodynamic Disk Braking
C. Y. Wang

267 The Role of Axial Edge Effects and Cavitation in Lubrication for Short Journal Bearings (85-APM-8)
R. H. Buckholz, J. Lin, and C. H. T. Pan

274 Temperature Field Due to a Moving Heat Source: A Moving Mesh Finite Element Analysis (85-APM-19)
Z.-B. Kuang and S. N. Atluri

281 Effect of Inertia on Finite Near-Tip Deformation for Fast Mode-III Crack Growth
J. D. Achenbach and N. Nishimura

287 Dynamic Impact Over a Subsurface Crack: Applications to the Dynamic Tear Test (85-APM-17)
L. M. Brock, M. Jolles, and M. Schroedl

291 A Stress Intensity Factor Tracer (85-APM-12)
K.-S. Kim

298 A Two Surface Model for Transient Nonproportional Cyclic Plasticity: Part 1 Development of Appropriate Equations (85-APM-9)
D. L. McDowell

303 A Two Surface Model for Transient Nonproportional Cyclic Plasticity: Part 2 Comparison of Theory With Experiments (85-APM-10)
D. L. McDowell

309 The Mechanics of High-Speed Rolling of Viscoplastic Materials (85-APM-6)
J. Tirosh, D. Iddan, and O. Pawelski

319 Three-Dimensional Fully Plastic Solutions for Plates and Cylinders With Through-Wall Cracks
G. Yagawa, Y. Takahashi, and H. Ueda

326 Asymptotic Solutions of the Von Karman Equation for a Circular Plate Under a Concentrated Load
J. P. Frakes and J. G. Simmonds

331 A Mixture Theory for Wave Propagation in Angle-Ply Laminates Part 1: Theory
H. Murakami

338 A Mixture Theory for Wave Propagation in Angle-Ply Laminates Part 2: Application
H. Murakami and A. Akiyama

345 Linear Dynamic Poroelasticity With Microstructure for Partially Saturated Porous Solids
J. G. Berryman and L. Thigpen

351 Modeling Shrinkage Mechanisms in Porous Elastic Solids (85-APM-20)
S. C. Cowin

356 Response of an Elastic Plate to Localized Transient Sources
N. Vasudevan and A. K. Mal

363 Optimal Boundary Tractions for Solids With Initial Strains
R. A. Meric

368 On the Theory of a Cosserat Point and Its Application to the Numerical Solution of Continuum Problems
M. B. Rubin

373 On the Numerical Solution of One-Dimensional Continuum Problems Using the Theory of a Cosserat Point
M. B. Rubin

379 Groove Bottom Contours of Minimum Stress Concentration for Antiplane Shear Deformation (85-APM-18)
B. H. Eldiwany and L. T. Wheeler

385 Large Inextensional Deformation of Orthotropic Cantilevered Plates With Distributed Loads (85-APM-7)
P. Darmon and R. C. Benson

389 Dynamics and Stability of Coaxial Cylindrical Shells Conveying Viscous Fluids
M. P. Paidoussis, A. K. Misra, and S. P. Chan

397 Free Vibration of Rectangular Plates Stiffened With Viscoelastic Beams
K. Ohtomi

(Contents continued on Inside Back Cover)

Downloaded 04 May 2010 to 171.66.16.49. Redistribution subject to ASME license or copyright; see http://www.asme.org/terms/Terms_Use.cfm

CONTENTS (CONTINUED)

402 **Buckling of Truncated Conical Shells Under Combined Axial Load, Pressure, and Heating**
J. Tani

409 **Pretwist and Shear Flexibility in the Vibrations of Turbine Blades**
S. Krenk and O. Gunneskov

416 **A Beam Theory for Anisotropic Materials**
O. A. Bauchau

423 **Theoretical Estimation of the Response of Helically Armored Cables to Tension, Torsion, and Bending** (85-APM-13)
J. Lanteigne

433 **Edge Vibrations in Laminated Composite Plates** (85-APM-16)
S. B. Dong and K. H. Huang

439 **Dynamic Rate Effects on Timoshenko Beam Response** (85-APM-21)
T. J. Ross

446 **Period-Doubling Bifurcations and Modulated Motions in Forced Mechanical Systems**
S. Tousi and A. K. Bajaj

453 **The Dynamics of a Harmonically Excited System Having Rigid Amplitude Constraints Part 1: Subharmonic Motions and Local Bifurcations** (85-APM-14)
S. W. Shaw

459 **The Dynamics of a Harmonically Excited System Having Rigid Amplitude Constraints Part 2: Chaotic Motions and Global Bifurcations** (85-APM-15)
S. W. Shaw

465 **Formulation of Equations of Motion for Systems Subject to Constraints**
C. Wampler, K. Buffinton, and J. Shu-hui

471 **Dissipativeness and Stability of a Class of Distributed Parameter Systems**
M. S. Bhat and S. K. Shrivastava

BRIEF NOTES

Influence of Fiber Inertia on the Stress Intensity Around a Subsurface Elastic Fiber 477
R. L. Ryan and S. Mall

Circumferential Part-Through Cracks in Cylindrical Shells Under Tension 478
J. A. Alabi and J. L. Sanders, Jr.

Modulation-Function Technique in Nonuniform Mechanical Systems 479
Y. Frostig and G. Rosenhouse

A Note on Numerical Analysis of Dynamic Coupled Thermoelasticity 483
W. K. Liu and H. G. Chang

Deformation of a Wedged Elastic Sheet due to Pressure 485
C. Y. Wang

Instability Characteristics of the Asymptotic Suction Profile 487
I. H. Herron, C. H. Von Kerczek, and J. Tozzi

488 *Wave Motion in Liquid Films on Rotating Plates*
A. T. Kirkpatrick, M. A. El-Masri, and J. F. Louis

490 *On the Size of the Cohesive Zone at the Crack Tip*
N. C. Huang

492 *Centrifugal Instability of Turbulent Wall Jets Along Strongly Concave Surfaces*
N. Fujisawa, R. Kobayashi, and H. Shirai

493 *On Nonlinear Oscillation of Moving String*
K. R. Korde

494 *Thermally Induced Roof Noise*
C. H. Ellen, C. V. Tu, and W. Y. D. Yuen

496 *Unsteady Nonsimilar Laminar Incompressible Boundary-Layer Flow Over a Yawed Infinite Circular Cylinder*
R. Vasantha and G. Nath

DISCUSSION

499 *Discussion on previously published paper* by **T. R. Roy**

BOOK REVIEWS

500 ***Fracture Mechanics Methodology*** edited by **G. C. Sih** and **L. Faria** . . . Reviewed by **C. H. Popelar**

Incompressible Flow by **Ronald L. Panton** . . . Reviewed by **S. A. Berger**

501 ***Flexible Shells, Theory and Application*** edited by **E. L. Axelrad** and **F. A. Emmerling** . . . Reviewed by **R. C. Benson**

Elastic Stability of Circular Cylindrical Shells by **N. Yamaki** . . . Reviewed by **G. J. Simitses**

502 ***Measuring Techniques in Gas-Liquid Two-Phase Flows*** edited by **J. M. Delhaye** and **G. Cognet** . . . Reviewed by **R. DiPippo**

Books Received by the office of the Technical Editor

476, 503, 504	Worldwide Mechanics Meeting List
252, 273, 280, 297, 318	Applied Mechanics Symposium Proceedings
355, 388, 401, 422	Applied Mechanics Symposium Proceedings
344	Change of Address Form
438	IUTAM Symposia

Downloaded 04 May 2010 to 171.66.16.49. Redistribution subject to ASME license or copyright; see http://www.asme.org/terms/Terms_Use.cfm

M. R. Müller
Associate Professor.
Assoc. Mem. ASME

P. C. Shang[1]
Graduate Student.
Assoc. Mem. ASME

Department of Mechanical and Aerospace Engineering,
Rutgers University,
New Brunswick, N.J. 08903

The Generation of Internal Gravity Waves in a Multilayered Moving Fluid by a Flap-Type Wave Maker

Experiments have examined the waveforms generated by a flap-type wave maker in a moving, three-layer fluid. Results show that the observed modulating waveforms could be predicted accurately for low frequencies and that if the two interfaces are sufficiently close together, both mode-one waves (whose amplitude vary in the vertical such that there is only one maximum) and mode-two waves (with a vertical amplitude structure that contains two relative maxima) are generated of similar amplitude. This results in downstream shifts from sinuous to varicose modes of oscillation.

1 Introduction

Research on internal gravity waves in layered fluids (both analytical and experimental) has centered on a number of areas that have bearing on this present study. These include investigations of possible generation mechanisms for naturally occurring oscillatory internal waves (see reference [1] for a review), wave-wave interactions (both resonant and otherwise), effects of waves on a mean flow [2], and the effects of a mean flow on the propagation of waves [3].

It seems probable that most of the energy observed in waves in the oceans and atmospheres is obtained through shear instability, where energy is pumped from the kinetic energy of the flow, or through external forcing. Theoretically, external forcing has been modeled as an oscillatory pressure distribution by a number of workers [4–6], providing interesting results but little experimental verification. If the waves that one observes are of small amplitude and there is no appreciable shear present, the waveforms can be assumed to be linear and therefore depend on the details of the initial conditions under which they were formed and the dispersion relations of the possible wave modes of the flow. By knowing the vertical structure of the wave field at one horizontal position, the waveforms at all other positions can be predicted. However, sufficient knowledge of the initial conditions is difficult to achieve and is one reason why little experimental work on the generation of linear internal waves appears in the literature.

In this paper we will discuss experiments where linear internal waves were externally forced in the laboratory by a flap-type wave maker in a fluid with three layers of distinctly different temperatures separated by sharp interfaces. Both the flow and the disturbances created by the wave maker will be modeled allowing one to predict the relative sizes of the different wave modes present in the flow and also their actual amplitudes.

While the results reported here can be viewed as pertaining to what can be achieved in the laboratory, they are also relevant to geophysical flows where the wave energy source is traveling at a velocity different than the mean flow. One such example in the ocean would be topographically generated waves in the gulf stream [7].

2 Theoretical Considerations

To predict the amplitudes of the interface deflections measured in the experiments discussed in Section 3, it is necessary to model both the flow and the wave maker. The flow under consideration is a two-dimensional, inviscid flow having a mean velocity U with a density stratification consisting of three layers of fluid with different densities separated by two relatively thin interfaces. The fluid is bounded above and below by solid horizontal walls. The different modes of internal wave propagation in such a flow are governed by the Taylor-Goldstein equation, which is the zeroth-order solution of the linearized vorticity equation. It can be written as [8]:

$$\left\{\frac{d^2}{dz^2}-\left(k^2-\frac{N^2(z)}{(U-c)^2}+\frac{U''(z)}{(U-c)}\right)\right\}\psi=0 \qquad (1)$$

where ψ is the amplitude function, which must go to zero at the upper and lower boundaries, $N(z)$ is the buoyancy frequency, which must be prescribed, k is the wave number and c the phase velocity of a particular wave mode, and U'' is the vertical gradient of the shear. In this problem, the background shear is negligible and the term containing U'' will be ignored.

[1] Present address: David M. Taylor Naval Ship Research and Development Center, Bethesda, Md. 20084.

Contributed by the Applied Mechanics Division for publication in the JOURNAL OF APPLIED MECHANICS.

Discussion on this paper should be addressed to the Editorial Department, ASME, United Engineering Center, 345 East 47th Street, New York, N.Y. 10017, and will be accepted until two months after final publication of the paper itself in the JOURNAL OF APPLIED MECHANICS. Manuscript received by ASME Applied Mechanics Division, December, 1983.

Copyright © 1985 by ASME
Downloaded 02 May 2010 to 171.66.16.54. Redistribution subject to ASME license or copyright; see http://www.asme.org/terms/Terms_Use.cfm

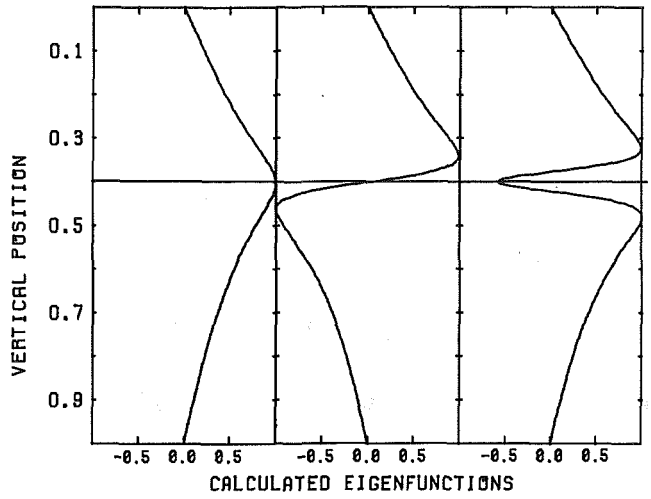


Fig. 1(*a*) Single interface

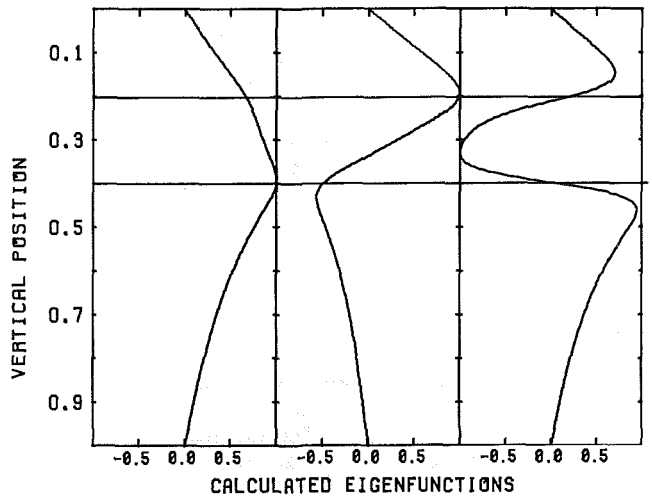


Fig. 1(*b*) Double interface

Fig. 1 Calculated eigenfunctions for the first three modes in a flow

Waves propagating in stratified fluids with nonzero mean velocities have a number of properties that differ from waves in still fluids. Note that if the fluid velocity U is set to zero, equation (1) will admit wavelike solutions only for oscillations whose frequency is less than the buoyancy frequency. When even a small amount of mean flow is present, there is no such constraint and waves of any frequency are theoretically possible. Waves of all frequencies cannot propagate in moving fluids, however, because if the slope of the wave gets sufficiently steep wave breakdown will occur [9]. Of interest here is the case where the mean flow is much faster than the propagation velocities of any mode of internal wave in a still fluid. An observer upstream of the wave maker will see no perturbations, while downstream the (two-dimensional) equations of motion predict a double infinity of possible waves, two wave trains corresponding to each wave mode in the still fluid case. The wave trains that travel slower than the mean flow have been shown by Cairns [10] to be "negative" energy waves. Some investigators have neglected the effects of a mean flow by stating that if one's frame of reference travels with the wave's phase speed, the role of velocity will drop out. But this analogy does not hold in cases where the wave generator (or wave energy source) is not moving with the mean flow. The resultant Doppler shift creates separate dispersion relations for waves traveling faster than the mean flow and those traveling more slowly regardless of the frame of reference in which the analysis is performed.

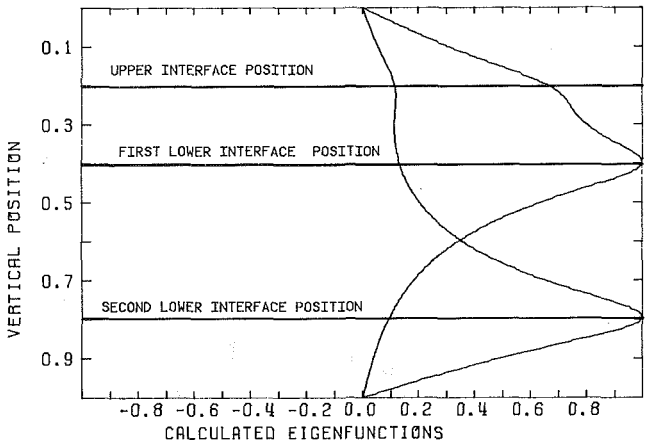


Fig. 2 Calculated mode-one eigenfunctions for two different interface displacements

The density is modeled by combining two hyperbolic tangent profiles with centers located in the middle of the two interfaces. The buoyancy frequency can then be determined at any location by:

$$N^2 = \frac{2g}{\epsilon_1}\beta_1\left\{1-\tanh^2\left[\frac{2(z-d_1)}{\epsilon_1}\right]\right\} + \frac{2g}{\epsilon_2}\beta_2\left\{1-\tanh^2\left[\frac{2(z-d_2)}{\epsilon_2}\right]\right\} \quad (2)$$

where ϵ is the interface thickness, β represents the dimensionless density decrease across the interface, and d is the vertical position of the interface. The subscripts identify the two different interfaces. Using this expression, equation (1) can be numerically integrated (in this case by a specially adapted fifth-order predictor/corrector method) for the eigenfunctions of all possible wave modes. An example of the first three eigenfunctions for waves traveling faster than the mean flow are shown in Fig. 1(*a*) for a flow with a single interface and in Fig. 1(*b*) for the double interface case.

Making the assumption that all waves present in the flow are linear, the waves that actually appear will depend entirely on the initial conditions. The wave maker will be modeled as a very thin two-dimensional flap which oscillates through a small angle about one end of the flap located at $x=0$. The vertical location of the wave maker will be in the center of one of the density interfaces. The amplitude of the disturbance created by the wave maker will be assumed to decay vertically away from the wave-maker level in a symmetric fashion. This means that if the magnitude of the eigenfunctions of the different wave modes present in the flow were known, their linear sum should produce a composite eigenfunction that is symmetric about the wave-maker level. The eigenfunctions shown in Fig. 1(*a*) indicate that if waves are excited at the center of the interface, a composite eigenfunction made up of only mode-one waves would be nearly symmetric. Small-amplitude second and third mode waves can be expected to be present in order to make the symmetry more complete. Earlier experimental work by Müller and Karlsson [11] support this finding. However, in Fig. 1(*b*), the mode-one eigenfunction has a kink in it resulting from the presence of the second interface. This effect is shown more clearly in Fig. 2 where the eigenfunctions of the downstream traveling mode-one wave trains are plotted in two cases, one where the interfaces are close together and one where they are farther apart. When the interfaces are located far apart the two interfaces act independently from each other while in the case when the two interfaces are near each other, the mode-one eigenfunction is quite nonsymmetric. Therefore both mode-two and mode-one waves must be of significant size in a flow where two in-

Downloaded 02 May 2010 to 171.66.16.54. Redistribution subject to ASME license or copyright; see http://www.asme.org/terms/Terms_Use.cfm

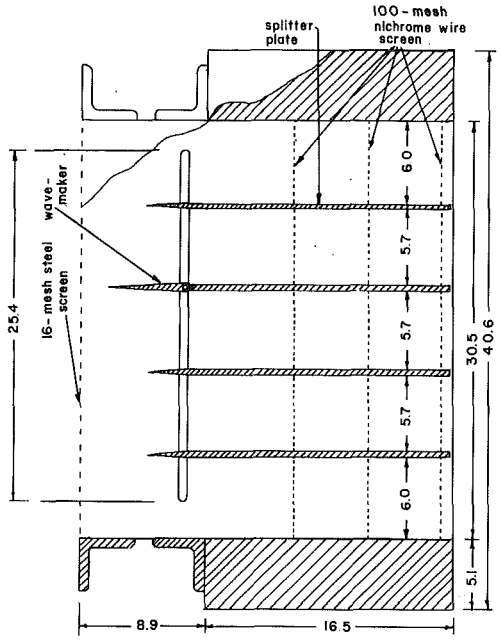


Fig. 3 The heating grid. Flow is from right to left.

terfaces exist close together and waves are forced at one of the interfaces. This is necessary to create a symmetric composite eigenfunction.

The flap-type wave maker being modeled provides additional constraints on the amplitudes and initial phase relationships between the different wave modes. Since the wave maker pivots around its leading edge, at that point the amplitudes must sum to zero. Using this and the symmetry condition, the relative amplitudes of the different wave modes (two mode-one and two mode-two) could then be found by the following procedure. After selecting the necessary input parameters to model the experiment, the Taylor-Goldstein equation was integrated to find both mode-one and mode-two eigenfunctions. A composite eigenfunction was then constructed by assigning an arbitrary amplitude to the downstream traveling mode-one wave, guessing an amplitude for the downstream traveling mode-two wave and then solving for the amplitude of the two upstream traveling wave trains based on a criteria of zero amplitude at the base of the wave maker. The second derivative of the composite eigenfunction was then examined for symmetry about the location of the wave maker and a search was made to determine the set of wave amplitudes that provided the best symmetry.

The actual size of the vertical velocity perturbation caused by the oscillation of the wave maker was crudely estimated by determining the average vertical velocity imparted to a fluid parcel traveling near the surface of the wave maker over its length. The average vertical velocity imposed on any particle during its time in residence over the wavemaker is

$$\bar{V}=\Upsilon\int_0^{\Upsilon}\frac{Ax}{L}\,\Omega\sin(\Omega t+\phi)\,dt \tag{3}$$

where A is the amplitude of the tip of the wavemaker, L is the length, Υ is the residence time ($=L/U$), Ω is the wave-maker frequency, and ϕ represents the initial phase of the wave maker when the particle is located at the base. Writing x as Ut, the integral becomes

$$\bar{V}=\frac{A}{\Omega\mathrm{T}^2}\sin(\phi+\theta)(P^2+Q^2)^{1/2} \tag{6}$$

where

$$P=\sin\Omega\mathrm{T}-\Omega\mathrm{T}\cos\Omega\Upsilon$$

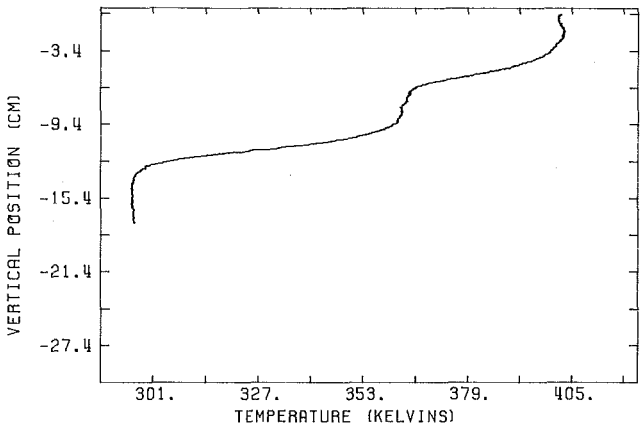


Fig. 4 Typical temperature profile for a three-layer flow

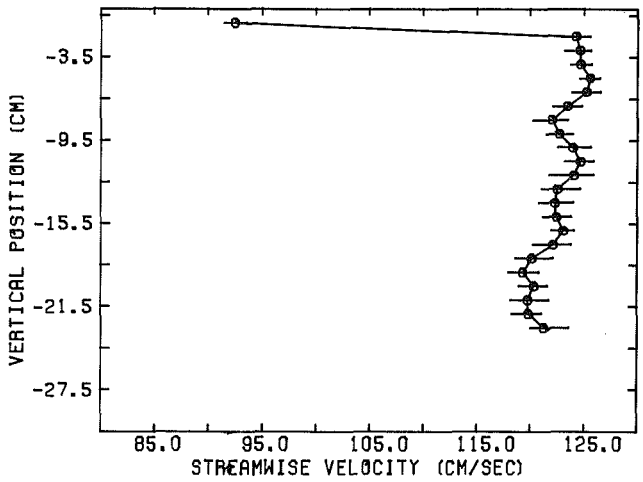


Fig. 5 Typical velocity profile

$$Q=\cos\Omega\Upsilon-\Omega\Upsilon\sin\Omega\Upsilon-1$$

and

$$\theta=\tan^{-1}(P/Q)$$

leaving an expression for the maximum vertical velocity of

$$\bar{V}_{max}=\frac{(P^2+Q^2)^{1/2}A}{\Omega\Upsilon^2} \tag{7}$$

The model will break down as the frequency becomes large and the average vertical velocity becomes meaningless. But, for low frequencies, wave amplitudes can be determined by matching the maximum vertical velocity predicted by the composite eigenfunction to the maximum average vertical velocity imparted by the wave maker.

3 Design of the Experiment

The experiments described here were performed in an open-circuit, induction-type wind tunnel with air being drawn from the laboratory and discharged outside of the laboratory building. The tunnel wind speeds were variable giving workable test section velocities from 90–140 cm/sec. A heater section was located between the acceleration chamber and the test section (see Fig. 3), where the flow was divided into five separate air streams by means of four splitter plates. Within each layer three 100-mesh Nichrome wire screens were stretched normal to the flow and by supplying AC power to some or all of the screens many different thermal profiles could be obtained. The test section was 0.305 × 0.457 × 1.524 meters, with transparent sidewalls for visualizing probe placements.

Downloaded 02 May 2010 to 171.66.16.54. Redistribution subject to ASME license or copyright; see http://www.asme.org/terms/Terms_Use.cfm

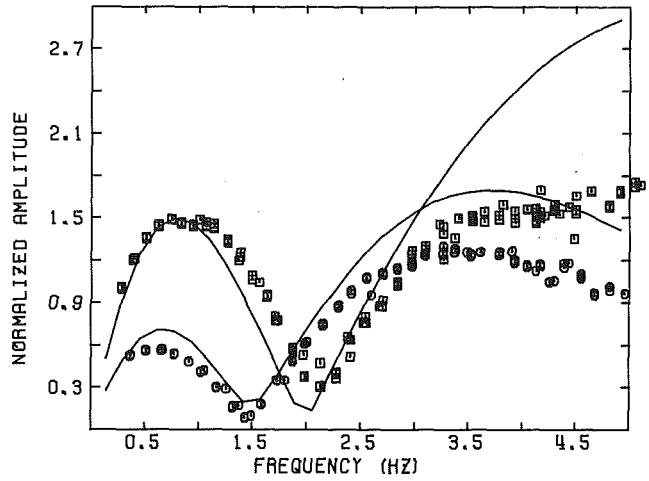


Fig. 6(*a*) Amplitude

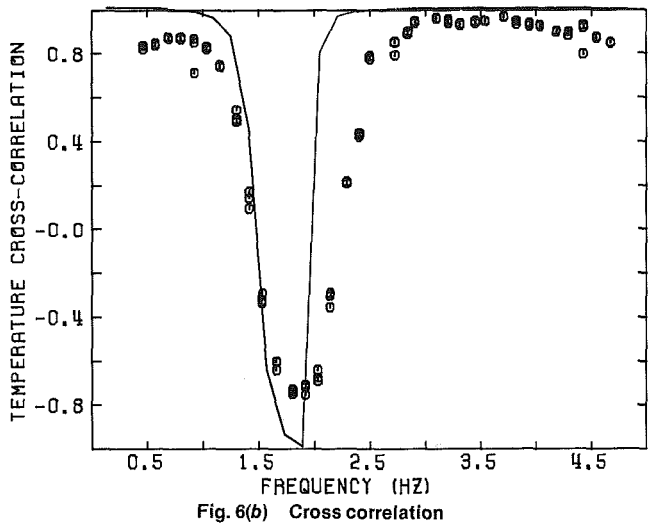


Fig. 6(*b*) Cross correlation

Fig. 6 Comparison of measured interface defections and model predictions for the lower interface excited case

Disturbances were generated by an oscillating tapered vane attached to the downstream end of any splitter plate chosen (again, see Fig. 3). The other splitter plates were fitted with sharp trailing edges to reduce the wake velocity defects. Sinusoidal disturbances were generated when the tapered vane was allowed to pivot about its axis following the motion of a connecting rod externally attached to a scotch yoke mechanism. The maximum peak-to-peak displacement of the downstream tip of the vane was 1.27 cm or 5.5 deg about the splitter plate. Typical operating values had peak-to-peak displacements of 2.5 mm. The rotational speed of the scotch yoke mechanism was controlled by a DC motor over a range of 10 to 517 rpm. By mounting an opaque light chopper on the rotational arm of the motor, the frequency of the disturbances could be monitored and were found to show less than 1 percent deviation from nominal for indefinite periods.

Velocity and temperature measurements were made with DISA constant temperature hot-wire anemometers and cold-wire temperature sensors. The probes were either installed on a probe support which was fed through holes in the floor of the test section, or placed on a mobile probe support which had three degrees of freedom. A 16-bit LSI 11/23 minicomputer system was used for the collection and reduction of experimental data. Included in the system was an 8-channel, 12-bit A/D converter which had a maximum throughput rate of 17 kHz.

4 Experimental Results

All of the experiments reported in this paper were performed with similar temperature and velocity profiles, examples of which are shown in Figs. 4 and 5. The velocity profile contains certain spatial variations of velocity which are troublesome. The background turbulence level was kept as small as possible (a mean RMS value of 0.6 percent) in order to maximize the signal to noise ratio in the temporally acquired data. This had the unwelcome side effect of suppressing the decay of the wake velocity defects caused by the splitter plates which resulted in the variations.

The waveforms created by the disturbance generator were observed by placing temperature sensors in the center of an interface and relating the temperature change measured with the interface deflection. The quality of the waveforms depended on their amplitudes over background noise and were consistantly better on the excited interface than on the adjacent interface. Power spectral density curves obtained from temperature recordings with a probe located at the center of the lower, excited interface showed that the energy in the second harmonic was typically 30 db down from the fundamental and higher harmonics appeared with even less energy. This waveform quality is comparable or better than other quantitative studies of internal waves (for instance see reference [12]).

Since there is only one disturbance generator, all of the excited wave modes will have the same frequency. Each mode will have a different wavelength so the amplitude of the interface deflections due to the waves will vary downstream due to a "beating" between the different waves. By studying the spatial variations of the interface deflections on both interfaces and the phase differences, the amplitudes of the different wave modes present in the flow could be educed. The amplitude of the interface deflections was determined by placing the temperature probe in the center of the interface and then recording the fluctuating temperature signal over several wave cycles. To obtain a repeatable average, the digitally recorded temperatures were first low-pass filtered (using a four-pole Butterworth digital filter) and then phase averaged using a signal from the wave maker as a trigger. Typically about 40 wave cycles were recorded during one sampling period, an average fluctuation level determined and a repeat sampling taken to estimate errors. The magnitude of the temperature fluctuations could then be related to an interface deflection by correlating the data with a temperature profile obtained in an undisturbed test section.

The initial conditions assumed by the model as well as extrapolation of experimental results indicated that the base of the flap-type wave maker serves as an absolute amplitude minimum for all frequencies. As the frequency of the wave maker varies, the wave numbers of the excited waves will change and the spatial modulations will be different. This can be put to advantage by measuring the amplitude of the deflections of the interface as a function of frequency. Figure 6(*a*) shows the observed amplitude of the interface deflections (both upper and lower) as a function of frequency measured at a point 128 cm downstream from the trailing edge of the wave maker, which was located at the center of the lower (more buoyant) interface. The amplitudes are scaled by the peak to peak amplitude of the wave maker. The amplitude of the deflections on the lower interface are in general larger than the deflections on the upper and get as large as 1.8 times the excitation amplitude. The waves on the upper interface get as large as 1.4 times the excitation amplitude. Also included in Fig. 6(*a*) is the theoretically predicted interface deflections determined using the method discussed in Section 2. The fit is acceptable when the frequency of the wave generator is low, and then the model begins to falter as the frequency is increased. The model will certainly fail at high frequency, but it

Downloaded 02 May 2010 to 171.66.16.54. Redistribution subject to ASME license or copyright; see http://www.asme.org/terms/Terms_Use.cfm

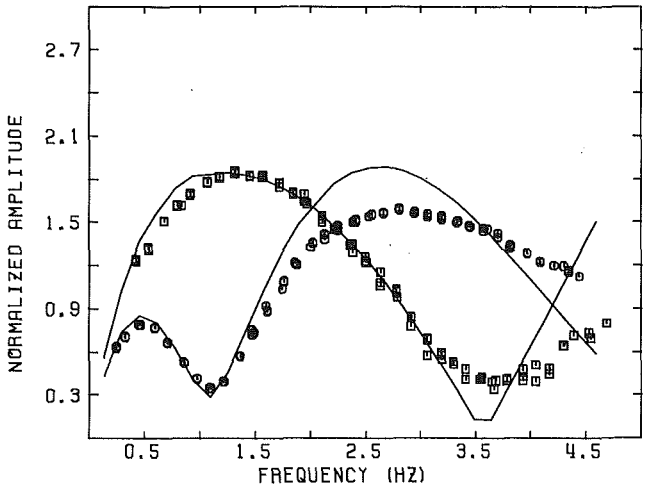


Fig. 7(a) Amplitude

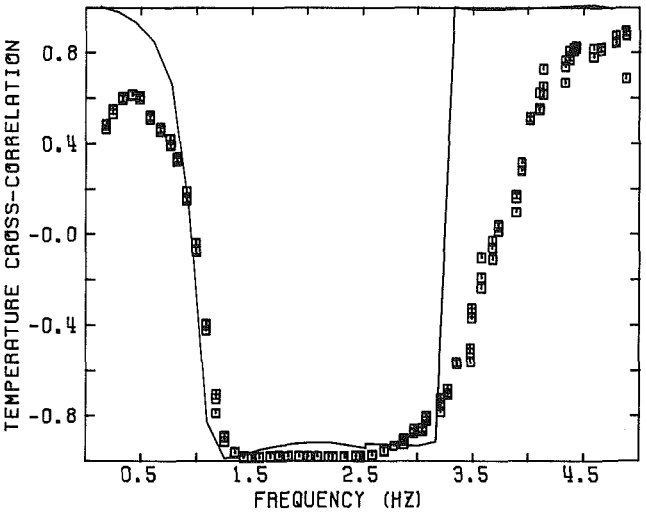


Fig. 7(b) Cross correlation

Fig. 7 Interface deflection as a function of frequency for the upper interface excited case

is felt that the large amplitudes predicted by the theory are sufficient to cause nonlinear terms to be important. Experiments were performed to determine the effect on the amplitude modulations of changing the amplitude of the wave maker. With the wave maker amplitude varying from 1.0–7.0 mm peak-to-peak, the qualitative features of the amplitude modulations did not change. This argued strongly that the wave generation mechanism being used produced linear waves.

These results indicate that the two mode-one waves and the two mode-two waves will have significant amplitudes. The figure does not provide information on the individual wave amplitudes, only a confirmation that the model will predict amplitudes with sufficient accuracy for frequencies under 15 rad/sec. In those cases, the two mode-two waves were always close in amplitude (within a few percent) as well as the two mode-one waves. The ratio of mode-two amplitude to mode-one amplitude varied from 24 percent at the low frequency end to 30 percent at the 15 rad/sec cutoff. With the mode-one wave being larger than the mode-two, the two interfaces will deflect in phase (sinuous oscillation) most of the time. However, when the two mode-one waves destructively interfere, the interfaces will deflect primarily due to mode-two waves and will be directly out of phase (varicose oscillation). The phase difference between oscillations on the two interfaces at a single point as a function of frequency were measured and are presented in Fig. 6(*b*) as the cross correlation between temperature fluctuations obtained during the same experiment shown in Fig. 6(*a*). A small region can be seen where the interfaces oscillated out of phase. Also plotted are results from the model again showing good agreement for low frequency waves.

Experiments were performed with the wave maker located on the upper and less buoyant interface. In general, the mode-two waves should be dominant with mode-one waves present in sufficient amplitude to smooth the composite eigenfunction. Figure 7(*a*) plots the results of such an experiment and shows qualitative differences in the interface deflections. Also plotted are the predictions of the model which again agree favorably with the experiment for low frequencies but break down as the frequencies get large. As in the first case studied, the two mode-two waves are generally very close in amplitude as are the two mode-one waves, but in this case the ratio of mode-two to mode-1 amplitude is 1.69 on average with little variation over the frequency range.

With larger mode-two waves, it should be expected that the variations in interface deflection between sinuous and varicose modes should be more pronounced. Figure 7(*b*) shows a plot of the measured temperature cross correlation between interfaces as a function of frequency and shows a large area of varicose propagation. The model adequately predicts this region as well which represents an area where the mode-one waves are either destructively interfering or are in phase with the mode-two waves on the lower interface making the size of the interface deflection on the lower interface large and consequently for a strong varicose oscillation.

5 Discussion of Results

The results of these experiments provide insight into generation mechanisms of internal waves of different natural modes. When waves are observed in nature, it is an enormously difficult task to determine the source of the wave energy that produced the waves [13]. One reason for this is the possible short-lived nature of the initial waveforms since they are subject to many instabilities which have been discussed in detail in the literature. Clearly if waves change their character rapidly, little can be said about their origin. On the other hand, many instability mechanisms rely to a large part on nonlinear effects in the waves and result in relatively slow growth rates. It is therefore possible that waves of small slope (linear) will keep their identity for some time and allow their origins to be traced. The experiments reported here indicate that multilayered flows can be good indicators of the source of external forcing, at least to whether the forcing comes from above or below. If mode-one waves are larger than mode-two, the energy arrived first at the stronger of the two interfaces. If mode-two waves are large, the energy arrived first at the weaker interface.

It is also of importance to have a model that will predict amplitudes if one is to examine many of the different nonlinear wave interaction theories which have been proposed. As an example, consider the 'explosive' resonant interaction of Craik and Adam [14]. They show a great many different interactions which depend in part on the size of the individual wave modes in the flow. In planning an experiment, it is necessary to know what the amplitudes of the different wave modes will be when artificially excited. In addition, the presence of four separate wave trains (in the three layer case) makes accurate prediction essential. The amplitudes modulate spatially so rapidly that it would be impossible to discern nonlinear growth without detailed knowledge of the original wave amplitudes.

This study also shows that flap-type wave makers could be useful in studying the nonlinear properties of waves and wave

Downloaded 02 May 2010 to 171.66.16.54. Redistribution subject to ASME license or copyright; see http://www.asme.org/terms/Terms_Use.cfm

breakdown. The initial oscillation of the flow field at the wave-maker is always sinuous, and the distance between the two interfaces varies only up to the difference in amplitude of the deflections. Downstream, when the interfaces begin to oscillate in a varicose mode, the distance between the interfaces ranges over the sum of the amplitudes. This greater variation in distance allows the possibility of a careful study of second-order effects.

Acknowledgment

This work was supported by NSF Grant No. CME 80-06735, which is gratefully acknowledged.

References

1 Thorpe, S. A., "The Excitation, Dissipation, and Interaction of Internal Waves in the Deep Ocean," *J. Geophys. Res.*, Vol. 80, 1975, pp. 1–27.

2 Bretherton, Francis P., "On the Mean Motion Induced by Internal Gravity Waves," *J. Fluid Mech.*, Vol. 36, 1969, pp. 785–803.

3 Thomas, G. P., "Wave-Current Interactions: An Experimental and Numerical Study Part 1. Linear Waves," *J. Fluid Mech.*, Vol. 110, 1981, pp. 457–474.

4 Pramanik, A. K., "Waves Due to a Moving Oscillatory Surface Pressure in a Stratified Fluid," ASME JOURNAL OF APPLIED MECHANICS, Vol. 41, 1974, pp. 571–574.

5 Mahanti, N. C., "Oscillations Modes in Superposed Fluids," ASME JOURNAL OF APPLIED MECHANICS, Vol. 45, 1978.

6 Manna, R. K., "Forced Oscillation in a Two-Layer Fluid of Finite Depth," ASME JOURNAL OF APPLIED MECHANICS, Vol. 45, 1983, pp. 506–510.

7 Wunsch, C., "Geographical Variability of the Internal Wave Field: A Search for Sources and Sinks," *J. Phys. Ocean.*, Vol. 6, 1976, pp. 471–485.

8 Thorpe, S. A., "On the Shape and Breaking of Finite Amplitude Internal Gravity Waves in a Shear Flow," *J. Fluid Mech.*, Vol. 85, 1978, pp. 8–31.

9 Muller, M. R., and Karlsson, S. K. F., "A Shear Instability Induced by a Composite Internal Wave," *Phys. Fluids*, Vol. 25, 1982, pp. 1705–1712.

10 Cairns, R. A., "The Role of Negative Energy Waves in Some Instabilities of Parallel Flows," *J. Fluid Mech.*, Vol. 92, 1979, pp. 1–14.

11 Muller, M. R., and Karlsson, S. K. F., "Experiments on the Propagation of Composite Internal Wave Trains," *Phys. Fluids*, Vol. 24, 1981, pp. 1937–1943.

12 Lewis, J. E., Lake, B. M., and Ko, D. R. S., "On the Interaction of Internal Waves and Surface Gravity Waves," *J. Fluid Mech.*, Vol. 63, 1974, pp. 773–800.

13 Hines, C. O., "The Upper Atmosphere in Motion," AGU Geophysical Monograph No. 18, 1974, pp. 659–660.

14 Craik, A. D. D., and Adam, J. A., " 'Explosive' Resonant Wave Interactions in a Three-Layer Fluid Flow," *J. Fluid Mech.*, Vol. 92, 1979, pp. 15–33.

Downloaded 02 May 2010 to 171.66.16.54. Redistribution subject to ASME license or copyright; see http://www.asme.org/terms/Terms_Use.cfm

A Finite Element Study of Low Reynolds Number Two-Phase Flow in Cylindrical Tubes

E. I. Shen
Research Assistant.

K. S. Udell
Assistant Professor.
Assoc. Mem. ASME

Department of Mechanical Engineering,
University of California,
Berkeley, Calif. 94720

A finite element solution to the steady-state problem of an inviscid bubble flowing at low Reynolds number in a cylindrical tube occupied by a second viscous phase was obtained. Interfacial tension forces were balanced against the viscous and pressure forces in order to locate the position of bubble-liquid interface. Velocities, pressures, and film thicknesses were obtained as a function of the capillary number. Specific applications of these results include the description of multiphase flow in tubes and porous media, and blood cell movement in small capillaries. The numerical results are compared with published theories and experiments.

1 Introduction

Bubble flow in small tubes is of interest in connection with two-phase flow through porous media as in the displacement of hydrocarbons from oil-bearing strata, the intrusion of air into water-saturated networks of fibers in papermaking, and also the flow of emulsions or foams through narrow capillaries. Flowing bubble systems may also be of considerable importance for the understanding of blood flow through the capillary system of the body. For example, Prothero and Burton [1] used the flow of a series of air bubbles through capillary tubes containing water as a model for blood cell displacement.

Bubble flows in straight tubes have been studied experimentally by Fairbrother and Stubbs [2], Taylor [3], Cox [4], and Goldsmith and Mason [5]. For the case of bubble phase nonwetting to the tube wall, Goldsmith and Mason showed experimentally that there will be a region of uniform thickness behind the front meniscus as shown in Fig. 1.

Theoretical studies of such flows were limited in the past to the use of the lubrication approximation due to the complicated boundary conditions on the bubble free surface. Bretherton [6] pioneered such a theory by assuming that the viscous stresses modify the bubble profile only very near the wall while in the center of the tube the bubble profile is static, as shown by regions II and III in Fig. 1. In region II, the lubrication approximation gives a good description of the flow and of the profile. His results, however, did not give a unified description for the bubble flow and were restricted to very low flow speed due to the assumption of a static bubble front.

The specific problem considered in this paper concerns a long bubble of a fluid of negligible viscosity moving in a tube filled with a perfectly wetting viscous liquid. Inertial effects are considered negligible and the interfacial tension is constant. The ratio of gravitational forces to interfacial forces (Bond number) is assumed small; thus gravitational forces are neglected.

In the present study a method was developed utilizing the finite element technique in order to describe bubble flow in tubes. The shapes of the bubble menisci which were unknown a priori were located by balancing the surface tension forces against the viscous and pressure forces. The effects of capillary number on the bubble shape and flow field are examined.

2 Finite Element Formulation

For incompressible, creeping viscous flow in a tube, the continuity and momentum equations, neglecting inertial and body forces, can be written in axisymmetrically cylindrical coordinates (z, r):

$$\frac{\partial u}{\partial z} + \frac{1}{r}\frac{\partial}{\partial r}(rv) = 0, \tag{1}$$

$$\rho\frac{\partial u}{\partial t} = -\frac{\partial p}{\partial z} - \left(\frac{1}{r}\frac{\partial}{\partial r}(r\tau_{rz}) + \frac{\partial \tau_{zz}}{\partial z}\right), \tag{2}$$

$$\rho\frac{\partial v}{\partial t} = -\frac{\partial p}{\partial r} - \left(\frac{1}{r}\frac{\partial}{\partial r}(r\tau_{rr}) - \frac{\tau_{\phi\phi}}{r} + \frac{\partial \tau_{rz}}{\partial z}\right),$$

$$\tau_{zz} = -2\mu\frac{\partial u}{\partial z}, \quad \tau_{rr} = -2\mu\frac{\partial v}{\partial r}, \quad \tau_{\phi\phi} = -2\mu\frac{v}{r},$$

$$\tau_{zr} = \tau_{rz} = -\mu\left(\frac{\partial u}{\partial r} + \frac{\partial v}{\partial z}\right), \tag{3}$$

where u and v are the velocity components in the direction of z and r, respectively, and τ_{zz} etc. are the stress components.

Through the analogy between an incompressible elastic solid and an incompressible viscous fluid [7], the finite element model is formulated based on the principle of virtual work typically used in solid mechanics. The continuity equation is retained instead of a penalty formulation known

Contributed by the Applied Mechanics Division for publication in the JOURNAL OF APPLIED MECHANICS.

Discussion on this paper should be addressed to the Editorial Department, ASME, United Engineering Center, 345 East 47th St., New York, N.Y. 10017 and will be accepted until two months after final publication of the paper itself in the JOURNAL OF APPLIED MECHANICS. Manuscript received by ASME Mechanics Division, February, 1984; final revision, July, 1984.

Copyright © 1985 by ASME
Downloaded 02 May 2010 to 171.66.16.54. Redistribution subject to ASME license or copyright; see http://www.asme.org/terms/Terms_Use.cfm

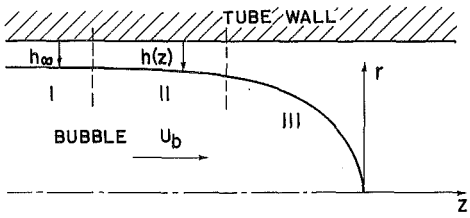


Fig. 1 Steady state profile of an inviscid moving bubble in a cylindrical tube

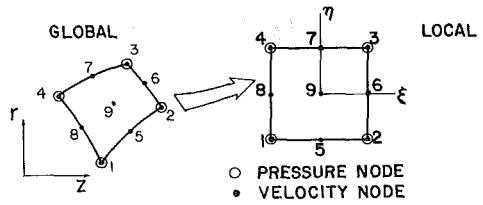


Fig. 2 Basic quadrilateral element and isoparametric mapping

to have its drawback in treating transient flows [8, 9]. This formulation results in the following integral equations:

$$\int_V \delta\epsilon^t \mathbf{D}\epsilon dV - \int_V \rho \frac{\partial \mathbf{v}^t}{\partial t}\delta\mathbf{v} dV = \int_S \delta\mathbf{v}^t \mathbf{T}\, r\, ds, \tag{4}$$

$$\epsilon = \left[\frac{\partial u}{\partial z}, \frac{\partial u}{\partial r}, \frac{\partial v}{\partial z}, \frac{\partial v}{\partial r}, \frac{v}{r}, p\right],$$

$$\mathbf{v} = [u, v],$$

and

$$\mathbf{T} = [T_z, T_r],$$

where $\mathbf{D}$ is the 6×6 constitutive matrix, with nonzero elements $d_{11} = d_{44} = d_{55} = 2\mu$, $d_{22} = d_{33} = d_{23} = d_{32} = \mu$ and $d_{16} = d_{46} = d_{56} = d_{61} = d_{64} = d_{65} = -1$. Note that application of the Galerkin method of weighted residuals to equations (1)–(3) would also yield the identical equations.

A quadrilateral element was employed as shown in Fig. 2 with mixed interpolation consisting of nine-node biquadratic functions for velocity components and four-node bilinear functions for pressure. While the utilization of such elements in solving viscous flows for axisymmetrical coordinates has not been tested nor reported in the literature, there has been little difficulty in their use in this study. The free meniscus is interpolated with quadratic functions for the flow field calculation. Cubic splines with tension [10] were used for the calculation of derivatives of the meniscus location with respect to the axial coordinate.

The interpolation functions chosen for approximating the velocity and pressure components are:

$$u = \sum_{j=1}^{n} H_j(z,r)\, u_j, \tag{5}$$

$$v = \sum_{j=1}^{N} H_j(z,r)\, v_j, \tag{6}$$

and

$$p = \sum_{k=1}^{M} H_k^p(z,r)\, p_k. \tag{7}$$

The curvilinear (z, r) element is mapped isoparametrically into the fixed (ξ, η) domain as shown in Fig. 2; that is,

$$z = \sum_{j=1}^{N} H_j(\xi,\eta)\, Z_j, \tag{8}$$

and

$$r = \sum_{j=1}^{N} H_j(\xi,\eta)\, R_j, \tag{9}$$

where Z_j and R_j are the coordinates for the jth node in the element.

Equation (4) is particulary convenient for the free surface problem since the surface traction can readily be incorporated into the boundary term on the right-hand side. The traction term of equation (4) can be decomposed into normal and tangential parts:

$$\mathbf{T} = T_n \mathbf{n} + T_t \mathbf{t}. \tag{10}$$

The directions of normal and tangential vectors are determined as follows:

$$\mathbf{n} = [\sin\theta, -\cos\theta], \tag{11}$$

and

$$\mathbf{t} = [-\cos\theta, -\sin\theta], \tag{12}$$

where the angle θ is defined by $\theta = \tan^{-1}(dr/dz)$.

By substituting the stress vector and equations (5)–(7) into equation (4), the following is obtained:

$$[\mathbf{K} + \mathbf{M}]\mathbf{v}_o = \mathbf{F}, \tag{13}$$

where

$$\mathbf{K} = \int_V \mathbf{B}^t \mathbf{D}\mathbf{B} r\, dr\, dz,$$

$$\mathbf{M} = -\int_V \rho \alpha^t \alpha \dot{\mathbf{v}}\, r\, dr\, dz,$$

and

$$\mathbf{F} = \int_S \alpha^t \mathbf{T}\, r\, ds.$$

For the steady state problem considered in this work, $\mathbf{M} = 0$.

When the reference frame is chosen to be fixed at the bubble front, the boundary conditions, besides those on the free surface, are:

$$u = -U_b, \quad v = 0, \quad p = -\frac{\sigma}{R_\infty}, \quad \text{as} \quad z \to -\infty,$$

$$u = -U_b + 2U_b\left(\frac{R_\infty}{R_t}\right)^2\left(1 - \left(\frac{r}{R_t}\right)^2\right), \quad v = 0, \quad \text{as} \quad z \to \infty,$$

$$u = -U_b, \quad v = 0, \quad \text{on} \quad r = R_t,$$

$$T_z = 0, \quad v = 0, \quad \text{along the centerline.} \tag{14}$$

Note that the pressure at $z = -\infty$ and axial velocity at $z = +\infty$ are both functions of the radial location of the end node on the bubble free surface.

The location of the free surface is determined by three boundary conditions:

(*i*) The kinematic flow condition that defines the free surface as a streamline (or streamtube for axisymmetrical coordinates)

$$u\frac{\partial r}{\partial z} = v, \tag{15}$$

(*ii*) the dynamic flow conditions where tangential stresses along free surfaces are absent since there is no surface tension gradient

$$T_t = 0, \text{ and} \tag{16}$$

(*iii*) normal stresses consisting of pressure and normal viscous stresses are balanced by interfacial tension forces at the free surfaces.

$$T_n N_{Ca} = \frac{1}{r\left[1 + \left(\frac{\partial r}{\partial z}\right)^2\right]^{1/2}} - \frac{\frac{\partial^2 r}{\partial z^2}}{\left[1 + \left(\frac{\partial r}{\partial z}\right)^2\right]^{3/2}}, \tag{17}$$

where the capillary number is defined as $N_{Ca} = \mu U_b/\sigma$.

Downloaded 02 May 2010 to 171.66.16.54. Redistribution subject to ASME license or copyright; see http://www.asme.org/terms/Terms_Use.cfm

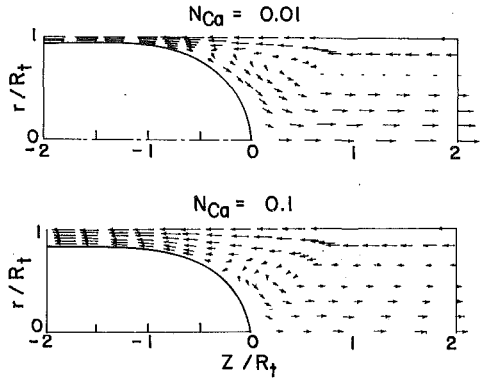


Fig. 3 Flow velocity fields for N_{Ca} = 0.01 and 0.1

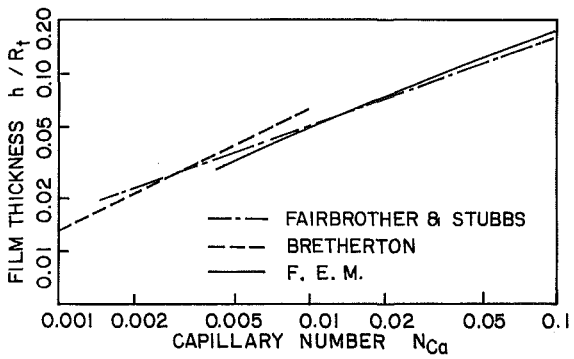


Fig. 4 Film thickness as a function of capillary number

Upon substitution of the equations (14)–(16) into equations (13), the finite element formulation is closed and can be solved as a fixed boundary problem. When the viscous flow field is obtained, the normal stresses at the free surface are calculated through the following expression:

$$T_n N_{Ca} = -p - (\tau_{zz} \sin^2\theta + \tau_{rr} \cos^2\theta - \tau_{rz} \sin 2\theta). \quad (18)$$

The third boundary condition, equation (17), is an initial-value ordinary differential problem with two initial conditions:

$$r(z=z_1) = r_1, \quad (19)$$

and

$$r_z(z=z_1) = \left(\frac{\partial r}{\partial z}\right)_1. \quad (20)$$

Given (19) and (20), equation (17) is integrated using a fourth-order Runge-Kutta integration scheme. Since T_n is known only at discrete points along the surface, a cubic splines fit for T_n was used. The difficulty of having a singularity at the origin is bypassed by assuming a spherical cap at the bubble front. The initial values are calculated from the average normal stress for the node next to the origin:

$$r_1 = (R_f^2 - (z+R_f)^2)^{1/2}, \quad (21)$$

$$\left(\frac{\partial r}{\partial z}\right)_1 = -\frac{z+R_f}{r_1}, \quad (22)$$

$$R_f = \frac{2}{T_n N_{Ca}}, \quad (23)$$

where R_f is the radius of the front meniscus. The new profile resulting from the numerical integration is checked against the previous profile. If the two profiles do not agree within the specified tolerance, an underrelaxation scheme is called to correct the positions of the free surface nodes, i.e.,

$$r_i^{(k+1)} = r_i^{(k)} + \beta_i^{(k)} (r_i - r_i^{(k)}), \quad (24)$$

where

$\beta_i^{(k)} = (\beta_o + (k/k_{\max})^n (\beta_{\max} - \beta_o))/\alpha^{i-1}$

= underrelaxation factor for ith node at kth iteration;

r_j = radial position of the ith free surface node resulting from the integration of equation (17).

The form of the underrelaxation factor $\beta_i^{(k)}$ used in this study was chosen to compensate for the effect of the cumulative error in the free surface location as the integration proceeded farther from the origin. Without underrelaxation, the error in the normal stress given by equation (18) for an unbalanced free surface was accentuated in the calculation of the surface location of the next iteration. As convergence was approached, the change in the normal stress from the previous iteration became slight, and convergence could be accelerated by increasing the underrelaxation factor. Usually 20 to 40 iterations were required if a good initial estimation of the free surface location was specified. For the cases in the present study, values of $\beta_0 = 0.05$, $\beta_{max} = 0.20$, $k_{max} = 40$, $n = 2$ to 4, and $\alpha = 1.02$ to 1.1 worked well.

A computer code was written to facilitate the finite element calculations. In each iteration, a semiautomatic mesh generator produces the mesh pattern and appropriate boundary conditions. The system matrix is symmetrically banded and was solved using a Gaussian elimination routine with partial pivoting.

The numerical solution of equations (1)–(3) was successively tested against the single-phase Poiseuille flow and entrance flow solutions. The calculations of Lee and Fung [11] for single-phase flow through a constricted tube were also reproduced using this code in order to demonstrate the ability to handle curved boundaries.

3 Results and Discussions

Finite element solutions of the momentum and continuity equation particular to an inviscid bubble flowing in a smooth capillary tube were obtained for capillary numbers ranging between 5×10^{-3} and 2×10^{-1}. Typical velocity fields for capillary numbers of 1×10^{-2} and 1×10^{-1} are shown in Fig. 3. As illustrated in this figure, flow recirculation occurred ahead of the moving bubble in both cases. The recirculation observed through fixing the axial coordinate to the bubble front results from a partial entrainment of the viscous fluid into the film region above the stagnation point. The location of the stagnation point was observed to move toward the centerline for increasing capillary number. The shape of the bubble was found to change from a profile with a blunt spherical front, as assumed by Bretherton at low N_{Ca}, to a more slender profile as N_{Ca} was increased.

Solutions for capillary numbers greater than 0.2 were attempted with oscillations occurring in the meniscus profile. The oscillations were probably caused by insufficient resolution of the flow field near the bubble front where the stagnation point is expected to be located. Small variations in the normal stress distribution in this region would be magnified at higher N_{Ca} through the integration of equation (17).

Film thicknesses were obtained as a function of capillary number. The calculated values are compared to the theoretical results of Bretherton [6] and the experimental correlation of Fairbrother and Stubbs [2] in Fig. 4. A unique feature of these calculations is that the predicted film thicknesses agrees well with Bretherton's results at low capillary number while excellent agreement with Fairbrother and Stubbs' empirical correlation was obtained at higher capillary numbers. It was found that Bretherton's two-third power law for film thickness, given in the following, overpredicts the finite element values for capillary number greater than 5×10^{-3}.

Downloaded 02 May 2010 to 171.66.16.54. Redistribution subject to ASME license or copyright; see http://www.asme.org/terms/Terms_Use.cfm

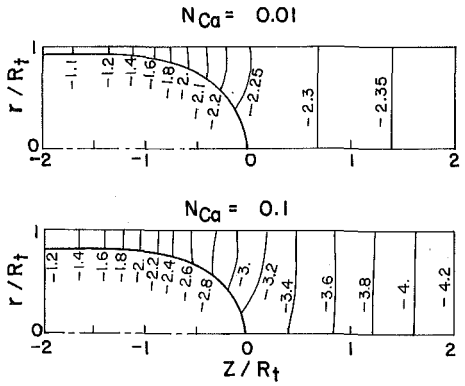


Fig. 5 Isobars (constant pR_t/σ) for N_{Ca} = 0.01 and 0.1

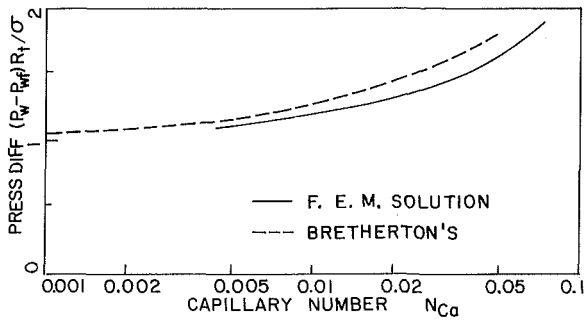


Fig. 6 Pressure drop as a function of capillary number

$$\frac{h}{R_t} = 0.643\,(3\,N_{Ca})^{2/3}. \tag{25}$$

Goldsmith and Mason [5] have shown that equation (25) agrees with experimental data to within 5 percent for capillary numbers less than 3×10^{-3}. For larger capillary numbers, the following empirical equation of Fairbrother and Stubbs appears to be accurate

$$\frac{h}{R_t} = 0.5\,(N_{Ca})^{1/2}. \tag{26}$$

During the finite element calculation at low capillary numbers, it was found that shorter bubble lengths resulted in a predicted film thickness two to four times less than the results mentioned above. In this case the lubrication region was too short for the pressure drop to develop across the bubble front. As a result, the bubble shape was unrealistically adjusted in order to absorb the excessive stresses. The present study shows that for capillary number below 5×10^{-3} a bubble length of at least 2.5 tube radii should be used.

The calculated pressure distributions, scaled with respect to σ/R_t, are shown in Fig. 5 for capillary numbers of 1×10^{-2} and 1×10^{-1}. A comparison of the two pressure maps shown in this figure reveals the fact that the pressure gradient for low N_{Ca} flow is concentrated in the thin film region. For higher N_{Ca}, the pressure is more evenly distributed, with gradients near $z = 0$ becoming more significant. As expected, the recirculation was found to occur ahead of the regions of larger pressure gradients for both cases shown in the figure.

The dimensionless pressure drop across the bubble front as a function of capillary number is shown in Fig. 6, where P_w is the film pressure at $z = -\infty$ and p_{wf} is the wetting phase pressure at $z = 0$, $r = 0$. Bretherton's equation, given in the following, is also shown for comparison.

$$\frac{(p_w - p_{wf})R_t}{\sigma} - 1 = 2.93\,(3\,N_{Ca})^{2/3}. \tag{27}$$

As illustrated in Fig. 6, the finite element prediction of the pressure drop agrees well with equation (27) for small capillary numbers. This result is expected since the asymptotic limit as $N_{Ca} \to 0$ must correspond to a spherical bubble of radius R_t, i.e., the film thickness approaching zero. For larger capillary numbers, the Bretherton solution overpredicts the finite element values by a significant amount. This discrepancy is due to the violation of Bretherton's assumption of a static bubble front, which is valid only at low capillary numbers. Thus, the pressure drop given by the finite element solution is expected to be more realistic for capillary numbers greater than 10^{-2}.

4 Conclusions

The present study of flow of bubbles in straight capillary tubes leads to the following conclusions:

1. The finite element formulation of the free surface problem presented in this work gives excellent predictions of the flow field, meniscus shape, and pressure distributions.
2. A flow recirculation is seen to occur at low capillary numbers with the stagnation point on the free surface shifting toward the centerline as the capillary number is increased.
3. Both bubble shapes and flow fields are strong functions of capillary number. The viscous effects are more pronounced near the tube wall for very low capillary number in which case the bubble front can be approximated by a portion of a sphere. The assumption of a static bubble front in Bretherton's lubrication theory begins to fail for capillary numbers where the viscous effects on the bubble surface extend further from the tube wall.
4. The pressure drop across the bubble front increases with increasing capillary number. For capillary numbers greater than 10^{-2}, the pressure calculations presented in this work are expected to be the most accurate available.

References

1 Prothero, J., and Burton, A. C., "The Physics of Blood Flow in Capillaries," *J. Biophysics*, Vol. 2, 1961, pp. 525-572.

2 Fairbrother, F., and Stubbs, A., "Studies in Electroendosmosis. Part VI. The Bubble-Tube Methods of Measurement," *J. Chem. Sc.*, Vol. 1, 1935, pp. 527-529.

3 Taylor, G. I., "Deposition of a Viscous Fluid on the Wall of a Tube," *J. Fluid Mech.*, Vol. 10, 1961, pp. 161-165.

4 Cox, B. G., "On Driving a Viscous Fluid Out of a Tube," *J. Fluid Mech.*, Vol. 14, 1962, pp. 81-98.

5 Goldmsith, H. L., and Mason, S. G., "The Flow of Suspensions Through Tubes: II Single Large Bubbles," *J. Colloid Sc.*, Vol. 18, 1963, pp. 237-261.

6 Bretherton, F. P., "The Motion of Long Bubbles in Tubes," *J. Fluid Mech.*, Vol. 10, 1961, pp. 166-188.

7 Zienkiewicz, O. C., *The Finite Element Methods*, 3rd ed., McGraw-Hill, London, 1977.

8 Hughes, T. J. R., Liu, W. K., and Brooks, A., "Finite Element Analysis of Incompressible Viscous Flows by the Penalty Function Formulation," *J. of Comput. Physics*, Vol. 30, 1979, pp. 1-60.

9 Oden, J. T., "RIP-Methods for Stokesian Flows," Chapter 15 in: *Finite Elements in Fluids*, Vol. 4, Wiley, New York, 1982, pp. 305-317.

10 Rubin, S. G. and Graves, R. A., "A Cubic Spline Approximation for Problems in Fluid Mechanics," Langley Research Center, NSA TR R-436, 1975.

11 Lee, J. S., and Fung, Y. C., "Flow in Locally Constricted Tubes at Low Reynolds Numbers," ASME JOURNAL OF APPLIED MECHANICS, Vol. 37, 1970, pp. 9-16.

Downloaded 02 May 2010 to 171.66.16.54. Redistribution subject to ASME license or copyright; see http://www.asme.org/terms/Terms_Use.cfm

Nonuniqueness in Steady-State Heat Transfer in Prestressed Duplex Tubes—Analysis and Case History

M. G. Srinivasan

D. M France[1]

Mechanical Engineers,
Components Technology Division,
Argonne National Laboratory,
Argonne, Ill. 60439
Mems. ASME

More than one steady-state solution is shown to exist for the problem of steady-state heat transfer across the walls of a duplex tube when the initial prestress between the inner and outer tubes is sufficiently low. This determination was used in explaining the apparently erratic heat-transfer performance of prestressed duplex tubes in the steam generating system of the Experimental Breeder Reactor II. The importance of the results lies not only in showing that nonuniqueness of steady-state solution applies to more complex geometries than heretofore analyzed, but also in demonstrating that such multiple steady-state conditions appear in practical situations.

Introduction

The lack of uniqueness of the solution for a problem of steady-state heat conduction through a solid-to-solid contact was described by Comninou and Dundurs [1]. They found that different steady-state solutions, satisfying the same boundary conditions but involving localized separation between the solids, may exist if the contacting solids are of different materials and heat flows into the material with the larger distortivity. In subsequent papers, Barber and coworkers [2, 3] investigated the stability of solutions involving thermoelastic contact. These investigations concerned one-dimensional heat flow in rods. The pioneering work described in these papers is of great interest in itself even though the problems considered in them do not represent any practical situations. This paper considers a problem of thermoelastic contact in prestressed double-walled (duplex) tubes of an operational heat-exchanger and explains the seemingly erratic heat transfer performance observed in the heat exchanger by showing existence of multiple steady-state solutions.

In a mechanically bonded duplex tube, an inner tube and an outer tube – both made of the same material – are interference-fitted during manufacture such that a radial prestress is obtained between the walls when both the walls are at the constant reference temperature. Numerical solution to the problem of counterflow heat transfer through the double wall, from a hotter fluid flowing parallel to the length of the tube on the outside to a colder fluid flowing in the opposite direction inside the tube, reveals the existence of multiple solutions for given mass flow and inlet temperature of the fluids, if the prestress at the reference temperature is sufficiently low. The apparently erratic heat-transfer performance of duplex tubes in the steam generator of the Experimental Breeder Reactor II (EBR-II) is explainable from this finding.

The two superheaters of the steam generator system of the EBR-II are of the shell-and-tube type in which high pressure steam flowing inside the straight duplex tubes is heated by liquid sodium, counterflowing on the shell side. The duplex tubes of one of the superheaters were the interference-fitted (mechanically bonded) type while those of the other were the metallurgically bonded type. Otherwise the two superheaters were identical. The superheater with mechanically bonded duplex tubes had begun to show erratic reductions of outlet steam temperature after about eight years of normal operation. The reduction of outlet steam temperature continued to increase with time over a period of the next eight years. This was attributable to the progressive relaxation of the prestress with time and the consequent increase in thermal resistence at the interface between the inner and outer tubes. However, the temperature measurements at the outer surface of the inner tube near the steam outlet for many different operating conditions showed not only that there was a large variation of heat-transfer performance from tube to tube for a given plant condition, but also that different plant runs culminating in nearly the same steady-state boundary conditions for a tube produced widely different steady-state heat transfer rates in that tube.

The purpose of this investigation is to obtain an explanation for this anomalous behavior through analytical modeling of the steady-state counterflow heat transfer in a duplex tube. The method used involved the expression of the condition of the interface (contact pressure or gap) as a

[1] Presently at Department of Mechanical Engineering, University of Illinois in Chicago.

Contributed by the Applied Mechanics Division for publication on the JOURNAL OF APPLIED MECHANICS.

Discussion on this paper should be addressed to the Editorial Department, ASME United Engineering Center, 345 East 47th Street, New York, N.Y. 10017, and will be accepted until two months after final publication of the paper itself in the JOURNAL OF APPLIED MECHANICS. Manuscript received by ASME Applied Mechanics Division, January, 1984; final revision, August, 1984.

Copyright © 1985 by ASME
Downloaded 02 May 2010 to 171.66.16.54. Redistribution subject to ASME license or copyright; see http://www.asme.org/terms/Terms_Use.cfm

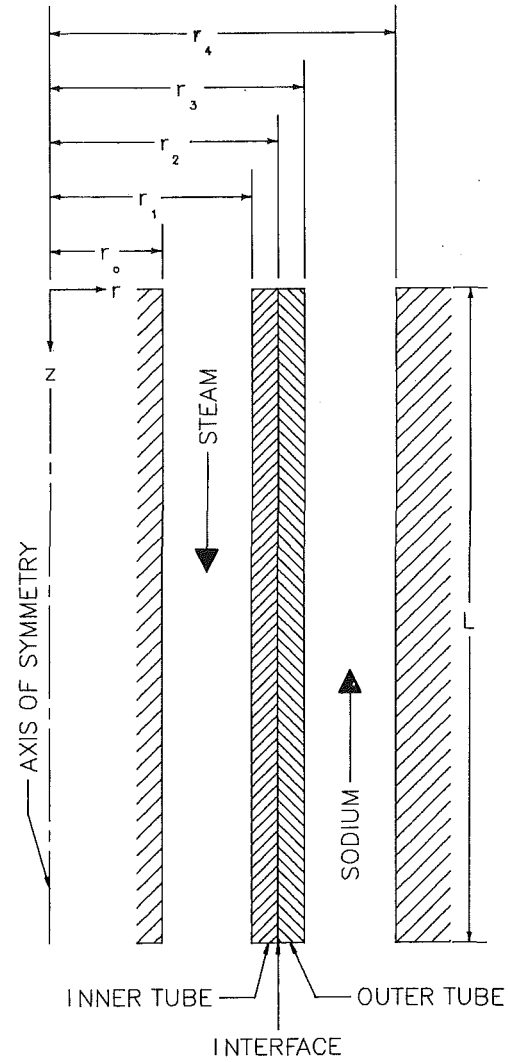


Fig. 1 Schematic geometry of counterflow in duplex tube

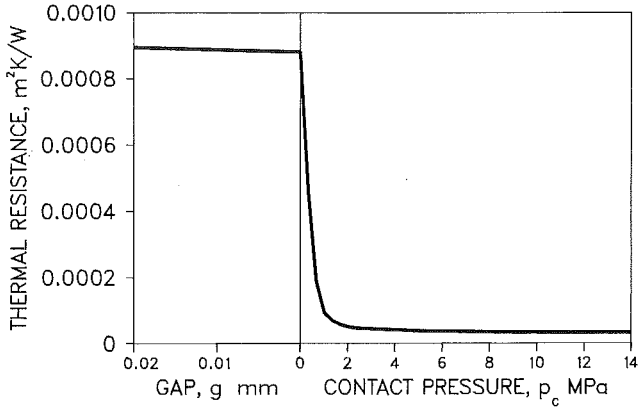


Fig. 2 Thermal resistance at interface as function of contact pressure and size of gap

function of the temperature distribution across the wall, the use of an empirical relationship between the interface condition and the contact thermal resistance, and a numerical solution for the temperature distribution in the radial and longitudinal directions of the tube.

Geometry and Boundary Conditions

The longitudinal section of a duplex tube is shown schematically in Fig. 1. Steam flows in an annular space $r_o < r < r_1$, where r_o is the outer radius of a core tube and r_1 is the inner radius of the inner tube. (The presence of the core tube is not analytically significant. The EBR-II superheater tubes have the core tube to increase steam velocity for better heat transfer.) Sodium flows in the opposite direction in the outer annular space $r_3 < r < r_4$, where r_3 is the outer radius of the outer tube and r_4 is the radius of a fictitious conduit determined from the geometrical arrangement of the tube bundle in the shell of a superheater. The interface is defined by $r = r_2$. If the inner and outer tubes separate, giving rise to a gap, g, the nominal radius of the interface would still be r_2 since $g << r_2$. The length of the tube over which heat transfer takes place is the distance between the steam inlet ($z = 0$) and outlet ($z = L$).

The mechanical boundary conditions at the ends of the tube in the superheater do not correspond to either plane stress or plane strain condition. However, it has been shown by Tseng [4] that for the present purpose the plane stress assumption does not introduce significant error. Therefore the ends $z = 0$, and $z = L$ were considered stress-free, and plane stress conditions were assumed to prevail for all z. At the boundaries $r = r_1$ and $r = r_3$, steam and sodium pressures were known. At the interface $r = r_2$, it was assumed that when the inner and outer tubes are in intimate contact there is no friction and hence no shear stress. The normal stress at $r = r_2$, which is continuous when the tube walls are in contact, is zero when the walls are not in contact.

The thermal boundary conditions at $r = r_o$ and $r = r_4$ correspond to insulated surfaces. The other boundry conditions specified were the steam mass flow rate and inlet temperature at $z = 0$, and the sodium mass flow rate and inlet temperature at $z = L$. The temperature distribution at any cross section was assumed to be axisymmetric.

Interface Condition

Among the thermal properties that must be specified for the solution of the heat-transfer problem, the contact thermal resistance at the interface requires special treatment since it is this that strongly couples the thermomechanical deformations of the tube walls and the heat transfer between them. At the interface at any cross section, there may be contact between the inner and outer tubes, or there may be a separation of the tubes giving rise to a gap between them. The thermal resistance at the interface is a function of the contact pressure or the gap thickness, which in turn is a function of the temperature distribution across the thickness of the inner and outer tubes and the internal and external pressures on the duplex tube. Since the temperature distribution in the tube wall is part of the solution to be determined, it is not possible to explicitly prescribe the thermal resistance at the interface a priori. In the present case, an iterative procedure was adopted to correctly represent the thermal resistance at the interface. Initially, an arbitrary longitudinal distribution of temperature differential between the inner and outer tubes was assumed. The interface condition along the length (i.e., contact pressure or gap size) was determined as a function of the assumed temperature differential. The thermal resistance was then obtained from the relationship between the interface condition and the thermal resistance, which was taken in this case as shown in Fig. 2. This curve was developed in two steps. The right half of the figure, giving the thermal resistance as a function of contact pressure, was based on experimental data provided by H. W. Buschman [5] for contact pressures greater than 0.35 MPa, and obtained by extrapolation for contact pressures in the range of 0–0.35 MPa. The thermal resistance as a function of gap size was calculated assuming heat conduction in the annular gap space through stagnant air. With

Downloaded 02 May 2010 to 171.66.16.54. Redistribution subject to ASME license or copyright; see http://www.asme.org/terms/Terms_Use.cfm

the thermal resistance specified at nodes along the length of the tube, the heat transfer problem was numerically solved. From this computed solution, the temperature differential between the inner and outer tubes was determined and compared with the assumed distribution of the temperature differential. If the two distributions did not coincide, the procedure was repeated with the last-computed distribution replacing the previously assumed one.

The expression of the interface condition, in terms of the temperature differential between the inner and outer tubes, is derived in the following. Since plane-stress conditions and axial symmetry were assumed, only the radial distribution of temperature at any cross section is relevant for the following.

The interference, δ, at the room-temperature (or reference temperature) is given by [6]

$$\delta = \frac{pr_2}{E}\left\{\frac{r_2^2+r_1^2}{r_2^2-r_1^2}+\frac{r_3^2+r_2^2}{r_3^2-r_2^2}\right\} \tag{1}$$

where p is the room-temperature contact pressure at the interface, and E is the Young's modulus of the tube, both of which were assumed.

Let $T(r)$ be the increase in temperature (from the reference temperature) at any radius during steady-state operation. Then the mean temperature increase of the inner tube wall, $\bar{T}_i$, is given by

$$\bar{T}_i = \frac{2}{r_2^2-r_1^2}\int_{r_1}^{r_2} Trdr \tag{2}$$

The unrestrained radial displacement, u_i, of the outer radius of the inner tube to due this temperature increase is [7]

$$u_i = \alpha \bar{T}_i r_2 \tag{3}$$

where α is the mean coefficient of thermal expansion. Similarly, for the outer tube

$$\bar{T}_o = \frac{2}{r_3^2-r_2^2}\int_{r_2}^{r_3} Trdr \tag{4}$$

and the unrestrained radial displacement, u_o, of the inner radius due to this temperature increase is given by

$$u_o = \alpha \bar{T}_o r_2 \tag{5}$$

Since $\bar{T}_o > \bar{T}_i$ under operating conditions, $u_o > u_i$, and consequently the change in the interference between the inner and outer tubes is negative and is given by

$$\Delta\delta = u_i - u_o = \alpha r_2(\bar{T}_i - \bar{T}_o) \tag{6}$$

Since the change in dimensions r_1, r_2, and r_3 due to the increase in temperature is negligible, the $p-\delta$ relationship of equation (1) gives Δp^T, the change in contact pressure due to the increase in temperature as

$$\Delta p^T = \frac{E\Delta\delta}{r_2}\,\frac{(r_2^2-r_1^2)(r_3^2-r_2^2)}{2r_2^2(r_3^2-r_1^2)}$$

which, after substitution for $\Delta\delta$ from (6), becomes

$$\Delta p^T = -E\alpha\,\frac{(r_2^2-r_1^2)(r_3^2-r_2^2)}{2r_2^2(r_3^2-r_1^2)}\,\Delta T \tag{7}$$

where

$$\Delta T = \bar{T}_o - \bar{T}_i \tag{8}$$

Considering the pressure loads, p_s, the steam pressure on the inner surface, and p_n, the sodium presure on the outer surface, the change in contact pressure, Δp^p, is given by $-\sigma_r$(at $r=r_2$) due to internal pressure p_s and external pressure p_n. From Timoshenko [6],

$$\Delta p^p = \frac{r_1^2(r_3^2-r_2^2)p_s + r_3^2(r_2^2-r_1^2)p_n}{r_2^2(r_3^2-r_1^2)} \tag{9}$$

The contact pressure at operating condition, p_c, is then,

$$p_c = p + \Delta p^T + \Delta p^p$$

which, using equations (7) and (9), may be expressed as:

$$p_c = p - \frac{E\alpha(r_2^2-r_1^2)(r_3^2-r_2^2)}{2r_2^2(r_3^2-r_1^2)}\Delta T + \frac{r_1^2(r_3^2-r_2^2)p_s + r_3^2(r_2^2-r_1^2)p_n}{r_2^2(r_3^2-r_1^2)} \tag{10}$$

In equation (10), ΔT is the difference between the mean wall temperature of the outer and inner tubes. This equation is valid for $p_c \geq 0$ or $\Delta T \leq \Delta T^*$ where ΔT^* is the value of ΔT for which p_c becomes zero. Letting $p_c = 0$ in equation (10), gives ΔT^* as

$$\Delta T^* = \frac{2r_2^2(r_3^2-r_1^2)}{E\alpha(r_2^2-r_1^2)(r_3^2-r_2^2)} \times\left\{p + \frac{r_1^2(r_3^2-r_2^2)p_s + r_3^2(r_2^2-r_1^2)p_n}{r_2^2(r_3^2-r_1^2)}\right\} \tag{11}$$

If $\Delta T > \Delta T^*$, the two surfaces at the interface separate, giving rise to a gap of thickness, g, at the interface. From the relationships given by equation (3) and (5), it is seen that the gap thickness may be expressed as,

$$g = \alpha r_2(\Delta T - \Delta T^*)$$

which becomes, after substitution for ΔT^*,

$$g = \alpha r_2 \Delta T - \frac{2r_2^3(r_3^2-r_1^2)}{E(r_2^2-r_1^2)(r_3^2-r_2^2)} \times\left\{p + \frac{r_1^2(r_3^2-r_2^2)p_s + r_3^2(r_2^2-r_1^2)p_n}{r_2^2(r_3^2-r_1^2)}\right\} \tag{12}$$

Heat-Transfer Analysis for Steady-State Solution

The thermal analysis for the steady-state counterflow heat-transfer solution follows the general approach used for single-phase fluid heat exchangers, except for the previously described iterative procedure for reconciling the thermal resistance assumed at the interface with the interface condition indicated by the solution. The fluid parameters specified are the mass flow rate and inlet temperature of sodium and steam. One-dimensional energy equations for sodium and steam and a relation for the conductive heat transfer across the duplex tube walls were employed in the usual manner. Thermal properties and heat-transfer coefficients were assumed as functions of temperature. The numerical analysis was started at the axial location $z=0$ where saturated steam was assumed to enter the tube. The outlet sodium temperature at the same location was unknown and was estimated to start the solution. The heat transfer from the sodium to the steam was then calculated as discrete points along the length of the tube, spaced at Δz, until $z=L$ was reached. The calculated sodium inlet temperatures at $z=L$ was then compared with the specified value, and if the comparison did not satisfy the convergence criterion, a new estimate for the sodium outlet temperature at $z=0$ was made. Then the incremental heat-transfer computations were repeated and a newly calculated value of sodium inlet temperature was obtained. This iterative procedure continued until the solution converged to the specified sodium inlet temperature.

The dimensions of the tube were defined by the following: $r_o = 10.3$ mm, $r_1 = 13.53$ mm, $r_2 = 15.88$ mm, $r_3 = 18.27$ mm, $r_4 = 31.7$ mm, and $L = 6858$ mm. The boundary conditions for the tube, tabulated in the following correspond to the full-power, steady-state operating condition of the EBR-II superheaters given in [8].

Downloaded 02 May 2010 to 171.66.16.54. Redistribution subject to ASME license or copyright; see http://www.asme.org/terms/Terms_Use.cfm

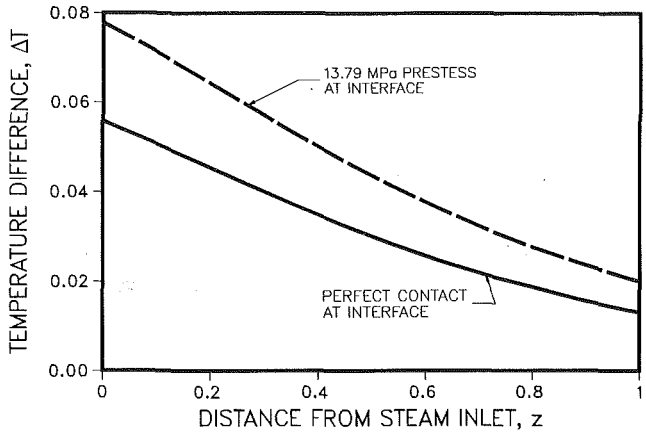


Fig. 3 Difference between mean wall temperature of inner and outer tubes along length. (ΔT and z are nondimensional.)

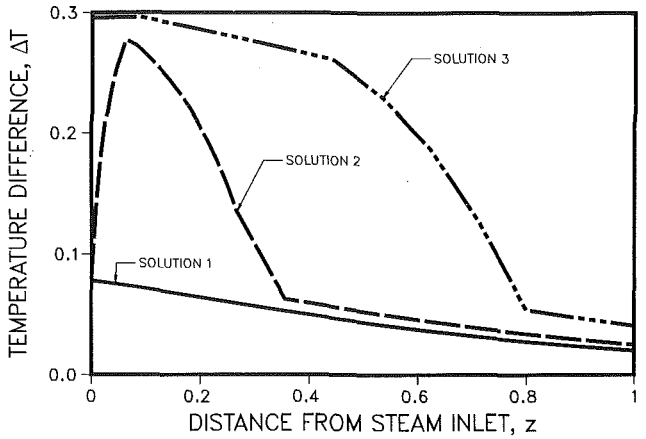


Fig. 4 Difference between mean wall temperature of inner and outer tubes along length. Three solutions for the case of uniform room temperature prestress of 10.34 MPa (1500 psi). (ΔT and z are nondimensional.)

1.	Mass flow rate of sodium	:2.054 kg/s
2.	Mass flow rate of steam	:0.216 kg/s
3.	Temperature of sodium at inlet	:468°C
4.	Temperature of steam at inlet	:304°C
5.	Sodium pressure, p_n	:0.31 MPa
6.	Steam pressure, p_s	:9.14 MPa

The numerical code was first tested for accuracy by comparing its prediction of the rate of total heat transfer with that measured for metallurgically bonded tubes since there was no anomaly associated with the behavior of the metallurgically bonded tubes. For this case, the interface thermal resistance is always zero. The computed value of the rate of total heat transferred was within 5 percent of the measured value, and this agreement is generally considered to be sufficiently accurate. However, for the purpose of establishing a good basis for comparison, it was decided to adjust the empirical heat transfer parameters used in the code to predict the measurement for metallurgically bonded tubes exactly. Except for the interface thermal resistance no changes were made in the code after the foregoing adjustment was made.

Computational Results

The results for the test case noted in the preceding paragraph are useful as a basis of comparison for subsequent computations since the only difference between the test case and the subsequent cases is the condition at the interface. The longitudinal distribution of ΔT, the difference between the mean wall temperature of the outer and inner tubes, is shown by the solid curve in Fig. 3. ΔT is used throughout the following discussion as a typical measure of the heat transfer solution. The abscissa of Fig. 3 is the distance from steam inlet, nondimensionalized with respect to L, and the ordinate is the temperature difference ΔT, nondimensionalized with respect to the steam inlet temperature. The first row of Table 1 gives the nondimensionalized values of rate of total heat transferred and the steam outlet temperature for this case. The rate of total heat transferred was nondimensionalized with respect to the corresponding value for this case, and hence is unity. The outlet steam temperature was nondimensionalized with respect to the inlet steam temperature.

It is obvious that the rate of total heat transferred for mechanically bonded tubes can never exceed that for the test case. It is also evident that the ΔT distribution for the test case is a lower bound of all ΔT distributions possible for mechanically bonded tubes. The solution in the case of the mechanically bonded tube is obviously influenced by the interface condition which in turn depends on the room-temperature contact pressure. The case of a mechanically bonded tube with a uniform room temperature prestress of 13.79 MPa (2000 psi) was considered next. It was assumed that this contact pressure is in the range of the radial prestress of the mechanically bonded tubes of the EBR-II superheater. With all other dimensions, material properties and boundary conditions being the same as for the previous case, a solution was obtained for this case. The ΔT distribution for this solution is shown by the dashed line of Fig. 3, and the rate of total heat transfer, etc., are given in the second row of Table 1. To obtain this solution, an initial trial distribution of ΔT was necessary, and it was found that many different initial trial distributions of ΔT always converged to the solution indicated by the dashed line of Fig. 3. Thus the uniqueness of the solution was demonstrated. From equation (10) it can be shown, that the interface contact pressure at the steady-state operating condtion, corresponding to the dashed line curve of Fig. 3, varies monotonically from a minimum of 12.85 MPa (1863 psi) at the steam inlet to a maximum of 16.34 MPa (2370 psi) at the steam outlet. Due to this relatively high value of contact pressure throughout the length of tube, the thermal resistance at the interface is relatively low. Consequently, the reduction in the rate of heat transfer and the outlet steam temperature, from the corresponding values for the perfectly bonded tube, is only slight as seen from Table 1.

Since the heat-transfer degradation observed in the EBR-II superheater was much greater than the reduction indicated in Table 1 for the prestress of 13.79 MPa, it was apparent that the room-temperature radial prestress in the tube was lower than the 13.79 MPa assumed. Therefore, the next case considered was that of a duplex tube with an assumed uniform room-temperature prestress of 10.34 MPa (1500 psi). All the parameters of the problem except the radial prestress were taken to be the same as for the previous case. The results for this case showed a very important difference, namely, that different trial distributions for ΔT assumed for starting solutions did not converge to the same final solution. Since the initial trial distributions were arbitrary, if the problem is characterized by a unique solution then it would be expected that any arbitrary initial trail should either converge to the correct solution or not converge at all. In the present case, however, it was found that four different arbitrary trial solutions employed converged to one or the other of the three solutions indicated by the three ΔT distributions shown in Fig. 4. The corresponding sets of values for rate of heat transfer and steam outlet temperature are given in Table 2.

Two different trial distributions of ΔT converged to the line shown as solution 1 of Fig. 4. Since the heat-transfer rate corresponding to this solution (given in the first row of Table

Downloaded 02 May 2010 to 171.66.16.54. Redistribution subject to ASME license or copyright; see http://www.asme.org/terms/Terms_Use.cfm

Table 1 Cases of unique steady-state solutions

Case	Tube type	Rate of total heat transferred (nondimensional)	Outlet steam temperature (nondimensional)	Interface conditions
1	Metallurgically	1.0000	1.4090	Perfect contact at all temperatures
2	Mechanically bonded with prestress	0.9819	1.3991	Contact pressure: at room temperature 13.79 MPa uniform, at operating conditions varies from 12.85 to 16.34 MPa

Table 2 Multiple steady-state solutions for tube with uniform room-temperature prestress of 10.34 MPa (1500 psi)

Solution No.	Rate of total heat transferred (nondimensional)	Outlet steam temperature (nondimensional)	Interface condition at steady-state operating condition			
			Region of contact	Maximum contact pressure, MPa	Region of separation	Maximum gap size, mm
1	0.9815	1.3990	$0 \le z/L \le 1$	12.89	none	–
2	0.9324	1.3731	$0 \le z/L < 0.044$ and $0.142 \le z/L \le 1$	12.62	$0.044 \le z/L \le 0.142$	0.0024
3	0.7670	1.2881	$0.498 < z/L \le 1$	11.71	$0 \le z/L \le 0.498$	0.0045

2) is only very slightly lower than that corresponding to the unique solution of the case of uniform prestress of 13.79 MPa (2000 psi) and since this solution corresponds to good contact along entire length of the tube, it is clear that no other solution giving a ΔT distribution lying below solution 1 line of Fig. 4 exists for this case. However, from the broken line solutions of Fig. 4 it is evident that other solutions resulting in poorer heat transfer exist for the same specified boundary conditions. The trial ΔT distribution that converged to solution 2 of Fig. 4 was assumed arbitrarily to be: $\Delta T = \Delta T^*$ at $z/L = 0.06$ and $\Delta T = 0$ for all other z. This solution corresponds to contact over most of the length of the tube and separation of the tubes over a relatively short length in the neighborhood of $z/L = 0.06$. Solution 3 of Fig. 4 was obtained by the convergence of a trial ΔT distribution given by $\Delta T = \text{constant} >> \Delta T^*$. This solution corresponds to a separation of the tubes over about two-thirds of the length on the inlet side, and contact over the remaining part of length on the outlet side. From Table 2 it is seen that this solution corresponds to a significant loss in heat-transfer efficiency. The reduction in heat transfer for this solution was of the right order of magnitude to account for the heat-transfer degradation observed in some steady-state runs of the EBR-II superheater.

The occurrence of multiple solutions, dependent on the arbitrarily assumed trial solutions, spurred a renewed search for other possible solutions in the case of uniform prestress of 13.79 MPa (2000 psi). Although many new trial ΔT distributions, including the ones that gave rise to different solutions for the case of uniform prestress of 10.34 MPa (1500 psi), were assumed, they all converged to the same solution obtained before.

Discussion

The most significant outcome of this study is the determination that more than one solution may exist for the problem of steady-state heat conduction through a solid-to-solid contact even when the two solids are made of the same material. It is not difficult to see how this determination explains the erratic behavior observed in the EBR-II superheater. The mechanically bonded duplex tubes of the EBR-II superheater had a certain room-temperature prestress distribution at the time the superheater was put into operation. This prestress distribution was sufficiently high to exclude the existence of all but the one solution (corresponding to good contact throughout the length of the tube) for the given steady-state boundary conditions, as demonstrated by the case of uniform prestress of 13.79 MPa (2000 psi). As the duplex tubes operate in a high-temperature environment (~430°C) the prestress gradually relaxed with time. In the case of EBR-II, it appears that the relaxation of prestress at the end of the first eight years of operation was sufficient to lower the prestress distribution in some tubes below a critical level. It was demonstrated in this study that for the same boundary conditions, whereas only one solution exists when the uniform prestress is 13.79 MPa (2000 psi), multiple solutions may exist if the uniform prestress is lowered to 10.34 MPa (1500 psi). In the EBR-II superheater, when the room-temperature prestress in tube has sufficiently relaxed, the tube appears to behave erratically since it may assume an interface configuration corresponding to any one of the multiple steady-state solutions for the same boundary conditions. Since the heat-transfer rate corresponding to some of these multiple solutions is significantly lower than one for the case of contact over the full tube length, the heat-transfer rate in the tube would be lower by different amounts in different runs even when all the runs reach the same steady-state conditions. During the second eight years of operation, the progressive relaxation of prestress resulted in a corresponding increase in the degradation of heat transfer and the erraticism of the behavior.

Although only three different solutions were determined for the case of the tube with a uniform room temperature prestress of 10.34 MPa, it was not established in this analysis that no more than these three solutions exist for this case. The analysis has only shown the nonuniqueness of the steady-state solution. It must, however, be noted that even where the steady-state heat-transfer analysis indicates the existence of multiple steady-state solutions, the actual steady-state condition reached by a tube may be uniquely determined if a nonsteady-state analysis that takes into account the time-variation of boundary conditions can be performed. In the case of the EBR-II tubes, only the steady-state boundary conditions were known for individual tubes and hence there does not appear to be any means of determining which of the many steady-state solutions would be obtained for a specific run of the plant. In a sense the computational iterations by

Downloaded 02 May 2010 to 171.66.16.54. Redistribution subject to ASME license or copyright; see http://www.asme.org/terms/Terms_Use.cfm

which the thermal resistance at the interface is reconciled with the ΔT distribution may be considered to be analogous to the time evolution of the interface condition during nonsteady conditions. However, the trial solutions assumed in the present case are arbitrary and do not have to be physically realizable.

The mechanism responsible for the existence of multiple steady-state solutions for prestressed duplex tubes is related to the nature of the thermal resistance curve of Fig. 2. Even though the idealization in the present case is not as strong as that of [1], this semiempirical curve also exhibits a steep gradient in the region of zero contact pressure. If the time variation of the boundary conditions during an ascent-to-power run of the plant were such that the contact pressure at the interface throughout the length of the tube was in the flat region on the right side of the curve, the steady-state reached would correspond to the solid curve of Fig. 4. Conversely, if a transient event caused a low interface contact pressure over some part of the tube, then the thermal resistance may increase sufficiently to cause a local increase in ΔT which in turn could cause further loss of contact ultimately leading to separation of the tubes over a short length (solution 2 of Fig. 4) or over a larger part of the length (solution 3 of Fig. 4) at steady-state operating conditions.

It was demonstrated that multiple solutions occur only when the reference-temperature prestress is lowered from a uniform value of 13.79 MPa (2000 psi) to 10.34 MPa (1500 psi). This result leads to the interpretation that for a given set of steady-state boundary conditions, there may be one or more critical or optimum prestress distributions along the length that might separate the regimes of unique solution from that of multiple solutions. Although no effort was made in the present study to investigate such critical prestress distributions, it appears that this problem is related to the question of stability of the multiple solutions.

Conclusions

Analytical determination of steady-state heat transfer in mechanically bonded tubes may show the existence of multiple solutions depending on the reference-temperature prestress at the interface. For given steady-state boundary conditions, if the reference-temperature prestress is sufficiently low these multiple solutions are obtained. The progressive loss of heat-transfer performance of EBR-II duplex tubes was explained by the progressive relaxation of the prestress. The existence of multiple solutions, together with the dependence of the actual steady-state solution on the history of nonsteady boundary conditions preceding the steady-state explain the significantly different performances of EBR-II tubes for nearly the same steady-state operating conditions.

Questions relating to the stability of the solutions, which are not addressed in this paper, require further investigations to establish the minimum levels of prestress that will ensure optimum heat transfer, irrespective of the history of the nonsteady boundary conditions.

Acknowledgments

The thermal resistance curve used in this analysis was constructed partially on the basis of data provided by H. W. Buschman of Argonne National Laboratory. The authors also gratefully acknowledge the assistance and encouragement given to them by H. J. Haupt and A. R. Brunsvold of Argonne National Laboratory in performing the analysis.

References

1 Comninou, M., and Dundurs, J., "On Lack of Uniqueness in Heat Conduction Through a Solid to Solid Contact," ASME *Journal of Heat Transfer*, Vol. 102, 1980, pp. 319–323.

2 Barber, J. R., Dundurs, J., and Comninou, M., "Stability Considerations in Thermoelastic Contact," ASME JOURNAL OF APPLIED MECHANICS, Vol. 47, 1980, pp. 871–874.

3 Barber, J. R., "Stability of Thermoelastic Contact for the Aldo Model," ASME JOURNAL OF APPLIED MECHANICS, Vol. 48, 1981, pp. 555–558.

4 A. A. Tseng, "Prestressing Evaluation of a Grooved Duplex Tube," *International Journal of Pressure Vessels and Piping*, Vol. 11 1983, pp. 191–205.

5 Buschman, H. W., Private Communication.

6 Timoshenko, S., *Strength of Materials, Part II: Advanced Theory and Problems*, 3rd ed., D. Van Nostrand, New York, 1956, pp. 205–213.

7 Boley, B. A., and Weiner, J. H., *Theory of Thermal Stresses*, Wiley, New York, 1960, p. 290.

8 Buschman, H. W., Penney, H., Quilici, M. D., and Radtke, W. H., "Operating Experiences of the EBR-II Steam Generating System," ASME Paper 81-JPGC-NE-4, Oct. 1981.

Downloaded 02 May 2010 to 171.66.16.54. Redistribution subject to ASME license or copyright; see http://www.asme.org/terms/Terms_Use.cfm

C. Y. Wang
Professor,
Departments of Mathematics and Mechanical Engineering,
Michigan State University,
East Lansing, Mich. 48824
Mem. ASME

Hydrodynamic Disk Braking

A viscous fluid separates a rotating disk and a parallel nonrotating disk. As the two disks are squeezed closer together, increased viscous torque is transmitted to the rotating disk. The Navier-Stokes equations are solved using a perturbation in the small squeeze number. Two cases of squeezing are studied: constant velocity approach and constant force approach.

Introduction

Braking is an important mechanism for the dissipation of excess kinetic energy. The most commonly used braking method utilizes dry friction between moving solid parts. This method, although efficient, causes irreparable wear and tear on the contact surfaces which must be later replaced. In a previous paper [1], a novel braking method is suggested. A very viscous fluid is introduced between a laterally moving plate and a parallel, fixed braking plate. As the two plates are brought closer together the viscous hydrodynamic drag acts on the moving plate and thus causes braking. Since solid-to-solid contact is avoided, the wear on the surfaces is greatly reduced. The viscous braking fluid can also be easily replenished or renewed.

In the present paper we consider the related problem of the hydrodynamic braking of a rotating disk by a parallel nonrotating disk. Due to the dominant effect of centrifugal forces, the problem will be much more difficult than the linear motion studied in reference [1]. Disk brakes are important in all rotating machinery.

Formulation

Figure 1 shows a rotating disk with angular velocity $\Omega C(t/T)$ situated at $z = 0$. Here Ω is a characteristic rotation speed, C is a time function of order unity, t is the time, and T is a characteristic time to be defined later. The nonrotating top braking disk is at $z = aZ(t/T)$, $r \le R$, where Z is also a time function of order unity. We assume the characteristic gap width a is much smaller than the radius R such that end effects can be ignored.

Let (u, v, w) be the velocity components in the cylindrical coordinates (r, θ, z), respectively. The unsteady axisymmetric Navier-Stokes equations are

$$u_t + uu_r + wu_z - v^2/r = -p_r/\rho + \nu(\nabla^2 u - u/r^2) \tag{1}$$

$$v_t + uv_r + wv_z + uv/r = \nu(\nabla^2 v - v/r^2) \tag{2}$$

$$w_t + uw_r + ww_z = -p_z/\rho + \nu\nabla^2 w \tag{3}$$

$$(ru)_r + rw_z = 0 \tag{4}$$

Contributed by the Applied Mechanics Division for publication in the JOURNAL OF APPLIED MECHANICS.
Discussion on this paper should be addressed to the Editorial Department, ASME, United Engineering Center, 345 East 47th Street, New York, N.Y. 10017, and will be accepted until two months after final publication of the paper itself in the JOURNAL OF APPLIED MECHANICS. Manuscript received by ASME Applied Mechanics Division, June, 1983.

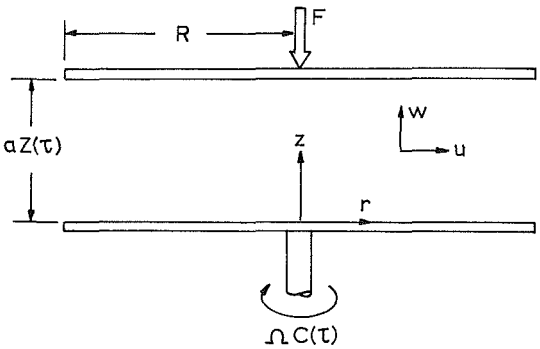


Fig. 1 The coordinate system

where

$$\nabla^2 = \frac{\partial^2}{\partial r^2} + \frac{1}{r}\frac{\partial}{\partial r} + \frac{\partial^2}{\partial z^2} \tag{5}$$

p is the pressure, ρ is the density, and ν is the viscosity of the viscous fluid. The boundary conditions are

$$\text{at} \quad z=0, \quad u=w=0, \quad v=\Omega rC(\tau) \tag{6}$$

$$\text{on} \quad z=aZ(t/T), \quad u=v=0, \quad w=z_t=aZ_\tau/T \tag{7}$$

Since the boundary is moving, set

$$\tau \equiv \frac{t}{T}, \quad \eta \equiv \frac{z}{aZ(\tau)} \tag{8}$$

The physical situation suggests both u and v are linearly proportional to r and w is independent of r. To satisfy continuity, let

$$u = -\frac{r}{2T}\frac{Z_\tau}{Z} f_\eta(\eta,\tau), \quad v=\Omega r g(\eta,\tau), \quad w=\frac{aZ_\tau}{T} f \tag{9}$$

Equation (3) can be integrated once

$$\int w_t dz + \frac{1}{2} w^2 = -p/\rho + \nu w_z + \text{function of } (r,t) \tag{10}$$

Let P_0 be the constant pressure at the edge of the top disk. Equations (1) and (9) indicate the pressure is parabolic in r. Thus

$$p = P_0 + \rho\left[\nu w_z - \frac{1}{2} w^2 + \frac{a^2 Z_\tau^2}{2T^2} - \int_{aZ}^{z} w_t dz - \frac{A(\tau)\nu Z_\tau}{4a^2 TZ^3}(r^2 - R^2)\right] \tag{11}$$

Copyright © 1985 by ASME
Downloaded 02 May 2010 to 171.66.16.54. Redistribution subject to ASME license or copyright; see http://www.asme.org/terms/Terms_Use.cfm

where $A(\tau)$ is a function to be determined. Using equations (1)–(4), (9), and (11) the governing equations simplify to

$$S\left[\frac{Z^3}{Z_\tau}\left(\frac{\partial}{\partial\tau}-\frac{Z_\tau}{Z}\eta\frac{\partial}{\partial\eta}\right)\left(\frac{Z_\tau}{Z}f_\eta\right)+ZZ_\tau(ff_{\eta\eta}-f_\eta^2/2)\right.$$
$$\left.+2(\Omega T)^2\frac{Z^3}{Z_\tau}g^2\right]=f_{\eta\eta\eta}-A \tag{12}$$

$$S\left[Z^2\left(\frac{\partial}{\partial\tau}-\frac{Z_\tau}{Z}\eta\frac{\partial}{\partial\eta}\right)g+ZZ_\tau(fg_\eta-f_\eta g)\right]=g_{\eta\eta} \tag{13}$$

Here $S \equiv a^2/\nu T$, defined as the "squeeze number," represents the relative importance of inertial effects of the squeezing motion to the viscous effects. We assume small gap width and high viscosity such that S is small. On the other hand, the rotation is usually fast such that $S(\Omega T)^2 \equiv \Lambda = 0(1)$. The boundary conditions are

$$f(0,\tau)=f_\eta(0,\tau)=f_\eta(1,\tau)=0, \quad f(1,\tau)=1 \tag{14}$$

$$g(0,\tau)=C(\tau), \qquad g(1,\tau)=0 \tag{15}$$

The initial conditions are

$$f(\eta,0)=F(\eta), \qquad g(\eta,0)=G(\eta) \tag{16}$$

where F and G are given functions.

The Transient

For small S, equations (12) and (13) are singular in τ. Thus there exists a time boundary layer of order S where the rates of change of f and g are important. Introduce the stretched time variable $\lambda \equiv \tau/S = 0(1)$. The leading terms of equations (12) and (13) are

$$Z^2(0)f_{\eta\lambda}+2\Lambda\frac{Z^3(0)}{Z_\tau(0)}g^2=f_{\eta\eta\eta}-A(0) \tag{17}$$

$$Z^2(0)g_\lambda=g_{\eta\eta} \tag{18}$$

The solution to equation (18), satisfying all conditions is

$$g=C(\tau)(1-\eta)+\sum_{m=1}^{\infty}C_m\exp\left[-\left(\frac{m\pi}{Z(0)}\right)^2\lambda\right]\sin m\pi\eta \tag{19}$$

where

$$C_m=2\int_0^1[G(\eta)-C(0)(1-\eta)]\sin m\pi\eta\, d\eta \tag{20}$$

The first term on the right-hand side of equation (19) is a linear quasisteady flow while the sum is a fast decaying transient. The square of this transient is

$$\left(\sum_{m=1}^{\infty}C_m\exp\left[-\left(\frac{m\pi}{Z(0)}\right)^2\lambda\right]\sin m\pi\eta\right)^2$$
$$=\sum_{l=1}^{\infty}\sum_{n=1}^{\infty}\frac{C_lC_n}{2}\exp\left[-\frac{\pi^2}{z(0)}(l^2+n^2)\lambda\right]$$
$$[\cos\pi(l-n)\eta-\cos\pi(l+n)\eta] \tag{21}$$

Equation (17) is then solved with equation (19). The solution f has similar transients:

$$f=3\eta^2-2\eta^3+\sum_{m=1}^{\infty}B_m\exp\left[-\left(\frac{2m\pi}{Z(0)}\right)^2\lambda\right]$$
$$(\cos 2m\pi\eta-1)+J(\lambda,\eta) \tag{22}$$

$$J(\lambda,\eta)\equiv 2\Lambda\frac{Z^3(0)}{Z_\tau(0)}\left\{C^2(0)\left(\frac{\eta^5}{30}-\frac{\eta^4}{6}+\frac{7\eta^3}{30}-\frac{\eta^2}{10}\right)\right.$$
$$\left.+2C(0)\sum_{m=1}^{\infty}C_m\exp\left[-\left(\frac{m\pi}{Z(0)}\right)^2\lambda\right]K_m(\eta)\right. \tag{23}$$
$$\left.+\sum_{l=1}^{\infty}\sum_{n=1}^{\infty}\frac{C_lC_n}{2}\exp\left[-\frac{\pi^2}{Z(0)}(l^2+n^2)\lambda\right]L_{ln}(\eta)\right.$$

$$B_m=2\int_0^1[F(\eta)-3\eta^2+2\eta^3-J(0,\eta)]\cos 2m\pi\eta\, d\eta \tag{24}$$

Since the functions K_m and L_{ln} can be obtained easily we will not go into the details of the transient solution. In what follows let us concentrate on the quasisteady period ($\tau > 0(S)$), when the transients have decayed and the braking action becomes important.

General Solution for Arbitrary Braking

Consider given arbitrary vertical movement of the top plate $Z(\tau)$ and arbitrary rotation $C(\tau)$ of the bottom plate. Since S is small, the following expansions are appropriate:

$$f=f_0(\eta,\tau)+Sf_1(\eta,\tau)+\ \ldots$$
$$g=g_0(\eta,\tau)+Sg_1(\eta,\tau)+\ \ldots$$
$$A=A_0(\tau)+SA_1(\tau)+\ \ldots \tag{25}$$

Equations (12)–(15) yield the successive equations

$$g_{0\eta\eta}=0, \quad f_{0\eta\eta\eta}-A_0=2\Lambda\frac{Z^3}{Z_\tau}g_0^2 \tag{26}$$

$$f_0(0,\tau)=f_{0\eta}(0,\tau)=f_{0\eta}(1,\tau)=0, \quad f_0(1,\tau)=1$$
$$g_0(0,\tau)=C(\tau) \quad g_0(1,\tau)=0 \tag{27}$$

$$g_{1\eta\eta}=Z^2\left(\frac{\partial}{\partial\tau}-\frac{Z_\tau}{Z}\eta\frac{\partial}{\partial\eta}\right)g_0+ZZ_\tau(f_0g_{0\eta}-f_{0\eta}g_0) \tag{28}$$

$$f_{1\eta\eta\eta}-A_1=4\Lambda\frac{Z^3}{Z_\tau}g_0g_1+\frac{Z^3}{Z_\tau}\left(\frac{\partial}{\partial\tau}-\frac{Z_\tau}{Z}\eta\frac{\partial}{\partial\eta}\right)\left(\frac{Z_\tau}{Z}f_{0\eta}\right)$$
$$+ZZ_\tau\left(f_0f_{0\eta\eta}-\frac{f_{0\eta}^2}{2}\right) \tag{29}$$

$$f_1(0,\tau)=f_{1\eta}(0,\tau)=f_1(1,\tau)=f_{1\eta}(1,\tau)$$
$$=g_1(0,\tau)=g_1(1,\tau)=0 \tag{30}$$

The zeroth-order solution

$$g_0=C(\tau)(1-\eta) \tag{31}$$

$$f_0=3\eta^2-2\eta^3+\gamma\left(\frac{\eta^5}{30}-\frac{\eta^4}{6}+\frac{7\eta^3}{30}-\frac{\eta^2}{10}\right) \tag{32}$$

$$A_0=-12-\frac{3}{5}\gamma \tag{33}$$

where $\gamma(\tau) \equiv C^2\,\Lambda\,Z^3/Z_\tau$. Terms containing γ represent the effect of centrifugal forces due to rotation. The first-order solution is more difficult. After some work, we find

$$g_1=Z^2C_\tau\left(-\frac{\eta^3}{6}+\frac{\eta^2}{2}-\frac{\eta}{3}\right)$$
$$+Z_\tau ZC\left(-\frac{1}{5}\eta^5+\frac{3}{4}\eta^4-\frac{5}{6}\eta^3+\frac{17}{60}\eta\right)$$
$$+Z_\tau ZC\gamma\left(\frac{1}{315}\eta^7-\frac{1}{45}\eta^6+\frac{17}{300}\eta^5-\frac{1}{15}\eta^4+\frac{1}{30}\eta^3-\frac{3}{700}\eta\right) \tag{34}$$

$$f_1=\frac{Z^3}{Z_\tau}\left(\frac{Z_\tau}{Z}\right)_\tau\left[\left(-\frac{1}{10}\eta^5+\frac{1}{4}\eta^4-\frac{1}{5}\eta^3+\frac{1}{20}\eta^2\right)\right.$$
$$\left.+\gamma\left(\frac{1}{1260}\eta^7-\frac{1}{180}\eta^6+\right.\right.$$

Downloaded 02 May 2010 to 171.66.16.54. Redistribution subject to ASME license or copyright; see http://www.asme.org/terms/Terms_Use.cfm

$$+\frac{7}{600}\eta^5-\frac{1}{120}\eta^4-0.000079365\eta^3+0.0015079\eta^2\Big)\Big]$$

$$+Z_\tau Z\,N_1(\eta)+4\Lambda\frac{Z^3}{Z_\tau}N_2(\eta) \tag{35}$$

$$N_1=\frac{1}{35}\eta^7-\frac{1}{10}\eta^6+\frac{1}{5}\eta^5-\frac{1}{4}\eta^4$$

$$+0.157143\eta^3-0.035714\eta^2$$

$$+\gamma\Big(\frac{-11}{7650}\eta^9+\frac{1}{105}\eta^8-\frac{38}{1575}\eta^7$$

$$+\frac{19}{600}\eta^6-\frac{7}{300}\eta^5+\frac{1}{120}\eta^4$$

$$+0.000343915\,\eta^3-0.000952381\eta^2\Big)+\gamma^2\Big(\frac{1}{118800}\eta^{11}$$

$$-\frac{1}{10800}\eta^{10}+\frac{177}{453600}\eta^9-\frac{41}{50400}\eta^8$$

$$+\frac{109}{126000}\eta^7-\frac{7}{18000}\eta^6$$

$$+0.0000446128\eta^3-0.0000133478\eta^2\Big) \tag{36}$$

$$N_2=Z^2C_\tau C\Big(\frac{1}{1260}\eta^7-\frac{1}{180}\eta^6$$

$$+\frac{1}{72}\eta^5-\frac{1}{72}\eta^4+0.00436508\eta^3$$

$$+0.000396825\eta^2\Big)+Z_\tau ZC^2\Big(\frac{1}{2520}\eta^9-\frac{19}{6720}\eta^8$$

$$+\frac{19}{2520}\eta^7$$

$$-\frac{1}{144}\eta^6-\frac{17}{3600}\eta^5+\frac{17}{1440}\eta^4$$

$$-0.00517857\eta^3-0.00006944\eta^2\Big)$$

$$+Z_\tau ZC^2\gamma\Big(\frac{-1}{311850}\eta^{11}+\frac{1}{28350}\eta^{10}$$

$$-\frac{71}{453600}\eta^9+\frac{37}{100800}\eta^8$$

$$-\frac{1}{2100}\eta^7+\frac{1}{3600}\eta^6+\frac{1}{14000}\eta^5-\frac{1}{5600}\eta^4$$

$$+0.00005267\eta^3+0.000010281\eta^2\Big) \tag{37}$$

$$A_1=\frac{Z^3}{Z_\tau}\Big(\frac{Z_\tau}{Z}\Big)_\tau(-1.2-0.00047619\gamma)+Z_\tau Z(0.942858$$

$$+0.00206349\gamma+0.00026768\gamma^2)$$

$$+4\Lambda\frac{Z^3}{Z_\tau}(0.02619048Z^2C_\tau C$$

$$-0.0310714Z_\tau ZC^2+0.00031602Z_\tau ZC^2\gamma) \tag{38}$$

When the functions $A(\tau)$ and $g(\eta,\tau)$ are found, the net force on the top disk is

$$F=2\pi\int_0^R(p|_{\eta=1}-P_0)rdr=\frac{\pi\mu R^4Z_\tau}{8a^2TZ^3}A(\tau) \tag{39}$$

where μ is the viscosity. The torque on the bottom disk is

$$M=-2\pi\int_0^R\mu\frac{\partial v}{\partial z}\Big|_{\eta=0}r^2dr=\frac{-\pi\mu\Omega R^4}{2aZ}g_\eta(0,\tau) \tag{40}$$

where

$$g_\eta(0,\tau)=-C(\tau)+S\Big(-\frac{1}{3}Z^2C_\tau+\frac{17}{60}Z_\tau ZC$$

$$-\frac{3}{700}Z_\tau ZC\gamma\Big)+0(S^2) \tag{41}$$

Thus for given vertical motion $Z(\tau)$ of the top disk and a given rotation $C(\tau)$ of the bottom disk, the fluid dynamic braking characteristics can be calculated from equations (39) and (40).

Constant Velocity Squeezing

Let V be the velocity of the top disk. The natural time scale is $T=a/V$ and $Z=1-\tau$. Equations (39) and (40) yield

$$\frac{F}{\frac{\pi\mu R^4V}{8a^3}}=\frac{-1}{(1-\tau)^3}\Big[-12-\frac{3}{5}\gamma+SA_1(\tau)\Big]+0(S^2) \tag{42}$$

$$\frac{M}{\frac{\pi\mu\Omega R^4}{2a}}=\frac{1}{(1-\tau)}\Big[C(\tau)+S\Big\langle\frac{1}{3}(1-\tau)^2C_\tau+\frac{17}{60}(1-\tau)C$$

$$-\frac{3}{700}(1-\tau)C\gamma\Big\rangle\Big]+0(S^2) \tag{42}$$

If the bottom disk is rotating with constant velocity, $C(\tau)=1$. We see that both force F and torque M approach infinity at $\tau=1$, when the two disks come into direct contact. Notice also the effect of rotation γ or C is of primary importance.

If the bottom disk is massed but free, its rotation will be stopped at $\tau=1$. We can solve for the rotation speed $C(\tau)$ by balancing torque with the change of angular momentum

$$M=I\frac{d(\Omega C)}{dt}=\frac{I\Omega}{T}\frac{dC}{d\tau} \tag{44}$$

where I is the moment of inertia of the bottom disk. Using the expansion

$$C=C_0(\tau)+SC_1(\tau)+\ldots \tag{45}$$

Equations (43) and (44) yield

$$C_0=(1-\tau)^{-k},$$

$$C_1=-\Big(\frac{k^2}{3}+\frac{17}{60}k\Big)[(1-\tau)^{-k+1}-(1-\tau)^{-k}]$$

$$-\frac{3\Lambda}{1400}\frac{k}{(2-k)}[(1-\tau)^{-3k+4}-(1-\tau)^{-k}] \tag{46}$$

where $k=\pi\mu R^4/2VI$. The number of revolutions turned before stopping can be found by

$$N=\frac{\Omega}{2\pi}\int_0^1C(\tau)d\tau \tag{47}$$

Constant Force Squeezing

In this case F is given while $Z(\tau)$ is unknown. We define the

Downloaded 02 May 2010 to 171.66.16.54. Redistribution subject to ASME license or copyright; see http://www.asme.org/terms/Terms_Use.cfm

time scale by $T = \pi\mu R^4/8a^2|F|$. Both $Z(\tau)$ and $A(Z(\tau))$ are expanded in S:

$$Z = Z_0(\tau) + SZ_1(\tau) + \ldots$$

$$A = A_0(Z) + SA_1(Z) + \ldots$$

$$= \bar{A}_0(Z_0) + S\bar{A}_1(Z_0, Z_1) + \ldots \tag{48}$$

We find

$$\bar{A}_0 = -12 - \frac{3}{5} C^2 \Lambda Z_0^3 / Z_{0\tau}$$

$$\bar{A}_1 = -\frac{3}{5} C^2 \Lambda \frac{Z_0^3}{Z_{0\tau}} \left(\frac{3Z_1}{Z_0} - \frac{Z_{1\tau}}{Z_{0\tau}} \right) + A_1(Z_0, Z_{0\tau}, Z_{0\tau\tau}) \tag{49}$$

Equation (39) yields the successive orders

$$Z_0^3 = \bar{A}_0(Z_0, Z_{0\tau}) Z_{0\tau}, \quad Z_0(0) = 1 \tag{50}$$

$$3Z_0^2 Z_1 = \bar{A}_0 Z_{1\tau} + \bar{A}_1 Z_{0\tau}, \quad Z_1(0) = 0 \tag{51}$$

Equation (50) is highly nonlinear while equation (51) is linear with variable coefficients. In what follows we only consider the constant rotation ($C(\tau) = 1$) case. It is fortunate that a solution to equation (50) can be obtained

$$Z_0 = (1 + L\tau)^{-\frac{1}{2}}, \quad L \equiv \frac{1}{6} \left(\frac{3}{5} \Lambda + 1 \right) \tag{52}$$

For constant force, the distance decay algebraically to zero as time increases. Equation (51) gives the first-order correction:

$$Z_{1\tau} + \frac{3L}{2(1 + L\tau)} Z_1 = -\frac{L^2 K}{24} (1 + L\tau)^{-\frac{7}{2}}$$

$$K \equiv 0.728571 - 0.123135 \frac{\Lambda}{L} - 0.0030635 \frac{\Lambda^2}{L^2} \tag{53}$$

The solution is

$$Z_1 = \frac{LK}{24} [(1 + L\tau)^{-\frac{5}{2}} - (1 + L\tau)^{-\frac{3}{2}}] \tag{54}$$

Using equations (40), (41), (52), and (54) the torque on the rotating disk is

$$\frac{M}{\frac{\pi\mu\Omega R^4}{2a}} = (1 + L\tau)^{\frac{1}{2}} + S\left[(1 + L\tau)^{-\frac{3}{2}} \left(\frac{17L}{120} - \frac{LK}{24} + \frac{3\Lambda}{700} \right) + \frac{LK}{24} (1 + L\tau)^{-\frac{1}{2}} \right] + 0(S^2) \tag{55}$$

The torque grows as $\tau^{1/2}$ which would eventually stop the rotation.

Discussion

The squeezing of a fluid between two disks was studied by Ishizawa [2] and others. However, the disks are nonrotating and thus process does not apply to braking. In this paper rotation is of primary importance and is not a minor perturbation. Due to centrifugal effects the problem becomes much more difficult than the translational braking of reference [1].

We did not calculate the $0(S^2)$ terms since they are tedious and their effects are comparatively small due to the smallness of the coefficients. Because of inherent nonlinearity enters the zeroth-order equation, we are not able to obtain analytical solutions of the constant power case studied in reference [1], although numerical integration may be possible. On the other hand, the equation governing the massed free plate in reference [1] is incorrect. It should contain a first-order derivative as in our equation (44).

The present paper shows hydrodynamic disk braking is a possible means of stopping rotation. The results may also be applied to disk brakes intended for dry friction, where a fluid was inadvertantly introduced, such as the seepage of water or oil between the braking surfaces.

References

1 Wang, C. Y., "Hydrodynamic Braking," *Int. J. Eng. Sci.*, Vol. 19, 1981, pp. 891–900.

2 Ishizawa, S., "The Unsteady Laminar Flow Between Two Parallel Disks With Arbitrarily Varying Gap Width," *Bull. Jap. Soc. Mech. Eng.*, Vol. 9, 1966, pp. 533–550.

Downloaded 02 May 2010 to 171.66.16.54. Redistribution subject to ASME license or copyright; see http://www.asme.org/terms/Terms_Use.cfm

The Role of Axial Edge Effects and Cavitation in Lubrication for Short Journal Bearings

R. H. Buckholz

J. Lin

C. H. T. Pan

Department of Mechanical Engineering,
Columbia University,
New York, N.Y. 10027

Questions concerning the role of axial edge effects in short bearing theory are investigated using the method of matched asymptotic expansion applied to Reynolds lubrication equation. Attention was initially directed to this problem by other studies that indicate regions of nonconformity in the short bearing solution (i.e., small length to diameter ratio). In the present theory a matched asymptotic expansion method—using the bearing slenderness ratio as the small parameter—is appied to journal bearings. The axial inlet fluid film edge and axial cavitation boundary layers are examined. The axial boundary layers are shown to scale on the bearing slenderness ratio; these boundary layers are necessary to adjust the pressure to the prescribed boundary value. Cavitation boundary shapes, as determined from Reynolds' free surface condition, are shown to be independent of the bearing eccentricity ratio. A reduction in load capacity—relative to previous theories—is shown. Pressure profiles obtained by the present theory are compared to previously reported short bearing results.

1 Introduction

The flow generated between eccentric cylinder sections having nearly identical radius forms the basis for understanding isoviscous, steady, laminar, incompressible lubrication. It is usually the case that the inner cylinder rotates. Complete details of the flow field can be obtained from solutions to the Navier-Stokes and mass conservation equations. However, is usually the case—in classical lubrication theory—that the modified Reynolds number is small. Therefore, Stokes approximation is valid for describing the flow field. The basic geometrical configuration (i.e., small gap between the eccentric cylinder surfaces) justifies the traditional lubrication assumption; thus, the local flow field is synthesized from a combination of Couette and Poiseuille flows. Reynolds [6] used this flow field synthesis and mass conservation to develop an equation for the fluid pressure in the gap between the two cylindrical surfaces. The resulting pressure equation, Reynolds equation, is linear and elliptic with nonconstant coefficients. The Reynolds equation is usually solved by numerical methods; except—as has been pointed out by many investigators—where geometrical considerations permit some asymptotic approximation of Reynolds equation. Two approximations have been explored, they are the long bearing approximation and the short bearing approximation. Each of these approximations has regions of invalidity. In this paper the small slenderness ratio strategy is studied. The approximate equations, for small slenderness ratio, have not been completely explored and more accurate results are needed. The Reynolds equation for long bearings (i.e., large slenderness ratio) has been explored by Sommerfeld. The long bearing assumption does not allow axial pressure gradients; therefore, the approximation is especially poor near the azimuthal bearing edge. Singular perturbation theories taking into account the nonuniformity, in this large aspect ratio approximation, have been properly explored by several authors. However, the similar approximate analytical solution, for the small slenderness ratio, has not been completely explored. Plain journal bearings—having a small slenderness ratio—were first studied by Michell [3] and Cardullo [1]. Their analysis was extended by Ocvirk [2], who calculated journal bearing performance characteristics using the short bearing pressure distribution. Ocvirk [2] was also the first to show good agreement between experimental studies of short bearings and the small slenderness ratio bearing theory. As a result, Ocvirk is often credited with the short bearing pressure distribution result. He calculated design parameters such as load capacity, attitude angle, friction factor, oil flow number, and peak pressure ratio. In practical design cases, the small slenderness ratio results have worked surprisingly well for slenderness ratio up to one, which is well beyond reasonable expectations. Thus, the small slenderness ratio approximations have been validated as powerful analytical methods to estimate journal bearing performance.

An edge effect correction for slider bearings was first given by Schuss and Etsion [7]. They used the method of matched

Contributed by the Applied Mechanics Division for presentation at the 1985 Joint ASME/ASCE Applied Mechanics, Fluids Engineering, and Bioengineering Conference, Albuquerque, N. Mex., June 24-26, 1985 of THE AMERICAN SOCIETY OF MECHANICAL ENGINEERS.

Discussion on this paper should be addressed to the Editorial Department, ASME, United Engineering Center, 345 East 47th Street, New York, N.Y. 10017, and will be accepted until two months after final publication of the paper itself in the JOURNAL OF APPLIED MECHANICS. Manuscript received by ASME Applied Mechanics Division, December, 1983; final revision, July, 1984. Paper No. 85-APM-8.

Copies will be available until February, 1986.

Copyright © 1985 by ASME

Downloaded 02 May 2010 to 171.66.16.54. Redistribution subject to ASME license or copyright; see http://www.asme.org/terms/Terms_Use.cfm

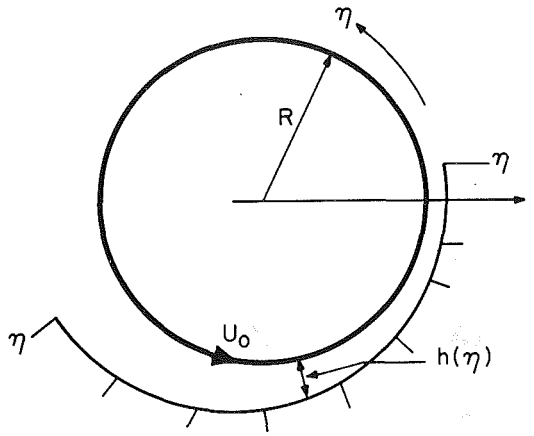


Fig. 1 Sketch to show notation. The length scales are not mutually consistent.

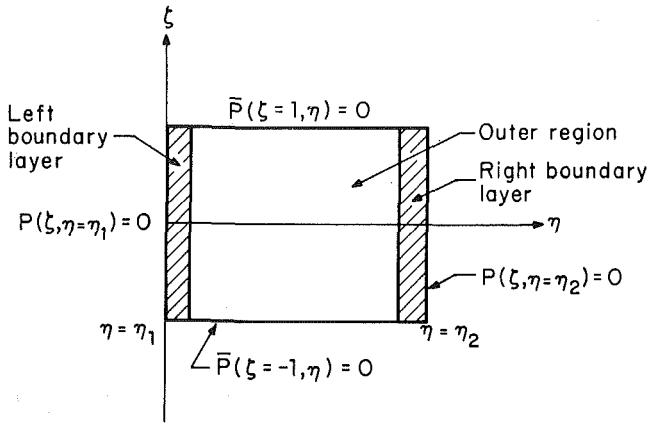


Fig. 2 Qualitative sketch showing the left and right boundary layers, the outer region, and pressure boundary conditions on the film edges

asymptotic expansions to correct for fluid entrance and exit edge boundary conditions. Composite solutions including the edge regions were not fully investigated and fluid film cavitation via Reynolds condition was not studied.

Recent interest in short journal bearings as squeeze-film dampers is discussed by Pan [5]. The work presented here is motivated by nonuniformities in Pan's solution to Reynolds equation subject to the $\lambda \ll 1$ approximation. To examine the source of these nonuniformities we return to Ocvirk's small λ formulation; it is noted that a balance between azimuthal mass flux and axial mass flux driven by a pressure gradient is required. It is important to note that axial boundary conditions on the pressure cannot be imposed; this is because the slenderness ratio multiplies the highest derivative in the azimuthal direction. This is the telltale sign of a singular perturbation problem.

In this paper the effects of finite azimuthal length on short bearings are studied using the method of matched asymptotic expansions, Nayfeh [5]. Leading-order uniformly valid perturbation solutions are developed for two specific cases; the first is the case of a short bearing with constantly converging gaps in the flow direction (this is a specialization of the Schuss [7] solution to partial arc journal bearings), and the second is the case of converging then diverging gaps in the flow direction. In the latter case, subambient pressures in the diverging gap are not allowed to develop; the location of a free surface at the fluid film termination is described using the Reynold's cavitation condition.

(a) Orientation. To examine the consequences of axial edge effects in short bearing theory it is necessary to introduce the Reynolds equation for incompressible liquids. Fluid inertia effects are neglected. The geometric approximation of small gap is then applied to the Stokes flow equation. The variation in gap thickness due to the cylindrical arc eccentricities is $h(x)$; the inner cylindrical surface rotates with surface speed U_0. The notation used is shown in Fig. 1.
The Reynolds equation for the fluid film pressure is given in the following

$$\frac{\partial}{\partial x}\left(\frac{h^3}{12\mu}\frac{\partial P}{\partial x}\right)+\frac{\partial}{\partial z}\left(\frac{h^3}{12\mu}\frac{\partial P}{\partial z}\right)=\frac{1}{2}U_0\frac{\partial h}{\partial x} \tag{1.1}$$

where

$$h=C(1-\epsilon\,\mathrm{Cos}\eta) \tag{1.2}$$

The nondimensional scalings used are shown in the following. This nondimensional pressure scale is specifically selected to reflect finite axial length bearings. Hence we may write

$$\lambda=L/2R \tag{1.3a}$$

$$\bar{h}(\eta)=h/C=(1-\epsilon\,\mathrm{Cos}\eta) \tag{1.3b}$$

$$\bar{P}=4PC^2/6\mu\omega L^2 \tag{1.3c}$$

$$\xi=2z/L \tag{1.3d}$$

$$\eta=x/R \tag{1.3e}$$

With the aid of the preceding scaling we may write the Reynolds equation as

$$\lambda^2\frac{\partial}{\partial\eta}\left(\bar{h}^3\frac{\partial\bar{P}}{\partial\eta}\right)+\frac{\partial}{\partial\xi}\left(\bar{h}^3\frac{\partial\bar{P}}{\partial\xi}\right)=\epsilon\,\mathrm{Sin}\eta \tag{1.4}$$

Additional consideration of boundary conditions are required. We assume the pressure is ambient at the ends $\xi = \pm 1$, and also prescribe the pressures along axial edges $\eta = \eta_1$ and $\eta = \eta_2$. Provided the boundary locations η_1 and η_2 are given, no additional conditions are required.

(b) Ocvirk's Short Bearing Solution. Ocvirk [2] presented a solution to (1.4) applicable to the case where $\lambda \to 0$. It is assumed that azimuthal derivatives in Reynolds equation can be neglected; the argument as presented is intuitive and nondimensional scaling arguments are not well developed. As originally proposed the short bearing Reynolds equation is

$$\frac{\partial}{\partial\xi}\left(\bar{h}^3\frac{\partial\bar{P}}{\partial\xi}\right)=\epsilon\,\mathrm{Sin}\eta \tag{1.5}$$

with boundary conditions

$$\bar{P}(\eta,\xi=\pm)=0 \tag{1.6}$$

Ocvirk's solution to (1.5) with boundary conditions (1.6) is:

$$\bar{P}=\frac{-1}{2}(1-\xi^2)\epsilon\,\mathrm{Sin}\eta/(1-\epsilon\,\mathrm{Cos}\eta)^3 \tag{1.7}$$

Equation (1.7) is an asymptotic result for the fluid film pressure. This classical solution is only uniformly valid for semicircular short bearings (i.e., $p = 0$ when $\eta = 0$ and $\eta = \pi$). This is a serious defect in modeling the pressure, the quantity from which practical design estimates are made.

It is desirable to obtain uniformly valid pressures for short journal bearings with azimuthal extent less than π. In this circumstance the Ocvirk solution can not provide a zero pressure along the axial fluid film edge. A procedure that permits imposing azimuthal edge boundary conditions, similar to that given by Schuss, is needed.

Meanwhile, consideration of fluid film cavitation requires a pair of azimuthal boundary conditions along the cavitation boundary. The general question of cavitation has been a subject of much controversy; it is clear that Ocvirk's simple

Downloaded 02 May 2010 to 171.66.16.54. Redistribution subject to ASME license or copyright; see http://www.asme.org/terms/Terms_Use.cfm

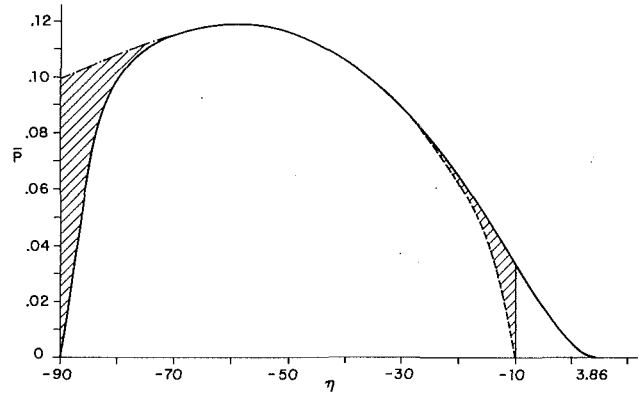


Fig. 3(a)

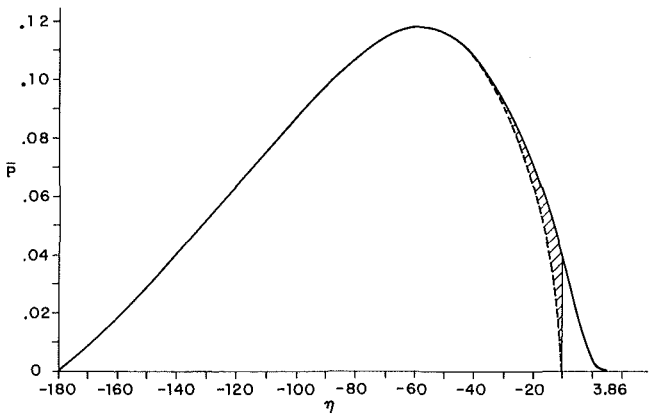


Fig. 3(b)

Fig. 3 (*a*, *b*) Plot of centerline pressure distribution for slenderness ratio equal to 0.1, and eccentricity ratio equal to 0.2. (*a*) the solid curve, (——), indicates the pressure profile for $P(\xi, \eta_1 = -90) = 0$ and $\partial P(\xi, \eta)/\partial\eta = 0$; the curve (·····) shows the boundary layer at the bearing trailing edge if $P(\xi, \eta_2 = -10) = 0$; and the curve (·-·-·) shows the Ocvirk pressure prediction near the bearing entrance region. (*b*), the solid curve is for $P(\xi, \eta_1 = -180) = 0$ and $\partial P(\xi, \eta_2)/\partial\eta = 0$; and the curve (·····) shows the trailing edge pressure profile for $P(\xi, \eta_2 = -10) = 0$.

model can not cope with this phenomena. Previously, the short bearing theory had only been for converging gaps; Pan [5] extended this classical treatment to include diverging gaps. Pan sought the cavitation boundary location using the Reynolds free surface condition—the gradient of the film pressure must vanish at the ruptured boundary. However, he applied the Reynolds free surface condition to the Ocvirk short bearing solution. A more precise treatment, using Reynolds' cavitation condition is needed near the leading edge of film rupture.

2 A Method of Improving the Ocvirk Approximation Using Matched Asymptotic Theory

The version of the small slenderness ratio theory presented here describes inner and outer expansions and a matching technique for journal bearings. It is impossible to satisfy the pressure condition along axial film edges using Ocvirk's approximation. Azimuthal pressure derivatives are needed in the neighborhood of the axial film edge; and retaining this term in Reynolds' equation turns out to be decisive in enabling us to specify axial film edge conditions. To determine a uniformly valid solution the method of composite solutions is adopted, where the outer flow is that region away from the axial film edge, and the inner regions are near the film edge. The respective locations of inner and outer flow regions are shown; Fig. 2.

A complete examination of this problem suggests that two different cases be treated separately. In the first case, a journal bearing with azimuthal extent less than π is studied. The corresponding axial edge boundary conditions are

$$-\pi < \eta_1 \qquad \text{and} \qquad \eta_2 = \eta_{\text{exit}} < 0 \text{ deg}$$
$$\bar{P}(\xi, \eta_1) = 0$$
$$\bar{P}(\xi, \eta_2) = 0 \tag{2.1}$$

In the second case, the pressure at the film entrance is specified. The wetted bearing surface extends into the diverging portion of the gap where pressures go negative and film rupture occurs; this film rupture curve can be regarded as a free surface. The boundary conditions are

$$0 < \eta_2 < \eta_{\text{exit}}$$
$$\bar{P}(\xi, \eta_1) = 0$$
$$\bar{P}(\xi, \eta_2) = 0 \tag{2.2}$$

An additional consideration is required since $\eta_2 = \eta_2(\xi)$ is unknown; the straightforward procedure used here is to apply Reynolds' condition. This requires vanishing pressure gradient on the cavitation boundary.

$$\underline{\nabla}\ \bar{p} = 0 \qquad \text{on} \qquad \eta_2 = \eta_2(\xi)$$

Solutions for $\bar{P}$ (ξ, η) and for $\eta_2 = \eta_2(\xi)$ are given in the following sections.

***(a)* The Outer Problem.** Consider a straightforward expansion in the slenderness ratio λ. The pressure is expanded in an asymptotic series

$$\bar{P} = \sum_{n=1}^{\infty} \nu_n(\lambda)\, \bar{P}_{01}(\xi, \eta) \tag{2.3}$$

where ν_n (λ) is an asymptotic sequence. Substituting this asymptotic series (2.3) into (1.4) and taking the limit ($\lambda \to 0$, η fixed) we obtain ν_1 $(\lambda) = 1$ and

$$\frac{\partial}{\partial\xi}\left(\bar{h}^3 \frac{\partial \bar{P}_{01}}{\partial\xi}\right) = \epsilon\, \text{Sin}\eta \tag{2.4}$$

As a consequence, of this limiting procedure, the partial differential equation is reduced to an ordinary differential equation in the axial coordinate. Therefore, only the azimuthal edge boundary conditions can be satisfied.

$$\bar{P}_{01}(\xi = \pm 1, \eta) = 0$$

The solution is identical to that obtained by Ocvirk,

$$\bar{P}_{01} = -\frac{1}{2}(1 - \xi^2)\epsilon\, \text{Sin}\eta/(1 - \epsilon\, \text{Cos}\eta)^3 \tag{2.5}$$

This expansion is valid away from the axial edges where $\eta = \eta_1$ and where $\eta_2 = \eta_2(\xi)$. The limiting pressure behavior near the axial edges is described by rescaling the azimuthal coordinate η.

***(b)* Inner Problem.** It remains to obtain coordinate scalings for the two inner regions. Left and right boundary layers are treated separately, but the axial coordinate scaling is the same. On the left boundary, near $\eta = \eta_1$, the new independent variable in the azimuthal direction is η^* and it is defined as

$$\eta^* = (\eta - \eta_1)/\lambda$$

We consider the following asymptotic expansion for pressure on the left boundary.

$$\bar{P}^* = \sum_{\eta=1}^{\infty} \nu_n{}^*(\lambda)\, \bar{P}_{0n}{}^*((\xi, \eta^*) \tag{2.6}$$

A single star represents the left boundary layer. The

Downloaded 02 May 2010 to 171.66.16.54. Redistribution subject to ASME license or copyright; see http://www.asme.org/terms/Terms_Use.cfm

asymptotic series (2.6) is substituted into the Reynolds equation (1.4). The azimuthal coordinate is rescaled to η^*, then the inner limit ($\lambda \to 0$, η^* fixed) is applied. The result is:

$$\frac{\partial}{\partial \eta^*}(\bar{h}^3(\eta_1)\frac{\partial \bar{P}_{01}^*}{\partial \eta^*} + \frac{\partial}{\partial \xi}(\bar{h}^3(\eta_1)\frac{\partial \bar{P}_{01}^*}{\partial \xi} = \epsilon \operatorname{Sin}\eta_1 \tag{2.7}$$

and boundary conditions on P are expressed as

$$\bar{P}_{01}{}^*(\xi, \eta^* = 0) = 0$$

$$\bar{P}_{01}{}^*(\xi = \pm 1, \eta^*) = 0$$

The inner solution must be compatible via matching to the outer solution; for the present purpose of matching, it is sufficient to use the relatively simple method that

inner limit (outer solution) = outer limit (inner solution)

Here we require that

$$\operatorname*{Limit}_{\eta \to \eta_1}\left[\sum_{n=1}^{\infty} \nu_n(\lambda)\bar{P}_{0n}(\xi,\eta)\right] = \operatorname*{Limit}_{\eta^* \to \infty}\left[\sum_{n=1}^{\infty} \nu_n{}^*(\lambda)\bar{P}_{0n}{}^*(\xi,\eta^*)\right] \tag{2.8}$$

Likewise, for the right boundary near $\eta = \eta_2$, the azimuthal coordinate is rescaled

$$\eta^{**} = (\eta_2 - \eta)/\lambda$$

We assume that the pressure near $\eta = \eta_2$ can be expanded in an asymptotic series, the series is

$$\bar{P}^{**} = \sum_{n=0}^{\infty} \nu_n{}^{**}(\lambda)\bar{P}_{0n}^{**}(\xi,\eta^{**}) \tag{2.9}$$

where $\nu_n{}^{**}(\lambda)$ is an asymptotic sequence, here a double star represents the right boundary layer. The asymptotic series (2.9), coupled with Reynolds equation (1.4) rescaled to η^{**} yields

$$\frac{\partial}{\partial \eta^{**}}\bar{h}^3(\eta_2)\frac{\partial \bar{P}_{01}{}^{**}}{\partial \eta^{**}} + \frac{\partial}{\partial \xi}\bar{h}^3(\eta_2)\frac{\partial \bar{P}_{01}{}^{**}}{\partial \xi} = \epsilon \operatorname{Sin}\eta_2 \tag{2.10}$$

and boundary conditions on $\bar{P}_{01}{}^{**}$ can be expressed as

$$\bar{P}_{01}{}^{**}(\xi, \eta^{**} = 0) = 0$$

$$\bar{P}_{01}{}^{**}(\xi = \pm 1, \eta^{**}) = 0$$

Following the stated matching procedure we obtain:

$$\operatorname*{Limit}_{\eta \to \eta_2}\left(\sum_{\eta=1}^{\infty} \nu_n(\lambda)\bar{P}_{0n}(\xi,\eta)\right)$$

$$= \operatorname*{Limit}_{\eta^{**} \to \infty}\left(\sum_{n=1}^{\infty} \nu_n{}^{**}(\lambda)\bar{P}_{01}{}^{**}(\xi,\eta^{**})\right) \tag{2.11}$$

The procedure to amend Ocvirk's solution requires solving the foregoing linear elliptic boundary value problems on the left and right axial film edges.

(c) Boundary Layer and Composite Solution—Case (a). A solution to the boundary value problem stated previously is obtained; on the left boundary layer homogeneous solution is Q^* and the particular solution is $A^*(1 - \xi^2)$. Thus

$$\bar{P}_{01}{}^* = Q^* - A^*(1 - \xi^2)$$

where the constant A^* is:

$$A^* = \epsilon \operatorname{Sin}\eta_1/2(1 - \epsilon \operatorname{Cos}\eta_1)^3$$

The associated boundary value problem for the homogeneous solution Q^* is

$$\nabla^2 Q^* = 0$$

$$Q^*(\xi, \eta^* = 0) = (\epsilon \operatorname{Sin}\eta_1/2(1 - \epsilon \operatorname{Cos}\eta_1)^3)(1 - \xi^2)$$

$$Q^*(\xi = \pm 1, \eta^*) = 0 \tag{2.12}$$

After applying the matching condition to the boundary layer pressure result, the following condition on the homogeneous solution is found.

$$Q^*(\eta^* \to \infty, \xi) = 0$$

The homogeneous solution is determined by separation of variables. The eigenfunction orthogonality condition is used to determine the unknown constants in a eigenfunction expansion. The resulting expression for Q^* is

$$Q^* = \sum_{n=0}^{\infty} \frac{2\epsilon \operatorname{Sin}\eta_1(-1)^n}{(1 - \epsilon \operatorname{Cos}\eta_1)^3 \gamma_n{}^3} \operatorname{Cos}\gamma_n \xi e^{-\gamma_n \eta^*} \tag{2.13}$$

where eigenvalues γ_n are

$$\gamma_n = \left(n + \frac{1}{2}\right)\pi$$

The preceding inner solution is matched to the outer or Ocvirk solution. The leading order term in the matched asymptotic expansion is

$$\bar{P}_{01}{}^* = \frac{\epsilon \operatorname{Sin}\eta_1}{2(1 - \epsilon \operatorname{Cos}\eta_1)^3}\left[-(1 - \xi^2) + \sum_{n=0}^{\infty} \frac{4(-1)^n}{\gamma_n{}^3} \operatorname{Cos}\gamma_n \xi e^{-\gamma_n \eta^*}\right] \tag{2.14}$$

Similar considerations apply to the right boundary layer in the neighborhood of $\eta = \eta_2$. The pressure equation in this inner region is again a Poisson equation. Corresponding equations and boundary conditions are conveniently similar to the left boundary layer; the solution is obtained by the previous straightforward method,

$$\bar{P}_{01}{}^{**} = \frac{\epsilon \operatorname{Sin}\eta_2}{2(1 - \epsilon \operatorname{Cos}\eta_2)^3}\left[-(1 - \xi^2) + \sum_{n=0}^{\infty} \frac{4(-1)^n}{\gamma_n{}^3} \operatorname{Cos}\gamma_n \xi e^{-\gamma_n \eta^{**}}\right] \tag{2.15}$$

It remains to give an expression for the composite solution, P_{cs}; here leading-order terms from inner and outer asymptotic expansions are required. The procedure used here is to add the three asymptotic expansions and subtract off the common part, we write

$$\bar{P}_{cs} = \bar{P}_{01} + \bar{P}_{01}{}^* + \bar{P}_{01}{}^{**} - \bar{P}_{cp}{}^* - \bar{P}_{cp}{}^{**}$$

where $\bar{P}_{cp}{}^*$ and $\bar{P}_{cp}{}^{**}$ are common parts from left and right boundary layers, respectively. This straightforward procedure for the composite pressure is achieved in the following,

$$\bar{P}_{cs} = -\frac{1}{2}(1 - \xi^2)\epsilon \operatorname{Sin}\eta/(1 - \epsilon \operatorname{Cos}\eta)^3 + \frac{\epsilon \operatorname{Sin}\eta_1}{2(1 - \epsilon \operatorname{Cos}\eta_1)^3}\sum_{n=0}^{\infty} \frac{4(-1)^n}{\gamma_n{}^3} \operatorname{Cos}\gamma_n \xi e^{-\gamma_n(\eta - \eta_1)/\lambda} + \frac{\epsilon \operatorname{Sin}\eta_2}{2(1 - \epsilon \operatorname{Cos}\eta_2)^3}\sum_{n=0}^{\infty} \frac{4(-1)^n}{\gamma_n{}^3} \operatorname{Cos}\gamma_n \xi e^{-\gamma_n(\eta_2 - \eta)/\lambda} \tag{2.16}$$

(d) Boundary Layer and Composite Solution—Case (b). We may now return to the question of fluid film breakup in the diverging portion of the gap. The lubricant film is allowed to, in some cases, sustain a subambient pressure; however, here we take the cavitation pressure to be

Downloaded 02 May 2010 to 171.66.16.54. Redistribution subject to ASME license or copyright; see http://www.asme.org/terms/Terms_Use.cfm

zero. The film breakup, or cavitation, will extend along the axial direction. It follows that cavitation depends on the local film properties. The presence of such a free surface requires an additional boundary condition, a commonly accepted free surface condition is Reynolds'

$$\nabla \bar{P}_{cs} = 0 \qquad \bar{P}_{cs} = 0$$

The fluid inertia forces, along with capillary effects, are neglected. No explicit description of the flow is given after film breakup. The present simplified theory has the advantage of avoiding specific details of flow in the cavitation region, while still locating the cavitation boundary.

For case (*b*) the left boundary layer remains exactly the same; however the location η_2 is unknown. The pressure field is still given by equation (2.16); the location of the cavitation boundary is determined by applying Reynolds' condition

$$\left.\frac{\partial \bar{P}_{cs}}{\partial \eta}\right|_{\eta=\eta_2} = 0$$

This condition results in the following equation

$$-\frac{(1-\xi^2)}{2}\left[\frac{\epsilon \operatorname{Cos}\eta_2 - 3\epsilon^2 + 2\epsilon^2 \operatorname{Cos}^2\eta^2}{(1-\epsilon \operatorname{Cos}\eta_2)^4}\right]$$

$$+\frac{\epsilon \operatorname{Sin}\eta_2}{2\lambda(1-\epsilon \operatorname{Cos}\eta_2)^3}\sum_{n=0}^{\infty}\frac{4(-1)^n}{\gamma_n{}^2}\operatorname{Cos}\gamma_n\xi = 0 \qquad (2.17)$$

Equation (2.17) gives the cavitation boundary location as a function of axial position; admittedly, this implicit function is not simple. But in general, the cavitation incipience occurs near the minimum gap; thus, values of η_2 are estimated to be 0 (λ). The relationship (2.17) is substantially simplified using cos $\eta_2 \cong 1$ and sin $\eta_2 = \eta_2$. These conditions immediately lead to the asymptotic result

$$\eta_2 \cong \frac{\lambda(1-\xi^2)}{4}\Big/\sum_{n=0}^{\infty}\frac{(-1)^n}{\gamma_n{}^2}\operatorname{Cos}\gamma_n\xi \qquad (2.18)$$

The series in (2.18) is summed, and the equivalent integral expression is given in the appendix. Thus

$$\eta_2 \cong \lambda(1-\xi^2)\Big/\left(\frac{2}{\pi}\left(2G - \int_0^{\xi} Ln\left(\frac{1+\operatorname{Sin}x}{1-\operatorname{Sin}x}\right)^{1/2} dx\right)\right) \qquad (2.19)$$

The preceding model of film rupture is based on a separation of variables solution of the homogeneous inner boundary layer problem. It should be mentioned at this stage that axial variation of the cavitation boundary, $\eta_2 = \eta_2(\lambda, \xi)$, is not strictly consistent with the separation of variables scheme. Here we now expand η_2 in an asymptotic series

$$\eta_2 = \sum_{n=0}^{\infty}\beta_n(\lambda)\eta_{2n}(\xi) \qquad (2.20)$$

where $\beta_n(\lambda)$ is an asymptotic sequence. This scheme is suggested in view of the foregoing analysis; the actual form of the first term in (2.20) is given by (2.19), $\beta_0(\lambda) = \lambda$. In this situation the slow axial variation of η_2 is consistent, to a first approximation, with the separation of variables method used. Cavitation regions where $\beta_0(\lambda) = 0$ cannot be treated by this separation of variables approach.

3 Results

There is no difficulty now in calculating fluid film pressure fields for specific cases. As an example, bearing centerline pressure distributions are calculated for eccentricity ratio 0.2 and 0.8. The results are shown in Figs. 3(*a*) and 3(*b*), respectively.

At eccentricity ratio 0.2, and slenderness ratio 0.1, the centerline pressure profile for $\eta_1 = -90$ and $\eta_2 = -10$ is presented in Fig. 3(*a*). It is quickly seen that a reduction in load capacity is predicted by the new matched asymptotic theory as compared to Ocvirk's theory. The magnitude of Ocvirk's overestimate is indicated by the shaded region, Fig. 3(*a*). A second result for centerline pressure profiles with film rupture is also shown, Fig. 3(*a*); the fluid film is shown to extend 3.86 deg beyond the minimum gap thickness. For eccentricity ratio 0.2, slenderness ratio 0.1, $\eta_1 = -180$, and $\eta_2 = -10$, the centerline pressure is generated from equation (2.16) and shown in Fig. 3(*b*); a second result for film rupture is again shown to extend the fluid film 3.86 beyond the minimum gap thickness. An interesting feature of the solution here is the vanishing of the entrance boundary layer when the fluid film starts at the maximum gap; the mathematical reason for this lies in specification of the axial fluid film edge location and pressure to exactly that given by Ocvirk's solution.

For the conditions, eccentricity ratio = 0.8, slenderness ratio = 0.1, $\eta_1 = -90$, and $\eta_2 = -10$, the centerline pressure profiles are shown in Fig. 4(*a*). In this situation, the newly predicted load capacity is again lower than Ocvirk's. Should the fluid film be extended past the minimum gap into the diverging gap, the film rupture is predicted to occur at 3.86 deg. Figure 4(*b*) shows the tendency for the entrance boundary layer to vanish as η_1 approaches the maximum gap. The effect of terminating the fluid film at $\eta_2 = -10$ is also shown in Fig. 4(*b*); the role of the boundary layer is to drag the pressure down to zero in the 0 (λ) edge region. Since the axial edge boundary layers drag the outer solution pressure profile down to zero in a 0 (λ) region. It is not unexpected to see a decrease in load capacity. It is noted that when $\eta_1 =$ –

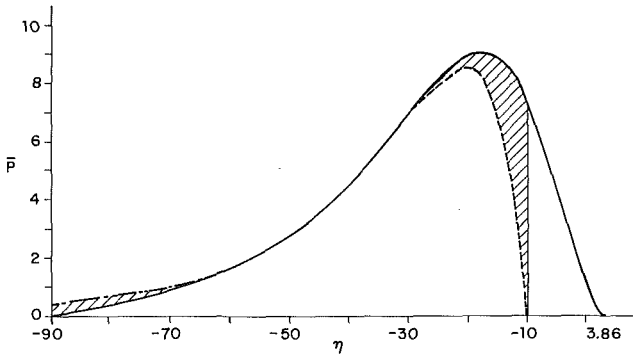


Fig. 4(*a*)

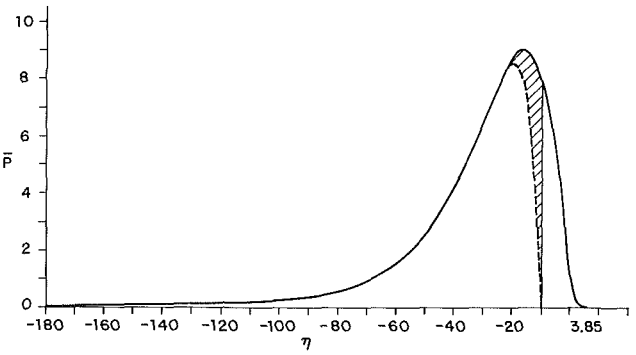


Fig. 4(*b*)

Fig. 4 (*a*, *b*) Plot of centerline pressure distribution for slenderness ratio equal to 0.1 and eccentricity ratio 0.8. (*a*), the solid line shows the matched asymptotic theory for $P(\xi, \eta_1 = 90) = 0$ and $\partial P(\xi, \eta_2)/\partial \eta = 0$; the curve (-·-·-) shows the Ocvirk pressure prediction near $\eta = -90$ and the curve (·····) shows the trailing edge prediction for $P(\xi, \eta_2 = -10) = 0$. (*b*), the solid curve shows the pressure for $P(\xi, \eta_1 = -180)$ and $\partial P(\xi, \eta_2)/\partial\eta = 0$; the curve (·····) shows the trailing edge boundary layer for $P(\xi, \eta_2 = -10) = 0$.

Downloaded 02 May 2010 to 171.66.16.54. Redistribution subject to ASME license or copyright; see http://www.asme.org/terms/Terms_Use.cfm

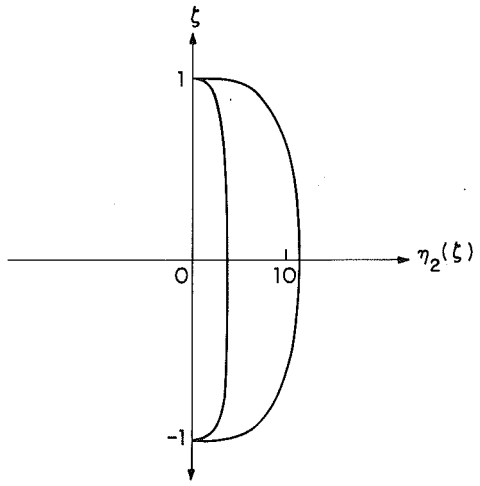


Fig. 5 Cavitation boundary shape for axial film rupture, slenderness ratios 0.1 and 0.3

180, or $\eta_2 = 0$ the outer solution automatically satisfies the zero pressure edge condition. It is shown that for $\eta_2 = 0$ no boundary layer is necessary. And if film rupture is allowed to occur the effect of including the term

$$\lambda^2 \frac{\partial}{\partial \eta} \bar{h}^3(\eta) \frac{\partial \bar{P}}{\partial \eta}$$

has the primary feature of adjusting the pressure profile slope near rupture. Thus relatively little change in predicted load capacity occurs between this matched asymptotic theory for film rupture and the previous short bearing theory.

The cavitation boundary shape, via Reynolds condition, emerged from the analysis. An unexpected feature of this result is the absence of any eccentricity dependence. Cavitation boundary shapes, calculated from equation (2.19), are shown in Fig. 5.

4 Discussion

The present work was undertaken primarily to resolve the question of how to handle fluid film edges in short bearing theory. This is answered by locating boundary layers at each of the axial film edges. Previous short bearing theory is treated as the outer solution and thus fully reconciled to this theory. The mathematical reason for the previous difficulties lies in a change in character of Reynolds equation when

$$\lambda^2 \frac{\partial}{\partial \eta} \bar{h}^3(\eta) \frac{\partial \bar{P}}{\partial \eta}$$

is completely neglected. This solution gives leading order composite functions for fluid film pressures. Boundary layer thickness is shown to scale on bearing slenderness ratio, λ, to the first power.

A new feature that emerges is the physical significance associated with these inner and outer regions. The leading order term in the outer region—Ocvirk's solution—is characterized by a balance between, axial mass flux that is driven by an axial pressure gradient, and the azimuthal mass flux caused by Couette flow in a variable thickness gap. The pressure in the inner flow joins smoothly to the outer; and here it is possible to characterize the inner pressure field in two parts that corresponded to the previously stated particular and homogeneous solutions. The first part, the particular solution, is associated with a balance between azimuthal mass flux through a linearly changing gap, and axial mass flux due to a corresponding axial pressure gradient. The second part, the homogeneous solution, is essentially a Hele-Shaw type flow; near the exit, fluid is driven through a constant thickness gap by the outer pressure field. The imposed outer pressure field possesses axial variation; corresponding fluid motion is then in both azimuthal and axial directions.

An unexpected feature of this solution is the independence of the cavitation boundary from journal eccentricity. This was not anticipated at the outset; the extent to which this may be true in higher order terms is not known. An obvious fact is that cavitation boundary response to local fluid film geometry and to local gap thickness can be included by modification of the film breakup to include capillary forces. This is a difficult complication for which limited experimental and theoretical guides can be found; the capillary effect remains an open question. In the interest of brevity the parametric range of λ and ϵ for which short bearing theory can be applied is to be a separate publication.

Acknowledgment

This work was partially supported by the National Science Foundation under Grant NSF MEA 81 06447.

References

1 Buckholz, R. H., et al., "The Accuracy of Short Bearing Theory," in preparation, 1984.

2 Cardullo, F. E., "Some Practical Deductions From Theory of Lubrication of Short Cylindrical Bearings," ASME MSP-51-12, Vol. 52, 1930, pp. 143-153.

3 Dubois, G. B., and Ocvirk, F. W., "Analytical Derivation of Short Bearing Approximation for Full Journal Bearings," NACA Report 1157, 1953.

4 Michell, A. G. M., "Progress in Fluid-Film Lubrication," ASME, MSP-51-21, Vol. 51, 1929, pp. 153-163.

5 Nayfeh, A., *Perturbation Methods*, Wiley, New York, 1973.

6 Pan, C. H. T., "An Improved Short Bearing Analysis for the Submerged Operation of Plain Journal Bearings and Squeeze-Film Dampers," ASME *Journal of Lubrication Technology*, Vol. 102, No. 3, 1980, pp. 320-332.

7 Reynolds, O., "On the Theory of Lubrication and Its Application to Mr. Beauchampt Tower's Experiments, Including an Experimental Determination of the Viscosity of Olive Oil," *Phil. Trans. Roy. Soc.*, London, Series *A*, Vol. 177, 1886, pp. 157-234.

8 Schuss, Z., and Etsion, I., "On the Solution of Lubrication Problems Involving Narrow Configurations," ASLE Vol. 24, No. 2, 1981, pp. 186-190.

APPENDIX

In case (*b*) fluid film rupture was considered; here the series in (2.18) is expressed as an integral. The derivation is given from the following expansion

$$\text{Sec } x = 2(\text{Cos } x - \text{Cos } 3x - \text{Cos } 5x - \text{Cos } 7x \ldots), \tag{A1}$$

both sides are integrated with respect to x

$$\int_0^x \text{Sec } x' dx' = Ln\left(\frac{1+\text{Sin } x}{1-\text{Sin } x}\right)^{1/2} \tag{A2}$$

and

$$\int_0^x 2(\text{Cos } x' - \text{Cos } 3x' + \text{Cos } 5x' - \ldots .)dx' = 2\left(\text{Sin } x - \frac{\text{Sin } 3x}{3} + \frac{\text{Sin } 5x}{5} - \ldots .\right) \tag{A3}$$

thus

$$Ln\left(\frac{1+\text{Sin } x}{1-\text{Sin } x}\right)^{1/2} = 2\left(\text{Sin } x - \frac{\text{Sin } 3x}{3} + \frac{\text{Sin } 5x}{5} - \ldots .\right) \tag{A4}$$

The equation (*A*4) is integrated a second time,

$$\int_0^x Ln\left(\frac{1+\text{Sin } x'}{1-\text{Sin } x'}\right)^{1/2} dx' = 2\int_0^x \left(\frac{\text{Sin } x'}{1} - \frac{\text{Sin } 3x'}{3}\right.$$

Downloaded 02 May 2010 to 171.66.16.54. Redistribution subject to ASME license or copyright; see http://www.asme.org/terms/Terms_Use.cfm

$$+\frac{\text{Sin } 5x'}{5}-\ldots\Big)dx' \tag{A5}$$

$$=2\Big(\frac{\text{Cos } x}{1\cdot 1}-\frac{\text{Cos } 3x}{3\cdot 3}+\frac{\text{Cos } 5x}{5\cdot 5}-\ldots\Big)$$

$$-2\Big(1-\frac{1}{3^2}+\frac{1}{5^2}-\ldots\Big)$$

The final result for representing the series as an integral is given in the following

$$-\int_0^x Ln\Big(\frac{1+\text{Sin } x'}{1-\text{Sin } x'}\Big)^{1/2}dx'$$

$$=2\sum_{n=0}^{\infty}\frac{(-1)^n\text{Cos}(2n+1)x}{(2n+1)^2}-2G \tag{A6}$$

and we have the following result to substitute into equation (2.18)

$$\sum_{n=0}^{\infty}\frac{(-1)^n 4\text{Cos}(2n+1)\pi x}{(2n+1)^2\pi^2}$$

$$=\frac{2}{\pi^2}\Big\{2G-\int_0^x Ln\Big(\frac{1+\text{Sin } x'}{1-\text{Sin } x'}\Big)^{1/2}dx'\Big\} \tag{A7}$$

where

$$G=\Big(1-\frac{1}{3^2}+\frac{1}{5^2}-\ldots.\Big)=0.915965 \tag{A8}$$

Downloaded 02 May 2010 to 171.66.16.54. Redistribution subject to ASME license or copyright; see http://www.asme.org/terms/Terms_Use.cfm

Z-B. Kuang[1]

S. N. Atluri
Mem. ASME

Center for the Advancement
of Computational Mechanics,
School of Civil Engineering,
Georgia Institute of Technology,
Atlanta, Ga. 30332

Temperature Field Due to a Moving Heat Source: A Moving Mesh Finite Element Analysis

The transient temperature field (as seen by a moving observer) due to a moving heat source, such as the process zone near a dynamically propagating crack tip or an external agent as in the case of welding, is analyzed by a moving-mesh finite element procedure. The effects of the temperature-dependent material properties, and of the loss of heat to the surrounding medium through convection and radiation, are studied. Situations under which conditions in the process zone may be labeled as "isothermal" or "adiabatic" are explored. Estimates of temperature rise near the tip of a crack propagating at realistic speeds in structural steels are made.

1 Introduction

The problem of temperature distribution in a solid due to a propagating heat source is of relevance in several seemingly distinct problems such as dynamic crack propagation in an inelastic solid, welding, etc. The criteria governing fast crack propagation in inelastic solids are still undergoing intense scrutiny and development. Even under quasistatic elastic-plastic crack-growth conditions, the futility of using "energy release" type of approaches has been generally recognized, based on a study by Rice [1] who showed that the rate of energy release (per unit of crack growth in the limit of vanishing crack-growth increment) to the crack tip is in fact zero for materials in which stress saturates to a finite value at large strain. Thus, in this case, the elastic energy release rate is exactly equal to the plastic dissipation rate; a major portion of which is converted to heat. Even under brittle fracture conditions, the difference between the elastic energy released to the crack tip and the specific surface energy of the material is mostly converted to heat (Schönert and Weichert [2] and Doll [3]). Thus, the analysis of temperature rise at the tip of a moving crack and its influence on the behavior of the material near the crack tip, are of interest in understanding the process of fracture.

In general, one may postulate, near the crack tip, a fracture process zone in which intense irreversible deformation occurs. In ductile fracture, the dimensions of this process zone, wherein void nucleation, growth, and coalescence may take place, are of the order of crack-tip stretch. On the other hand, in fracture of the cleavage type, the fracture process zone is generally of the order of the grain size of the material. In this paper we postulate, in the context of fracture, a moving heat source of a size comparable to that of the "Process zone" near the propagating crack tip. On the other hand, in the context of welding, the dimensions of the heat source may be much larger.

Weichert and Schönert [4-6] have earlier presented a series of studies concerning the temperature rise near a moving heat source. These studies were, however, limited to the linear and "steady-state" case, i.e., the one in which the temperature field appears invariant to an observer moving along with the heat source, at the same speed. Weichert and Schönert [4] first studied the case of a circular-shaped heat source; late [5, 6] they considered the case of a rectangular heat source. Also, in their studies, Weichert and Schönert: (*i*) considered the thermal conductivity and diffusivity to be independent of temperature and (*ii*) neglected the loss of heat to the surrounding medium due to convection and radiation. In this paper, for various velocities of propagation of the heat source in the range of 0.762-762 m/sec [ie., 2.5-2500 ft/sec], we (*i*) analyze the transient (i.e., time-dependent when observed by an observer moving with the heat source, at the same velocity) temperature state near the propagating heat source, (*ii*) include the effects of temperature-dependent material properties, and (*iii*) include effects of convective and radiative heat losses to the surrounding medium. For cases (*ii*) and (*iii*), the problem becomes strongly nonlinear. We characterize the situations under which the conditions in the process zone may be labeled "isothermal" or "adiabatic." An estimate of the possible temperature rise near a tip of a propagating crack in structural steels is given. We present a discussion of the possible effect of the temperature rise near the crack tip on the fracture process itself.

In studying problems of the crack-propagation type, we assume that the total heat generated per unit of crack extension is of a constant value. Thus, in this case, the rate of heat generated per unit time varies linearly with the velocity of propagation of the crack and, hence, of the heat source itself.

[1] Visitor from the Department of Mechanics, Xian Jiaotong University, Xian, China.

Contributed by the Applied Mechanics Division for presentation at the 1985 joint ASME/ASCE Applied Mechanics, Bioengineering, and Fluids Engineering Conference, Albuquerque, N. Mex., June 24-26, 1985 of THE AMERICAN SOCIETY OF MECHANICAL ENGINEERS.

Discussion on this paper should be addressed to the Editorial Department, ASME, United Engineering Center, 345 East 47th Street, New York, NY. 10017, and will be accepted until two months after final publication of the paper itself in the JOURNAL OF APPLIED MECHANICS. Manuscript received by ASME Applied Mechanics Division, July, 1984; final revision, September, 1984. Paper No. 85-APM-19.

Copies will be available until February, 1986.

Copyright © 1985 by ASME
Downloaded 02 May 2010 to 171.66.16.54. Redistribution subject to ASME license or copyright; see http://www.asme.org/terms/Terms_Use.cfm

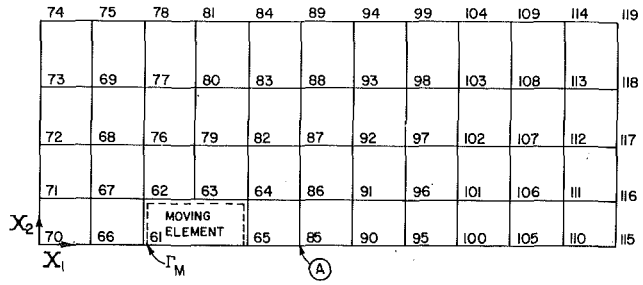


Fig. 1(*a*) Finite element model of the upper half of the domain

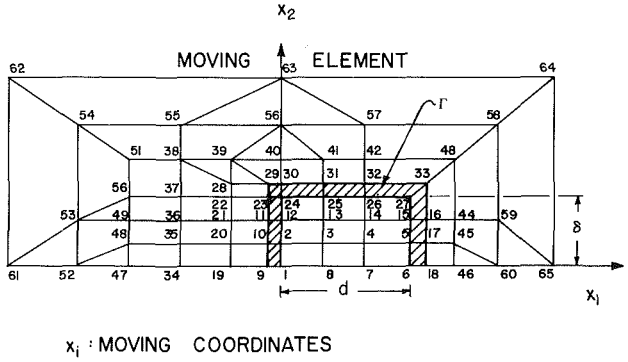


Fig. 1(*b*) Details of the moving element (bounded by Γ_M as shown in Fig. 1(*a*)). Γ is the boundary of the heat source. When $\dot{q}$ is assumed to be uniform, the intensity reduces from a constant value to zero within the thin hatched layer.

Fig. 1

On the other hand, in a problem of welding, we may assume that the heat generated per unit time is of a constant value.

2 Numerical Treatment of the Moving Heat Source Problem

We consider a fixed cartesian coordinate system X_i (i = 1,2,3) with X_1 and X_2 being the "inplane" coordinates, and X_3 in the direction of the thickness, which is considered to be much smaller than the lateral dimensions of the body. We consider, in general, a rectangular heat source that moves at a constant velocity v. We consider a moving coordinate system x_i, centered at the propagating crack tip, such that $x_1 = X_1 - vt$ and $x_2 = X_2$; $x_3 = X_3$. See Figs. 1(*a*) and (*b*) for the geometry (along with a finite element mesh) of the upper half ($X_2 > 0$) of the symmetric domain and the upper half of the heat source, respectively. The differential equation governing the unsteady heat conduction problem is:

$$(kT_{,i})_{,i} + \dot{q} = \rho c \frac{\partial T}{\partial t} \quad \text{in} \quad V \tag{2.1}$$

where V is the volume of the body; T is the temperature; k the thermal conductivity (possibly dependent on T) of the material; $\dot{q}$ is the strength of the heat source (per unit volume per unit time); ρ is the density of the material; C the specific heat of the material; t the time; and $(\ )_{,i}$ denotes a partial derivative of $(\ )$ with respect to X_i. The initial condition is:

$$T(X_i,0) = T_0(X_i) \tag{2.2}$$

Four types of boundary conditoins are considered:

$$T - T_0 = 0 \quad \text{on} \quad S_1 \tag{2.3a}$$

$$k\, n_i T_{,i} + q = 0 \quad \text{on} \quad S_2 \tag{2.3b}$$

$$k\, n_i T_{,i} + h(T - T_\infty) = 0 \quad \text{on} \quad S_3 \tag{2.3c}$$

$$k\, n_i T_{,i} + h_r(T - T_\infty) = 0 \quad \text{on} \quad S_4 \tag{2.3d}$$

where

$$h_r = F\sigma\epsilon(T + T_\infty)(T^2 + T_\infty^2) \tag{2.3e}$$

where, n_i are direction cosines of a unit normal to the surface; q is the boundary heat flux, h is the coefficient of convective heat transfer; T_∞ is the temperature of the surrounding medium; ϵ is the emissivity of the surface, σ is the Stefan-Boltzmann constant; and h_r is the radiation boundary conductance.

In the present calculations, the total heat production, Q, per unit of source travel (or, equivalently, per unit of crack extension) is assumed to be constant, even though such an assumption is not essential for the numerical scheme employed. Thus, the rate of total heat production per unit time, i.e., $\dot{q}$, is Qv. The spatial distribution of $\dot{q}$, in the rectangular heat source, is assumed, alternatively, to be: (*i*) uniformly distributed within the rectangular region ($x_1 = D$) × ($x_2 = 2\delta$), and (*ii*) $\dot{q}$ has a ($1/r$) type of behavior near $x_1 = x_2 = 0$. When it is uniformly distributed, for numerical convenience, $\dot{q}$ is assumed to decay linearly, from its constant value, to zero within a thin layer as shown in Fig. 1(*b*).

In a finite-element approximation, we assume within each element,

$$T = N_\alpha(X_k)\, T_\alpha^{(e)} \quad = 1 \ldots N \tag{2.4}$$

where N_α are basis functions, and $T_\alpha^{(e)}$ are nodal temperatures at N nodes of the element. The solid is discretized into M finite elements, V_m, $m = 1..M$. We assume that the trial functions (2.4) may be made to satisfy the lower-order condition (2.3*a*) in the usual way (i.e., by setting the nodal values of T to prescribed values after the finite element algebraic equations are obtained). By using the standard Galerkin weighted residual formulation (i.e., the one in which the trail and test function spaces are identical), the weak form of equations (2.1) and (2.3*b*,*c*,*d*) may be written as:

$$\sum_m \Big\{ \int_{V_m} \Big\{ k\, N_{\alpha,i} N_{\beta,i} T_\beta^{(e)} + \rho c\, N_\alpha N_\beta \frac{\partial T_\beta^e}{\partial t} \Big\} dV + \int_{S_{3m}} h\, N_\alpha N_\beta T_\beta^{(e)} dS + \int_{S_{4m}} h_r N_\alpha N_\beta T_\beta^{(e)} dS \Big\} = \sum_m \Big\{ \int_{V_m} \dot{q}\, N_\alpha dV - \int_{S_{2m}} q\, N_\alpha dS + \int_{S_{3m}} h\, T_\infty N_\alpha dS + \int_{S_{4m}} h_r N_\alpha T_\infty dS \Big\} \quad (\alpha = 1 \ldots \mathrm{N}, \beta = 1 \ldots N) \tag{2.5}$$

wherein a sum over repeated indices is implied; S_{2m}, S_{3m}, and S_{4m} are those parts of external surfaces S_2, S_3, and S_4, respectively, which coincide with the boundary ∂V_m of the element V_m. Equation (2.5) is cast in the familiar matrix form as:

$$\underline{\underline{C}}\, \frac{\partial \underline{T}}{\partial t} + \underline{\underline{\mathbf{K}}}(T)\underline{T} = \underline{R}(T) \tag{2.6}$$

where $(\sim)$ denotes a matrix, $(_)$ denotes a vector, $\underline{T}$ denotes the vector of nodal temperatures. It is seen that: (*i*) when the thermal conductivity, k, is a function of temperature and/or (*ii*) when radiative heat transfer through S_4 is accounted for, equation (2.6) represents a set of *nonlinear*, first-order, ordinary differential equations An Euler backward difference method, described in detail, for instance, by Bathe and Koshgoftaar [7] is used to solve equation (2.6), in conjunction with the "moving element" procedure for modeling the moving heat source as described below.

The numerical modeling of the moving heat source is carried out as follows. In the time increment, Δt, used in the time-integration of equation (2.6) the heat source propagates by ($v\Delta t$). The crack tip, likewise, also propagates by ($v\Delta t$). In the parallel mechanical problem of dynamic crack-propagation under some external dynamic loading, two general procedures have been suggested in prior literature.

Downloaded 02 May 2010 to 171.66.16.54. Redistribution subject to ASME license or copyright; see http://www.asme.org/terms/Terms_Use.cfm

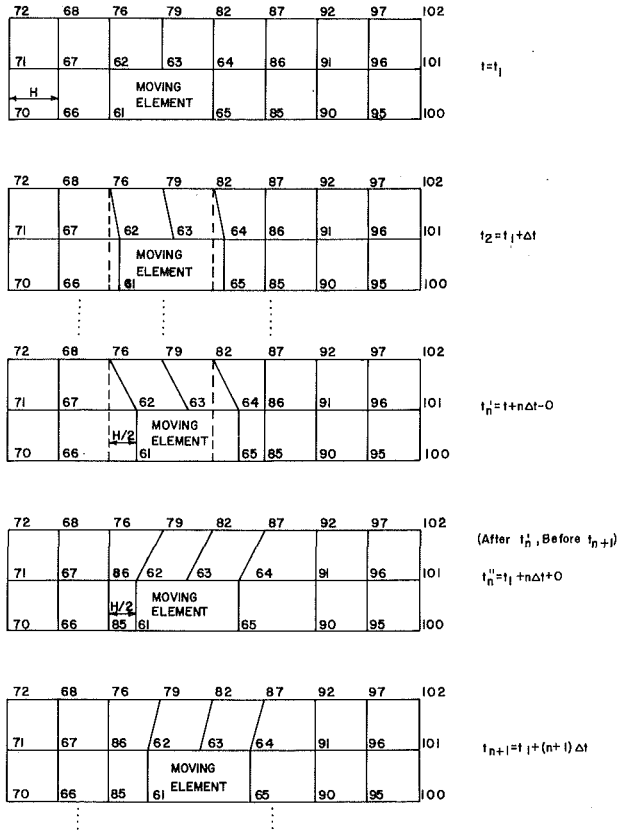


Fig. 2 Schematic of the "moving-element" procedure for modeling the propagating heat source

One is the so-called moving crack-tip element procedure as developed, for instance, by Atluri, Nishioka, and Nakagaki [8] and Nishioka and Atluri [9]. The other is the so-called node-release technique, the history of development and details of which were recently discussed by Brickstad [10]. One of the principal differences between the two approaches concerns the required spacing of finite element nodes along the crack path. In the node-release technique, wherein the crack tip at times t and $t + \Delta t$, respectively, is represented by two adjacent nodes, their spacing must be equal to $(v\Delta t)$. Thus, when v is not a constant, the time step is governed by the requirements of both the accuracy/stability-of-time-integration, as well as node spacing along the crack path. On the other hand, in the propagating element method, moving elements may be shifted by an arbitrary amount in each time increment, Δt.

In this paper, we use the moving-mesh procedure. Referring to Fig. 1(*a*), the mesh near the tip, bounded by the curve Γ_M, is made to propagate rigidly along with the crack tip. When the time step Δt is chosen from the requirements of accuracy and stability of the finite difference scheme, the contour Γ_M and the elements within it are rigidly translated by $C = v\Delta t$ (where v may depend on time); and thus, the crack tip (node 1 in Fig. 1(*b*)) also moves by ΔC. Note that the propagating heat source, bounded by the curve Γ in Fig. 1(*b*), is enclosed within Γ_M. The sequence of this propagating-mesh procedure is illustrated in Fig. 2. As shown in this figure, while the mesh within Γ_M is translated, (*i*) the numbering of nodes of the elements in Γ_M remains unchanged, (*ii*) the shape of elements within Γ_M remains unchanged, and (*iii*) the elements immediately *surrounding* Γ_M get continuously distorted. This continuous distortion of elements surrounding Γ_M, between the times t_1 and t_n, is shown in Fig. 2. The distortion of elements around Γ_M at time t_n may, however, be so severe as to cause numerical problems. (It is well known that a severe distortion of isoparametric elements leads to numerical ill-conditioning of the associated element matrices.) Thus, prior to proceeding with time integration from t_n, the mesh is readjusted as t_n, as shown in Fig. 2. Also, as is well known, the finite difference method of integrating equation (2.6) involves the vectors of nodal temperatures, at two successive instants of times, say t_1 and $t_2 = t_1 + \Delta t$. While the numbering of nodes at t_2 remains unchanged from that at t_1, note that the nodes at t_2 are at spatial locations different from those at t_1. Thus, from the known data at time t_1, the temperature at the spatial location of the nodes at time t_2 is obtained through simple interpolation procedures.[2] These procedures are analogous to the corresponding *deformation* problem of dynamic crack propagation treated, for instance, by Atluri, Nishioka, and Nakagaki [8, 9]; and their further discussion is omitted here.

3 Results

An edge-cracked steel panel of width $w(= 0.6096$ m or 2 ft), semiheight $h(= 0.3\ w)$, and an initial crack length of $a_0(= 0.3\ w)$ is considered. The material properties, ρ and c are taken (see, for instance, Eckert and Drake, [11]) to be such that: $\rho c = 3.64 \times 10^6$ J/m^3 °C (54.28 Btu/ft^3 °F).

In the first series of calculations, designated henceforth as "linear analyses," (*i*) the thermal conductivity is assumed to be independent of temperature and of constant value $k = 1.93 \times 10^5$ J/m hr °C (31.0 Btu/ft hr °F) and (*ii*) the heat transfer due to convection and radiation are ignored. The heat source, as shown in Fig. 1(*b*) is taken to be of width $(0.193\ a_0)$ and semiheight $(0.1\ a_0)$ and thus is of a nearly square shape. The panel is considered to be of unit thickness. The boundary conditions used are: (*i*) $T = T_0$ at the outer boundary segments, i.e., at $X_1 = 0$, $X_1 = w$, and at $X_2 = h$, of the specimen, (*ii*) symmetry condition $T_{,2} = 0$ at the crack plane $X_2 = 0$ (assuming that the crack is simply a surface of discontinuity). Note that these two conditions are also applicable to the problem of an uncracked symmetric panel with a moving heat source symmetric about $x_2 = 0$, and hence the temperature distribution $T(x_1,x_2)$ is also symmetric about $x_2 = 0$. Thus, the present numerical results may be deemed to be applicable both in crack propagation as well as welding type of problems. The intensity of the heat source is first assumed to be uniform in the region Γ (minus the narrow hatched strip) as shown in Fig. 1(*b*) and to be of magnitude: $\dot{q} = (37.26 \times 10^9\ v)$J/m^3 hr ($10^6$ v Btu/ft^3 hr); and four different values of v, viz, $v = 0.762$, 7.62, 76.2, and 762 m/sec (2.5, 25, 250, 2500 ft/sec), respectively, are considered. Figure 3 shows, for $v = 76.2$ m/sec (250 ft/sec), the variation of the temperature with time at fixed locations in the moving coordinate system x_i (i.e., at points with unchanging node numbers in the moving mesh). It is seen that points at fixed locations (in the moving coordinate system x_i) ahead of the propagating heat source are the first ones to reach a condition of steady state. The points (in the x_i system) behind the propagating heat source reach steady-state in a progressive fashion, i.e., the farther the location behind the source, the later is the time for attaining steady state. Similar results (not shown here for space reasons) were obtained for other values of v, and these reveal that the higher the velocity, the shorter is the time, in general, to reach steady state (in the moving coordinate system).

Next, the case of a heat source with $(1/r)$ type[3] of distribution near the origin, i.e., $x_1 = x_2 = 0$, in the moving

[2] Thus the treatment and modeling of the material derivative of temperature in the present paper is entirely analogous to that of the material acceleration in references [8, 9, and 12].

[3] In problems of welding, the heat source may be assumed to be uniformly distributed. However, in problems of crack propagation, the strain-energy density usually has a $(1/r)$ variation near the crack tip. Thus, it is assumed here that the plastically dissipated energy, and hence the heat production, has a $(1/r)$ type variation.

Downloaded 02 May 2010 to 171.66.16.54. Redistribution subject to ASME license or copyright; see http://www.asme.org/terms/Terms_Use.cfm

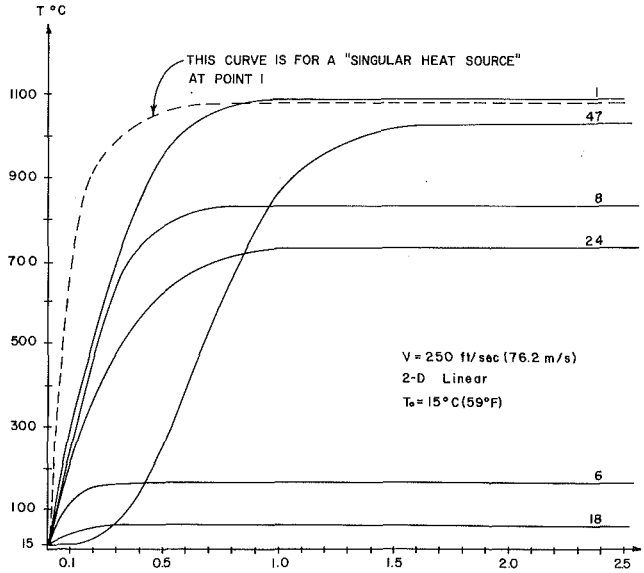


Fig. 3 Variation, with time, of temperature at fixed locations in the moving coordinate system, for v = 76.2 m/sec.

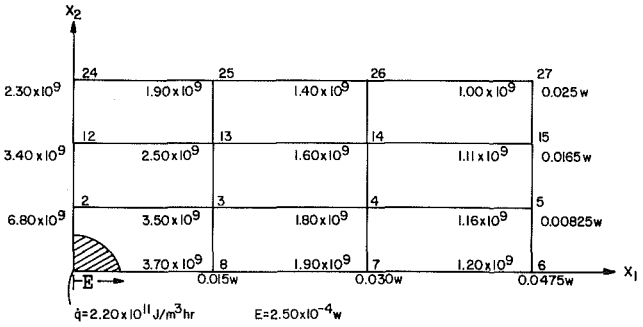


Fig. 4 Nature of "singular distribution" of intensity of the heat source, v = 76.2 m/sec

coodinate system was considered. This singular type distribution is shown in Fig. 4, when the velocity of the heat source is taken to be v = 76.2 m/sec (250 ft/sec). The *total* strength of the heat source described in Fig. 4 is 1.261×10^{10} J/m hr (3.38×10^5 Btu/ft hr). The temperature at the crack tip ($x_1 = x_2 = 0$ in the moving coordinate system or node 1 in the moving mesh of Fig. 1(*b*) shown, as a function of time, in Fig. 3, is nearly identical [i.e., $(T - T_0) \simeq 1097°C(1975°F)$] in steady state for both the cases of uniform as well as singular distributions of heat source. However, the total strength of the heat source for the uniformly distributed case is 5.403×10^{10} J/m hr (1.45×10^6 Btu/ft hr). Thus, while $(T - T_0)$ at the crack tip is nearly the same, the total heat production per unit time in the uniformly distributed case is roughly 4.3 times greater than that when the source distribution is of a singular type. Next, we consider the temperature variations at fixed locations in the stationary coordinate system X_i, such as point A (in the X_i system) as shown in Figs. 1 and 2. The variation with crack growth $(a - a_0)$ $[= v\,x(t - t_0)]$ of the temperature at A is shown for four different cases of v = 0.762, 7.62, 76.2, 762 m/sec (2.5 to 2500 ft/sec), respectively, in Fig. 5. It is seen that in all cases, the temperature at A changes very slowly prior to the arrival of the heat source at A and increases rapidly as the heat source arrives. The temperature at A reaches a maximum when the crack tip (or the origin $x_1 = x_2 = 0$ of the heat source) is almost at A; and as the heat source (and the crack-tip) moves past A, the temperature at A begins to fall. It is seen from Fig. 5 that the temperature variation as well as the maximum temperature at A are nearly identical for the cases v = 76.2 and 762 m/sec, respectively,

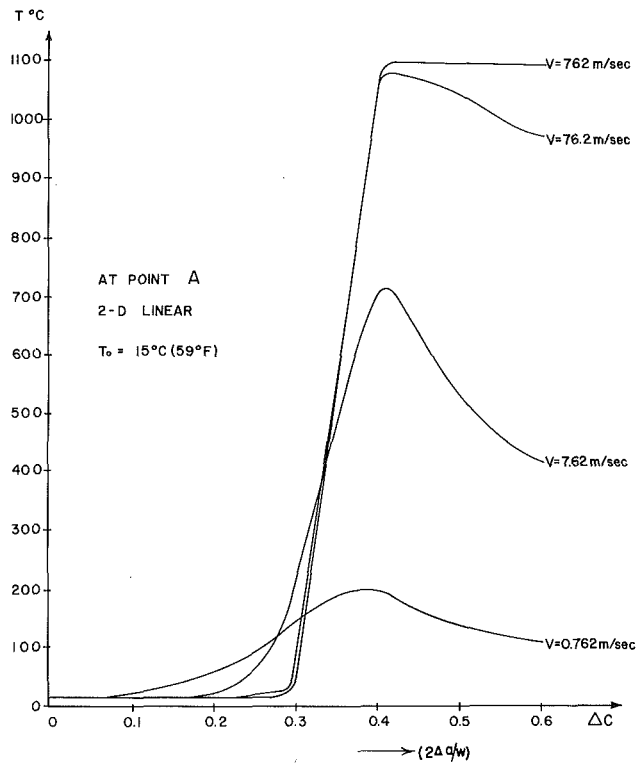


Fig. 5 Variation of temperature, with crack growth at point A, fixed in the stationary coordinate system (see Fig. 1(*a*)) for various values of v

until the arrival of the crack tip, after which time the temperature at A remains nearly the same for the higher velocity, while it drops for v = 76.2 m/sec.

In the next set of calculations, the thermal conductivity, k, was assumed to be a function of temperature in the following fashion. The complete set of data in Table 1 may be found in Eckert and Drake [11]. This set of calculations will henceforth be referred to as "nonlinear calculations."

In the final set of calculations, we assume that the temperature distribution is uniform in the thickness direction (X_3), and include the effects of both convective and radiative heat transfer through the lateral surfaces (i.e., surfaces normal to X_3 axis) of the panel. Henceforth we refer to these as "approximate three-dimensional" calculations, while recognizing that these, at the same time, are also strongly nonlinear calculations. We note that in these approximate three-dimensional calculations, the effect of temperature dependence of conductivity, k, is also simultaneously included. Two different values of the thickness of the plate are considered in these approximate three-dimensional analyses: (*i*) 10mm and (*ii*) 1mm, respectively. For each of the two lateral surfaces, we assume the respective values: h = 9.052 J/hr m^2 °C and $F\epsilon\sigma = 1.848 \times 10^{-4}$ J/hr m^2 °C^4 (0.155×10^{-8} Btu/hr ft^2 °F^4).

The steady-state temperature distributions at fixed locations in the moving coordinate system x_i are shown, when v = 76.2 m/sec, in Figs. 6(*a*) and (*b*) respectively, for each of the four cases considered: (*i*) linear calculation, (*ii*) nonlinear calculation, (*iii*) approximate three-dimensional calculation with thickness of 10mm, and (*iv*) approximate three-dimensional calculation with thickness of 1mm. Similar results where obtained for the cases v = 0.762, 7.62, 762 m/sec, respectively, but are not shown here for space reasons. In Fig. 6(*a*, *b*), the heat source is assumed to have a uniform distribution.

Now, an examination of Fig 6(*a*, *b*) for the case v = 76.2 m/sec reveals that: (*i*) in the nonlinear calculation the steady-state temperatures at locations in the moving coordinate

Downloaded 02 May 2010 to 171.66.16.54. Redistribution subject to ASME license or copyright; see http://www.asme.org/terms/Terms_Use.cfm

Table 1 Dependence of k on Temperature

°C :	0	100	200	300	400	600	800	1161	3316
k : (J/m hr °C) × 10^4	19.76	18.68	17.26	16.18	15.10	12.58	11.14	11.14	11.14

Table 2 Ratio (heat outflow through Γ/total heat in source)

vel: m/s	$v = 0.762$	7.62	76.2	762
two-dimensional linear	(0.8861[a]) 0.9398	(0.3120[a]) 0.4857	0.1014 (0.0278[a])	0.0179 (0.004045[a])
two-dimensional nonlinear	0.8828	0.3963	0.0884	0.0150
three-dimensional (t = 10mm)	0.9583	0.5140	0.1043	0.0167
three-dimensional (t = 1mm)	0.9857	0.8009	0.2203	0.0315

[a]Singular Source

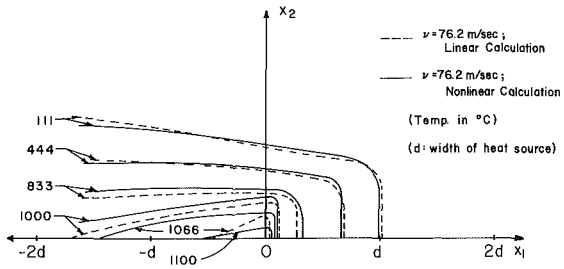


Fig. 6(*a*) Steady-state temperature distribution in the moving coordinate system: v = 76.2 m/sec; linear and nonlinear calculations

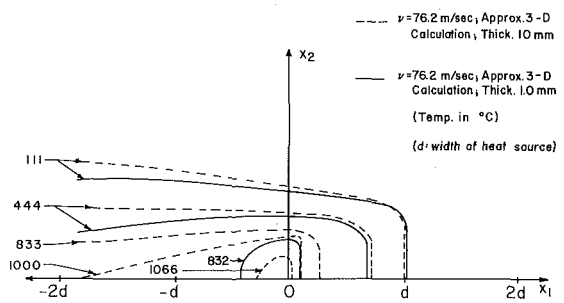


Fig. 6(*b*) Steady-state temperature distribution in the moving coordinate system; v = 76.2 m/sec., approximate three-dimensional calculation, thickness = 10mm and 1mm, respectively

Fig. 6

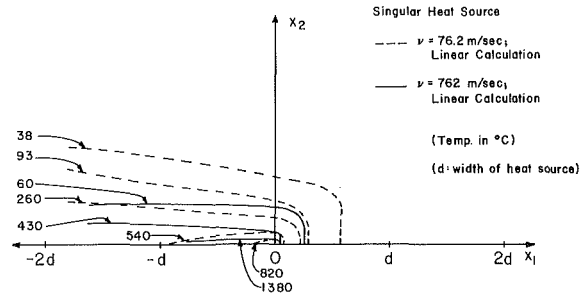


Fig. 7 Steady-state temperature distribution in the moving coordinate system, for "linear calculations," and v = 76.2 m/sec and 762 m/sec, *respectively, for a singular heat-source*

system behind the heat source, as well as in the region $0 < x_1 < (d/20)$ of the heat source itself, are higher than in the linear case. On the other hand, the temperature at locations ahead of the heat source, as well as in the region $(d/2) < x_1 < 0$, is somewhat lower in the nonlinear case than that in the linear case. In both linear and nonlinear calculations, the temperature ahead of the heat source quickly reduces to the ambient temperature T_0(= 15°C); (*ii*) in the case of approximate three-dimensional calculations for the thick specimen, the steady-state temperature distribution is more or less analogous to that in the linear case. Thus, in this case, the effects of reduced thermal conductivity at higher temperatures and those of convective and radiative heat transfer from the lateral surfaces, appear to nullify each other; (*iii*) in the case of approximate three-dimensional calculation for the thin specimen, the steady-state temperature distribution in the moving coordinate system is of significantly lower magnitude than that in the linear case. Thus, in thin panels, the effect of convection and radiation from lateral surfaces is predominant. Observations from results (not shown here for space reasons) for lower velocities (v = 0.762, 7.62 m/sec) and higher velocity (v = 762 m/sec) include: (*i*) for lower velocities, the temperature, at fixed locations in the moving coordinate system, *all around the heat source* is significantly higher in the nonlinear case than the linear case; (*ii*) the contours of constant temperature become "narrower" (i.e., they become parallel to the x_1 axis, and of very small "height") as the speed increases; and (*iii*) in general, the effects of temperature-dependence of thermal conductivity and convective and radiative heat transfer, which play a dominant role at smaller velocities (≤76.2 m/sec), become unimportant as the speed of the heat source increases (≥ 600 m/sec).

Finally, the steady-state temperature contours in the moving coordinate system, from a linear calculation, for the case of a singular-distribution of the heat source as shown in Fig. 4, are shown in Fig. 7 for v = 76.2 and 762 m/sec, respectively. It is seen that for v = 76.2 m/sec, the maximum temperature at the propagating origin of the heat source (or the crack-tip) is roughly the same as that in Fig. 6(*a*) for a uniformly distributed heat source even though the total heat in the latter case is roughly 4.3 times that in the former case. However, the zone of high temperature is much smaller in the singular source case. The effect of a singular heat source is much more pronounced at higher velocities (v = 762 m/sec).

We now present results for the outflow of heat from a contour Γ, shown in Fig. 1(*b*), which is the boundary of the heat source. Note that Γ moves rigidly along with the heat source. The ratio of the heat outflow through Γ and the total heat in the source is shown in Table 2 for various cases. It is seen from Table 2 that the heat flow through Γ decreases very rapidly with velocity; and at around $v \sim 609.6$ m/sec, it is less than 2 percent; thus the conditions in the process zone become nearly adiabatic.

4 A Brief Discussion of the Fracture Problem

In the "linear calculation," for a rectangular (height 2δ, width d) heat source wioth uniform intensity, the maximum temperature occurs at the center of the heat source for low velocities, while at higher velocities, the maximum temperature may exist behind the heat source in the moving coordinate system. We may write:

Downloaded 02 May 2010 to 171.66.16.54. Redistribution subject to ASME license or copyright; see http://www.asme.org/terms/Terms_Use.cfm

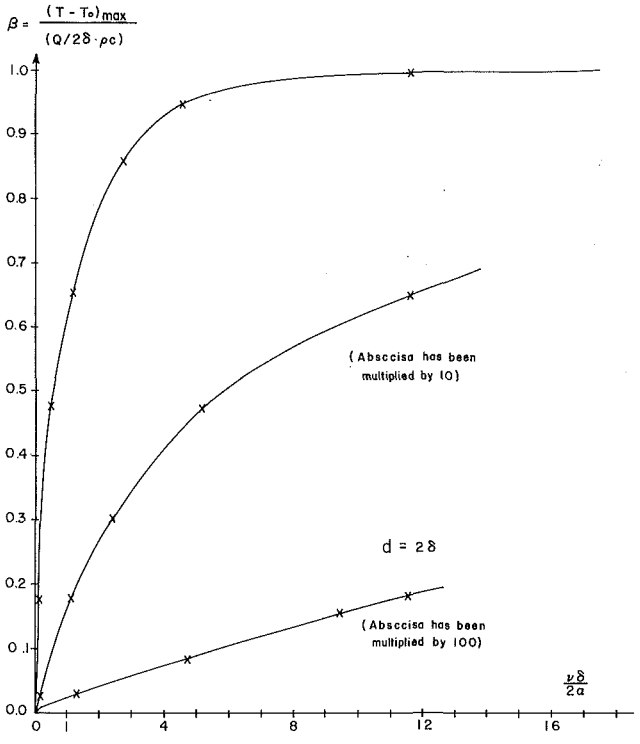


Fig. 8 The function $\beta(\psi)$ of equation (4.1)

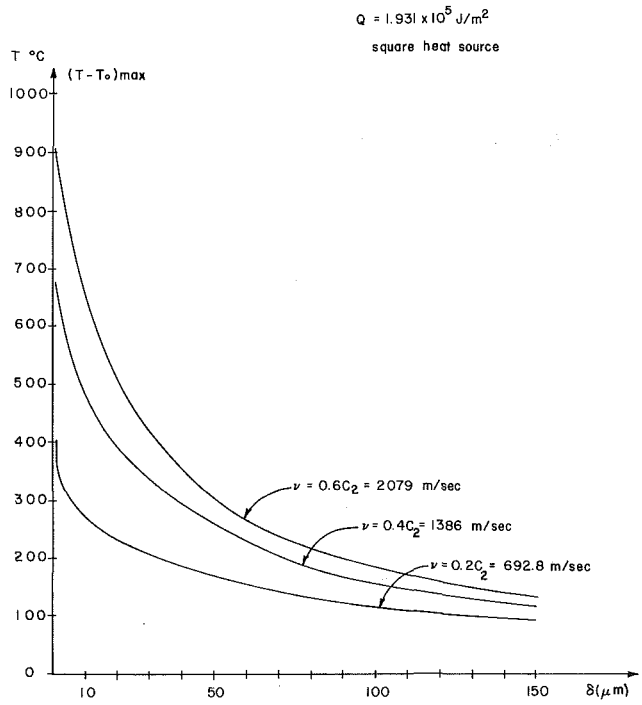


Fig. 9 Maximum temperature near a propagating crack-tip for various values of v (velocity of propagation) and δ (heat source size)

$$(T-T_0)_{\max} = \frac{Q}{(2\delta)(\rho c)}\,\beta(\psi,d) \tag{4.1}$$

where

$$\psi = \left(\frac{v\delta}{2\alpha}\right) \tag{4.2}$$

for a roughly square-shaped source. In the foregoing, α is the thermal conductivity coefficient. The dependence of β on ψ, as discerned from the presently computed results is shown in Fig. 8. It is seen from Fig. 8 that if, while keeping v = constant, δ is made to tend to zero, then $\beta \to 0$. Thus, in the case of a heat source of given strength Q, the temperature near the heat source would be of a finite value even when the heat source is of a very small size. This conclusion is at variance with that of Weichert and Schonert [6] who first consider a heat source of a given *constant size* δ, and find that $\beta \to 1$ as v tends to be very large (and thus $v\delta$ tends to be very large). They then conclude from (4.1) that $(T - T_0)_{\max} = [Q/(2\delta)(\rho C)]$, i.e., $(T - T_0)_{\max}$ varies as $(1/\delta)$.

Following Weichert and Schonert [6], we assume that in the case of structural steels, the total of inelastically dissipated energy and "surface energy" per unit of crack extension is of the order of 10^5 J/m^2 ($\approx$8.805 Btu/ft.^{2}). Specifically, we assume that the total heat generated Q, per unit of crack extension, is 1.931×10^5 J/m^2. We now proceed to estimate the maximum temperature in the vicinity of the tip of a crack propagating at plausible velocities, with a plausible size for the propagating heat source. First suppose that $\delta = 10\mu$m ($\approx 3.3 \times 10^{-5}$ ft). Let $v = 0.6C_2$ (C_2 being the shear-wave speed) i.e., v = 2078 m/sec. ($\approx$6820 ft./sec.). We take $\rho C = 3.64 \times 10^6$ J/m^3 °C and α = .0549 m^2/hr. From Fig. 8, we see that for the postulated value of $\psi(= v\delta/2\alpha)$ of 0.19, $\beta \simeq 0.26$. Thus, we calculate $(T - T_0)_{\max}$ to be about 668°C. Using similar procedures, $(T - T_0)_{\max}$ values are computed for various values of δ and v, respectively, and are shown in Fig. 9. Considering the microstructure of a typical steel, the grain size is roughly 10μm. The regions wherein finite strains are present near the crack tip, and the process zone itself, are roughly of the size of the order of several grain sizes. Further, the speed of fast crack propagation in steel is usually less than $0.6C_2$. Hence, we may conclude that the maximum temperature near the propagating crack-tip in steel may be less than 666°C. In the preceding discussion, the distribution of the intensity of the heat source has been assumed to be uniform. Instead, a heat source wherein the distribution of intensity is singular, as in Fig. 4, may be assumed. Recall that in Fig. 4, the radius of the zone of strong intensity is: $E \approx 5.26 \times 10^{-3} d$. The maximum temperature produced in this case has been shown to be nearly the same (at v = 76.2 m/sec) or higher (when v = 762 m/sec) as in the uniformly distributed case, while the total heat in the singular case is roughly 4.3 times smaller. However, in the realistic case of crack propagation, if a singular heat distribution is assumed, the value of E cannot be as small as 5×10^{-3} the size of the process zone. A reasonable assumption may be to consider the extreme case when the heat source is uniformly distributed over a very small region, say $d = 1\mu$m, below which a continuum analysis may be questionable. Even for this extreme value of d, Fig. 9 indicates that the maximum temperature near the crack tip may be about 1660°F (900°C).

Also from the contours of constant temperature in Fig. 6 (and others not included here), and the dependence of the quantity of heat outflow from a contour close to and rigidly moving with the heat source as shown in Table 2, it may be seen that the conditions near the propagating crack tip are isothermal for low velocities ($\psi << 1$) and adiabatic at high velocities ($\psi >> 10$) of crack propagation. This is also in accord with the observations of Weichert and Schonert [6].

The present analysis indicates that at larger, but realistic, speeds of crack-propagation, while the front of the propagating heat source remains cold, higher temperatures (of the order of 1000°C) may persist behind the propagating heat source even at distances of the order of the size of the heat source. Thus, in dynamic fracture, higher temperatures may prevail in the wake of the propagating crack-tip and process zone. The authors are currently studying a coupled thermoplastic problem to assess the effects, if any, of the forementioned temperature rise near the crack tip propagating under external mechanical action.

Downloaded 02 May 2010 to 171.66.16.54. Redistribution subject to ASME license or copyright; see http://www.asme.org/terms/Terms_Use.cfm

Acknowledgments

The first author (Z-B. K.) acknowledges support from Xian Jiaotong University during his stay at Georgia Institute of Technology. Partial support from the U.S. Office of Naval Research under Contract N00014-78-C-0636 to Georgia Institute of Technology and the encouragement of Dr. Y. Rajapakse are thankfully acknowledged. It is a pleasure to record here our thanks to Ms. J. Webb for her assistance in the preparation of this manuscript.

References

1 Rice, J. R., "An Examination of the Fracture Mechanics Energy Balance from the Point of View of Continuum Mechanics," *proc. Ist Int. Congr. Fract.*, Yokobori, T., et al., eds., Japanese Soc. for Strength and Fract., Tokyo, Vol. 1, 1966, eds., pp. 309–340.

2 Schönert, K., and Weichert, R., "Die Wärmetönung des Bruches in Eisen und ihre Abhängigkeit von der Ausbreitungsgeschwindigkeit," *Chem. Ing. Technique*, Vol. 41, 1969, p. 295.

3 Döll, W., "Application of an Energy Balance and an Energy Method to Dynamic Crack Propagation," *Int. J. of Fract.*, Vol. 12, 1976, pp. 595–605.

4 Weichert, R., and Schönert, K., "On the Temperature Rise at the Tip of a Fast Running Crack," *J. Mech. Phys. Solids*, Vol. 22, 1974, pp. 127–133.

5 Weichert, R., and Schönert, K., "Temperature Distribution Produced by a Moving Heat Source," *Q. J. Mech. Appl. Math.*, Vol. XXXI, Part 3, 1978, pp. 363–379.

6 Weichert, R., and Schönert, K., "Heat Generation at the Tip of a Moving Crack," *J. Mech. Phys. Solids*, Vol. 26, 1978, pp. 151–161.

7 Bathe, K. J., and Khoshgoftaar, "Finite Element Formulation and Solution of Nonlinear Heat Transfer," *J. Nuclear Eng. and Design*, Vol. 51, 1979, pp. 389–401.

8 Atluri, S. N., Nishioka, T., and Nakagaki, M., "Numerical Modeling of Dynamic and Nonlinear Crack Propagation in Finite Bodies, by Moving Singular-Elements," in *Nonlinear and Dynamic Fracture Mechanics*, Perrone, N., and Atluri, S. N., eds., ASME-AMD, Vol. 35, 1979, pp. 37–66.

9 Nishioka, T., and Atluri, S. N., "Numerical Modeling of Dynamic Crack Propagation in Finite Bodies by Moving Singular Elements—Part I: Formulation, Part II: Results," ASME JOURNAL OF APPLIED MECHANICS, Vol. 47, 1980, pp. 570–582.

10 Brickstad, B., "A Viscoplastic Analysis of Rapid Crack Propagation Experiments in Steel," *J. Mech. Phys. Solids*, Vol. 31, 1983, pp. 307–327.

11 Eckert, E. R. G., and Drake, R. M., *Analysis of Heat and Mass Transfer*, McGraw Hill, 1972.

12 Stonesifer, R. B., Nishioka, T., and Atluri, S. N., "An Evaluation of Several Moving Singularity Finite Element Models for Fast Fracture Analysis," *Engineering Fracture Mechanic*, Vol. 15, No. 2, 1981, pp. 205–218.

Downloaded 02 May 2010 to 171.66.16.54. Redistribution subject to ASME license or copyright; see http://www.asme.org/terms/Terms_Use.cfm

Effect of Inertia on Finite Near-Tip Deformation for Fast Mode-III Crack Growth

J. D. Achenbach
Fellow ASME

N. Nishimura

Department of Civil Engineering,
Northwestern University,
Evanston, Ill. 60201

The combined effects of finite deformation and material inertia have been analyzed for fast crack growth under antiplane loading conditions. A steady-state dynamic solution has been obtained for the finite strain on the crack line, from the moving crack tip to the moving transition boundary with the zone of small strains. The crack propagates in a material with a response curve in uniform shear that is linear at small strains, and which remains constant once a critical strain has been exceeded. The corresponding quasi-static solution is given in the full zone of large deformation. For the dynamic formulation, an explicit expression for the crack-line strain has been obtained by expanding the displacement in a power series in the distance to the crack line, with coefficients that depend on the distance to the moving crack tip. Substitution in the equation of motion yields a nonlinear ordinary differential equation for the relevant coefficient, which can be solved rigorously. The finite deformation crack-line fields have been matched to appropriate small-strain fields at the transition boundary. The principal result is that the dynamic strain remains bounded at the crack tip, apparently due to the effect of material inertia. The crack-line strain has been plotted for several crack-tip speeds. It decreases with higher crack-tip speed. An explicit expression has been given for the extent of the zone of finite deformation, as a function of the crack tip speed and the far-field loading.

1 Introduction

Several recent investigations have been concerned with the effects of finite deformations on the fields of stress and deformation near a crack tip. Most notable are a series of papers by Knowles and Knowles and Sternberg, in which full nonlinear equilibrium theory of homogeneous and isotropic, incompressible elastic solids has been employed to construct fields near the tip of a crack. A summary has been presented in reference [1]. The most complete results have been obtained for a crack in a body subjected to finite antiplane shear, as reported in references [2, 3]. Related work for the antiplane shear case has been carried out by Lo [4], who found that for certain forms of the strain energy density, the formulation of the problem becomes formally indentical to those of certain previously studied small strain elastic-plastic problems.

The present paper is also concerned with finite deformations near a crack tip under antiplane shear loading. The formulation of the governing equations follows by-and-large references [2, 3]. A notable difference is, however, that we study a growing crack, and that the effects of inertia have been included in the formulation. We consider a strain energy density that yields a response curve for uniform shear which is linear at small strains, and which maintains a constant plateau once a certain critical strain has been exceeded.

The method of solution employs power series expansions in the distance to the crack line, with coefficients that depend on the distance to the crack tip. To analyze small strain crack line fields in elastic perfectly-plastic materials, such expansions have previously been used by Achenbach and Dunayevsky [5] and Achenbach and Li [6] for quasistatic problems, and by Achenbach and Li [7] for dynamic crack growth cases. Substitution of a displacement expansion in the equation of motion yields a nonlinear ordinary differential equation for the relevant coefficient, which can be solved rigorously. The crack-line fields have been matched to appropriate small strain elastic fields at a transition boundary.

The paper also includes a section that shows that for dynamic crack growth the stresses and the displacement gradients are continuous across the moving transition boundary that precedes the crack tip, at least near the crack line. Continuity of these quantities all around the transition boundary has been shown for the quasistatic case. Furthermore, the full quasistatic field has been obtained in the zone of large deformation. For the elastic material that is considered in this paper, the static fields for a moving and a stationary crack are identical for coordinates centered at the crack tip. The quasistatic crack-tip strain is shown to be singular. An independent application of the expansion

Contributed by the Applied Mechanics Division for publication in the JOURNAL OF APPLIED MECHANICS.

Discussion on this paper should be addressed to the Editorial Department, ASME, United Engineering Center, 345 East 47th Street, New York, N.Y. 10017, and will be accepted until two months after final publication of the paper itself in the JOURNAL OF APPLIED MECHANICS. Manuscript received by ASME Applied Mechanics Division, March, 1984; final revision, July, 1984.

Copyright © 1985 by ASME
Downloaded 02 May 2010 to 171.66.16.54. Redistribution subject to ASME license or copyright; see http://www.asme.org/terms/Terms_Use.cfm

method yields the correct crack-line approximation to the exact solution.

The analysis of the crack-line fields for steady-state dynamic crack growth has yielded the most surprising result of this paper. It is shown that the effect of inertia is to remove the strain singularity at the crack tip. Thus, for the dynamic problem both the stress and the strain are bounded at the crack tip. Curves are presented that plot the strain versus distance along the crack tip. An expression has been obtained for the length of the zone of large deformation as a function of the crack-tip speed.

2 Governing Equations

The equations that govern finite antiplane shear deformation in an unbounded body containing a crack have been formulated by Knowles [2] and Knowles and Sternberg [3]. In this section we briefly review the formulation of [2] and [3] in a slightly different notation, we introduce a different strain-energy density than was used in these papers, and we extend the formulation to the dynamic case.

Let X_i and x_i be the Cartesian coordinates of a typical point in the undeformed and deformed states, respectively. For antiplane strain we have

$$x_3 = X_3 + U(X_1, X_2, t), \quad x_\alpha = X_\alpha \qquad \alpha = 1,2 \tag{2.1}$$

The corresponding components of the deformation gradient $\mathbf{F}$ are

$$F_{ij} = \frac{\partial x_i}{\partial X_j} = \begin{pmatrix} \delta_{\alpha\beta} & 0 \\ U_{,\beta} & 1 \end{pmatrix} \tag{2.2}$$

and the first fundamental scalar invariant is

$$I_1 = tr(F^T F) = 3 + \epsilon^2, \tag{2.3}$$

where

$$\epsilon^2 = U_{,\alpha} U_{,\alpha}, \qquad U_{,\alpha} = \partial U / \partial X_\alpha \tag{2.4a,b}$$

We consider an incompressible material. Hence the deformation is locally volume preserving, and the Jacobian of the mapping (2.1) is

$$J = \det(\mathbf{F}) = 1 \tag{2.5}$$

Let τ be the actual (Cauchy) stress tensor field in the deformed body, and let $S(X_\alpha, t)$ be the corresponding nominal (Piola) stress field in the undeformed configuration. Then

$$\tau = SF^T, \qquad S = \tau(\mathbf{F}^T)^{-1} \tag{2.6a,b}$$

The analysis of this paper is restricted to the class of incompressible solids for which W depends on I_1 only

$$W = W(I_1) \qquad \text{for all} \qquad I_1 \geq 3, \quad W(3) = 0 \tag{2.7}$$

As discussed by Knowles [1], we then have

$$\tau_{3\alpha} = \tau_{\alpha 3} = S_{3\alpha} = S_{\alpha 3} = 2W'(I_1) U_{,\alpha}, \tag{2.8}$$

$$\tau_{\alpha\beta} = S_{\alpha\beta} = S_{33} = 0, \qquad \tau_{33} = 2W'(I_1)\epsilon^2 \tag{2.9}$$

where ϵ is defined by (2.4a,b), and

$$W'(I_1) = dW/dI_1, \tag{2.10}$$

For dynamic problems these equations are supplemented by

$$S_{3\alpha,\alpha} = \rho_0 \ddot{U}, \qquad (\dot{}) = \partial/\partial t, \tag{2.11}$$

where ρ_0 is the mass density in the reference configuration.

To define the desired relation between $S_{3\alpha}$ and $U_{,\alpha}$, we consider the static problem of an unbounded body, which is subjected to the following condition at infinity

$$U(X_1, X_2) = \kappa X_2 + 0(1) \qquad \text{as} \qquad X_\alpha X_\alpha \to \infty \tag{2.12}$$

The solution then is

$$U(X_1, X_2) = \kappa X_2 \qquad \text{for all} \qquad (X_1, X_2) \tag{2.13}$$

and

$$\tau_{23} = \tau_{32} = \tau(\kappa) = 2W'(3 + \kappa^2)\kappa,$$

$$\tau_{33} = \tau(\kappa)\kappa \quad (0 \leq \kappa < \infty) \tag{2.14a,b}$$

The graph of τ versus $\kappa (0 \leq \kappa < \infty)$ is called the response curve in simple shear. In this paper we wish to consider a response curve of the form shown in Fig. 1, which is defined by

$$\tau(\kappa) = \begin{cases} \mu\kappa & \kappa \leq \epsilon_0 \qquad (2.15a) \\ \mu\epsilon_0 & \kappa \geq \epsilon_0 \qquad (2.15b) \end{cases}$$

The corresponding strain energy density for an incompressible elastic solid then follows from (2.14a) as

$$W(I_1) = \int_0^{(I_1 - 3)^{1/2}} \tau(\kappa)\, d\kappa \qquad (3 \leq I_1 < \infty) \tag{2.16}$$

Substitution of (2.15a,b) into (2.16) yields

$$W(I_1) = \begin{cases} \frac{1}{2}\mu(I_1 - 3) & 3 \leq I_1 \leq 3 + \epsilon_0^2 \qquad (2.17a) \\ \mu[(I_1 - 3)\epsilon_0^2]^{1/2} - \frac{1}{2}\mu\epsilon_0^2 & 3 + \epsilon_0^2 \leq I_1 \qquad (2.17b) \end{cases}$$

The stress-strain relations follow from (2.8) and (2.17) as

$$S_{3\alpha} = \mu U_{,\alpha} \qquad \text{for} \quad 0 \leq \epsilon \leq \epsilon_0, \tag{2.18}$$

$$S_{3\alpha} = S_0 U_{,\alpha}/\epsilon \quad \text{for} \quad \epsilon \geq \epsilon_0, \tag{2.19}$$

where

$$S_0 = \mu\epsilon_0 \tag{2.20}$$

It is noted that (2.19) implies that for $\epsilon > \epsilon_0$ we have

$$S_{31}^2 + S_{32}^2 = S_0^2. \tag{2.21}$$

Unfortunately, the Cauchy stresses τ_{ij} do not satisfy a relation of analogous simplicity.

3 Discontinuities Across a Propagating Transition Boundary

A surface that separates regions where the constitutive behavior is defined by (2.18) and (2.19), respectively, will be called a transition boundary. In this section we examine the possibility of propagating discontinuities in the stress, $S_{ij}(\mathbf{X}, t)$, the displacement gradient, $F_{ij}(\mathbf{X}, t)$, and the particle velocity, $\dot{x}_i(\mathbf{X}, t)$, across a propagating transition boundary, for the case that the linear relation (2.18) holds ahead of the moving surface, while the nonlinear relation (2.19) applies behind it.

The propagating surface is represented by the relation

$$\Sigma(X, t) = 0 \tag{3.1}$$

The unit normal to the surface is denoted by $\mathbf{N}$. The speed of propagation V_N, which is the speed with which the surface traverses the material, is positive when the surface moves in the direction of $\mathbf{N}$. A discontinuity of a field quantity, say $G(X, t)$, is denoted in the usual manner by

$$[[G]] \equiv G^+ - G^- \tag{3.2}$$

where G^+ and G^- are the limits as $\mathbf{X}$ approaches a point on the surface along paths entirely ahead of and entirely behind it.

The displacement is continuous, and hence deformation gradients in the surface are also continuous

$$[[\partial x_i / \partial \Gamma_\beta]] = 0, \qquad \beta = 1,2 \tag{3.3}$$

where Γ_1 and Γ_2 are two independent coordinates in the surface $\Sigma(X, t) = 0$. The balance of linear momentum yields the well-known relation

$$[[S_{ij}]] N_j = -\rho_0 V_N [[\dot{x}_i]], \tag{3.4}$$

where ρ_0 is the mass density in the reference configuration, and $\dot{\mathbf{x}}$ denotes the particle velocity. From the balance of

Downloaded 02 May 2010 to 171.66.16.54. Redistribution subject to ASME license or copyright; see http://www.asme.org/terms/Terms_Use.cfm

energy it follows that the energy dissipated locally as the surface passes, may be written as

$$H=[[W+\frac{1}{2}\rho_0\dot{x}_i\dot{x}_i]]V_N+[[\dot{x}_iS_{ij}]]N_j, \tag{3.5}$$

where $W(X,t)$ is the strain energy density. It is assumed that

$$H\geq 0, \tag{3.6}$$

i.e., the energy dissipation across a propagating transition boundary cannot be negative [8].

It can be verified that H may be rewritten as

$$H=[[W-\frac{1}{2}\rho_o\dot{x}_i\dot{x}_i]]V_N+\dot{x}_i^+[[\rho_0\dot{x}_iV_N+S_{ij}N_j]]$$
$$+[[\dot{x}_i]](\rho_0\dot{x}_iV_N+S_{ij}N_j)^- \tag{3.7}$$

The second term on the right-hand side cancels by virtue of equation (3.4). A further rearrangement of H yields

$$H=([[W]]-\frac{1}{2}\rho_0[[\dot{x}_i]][[\dot{x}_i]])V_N+[[\dot{x}_i]]\bar{S_{ij}}N_j, \tag{3.8}$$

or, by the use of (3.4) in the second term,

$$H=[[W]]V_N+\frac{1}{2}[[\dot{x}_i]]([[S_{ij}]]N_j+2\bar{S_{ij}}N_j)$$

$$=[[W]]V_N+\frac{1}{2}[[\dot{x}_i]](S_{ij}^++\bar{S_{ij}})N_j \tag{3.9}$$

By using the compatibility relation

$$[[\dot{x}_i]]=-[[\partial x_i/\partial N]]V_N, \tag{3.10}$$

we finally find

$$H=\{[[W]]-\frac{1}{2}[[\partial x_i/\partial N]](S_{ij}^++\bar{S_{ij}})N_j\}V_N \tag{3.11}$$

For antiplane shear, equation (3.11) reduces to

$$H=\{[[W]]-\frac{1}{2}[[\partial x_3/\partial N]](S_{3\alpha}^++\bar{S_{3\alpha}})N_\alpha\}V_N \tag{3.12}$$

where $\alpha=1, 2$. An expression similar to (3.11) has been presented in [9].

In this paper the interest is focussed on a field $x_3(X_1,X_2,t)$ which is antisymmetric with respect to the X_1 axis, but which has discontinuities across a transition boundary which is symmetric relative to $X_2=0$, and on which $V_N>0$. This case applies, for example, to a transition boundary ahead of a Mode-*III* crack tip. The condition $H\geq 0$ then becomes

$$\bar{H}=H/V_N=[[W]]-\frac{1}{2}[[\partial x_3/\partial N]](S_{3\alpha}^++\bar{S_{3\alpha}})N_\alpha\geq 0 \tag{3.13}$$

Let us first consider the intersection point on $X_2=0$, which is defined by $X_2=0, X_1=X_0(t)$. Because of antisymmetry we have $x_3(X_1,0,t)\equiv 0$, and hence

$$\partial x_3/\partial X_1\equiv 0, \tag{3.14}$$

while (3.3) implies

$$\epsilon^-=\epsilon^+=\partial x_3/\partial X_2=\epsilon_0 \tag{3.15}$$

where ϵ is defined by (2.4*a*). By using the expressions for W given by (2.17*a*) and (2.17*b*), it then follows that

$$\bar{H}=[[W]]=\frac{1}{2}\mu(\epsilon^+)^2-\mu\epsilon^-\epsilon_0+\frac{1}{2}\mu\epsilon_0^2=0 \tag{3.16}$$

Next we consider a position (X_0,dX_2). Here we have by (3.13) and (3.16)

$$d\bar{H}\geq 0, \tag{3.17}$$

where

$$d\bar{H}=\mu\epsilon^+d\epsilon^+-\mu\epsilon_0d\epsilon^--\frac{1}{2}(\epsilon_N^+-\epsilon_N^-)\left(\mu d\epsilon_N^+\right.$$

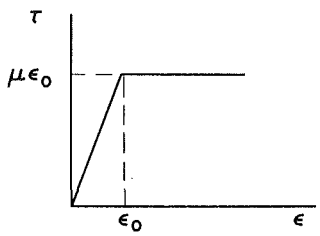


Fig. 1 Response curve in simple shear

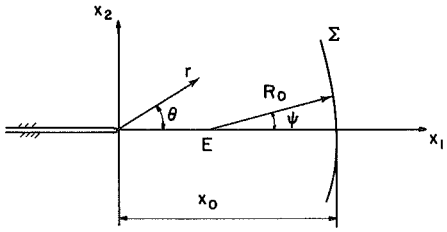


Fig. 2 Geometry of crack tip and transition boundary

$$\left.+\frac{\mu\epsilon_0}{\epsilon^-}d\epsilon_N^--\frac{\mu\epsilon_0\epsilon_N^-}{(\epsilon^-)^2}d\epsilon^-\right)$$
$$-\frac{1}{2}(d\epsilon_N^+-d\epsilon_N^-)(\mu\epsilon_N^++\mu\epsilon_0\frac{\epsilon_N^-}{\epsilon^-}) \tag{3.18}$$

In (3.18),

$$\epsilon_N=\partial x_3/\partial N \tag{3.19}$$

Since $\epsilon^+=\epsilon^-=\epsilon_0$ and $\epsilon_N^+=\epsilon_N^-=0$, equation (3.18) reduces to

$$\mu\epsilon_0(d\epsilon^+-d\epsilon^-)\geq 0 \tag{3.20}$$

In the domain of small deformation the quantity ϵ cannot increase with distance from the crack line, hence $d\epsilon^+\leq 0$. On the other hand, ϵ maintains the condition of large deformation, $\epsilon\geq\epsilon_0$, behind the transition boundary, and hence $d\epsilon^-\geq 0$. Consequently (3.20) can be satisfied only if

$$d\epsilon^+=d\epsilon^-\equiv 0 \tag{3.21}$$

Equations (3.15) and (3.21) imply

$$[[\epsilon]]=0 \tag{3.22}$$

Equation (3.22), together with the constitutive equations, (2.18) and (2.19), give

$$[[S_\alpha]]=\mu[[\partial x_3/\partial X_\alpha]]=\mu N_\alpha[[\partial x_3/\partial N]] \tag{3.23}$$

where (3.3) has also been used. Next (3.4) and (3.10) yield

$$[[S_{3\alpha}]]N_\alpha-\rho_0V_N^2[[\partial x_3/\partial N]]=0 \tag{3.24}$$

Substitution of (3.23) subsequently gives

$$\mu(1-M_N^2)[[\partial x_3/\partial N]]=0, \tag{3.25}$$

where $M_N^2=\rho_0V_N^2/\mu$. It follows that

$$[[\partial x_3/\partial N]]=0 \tag{3.26}$$

provided that $M_N<1$. Equation (3.26) in turn implies by (3.10) that $[[\dot{x}_3]]=0$, and

$$[[S_{3\alpha}]]=0 \tag{3.27}$$

by (3.23). We have thus proven the continuity of the relevant quantities across the transition boundary near the crack line, for dynamic problems.

In (quasi) static problems ($\rho_0=0$), we can prove the same results all along the transition boundary. Indeed, equations (3.3) and (3.4) give [10]

$$[[S_{3\alpha}]][[\partial x_3/\partial X_\alpha]]=0, \tag{3.28}$$

which is written explicitly as

Downloaded 02 May 2010 to 171.66.16.54. Redistribution subject to ASME license or copyright; see http://www.asme.org/terms/Terms_Use.cfm

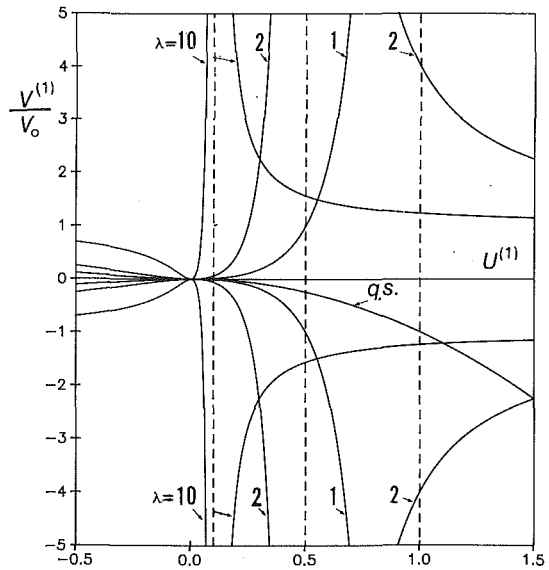


Fig. 3 $V^{(1)}/V_0$ versus $U^{(1)}$ for $\lambda = 10$, $\lambda = 2$, and $\lambda = 1$. The corresponding quasistatic curve of $\epsilon_0 X_0 V^{(1)}_{qs}$ versus $U^{(1)}_{qs}$ is indicated by *q.s.*

$$I = \{\mu(\partial x_3/\partial X_\alpha)^+ - S_0(\partial x_3/\partial X_\alpha)^-/\epsilon^-\}\{(\partial x_3/\partial X_\alpha)^+ - (\partial x_3/\partial X_\alpha)^-\} = 0 \tag{3.29}$$

It follows that

$$I = \mu(\epsilon^+)^2 + S_0\epsilon^- - S_0(\partial x_3/\partial X_\alpha)^+(\partial x_3/\partial X_\alpha)^-/\epsilon^- - \mu(\partial x_3/\partial X_\alpha)^+(\partial x_3^-/\partial X_\alpha)^- \tag{3.30}$$

By using the inequality

$$|x^+_{3,\alpha}x^-_{3,\alpha}| \le (x^+_{3,\alpha}x^+_{3,\alpha})^{1/2}(x^-_{3,\beta}x^-_{3,\beta})^{1/2}, \tag{3.31}$$

it follows from (3.30) that

$$I \ge \mu(\epsilon^+)^2 + S_0\epsilon^- - S_0\epsilon^+ - \mu\epsilon^+\epsilon^- = \mu[(\epsilon^+)^2 + \epsilon_0\epsilon^- - \epsilon_0\epsilon^+ - \epsilon^+\epsilon^-] = \mu(\epsilon^+ - \epsilon^-)(\epsilon^+ - \epsilon_0) \ge 0, \tag{3.32}$$

since $\epsilon^+ \le \epsilon^-$ and $\epsilon^+ \le \epsilon_0$. But (3.28) and (3.32) will be in conflict, unless $\epsilon^+ = \epsilon_0$ on the transition boundary (note that $\epsilon^+ = \epsilon^-$ will lead to $\epsilon^+ = \epsilon_0$ also). It can be shown that this result, together with (3.3) and (3.4), yield either $\epsilon^+ = \epsilon^-$, or **N** layer $\nabla x_3 = 0$ (i.e., x_3 is locally constant) on the transition boundary. As will be seen later, we may exclude the latter possibility for the present application. We thus conclude that $\epsilon^+ = \epsilon^- = \epsilon_0$ on the transition boundary. With this result, we can follow the procedures in equations (3.23)–(3.27) to prove continuity of $S_{3\alpha}$, $\partial x_3/\partial N$ and $\dot{x}_3$.

4 Static Fields Near a Crack Tip

In the immediate vicinity of a crack tip the deformation is large, i.e., $\epsilon > \epsilon_0$, and consequently equations (2.19) and (2.21) hold. Outside the region of large deformation, linearized elasticity according to equation (2.18) applies. The two regions are separated by a transition boundary. In this section it is assumed that the largest length dimension of the region of large deformation is small as compared to the length of the crack. This assumption implies that the crack may be taken as semi-infinite, and that the displacement outside the region of large deformation may be represented by the well-known square-root solution according to linearized elasticity.

The conditions on the faces of the crack are

$$U_{,2}(X_1, 0^\pm) = 0 \qquad -\infty < X_1 < 0 \tag{4.1}$$

The equation that governs the displacement field in the zone of large deformation is obtained by substituting (2.19) into the balance equation for static equilibrium. The result is

$$(U_{,2})^2 U_{,11} - 2U_{,1}U_{,2}U_{,21} + (U_{,1})^2 U_{,22} = 0. \tag{4.2}$$

Equation (4.2) can be rewritten as

$$(1/U_{,1})\mathcal{L}\{U_{,1}\} - (1/U_{,2})\mathcal{L}\{U_{,2}\} = 0, \tag{4.3}$$

where the differential operator $\mathcal{L}$ is defined as

$$\mathcal{L} = (\partial/\partial X_1) - (U_{,1}/U_{,2})(\partial/\partial X_2) \tag{4.4}$$

It is now noted that $\mathcal{L}$ is a total differential along the characteristic line defined by

$$dX_2/dX_1 = -U_{,1}/U_{,2} \tag{4.5}$$

Along such a line (4.3) can be integrated to yield

$$\ln(U_{,1}/U_{,2}) = C, \qquad \text{or} \qquad U_{,1}/U_{,2} = -D, \tag{4.6a,b}$$

where C and D are constants. By combining (4.5) and (4.6*b*), we conclude that the characteristics are straight lines:

$$dX_2/dX_1 = D \tag{4.7}$$

On these characteristics the displacement U is constant, because it follows from (4.5) that

$$dU = 0 \tag{4.8}$$

The problem formulation in the zone of the large deformation as defined by equations (2.21) and (4.8) is now identical to the one for small strain deformation near a crack in an elastic perfectly-plastic material with the Huber-Mises yield condition. The solution to the latter problem was given first by Hult and McClintock [11]. It was discussed in some detail by Rice [12]. In the present context the Hult-McClintock solution shows that the zone of large deformation is a circle of radius

$$R_0 = \frac{1}{2\pi}(K_{III}/S_0)^2, \tag{4.9}$$

which is centered at a point E on the crack line (see Fig. 2), a distance R_0 ahead of the crack tip. In the zone of large deformation we have [11, 12]:

$$U = \left(\frac{R_0}{2\pi}\right)^{1/2}\frac{2}{\mu}K_{III}\sin\theta \tag{4.10}$$

$$S_{31} = -S_0\sin\theta, \qquad S_{32} = S_0\cos\theta \tag{4.11a,b}$$

In the region of linearized elasticity we have

$$U = \left(\frac{R}{2\pi}\right)^{1/2}\frac{2}{\mu}K_{III}\sin\frac{1}{2}\psi \tag{4.12}$$

$$S_{31} = -\left(\frac{1}{2\pi R}\right)^{1/2}K_{III}\sin\frac{1}{2}\psi \tag{4.13}$$

$$S_{32} = \left(\frac{1}{2\pi R}\right)^{1/2}K_{III}\cos\frac{1}{2}\psi \tag{4.14}$$

where (R, ψ) are polar coordinates centered at the point E. Thus, equations (4.10) and (4.11*a,b*) hold for $R < R_0$, while (4.12)–(4.14) are valid for $R > R_0$.

We conclude this section by rederiving the field on the crack line in the zone of large deformation, by the use of an expansion method. This method can be used for problems that are not otherwise solvable. The method is shown here to demonstrate its utility, and as a preliminary to its application in the next section to the problem of dynamic crack growth. Following the approach of Achenbach and Dunayevsky [5] and Achenbach and Li [6], we seek a solution to equation (4.2) for small values of $X_2 (X_2/X_1 << 1)$, in the form

$$U = U^{(1)}(X_1)X_2 + U^{(3)}(X_1)X_2^3 + O(X_2^5) \tag{4.15}$$

Substitution of (4.15) into (4.2) followed by collection of terms of order X_2 yields

$$U^{(1)}_{,1}U^{(1)} - 2(U^{(1)}_{,1})^2 = 0 \tag{4.16}$$

Equation (4.16) is satisfied by

Downloaded 02 May 2010 to 171.66.16.54. Redistribution subject to ASME license or copyright; see http://www.asme.org/terms/Terms_Use.cfm

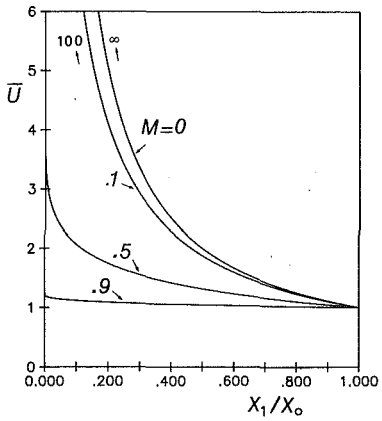


Fig. 4 Normalized crack-line strain in zone of large deformation

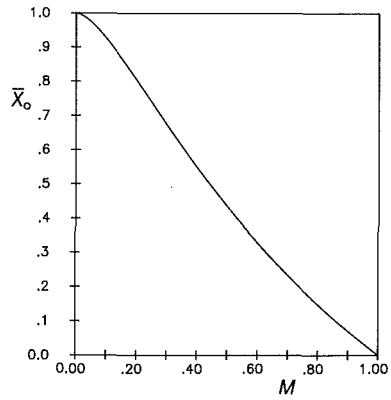


Fig. 5 Dimensionless length of zone of large deformation versus M; $\bar{X}_0 = (S_0/K_{III})^2 \pi X_0$

$$U^{(1)}_{,1} = (1/C)(U^{(1)})^2 \tag{4.17}$$

where C is a constant. The general solution to (4.17) is $U^{(1)} = -C/(X_1 + D)$. A singular and multiple-valued solution at the crack tip is obtained by setting $D = 0$. Hence

$$U^{(1)} = \bar{C}/X_1 \tag{4.18}$$

where $\bar{C}$ is a still to be determined constant. At $X_1 = X_0$, $X_2 = 0$, we have $U^{(1)} = \epsilon_0$, and thus $\bar{C} = X_0\epsilon_0$ where X_0 is the X_1 coordinate of the transition boundary on the crack line. It follows that

$$U = (X_0/X_1)\epsilon_0 X_2 + O(X_2^3) \tag{4.19}$$

The corresponding stresses at the transition boundary follow from (2.19) as

$$S_{31} = -S_0(X_2/X_0), \qquad S_{32} = S_0 \tag{4.20a,b}$$

Near the crack line in the zone of linearized elasticity, we now *assume* solutions of the general form (4.12)–(4.14). Continuity of S_{31} and S_{32} then yields by the use of (4.13) and (4.14)

$$\theta \equiv X_2/X_0 = \frac{1}{2}\psi \tag{4.21}$$

which implies that $X_0 = 2R_0$. It is now easily verified that for $\theta << 1$, (4.19) and (4.20a,b) do indeed correspond to (4.10), (4.11a,b) with (4.9), respectively.

As a final comment we note that the results derived in this section also apply to the crack line fields for quasistatic crack growth. For a propagating crack it is convenient to define the coordinate system (X_1, X_2) as moving with the crack tip. Stationary coordinates (X, Y) and moving coordinates (X_1, X_2) are related by

$$X_1 = X - a(t), \qquad X_2 = Y, \tag{4.22a,b}$$

where $X = a(t)$, $Y = 0$ defines the position of the crack tip in the (X, Y) system. In the moving (X_1, X_2) system, the material time derivative is defined as

$$(\dot{}) = (\partial/\partial t) - \dot{a}(\partial/\partial X_1), \tag{4.23}$$

where $\dot{a} = da/dt$ is the crack-tip speed. Spatial derivatives are the same in the two systems. Since the time derivatives do not appear in the elastic consitutive equations used in this paper, they do not enter the formulation of the quasistatic crack growth problem. Hence, the governing equations and, therefore, the fields are identical for the stationary and the moving crack tip, provided that they are defined relative to a coordinate system that is centered at the (stationary or moving) crack tip.

5 Dynamic Fields Near a Moving Crack Tip

It is convenient to formulate the governing equations in the moving coordinates (X_1, X_2) defined by (4.22a,b), with the material time derivative as defined by (4.23). In this section we will restrict the attention to the steady-state field near a crack tip which moves with a constant speed c. The material time derivatives then reduce to

$$(\dot{}) = -c(\partial/\partial X_1), \qquad (\ddot{}) = c^2(\partial^2/\partial X_1^2) \tag{5.1a,b}$$

Relative to the moving coordinate system, the equation of motion (2.11) becomes

$$S_{3\alpha,\alpha} = \rho_0 c^2 U_{,11}, \qquad \text{where} \quad \alpha = 1,2 \tag{5.2}$$

Substitution of (2.19) into (5.2) yields in the zone of large deformation

$$(U_{,2})^2 U_{,11} - 2U_{,1}U_{,2}U_{,12} + (U_{,1})^2 U_{,1})^2 U_{,22} = \lambda[(U_{,1})^2 + (U_{,2})^2]^{3/2} U_{,11} \tag{5.3}$$

where

$$\lambda = c^2\rho_0/S_0 \tag{5.4}$$

A solution in the vicinity of the crack line can be obtained by using the expansion given by equation (4.15). By substituting (4.15) into (5.3) and collecting terms of order X_2 we find

$$U^{(1)}_{,11}U^{(1)} - 2(U^{(1)}_{,1})^2 = \lambda(U^{(1)})^2 U^{(1)}_{,11} \tag{5.5}$$

For $\lambda = 0$, (5.5) reduces to (4.16). It is convenient to define

$$V^{(1)} = U^{(1)}_{,1}, \tag{5.6}$$

and to rewrite (5.5) in the form

$$\frac{dU^{(1)}}{U^{(1)}(1 - \lambda U^{(1)})} = \frac{dV^{(1)}}{2V^{(1)}} \tag{5.7}$$

This equation can be integrated to yield

$$\left(\frac{U^{(1)}}{U^{(1)} - 1/\lambda}\right)^2 = \pm\frac{V^{(1)}}{V_0}, \tag{5.8}$$

where V_0 is a positive constant, and the sign is chosen so as to make the right-hand side positive. For a few values of λ, $\pm V^{(1)}/V_0$ has been plotted in Fig. 3. Also plotted in Fig. 3 is the corresponding relation for $\lambda \equiv 0$, which follows from (4.19) and (5.6) as

$$\epsilon_0 X_0 V^{(1)}_{qs} = -(U^{(1)}_{qs})^2 \tag{5.9}$$

Since we expect that $U^{(1)} \to U^{(1)}_{qs}$ and $V^{(1)} \to V^{(1)}_{qs}$ as $\lambda \to 0$, it can be seen from Fig. 3 that the relevant dynamic solution for $U^{(1)}$ and $V^{(1)}$ should be located in the part of the phase plane defined by

$$0 < U^{(1)} < 1/\lambda, \qquad V^{(1)} < 0 \tag{5.10a,b}$$

Hence, for $V_0 > 0$, the minus sign applies in equation (5.8). An important consequence of (5.10a) is that $U^{(1)}$ remains bounded for $\lambda \neq 0$.

We now return to equation (5.6), and we write

Downloaded 02 May 2010 to 171.66.16.54. Redistribution subject to ASME license or copyright; see http://www.asme.org/terms/Terms_Use.cfm

$$\frac{dX_1}{dU^{(1)}} = \frac{1}{V^{(1)}} = -\frac{(U^{(1)} - 1/\lambda)^2}{V_0 (U^{(1)})^2} \tag{5.11}$$

where (5.8) has also been used. Integration yields

$$X_1 = -\frac{1}{V_0}\left\{U^{(1)} - \frac{2}{\lambda}\ln U^{(1)} - \frac{1}{\lambda^2}\frac{1}{U^{(1)}}\right\} + C \tag{5.12}$$

This expression contains two constants, V_0 and C, which can be obtained from the conditions at $X_1 = 0$ and $X_1 = X_0$, where X_0 is the intersection of the transition zone with the X_1 axis in the moving coordinate system. We have

$$U^{(1)} = \epsilon_0 \qquad \text{at} \qquad X_1 = X_0 \tag{5.13}$$

The only place on the crack line where singularities can be expected is $X_1 = 0$. Since equation (5.8) shows that $V^{(1)} \to \infty$ as $U^{(1)} \to 1/\lambda$, we conclude

$$U^{(1)} = 1/\lambda \qquad \text{at} \quad X_1 = 0 \tag{5.14}$$

Application of (5.13) and (5.14) to (5.12) yields

$$C = (2/\lambda V_0)\ln\lambda \tag{5.15}$$

$$V_0 = (-M^2 + 2\ln M^2 + 1/M^2)/\lambda X_0 \tag{5.16}$$

where M is the Mach number

$$M^2 = c^2/(\mu/\rho_0) \tag{5.17}$$

Substitution of (5.15) and (5.16) into (5.12) yields

$$\frac{X_1}{X_0} = \frac{1 - M^4\bar{U}^2 + 2M^2\bar{U}\ln(M^2\bar{U})}{(1 - M^4 + 2M^2\ln M^2)\bar{U}} \tag{5.18}$$

Here $\bar{U}$ is the normalized strain

$$\bar{U} = U^{(1)}/\epsilon_0 \tag{5.19}$$

The condition that the crack tip is in the zone of large deformation implies $1/\lambda > \epsilon_0$, and hence $M^2 < 1$, since $M^2 = \epsilon_0\lambda$.

Plots of $\bar{U}$ versus X_1/X_0 can be obtained from (5.18). Results are shown in Fig. 4, for various values of M. For $M > 0$, $\bar{U}$ remains finite (and equal to $1/M^2$) at $X_1 = 0$. In the limit $M \to 0$ we find

$$X_1/X_0 = 1/\bar{U}, \qquad \text{or} \qquad U^{(1)} = (X_0/X_1)\epsilon_0, \tag{5.20}$$

in agreement with the quasistatic results given by (4.19).

Equation (5.18) is the main result of this paper. It is, however, desirable to determine an explicit expression for X_0 in terms of the crack-tip speed and the far-field loading, albeit by approximation. In Section 3 it was shown that $\partial x_3/\partial N$ (or $\partial U/\partial N$), and $S_{3\alpha}$ are continuous at the transition boundary. Thus, the fields of large deformation can, in principle, be matched to corresponding linearly elastic fields, to yield an expression for X_0. Under the assumption that the zone of large deformation is small, the small strain fields are taken as the asymptotic near-tip fields for a crack in a linearly elastic solid. For the quasistatic case the solution (4.12)–(4.14) shows that exact matching can be achieved, provided that the center of the small strain field is shifted to a point on the crack line ahead of the actual crack tip. For the dynamic problem we do not expect that the zone of large deformation will be circular, and hence it is unlikely that a simple solution valid along the complete transition boundary can be obtained. In any event we have expressions for the large deformation fields only in the immediate vicinity of the crack line. It is, however, noted that to first order in X_2 the small-strain quasistatic and steady-state dynamic solutions are both of the general form, given by (4.12)–(4.14). Hence it seems reasonable to assume linearly elastic fields of the type (4.12)–(4.14), at least near the crack line, but where K_{III} should now be interpreted as an elastodynamic Mode-*III* stress intensity factor. For a semi-infinite crack the elastodynamic and quasistatic stress-intensity factor are related by $(K_{III})_{dyn} = (1-M)^{1/2}(K_{III})_{qs}$, see e.g., [13, p.35]. It follows that (4.9) also holds for the dynamic problem, but with the understanding that R_0 is the local radius of curvature of the transition boundary at its intersection with the crack line.

Near the crack line continuity of $\partial U/\partial N$ implies continuity of $V^{(1)}$. At the transition boundary we then have

$$S_{31} = \mu X_2 V^{(1)}\Big|_{X=X_0} = -\mu X_2 V_0\left(\frac{\epsilon_0}{\epsilon_0 - 1/\lambda}\right)^2 \tag{5.21}$$

$$S_{32} = S_0, \tag{5.22}$$

where (5.8) has been used. Continuity of S_{31} and S_{32} yields by the use of (4.13) and (4.14)

$$\mu X_2 V_0\left(\frac{M^2}{1-M^2}\right)^2 / S_0 \cong \frac{1}{2}\psi = \frac{1}{2}\frac{X_2}{R_0} \tag{5.23}$$

Substitution of V_0 and R_0 as given by (5.16) and (4.9) finally yields

$$X_0 = \frac{1}{\pi}\left(\frac{K_{III}}{S_0}\right)^2 \frac{1 - M^4 + 2M^2\ln M^2}{(1-M^2)^2} \tag{5.24}$$

The dimensionless form $(S_0/K_{III})^2\pi X_0$ has been plotted versus M in Fig. 5. It is noted that the zone of large deformation ahead of the crack tip decreases as M increases.

Acknowledgment

This paper was prepared in the course of research sponsored by the Office of Naval Research under Contact N00014-76-C-0063 with Northwestern University.

References

1 Knowles, J. K., "Crack Problems in Finite Elastostatics," in *Fracture Mechanics*, Burridge, R., ed., Vol. XII, SIAM-AMS Proceedings, American Mathematical Society, 1978, pp. 81–96.

2 Knowles, J. K., "The Finite Anti-Plane Shear Field Near the Tip of a Crack for a Class of Incompressible Elastic Solids," *Int. J. of Fracture*, Vol. 13, 1977, p. 611.

3 Knowles, J. K., and Sternberg, E., "Discontinuous Deformation Gradients Near the Tip of a Crack in Finite Anti-Plane Shear: an Example," *J. of Elasticity*, Vol. 10, 1980, pp. 81–110.

4 Lo, K. K., "Finite Deformation Crack in an Infinite Body Under Anti-Plane Shear," *Int. J. Solids and Structures*, Vol. 13, 1977, pp. 1219–1224.

5 Achenbach, J. D., and Dunayevsky, V., "Crack Growth Under Plane Stress Conditions in an Elastic Perfectly-Plastic Material," *J. Mech. Phys. Solids*, Vol. 32, 1984, pp. 89–100.

6 Achenbach, J. D., and Li, Z., "Plane-Stress Crackline Fields for Crack Growth in an Elastic Perfectly-Plastic Material," *J. Eng. Fract. Mech.*, in press.

7 Achenbach, J. D., and Li, Z., "Plastic Deformation Near a Rapidly Propagating Crack Tip," in *Fundamentals of Deformation and Fracture*, Miller, K. J., ed., Cambridge University Press, Cambridge, in press.

8 Knowles, J. K., "On the Dissipation Associated With Equilibrium Shocks in Finite Elasticity," *J. of Elasticity*, Vol. 9, 1979, p. 2.

9 Malek-Madani, R., "Energy Criteria for Finite Hyperelasticity," *Arch. Rat. Mech. Anal.*, Vol. 77, 1981, pp. 177–188.

10 Yatomi, C., and Nishimura, N., "On the Dissipation Inequality in Equilibrium Shocks," *J. of Elasticity*, Vol. 13, 1983, pp. 311–317.

11 Hult, J. A., and McClintock, F. A., "Elastic-Plastic Stress and Strain Distributions Around Sharp Notches under Repeated Shear," *Proc. 9th Int. Congr. Appl. Mech.*, Vol. 8, 1956, pp. 51–58.

12 Rice, J. R., "Mathematical Analysis in the Mechanics of Fracture," in *Fracture II*, Liebowitz, H., ed., Academic Press, New York, 1968, pp. 191–311.

13 Achenbach, J. D., "Dynamic Effects in Brittle Fracture," in *Mechanics Today*, Vol. 1, Nemat-Nasser, S., ed., Pergamon Press, Oxford and New York, 1974, pp. 1–57.

Downloaded 02 May 2010 to 171.66.16.54. Redistribution subject to ASME license or copyright; see http://www.asme.org/terms/Terms_Use.cfm

Dynamic Impact Over a Subsurface Crack: Applications to the Dynamic Tear Test

L. M. Brock
Engineering Mechanics Department,
University of Kentucky,
Lexington, Ky. 40506

M. Jolles

M. Schroedl

Code 6382,
Naval Research Laboratory,
Washington, D.C. 20375

Dynamic fracture is often studied by means of the dynamic tear (DT) test, which involves transverse impact by a mass on a beam. This process generates a complicated elastic wave pattern in the beam which, however, consists of two wave types: impact waves and reflected waves. The former are the compression wave radiating from the impact line and its diffractions at the notch end, while the latter are all waves originated by reflections from the beam surfaces. To gain insight into the role of specific waveforms in generating the fracture at the notch end in this process, the effects of the impact waves on the dynamic notch end stress field is studied. For both an idealized and an experimentally determined impact force, these waves are shown to initially place the notch end in compression. Moreover, even when a tensile stress state is eventually achieved, the stress intensity factor levels lie well below experimentally determined fracture toughness values. These results suggest that reflected waves generate the fracture, which agrees with experimental evidence.

Introduction

The failure of a notched beam by transverse impact is often used [1-5] to study dynamic fracture. In a version of this process called the dynamic tear (*DT*) test, a mass strikes across the width of the unnotched side of a simply supported rectangular bar. As indicated schematically in Fig. 1(*a*), the impact line and notch plane lie midway between the bar supports, so that the resulting elastic waves approximately generate a Mode *I* stress state at the notch end.

The elastic waves are not treated explicitly in studies such as [1-5], due in part perhaps to the complicated wave patterns arising in even two-dimensional geometries. As pointed out in [6], however, determination of the loading wave-forms associated with dynamic fracture can be important in characterizing the process. In this light, the complicated wave pattern can be viewed as a combination of two wave types: impact waves and reflected waves. The former consist of the compression wave radiating from the impact line and its diffractions at the notch end, the latter consist of all waves originated by reflections from the beam surfaces. However, it is noted in [5] that fracture at the notch end is not instantaneous, but occurs after at least one wave travel time between the impact line, bar ends, and notch. Therefore, the roles that the two wave types play in generating fracture is not clear.

As a first step in gaining insight into these roles we here study the effect of impact waves by analyzing an idealized yet relevant problem: Consider the isotropic, homogeneous,

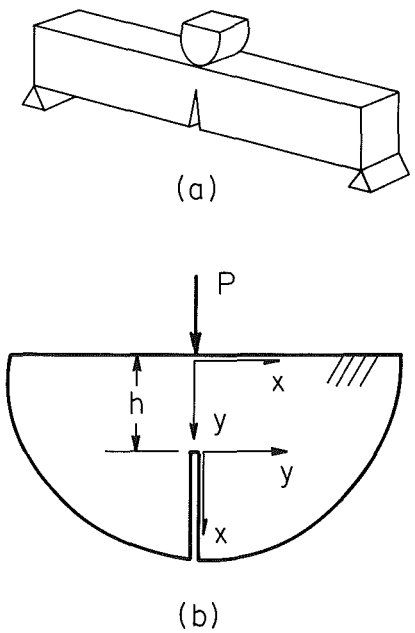


Fig. 1 (*a*) **Schematic of DT test, and** (*b*) **point force on cracked half-plane**

Contributed by the Applied Mechanics Division for presentation at the 1985 Joint ASME/ASCE Applied Mechanics, Fluids Engineering, and Bioengineering Conference, Albuquerque, N. Mex., June 24-26, 1985 of THE AMERICAN SOCIETY OF MECHANICAL ENGINEERS.

Discussion on this paper should be addressed to the Editorial Department, ASME, United Engineering Center, 345 East 47th Street, New York, N.Y. 10017, and will be accepted until two months after final publication of the paper itself in the JOURNAL OF APPLIED MECHANICS. Manuscript received by ASME Applied Mechanics Division, February, 1984; final revision, July, 1984. Paper No. 85-APM-17.

Copies will be available until February, 1986.

Copyright © 1985 by ASME
Downloaded 02 May 2010 to 171.66.16.54. Redistribution subject to ASME license or copyright; see http://www.asme.org/terms/Terms_Use.cfm

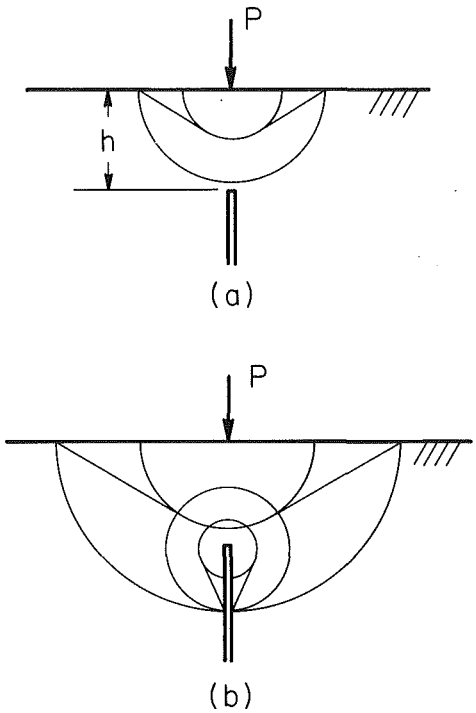


Fig. 2 (*a*) Wave pattern for $0<s<h$, and (*b*) wave pattern for $h<s<mh$

linearly elastic half-plane shown in Fig. 1(*b*) with a crack extending from infinity normal to the half-plane surface to a distance h from the surface. This cracked half-plane is at rest until $s=0$ when a normal point force (line load in the out-of-plane direction) of constant magnitude P is applied to the surface directly above the crack edge. Here s is the time multiplied by the half-plane dilatational wave speed.

The resulting impact wave pattern for $0<s<h$ is shown in Fig. 2(*a*). At $s=h$ and $s=mh$, respectively, the dilatational and rotational wave components of this pattern reach the crack edge, where $1/m$ is the rotational wave speed divided by the dilatational wave speed, so that $m>1$. In this paper, all speeds are nondimensionalized in this manner. The resulting diffraction pattern for $h<s<mh$ is shown in Fig. 2(*b*).

Until $s=3h$, the crack edge stress field is governed by the impact wave diffraction pattern, and can therefore be determined by superposition of the following problems: Problem 1 treats the point force acting on the same half-plane with the crack removed. Problem 2 examines a semi-infinite crack in an unbounded plane whose surfaces are subjected to the negatives of the Problem 1 tractions induced on the region that would be occupied by the Fig. 1(*b*) crack. This superposition is at first glance simply another variation on a standard [7] approach for analyzing crack problems. However, the crack depth h gives Problem 2 a characteristic length which makes a direct solution by standard techniques difficult. As will be seen, therefore, Problem 2 is not attacked directly.

In the next section, Problem 1 is formally stated and solved. Subsequently, Problem 2 is addressed and the crack edge stress field for $0<s<3h$ extracted by superposition. The field is studied and then modified to consider an experimentally determined impact force.

Problem 1

Problem 1 is, of course, Lamb's problem [8], but is stated here because many of the equations also govern Problem 2. As indicated in Fig. 1(*b*), we define the half-plane in terms of Cartesian coordinates as $y>0$ and locate the point force at $(x, y)=0$ for $s\geq 0$. Thus, along $y=0$

$$\sigma_{xy}=0, \quad \sigma_y=PH(s)\delta(x) \tag{1a,b}$$

where $H(\ )$ and $\delta(\ )$ are the Heaviside and Dirac functions. For $y, s>0$

$$\nabla^2(u,v)+(m^2-1)\left(\frac{\partial}{\partial x},\frac{\partial}{\partial y}\right)\Delta=m^2\frac{\partial^2}{\partial s^2}(u,v) \tag{2}$$

$$\frac{1}{\mu}\sigma_x=m^2\frac{\partial u}{\partial x}+(m^2-2)\frac{\partial v}{\partial y}, \quad \frac{1}{\mu}\sigma_{xy}=\frac{\partial v}{\partial x}+\frac{\partial u}{\partial y} \tag{3}$$

where $u(x, y, s)$ and $v(x, y, s)$ are the x and y-displacements, Δ is the dilatation, μ is the shear modulus, and σ_y follows from σ_x by interchanging the derivatives. In addition,

$$(u,v)\equiv 0(s\leq 0) \tag{4}$$

and (u, v) must satisfy appropriate radiation conditions as $s\to\infty$ [9].

This problem is easily solved by Laplace and Fourier transform techniques [10] and, in particular, the tractions generated along $x=0$ are found to be

$$\sigma_{xy}=0, \quad y\sigma_x=S(k)H(k-1),$$

$$\frac{\pi}{P}S(k)=\frac{S_1(k)}{\alpha}-S_2(k)H(k-m) \tag{5a-c}$$

$$k=\frac{s}{y}, \quad S_1(k)=\frac{kTM}{M^2-4kB\alpha^2}, \quad S_2(k)=\frac{4\beta Ak^2}{T^2-4kA\beta^2} \tag{6}$$

$$T=2k^2-m^2, \quad M=2k^2+m^2-2,$$

$$A=\sqrt{(1-m^2+k^2)}, \quad B=\sqrt{(m^2-1+k^2)} \tag{7}$$

$$\alpha=\sqrt{(k^2-1)}, \quad \beta=\sqrt{(k^2-m^2)} \tag{8}$$

Problem 2

With Fig. 1(*b*) in mind, we define a semi-infinite crack in an unbounded plane in terms of Cartesian coordinates as $y=0$, $x>0$. Prior to $s=h$ the cracked plane is at rest. Subsequently, negatives of the tractions corresponding to (5) appear along both crack faces. Since the tractions are symmetric with respect to the crack plane, analysis can be confined to the region $y>0$. In this region, (2)–(4) and the radiation conditions again hold, with $s\leq h$ replacing $s\leq 0$ in (4), but along $y=0$ we now have the mixed conditions

$$\sigma_{xy}=0, \quad v=0(x<0),$$

$$\sigma_y=\frac{-1}{x+h}S\left(\frac{s}{x+h}\right)H\left(\frac{s}{x+h}-1\right)(x>0) \tag{9a-c}$$

where the form of (9*c*) follows from (5*b*) and the relationship indicated in Fig. 1(*b*) between the coordinate systems used in the two problems.

Problem 2 is of a type that could generally be handled by the transform techniques used in Problem 1 and the Wiener-Hopf technique were it not for the characteristic length h in (9*c*). Unfortunately, this length leads to ill-defined regions of analyticity in the transform space, which are not of the standard Wiener-Hopf type. However, (9*c*) also indicates that, for a given value of the ratio $(x+h)/s$ – say c, the corresponding value $S(1/c)$ in the imposed crack surface traction in effect travels with the non-dimensionalized speed c. Since $s>x+h$, the speed at which $S(1/c)$ leaves $x=0$ at a given s is h/s and the speeds for all the S-values on the crack surface at a given s will lie in the range $h/s<c<1$. This observation suggests that to solve Problem 2, we consider first the following simple problem:

Simple Problem

In this problem, the cracked plane is at rest until $s=0$. Subsequently, we let (2)–(4), the radiation conditions and (9*a*, *b*) remain valid, but replace (9*c*) with the traveling stress impulse

Downloaded 02 May 2010 to 171.66.16.54. Redistribution subject to ASME license or copyright; see http://www.asme.org/terms/Terms_Use.cfm

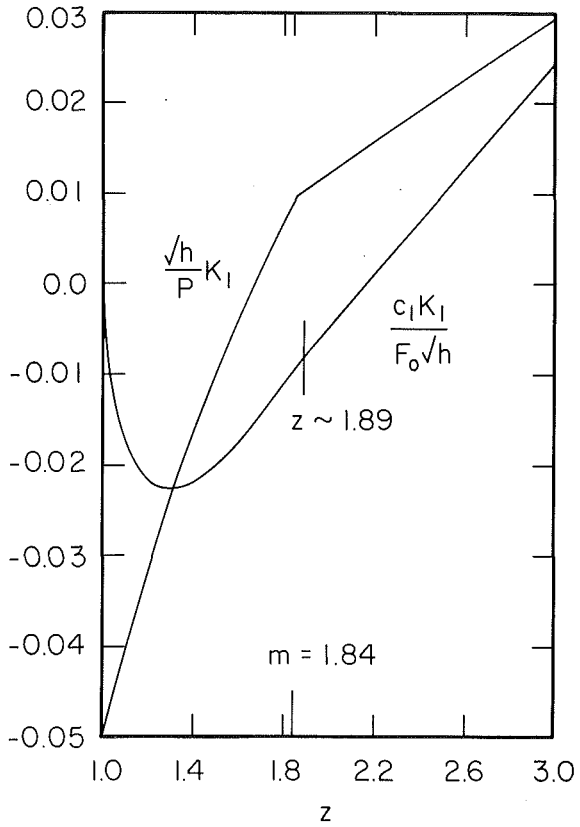


Fig. 3 Dynamic stress intensity factors for impact forces

$$\sigma_y = \sigma \frac{s}{x}\delta(cs-x)(x>0) \tag{10}$$

where σ is a real constant and the real variable c is a non-dimensionalized speed that lies in the range $0<c<1$. This problem has no characteristic length and is, thus, easily solved by standard transform and Wiener-Hopf techniques. Indeed, the problem is a special case of a standard problem presented in [7], and it can be shown that any scalar field variable in the solution has the general form $\sigma f(x, y, s, c)$. In particular, on the crack plane $y=0$ just ahead of the crack $(x=0-)$, $f=0$ for σ_{xy} while for σ_y,

$$f = -\frac{Q(k)}{\sqrt{(s\,|x|)}}, \quad Q(k) = \frac{a_+(k)}{(k+n)G_+(k)}, \quad k=\frac{1}{c} \tag{11}$$

where $1/n$ is the nondimensionalized Rayleigh wave speed $(n>m>1)$ and

$$b=\sqrt{(m^2-k^2)}, \quad a_+ = \sqrt{(1+k)} \tag{12}$$

$$\ln G_+(k) = -\frac{1}{\pi}\int_1^m \frac{1}{w+k}\tan^{-1}\left(\frac{4w^2\alpha b}{T^2}\right)dw \tag{13}$$

Now, if the stress impulse first leaves the crack edge at $s=h/c$ instead of $s=0$ and σ is replaced by $-S(1/c)dc$, the general form noted in the foregoing becomes $-S(1/c)f(x, y, s-h/c, c)dc$ and can be summed with respect to c over the range $h/s<c<1$ to give the corresponding scalar field variable for Problem 2. This idea of summing over a speed parameter to obtain a solution that exhibits a characteristic length was developed in [11] and has been used in [12].

Complete Solution: Crack Edge Stress

The preceding discussion implies that if (F, F_1, F_2) are corresponding scalar field variables near the crack edge for, respectively, the original problem and Problems 1 and 2, then for $0<s<3h$

$$F = F_1 + F_2 H(s-h) \tag{14}$$

$$F_2 = -\int_{h/s}^1 S(1/c)f(x,y,s-h/c,c)dc \tag{15}$$

As a demonstration, consider $F_2=\sigma_y$ for $y=0$, $x>0$. Equation (10) shows that

$$f = \frac{s-h/c}{x}\delta(cs-h-x) \tag{16}$$

in (15) so that the integral appropriately yields, by the sifting property of the Dirac function, (9c).

Substitution of (11) into (14), changing the integration variable from c to k, and recognizing that Problem 1 in general has no singular behavior at the crack edge gives $\sigma_{xy}=0$ and

$$\sqrt{|x|}\,\sigma_y \sim \frac{1}{\pi}\int_1^{s/h}\frac{Q(k)S(k)}{\sqrt{(s-kh)}}\frac{dk}{k^2} = K_1 \tag{17}$$

for $h<s<3h$, $y=0$, $x=0^-$. Here K_1 is the Mode I dynamic stress intensity factor. Substitution of (6) and making the additional integration variable changes $k=k_1$ and $k=k_2$, where

$$2k_1 = z+1+(z-1)\sin\Omega, \quad 2k_2 = z+m+(z-m)\sin\Omega, \quad z=\frac{s}{h} \tag{18}$$

in the first and second terms, respectively, in $S(k)$ yields the computationally more convenient nonsingular integration

$$K_1(z) = \frac{P}{\pi^2\sqrt{h}}\int\left[\frac{q_1(k_1)}{a_+(k_1)}H(z-1) - q_2(k_2)\sqrt{(k_2-m)}H(z-m)\right]d\Omega, \quad q_i = \frac{Q_i S_i}{k_i^2} \tag{19}$$

along the strip $(-\pi/2, \pi/2)$ of the Ω-axis, where $1<z<3$.

Clearly, $z=1$ and $z=m$ signal the arrivals of, respectively, the point force generated dilatational and rotational impact wave at the crack edge. Examination of (19) shows that at $z=1$ the second term does not appear while $k_1=1$. Therefore,

$$K_1(1) = -\frac{PQ(1)(m^2-2)}{\sqrt{(2h)}m^2\pi} \tag{20}$$

Since $Q(1)>0$ and it can be shown that $m>\sqrt{2}$ for plane strain or stress, (20) shows that the dilatational wave arrival instantaneously places the crack edge in compression. To see what happens subsequently, the factor K_1 is plotted in Fig. 3 versus $z>1$ for A517 steel $(m=1.84)$. Figure 3 shows that the crack edge stress field changes from compression to tension prior to the rotational wave arrival $(z=m)$. The tension field grows subsequently, although it should be remembered that (19) is valid only for $1<z<3$.

Realistic Impact Load: Crack Edge Stress

The actual forces transmitted by mass impact to A517 steel and 6061 aluminum bars of the Fig. 1(*a*) configuration have been measured experimentally [5]. The results show that (1*b*) is a useful but severe approximation. For the steel, the impact force until fracture initiation, which corresponds roughly to the range $0<s<14h$ in the present analysis, can accurately be represented as a point force with a time-varying P given by

$$P = \frac{F_0}{c_1}s_p t\left(1+\frac{3t}{10}-\frac{8t^2}{15}\right), \quad t=\frac{s}{s_p} \tag{21}$$

$$s_p = 0.35\text{m}, \quad c_1 = 5790\text{m/sec}, \quad F_0 = 1.4(10^5)\text{MN/m}-\text{sec} \tag{22}$$

where s_p corresponds to the instant of peak impact force $(s\sim 12h)$, c_1 is the dilatational wave speed, and F_0 is the initial slope of the impact force-time curve divided by the bar width. It should be noted, however, that the notch and bar lengths

Downloaded 02 May 2010 to 171.66.16.54. Redistribution subject to ASME license or copyright; see http://www.asme.org/terms/Terms_Use.cfm

considered in [5] are such that the analysis is now valid only in a time range corresponding to $0<s<1.89h$. At $s\sim 1.89h$ the first reflections from the notched side of the bar reach the notch end.

By simple convolution over time, the solution for this impact load follows from the previous results. In particular, (19) becomes

$$K_1(z)=\frac{F_0\sqrt{h}}{\pi^2 c_1}\int\left[\frac{q_1(k_1)}{a_+(k_1)}I(k_1)H(z-1)\right.$$

$$\left.-q_2(k_2)\sqrt{(k_2-m)}I(k_2)H(z-m)\right]d\Omega \tag{23}$$

$$I(k)=\left[2+\frac{1}{15}(z-k)-\frac{8}{15(45)}(z-k)^2\right]\sqrt{(z-k)} \tag{24}$$

for $1<z<1.89$. In this case, $K_1(1)=0$, but a plot of (23) also given in Fig. 3 shows that the crack edge stress field is now compressive until the arrival ($z\sim 1.89$) of the first reflected waves.

Discussion

There is experimental data [13, 14] to show that for steels such as that studied in [5] the dynamic fracture toughness K_{1D} at the onset of quasi-brittle fracture lies in the range

$$20\frac{\text{MN}}{\text{m}^{3/2}}<K_{1D}<50\frac{\text{MN}}{\text{m}^{3/2}} \tag{25}$$

In [6] the parameter h is 0.0286m so that

$$\frac{F_0}{c_1}\sqrt{h}=4.08\frac{\text{MN}}{\text{m}^{3/2}} \tag{26}$$

Then, from Fig. 3 we find

$$K_1(1.89)=-0.03\frac{\text{MN}}{\text{m}^{3/2}} \tag{27}$$

As already indicated, the first reflections from the impact line reach the notch end at $s=3h$, while the impact force peaks at $s\sim 12h$ and fracture initiates at $s\sim 14h$. From [5] it can also be shown that the first reflections from the bar ends reach the notch end at $s\sim 7h$. All these arrivals occur beyond the range of analysis validity. However, insight into the effects of impact waves partially uncoupled from reflection effects can be gained by studying (23) for the full range of validity for (21). Then, from (23) and (26) we find

$$K_1(3)=0.01\frac{\text{MN}}{\text{m}^{3/2}},\quad K_1(7)=0.67\frac{\text{MN}}{\text{m}^{3/2}},$$

$$K_1(12)=1.29\frac{\text{MN}}{\text{m}^{3/2}},\quad K_1(14)=1.46\frac{\text{MN}}{\text{m}^{3/2}} \tag{28}$$

All four of these values lie well below the range defined by (25). This would seem to indicate that it is the reflected waves that essentially generate quasi-brittle fracture at the notch end. Certainly, this conclusion would agree with the aforementioned [5] time lag between impact and fracture initiations.

The K_1 derived here, of course, does not account for microcracks, inclusions or dislocations existing near the notch end. In particular, Brock [15] has shown that the triggering of screw dislocation motion into a crack edge by an *SH*-wave can theoretically either increase or decrease the Mode *III* dynamic stress intensity factor from the values achieved by crack edge wave diffraction alone. Nevertheless, when viewed in conjunction with experimental data [5, 13, 14], the present results indicate that fracture in the *DT* test occurs due to a notch end stress state generated by a complicated pattern of impact and reflected waves. Thus, the notch is acutely "aware" of the beam geometry, and care is therefore required in using *DT* test data to characterize the dynamic fracture properties of a specific material.

Acknowledgment

This work was done while LMB was a 1983 Navy/ASEE Summer Faculty Fellow at the Naval Research Laboratory in Washington, D.C.

References

1 Timoshenko, S. P., "Zur Frage nach der Wirkung eines Stosse auf einen Balken," *Zeitschrift für Mathematik und Physik*, Vol. 62, 1913, pp. 198–209.

2 Mason, H. L., "Impact on Beams," *Transactions of the ASME*, Vol. 58, 1936, pp. *A*55–*A*61.

3 Lee, E. H., "Impact of a Mass Striking a Beam," *Transactions of the ASME*, Vol. 62, 1940, pp. *A*129–*A*138.

4 Eringen, A. C., "Transverse Impact on Beams and Plates," ASME JOURNAL OF APPLIED MECHANICS, Vol. 20, 1953, pp. 461–468.

5 Nash, G. E., and Lange, E. A., "Mechanical Aspects of the Dynamic Tear Test," ASME *Journal of Basic Engineering*, Vol. 91, 1969, p. 535–543.

6 Kolsky, H., "Recent Work on the Relations Between Stress Pulses and Fracture," in *Dynamic Crack Propagation*, Sih, G. C., ed., Noordhoff, Leyden, 1973, pp. 399–414.

7 Achenbach, J. D., *Wave Propagation in Elastic Solids*, North-Holland, Amsterdam, 1973.

8 Lamb, H., "On the Propagation of Tremors over the Surface of an Elastic Solid," *Philosophical Transactions of the Royal Society*, London, Series *A*, Vol. 203, 1904, pp. 1–42.

9 Carrier, G. F., and Pearson, C. E., *Partial Differential Equations*, Academic Press, New York, 1976.

10 Sneddon, I. N., *The Use of Integral Transforms*, McGraw-Hill, New York, 1972.

11 Freund, L. B., "The Stress Intensity Factor due to Normal Impact Loading of the Faces of a Crack," *International Journal of Engineering Science*, Vol. 12, 1974, pp. 179–190.

12 Brock, L. M., "Shear and Normal Impact Loadings on One Face of a Narrow Slit," *International Journal of Solids and Structures*, Vol. 18, 1982, pp. 467–477.

13 Congleton, J., "Practical Applications of Crack-Branching Measurements," in *Dynamic Crack Propagation*, Sih, G. C., ed., Noordhoff, Leyden, 1973, pp. 427–438.

14 Shockey, D. A., Kalthoff, J. F., Klemm, W., and Winkler, S., "Simultaneous Measurements of Stress Intensity and Toughness for Fast-Running Cracks in Steel," *Experimental Mechanics*, Vol. 23, 1983, pp. 140–145.

15 Brock, L. M., "The Dynamic Stress Intensity Factor Due to Arbitrary Screw Dislocation Motion," ASME JOURNAL OF APPLIED MECHANICS, Vol. 50, 1983, pp. 383–389.

Downloaded 02 May 2010 to 171.66.16.54. Redistribution subject to ASME license or copyright; see http://www.asme.org/terms/Terms_Use.cfm

A Stress Intensity Factor Tracer

K.-S. Kim
Assistant Professor,
Department of Theoretical
and Applied Mechanics,
University of Illinois
at Urbana-Champaign,
Urbana, Ill. 61801

A new optical method, Stress Intensity Factor Tracer (SIFT), has been developed. The device measures ***continuously*** *the* ***real-time*** *stress intensity factor variation, $K_I(t)$, of a* ***moving*** *crack tip using a* ***single, stationary*** *photodetector. The method uses the fact that any variation in $K_I(t)$ leads to a change in the intensity of light, $I(t)$, impinging on a fixed finite area, Γ, on the focal plane. The focal plane is defined as the plane on which initially parallel light rays transmitted through a transparent fracture specimen (or reflected from the surface of an opaque specimen) are focused by a converging lens. Provided that the light detecting area, Γ, excludes the focal point, a simple relation, $I(t) = B[K_I(t)]^{4/3}$, has been obtained for a K_I-dominant field. The constant, B, is a product of several experimental parameters including a "shape factor" of the sampling area, Γ, where $I(t)$ is measured. A significant feature of this method is that $I(t)$ is independent of the location of the crack tip in the illuminated zone on the specimen plane. The technique may therefore be applied to dynamic fracture studies without using high-speed photography. Only the constant, B, becomes a function of crack velocity for the dynamic K_I-field. This paper presents the theoretical development of the SIFT method, including the wave optics of the system. Experimental results supporting the theory are included.*

Introduction

During the past three decades the stress intensity factor (SIF) has been used as a parameter to characterize the loading on cracks in practical fracture tests, e.g., fatigue crack growth or dynamic fracture, in which the small scale yielding condition prevails. However, measuring the *continuous* time history of the stress intensity factor, $K(t)$, has been difficult for a rapidly *moving* crack using conventional methods such as photoelasticity [1-3], optical method of caustics [4-6], strain gauges [7, 8], and compliance methods [9], etc. Although the compliance method has been well adapted for the studies of slow crack growth such as fatigue crack growth or ductile stable crack growth, it has limitations on real-time measurement of $K(t)$. Strain gauges are useful for stationary cracks; however, data reduction for rapidly moving cracks is difficult. Conventional optical techniques have been widely applied to dynamic fracture testing; nonetheless, these techniques require high-speed photography.

If the deformation field, such as stress or strain, is measured at a material point of the specimen containing a moving crack, the measured quantities depend not only on the functional form of the deformation field in terms of the relative position vector to the crack tip but also on the location of the crack tip in the specimen. On the other hand, the SIF is determined only by the functional form of the near-tip stress field (or the spatial gradient of the field). Thus high-speed photography is conventionally used in dynamic fracture to freeze the location of the crack tip at the instance of exposure. Then the SIF is extracted from the stress distribution (or the spatial gradient of the stress field) at the vicinity of the crack tip by photoelasticity (or optical method of caustics). This conventional technique inevitably provides only a limited number of data ponts of the SIF at discrete times.

In this paper, a new *simple* optical method is introduced to measure the SIF of an *arbitrarily running* crack, *continuously* and in *real-time*, with a *single stationary* photodetector. Moving light sources or light detectors are not necessary, neither is high-speed photography. This optical device is the "Stress Intensity Factor Tracer (SIFT)." The principle behind this device lies in the theory of focal-plane mapping [12]. A schematic of focal-plane mapping and the definition of the focal plane is illustrated in Fig. 1. Focal-plane mapping has the following properties: (1) the focal point does not move at all, irrespective of any motion of the crack tip; (2) the position vector on the focal plane represents the spatial gradient of the first invariant of the in-plane stress field in the specimen plane; (3) any optical quantity that is a scalar function of the position vector on the focal plane has a functional relation to the SIF; and (4) selection of light on the focal plane can be considered as an optical filtering. The light intensity distribution on the focal plane is a scalar function of the position vector and property (3) of the focal plane tells us that it is related to SIF. If the intensity of the beam is uniformly distributed on the specimen plane, the distribution of light intensity on the focal plane is independent of the location of the crack tip in the specimen plane. Furthermore, light can be exclusively selected from the K_I-dominant annulus region around the crack tip, using the properties (3) and (4) of the focal plane. The optical filtering scheme, in principle, is

Contributed by the Applied Mechanics Division for presentation at the 1985 Joint ASME/ASCE Applied Mechanics, Fluids Engineering, and Bioengineering Conference, Albuquerque, N. Mex., June 24-26, 1985 of THE AMERICAN SOCIETY OF MECHANICAL ENGINEERS.

Discussion on this paper should be addressed to the Editorial Department, ASME, United Engineering Center, 345 East 47th Street, New York, N.Y. 10017, and will be accepted until two months after final publication of the paper itself in the JOURNAL OF APPLIED MECHANICS. Manuscript received by ASME Applied Mechanics Division, April, 1984, final revision August, 1984. Paper No. 85-APM-12.

Copies will be available until February, 1986.

Copyright © 1985 by ASME
Downloaded 02 May 2010 to 171.66.16.54. Redistribution subject to ASME license or copyright; see http://www.asme.org/terms/Terms_Use.cfm

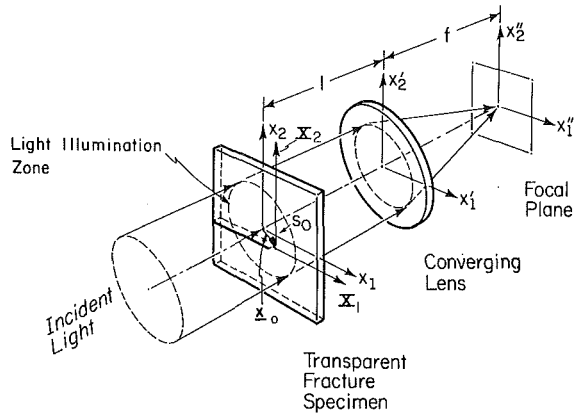


Fig. 1 Optical setup for SIFT

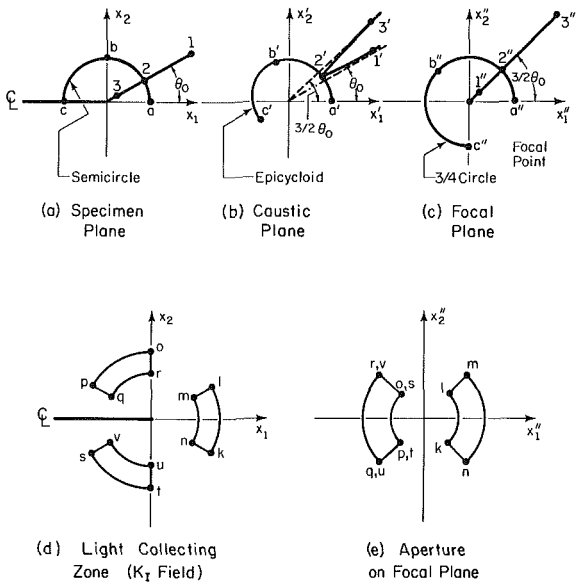


Fig. 2 Schematics of optical-shadow mapping [(*a*)-(*b*)] and focal-plane mapping [(*a*)-(*c*)] of Mode *I* crack, and the optimum optical filtering of the K_I-field zone

similar to those of the Schlieren technique [10] or generalized Fourier filtering [11]. Theoretical analysis shows that the light intensity, $I(t)$, monitored by a *stationary* photodetector at a proper filtering spot of the focal plane, is proportional to $[K_I(t)]^{4/3}$ all the time, as long as the crack tip is within the uniform light illumination zone. The SIF, $K_I(t)$, is for an arbitrarily *moving* crack tip.

Following the theoretical development, the paper describes experiments conducted to verify the relationship of $I(t) - K_I(t)$ in the quasistatic case, using Homalite 100. Compact tension (CT) and double cantilever beam (DCB) specimen geometries were used. Light intensity on the focal plane was detected using a photodiode. The SIF was obtained via load and mouth-opening displacement measurements. Experiment and theory show good agreement, within 3 percent error of $I(t)$, if the photodetector is placed in the proper place on the focal plane. The SIFT method is expected to be useful in many applications that require the continuous measurement of $K_I(t)$ for either a stationary or moving crack tip.

SIFT for K_I Field

To understand the SIFT system, consider the optical setup shown in Fig. 1. A light beam initially collimated parallel is transmitted through (or reflected from) a flat transparent (or opaque) fracture specimen and focused by a converging lens. In this arrangement, the light ray from a generic point, $\mathbf{X}$, on the specimen plane[1] with the origin of the axis at the crack tip will be mapped on to a point $\mathbf{x}''$ on the focal plane, which is parallel to the specimen plane and has its origin at the focal point of the converging lens. Then the mapping of the K_I-field, $\mathbf{x}''(\mathbf{X})$, which is identical to the deflection vector in the optical method of caustics [6] can be expressed as (see Appendix *A*)

$$x_1'' = (K_I cfd/\sqrt{2\pi}) r^{-3/2} \cos(3\theta/2)$$
$$x_2'' = (K_I cfd/\sqrt{2\pi}) r^{-3/2} \sin(3\theta/2) \quad (1)$$

where $r = |\mathbf{X}| = (X_1^2 + X_2^2)^{1/2}$, $\theta = \tan^{-1}(X_2/X_1)$, c is the shadow optical constant [6] of the specimen, f is the focal length of the convering lens, d is the thickness of the specimen, and K_I is the opening mode SIF. The mapping can be also expressed in polar coordinate on the focal plane as $r'' = Ar^{-3/2}$, $\theta'' = 3/2\ \theta$, where $r'' = |\mathbf{x}''|$, $\theta'' = \tan^{-1}(x_2''/x_1'')$, and $A = K_I cfd/\sqrt{2\pi}$.

An illustrative schematic of focal-plane mapping is shown in Fig. 2 and compared with caustic mapping. In the conventional caustic mapping of the K_I-field, the initial curve of the epicycloid caustic, a'-b'-c' in Fig. 2(*b*), is a circle, a-b-c in Fig. 2(*a*). The radial line, e.g., line 1-2-3 on the specimen plane in Fig. 2(*a*), is mapped to a hyperbolic curve, 1′-2′-3′ on the caustic plane in Fig. 2(*b*). On the other hand, for focal-plane mapping, the radial line on the specimen plane is mapped to another radial line, but is inverted, 1″-2″-3″ on the focal plane in Fig. 2(*c*). The circle, which has its center at the crack tip, is mapped to a circle, the center of which is at the focal point, on the focal plane but the angular span of the mapping is stretched by the factor of 3/2 as shown in Fig. 2(*c*). This mapping makes it easy to select the light from the annulus region of the K_I-field because an annulus around the focal point on the focal plane corresponds to an annulus around the crack tip on the specimen plane. The best light-collecting areas on the focal plane are the areas of $(-\pi/4 \le \theta'' \le \pi/4,\ r_1'' < r'' < r_2'')$ and $(3/4\pi \le \theta'' \le 5/4\pi,\ r_1'' \le r'' \le r_2'')$ as shown in Fig. 2(*e*). The corresponding areas on the specimen are shown in Fig. 2(*d*). The sectors of $\pi/4 \le |\theta''| \le 3\pi/4$ are excluded because the crack itself is a slit, on the specimen plane, which causes light diffraction in the X_2-direction and the diffracted light will be mapped along the x_2'' axis. The radii, r_1'' and r_2'', should be decided to select the light from the K_I-dominant field, excluding the near-tip nonlinear zone by r_2'' and the far field zone by r_1'', where the stress states are no longer represented by the K_I singular term expression. The existence of r_1'' and r_2'' to select the K_I-dominant field is verified by the experiments in the next section.

With this mapping, the distribution of the light intensity, $\Omega''(\mathbf{x}'')$, on the focal plane can be expressed as (see Appendix *A*)

$$\Omega''(\mathbf{x}'') = \Omega(\mathbf{X}(\mathbf{x}'') + \mathbf{x}_0)/J$$
$$= \frac{4}{9} (K_I cfd/\sqrt{2\pi})^{4/3} (r'')^{-10/3} \Omega(\mathbf{X}(\mathbf{x}'') + \mathbf{x}_0) \quad (2)$$

where J is the Jacobian of the mapping, $\Omega(\mathbf{X}(\mathbf{x}'') + \mathbf{x}_0)$ is the distribution of the transmitted (or reflected) light intensity on the specimen plane, and $\mathbf{x}_0$ is the crack-tip position vector in the specimen plane, as illustrated in Fig. 1. The existence of the local inverse mapping $\mathbf{X}(\mathbf{x}'')$ is assumed. If a uniform intensity distribution of light $(\Omega(\mathbf{X}(\mathbf{x}'') + \mathbf{x}_0) = \Omega_0)$ is provided on the specimen plane, the light intensity distribution, $\Omega''(\mathbf{x}'')$, on the focal plane is not a function of $\mathbf{x}_0$ [see equation (2)]. Then the total light intensity, I, collected on a

[1] Because the thickness of the specimen is much smaller than the focal length of the lens, midplane between two faces of the specimen can be considered as the specimen plane for a transparent specimen.

Downloaded 02 May 2010 to 171.66.16.54. Redistribution subject to ASME license or copyright; see http://www.asme.org/terms/Terms_Use.cfm

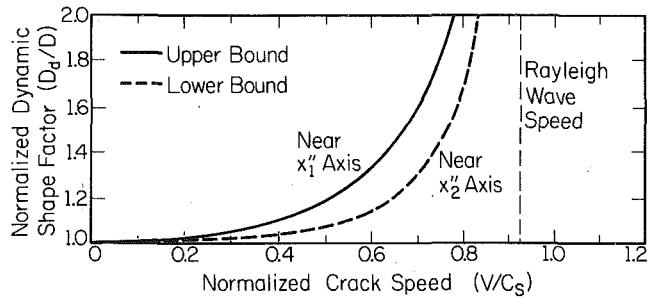


Fig. 3 Dynamic shape factor as a function of crack speed ($\nu = 0.33$)

set of finite area, Γ, of the focal plane, excluding the focal point, can be given as

$$I = \int_{\Gamma} \Omega'' dS'' = BK_I^{4/3} \tag{3}$$

$$B = \frac{4}{9}\Omega_0 D(cfd/\sqrt{2\pi})^{4/3}, D = \int_{\Gamma^+ + 2\Gamma^-} (r'')^{-10/3} dS'' \tag{4}$$

where Γ^+ is the part of Γ for which $x_1'' \geq 0$ and Γ^- is the other part of $\Gamma(x_1'' < 0)$. D is a shape factor that depends only on the shape of the light-collecting aperture.

When a crack tip moves in the specimen plane, $I(t)$ is still independent of crack-tip motion because it is not a function of $\mathbf{x}_0$, as shown in equations (2), (3), and (4). However, all the points, $\{\mathbf{X}(\mathbf{x}''); \mathbf{x}'' \in \Gamma\}$, must be in the uniform illumination zone on the specimen plane to satisfy the condition $\Omega(\mathbf{X}(\mathbf{x}'') + \mathbf{x}_0) = \Omega_0$. Also, the static K_I-field must be replaced in the derivation by the dynamic K_I-field to account for the inertia effect. For the dynamic K_I-field, equation (3) still holds with some changes in the expression of the shape factor, D. The dynamic shape factor, D_d, is a function of the speed of the crack, v, as (see Appendix B)

$$D_d = \beta(v)\left[\int_{\Gamma^+ + 2\Gamma^-} \{(x_1'')^2 + (x_2'')^2/\alpha_1^2\}^{-5/3} dS''\right] \tag{5}$$

$$\beta(v) = [(1+\alpha_2^2)(\alpha_1^2 - \alpha_2^2)/\{4\alpha_1\alpha_2 - (1+\alpha_2^2)^2\}]^{4/3}/\alpha_1^2,$$
$$\alpha_1 = (1 - v^2/c_l^2)^{1/2}, \alpha_2 = (1 - v^2/c_s^2)^{1/2} \tag{6}$$

where c_l and c_s are the longitudinal and the transverse wave speeds. The normalized dynamic shape factor, D_d/D, for Poisson's ratio $\nu = 0.33$, is shown as a function of the crack speed in Fig. 3. For a given speed of the crack, D_d/D has a value between the maximum and the minimum, where the extremes are obtained when the light-collecting area, Γ, is a slit along the x_1'' and x_2'' axes, respectively.

In a laboratory experiment, the distribution of light intensity, Ω, can be made relatively uniform on a chosen (simply connected) area, S_0, of the specimen plane containing a crack tip by using an aperture of illumination for an expanded and collimated laser beam. Then equation (3) can be normalized as

$$I(t)/I_0 = [K_I(t)/K_n]^{4/3} \tag{7}$$

$$K_n = (3\sqrt{3\pi}S_0^{3/4})/(2D^{3/4}cfd) \tag{8}$$

where I_0 is the total intensity of light transmitted through (or reflected from) area S_0 of the specimen plane. For the given range of $K_I(t)$, the sensitivity of $I(t)/I_0$ can be controlled by the normalizing parameter, K_n, the dimension of which is equal to that of SIF.

Experiments and Discussions

Experiments were carried out with two different specimens, i.e, the CT specimen and the DCB specimen, to verify the relations derived in the preceding section. However, mainly the CT specimen was used throughout the experiments. The DCB specimen was only used to test the boundary effect on the K_I-dominant field. Both specimens were made of Homalite 100, which has its shadow optic constant, c, of $1.0 \times 10^{-10} m^2/N$ for the test conditions of approximately 2 $MN/m^{3/2}/min$ loading rate at room temperature. Although Homalite 100 is optically anisotropic, the anisotropy constant, λ [6], is so small that the SIFT formula of an optically isotropic material was used as an approximation. The dimensions of the CT specimen were: the height of each loading arm was 81.3 mm; the effective crack length and the unfractured ligament were each 68.3 mm long; and the thickness of the specimen was 6.0 mm. The load lines were 56.3 mm apart from the crack faces. The dimensions of the DCB specimen were 63 mm × 254 mm, 11.2 mm thickness with a 150 mm long crack loaded at the points on the centerline of each arm, 138 mm behind the crack tip.

The specimens were loaded in the opening mode by an Instron machine. For the CT specimen, the load-cell output that is proportional to the SIF was connected to the X input of an X-Y chart recorder, while the SIFT photodetector output was connected to the Y input of the recorder. Then the load scale (max. 450N) was converted to the SIF scale by the conversion formula [13]. For the DCB specimen, the clip-gauge output of crack-opening displacement, which is also proportional to the SIF was used instead of load-cell output. The clip gauge was attached to the end faces of the two arms of the specimen.

A 3 mW He-Ne laser was used as a light source for the SIFT system. The laser beam was expanded, collimated, and cut by an aperture of illumination with a diameter of 50 mm. Because the expanded beam has Gaussian distribution of light intensity, the aperture was arranged to pass only the central portion of the expanded beam, so that the illuminated area had uniform light intensity within ±3 percent variation. The transmitted beam was focused by a concave Schlieren mirror with a focal length of 1.5 m and a diameter of 10 cm. Then the SIFT system was tested by measuring the light intensities at various positions along the x_1'' axis on the focal plane with a photodiode that had a circular active area with a diameter of 2.5 mm.

The experimental results are shown in Fig. 4 with the theoretical prediction, $I/B = K_I^{4/3}$, plotting the normalized light intensity, I/B, against the SIF, K_I, for different photodetector positions. The normalizing factor, B, was estimated by equation (4) based on K_I-field approximation. For the estimation, the shape factor, D, of the circular photodetector was evaluated by carrying out the integration of equation (4) in polar coordinate. The shape factor as a function of the location of the photodetector on the focal plane can be expressed as

$$D(\beta) = \frac{3}{2}\left(\frac{\beta}{r_0}\right)^{4/3} \int_0^{\sin^{-1}\beta} [\{\cos\theta - (1 - \beta^2\sin^2\theta)^{1/2}\}^{-4/3} - \{\cos\theta + (1 - \beta^2\sin^2\theta)^{1/2}\}^{-4/3}] d\theta \tag{9}$$

where $\beta = r_0/h$, and r_0 is the radius of the photodetector and h is the distance between the focal point and the center of the photodetector.

The shape factor, $D(\beta)$, can also be obtained by integrating equation (3) from 0 to K_{I0} as

$$D(\beta) = \frac{21(2\pi)^{2/3}}{4\Omega_0(cfd)^{4/3}K_{I0}^{7/3}} \int_0^{K_{I0}} I(K_I, \beta) dK_I \tag{10}$$

The shape factors were evaluated for various β values by

Downloaded 02 May 2010 to 171.66.16.54. Redistribution subject to ASME license or copyright; see http://www.asme.org/terms/Terms_Use.cfm

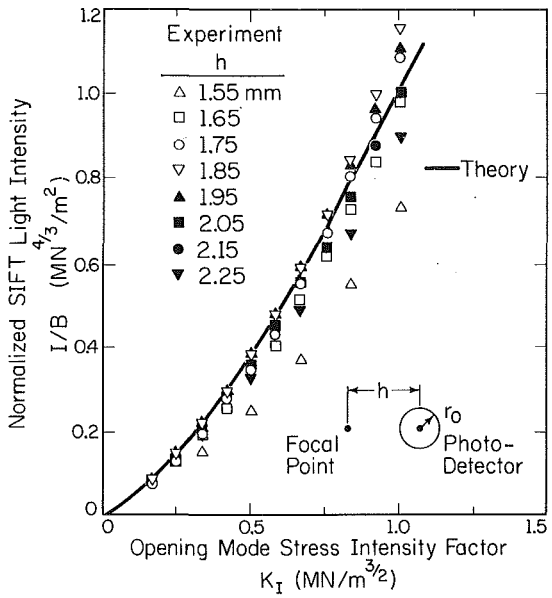


Fig. 4 Light intensity-stress intensity factor relation of the SIFT with a circular apperture

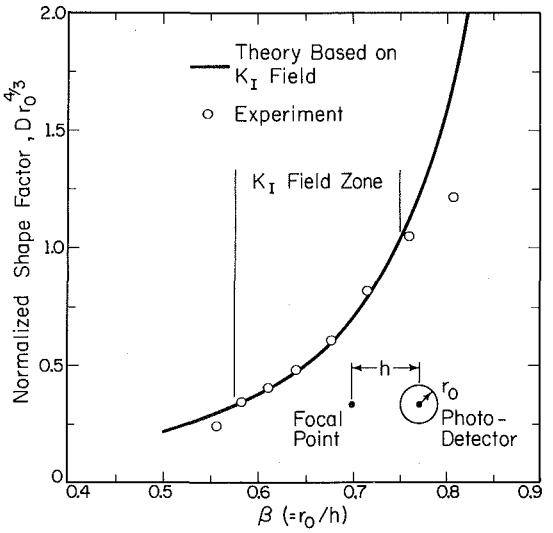


Fig. 5 An average light intensity (expressed as a shape factor) distribution near the focal point

carrying out the integration in equation (10) up to $K_{I0} = 1.0$ MN/m$^{3/2}$ with the experimentally obtained light intensity-stress intensity factor relations $I(K_I,\beta)$. In Fig. 5 the experimental shape factors are compared with the theoretical ones of the K_I-field given by equation (9).

As shown in Figs. 4 and 5, the experimental and the theoretical results match very well for the range of 1.75 mm $\leq h \leq$ 2.15 mm, which spans 0.5 mm $\leq x_1'' \leq$ 3.4 mm for the photodetector with a diameter of 2.5 mm. However, when the photodetecting area includes regions very close to the focal point, $x_1'' \leq 0.4$ mm for this setup, the deviation of the theoretical prediction from the experimental observation is significant (more than 10 pecent). This deviation is believed to be because the theoretical prediction is based only on the K_I-field whereas the actual light collection contains contributions from the higher-order terms of the series expansion of the crack-tip stress field. The closer the photodetector is to the focal point the more significant the higher-order effect is because the closer photodetector receives light from regions far away from the crack tip [see reciprocal mapping of Figs. 2(*a*) and 2(*c*)]. In addition more error sources are near the focal point, such as those caused by light scattering and refraction from the inhomogeneity of the specimen, the lens aberration, and aperture diffraction. The diffraction effect is particularly significant because the geometrical optics, which is the first-order approximation of the wave optics, can no longer predict the light intensity distribution accurately near the focal point.

If the photodetector is too far away from the focal point, the theoretical prediction also deviates from the experimental observation. In this case the photodetector collects light from regions very close to the crack tip, so that the stress state in the region is no longer close to the K_I-field because of the bluntness (and/or local plastic deformation) of the crack tip. In addition, in the practical laboratory specimen, if the light-collecting region on the specimen plane is within the distance of a quarter of the thickness of the specimen from the crack tip, plane stress approximation for the K_I-field is no longer valid. In this region, the deflection of the light ray is smaller than that expected by the plane stress K_I-field approximation, so that the light intensity of the SIFT is also smaller than expected, as shown in Fig. 5.

These experiments show that a wide enough K_I-field zone on the focal plane exists, where the K_I value can be measured accurately. In this moderate range of photodetector location the increase of the light intensity, for the increase of K_I, is slightly steeper than $K_I^{4/3}$ when the K_I value is large, which indicates that the light-collecting area on the specimen is expanding at a greater rate than expected as the load increases. The tendency is more profound in the DCB specimen test [14]. This deviation slightly overestimates the SIF when K_I is very large, if the SIFT is used with the formulas based on K_I-field approximation. However the deviation is insignificant for estimating of K_I values because the I-K_I relationship of the SIFT is concave up as shown in Fig. 4. In practical applications, the calibration curve of the I-K_I relationship can also be used instead of formulas based on K_I-field approximation.

The SIFT is insensitive to rigid body motion of the specimen if the transmitted light is used for a transparent specimen. On the other hand, it is highly sensitive to rigid body motion of the specimen if reflected light is used, so that a compensation technique of the rigid body motion has to be employed for the reflected scheme. The compensation can be easily made by reprojecting the light reflected from the front face on to the back face of the specimen to use the doubly reflected light for the SIFT. Although the SIFT can be arranged to be insensitive to the rigid body motion of the specimen, it is always sensitive to the motion of the rest of the optical elements. To eliminate this sensitivity, the optical setup has to be mounted on a vibration-isolated optical table separated from the loading system. Despite these difficulties the SIFT developed here has been successfully applied to the experimental analysis of the stress intensity variation of a DCB specimen under vibrational loading and of a dynamic crack propagation in a large Homalite 100 specimen subjected to impulsive loading on the crack faces. The results of those analyses are presented elsewhere [14, 15].

An important application for the SIFT method is in real-time measurement of $K_I(t)$ for rapidly moving cracks. As explained earlier, this technique is well suited for such experiments because the focal-plane mapping is independent of the crack-tip position as long as the light-collecting zone lies within the uniform incident beam in the specimen plane. Moving light sources and moving light detectors are not needed; neither is any high-speed photography.

Concluding Remarks

A new optical technique, the Stress Intensity Factor Tracer (SIFT) has been developed to measure, with a *single stationary* photodetector, the *continuous* analog time trace of

Downloaded 02 May 2010 to 171.66.16.54. Redistribution subject to ASME license or copyright; see http://www.asme.org/terms/Terms_Use.cfm

the stress intensity factor *regardless of crack-tip motion.* Theoretical analysis has been carried out for both the static and dynamic K_I-fields, to derive the light intensity-stress intensity factor relation as $I=B(v)\ K_I^{4/3}$ for the opening mode crack. $B(v)$ is a known function of the speed of the crack. The theoretical analysis of the optical system, based on wave optics and crack tip K_I-field approximation, shows good agreement with experimental observations. Experiments also show that a K_I-field annulus region exists around the crack tip, where the SIFT formula based on K_I-field approximation gives excellent agreement with the experimental results. Preliminary analysis indicates that the SIFT measures $\sqrt{K_I^2+K_{II}^2}$ for a mixed mode crack opening, where K_{II} is a mode *II* stress intensity factor. The usefulness of SIFT is expected to be shown in many types of time-dependent fracture tests, such as fatigue crack growth tests and dynamic fracture tests. Its application to dynamic fracture is illustrated elsewhere [15].

Acknowledgment

This project was supported by the Research Board and the Department of Theoretical and Applied Mechanics, University of Illinois at Urbana-Champaign.

References

1 Post, D., "Photoelastic Stress Analysis for an Edge Crack in a Tensile Field," *Proc. Society for Experimental Stress Analysis*, Vol. 12, 1954, pp. 99–116.

2 Wells, A., and Post, D., "The Dynamic Stress Distribution Surrounding a Running Crack—a Photoelastic Analysis," *Proc. Society for Experimental Stress Analysis*, Vol. 16, 1958, pp. 69–92.

3 Smith, D. G., and Smith , C.W., "Photoelastic Determination of Mixed Mode Stress Intensity Factors," *Journal of Engineering Fracture Mechanics*, Vol. 4, 1972, pp. 357–366.

4 Manogg, P., "Anwendung der Schattenoptik zur Untersuchung des Zerreissvorganges Von Platten," Ph.D. Dissertation, University of Freiburg, 1964.

5 Theocaris, P. S., and Gdoutos, E. E., "An Optical Method for Determining Opening-Mode and Edge Sliding-Mode Stress Intensity Factors," ASME JOURNAL OF APPLIED MECHANICS, Vol. 39, 1972, pp. 91–97.

6 Beinert, J., and Kalthoff, J. F., "Experimental Determination of Dynamic Stress Intensity Factors by the Method of Shadow Patterns," in *Mechanics of Fracture*, Vol. 7, Sih, G. C., 1981.

7 Hall, W. J., Mosborg, R. J., and McDonald, V. J., "Brittle Fracture Propagation in Wide Steel Plates," *The Welding Journal*, Vol. 35, No. 1, 1957, Research Supplement, pp. 1–8.

8 Kinra, V. K., and Bowers, C. L., "Brittle Fracture of Plates in Tension. Stress Field Near the Crack," *International Journal of Solids and Structures*, Vol. 17, 1981, pp. 175–181.

9 Schra, L., Boerema, P. J., and Van Leeuwen, H. P., "Experimental Determination of the Dependence of Compliance on Crack Tip Configuration of a Tapered DCB Specimen," Nat. Aerospace Inst. Amsterdam Rept. TR 73025, 1973.

10 Töplen, A., "Beobachtungen nach einer neuen optischen Methode," Bonn, 1864.

11 Goodman, J. W., *Fourier Optics*, McGraw-Hill, New York 1968.

12 Kim, K. S., and Phillips, J. W., "Focal-Plane Analysis of the Optical Pattern Produced by Mode-I Crack," *Proc. Society of Engineering Science*, Vol. 18, 1981, p. 173.

13 Tada, H., Paris, P. C., and Irwin, G. R., *The Stress Analysis of Cracks Handbook*, 1973.

14 Kim, K. S., "A Stress Intensity Factor Tracer and Its Application to Time Dependent Fracture Testing," to appear *International Congress on Fracture 6th*, New Delhi, India, Dec. 1984.

15 Kim, K. S., "Dynamic Fracture Under Normal Impact Loading of the Crack Faces," ASME JOURNAL OF APPLIED MECHANICS, to appear.

16 Pauli, W., *Pauli Lectures on Physics—Vol. 2 Optics and the Theory of Electrons*, by Enz, C. P., ed., 4th ed., MIT Press, 1981.

17 Born, M., and Wolf, E., *Principle of Optics*, 2nd Ed., Academic Press New York, 1964.

18 Williams, M. L., "On the Stress Distribution at the Base of a Stationary Crack," ASME JOURNAL OF APPLIED MECHANICS, Vol. 24, 1957, pp. 109–114.

19 Freund, L. B., and Clifton, R. J., "On the Uniqueness of Elastodynamic Solutions for Running Cracks," *Journal of Elasticity*, Vol. 4, 1974, pp. 293–299.

APPENDIX A

Wave Optics for SIFT

In Fig. 1 the optical mapping of $\mathbf{x}\rightarrow\mathbf{x}'$ can be considered as a steady electromagnetic wave propagation governed by

$$\nabla^2\mathbf{E}=\frac{1}{C^2}\frac{\partial^2\mathbf{E}}{\partial t^2} \tag{A}$$

with the boundary condition on $\mathbf{x}$ plane as

$$\mathbf{E}(\mathbf{x})=\mathbf{A}(\mathbf{x})e^{i(\omega t-k\Delta s(\mathbf{x})-\phi_0)},\ \mathbf{x}\epsilon S_0 \tag{A2}$$

where $\mathbf{E}$, C, $\mathbf{A}$, ω, and k are the electric field, the speed, the amplitude, the angular frequency, and the wave number of the light. $\Delta s(\mathbf{x})$ is the perturbation of optical path length caused by the deformation of the specimen so that $k\Delta s(\mathbf{x})$ is the phase perturbation on the $\mathbf{x}$ plane. ϕ_0 is a constant phase determined by the incident plane harmonic wave on to the specimen. S_0 is the region of illumination on the specimen plane. The notation S_0 is also used as the area of the region itself. Then the solution of the Helmholtz equation, which is the governing equation of the spatial part of the electric field, is readily available by the so-called Kirchhoff's solution [16] as

$$\mathbf{E}(\mathbf{x}')=-ike^{i\omega t}\int\int_{S_0}\frac{\mathbf{A}(\mathbf{x})}{2\pi\bar{l}}\left(\frac{l}{\bar{l}}\right)\left(1+\frac{1}{ik\bar{l}}\right)e^{-ik\{\bar{l}+\Delta s(\mathbf{x})+\phi_0/k\}}dx_1dx_2 \tag{A3}$$

where $\bar{l}=\{l^2+|\mathbf{x}'-\mathbf{x}|^2\}^{1/2}$ and l is the distance between the $\mathbf{x}$ and $\mathbf{X}'$ planes.

Similarly, the electric field expression of the light on the $\mathbf{x}''$ plane can be given by

$$\mathbf{E}(\mathbf{x}'')=-ike^{i\omega t}\int\int_{S_l}\frac{\mathbf{A}'(\mathbf{x}')}{2\pi\bar{f}}\left(\frac{f}{\bar{f}}\right)\left(1+\frac{1}{ik\bar{f}}\right)e^{-ik\{\bar{f}+\Delta s_l(\mathbf{x}')+\phi(\mathbf{x}')\}}dx_1'dx_2' \tag{A4}$$

where $\bar{f}=\{f^2+|\mathbf{x}''-\mathbf{x}'|^2\}^{1/2}$, f is the focal length of the converging lens, S_l is the area of the lens plane, and $\Delta s_l(\mathbf{x}')$ is the effective optical path length change caused by the presence of the lens. $\Delta s_l(\mathbf{x}')$ of a converging lens with focal length f is given by

$$\Delta s_l(\mathbf{x}')=\Delta s_l^0-|\mathbf{x}'|^2/(2f) \tag{A5}$$

where Δs_l^0 is a constant representing the optical path length change at the center ($\mathbf{x}'=\mathbf{O}$) of the lens. For the far field approximation ($k\bar{f}>>1, k\bar{l}>>1$), the electric field on the focal plane can also be expressed in terms of $\mathbf{x}$ from equations (*A*3) and (*A*4) as

$$\mathbf{E}(\mathbf{x}'')=-k^2e^{i\omega t}\int\int_{S_l}\int\int_{S_0}\frac{lf\mathbf{A}(\mathbf{x})}{(2\pi\bar{l}\bar{f})^2}e^{-ikF(\mathbf{x}'',\mathbf{x}',\mathbf{x},l,f)}dx_1dx_2dx_1'dx_2' \tag{A6}$$

where

$$F(\mathbf{x}'',\mathbf{x}',\mathbf{x},l,f)=\bar{f}+\bar{l}+\Delta s(\mathbf{x})+\Delta s_l(\mathbf{x}')+(\phi_0/k) \tag{A7}$$

The asymptotic behavior, for large k, of equation (*A*6) can be described by the method of stationary phase, which essentially provides the ray optics. The evaluation of the integral in equation (*A*6), for the method of stationary phase, is based on the Taylor series of F and the nonexponential term of the integrand on the set

$$C_F=\{(\mathbf{x}'',\mathbf{x}',\mathbf{x})\,|\,\mathrm{grad}_{\mathbf{x}}F=\mathbf{O},\ \mathrm{grad}_{\mathbf{x}'}F=\mathbf{O}\} \tag{A8}$$

The subscripts on grad indicate the independent variables for the gradient operator. The reason to have the Taylor series on C_F is that the integrand of equation (*A*6) oscillates very rapidly for large k and the oscillations tend to cancel out away

Downloaded 02 May 2010 to 171.66.16.54. Redistribution subject to ASME license or copyright; see http://www.asme.org/terms/Terms_Use.cfm

from C_F. Actually C_F itself indicates Fermat's principles [17]. Equations (A7) and (A8) provide

$$\text{grad}_{\mathbf{x}} F = \frac{\mathbf{x}-\mathbf{x}'}{\bar{l}} + \text{grad}_{\mathbf{x}} \Delta s(\mathbf{x}) = \mathbf{O} \tag{A9}$$

$$\text{grad}_{\mathbf{x}'} F = \frac{\mathbf{x}'-\mathbf{x}''}{\bar{f}} + \frac{\mathbf{x}'-\mathbf{x}}{\bar{l}} - \frac{\mathbf{x}'}{f} = \mathbf{O} \tag{A10}$$

The equation (A9) is the mapping for optical shadow (or for the caustics for special cases). The addition of equations (A9) and (A10) gives

$$-\frac{\mathbf{x}''}{\bar{f}} + \text{grad}_{\mathbf{x}} \Delta s(\mathbf{x}) = \frac{\bar{f}-f}{\bar{f}f}\mathbf{x}' = 0\left(\frac{|\mathbf{x}''-\mathbf{x}'|^2}{f^3}\mathbf{x}'\right) \tag{A11}$$

where 0( ) is an order sign. For a shallow deflection of light rays, i.e., $|\text{grad}_{\mathbf{x}} \Delta s(\mathbf{x})| < L/f$ and $L/f << 1$ (L is the aperture radius of the lens), the mapping becomes

$$\mathbf{x}'' = \left[1 + 0\left(\frac{L^2}{f^2}\right)\right] f \,\text{grad}_{\mathbf{x}} \Delta s(\mathbf{x}) + 0\left(\frac{L^3}{f^2}\right) \cong f \,\text{grad}_{\mathbf{X}} \Delta \tilde{s}(\mathbf{X}) \tag{A12}$$

where $\Delta \tilde{s}(\mathbf{X}) = \Delta s(\mathbf{X}+\mathbf{x}_0)$, and $\mathbf{X}$ is a position vector with respect to the crack tip on the specimen plane. Here the location of the crack tip is denoted by $\mathbf{x}_0$, as illustrated in Fig. 1. The error term $0(L^2/f^2)$ in [ ] represents the coma of the lens and the error term $0(L^3/f^2)$ indicates the spherical aberration of the lens. Equation (A12) indicates that the focal-plane mapping $\mathbf{x}''(\mathbf{X})$ is identical to the deflection vector at the distance of focal length from the specimen. For a moving crack, Δs near the tip changes in such a way that $\Delta \tilde{s}$ is only a function of $\mathbf{X}$. This provides the insensitivity of the focal-plane mapping to the location of the crack tip when applied to a fracture specimen.

The optical path length change, $\Delta s(\mathbf{x})$, can be expressed as a function of the stresses, as well explained in reference [6], by the use of stress-optic constitutie relations. An optically isotropic and elastic material of shadow optic constant, c, and of thickness, d, has the relation as

$$\Delta \tilde{s}(\mathbf{X}) = cd\sigma(\mathbf{X}) \tag{A13}$$

where σ $(= \sigma_{11} + \sigma_{22})$ is the first invariance of the in-plane stresses. For the K_I-dominant field of a quasistatic crack [18],

$$\sigma(\mathbf{X}) = \sqrt{\frac{2}{\pi}}\frac{K_I}{\sqrt{r}}\cos\frac{\theta}{2} + \sigma_{0x} \tag{A14}$$

where σ_{0x} is a constant representing the far field tensile stress in the x_1 direction. Combining equations (A12), (A13), and (A14) leads to equation (1) of the main text.

When the integration of equation (A6) is carried out by the method of stationary phase, not very near the critical points such as caustics or a focal point, the electric field representation of light $\mathbf{E}(\mathbf{x}'')$ becomes

$$\mathbf{E}(\mathbf{x}'') \cong -ke^{i\omega t}\int\int_{S_l} \frac{ilf\mathbf{A}[\mathbf{x}(\mathbf{x}')]e^{-ikF[\mathbf{x}'',\mathbf{x}',\mathbf{x}(\mathbf{x}'),l,f]}}{2\pi\bar{l}f^2[\det(F_{,ij}|\mathbf{x}(\mathbf{x}'))]^{1/2}}dx_1'dx_2'$$

$$\cong \mathbf{A}[\mathbf{x}(\mathbf{x}'')]\frac{\mathbf{If}}{\bar{l}f}e^{i(\omega t - kF_0)}/\left[\det\left(F_{,ij}\Big|_{\mathbf{x}'(\mathbf{x}'')}^{\mathbf{x}(\mathbf{x}'')}\right)\det\left(F_{,i'j'}\Big|_{\mathbf{x}'(\mathbf{x}'')}^{\mathbf{x}(\mathbf{x}'')}\right)\right]^{1/2}$$

$$\cong \mathbf{A}[\mathbf{x}(\mathbf{x}'')]e^{i(\omega t - kF_0)}/\sqrt{J} \tag{A15}$$

where $F_{,ij} = \partial^2 F/\partial x_i \partial x_j$ and $F_{,i'j'} = \partial^2 F/\partial x_i' \partial x_j'$ and J is the Jacobian, $\det[\partial x_i''/\partial x_j]$. The notations $\mathbf{x}(\mathbf{x}'')$ or $\mathbf{x}'(\mathbf{x}'')$ on the right side of the bar in the Hessian determinant indicates that the variable $\mathbf{x}$ or $\mathbf{x}'$ of the Hessian should be expressed in terms of $\mathbf{x}''$ with the mapping relation given by equations (A9) and (A10). F_0 is the first-order approximation of the phase variation on the focal plane, expressed as

$$F_0(\mathbf{x}'', \mathbf{x}'(\mathbf{x}''), \mathbf{x}(\mathbf{x}''), l, f)$$

$$= f\left(1 + \frac{|\mathbf{x}''-\mathbf{x}'|^2}{2f^2}\right) + l\left(1 + \frac{|\mathbf{x}'-\mathbf{x}|^2}{2l^2}\right) + \Delta s(\mathbf{x}) + \Delta s_l^0$$

$$- |\mathbf{x}'|^2/2f + \phi_0/k = c_0 - \frac{\mathbf{x}''\cdot\mathbf{x}(\mathbf{x}'')}{f}\left[1 + 0\left(\frac{L^2}{f^2}\right)\right]$$

$$+ \frac{|\mathbf{x}''|^2}{2f}\left\{1 - \frac{l}{f} + 0\left(\left[\frac{L}{f}\right]^2 |\nabla(\Delta s)|^2\right)\right\} + \Delta s[\mathbf{x}(\mathbf{x}')]$$

$$\cong c_0 - \frac{\mathbf{x}''\cdot\mathbf{X}(\mathbf{x}'')}{f} - \frac{\mathbf{x}''\cdot\mathbf{x}_0}{f} + \frac{|\mathbf{x}''|^2}{2f}\left(1 - \frac{l}{f}\right) + \Delta \tilde{s}[\mathbf{X}(\mathbf{x}'')], \tag{A16}$$

where $c_0 = f + l + \Delta s_l^0 + \phi_0/k$. The light intensity distribution can then be easily obtained from equation (A15) as

$$\Omega''(\mathbf{x}'') = \mathbf{E}(\mathbf{x}'')\cdot\mathbf{E}^*(\mathbf{x}'') = |\mathbf{A}[\mathbf{x}(\mathbf{x}'')]|^2/J = \Omega(\mathbf{x}(\mathbf{x}''))/J \tag{A17}$$

where $\mathbf{E}^*(\mathbf{x}'')$ indicates the complex conjugate of $\mathbf{E}(\mathbf{x}'')$. The argument of function Ω can be also replaced by $\mathbf{X}(\mathbf{x}'') + \mathbf{x}_0$, because $\mathbf{x} = \mathbf{X} + \mathbf{x}_0$.

APPENDIX B

Dynamic Shape Factor

When the SIFT system is applied to a rapidly running crack, the near-tip dynamic K_I-field including the inertia effect, has to be used to derivate of the relationship between the light intensity and the stress intensity factor. In place of equation (A14) of the quasistatic K_I-field, the dynamic K_I-field gives [19]

$$\sigma(\mathbf{X}) = H(v)\sqrt{\frac{2}{\pi}}\frac{K_I}{\sqrt{r_\xi}}\cos\frac{\theta_\xi}{2} + \sigma_{0x} \tag{B1}$$

$$H(v) = (\alpha_1^2 - \alpha_2^2)(1+\alpha_2^2)/\{4\alpha_1\alpha_2 - (1+\alpha_2^2)^2\} \tag{B2}$$

where α_1 and α_2 are functions of crack speed, v, as given in equation (6) of the main text. r_ξ and θ_ξ are the polar coordinates of ξ-plane defined as

$$\xi_1 = r_\xi \cos\theta_\xi = X_1$$
$$\xi_2 = r_\xi \sin\theta_\xi = \alpha_1 X_2 \tag{B3}$$

then equations (A12), (A13), (B1), and (B3) give

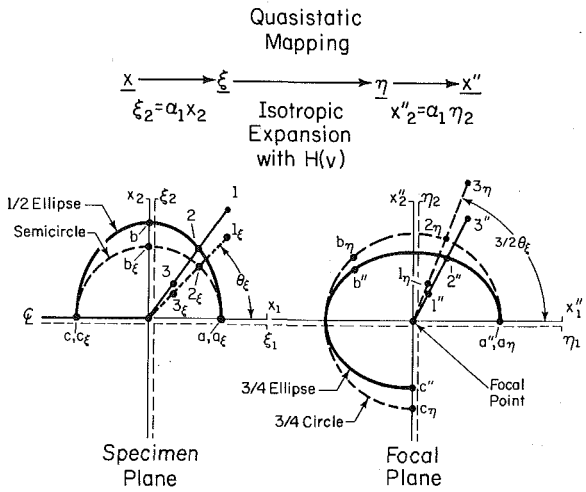


Fig. B1 Focal-plane mapping of a running Mode I crack

Downloaded 02 May 2010 to 171.66.16.54. Redistribution subject to ASME license or copyright; see http://www.asme.org/terms/Terms_Use.cfm

$$x_1'' = cfd\frac{\partial\sigma}{\partial X_1} = cfd\frac{\partial\sigma}{\partial\xi_1} = H(v)\,(K_I cfd/\sqrt{2\pi})r_\xi^{-3/2}\cos(3\theta_\xi/2)$$

$$x_2'' = cfd\frac{\partial\sigma}{\partial X_2} = \alpha_1 cfd\frac{\partial\sigma}{\partial\xi_2} = \alpha_1 H(v)\,(K_I cfd/\sqrt{2\pi})r_\xi^{-3/2}\sin(3\theta_\xi/2) \quad (B4)$$

If we introduce an intermediate mapping variable η such as

$$\eta_1 = r_\eta\cos\theta_\eta = x_1''$$
$$\eta_2 = r_\eta\sin\theta_\eta = x_2''/\alpha_1 \quad (B5)$$

then, the intermediate mapping $\xi\rightarrow\eta$ is identical to the quasistatic mapping except for the scalar multiplication factor $H(v)$. The mapping can be expressed in polar coordinates as, $r_\eta = A_d\, r_\xi^{-3/2}$, $\theta_\eta = 3/2\theta_\xi$ and $A_d = H(v)K_I cfd/\sqrt{2\pi}$, so that a circle on the ξ plane maps to another circle on the η plane as for the quasistatic focal-plane mapping. Considering the mappings $\mathbf{X}\rightarrow\xi$ and $\eta\rightarrow\mathbf{x}''$ are the shrinkage of X_2 coordinate and η_2 coordinate, respectively, by the factor of α_1, we can see that an ellipse of eccentricity, v/c_l, on the specimen plane, $\mathbf{X}$, with the major axis on the X_2 axis and the center on the crack tip maps to another ellipse of eccentricity, v/c_l, on the focal plane, with the major axis on the x_1'' axis and the center on the focal point. A schematic of the mapping is shown in Fig. $B1$.

The light intensity distribution $\Omega''(\mathbf{x}'')$ on the focal plane can be obtained by equation ($A17$) with the estimation of the Jacobian, J, of the mapping as,

$$1/J = det\left(\frac{\partial X_i}{\partial x_j''}\right) = det\left(\frac{\partial X_i}{\partial\xi_j}\right)\cdot\det\left(\frac{\partial\xi_i}{\partial\eta_j}\right)\cdot det\left(\frac{\partial\eta_i}{\partial x_j''}\right) \quad (B6)$$

where

$$det\left(\frac{\partial X_i}{\partial\xi_j}\right) = det\left(\frac{\partial\eta_i}{\partial x_j''}\right) = 1/\alpha_1, \quad (B7)$$

$$det\left(\frac{\partial\xi_i}{\partial\eta_j}\right) = \frac{4}{9}A_d^{4/3}r_\eta^{-10/3}, \quad (B8)$$

so that

$$\Omega''(\mathbf{x}'') = \frac{4}{9\alpha_1^2}[H(v)K_I cfd/\sqrt{2\pi}]^{4/3}\cdot[(x_1'')^2 + (x_2'')^2/\alpha_1^2]^{-5/3}\Omega(\mathbf{x}(\mathbf{x}'')) \quad (B9)$$

Then equation ($B9$) and equation (3) of the main text give the dynamic shape factor given in equations (5) and (6) of the main text.

Downloaded 02 May 2010 to 171.66.16.54. Redistribution subject to ASME license or copyright; see http://www.asme.org/terms/Terms_Use.cfm

A Two Surface Model for Transient Nonproportional Cyclic Plasticity:

Part 1 Development of Appropriate Equations

D. L. McDowell
Assistant Professor,
School of Mechanical Engineering,
Georgia Institute of Technology,
Atlanta, Ga. 30332
Assoc. Mem. ASME

A two surface stress space model is introduced with internal state variable repositories for fading memory of maximum plastic strain range and nonproportionality of loading. Evolution equations for isotropic hardening variables are prescribed as a function of these internal variables and accumulated plastic strain, and reflect dislocation interactions that occur in real materials. The hardening modulus is made a function of prior plastic deformation and the distance of the current stress point from the limit surface. The kinematic hardening rules of Mroz and Prager are used for the yield and limit surfaces, respectively. The structure of the model is capable of representing essential aspects of complex nonproportional deformation behavior, including direction of the plastic strain rate vector, memory of plastic strain range, cross-hardening effects, variation of hardening modulus, cyclic hardening or softening, cyclic racheting, and mean stress relaxation.

Introduction

The presence of cyclic plasticity in a multiaxial stress-strain field is a serious fatigue design consideration in the nuclear, aircraft, and ground vehicle industries [1–4]. When the stress rate is nonradial in deviatoric stress space at some interval of each loading cycle, the analysis is complicated by nonproportionality effects [5].

Nonproportional loading places additional requirements on the constitutive equations for transient cyclic plasticity. In particular, the plastic strain rate vector direction, memory of plastic strain range, magnitude of the plastic hardening modulus, and cross-hardening effects are of critical importance. The objective of this work is to introduce a two surface model based on the assumptions of time and rate-independent plasticity theory which is capable of predicting results from cyclic, nonproportional, room-temperature tests performed by the author [6, 7], including cyclic hardening effects. A companion paper demonstrates the quantitative behavior of this model for nonproportional strain cycling experiments conducted by the author on type 304 stainless steel.

Contributed by the Applied Mechanics Division for presentation at the 1985 Joint ASME/ASCE Applied Mechanics, Fluids Engineering, and Bioengineering Conference, Albuquerque, N. Mex., June 24–26, 1985 of THE AMERICAN SOCIETY OF MECHANICAL ENGINEERS.

Discussion on this paper should be addressed to the Editorial Department, ASME, United Engineering Center, 345 East 47th Street, New York, N.Y. 10017, and will be accepted until two months after final publication of the paper itself in the JOURNAL OF APPLIED MECHANICS. Manuscript received by ASME Applied Mechanics Division, April, 1984; final revision, August, 1984. Paper No. 85-APM-9.

Copies will be available until February, 1986.

Motivation From Previous Work

Plastic Strain Rate Direction. With regard to the direction of the plastic strain rate vector during nonproportional cyclic loading there are two approaches. The first approach, motivated chiefly by yield surface probing experiments during nonproportional straining [8–11], requires the formulation of an anisotropic yield surface [12–15]. This surface can distort, expand, or contract to reflect deformation-induced anisotropy and isotropic hardening.

It is reasonable to assume for cyclic plasticity applications that deformation-induced anisotropy can be accounted for by a kinematic backstress α. The yield surface may contract or expand but not distort. These assumptions result in a computationally more efficient form of the yield surface than most formulations that permit distortion:

$$f = f(\sigma - \alpha, R) = 0 \tag{1}$$

where $\dot{\alpha}$ is determined from the consistency condition $\dot{f} = 0$ during plastic flow and the ratio of kinematic to isotropic hardening [16].

As usual, the conditions for plastic flow are

$$\dot{\epsilon}^p = \dot{m}(\partial f/\partial \sigma) \quad \text{if} \quad f = 0 \quad \text{and} \quad \dot{\sigma}:(\partial f/\partial \sigma) \geq 0 \tag{2}$$

$$\dot{\epsilon}^p = \mathbf{0} \quad \text{otherwise} \tag{3}$$

where $\dot{m}$ is a scalar multiplier, and σ is the stress tensor. Here the usual decomposition of the total small strain rate into elastic and plastic components is assumed, i.e., $\dot{\epsilon} = \dot{\epsilon}^e + \dot{\epsilon}^p$. The scalar product $\dot{\sigma}_{ij}\ (\partial f/\partial \sigma_{ij})$ is denoted by $\dot{\sigma}:(\partial f/\partial \sigma)$.

Lamba [17, 18], McDowell et al. [19, 20], and Garud [21, 22] have demonstrated the applicability of equations (1)–(3)

Copyright © 1985 by ASME
Downloaded 02 May 2010 to 171.66.16.54. Redistribution subject to ASME license or copyright; see http://www.asme.org/terms/Terms_Use.cfm

for proper plastic strain rate direction under conditions of nonproportional straining at cyclically stable conditions when the hardening rule is obtained from a nested surface approach. The yield surface radius R can be determined for cyclic hardening or softening from a relation that defines R as a function of accumulated plastic strain $\eta = \int_t \sqrt{(\dot{\epsilon}^p : \dot{\epsilon}^p)}\, dt$ [23].

Plastic Strain Range Effects. It is well known that the evolution of the isotropic hardening parameter R depends on plastic strain range [24–26], particularly for the austenitic stainless steels. Analytical description of this dependence requires a more detailed repository for history dependence than η. At the very least, a measure of the metric plastic strain accumulation from a point of recent unloading is necessary [27, 28]. A plastic strain range memory parameter q was introduced by Chaboche et al. [29] and Nouailhas et al. [30] for cyclic loading. The evolution of q follows from

$$\dot{q} = \frac{1}{2} H(F)\, \mathbf{n} : \mathbf{n}^* \dot{\eta} (2/3)^{1/2} \tag{4}$$

where $H(F) = 1$ if $F = 0$ and $H(F) = 0$ if $F < 0$. The normal to the yield surface f at the current stress point is denoted by $\mathbf{n}$, where $\mathbf{n} = (\partial f/\partial \sigma) \,/\, \|\partial f/\partial \sigma\|$. The notation $\|\partial f/\partial \sigma\|$ denotes the norm $(\partial f/\partial \sigma : \partial f/\partial \sigma)^{1/2}$. Here, F is the plastic strain memory surface defined in second invariant form by

$$F = (2/3)(\epsilon^p - \alpha^p) : (\epsilon^p - \alpha^p) - q^2 = 0 \tag{5}$$

where α^p is the center of the memory surface in plastic strain space. Note that $\mathbf{n}^*$ is the normal to the surface F at the point ϵ^p defined by $\mathbf{n}^* = (\partial F/\partial \epsilon^p) \,/\, \|\partial F/\partial \epsilon^p\|$. For completely reversed uniaxial cycling, q represents half the axial plastic strain range. The surface F is shown in Fig. 1 in plastic strain space.

There is a rather severe problem with this formulation of plastic strain range memory. If an overload cycle occurs in which the plastic strain range is doubled, for example, continued cycling at the smaller strain range may not result in a saturated isotropic hardening state that corresponds to the overload cycle. Yet q would correspond to the plastic strain range of the overload cycle. The actual plastic strain range "remembered" by the material would lie somewhere between that of the small and large cycles [25, 31]. This lack of evanescence can be corrected by introduction of a fading memory term in equation (4)

$$\dot{q} = \left[\frac{1}{2} H(F)\, \Gamma (2/3)^{1/2} - \Lambda(q) \right] \dot{\eta} \tag{6}$$

where $\Lambda(q)$ is the memory loss-rate function and Γ is a scalar to be defined later. This capability of fading memory is also necessary to allow for the possibility of readjustment of the isotropic hardening or softening response when reducing the applied strain range during cyclically stable conditions.

Expressing the flow rule in equation (2) in an equivalent form $\dot{\epsilon}^p = (1/h)\ (\dot{\sigma} : \mathbf{n})\mathbf{n}$ allows interpretation of h as a generalized plastic modulus or hardening modulus. It is particularly attractive to define h through a multiple nested surface scheme as in the approach of Mroz [32–34]. Path dependence of h and $\dot{\epsilon}^p$ is achieved through the translation of the yield and loading surfaces.

Cross-Hardening Effects. It is experimentally observed for a number of metals [7, 17, 30, 35] that nonproportional cycling leads to an increase in the size of the region of elastic response above that corresponding to proportional cycling at the same effective strain range. This additional isotropic hardening apparently results from increased dislocation interaction and is not included in conventional theories. Brown and Miller [35] were able to correlate this additional hardening for out-of-phase sinusoidal straining of 1 percent Cr-Mo-V steel by introducing a rotation factor

$$RF = \frac{\text{shear strain range at 45 deg to maximum shear plane}}{\text{maximum shear strain range}} \tag{7}$$

For proportional straining, defined in this work as loading for which the total strain rate is collinear with the total strain, $RF = 0$. For the case of sinusoidal tension-torsion straining of a thin-walled tubular specimen with an engineering shear to axial strain amplitude ratio of $\gamma_a/\epsilon_a = (1+\nu)$ and a phase angle of 90 deg, $RF = 1$. Here, ν is Poisson's ratio. The latter case defines every plane in the specimen wall as a maximum shear strain plane of equal shear strain range at some point in the loading cycle. The maximum shear planes rotate at a constant rate. This case also yielded the most additional cyclic hardening observed by Brown and Miller within a rather coarse matrix of phase angle and strain amplitude ratio tests.

Brown and Miller achieved a correlation coefficient of 0.836 for various phase angle and strain amplitude ratios by assuming a linear relation between cyclically stable flow stress and rotation factor based on a maximum shear stress-strain Ramberg-Osgood relation analogous to the uniaxial cyclic stress-strain curve [24].

Nouailhas et al. [30] point out that inclusion of plastic strain range dependence through the memory parameter q of equations (5) and (6) is highly insufficient to correlate the significant additional hardening of type 316 stainless steel subjected to 90 deg out-of-phase tension-torsion loading. Hence, the need to define another state variable to account for the additional hardening during nonproportional loading is well established.

McDowell [6, 7, 31] introduced an instantaneous measure J of the nonproportionality of the strain rate tensor

$$J = |\dot{\gamma}_{\max}(\epsilon)/g(\gamma_{\max}(\dot{\epsilon}))| \tag{8}$$

$$\dot{\gamma}_{\max}(\epsilon) = d/dt(\epsilon_1 - \epsilon_3) \tag{9}$$

$$\gamma_{\max}(\dot{\epsilon}) = (\dot{\epsilon})_1 - (\dot{\epsilon})_3 \tag{10}$$

where ϵ_1, ϵ_3 are the largest and smallest principal strains, and $(\dot{\epsilon})_1$, $(\dot{\epsilon})_3$ are the largest and smallest principal values, respectively, of the strain rate tensor at each point in time. The function g is defined by $g(x) = 1$ if $x = 0$; $g(x) = x$ if $x \neq 0$.

There is a physical interpretation for this definition of J. Under conditions of proportional straining, $\dot{\gamma}_{\max}(\epsilon) = \gamma_{\max}(\dot{\epsilon})$ and $J = 1$. In this case, the principal axes of strain are fixed with respect to material axes. For the case of sinusoidal tension-torsion straining of a thin-walled tubular specimen with a shear to axial strain amplitude ratio of $\gamma_a/\epsilon_a = (1+\nu)$ and a phase angle of 90 deg, $\dot{\gamma}_{\max}(\epsilon) = 0$ and $J = 0$ since $\gamma_{\max}(\dot{\epsilon})$ is nonzero. Again, this is the case of maximum additional cyclic hardening observed experimentally by Brown and Miller. Hence, $0 \leq J \leq 1$ with decreasing values of J indicative of higher degrees of instantaneous nonproportionality.

Since J is an instantaneous measure of nonproportionality, the degree of nonproportionality, ϕ, representative of several complete cycles of loading can be expressed as a functional of J such that $0 \leq \phi \leq 1$; ϕ is directly analogous to RF in equation (7), but evolves continuously. A specific rate form for the state variable ϕ will be proposed later.

It should also be noted that the form for J in equations (8)–(10) is valid for proportional straining or for conditions of nonproportional loading where the principal strain directions rotate continuously at some or all points of a loading cycle, as in axial-torsion tests of thin-walled tubular specimens. Nonproportional variations of principal strains with fixed principal directions will not be considered in this study.

Downloaded 02 May 2010 to 171.66.16.54. Redistribution subject to ASME license or copyright; see http://www.asme.org/terms/Terms_Use.cfm

Description of Model

It should be noted that the formulation for memory of plastic strain range and nonproportionality of loading discussed in the previous sections are strain-based. Hence, the possibility of including these parameters in a strain space plasticity theory [36–38] appears physically meaningful. However, the memory of plastic strain range would still necessitate a separate plastic strain memory surface or analogous formulation. In addition, accurate modeling of modulus and kinematic hardening for nonproportional cyclic loading would probably require a multiple surface strain space formulation [38]. Therefore, the present paper will consider a more conventional stress space formulation for the yield surface, with the addition of a plastic strain memory surface.

A two surface, stress-space, cyclic plasticity model similar to that of Dafalias and Popov [27] and Krieg [34] is considered. This model includes plastic strain range and nonproportionality dependence in the isotropic hardening formulation. It is valid for complex, nonproportional, cyclic loading with transient hardening or softening behavior. Only small strains are considered.

The yield and limit surfaces are defined as $f(\mathbf{s} - \boldsymbol{\alpha}, R) = 0$ and $f^*(\mathbf{s}^* - \boldsymbol{\alpha}^*, R^*) = 0$, respectively, where

$$f = (3/2)\boldsymbol{\xi}:\boldsymbol{\xi} - R^2 \tag{11}$$

$$f^* = (3/2)\boldsymbol{\xi}^*:\boldsymbol{\xi}^* - (R^*)^2 \tag{12}$$

where $\mathbf{s} = \boldsymbol{\sigma} - (1/3)(\boldsymbol{\sigma}:\mathbf{I})\mathbf{I}$, $\boldsymbol{\xi} = \mathbf{s} - \boldsymbol{\alpha}$, $\boldsymbol{\xi}^* = \mathbf{s}^* - \boldsymbol{\alpha}^*$, and where $\boldsymbol{\alpha}$, R, and $\boldsymbol{\alpha}^*$, R^* denote the vector position of the center and radius of the yield and limit surfaces, respectively. The vectors $\mathbf{s}$ and $\mathbf{s}^*$ are position vectors of generic points on the yield and limit surfaces, respectively, in deviatoric stress space. The identity tensor is denoted by $\mathbf{I}$. The flow rule can be stated as $\dot{\boldsymbol{\epsilon}}^p = (1/h)(\dot{\mathbf{s}}:\mathbf{n})\mathbf{n}$ if $f = 0$ and $\dot{\mathbf{s}}:\mathbf{n} \geq 0$, with $\dot{\boldsymbol{\epsilon}}^p = \mathbf{0}$ otherwise where $h = (2/3)(d\sigma/d\epsilon^p)$ is determined from a stable uniaxial cyclic stress-strain curve, and $\mathbf{n} = (\partial f/\partial \mathbf{s}) / \|\partial f/\partial \mathbf{s}\|$.

To formulate hardening rules and the form of the function h for multiaxial loading, it is necessary to consider previous nonproportional cyclic loading experiments. The work of Lamba [17, 18] points to the use of a Mroz-type [32, 33] kinematic-isotropic hardening rule. The kinematic hardening rules of Prager [39] and Ziegler [40] prove to be inadequate for nonproportional cyclic loading [17, 18]. Hence, the use of two surfaces in the stress space formulation is both minimal and capable of accuracy.

The following simple hardening rules are representative of popular two surface models and can include all essential aspects of reality [23] such as cyclic hardening and softening, cyclic mean stress relaxation, and cyclic creep or racheting:

$$\dot{\boldsymbol{\alpha}} = \dot{\mu}_\alpha \boldsymbol{\nu} \tag{13}$$

$$\dot{R} = \Sigma \dot{\eta} \tag{14}$$

$$\dot{\boldsymbol{\alpha}}^* = \kappa \dot{\eta}\, \mathbf{n} \tag{15}$$

$$\dot{R}^* = \zeta \dot{\eta} \tag{16}$$

Equations (13) and (15) define kinematic hardening of f and f^*, respectively. Isotropic hardening is defined in equations (14) and (16). In these equations, $\boldsymbol{\nu} = (\mathbf{s}^* - \mathbf{s}) / \|\mathbf{s}^* - \mathbf{s}\|$, $\dot{\eta} = (\dot{\boldsymbol{\epsilon}}^p : \dot{\boldsymbol{\epsilon}}^p)^{1/2} = \|\dot{\boldsymbol{\epsilon}}^p\|$ and $\kappa = (2/3)(d\sigma/d\epsilon^p)_\infty$ where $d\sigma$ and $d\epsilon^p$ are measured from a uniaxial cyclic stress-strain curve. Hence, κ represents the asymptotic plastic modulus. In practice, κ is selected to best fit the asymptotic stress-strain response. The functions Σ and ζ will be discussed later.

In the Mroz rule of equation (13) $\mathbf{s}^*$ defined as the point on the surface f^* which has the same outward normal as the normal, $\mathbf{n}$, to the yield surface f at the current stress state, $\mathbf{s}$:

$$\mathbf{s}^* = \boldsymbol{\alpha}^* + (R^*/R)\boldsymbol{\xi} \tag{17}$$

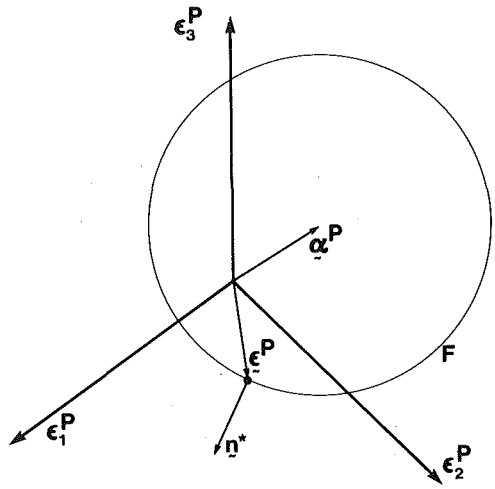


Fig. 1 Plastic strain memory surface F when the current plastic strain lies on F

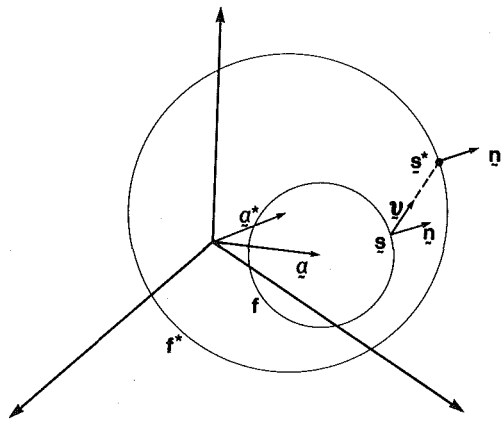


Fig. 2 Surfaces f and f^* in deviatoric stress space

The rate scalar $\dot{\mu}_\alpha$ is determined from the consistency condition $\dot{f} = 0$ during the plastic flow, which upon the substitution $\dot{\boldsymbol{\alpha}} = \dot{\mu}_\alpha \boldsymbol{\nu}$ leads to

$$\dot{\mu}_\alpha = (\boldsymbol{\xi}:\dot{\mathbf{s}} - (2/3)R\dot{R}) / (\boldsymbol{\xi}:\boldsymbol{\nu}) \tag{18}$$

The surfaces f and f^* and the parameters $\boldsymbol{\alpha}$, $\boldsymbol{\alpha}^*$, $\mathbf{n}$ and $\boldsymbol{\nu}$ are illustrated in Fig. 2 in deviatoric stress space. The hardening modulus, h, can be expressed as a function of $\|\mathbf{s}^* - \mathbf{s}\|$. As noted by Krieg [34], the stiffness decreases as $\|\mathbf{s}^* - \mathbf{s}\|$ decreases until we approach the asymptotic state characterized by κ at some significant level of plastic strain. In the absence of accurate knowledge of the variation of the hardening modulus during nonproportional plastic flow, it is assumed that the limit surface f^* is of primary importance in defining h. The functional relationship for h can then be determined from a stable uniaxial cyclic stress-strain curve as shown in Fig. 3. Since this curve is representative of cyclically stable response, $\dot{R} = \dot{R}^* = 0$ and hardening is purely kinematic. The radii R^* and R determined from this uniaxial cyclic stress-strain curve will be denoted as $\bar{R}^*(0, q)$ and $\bar{R}(0, q)$, respectively, where q is the maximum plastic strain amplitude in the incremental step test used to determine the curve. Small offset or deviation from linearity definitions of yield could be used. The hardening modulus could be generally written as

$$h = h(\|\mathbf{s}^* - \mathbf{s}\| / (\theta(R^* - R)), \kappa) \tag{19}$$

As $\|\mathbf{s}^* - \mathbf{s}\| \to 0$, $h \to \kappa$. The asymptotic slope $(2/3)(d\sigma/d\epsilon^p)_\infty$ defines κ as shown in Fig. 3. The radii R and R^* are the $\Delta\epsilon^p/2 = 0$ ordinate intercepts defined by a deviation

Downloaded 02 May 2010 to 171.66.16.54. Redistribution subject to ASME license or copyright; see http://www.asme.org/terms/Terms_Use.cfm

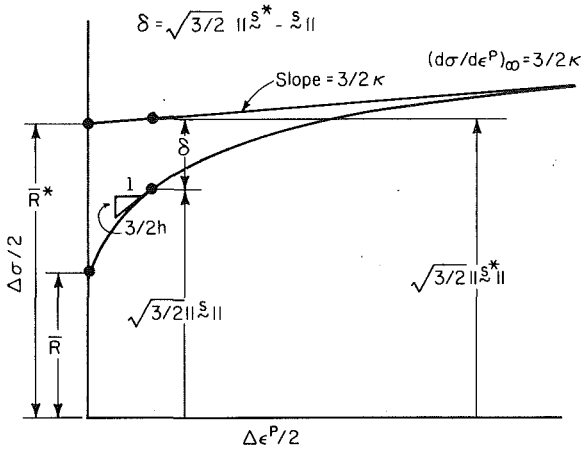


Fig. 3 Determination of parameters in two surface model from a uniaxial cyclic stress-strain curve

from linearity, perhaps, and back extrapolation of the asymptotic plastic response defined by κ, respectively. Thus, R is the uniaxial yield strength of the material.

The θ parameter in equation (19) introduces memory of the most recent point of elastic unloading. It is a measure of the effects of plastic deformation accumulated during the last loading reversal. From an alternative viewpoint, it is a measure of the initial distance to the asymptotic plastic state from the point of initial yielding for the current plastic trajectory. Hence, the use of θ has the same qualitative effect on the plastic modulus function as the delta parameter introduced by Dafalias and Popov [27] to describe the experimental observation that h is not strictly just a function of current distance from the limit surface. A simple, reasonable choice for θ for each plastic strain trajectory would be

$$\theta = \|\mathbf{s}_0^* - \mathbf{s}_0\| / (R_0^* - R_0) \tag{20}$$

where all zero subscripted variables correspond to values at the most recent point of initial yielding following a change in loading direction.

The hardening rules in equations (13)–(16) allow the surfaces f and f^* to expand and translate independently without intersecting. The limit surface translates more slowly and, possibly, in a different direction than the yield surface when the stress point lies within f^*. When $\|\mathbf{s}^* - \mathbf{s}\| \to 0$ and $\dot{R} = \dot{R}^* = 0$, the surfaces approach tangential contact and translate according to $\dot{\alpha} \to \dot{\alpha}^* = \kappa\dot{\eta}\mathbf{n}$ since $h \to \kappa$. When $\|\mathbf{s}^* - \mathbf{s}\| = 0$, we can heuristically take $\nu = \mathbf{n}$.

The use of this stress space formulation is restricted to strain-hardening behavior for which $(\partial f/\partial \mathbf{s})$: $\dot{\mathbf{s}} > 0$ during plastic flow, a condition almost universally met by metals of structural interest at typical cyclic strain magnitudes.

The isotropic hardening functions Σ and ζ can be written as

$$\dot{R} = \mu(\bar{R}(\phi,q) - R)\psi\dot{\eta} \tag{21}$$

$$\dot{R}^* = \mu(\bar{R}^*(\phi,q) - R^*)\psi^*\dot{\eta} \tag{22}$$

where $\bar{R}$ and $\bar{R}^*$ represent cyclically stable values of R and R^* corresponding to the current values of state variables ϕ and q. The rate of approach to the cyclically stable state is governed by μ. The admissibility functions ψ and ψ^* place restrictions on the stable states that can actually be attained. They are necessary for complex loading because a formulation based on internal state variables that do not necessarily monotonically increase (i.e., plastic strain range q and nonproportionality of loading ϕ) implies reversibility; yet isotropic hardening is known to be largely irreversible for planar slip metals [25, 26], and nearly reversible for wavy slip materials of structural interest. In the event of nonfading memory for cyclically hardening metals, ψ and ψ^* could be represented by Heaviside functions $u(\bar{R}(\phi,q) - R)$ and $u(\bar{R}^*(\phi,q) - R^*)$, respectively. In contrast, completely fading memory can be described by $\psi = \psi^* = 1$.

The variable ϕ represents the integrated effects of mobile dislocation interactions during cycling. The evolution of ϕ can be described by

$$\dot{\phi} = \mu^*(1 - J - \phi)\dot{\eta}\, u(1 - J - \phi_{\text{limit}}) \tag{23}$$

where $\phi = 0$ at time $t = 0$ or $\int_t \dot{\eta} dt = 0$. Inclusion of the Heaviside function $u(1 - J - \phi_{\text{limit}})$ is based on the assumption that additional hardening due to interaction of slip systems during nonproportional loading is determined primarily by those portions of each loading cycle for which the maximum shear planes rotate during plastic flow. The threshold value ϕ_{limit} may be defined as a small number in the range 0.01 to 0.03 so that virtually all deviations from proportionality are included. The calculation of ϕ is insensitive to the magnitude of ϕ_{limit} if ϕ_{limt} is less than 0.10, particularly for moderate to severe degrees of nonproportionality of loading. For proportional straining, $\phi = 0$. For $\gamma_a/\epsilon_a = (1 + \nu)$ during sinusoidal tension-torsion straining with a phase angle between applied axial and shear strains of 90 deg, $\phi \to 1$ as $\int_t \dot{\eta} dt \to \infty$. The evolution of q, the plastic strain range variable, is defined by equation (6). Introducing a kinematic hardening rule for F in equation (5),

$$\dot{\alpha}^p = (H(F)/2)(\dot{\epsilon}^p : \mathbf{n}^*)\mathbf{n}^* \tag{24}$$

Hence, the surface F can evolve only if $F = 0$ and ϵ^p lies on F. Enforcing the consistency condition $\dot{F} = 0$ during plastic flow when $F = 0$ $(H(F) = 1)$,

$$(\partial F/\partial \epsilon^p) : \dot{\epsilon}^p + (\partial F/\partial \alpha^p) : \dot{\alpha}^p - 2q\dot{q} = 0 \tag{25}$$

which, after some substitution and manipulation, leads to

$$\Gamma = \mathbf{n}^* : \mathbf{n} + \sqrt{6}\Lambda(q) \tag{26}$$

All that remains in the isotropic hardening formulation is assignment of the functions $\bar{R}(\phi, q)$ and $\bar{R}^*(\phi, q)$ in equations (21) and (22). McDowell [6, 7] demonstrated the applicability of the linear form

$$\bar{R}(\phi,q) = \phi[\bar{R}(1,q) - \bar{R}(0,q)] + \bar{R}(0,q) \tag{27}$$

$$\bar{R}^*(\phi,q) = \phi[\bar{R}^*(1,q) - \bar{R}^*(0,q)] + \bar{R}^*(0,q) \tag{28}$$

where $\bar{R}(1, q)$ and $\bar{R}^*(1, q)$ can be obtained, for example, from the cyclic stress-strain response during proportional loading immediately following cyclically stable 90 deg out-of-phase tension-torsion loading of thin-walled tubular specimens at a shear to axial strain amplitude ratio of $\gamma_a/\epsilon_a = (1 + \nu)$.

Conclusions

The proposed model, while limited in scope to time and rate-independent behavior, is significant in two respects. First, the effects of changes in plastic strain range and nonproportionality of loading are incorporated in the evolution of isotropic hardening via two additional state variables q and ϕ. It is fully expected that either or both of these variables could be included in virtually any constitutive framework. Abrahamson [41] incorporated an analogous form of ϕ proposed by McDowell [7] into a state variable constitutive framework valid for cyclic viscoplasticity.

It is noted that the structure of the proposed theory is capable of representing those aspects of material behavior perceived as most essential and relevant by Drucker and Palgen [23] for time-independent cyclic plasticity including erasure of memory of prior deformation by overload excursions, cyclic hardening or softening under symmetric cycles of stress or strain in the plastic range, progressive creep or racheting of the hysteresis response during unsymmetric cycles of stress in the plastic range, and progressive relaxation of mean stress during unsymmetric cycles of strain in the

Downloaded 02 May 2010 to 171.66.16.54. Redistribution subject to ASME license or copyright; see http://www.asme.org/terms/Terms_Use.cfm

plastic range. The accuracy of the racheting or mean stress relaxation capability of this model would be enhanced by admitting dependence of κ and h on (1/2) (s:s), the second invariant of deviatoric stress.

Acknowledgments

The author wishes to acknowledge the National Science Foundation (Grant No. MEA-8404080; Program Manager, C. J. Astill) for continuing research support on the subject of this paper.

References

1 Krempl, E., *The Influence of State of Stress on Low-Cycle Fatigue of Structural Materials*, ASTM STP 549, 1974.

2 Brown, M. W., and Miller, K. J., "Two Decades of Progress in the Assessment of Multiaxial Low-Cycle Fatigue Life," *Low-Cycle Fatigue and Life Prediction*, ASTM STP 770, 1982, pp. 482-499.

3 Fash, J. W., Socie, D. F., and McDowell, D. L., "Fatigue Life Estimates for a Simple Notched Component Under Biaxial Loading," to appear in ASTM STP 853.

4 Garud, Y. S., "MULTI-AXIAL FATIGUE: A Survey of the State of the Art," Proceedings of the ASTM/SAE Workshop on Elasto-Plastic Materials Behavior and Component Fatigue Analysis, Minneapolis, April 1980.

5 Laflen, J. H., and Cook, T. S., "Equivalent Damage—A Critical Assessment," NASA CR-167874, Nov. 1982.

6 McDowell, D. L., "On the Path Dependence of Transient Hardening and Softening to Stable States Under Complex Biaxial Cyclic Loading," *Proceedings of the International Conference on Constitutive Laws for Engineering Materials*, Desai and Gallagher, Eds., Tucson, Ariz., Jan. 1983, pp. 125-132.

7 McDowell, D. L., "Transient Nonproportional Cyclic Plasticity," Ph.D. thesis, Design and Materials Division, Report No. 107, Department of Mechanical and Industrial Engineering, University of Illinois at Urbana-Champaign, June 1983.

8 Liu, K. C., and Greenstreet, W. L., "Experimental Studies to Examine Elastic-Plastic Behaviors of Metal Alloys Used in Nuclear Structures," *Constitutive Equations in Viscoplasticity: Computational and Engineering Aspects*, AMD, ASME, Vol. 20, 1976, pp. 35-56.

9 Hecker, S. S., "Experimental Studies of Yield Phenomena in Biaxially Loaded Metals," *Constitutive Equations in Viscoplasticity: Computational and Engineering Aspects*, AMD, ASME, Vol. 20, 1976, pp. 1-32.

10 Phillips, A., Tang, J. L., and Ricciuti, M., "Some New Observations on Yield Surfaces," *Acta Mechanica*, Vol. 20, 1974, pp. 23-39.

11 Ohashi, Y., Kawashima, K., and Yokochi, T., "Anisotropy Due to Plastic Deformation of Initially Isotropic Mild Steel and Its Analytical Formulation," *Journal of the Mechanics and Physics of Solids*, Vol. 23, 1975, pp. 277-294.

12 Phillips, A., and Weng, G. J., "An Analytical Study of an Experimentally Verified Hardening Law," ASME JOURNAL OF APPLIED MECHANICS, Vol. 42, June 1975, pp. 375-378.

13 Shiratori, E., Ikegami, K., and Yoshida, F., "Analysis of Stress-Strain Relations by Use of an Anisotropic Hardening Plastic Potential," *Journal of the Mechanics and Physics of Solids*, Vol. 27, 1979, pp. 213-229.

14 Drucker, D. C., "Some Implications of Work Hardening and Ideal Plasticity," *Quarterly of Applied Mathematics*, Vol. 7, No. 4, Jan. 1950, pp. 411-418.

15 Mair, W. M., and Pugh, H., "Effect of Prestrain on Yield Surfaces in Copper," *Journal Mechanical Engineering Science*, Vol. 6, No. 2, 1964, pp. 150-163.

16 Newman, J. C., Jr., "Finite Element Analysis of Crack Growth Under Monotonic and Cyclic Loading," *Cyclic Stress-Strain and Plastic Deformation Aspects of Fatigue Crack Growth*, ASTM STP 637, 1977, pp. 56-80.

17 Lamba, H. S., "Nonproportional Cyclic Plasticity," TAM Report No. 413, Department of Theoretical and Applied Mechanics, University of Illinois of Urbana-Champaign, 1976.

18 Lamba, H. S., and Sidebottom, O. M., "Proportional Biaxial Cyclic Hardening of Annealed Oxygen-Free High-Conductivity Copper," *Journal of Testing and Evaluation*, ASTM, Vol. 6, No. 4, 1978, pp. 260-267.

19 McDowell, D. L., "Multiaxial Nonproportional Cyclic Deformation," Report No. 102, Design and Materials Division, Department of Mechanical and Industrial Engineering, University of Illinois at Urbana-Champaign, May 1981.

20 McDowell, D. L., Socie, D. F., and Lamba, H. S., "Multiaxial Nonproportional Cyclic Deformation," *Low-Cycle Fatigue and Life Prediction*, ASTM STP 770, 1982, pp. 500-518.

21 Garud, Y. S., "A New Approach to the Evaluation of Fatigue Under Multiaxial Loadings," *Proceedings, Symposium on Methods for Predicting Material Life in Fatigue*, ASME, Dec. 1979, pp. 247-263.

22 Garud, Y. S., "Prediction of Stress-Strain Response Under General Multiaxial Loading," *Mechanical Testing for Deformation Model Development*, ASTM STP 765, 1982, pp. 223-238.

23 Drucker, D. C., and Palgen, L., "On Stress-Strain Relations Suitable for Cyclic and Other Loading," TAM Report No. 443, Department of Theoretical and Applied Mechanics, University of Illinois at Urbana-Champaign, July 1980.

24 Landgraf, R. W., Morrow, J., and Endo, T., "Determination of the Cyclic Stress-Strain Curve," *Journal of Materials*, ASTM, Vol. 4, No. 1, Mar. 1969, pp. 176-188.

25 Lukas, P., and Polak, J., "Cyclic Stress-Strain Response in Low Amplitude Region," *Proceedings of the Symposium on Work Hardening in Tension and Fatigue*, AIME, Cincinnati, Nov. 1975, pp. 177-205.

26 Landgraf, R. W., "Cyclic Stress-Strain Responses in Commercial Alloys," *Proceedings of the Symposium on Work Hardening in Tension and Fatigue*, AIME, Cincinnati, Nov. 1975, pp. 240-259.

27 Dafalias, Y. F., Popov, E. P., "A Model of Nonlinearly Hardening Materials for Complex Loading," *Acta Mechanica*, Vol. 21, 1975, pp. 173-192.

28 Eisenberg, M. A., "A Generalization of Plastic Flow Theory With Application to Cyclic Hardening and Softening Phenomena," ASME *Journal of Engineering Materials and Technology*, Vol. 98, 1976, pp. 221-228.

29 Chaboche, J.-L., Dang Van, K., and Cordier, G., "Modelization of the Strain Memory Effect on the Cyclic Hardening of 316 Stainless Steel," *Proceedings of the 5th International Conference on Structural Mechanics in Reactor Technology*, Berlin, 1979.

30 Nouailhas, D., Policella, H., and Kaczmarek, H., "On the Description of Cyclic Hardening Under Complex Loading Histories," *Proceedings of the International Conference on Constitutive Laws for Engineering Materials*, Desai and Gallagher, Eds., Tucson, Ariz., Jan. 1983, pp. 45-49.

31 McDowell, D. L., and Socie, D. F., "Transient and Stable Deformation Behavior Under Cyclic Nonproportional Loading," to appear in ASTM STP 853.

32 Mroz, Z., "Mathematical Models of Inelastic Material Behavior," Solid Mechanics Division, University of Waterloo, Waterloo, Ontario, 1973.

33 Mroz, Z., "An Attempt to Describe the Behavior of Metals Under Cyclic Loads Using a More General Workhardening Model," *Acta Mechanica*, Vol. 7, 1967, pp. 199-212.

34 Krieg, R. D., "A Practical Two Surface Plasticity Theory," ASME JOURNAL OF APPLIED MECHANICS, Vol. 42, Sept. 1975, pp. 641-646.

35 Brown, M. W., and Miller, K. J., "Cyclic Deformation of 1 Percent Cr-Mo-V Steel Under Out-of-Phase Loads," *Fatigue of Engineering Materials and Structures*, Vol. 2, 1979, pp. 217-228.

36 Casey, J., and Naghdi, P. M., "On the Characterization of Strain-Hardening in Plasticity," ASME JOURNAL OF APPLIED MECHANICS, Vol. 48, 1981, pp. 285-296.

37 Casey, J., and Naghdi, P. M., "On the Nonequivalence of the Stress Space and Strain Space Formulations of Plasticity Theory," ASME JOURNAL OF APPLIED MECHANICS, Vol. 50, 1983, pp. 350-354.

38 Yoder, P. J., and Iwan, W. D., "On the Formulation of Strain-Space Plasticity With Multiple Loading Surfaces," ASME JOURNAL OF APPLIED MECHANICS, Vol. 48, 1981, pp. 773-778.

39 Prager, W., "A New Method of Analyzing Stress and Strain in Workhardening, Plastic Solids," ASME JOURNAL OF APPLIED MECHANICS, Vol. 23, 1956, p. 493.

40 Ziegler, H., "A Modification of Prager's Hardening Rule," *Quarterly of Applied Mathematics*, Vol. 17, 1959, pp. 55-60.

41 Abrahamson, T. E., "Modeling the Behavior of Type 304 Stainless Steel with a Unified Creep-Plasticity Theory," Ph.D. thesis, Department of Mechanical and Industrial Engineering, University of Illinois at Urbana-Champaign, 1983.

Downloaded 02 May 2010 to 171.66.16.54. Redistribution subject to ASME license or copyright; see http://www.asme.org/terms/Terms_Use.cfm

A Two Surface Model for Transient Nonproportional Cyclic Plasticity:

Part 2 Comparison of Theory With Experiments

D. L. McDowell
Assistant Professor,
School of Mechanical Engineering,
Georgia Institute of Technology,
Atlanta, Ga. 30332
Assoc. Mem. ASME

For the two surface cyclic plasticity model introduced in Part 1, methods for determination of model parameters are described. The model is specialized to axial-torsional loading of a thin-walled tubular specimen, and applied to nonproportional, room-temperature cycling of type 304 stainless steel. Computer simulations for two complex histories show good general agreement with experimental data obtained by the author.

Introduction

In Part 1 of this two-part paper, a two surface cyclic plasticity model was developed which includes the essential aspects of cyclic nonproportional loading. In this part, the material constants and model parameters are determined for type 304 stainless steel. The model is specialized to axial-torsional loading and compared with nonproportional, cyclic histories consisting of several sequential blocks, each consisting of different strain-controlled paths. It is shown that the model gives quantitatively good agreement for these complex histories and that the nonproportional state variable is necessary for this agreement.

Type 304 stainless steel is widely used in applications that involve cyclic nonproportional loading such as boiling water and liquid-metal-cooled fast breeder reactors and gas turbine engines. Such applications have warranted a relatively high research effort with regard to room and high-temperature cyclic deformation characteristics [1–4] related to fatigue and creep-fatigue interaction [5, 6].

Determination of Model Parameters

Most of the parameters of the two surface model presented in companion paper can be determined from uniaxial tests. The model requires well-defined nonproportional, biaxial tests to determine saturated or cyclically stable isotropic hardening variables.

1. Parameters $\bar{R}$ (0, q), $\bar{R}^*$ (0, q), κ and h. The radii $\bar{R}$ (0, q) and $\bar{R}^*$ (0, q) of the yield and limit surfaces, respectively, can be determined from stable uniaxial cyclic stress-strain curves [7] determined at several maximum strain amplitudes across the range of interest. The strain rate of the tests should be of the same order of magnitude as that of the histories to be modeled.

It should be noted that the asymptotic slope $(d\sigma/d\epsilon^P)_\infty = (3/2)\ \kappa$ is also a function of nonproportionality and strain range, $\bar{\kappa} = \bar{\kappa}(\phi, q)$, where $\bar{\kappa}$ denotes the slope for cyclically stable response corresponding to current values of ϕ and q. The variables σ and ϵ^P are applied stress and plastic strain in the axial direction.

The function $\bar{\kappa} = \bar{\kappa}(0, q)$ is defined by fitting the slope $(2/3)(d\sigma/d\epsilon^P)_\infty$ of the cyclic stress-strain curves at several q values.

Having determined $\bar{R}$, $\bar{R}^*$, and $\bar{\kappa}$, we can compute h from the uniaxial cyclic stress-strain curve at a selected value of $q = q'$

$$h = \frac{2}{3}\frac{d\sigma}{d\epsilon^P} = h(\delta/\delta_0, \bar{\kappa}(0,q')) \tag{1}$$

where

$$\delta = \sqrt{3/2}\|\mathbf{s}^* - \mathbf{s}\| \text{ and } \delta_0 = \sqrt{3/2}\|\mathbf{s}_0^* - \mathbf{s}_0\| = \bar{R}^*(0,q') - \bar{R}(0,q) \tag{2}$$

The quantity δ is shown in Fig. 3 of Part 1.

2. Parameters $\bar{R}(1, q)$, $\bar{R}^*$ (1, q), and $\bar{\kappa}(1, q)$. It is necessary to determine the $\bar{R}$ (1, q) and $\bar{R}^*$ (1, q) functions in equations (27) and (28) of Part 1 by running appropriate biaxial tests. Tension-torsion tests can be run at several strain amplitude levels with a phase angle between applied sinusoidal axial and engineering shear strain of 90 deg and a shear to axial strain amplitude ratio $\gamma_a/\epsilon_a = (1 + \nu)$. The parameters $\bar{R}$ (1, q), $\bar{R}^*$ (1, q) and $\bar{\kappa}$ (1, q) are determined in

Contributed by the Applied Mechanics Division for presentation at the 1985 joint ASME/ASCE Applied Mechanics, Fluids Engineering, and Bioengineering Conference, Albuquerque, N. Mex., June 24–26, 1985 of THE AMERICAN SOCIETY OF MECHANICAL ENGINEERS.

Discussion on this paper should be addressed to the Editorial Department, ASME, United Engineering Center, 345 East 47th Street, New York, N.Y. 10017, and will be accepted until two months after final publication of the paper itself in the JOURNAL OF APPLIED MECHANICS. Manuscript received by ASME Applied Mechanics Division, April 1984; final revision, August, 1984. Paper No. 85-APM-10.

Copies will be available until February, 1986.

Copyright © 1985 by ASME
Downloaded 02 May 2010 to 171.66.16.54. Redistribution subject to ASME license or copyright; see http://www.asme.org/terms/Terms_Use.cfm

analogy to the uniaxial case from half of the hysteresis loops obtained by subsequent axial loading after reaching cyclically stable response, or from a stable cyclic effective stress-strain curve obtained by connecting effective stress points at maxima of effective strain.

3. Parameters $\Lambda(q)$ and μ. The function $\Lambda(q)$ in equations (6) and (26) of Part 1 can be determined by running completely reversed uniaxial tests at a strain amplitude ϵ_{a2} until cyclically stable, increasing the strain amplitude to ϵ_{a1} for three cycles, and then decreasing to ϵ_{a2} for 10 cycles. After decreasing to ϵ_{a2}, the cyclic stress amplitude is compared to that corresponding to ϵ_{a2} if cycling were continued at amplitude ϵ_{a1}. We can heuristically define $\Lambda(q) = Cq$, where C is a constant, based on limited experiments. Upon decreasing the strain range to ϵ_{a2} and integrating equation (6) of Part 1 from this point on with $H(F) = 0$,

$$C = -1n[q^*/(\epsilon_{a1}{}^P)]/[40\epsilon_{a2}{}^P(3/2)^{1/2}] \tag{3}$$

where $\epsilon_{a1}{}^P$ and $\epsilon_{a2}{}^P$ are the plastic strain amplitudes corresponding to ϵ_{a1} and ϵ_{a2}, just before and after the amplitude reduction, respectively, and q^* is some plastic strain amplitude between $\epsilon_{a1}{}^P$ and $\epsilon_{a2}{}^P$. From the stress-strain response after unloading from $\epsilon_{a1}{}^P$ to 10 cycles of loading at $\epsilon_{a2}{}^P$, the value of q^* can be determined by setting $\bar{R}(0, q^*) = R$ since $\bar{R}(0, q)$ is known, for example. In general, $\beta_i(0, \epsilon_{a2}{}^P) \neq \beta_i(0, q^*)$ where $\beta_i = \bar{R}, \bar{R}^*$ and $\bar{\kappa}$, respectively, for $i = 1, 2, 3$. Note that q^* is the maximum plastic strain amplitude that is "remembered" by the material after the three cycle overload.

The parameter μ can be approximated as a constant for a range of strain amplitudes as demonstrated in previous uniaxial and proportional biaxial tests [8, 9, 10]. In the current rate formulation for ϕ, constant μ^* may be taken to fit transient response under conditions of nonproportional loading. For uniaxial tests, $\phi = \dot{\phi} = 0$ and μ is easily found from tests in which the strain range is suddenly increased. Denote the values of $\bar{R}$, $\bar{R}^*$, and $\bar{\kappa}$ pertaining to cyclically stable response at a completely reversed uniaxial strain amplitude q_a as $\beta_i(0, q_a)$. If the plastic strain amplitude is increased to q_b at time $t = 0$ such that $q_b > q_a$, integration of equations (21) and (22) of Part 1 and equation (15) of Part 2 (to be introduced) with all ψ values equal to 1 gives

$$X_i - \beta_i(0,q_b) = [\beta_i(0,q_a) - \beta_i(0,q_b)]\exp\left[-\mu\int_0^t \dot{\eta}dt\right] \tag{4}$$

where $X_i = R, R^*$, and κ, respectively, for $i = 1, 2, 3$. Since the $\beta_i(0, q)$ functions are known from previous uniaxial tests, X_i can be determined from the hysteresis loops as a function of $\int_0^t \dot{\eta}dt$ and a representative value for μ can then be determined from equation (4). For simplicity, the stress amplitude could be used to determine μ in equation (4) instead of X_i and β_i. If the transient response of a virgin specimen is used, the $\beta_i(0, q_a)$ parameters in equation (4) could be replaced by initial values of R, R^*, and κ.

4. Parameters ψ, ψ^*, ψ_κ, and μ^*. The form of the ψ, ψ^*, and ψ_κ functions in equations (21) and (22) of Part 1 and equation (15) of Part 2 must be determined for each material. Minimally, uniaxial tests would be necessary in which the strain amplitude is suddenly decreased from q_b corresponding to cyclically stable conditions to q_a where $q_b > q_a$. The ψ functions could be constructed from a number of such tests since $\bar{R}$, $\bar{R}^*$, and $\bar{\kappa}$ are known in the evolution equations for R, R^*, and κ. Since the ψ functions may be history-dependent, it may be sufficiently accurate to heuristically assume simple forms for wavy and planar slip materials as stated in Part 1.

The choice of μ^* can be made by fitting the rate of approach to the new cyclically stable state after switching from cyclically stable uniaxial loading. Let J' be defined as the degree of nonproportionality for the subsequent cycles (approximated as a constant). If the effective strain range is not substantially increased or decreased, we can approximate $q = q''$ as a constant. Then, equations (23), (21), or (22), and (27) or (28) of Part 1 can be combined into the differential equation

$$\frac{dX_i}{d\eta} + \mu X_i = \mu(1-J')(1-e^{-\mu^*\eta})\{\beta_i(1,q'') - \beta_i(0,q'')\} + \mu\beta_i(0,q'') \tag{5}$$

with the initial condition $X_i = \beta_i(0, q'')$ at $\eta = 0$. The solution to this equation is

$$X_i = \beta_i(0,q'') + (1-J')\{\beta_i(1,q'') - \beta_i(0,q'')\}[1 + (\mu^* e^{-\mu\eta} - \mu e^{-\mu'\eta})/(\mu - \mu^*)] \tag{6}$$

for $i = 1, 2, 3$. The maximum effective stress amplitude could be used in equation (6) to determine μ^* instead of X_i and β_i. The constant μ^* can be approximated by fitting equation (6) to the observed X_i versus η response, since μ is known.

Specialization to Axial-Torsional Loading

For a thin-walled tubular section subjected to combined tension and torsion, the deviatoric stress components can be expressed in terms of the nonzero stress components σ_{11} and σ_{12} as follows:

$$s_{11} = (2/3)\sigma_{11}, s_{22} = s_{33} = -(1/2)s_{11}, s_{12} = \sigma_{12} \tag{7}$$

$$\xi_{11} = s_{11} - \alpha_{11}, \xi_{22} = \xi_{33} = -(1/2)\xi_{11}, \xi_{12} = s_{12} - \alpha_{12} \tag{8}$$

since $\alpha_{22} = \alpha_{33} = -(1/2)\alpha_{11}$. Also, $s_{23} = s_{13} = \alpha_{13} = \alpha_{23} = 0$. Here, the subscripts 1, 2, 3 denote the axial, circumferential, and radial directions of the tubular test specimen, and $\mathbf{s}$ is the deviatoric stress tensor.

The $\mathbf{s}$ and $\boldsymbol{\alpha}$ tensors are, of course, symmetric. In this case the yield surface is expressed as $f = \sigma_{11}{}^2 + 3\sigma_{12}{}^2 - R^2 = 0$.

The components of the normal $\mathbf{n} = \boldsymbol{\xi}/\|\boldsymbol{\xi}\|$ are $n_{11} = \xi_{11}/P_\xi$ and $n_{12} = \xi_{12}/P_\xi$ where $P_\xi = ((3/2)\xi_{11}{}^2 + 2\xi_{12}{}^2)^{1/2}$ and $n_{33} = n_{22} = -(1/2)n_{11}$. For the case of tension-torsion loading of a thin-walled tubular specimen, the instantaneous measure of nonproportionality is expressed as

$$J = |(\epsilon_{11}\dot{\epsilon}_{11}(1+\nu)^2 + 4\epsilon_{12}\dot{\epsilon}_{12}) / [(\epsilon_{11}{}^2(1+\nu)^2 + 4\epsilon_{12}{}^2)(\dot{\epsilon}_{11}{}^2(1+\nu)^2 + 4\dot{\epsilon}_{12}{}^2)]^{1/2}| \tag{9}$$

The kinematic hardening rule for the yield surface becomes $\dot{\alpha}_{11} = Z(s_{11}^* - s_{11})$ and $\dot{\alpha}_{12} = Z(s_{12}{}^* - s_{12})$ where

$$Z = [(3/2)\xi_{11}\dot{s}_{11} + 2\xi_{12}\dot{s}_{12} - (2/3)R\dot{R}] / [\xi_{11}(s_{11}{}^* - s_{11})(3/2) + 2\xi_{12}(s_{12}{}^* - s_{12})] \tag{10}$$

and $s_{11}{}^* = \alpha_{11}{}^* + (R^*/R)\xi_{11}$, $s_{12}{}^* = \alpha_{12}{}^* + (R^*/R)\xi_{12}$. The flow rule can be written in component form as $\dot{\epsilon}_{11}{}^P = (1/h)P_\epsilon n_{11}$ and $\dot{\epsilon}_{12}{}^P = (1/h)P_\epsilon n_{12}$ if $P_\epsilon = ((3/2)\dot{s}_{11}n_{11} + 2\dot{s}_{12}n_{12}) \geq 0$; $\dot{\epsilon}_{11}{}^P = \dot{\epsilon}_{12}{}^P = 0$ otherwise. Here, h is determined from equation (1). Kinematic hardening of the limit surface f^* follows the Prager rule $\dot{\alpha}_{11}{}^* = \kappa n_{11}\dot{\eta}$ and $\dot{\alpha}_{12}{}^* = \kappa n_{12}\dot{\eta}$ where $\dot{\eta} = ((3/2)(\dot{\epsilon}_{11}{}^P)^2 + 2(\dot{\epsilon}_{12}{}^P)^2)^{1/2}$.

Isotropic and kinematic hardening rules for the plastic strain memory surface are written, respectively, as

$$\dot{q} = [\{((3/2)n_{11}n_{11}{}^* + 2n_{12}n_{12}{}^*) + \sqrt{6}\Lambda(q)\}(2/3)^{1/2}H(F)/2 - \Lambda(q)]\dot{\eta} \tag{11}$$

$$\dot{\alpha}_{11}{}^P = P_\alpha n_{11}{}^*, \quad \dot{\alpha}_{12}{}^P = P_\alpha n_{12}{}^* \tag{12}$$

where $P_\alpha = H(F)((3/2)n_{11}n_{11}{}^* + 2n_{12}n_{12}{}^*)\dot{\eta}/2$; $H(F) = 1$ if $F = 0$ and $H(F) = 0$ if $F < 0$. In the preceding equations, $\eta_{11}{}^* = (\epsilon_{11}{}^P - \alpha_{11}{}^P)/\Delta$ and $n_{12}{}^* = (\epsilon_{12}{}^P - \alpha_{12}{}^P)/\Delta$ where

$$\Delta = ((3/2)(\epsilon_{11}{}^P - \alpha_{11}{}^P)^2 + 2(\epsilon_{12}{}^P - \alpha_{12}{}^P)^2)^{1/2} \tag{13}$$

Isotropic hardening rules for the yield and limit surfaces reduce to $\dot{R} = \mu(\bar{R}(\phi, q) - R)\psi\dot{\eta}$ and $\dot{R}^* = \mu(\bar{R}^*(\phi, q) -$

Downloaded 02 May 2010 to 171.66.16.54. Redistribution subject to ASME license or copyright; see http://www.asme.org/terms/Terms_Use.cfm

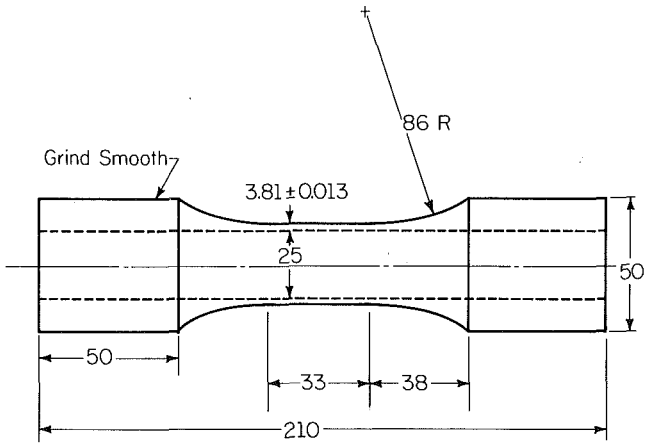


Fig. 1 Tubular biaxial specimen; dimensions in mm

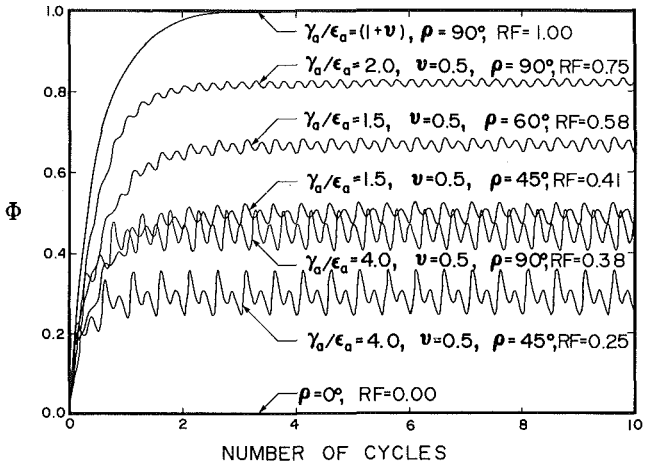


Fig. 2 Nonproportional state variable ϕ versus number of cycles for sinusoidal loading with $\epsilon_a = 0.005$ and various γ_a/ϵ_a and ρ values. The rotation factor *RF* from Brown and Miller's theory is included for comparison in each case.

$R^*)\psi^*\dot{\eta}$ where ϕ evolves according to the equation

$$\dot{\phi} = \mu^*(1 - J - \phi)\,\dot{\eta}\; u(1 - J - \phi_{\text{limit}}) \tag{14}$$

with $\phi_{\text{limit}} = 0.02$ (i.e., small) and q is obtained from integration of equation (11).

To obtain an accurate representation of the change in asymptotic plastic modulus κ during cyclic hardening, it is possible to write an evolution equation

$$\dot{\kappa} = \mu(\bar{\kappa}(\phi, q) - \kappa)\,\psi_\kappa \dot{\eta} \tag{15}$$

where ψ_κ is an appropriate admissibility function analogous to ψ and ψ^*.

Hence, we have established a set of first order evolution equations for α, ϵ^P, α^*, η, q, α^P, R, R^*, ϕ, and κ, respectively. For a given strain or stress history, they may be integrated to give the resulting stress or strain response, respectively. For a known strain history, assuming isotropic elastic response,

$$\dot{\sigma}_{11} = E(\dot{\epsilon}_{11} - \dot{\epsilon}_{11}{}^P), \qquad \dot{\sigma}_{12} = 2G(\dot{\epsilon}_{12} - \dot{\epsilon}_{12}{}^P) \tag{16}$$

Using the equations $\dot{\epsilon}_{11}{}^P = (1/h)\;(\dot{\mathbf{s}}:\mathbf{n})n_{11}$, $\dot{\epsilon}_{12}{}^P = (1/h)\;(\dot{\mathbf{s}}:\mathbf{n})n_{12}$, $E = 2G(1 + \nu_e)$, $\dot{\sigma}_{11} = (3/2)\dot{s}_{11}$, and $\dot{\sigma}_{12} = \dot{s}_{12}$, we can substitute into equations (16) to obtain $\dot{s}_{11}$ and $\dot{s}_{12}$, since $\dot{\epsilon}_{11}$ and $\dot{\epsilon}_{12}$ are known. Here, ν_e is the value of Poisson's ratio from purely elastic response.

Application to Complex Nonproportional Histories

Determination of Parameters for Type 304 Stainless Steel. A series of room-temperature, strain-controlled uniaxial and tension-torsion tests were run to determine the parameters of the two surface model for type 304 stainless steel. All specimens were heat treated at 1100°C for 40 minutes in a vacuum and furnace cooled to achieve an isotropic grain structure with an average grain diameter of 0.16 mm. A schematic of a tension-torsion specimen is shown in Fig. 1.

The biaxial tests were performed on a computer-contolled, closed-loop, servohydraulic test machine. A computer program was written so that any combination of line segments in strain space could be joined end-to-end to define a loading cycle. A block was defined as an arbitrary number of identical cycles. Furthermore, the program allowed the user to define any number of blocks, each containing a different cycle loading path. The effective strain rate $\dot{\bar{\epsilon}} = (\dot{\epsilon}_{11}{}^2 + 4\dot{\epsilon}_{12}{}^2/3)^{1/2}$ was kept constant along each segment.

Several uniaxial incremental step tests and out-of-phase step tests at maximum strain amplitudes ranging from 0.003 to 0.01 were run to establish the plastic strain range dependence of $\bar{R}(0, q)$, $\bar{R}^*(0, q)$, $\bar{\kappa}(0, q)$, $\bar{R}(1, q)$, $\bar{R}^*(1, q)$ and $\bar{\kappa}(1, q)$. From four uniaxial tests at $\dot{\bar{\epsilon}} = 0.002$ sec^{-1}, linear relationships were fit as a satisfactory approximation for $\bar{R}(0, q)$, $\bar{R}^*(0, q)$ and $\bar{\kappa}(0, q)$:

$$\bar{R}(0,q) = 171 + (q - 0.005)4000 \text{ MPa} \tag{17}$$

$$\bar{R}^*(0,q) = 295 + (q - 0.005)20690 \text{ MPa} \tag{18}$$

$$\bar{\kappa}(0,q) = 4370 - (q - 0.005)196100 \text{ MPa} \tag{19}$$

A plastic strain offset of 0.0005 was used to define yield. The hardening modulus was determined from the uniaxial cyclic stress-strain curve with $q = 0.0068$ as

$$h = \kappa\left(1 + (91960/\kappa)\left\{\sinh\left\{\frac{\|\mathbf{s}^* - \mathbf{s}\|}{\|\mathbf{s}_0^* - \mathbf{s}_0\|}\right\}\right\}^{1.1}\right) \tag{20}$$

From three sinusoidal tension-torsion tests described by

$$\epsilon = \epsilon_{11} = \epsilon_a \sin\,\omega t, \qquad \gamma = 2\epsilon_{12} = \gamma_a \sin(\omega t - \rho) \tag{21}$$

with $\epsilon_{22} = \epsilon_{33} = -\nu\epsilon_{11}$, $\epsilon_{23} = \epsilon_{13} = 0$, $\gamma_a/\epsilon_a = 1.5$ and $\rho = 90$ deg, $\bar{R}(1, q)$, $\bar{R}^*(1, q)$, and $\bar{\kappa}(1, q)$ were approximated by

$$\bar{R}(1,q) = 405 \text{ MPa}, \bar{R}^*(1,q) = 565 \text{ MPa}, \bar{\kappa}(1,q) = 4046 \text{ MPa} \tag{22}$$

From uniaxial tests where the strain range was increased or decreased, constants μ and C were taken as $\mu = 10$ and $C = 0.6$. The value of μ^* was taken to be 50 based on a transition from stable proportional to nonproportional cycling. Plots of ϕ versus number of cycles for the loading described in equations (21) appear in Fig. 2. For the type 304 stainless steel of this investigation, ψ and ψ^* were taken as Heaviside functions $u(\beta_i - X_i)$ for $i = 1$ and 2, respectively. The parameter ψ_κ was taken as the Heaviside function $u(\kappa - \bar{\kappa})$. Significant fading memory of prior cyclically stable states was not observed even for nonproportional loading followed by proportional loading. All tests were conducted at effective strain rates ranging from 0.001 sec^{-1} to 0.003 sec^{-1}.

Correlation of Theory With Experiments. Results of two separate strain-controlled tension-torsion tests are reported in this investigation. Young's modulus and the shear modulus were respectively determined as $E = 188$ GPa and $G = 77$ GPa.

To compare the experimental results with the proposed two surface theory, the same strain histories were introduced in the constitutive equations. The specialized axial-torsional equations were integrated using a first-order predictor-corrector method [11, 12]. The state equations can be expressed as $\dot{\mathbf{x}} = \mathbf{F}(\mathbf{x}, t)$ where

$$\mathbf{x} = \{\alpha_{11}\alpha_{12}\epsilon_{11}{}^P\epsilon_{12}{}^P\alpha_{11}{}^*\alpha_{12}{}^*\eta\; q\; \alpha_{11}{}^P\alpha_{12}{}^P R\; R^*\phi\; \kappa\; s_{11}s_{12}\}^T \tag{23}$$

Downloaded 02 May 2010 to 171.66.16.54. Redistribution subject to ASME license or copyright; see http://www.asme.org/terms/Terms_Use.cfm

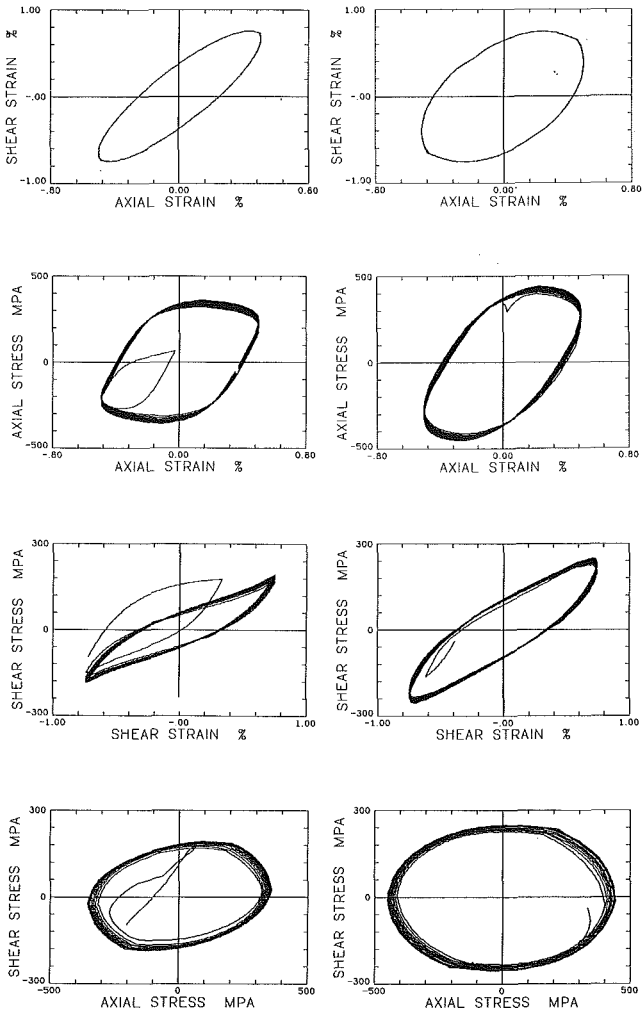


Fig. 3 Experimental results for History 1: (left column) cycles 1 to 10 of block 2, and (right column) cycles 1 to 10 of block 3

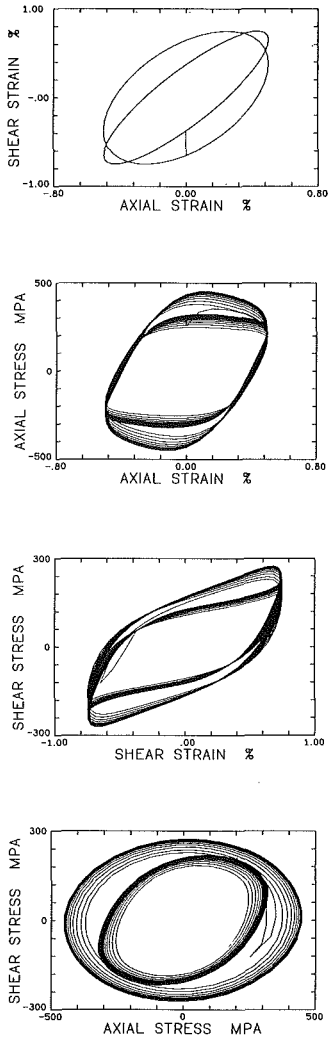


Fig. 4 Predicted results for History 1: 25 cycles of block 2 and first 10 cycles of block 3

Define $\mathbf{x}_{k+1}{}^{P}$ and $\mathbf{x}_{k+1}{}^{c}$ as predicted and corrected values of $\mathbf{x}$, respectively, at the $(k + 1)$th time step. The corrector algorithm was repeated until the norm of the error vector

$$\bar{E} = \left(\sum_{i=1}^{16} \left(|(\mathbf{x}_{k+1}{}^{c} - \mathbf{x}_{k+1}{}^{P})_i| / |(\mathbf{x}_{k+1}{}^{c})_i| \right)^2 \right)^{1/2} \tag{24}$$

was acceptable where $(\mathbf{x}_{k+1}{}^{c} - \mathbf{x}_{k+1}{}^{P})_i$ and $(\mathbf{x}_{k+1}{}^{c})_i$ are the ith components of $(\mathbf{x}_{k+1}{}^{c} - \mathbf{x}_{k+1}{}^{P})$ and $\mathbf{x}_{k+1}{}^{c}$, respectively. Then, the accepted value of $\mathbf{x}_{k+1}$ is $\mathbf{x}_{k+1} = (4/5)\mathbf{x}_{k+1}{}^{c} + (1/5)\mathbf{x}_{k+1}{}^{P}$. Automatic time-step control was included to reduce (increase) the time step Δt_k if $\bar{E}$ was greater (less) than a selected maximum value at a selected iteration. All calculations were performed on the Georgia Tech Cyber 835.

History 1: Specimen SS09. This specimen was subjected to 10 cycles of a proportional incremental step test with maximum strain amplitudes of $\epsilon_a = 0.007$, $\gamma_a = 0.0105$, and a strain rate $\dot{\bar{\epsilon}} = 0.001$ sec^{-1}. Subsequently, three blocks of different loading cycles were applied. Block 1 consisted of 16 cycles of proportional loading on the same maximum shear planes with $\rho = 0°$, $\epsilon_a = 0.005$, and $\gamma_a = 0.0075$. Block 2 consisted of 25 cycles of sinusoidal loading with $\rho = 30$ deg, $\gamma_a = 0.0075$, and $\epsilon_a = 0.005$. Block 3 consisted of 25 cycles of sinusoidal loading with $\rho = 60$ deg, $\gamma_a = 0.0075$, and $\epsilon_a = 0.005$.

The imposed cyclic strain history for blocks 2 and 3 is shown in Fig. 3 along with the experimentally observed axial stress-strain, shear stress-engineering strain and shear stress-axial stress responses. Block 1 is not included since no additional transient cyclic hardening occurred. Since data were taken in cycles 1 to 10 and geometrically increasing powers-of-two beyond cycle 10 of each block, only cycles 1 to 10 for blocks 2 and 3 appear in Fig. 3. Very little additional hardening occurred between cycles 10 and 25 [9, 10].

It should be noted that any measure of effective plastic strain range (e.g., octahedral or maximum shear) does not increase for each subsequent block, yet additional isotropic hardening occurs at the beginning of blocks 2 and 3. Computer-generated plots of the blocks 2 and 3 from two surface plasticity theory, shown in Fig. 4, demonstrate the capability of state variable ϕ to correlate this additional hardening. In the analysis, the initial values $R = 170$ MPa, $R^* = 291$ MPa, and $\kappa = 4427$ MPa were used, based on the hysteresis loop response from the stable cycles of block 1. Cyclic hardening in each block is predicted well by the model. Since the points from numerical integration were plotted at effective strain increments of 0.0005 to 0.001 and connected by straight lines, the plotted results have a piecewise linear appearance. Of course, the time steps used in integration were considerably smaller.

For block 3, the yield and limit surfaces are in contact for most, if not all, of each cycle. The evolution of R, R^*, q, and ϕ in the model is plotted for this history in Fig. 5 as a function of time. Note that q exhibits a general decay in each block as cyclic hardening accumulates. Also, ϕ increases, as expected,

Downloaded 02 May 2010 to 171.66.16.54. Redistribution subject to ASME license or copyright; see http://www.asme.org/terms/Terms_Use.cfm

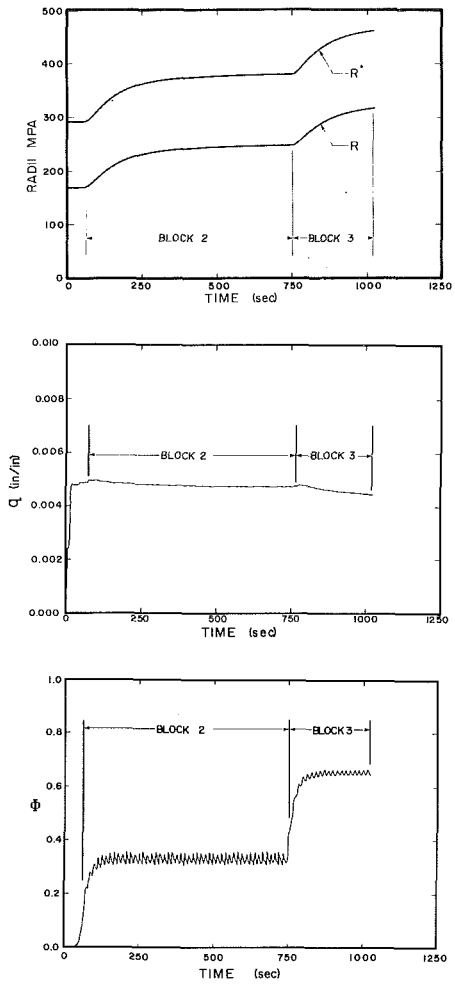


Fig. 5 Evolution of R, R^*, q, and ϕ for blocks 2 and 3 of History 1

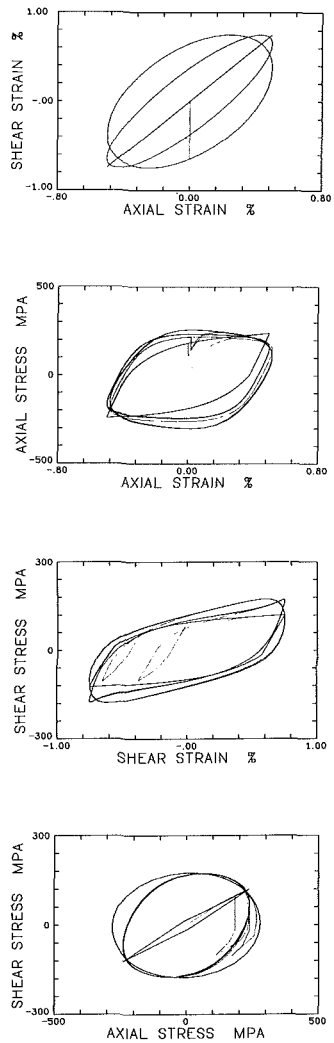


Fig. 6 Predicted results for History 1 if $\phi = 0$. The underestimation of hardening predicted in blocks 2 and 3 illustrates the inaccuracy of extrapolating uniaxial test results to nonproportional loading.

for each block. In the numerical integration, the norm $\tilde{E}$ of the error vector was kept below 10^{-3}. Poisson's ratio in equation (9) was taken as an effective value based on the ratio of maximum effective plastic strain range to maximum effective total strain range.

To illustrate the consequences of neglecting nonproportional cross-hardening effects in the analysis, the model was used to predict the same imposed strain history with $\phi = 0$ always. This would be the case if, as usually is done, only uniaxial test results were used as a reference in models for nonproportional histories. Figure 6 shows the responses predicted in this case for blocks 1, 2, and 3 of History 1. The lack of transient hardening in blocks 2 and 3 is noted. Hence, the use of uniaxial baseline data for nonproportional histories obviously can be quite inaccurate for this material.

History 2: Specimen SS01. This specimen was subjected to three blocks of dissimilar cylces. Block 1 consisted of proportional loading from the virgin state for 25 cycles with $\epsilon_a = 0.0041$, $\gamma_a = 0.006$, and $\dot{\bar{\epsilon}} = 0.003$ sec^{-1}. Block 2 consisted of another 25 cycle path, introducing another discrete set of maximum shear strain planes at the same axial and shear strain amplitudes. Block 3 consisted of another 25 cycle path that joined the previous two paths by continuously rotating the maximum shear strain planes between the tips. The three blocks of loading paths are shown in Fig. 7 along with the experimentally observed axial stress-strain, shear stress-engineering strain, and shear stress-axial stress responses. All responses are from the first 10 cycles of each block with the exception of the shear-stress–axial stress responses for blocks 1 and 2, which are from cycle 24. Again, little additional transient hardening was observed for cycles 10 to 25. The tips of the strain paths are numbered to denote sequence of loading. The response for block 2 was nearly stable immediately following block 1. It is clear that the stress response in block 3 is not symmetric and distortion and/or translation of the limit or large offset strain yield surface has occurred. Again, the isotropic hardening accrued in block 3 considerably exceeds that predicted by using a uniaxial cyclic stress-strain curve a the same maximum plastic strain range.

Results from the model are shown in Fig. 8 for each block. Note that the transient response in block 3 is well represented by the model, but the model predicts unloading from the limit surface near the maximum axial stress amplitude while the experimental results do not clearly reveal such a phenomenon. Hence, the peak axial stress amplitude is underestimated. The rate of hardening in block 3 is reasonably accurate, even though the loading is quite complex. In the analysis, the initial values $R = 148$ MPa, $R^* = 192$ MPa, and $\kappa = 8366$ MPa were used, based on the monotonic stress-strain curve for the annealed type 304 stainless steel. Initial values for all other variables were taken as zero. Again, the norm of the error vector was maintained below 10^{-3}.

Conclusions

It has been demonstrated that the proposed two surface

Downloaded 02 May 2010 to 171.66.16.54. Redistribution subject to ASME license or copyright; see http://www.asme.org/terms/Terms_Use.cfm

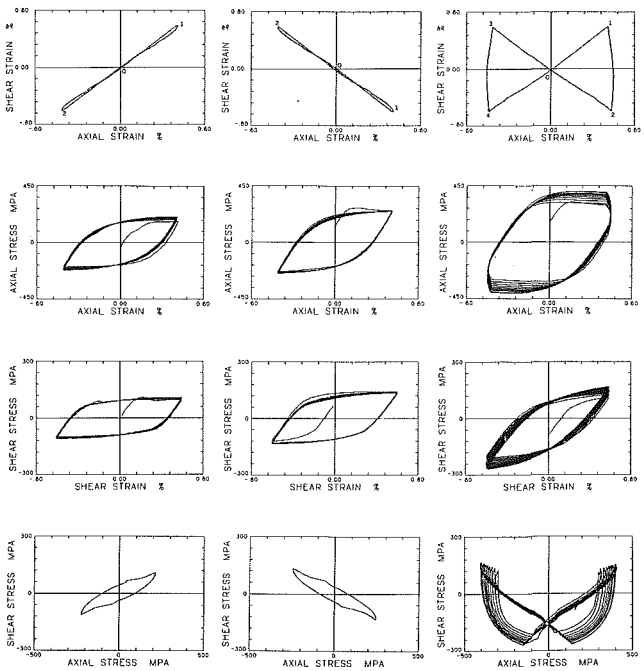


Fig. 7 Experimental results for History 2: (left column) cycles 1 to 10 of block 1, (center column) cycles 1 to 10 of block 2, and (right column) cycles 1 to 10 of block 3

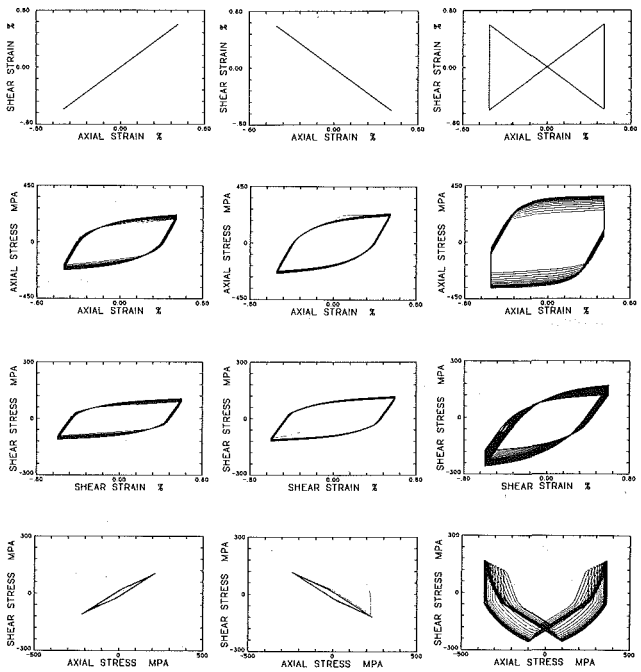


Fig. 8 Predicted results for History 2: (left column) cycles 1 to 25 of block 1, (center column) cycles 1 to 25 of block 2, and (right column) cycles 1 to 25 of block 3

theory is capable of reasonably accurate prediction of stress-strain response for complex nonproportional loading. The model combines an appropriate kinematic hardening rule based on the theory of Mroz with an isotropic hardening rule that accounts for dependence on plastic strain range and nonproportionality of loading, both of which can be significant for a number of materials of structural interest. Hence, the model is sophisticated enough to describe essential aspects of transient, cyclic, nonproportional deformation behavior.

To achieve this necessary sophistication, some concessions were made. To model plastic strain range dependence, state variables $\boldsymbol{\alpha}^P$ and q are introduced. State variables R^*, $\boldsymbol{\alpha}^*$ and κ were introduced in addition to the usual variables R and $\boldsymbol{\alpha}$ to produce an acceptable description of plastic strain rate direction and hardening modulus during nonproportional plastic flow. State variable ϕ was defined to account for additional isotropic hardening during nonproportional loading. Even with these additional parameters, the model is simple in the respect that the yield surface is not allowed to distort.

Methods for experimental determination of model parameters have been set forth, although there is freedom to adapt the model to peculiar characteristics of each material of interest. For example, the functions $\Lambda(q)$, ψ, ψ^*, and ψ_κ may be determined to any desired degree of precision. The function θ may be selected to give smooth reloading response after unloading for small subcycles, or to accurately fit cyclic creep racheting response. Even with the relatively small number of tests run in this investigation to determine $\bar{R}$, $\bar{R}^*$, $\bar{\kappa}$, C, and μ, it is seen that the theory satisfactorily models the more complex histories of this study. No claim can be made regarding the sufficiency of experimental characterization of the $\Lambda(q)$ and ψ functions in this study, since the histories to be predicted did not include overload sequence effects. It seems that the choice of the structure of the model is more important than exhaustive experimental characterization, as evidenced by the poor predictions obtained when ϕ was neglected.

Acknowledgments

The author wishes to acknowledge the National Science Foundation (Grant No. MEA-8404080; Program Manager, C. J. Astill) for continuing research support on the subject of this paper.

References

1 Miller, A., "An Inelastic Constitutive Model for Monotonic, Cyclic, and Creep Deformation: Part II—Application to Type 304 Stainless Steel," ASME *Journal of Engineering Materials and Technology*, Vol. 98, 1976, pp. 106–113.

2 Liu, M. C. M., Krempl, E., and Nairn., D. C., "An Exponential Stress-Strain Law for Cyclic Plasticity," ASME *Journal of Engineering Materials and Technology*, Vol. 98, 1976, pp. 322–329.

3 Wu, H. C., and Yip, M. C., "Endochronic Description of Cyclic Hardening Behavior for Metallic Materials," ASME *Journal of Engineering Materials and Technology*, Vol. 103, 1981, pp. 212–217.

4 Eisenberg, M. A., "A Generalization of Plastic Flow Theory With Application to Cyclic Hardening and Softening Phenomena," ASME *Journal of Engineering Materials and Technology*, Vol. 98, 1976, pp. 221–228.

5 Koterazawa, R., and Iwata, Y., "Fracture Mechanics and Fractography of Creep and Fatigue Crack Propagation at Elevated Temperature," ASME *Journal of Engineering Materials and Technology*, Vol. 98, 1976, pp. 296–304.

6 Cheng, C. Y., and Diercks, D. R., "Effects of Hold Time on Low-Cycle Fatigue Behavior of AISI Type 304 Stainless Steel at 593°C," *Metallurgical Transactions*, Vol. 4, 1973, pp. 615–617.

7 Landgraf, R. W., Morrow, J., and Endo, T., "Determination of the Cyclic Stress-Strain Curve," *Journal of Materials*, ASTM, Vol. 4, No. 1, Mar. 1969, pp. 176–188.

8 Lamba, H. S., and Sidebottom, O. M., "Proportional Biaxial Cyclic Hardening of Annealed Oxygen-Free High-Conductivity Copper," *Journal of Testing and Evaluation*, ASTM, Vol. 6, No. 4, 1978, p. 260–267.

9 McDowell, D. L., "Transient Nonproportional Cyclic Plasticity," Ph.D. thesis, Report No. 107, Design and Materials Division, Department of Mechanical and Industrial Engineering, University of Illinois at Urbana-Champaign, June 1983.

10 McDowell, D. L., "On the Path Dependence of Transient Hardening and Softening to Stable States Under Complex Biaxial Cyclic Loading," *Proceedings of the International Conference on Constitutive Laws for Engineering Materials*, Desai and Gallagher, Eds., Tucson, Ariz., Jan. 1983, pp. 125–132.

11 Kumar, V., Morjaria, M., and Mukherjee, S., "Numerical Integration of Some Stiff Constitutive Models of Inelastic Deformation," ASME *Journal of Engineering Materials and Technology*, Vol. 102, 1980, pp. 92–96.

12 Hilderbrand, F. B., Finite-Difference Equations and Simulations, Prentice-Hall, Englewood Cliffs, N.J., 1968.

Downloaded 02 May 2010 to 171.66.16.54. Redistribution subject to ASME license or copyright; see http://www.asme.org/terms/Terms_Use.cfm

J. Tirosh
Faculty of Mechanical Engineering,
Technion-Israel Institute
of Technology,
Haifa, Israel
Mem. ASME

D. Iddan
Senior Engineer,
Rafael,
Haifa, Israel

O. Pawelski
Max Planck Institut
für Eisenforschung,
Düsseldorf, West Germany

The Mechanics of High-Speed Rolling of Viscoplastic Materials

In the present work a consideration is given to the speed effect on the mechanical performance of strip rolling process with time-dependent materials. The speed-governing dimensionless groups (Euler number and Bingham number) are identified. The suggested approach includes, in an upper bound sense (mixed with stress-equilibrium solutions), the dynamic stress distribution of a Bingham-like viscoplastic material, the speed-dependent energy dissipations, the self-heated surface temperature, and the associated material softening. All these effects are coupled and contributed for explaining the apparently puzzling empirical evidence showing ***reduction*** *in the roll torque and separation force while* ***increasing*** *the rolling speed. For a relativelyl slow speed, the predicted roll separtion force matches very well an available experimental data as well as Kobayashi's rigid-plastic finite element analysis. The predicted torque, however, is somewhat higher than the experiments, in particular when the roll-flatness correction is incorporated. The capability of forecasting the variation of roll force with various speeds (reaching high speeds), was checked versus Ford's measurements and a satisfactory agreement is demonstrated.*

1 Introduction

Experimental facts have been accumulated during the last few decades on the marked effect of rolling speed on roll force and roll torque of thin strips [1, 2]. Such dependency cannot be explained by the classical time-independent plasticity. Ford [1] was apparently the first to accentuate the complexity of this phenomena. Via an extensive data and associated estimations, Ford concluded that neither the dependence of yield stress on deformation rate nor the effect of temperature rise (resulting from the work of deformation and frictional shear) can provide satisfactory explanation to the speed-sensitive rolling loads. The need for better understanding of this phenomenon stems from the practical importance of maintaining the precision of the product gauge independent of rolling speed. Such difficulties stimulated a closer look into this problem.

In the last few years progress has been achieved in introducing speed effect into plastic forming processes. One possible way elaborated widely by Cristescu [3] is to superpose the viscous effect on the constitutive equation of perfectly plastic materials in Bingham-type sense. In this approach the velocity of the operation is coupled with the viscosity parameter of the flowing metal. Cristescu's example of wire drawing reveals that either higher viscosity or higher speed (or both) increases the required load which matches better experimental results.

Another approach to bring speed effect into time-independent material is used in references [4, 5]. In these studies, account was given to the dynamic load needed for accelerating the plastic flow. Consequently, velocity-dependent terms somewhat improved the ability to forecast the active (and reactive) loads in forming processes.

In the present work we attempt to study the speed effect in cold rolling process of metals. This is done by considering both the viscoplastic nature of the metal, the inertia effects, the temperature rise, and the strength softening associated with high-speed rolling. The outcome is a versatile expression capable of estimating in an approximate way the dynamic stress distribution in the roll gap, the overall roll separation force, and roll torque as a function of the speed at which the process is conducted. The relationship is highly nonlinear (cubic polynomial in the speed) and presented in terms of universal dimensionless numbers (Bingham number and Euler number).

Agreement with roll force and torque measurements taken from Ford [1], Al-Salehi et al. [6], and Shida et al. [14] is very satisfactory. Comparisons to calculations by rigid-plastic finite elements from Li and Kobayashi [7] is excellent in few cases, and satisfactory in others.

2 Dynamic Stress Analysis

Consider a rolling process of a sheet material with initial thickness h_i and final thickness h_f having a relatively large width, such that h_i and $h_f << $ width.

The process is achieved by two rollers of diameter D^{ϕ} revolving with angular speed ω as shown in Fig. 1. The

Contributed by the Applied Mechanics Division for presentation at the 1985 Joint ASME/ASCE Applied Mechanics, Fluids Engineering, and Bioengineering Conference, Albuquerque, N. Mex., June 24-26, 1985 of THE AMERICAN SOCIETY OF MECHANICAL ENGINEERS.

Discussion on this paper should be addressed to the Editorial Department, ASME, United Engineering Center, 345 East 47th Street, New York, N.Y. 10017, and will be accepted until two months after final publication of the paper itself in the JOURNAL OF APPLIED MECHANICS. Manuscript received by ASME Applied Mechanics Division, February, 1984; final revision, July, 1984. Paper No. 85-APM-6.

Copies will be available until February, 1986.

Copyright © 1985 by ASME
Downloaded 02 May 2010 to 171.66.16.54. Redistribution subject to ASME license or copyright; see http://www.asme.org/terms/Terms_Use.cfm

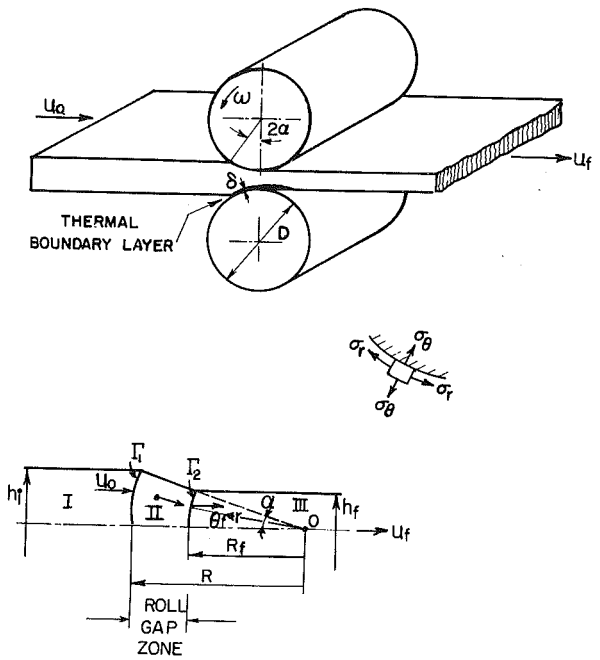


Fig. 1 Schematic view of strip rolling process

material is assumed to respond in a viscoplastic manner (according to the so-called Bingham model) where the viscous strain rate and the plastic strain rate are alike. Thus the stress deviator S_{ij} $(=\sigma_{ij} - 1/3\ \sigma_{kk}\delta_{ij})$ is related to strain by

$$S_{ij}=(2\eta+K/\sqrt{I_2})\dot{\epsilon}_{ij} \quad \text{or equivalently} \quad S_{ij}=\frac{2\eta}{1-K/\sqrt{J_2}}\dot{\epsilon}_{ij} \tag{1}$$

where η is the viscosity of the material, K is the yielding stress in shear, provided $K<\sqrt{J_2}$. I_2 and J_2 are the second invariant of strain rate and stress deviator, respectively, namely

$$I_2=1/2\ \dot{\epsilon}_{ij}\dot{\epsilon}_{ij}, \qquad J_2=1/2\ S_{ij}S_{ij} \tag{2}$$

Since the arc of contact area is practically small ($\alpha \simeq 5$ deg) and the thickness of the sheet is small with respect to the roller diameter, one can replace the arc of the contact area by a straight line. Consequently the flow pattern can be described as a radially converging flow (like planar strain extrusion) with moving inclined dies. The "moving dies," due to their frictional shear with the material, constitute the *driving force* of the process. Additional possibility of applying force is through a backward and/or forward push/pull. It is not essential to our analysis and will be skipped for clarity purposes.

By assuming a radial flow, the admissible velocity field, u_i^*, is solved from the incompressiblity condition $\dot{\epsilon}_{ii}^* = 0$ which yields

$$\frac{\partial u_r^*}{\partial r}+\frac{u_r^*}{r}=0 \tag{3}$$

Since u_r^* depends on two space variables only (r, θ) the solution to (3) is

$$u_z^*=0 \qquad u_r^*=-f(\theta)/r \qquad u_\theta^*=0 \tag{4}$$

where $f(\theta)$ is an angular variable to be determined from the predetermined lines of velocity discontinuities at inlet and outlet of the roll gap shown is Fig. 1.

The continuity of the radial component of u_0 across Γ_1 leads to

$$f(\theta)=u_0R\cos\theta \tag{5}$$

Consequently, the nonzero strain rate components derived from (4) and (5) via the kinematic relationship

$$\dot{\epsilon}_{ij}^*=1/2(u_{i,j}^*+u_{j,i}^*) \tag{6}$$

are:

$$\dot{\epsilon}_r^*=\partial u_r^*/\partial r=u_0R\cos\theta/r^2$$
$$\dot{\epsilon}_\theta^*=-\dot{\epsilon}_r^*(\text{since } \dot{\epsilon}_z^*=0) \tag{7}$$
$$\dot{\epsilon}_{r\theta}^*=\frac{1}{2r}\frac{\partial u_r}{\partial\theta}=1/2\ u_0R(\sin\theta)/r^2$$

u_0 and R are the ingoing speed and radial distance, respectively (see Fig. 1). Also, for plane strain situation (where $\sigma_z = 1/2\ (\sigma_r + \sigma_\theta)$), one gets the second stress deviator invariant as

$$J_2=1/2\ S_{ij}S_{ij}=1/4(\sigma_r-\sigma_\theta)^2+\tau_{r\theta}^2 \tag{8}$$

The equations of motion ($\sigma_{ij,j} = \rho\dot{u}_i$) when specialized to this case are

$$\frac{\partial\sigma_r}{\partial r}+\frac{1}{r}\frac{\partial\tau_{r\theta}}{\partial\theta}+\frac{\sigma_r-\sigma_\theta}{r}=\left[\frac{\partial u_r}{\partial t}+u_r\left(\frac{\partial u_r}{\partial r}\right)\right]\rho \tag{9}$$

$$\frac{1}{r}\frac{\partial\sigma_\theta}{\partial\theta}+\frac{\partial\tau_{r\theta}}{\partial r}+\frac{2\tau_{r\theta}}{r}=0 \tag{10}$$

By using (7), the constitutive relation (1) can be expressed alternatively in terms of the admissible field, namely

$$\dot{\epsilon}_r^*=u_0R(\cos\theta)/r^2=1/(2\eta)(1-K/\sqrt{J_2})\,(\sigma_r-\sigma_\theta)/2 \tag{11}$$

$$\dot{\epsilon}_{r\theta}^*=\frac{1}{2}u_0R(\sin\theta)/r^2=1/(2\eta)(1-K/\sqrt{J_2})\,\tau_{r\theta} \tag{12}$$

The unknowns dynamic stress components σ_r, σ_θ, $\tau_{r\theta}$, and J_2 are solvable via (8)–(12) with the boundary condition that the radial stress is zero (or equal to the back push traction if imposed).

Leaving the algebra aside, the outcome for the normalized dynamic stress components ($\hat{\sigma}_r=\sigma_r/K$, $\hat{\sigma}_\theta=\sigma_\theta/K$, $\hat{\tau}_{r\theta}=\tau_{r\theta}/K$) reads

$$(\hat{\sigma}_r)_{\text{dyn}}=(\hat{\sigma}_r)_{st}+\frac{5}{2}N[(R/r)^2\cos\theta-1]$$
$$+\frac{1}{2}\text{Eu}[(R/r)^2\cos^2\theta-1] \tag{13}$$

$$(\hat{\sigma}_\theta)_{\text{dyn}}=(\hat{\sigma}_\theta)_{st}-\frac{3}{2}N\left[(R/r)^2\cos\theta+\frac{5}{3}\right]$$
$$+\frac{1}{2}\text{Eu}[(R/r)^2\cos^2\theta-1] \tag{14}$$

$$(\hat{\tau}_{r\theta})_{\text{dyn}}=(\hat{\tau}_{r\theta})_{st}+N(R/r)^2\sin\theta \tag{15}$$

where the two nondimensional groups with velocity terms used in the foregoing, N and Eu, are defined as

$$N=\eta u_0/(KR) \tag{16}$$

known as "speed parameter" [3] or "(Bingham number)$^{-1}$" and

$$\text{Eu}=\rho u_0^2/K \tag{17}$$

known as Euler number.

The "static" values of the stress components $(\hat{\sigma}_{ij})_{st}$ (the stresses that arise in quasistatic operation) appear to be

$$(\hat{\sigma}_r)_{st}=2/\sqrt{3}\ln[\cos\theta+(\cos^2\theta+1/3)^{1/2}]$$
$$+4\cos\theta/(3\cos^2\theta+1)^{1/2}+5/2\ln(R/r)-2.8864 \tag{18}$$

$$(\hat{\sigma}_\theta)_{st}=2/\sqrt{3}\ln[\cos\theta+(\cos^2\theta+1/3)^{1/2}$$
$$+5/2\ln(R/r)-2.8864 \tag{19}$$

$$(\hat{\tau}_{r\theta})_{st}=\sin\theta/(3\cos^2\theta+1)^{1/2} \tag{20}$$

The role of the speed u_0 in increasing tension in the longitudinal direction (σ_r) and enhancing *compressive* load on the rollers ($\sigma_\theta(r, \alpha)$) is exhibited in Figs. 2 and 3.

Since the admissible velocity field and associated lines of

Downloaded 02 May 2010 to 171.66.16.54. Redistribution subject to ASME license or copyright; see http://www.asme.org/terms/Terms_Use.cfm

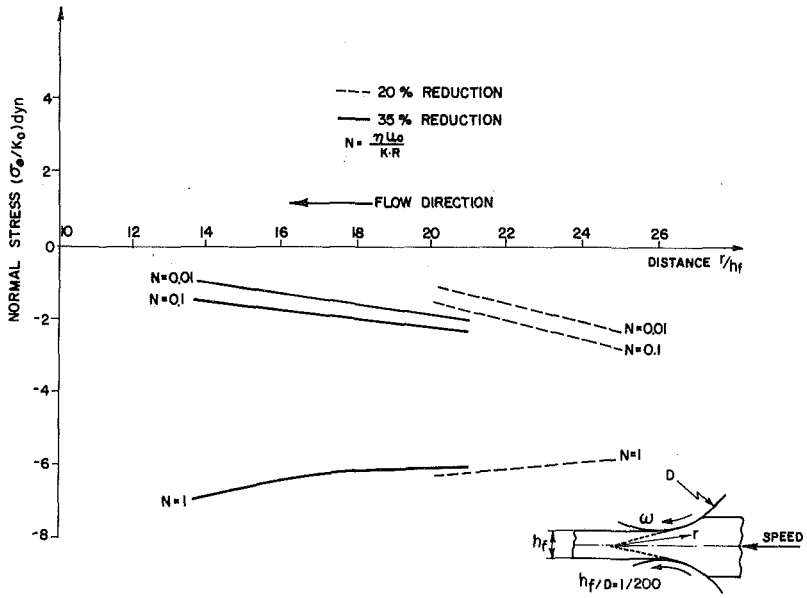


Fig. 2 Approximate dynamic tangential stress distribution (normal to the rolls) with respect to the speed parameter *N*. It is seen that high speeds cause an increase in the compressive load on the rolls.

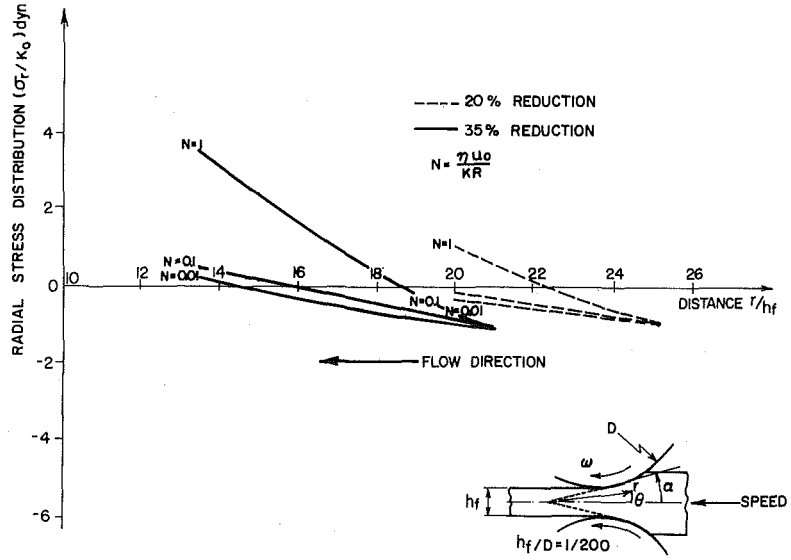


Fig. 3 Approximate dynamic radial stress distribution under the rolls (along the flow) with respect to the speed parameter *N*. It is seen that high speeds cause an increase in tensile stresses. The strip enters in compressive stress and may end in tension.

velocity discontinuities are assumed a priori, the resolved stresses are unavoidably approximate in nature. They satisfy all static and kinematic conditions in the domain of the roll gap but they do not necessarily satisfy, except along the symmetry line, the zero traction boundary conditions on Γ_1 and Γ_2. Otherwise it would have been an exact solution. There is seemingly no way to estimate the error involved in such a solution unless a rigorous lower bound can be established to this problem.

3 Recapitulation of the Dynamic Upper Bound

Define a control volume whose border is designated by S_T and S_u (as shown in Fig. 1) according to whether the traction or the velocity is prescribed, respectively.

Consider a pair of strain rate states. A true state $\dot{\epsilon}_{ij}$ and an admissible state $\dot{\epsilon}^*_{ij}$ with corresponding stress states σ_{ij} and σ^*_{ij}. The postulate of material stability (Drucker [8]) ["convexity of yield surface"] and the existence of plastic potential (Hill [9]) ["normality of plastic strain to yield surface"] leads to the basic inequality at each point

$$(\sigma_{ij} - \sigma^*_{ij})\,\dot{\epsilon}^*_{ij} \leq 0 \tag{21}$$

By assuming homogeneity of the material (obeying any constitutive law) and accounting for accelerating flow via the equation of motion

$$\sigma_{ij,j} = \rho \dot{u}_i \ (u_i = \text{a true velocity field}) \tag{22}$$

one can readily show (Tirosh and Kobayashi [4]) that (21) is representable by

$$\int_{S_u} T_i u_i ds \leq \int_V \sigma^*_{ij}\dot{\epsilon}^*_{ij} dV + \int_V \rho \dot{u}_i u^*_i dV - \int_{S_T} T_i u^*_i ds \tag{23}$$

where T_i are the actual traction components defined as $T_i = \sigma_{ij} n_j$ on S_T. It has been shown [4, 5] that for incompressible material undergoing steady state deformation (e.g., rolling process), the true acceleration $\dot{u}_i$ can be replaced by an "admissible" acceleration $\dot{u}^*_i$ (material denvative (u^*_i)) without

Downloaded 02 May 2010 to 171.66.16.54. Redistribution subject to ASME license or copyright; see http://www.asme.org/terms/Terms_Use.cfm

introducing any inaccuracy in (23) and it will be used so in the sequel.

4 Upper Bound in Rolling Process

The left-side term of (23) $\int_{S_u} T_i u_i ds$ can be split into its normal and tangential components

$$\int_{S_u} T_n u_n ds + \int_{S_u} T_t [u_t] ds \tag{24}$$

when [ ] signifies a jump in u_t across S_u. In the rolling process the power is transmitted to the material by frictional shear only, so that the first term in (24) is zero (due to $u_n = 0$ on S_u). The associated tangential jump $[u_t]$ between the roller angular speed ω and the flowing material (known also as "relative speed") is given by

$$[u_t] = \omega\, D/2 - u_r^*(\alpha, r) \tag{25}$$

where D is the roller's diameter and $u_r^*(\alpha, r)$ is the absolute material velocity along the interface with the roller.

The required roll torque M is related to the frictional shear τ_f by equating the powers as

$$2M\omega = \int_{S_u} 2\tau_f (\omega\, D/2) ds \tag{26}$$

Consequently (23) can be rewritten for estimating the rolling power as

$$J^* = \int_V \sigma_{ij}^* \dot{\epsilon}_{ij}^* dV + \int_{S_u} \tau_f u_r^*(\alpha, r)\, ds + \int_V \rho \dot{u}_i^* \cdot u_i^* dV \tag{27}$$

where J^* is the upper bound value of the $2M\omega$, $J^* \geq 2M\omega$.

A rigorous evaluation of (27) needs still a physical description of the frictional traction τ_f. Three classical models have been used as candidates for competing for the *best fit* with experiments.

$$(a) \qquad \tau_f = \mu \sigma_\theta^* (u_i^*, \rho, \text{geometry}, \sigma_0)\Big|_{S_u} \tag{28}$$

where σ_θ^* is the normal component of the dynamic stress distribution (given in (14)) resolved from the associated admissible field u_i^* and evaluated on S_u.

$$(b) \qquad \tau_f = m\sqrt{J_2}\Big|_{S_u} \quad 0 \leq m \leq 1 \tag{29}$$

where the invariant J_2 (defined in (2)) includes the viscoplastic response and yields

$$\sqrt{J_2} = K + (u_0 \eta / R) \cdot (R/r)^2 (3\cos^2\theta + 1)^{1/2}. \tag{30}$$

For the limiting case where the material viscosity vanishes then $\sqrt{J_2} = K$ as is in perfectly plastic materials.

$$(c) \qquad \tau_f = \mu p\Big|_{S_u} \tag{31}$$

where p is the pressure distribution on S_u solved from the well-known static slab-method-type analysis [8].

5 Energy Consumptions

To estimate the power $2M\omega$ one needs to evaluate the discrete energy-rate terms of (27). This will be done here in a brief way leaving aside all the algebra involved.

(a) Internal Energy-Rate ($\dot{W}_{id}^*$).

$$\dot{W}_{id}^* \left(= \int \sigma_{ij}^* \dot{\epsilon}_{ij}^* dV\right) = 2\eta \int \dot{\epsilon}_{ij}^* \dot{\epsilon}_{ij}^* dV + \sqrt{2} K \int (\dot{\epsilon}_{ij}^* \dot{\epsilon}_{ij}^*)^{1/2} dV \tag{32}$$

When using the admissible field given by (7) in (32), the final expression which resulted is

$$\dot{W}_{id}^* = 4Ku_0 R\, \alpha \ln(R/R_f) + \eta u_0^2 \left(\frac{5}{2}\alpha + \frac{3}{4}\sin(2\alpha)\right)[(R/R_f)^2 - 1] \tag{33}$$

(b) Energy Rate Due to Velocity Discontinuity: ($\dot{W}_\Gamma^*$ on the surfaces Γ_1 and Γ_2 shown in Fig. 1).

The general expression is

$$\dot{W}_\Gamma^* = \int_{S_\Gamma} \sqrt{J_2}[u] ds \tag{34}$$

where the discontinuities $[u] = u_0 \sin\theta$ on Γ_1 and $u_f \sin\theta$ on Γ_2, and J_2 is given in (31). The results of (34) are

$$\dot{W}_\Gamma^* = 4Ku_0 R(1 - \cos\alpha) + 2\eta u_0^2 [1 + (R/R_f)^2] \Big\{ 1.3802 - \frac{1}{2}[\cos\alpha \sqrt{3\cos^2\alpha + 1} + \frac{1}{\sqrt{3}} \ln(\sqrt{3}\cos\alpha + \sqrt{3\cos^2\alpha + 1})] \Big\} \tag{35}$$

(c) Frictional Dissipation Rate ($\dot{W}_{fr}^*$).

The general expression is given in (27) as

$$\dot{W}_{fr}^* = \int_{S_u} \tau_f u_r^*(\alpha, r)\, ds \tag{36}$$

Case a ($\tau = \mu\sigma_\theta^*$). Consider τ_f of case *a* in (28), then

$$\dot{W}_{fr}^* = \int \mu \sigma_\theta^* u_r^*(\alpha, r)\, ds \tag{37}$$

$$\dot{W}_{fr}^* = \mu K u_0 R \cos\alpha \Big\{ 5.77 + 5\ln(R/R_f) - \frac{4}{3}\ln(\cos\alpha + \sqrt{\cos^2\alpha + 1/3}) \Big\} \ln(R/R_f) + \mu\eta u_0^2 \cos\alpha \Big\{ \frac{3}{2}[(R/R_f)^2 - 1]\cos\alpha + 5 \Big\} + \mu\rho u_0^3 R \cos\alpha \Big\{ \ln(R/R_f)^2 - \frac{1}{2}[(R/R_f)^2 - 1]\cos^2\alpha \Big\} \tag{38}$$

Case b ($\tau = m\sqrt{J_2}$).

$$\dot{W}_{fr}^* = \int m\sqrt{J_2} u_r^*(\alpha, r)\, ds \tag{39}$$

$$= 2mKu_0 R \cos\alpha \ln(R/R_f) + m\eta u_0^2 (\cos\alpha)(3\cos_\alpha^2 + 1)^{1/2}[(R/R_f)^2 - 1] \tag{40}$$

Case c ($\tau = \mu p$).

$$\dot{W}_{fr}^* = 2\left[\int \mu p^{(-)} u_r^*(\alpha, r)\, ds + \int \mu p^{(+)} u_r^*(\alpha, r)\, ds\right] \tag{41}$$

where $p^{(-)}$ and $p^{(+)}$ are the pressure distribution [10] before and after the point of no-slip (usually called the neutral point) at which the pressure has a peak. The final results is

$$(\dot{W}_{fr}^*) = 4u_0 K R(\cos\alpha)(h_f/D)/\mu \cdot \{1 + (\mu H_n - 1)e^{\mu H_n} + \left(\frac{h_f}{h_i}\right)[e^{\mu(H_i - H_n)}(\mu H_n + 1) - (\mu H_i + 1)]\} \tag{42}$$

where

$$H_i = 2\left(\frac{D}{2h_f}\right)^{1/2}\left(\frac{h_i}{h_f} - 1\right)^{1/2}$$

$$H_n = \frac{1}{2}\left[H_i - \frac{1}{\mu}\ln(h_i/h_f)\right] \tag{43}$$

(d) The Dynamic Energy Rate Term ($\dot{W}_{\text{dyn}}^*$). This term is contributed by the convective acceleration field as,

$$\dot{W}_{\text{dyn}}^* = \int \rho u_i^* \dot{u}_i^* dV = \frac{1}{3}\rho u_0^3 R[(R/R_f)^2 - 1](\sin\alpha)(2 + \cos^2\alpha) \tag{44}$$

Downloaded 02 May 2010 to 171.66.16.54. Redistribution subject to ASME license or copyright; see http://www.asme.org/terms/Terms_Use.cfm

It appears in the present situation to be small compared with other energy-rate terms $0(10^{-6})$.

As a summary, the upper bound formulation for the power $2M\omega \le J^*$ for the three different friction cases ($j = a, b, c$) is generally a cubic polynomial with respect to the income speed u_0 according to:

$$J_j^* = A_j K R u_0 + B_j \eta u_0^2 + C_j \rho R u_0^3 \quad (j = a,b,c) \tag{45}$$

where

$$\left.\begin{aligned}
A_a &= 4\alpha \ln(R/R_f) + 4(1-\cos\alpha) \\
&\quad + \mu\cos\alpha \ln(R/R_f)[5.7728 \\
&\quad + 5\ln(R/R_f) - \frac{4}{3}\ln(\cos\alpha + \sqrt{\cos^2\alpha + 1/3})] \\
B_a &= [(R/R_f)^2 - 1]\left(\frac{5}{2}\alpha + \frac{3}{4}\sin 2\alpha\right) \\
&\quad + 2[1 + (R/R_f)^2]\{1.3802 \\
&\quad - 1/2[\cos\alpha\sqrt{3\cos^2\alpha + 1} \\
&\quad + 1/\sqrt{3}\ln(\sqrt{3}\cos\alpha + \sqrt{3\cos^2\alpha + 1})]\} \\
&\quad + \mu\cos\alpha\{[3/2(R/R_f)^2 - 1]\cos\alpha + 5]\} \\
C_a &= 1/3 \sin\alpha(2 + \cos^2\alpha)[(R/R_f)^2 - 1] \\
&\quad + \mu\cos\alpha(\ln(R/R_f) - 1/2[(R/R_f)^2 - 1]\cos^2\alpha)
\end{aligned}\right\} \tag{46}$$

$$\left.\begin{aligned}
A_b &= 4\alpha \ln(R/R_f) + 4(1-\cos\alpha) \\
&\quad + 2m\cos\alpha \ln(R/R_f) \\
B_b &= [(R/R_f)^2 - 1]\left(\frac{5}{2}\alpha + \frac{3}{4}\sin 2\alpha\right) \\
&\quad + 2\left[1 + (R/R_f)^2\right]\left\{1.3802 \right. \\
&\quad \left. - \frac{1}{2}\left[\cos\alpha\sqrt{3\cos^2\alpha + 1} + \frac{1}{\sqrt{3}}\ln\left(\sqrt{3}\cos\alpha \right.\right.\right. \\
&\quad \left.\left.\left. + \sqrt{3\cos^2\alpha + 1}\right)\right]\right\} \\
&\quad + m\cos\alpha(3\cos^2\alpha + 1)^{1/2}[(R/R_f)^2 - 1] \\
C_b &= \frac{1}{3}\sin\alpha(2 + \cos^2\alpha)[(R/R_f)^2 - 1]
\end{aligned}\right\} \tag{47}$$

$$\left.\begin{aligned}
A_c &= 4\alpha \ln(R/R_f) + 4(1-\cos\alpha) \\
&\quad + 4\cos\alpha(h_f/D)/\mu\{1 + (\mu H_n - 1)e^{\mu H_n} \\
&\quad + (h_f/h_i)[e^{\mu(H_i - H_n)}(\mu H_n + 1) - (\mu H_i + 1)]\} \\
B_c &= [(R/R_f)^2 - 1]\left(\frac{5}{2}\alpha + \frac{3}{4}\sin 2\alpha\right) \\
&\quad + 2[1 + (R/R_f)^2\{1.3802 \\
&\quad - 1/2[\cos\alpha\sqrt{3\cos^2\alpha + 1} \\
&\quad + \frac{1}{\sqrt{3}}\ln(\sqrt{3}\cos\alpha + \sqrt{3\cos^2\alpha + 1})]\} \\
C_c &= 1/3 \sin\alpha(2 + \cos^2\alpha)[(R/R_f)^2 - 1].
\end{aligned}\right\} \tag{48}$$

The geometrical relations that appear in (46)–(48) are:

$$\left.\begin{aligned}
R/R_f &= h_i/h_f \\
\alpha &= \frac{1}{2}\arccos\{1 - (h_i - h_f)/D\} \\
R &= h_i\sqrt{D/[2(h_i - h_f)]} \\
H_i &= 2\sqrt{D/(2h_f)}\ \sqrt{h_i/h_f - 1} \\
H_n &= 1/2[H_i - 1/\mu \ln(h_i/h_f)].
\end{aligned}\right\} \tag{49}$$

6 Bounds on Temperature

Consider a material undergoing plastic deformation as a thermodynamic system. The initial state of the internal energy E_1 will be changed to its final state E_2 by mechanical work rate $J = 2M\omega$ and possibly with net heat transfer $(Q_2 - Q_1)$. The time rate of the energy balance (first law of thermodynamics) is given in this case as

$$\dot{E}_2 - \dot{E}_1 = \dot{Q}_2 - \dot{Q}_1 + J, \tag{50}$$

or, in terms of the upper bound formulation for J ($J^* \ge J$)

$$\Delta\dot{E} \le \Delta\dot{Q} + J^*. \tag{51}$$

If the process is conducted fast enough, it can tacitly be regarded as an adiabatic process so that $\dot{Q}_2 - \dot{Q}_1 = 0$ in (50).

As noted by Tanner and Johnson [11], the increase in internal energy in plastic forming by mechanical work is mainly manifested by temperature rise (approximately 90 percent) whereas the rest of the energy is stored in the alteration of the crystal lattice structure into a higher strained state (work hardening).

In the sequel we will ignore this energy partition and assume[1] that the totality of the mechanical work reappears as heat. Therefore the temperature rise will follow

$$(E_2 - E_1) = \int \rho C(T_2 - T_1)dV, \tag{52}$$

where C is the specific heat at constant volume and ρ is the material density. Taking the time derivative of (52) and substituting in (51) one gets

$$J^* \ge \frac{D}{Dt}\int(\rho C\Delta T)\,dV. \tag{53}$$

Assuming that ρ and C are temperature-independent, the right-hand side of (53) can be expressed equivalently within a control volume whose control surfaces are crossing the entrance and exit of the rolled strip;

$$D/Dt\int(\rho C\Delta T)\,dV = \rho C\left[\int_V \frac{\partial(\Delta T)}{\partial t}dV + \oint_{c.s.} u_i \Delta T n_i ds\right]. \tag{54}$$

In steady state rolling $(\Delta T)/\partial t = 0$. Also, the material enters the control surface at an ambient temperature T_0 therefore $\Delta T = 0$ at the entrance cross section. Equation (54) is hence reduced to

$$\frac{D}{Dt}\int_V (\rho C\Delta T)\,dV = \rho C u_f h_f (T_f - T_0), \tag{55}$$

where T_f is an average temperature of the product at the exit cross section where its final speed is u_f.

From (53) and (55) the average exit temperature T_f can be assessed in an upper bound sense as

$$T_f \le T_0 + \frac{1}{\rho C u_f h_f}(\dot{W}_{id}^* + \dot{W}_\Gamma^* + \dot{W}_{fr}^*). \tag{56}$$

Note that all terms of J^* beside the dynamic term $\int \rho \dot{u}_i^* u_i^* dV$ appears in (56). The dynamic term is nondissipative and does not contribute to the temperature rise.

[1] This assumption becomes a true fact in cases where the metal may reach temperature beyond its recrystalization temperature, so that the stored energy in the lattice is regained. In high-speed rolling this may indeed occur.

Downloaded 02 May 2010 to 171.66.16.54. Redistribution subject to ASME license or copyright; see http://www.asme.org/terms/Terms_Use.cfm

7 Surface Temperature

The upper bound estimation of the final temperature in (56) can be refined somewhat by considering the nonuniformity of the energy dissipation attributed to each term.

The first term ($\dot{W}^*_{id}$) causes change in temperature proportional to the intensity of the shear strain distribution. In rolling processes it is indeed close to uniformity and will be considered as such. The energy dissipation along lines of velocity discontinuities ($\dot{W}^*_{\Gamma}$) causes temperature jumps across these lines. The jump in temperature is expected to be of the order of the tangential velocity discontinuity (Johnson and Mellor [10]). In the admissible field considered here the shear strain is of the order of $(\Delta u_t/u_n) \simeq u_0 \sin\alpha/u_0 \simeq \alpha \simeq 0.1$ and considered small. The frictional energy ($\dot{W}^*_{fr}$) generates heat along the contact area with the roller and raises the temperature of the adjacent layer. The thickness of this layer (δ) is finite (or otherwise the temperature will be infinite) and presumably velocity-dependent by some empirical law, as shown by Bowden and Tabor [12] for moderate speeds (of 0(1m/s))

$$\delta = \lambda h_i/u_0 \tag{57}$$

where λ is a free parameter that will be adjusted to match experimental data. It is therefore possible to assess the highest temperature at the boundary layer T_L by adding the aforementioned contributions, namely

$$T_L = T_0 + \Delta T_b + \Delta T_L, \tag{58}$$

where ΔT_b is the (bulk) temperature rise due to internal energy rate evaluated as follows

$$\Delta T_b = (\dot{W}^*_{id} + \dot{W}^*_{\Gamma})/(\rho C h_i u_0), \tag{59a}$$

and ΔT_L is the temperature rise in the boundary layer, due to friction dissipation, namely

$$\Delta T_L = \int_{S_u} \tau_f (u^*_r - \omega D/2) dS/(2\rho C u^*_{a\dot{v}} \delta). \tag{59b}$$

Using the upper bound equation (27), the outcome solution for T_L (after some algebra) resulted as:

$$T_L = T_0 + (\dot{W}^*_{id} + \dot{W}^*_{\Gamma})/(\rho C\, u_0 h_i)\left\{1 + \frac{u_0}{(1+h_i/h_f)\lambda\cos\alpha}\right\}. \tag{59c}$$

8 Material Softening and Final Expressions

For more realistic results one may correct the overestimated temperature in (56) by allowing the yield stress in shear (K) to depend on temperature by a relevant empirical law, given in [13] for copper as

$$K = K_0(1.42 - 0.0014T) \quad \text{where} \quad 300°\text{k} \le T \le 600°\text{k} \tag{60}$$

Thus, high temperature of the product leads to a softer material which requires less mechanical work to activate the plastic flow. It hence leads to a decrease in the applied torque (M) and the separation force (F). The computation of M and F are done via the following simplified relationships,

$$M = J^*/(2\omega), \bar{p} = J^*/[2\mu\alpha D u_0 (h_i/h_f)], F = 1/2\int_0^{2\alpha} pD'\,d\alpha \tag{61}$$

$\bar{p}$ is the average of p and D' is the "new" diameter of the rollers, which accounts for their local flatening according to Hitchcock (or similarly to Bland and Ford [15]):

$$D' = D\left(1 + \frac{F}{E(h_i - h_f)}\right) \tag{62}$$

(Here E stands for Young modulus). The speed-dependent friction coefficient $\mu = \mu(u)$ is taken from reference [2] and reads

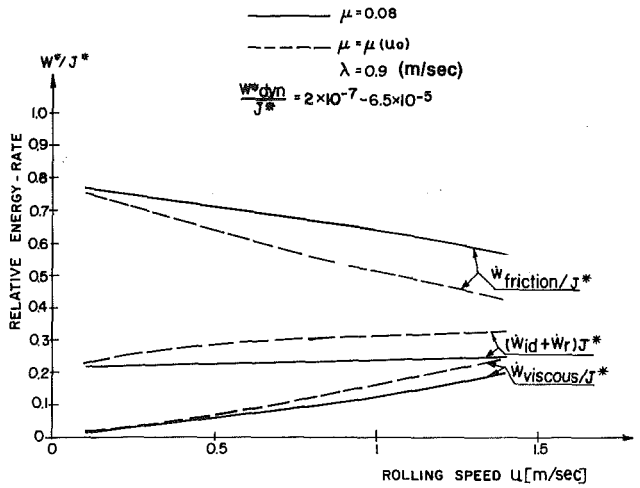


Fig. 4 The variation of normalized energy-rates terms consumed in strip rolling at 30 percent reduction with respect to the incoming rolling speed. The dynamic term (W^*_{dyn}/J^*) appears to be negligibly small 0(10^{-6}). Both constant friction coefficient and velocity-dependent friction coefficient (given experimentally in reference [2] for copper) are drawn.

$$\mu = 0.08\, e^{-0.54u_0} \quad \text{for} \quad 0 \le u_0 \le 0.25 \text{ m/sec}$$

and

$$\mu = 10^{-3}\exp[4\ u_0{}^{-0.038}] \quad \text{for} \quad 0.25 \text{ m/sec} \le u_0 \le 1.5 \text{ m/sec} \tag{63}$$

The solution to the load for such friction coefficients (63) versus speed (for different reductions) needs an iterative scheme using (45), (58), (59), (60), (62), and (63). The graphical representation is given in Figs. 4, 5, and 7 in comparisons with the constant friction solutions. In general no significant deviations between them are exhibited.

For comparison purposes the pertinent constitutive equation tried in the previous scheme was

$$\bar{\sigma} = \frac{\sigma_0}{\bar{\epsilon}_f}\int_0^{\bar{\epsilon}_f}\left(1 + \frac{\epsilon}{b}\right)^n d\epsilon \tag{64}$$

where b and n are material constants taken from [7] to match materials tested by [6] and [14]. $\bar{\epsilon}_f$ is the equivalent strain at a given reduction, $\bar{r}$, at which the test was conducted.

The evaluation of (64) is

$$\bar{\sigma} = \frac{\sigma_0 b}{(n+1)\bar{\epsilon}_f}\left[\left(1 + \frac{\bar{\epsilon}_f}{b}\right)^{n+1} - 1\right],$$

$$\bar{\epsilon}_f = \frac{2}{\sqrt{3}}\ln\left(\frac{1}{1-\bar{r}}\right), \qquad \bar{r} = 1 - h_f/h_i \tag{65}$$

The n and b values are listed in the figures as needed.

9 Results and Discussion

As mentioned earlier, the dynamic stress distribution given in equations (13) and (14) (and plotted in Figs. 2 and 3) are only an approximation. It satisfies the kinematics of the motion and the dynamic stress-equilibrium equations based on an admissible velocity field. It differs from the exact solution by not satisfying the stress-free boundary conditions at entrance and exit locations. There is not yet any procedure to measure the amount of deviation from the exact solution, since even counterpart numerical solutions are not available. The benefit of developing the foregoing approximate solution is by *revealing the role of the rolling speed on the stress distribution*. It is done via the two dimensionless groups: the speed parameter ($N = \eta u_0/KR$) which accentuate the viscous character of the material, and the Euler number (Eu = $\rho u_0^2/K$) which accentuates the dynamic nature of the high-speed rolling. By viewing a typical example of rolling copper

Downloaded 02 May 2010 to 171.66.16.54. Redistribution subject to ASME license or copyright; see http://www.asme.org/terms/Terms_Use.cfm

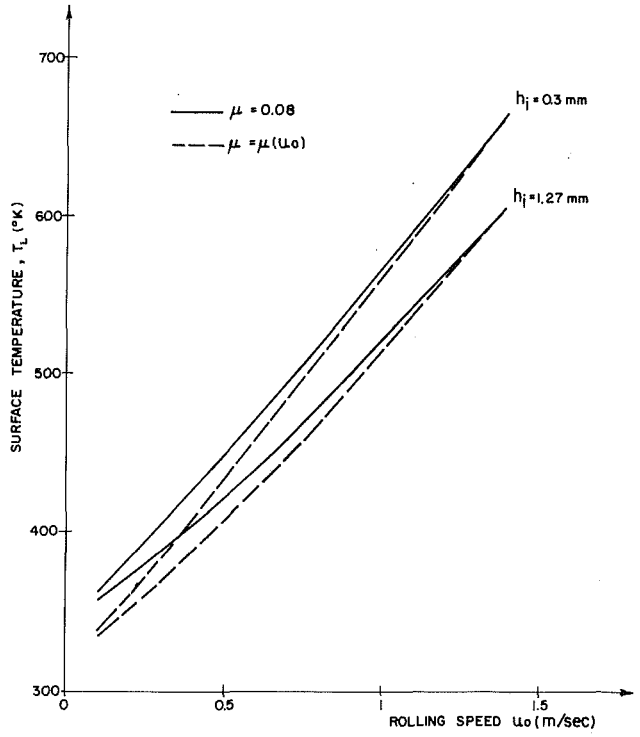


Fig. 5 Predicted surface temperature versus rolling speed for different initial thickness of constant and speed-dependent friction coefficients. λ = 0.09 [m/sec].

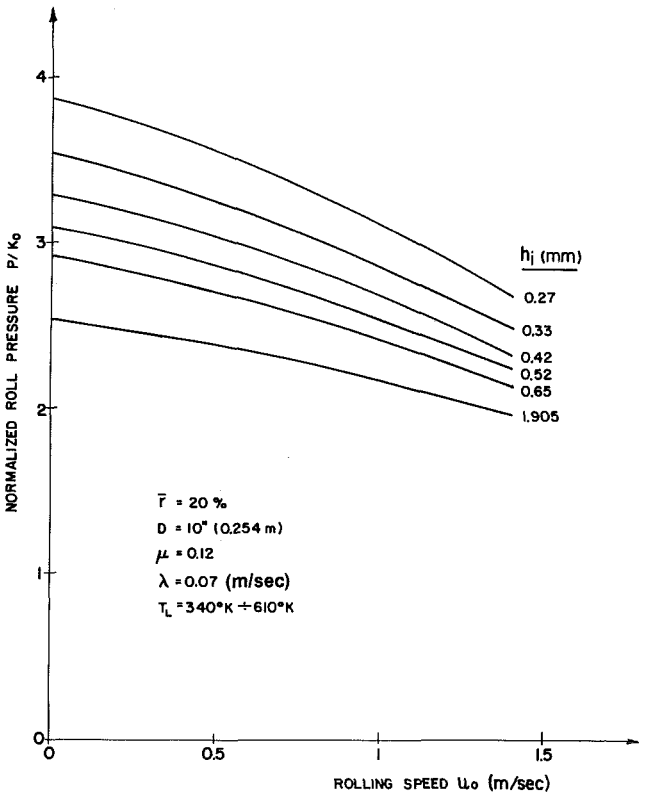


Fig. 6 Normalized roll pressure versus rolling speed for copper, with different initial thickness at $\bar{r}$ = 20 percent

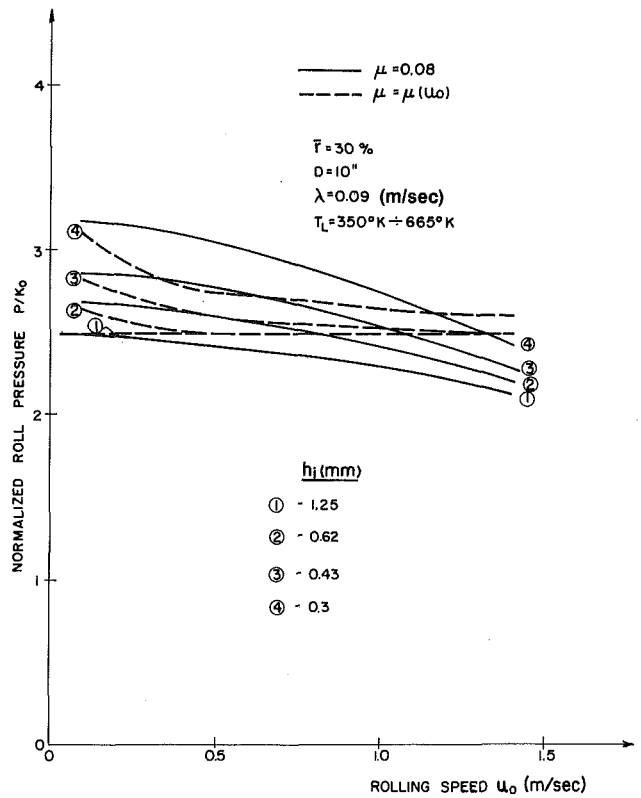


Fig. 7 Normalized roll pressure versus speed for copper strips with different initial thickness for constant and speed-dependent friction coefficients at $\bar{r}$ = 30 percent

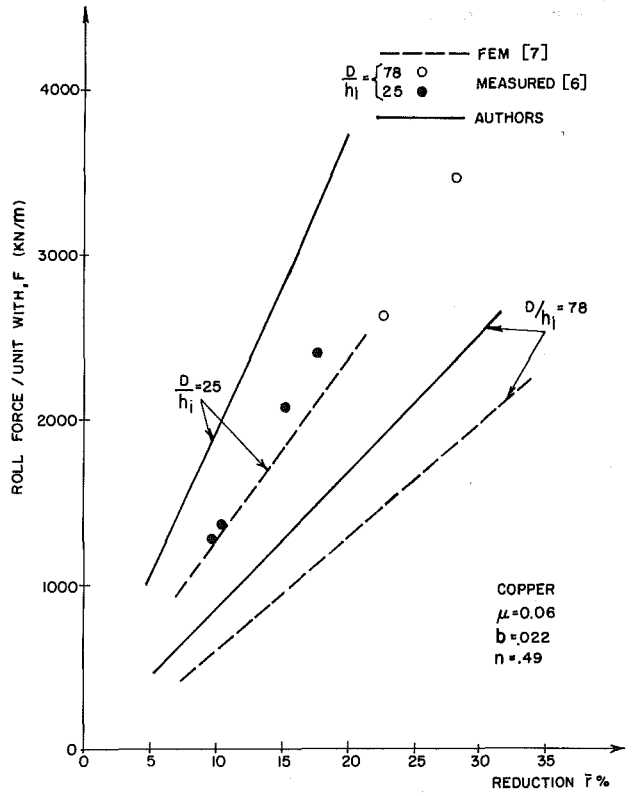


Fig. 8 Comparisons between measured predicted and computed roll force versus reduction for copper (σ_0 = 70.3 N/mm^2)

strips ($\eta = 2.78 \times 10^5$ N/m^{2}sec^{-1}, [3]) shown in Fig. 4, it is clear that the energy consumed by the process to accelerate the flow (in the considered dimensions and speeds) is relatively small and practically may be disregarded. The major contribution to the total energy-rate (J^*) comes from the friction $\dot{W}_f^*$. As the speed accelerates, this contribution is reduced and the viscous dissipation becomes larger. This trend is somewhat more pronounced if the friction coefficient is velocity-dependent.

The ideal work and redundant work remain nearly constant

Downloaded 02 May 2010 to 171.66.16.54. Redistribution subject to ASME license or copyright; see http://www.asme.org/terms/Terms_Use.cfm

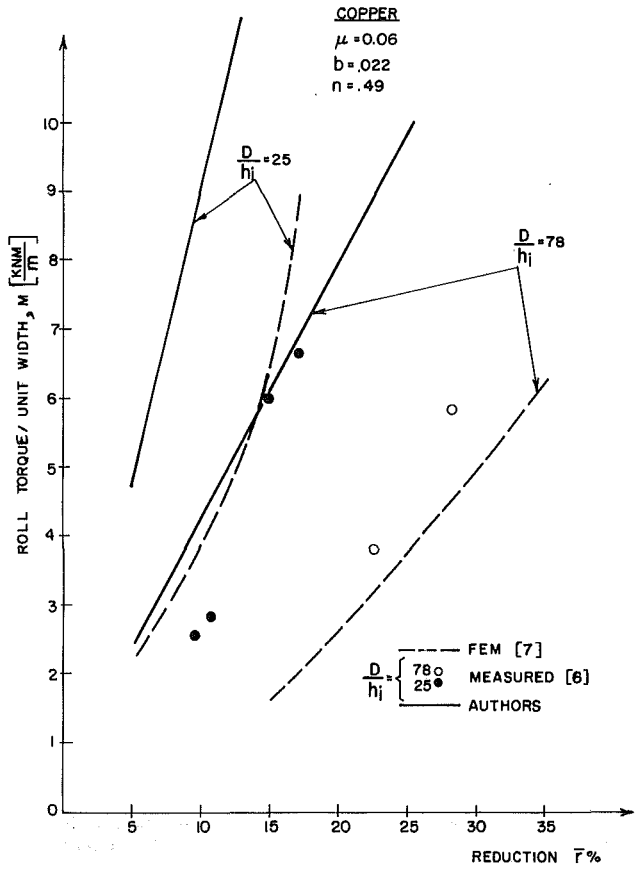


Fig. 9 Comparisons between measured predicted and computed roll torque versus reduction for copper (σ_0 = 70.3 N/mm^2)

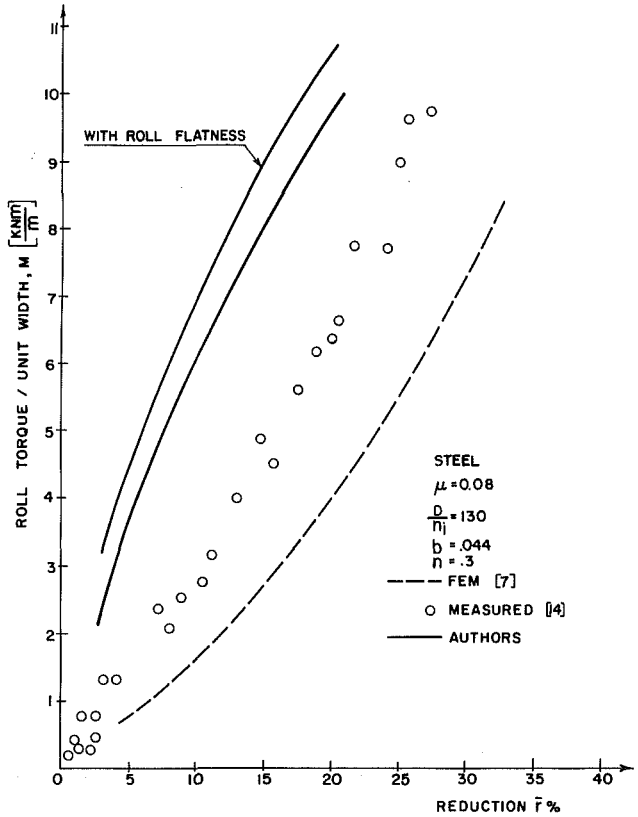


Fig. 11 Comparisons between measured, predicted, and computed roll torque versus reduction for steel at D/h_i = 130 (σ_0 = 358.0 N/mm^2)

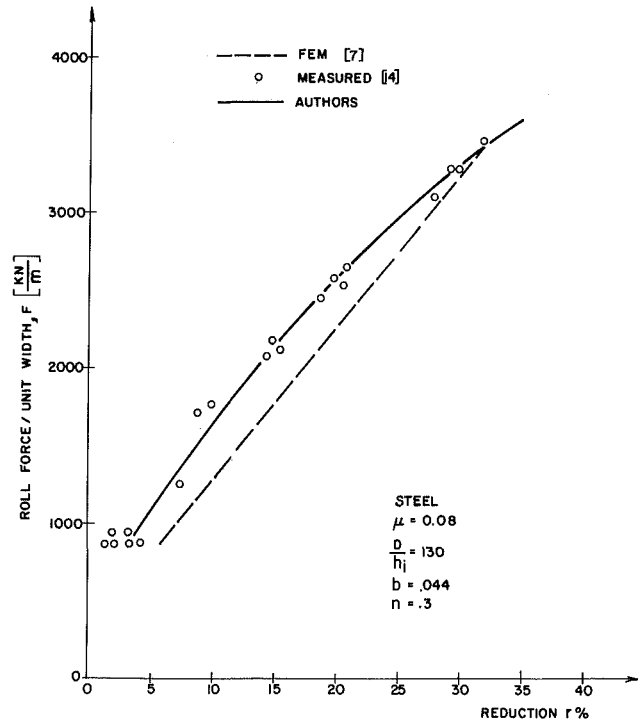


Fig. 10 Comparisons between measured, predicted, and computed roll force versus reduction for steel at D/h_i = 130 (σ_0 = 358.0 N/mm^2)

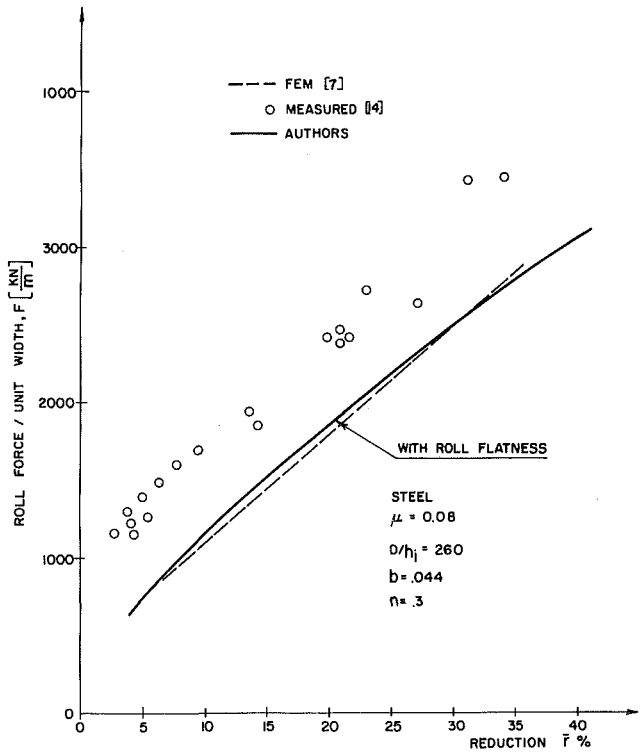


Fig. 12 Comparisons between measured, predicted, and computed roll force versus reduction for steel at D/h_i = 260 (σ_0 = 358.0 N/mm^2)

at growing speeds. The associated surface temperature increases with speed according to (59*c*) shown in Fig. 5. The boundary layer thickness, δ, represents the free parameter to adjust experimental data on surface temperature (not yet available in the literature).

If the reduction is done in several passes, like in practical rolling, the effect of the initial strip thickness appears to be pronounced in determining the separation load (see Fig. 6). The thinner the strip the higher the load and the sensitivity to speed. This was revealed computationally by utilizing the Coulomb friction model ($\tau = \mu p$). The other two models ($\tau =$

Downloaded 02 May 2010 to 171.66.16.54. Redistribution subject to ASME license or copyright; see http://www.asme.org/terms/Terms_Use.cfm

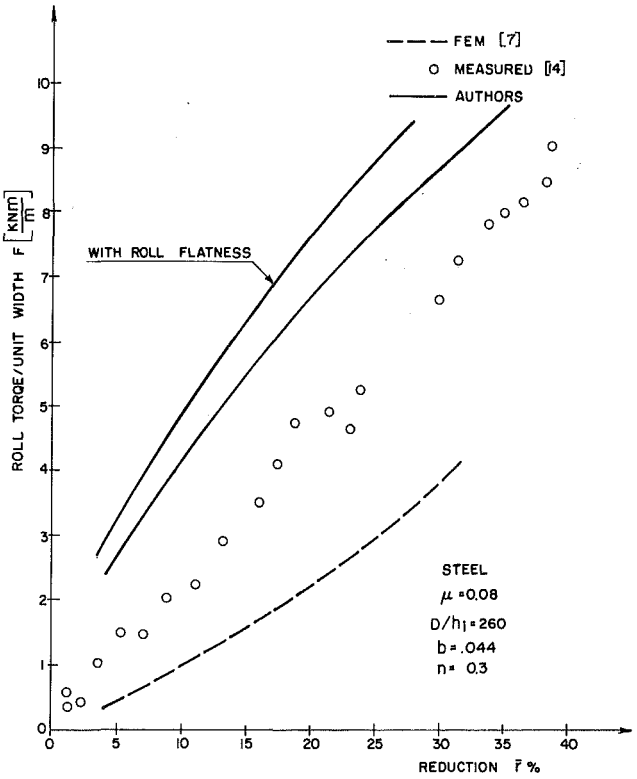


Fig. 13 Comparisons between measured, predicted, and computed roll torque versus reduction for steel at $D/h_i = 260$ ($\sigma_0 = 358.0$ N/mm^2)

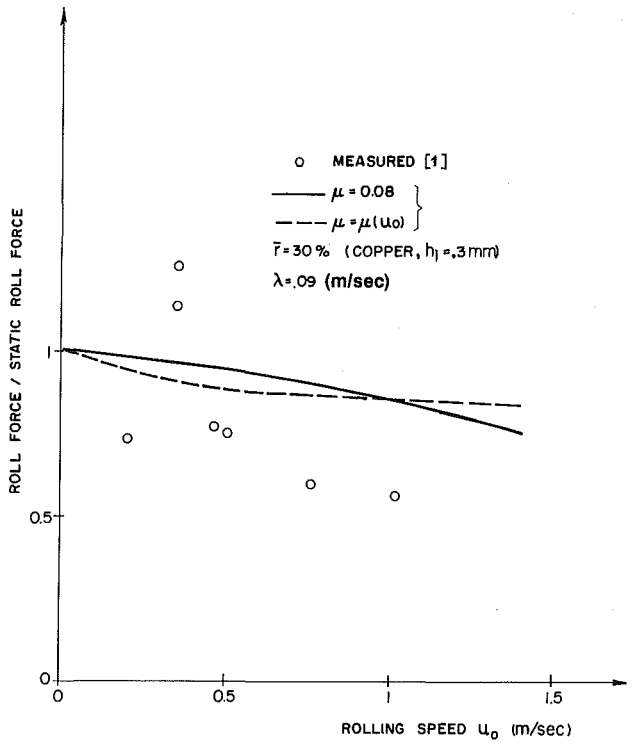


Fig. 14 Comparisons between measured and predicted roll force versus speed (copper, $\bar{r} = 30$ percent)

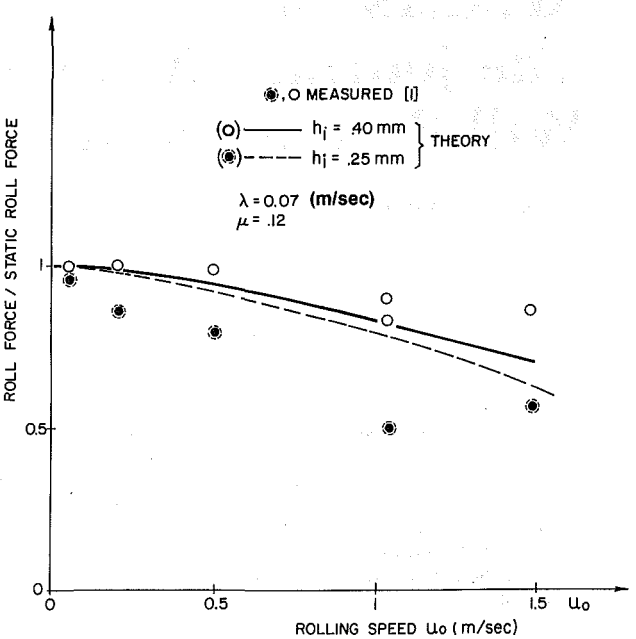


Fig. 15 Comparisons between measured and predicted roll force versus speed (copper, $\bar{r} = 20$ percent)

$m\sqrt{J_2}$, $\tau = \mu\sigma_\theta$) lacked this essential feature and hence were not explored further. With speed-dependent friction, (as in Fig. 7) the character of the plotted lines is changed but insignificantly. It indicates that assessment of separation force and torque based on constant friction coefficient is not far from reality even for very high speeds (at least in rolling of copper strips where the relationship is empirically known [2]).

Figures 8–13 demonstrate the agreement between the force and torque predicted by the suggested model and experimental measurements given by Al-Salehi et al. [6] and Shida et al. [14]. In addition, a numerical solution resulting from Kobayashi's rigid-plastic finite elements analysis (given by Li and Kobayashi [7]) is favorably matched too. In particular, Figs. 8, 10, and 12, which deal with assessments of roll force in copper and steel, show an excellent fit between numerical results [7] and the suggested formulation. Both solutions are close to the experimental data. In Figs. 9, 11, and 13 where the roll torque is assessed, the numerical FEM solution and the suggested formulation are deviated quite appreciably one from the other. However, the experimental results fall somewhere in between showing that the present solution is in conformity with the upper bound concept.

In these figures relatively slow speeds (0.16 and 0.25 m/sec) were depicted, so that the speed effect considered in the present formulation is not fully manifested. A large volume of data recording the reduction of rolling force as rolling speed is increased was given by Ford [1] and plotted in Figs. 14 and 15. A satisfactory agreement with the present formulation is seen. Consequently one may explain this force reduction phenomenon by the coupling effects between the viscoplastic response of the material and the temperature rise in a relatively narrow layer beneath the rolls. It leads to material softening causing reduction in the energy-rate consumption and hence to less torque and force.

The speed dependency of the friction coefficient was shown here to be relatively insignificant. However, if variation of the viscosity with speed could be measured it is plausible that the decrease of the viscosity coefficient (with the increase of the strain rate) might contribute to the torque reduction phenomenon too.

Acknowledgments

The authors are indebted to Prof. J. Lennard from New Brunswick, Canada, for his comments. The financial assistance of the Volkswagen Fund (W. Germany) coordinated by Dr. Plate and Dr. Forschner and the continuation of support given by the Center of Manufacturing Systems and Robotics at the Faculty of Mechanical Engineering, Technion, are gratefully acknowledged.

Downloaded 02 May 2010 to 171.66.16.54. Redistribution subject to ASME license or copyright; see http://www.asme.org/terms/Terms_Use.cfm

References

1 Ford, H., "The Effect of Speed of Rolling in the Cold-Rolling Process," *Journal of the Iron and Steel Institute*, 1947, pp. 380–398.

2 Sims, R. B., and Arthur, D. F., "Speed Dependent Variables in Cold Strip Rolling," *Journal of Iron and Steel Institute*, B.I.S.R.A., 1952, pp. 285–295.

3 Cristescu, N., "Plastic Flow Through Conical Converging Dies, Using a Viscoplastic Constitutive Equation," *International Journal of Mechanical Sciences*, Vol. 17, 1975, pp. 425–433.

4 Tirosh, J., and Kobayashi, Shiro, "Kinetic and Dynamic Effects on the Upper Bound Loads in Metal Forming Processes," ASME JOURNAL OF APPLIED MECHANICS, Vol. 43, 1976, pp. 214–318.

5 Tirosh, J., "Assessment of the Kinetic and Dynamic Loads Sustained by Stationary Tools During High-Rate Plastic Forming," *International Journal of Mechanical Sciences*, Vol. 26, 1984, pp. 73–78.

6 Al-Salehi, F. A. R., Fairbank, T. C., and Lancester, P. B., "An Experimental Determination of the Roll Pressure Distribution in Cold Rolling," *International Journal of Mechanical Sciences*, Vol. 15, 1973, pp. 693–710.

7 Li, Guo-Ji, and Kobayashi, S., "Rigid-Plastic Finite Element Analysis of Plane Strain Rolling," ASME *Journal of Engineering for Industry*, Vol. 104, 1983, pp. 55–64.

8 Drucker, D. C., "A Definition of Stable Inelastic Materials," ASME JOURNAL OF APPLIED MECHANICS, Vol. 26, 1959, pp. 101–106.

9 R. Hill, The mathematical theory of plasticity, Clarendon Press, Oxford (1950).

10 Johnson, W., and Mellor, P. P., *Engineering Plasticity*, van Nostrand Reinhold, 1973.

11 Tanner, R. I., and Johnson, W., "Temperature Distribution in Some Fast Metal Working Operations," *International Journal of Mechanical Sciences*, Vol. 1, 1960, pp. 28–33.

12 Bowden, F. P., and Tabor, D., *The Friction and Lubrication of Solids*, Oxford University Press, London, 1954.

13 ASM, Metals Handbook, 9th edition, Vol. 2: Properties and Selection; Nonferrous Alloys and Pure Metals," 1982.

14 Shida, S., and Awazuhara, H., "Rolling Load and Torque in Cold Rolling," *Journal of Japan Society for Technology and Plasticity*, Vol. 14, 1973, pp. 267–272.

15 Bland, D. R., and Ford, H., "The Calculation of Roll Force and Torque in Cold Strip Rolling With Tension," *Proceedings of the Institution of Mechanical Engineers*, Vol. 159, 1948, p. 144.

Downloaded 02 May 2010 to 171.66.16.54. Redistribution subject to ASME license or copyright; see http://www.asme.org/terms/Terms_Use.cfm

G. Yagawa
Professor,
Department of Nuclear Engineering,
University of Tokyo, Bunkyoku,
Tokyo, Japan
Mem. ASME

Y. Takahashi
Research Engineer,
Central Research Institute of
Electric Power Industry,
Komaeshi, Tokyo, Japan

H. Ueda
Graduate Student,
Department of Nuclear Engineering,
University of Tokyo,
Bunkyoku, Tokyo, Japan

Three-Dimensional Fully Plastic Solutions for Plates and Cylinders With Through-Wall Cracks

In the finite element method with the incremental procedure based on the flow theory of plasticity, which is now widely employed, a great amount of load increments and specially trained analysts are necessary to obtain sufficiently accurate results. Thus, the method is not suitable for the routine evaluation or parametric analysis of cracked structures in the plastic regime. With this consideration, an alternative evaluation method, called the engineering approach, has been developed, where the fully plastic solutions are utilized with the linear-elastic solutions to estimate the entire elastic-plastic behavior of cracked bodies. In this paper, a Selective Reduced Integration/Penalty Function (SRI/PF) method is developed for the analysis of three-dimensional fully plastic solutions. It is demonstrated through the calculation of center-cracked plates under plane strain condition that accurate solutions can be obtained with the present method. Then, using the method, fully plastic solutions for cylinders with a circumferential through-wall crack subjected to remote uniform tension are calculated and tabulated as functions of the crack angle and the hardening exponent.

Introduction

With the wide use of ductile materials in pressure vessels and piping, the importance of nonlinear fracture mechanics is growing as a tool for the evaluation of structural integrity under the presence of cracks. Especially, J-integral and its variations are applied to many situations relating to nonlinear fracture phenomena. Since analytical solutions are very hard to obtain for the configurations of the actual components, numerical techniques, especially the finite element method, are known to play important roles in the practical applications.

However, in the finite element analysis with the incremental procedure based on the flow theory of plasticity, a great amount of load increments and specially trained analysts are necessary to obtain sufficiently accurate results. Thus, the method is not suitable for the routine evaluation or parametric analysis of cracked structures in the plastic regime.

With this consideration, an alternative evaluation method, called the engineering approach, has been developed [1–7], where the fully plastic solutions are utilized with the linear-elastic solutions to estimate the entire elastic-plastic behaviors of cracked bodies. The fully plastic solutions are based on the deformation theory of plasticity and the power-law hardening property.

Under these assumptions, it was shown [1] that the J-integral J, and the displacement at some arbitrary point D, can be normalized thanks to Ilyushin's principle [8] in the following manners:

$$J = \kappa\sigma_0\epsilon_0 l \left(\frac{P}{P_0}\right)^{n+1} \tilde{J} \tag{1}$$

$$D = \kappa\epsilon_0 l \left(\frac{P}{P_0}\right)^{n} \tilde{D} \tag{2}$$

where l, P, and P_0 are the characteristic length, the applied load, and the reference load defined properly, respectively. In equations (1) and (2), $\tilde{J}$ and $\tilde{D}$ are the nondimensionalized J-integral and displacement, respectively, both of which are dependent only on the value of n and the structural configuration. These expressions with the values of $\tilde{J}$ and $\tilde{D}$ enable one to evaluate the J-integral and the displacement at any magnitude of applied load without detailed time-consuming computations.

For the given specimen configurations, $\tilde{J}$ and $\tilde{D}$ are factorized into suitable forms. Many solutions for the two-dimensional problem, i.e., plane stress, plane strain, and axisymmetrical conditions have been obtained by Shih and Kumar [1] and Kumar et al. [2]. From the viewpoint of practical applications, however, fully plastic solutions for three-dimensional problems are highly desired.

As in the case of the plane strain and axisymmetrical conditions, the incompressibility of plastic deformation under the three-dimensional condition introduces unacceptable inaccuracy into the finite element solutions as far as the usual displacement method is employed. The reason for this was made clear by some mathematical consideration [9] and several remedies were also proposed. Parks [10] among others

Contributed by the Applied Mechanics Division for publication in the JOURNAL OF APPLIED MECHANICS.
Discussion on this paper should be addressed to the Editorial Department, ASME, United Engineering Center, 345 East 47th Street, New York, N.Y. 10017, and will be accepted until two months after final publication of the paper itself in the JOURNAL OF APPLIED MECHANICS. Manuscript received by ASME Applied Mechanics Division, April, 1984.

Copyright © 1985 by ASME
Downloaded 02 May 2010 to 171.66.16.54. Redistribution subject to ASME license or copyright; see http://www.asme.org/terms/Terms_Use.cfm

utilized the Lagrangian multiplier method [11] in the calculation of the fully plastic solutions for center-cracked plates under plane strain condition. The Selective Reduced Integration/Penalty Function (SRI/PF) method [12] is another technique that has been employed also in the fully plastic analyses for plane strain problems [13–15]. In the analyses for the two-dimensional problems, Shih and Kumar [1] and Kumar et al. [2] employed the four-noded quadrilateral elements composed of four constant-strain triangle elements, whose effectiveness was theoretically shown in [16]. This method, however, seems to lack generality and cannot be extended directly to the three-dimensional analysis.

In this paper, we newly developed the method for calculating the three-dimensional fully plastic solutions. This method is actually based on the SRI/PF method, which is essentially the extension of the two-dimensional analysis method [13–15] to the three-dimensional case, but a more tractable formulation for the J-integral calculations is developed here.

Basic Equations and Method of Solution

The fully plastic solutions for the J-integral and the other parameters such as the crack-opening displacement and the residual load point displacement are based on the assumption of the following power-law hardening constitutive relation with the J_2-deformation theory:

$$\frac{\bar{\epsilon}}{\epsilon_0} = \kappa\left(\frac{\bar{\sigma}}{\sigma_0}\right)^n \tag{3}$$

where κ, ϵ_0, σ_0, and n are material constants while $\bar{\epsilon}$ and $\bar{\sigma}$ are the equivalent strain and the equivalent stress defined as

$$\bar{\epsilon} = \sqrt{\frac{2}{3}\epsilon_{ij}\epsilon_{ij}} \tag{4}$$

$$\bar{\sigma} = \sqrt{\frac{3}{2}s_{ij}s_{ij}} \tag{5}$$

respectively. Here, ϵ_{ij} represents the strain components and s_{ij} the deviatoric stress components defined as follows:

$$s_{ij} = \sigma_{ij} - \frac{1}{3}\delta_{ij}\sigma_{mm} \tag{6}$$

where σ_{ij} is the stress components and δ_{ij} is the Kronecker's delta.

According to the J_2-deformation theory, the multiaxial constitutive relations are written as follows:

$$\frac{s_{ij}}{\sigma_0} = \frac{2}{3}\left(\frac{\bar{\epsilon}}{\kappa\epsilon_0}\right)^{\frac{1}{n}}\bar{\epsilon}^{1-n}\epsilon_{ij} \tag{7}$$

$$\epsilon_{ii} = 0 \tag{8}$$

where equation (8) refers to the material incompressibility.

In the present method, the incompressibility was introduced by the penalty function method. For simplicity, κ, σ_0, and ϵ_0 were assumed to be unity in the calculation. Permitting some compressibility in material, the constitutive relation can be written instead of equations (7) and (8) as follows:

$$s_{ij} = \frac{2}{3}\bar{e}^{\frac{1-n}{n}}e_{ij} \tag{9}$$

$$\sigma_m = K\epsilon_{ii} \tag{10}$$

where σ_m and K are the mean stress and the modulus of volume expansion, respectively. e_{ij} is the deviatoric strain component and $\bar{e}$ is defined as follows:

$$\bar{e} = \sqrt{\frac{2}{3}e_{ij}e_{ij}} \tag{11}$$

As can be seen in equation (10), K controls the material incompressibility and, if we assume an infinite value for K, the material incompressibility is realized perfectly. In the numerical calculation, however, the use of the finite but sufficiently large value of K makes the material sufficiently close to incompressibility. Thus, K can be regarded as a penalty factor in the analysis of the incompressible materials.

In the absence of the body force, the virtual work principle is written as

$$\int_V \sigma_{ij}\delta\epsilon_{ij}dV - \int_{S_\sigma} T_i\delta u_i dS = 0 \tag{12}$$

or as

$$\int_V (s_{ij} + \delta_{ij}\sigma_m)\delta\epsilon_{ij}dV - \int_{S_\sigma} T_i\delta u_i dS = 0 \tag{13}$$

where V is the volume of a cracked body, S_σ is the boundary on which the traction force T_i is prescribed, u_i is the displacement, and δ represents the variation.

Then, obeying the usual procedure of the finite element discretization, the following simultaneous equation for the nodal displacement vector $\{d\}$ is derived:

$$\left\{\sum_e\left(\int_{V_e}[B]^t[D_s][B]dV + \int_{V_e}[B]^t[D_v][B]dV\right)\right\}\{d\} = \{F\} \tag{14}$$

where $\{F\}$ is the equivalent nodal force, and V_e and $\sum_e$ represent the volume of the element and the summation on all elements, respectively. $[B]$, $[D_s]$, and $[D_v]$ are matrices defined, respectively, by the following equations:

$$\{\epsilon\} = [B]\{d\} \tag{15}$$

$$\{s\} = [D_s]\{\epsilon\} \tag{16}$$

$$\{\sigma_m\} = [D_v]\{\epsilon\} \tag{17}$$

where

$$\{\epsilon\} = \begin{Bmatrix} \epsilon_{xx} \\ \epsilon_{yy} \\ \epsilon_{zz} \\ \gamma_{xy} = 2\epsilon_{xy} \\ \gamma_{yz} = 2\epsilon_{yz} \\ \gamma_{zx} = 2\epsilon_{zx} \end{Bmatrix} \tag{18}$$

$$\{s\} = \begin{Bmatrix} s_{xx} \\ s_{yy} \\ s_{zz} \\ s_{xy} = \sigma_{xy} \\ s_{yz} = \sigma_{yz} \\ s_{zx} = \sigma_{zx} \end{Bmatrix} \tag{19}$$

$$\{\sigma_m\} = \begin{Bmatrix} \sigma_m \\ \sigma_m \\ \sigma_m \\ 0 \\ 0 \\ 0 \end{Bmatrix} \tag{20}$$

Since the matrix $[D_s]$ is a function of strain, equation (14) is nonlinear regarding $\{d\}$ and must be solved by some iterative procedure. The Newton-Raphson method was employed here, and at the $(i+1)$th step of the Newton-Raphson iteration, the following equation was solved instead of equation (14):

$$([K_s] + [K_v]\{\Delta d\} = \{F\} - \{f_{s(i)}\} - \{f_{v(i)}\} \tag{21}$$

where

$$[K_s] = \sum_e\int_{V_e}[B]^t[D_s^t][B]dV \tag{22}$$

Downloaded 02 May 2010 to 171.66.16.54. Redistribution subject to ASME license or copyright; see http://www.asme.org/terms/Terms_Use.cfm

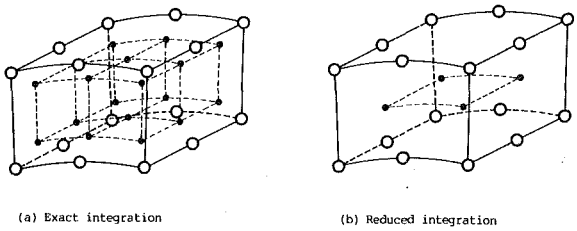


Fig. 1 Finite elements and integration points

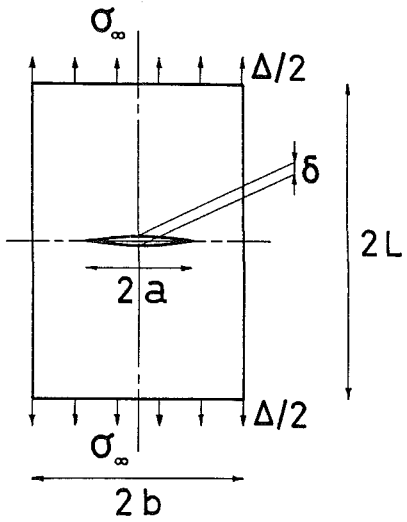


Fig. 2 Center-cracked plate under plane strain condition

$$[K_v] = \sum_e \int'_{V_e} [B]^t [D_v][B] dV \tag{23}$$

$$\{f_{s(i)}\} = \sum_e \int_{V_e} [B]^t \{s_{(i)}\} dV \tag{24}$$

$$\{f_{v(i)}\} = \sum_e \int'_{V_e} [B]^t \{\sigma_{m(i)}\} dV \tag{25}$$

Here, $[D'_s]$ is the matrix defined by

$$\{\Delta s\} = [D'_s]\{\Delta \epsilon\} \tag{26}$$

and its component can be calculated as

$$[D'_s] = \frac{2}{3} \bar{\epsilon}_{(i)}^{\frac{1-n}{n}} \left([A] + \frac{2}{3} \frac{1-n}{n} \frac{1}{\bar{\epsilon}^2_{(i)}} [A]\{\epsilon_{(i)}\} \lfloor \epsilon_{(i)} \rfloor [A] \right) \tag{27}$$

where $[A]$ is the matrix defined by

$$\{e\} = [A]\{\epsilon\} \tag{28}$$

In equations (22)–(25), $\int$ and $\int'$ mean the exact and reduced integrations, respectively.

Initiating the calculation from linear material ($n = 1$), the nodal displacements obtained there were used as an initial guess in the calculation for the hardening exponent $n = 2$. Similarly, the converged solution for the hardening exponent n was used as an initial guess in the calculation for the hardening exponent ($n = n + 1$).

It was assumed in this study that the convergence was achieved when

$$\left| \frac{\Pi_{(i)} - \Pi_{(i-1)}}{\Pi_{(ii)}} \right| < 10^{-4} \tag{29}$$

where $\Pi_{(i)}$ and $\Pi_{(i-1)}$ denote, respectively, the values of the potential energy Π at the ith and the $(i-1)$th iteration stages. Here, Π is defined as

$$\Pi = \sum_e \left(\int_{V_e} W_s dV - \int'_{V_e} W_v dV \right) - \lfloor F \rfloor \{d\} \tag{30}$$

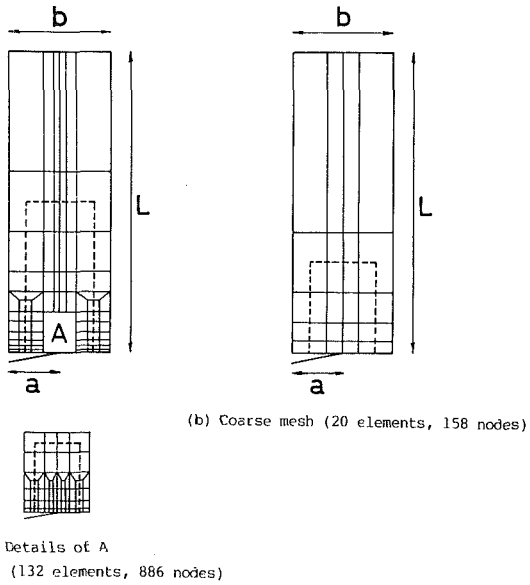


Fig. 3 Finite element subdivisions for one-quarter of a plate

where W_s and W_v represent the deviatoric and compressible strain energy densities, respectively, i.e.,

$$W_s = \frac{n}{n+1} \bar{\sigma}^{n+1} \tag{31}$$

$$W_v = \frac{\sigma_m^2}{2K} \tag{32}$$

Utilized here for J-integral calculation was the Virtual Crack Extension (VCE) method developed by Parks [10]. This method is based on the potential energy release-rate definition of the J-integral and can be applied to the three-dimensional problems as well as to the two-dimensional cases. To make the calculation consistent with the previous formulations, the following formula for J was used:

$$J = -\frac{1}{\delta A} \sum_e \left\{ \int_{V_e} (W_s \delta \det[J] + \{s\}[\delta B]\{d\} \det[J]) d\xi d\eta d\zeta + \int'_{V_e} (W_v \delta \det[J] + \{\sigma_m\}[\delta B]\{d\} \det[J]) d\xi d\eta d\zeta \right\} \tag{33}$$

where A is the crack area and δ means the variation with the small change of the crack area δA. (ξ, η, ζ) are the curvilinear coordinates and det $[J]$ is the Jacobian of coordinate transformation. It should be noted that this formulation is easier to implement in the finite element code than the line-integral in the two-dimensional problem or the surface-integral in the three-dimensional problem. Moreover, in this method, there is no need to make use of special interpolation technique such as that used in reference [15].

Finite Elements

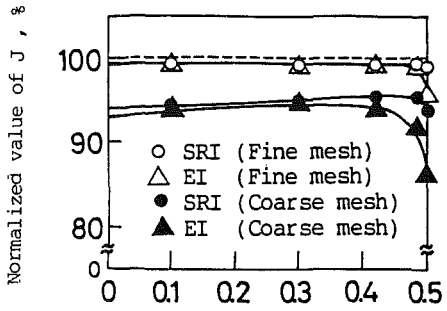
Here, the analyses for through-wall cracks in plates and cylinders were performed. Used were the 16-noded isoparametric elements. The configuration of the element is shown in Fig. 1. As can be seen in the figure, this element has the midside nodes on eight edges along two directions with no midside nodes on four edges along one direction. The latter direction was taken to coincide with the wall thickness direction of plates or cylinders. The matrix $[B]$ as well as the interpolation functions were composed on the base of the Cartesian and cylindrical coordinates for plates and cylinders, respectively.

In this element, the exact integration can be carried out with the use of $3 \times 3 \times 2$ Gaussian integration points indicated in

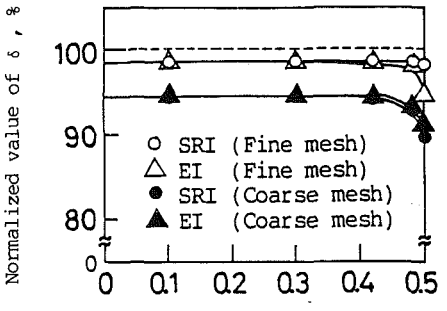
Downloaded 02 May 2010 to 171.66.16.54. Redistribution subject to ASME license or copyright; see http://www.asme.org/terms/Terms_Use.cfm

Table 1 Fully plastic solutions for center cracked plate under tension ($a/b = 1/2$)

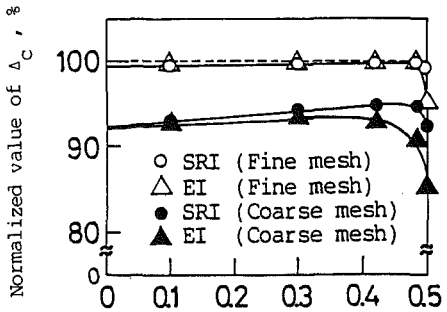
		$n=1$	$n=2$	$n=3$	$n=5$	$n=7$	$n=10$
h_1	Present	2.19	2.27	2.18	1.93	1.71	1.44
	Shih and Kumar [1]	2.19	2.27	2.18	1.93	1.71	1.44
h_2	Present	2.03	1.82	1.58	1.22	0.985	0.766
	Shih and Kumar [1]	2.09	1.87	1.61	1.23	0.996	0.776
h_3	Present	0.794	1.06	1.15	1.09	0.952	0.767
	Shih and Kumar [1]	0.798	1.06	1.15	1.10	0.959	0.771



(a) J versus ν



(b) δ versus ν



(c) Δ_c versus ν

Fig. 4 J, δ, and Δ_c versus Poisson's ratio (elastic solutions)

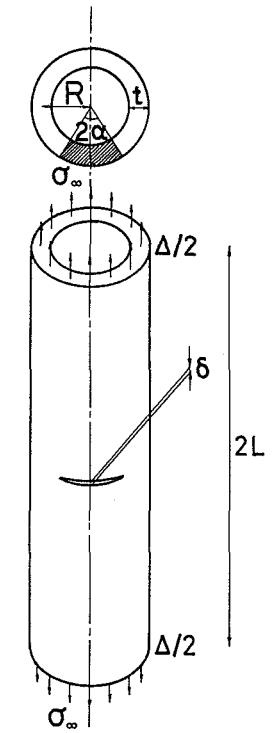


Fig. 5 Circumferentially through-wall cracked cylinder

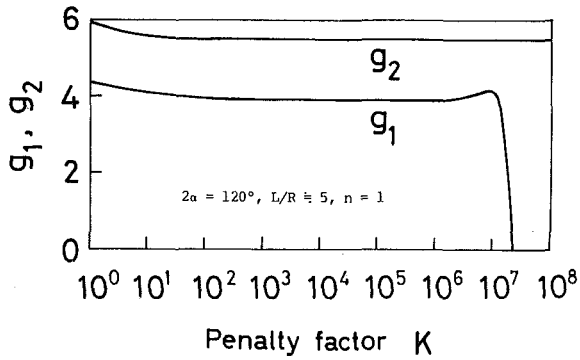


Fig. 6 Influence of magnitude of penalty factor on numerical results

Fig. 1(*a*). On the other hand, the reduced integration is performed with $2\times2\times1$ integration points as shown in Fig. 1(*b*).

Analysis of Center-Cracked Plates Under Plane Strain Condition

For the verification of the present method, analyzed first was center-cracked plates made of power-hardening materials under plane strain condition. The solutions calculated were compared with the reference values for elastic and fully plastic conditions [17, 1]. The configuration of the plate analyzed is shown in Fig. 2, where the crack length $2a$, and the plate length $2L$, are taken to be one-half and three times of the plate width $2b$, respectively.

Due to symmetry of the geometry and the loading, only one-quarter part of the whole plate was discretized. Two kinds of finite element subdivision as shown in Fig. 3 were employed. Only one layer of the elements was used in the thickness direction and all nodal displacements in this

Downloaded 02 May 2010 to 171.66.16.54. Redistribution subject to ASME license or copyright; see http://www.asme.org/terms/Terms_Use.cfm

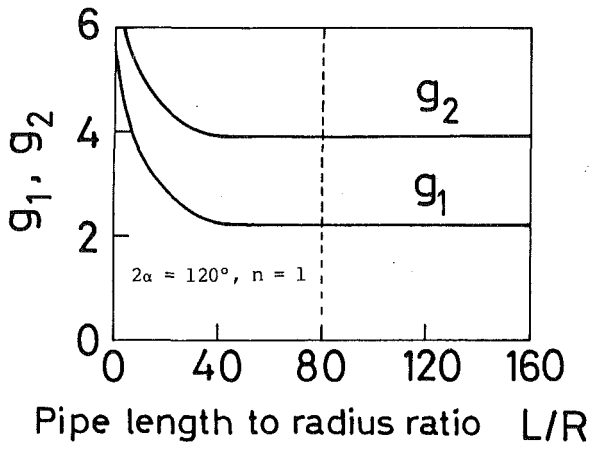


Fig. 7 Influence of pipe length on numerical results

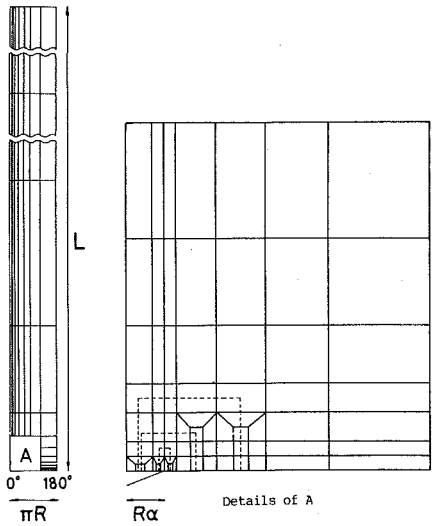


Fig. 8(*a*) Finite element subdivision for one-quarter of circumferentially through-wall cracked cylinder ($2\alpha = 30$ deg, $L/R = 80$, 119 elements, 816 nodes)

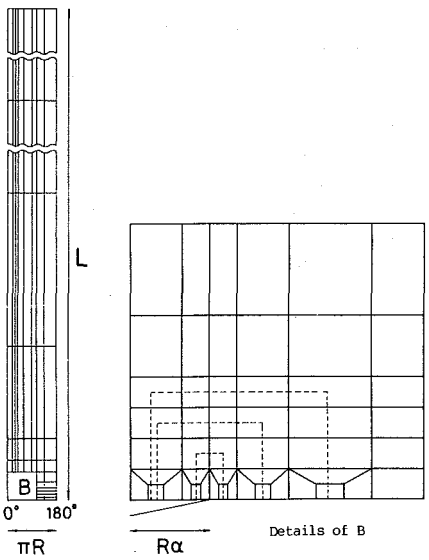


Fig. 8(*b*) Finite element subdivision for one-quarter of circumferentially through-wall cracked cylinder ($2\alpha = 60$ deg, $L/R = 80$, 111 elements, 768 nodes)

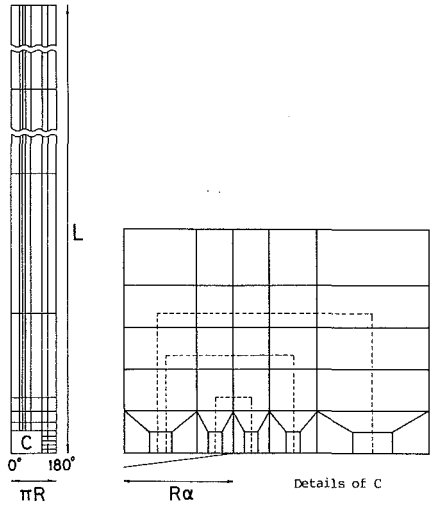


Fig. 8(*c*) Finite element subdivision for one-quarter of circumferentially through-wall cracked cylinder ($2\alpha = 90$ deg, $L/R = 80$, 99 elements, 692 nodes)

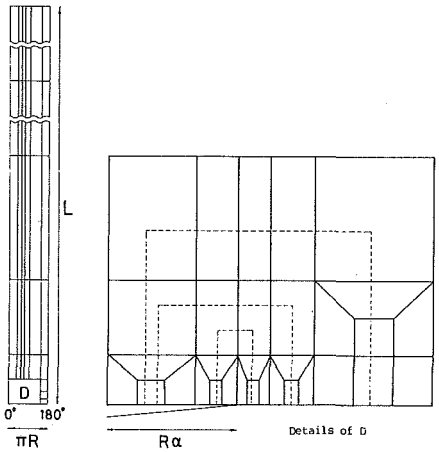


Fig. 8(*d*) Finite element subdivision for one-quarter of circumferentially through-wall cracked cylinder ($2\alpha = 120$ deg, $L/R = 80$, 65 elements, 468 nodes)

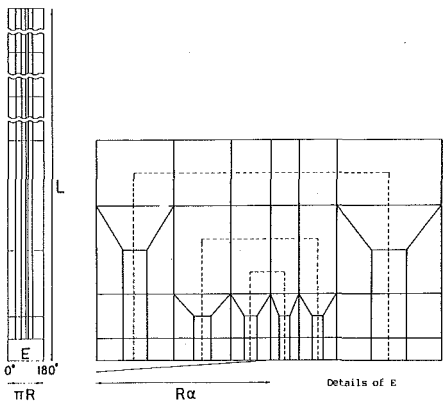


Fig. 8(*e*) Finite element subdivision for one-quarter of circumferentially through-wall cracked cylinder ($2\alpha = 180$ deg, $L/R = 160$, 94 elements, 654 nodes)

Fig. 8

Downloaded 02 May 2010 to 171.66.16.54. Redistribution subject to ASME license or copyright; see http://www.asme.org/terms/Terms_Use.cfm

Table 2 Normalized stress intensity factors for circumferentially through-wall cracked cylinder under tension

	$2\alpha = 30$deg	$2\alpha = 60$deg	$2\alpha = 90$deg	$2\alpha = 120$deg
Present	1.122	1.392	1.637	1.792
Delale and Erdogan [18]	1.112	1.327	1.549	1.750

Table 3 Fully plastic solutions for circumferentially through-wall cracked cylinder under tension

	2α	$n=1$	$n=2$	$n=3$	$n=4$	$n=5$
g_1	30 deg	3.00	3.93	4.48	4.80	4.97
	60 deg	3.31	3.88	3.85	3.45	2.96
	90 deg	3.03	2.71	2.02	1.39	0.918
	120 deg	2.20	1.49	0.843	0.446	0.232
	180 deg	0.776	0.275	0.0796	0.0223	0.00629
g_2	30 deg	3.75	4.48	4.94	5.22	5.35
	60 deg	4.16	4.46	4.26	3.87	3.31
	90 deg	4.33	3.72	2.74	1.87	1.23
	120 deg	3.90	2.49	1.38	0.730	0.378
	180 deg	2.51	0.736	0.197	0.0515	0.0135
g_3	30 deg	0.236	0.440	0.646	0.842	1.02
	60 deg	0.514	0.842	1.06	1.18	1.20
	90 deg	0.779	1.02	1.01	0.857	0.670
	120 deg	0.913	0.901	0.664	0.427	0.254
	180 deg	0.873	0.389	0.132	0.0401	0.0116

direction were constrained to impose the plane strain condition. The rings used for the J-integral calculation by the VCE method are also shown in the same figures by the broken lines.

At first, the analysis for the linear-elastic material ($n=1$) was performed. Figure 4 shows the comparison of the J-integral J, the crack-opening displacement at crack center δ, and the residual load-point displacement Δ_c calculated by the selective reduced integration and the exact integration for Poisson's ratio of 0–0.5 ($\Delta_c = \Delta - \Delta_{nc}$, where Δ is the total load point displacement and Δ_{nc} is the load point displacement of uncracked plates). The value of Poisson's ratio ν is a function of K defined as follows:

$$\nu = \frac{9K-2}{18K+2} \tag{34}$$

where κ, ϵ_0, and σ_0 are assumed to be unity. These values obtained were normalized by the values in the handbook [17]. Comparing the results with the Exact Integration (EI) and the Selective Reduced Integration (SRI), the decrease in the accuracy is seen with Poisson's ratio approaching 0.5 in the former case. It is also seen in the figure that, with the fine mesh and the SRI method, very good agreements with the reference values are achieved for the three parameters. This indicates the effectiveness of the SRI method in the analysis for the incompressible as well as compressible linear-elastic materials.

For the center-cracked plate made of power-hardening materials, the following normalization for the J-integral, δ and Δ_c are usually employed:

$$J = \kappa\sigma_0\epsilon_0 a\left(1-\frac{a}{b}\right)h_1\left(\frac{a}{b},n\right)\left(\frac{P}{P_0}\right)^{n+1} \tag{35}$$

$$\delta = \kappa\epsilon_0 a h_2\left(\frac{a}{b},n\right)\left(\frac{P}{P_0}\right)^{n} \tag{36}$$

$$\Delta_c = \kappa\epsilon_0 a h_3\left(\frac{a}{b},n\right)\left(\frac{P}{P_0}\right)^{n} \tag{37}$$

where P_0 is the limit load for the perfectly plastic material defined as

$$P_0 = \frac{4}{\sqrt{3}}(b-a)\sigma_0 \tag{38}$$

In equations (35)–(37), h_1, h_2, and h_3 are the fully plastic solutions for the respective three parameters. The convergence of the solutions for each n was really achieved after two or three Newton-Raphson iterations. The amount of the virtual crack extension for J-integral calculation was set to be some value between 10^{-7} and 10^{-8} times of b. The solutions obtained by the SRI method with the fine mesh are listed with the values by Shih and Kumar [1] in Table 1. Excellent agreements are again achieved for all the parameters and this indicates the soundness of the present method even in the nonlinear fully plastic analysis.

Analysis of Cylinders With a Circumferential Through-Wall Crack

In this section, the fully plastic analyses were performed to obtain the solutions for the cylinder with a circumferential through-wall crack using the method described in the foregoing.

The configuration of an analyzed model is shown in Fig. 5. The cylinder has a circumferential through-wall crack and is subjected to uniform tensional stress σ_∞ at the section remote from the crack. The mean radius and thickness of the cylinder are denoted by R and t, respectively. The analysis was performed for five crack angles 2α, namely 30, 60, 90, 120, and 180 deg. The thickness-to-inner radius ratio was fixed at 0.1, which corresponds to typical 26-in. diameter pipes of BWR and PWR nuclear power plants.

Three parameters calculated here were the J-integral J, the crack-opening displacement at crack center δ, and the residual load-point displacement Δ_c. The value of δ was defined as an averaged value of the displacements of inner and outer nodes at the crack center. The value of Δ_c was determined from a mean value of the maximum and the minimum displacements of all the nodes that locate on the loaded section. Using the notations $a=\alpha R$ and $b=\pi R$, the fully plastic solutions g_1, g_2, and g_3 were defined in the similar way as in equations (35)–(37), i.e.,

$$J = \kappa\sigma_0\epsilon_0 a\left(1-\frac{a}{b}\right)g_1\left(\frac{a}{b},n,\frac{t}{R}\right)\left(\frac{P}{P_0}\right)^{n+1} \tag{39}$$

$$\delta = \kappa\epsilon_0 a g_2\left(\frac{a}{b},n,\frac{t}{R}\right)\left(\frac{P}{P_0}\right)^{n} \tag{40}$$

$$\Delta_c = \kappa\epsilon_0 a g_3\left(\frac{a}{b},n,\frac{t}{R}\right)\left(\frac{P}{P_0}\right)^{n} \tag{41}$$

Downloaded 02 May 2010 to 171.66.16.54. Redistribution subject to ASME license or copyright; see http://www.asme.org/terms/Terms_Use.cfm

where P is the applied load given by

$$P=2\pi\sigma_\infty Rt \tag{42}$$

and P_0 is the limit load for the perfectly plastic material given by [3]

$$P_0=2\sigma_0 Rt\left\{\pi-\alpha-2\arcsin\left(\frac{1}{2}\sin\alpha\right)\right\} \tag{43}$$

Before going into the fully plastic calculations for various crack angles, influences of the penalty factor K and the pipe length L on the solutions were examined in the linear case.

Figure 6 shows the effect of the penalty factor on the solutions g_1 and g_2 in the case of the double-precision computation (32 bits/word) with HITAC M280H system. It can be seen in the figure that wide range of the penalty factor, i.e., from 10^3 to 10^6 gives essentially the same results. From this figure, one could use safely any value between 10^4 and 10^6 as the penalty factor in the practical calculations.

Next, the effect of the pipe length on the solutions was studied in the linear calculation. The results for a cylinder with a crack of 120 deg are shown in Fig. 7, which indicates that quite large pipe length, e.g., $L=80R$, is necessary to have a solution almost independent of the pipe length. One should be careful of this fact in the calculation and the application of the solutions. The pipe length actually employed for each crack angle is shown in Fig. 8(*a*)-(*e*). It was presumed that the length thus determined is enough for the nonlinear cases as well, since in the nonlinear material, deformation may be more confined to the neighborhood of the crack tip. The finally employed finite element models for a one-quarter part of the whole cylinder are also shown in Fig. 8(*a*)-(*e*) with rings for the VCE J-integral calculations.

An integral equation method for the stress intensity factor for this problem was developed by Delale and Erdogan [18] using the shell theory, which takes account of the transverse shear effect. Their solutions were compared with the present solutions for 2α of 30 to 120 deg in Table 2. Differences between both are within 6 percent as shown in the table.

The present nonlinear solutions were found to converge with two or three iterations for each value of n from 2 to 5. They are listed in Table 3 as a function of n and crack angle 2α.

Conclusion

In this paper, we studied a Selective Reduced Integration/Penalty Function (SRI/PF) method for the analysis of three-dimensional fully plastic solutions. It was demonstrated through the calculation of center-cracked plates under plane strain condition that accurate solutions can be obtained with the present method. Then, using the method, fully plastic solutions for cylinders with a circumferential through-wall crack subjected to remote uniform tension were calculated and tabulated as a function of crack angle and the hardening exponent. This method is believed to have very large potential in the application to other three-dimensional problems.

Acknowledgment

The present study was partially supported by the Grant-in-Aid for Scientific Research from the Ministry of Education, Science, and Culture.

References

1 Shih, C. F., and Kumar, V., "Estimation Technique for the Prediction of Elastic-Plastic Fracture of Structural Components of Nuclear Systems," RP1237-1, First Semianual Report for EPRI, General Electric Company, 1979.

2 Kumar, V., German, M. D., and Shih, C. F., "An Engineering Approach for Elastic-Plastic Fracture Analysis," EPRI NP-1931, Project 1237-1, Topical Report, 1981.

3 German, M. D., Andrews, W. R., Kumar, V., Shih, C. F., deLorenzi, H. G., and Mowbray, D. F., "Elastic-Plastic Fracture Analysis of Flawed Stainless Steel Pipes," Final Report to EPRI, Research Project T118-8, General Electric Company, 1982.

4 Goldman, N. L., and Hutchinson, J. W., "Fully Plastic Crack Problem: The Center-Cracked Strip Under Plane Strain," *Int. J. Solids and Struct.*, Vol. 11, 1975, pp. 575-591.

5 Shih, C. F., "J-integral Estimates for Strain Hardening Materials in Antiplane Shear Using Fully Plastic Solution," ASTM STP 590, 1976, pp. 3-26.

6 Shih, C. F., and Hutchinson, J. W., "Fully Plastic Solutions and Large Scale Yielding Estimates for Plane Stress Crack Problems," ASME *Journal of Engineering Materials and Technology*, Vol. 98, 1976, pp. 289-295.

7 Hutchinson, J. W., Needleman, A., and Shih, C. F., "Fully Plastic Problems in Bending and Tension," MECH-6, Harvard University, Cambridge, Mass., 1978.

8 Ilyushin, A. A., "The Theory of Small Elastic-Plastic Deformations," *Prikadnaia Matematika i Mekhanika (P.M.M.)*, Vol. 10, 1946, p. 347.

9 Nagtegaal, J. C., Parks, D. M., and Rice, J. R., "On Numerically Accurate Finite Element Solutions in the Fully Plastic Range," *Comp. Meth. Appl. Mech. Eng.*, Vol. 4, 1974, pp. 153-178.

10 Parks, D. M., "Virtual Crack Extension: A General Finite Element Technique for J-Integral Evaluation," *Proc. 1st Int. Conf. in Num. Fract. Mech.*, 1978, pp. 464-478.

11 Herrmann, L. R., "Elasticity Equations for Incompressible and Nearly Incompressible Materials by Variational Theorem," *AIAA*, Vol. 3, 1965, pp. 1896-1900.

12 Zienkiewicz, O. C., and Godbole, P. N., "A Penalty Function Approach to Problems of Plastic Flow of Metals With Large Surface Deformation," *J. Strain Analysis*, Vol. 10, 1975, pp. 180-185.

13 Yagawa, G., Aizawa, T., and Ando, Y., "Linear and Nonlinear Elastic Analysis of Cracked Plate: Application of a Penalty Function and Superposition Method," *Int. J. Num. Meth. Eng.*, Vol. 17, 1981, pp. 719-733.

14 Yagawa, G., and Aizawa, T., "A Superposition Method for Nonlinear Crack Problems," ASTM STP 803, 1983, pp. I354-I369.

15 Shih, C. F., and Needleman, A., "Fully Plastic Crack Problems: Solution by a Penalty Method That Pass the Consistency Check," U.S. Department of Energy, Contract DE-AC02-80-ER10556, Technical Report No. 95, Brown University, 1983.

16 Needleman, A., and Shih, C. F., "A Finite Element Method for Plane Strain Deformation of Incompressible Solids," *Comp. Meth. Appl. Mech. Eng.*, Vol. 15, 1978, pp. 223-240.

17 Tada, H., Paris, P. C., and Irwin, G. R., *The Stress Analysis of Crack Handbook*, Del Research Corporation, 1973.

18 Delale, F., and Erdogan, F., "Transverse Shear Effect in a Circumferentially Cracked Cylinder Shell," *Quarterly App. Math.*, 1979, pp. 239-258.

Downloaded 02 May 2010 to 171.66.16.54. Redistribution subject to ASME license or copyright; see http://www.asme.org/terms/Terms_Use.cfm

Asymptotic Solutions of the Von Karman Equations for a Circular Plate Under a Concentrated Load[1]

J. P. Frakes

J. G. Simmonds
Mem. ASME

Department of Applied Mathematics,
University of Virginia,
Charlottesville, Va. 22901

Reissner's form of the axisymmetric von Karman equations for a centrally, point-loaded plate are written in dimensionless differential and integral form. To concentrate on essentials, we take Poisson's ratio to be one-third (so that the limiting Föppl membrane equations have one-term solutions) and boundary conditions of simple support. A dimensionless parameter β measures the relative bending stiffness. A nine-term perturbation solution in powers of $\epsilon=\beta^{-6}$, the first term of which corresponds to linear plate theory, is constructured using MACSYMA. Although the resulting deflection-load power series appears to converge only if $|\epsilon| < 1/40$, successive Aitken-Shanks' transformations yield an expression valid up to $\epsilon \approx 1$. Solutions as $\beta \to 0$ are constructed using singular perturbation methods and two terms of the deflection-load curve are computed numerically, the first term corresponding to the exact nonlinear membrane solution. A graph shows that there is a region of overlap of the large and small β-approximations to the deflection-load curve.

Introduction

If an elastically isotropic, circular membrane is fixed at its outer radius a and subject to a downward concentraed load P at its center, then within the Föppl theory [1] (which neglects squares of angles of rotation compared to unity and assumes linear stress-strain relations) there is an exact solution [2, 3] for the *downward* vertical deflection W that has a cusp at the load point. In particular, if Poisson's ratio $\nu = 1/3$,

$$\frac{W}{a}=\left(\frac{3P}{\pi Eah}\right)^{1/3}\left[1-\left(\frac{r}{a}\right)^{2/3}\right], \tag{1}$$

where h is the thickness of the membrane, E is Young's modulus, and r is radial distance; h and E are constants.

What happens to (1) if there is bending stiffness? We will answer this and related questions by using perturbation and numerical methods to obtain approximate solutions of Reissner's form of the axisymmetric, twice-integrated von Karman equations [4],

$$A(r^2\Psi''+r\Psi'-\Psi)=-\frac{1}{2}r\Phi^2 \tag{3}$$

$$D(r^2\Phi''+r\Phi'-\Phi)=r(\Psi\Phi-P/2\pi). \tag{4}$$

Here $D = E_bh^3$ is the bending stiffness and $A = 1/E_sh$ is the stretching compliance, where E_b and E_s are Young's moduli of bending and stretching. (Conventionally, $E_b = E/12(1-\nu^2)$, $E_s = E$.) Further, Ψ is a stress function, $\Phi = -W'$, and a prime denotes differentiation with respect to r. The hoop strain and radial bending moment are given, respectively, by

$$\epsilon_\theta=r^{-1}U=A(\Psi'-\nu r^{-1}\Psi) \tag{5}$$

$$M_r=-D(\Phi'+\nu r^{-1}\Phi), \tag{6}$$

where U is horizontal displacement. The downward displacement of the plate, if taken zero at the edge, is given by

$$W=\int_r^a \Phi dr. \tag{7}$$

It is convenient to change variables and to non-dimensionalize. Thus, with

$$\alpha=2\left(\frac{AP}{2\pi a}\right)^{1/3}=2\left(\frac{P}{2\pi E_sah}\right)^{1/3} \tag{8}$$

$$\beta^2=\frac{8\pi D\alpha}{Pa}=8\left(\frac{E_b}{E_s}\right)\left(\frac{2\pi E_sah}{P}\right)^{2/3}\left(\frac{h}{a}\right)^2 \tag{9}$$

$$r^2=a^2x,\quad \Psi=\left(\frac{P}{2\pi\alpha}\right)x^{-1/2}f,\quad \Phi=\alpha x^{1/2}g \tag{10}$$

$$\epsilon_\theta=\left(\frac{AP}{2\pi\alpha a}\right)e,\quad M_r=-\left(\frac{D\alpha}{a}\right)m \tag{11}$$

$$U=\left(\frac{AP}{2\pi\alpha}\right)u,\quad W=\left(\frac{\alpha a}{2}\right)w, \tag{12}$$

equations (3)–(7) reduce to

$$f''=-g^2 \tag{13}$$

[1]This work was supported by the National Science Foundation under grant CEE-8117103.

Contributed by the Applied Mechanics Division for publication in the JOURNAL OF APPLIED MECHANICS.

Discussion on this paper should be addressed to the Editorial Department, ASME, United Engineering Center, 345 East 47th Street, New York, N.Y. 10017, and will be accepted until two months after final publication of the paper itself in the JOURNAL OF APPLIED MECHANICS. Manuscript received by ASME Applied Mechanics Division, March, 1984.

Copyright © 1985 by ASME
Downloaded 02 May 2010 to 171.66.16.54. Redistribution subject to ASME license or copyright; see http://www.asme.org/terms/Terms_Use.cfm

$$\beta^2 x(xg)'' = fg - 1 \tag{14}$$

$$e = x^{-1/2}u = 2f' - x^{-1}(1+\nu)f \tag{15}$$

$$m = 2xg' + (1+\nu)g \tag{16}$$

$$w = \int_x^1 g\,dx, \tag{17}$$

where a prime now denotes differentiation with respect to x. The Föppl equations follow upon setting $\beta = 0$ and ignoring (16).

The von Karman equations remedy two deficiencies of Föppl's. First, the presence of bending stiffness, manifested by the parameter β, removes the cusp in W under the concentrated load. And second, the assumption that $\Phi^2 + 1 \approx 1$, which is embedded in *both* the Föppl and von Karman equations, but which is inescapably violated in the Föppl equations because the cusp, is satisfied by the von Karman equations if α is small – a comparison of the large rotation plate equations of Reissner [5] with those of von Karman, carried out in [6], shows that the relative pointwise errors in the latter are $O(\alpha^2)$.

To focus on how bending stiffness modifies the effect of a point load on a membrane and to keep the analysis simple, we take $\nu = 1/3$ and boundary conditions of simple support, viz.,

$$u(1) = 2f'(1) - (4/3)f(1) = 0 \tag{18}$$

$$m(1) = 2g'(1) + (4/3)g(1) = 0. \tag{19}$$

As the center of the plate is approached the slope of the deformed midsurface must approach zero and the vertical load must be equilibrated by the radial transverse shear stress resultant. These conditions imply that

$$f \sim \beta^{-4}Ax, \quad g \sim \beta^{-2}(-\ln x + B) \quad \text{as} \quad x \to 0, \tag{20}$$

where A and B are unknown functions of β.

Herein, we present asymptotic solutions for f and g for large and small values of β plus expressions for the central deflection of the plate as a function of the load. In carrying out our work, we have made extensive use of MACSYMA, a symbol manipulating program developed at MIT. By applying the Aitken-Shanks transformation [7] that accelerates the convergence of sequences (or, in some cases, renders divergent sequences convergent), we have been able to extend the deflection-load curve for $\beta >> 1$ so that it overlaps the deflection-load curve for $\beta << 1$.

Chien and Yeh [8] and Schmidt [9, 10] have obtained, for various boundary conditions, deflection-load and load-deflection formulas, respectively, by assuming perturbation expansions in powers of a load or deflection parameter. Their work is summarized in the book by Chia [11]. The convergence of Chien's perturbation solution is discussed by Chen [12]. Watson and Chudobiak [13] applied an Aitken-Shanks transformation to three-term perturbation series for the deflection and stresses in a uniformly loaded plate.

None of the preceding authors discuss the behavior of a centrally, point-loaded plate as the bending stiffness approaches zero, although such an analysis is given by Chien [14], Bromberg [15], and Keller and Reiss [16] for plates under uniform pressure.

Solution for Relatively Large Bending Stiffness ($\beta >> 1$)

Let

$$f = \epsilon^{2/3}F, \quad g = \epsilon^{1/3}G, \quad \epsilon = \beta^{-6}. \tag{21}$$

Then (13), (14), and (18)–(20) take the form

$$F'' = -G^2 \tag{22}$$

$$x(xG)'' = \epsilon FG - 1 \tag{23}$$

$$F'(1) = (2/3)F(1) \tag{24}$$

$$G'(1) = -(2/3)G(1) \tag{25}$$

$$F \sim Ax, \quad G \sim -\ln x + B \quad \text{as} \quad x \to 0. \tag{26}$$

By integrating (22) and (23) twice, using the iterated integral formula

$$\int_0^x \int_0^\xi y(t)\,dt\,d\xi = \int_0^x (x-t)y(t)\,dt, \tag{27}$$

and imposing the boundary conditions (24)–(26), we convert (22)–(26) into the coupled, nonlinear integral equations

$$F(x,\epsilon) = \int_0^1 K(x,t)G^2(t,\epsilon)\,dt \equiv \mathcal{K}\{G^2\} \tag{28}$$

$$G(x,\epsilon) = \int_0^1 L(x,t)[1 - \epsilon F(t,\epsilon)G(t,\epsilon)]\,dt \equiv -\ln x + 3/2 - \epsilon\mathcal{L}\{FG\}, \tag{29}$$

where

$$K(x,t) = \begin{cases} (1+2x)t, & t < x \\ (1+2t)x, & x < t \end{cases} \tag{30}$$

$$L(x,t) = \begin{cases} \dfrac{1}{x} + \dfrac{1}{2}, & t < x \\ \dfrac{1}{t} + \dfrac{1}{2}, & x < t \end{cases} \tag{31}$$

The unknown constants A and B in (26) are given by

$$A(\epsilon) = \int_0^1 (1+2x)G^2(x,\epsilon)\,dx \tag{32}$$

$$B(\epsilon) = \frac{3}{2} - \epsilon\int_0^1 \left(\frac{1}{x} + \frac{1}{2}\right)F(x,\epsilon)G(x,\epsilon)\,dx. \tag{33}$$

Integral equations analogous to (28) and (29) for plates under uniform pressure are given by Keller and Reiss [16] who use them to obtain bounds on the solution. Chen [12] uses integral equations to estimate the errors and radius of convergence of Chien's perturbation method for uniform or concentrated normal loads.

An attempt to solve (28) and (29) by either iteration or perturbation yields, formally, solutions of the same form: power series in ϵ. Thus assuming

$$F(x,\epsilon) \sim \sum_0^N \epsilon^n F_n(x), \quad G(x,\epsilon) \sim \sum_0^N \epsilon^n G_n(x), \tag{34}$$

we have, upon substituting (34) into (28) and (29) and equating coefficients of like powers of ϵ,

$$F_n = \mathcal{K}\left\{\sum_0^n G_k G_{n-k}\right\} \tag{35}$$

$$G_{n+1} = -\mathcal{L}\left\{\sum_0^n F_k G_{n-k}\right\}, \quad G_0 = -\ln x + 3/2. \tag{36}$$

Substituting (34) into (32) and (33), we have

$$A(\epsilon) \sim \sum_0^N \epsilon^n \sum_0^n \int_0^1 (1+2x)G_k(x)G_{n-k}(x)\,dx \equiv \sum_0^N \epsilon^n A_n \tag{37}$$

$$B(\epsilon) \sim \frac{3}{2} - \sum_0^N \epsilon^{n+1} \sum_0^n \int_0^1 \left(\frac{1}{x} + \frac{1}{2}\right)F_k(x)G_{n-k}(x)\,dx$$

Downloaded 02 May 2010 to 171.66.16.54. Redistribution subject to ASME license or copyright; see http://www.asme.org/terms/Terms_Use.cfm

Table 1 Values of A_n, B_n, and V_n

n	A_n	B_n	V_n
0	$\frac{23}{2}$	$\frac{3}{2}$	$\frac{5}{2}$
1	$-\frac{9369535}{62208}$	$-\frac{21731}{864}$	$-\frac{43087}{2592}$
2	$\frac{3878467058038397}{1049760000000}$	$\frac{804999226279}{1555200000}$	$\frac{1368344804549}{3888000000}$

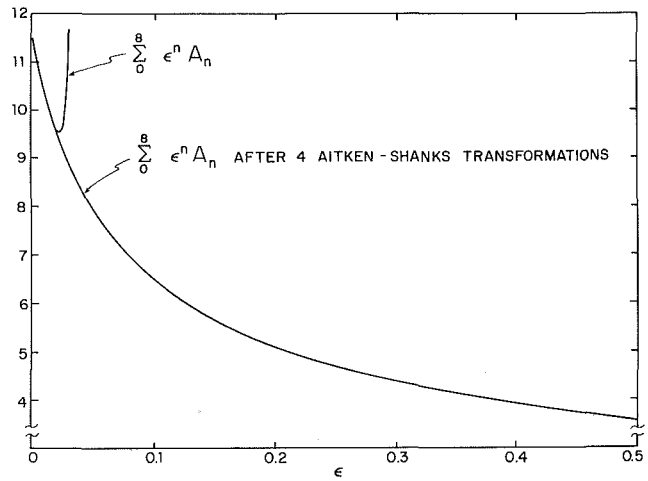


Fig. 1 $A \sim \Sigma_0^8 \epsilon^n A_n$ before and after four Aitken-Shanks transformations; see equation (37)

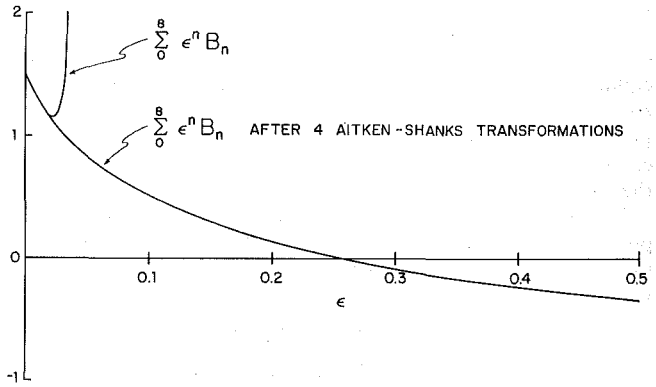


Fig. 2 $B \sim \Sigma_0^8 \epsilon^n B_n$ before and after four Aitken-Shanks transformations; see equation (38)

$$\equiv \sum_0^N \epsilon^n B_n. \tag{38}$$

From (12), (17), (21), and (34), a dimensionless downward vertical displacement at the center of the plate may be defined by

$$\beta^2 w(0) = \int_0^1 G(x,\epsilon)\,dx \sim \sum_0^N \epsilon^n \int_0^1 G_n(x)\,dx \equiv \sum_0^N \epsilon^n V_n, \tag{39}$$

Using MACSYMA we have computed the first nine terms of the sequences $\{F_n, G_n, A_n, B_n, V_n\}$. In particular,

$$F_0 = -(x/8)(4x\ln^2 x - 24x\ln x + 41x - 92) \tag{40}$$

$$G_1 = (1/864)[72x^2\ln^3 x - 720x^2\ln^2 x + (2514x^2 - 4968x)\ln x - 2962x^2 + 14904x - 21713]. \tag{41}$$

The number of terms in the successive functions F_1, G_2, ... grows explosively and no attempt is made to list them here. A few terms in the numerical sequences $\{A_n, B_n, V_n\}$ are given in Table 1.

Graphs of $\sum_0^8 \epsilon^n \{A_n, B_n\}$ are presented in Figs. 1 and 2 along with the graphs obtained by applying four Aitken-Shanks transformations, denoted by $s_n^{(4)}$ in [7].

Solution for Relatively Small Bending Stiffness ($\beta << 1$)

We expect a circular plate, if very thin, to behave essentially like a membrane except near its edge and near the central point load. We now formalize this.

Edge-Zone Solutions. To analyze edge-zone behavior let

$$x = 1 - \beta y, \quad xg = p. \tag{42}$$

Then (13) and (14) and the boundary conditions (18) and (19) take the form

$$(1-\beta y)^2 f'' = -\beta^2 p^2 \tag{43}$$

$$(1-\beta y)^2 p'' = fp - 1 + \beta y \tag{44}$$

$$f'(0) = -(2/3)\beta f(0) \tag{45}$$

$$p'(0) = -(1/3)\beta p(0), \tag{46}$$

where a prime now denotes differentiation with respect to y. As $y \to \infty$ and $x \to 1$, the edge-zone and interior solutions must match.

Assuming

$$f \sim \sum_0^N \beta^n f_n(y), \quad p \sim \sum_0^N \beta^n p_n(y), \tag{47}$$

substituting (47) into (43)-(46), and equating like powers of β, we obtain a sequence of differential equations and boundary conditions. Using earlier equations to eliminate second derivatives of lower order terms in later equations, we obtain

$$f_0'' = 0, \quad f_0'(0) = 0 \tag{48}$$

$$p_0'' - f_0 p_0 = -1, \quad p_0'(0) = 0 \tag{49}$$

$$f_1'' = 0, \quad f_1'(0) = -(2/3)f_0(0) \tag{50}$$

$$p_1'' - f_0 p_1 = f_1 p_0 + (2f_0 p_0 - 1)y, \quad p_1'(0) = -(1/3)p_0(0) \tag{51}$$

$$f_2'' = -p_0^2, \quad f_2'(0) = -(2/3)f_1(0) \tag{52}$$

$$p_2'' - f_0 p_2 = f_1 p_1 + f_2 p_0 + 2(f_0 p_1 + f_1 p_0)y + (3f_0 p_0 - 1)y^2$$
$$p_2'(0) = -(1/3)p_1(0), \tag{53}$$

etc.

Solving these equations in sequence, we have

$$f_0 = A_0, \quad p_0 = A_0^{-1} \tag{54}$$

$$f_1 = A_1 - (2/3)A_0 y, \quad p_1 = -A_0^{-2}[A_1 + (1/3)A_0 y] \tag{55}$$

$$f_2 = A_2 - (2/3)A_1 y - (1/2)A_0^{-2} y^2$$
$$p_2 = A_0^{-3}\{A_0^{-2} - (4/9)A_0 + A_1^2 - A_2 A_0 + (1/3)A_0 A_1 y + [(1/2)A_0^{-1} - (2/9)A_0^2]y^2\}. \tag{56}$$

So far no exponential terms have appeared; (54)-(56) are merely the membrane contribution to f and g near the edge.

Downloaded 02 May 2010 to 171.66.16.54. Redistribution subject to ASME license or copyright; see http://www.asme.org/terms/Terms_Use.cfm

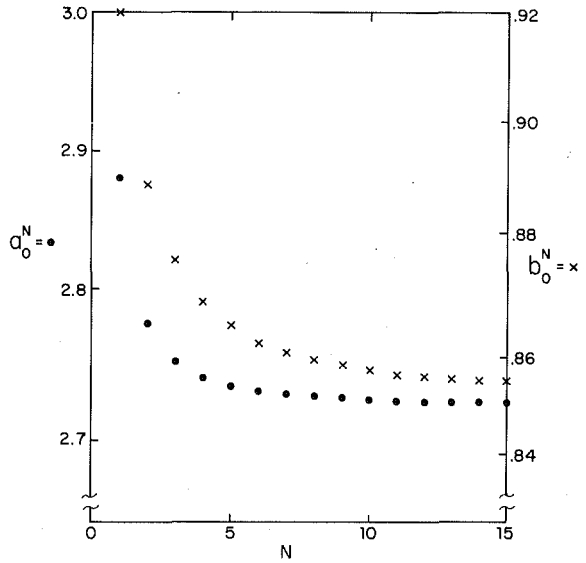


Fig. 3 The iterates a_0^N and b_0^N; see equation (77)

We expect this because of the boundary conditions of simple support.

Interior Solutions. Here we seek solutions of (13) and (14) of the form

$$f \sim \sum_0^N \beta^{2n} \bar{f}_n(x), \quad g \sim \sum_0^N \beta^{2n} \bar{g}_n(x). \tag{57}$$

Substituting (57) into (13) and (14) and equating coefficients of like powers of β^2, we obtain the sequence of equations

$$\bar{g}_n = \bar{f}_0^{-1}\left[x(x\bar{g}_{n-1})'' - \sum_1^n \bar{f}_k \bar{g}_{n-k}\right], \quad \bar{g}_0 = \bar{f}_0^{-1} \tag{58}$$

$$\bar{f}_n'' = -\sum_0^n \bar{g}_k \bar{g}_{n-k}. \tag{59}$$

Because we chose $\nu = 1/3$, we know that $\bar{f}_0$ and $\bar{g}_0$ must be the one-term Schwerin solutions [2]

$$\bar{f}_0 = (9/2)^{1/3} x^{2/3}, \quad \bar{g}_0 = (2/9)^{1/3} x^{-2/3} \tag{60}$$

which satisfy (13) and (14) with $\beta = 0$ as well as the boundary condition (18). Setting $n = 1$ in (58) and (59) and inserting (60), we get

$$\bar{g}_1 = -(2/9)^{2/3}(2/9 + \bar{f}_1)x^{-4/3} \tag{61}$$

$$x^2\bar{f}_1'' - (4/9)\bar{f}_1 = 8/81 \tag{62}$$

which have the solution

$$\bar{f}_1 = \bar{A}_1 x^{4/3} + \bar{B}_1 x^{-1/3} - 2/9 \tag{63}$$

$$\bar{g}_1 = -(2/9)^{2/3}(\bar{A}_1 + \bar{B}_1 x^{-5/3}). \tag{64}$$

Matching (57) to (47) verifies what is obvious physically:

$$|f(x) - (9/2)^{1/3}x^{2/3}| = O(\beta^2),$$

$$|g(x) - (2/9)^{1/3}x^{-2/3}| = O(\beta^2), \tag{65}$$

uniformly on $0 < \delta \le x \le 1$.

Solutions in a Neighborhood of the Point Load. Let

$$f = \beta^2\phi, \quad g = \beta^{-2}\gamma, \quad x = \beta^3\xi \tag{66}$$

$$A = \beta^3 a, \quad B = 3\ln\beta - b. \tag{67}$$

Then (13), (14), and (20) reduce to

$$\phi'' = -\gamma^2 \tag{68}$$

$$\xi(\xi\gamma)'' = \phi\gamma - 1 \tag{69}$$

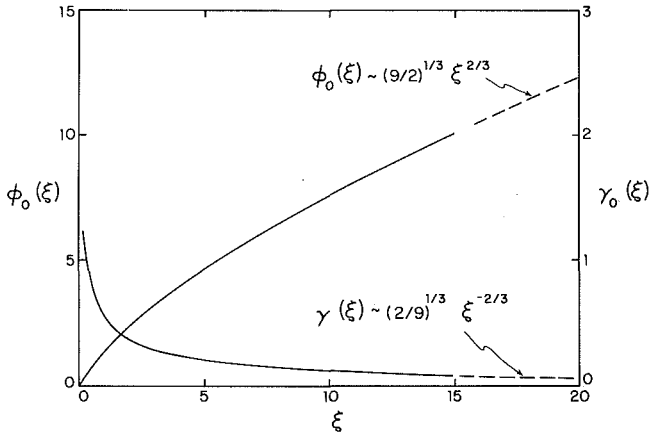


Fig. 4 Lowest-order solutions in a neighborhood of the point load; see equations (68), (69), (73), and (74)

$$\phi \sim a\xi, \quad \gamma \sim -\ln\xi - b \quad \text{as} \quad \xi \to 0, \tag{70}$$

where a prime now denotes differentiation with respect to ξ.

Boundary conditions for large ξ are obtained by matching with the interior solutions. This may be carried out via an intermediate variable ζ by setting

$$\xi = \beta^{-3/2}\zeta, \quad x = \beta^{3/2}\zeta \tag{71}$$

and then requiring that, for *fixed* ξ,

$$\beta^2\phi(\xi,\beta) = \beta^2\phi(\beta^{-3/2}\zeta,\beta) \sim \sum_0^N \beta^{2n}\bar{f}_n(\beta^{3/2}\zeta)$$

$$\beta^{-2}\gamma(\xi,\beta) = \beta^{-2}\gamma(\beta^{-3/2}\zeta,\beta) \sim \sum_0^N \beta^{2n}\bar{g}_n(\beta^{3/2}\zeta) \tag{72}$$

as $\beta \to 0$. To lowest order, (60) and (72) imply that

$$\phi_0(\xi) \equiv \phi(\xi,0) \sim (9/2)^{1/3}\xi^{2/3},$$

$$\gamma_0(\xi) \equiv \gamma(\xi,0) \sim (2/9)^{1/3}\xi^{-2/3} \quad \text{as} \quad \xi \to \infty. \tag{73}$$

Thus ϕ_0 and γ_0 satisfy the differential equations (68) and (69) plus the boundary conditions (73) and, from (70),

$$\phi_0 \sim a_0\xi, \quad \gamma_0 \sim -\ln\xi - b_0 \quad \text{as} \quad \xi \to 0, \tag{74}$$

where a_0 and b_0 are the values of $a(\beta)$ and $b(\beta)$ at $\beta = 0$. It may be shown either from (32), (33), and (67) or else, directly, from (68), (69), (73), and (74) that

$$a_0 = \int_0^\infty \gamma_0^2(\xi)\,d\xi \tag{75}$$

$$b_0 = \int_0^1 \frac{\phi_0(\xi)\gamma_0(\xi)}{\xi}\,d\xi + \int_1^\infty \frac{\phi_0(\xi)\gamma_0(\xi) - 1}{\xi}\,d\xi - 1. \tag{76}$$

The nonlinear boundary value problem for $\phi_0(\xi)$ and $\gamma_0(\xi)$ is singular in three ways: $\xi \in (0,\infty)$ and the differential equations are singular at $\xi = 0,\infty$. We used the following procedure to obtain approximate solutions for $\phi_0(\xi)$ and $\gamma_0(\xi)$ and approximate values for a_0 and b_0.

To start the numerical integration of (68) and (69), we moved away from the singular point $\xi = 0$ to a regular point $\xi = H$. This was done by choosing trial values of a_0 and b_0 and then computing $\phi_0(H, a_0, b_0)$ and $\gamma_0(H, a_0, b_0)$ as limits of a sequence of analytic iterates generated by MACSYMA. Using these as starting values and choosing a mesh size h such that $0 < h << H < 1$, (68) and (69) were integrated numerically to $\xi = N$, $N = 1, 2, \cdots$. Newton's method was then applied to adjust the trial values of a_0 and b_0 until the "mock" boundary conditions

$$\phi_0(N, a_0^N, b_0^N) = (9/2)^{1/3}N^{2/3},$$

$$\gamma_0(N, a_0^N, b_0^N) = (2/9)^{1/3}N^{-2/3} \tag{77}$$

Downloaded 02 May 2010 to 171.66.16.54. Redistribution subject to ASME license or copyright; see http://www.asme.org/terms/Terms_Use.cfm

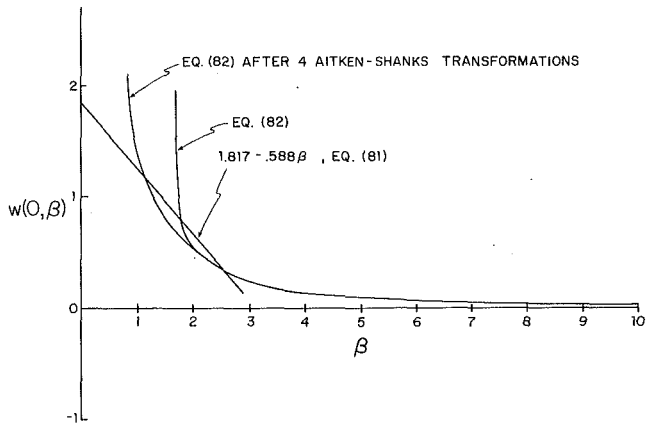


Fig. 5 Dimensionless deflection-load curve; see equations (9) and (37)

were met. N was then incremented and the procedure repeated. This produced a sequence of values a_0^N and b_0^N that approached 2.717 . . . and 0.852 . . . , respectively. (a_0 is tantalizingly close to e = 2.718 . . . ,) Graphs of a_0^N and b_0^N versus N are given in Fig. 3 and the graphs of the converged values of $\phi_0(\xi, a_0, b_0)$ and $\gamma_0(\xi, a_0, b_0)$ are given in Fig. 4. Equations (75) and (76) served as consistency checks on the converged values of a_0 and b_0. For more details of the numerical procedure see [17].

Deflection Under a Point Load

From (17) and (66) we have

$$w(0,\beta) = \int_0^1 g(x,\beta)\,dx = \beta\int_0^{\beta^{-3}} \gamma(\xi,\beta)\,d\xi. \tag{78}$$

Now (57), (60), (64), and (72) imply, in terms of the intermediate variable $\zeta = \beta^{3/2}\xi$, that

$$\gamma \sim (2/9)^{1/3}\beta\xi^{-2/3} - (2/9)^{2/3}\bar{B}_1\beta^{3/2}\zeta^{-5/3} + \cdots, \quad \zeta = O(1)$$
$$= (2/9)^{1/3}\xi^{-2/3} - (2/9)^{2/3}\bar{B}_1\beta^{-1}\xi^{-5/3} + \cdots \quad \text{as} \quad \xi \to \infty. \tag{79}$$

This asymptotic behavior suggests that we rewrite (78) as

$$w(0,\beta) = (2/9)^{1/3}\beta\int_0^{\beta^{-3}} \xi^{-2/3}\,d\xi + \beta\int_0^{\infty} [\gamma(\xi,\beta) - (2/9)^{1/3}\xi^{-2/3}]\,d\xi - \beta\int_{\beta^{-3}}^{\infty} [\gamma(\xi,\beta) - (2/9)^{1/3}\xi^{-2/3}]\,d\xi. \tag{80}$$

The first integral in (80) may be evaluated exactly, while according to (79), the last line in (80) is $O(\beta^2)$. Thus, if we replace γ by γ_0 in the middle integral in (80), we have

$$w(0,\beta) \sim 3(2/9)^{1/3} + \beta\int_0^{\infty} [\gamma_0(\xi) - (2/9)^{1/3}\xi^{-2/3}]\,d\xi \approx 1.817\cdots - (0.588\cdots)\beta. \tag{81}$$

As $\beta \to \infty$, we have, from (21), (39), and Table 1,

$$w(0,\beta) \sim \frac{1}{\beta^2}\left[\frac{5}{2} - \frac{43087}{2592}\,\frac{1}{\beta^6} + O\left(\frac{1}{\beta^{12}}\right)\right]. \tag{82}$$

Inverted, equation (82) yields

$$q = \frac{2}{5}V + \frac{43087}{202500}V^3 + O(V^5), \tag{83}$$

where

$$q = \sqrt{2}\beta^{-3} = \frac{Pa^2E_s^{1/2}}{32\pi h^4 E_b^{3/2}} \tag{84}$$

is a dimensionless load and

$$V = \frac{1}{2}\left(\frac{E_s}{E_b}\right)^{1/2}\frac{W(0)}{h}$$

is a dimensionless vertical displacement. Equation (83) agrees with equation (52) of Chien and Yeh [8] upon taking Poisson's ratio equal to one-third in their equation (53*b*). Figure 5 displays a graph of the last line of (81) and the series $\beta^{-2}\Sigma_0^8\beta^{-6n}V_n$. Also shown is the result of applying to the latter series several Aitken-Shanks transformations. This is seen to be powerful enough to produce a region of overlap for the two expansions of $w(0, \beta)$.

Conclusions

In nonlinear problems with solutions expressible as regular perturbation expansions, it is often feasible to compute by hand only two or three terms. For point loaded circular plates, we have shown by using MACSYMA to generate longer perturbations expansions (the terms of which never need be seen) and by applying Aitken-Shanks transformations to the results, that we can extend dramatically the range of usefulness of the expansions. Moreover, by using MACSYMA to aid in the numerical solution of a complementary singular boundary-value problem, we have been able to obtain a good, approximate deflection-load curve that is valid over the full, semi-infinite range (0, ∞) of the load-stiffness parameter β.

References

1 Föppl, A., *Vorlesungen über technische Mechanik*, Vol. 3, Teubner, Leipzig, 1905, pp. 298–299.

2 Schwerin, E., "Über Spannungen und Formänderungen kreisringförminger Membranen," *Zeit. f. Tech. Physik*, Vol. 12, 1929, pp. 651–659.

3 Jahsman, W. E., Field, F. A., and Holms, A. M. C., "Finite Deformations in a Prestressed, Centrally Loaded Circular Elastic Membrane," *Proc. 4th Nat. Cong. Appl. Mechs.*, Vol. 1, 1962, pp. 585–594.

4 Reissner, E., "On Finite Deflections of Circular Plates," *Proc. Symposia Appl. Math.*, Vol. 1, Am. Math. Soc., 1949, pp. 213–219.

5 Reissner, E., "On the Equations for Finite Symmetrical Deflections of Thin Shells of Revolution," *Progress in Applied Mechanics* (The Prager Anniversary Volume), Drucker, D. C., ed., MacMillian, New York, 1963, pp. 171–178.

6 Simmonds, J. G., "Closed-Form, Axisymmetric Solution of the von Karman Plate Equations for Poisson's Ratio One-Third," ASME JOURNAL OF APPLIED MECHANICS, Vol. 50, 1983, pp. 897–898.

7 Greenberg, M. D., *Foundations of Applied Mathematics*, Prentice-Hall, Englewood Cliffs, N.J., 1978, pp. 38–41.

8 Chien, W.-Z., and Yeh, K.-Y., "On the Large Deflection of Circular Plate," *Scientia Sinica*, Vol. 3, 1954, pp. 405–436.

9 Schmidt, R., "Large Deflections of a Clamped Circular Plate," *J. Eng. Mechs. Div., ASCE*, Vol. 94, 1968, pp. 1603–1606.

10 Schmidt, R., "Finite Deflections of a Loosely Clamped Circular Plate Loaded at its Center," *J. Indust. Math. Soc.*, Vol. 23, 1973, pp. 45–51.

11 Chia, C.-Y., *Nonlinear Analysis of Plates*, McGraw-Hill, New York, 1980, pp. 117–121.

12 Chen, S.-L., "Chien's Solution and Its Asymptotic Behavior in Large Deflection of Circular Plates," *Applied Mathematics and Mechanics* (transl. from Chinese), Vol. 3, 1982, pp. 557–562.

13 Watson, L. G., and Chudobiak, J. M., "Solution of von Karman Plate Equations With Perturbation and Series Summation," *Research in Structural and Solid Mechanics—1982*, NASA Conference Publication 2245, 1982, pp. 349–361.

14 Chien, W.-Z., "Asymptotic Behavior of a Thin Clamped Circular Plate Under Uniform Normal Pressure at Very Large Deflection," National Tsing Hua University Sci. Repts., Vol. 5, 1948, pp. 71–94.

15 Bromberg, E., "Nonlinear Bending of a Circular Plate Under Normal Pressure," *Comm. Pure Appl. Math.*, Vol. 9, 1956, pp. 633–659.

16 Keller, H. B., and Reiss, E. L., "Iterative Solutions for the Nonlinear Bending of Circular Plates," *Comm. Pure Appl. Math.*, Vol. 11, 1958, pp. 273–292.

17 Frakes, J. P., "Analytic-Numeric Solutions With the Aid of MACSYMA of the von Karman Equations for a Circular Plate Under a Concentrated Load," Master's thesis, University of Virginia, 1984.

Downloaded 02 May 2010 to 171.66.16.54. Redistribution subject to ASME license or copyright; see http://www.asme.org/terms/Terms_Use.cfm

A Mixture Theory for Wave Propagation in Angle-Ply Laminates

Part 1: Theory

H. Murakami
Assistant Professor,
Department of Applied Mechanics and Engineering Sciences,
University of California,
San Diego, Calif. 92093

In an effort to construct a continuum model with microstructure for elastic angle-ply laminates, an asymptotic mixture theory with multiple scales is presented in this two-part paper. The theory, which is in the form of a binary mixture, can simulate wave propagation in linearly elastic laminated composites with orthotropic lamina. Reissner's new variational principle has been adopted to avoid the numerous solution procedures of microstructure boundary value problems (MBVP's), which are required to find mixture properties in terms of the geometrical and material properties of the two constituents of the composite. For the special case of isotropic lamina the variational approach yields the same results as those derived by the asymptotic mixture theory with multiple scales [10] which requires the solution of the MBVP's. The advantage of the variational approach over the alternative is that it makes the application of the technique feasible to wave propagation in fiber-reinforced and particulate composites. The application of the mixture model to angle-ply laminates is deferred to the second part of the paper, which also contains a study of dispersion of time harmonic waves in angle-ply laminates.

1 Introduction

Many practical structural composites fall into the category of laminas. One of the most important examples of such materials is angle-ply laminate. Because of their extraordinary "shock-absorbing" capabilities, angle-ply laminates are frequently used in a dynamic load environment.

In an effort to clarify wave phenomena in anisotropic layered composites, Nemat-Nasser and Yamada [1] examined harmonic waves in layered, transversely isotropic composites. An efficient quotient method was proposed for furnishing approximate solutions to the phase velocity spectra. It has been observed that the effect of anisotropy becomes prominent for wave propagation in the direction of layering. For antiplane and plane strain motions, Shah and Datta [2] proposed a stiffness method to compute dispersion spectra in which equations were developed for both isotropic and anisotropic layers. It is noted that phase velocity data provide an accuracy measure for dispersive continuum models and therefore such data are of considerable importance.

In addition to phase-velocity spectra studies, a number of investigators have attempted to construct anisotropic continuum models of elastic layered composites. In an early study, Moon [3] proposed a continuum model based on the effective modulus concept [4, 5]. This formulation leads to a theory that is nondispersive and therefore somewhat limited. In a more recent study, an anisotropic continuum model for elastic-angle-ply laminates was proposed by Murakami and Hegemier [6] for waveguide-type problems. Although continuum models exist that can simulate wave propagation in arbitrary directions in the case of isotropic constituents [7–10], these models have not been extended to laminated composites with anisotropic constituents.

In this two-part paper [11], an asymptotic mixture theory of multiple scale [10] is applied to construct a continuum model for wave propagation in linearly elastic laminated composites with orthotropic laminas. The resulting model is applied to an angle-ply laminate of symmetric stacking sequence in Part 2 [11] in which the excellent accuracy of the model has been demonstrated by comparison of the dispersion spectra with the numerically obtained exact spectra.

In this paper, the asymptotic mixture theory with multiple scales [10] has been recast in a variational form. It is understood that the success of the asymptotic mixture theory comes from an appropriate displacement and stress microstructure that satisfies basic continuity conditions at the interface of two constituents, which is used for the model construction. Such microstructure is obtained by an asymptotic procedure that yields a series of microboundary value

Contributed by the Applied Mechanics Division for publication in the JOURNAL OF APPLIED MECHANICS.
Discussion on this paper should be addressed to the Editorial Department, ASME, United Engineering Center, 345 East 47th Street, New York, N.Y. 10017, and will be accepted until two months after final publication of the paper itself in the JOURNAL OF APPLIED MECHANICS. Manuscript received by ASME Applied Mechanics Division, February, 1984; final revision, August, 1984.

Copyright © 1985 by ASME
Downloaded 02 May 2010 to 171.66.16.54. Redistribution subject to ASME license or copyright; see http://www.asme.org/terms/Terms_Use.cfm

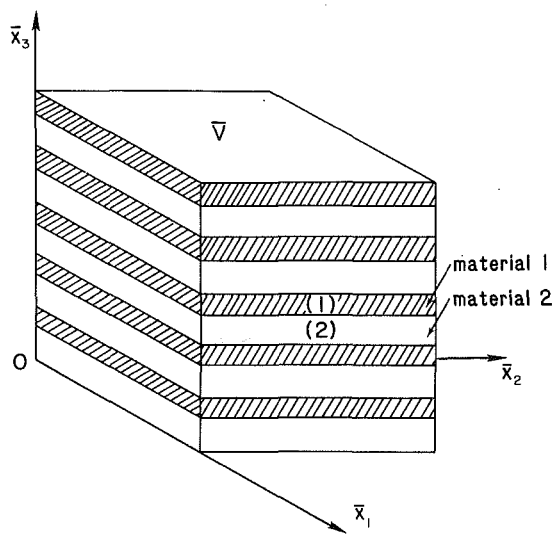


Fig. 1 A laminated composite and a coordinate system

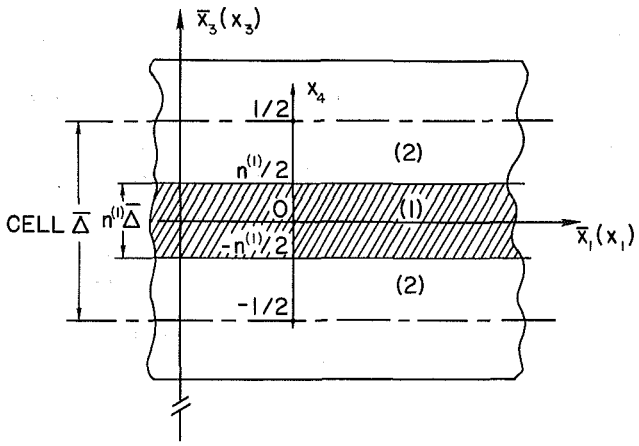


Fig. 2 A unit cell

problems (MBVP's) defined over a unit cell [10, 12, 13]. Thus, it is desirable to reduce the number of MBVP's that are to be solved to extract the information on the displacement and stress variation over a cell.

To this end, Reissner's variational principle derived for plates [14], which allows approximations for displacements and transverse stresses (but not for in-plane stresses), has been applied to cast the governing equations for a synthesized field by the multivariable representation [10] in a modified form of the principle of virtual work. Using the solutions of two MBVP's as trial displacements and transverse stresses, mixture equations have been derived. It has been proven that the results are *exactly* the same as the ones obtained by solving a series of MBVP's. The advantage of the variational approach over [10] is that it reduces the number of MBVP's to be solved significantly and makes the application of the technique feasible to composites with more complex microstructures. Furthermore, it has been confirmed that the variational approach allows the introduction of inelastic behavior by incremental constitutive relations [15].

2 Formulation

Consider a domain $\bar{V}$ that contains a large number of two alternating linearly elastic orthotropic laminas with perfect interface bonds as shown in Fig. 1. Let a rectangular Cartesian reference system $\bar{x}_1$, $\bar{x}_2$, $\bar{x}_3$ be selected with $\bar{x}_3$ normal to the middle plane of a lamina defined by $\bar{x}_1$ and $\bar{x}_2$. When the principal directions of orthotropy do not coincide with the coordinates $\bar{x}_1$ and $\bar{x}_2$, each lamina is monoclinic with respect to the $\bar{x}_3$-axis. A typical cell that represents the geometrical microstructure of the composite is shown in Fig. 2.

For notational convenience forms $(\ )^{(\alpha)}$, $\alpha = 1,2$ denote quantities associated with material α. Where appropriate, the usual Cartesian indicial notation will be employed in which Latin indices range from 1 to 3 and repeated indices imply the summation convention unless otherwise noted. In addition, the notations $(\ )_{,i} \equiv \partial(\ )/\partial\bar{x}_i$ and $(\dot{\ }) \equiv \partial(\ )/\partial\bar{t}$ will be employed where $\bar{t}$ represents time. Quantities of the form $(\bar{\ })$ and $(\ )$ denote dimensional and nondimensional variables, respectively.

With the aid of the foregoing notation, the governing relations for the displacement vector $\bar{u}_i^{(\alpha)}$ and the stress tensor $\bar{\sigma}_{ij}^{(\alpha)}$ in the two constituents are:

(a) Equations of Motion.

$$\bar{\sigma}_{ji,j}^{(\alpha)} = \bar{\rho}^{(\alpha)}\ddot{\bar{u}}^{(\alpha)}, \bar{\sigma}_{ji}^{(\alpha)} = \bar{\sigma}_{ij}^{(\alpha)} \tag{1}$$

where $\bar{\rho}^{(\alpha)}$ is the mass density;

(b) Constitutive Relations for Monoclinic Materials.

$$\begin{bmatrix} \bar{\sigma}_{11} \\ \bar{\sigma}_{22} \\ \bar{\sigma}_{33} \\ \bar{\sigma}_{23} \\ \sigma_{31} \\ \bar{\sigma}_{12} \end{bmatrix}^{(\alpha)} = \begin{bmatrix} \bar{C}_{11} & \bar{C}_{12} & \bar{C}_{13} & 0 & 0 & \bar{C}_{16} \\ \bar{C}_{12} & \bar{C}_{22} & \bar{C}_{23} & 0 & 0 & \bar{C}_{26} \\ \bar{C}_{13} & \bar{C}_{23} & \bar{C}_{33} & 0 & 0 & \bar{C}_{36} \\ 0 & 0 & 0 & \bar{C}_{44} & \bar{C}_{45} & 0 \\ 0 & 0 & 0 & \bar{C}_{45} & \bar{C}_{55} & 0 \\ \bar{C}_{16} & \bar{C}_{26} & \bar{C}_{36} & 0 & 0 & \bar{C}_{66} \end{bmatrix}^{(\alpha)} \begin{bmatrix} e_{11} \\ e_{22} \\ e_{33} \\ 2e_{23} \\ 2e_{31} \\ 2e_{12} \end{bmatrix}^{(\alpha)} \tag{2a}$$

or in abbreviated form

$$\bar{\boldsymbol{\sigma}}^{(\alpha)} = [\bar{C}]^{(\alpha)}\mathbf{e}^{(\alpha)}, \tag{2b}$$

where $\bar{C}_{\beta\gamma}^{(\alpha)}$ ($\beta, \gamma = 1$ to 6) are elastic moduli;

(c) Strain-Displacement Relations.

$$e_{ij}^{(\alpha)} = \frac{1}{2}(\bar{u}_{i,j}^{(\alpha)} + \bar{u}_{j,i}^{(\alpha)}); \tag{3}$$

(d) Interface Continuity Conditions.

$$\bar{u}_i^{(1)} = \bar{u}_i^{(2)}, \bar{\sigma}_{3i}^{(1)} = \bar{\sigma}_{3i}^{(2)} \quad \text{on interfaces;} \tag{4}$$

(e) Initial Conditions at $\bar{t} = 0$ and Appropriate Boundary Data Along the Boundary of $\bar{V}$. Conditions (*a*)–(*e*) define a well-posed initial boundary value problem. The direct solution to this problem is, however, extremely difficult due to the large number of interfaces in most cases of practical interest. The objective of the subsequent analysis is to alleviate such difficulties by deriving a set of partial differential equations with constant coefficients whose solution can be utilized to approximate the solution of the problem defined by (*a*)–(*e*). This effort is facilitated by a scaling of both dependent and independent variables. To this end the following quantities are introduced:

$\bar{\Lambda}$	typical macrosignal wavelength or macrodimension;
$\bar{\Delta}$	composite cell length;
$\bar{c}_{(m)}, \bar{\rho}_{(m)}$	reference wave velocity and macrodensity;
$\bar{E}_{(m)} = \bar{\rho}_{(m)}\bar{c}_{(m)}^2$	reference composite elastic modulus;
$\bar{t}_{(m)} = \bar{\Lambda}/\bar{c}_{(m)}$	typical macrosignal travel time;
$\epsilon = \bar{\Delta}/\bar{\Lambda}$	ratio of micro-to-macro dimensions.

With the aid of the foregoing notation, the following nondimensional quantities are now defined:

Downloaded 02 May 2010 to 171.66.16.54. Redistribution subject to ASME license or copyright; see http://www.asme.org/terms/Terms_Use.cfm

$$(x_1, x_2, x_3) = (\bar{x}_1, \bar{x}_2, \bar{x}_3)/\bar{\Lambda}, t = \bar{t}/\bar{t}_{(m)},$$
$$u_i^{(\alpha)} = \bar{u}_i^{(\alpha)}/\bar{\Lambda},\ \sigma_{ij}^{(\alpha)} = \bar{\sigma}_{ij}^{(\alpha)}/\bar{E}_{(m)}, i,j = 1-3, \tag{5}$$
$$\rho^{(\alpha)} = \bar{\rho}^{(\alpha)}/\bar{\rho}_{(m)}, C_{\beta\gamma}^{(\alpha)} = \bar{C}_{\beta\gamma}^{(\alpha)}/\bar{E}_{(m)}, \beta,\gamma = 1-6.$$

With the variables defined accoridng to (5), the material properties are seen to be periodic in the x_3-direction with period ϵ. Thus, the field variables are expected to vary significantly over two length scales along the x_3-direction. One such scale is of the order of the signal wavelength, which is unity in the scaled system. The other length scale is of the order of the cell dimension $\epsilon(<<1)$. This suggests a two-variable expansion procedure [16, 17]. Therefore, all field variables are considered to be functions of the micro-variable $x_4 = x_3/\epsilon$ as well as the macrovariable x_i, $i = 1-3$:

$$f(x_1, x_2, x_3, t; \epsilon) = f^*(x_1, x_2, x_3, x_4, t; \epsilon) \tag{6a}$$

For any field variable (6*a*) one obtains

$$\frac{\partial}{\partial x_3} f(x_1, x_2, x_3, t; \epsilon) = \frac{\partial}{\partial x_3} f^*(x_1, x_2, x_3, x_4, t; \epsilon)$$
$$+ \frac{1}{\epsilon} \frac{\partial}{\partial x_4} f^*(x_1, x_2, x_3, x_4, t; \epsilon) \tag{6b}$$

In the sequel f^* will be replaced by f for notational simplicity. When written in terms of x_i, x_4 and in nondimensional form, equations (1)–(4) are rewritten as:

$$\sigma_{ji,j}^{(\alpha)} + \frac{1}{\epsilon} \sigma_{3i,4}^{(\alpha)} = \rho^{(\alpha)} \ddot{u}_i^{(\alpha)}, \sigma_{ji}^{(\alpha)} = \sigma_{ij}^{(\alpha)}, \tag{7}$$

$$\boldsymbol{\sigma}^{(\alpha)} = [C]^{(\alpha)} \mathbf{e}^{(\alpha)} \tag{8a}$$

in which

$$e_{ij}^{(\alpha)} = \frac{1}{2}(u_{i,j}^{(\alpha)} + u_{j,i}^{(\alpha)}) + \frac{1}{2\epsilon}(\delta_{i3} u_{j,4}^{(\alpha)} + \delta_{j3} u_{i,4}^{(\alpha)}) \tag{8b}$$

and δ_{ij} is the usual Kronecker delta;

$$u_i^{(1)} = u_i^{(2)}, \sigma_{3i}^{(1)} = \sigma_{3i}^{(2)} \qquad \text{on interfaces.} \tag{9}$$

Equations (7)–(9) can be viewed as a set of partial differential equations in x_i, x_4, and t, in which the coefficients are independent of x_i, t but are functions of x_4 with a unit period. If the domain of definition was $-\infty < \bar{x}_3 < \infty$, which corresponds to $\epsilon \to 0$, and if the initial data was quiescent or periodic in x_4, it would follow from the Floquet theory [18, 19] that there exists a set of solution of (7)–(9) which are periodic in x_4 with unit length. This periodicity condition is expected to persist at least in the interior of the domain in which the solution is sought, as long as the length of the domain in the x_3-direction is sufficiently large. Consequently, equations (7)–(9) will be analyzed under the premise that all field variables are periodic in the microcoordinate x_4 with the understanding that such an analysis may not be accurate at the boundary domain where a boundary layer solution should be sought for some kinds of boundary conditions.

As a result of the assumed periodicity condition on the microscale, it is necessary to treat only a typical unit cell associated with the x_3-direction. With no loss in generality, it will be convenient to define the cell (see Fig. 2) by

$$A^{(1)} = [x_4 \mid |x_4| < n^{(1)}/2], \quad A^{(2)} = \left[x_4 \mid n^{(1)}/2 < |x_4| < \frac{1}{2}\right]. \tag{10}$$

In (10), $A^{(\alpha)}$ denotes the domain occupied by material α in the cell and $n^{(\alpha)}$ is the volume fraction that satisfies

$$n^{(1)} + n^{(2)} = 1. \tag{11}$$

With the preceding choice of the unit cell, the interface conditions (9) must be satisfied at $|x_4| = n^{(1)}/2$ and the periodicity conditions is given by

$$f_i(x_k, -1/2, t; \epsilon) = f_i(x_k, 1/2, t; \epsilon) \tag{12}$$

where f represents any field variable.

The key elements introduced are: (*a*) the multivariable representation of all field variables (6); and (*b*) the periodicity of all field variables in the microcoordinate x_4.

3 Mixture Equations

Binary mixture equations for the composite can be immediately obtained by introducing an average operation according to

$$f^{(\alpha a)}(x_i, t; \epsilon) \equiv \frac{1}{n^{(\alpha)}} \int_{A^{(\alpha)}} f^{(\alpha)}(x_i, x_4, t; \epsilon) dx_4. \tag{13}$$

Upon averaging (7) with use of the periodicity condition for $\sigma_{3i}^{(2)}$, one obtains the momentum equations

$$\sigma_{ji,j}^{(\alpha p)} + (-1)^{\alpha+1} P_i = \rho^{(\alpha p)} \ddot{u}_i^{(\alpha a)} \tag{14}$$

where P_i denotes the components of an interaction body force vector per unit volume, given by

$$P_i \equiv \frac{1}{\epsilon} \left\{ \sigma_{3i}^{(\alpha)} \mid_{x_4 = n^{(1)}/2} - \sigma_{3i}^{(\alpha)} \mid_{x_4 = -n^{(1)}/2} \right\}. \tag{15}$$

In (14), the definitions for "partial" quantities:

$$\sigma_{ij}^{(\alpha p)} \equiv n^{(\alpha)} \sigma_{ij}^{(\alpha a)}, \rho^{(\alpha p)} \equiv n^{(\alpha)} \rho^{(\alpha)} \tag{16}$$

have been used.

The momentum equations (14) are complemented by mixture constitutive equations obtained by averaging (8) and applying the periodicity condition. This yields

$$\begin{bmatrix} \sigma_{11} \\ \sigma_{22} \\ \sigma_{33} \\ \sigma_{23} \\ \sigma_{31} \\ \sigma_{12} \end{bmatrix}^{(\alpha p)} = n^{(\alpha)} \begin{bmatrix} C_{11} & C_{12} & C_{13} & 0 & 0 & C_{16} \\ C_{12} & C_{22} & C_{23} & 0 & 0 & C_{26} \\ C_{13} & C_{23} & C_{33} & 0 & 0 & C_{36} \\ 0 & 0 & 0 & C_{44} & C_{45} & 0 \\ 0 & 0 & 0 & C_{45} & C_{55} & 0 \\ C_{16} & C_{26} & C_{36} & 0 & 0 & C_{66} \end{bmatrix}^{(\alpha)}$$
$$\begin{bmatrix} u_{1,1} \\ u_{2,2} \\ u_{3,3} \\ u_{2,3} + u_{3,2} \\ u_{3,1} + u_{1,3} \\ u_{1,2} + u_{2,1} \end{bmatrix}^{(\alpha a)} + (-1)^{\alpha+1} \begin{bmatrix} 0 & 0 & C_{13} \\ 0 & 0 & C_{23} \\ 0 & 0 & C_{33} \\ C_{45} & C_{44} & 0 \\ C_{55} & C_{45} & 0 \\ 0 & 0 & C_{36} \end{bmatrix}^{(\alpha)} \begin{bmatrix} \overset{3}{S}_1 \\ \overset{3}{S}_2 \\ \overset{3}{S}_3 \end{bmatrix} \tag{17}$$

where

$$\overset{3}{S}_i \equiv \frac{1}{\epsilon} \left\{ u_i^{(\alpha)} \mid_{x_4 = n^{(1)}/2} - u_i^{(\alpha)} \mid_{x_4 = -n^{(1)}/2} \right\}. \tag{18}$$

The new displacement variable $\overset{3}{S}_i(x_k, t)$ designates director displacement associated with the discrete microstructure oriented along the x_3-axis. To "close" the mixture relations, it is necessary to construct: (*a*) appropriate conservation equations associated with the director; and (*b*) constitutive equations for P_i and stress-type quantities associated with the director displacements. To this end, an asymptotic procedure may be useful to extract vital information on the variation of field variables over the cell [6, 10, 13].

4 Asymptotic Analysis

The premise that the composite macrodimension is much larger than the microdimension, $\epsilon << 1$, and the form of scaled equations (7) and (8) suggest the expansion of the dependent variables in the asymptotic series:

Downloaded 02 May 2010 to 171.66.16.54. Redistribution subject to ASME license or copyright; see http://www.asme.org/terms/Terms_Use.cfm

$$\{u_i,\sigma_{ij}\}^{(\alpha)}(x_k,x_4,t;\epsilon)=\sum_{n=0}^{\infty}\epsilon^n\{u_{i(n)},\sigma_{ij(n)}\}^{(\alpha)}(x_k,x_4,t). \tag{19}$$

If (19) is substituted into (7) and (8) and the coefficients of different powers of ϵ are equated to zero, a sequence of problems is obtained. The first of the equations in this sequence furnishes

$$\sigma^{(\alpha)}_{3i(0),4}=u^{(\alpha)}_{i(0),4}=0. \tag{20}$$

Thus, the quantities $\sigma^{(\alpha)}_{3i(0)}$ and $u_i{}^{(\alpha)}_{(0)}$ are independent of the microcoordinate x_4, i.e.,

$$\{u_i,\sigma_{ij}\}^{(\alpha)}_{(0)}=\{u_i,\sigma_{ij}\}_{(0)}(x_k,t) \tag{21}$$

where the zeroth-order expansions of the interface condition (9) have been utilized. The remaining system of equations obtained from (7), (8), and (19) are

$$\sigma^{(\alpha)}_{ji(n),j}+\sigma^{(\alpha)}_{3i(n+1),4}=\rho^{(\alpha)}\ddot{u}_i{}^{(\alpha)}_{(n)},\sigma^{(\alpha)}_{ji(n)}=\sigma^{(\alpha)}_{ij(n)}, \tag{22}$$

$$\sigma^{(\alpha)}_{(n)}=[C]^{(\alpha)}\mathbf{e}^{(\alpha)}_{(n)} \tag{23a}$$

where

$$\mathbf{e}^{(\alpha)}_{(n)}=[u_{1(n),1},u_{2(n),2},u_{3(n),3}+u_{3(n+1),4},u_{2(n),3}+u_{3(n),2}+u_{2(n+1),4},$$
$$u_{3(n),1}+u_{1(n),3}+u_{1(n+1),4},u_{1(n),2}+u_{2(n),1}]^T \tag{23b}$$

Because of (21), the higher-order terms in (19) must satisfy a normalization condition; a convenient choice is

$$u^{(1)}_{i(n)}=\sigma^{(1)}_{3i(n)}=0 \quad \text{at} \quad x_4=0,n\geq 1. \tag{24}$$

From (21)–(23) one concludes that, for $n\geq 1$,

$u^{(\alpha)}_{i(2n)}$ and $\sigma^{(\alpha)}_{3i(2n)}$ are even functions of x_4, (25a)

$u^{(\alpha)}_{i(2n-1)}$ and $\sigma^{(\alpha)}_{3i(2n-1)}$ are odd functions of x_4. (25b)

In view of (25) and the periodicity condition (12), one also obtains

$$u_i{}^{(2)}_{(2n-1)}=\sigma^{(2)}_{3i(2n-1)}=0 \quad \text{on} \quad x_4=\pm 1/2,n\geq 1. \tag{26}$$

To be added to the foregoing are the interface condition of displacement and traction vectors (9):

$$u_i{}^{(1)}_{(n)}=u_i{}^{(2)}_{(n)},\sigma^{(1)}_{3i(n)}=\sigma^{(2)}_{3i(n)} \quad \text{on} \quad x_4=\pm n^{(1)}/2. \tag{27}$$

As demonstrated by Murakami, Maewal, and Hegemier [10], it is possible to close the theory by solving a series of microboundary value problems (MBVP's) defined over the cell. However, the drawback of the asymptotic method with MBVP's is that the number MBVP's to be solved is quite large.

To overcome these difficulties, an alternative procedure is adopted in the sequel which utilizes the modified principle of virtual work which has (7) as one of the Euler-Lagrange equations. The procedure requires a trial displacement field over the cell. This microstructural information on displacements and some stresses is extracted by solving only a couple of simple MBVP's. In the sequel, the new Reissner variational principle [14] will be used which allows the approximation of displacements $u_i{}^{(\alpha)}$ and transverse stresses $\sigma^{(\alpha)}_{3i}$. To obtain the lowest order mixture theory it is necessary to obtain the microstructure of displacements and transverse stresses to $O(\epsilon)$. Since the $O(1)$ terms are known by (21), it is only necessary to find the microstructure of $u_i{}^{(\alpha)}_{(1)}$ and $\sigma^{(\alpha)}_{3i(1)}$ by the asymptotic procedure.

5 First-Order Displacements and Transverse Stresses

Equations (21) and (23) for $n=0$ furnish

$$u^{(\alpha)}_{i(1),4}=B_i{}^{(\alpha)}(x_k,t). \tag{28}$$

The function $B_i{}^{(\alpha)}$ is related to the director displacement if $u_i{}^{(\alpha)}$ is represented in (18) by terms up to and including $O(\epsilon^2)$, in (19) with the result

$$u^{(\alpha)}_{i(1)}=\overset{3}{S}_i(x_k,t)g^{(\alpha)}(x_4) \tag{29}$$

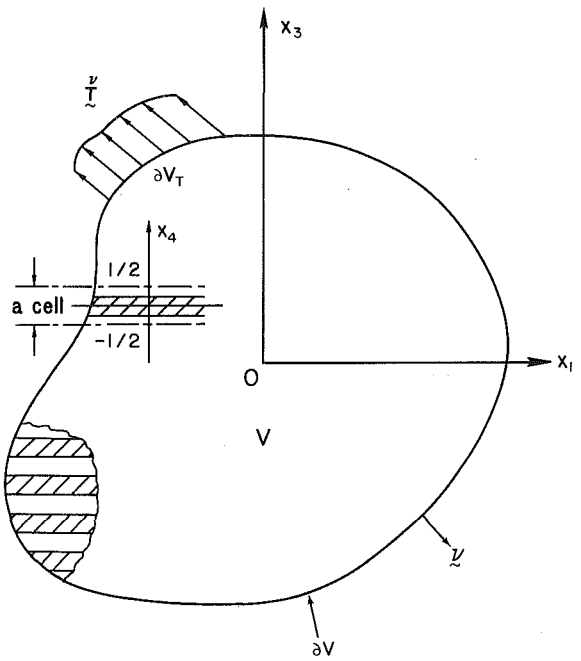


Fig. 3 A mixture continuum that represents the laminated composite

where

$$g^{(1)}(x_4)=x_4/n^{(1)},g^{(2)}(x_4)=\left(\frac{1}{2}sgnx_4-x_4\right)/n^{(2)} \tag{30}$$

in which $sgn(x_4)$ implies the algebraic sign of x_4. Equations (24)–(26) have been used in the derivation of (28) and (29).

Equation (22) for $n=0$, together with (21), yields

$$\sigma^{(\alpha)}_{3i(1),4}=D_i{}^{(\alpha)}(x_k,t). \tag{31}$$

If (31) is now integrated over $A^{(\alpha)}$ and use is made of (15), (19), (25), and (26), one obtains

$$D_i{}^{(\alpha)}(x_k,t)=(-1)^{\alpha+1}P_i/n^{(\alpha)}. \tag{32}$$

Whence

$$\sigma^{(\alpha)}_{3i(1),4}=(-1)^{\alpha+1}P_i/n^{(\alpha)}. \tag{33}$$

Instead of introducing MBVP's for $u^{(\alpha)}_{i(2)}$ as [10], equation (36) is integrated with (26b) for $n=1$. Thus, one obtains

$$\sigma^{(\alpha)}_{3i(1)}=P_ig^{(\alpha)}(x_4). \tag{34}$$

Equations (21), (29), and (34) supply vital information on the microstructure of displacements and transverse stresses up to $O(\epsilon)$ terms. Anticipating the $O(\epsilon^2)$ differences of $u_i{}^{(\alpha)}$ and $\sigma^{(\alpha)}_{3i}$ one may select the following trial functions:

$$u_i{}^{(\alpha)}(x_k,x_4,t;\epsilon)=U_i{}^{(\alpha)}(x_k,t)+\epsilon\overset{3}{S}_i(x_k,t)g^{(\alpha)}(x_4), \tag{35a}$$

$$\sigma^{(\alpha)}_{3i}(x_k,x_4,t;\epsilon)=\tau^{(\alpha)}_{3i}(x_k,t)+\epsilon P_i(x_k,t)g^{(\alpha)}(x_4). \tag{35b}$$

6 The Modified Principle of Virtual Work

Using the equations of motion (7), Gauss' theorem, the periodicity condition (12), and the continuity of traction vectors across interfaces (9b), it can be demonstrated that the principle of virtual work for the synthesized fields by the multivariable representation takes the form:

$$\iiint_V\left\{\sum_{\alpha=1}^{2}\int_{A^{(\alpha)}}\sigma^{(\alpha)}_{ij}\delta e^{(\alpha)}_{ij}dx_4\right\}dx_1dx_2dx_3$$
$$=\iiint_V\left\{\sum_{\alpha=1}^{2}\int_{A^{(\alpha)}}(-\rho^{(\alpha)}\ddot{u}_i{}^{(\alpha)})\delta u_i{}^{(\alpha)}dx_4\right\}dx_1dx_2dx_3$$
$$+\iint_{\partial V_T}\left\{\sum_{\alpha=1}^{2}\int_{A^{(\alpha)}}\overset{V}{T}_i{}^{(\alpha)}\delta u_i{}^{(\alpha)}dx_4\right\}dA \tag{36}$$

Downloaded 02 May 2010 to 171.66.16.54. Redistribution subject to ASME license or copyright; see http://www.asme.org/terms/Terms_Use.cfm

in which $\delta u_i^{(\alpha)}$ is a virtual displacement and $e_{ij}^{(\alpha)}$ is defined by (8*b*). With reference to Fig. 3, $\overset{p}{T}_i^{(\alpha)}$ denotes the traction vector on the surface ∂V_T where the traction is specified, and dA is an infinitesimal surface element on the boundary of $V: \partial V$. In (36) the integrations with respect to the microcoordinate are carried out only over the typical cell. The integration with respect to the macrocoordinates are carried out over the entire domain V, occupied by the composite.

Equation (36) is modified to allow the variation of transverse stresses and allow discontinuous displacements based on the new Reissners' variational principle [14] as follows:

$$\iiint_V \Bigg[\sum_{\alpha=1}^{2} \int_{A^{(\alpha)}} \delta e_{11}^{(\alpha)} \sigma_{11}^{(\alpha)} + \delta e_{22}^{(\alpha)} \sigma_{22}^{(\alpha)} + 2\delta e_{12}^{(\alpha)} \sigma_{12}^{(\alpha)} + \delta e_{33}^{(\alpha)} \sigma_{33}^{(\alpha)} + 2\delta e_{23}^{(\alpha)} \sigma_{23}^{(\alpha)} + 2\delta e_{31}^{(\alpha)} \sigma_{31}^{(\alpha)} + \delta\sigma_{33}^{(\alpha)} \left(u_{3,3}^{(\alpha)} + \frac{1}{\epsilon} u_{3,4}^{(\alpha)} - e_{33}^{(\alpha)}(\ldots) \right) + \delta\sigma_{23}^{(\alpha)} \left(u_{2,3}^{(\alpha)} + u_{3,2}^{(\alpha)} + \frac{1}{\epsilon} u_{2,4}^{(\alpha)} - 2e_{23}^{(\alpha)}(\ldots) \right) + \delta\sigma_{31}^{(\alpha)} \left(u_{3,1}^{(\alpha)} + u_{1,3}^{(\alpha)} + \frac{1}{\epsilon} u_{1,4}^{(\alpha)} - 2e_{31}^{(\alpha)}(\ldots) \right) \Bigg\} dx_4 + P_i(\delta U_i^{(2)} - \delta U_i^{(1)}) + \delta P_i (U_i^{(2)} - U_i^{(1)}) \Bigg] dx_1 dx_2 dx_3$$

$$= \iiint_V \Bigg\{ \sum_{\alpha=1}^{2} \int_{A^{(\alpha)}} (-\rho^{(\alpha)} \ddot{u}_i^{(\alpha)}) \delta u_i^{(\alpha)} dx_4 \Bigg\} dx_1 dx_2 dx_3 + \iint_{\partial V_T} \left(\sum_{\alpha=1}^{2} \int_{A^{(\alpha)}} \overset{p}{T}_i^{(\alpha)} \delta u_i^{(\alpha)} dx_4 \right) dA \tag{37}$$

where

$$2e_{ij}^{(\alpha)} = U_{i,j}^{(\alpha)} + \epsilon(\overset{3}{S}_{i,j} + \overset{3}{S}_{j,i}) g^{(\alpha)}(x_4),$$

$$2\delta e_{i,j} \equiv \delta U_{i,j}^{(\alpha)} + \delta U_{i,j}^{(\alpha)} + \epsilon(\delta \overset{3}{S}_{i,j} + \delta \overset{3}{S}_{j,i}) g^{(\alpha)}(x_4), \quad i,j = 1,2 \tag{38}$$

$$e_{33}^{(\alpha)}(\ldots) \equiv \sigma_{33}^{(\alpha)} / C_{33}^{(\alpha)} - \{ (C_{13}/C_{33})^{(\alpha)} e_{11}^{(\alpha)} + (C_{23}/C_{33})^{(\alpha)} e_{22}^{(\alpha)} + (C_{36}/C_{33})^{(\alpha)} 2e_{12}^{(\alpha)} \},$$

$$\delta e_{33}^{(\alpha)} \equiv \delta U_{3,3}^{(\alpha)} + (-1)^{\alpha+1} \delta \overset{3}{S}_3 / n^{(\alpha)} + \epsilon \delta \overset{3}{S}_{3,3} g^{(\alpha)}(x_4),$$

$$\begin{bmatrix} 2e_{23} \\ 2e_{31} \end{bmatrix}^{(\alpha)} \equiv \begin{bmatrix} C_{44} & C_{45} \\ C_{45} & C_{55} \end{bmatrix}^{(\alpha)-1} \begin{bmatrix} \sigma_{23} \\ \sigma_{31} \end{bmatrix}^{(\alpha)} = \begin{bmatrix} \tilde{C}_{55} & -\tilde{C}_{45} \\ -\tilde{C}_{45} & \tilde{C}_{44} \end{bmatrix}^{(\alpha)} \begin{bmatrix} \sigma_{23} \\ \sigma_{31} \end{bmatrix}^{(\alpha)},$$

$$2\delta e_{i,3}^{(\alpha)} \equiv \delta U_{i,3}^{(\alpha)} + \delta U_{3,i}^{(\alpha)} + (-1)^{\alpha+1} \delta \overset{3}{S}_i / n^{(\alpha)} + \epsilon(\delta \overset{3}{S}_{i,3} + \delta \overset{3}{S}_{3,i}) g^{(\alpha)}(x_4), i = 1,2 \tag{39}$$

$$\delta u_i^{(\alpha)} = \delta U_i^{(\alpha)} + \epsilon \delta \overset{3}{S}_i g^{(\alpha)}(x_4),$$

$$\ddot{u}_i^{(\alpha)} = \ddot{U}_i^{(\alpha)} + \epsilon \ddot{\overset{3}{S}}_i g^{(\alpha)}(x_4), \tag{40}$$

$$\sigma_{31}^{(\alpha)} = \tau_{3i}^{(\alpha)} + \epsilon P_i g^{(\alpha)}(x_4), \delta\sigma_{3i}^{(\alpha)} = \delta\tau_{3i}^{(\alpha)} + \epsilon \delta P_i g^{(\alpha)}(x_4). \tag{41}$$

In (37) basic variables are the displacements $u_i^{(\alpha)}$ and transverse stresses $\sigma_{3i}^{(\alpha)}$. Transverse strains $e_{3i}^{(\alpha)}$ are to be computed in terms of transverse stresses $\sigma_{3i}^{(\alpha)}$ and in-plane strains $e_{ij}^{(\alpha)}$, $i,j = 1,2$ which are defined by (38).

Substituting (38)–(41) into (37) one obtains

$$\iint_{\partial V_T} \Bigg\{ \sum_{\alpha=1}^{2} \delta U_i^{(\alpha)} (\sigma_{ji}^{(\alpha p)} \nu_j - \overset{p}{T}_i^{(\alpha p)}) + \epsilon^2 \delta \overset{3}{S}_i (\overset{3}{M}_{ji} \nu_j - \overset{3p}{T}_i) \Bigg\} dA$$

$$- \iiint_V \Bigg\{ \sum_{\alpha=1} \Big[\delta U_i^{(\alpha)} (\sigma_{ji,j}^{(\alpha p)} + (-1)^{\alpha+1} P_i - \rho^{(\alpha p)} \ddot{U}_i^{(\alpha)}) + n^{(\alpha)} \delta\tau_{33}^{(\alpha)} \Big\{ U_{3,3}^{(\alpha)} + (-1)^{\alpha+1} \overset{3}{S}_3 / n^{(\alpha)} - \tau_{33}^{(\alpha)} / C_{33}^{(\alpha)} + (C_{13}/C_{33})^{(\alpha)} U_{1,1}^{(\alpha)} + (C_{23}/C_{33})^{(\alpha)} U_{2,2}^{(\alpha)} + (C_{36}/C_{33})^{(\alpha)} (U_{1,2}^{(\alpha)} + U_{2,1}^{(\alpha)}) \Big\}$$

$$+ n^{(\alpha)} \delta\tau_{23}^{(\alpha)} \Big\{ U_{2,3}^{(\alpha)} + U_{3,2}^{(\alpha)} + (-1)^{\alpha+1} \overset{3}{S}_2 / n^{(\alpha)} - \tilde{C}_{55}^{(\alpha)} \tau_{23}^{(\alpha)} + \tilde{C}_{45}^{(\alpha)} \tau_{31}^{(\alpha)} \Big\}$$

$$+ n^{(\alpha)} \delta\tau_{31}^{(\alpha)} \Big\{ U_{3,1}^{(\alpha)} + U_{1,3}^{(\alpha)} + (-1)^{\alpha+1} \overset{3}{S}_1 / n^{(\alpha)} + \tilde{C}_{45}^{(\alpha)} \tau_{23}^{(\alpha)} - \tilde{C}_{44}^{(\alpha)} \tau_{31}^{(\alpha)} \Big\} \Big]$$

$$+ \epsilon^2 \delta \overset{3}{S}_i \Big\{ \overset{3}{M}_{ji,j} + (\tau_{3i}^{(2)} - \tau_{3i}^{(1)})/\epsilon^2 - \overset{3}{I} \ddot{\overset{3}{S}}_i \Big\}$$

$$+ \epsilon^2 \delta P_3 / 12 \Big\{ 12(U_3^{(2)} - U_3^{(1)})/\epsilon^2 + \overset{3}{S}_{3,3} - \sum_\alpha (n^{(\alpha)}/C_{33}^{(\alpha)}) P_3 + \sum_\alpha (n^{(\alpha)} C_{13}^{(\alpha)}/C_{33}^{(\alpha)}) \overset{3}{S}_{1,1} + \sum_\alpha (n^{(\alpha)} C_{23}^{(\alpha)}/C_{33}^{(\alpha)}) \overset{3}{S}_{2,2} + \sum_\alpha (n^{(\alpha)} C_{36}^{(\alpha)}/C_{33}^{(\alpha)}) (\overset{3}{S}_{1,2} + \overset{3}{S}_{2,1}) \Big\}$$

$$+ \epsilon^2 \delta P_2 / 12 \Big\{ 12(U_2^{(2)} - U_2^{(1)})/\epsilon^2 + (\overset{3}{S}_{2,3} + \overset{3}{S}_{3,2}) - \sum_\alpha (n^{(\alpha)} \tilde{C}_{55}^{(\alpha)}) P_2 + \sum_\alpha (n^{(\alpha)} \tilde{C}_{45}^{(\alpha)}) P_1 \Big\}$$

$$+ \epsilon^2 \delta P_1 / 12 \Big\{ 12(U_1^{(2)} - U_1^{(1)})/\epsilon^2 + (\overset{3}{S}_{3,1} + \overset{3}{S}_{1,3}) + \sum_\alpha (n^{(\alpha)} \tilde{C}_{45}^{(\alpha)}) P_2 - \sum_\alpha (n^{(\alpha)} \tilde{C}_{44}^{(\alpha)}) P_1 \Big\} \Bigg\} dx_1 dx_2 dx_3 = 0 \tag{42}$$

where

$$\sigma_{ij}^{(\alpha p)} \equiv \int_{A^{(\alpha)}} \sigma_{ij}^{(\alpha)} dx_4, i,j = 1,2,$$

$$\sigma_{3i}^{(\alpha p)} \equiv n^{(\alpha)} \tau_{3i}^{(\alpha)} \quad i = 1,2,3, \tag{43}$$

$$\epsilon \overset{3}{M}_{ij} \equiv \sum_{\alpha=1}^{2} \int_{A^{(\alpha)}} \sigma_{ij}^{(\alpha)} g^{(\alpha)}(x_4) dx_4, i,j = 1,2,$$

$$\overset{3}{M}_{3i} = P_i / 12, \tag{44}$$

Downloaded 02 May 2010 to 171.66.16.54. Redistribution subject to ASME license or copyright; see http://www.asme.org/terms/Terms_Use.cfm

$$\overset{p}{T}{}_i^{(\alpha p)} \equiv \int_{A^{(\alpha)}} \overset{p}{T}{}_i^{(\alpha)} dx_4, \epsilon^{3p}\overset{3}{T}_i \equiv \sum_{\alpha=1}^{2} \int_{A^{(\alpha)}} \overset{p}{T}{}_i^{(\alpha)} g^{(\alpha)}(x_4) dx_4, \tag{45}$$

$$\overset{3}{I} \equiv \sum_{\alpha=1}^{2} \int_{A^{(\alpha)}} \rho^{(\alpha)} g^{(\alpha)2}(x_4) dx_4 = \frac{1}{12} \sum_{\alpha} n^{(\alpha)} \rho^{(\alpha)} = \frac{1}{12} \rho_{(m)}. \tag{46}$$

The Euler-Lagrange equations of (42) are, in V

$$\sigma_{ji,j}^{(\alpha p)} + (-1)^{\alpha+1} P_i = \rho^{(\alpha p)} \ddot{U}_i^{(\alpha)}, \tag{47}$$

$$\overset{3}{M}_{ji,j} + (\tau_{3i}^{(2)} - \tau_{3i}^{(1)})/\epsilon^2 = \overset{3}{I}\ddot{\overset{3}{S}}_i, \tag{48}$$

$$\sigma_{33}^{(\alpha p)} = n^{(\alpha)} \tau_{33}^{(\alpha)} = C_{33}^{(\alpha)} \left\{ n^{(\alpha)} U_{3,3}^{(\alpha)} + (-1)^{\alpha+1} \overset{3}{S}_3 \right\}$$
$$+ n^{(\alpha)} C_{13}^{(\alpha)} U_{1,1}^{(\alpha)} + n^{(\alpha)} C_{23}^{(\alpha)} U_{2,2}^{(\alpha)}$$
$$+ n^{(\alpha)} C_{36}^{(\alpha)} (U_{1,2}^{(\alpha)} + U_{2,1}^{(\alpha)}), \tag{49a}$$

$$\begin{bmatrix} \sigma_{23} \\ \sigma_{31} \end{bmatrix}^{(\alpha p)} = n^{(\alpha)} \begin{bmatrix} \tau_{23} \\ \tau_{31} \end{bmatrix}^{(\alpha)} = \begin{bmatrix} C_{44} & C_{45} \\ C_{45} & C_{55} \end{bmatrix}^{(\alpha)}$$
$$\begin{bmatrix} n^{(\alpha)}(U_{2,3}^{(\alpha)} + U_{3,2}^{(\alpha)}) + (-1)^{\alpha+1} \overset{3}{S}_2 \\ n^{(\alpha)}(U_{3,1}^{(\alpha)} + U_{1,3}^{(\alpha)}) + (-1)^{\alpha+1} \overset{3}{S}_1 \end{bmatrix}, \tag{49b}$$

$$P_3 = C_{33(n)} \left\{ 12(U_3^{(2)} - U_3^{(1)})/\epsilon^2 + \overset{3}{S}_{3,3} + \sum_{\alpha} (n^{(\alpha)} C_{13}^{(\alpha)}/C_{33}^{(\alpha)}) \overset{3}{S}_{1,1} \right.$$
$$\left. + \sum_{\alpha} (n^{(\alpha)} C_{23}^{(\alpha)}/C_{33}^{(\alpha)}) \overset{3}{S}_{2,2} + \sum_{\alpha} (n^{(\alpha)} C_{36}^{(\alpha)}/C_{33}^{(\alpha)})(\overset{3}{S}_{1,2} + \overset{3}{S}_{2,1}) \right\},$$

$$\begin{bmatrix} \sum_{\alpha} n^{(\alpha)} \tilde{C}_{44}^{(\alpha)} & -\sum_{\alpha} n^{(\alpha)} \tilde{C}_{45}^{(\alpha)} \\ -\sum_{\alpha} n^{(\alpha)} \tilde{C}_{45}^{(\alpha)} & \sum_{\alpha} n^{(\alpha)} \tilde{C}_{55}^{(\alpha)} \end{bmatrix} \begin{bmatrix} P_1 \\ P_2 \end{bmatrix} \tag{50a}$$

$$= \begin{bmatrix} 12(U_1^{(2)} - U_1^{(1)})/\epsilon^2 + (\overset{3}{S}_{3,1} + \overset{3}{S}_{1,3}) \\ 12(U_2^{(2)} - U_2^{(1)})/\epsilon^2 + (\overset{3}{S}_{2,3} + \overset{3}{S}_{3,2}) \end{bmatrix} \tag{50b}$$

where

$$C_{33(n)} = 1/\left(\sum_{\alpha} n^{(\alpha)}/C_{33}^{(\alpha)} \right). \tag{51}$$

The remaining constitutive relations are computed from

$$\begin{bmatrix} \sigma_{11} \\ \sigma_{22} \\ \sigma_{12} \end{bmatrix}^{(\alpha)} = \begin{bmatrix} C_{11} & C_{12} & C_{13} & C_{16} \\ C_{12} & C_{22} & C_{23} & C_{26} \\ C_{16} & C_{26} & C_{36} & C_{66} \end{bmatrix}^{(\alpha)}$$
$$\begin{bmatrix} e_{11} \\ e_{22} \\ e_{33}(\ldots) \\ 2e_{12} \end{bmatrix}^{(\alpha)}. \tag{52}$$

By substituting (38) and (39) into (43) and (44) one obtains

$$\begin{bmatrix} \sigma_{11} \\ \sigma_{22} \\ \sigma_{12} \end{bmatrix}^{(\alpha p)} = n^{(\alpha)} \begin{bmatrix} C_{11} & C_{12} & C_{13} & C_{16} \\ C_{12} & C_{22} & C_{23} & C_{26} \\ C_{16} & C_{26} & C_{36} & C_{66} \end{bmatrix}^{(\alpha)}$$
$$\begin{bmatrix} U_{1,1} \\ U_{2,2} \\ U_{3,3} \\ U_{1,2} + U_{2,1} \end{bmatrix}^{(\alpha)} + (-1)^{\alpha+1} \begin{bmatrix} C_{13} \\ C_{23} \\ C_{36} \end{bmatrix} \overset{3}{S}_3, \tag{53}$$

$$\overset{3}{M}_{11} = \frac{1}{12} \left\{ \sum_{\alpha} n^{(\alpha)} (C_{11}^{(\alpha)} - C_{13}^{(\alpha)2}/C_{33}^{(\alpha)}) \overset{3}{S}_{1,1} \right.$$
$$+ \sum_{\alpha} n^{(\alpha)} (C_{12}^{(\alpha)} - C_{13}^{(\alpha)} C_{23}^{(\alpha)}/C_{33}^{(\alpha)}) \overset{3}{S}_{2,2}$$
$$+ \sum_{\alpha} n^{(\alpha)} (C_{16}^{(\alpha)} - C_{13}^{(\alpha)} C_{36}^{(\alpha)}/C_{33}^{(\alpha)})(\overset{3}{S}_{1,2} + \overset{3}{S}_{2,1})$$
$$\left. + \sum_{\alpha} (n^{(\alpha)} C_{13}^{(\alpha)}/C_{33}^{(\alpha)}) P_3 \right\}, \tag{54a}$$

$$\overset{3}{M}_{22} = \frac{1}{12} \left\{ \sum_{\alpha} n^{(\alpha)} (C_{12}^{(\alpha)} - C_{23}^{(\alpha)} C_{13}^{(\alpha)}/C_{33}^{(\alpha)}) \overset{3}{S}_{1,1} \right.$$
$$+ \sum_{\alpha} n^{(\alpha)} (C_{22}^{(\alpha)} - C_{23}^{(\alpha)2}/C_{33}^{(\alpha)}) \overset{3}{S}_{2,2}$$
$$+ \sum_{\alpha} n^{(\alpha)} (C_{26}^{(\alpha)} - C_{23}^{(\alpha)} C_{36}^{(\alpha)}/C_{33}^{(\alpha)})(\overset{3}{S}_{1,2} + \overset{3}{S}_{2,1})$$
$$\left. + \sum_{\alpha} (n^{(\alpha)} C_{23}^{(\alpha)}/C_{33}^{(\alpha)}) P_3 \right\}, \tag{54b}$$

$$\overset{3}{M}_{12} = \frac{1}{12} \left\{ \sum_{\alpha} n^{(\alpha)} (C_{16}^{(\alpha)} - C_{13}^{(\alpha)} C_{36}^{(\alpha)}/C_{33}^{(\alpha)}) \overset{3}{S}_{1,1} \right.$$
$$+ \sum_{\alpha} n^{(\alpha)} (C_{26}^{(\alpha)} - C_{23}^{(\alpha)} C_{36}^{(\alpha)}/C_{33}^{(\alpha)}) \overset{3}{S}_{2,2}$$
$$+ \sum_{\alpha} n^{(\alpha)} (C_{66}^{(\alpha)} - C_{36}^{(\alpha)2}/C_{33}^{(\alpha)})(\overset{3}{S}_{1,2} + \overset{3}{S}_{2,1})$$
$$\left. + \sum_{\alpha} (n^{(\alpha)} C_{36}^{(\alpha)}/C_{33}^{(\alpha)}) P_3 \right\}. \tag{54c}$$

The associated boundary conditions are

$$\sigma_{ji}^{(\alpha p)} \nu_j = \overset{p}{T}{}_i^{(\alpha p)} \quad \text{or} \quad \delta U_i^{(\alpha)} = 0 \quad \text{on} \quad \partial V, \tag{55}$$

$$\overset{3}{M}_{ji} \nu_j = \overset{3p}{T}_i \quad \text{or} \quad \delta \overset{3}{S}_i = 0 \quad \text{on} \quad \partial V. \tag{56}$$

Equations (47)–(56) and the initial condition

$$U_i^{(\alpha)}, \overset{3}{S}_i, \dot{U}_i^{(\alpha)}, \dot{\overset{3}{S}}_i \quad \text{at} \quad t = 0 \quad \text{in} \quad V \tag{57}$$

define a well-posed initial boundary value problem. It has been proven that the procedure that solves a series of MBVP's yields *exactly* the same set of equations if one sets $u_i^{(\alpha\alpha)} = U_i^{(\alpha)}$. This can be confirmed by specializing the results for isotropic laminas in which

$$C_{11}^{(\alpha)} = C_{22}^{(\alpha)} = C_{33}^{(\alpha)} = (\lambda + 2\mu)^{(\alpha)}, \quad C_{12}^{(\alpha)} = C_{13}^{(\alpha)} = C_{23}^{(\alpha)} = \lambda^{(\alpha)},$$
$$C_{44}^{(\alpha)} = C_{55}^{(\alpha)} = C_{66}^{(\alpha)} = \mu^{(\alpha)}, C_{45}^{(\alpha)} = C_{16}^{(\alpha)} = C_{26}^{(\alpha)} = C_{36}^{(\alpha)} = 0 \tag{58}$$

where $\lambda^{(\alpha)}$ and $\mu^{(\alpha)}$ are Lame's constants. If one substitutes (58) into (49)–(54), it can be easily shown that equations (47)–(54) reduce to the equations (15), (31), (18), (42), (46) of reference [10].

7 Concluding Remarks

An asymptotic mixture theory with multiple scales has been

Downloaded 02 May 2010 to 171.66.16.54. Redistribution subject to ASME license or copyright; see http://www.asme.org/terms/Terms_Use.cfm

presented in a variational form using Reissner' displacement and partial stress variational principle [14]. The theory has been developed for laminated composites with orthotropic laminas and periodic microstructure. The theory yields exactly the same results as the ones that are obtained by the asymptotic mixture theory whereby the solution of a series of microboundary value problems (MBVP's) is required to close the mixture theory [10]. The introduction of the new Reissner variational principle not only reduces the number of MBVP's to be solved and simplifies the theory, but also allows the application of the theory to fiber-reinforced and particulate composites with periodic microstructure.

Acknowledgment

The author is thankful to Professor Eric Reissner for showing his unpublished paper on the improved stress-displacement variational principle.

References

1 Nemat-Nasser, S., and Yamada, M., "Harmonic Waves in Layered Transversely Isotropic Composites," *Journal of Sound and Vibration*, Vol. 79, 1981, pp. 161–170.

2 Shah, A. H., and Datta, S. K., "Harmonic Waves in a Periodically Laminated Medium," *International Journal of Solids and Structures*, Vol. 18, 1982, pp. 397–410.

3 Moon, F. C., "Wave Surfaces Due to Impact on Anisotropic Plates," *Journal of Composite Materials*, Vol. 8, 1972, pp. 62–79.

4 Postma, G. W., "Wave Propagation in Stratified Medium," *Geophysics*, Vol. 20, 1955, pp. 780–806.

5 Rytov, S. M., "Acoustical Properties of a Thinly Laminated Medium," *Soviet Physics, Acoustics*, Vol. 2, 1956, pp. 68–80.

6 Murakami, H., and Hegemier, G. A., "A Mixture Theory for Wave Propagation in Anisotropic Angle-Ply Laminates," *Mechanics Today*, Vol. 5, Nemat-Nasser, S. ed., 1980, pp. 329–349.

7 Sun, C. T., Achenbach, J. D., and Herrman, G., "Continuum Theory for a Laminated Medium," ASME JOURNAL OF APPLIED MECHANICS, Vol. 35, 1968, pp. 467–475.

8 Drumheller, D. S., and Bedford, D., "Wave Propagation in Elastic Laminates Using a Second Order Microstructure Theory," INTERNATIONAL JOURNAL OF SOLIDS AND STRUCTURES, Vol. 10, 1974, pp. 61–76.

9 Mengi, Y., Birlik, A., and McNiven, H. D., "A New Approach for Developing Dynamic Theories for Structural Elements, Part 2: Application to Thermoelastic Layered Composites," *International Journal of Solids and Structures*, Vol. 16, 1980, pp. 1169–1186.

10 Murakami, H., Maewal, A., and Hegemier, G. A., "A Mixture Theory With a Director for Linear Elastodynamics of Periodically Laminated Media," *International Journal of Solids and Structures*, Vol. 17, 1981, pp. 155–173.

11 Murakami, H., and Akiyama, A., "A Mixture Theory for Wave Propagation in Angle-Ply Laminates, Part 2: Application," ASME JOURNAL OF APPLIED MECHANICS, Vol. 52, 1985, pp. 337–343.

12 Hegemier, G. A., "Finite Amplitude Elastic-Plastic Wave Propagation in Laminated Composites," *Journal of Applied Physics*, Vol. 45, 1974, pp. 4248–4253.

13 Murakami, H., Maewal, A., and Hegemier, G. A., "Mixture Theory for Longitudinal Wave Propagation in Unidirectional Composites With Cylindrical Fibers of Arbitrary Cross Section-I. Formulation," *International Journal of Solids and Structures*, Vol. 15, 1979, pp. 325–334.

14 Reissner, E., "On a Certain Mixed Variational Theorem and a Proposed Application," *International Journal for Numerical Methods in Engineering*, Vol. 20, 1984, pp. 1366–1368.

15 Hegemier, G. A., Read, H., Murakami, H., Hageman, L. J., and Herrmann, R. G., "Development of Advanced Constitutive Model for Reinforced Concrete," Report SSS-R-83-6112, S-cubed, La Jolla, Calif., April 1983.

16 Cole, J. D., *Perturbation Methods in Applied Mathematics*, Blaisdell, Waltham, Mass., 1968.

17 Nayfeh, A. H., *Perturbation Methods*, Wiley, New York, 1973.

18 Brillouin, L., *Wave Propagation in Periodic Structures*, Dover, New York, 1953.

19 Kohn, W., Krumhasl, J. A., and Lee, E. H., "Variational Methods for Dispersion Relations and Elastic Properties of Composite Materials," ASME JOURNAL OF APPLIED MECHANICS, Vol. 39, 1972, pp. 327–336.

Downloaded 02 May 2010 to 171.66.16.54. Redistribution subject to ASME license or copyright; see http://www.asme.org/terms/Terms_Use.cfm

A Mixture Theory for Wave Propagation in Angle-Ply Laminates

Part 2: Application

H. Murakami
Assistant Professor.

A. Akiyama
Graduate Student.

Department of Applied Mechanics
and Engineering Sciences,
University of California,
San Diego, Calif. 92093

A binary mixture theory with microstructure is constructed for symmetric angle-ply laminates with orthotropic laminas for wave motion in arbitrary directions. A numerical study of phase-velocity spectra associated with the resulting theory reveals that dispersion is most prominent in waveguide propagation. Further, it is directionally dependent and may be strong depending on the propagation direction and lay-up angle. Typical results are presented for a graphite/epoxy composite. To assess the accuracy of the mixture model, a finite element eigenvalue analysis has been carried out. The comparisons of exact versus mixture phase-velocity spectra imply that the theory provides a tool with which one may efficiently study the rather extraordinary capability of angle-ply laminates to act as "shock absorbers."

1 Introduction

Certain material and geometric combinations lead to laminated composites with superior strength and ductility characteristics. Angle-ply laminates, for example, often exhibit extraordinary strength/weight and "shock-absorbing" characteristics. As a result, such composites are frequently used in a dynamic load environment which may, in turn, require a material model that can be used to simulate wave phenomena. For those cases in which the composite consists of many laminas, it is computationally advantageous to describe the composite by a continuum model wherein the heterogeneities are "smoothed" or "homogenized." Since the laminas of most practical composites are anisotropic, the foregoing model must properly reflect material anisotropy.

In an early study, Moon [1] proposed a continuum model based on the nondispersive effective modulus theory [2, 3]. A dispersive model was proposed by Murakami and Hegemier [4] for waveguide type problems.

To extend the results for wave propagation in arbitrary directions, a binary mixture theory was developed for wave propagation in laminated composites with orthotropic laminas in the first part of this paper [5]. Here, those results are applied for wave propagation in angle-ply laminates. Following the development of basic equations, the dispersion of time-harmonic waves in a graphite/epoxy composite with various lay-up angles is studied. The phase-velocity spectra for a variety of lay-up angles and propagation directions have revealed that the dispersion is most prominent in waveguide propagation and directionally dependent.

Finally, to assess the accuracy of the mixture model, the numerically obtained exact dispersion spectra have been computed for the wave propagation in the graphite/epoxy composite. To this end, the variational equation developed by Kohn, Krunhansl, and Lee [6] has been utilized. In the comparison of exact versus mixture phase velocity spectra, excellent agreements have been observed. This indicates that the model is useful for studying the dynamic behavior of angle-ply laminates by finite element or finite difference methods in the time domain.

2 Summary of Basic Equations

Consider a periodic and symmetric angle-ply stacking sequence of two linearly, elastic orthotropic, homogeneous laminas with perfect interface bonds. Let a rectangular Cartesian reference system x_1, x_2, x_3 be selected with x_3 normal to the middle plane of a lamina defined by x_1 and x_2. With reference to Fig. 1 each lamina is monoclinic with respect to the x_3-axis for cases in which the coordinate system and the principal material directions of orthotropy do not coincide with each other.

In the following notations all variables are dimensionless quantities and the same notation introduced in the first part [5] will be used. Lowercase Latin indices range from 1 to 3 and repeated indices imply summation convention unless otherwise noted. In addition, the notations $(\ )_{,i} \equiv \partial(\ )/\partial x_i$ and $(\dot{\ }) \equiv \partial(\ )/\partial t$ are employed.

The basic equations of the mixture theory for average displacement $U_i^{(\alpha)}$, director displacement $\overset{3}{S}_i$, partial stress $\sigma_{ij}^{(\alpha p)}$ and moment $\overset{3}{M}_{ij}$ for material $\alpha\,(=1, 2)$ are:

Contributed by the Applied Mechanics Division for publication in the JOURNAL OF APPLIED MECHANICS.

Discussion on this paper should be addressed to the Editorial Department, ASME, United Engineering Center, 345 East 47th Street, New York, N.Y. 10017, and will be accepted until two months after final publication of the paper itself in the JOURNAL OF APPLIED MECHANICS. Manuscript received by ASME Applied Mechanics Division, February, 1984; final revision, August, 1984.

Copyright © 1985 by ASME
Downloaded 02 May 2010 to 171.66.16.54. Redistribution subject to ASME license or copyright; see http://www.asme.org/terms/Terms_Use.cfm

(a) Equations of motion.

$$\sigma_{ji,j}^{(\alpha p)} + (-1)^{\alpha+1} P_i = \rho^{(\alpha p)} \ddot{U}_i^{(\alpha)}, \tag{1}$$

$$\overset{3}{M}_{ji,j} + (\tau_{3i}^{(2)} - \tau_{3i}^{(1)})/\epsilon^2 = \overset{3}{I}\ddot{\overset{3}{S}}_i, \tag{2}$$

where

$$\rho^{(\alpha p)} = n^{(\alpha)} \rho^{(\alpha)}, \quad \overset{3}{I} = \sum_{\alpha=1}^{2} \rho^{(\alpha p)}/12; \tag{3}$$

(b) Constitutive Relations for Stress Variables.

$$\begin{bmatrix} \sigma_{11} \\ \sigma_{22} \\ \sigma_{12} \end{bmatrix}^{(\alpha p)} = n^{(\alpha)} \begin{bmatrix} C_{11} C_{12} C_{13} C_{16} \\ C_{12} C_{22} C_{23} C_{26} \\ C_{16} C_{26} C_{36} C_{66} \end{bmatrix}^{(\alpha)} \begin{bmatrix} U_{1,1} \\ U_{2,2} \\ U_{3,3} \\ U_{1,2} + U_{2,1} \end{bmatrix}^{(\alpha)}$$

$$+ (-1)^{\alpha+1} \begin{bmatrix} C_{13} \\ C_{23} \\ C_{36} \end{bmatrix}^{(\alpha)} \overset{3}{S}_3, \tag{4a}$$

$$\sigma_{33}^{(\alpha p)} = n^{(\alpha)} \tau_{33}^{(\alpha)} = C_{33}^{(\alpha)} \{ n^{(\alpha)} U_{3,3}^{(\alpha)} + (-1)^{\alpha+1} \overset{3}{S}_3 \}$$
$$+ n^{(\alpha)} \{ C_{13}^{(\alpha)} U_{1,1}^{(\alpha)} + C_{23}^{(\alpha)} U_{2,2}^{(\alpha)} + C_{36}^{(\alpha)} (U_{1,2}^{(\alpha)} + U_{2,1}^{(\alpha)}) \}, \tag{4b}$$

$$\begin{bmatrix} \sigma_{23} \\ \sigma_{31} \end{bmatrix}^{(\alpha p)} = n^{(\alpha)} \begin{bmatrix} \tau_{23} \\ \tau_{31} \end{bmatrix}^{(\alpha)} = \begin{bmatrix} C_{44} C_{45} \\ C_{45} C_{55} \end{bmatrix}^{(\alpha)}$$

$$\begin{bmatrix} n^{(\alpha)} (U_{2,3}^{(\alpha)} + U_{3,2}^{(\alpha)}) + (-1)^{\alpha+1} \overset{3}{S}_2 \\ n^{(\alpha)} (U_{3,1}^{(\alpha)} + U_{1,3}^{(\alpha)}) + (-1)^{\alpha+1} \overset{3}{S}_1 \end{bmatrix}, \tag{4c}$$

$$\overset{3}{M}_{11} = \frac{1}{12} \sum_{\alpha} n^{(\alpha)} \{ (C_{11}^{(\alpha)} - C_{13}^{(\alpha)2}/C_{33}^{(\alpha)}) \overset{3}{S}_{1,1}$$
$$+ (C_{12}^{(\alpha)} - C_{13}^{(\alpha)} C_{23}^{(\alpha)}/C_{33}^{(\alpha)}) \overset{3}{S}_{2,2}$$
$$+ (C_{16}^{(\alpha)} - C_{13}^{(\alpha)} C_{36}^{(\alpha)}/C_{33}^{(\alpha)})(\overset{3}{S}_{1,2} + \overset{3}{S}_{2,1})$$
$$+ (C_{13}^{(\alpha)}/C_{33}^{(\alpha)}) P_3 \}, \tag{5a}$$

$$\overset{3}{M}_{22} = \frac{1}{12} \sum_{\alpha} n^{(\alpha)} \{ (C_{12}^{(\alpha)} - C_{23}^{(\alpha)} C_{13}^{(\alpha)}/C_{33}^{(\alpha)}) \overset{3}{S}_{1,1}$$
$$+ (C_{22}^{(\alpha)} - C_{23}^{(\alpha)2}/C_{33}^{(\alpha)}) \overset{3}{S}_{2,2}$$
$$+ (C_{26}^{(\alpha)} - C_{23}^{(\alpha)} C_{36}^{(\alpha)}/C_{33}^{(\alpha)})(\overset{3}{S}_{1,2} + \overset{3}{S}_{2,1})$$
$$+ (C_{23}^{(\alpha)}/C_{33}^{(\alpha)}) P_3 \}, \tag{5b}$$

$$\overset{3}{M}_{12} = \frac{1}{12} \sum_{\alpha} n^{(\alpha)} \{ (C_{16}^{(\alpha)} - C_{13}^{(\alpha)} C_{36}^{(\alpha)}/C_{33}^{(\alpha)}) \overset{3}{S}_{1,1}$$
$$+ (C_{26}^{(\alpha)} - C_{23}^{(\alpha)} C_{36}^{(\alpha)}/C_{33}^{(\alpha)}) \overset{3}{S}_{2,2}$$
$$+ (C_{66}^{(\alpha)} - C_{36}^{(\alpha)2}/C_{33}^{(\alpha)}) (\overset{3}{S}_{1,2} + \overset{3}{S}_{2,1})$$
$$+ (C_{36}^{(\alpha)}/C_{33}^{(\alpha)}) P_3 \}, \tag{5c}$$

$$\overset{3}{M}_{3i} = P_i/12, \quad i = 1,2,3 \tag{5d}$$

where

$$\sigma_{ij}^{(\alpha p)} = \sigma_{ji}^{(\alpha p)}, \quad \overset{3}{M}_{ij} = \overset{3}{M}_{ji}; \tag{6}$$

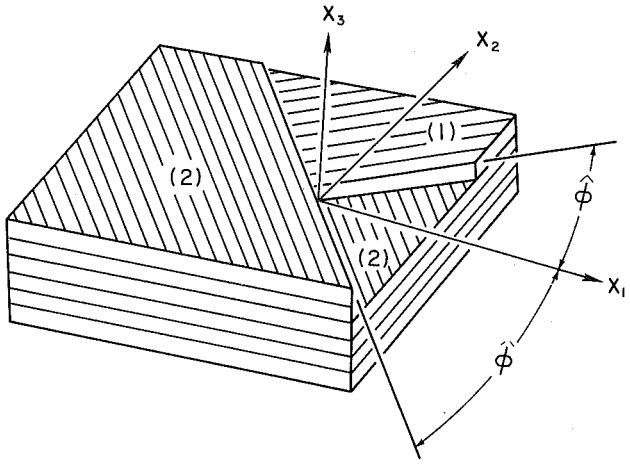


Fig. 1 A typical angle-ply laminate

(c) Constitutive Relations for Interaction Body Forces.

$$\begin{bmatrix} \sum_{\alpha} n^{(\alpha)} \hat{C}_{44}^{(\alpha)} & -\sum_{\alpha} n^{(\alpha)} \hat{C}_{45}^{(\alpha)} \\ -\sum_{\alpha} n^{(\alpha)} \hat{C}_{45}^{(\alpha)} & \sum_{\alpha} n^{(\alpha)} \hat{C}_{55}^{(\alpha)} \end{bmatrix} \begin{bmatrix} P_1 \\ P_2 \end{bmatrix}$$
$$= \begin{bmatrix} 12(U_1^{(2)} - U_1^{(1)})/\epsilon^2 + (\overset{3}{S}_{3,1} + \overset{3}{S}_{1,3}) \\ 12(U_2^{(2)} - U_2^{(1)})/\epsilon^2 + (\overset{3}{S}_{2,3} + \overset{3}{S}_{3,2}) \end{bmatrix}, \tag{7a,b}$$

$$P_3 = C_{33(n)} \Big[12(U_3^{(2)} - U_3^{(1)})/\epsilon^2 + \overset{3}{S}_{3,3}$$
$$+ \sum_{\alpha=1}^{2} n^{(\alpha)} \{ (C_{13}^{(\alpha)}/C_{33}^{(\alpha)}) \overset{3}{S}_{1,1} + (C_{23}^{(\alpha)}/C_{33}^{(\alpha)}) \overset{3}{S}_{2,2}$$
$$+ (C_{36}^{(\alpha)}/C_{33}^{(\alpha)}) (\overset{3}{S}_{1,2} + \overset{3}{S}_{2,1}) \} \Big] \tag{7c}$$

where

$$C_{33(n)} = 1/\Big(\sum_{\alpha} n^{(\alpha)}/C_{33}^{(\alpha)} \Big),$$

$$\begin{bmatrix} \hat{C}_{55} - \hat{C}_{45} \\ -\hat{C}_{45} \quad \hat{C}_{44} \end{bmatrix}^{(\alpha)} = \begin{bmatrix} C_{44} C_{45} \\ C_{45} C_{55} \end{bmatrix}^{(\alpha)^{-1}}; \tag{8}$$

(d) Boundary Conditions Along the Boundary of the Domain.

$$\sigma_{ji}^{(\alpha p)} \nu_j \quad \text{or} \quad U_i^{(\alpha)} \quad \text{prescribed}, \tag{9}$$

$$\overset{3}{M}_{ji} \nu_j \quad \text{or} \quad \overset{3}{S}_i \quad \text{prescribed}; \tag{10}$$

(e) Initial Conditions.

$$U_i^{(\alpha)}, \overset{3}{S}_i, \dot{U}_i^{(\alpha)} \quad \text{and} \quad \dot{\overset{3}{S}}_i \quad \text{prescribed at} \quad t = 0. \tag{11}$$

3 Application to Angle-Ply Laminates

The mixture equations of the preceding section are now specialized to the case of symmetric angle-ply laminates with the *same orthotropic laminas*, i.e., each lamina consists of the same orthotropic material and is of equal volume fraction

$$n^{(1)} = n^{(2)} = 0.5. \tag{12}$$

This constitutes a reasonable model of angle-ply laminates as illustrated in Fig. 1. Here $2\hat{\phi}$ denotes the lay-up angle of two material principal axes, and the x_1-axis is selected as the bisecting line of these two principal directions.

Downloaded 02 May 2010 to 171.66.16.54. Redistribution subject to ASME license or copyright; see http://www.asme.org/terms/Terms_Use.cfm

With respect to the local coordinate system that coincides with the material principal axes, the stress and strain relation for the orthotropic materials becomes [7]

$$\begin{bmatrix} \sigma_{11} \\ \sigma_{22} \\ \sigma_{33} \end{bmatrix} = \begin{bmatrix} T_{11} T_{12} T_{13} \\ T_{12} T_{22} T_{23} \\ T_{13} T_{23} T_{33} \end{bmatrix} \begin{bmatrix} e_{11} \\ e_{22} \\ e_{33} \end{bmatrix},$$

$$\begin{bmatrix} \sigma_{23} \\ \sigma_{31} \\ \sigma_{12} \end{bmatrix} = \begin{bmatrix} T_{44} & 0 & 0 \\ 0 & T_{55} & 0 \\ 0 & 0 & T_{66} \end{bmatrix} \begin{bmatrix} 2e_{23} \\ 2e_{31} \\ 2e_{12} \end{bmatrix}. \tag{13}$$

In (13) the elements may be expressed in terms of Young's moduli, Poisson's ratio, and shear moduli as follows:

$$T_{11} = \frac{1-\nu_{23}\nu_{32}}{E_2E_3d}, \qquad T_{12} = \frac{\nu_{21}+\nu_{31}\nu_{23}}{E_2E_3d},$$

$$T_{13} = \frac{\nu_{31}+\nu_{21}\nu_{32}}{E_2E_3d}, \qquad T_{22} = \frac{1-\nu_{13}\nu_{31}}{E_1E_3d},$$

$$T_{23} = \frac{\nu_{32}+\nu_{12}\nu_{31}}{E_1E_3d}, \qquad T_{33} = \frac{1-\nu_{12}\nu_{21}}{E_1E_2d},$$

$$T_{44} = G_{23},\ T_{55} = G_{31}, T_{66} = G_{12},\ T_{ij} = T_{ji}\ (i,j = 1\text{–}6) \tag{14}$$

where

$$d \equiv \frac{1-\nu_{12}\nu_{21}-\nu_{23}\nu_{32}-\nu_{31}\nu_{13}-2\nu_{21}\nu_{32}\nu_{13}}{E_1E_2E_3} \tag{15}$$

and where

E_1, E_2, E_3 = Young's moduli in the x_1, x_2, and x_3 directions, respectively;

ν_{ij} = Poisson's ratios for transverse strain in the x_j direction when stressed in the x_i direction;

G_{23}, G_{31}, G_{12} = shear moduli in the $x_2 - x_3$, $x_3 - x_1$, and $x_1 - x_2$ planes, respectively;

$$\nu_{ij}/E_i = \nu_{ji}/E_j \quad \text{no sum on } i \text{ and } j. \tag{16}$$

Thus, nine independent constants are required to define the orthotropic lamina. The appropriate constraints on these may be found in [7].

For the coordinate system shown in Fig. 1 in which the principal material axes and the coordinate axes do not coincide, the stiffness matrix for each material is obtained by appropriate transformation of the [T] matrix. Here one finds

$$C_{11}^{(1)} = C_{11}^{(2)} = T_{11}\cos^4\hat{\phi} + \left(\frac{1}{2}T_{12} + T_{66}\right)\sin^2(2\hat{\phi}) + T_{22}\sin^4\hat{\phi},$$

$$C_{12}^{(1)} = C_{12}^{(2)} = \frac{1}{4}(T_{11} + T_{22} - 4T_{66})\sin^2(2\hat{\phi}) + T_{12}(\sin^4\hat{\phi} + \cos^4\hat{\phi}),$$

$$C_{13}^{(1)} = C_{13}^{(2)} = T_{13}\cos^2\hat{\phi} + T_{23}\sin^2\hat{\phi},$$

$$C_{16}^{(1)} = -C_{16}^{(2)} = \frac{1}{2}\left\{(T_{11}\cos^2\hat{\phi} - T_{22}\sin^2\hat{\phi})\sin(2\hat{\phi}) - \left(\frac{1}{2}T_{12} + T_{66}\right)\sin(4\hat{\phi})\right\},$$

$$C_{22}^{(1)} = C_{22}^{(2)} = T_{11}\sin^4\hat{\phi} + \left(\frac{1}{2}T_{12} + T_{66}\right)\sin^2(2\hat{\phi}) + T_{22}\cos^4\hat{\phi},$$

$$C_{23}^{(1)} = C_{23}^{(2)} = T_{13}\sin^2\hat{\phi} + T_{23}\cos^2\hat{\phi},$$

$$C_{26}^{(1)} = -C_{26}^{(2)} = \frac{1}{2}\left\{(T_{11}\sin^2\hat{\phi} - T_{22}\cos^2\hat{\phi})\sin(2\hat{\phi}) + \left(\frac{1}{2}T_{12} + T_{66}\right)\sin(4\hat{\phi})\right\},$$

$$C_{33}^{(1)} = C_{33}^{(2)} = T_{33},$$

$$C_{36}^{(1)} = -C_{36}^{(2)} = \frac{1}{2}(T_{13} - T_{23})\sin(2\hat{\phi}),$$

$$C_{44}^{(1)} = C_{44}^{(2)} = T_{44}\cos^2\hat{\phi} + T_{55}\sin^2\hat{\phi},$$

$$C_{45}^{(1)} = -C_{45}^{(2)} = \frac{1}{2}(T_{55} - T_{44})\sin(2\hat{\phi}),$$

$$C_{55}^{(1)} = C_{55}^{(2)} = T_{44}\sin^2\hat{\phi} + T_{55}\cos^2\hat{\phi},$$

$$C_{66}^{(1)} = C_{66}^{(2)} = \frac{1}{4}(T_{11} - 2T_{12} + T_{22})\sin^2(2\hat{\phi}) + T_{66}\cos^2(2\hat{\phi})$$

$$C_{ij}^{(\alpha)} = C_{ji}^{(\alpha)}\ (i, j = 1 \text{ to } 6). \tag{17}$$

The mixture equations for the preceding laminate can now be summarized as follows:

(*a*) Equations of Motion.

$$\sigma_{ji,j}^{(\alpha p)} + (-1)^{\alpha+1}P_i = \rho^{(\alpha p)}\ddot{U}_i^{(\alpha)}, \tag{18}$$

$$\overset{3}{M}_{ji,j} + (\tau_{3i}^{(2)} - \tau_{3i}^{(1)})/\epsilon^2 = \overset{3}{I}\overset{3}{S}_i, \tag{19}$$

where

$$\rho^{(1p)} = \rho^{(2p)} = 0.5\rho^{(1)}, \quad \overset{3}{I} = \rho^{(1)}/12;$$

(*b*) Constitutive Relations for Stress Variables.

$$\begin{bmatrix} \sigma_{23} \\ \sigma_{31} \end{bmatrix}^{(\alpha p)} = \frac{1}{2}\begin{bmatrix} \tau_{23} \\ \tau_{31} \end{bmatrix}^{(\alpha)} = \begin{bmatrix} C_{44} & (-1)^{\alpha+1}C_{45} \\ (-1)^{\alpha+1}C_{45} & C_{55} \end{bmatrix}^{(1)} \begin{bmatrix} (U_{2,3}^{(\alpha)} + U_{3,2}^{(\alpha)})/2 + (-1)^{\alpha+1}\overset{3}{S}_2 \\ (U_{3,1}^{(\alpha)} + U_{1,3}^{(\alpha)})/2 + (-1)^{\alpha+1}\overset{3}{S}_1 \end{bmatrix}. \tag{20}$$

$$\sigma_{33}^{(\alpha p)} = \frac{1}{2}\tau_{33}^{(\alpha)} = C_{33}^{(1)}\{U_{3,3}^{(\alpha)}/2 + (-1)^{\alpha+1}\overset{3}{S}_3\} + \{C_{13}^{(1)}U_{1,1}^{(\alpha)} + C_{23}^{(1)}U_{2,2}^{(\alpha)} + (-1)^{\alpha+1}C_{36}^{(1)}(U_{1,2}^{(\alpha)} + U_{2,1}^{(\alpha)})\}/2,$$

$$\overset{3}{M}_{11} = \{(C_{11}^{(1)} - C_{13}^{(1)2}/C_{33}^{(1)})\overset{3}{S}_{1,1} + (C_{12}^{(1)} - C_{13}^{(1)}C_{23}^{(1)}/C_{33}^{(1)})\overset{3}{S}_{2,2} + (C_{13}^{(1)}/C_{33}^{(1)})P_3\}/12,$$

$$\overset{3}{M}_{22} = \{(C_{12}^{(1)} - C_{23}^{(1)}C_{13}^{(1)}/C_{33}^{(1)})\overset{3}{S}_{1,1} + (C_{22}^{(1)} - C_{23}^{(1)2}/C_{33}^{(1)})\overset{3}{S}_{2,2} + (C_{23}^{(1)}/C_{33}^{(1)})P_3\}/12,$$

$$\overset{3}{M}_{12} = (C_{66}^{(1)} - C_{36}^{(1)2}/C_{33}^{(1)})(\overset{3}{S}_{1,2} + \overset{3}{S}_{2,1})/12,$$

$$\overset{3}{M}_{3i} = P_i/12, \qquad i = 1,2,3; \tag{21}$$

(*c*) Constitutive Relations for Interaction Body Forces.

$$P_1 = (C_{55}^{(1)} - C_{45}^{(1)2}/C_{44}^{(1)})\{12(U_1^{(2)} - U_1^{(1)})/\epsilon^2 + (\overset{3}{S}_{3,1} + \overset{3}{S}_{1,3})\},$$

$$P_2 = (C_{44}^{(1)} - C_{45}^{(1)2}/C_{55}^{(1)})\{12(U_2^{(2)} - U_2^{(1)})/\epsilon^2 + (\overset{3}{S}_{2,3} + \overset{3}{S}_{3,2})\},$$

$$P_3 = C_{33}^{(1)}\{12(U_3^{(2)} - U_3^{(1)})/\epsilon^2 + \overset{3}{S}_{3,3} + (C_{13}^{(1)}/C_{33}^{(1)})\overset{3}{S}_{1,1} + (C_{23}^{(1)}/C_{33}^{(1)})\overset{3}{S}_{2,2}\}. \tag{22}$$

Downloaded 02 May 2010 to 171.66.16.54. Redistribution subject to ASME license or copyright; see http://www.asme.org/terms/Terms_Use.cfm

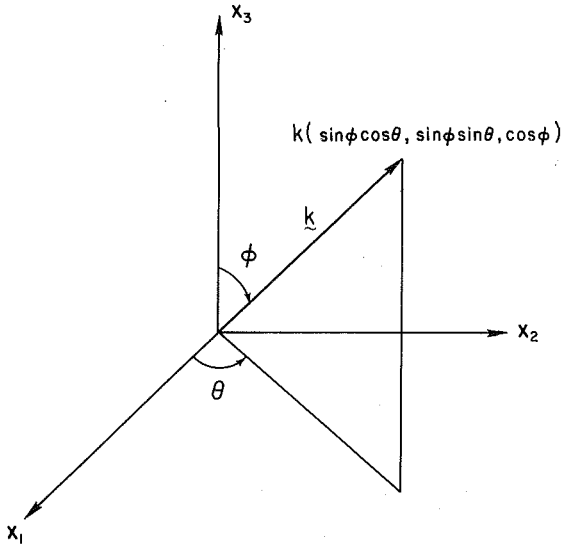


Fig. 2 The definition of wave vector

$$\mathbf{k} = k[\sin\phi\cos\theta,\ \sin\phi\sin\theta,\ \cos\phi]^T. \tag{24}$$

Substitution of (23) into (18)–(22) yields an eigenvalue problem for $\epsilon\omega$ of the form:

$$[K]\mathbf{U}^* = (\epsilon\omega)^2[M]\mathbf{U}^* \tag{25}$$

where $[K]$ and $[M]$ are 9×9 matrices, the elements of which are functions of the mixture constants and the wave vector, and

$$\mathbf{U}^* = [U_1^{*(1)}, U_1^{*(2)}, U_2^{*(1)}, U_2^{*(2)}, U_3^{*(1)}, U_3^{*(2)}, s_1, s_2, s_3]^T. \tag{26}$$

Upon calculation of the eigenvalue $\epsilon\omega$ for a given ϵk, one obtains the phase velocity C_p as

$$C_p = (\epsilon\omega)/(\epsilon k). \tag{27}$$

Since the two laminas consist of the same material, $\bar{E}^{(1)}$ and $\bar{\rho}^{(1)}$ are used for the scaling in (5) of reference [5]. The phase velocity is normalized with respect to the bar velocity $\bar{C}_0 = \sqrt{\bar{E}_1/\bar{\rho}^{(1)}}$.

A numerical study of phase-velocity spectra has been carried out for a graphite/epoxy composite, the material properties of which are shown in Table 1. In this study a premise of transverse isotropy was adopted; thus

$$\nu_{23} = \nu_{32},\ E_2 = E_3,\ \nu_{21} = \nu_{31},\ \nu_{12} = \nu_{13}. \tag{28}$$

4 Phase-Velocity Spectra

Considerable information regarding the influence of lay-up angle and propagation direction on dispersion can be obtained by investigating the phase-velocity spectrum of the mixture equations (18)–(22). For this purpose let us consider harmonic wave propagation in a full space of the form

$$[U_1^{(1)}, U_1^{(2)}, U_2^{(1)}, U_2^{(2)}, U_3^{(1)}, U_3^{(2)}, \overset{3}{S}_1, \overset{3}{S}_2, \overset{3}{S}_3]^T$$
$$= \exp\{ik(x_1\sin\phi\cos\theta + x_2\sin\phi\sin\theta + x_3\cos\phi) - i\omega t\}$$
$$[U_1^{*(1)}, U_1^{*(2)}, U_2^{*(1)}, U_2^{*(2)}, U_3^{*(1)}, U_3^{*(2)}, iks_1, iks_2, iks_3]^T \tag{23}$$

where $[\ ]^T$ denotes the transpose of $[\ ]$. In (23) $U_i^{*(\alpha)}$ and s_i are constant amplitudes, k denotes wave number, ω represents angular frequency, ϕ is azimuth, and θ is longitude; the direction of the wave propagation may be best represented by the wave vector $\mathbf{k}$ as shown in Fig. 2:

Phase-velocity contours versus wave direction θ, $0 < \theta < \pi/2$ are computed for nondimensional wave numbers $\epsilon k = 0$, 0.8, and 1.6, and shown in Figs. 3–6 for lay-up angles of 0 deg, ±15 deg, ±30 deg, and ±45 deg, respectively. Two fundamental modes of propagation are observed: one corresponds to a "gross" longitudinal mode, the other corresponds to a "gross" shear mode. In each figure the phase-velocity contours are shown for each different azimuth ϕ; the first to the fourth quadrant shows the results for $\phi = 0$ deg, 30 deg, 60 deg, and 90 deg, respectively.

Table 1 Material properties used for computation of phase-velocity contours

Composite \ Moduli	$\bar{E}_1$	$\bar{E}_2$	$\bar{G}_{12}$	ν_{12}	ν_{23}
Graphite/Epoxy	30	0.75	0.375	0.25	0.25

Because the two constituents are the same material, no dispersion is observed in the first quadrant of each figure, which corresponds to the normal incidence to the layering, i.e., $\phi = 0$ deg. When the lay-up angle $\hat{\phi} = 0$ deg, the composite becomes a homogeneous material, with the result that the material does not yield dispersion as shown in Fig. 3.

Pronounced dispersion can be seen to occur in the third and the fourth quadrants, $\phi = 60$ deg and 90 deg, in Figs. 4–6. The strongest dispersion is observed in the waveguide type of propagation, $\phi = 90$ deg. The dispersion effect decreases as the azimuth ϕ decreases from 90 deg to 0 deg in which no dispersion occurs. With respect to the latitude θ, the strongest dispersion is observed for the propagation directions that are almost parallel to the bisectors of the acute lay-up angle, i.e., $\theta = 0$ deg. The results for the waveguide type of propagation, $\phi = 90$ deg, agree with the ones reported in reference [4].

A different view of the spectra in Fig. 5 is provided in Figs. 7(*a–c*) which correspond to $\phi = 30$ deg, 60 deg, and 90 deg, respectively, for $\theta = 0$ deg, 45 deg, and 90 deg. In Fig. 7, strong dispersion is observed in a gross longitudinal mode for the propagation direction $\theta = 0$ deg. This is prominent in Figs. 4–6 even if $\epsilon k = 0.8$ for which the wavelength is approximately eight times the cell dimension. This observation explains the unique capability of angle-ply laminates to serve as "shock observers": a sharp wave front induced by an impact is transmitted in the acute bisector directions more rapidly than in any other directions, and takes place with strong dispersion which in turn leads to "rounding" or "spreading" of the wave front.

Since most ply-angle laminates are constructed with fiber-reinforced laminas, it is instructive to compare the dispersion due to the lay-up angle with the one due to fiber reinforcing. The latter has been examined in [8], and a comparison with results reported therein reveals that the influence on dispersion of lay-up angle is significantly greater than that of fiber reinforcing alone.

Finally, it is noted that, in the limit $\epsilon k \to 0$, the contour essentially reduces to that of reference [1]; slight pattern differences are due to small differences in the material constants used in the numerical computations. The analysis of reference [1] was based on the "effective modulus" theory and is nondispersive.

5 Exact Dispersion Spectra

To assess the accuracy of the mixture model, the preceding dispersion spectra have to be compared with the exact ones. This task is accomplished by a finite element discretization applied to the variational equation obtained by Kohn, Krumhansl, and Lee [6]. In evaluating eigenvalues based on the Rayleigh-Ritz procedure, they adopted Fourier expansion form as a trial displacement function defined over the cell, and experienced slow convergence. This is caused by the trial functions that do not satisfy the continuity of traction vectors at material interfaces. This drawback has been circumvented by the finite element method, which introduces the interpolation of displacements on each element, but not on the whole domain, with fine elements near material interfaces.

Downloaded 02 May 2010 to 171.66.16.54. Redistribution subject to ASME license or copyright; see http://www.asme.org/terms/Terms_Use.cfm

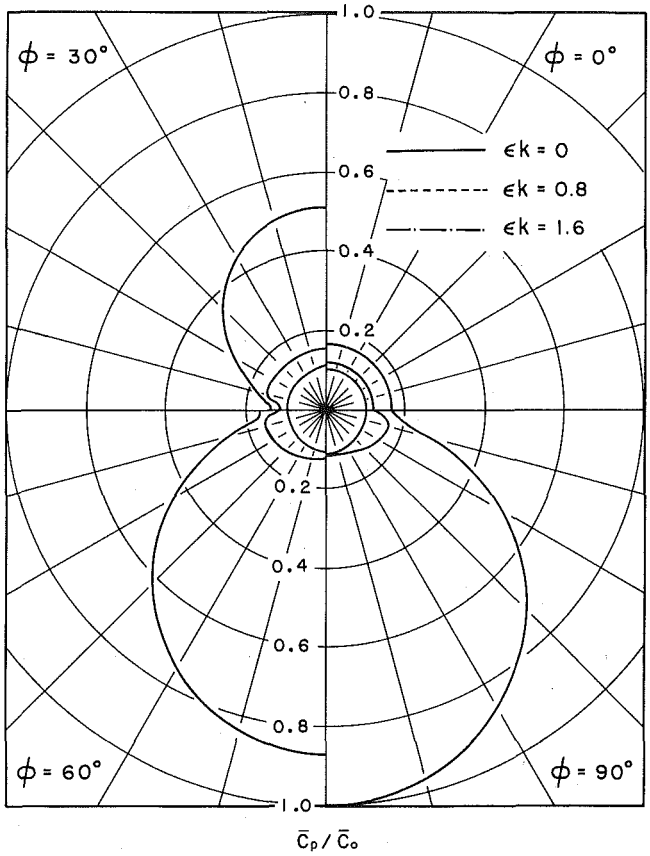


Fig. 3 Phase-velocity contours for graphite/epoxy laminate with lay-up angle $\hat{\phi} = 0$ deg

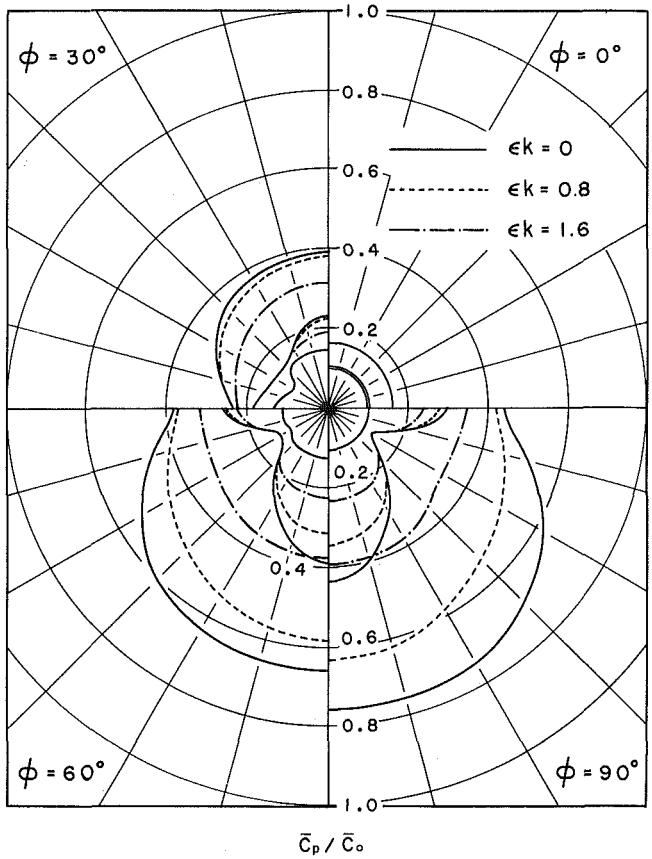


Fig. 5 Phase-velocity contours for graphite/epoxy laminate with lay-up angle $\hat{\phi} = \pm 30$ deg

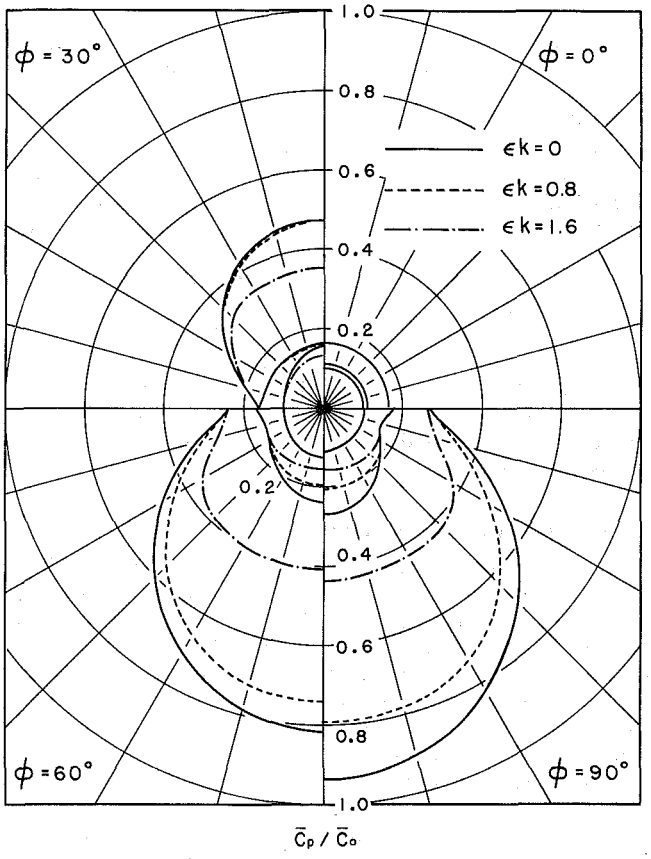


Fig. 4 Phase-velocity contours for graphite/epoxy laminate with lay-up angle $\hat{\phi} = \pm 15$ deg

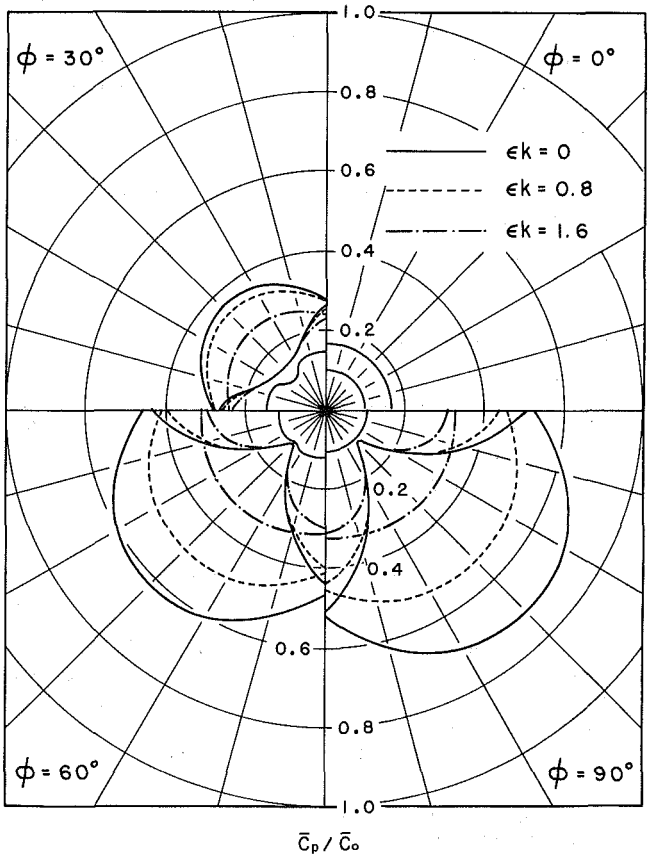


Fig. 6 Phase-velocity contours for graphite/epoxy laminate with lay-up angle $\hat{\phi} = \pm 45$ deg

Downloaded 02 May 2010 to 171.66.16.54. Redistribution subject to ASME license or copyright; see http://www.asme.org/terms/Terms_Use.cfm

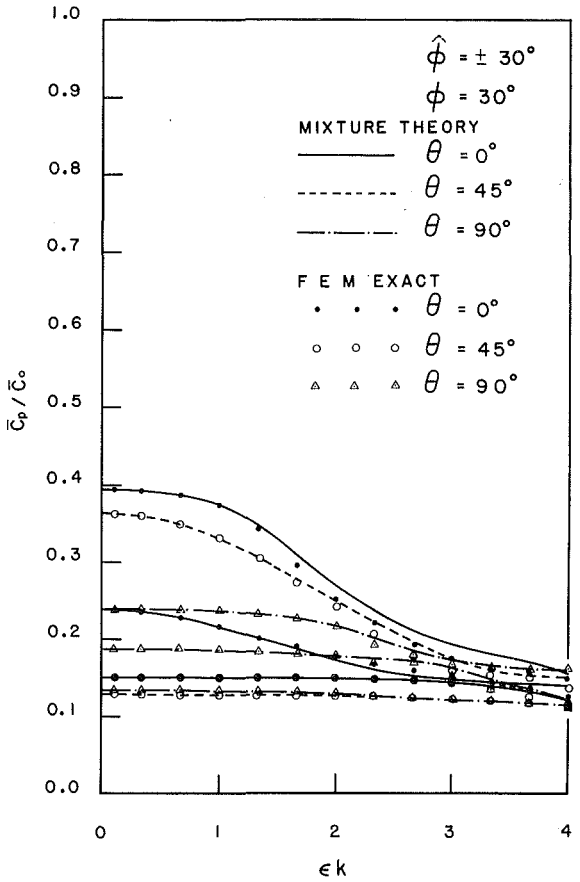


Fig. 7(a) Phase-velocity spectra of ±30 deg graphite/epoxy for ϕ = 30 deg

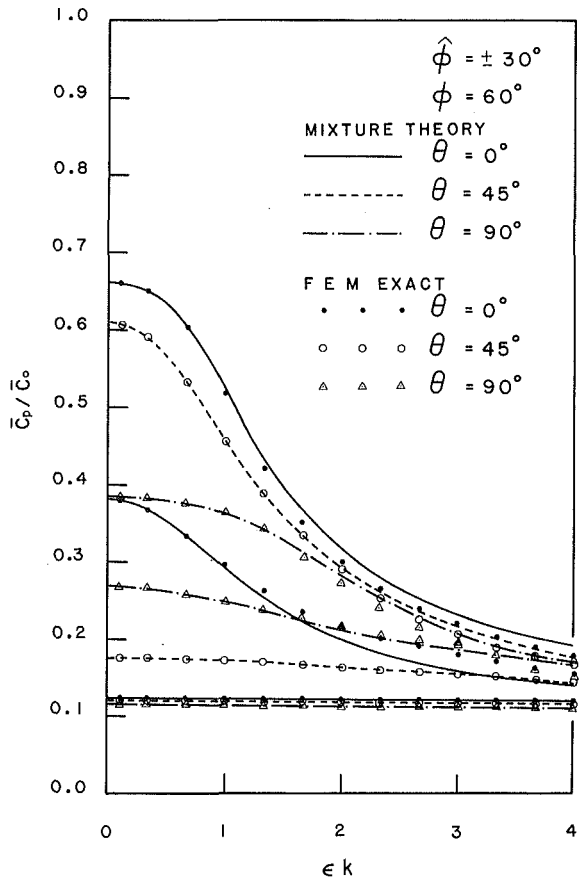


Fig. 7(b) Phase-velocity spectra of ±30 deg graphite/epoxy for ϕ = 60 deg

Let us consider a harmonic wave motion of the form

$$\hat{\sigma}_{ij}(x_k,t) = \sigma_{ij}(x_k,\omega)\exp(i\omega t),$$
$$\hat{u}_i(x_k,t) = u_i(x_k,\omega)\exp(i\omega t). \tag{29}$$

The functional for the cell with the cell length ϵ is obtained as follows:

$$J(u_l,u_l^*) = \int_{-\epsilon/2}^{\epsilon/2} (-\sigma_{ij}e_{ij}^* + \rho\omega^2 u_i u_i^*)\, dx_3, \tag{30}$$

where ( )* denotes the complex conjugate of ( ). The Euler-Lagrange equations of (30) are

$$\sigma_{ji,\,j} + \rho\omega^2 u_i = 0 \qquad \text{on} \quad |x_3| \le \epsilon/2, \tag{31}$$

$$\delta u_i^*(x_1,x_2,\epsilon/2,\omega)\,\sigma_{3i}(x_1,x_2,\epsilon/2,\omega)$$
$$= \delta u_i^*(x_1,x_2,-\epsilon/2,\omega)\,\sigma_{3i}(x_1,x_2,-\epsilon/2,\omega), \tag{32}$$

while the following relations are considered to be definitions:

$$\sigma_{ij} \equiv C_{ijkl}e_{kl},\ e_{kl} \equiv \frac{1}{2}(u_{k,l} + u_{l,k}) \tag{33}$$

where C_{ijkl} is an elastic modulus tensor. The kinematic boundary conditions are

$$u_i^{(1)} = u_i^{(2)} \qquad \text{at} \quad x_3 = \pm\epsilon n^{(1)}/2 \tag{34}$$

and the quasiperiodicity condition for the displacement:

$$u_i^{(2)}(x_1,x_2,\epsilon/2,\omega) = u_i^{(2)}(x_1,x_2,-\epsilon/2,\omega)\exp(i\epsilon k_3) \tag{35}$$

where $k_3 = k\cos\phi$ is the x_3-component of the wave vector defined by (24). To satisfy the quasiperiodicity condition (35) it is convenient to express u_i in the form:

$$u_i = U_i(x_3,k_j)\exp i(k_l x_l - \omega t). \tag{36}$$

Then equation (35) becomes

$$U_i(\epsilon/2,k_j) = U_i(-\epsilon/2,k_j). \tag{37}$$

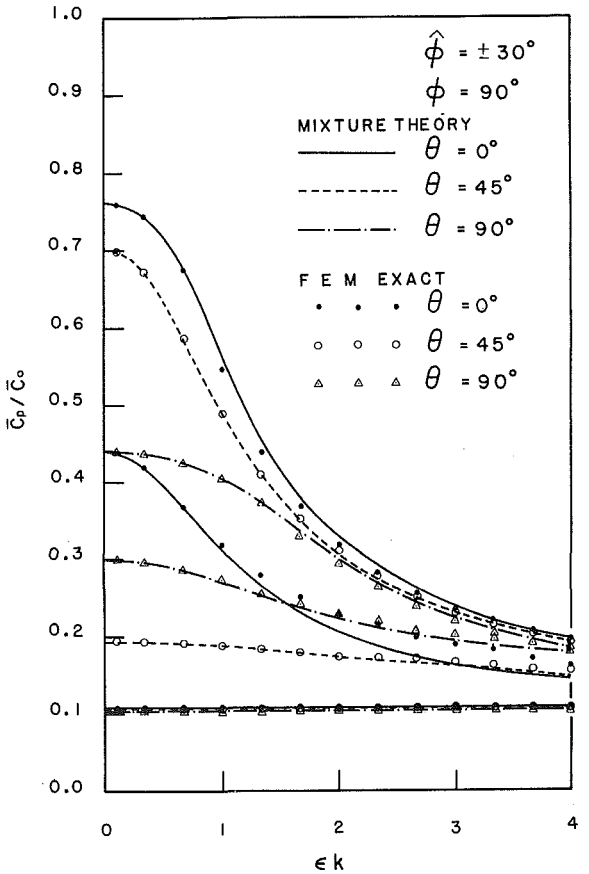


Fig. 7(c) Phase-velocity spectra of ±30 deg graphite/epoxy for ϕ = 90 deg

Downloaded 02 May 2010 to 171.66.16.54. Redistribution subject to ASME license or copyright; see http://www.asme.org/terms/Terms_Use.cfm

In (36) and (37) there should not be any confusion between U_i in (36) and $U_i^{(\alpha)}$ used for $u_i^{(\alpha a)}$ in the mixture equations (18–21).

By discretizing the domain $|x_3| \leq \epsilon/2$ into two node finite elements one interpolates the displacement $\mathbf{u}$ by nodal displacements $\mathbf{W}$. Using the finite element approximation in each element for the first variation of (30) assembling process yields an eigenvalue problem of the form

$$\delta \mathbf{W}^* [\underline{\mathbf{K}} - \omega^2 \underline{\mathbf{M}}] \mathbf{W} + c.c. = 0 \tag{38}$$

where $\underline{\mathbf{K}}$ is a hermitian stiffness matrix, while $\underline{\mathbf{M}}$ is a symmetric real mass matrix and where "*c.c.*" denotes the complex conjugate of the preceding terms. In the assembling process it is understood that the kinematic boundary condition (37) is incorporated. This process changes $\underline{\mathbf{K}}$ from a banded matrix to a fully populated matrix. Solving the eigenvalue problem defined by (38) for arbitrary $\delta \mathbf{W}^*$ one can obtain $\epsilon\omega$ for a given ϵk, and eventually compute C_p by (27).

The foregoing algorithm has been used to compute the exact phase-velocity spectra for the graphite/epoxy composite using 20 elements. The representative results are shown in Figs. 7. It has been observed that the agreement between the mixture phase-velocity spectra and the exact ones is excellent. It can be concluded from Figs. 7 that the mixture theory can predict the dispersion phenomena in the angle-ply laminates.

The accuracy of the finite element procedure was tested by comparing the phase-velocity spectra of an isotropic laminated composite with exact spectra obtained analytically by Sve [9]. For the composite treated by Sve the error of phase velocity computed with 20 elements was less than 3 percent even at $\epsilon k = 4$.

6 Concluding Remarks

The mixture equations developed in reference [5] for laminated composites with orthotropic laminas have been applied to angle-ply laminates. A significant feature of this model is its ability to account for dispersion due to lay-up angle. Numerical computations on a graphite/epoxy composite have demonstrated that such dispersion is directionally dependent, and may be very strong for certain preferred directions.

To assess the accuracy of the model, a finite element, eigenvalue analysis was carried out using the functional obtained by Kohn, Kramhansl, and Lee [6]. The comparisons of exact versus mixture phase-velocity spectra imply that the theory provides a tool with which one may efficiently study the rather extraordinary capability of angle-ply laminates to act as "shock absorbers."

References

1 Moon, F. C., "Wave Surfaces Due to Impact on Anisotropic Plates," *Journal of Composite Materials*, Vol. 8, 1972, pp. 62–79.

2 Postma, G. W., "Wave Propagation in Stratified Medium," *Geophysics*, Vol. 20, 1955, pp. 780–806.

3 Rytov, S. M., "Acoustical Properties of a Thinly Laminated Medium," *Soviet Physics, Acoustics*, Vol. 2, 1956, pp. 68–80.

4 Murakami, H., and Hegemier, G. A., "A Mixture Theory for Wave Propagation in Anisotropic Angle-Ply Laminates," *Mechanics Today*, Vol. 5, Nemat-Nassar, S., ed., 1980, pp. 329–349.

5 Murakami, H., "A Mixture Theory for Wave Propagation in Angle-Ply Laminates, Part 1: Theory," ASME JOURNAL OF APPLIED MECHANICS, Vol. 52, 1985, pp. 331–337.

6 Kohn, W., Krunhansl, J. A., and Lee, E. H., "Variational Methods for Dispersion Relations and Elastic Properties of Composite Materials," ASME JOURNAL OF APPLIED MECHANICS, Vol. 39, 1972, pp. 327–336.

7 Jones, R. M., *Mechanics of Composite Materials*, Scripta, Washington, D.C., 1975.

8 Murakami, H., Nonomura, S., and Shioya, S., "Effect of Constituent Anisotropy on Longitudinal Wave Propagation in Unidirectional Fiber Reinforced Composite" (in Japanese), *Transactions of the Japan Society of Mechanical Engineers*, Vol. 48-462A, 1982, pp. 230–238.

9 Sve, C., "Time-Harmonic Traveling Obliquely in a Periodically Laminated Medium," ASME JOURNAL OF APPLIED MECHANICS, Vol. 38, 1971, pp. 477–482.

Downloaded 02 May 2010 to 171.66.16.54. Redistribution subject to ASME license or copyright; see http://www.asme.org/terms/Terms_Use.cfm

J. G. Berryman

L. Thigpen

Lawrence Livermore National Laboratory,
P.O. Box 808, L-200,
Livermore, Calif. 94550

Linear Dynamic Poroelasticity With Microstructure for Partially Saturated Porous Solids[1]

Linear equations of motion are derived to describe the behavior of small disturbances in a porous solid containing both liquid and gas. Appropriate boundary conditions are derived to guarantee the uniqueness of the solutions of these equations.

Introduction

The linear theory of dynamic poroelasticity for fluid-saturated porous media was first presented by Biot [1] and has been studied extensively since its inception. Appropriate boundary conditions and uniqueness of solutions were established by Deresiewicz and Skalak [2]. The existence of the second (slow) compressional wave predicted by the theory was confirmed experimentally by Plona [3] with supporting theoretical evidence supplied by Berryman [4]. Further experimental evidence confirming the predicted attenuation of ultrasonic pulses has been presented by Salin and Schon [5]. The theory for fluid-saturated porous materials is therefore quite well established.

In contrast, the theory for partially saturated porous media – while of great practical importance – has not been developed to a significant extent. An important negative result by Mochizuki [6] has shown that the attenuation measurements of Murphy [7] on partially saturated samples cannot be explained using Biot's theory while assuming the liquid and gas in the pores act as a composite fluid. Bedford and Stern [8] have developed a model for porous media saturated with a bubbly liquid. A more general theory for partially saturated porous solids is needed.

The present authors have recently developed a nonlinear theory of dynamic poroelasticity [9] for fully saturated porous media. The framework of that theory is sufficiently versatile to allow the inclusion of multiple pore fluids with only a modest increase in effort required to derive the equations of motion. The discussion in the present paper will be limited to small-amplitude disturbances and will not treat capillary pressure effects. The resulting linear theory will then be examined to determine appropriate boundary conditions and to establish uniqueness of the solutions of these equations. The restriction to small (infinitesimal) disturbances is necessary at present because of the difficult conceptual problems that arise in formulating boundary conditions if finite volumes of liquid or gas escape through a free surface. These problems must be faced in a nonlinear theory but may be safely avoided here. The neglect of capillary pressure effects is not essential but it greatly simplifies the analysis of both the boundary conditions and the equations of motion.

Formulation

Our notation and definitions will be very similar to the Eulerian variational formulation of Bedford and Drumheller [10, 11]. However, we wish to stress that the goal of our approach is a Lagrangian formulation of the equations of motion so several differences arise. The same *linear* equations of motion derived here could be obtained in the Eulerian framework, but a Lagrangian formulation is more natural for studying elastic waves in porous solids. The changes required to obtain nonlinear equations of motion should be apparent once the variational principle has been presented.

The constituent solid and fluids are treated on average as continua. We assume that the solid and fluids in a ball of radius λ surrounding a point $\mathbf{X}$ (λ is some appropriate correlation length) can be assigned some average motion. In Cartesian tensor notation, the motion takes the form

$$x_{(\xi)i} = \chi_{(\xi)i}(\mathbf{X},t) \tag{1}$$

where $x_{(\xi)i}$ is the position vector of the ξ constituent ($\xi = s$ for the solid and $\xi = g$ for gas or l for liquid) and $\mathbf{X}$ is the specified reference configuration. The displacement vector is the nontrivial part of the motion given by

$$u_{(\xi)i} = x_{(\xi)i} - X_i. \tag{2}$$

In terms of the displacement vector, the velocity $v_{(\xi)i}$ and the acceleration $a_{(\xi)i}$ of the constituents are

$$v_{(\xi)i} = \frac{\partial}{\partial t} u_{(\xi)i} \tag{3}$$

$$a_{(\xi)i} = \frac{\partial^2}{\partial t^2} u_{(\xi)i}. \tag{4}$$

The Jacobian of the motion (1) is given by

$$J_{(\xi)} = \det\left(\frac{\partial x_{(\xi)i}}{\partial X_j}\right) = \det(x_{(\xi)i,j}). \tag{5}$$

[1] Dedicated to the memory of Frank A. Morrison, Jr.

Contributed by the Applied Mechanics Division for publication in the JOURNAL OF APPLIED MECHANICS.

Discussion on this paper should be addressed to the Editorial Department, ASME, United Engineering Center, 345 East 47th Street, New York, N.Y. 10017, and will be accepted until two months after final publication of the paper itself in the JOURNAL OF APPLIED MECHANICS. Manuscript received by ASME Applied Mechanics Division, May, 1984.

Copyright © 1985 by ASME
Downloaded 02 May 2010 to 171.66.16.54. Redistribution subject to ASME license or copyright; see http://www.asme.org/terms/Terms_Use.cfm

A comma preceding a subscript indicates a partial derivative with respect to the appropriate component of $\mathbf{X}$. The local density $\tilde{\rho}_{(\xi)}$ (mass per unit volume of constituent ξ) and volume fraction $\phi_{(\xi)}$ are related to the partial density (mass per unit total volume) by

$$\rho_{(\xi)} = \phi_{(\xi)} \tilde{\rho}_{(\xi)}. \tag{6}$$

For the porous media under consideration, the volume fractions satisfy

$$\sum_{\xi} \phi_{(\xi)} = \phi_{(s)} + \phi_{(l)} + \phi_{(g)} = 1. \tag{7}$$

In this case, the porosity ϕ (void volume per unit total volume) is given by $\phi = 1 - \phi_{(s)}$. It is well known that the conservation of mass leads to the identity

$$J_{(\xi)} = \frac{\rho_{(\xi)0}}{\rho_{(\xi)}} = \frac{\phi_{(\xi)0} \tilde{\rho}_{(\xi)0}}{\phi_{(\xi)} \tilde{\rho}_{(\xi)}} \tag{8}$$

where the value in the reference configuration is indicated by an 0 subscript.

If the (nonlinear) Lagrangian strain tensor $e_{(\xi)ij}$ for the ξ component is given by (see Eringen [12] or Green and Adkins [13])

$$2e_{(\xi)ij} = u_{(\xi)i,j} + u_{(\xi)j,i} + u_{(\xi)k,i} u_{(\xi)k,j}, \tag{9}$$

then the three strain invariants are given by

$$I_{(\xi)1} = tr(e_{(\xi)ij}) = e_{(\xi)ii} \tag{10}$$

$$I_{(\xi)2} = \frac{1}{2}(I^2_{(\xi)1} - e_{(\xi)ij} e_{(\xi)ji}) \tag{11}$$

$$\begin{aligned} I_{(\xi)3} &= \det(e_{(\xi)ij}) \\ &= \frac{1}{3}(e_{(\xi)ij} e_{(\xi)jk} e_{(\xi)ki} + 3I_{(\xi)1} I_{(\xi)2} - I^3_{(\xi)1}). \end{aligned} \tag{12}$$

The Jacobian can then be expressed in terms of the strain invariants as

$$J_{(\xi)} = (1 + 2I_{(\xi)1} + 4I_{(\xi)2} + 8I_{(\xi)3})^{1/2}, \tag{13}$$

in Lagrangian form.

Variational Principle

If a variation $\delta x_{(\xi)i}$ is added to the motion (1), the velocity and Jacobian of the ξ constituent are

$$\delta v_{(\xi)i} = \frac{\partial}{\partial t} \delta x_{(\xi)i} \tag{14}$$

and

$$\delta J_{(\xi)} = J_{(\xi)} \delta x_{(\xi)j,j}. \tag{15}$$

Equation (15) is a well-known result due to Jacobi (see Eringen [12]).

If K is the total kinetic energy, U is the internal energy, and W is the work due to external forces, then Hamilton's extended variational principle requires that any variation $\delta x_{(\xi)i}$ satisfy

$$\delta \int_{t_1}^{t_2} (K - U + W) dt = 0 \tag{16}$$

for arbitrary times t_1 and t_2.

Using the entropy inequality (from the second law of thermodynamics) to provide constraints on constitutive postulates in the manner of Coleman and Noll [14], Drumheller and Bedford [11] show that the internal energy can depend only on the deformation gradient $\partial \chi_{(\xi)i} / \partial X_j$ and on the local densities $\tilde{\rho}_{(\xi)}$. Thus, the internal energy for an isotropic fluid-saturated porous medium is in general of the form

$$U = \int d\Omega \sum_{\xi} \rho_{(\xi)} E_{(\xi)} \tag{17}$$

where

$$E_{(s)} = E_{(s)}(I_{(s)1}, I_{(s)2}, I_{(s)3}, \tilde{\rho}_{(s)}) \tag{18}$$

and

$$E_{(f)} = E_{(f)}(I_{(f)1}, \tilde{\rho}_{(f)}) = E_{(f)}(\tilde{\rho}_{(f)}) \quad \text{for} \quad f = g \text{ or } l. \tag{19}$$

Alternatively, equations (17)–(19) may simply be introduced as postulates for an elastic material saturated with compressible ideal fluids. The volume element $d\Omega$ is the solid volume element and satisfies the conservation of solid mass constraint

$$\delta(\rho_{(s)} d\Omega) = 0. \tag{20}$$

The assumption of isotropy guarantees that the strain energy functionals $E_{(\xi)}$ depend on the deformation gradient only through the strain invariants. The restriction of form in (19) follows from the idea that a fluid should not alter its material response after an arbitrary deformation that leaves the density unchanged. For a single-phase ideal fluid, there is no additional work corresponding to variations in fluid volume fraction so the dependence on deformation gradient may be dropped in (19).

The general form of (17) as the sum of separate terms for solid and fluid is a result of the immiscibility postulate of Drumheller and Bedford [11]. According to this postulate, the free energy of a given constituent depends only on the constitutive variables of that constituent. This form also neglects the possibility of any free energy associated with an interface between constituents.

The theory being developed depends on the microstructure of the fluid-saturated porous medium as evidenced by the presence of $\tilde{\rho}_{(\xi)}$ in (18) and (19). The total kinetic energy must also depend on these variables and, therefore, takes the form

$$\begin{aligned} 2K = \int d\Omega \Big[&\sum_{\xi} \rho_{(\xi)} \dot{u}_{(\xi)i} \dot{u}_{(\xi)i} + \sum_{\xi} \rho_{(\xi)} \Lambda_{(\xi)} \dot{\tilde{\rho}}^2_{(\xi)} \\ &+ \frac{1}{2} \sum_{\xi\zeta} \rho_{(\xi\zeta)} (\dot{u}_{(\xi)i} - \dot{u}_{(\zeta)i})(\dot{u}_{(\xi)i} - \dot{u}_{(\zeta)i}) \Big]. \end{aligned} \tag{21}$$

The first term in (21) is the usual kinetic energy due to particle motion. The second term is the microstructural kinetic energy due to local expansion and contraction of the constituents [11]. The third term is the virtual mass term due to relative flow of the constituents again assuming the medium is isotropic. The matrix of coefficients $\rho_{(\xi\zeta)}$ is chosen to be symmetric for convenience. The choice is permissible because the microscopic kinetic energy due to backflow depends only on relative speeds – not on which constituent is actually in motion. The possibility of overcounting the total kinetic energy for the virtual mass terms may be avoided by generalizing the arguments of Berryman [15] when determining the values of the coefficients $\rho_{(\xi\zeta)}$.

In the absence of capillary pressure effects, the virtual work to be substituted into (16) is

$$\delta W = \int d\Omega \sum_{\xi} [\rho_{(\xi)} b_{(\xi)i} + d_{(\xi)i}] \delta x_{(\xi)i} + \int dS \sum_{\xi} s_{(\xi)i} \delta x_{(\xi)i} \tag{22}$$

where $b_{(\xi)i}$ is an external body force density, $d_{(\xi)i}$ is the drag force, and $s_{(\xi)i}$ is the surface traction on the ξth constituent.

To complete the variational principle, we must account for the constraints summarized in (7), (8), and (13). Since the volume fractions play a secondary role in the analysis, it proves convenient to eliminate these variables altogether from the variation. To do so, we note that

$$\phi_{(\xi)} = \frac{\rho_{(\xi)0}}{J_{(\xi)} \tilde{\rho}_{(\xi)}} \tag{23}$$

so that (7) becomes

$$\sum_{\xi} \frac{\rho_{(\xi)0}}{J_{(\xi)} \tilde{\rho}_{(\xi)}} = 1. \tag{24}$$

We will associate a Lagrange multiplier λ_{ϕ} with the constraint (24). For the nonlinear analysis, it is convenient to introduce

Downloaded 02 May 2010 to 171.66.16.54. Redistribution subject to ASME license or copyright; see http://www.asme.org/terms/Terms_Use.cfm

additional Lagrange multipliers associated with the constraints in (13). However, for the linear analysis, it suffices to use the approximation

$$J_{(\xi)} \simeq 1 + I_{(\xi)1} \tag{25}$$

and to substitute (25) and

$$\bar{\rho}_{(\xi)} = \bar{\rho}_{(\xi)0} + \Delta\bar{\rho}_{(\xi)} \tag{26}$$

into (24) to obtain the linear approximation

$$\sum_{\xi} \phi_{(\xi)0}\left[I_{(\xi)1} + \frac{\Delta\bar{\rho}_{(\xi)}}{\bar{\rho}_{(\xi)0}}\right] = 0. \tag{27}$$

The variational principle for linear poroelasticity for partially saturated media is therefore

$$\delta\int_{t_1}^{t_2} dt\left\{K - U + W - \int d\Omega\lambda_\phi \sum_{\xi}\phi_{(\xi)0}\left[I_{(\xi)1} + \frac{\Delta\bar{\rho}_{(\xi)}}{\bar{\rho}_{(\xi)0}}\right]\right\} = 0. \tag{28}$$

To obtain linear equations of motion, the various terms of (28) needed only be quadratic functions of their variables. Hence, it is sufficient to replace $\rho_{(\xi)}$, $\Lambda_{(\xi)}$, and $\rho_{(\zeta\xi)}$ in (21) by their reference values. The energies in (17) are given by

$$\rho_{(s)0}E_{(s)} = \frac{1}{2}aI_{(s)1}^2 + bI_{(s)2} + cI_{(s)1}\Delta\bar{\rho}_{(s)} + \frac{1}{2}d\Delta\bar{\rho}_{(s)}^2 \tag{29}$$

and

$$\rho_{(f)0}E_{(f)} = \frac{1}{2}h_{(f)}\Delta\bar{\rho}_{(f)}^2 \qquad \text{for} \quad f = g, l. \tag{30}$$

The constraint term of (28) is also quadratic because λ_ϕ is a linear function of the variables $\bar{\rho}_{(\xi)}$ and $u_{(s)i}$ as we will show. The constants a, b, c, d must be chosen so that (29) is a positive definite function of its variables [16].

Equations of Motion and Uniqueness of Solutions

The equations of motion are obtained from (28) by making independent variations with respect to $u_{(\xi)i}$, $\bar{\rho}_{(\xi)}$, and λ_ϕ. For the present, only those motions are considered for which $\delta u_{(s)i}$ and the normal component of $\delta u_{(f)i}$ vanish at the surface of the material volume. The variation with respect to λ_ϕ just reproduces the constraint equation (27). The variation with respect to $\bar{\rho}_{(\xi)}$ gives

$$\int_{t_1}^{t_2} dt\int d\Omega\delta\bar{\rho}_{(\xi)}\left[-\rho_{(\xi)0}\Lambda_{(\xi)0}\ddot{\bar{\rho}}_{(\xi)} - \rho_{(\xi)0}\frac{\partial E_{(\xi)}}{\partial\bar{\rho}_{(\xi)}} - \lambda_\phi\phi_{(\xi)0}/\bar{\rho}_{(\xi)0}\right] = 0 \tag{31}$$

so the equations of motion for density are given by

$$\Lambda_{(\xi)0}\ddot{\bar{\rho}}_{(\xi)} = -\frac{\partial E_{(\xi)}}{\partial\bar{\rho}_{(\xi)}} - \frac{\lambda_\phi}{\bar{\rho}_{(\xi)0}^2}. \tag{32}$$

Variation for the solid motion $u_{(s)i}$ produces

$$\int_{t_1}^{t_2} dt\int d\Omega\Big\{[\rho_{(s)0}b_{(s)i} + d_{(s)i}]\delta u_{(s)i}$$

$$+\left[\rho_{(s)0}\dot{u}_{(s)i} + \sum_{f=g,l}\rho_{(sf)0}(\dot{u}_{(s)i} - \dot{u}_{(f)i})\right]\delta\dot{u}_{(s)i} \tag{33}$$

$$-\left[\rho_{(s)0}\frac{\partial E_{(s)}}{\partial u_{(s)i,j}} + \lambda_\phi\phi_{(s)0}\delta_{ij}\right]\delta u_{(s)i,j}\Big\} = 0$$

which, after integrating by parts, gives the equation of motion

$$\rho_{(s)0}\ddot{u}_{(s)i} + \sum_{f=g,l}\rho_{(sf)0}(\ddot{u}_{(s)i} - \ddot{u}_{(f)i})$$

$$= \left[\rho_{(s)0}\frac{\partial E_{(s)}}{\partial u_{(s)i,j}} + \lambda_\phi\phi_{(s)0}\delta_{ij}\right]_{,j} + d_{(s)i} + \rho_{(s)0}b_{(s)i}. \tag{34}$$

The corresponding results for the fluid constituents ($f = g$ or l) are

$$\int_{t_1}^{t_2} dt\int d\Omega\Big\{[\rho_{(f)0}b_{(f)i} + d_{(f)i}]\delta u_{(f)i}$$

$$+\left[\rho_{(f)0}\dot{u}_{(f)i} + \sum_{\xi\neq f}\rho_{(f)0}(\dot{u}_{(f)i} - \dot{u}_{(\xi)i})\right]\delta u_{(f)}$$

$$-[\lambda_\phi\phi_{(f)0}\delta_{ij}]\delta u_{(f)i,j}\Big\} = 0 \tag{35}$$

and

$$\rho_{(f)0}\ddot{u}_{(f)i} + \sum_{\xi\neq f}\rho_{(f\xi)0}(\ddot{u}_{(f)i} - \ddot{u}_{(\xi)i})$$

$$= \phi_{(f)0}(\lambda_\phi)_{,i} + d_{(f)i} + \rho_{(f)0}b_{(f)i}. \tag{36}$$

Equations (27), (32), (34), and (36) provide all the equations needed to solve for λ_ϕ, $\bar{\rho}_{(\xi)}$, and $u_{(\xi)i}$. Since the left-hand side of (32) is a linear function of $\bar{\rho}_{(\xi)}$ and since $E_{(\xi)}$ is a quadratic function of $\bar{\rho}_{(\xi)}$ (and $u_{(s)i}$ when $\xi = s$), equation (32) guarantees that λ_ϕ is a linear function of the other variables as mentioned at the end of the preceding section.

To establish uniqueness of the solutions of these equations, the analysis of Deresiewicz and Skalak [2] will be generalized to the partially saturated case. Consider the time rate of change of the total energy

$$\frac{d}{dt}(K+U) = \int d\Omega\Big\{\sum_{\xi}\rho_{(\xi)0}\Lambda_{(\xi)}\dot{\bar{\rho}}_{(\xi)}\ddot{\bar{\rho}}_{(\xi)}$$

$$+\sum_{\xi}\left[\rho_{(\xi)0}\dot{u}_{(\xi)i} + \sum_{\zeta\neq\xi}\rho_{(\xi\zeta)}(\dot{u}_{(\xi)i} - \dot{u}_{(\zeta)i})\right]\ddot{u}_{(\xi)i}$$

$$+\rho_{(s)0}\frac{\partial E_{(s)}}{\partial u_{(s)i,j}}\dot{u}_{(s)i,j} + \sum_{\xi}\rho_{(\xi)0}\frac{\partial E_{(\xi)}}{\partial\bar{\rho}_{(\xi)}}\dot{\bar{\rho}}_{(\xi)}$$

$$+\lambda_\phi\sum_{\xi}\phi_{(\xi)0}\left[\dot{u}_{(\xi)i,i} + \frac{\dot{\bar{\rho}}_{(\xi)}}{\bar{\rho}_{(\xi)0}}\right]\Big\}. \tag{37}$$

The final line of (37) has been added for convenience but clearly makes no contribution to the total integral due to the identity (27). After integrating by parts and then collecting terms, we have

$$\frac{d}{dt}(K+U) = \int d\Omega\Big\{\sum_{\xi}\dot{\bar{\rho}}_{(\xi)}\left[\rho_{(\xi)0}\Lambda_{(\xi)0}\ddot{\bar{\rho}}_{(\xi)}\right.$$

$$\left.+\rho_{(\xi)0}\frac{\partial E_{(\xi)}}{\partial\bar{\rho}_{(\xi)}} + \lambda_\phi\frac{\phi_{(\xi)0}}{\bar{\rho}_{(\xi)0}}\right]$$

$$+\sum_{\xi}\dot{u}_{(\xi)i}\Big[\rho_{(\xi)0}\ddot{u}_{(\xi)i} + \sum_{\zeta\neq\xi}\rho_{(\xi\zeta)}(\ddot{u}_{(\xi)i} - \ddot{u}_{(\zeta)i}) \tag{38}$$

$$-\left(\rho_{(s)0}\frac{\partial E_{(s)}}{\partial u_{(s)i,j}}\delta_{\xi s} + \lambda_\phi\phi_{(\xi)0}\delta_{ij}\right)_{,j}\Big]\Big\}$$

$$+\int dS\sum_{\xi}\dot{u}_{(\xi)i}\left(\rho_{(s)0}\frac{\partial E_{(s)}}{\partial u_{(s)i,j}}\delta_{\xi s} + \lambda_\phi\phi_{(\xi)0}\delta_{ij}\right)\eta_j.$$

In writing (38), we used the symmetry $\rho_{(\xi\zeta)} = \rho_{(\zeta\xi)}$ discussed briefly after equation (21). The final integral in (38) is a surface integral resulting from application of the divergence theorem to the terms in (37) proportional to $u_{(\xi)i,j}$. The expression η_j is the unit outward normal vector.

Substituting (32) into (38) shows that the first bracketed expression of (38) vanishes identically. Substituting (34) and (36) into (38) and considering the case when body forces are absent, we find that (38) reduces to

Downloaded 02 May 2010 to 171.66.16.54. Redistribution subject to ASME license or copyright; see http://www.asme.org/terms/Terms_Use.cfm

$$\frac{d}{dt}(K+U)=\int d\Omega \sum_{\xi} d_{(\xi)i}\dot{u}_{(\xi)i}$$

$$+\int dS\sum_{\xi}\dot{u}_{(\xi)i}[\tau_{(s)ij}\delta_{\xi s}+\lambda_{\phi}\phi_{(\xi)0}\delta_{ij}]\eta_j. \tag{39}$$

and the stress in the porous solid is

$$\tau_{(s)ij}=\rho_{(s)0}\frac{\partial E_{(s)}}{\partial u_{(s)i,j}}. \tag{40}$$

The authors have shown elsewhere [16] that the drag forces may be written in the form

$$d_{(\xi)i}=-\sum_{\zeta}C_{(\xi\zeta)}(\dot{u}_{(\zeta)i}-\dot{u}_{(s)i}) \tag{41}$$

where $C_{(\xi\zeta)}$ is a symmetric, positive-semidefinite matrix whose matrix elements satisfy

$$\sum_{\xi}C_{(\xi\zeta)}=0 \qquad \text{for} \quad \zeta=g \text{ or } l. \tag{42}$$

For the present purposes, we may take (41) and (42) as postulates of the theory. It follows easily from (41) and (42) that

$$\sum_{\xi}d_{(\xi)i}\dot{u}_{(\xi)i}=-\sum_{\xi\zeta}C_{(\xi\zeta)}(\dot{u}_{(\zeta)i}-\dot{u}_{(s)i})(\dot{u}_{(\xi)i}-\dot{u}_{(s)i}) \tag{43}$$

and it follows from the positive-semidefinite character of $C_{(\xi\zeta)}$ that (43) is nonpositive.

Defining the dissipation function per unit volume D_0 by

$$2D_0=-\sum_{\xi}d_{(\xi)i}\dot{u}_{(\xi)i}\geq 0 \tag{44}$$

and the volume dissipation integral D by

$$2D=\int d\Omega\, 2D_0, \tag{45}$$

we find that equation (39) becomes

$$\frac{d}{dt}(K+U)+2D=\int dS\sum_{\xi}\dot{u}_{(\xi)i}[\tau_{(s)ij}\delta_{\xi s}+\lambda_{\phi}\phi_{(\xi)0}\delta_{ij}]\eta_j. \tag{46}$$

Equation (46) shows that the surface integral on the right should be interpreted as the rate at which work is done on the partially saturated medium by surface forces.

To establish sufficient conditions for uniqueness of the solutions, consider a partially saturated porous medium with boundary B and suppose that two distinct solutions (1,2) to the equations exist for the same initial conditions. If we consider the equations of motion for the differences

$$\hat{\rho}_{(\xi)}\equiv\rho^{(1)}_{(\xi)}-\rho^{(2)}_{(\xi)} \qquad \text{and} \qquad \hat{u}_{(\xi)i}\equiv u^{(1)}_{(\xi)i}-u^{(2)}_{(\xi)i},$$

we find that *if*

$$\int_B dS\sum_{\xi}u_{(\xi)i}[\hat{\tau}_{(s)ij}\delta_{\xi s}+\hat{\lambda}_{\phi}\phi_{(\xi)0}\delta_{ij}]\eta_j=0 \tag{47}$$

then equation (46) implies that, since $\hat{K}(0)+\hat{U}(0)=0$,

$$\hat{K}(t)+\hat{U}(t)=-\int_0^t dt 2\hat{D}\leq 0. \tag{48}$$

Because of the positive-definite character of the kinetic and potential energies and the positive-semidefinite character of D, it follows that (48) can only be satisfied if $\hat{K}=\hat{U}=\hat{D}=0$ which, in turn, implies that the differences $\hat{\rho}_{(\xi)}$ and $\hat{u}_{(\xi)i}$ must all vanish. Thus, equation (47) is a sufficient condition for the uniqueness of the solutions. Note that, if we relax the equality of (47) and allow the surface integral on the left-hand side to be *less than or equal* to zero, the preceding argument may still be carried through to the conclusion that the solution is unique. The fact that (47) is *not* a *necessary* condition for uniqueness will be discussed in more detail following the section on boundary conditions.

Boundary Conditions

Although the sufficient condition (47) for uniqueness of solutions provides an important constraint on the boundary conditions for poroelasticity, considerable flexibility still exists in the final choice. Various physical arguments will be made to narrow the range of possibilities.

First, a variational derivation of the general constraints on the boundary conditions will be presented. Consider equation (28) and allow variations of $u_{(\xi)i}$ on the surface of the material volume [17]. Equations (33) and (35) are affected by this loosening of the variational constraints. The appropriate surface term from (22) should be added to (33) and (35). The variation for the volume integrals is the same so the bulk equations of motion (34) and (36) remain unchanged. However, the independent variation of the surface integrals leads to the new conditions valid at a material boundary

$$\int_{t_1}^{t_2}dt\int_B dS\{s_{(s)i}-\sigma_{(s)ij}\eta_j\}\delta u_{(s)i}=0 \tag{49}$$

where

$$\sigma_{(s)ij}=\tau_{(s)ij}+\lambda_{\phi}\phi_{(s)0}\delta_{ij} \tag{50}$$

and

$$\int_{t_1}^{t_2}dt\int_B dS[s_{(f)i}-\lambda_{\phi}\phi_{(f)0}\eta_i]\delta u_{(f)i}=0 \tag{51}$$

with

$$f=g \text{ or } l.$$

From (49) and (51), we conclude that for the solid constituent either the displacement $u_{(s)i}$ or the surface stress $\sigma_{(s)ij}\eta_j$ must be specified at a material boundary. This conclusion is consistent with the uniqueness condition (47) since $\dot{u}_{(s)i}|_B$ is also determined if $u_{(s)i}|_B$ is specified for all time.

Note that, in the absence of capillary pressure effects, the surface stresses for the fluid constituents cannot be specified arbitrarily if the displacements are not specified. The fluid stresses must satisfy

$$\lambda_{\phi}=s_{(g)i}\eta_i/\phi_{(g)0}=s_{(l)i}\eta_i/\phi_{(l)0}. \tag{52}$$

Equation (52) is physically reasonable if we assume, for example, a total surface stress s_i is applied to the medium and

$$s_{(\xi)i}=\phi_{(\xi)0}s_i \qquad \text{for all} \quad \xi. \tag{53}$$

Thus, $s_{(\xi)i}$ as given by (53) is just the partial surface stress for constituent ξ.

If no conditions are placed on the fluid displacement, we conclude that

$$\lambda_{\phi}=s_i\eta_i \tag{54}$$

at a material boundary. However, if the surface stress is not known, then (54) must be replaced by a single condition on all the fluid displacements (constraints on the individual fluid displacements would make the problem overdetermined). Using (53) and summing (51) over the fluids gives

$$\int_{t_1}^{t_2}dt\int dS[s_j\eta_j-\lambda_{\phi}]\sum_f\phi_{(f)0}\delta u_{(f)i}\eta_i=0. \tag{55}$$

We conclude that the single condition on the fluid displacement should be the specification of the normal component of the average fluid displacement $\sum_f\phi_{(f)}u_{(f)i}\eta_i$.

At the interface between two porous media, continuity of $\dot{u}_{(s)i}$ must be imposed on physical grounds if the two porous frames are to remain in contact during the motion. Furthermore, if fluid mass is to be conserved at the interface, then it can be shown [18] that the normal component of

$$\rho_{(f)0}[\dot{u}_{(f)i}-\dot{u}_{(s)i}] \tag{56}$$

must be continuous for each fluid at the interface. Dividing out a factor of $\bar{\rho}_{(f)0}$ common to the same fluid on either side of the interface, the resulting displacement condition is that the normal component of

$$w_{(f)i}\equiv\phi_{(f)0}[u_{(f)i}-u_{(s)i}] \tag{57}$$

must be continuous.

The continuity of (57) is an additional constraint on the possible variations of $u_{(\xi)i}$. Therefore, we must add the terms

Downloaded 02 May 2010 to 171.66.16.54. Redistribution subject to ASME license or copyright; see http://www.asme.org/terms/Terms_Use.cfm

$$\delta\int_{t_1}^{t_2} dt\int dS\lambda_{(f)}[w_{(f)i}^{(m)} - w_{(f)i}^{(m')}]\eta_i^{(m)} \tag{58}$$

to the variational equation (28) when the boundary is not a free surface but an interface between two porous media (say m and m') with different properties. The new variable $\lambda_{(f)}$ is a Lagrange multiplier associated with the fluid mass balance constraint. Recalling that $\eta_j^{(m)} = -\eta_j^{(m')}$ and that $\delta u_{(s)i}^{(m)} = \delta u_{(s)i}^{(m')}$ is guaranteed by the no-slip condition, it is not difficult to show that (49) and (51) are replaced by

$$\int_{t_1}^{t_2} dt\int dS\{[\sigma_{(s)ij}^{(m)} - \sum_f \lambda_{(f)}\phi_{(f)0}^{(m)}\delta_{ij}]$$

$$-[\sigma_{(s)ij}^{(m')} - \sum_f \lambda_{(f)}\phi_{(f)0}^{(m')}\delta_{ij}]\eta_j^{(m)}\delta u_{(s)i}^{(m)} = 0 \tag{59}$$

and

$$\int_{t_1}^{t_2} dt\int dS[(\lambda_\phi^{(m)} + \lambda_{(f)})\phi_{(f)0}^{(m)}\delta u_{(f)i}^{(m)}$$

$$-(\lambda_\phi^{(m')} + \lambda_{(f)})\phi_{(f)0}^{(m')}\delta u_{(f)i}^{(m')}]\eta_i^{(m)} = 0 \tag{60}$$

Equations (59) and (60) are not very useful individually because the values of the $\lambda_{(f)}$'s are not known. However, by summing (60) over the fluids and adding the result to (59), we find that

$$\int_{t_1}^{t_2} dt\int dS\{[T_{(s)ij}^{(m)} - T_{(s)ij}^{(m')}]\eta_j^{(m)}\delta u_{(s)i}^{(m)}$$

$$+[\lambda_\phi^{(m)} - \lambda_\phi^{(m')}]\sum_f \delta w_{(f)i}^{(m)}\eta_i^{(m)}\} = 0 \tag{61}$$

where the total stress is

$$T_{(s)ij}^{(m)} = \tau_{(s)ij}^{(m)} + \lambda_\phi^{(m)}\delta_{ij}, \tag{62}$$

and we have used the fact that $\delta w_{(f)i}^{(m)}\eta_i^{(m)} = \delta w_{(f)i}^{(m')}\eta_i^{(m)}$. Equation (61) is very convenient because the variations with respect to $u_{(s)i}$ and the $w_{(f)i}$ are all independent. Furthermore, at an interface the variation of $u_{(s)i}$ need not vanish in general so (61) shows that the total stress at the interface is continuous

$$T_{(s)ij}^{(m)}\eta_j^{(m)} = T_{(s)ij}^{(m')}\eta_j^{(m)}. \tag{63}$$

The possible variations of $w_{(f)i}$ may be limited by special conditions at the interface that restrict the flow. Some examples of such conditions include: (*a*) misalignment of the pores, (*b*) insertion of a thin impermeable membrane between the porous media, and (*c*) surface damage of one or both due to abrasion. If the flow at the interface has not been restricted, then the variations $\delta w_{(f)i}$ may be arbitrary. In this case, equation (61) leads to the conclusion that

$$\lambda_\phi^{(m)} = \lambda_\phi^{(m')}. \tag{64}$$

Equation (64) is essentially a statement of the continuity of the hydrostatic pressure at the interface. (This point will be elaborated in the Discussion section.) However, if the flow has been restricted, then the hydrostatic pressure may not be continuous. In this case, equation (61) shows that the sum of the variations of the $w_{(f)i}$'s must vanish. This variation will vanish if the sum is a constant. Since the constant is assumed to vanish in the quiescent state, we conclude that (64) is replaced by

$$\sum_f w_{(f)i}^{(m)}\eta_i^{(m)} = 0. \tag{65}$$

Equation (65) states that the normal component of the *average* fluid displacement equals the normal component of the solid displacement at the interface.

Equation (61) does not require that the individual terms of (65) vanish (e.g., $w_{(g)i}^{(m)}\eta_i^{(m)} = 0$ is not necessary). In fact, equation (65) replaces (64) with a single equation whereas requiring the individual terms of (65) to vanish would cause the problem to be overdetermined.

The boundary conditions for dynamic poroelasticity derived in this section may be summarized as follows:

At a material surface, specify either

$$\sigma_{(s)ij}\eta_j \quad \text{or} \quad u_{(s)i} \tag{66}$$

and either

$$\lambda_\phi \quad \text{or} \quad \sum_f \phi_{(f)0}u_{(f)i}. \tag{67}$$

At an interface between two porous media, the quantities

$$u_{(s)i} \tag{68}$$

$$T_{(s)ij}\eta_j \tag{69}$$

$$w_{(f)i}\eta_i \tag{70}$$

must all be continuous and either

$$\sum_f w_{(f)i}\eta_i = 0 \quad \text{or} \quad \lambda_\phi \text{ is continuous.} \tag{71}$$

The boundary conditions for interfaces between porous media and either pure fluids or nonporous elastic solids may be obtained from (68)–(71) by letting the appropriate volume fractions vanish on the nonporous side of the interface.

Discussion

This section will elaborate some of the details of the previous sections.

Uniqueness Versus Boundary Conditions. For a bounded porous medium, the equations of poroelasticity have been shown to have unique solutions if (47) is satisfied at the material surface. The boundary conditions (66) and (67) guarantee that (47) holds and therefore uniqueness is assured. However, whereas the variational calculation *requires* (66) and (67), the uniqueness condition (47) is *not necessary* but only *sufficient*. In fact, uniqueness is guaranteed as long as the left-hand side of (47) remains nonpositive. The importance of this observation may be elucidated by considering the uniqueness problem for two porous media in contact at an interface. It is not difficult to show that (47) is then replaced by

$$\int dS\{[\hat{T}_{(s)ij}^{(m)} - \hat{T}_{(s)ij}^{(m')}]\eta_j^{(m)}\hat{u}_{(s)i}^{(m)} + [\hat{\lambda}_\phi^{(m)} - \hat{\lambda}_\phi^{(m')}]\sum_f \hat{w}_{(f)i}^{(m)}\eta_i^{(m)}\} \le 0. \tag{72}$$

With the boundary conditions (68)–(71), equality holds in (72) so uniqueness is again guaranteed. However, Deresiewicz and Skalak [2] have considered relaxing the boundary condition (71) and allowing what is essentially a surface permeability to exist at the interface. For partially saturated solids, we might suppose that

$$\dot{w}_{(f)i}\eta_i = -\frac{\kappa\,\kappa_{rf}}{\mu_{(f)}}(\lambda_\phi^{(m)} - \lambda_\phi^{(m')}) \tag{73}$$

where κ is a surface permeability, κ_{rf} is a surface relative permeability, and $\mu_{(f)}$ is the shear viscosity of the fluid. Then

$$\sum_f \dot{w}_{(f)i}\eta_i = -\frac{\kappa}{\mu}(\lambda_\phi^{(m)} - \lambda_\phi^{(m')}) \tag{74}$$

where

$$1/\mu \equiv \sum_f \kappa_{rf}/\mu_{(f)}. \tag{75}$$

Using (68)–(70) and (74) in (72) gives

$$-\int dS\frac{\kappa}{\mu}(\hat{\lambda}_\phi^{(m)} - \hat{\lambda}_\phi^{(m')})^2 \le 0 \tag{76}$$

which is certainly satisfied if $\kappa \ge 0$ and $\mu \ge 0$ hold as we expect. Thus, replacing (71) by (74) has not affected the uniqueness of the solutions.

The variational calculation requires (71). Equation (74) is consistent with (71) only when $\kappa = 0$ (the closed pore case) or when $\kappa = \infty$ (the open pore case). Except for these two limits, equation (74) is not consistent with the variational calculation. Even though the use of (74) with the equations of poroelasticity would still lead to unique solutions, those

Downloaded 02 May 2010 to 171.66.16.54. Redistribution subject to ASME license or copyright; see http://www.asme.org/terms/Terms_Use.cfm

solutions might not be physically reasonable and, therefore (74) should be used (if at all) with great caution.

If a thin, low permeability film is sandwiched between two porous media, calculations may be performed without (74) by giving the thin film a finite thickness and using the boundary conditions (68)–(71) at both film interfaces.

Quasistatic Density Variations. The analysis has been carried through so far without making any restrictions on the microstructural equations for density variation (32). However, for practical problems it may often be found that the microinertial factors $\Lambda_{(\xi)0}$ are small or that the frequencies of interest are so low that the left-hand side of (32) may be neglected. If so, then (32) shows that, in the absence of capillary pressure effects,

$$\lambda_\phi = -\tilde{\rho}^2_{(\xi)0} \frac{\partial E}{\partial \tilde{\rho}_{(\xi)}} \equiv -P_{(\xi)} \tag{77}$$

where $P_{(\xi)}$ is the pressure for constituent ξ [11]. It follows from (77) that the subscript may be dropped from P since all the constituent pressures are equal. Thus, λ_ϕ is just the hydrostatic stress (the negative of the hydrostatic pressure).

With this quasistatic approximation for the density variations, the equations can be simplified considerably. For fully saturated solids, the equations may be shown to reduce to Biot's theory [1] and the various constants may be given simple physical interpretations in terms of measurable quantities [16].

Acknowledgments

This work was performed under the auspices of the U.S. Department of Energy by the Lawrence Livermore National Laboratory under contract No. W-7405-ENG-48 and supported specifically by the Nuclear Test Containment Program.

References

1 Biot, M. A., "Theory of Propagation of Elastic Waves in a Fluid-Saturated Porous Solid. I. Low-Frequency Range," *J. Acoust. Soc. Am.*, Vol. 28, 1956, pp. 168–178.

2 Deresiewicz, H., and Skalak, R., "On Uniqueness in Dynamic Poroelasticity," *Bull. Seismol. Soc. Am.*, Vol. 53, 1963, pp. 783–788.

3 Plona, T. J., "Observation of a Second Bulk Compressional Wave in a Porous Medium at Ultrasonic Frequencies," *Appl. Phys. Lett.*, Vol. 36, 1980, pp. 259–261.

4 Berryman, J. G., "Confirmation of Biot's Theory," *Appl. Phys. Lett.*, Vol. 37, 1980, pp. 382–384.

5 Salin, D., and Schon, W., "Acoustics of Water Saturated Packed Glass Spheres," *J. Phys. Lett.*, Vol. 42, 1981, pp. 477–480.

6 Mochizuki, S., "Attenuation in Partially Saturated Rocks," *J. Geophys. Res.*, Vol. 87, 1982, pp. 8598–8604.

7 Murphy, W. F., "Effects of Partial Water Saturation on Attenuation in Massilon Sandstone and Vycor Porous Glass," *J. Acoust. Soc. Am.*, Vol. 71, 1982, pp. 1458–1468.

8 Bedford, A., and Stern, M., "A Model for Wave Propagation in Gassy Sediments," *J. Acoust. Soc. Am.*, Vol. 73, 1983, pp. 409–417.

9 Berryman, J. G., and Thigpen, L., "Nonlinear and Semilinear Dynamic Poroelasticity With Microstructure," *J. Mech. Phys. Solids*, in press.

10 Bedford, A., and Drumheller, D. S., "A Variational Theory of Porous Media," *Int. J. Solids Struct.*, Vol. 15, 1979, pp. 967–980.

11 Drumheller, D. S., and Bedford, A., "A Thermomechanical Theory for Reacting Immiscible Mixtures," *Arch. Rational Mech. Anal.*, Vol. 73, 1980, pp. 257–284.

12 Eringen, A. C., *Nonlinear Theory of Continuous Media*, McGraw-Hill, New York, 1962.

13 Green, A. E., and Adkins, J. E., *Large Elastic Deformations*, Oxford University Press, London, 1960.

14 Coleman, B. D., and Noll, W., "The Thermodynamics of Elastic Materials With Heat Conduction and Viscosity," *Arch. Rational Mech. Anal.*, Vol. 13, 1963, pp. 167–184.

15 Berryman, J. G., "Effective Conductivity by Fluid Analogy for a Porous Insulator Filled With a Conductor," *Phys. Rev. B*, Vol. 27, 1983, pp. 7789–7792.

16 Thigpen, L., and Berryman, J. G., "Mechanics of Porous Elastic Materials Containing Multiphase Fluid," LLNL UCRL-90610, Mar. 1984, to be published.

17 Love, A. E. H., *A Treatise on the Mathematical Theory of Elasticity*, Dover, New York, 1944, pp. 166–167.

18 Thomas, T. Y., *Plastic Flow and Fracture in Solids*, Academic Press, New York, 1961, p. 18.

Downloaded 02 May 2010 to 171.66.16.54. Redistribution subject to ASME license or copyright; see http://www.asme.org/terms/Terms_Use.cfm

Modeling Shrinkage Mechanisms in Porous Elastic Solids

S. C. Cowin
Professor of Mechanics,
Department of Biomedical Engineering,
Tulane University,
New Orleans, La. 70118
Fellow, ASME

This paper concerns the applications of a method of modeling the mechanism of shrinkage in porous elastic materials. Examples of the effects of shrinkage in porous elastic materials include the cracks that appear in the sun-dried gumbo at the bottom of a former mud puddle or in concrete, and the warping and cracking of drying lumber. The model for shrinkage is applied here for drying wood, but with an emphasis on the method and the generality of the results with regard to shrinkage in other materials. The model is able to predict the stresses, strains, deformation, and warping associated with wood drying.

Introduction

A method of modeling shrinkage mechanisms in porous elastic materials was described in [1]. This method is based on the theory of elastic materials with voids [2, 3]. The purpose of this paper is to illustrate the method of modeling shrinkage by applying it to the shrinkage of wood induced by drying. The drying of a microporous material such as wood or concrete varies with time in a manner determined by the heat and mass transfer processes. In this paper only the net shrinkage induced by a reduction in moisture content is considered, and the intermediate heat and mass transfer processes are not considered. These processes are well treated elsewhere [4–8]. The emphasis is placed here on the modeling of the shrinkage induced by the reduced moisture content.

In general, the swelling and shrinking of solid materials is due to the presence of a second constituent dispersed within the solid matrix. There are at least three ways in which the second constituent can cause the solid matrix to swell or to shrink. The first way is by the second constituent's changing its concentration at constant specific volume, an example of which is the absorption of water by a microporous solid. The second way is by the second constituent's changing its specific volume at constant concentrations. This second way is obviously coupled with thermal effects, e.g., different coefficients of thermal expansion in the second constituent. Examples of this second way include soil heaving due to the freezing of internal water, and the swelling induced by the thermal expansion of small, distributed gas bubbles within the solid matrix. The third way is simply a combination of the first two, that is to say where the swelling or shrinking occurs by some combination of changes in the concentration and in the specific volume of the second constituent. An example here is the drying of most microporous materials where a change in phase of the second constituent from liquid to gas accompanies the process. An object is viewed here as capable of swelling or shrinking if the overall volume or shape of the object can be changed by the internal concentration or specific volume changes in the second constituent without a change in the surface tractions and/or gravitational force acting on the object.

The basic features of the model for shrinking, the linear theory of elastic materials with voids, are reviewed in the next section. In the two sections that follow, a model shrinkage induced in wood by drying is suggested and illustrated by example. The paper closes with a discussion of the relationship of the linear theory of elastic materials with voids to the theory of coupled thermoelasticity and to the Biot theory of consolidation of elastic porous media. Also discussed are previous models of shrinking and swelling.

The Theory of Elastic Materials With Voids

There does not appear to be a theory among the traditional continuum theories that permits a porous body to enlarge or reduce the overall volume it occupies in the absence of body tractions and gravitation. There is such a mechanism, however, in the theory of elastic materials with voids [2, 3]. In this theory there is a field representation of the balance of self-equilibrated force systems at each point in the continuum. These self-equilibrated force systems can induce overall changes in the local bulk volume of the material. The theory is briefly described in this section.

The basic concept underlying the theory of elastic materials with voids is that of a material for which the bulk density ρ is written as the product of two fields – the density field of the matrix material γ and the volume fraction field ν, i.e., $\rho = \gamma\nu$. This representation of the bulk density of the material introduces an additional degree of kinematic freedom in the theory, the solid volume fraction ν. The linear theory of elastic materials with voids deals with small changes from a reference configuration of a porous body. In the reference configuration $\rho = \gamma\nu$ can be written as $\rho_R = \gamma_R\nu_R$ and it is

Contributed by the Applied Mechanics Division for presentation at the 1985 Joint ASME/ASCE Applied Mechanics, Bioengineering, and Fluids Engineering Conference, Albuquerque, N. Mex., June 24-26, 1985 of THE AMERICAN SOCIETY OF MECHANICAL ENGINEERS.

Discussion on this paper should be addresed to the Editorial Department, ASME, United Engineering System, 345 East 47th Street, New York, N.Y. 10017, and will be accepted until two months after final publication of the paper itself in the JOURNAL OF APPLIED MECHANICS. Manuscript received by ASME Applied Mechanics Division, June, 1984; final revision, September, 1984. Paper No. 85-APM-20.

Copies will be available until February, 1986.

Copyright © 1985 by ASME
Downloaded 02 May 2010 to 171.66.16.54. Redistribution subject to ASME license or copyright; see http://www.asme.org/terms/Terms_Use.cfm

assumed here that ν_R is spatially constant. As is customary in linear elasticity the reference configuration is assumed to be stress-free and strain-free.

The independent kinematic variables in the linear theory are the displacement field $u_i(\mathbf{x}, t)$ from the reference configuration and the change in volume fraction from the reference volume fraction, $\phi(\mathbf{x}, t)$,

$$\phi(\mathbf{x},t) = \nu(\mathbf{x},t) - \nu_R, \tag{1}$$

where $\mathbf{x}$ is the spatial position vector in cartesian coordinates and t is time. The infinitesimal strain tensor $E_{ij}(\mathbf{x}, t)$ is determined from the displacement field u_i by the relation

$$E_{ij} = \tfrac{1}{2}(u_{i,j} + u_{j,i}), \tag{2}$$

where the comma followed by a lowercase Latin letter indicates a partial derivative with respect to the indicated coordinate axes.

The equations of motion governing a linear-elastic continuum with voids are the balance of linear momentum,

$$\rho\ddot{u}_i = T_{ij,j} + \rho b_i, \tag{3}$$

and the balance of equilibrated force,

$$\rho k\ddot{\phi} = h_{i,i} + g + q, \tag{4}$$

where T_{ij} is the symmetric stress tensor, b_i is the body force vector, h_i is the equilibrated stress vector, k is the equilibrated inertia, g is the intrinsic equilibrated body force, and q is the extrinsic equilibrated body force. The extrinsic equilibrated body force q, which was denoted by ρl in [2, 3], is of major importance in the problem at hand. The interpretation of q is as a force system like a center of dilation in classical elasticity, but it is a center of dilation that exists at every point in the medium and which either acts at a distance or is externally controllable. Jenkins [9] suggested that q be interpreted as an externally controlled pore pressure. In modeling the shrinking mechanism q is equivalent to an internal, self-equilibrated, center of contraction field that exerts no external surface tractions. This point is discussed in detail in [1].

The constitutive equations for the linear theory of elastic materials with voids relate the stress tensor T_{ij}, the equilibrated stress vector h_i, and the intrinsic equilibrated body force g to the strain E_{ij}, the change in volume fraction ϕ, the time rate of change of the volume fraction $\dot{\phi}$, and the gradient of the change in volume fraction $\phi_{,i}$. For a material that is anisotropic, but which has a center of symmetry, these equations take the form

$$T_{ij} = C_{ijkm}E_{km} + B_{ij}\phi, \tag{5}$$

$$g = -\xi\phi - \omega\dot{\phi} - B_{ij}E_{ij} \quad \text{and} \quad h_i = A_{ij}\phi_{,j}, \tag{6}$$

where C_{ijkm}, B_{ij}, A_{ij}, ω, and ξ are functions of ν_R. In the case of isotropy, these constitutive relations have the representation

$$T_{ij} = \kappa\delta_{ij}E_{kk} + 2\mu\left(E_{ij} - \frac{1}{3}\delta_{ij}E_{kk}\right) + \beta\phi\delta_{ij}, \tag{7}$$

$$g = -\xi\phi - \omega\dot{\phi} - \beta E_{kk}, \quad \text{and} \quad h_i = \alpha\phi_{,i}. \tag{8}$$

The coefficients μ, α, β, ξ, ω, and $\kappa = \lambda + \frac{2}{3}\mu$ all depend on ν_R and μ, α, ξ, ω, and κ must be positive and β must satisfy the inequality $\kappa\xi \geq \beta^2$.

In this paper, only homogeneous shrinking deformations are considered. The quantities T_{ij}, E_{ij}, and ϕ are all assumed to be independent of position and, since body forces are neglected and the motion is assumed to be quasistatic, the equations of equilibrium are satisfied and will not be considered further. Also, under these conditions the balance of equilibrated force reduces to

$$q = \xi\phi + \omega\dot{\phi} + B_{ij}E_{ij}, \tag{9}$$

where q represents local centers of compression or dilation due to swelling or shrinking and ω and ξ are material constants.

Modeling the Shrinking Mechanisms in Drying Wood

The water in wood is divided into two types, *free water* and *bound water* [10]. Bound water is chemically bound within the wood cell walls. Free water is any water content in the wood above bound water. When the moisture content of wood is progressively reduced, the moisture content at which the cell walls are completely saturated (that is to say, all the bound water retained) but no water exists in the cell cavities (no free water) is called the *fiber saturation point* [11]. The fiber saturation point is generally about 30 percent moisture content. This is the moisture content below which the physical and mechanical properties of wood begin to change as a function of moisture content. The process of wood drying is generally considered to be the process of removal of the bound water.

It is important to note that the mechanisms for the removal of free and bound water from wood are different. Free water movement is through the wood pores and follows Darcy's law, that is to say the fluid moves down the water pressure gradient. Bound water movement has a different diffusion mechanism. It follows Fick's law and moves down the moisture concentration gradient. The movement of bound water is by liquid water diffusion across cell walls and by water vapor diffusion across void structures [11].

The loss of bound water from a wood cell causes the wood cell to shrink. There is a specific mechanism in wood for excessive shrinkage or collapse displayed by some wood species upon drying. Tiemann [12] suggested that this excessive shrinkage is caused by capillary tension forces on the water which completely fills the cell lumen. This water tension causes the cell walls to be completely pulled into the lumen as the lumen water is evaporated, thus greatly increasing the shrinkage of the wood specimen [13]. This bears some analogy to the process of obtaining a prune from a plum.

From this discussion one can conclude that the decreasing moisture content below the fiber saturation point will cause wood tissue to shrink. The local mechanism of shrinkage is the contraction of the cell. It is suggested here that the local force system causing the cellular contraction be represented as a center of contraction q. A constitutive equation for q would relate q to the amount of local moisture content below the moisture content at the fiber saturation point. One can infer from some existing data that this constitutive relation might be linear in the moisture content. It would also appear that most of this discussion could apply to other microporous materials like concrete.

The relation between q and the moisture content is the connecting link between the mechanism for shrinkage suggested in [1] and the theories for multiphase heat transfer in porous materials [4–8]. These theories give a basis for relating the local moisture content to the local thermodynamic conditions, heat and mass transfer processes, and transport phenomena. If the moisture transport and shrinkage theories were uncoupled, one could solve a shrinking problem associated with wood drying by first employing one of these theories to determine the moisture content field in the wooden object as a function of time due to the thermal and moisture environment of the wooden object. One could then use the constitutive equation to determine the q field from the moisture content field. The q field determined from the moisture content distribution would then be used in conjunction with the theory of elastic materials with voids to determine the shrinkage.[1] However, the moisture transport

[1] Note that the wood is modeled as a porous solid in which the pores of the solid are the portions of the wood volume that might contain free water and the matrix of the porous solid is an elastic material with voids. The volume of the wood that might contain bound water is thus modeled as the void portion of an elastic material with voids.

Downloaded 02 May 2010 to 171.66.16.54. Redistribution subject to ASME license or copyright; see http://www.asme.org/terms/Terms_Use.cfm

and shrinkage theories will be coupled in the sense of thermoelasticity, rather than uncoupled, and the moisture transport and shrinkage will have to be determined simultaneously. In the next section an example of a shrinkage calculation is presented. To illustrate the mechanism of shrinkage, only the asymptotic final shrunken state is determined. All the diffusive and relaxation mechanisms associated with material relaxation and the heat and mass transfer processes are neglected and a constant, homogeneous field q is assumed. Given the homogeneous field q, the shape and volume changes induced by shrinkage in a wooden object are determined. While this approach neglects much of the physics of the problem, it is physics that is well understood and treated in other models. The emphasis is thus placed on the determination of the shrinkage.

An Example of a Shrinkage Calculation

A problem of homogeneous shrinkage in wood is considered. The shrinking wooden object is assumed to be under no surface tractions so the stresses T_{ij} in (5) are zero. Only the final shrunken state is considered so that the time effects associated with the heat transfer process of moisture removal and other relaxation phenomena can be neglected. Time effects are neglected in the shrinking mechanism model by setting ω in (9) equal to zero and taking the value of q to be its constant asymptotic value. Substituting the condition that T_{ij} is zero into (5) and introducing the compliance tensor K_{rsij}, which is related to C_{ijkm} by

$$K_{rsij}C_{ijkm}=\delta_{rk}\delta_{sm}, \tag{10}$$

and introducing also a scalar constant of dimension stress,

$$\sigma=\xi-K_{kmij}B_{km}B_{ij}, \tag{11}$$

and a second-rank constant tensor of dimension one upon stress,

$$S_{km}=-\frac{1}{\sigma}K_{kmij}B_{ij}, \tag{12}$$

the following important formula relating the strain tensor to q is obtained:

$$E_{km}=S_{km}q. \tag{13}$$

The strain field therefore has a constant value determined by the asymptotic value of q and the tensor of material constants S_{km}.

Wood is known to have a cylindrical orthotropic symmetry [10, 14]. That means that the tensor S_{km} will take on a diagonal form in the appropriate cylindrial coordinate system and in no other material coordinate system. It will be easy, therefore, to determine the displacement field associated with the constant strain field (13) in the appropriate cylindrical coordinate system. Substitution of (2) into (13) and subsequent conversion from cartesian to the cylindrical coordinate system (r, θ, z) as well as recognition of the fact that S_{km} will be in a diagonal form in the cylindrical coordinate system yields the following three partial differential equations for the components u_r, u_θ, u_z of the displacement vector:

$$S_{rr}q=\frac{\partial u_r}{\partial r}, \quad S_{\theta\theta}q=\frac{1}{r}\frac{\partial u_\theta}{\partial\theta}+\frac{u_r}{r}, \quad S_{zz}q=\frac{\partial u_z}{\partial z}. \tag{14}$$

The solution to this system of equations, subject to the condition that the displacements and the rotations vanish at $r=0, z=0$, is

$$u_r=qS_{rr}r, \quad u_\theta=r\theta q(S_{\theta\theta}-S_{rr}), \quad u_z=qS_{zz}z. \tag{15}$$

It is convenient for later calculations to introduce the notation Q for the ratio of $S_{\theta\theta}$ to S_{rr},

$$Q=S_{\theta\theta}/S_{rr}, \tag{16}$$

thus

$$u_\theta=\theta u_r(Q-1). \tag{17}$$

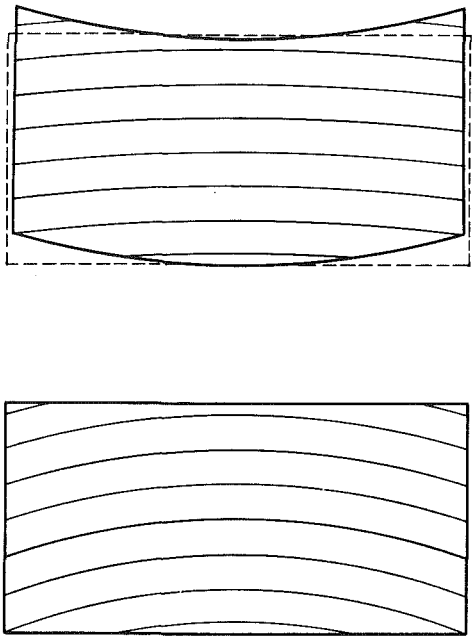


Fig. 1 The lower portion of this figure represents the transverse cross section of a piece of green lumber with a height-to-width ratio of 2:4. The circular arcs represent portions of growth rings. The upper portion of this figure represents the theoretically predicted transverse cross section after the shrinkage due to drying.

To illustrate the effect of this shrinking on an ordinary piece of lumber, it is convenient to transform the displacement field u_r, u_θ, u_z to cartesian components u_x, u_y and u_z. This transformation is accomplished by

$$u_x=u_r\cos\theta-u_\theta\sin\theta, \quad u_y=u_r\sin\theta+u_\theta\cos\theta, \quad u_z=u_z, \tag{18}$$

where

$$x=r\sin\theta, \quad y=r\cos\theta,$$

$$\theta=\tan^{-1}\frac{y}{x}, \quad r^2=x^2+y^2; \tag{19}$$

thus

$$u_x=qS_{rr}(x-\theta(Q-1)y), \quad u_y=qS_{rr}(y+\theta(Q-1)x),$$
$$u_z=qS_{zz}z. \tag{20}$$

Consider a piece of green lumber cut to a rectangular cross section with a ratio of 2:4. This piece of lumber is cut from a tree so that the long (four length units) edge is parallel to the tangent of the growth ring passing through its centroid and so that its centroid is six length units from the center of the tree. The cross section of this piece of lumber is illustrated in the lower portion of Fig. 1. The circular arcs in Fig. 1 represent growth rings. The cross-sectional shape of this piece of lumber will be determined in its shrunken, dried state using the displacement field (20) in cartesian coordinates. Multiples of u_x and u_y denoted by u and v, respectively, are defined by

$$u=\frac{u_x}{qS_{rr}}=x-\theta(Q-1)y, \quad v=\frac{u_y}{qS_{rr}}=y+\theta(Q-1)x \tag{21}$$

where Q is defined by (16). In this problem it is assumed that $Q = 1.4$, a very typical value for Q in wood. To determine the movement of the external edges of the two-by-four from its green to its shrunken dried state, the displacement u along the lines $x = 6\pm 1$, $|y| \le 2$,

$$u=6\pm1-0.4y\tan^{-1}\frac{y}{6\pm1}, \tag{22}$$

and v along the lines $y = \pm 2$, $5 \le x \le 7$,

Downloaded 02 May 2010 to 171.66.16.54. Redistribution subject to ASME license or copyright; see http://www.asme.org/terms/Terms_Use.cfm

$$v = \pm 2 + 0.4\tan^{-1}\frac{\pm 2}{x}, \tag{23}$$

are determined. These results are plotted with an arbitrary but uniform scale factor in the upper portion of Fig. 1. The increase in the radius of curvature of the growth rings due to the anisotropic shrinking process are also illustrated in Fig. 1.

This result illustrates the warping of wood in the plane of its transverse cross section. Significant warping is also observed in lumber along its long axis. This warping is manifested by the rotation of the transverse plane sections relative to one another. It would be obtained in the present model if one accounted for the actual conical orthotropic symmetry of wood rather than making the approximation of cylindrical orthotropic symmetry.

Discussion

There are two major and interrelated points to be made in this discussion. The first concerns the relationship of the theory of linear-elastic materials with voids to the theory of coupled thermoelasticity and to the Biot theory for the consolidation of elastic porous media. The second concerns certain previous suggestions for the modeling of shrinking or swelling in wood or composite materials.

Consider first the relationship of the theory of linear-elastic materials with voids to coupled thermoelasticity. The theory of coupled thermoelasticity is described by Boley and Weiner [15] and by Carlson [16]. If another theory has exactly the same structure of partial differential equations, but with different physical interpretation of the variable denoting temperature change in thermoelasticity, then the theory is said to be of the *quasistatic coupled thermoelastic type*. Quasistatic means that inertia terms are neglected. Biot [17] pointed out that his model of consolidating porous media (Biot [18, 19], see also Rice and Cleary [20]) was of the quasistatic coupled thermoelastic type. The fluid pressure in the pores of the Biot theory is analogous to the change in temperature in thermoelasticity. The quasistatic linear theory of elastic materials with voids is of the quasistatic coupled thermoelastic type if two changes are made in $(6)_1$. The first change is to set the constant ξ equal to zero and the second is to replace the term $B_{ij}E_{ij}$ by its time derivative $B_{ij}\dot{E}_{ij}$. In this case the change in solid volume fraction ϕ plays the same role as the change in temperature in thermoelasticity. This observation illuminates the three differences between the Biot theory or coupled thermoelasticity theory and the theory of linear-elastic materials with voids. First, the field variable that plays the role of the temperature change in thermoelasticity is fluid pressure in the Biot theory and change in volume fraction in the linear theory of elastic materials with voids. Second and third, the equation in the theory of elastic materials with voids analogous to the equation governing the temperature change in thermoelasticity (i.e., the conservation of energy) has one extra term in it and one term with a different structure. This extra term is proportional to the additional field variable and only vanishes when ξ is zero. The term with a different structure differs by a time derivative; the term $B_{ij}E_{ij}$ that appears in the theory of linear elastic materials with voids is replaced by the time derivative of this term in coupled thermoelasticity. Thus, there is both a physical and two mathematical differences between the Biot theory and the theory of elastic materials with voids. However, the mathematical difference between the two theories vanishes in the Laplace transform domain. This is because the Laplace transform of the derivative of a function is proportional to the Laplace transform of the function, hence Laplace transforms of functions can be combined with Laplace transforms of the derivatives of the same functions. It follows then that all three theories in the Laplace transform domain are of the quasistatic coupled thermoelastic type.

In linear thermoelasticity, the constitutive equation for stress relates the stress linearly to the strain and to the change in temperature from some reference temperature. Constitutive relations which are identical with the thermoelastic constitutive relation, but with the exception that some other variable plays the role of the temperature change, are said to be *constitutive relations of the linear thermoelastic type*. It is important to note that, while a theory of the quasistatic coupled thermoelastic type necessarily has a constitutive equation of the linear thermoelastic type, the existence in a theory of a constitutive equation of the linear thermoelastic type does not imply that the theory itself is of the quasistatic coupled thermoelastic type.

The constitutive equation (5) relates the stress to the strain and to the change in volume fraction. It is a constitutive relation of the linear thermoelastic type. One can view the first term on the right-hand side of (5), the term proportional to strain, as the elastic stress term and the second term, the term proportional to volume fraction, as the swelling stress or shrinking stress.

The first proposal for a constitutive equation of the linear thermoelastic type for swelling that has come to my attention is in the work of Halpin and Pagaro [21]. The connection and analogy to thermoelasticity is stated and explored by these authors. They introduce swelling strains and employ them in their study of anisotropic composites. The first proposal for a constitutive equation of the linear thermoelastic type for shrinking, which has come to my attention, is in the work of Gillis and Mark [22] who employed such a relation for the study of the shrinkage of pulp fibers. In a recent series of papers Lewis, Strada, and Comini [23], Lewis, Morgan, and Thomas [24], and Thomas [25] have analyzed the shrinkage induced in drying lumber using a constitutive relation of the thermoelastic type in conjunction with an elastic-plastic stress strain relation.

The theories for wood and for composites described in the foregoing, which involve constitutive relations of the thermoelastic type, are theories of the quasistatic *uncoupled* thermoelastic type. That is to say the shrinking strains are determined by a method independent of the elastic deformation of the body and are then used as input into a modified elasticity theory to determine the total stress and strain fields. Theories of this type do not allow for the interaction of the thermal field with the strain field that characterizes coupled thermoelasticity.

There are a number of distinctions to be made between the theory of shrinking discussed here and these earlier theories involving constitutive relations of the thermoelastic type. First, the present theory is coupled in the sense that it allows for the interaction between the shrinkage strain and the load-induced strain fields. Second, a kinematic variable is introduced in the presently proposed model to represent the solid volume fraction (or porosity) change. Third, self-equilibrated force systems are introduced to represent the shrinkage stresses. Fourth, the interaction of the porous elastic matrix with the shrinkage forces is represented by a constitutive relation. It is thought that most shrinkage mechanisms can be modeled with theories containing these features.

Acknowledgment

This work was supported by the Solid Mechanics Program of the National Science Foundation.

References

1 Cowin, S. C., "Mechanical Modeling of the Shrinking and Swelling of Porous Elastic Solids," *Advances in Rheology*, Vol. 3, *Polymers*, Mena, B., Garcia-Rejon, A., and Rangel-Nefaile, eds., Universedad Nacional Autonoma de Mexico, 1984, pp. 105–112; also to appear (with two additional figures) in *Journal of Rheology*.

2 Cowin, S. C., and Nunziato, J. W., "Linear Elastic Materials With Voids," *Journal of Elasticity*, Vol. 13, 1983, pp. 125–147.

Downloaded 02 May 2010 to 171.66.16.54. Redistribution subject to ASME license or copyright; see http://www.asme.org/terms/Terms_Use.cfm

3 Nunziato, J. W., and Cowin, S. C., "A Nonlinear Theory of Elastic Materials With Voids," *Archive for Rational Mechanics and Analysis*, Vol. 44, 1979, pp. 175-201.

4 Luikov, A. V., "Systems of Differential Equations of Heat and Mass Transfer in Capillary-Porous Bodies (Review)," *International Journal of Heat and Mass Transfer*, Vol. 18, 1975, pp. 1-14.

5 Huang, C. L. D., "Multi-Phase Moisture Transfer in Porous Media Subjected to Temperature Gradient," *International Journal of Heat and Mass Transfer*, Vol. 22, 1979, pp. 1295-1307.

6 Whitaker, S., "Toward a Diffusion Theory of Drying," *Ind. Eng. Chem. Fundam.*, Vol. 16, 1977, pp. 408-414.

7 Whitaker, S., "The Transport Equations for Multi-Phase Systems," *Chemical Engineering Science*, Vol. 28, 1973, pp. 139-147.

8 Harmathy, T. Z., "Simultaneous Moisture and Heat Transfer in Porous Systems With Particular Reference to Drying," *I/EC Fundamentals*, Vol. 8, 1969, pp. 92-103.

9 Jenkins, J. T., "Static Equilibrium of Granular Materials," ASME JOURNAL OF APPLIED MECHANICS, Vol. 42, 1975, pp. 603-608.

10 "Wood Handbook: Wood as an Engineering Material," U.S. Forest Products Laboratory, U.S. Government Printing Office, 1974.

11 Hart, C. A., *The Drying of Wood*, The North Carolina Agricultural Extension Service, Ext. Cir 471, Feb. 1968.

12 Tiemann, H. D., *Wood Technology*, Dilman, New York, 3rd ed., 1951.

13 Hart, C. A., Przestrzelski, P. J., and Wheeler, F. J., "Entrapped Lumen Water in Hickory During Desorption," *Wood Science*, Vol. 6, No. 4, 1974, pp. 356-362.

14 Gillis, P. P., "Orthotropic Elastic Constants of Wood," *Wood Science and Technology*, Vol. 6, 1972, pp. 138-156.

15 Boley, B. A., and Weiner, J. H., *Theory of Thermal Stresses*, Wiley, New York, 1960.

16 Carlson, D. E., "Linear Thermoelasticity," *Handbuch der Physik*, Vol. VI *a*/2, 1972, pp. 297-346.

17 Biot, M. A., "Thermoelasticity and Irreversible Thermodynamics," *Journal of Applied Physics*, Vol. 27, 1956, pp. 240-253.

18 Biot, M. A., "General Theory of Three-Dimensional Consolidation," *Journal of Applied Physics*, Vol. 12, 1941, pp. 155-164.

19 Biot, M. A., "Theory of Elasticity and Consolidation for a Porous Anisotropic Solid," *Journal of Applied Physics*, Vol. 26, 1955, pp. 182-185.

20 Rice, J. R., and Cleary, M. P., "Some Basic Stress Diffusion Solutions for Fluid-Saturated Elastic Porous Media With Compressible Constituents," *Rev. Geophysics Space Phys.*, Vol. 14, 1976, pp. 227-241.

21 Halpin, J. C., and Pagano, N. J., "Consequences of Environmentally Induced Dilatation in Solids," Air Force Materials Lab. Tech. Report 68-395, 1969.

22 Gillis, P. P., and Mark, R. E., "Analysis of Shrinkage, Swelling and Twisting of Pulp Fibers," *Cellulose Chemistry and Technology*, Vol. 7, 1973, pp. 209-234.

23 Lewis, R. W., Strada, M., and Comini, G., "Drying Induced Stresses in Porous Bodies," *International Journal of Numerical Methods in Engineering*, Vol. 11, 1977, pp. 1175-1184.

24 Lewis, R. W., Morgan, K., and Thomas, H. R., "Drying-Induced Stresses in Porous Bodies—An Elastoviscoplastic Model," *Computer Methods in Applied Mechanics and Engineering*, Vol. 20, 1979, pp. 291-301.

25 Thomas, H. R., "Numerical Analysis of Drying Induced Stresses in Timber: An Orthotropic Model," *Mechanics of Materials*, Vol. 2, 1983, pp. 249-263.

Downloaded 02 May 2010 to 171.66.16.54. Redistribution subject to ASME license or copyright; see http://www.asme.org/terms/Terms_Use.cfm

Response of an Elastic Plate to Localized Transient Sources

N. Vasudevan[1]

A. K. Mal

Professor.
Mem. ASME

Mechanical, Aerospace, and Nuclear Engineering Department, School of Engineering and Applied Science, University of California, Los Angeles, Calif. 90024

The surface response of an infinite, homogeneous elastic plate to an internal dislocation across an infinitestimal area is investigated. As a companion problem, the normal displacement of the plate surface due to a time-dependent surface load is also calculated. The first problem is relevant for the detection of crack initiation in structural materials through the analysis of high-frequency elastic waves generated by the event. The solution to the second problem is needed for the calibration of test equipment used in the detection of the waves. The problems are formulated by means of a classical integral transform in the frequency domain and the spectral response of the plate is expressed in terms of the modal contributions due to the real, imaginary, and complex roots of the Rayleigh-Lamb equation. Time histories of the response are obtained through the inversion of the spectra by a Fast Fourier Transform (FFT) routine.

1 Introduction

The response of an elastic plate to surficial and internal disturbances is primarily influenced by the nature of the source and by the dispersive wave motions that occur within the plate. Theoretical response curves are useful in studying the waveforms generated by dislocation type sources in order to characterize them. Surface load-generated motions can be used for the calibration of transducers that are employed in Acoustic Emission (AE) experiments.

Forced vibration problems of infinite and semi-infinite plates have been discussed by Miklowitz (1978) where references to early work can be found. More recently transient wave propagation in infinite plates due to point sources was given detailed attention in the work of Ceranoglu and Pao (1981). Although the generalized ray theory employed by these authors yields exact results within a specific time interval, it is much too cumbersome at radial distances of several plate thicknesses due to the large number of ray integrals that have to be numerically evaluated. Computations at field points beyond six plate thicknesses were not considered feasible by the authors. An attempt to overcome this drawback was made by Weaver and Pao (1983) using the method of normal modes. In this method the authors began with a finite plate whose response could be described by a double infinite sum over the wave number and the eigenfrequencies. As the radius of the plate becomes infinite the wave number sum is replaced by an integral. Thus the final result is the sum of modal responses each of which is an infinite integral over the wave number. The vertical displacements of the surface due to an applied vertical surface point force were calculated.

We present an alternative method based on a classical integral transform technique. Working in the frequency domain we first obtain the spectral response by summing the residues at the real, imaginary and complex roots of the Rayleigh-Lamb (RL) dispersion equation. An FFT inversion gives the transient response. We compare our results with those of Weaver and Pao (1983) for a concentrated step load. Additional results are presented for a pulse load of different nature and for an embedded dislocation type source.

2 The Dislocation Source at Depth

We assume that the plate has thickness H and its material has the P-wave speed α, S-wave speed β, density ρ, and shear modulus μ. A dislocation source is characterized by its depth z, direction of slip, and the inclination of the slip plane. We locate a coordinate system as shown in Fig. 1, and introduce parameters δ, λ, r, θ where:

δ = dip angle, angle between slip plane and x_1x_2 plane;
λ = rake angle, angle between slip direction and x_1 axis; and
r,θ = polar coordinates of the observation point.

Since it proves convenient for us to work in the frequency domain, the time dependence is eliminated by a Fourier transformation. For reasons to be given later, we introduce a complex frequency, $\omega - i\epsilon$ by adding to it a small imaginary part, $-i\epsilon$, where ω is real and ϵ is positive. For any general field varilable $p(\mathbf{x},t)$ and its transform $P(\mathbf{x}, \omega-i\epsilon)$ we define a Fourier transform pair by,

$$P(\mathbf{x},\omega-i\epsilon) = \int_0^\infty p(\mathbf{x},t)\, \exp(-i(\omega-i\epsilon)t)\, dt$$

$$p(\mathbf{x},t) = (1/2\pi) \int_{-\infty}^{+\infty} P(\mathbf{x},\omega-i\epsilon)\, \exp(\epsilon t + i\omega t)\, d\omega \quad (2.1)$$

[1] Present address: 105-50 Firestone Labs., Caltech, Pasadena, Calif. 91125.

Contributed by the Applied Mechanics Division for publication in the JOURNAL OF APPLIED MECHANICS.

Discussion on this paper should be addressed to the Editorial Department ASME, United Engineering Center, 345 East 47th Street, New York, N.Y. 10017, and will be accepted until two months after final publication of the paper itself in the JOURNAL OF APPLIED MECHANICS. Manuscript received by ASME Applied Mechanics Division, August, 1983; final revision, April, 1984. Paper No. 85-APM-11.

Copyright © 1985 by ASME
Downloaded 02 May 2010 to 171.66.16.54. Redistribution subject to ASME license or copyright; see http://www.asme.org/terms/Terms_Use.cfm

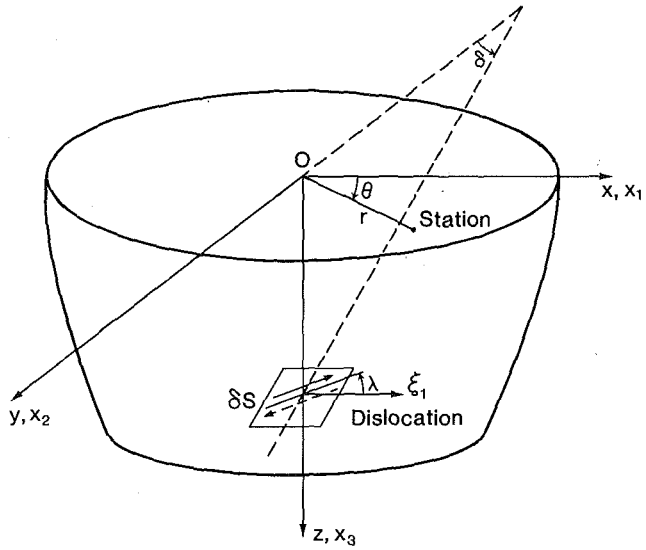


Fig. 1 The geometry of an embedded dislocation in the plate

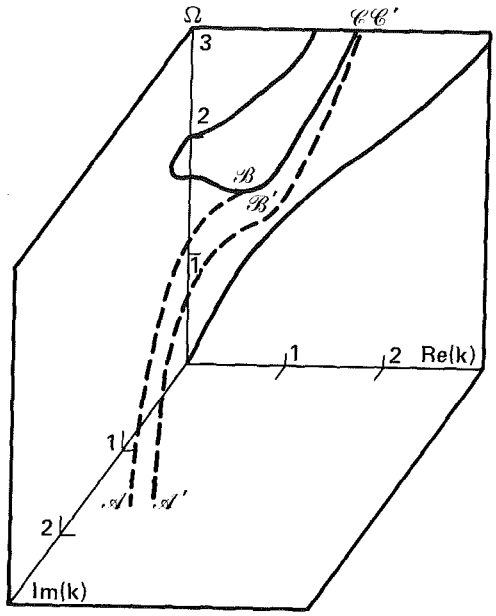


Fig. 2 Behavior of the second symmetric complex mode of the plate for complex frequencies

With the understanding that all variables have been time transformed as in (2.1) the displacement field may be expressed in the form (see, e.g., Mal, 1972, Kennett, 1983)

$$U_k(\mathbf{x},\omega) = \int_S [U_i(\xi,\omega)]^{+}_{-} T_{ij}^{(k)} n_j \, dS(\xi) \tag{2.2}$$

where

$U_k(\mathbf{x}, \omega)$ = displacement in k-direction at position $\mathbf{x}$. $[U_i(\xi, \omega)]^{+}_{-} = D_i F(\omega)$ = displacement jump across the dislocation at ξ. $F(\omega)$ = Fourier transform of the time-dependent part of the dislocation $f(t)$. $T_{ij}^{(k)}(\mathbf{x}, \xi)$ = ij-component of stress at ξ due to a unit force applied in k-direction at $\mathbf{x}$. n_j = j-component of unit normal vector to $dS(\xi)$. $dS(\xi)$ = elemental dislocation area.

Every infinitesimal area S contributes a displacement given by,

$$\delta U_k(\mathbf{x},\omega) = D_i F(\omega) T_{ij}^{(k)} n_j \, \delta S \tag{2.3}$$

The representation (2.3) forms the basis of our analysis of a point source of internal dislocation.

In what follows a subscript or superscript S indicates a shear dislocation and N indicates a normal dislocation. If D is the magnitude of a shear dislocation, then the cartesian components of the displacement due to the slip are given by (c. f. Harkrider, 1964),

$$\begin{aligned}\delta U_k^S(\mathbf{x},\omega) = (\delta M_S/\mu) F(\omega) \; (&(\cos\lambda\sin\delta) T_{23}^{(k)} \\ &- (\cos\lambda\cos\delta) T_{13}^{(k)} + (\sin\lambda\cos 2\delta) T_{21}^{(k)} \\ &+ (1/2)(\sin\lambda\sin 2\delta)(T_{33}^{(k)} - T_{22}^{(k)}))\end{aligned} \tag{2.4}$$

where δM_S is the seismic moment of the slip.

$$\delta M_S = \mu D_S \, \delta S \tag{2.5}$$

For the normal dislocation a similar analysis gives,

$$\begin{aligned}\delta U_k^N(\mathbf{x},\omega) = (\delta M_N/\mu) F(\omega) \; (&(\sin^2\delta) T_{22}^{(k)} \\ &+ (\cos^2\delta) T_{33}^{(k)} - (\sin 2\delta) T_{23}^{(k)})\end{aligned} \tag{2.6}$$

where

$$\delta M_N = \mu D_N \, \delta S \tag{2.7}$$

It should be noted that the application of the representation theorem (2.3) has reduced the dislocation problem to a well-posed boundary value problem of the plate in which no internal dislocation is present, but instead, a unit time-harmonic force acts at the field point on the plate surface. If the objective is the calculation of the k-component of the surface displacement at $\mathbf{x}$, then the point force must be applied along the x_k-axis at that location and the resulting traction components $T_{ij}^{(k)} n_j$ on the surface element dS in the interior of the plate must be calculated. The formal solution to this auxiliary problem can be obtained by standard integral transform methods. We have employed a Hankel transform technique followed by a propagator matrix formulation (see, e.g., Kennet, 1983) that has been widely used in the seismological literature. The main advantage of this formulation is that it can be easily extended to deal with the multilayered plate problem.

3 The Surface Source Problem

The displacement, velocity, and acceleration components normal to the plate surface ("vertical") are measured in most AE experiments. According we will restrict our calculations to the z-component of the surface displacement. We assume that a point force $F(\omega)\exp(i\omega t)$ acts along the z-axis at 0 (Fig. 1). Our task is to calculate the stress components $T_{ij}^{(3)} n_j \exp(i\omega t)$ at an interior point (x,y,z) for given normal vector n. In addition, as indicated earlier the vertical component of the displacement on the two faces of the plate, $z=0, H$ are also of interest. In subsequent discussions the time factor $\exp(+i\omega t)$ and the superscript (k) will be omitted for convenience.

For the normal force case the boundary conditions at $z=0$ may be expressed in the form,

$$T_{rz} = T_{\theta z} = 0$$

$$T_{zz} = -\delta(r)/(2\pi r) = -(F(\omega)/2\pi)\int_0^\infty k J_0(kr)\, dk \tag{3.1}$$

where $\delta(r)$ in the Dirac delta function and the last integral is its well-known representation.

Let $U(r,z)$ and $W(r,z)$ denote the radial and "vertical" components of the displacements within the plate and $S(r,z)$ and $T(r,z)$ the (zz) and (rz) components of the stress tensor. Further, let $\bar{U}, \bar{W}, \bar{S}, \bar{T}$ denote their Hankel transforms defined through the relations,

$$U(r,z) = (-F(\omega)/\omega)\int_0^\infty \bar{U}(k,z)\, k J_1(kr)\, dk$$

$$W(r,z) = (-iF(\omega)/\omega)\int_0^\infty \bar{W}(k,z)\, k J_0(kr)\, dk$$

Downloaded 02 May 2010 to 171.66.16.54. Redistribution subject to ASME license or copyright; see http://www.asme.org/terms/Terms_Use.cfm

$$S(r,z) = (+iF(\omega)) \int_0^\infty \bar{S}(k,z)\, k J_1(kr)\, dk$$

$$T(r,z) = F(\omega) \int_0^\infty \bar{T}(k,z)\, k J_0(kr)\, dk \tag{3.2}$$

In the propagator matrix formulation a "stress-displacement" vector $\bar{R}(k,z)$ is defined by,

$$\bar{R}(k;z) = [\bar{U}(k,z)/c,\ \bar{W}(k,z)/c,\ \bar{S}(k,z),\ \bar{T}(k,z)]^T \tag{3.3}$$

where $c = \omega/k$, and the explicit dependence of the field quantities on k has been suppressed.

It can be shown that $\bar{R}(z)$ satisfies a system of first-order ordinary differential equations in $0 < z < H$, and that its value at any level z_1 can be related to that at another level z_2 in the form,

$$\bar{R}(z_1) = P(z_1,z_2)\bar{R}(z_2),\ 0 < z_1, z_2 < H \tag{3.4}$$

where $P(z_1,z_2)$ is the propagator matrix (Kennet, 1983). Assuming $z_1 = 0$, $z_1 = H$ in the foregoing,

$$\bar{R}(H) = [A]\bar{R}(0) \tag{3.5}$$

The elements of $[A]$ can be found in Haskell (1953), Harkrider (1964), and also in Mal, Kundu, and Xu (1984).

It should be noted that the stress displacement vector is continuous across the welded interface between two dissimilar media, so that the preceding relations can also be applied to the multilayered plate problem with minor modifications.

For the given boundary conditions,

$$\bar{R}(0) = [\bar{U}(0)/c,\ \bar{W}(0)/c,\ -k/2\pi,\ 0]^T$$

and

$$\bar{R}(H) = \bar{U}(H)/c,\ \bar{W}(H)/c,\ 0,\ 0]^T \tag{3.6}$$

Thus, equation (3.5) gives four linear equations for the four unknown surface displacements. Their solution may be expressed in the form,

$$\begin{aligned}
\bar{U}(\bar{k},0) &= G_1/D_S + G_2/D_{AS} \\
\bar{U}(\bar{k},H) &= G_1/D_S - G_2/D_{AS} \\
\bar{W}(\bar{k},0) &= G_4/D_S + G_3/D_{AS} \\
\bar{W}(\bar{k},H) &= -G_4/D_S + G_3/D_{AS}
\end{aligned} \tag{3.7}$$

The expressions for G_1, G_2, G_3, G_4, D_s, and D_{AS} are given in Appendix A. The denominators D_S and D_{AS} are the familiar symmetric and antisymmetric RL expressions, respectively, for the time-harmonic motion in a plate of thickness H. The quantity $\bar{k}$ is a dimensionless wave number which is related to k through.

$$\bar{k} = kH/\pi \tag{3.8}$$

Equations (3.7) give the symmetric and antisymmetric parts of the Hankel transformed surface displacements on both faces of the plate. The stress-displacement vector in the interior of the plate can be determined by means of (3.4) and (3.7). The other stress components which appear in (2.4) and (2.6) can be directly calculated from the displacements components given by (3.2).

4 The Spectral Response

It can be seen from the foregoing that in both problems the calculation of the surface displacement spectra required the evalution of integrals of the form,

$$I(r,z,\omega) = \int_0^\infty (F_1(k)/D_S(k))\, kJ_n(kr)\, dk + \int_0^\infty (F_2(k)/D_{AS}(k))\, kJ_n(kr)\, dk \tag{4.1}$$

where n is either zero or one and the ω, z dependence of F_1, F_2 has been suppressed. For a given real value of frequency ω, both D_S and D_{AS} posses a finite number of real and infinite number of imaginary and complex zeros. These represent the symmetric and antisymmetric modes of the plate. For complex values of frequency $\omega - i\epsilon$, the zeros of D_S and D_{AS} are shifted off the real k-axis. In the limit as $\epsilon \to 0$, the poles for which $d\omega/dk > 0$ approach the real axis from below and those for which $d\omega/dk < 0$ approach it from above. Since the integrand in (4.1) is an odd function of k and is well behaved at $k = 0$ and $k = \infty$, we can rewrite it in the form,

$$I = (1/2)\int_{-\infty}^{+\infty} (F_1(k)/D_S(k))\, kH_n^{(2)}(kr)\, dk + (1/2)\int_{-\infty}^{+\infty} (F_2(k)/D_{AS}(k))\, kH_n^{(2)}(kr)\, dk \tag{4.2}$$

where $H_n^{(2)}$ is the Hankel function of the second kind. This choice of the Hankel function is the only one possible for the chosen time dependence, $\exp(i\omega t)$ that will ensure an outgoing wave field for large radial distances from the source. Further details of these and related aspects can be found in Ewing et al. (1957) and in Mal (1974). It can be shown that the integrands of (4.1) do not possess any branch points in the complex k-plane since they are even functions of the radicals η_α and η_β (defined in Appendix A) and satisfy Jordan's lemma on a large semicircle in the lower half plane. The path of integration can then be closed by a large semicircle in the lower half of the complex k-plane and the response of the plate can be written entirely as a sum of residues in the form,

$$I = i\pi \sum_j (F_1(k_j)/D_S'(k_j))\, k_j H_n^{(2)}(k_j r) + i\pi \sum_j (F_2(k_j)/D_{AS}'(k_j))\, k_j H_n^{(2)}(k_j r) \tag{4.3}$$

where the primes indicate differentiation with respect to k. The symmetric and antisymmetric modal responses can be calculated separately from (4.3).

5 Numerical Procedure and Results

5.1 Root Determination. The RL Spectrum is usually characterized in terms of the dimensionless wave number $\bar{k}$ and a frequency Ω defined by,

$$\Omega = \omega H/(\pi\beta) \tag{5.1}$$

The numerical calculations were carried out for a glass plate with properties, $\alpha = 5.76$ Km/sec, $\beta = 3.49$ Km/sec, and $\mu = 2.8E+13$ Kg/(Km sec^2), which correspond to a Poisson's ratio of 0.21. This was considered sufficient to illustrate the calculation procedure since the computer programs developed for this purpose can be used for arbitrary material properties. A thickness H of 0.96 cm was used for the force response problem and that of 1.0 cm for the dislocation problem.

The RL equations $D_S = 0$ and $D_{AS} = 0$ can be used directly to compute the real and purely imaginary wave numbers for preselected real values of frequency (Ω) and Poisson's ratio. Two bracketing methods, the bisection scheme as well as the method of false position (Regula Falsi) were used to determine the preceding roots. All complex roots lying within a given rectangular region were also determined. A subroutine available in the IMSL package utilizing an iterative procedure called Muller's method was very successful in determining these roots within 10–20 iterations. A guessed value for each root to be found is necessary as an input to the routine. It has been shown that the complex modes meet the real $\Omega - \bar{k}$ plane at points where the slope $d\Omega/d\bar{k} = 0$ (Mindlin, 1955). This occurs for the second S and the third AS modes within the range of frequencies of interest. The routine used in the foregoing was able to uncover a complex loop in the vicinity of the sixth AS mode as well.

Downloaded 02 May 2010 to 171.66.16.54. Redistribution subject to ASME license or copyright; see http://www.asme.org/terms/Terms_Use.cfm

5.2 The Use of the Complex Fourier Transform. The behavior of the integrand of (4.2) at the cutoff frequency of each mode is unlike its behavior at any other frequency point. As the wave number approaches zero for a fixed frequency equal to any of the nonzero cutoff frequencies either for an S or AS mode, the corresponding function D_S or D_{AS} approaches a double zero. However, the numerators of (4.2) also vanish simultaneously. It can be shown that the integrand then approaches a constant for some of the modes and a simple pole singularity for the others. This is true for both the force and dislocation problems. The case of $\omega = 0$ is an exception since here the singularity is of higher order than a simple pole. In all such cases the residue expression (4.3) is not valid. The use of complex frequency causes the numerator of (4.2) to be strictly nonzero and the denominator to have simple zeros at all frequencies. The given residue expression then holds good at each pole.

For a plate, higher-order singularities other than those at $\omega = 0$ also exist. In the frequency range of interest these are the *minima of the second S, the third AS, and the sixth AS* modes. As we approach these modes from above along the frequency axis they become two valued below their respective cutoffs and these two zeros approach each other as we tend to the minimum point. They ultimately coincide at the minimum and form a double pole. In the force response case, it can be seen by mere inspection of the expressions that the numerator is stricly nonzero here. This implies that the original Hankel inversion integrals are in fact not defined for such a frequency. If we invert this mode directly large sinusoidal oscillations (25 percent of the peak response values) are produced from $t = 0$ onward leading to pre P-wave arrivals.

The usefulness of complex frequency was first indicated by Folk et al. (1958) in a different context. Shown in Fig. 2 is the effect of complex frequency on the second symmetric mode denoted by the branch $\mathfrak{A}\,\mathfrak{B}\,\mathfrak{C}$. The dispersion curve for this code becomes detached from its mirror image (not shown) and pulls away form the real Ω-$\bar{k}$ plane toward negative imaginary $\bar{k}$ where it is denoted by $\mathfrak{A}'\mathfrak{B}'\mathfrak{C}'$. Exactly the same effect is produced on the mirror image branch in the positive real $\bar{k}$ direction. Numerically, one finds the effect of the double pole fading away as frequency is perturbed away from the real plane. To calculate the new wave number a Taylor series expanions about the real frequency gives the imaginary increment $-i\bar{\epsilon}\ (d\bar{k}/d\Omega)$ provided $\bar{\epsilon}$ is small enough for us to ignore higher order terms, where $\bar{\epsilon}$ is related to ϵ (defined earlier) through,

$$\bar{\epsilon} = \epsilon H/(\pi\beta) \tag{5.2}$$

It is only for positive $d\bar{k}/d\Omega$ that the roots are included in contour integration in the $\bar{k}$-plane.

Usually this complex increment is so small that a two-term series expansion proves sufficient. Two higher-order terms were computed to check the convergence of the series. The Taylor series for $\bar{k}$ as a function of Ω theoretically breaks down in the vicinity of the singular points discussed earlier. However, an approximate relationship of Ω as a function of $\bar{k}$ valid in the neighboring region can be written down at these points. This represents a solution of the RL equations in the immediate neighborhood of these singularities. If Ω is then perturbed the resulting value of $\bar{k}$ can be computed by inverting this relation. These calculations show that the Taylor series for $\bar{k}(\Omega)$ does not break down until we approach well within one frequency sampling division of the singular point.

5.3 The Force Response. The relation (3.2) written in the form (4.3) was used to compute the surface displacement for a given value of r. In principle the evaluation of (4.3) requires the knowledge of the infinite number of real, imaginary, and complex roots of the dispersion equation at each frequency. However, for numerical analysis, roots that lie beyond a certain distance above the real $\bar{k}$-axis can be ignored. Shown in Fig. 3 is the natural log of absolute value of the expression, $|\bar{W}(\bar{k},0)\,H_0^{(2)}(\bar{k}\pi r/H)|$, plotted versus distance above the real axis in the dimensionless wave number plane. The calculation is done for a frequency of 1MHz for the glass plate and for $\mathrm{Re}(\bar{k}) = 0.5$. The figure shows that on the top surface of the plate (where the load has been applied), the contribution from a complex root decreases rapidly with distance along the imaginary $\bar{k}$ axis. For an observation point at a radial distance of one-plate thickness the amplitude of the spectral displacement decreases by a factor of approximately exp (-10), and by exp(-20) at a radial distance of two-plate thicknesses, if the imaginary part of $\bar{k}$ changes by three units. This implies that for ranges beyond a single-plate thickness, roots lying beyond three units of imaginary $\bar{k}$ cannot contribute significantly to the spectra. This is also true for purely imaginary roots.

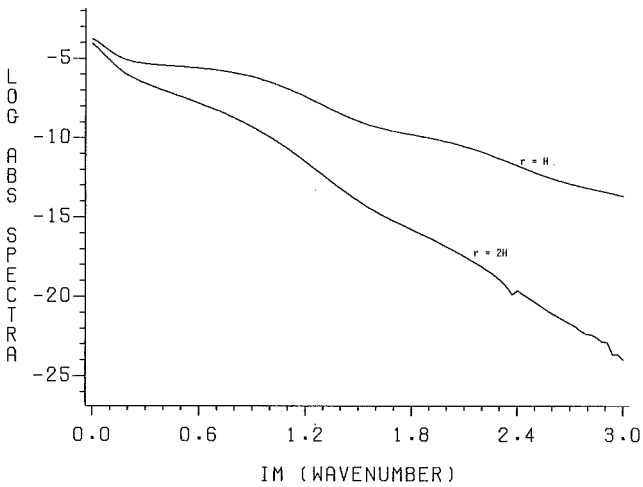


Fig. 3 Decay of a typical residue expression with imaginary wave number, for Re($\bar{k}$) = 0.5

The behavior of the spectra near $\omega = 0$ and ∞ has to be known before performing the inversion. An unbalanced force system typically leads to singularities in the frequency spectrum. For an applied step load, the frequency behavior shown by the first AS mode is given by, $C_1\ln(\omega)/\omega^2 + C_2/\omega^2 + 0(\ln\omega/\omega)$ as $\omega \to 0$, and by, $C_3\omega^{-1/2} + 0(\omega^{-3/2})$ as $\omega \to \infty$. The spectra in the first symmetric mode behaves like, $C_4\ln(\omega)/\omega + 0(\ln\omega)$ as $\omega \to 0$ and like, $C_5\omega^{-1/2} + 0(\omega^{-3/2})$ as $\omega \to \infty$ where C_1, C_2, C_3, C_4, C_5 are in general complex constants. The higher modes are nonexistant near $\omega = 0$ and their spectra approach logarithmic infinities near their respective cutoffs.

For a singularity of the type $1/\omega$ near $\omega = 0$, the FFT procedure can be used to invert the spectra directly without filtering out the static value (at $\omega = 0$) first. This leads to an accurate FFT inversion within any selected time window provided the frequency sampling interval is chosen sufficiently small. However, for the first AS mode the blowup near $\omega = 0$ is so rapid that numerical inversion using the FFT is difficult even for relatively small frequency intervals. Use of complex frequency does not alleviate the problems encountered in the first AS mode step response. Although there are other ways of inverting the first AS mode for the step load, the purpose of instrument calibration does not require this result.

The geometry for the force problem is the same as that used by Weaver and Pao (1983) except that their vertical coordinate is upward. To compare our results with theirs we show some individual modal responses of the vertical displacement 10 cm away from an applied step load. The plate properties are identical to those used by them. Our horizontal coordinate is a nondimensional time t^* defined by,

Downloaded 02 May 2010 to 171.66.16.54. Redistribution subject to ASME license or copyright; see http://www.asme.org/terms/Terms_Use.cfm

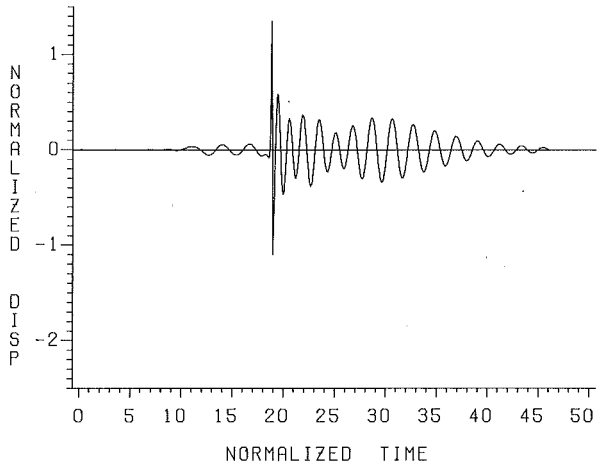


Fig. 4 Vertical displacement in the first *S* mode for a vertical step load. Plate thickness $H = 0.96$ cm for Figs. 4–7. $C = 0.924E(+11)$.

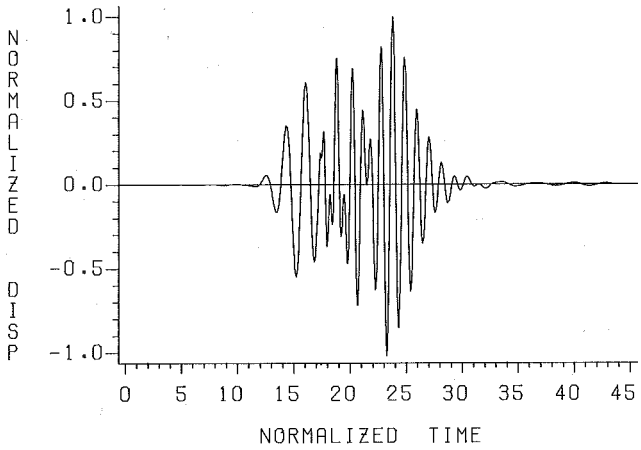


Fig. 5 Vertical displacement in the second *AS* mode, $C = 0.1213E(+11)$

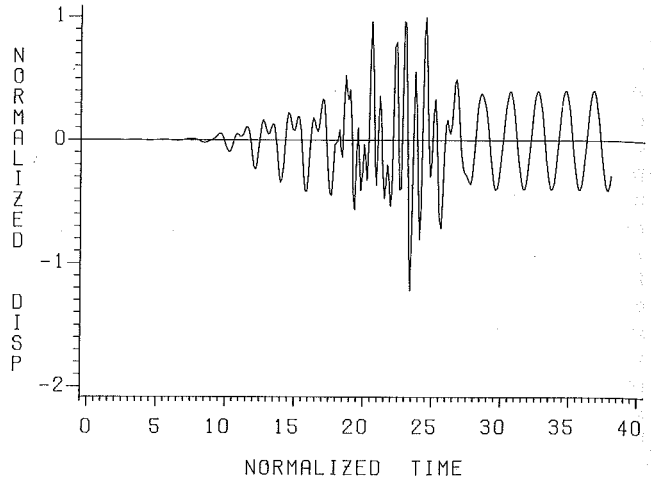


Fig. 6 Vertical displacement in the second *S* mode, $C = 0.8200E(+10)$

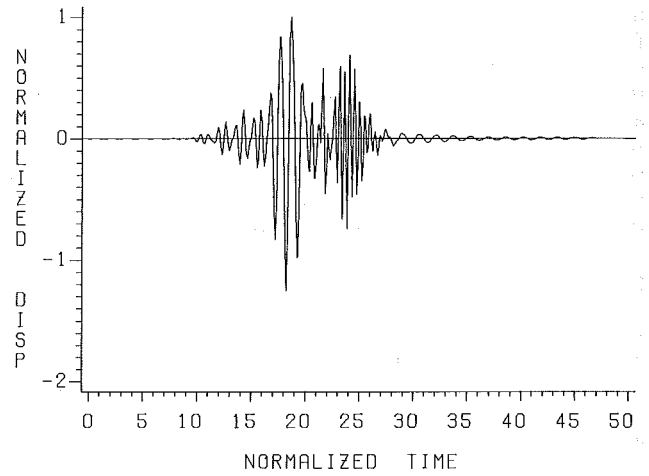


Fig. 7 Vertical displacement in the third *S* mode, $C = 0.1337E(+10)$

$$t^* = t\alpha/H$$

The vertical axis is a nondimensional displacement U^* given by,

$$U^* = U/[4\pi^3\mu\beta^2 C/H^2]$$

where C is the maximum positive value for that plot (shown in the figure). Knowing U^*, U can be calculated in suitable units. All results shown are lower in magnitude than those of Weaver and Pao by a factor of π. This discrepancy was previously point out by Hutchinson (1983). Figures 4–7 show the first S, second AS, second S and third S modes, respectively. These are to be compared with Figs. 6(*a*), 7(*b*), 6(*b*), and 6(*c*) of Weaver and Pao. In view of what has been discussed, the second S mode should present difficulties in inversion on the real frequency axis. We use a negative imaginary increment of 0.01 in the nondimensional frequency Ω. While a real frequency inversion gave spurious oscillations of large magnitude that began at $t=0$, use of complex frequency decreased the effect of the singularity and led to a much improved time domain result as shown. The first two complex branches and all imaginary loops less than a nondimensional frequency of about 4.0 were also included. These have negligible effect even at $r=2H$ and so their contribution at 10 cm is not noticeable. Our method is well suited for forces whose net impulse is zero over their duration since the strength of the singularity of the first AS mode is reduced.

For the total response calculations the convergence condition used is the same for both the force and dislocation problems. This condition ensures that the number of modes assumed is such that the change in the maximum amplitude of the spectra is less than one percent when an extra mode is added. In all the cases considered the contributions of the lowest S and AS complex modes are taken into account for radial distances that are less than ten plate thicknesses from the source. Shown in Fig. 8 is the total response due to a sinusoidal load $\sin(2\pi t)$ of duration 1 μs, of the first six modes (three S and three AS) at $r=20H$. Without the use of complex frequency there would be significant oscillations before the compressional wave arrival caused mainly by the second S mode. The amplitude and phase of the spectra corresponding to this case are shown in Figs. 9 and 10. The rapid oscillations of the phase are due mainly to the behavior of the Hankel function when its argument increases rapidly to large values. For the sake of convenience in plotting, the upper limit of frequency shown in the figure is smaller than the value used by us for inversion.

5.4 The Dislocation Response. Unlike the load response problem, the dislocation is equivalent to a self-equilibrated force system that implies that the response will be bounded for large times, and this is reflected in the spectra by their behavior at $\omega = 0$. For a source function with a permanent static offset, they go over to the Fourier transform of the step function, which is singular like $1/\omega$ as $\omega \to 0$. We have assumed a source function of the modulated ramp type in the time domain with a rise time of one microsecond. As indicated in the foregoing, such a singularity can be easily handled by the FFT code.

Downloaded 02 May 2010 to 171.66.16.54. Redistribution subject to ASME license or copyright; see http://www.asme.org/terms/Terms_Use.cfm

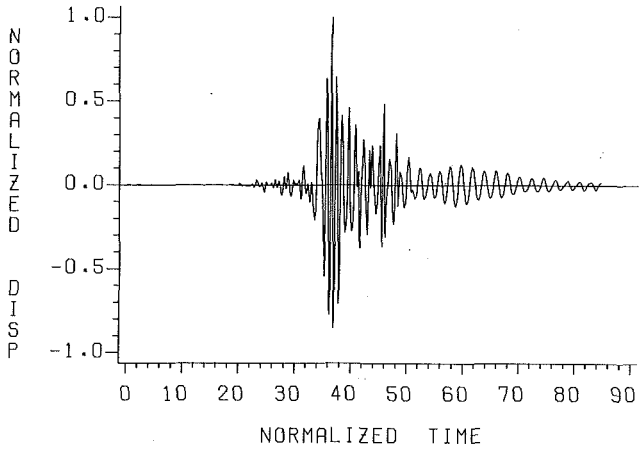


Fig. 8 Total vertical displacement for a sine load, sum of six modes at $r = 20H$, $C = 0.1370E(+12)$

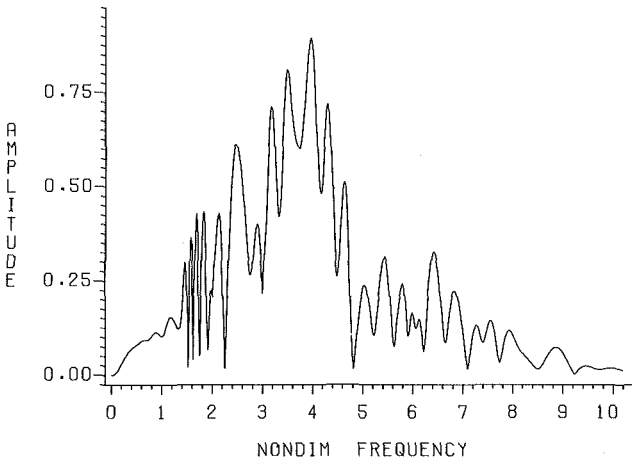


Fig. 9 Spectral amplitude for the response in Fig. 8, $\bar{\epsilon} = 0.01$

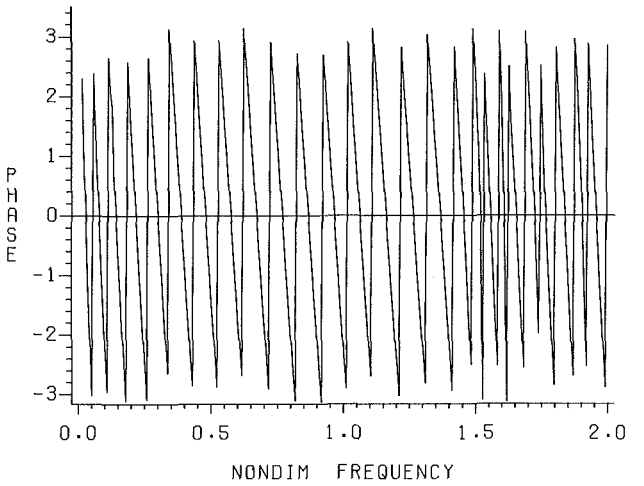


Fig. 10 Phase of the spectra for the response in Fig. 8

We consider a horizontal shear dislocation at the center of the plate with rake angle 0 deg and dip angle 0 deg. Shown in Figs. 11 and 12 are the total responses at $r = 3H$ and $50H$. The Rayleigh wave arrivals corresponding to the first AS mode are the most prominent arrivals in these responses. They then proceed to settle down to their static values. At $50H$ we encounter low-frequency oscillations due to the first flexural mode. Since the record persists for a long time we do not see

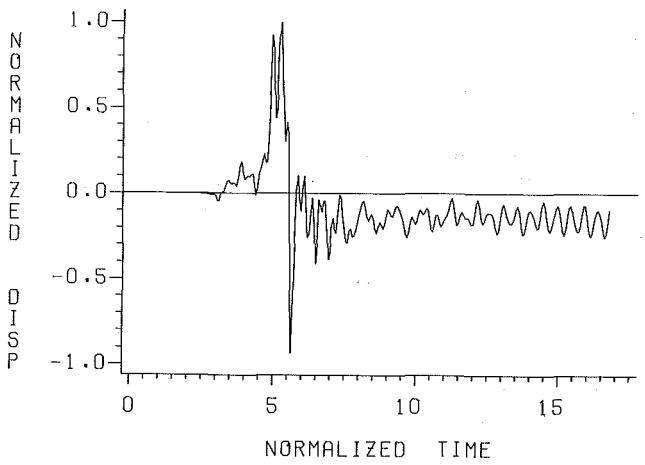


Fig. 11 Total vertical displacement for a shear dislocation, sum of 10 AS modes, $r = 3H$, $H = 1$cm; $\theta = 45$ deg, $C = 0.7770E(+08)$

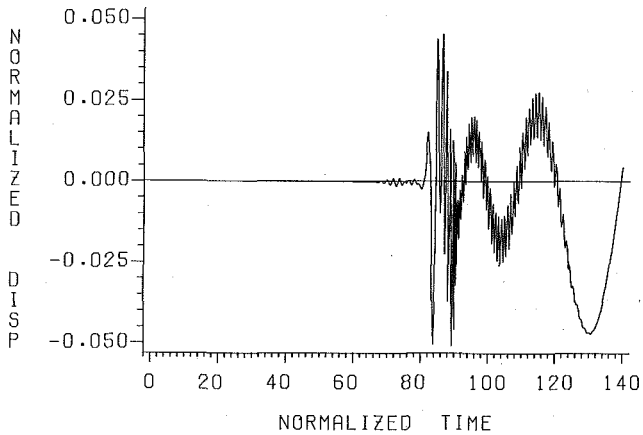


Fig. 12 Same geometry as in Fig. 11, $r = 50H$, $C = 0.3027E(+08)$

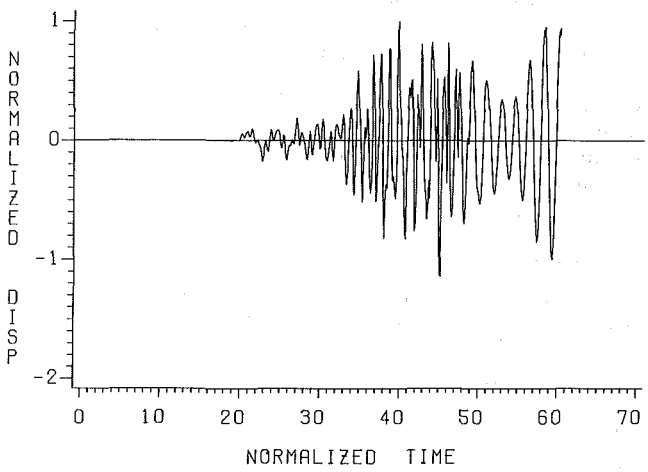


Fig. 13 Total vertical displacement for a normal dislocation, sum of six AS modes; $\delta = 90$ deg, $r = 20H$, $\theta = 45$ deg, $C = 0.2141E(+08)$

the static displacement in the plot. The higher modes manifest themselves as tiny oscillations that become smaller and smaller. Weaver and Pao (1983) have obtained a result showing very similar characteristics at $40H$ for the case of the applied surface step load.

Shown in Fig. 13 is the vertical displacement due to a normal opening crack of dip angle 90 deg located at the plate center. In contrast to the shear dislocation, which was governed by the AS modes we now see the effects of the S modes only. In the absence of the AS modes the response is highly oscillatory and does not settle to a static result quickly.

Downloaded 02 May 2010 to 171.66.16.54. Redistribution subject to ASME license or copyright; see http://www.asme.org/terms/Terms_Use.cfm

Notice also the sharp peak after the compressional wave arrival.

6 Conclusions

The technique that has been described in the preceding sections is one that although well known, has not heretofore been used for point source problems. We have attended to a number of theoretical and numerical details in implementing this procedure. As a result of these efforts we have developed a set of computer codes that are efficient and versatile. The maximum range of $r=50H$ used here does not represent an upper bound for the computer code that has been developed. Since at large distances the Hankel function oscillates rapidly, it becomes necessary to reduce the frequency sampling interval at which the spectra are being computed in order to capture this behavior. This is done at low cost because the effect of increasing radial distance is felt only by the Hankel function. One can then interpolate the remaining part of the spectra from its values at any previous computation. Only the Hankel function is recomputed at each new frequency point. This procedure is cheap and one could proceed to much larger distances than considered here. On the other hand, computation at epicentral distances between zero and 1.5 plate thicknesses presents some difficulties. This is due mainly to the fact that an increasingly larger number of real modes are needed to achieve convergence. The influence of the imaginary and complex branches are still so small that they could be safely neglected beyond a certain threshold.

One the roots of the RL equation are computed and stored, response calculations for surface point forces and dislocation sources of arbitrary depth and orientation can be performed with relative ease for numerous station distances. Another advantage of our approach is that physically acceptable dissipative mechanisms which can account for the attenuation of high-frequency waves can be easily incorporated into the model since we employ a frequency domain approach. In addition to the foregoing, the propagator matrix method used in solving the equations of motion can be extended to the multilayered plate problem in a straightforward manner. The disadvantge of the method lies primarily in its low convergence rate near the epicentral region.

In conclusion the frequency domain approach leads to a direct calculation of the spectra and the corresponding time domain modal responses. We expect that these features of the technique will prove useful in equipment calibration and in the analysis of *AE* signal for source characterization. Work along these lines is currently in progress.

7 Acknoweldgment

We wish to thank the referees for their detailed and constructive criticism of an earlier version of the paper. This research was supported by the National Science Foundation under grant MEA 82-19592.

References

Ceranoglu, A. N., and Pao, Y. H., 1981, "Propagation of Elastic Pulses and Acoustic Emission in a Plate," Parts I, II and III, ASME JOURNAL OF APPLIED MECHANICS, Vol. 48, pp. 125–147.

Ewing, M., Jardetsky, J., and Press, F., 1957, *Waves in Layered Media*, McGraw-Hill, New York.

Folk, R., Fox, G., Shook, C. A., and Curtis, C. W., 1958, "Elastic Strain Produced by the Sudden Application of Pressure to One End of a Cylindrical Bar, I. Theory," *J. Acoust. Soc. of Am.*, Vol. 30, No. 6, pp. 552–558.

Harkrider, D. G., 1964, "Surface Waves in Mutilayered Elastic Media," Vol. 54, pp. 627–679.

Haskell, N. A., 1953, "The Dispersion of Surface Waves on Multilayered Media," *B.S.S.A.*, Vol. 43, pp. 17–34.

Hutchinson, J. R., 1983, Discussion, ASME JOURNAL OF APPLIED MECHANICS, Vol. 50, pp. 699–700.

Kennet, B. L. N., *Seismic Wave Propagation in Stratified Media*, Cambridge University Press, 1983.

Mal, A. K., 1972, "Rayleigh Waves From a Moving Thrust Fault," *Bull. Seism. Soc. Am.*, Vol. 62, pp. 751–762.

Mal, A. K., "Applied Mechanics in Earthquake Engineering" in *Applications of Continuum Mechanics*, ASME Winter Annual Meeting, 1974, pp. 205–223

Mal, A. K., Kundu, T., and Xu, P. C., 1984, "On the Surface Response of a Multilayered Solid to a Dislocation Source," in *Earthquake Source Modelling, Ground Motion and Structural Response*, Proceedings of ASME Symposium, AMD-Vol. 80, pp. 29–48.

Miklowitz, J., 1978, *The Theory of Elastic Waves and Waveguides*, North Holland.

Mindlin, R. D., 1955, "An Introduction to the Mathematical Theory of the Vibrations of Elastic Plates", U.S. Army Signal Corps. Eng. Lab., monograph.

Vasudevan, N., 1984, "Response of an Infinite Elastic Plate to Point Dislocation Sources," Ph.D. Thesis, University of California, Los Angeles.

Weaver, R. L., and Pao, Y. H., 1983, "Axisymmetric Elastic Waves Excited by a Point Source in a Plate," ASME JOURNAL OF APPLIED MECHANICS, Vol. 49, pp. 821–836.

APPENDIX A

The functions G_1, G_2, G_3, G_4, D_S, D_{AS} which appear in (3.7) are defined in the following. We first define

$$P=\bar{k}\pi\eta_\alpha, \quad Q=\bar{k}\pi\eta_\beta,$$

where

$$\eta_q=(c^2/q^2-1)^{1/2} \qquad |c|>q$$
$$=-i(1-c^2/q^2)^{1/2} \qquad |c|<q$$

where q is either α or β.
Then G_1, G_2 etc become,

$$G_1=-\frac{\omega^3H^2}{8\pi^3\mu\beta^2}F_1 \tag{A-1}$$

$$G_2=-\frac{\omega^3H^2}{8\pi^3\mu\beta^2}F_2 \tag{A-2}$$

$$G_3=-\frac{i\omega^3H^2\bar{k}^2\eta_\alpha}{4\pi^3\mu\beta^2}F_3 \tag{A-3}$$

$$G_4=-\frac{i\omega^3H^2\bar{k}^2\eta_\alpha}{4\pi^3\mu\beta^2}F_4 \tag{A-4}$$

$$D_{AS}=4\bar{k}^4\eta_\alpha\eta_\beta\sin(Q/2)\cos(P/2)$$
$$+(2\bar{k}^2-\Omega^2)^2\cos(Q/2)\sin(P/2) \tag{A-5}$$

$$D_S=4\bar{k}^4\eta_\alpha\eta_\beta\sin(P/2)\cos(Q/2)$$
$$+(2\bar{k}^2-\Omega^2)^2\cos(P/2)\sin(Q/2) \tag{A-6}$$

where

$$F_1=((2\bar{k}^2-\Omega^2)\cos(P/2)\sin(Q/2))$$
$$F_2=((2\bar{k}^2-\Omega^2)\cos(Q/2)\sin(P/2))$$
$$F_3=(\cos(P/2)\cos(Q/2))$$
$$F_4=(\sin(P/2)\sin(Q/2))$$

Downloaded 02 May 2010 to 171.66.16.54. Redistribution subject to ASME license or copyright; see http://www.asme.org/terms/Terms_Use.cfm

Optimal Boundary Tractions for Solids With Initial Strains

R.A. Meric
TUBITAK,
Applied Mathematics Department,
Research Institute for Basic Sciences,
Gebze, Kocaeli, Turkey

Optimal boundary loading of solids with initial strains has been analyzed as a steady-state optimal control problem. Discretization of the optimality conditions, obtained by calculus of variations, is achieved by the finite element method, while the minimization of a performance index is done via the conjugate gradient method. Numerical results are provided for two plane strain problems with initial thermal strains.

Introduction

Static structural optimization problems in infinite dimensions may be viewed as a subclass of optimal control problems of distributed parameter systems (DPS). If the behavior of the system is influenced by mechanisms acting at the boundary, then the control problem may be termed as a boundary control problem. The objective of the control problem is usually to minimize a given performance index which is dependent on the state of the system and its controls. If the state of the physical system and controls are both time-independent, the control problem is termed as a steady-state control or static optimization problem.

Since necessary conditions for optimality of DPS are distributed in space, resort must be made to numerical methods in any realistic optimal control problem. In this study, the finite element method (FEM) as well as the conjugate gradient method (CGM) of optimization are utilized for the solution of optimal boundary loading of infinitely long cylinders under plane strain conditions and with initial thermal strains. The solution method is, however, general in that three-dimensional problems with any kind of initial strains and/or residual stresses can easily be accommodated.

Problem Statement

Consider an elastic, homogeneous and isotropic solid body of arbitrary geometry in three dimensions under a known temperature field. Using the displacements u_i as the state functions, the system equations (i.e., the Navier-Duhamel equations and relevant boundary conditions) may be written as follows:

The state problem:

$$\text{in } D \quad : \quad \mu u_{i,jj} + (\lambda+\mu) u_{j,ji} - (3\lambda+2\mu)\alpha T_{,i} = 0 \tag{1}$$

$$\text{on } S_1 \quad : \quad u_i = \bar{u}_i \tag{2}$$

$$\text{on } S_2 \quad : \quad \lambda u_{j,j} n_i + \mu(u_{i,j}+u_{j,i}) n_j - (3\lambda+2\mu)\alpha T n_i = \bar{t}_i \tag{3}$$

$$\text{on } S_3 \quad : \quad \lambda u_{j,j} n_i + \mu(u_{i,j}+u_{j,i}) n_j - (3\lambda+2\mu)\alpha T n_i = t_i \tag{4}$$

where D denotes the physical domain of interest with its boundary $S = S_1 + S_2 + S_3$; λ and μ are Lamé's constants; α is the coefficient of linear thermal expansion; T represents the prescribed temperature distribution of the solid body from a reference point; $\bar{u}_i$ are the given displacements on S_1; $\bar{t}_i$ denote the uncontrollable given boundary tractions and t_i are the (unknown) control tractions; n_i are the direction cosines of the unit vector normal to S.

In the present optimization problem, it is desired to have a displacement distribution on S_3 as close to zero as possible by applying a relatively minimum amount of control tractions t_i on S_3. The control tractions will balance the effects of the uncontrollable tractions $\bar{t}_i$ on S_2 as well as the initial strains (in this case, thermal strains).

The physical objectives may be cast into a mathematical form in terms of an integral functional $J[u_i, t_i]$ defined on S_3, the so-called performance index of the optimal control problem; thus

$$J[u_i,t_i] = \frac{1}{2}\int_{S_3} (u_i u_i + \beta t_i t_i)\, dS \tag{5}$$

where β is a given weighting parameter, enforcing a certain relative degree of achievement of the stated physical objectives according to its value.

The static optimization problem of optimal loading of solids with initial thermal strains may be stated as follows: "Find the optimal control functions t_i on S_3 from a set of admissible controls such that the performance index J is minimized under the system constraints (1)–(4)."

It is noted that there are no upper and/or lower bounds (i.e., hard constraints) on the control tractions t_i, and that concentrated loads are excluded from the analysis.

The present problem constitutes a special case of the more general problem which may be described as: "Given a body in some arbitrary state of stress and strain (due to some given loading), how do you apply boundary tractions to get close to desired distributions of displacements and/or stresses in the whole body or on its bounding surface while not using inordinately high surface tractions?"

Contributed by the Applied Mechanics Division for publication in the JOURNAL OF APPLIED MECHANICS.

Discussion on this paper should be addressed to the Editorial Department, ASME, United Engineering Center, 345 East 47th Street, New York, N.Y. 10017, and will be accepted until two months after final publication of the paper itself in the JOURNAL OF APPLIED MECHANICS. Manuscript received by ASME Applied Mechanics Division, February, 1984; final revision, July, 1984.

Copyright © 1985 by ASME
Downloaded 02 May 2010 to 171.66.16.54. Redistribution subject to ASME license or copyright; see http://www.asme.org/terms/Terms_Use.cfm

Although it might be argued that a direct analysis with prescribed displacements is sufficient without any optimization for the given J, any other type of performance indices involving stresses or displacements in the whole body would require an inverse procedure (i.e., an inverse problem). However, the present formulation and the solution method will be general in that performance indices defined in D or S may be handled with equal ease.

Necessary Conditions of Optimality

It is possible to adjoin the system state equation (1) with the performance index J by means of Lagrange multiplier functions ψ_i, obtaining a modified (or augmented) performance index $J^*[u_i, t_i, \psi_i]$, i.e.,

$$J^*[u_i,t_i,\psi_i] = J[u_i,t_i] + \int_D \psi_i[\mu u_{i,jj} + (\lambda+\mu)u_{j,ji} - (3\lambda+2\mu)\alpha T_{,i}]dD \quad (6)$$

The necessary condition for J^* to be stationary is that its first variation should be equal to zero for all permissible values of δu_i, δt_i, and $\delta\psi_i$, hence

$$\delta J^*[u_i,t_i,\psi_i] = 0 \quad (7)$$

By substituting equation (5) into equation (6), the preceding equation may be written in the following form:

$$\delta J^* = \int_{S_3} (u_i\delta u_i + \beta t_i \delta t_i)\, dS + \int_D \{\delta\psi_i[\mu u_{i,jj} + (\lambda+\mu)u_{j,ji} - (3\lambda+2\mu)\alpha T_{,i}] + \psi_i[\mu\delta u_{i,jj} + (\lambda+\mu)\delta u_{j,ji}]\}dD = 0 \quad (8)$$

Using Gauss' theorem and introducing the boundary conditions (2)–(4) into equation (8), the stationary conditions (i.e., the Euler-Lagrange equations) for the functional J^* may be derived (see Appendix). These conditions may be grouped under some headings in order to have a clear understanding of the iterative solution procedure which will be adopted later on. As such, the first group of equations is given under the title of "the state problem" in equations (1)–(4). The remaining conditions are grouped as follows:

The costate problem:

$$\text{in } D : \mu\psi_{i,jj} + (\lambda+\mu)\psi_{j,ji} = 0 \quad (9)$$

$$\text{on } S_1 : \psi_i = 0 \quad (10)$$

$$\text{on } S_2 : \lambda\psi_{j,j}n_i + \mu(\psi_{i,j} + \psi_{j,i})n_j = 0 \quad (11)$$

$$\text{on } S_3 : \lambda\psi_{j,j}n_i + \mu(\psi_{i,j} + \psi_{j,i})n_j = u_i \quad (12)$$

The gradient equation:

$$\text{on } S_3 : \psi_i + \beta t_i = 0 \quad (13)$$

Equations (1)–(4) and (9)–(13) are the necessary conditions for optimality of the performance index J subject to equations (1)–(4). The equations constitute a boundary value problem (BVP) in mathematical physics in terms of the unknowns u_i, t_i, and ψ_i. The field equations (1) and (9) defined in D are uncoupled second-order elliptic partial differeential equations (PDE). The coupling of the unknown functions occurs only in the boundary conditions since the present optimal control problem is of boundary control-boundary observation type.

It may be noted that the term "costate" comes from the fact that the Lagrange multiplier functions ψ_i are in fact serving as the costate (or adjoint) functions to the state functions u_i. Equation (13) denotes the gradient of the Lagrangian density of J^* with respect to the control functions t_i. This equation will be utilized in obtaining values for the next iteration step in an iterative solution procedure.

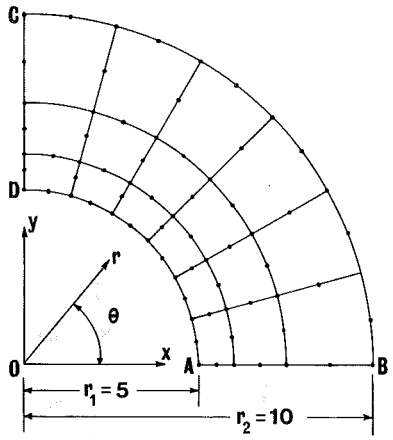


Fig. 1 Solution domain and mesh topology

Method of Solution

An iterative numerical method of solution will be adopted in order to find the optimal solutions. By taking an initial guess for t_i on S_3, the state problem, equations (1)–(4), describing a BVP may be solved for u_i. With this u_i, the costate problem, equations (9)–(12), describing another BVP, may consequently be solved for ψ_i. Better values for the control tractions t_i can then be found via optimization techniques by using the modified cost functional J^* and its gradient with respect to t_i.

Since the system state variables and the control are space dependent, both the state and costate problem have to be discretized in space by using discretization techniques, such as the finite element method (FEM), for a numerical solution. Through the space discretization of the variables, the static optimization problem can be treated as a standard mathematical programming (i.e., finite dimensional optimization) problem in which the function to be minimized is given by the discretized J^*.

Similar optimization problems in the field of heat transfer, i.e., static and dynamic optimal heating of solids by distributed heat sources and boundary heat fluxes, have been solved by the author utilizing the FEM [1–4] and the boundary integral equation method [5]. In the present problem of optimal traction loading of solids, knowing the temperature distribution T (or any other type of loading leading to initial strains) throughout the solid body, the state problem defined by equations (1)–(4) may efficiently be solved by the FEM under the influence of initially guessed control tractions t_i on S_3. Computer programs written in FORTRAN are available in the literature for the displacement solution of elastic bodies under initial (thermal) strains [6].

The costate problem equations (9)–(12) are very similar in form to the state problem equations, since the costate functions ψ_i are adjoint to the state functions u_i. This fact can be utilized to advantage by simply using the same decomposed stiffness matrices as in the state problem during the FEM solution of the costate problem.

Corresponding to an initial guess for the control tractions t_i, the displacements u_i and the costate functions ψ_i are thus found by the solution of the two BVP's via the FEM. At the present iteration step, the discretized modified cost functional J^* and its gradient can now be evaluated by using the following equations, derived from equations (6) and (13), respectively:

$$J^* = \sum_e \int_{S_3} [\{u\}^{eT}[N]^T[N]\{u\}^e + \beta\{t\}^{eT}[N]^T[N]\{t\}^e]dS \quad (14)$$

Downloaded 02 May 2010 to 171.66.16.54. Redistribution subject to ASME license or copyright; see http://www.asme.org/terms/Terms_Use.cfm

$$\frac{\partial J^*}{\partial \{t\}} = \sum_e \int_{S_3} [N]^T [[N]\{\psi\}^e + \beta[N]\{t\}^e] dS \qquad (15)$$

where $[N]$ is the usual shape function matrix; $\{u\}^e$ and $\{t\}^e$ are the element displacement and traction vectors, respectively; $\{t\}$ is the global traction vector defined on S_3 and the summations are over the finite elements next to S_3.

The discretized J^* (now, a function of $\{t\}$) can be minimized with respect to $\{t\}$ by using any first-order unconstrained optimization technique. The conjugate gradient method (CGM) is adopted in the present study, since the method requires a relatively small amount of computer storage compared to other quasi or modified Newton type of methods. A library routine from the Numerical Algorithms Group of England has successfully been utilized for the CGM of optimization [7].

Numerical Results and Discussion

Two example problems of optimal loading of solids with initial thermal strains were solved by the proposed numerical method described in the preceding section. Both problems involved infinitely long cylinders with plane strain conditions. In the first problem (indicated by Prob-*I*, henceforth) the cylinder was taken as a complete thick-walled hollow cylinder, while in the second problem (indicated by Prob-*II*, henceforth) the cross section was only a quadrant of an annulus. However, since radially symmetric conditions are imposed in Prob-*I*, consideration of only a quadrant of the whole annular region will be sufficient for the analysis, as in the case of Prob-*II*. Hence, the solution domain D and the finite element mesh topology with eight-noded isoparametric quadrilateral elements were the same for both problems, and are shown in Fig. 1. The inner radius was set as $r_1 = 5$ and the outer radius was fixed as $r_2 = 10$.

The boundary conditions were imposed differently for the two problems. In Prob-*I*, on sides AB and CD symmetry conditions pervailed with the normal components of displacements taken as zero. In Prob-*II*, however, both components of the displacements were prescribed as zero on the same sides (i.e., $\bar{u}_i = 0$). On side DA, prescribed tractions were taken with $p = 10$, where p denotes the compressive normal stress (pressure). The control tractions t_i were, on the other hand, applied on side BC for both problems.

The steady-state temperature distribution in the solid bodies was taken as a function of only the radial coordinate r in both problems, with no dependency on the polar coordinate angle θ. Specifically, T was set as $T(r) = k \log r$, where k is a given constant.

It may be noted at this point that Prob-*I* is a radially symmetric problem because of the nature of the boundary conditions and the radial temperature distribution in the solid. It is for this reason that the optimal control tractions, as well as other physical quantities of interest, will not depend on θ for this problem. On the other hand, Prob-*II* has a symmetry section only at $\theta = 45$ deg, which will result in the optimal tractions being dependent on the angle θ.

For the FEM solution of the state and costate problem, 18 quadratic quadrilateral elements were used with 73 total nodal points (see, Fig. 1). The control tractions on S_3 (i.e., on side BC) were also interpolated quadratically, and taken as continuous between the elements. It is noted that C° continuity of t_i is not required for the optimization problem, although the displacements u_i and the costate functions ψ_i have to be C° continuous in order that the finite elements be compatible for the state and costate problem, respectively.

During the iterative solution procedure, several initial guesses were tried to make sure that the numerical results corresponded to the solution of the optimal control problem at hand, since the CGM does not distinguish between local and global minima of functions. Computations have been performed on a DEC VAX-11/780 computer system with a 4 MB core memory. Double precision arithmetic was utilized in order to reduce roundoff errors.

Table 1 Optimal tractions and displacements corresponding to various weighting parameters in Prob-*I* ($E = 1000$, $k = 10$, $\alpha = 0.001$)

β	t_n/p	u_r/r_1
0.0	2.8841	3.2690×10^{-8}
10^{-15}	2.8841	3.2690×10^{-8}
10^{-10}	2.8839	3.0774×10^{-6}
10^{-6}	2.8625	5.0791×10^{-4}
10^{-5}	2.6890	4.7385×10^{-3}
10^{-3}	3.2674×10^{-1}	5.7685×10^{-2}
10^{-2}	3.6360×10^{-2}	6.4193×10^{-2}
10^{-1}	3.6775×10^{-3}	6.4925×10^{-2}
1.0	3.6817×10^{-4}	6.4999×10^{-2}

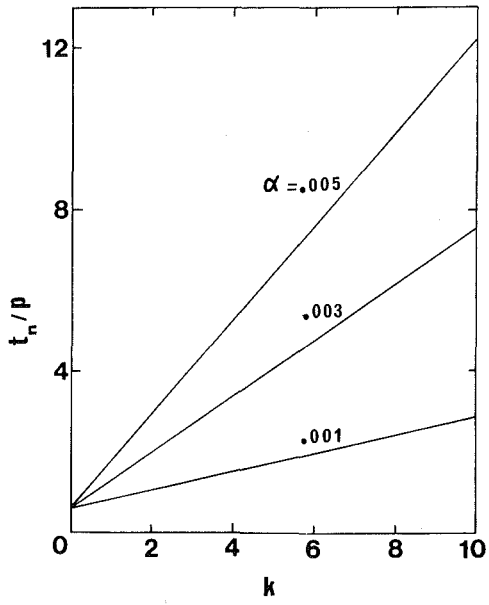


Fig. 2 Optimal normal tractions versus k for Prob-*I* ($E = 1000$)

The iterative numerical procedure of CGM typically needed 40 evaluations of J^* and its gradient, requiring approximately 1 minute of CPU time on the specific system. Most of the time, an initial guess of 5 for the normal components of control tractions and of zero shear componets were found as satisfactory for convergence, while the initial guess for J^* has been fixed as zero all the time. For convergence a tolerance of 10^{-15} has been adopted for the minimizing sequence of control tractions. Engineering constants for the elastic material, i.e., Young's modulus E and Poisson's ratio ν, were utilized instead of Lamé's constants λ and μ. Hence, the problem parameters are now the elastic constants E and ν, thermal constants α and k, and the weighting coefficient β. However, Poisson's ratio for both problems was fixed as $\nu = 0.3$.

Numerical results have been obtained for the two problems described earlier. The quantity t_n will indicate the normal component of the optimal traction vector on S_3, considered positive when directed into the solid, while t_s will denote the shear component of the optimal tractions, taken positive in the positive θ direction. The quantity shown by u_r will correspond to the radial component of displacements, while σ_r and σ_θ are the usual normal stresses in the polar coordinate directions.

In Table 1, the nondimensional forms of the optimal control traction t_n/p and the corresponding radial

Downloaded 02 May 2010 to 171.66.16.54. Redistribution subject to ASME license or copyright; see http://www.asme.org/terms/Terms_Use.cfm

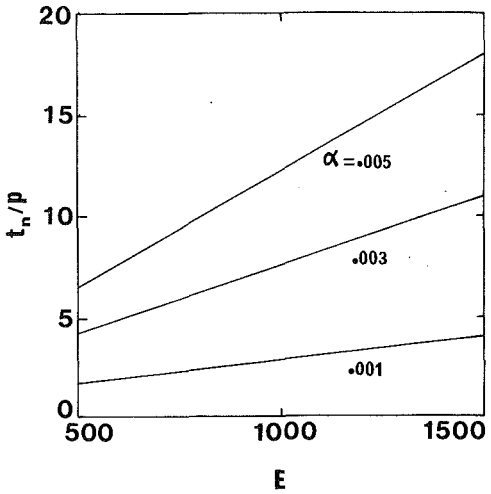


Fig. 3 Optimal normal tractions versus E for Prob-*I* (k = 10)

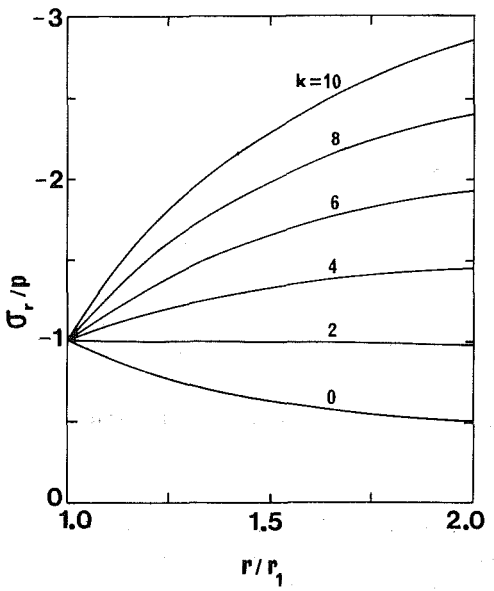


Fig. 4 Normal stress in r-direction as a function of radial distance for Prob-*I* (E = 1000, α = 0.001)

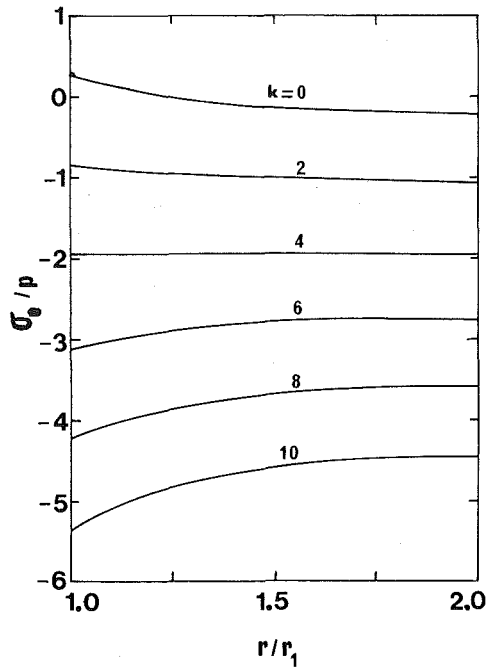


Fig. 5 Normal stress in θ-direction as a function of radial distance for Prob-*I* (E = 1000, α = 0.001)

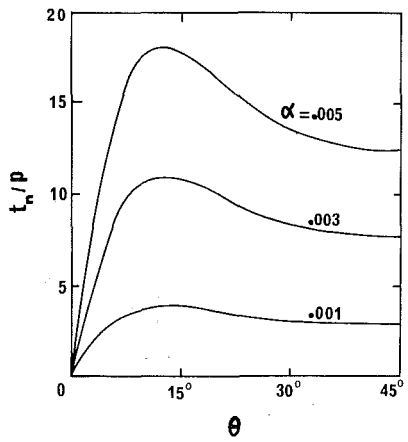


Fig. 6 Optimal normal tractions versus θ for Prob-*II* (E = 1000, k = 10)

displacement u_r/r_1 on S_3 (i.e., at $r = r_2$) are tabulated for various values of the weighting parameter β for Prob-*I* with E = 1000, α = 0.001, and k = 10. For this radially symmetric problem very small values of displacements are obtained on S_3, as desired in the optimization problem, when β is taken small. For these small values of β, however, relatively large amounts of control tractions were needed. At the other extreme, when β was set to larger values, the displacements on S_3 have increased, while the tractions have correspondingly decreased, as expected. Thus, the relative balance between the control tractions and displacements is being established with the value of the weighting parameter β.

For the following figures in this section, β has been set to a relatively small value of 10^{-6}, indicating our desire of achieving small displacements at $r = r_2$. Figures 2–5 relate to Prob-*I*, the radially symmetric problem with no θ-dependency. In Fig. 2, the nondimensional optimal control traction is shown as a function of the temperature distribution coefficient k for various values of the thermal linear expansion coefficient α for E = 1000. As expected, higher temperatures in the solid resulting in higher initial thermal strains require increasing amounts of control tractions which are being applied at $r = r_2$. Since the thermoelastic problem is a linear problem, the relationship between t_n/p and k is also a linear one.

The optimal tractions are plotted as a function of Young's modulus E for various values of α when k = 10 in Fig. 3. As seen in the figure, more rigid solids with higher values of E require larger amounts of control tractions, indicated by the positive slope in the figure.

Figures 4 and 5 denote the nondimensional normal stresses σ_r/p and σ_θ/p as a function of the radial distance r/r_1 in the solid for various values of k when E = 1000 and α = 0.001. When the temperature distribution is identically zero the coefficient k is adopted as zero in the figure. For small values of k between zero and 2, the normal stress σ_r/p is decreasing with the radial distance, while it is increasing for larger values. Similar trends have been found for the other normal stress σ_θ/p as shown in Fig. 5.

Figures 6–8 relate to Prob-*II*, with fixed sides AB and CD of the domain D, for which there is now θ-dependency of functions. Young's modulus and temperature distribution coefficient k have been set equal to 1000 and 10, respectively. Figures 6 and 7 show the nondimensional normal and shear

Downloaded 02 May 2010 to 171.66.16.54. Redistribution subject to ASME license or copyright; see http://www.asme.org/terms/Terms_Use.cfm

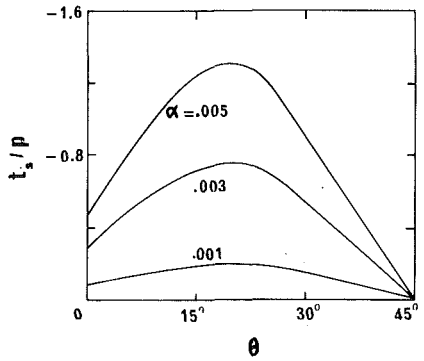


Fig. 7 Optimal shear tractions versus θ for Prob-II ($E = 1000, k = 10$)

component of the optimal control traction as a function of the polar angle θ for various values of α. Since there exists a plane of symmetry at $\theta = 45$ deg, the distributions are only shown for the range $\theta = 0$ to 45 deg. As the quadrant annular solid is fixed at $r = r_2$ when $\theta = 0$ deg, the normal tractions are zero there, while the shear tractions are zero at $\theta = 45$ deg due to the symmetry condition. The last figure, Fig. 8, denotes the normal stress σ_r/p versus θ at $r/r_1 = 1.466$ (a Gauss integration point) close to the midsection of the solid for various values of α. As expected, increasing values of stresses are obtained for higher values of α.

Conclusion

A model problem of optimal boundary loading of solids with initial strains has been analyzed by numerical methods. Although emphasis has been focused on thermal strains, any type of initial strains and/or stresses can easily be handled by the same solution procedure. One reason for taking thermal strains is that research is underway for coupled thermoelastic optimization problems in which heat transfer and elasticity BVP's are solved in a coupled way.

The problem formulation can also be extended for other types of performance indices involving displacements, tractions, and/or stresses either in the solid body or on its bounding surface.

References

1 Meric, R. A., "Finite Element Methods for an Optimal Steady-State Control Problem," *Int. J. Num. Meth. Eng.*, Vol. 12, 1978, pp. 1375-1382.

2 Meric, R. A., "Finite Elements for an Optimal Control Problem Governed by a Parabolic Equation," *Int. J. Num. Meth. Eng.*, Vol. 14, 1979, pp. 624-628.

3 Meric, R. A., "Finite Element Analysis of Optimal Heating of a Slab With Temperature-Dependent Thermal Conductivity," *Int. J. Heat Mass Transfer*, Vol. 22, 1979, pp. 1347-1353.

4 Meric, R. A., "Finite Element and Conjugate Gradient Methods for a Nonlinear Optimal Heat Transfer Control Problem," *Int. J. Num. Meth. Eng*, Vol. 14, 1979, pp. 1851-1863.

5 Meric, R. A., "Boundary Integral Equation and Conjugate Gradient Methods for Optimal Boundary Heating of Solids," *Int. J. Heat Mass Transfer*, Vol. 26, 1983, pp. 261-267.

6 Hinton, E., and Owen, D. R. J., *Finite Element Programming*, Academic Press, New York, 1977.

7 NAG Library, The Numerical Algorithms Group, Oxford, England.

APPENDIX

By the following identities

$$\lambda\psi_i\delta u_{j,ji} \equiv \lambda[(\psi_i\delta u_{j,j})_{,i} - (\psi_{i,i}\delta u_j)_{,j} + \psi_{i,ij}\delta u_j] \tag{A.1}$$

$$\mu\psi_i(\delta u_{i,j} + \delta u_{j,i})_{,j} \equiv \mu\{\psi_i(\delta u_{i,j} + \delta u_{j,i})]_{,j} - (\psi_{i,j}\delta u_i)_{,j} - (\psi_{i,j}\delta u_j)_{,j} + \psi_{i,jj}\delta u_i + \psi_{i,ji}\delta u_j\} \tag{A.2}$$

δJ^* can be rewritten from equation (8) as follows:

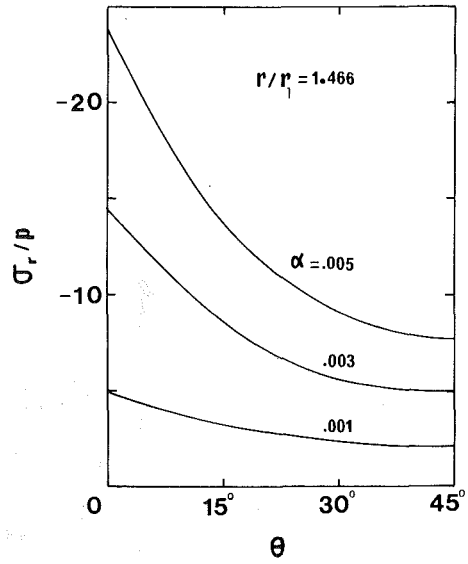


Fig. 8 Normal stress in r-direction versus θ for Prob-II ($E = 1000, k = 10$)

$$\delta J^* = \int_D \{\delta\psi_i[\mu u_{i,jj} + (\lambda+\mu)u_{j,ji} - (3\lambda+2\mu)\alpha T_{,i}] + \lambda[(\psi_i\delta u_{j,j})_{,i} - (\psi_{i,i}\delta u_j)_{,j} + \psi_{i,ij}\delta u_j] + \mu[\psi_i(\delta u_{i,j} + \delta u_{j,i})]_{,j} - \mu[(\psi_{i,j}\delta u_i)_{,j} + (\psi_{i,j}\delta u_j)_{,i} - \psi_{i,jj}\delta u_i - \psi_{i,ji}\delta u_j]\}dD + \int_{S_3}(u_i\delta u_i + \beta t_i\delta t_i)dS = 0 \tag{A.3}$$

Some of the domain integrals in equation (A.3) are converted into surface integrals by Gauss' theorem leading to the following equation:

$$\delta J^* = \delta J_D^* + \delta J_S^* = 0 \tag{A.4}$$

where

$$\delta J_D^* = \int_D \{\delta\psi_i[\mu u_{i,jj} + (\lambda+\mu)u_{j,ji} - (3\lambda+2\mu)\alpha T_{,i}] + \lambda\psi_{i,ij}\delta u_j + \mu\psi_{i,jj}\delta u_i + \mu\psi_{i,ji}\delta u_j\}dD \tag{A.5}$$

$$\delta J_S^* = \int_S \{\lambda(\psi_i\delta u_{j,j}n_i - \psi_{i,i}\delta u_j n_j) + \mu[\psi_i(\delta u_{i,j} + \delta u_{j,i})n_j - \psi_{i,j}\delta u_i n_j - \psi_{i,j}\delta u_j n_i]\}dS + \int_{S_3}(u_i\delta u_i + \beta t_i\delta t_i)dS \tag{A.6}$$

Introducing the variational forms of the boundary conditions (2)-(4) into equation (A.6), δJ_S^* may be rearranged as

$$\delta J_S^* = \int_{S_1}\mu\,\psi_i(\delta u_{i,j} + \delta u_{j,i})n_j dS - \int_{S_2}[\lambda\psi_{j,j}n_i + \mu(\psi_{i,j} + \psi_{j,i})n_j]\delta u_i dS + \int_{S_3}\{(\psi_i + \beta t_i)\delta t_i - [\lambda\psi_{j,j}n_i + \mu(\psi_{i,j} + \psi_{j,i})n_j - u_i]\delta u_i\}dS \tag{A.7}$$

Substitution of equations (A.5) and (A.7) into equation (A.4) leads to the variational statement for J^*. Since the variations δu_i, δt_i, and $\delta\psi_i$ are independent of each other, their coefficients can be set equal to zero separately. This yields the Euler-Lagrange equations given by equations (1)-(4) and (9)-(13).

Downloaded 02 May 2010 to 171.66.16.54. Redistribution subject to ASME license or copyright; see http://www.asme.org/terms/Terms_Use.cfm

On the Theory of a Cosserat Point and Its Application to the Numerical Solution of Continuum Problems

M. B. Rubin
Faculty of Mechanical Engineering,
Technion-Israel Institute of Technology,
Haifa, Israel,
Assoc. Mem. ASME

The theory of a Cosserat point is developed to describe motion of a body that is essentially a material point surrounded by some small volume. The development of this theory is motivated mainly by its applicability to the numerical solution of continuum problems. Attention is confined to the purely mechanical theory and nonlinear balance laws are proposed for Cosserat points with arbitrary constitutive properties. The linearized theory is developed and constitutive equations for an elastic material are discussed within the context of both the nonlinear and linear theories. Explicit constitutive equations for a linear-elastic isotropic Cosserat point are developed to model a parallelepiped composed of a linear-elastic homogeneous isotropic material.

Introduction

The general equations of continuum mechanics involve quantities that depend on three space variables and time. Even for a simple material like an elastic solid, the nonlinear equations of motion are exceedingly difficult to solve. Often, in practice, we encounter bodies that are shell-like or rod-like in nature which can be analyzed using simpler equations than those of the three-dimensional theory. For a shell-like body, one of its dimensions is much smaller than the other two and limited information can be obtained about the deformation of such a body by solving shell equations that depend on only two space variables and time. For a rod-like body, two of its dimensions are much smaller than the other one and the deformation can be analyzed by solving rod equations that depend on only one space variable and time. In this paper, we take this reduction in dimension one step further and consider a body that is essentially a point surrounded by some small volume. Equations will be developed to describe the deformation of such a continuum that depend only on time. The development of these equations is motivated mainly by their applicability to the numerical solution of continuum problems. This application is considered in detail for one-dimensional problems in a companion paper [1].

During the past fifteen years, considerable advancement in shell theory has been made by modeling a shell-like body as a Cosserat surface [2, 3]. Similar advances have been made in rod theory of modeling a rod-like body as a Cosserat curve [4–6]. Here, we will follow the basic procedures outlined in these papers to develop the theory of a Cosserat point.

In the next section we introduce the kinematics and kinetics associated with the theory of a Cosserat point and propose balance laws of the simplest theory that allows three-dimensional deformation of the continuum. In the main text of the paper we introduce the basic equations by direct approach whereas in the Appendix we provide a derivation from the three-dimensional equations. Since the basic equations are valid for arbitrary materials it is necessary to supplement them by constitutive equations. Here we describe nonlinear constitutive equations for elastic Cosserat points.

The two following sections are devoted to the linear theory. One section develops linearized equations valid for arbitrary linear-elastic Cosserat points and the other section specifies constitutive equations for an isotropic Cosserat point that models a rectangular parallelepiped composed of a three-dimensionally isotropic linear-elastic material. Finally, we briefly comment on the use of the theory of a Cosserat point as a basis of numerical solution procedures for continuum problems.

Basic Equations (Direct Approach)

Generally speaking, the theory of a Cosserat point is applicable to the analysis of a body that is essentially a material point surrounded by some small volume. Within the context of the theory we model the body as a material point attached to which is a set of three-dimensional vectors called directors. These directors provide limited information about the deformation of the body.

In the present configuration, at time t, the body occupies the region $\mathcal{R}$ bounded by the closed surface $\partial\mathcal{R}$ with sections $\partial\mathcal{R}_K$ $(K = 1, 2, \ldots . M)$. Furthermore, in the present configuration (see Fig. 1), the Cosserat point is defined by its

Contributed by the Applied Mechanics Division for publication in the JOURNAL OF APPLIED MECHANICS.
Discussion on this paper should be addressed to the Editorial Department, ASME, United Engineering Center, 345 East 47th Street, New York, N.Y. 10017, and will be accepted until two months after final publication of the paper itself in the JOURNAL OF APPLIED MECHANICS. Manuscript received by ASME Applied Mechanics Division, November, 1983; final revision April, 1984.

Copyright © 1985 by ASME
Downloaded 02 May 2010 to 171.66.16.54. Redistribution subject to ASME license or copyright; see http://www.asme.org/terms/Terms_Use.cfm

location $\mathbf{r}(t)$, relative to the origin of a fixed coordinate system, and by the three[1] directors $\mathbf{d}_i(t)$ $(i = 1, 2, 3)$. The position vector $\mathbf{r}$ and directors $\mathbf{d}_i$ are each a three-dimensional vector function of time only which in the reference configuration acquire the values $\mathbf{r} = \mathbf{R}$ and $\mathbf{d}_i = \mathbf{D}_i$. A motion of the Cosserat point is defined by

$$\mathbf{r}=\mathbf{r}(t), \quad \mathbf{d}_i=\mathbf{d}_i(t), \quad d^{1/2}=[\mathbf{d}_1\,\mathbf{d}_2\,\mathbf{d}_3]>0, \qquad (1a,b,c)$$

where the condition $(1c)$ ensures that the directors form a right-handed set of linearly independent vectors.

The vector functions $\mathbf{r}$ and $\mathbf{d}_i$ in (1) are assumed to be sufficiently smooth in the sense that they are differentiable with respect to time t as many times as required. Let $\mathbf{v}$ and $\mathbf{w}_i$, each a three-dimensional vector function of time, denote, respectively, the velocity of the material point and the director velocities at time t. Then

$$\mathbf{v}=\frac{d}{dt}(\mathbf{r})=\dot{\mathbf{r}}, \qquad \mathbf{w}_i=\frac{d}{dt}(\mathbf{d}_i)=\dot{\mathbf{d}}_i, \qquad (2a,b)$$

where a superposed dot denotes time differentiation.

For later convenience, we also introduce the reciprocal vectors $\mathbf{d}^i$ $(i = 1, 2, 3)$ of the directors $\mathbf{d}_i$ and record the kinematical definitions

$$h_{ij}=\mathbf{d}_i\cdot\mathbf{d}_j, \quad \mathbf{d}_i\cdot\mathbf{d}^j=\delta_i{}^j, \quad h^{ij}=\mathbf{d}^i\cdot\mathbf{d}^j, \qquad (3a,b,c)$$

where $\delta_i{}^j$ is the Kronecker delta symbol. In view of the restriction $(1c)$ and the definition $(3b)$ we realize that $\mathbf{d}^i$ also form a linearly independent set of vectors so that any three-dimensional vector quantity can be expressed as a linear combination of either of the sets $\mathbf{d}_i$ or $\mathbf{d}^i$. Using these definitions we may also introduce the strain γ_{ij} relative to the reference configuration through the expression

$$\gamma_{ij}=\tfrac{1}{2}(h_{ij}-H_{ij}), \qquad (4)$$

where H_{ij} is the reference value of h_{ij}.

We now turn to a statement of the conservation and balance laws of the theory and, with reference to the present configuration, define the following quantities: The mass $m(t)$ of the point; the contact force $\mathbf{n}_K(t)$ and contact director couples $\mathbf{m}_K{}^i(t)$, each a three-dimensional vector, applied to the section $\partial\mathcal{R}_K$ of the boundary $\partial\mathcal{R}$; the external body force $\mathbf{f}(t)$ and external body director couples $\mathbf{l}^i(t)$, each a three-dimensional vector; the intrinsic director couples $\mathbf{k}^i(t)$, each a three-dimensional vector that makes no contribution to the supply of angular momentum; and the constant inertia coefficients y^i and y^{ij}, with y^{ij} being a symmetric tensor. With the preceding definitions, and with reference to the present configuration we postulate the following conservation and balance laws for a Cosserat point:[2]

$$\frac{d}{dt}[m]=0, \qquad (5a)$$

$$\frac{d}{dt}[m(\mathbf{v}+y^i\mathbf{w}_i)]=\mathbf{f}+\sum_{K=1}^{M}\mathbf{n}_K, \qquad (5b)$$

$$\frac{d}{dt}[m(y^i\mathbf{v}+y^{ij}\mathbf{w}_j)]=\mathbf{l}^i+\sum_{K=1}^{M}\mathbf{m}_K{}^i-\mathbf{k}^i, \qquad (5c)$$

$$\frac{d}{dt}[\mathbf{r}\times m(\mathbf{v}+y^i\mathbf{w}_i)+\mathbf{d}_i\times m(y^i\mathbf{v}+y^{ij}\mathbf{w}_j)]$$

$$=\mathbf{r}\times\left[\mathbf{f}+\sum_{K=1}^{M}\mathbf{n}_K\right]+\mathbf{d}_i\times\left[\mathbf{l}^i+\sum_{K=1}^{M}\mathbf{m}_K{}^i\right]. \qquad (5d)$$

[1] The theory could be developed for a finite set of more than three directors but this level of generality is not pursued here.

[2] Throughout this paper we use the usual summation convention over repeated indices.

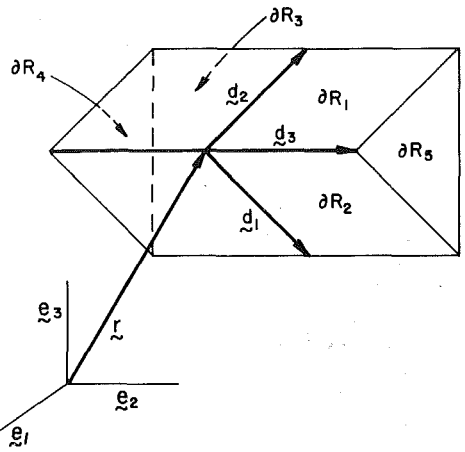


Fig. 1 Sketch of a typical Cosserat point modeling a triangular prism

Equation $(5a)$ represents the conservation of mass, $(5b)$ the balance of linear momentum, $(5c)$ the balance of director momentum, and $(5d)$ the balance of angular momentum.

Now with the help of $(5a)$–$(5c)$, the balance of angular momentum $(5d)$ may be written in the form:

$$\mathbf{d}_i\times\mathbf{k}^i=0 \qquad (6)$$

Component forms of the equations $(5b,c)$ and (6) can be obtained trivially when we refer all quantities to the base vectors $\mathbf{d}_i$, such as:

$$\mathbf{f}=\mathbf{f}^i\mathbf{d}_i, \qquad \mathbf{n}_K=n_K{}^i\mathbf{d}_i, \qquad (7a,b)$$

$$\mathbf{l}^i=\mathbf{l}^{ij}\mathbf{d}_j, \qquad \mathbf{m}_K{}^i=m_K{}^{ij}\mathbf{d}_j, \ \mathbf{k}^i=k^{ij}\mathbf{d}_j. \qquad (7c,d,e)$$

In particular, the component form of (6) states that the tensor k^{ij} is symmetric:

$$k^{ij}=k^{ji}, \qquad (8)$$

which is analagous to the consequences of angular momentum in the three-dimensional theory which states that the Cauchy stress tensor is symmetric.

For the general theory of a Cosserat point the equations of motion (5) must be supplemented by constitutive equations for the mass m, the inertia coefficients y^i and y^{ij}, and for the intrinsic director couples $\mathbf{k}^i$. The body force $\mathbf{f}$, contact forces $\mathbf{n}_K$, body director couples $\mathbf{l}^i$, and contact director couples $\mathbf{m}_K{}^i$ are specified for a particular problem.

With reference to the development of constitutive equations for the intrinsic director couples $\mathbf{k}^i$ and within the context of the purely mechanical theory it is convenient to define the mechanical power P by the expression:

$$P=\left(\mathbf{f}+\sum_{K=1}^{M}\mathbf{n}_K\right)\cdot\mathbf{v}+\left(\mathbf{l}^i+\sum_{K=1}^{M}\mathbf{m}_K{}^i\right)\cdot\mathbf{w}_i$$

$$-\frac{d}{dt}[\tfrac{1}{2}m(\mathbf{v}\cdot\mathbf{v}+2y^i\mathbf{v}\cdot\mathbf{w}_i+y^{ij}\mathbf{w}_i\cdot\mathbf{w}_j)], \qquad (9)$$

Using (3)–(5), (7), and (8), the expression (9) for the mechanical power can be rewritten in the reduced form

$$P=\mathbf{k}^i\cdot\mathbf{w}_i=k^{ij}\dot{\gamma}_{ij}. \qquad (10)$$

for a nonlinear elastic Cosserat point we assume the existence of a strain energy function ψ such that

$$P=\dot{\psi}, \qquad \psi=\hat{\psi}(\gamma_{ij},H_{ij}). \qquad (11a,b)$$

Substituting (11) into (10) we derive the constitutive equation

$$k^{ij}=\frac{\partial\psi}{\partial\gamma_{ij}} \qquad (12)$$

where the derivative in (12) is regarded as a symmetric func-

Downloaded 02 May 2010 to 171.66.16.54. Redistribution subject to ASME license or copyright; see http://www.asme.org/terms/Terms_Use.cfm

tion. Finally, it is worth mentioning that this theory can be shown to be properly invariant under superposed rigid body motions.

Linear Theory

In this section we develop linearized equations of motion and constitutive equations that describe small deformations of the Cosserat point relative to its reference configuration. For this linearized theory we assume that in its reference configuration the Cosserat point is in its natural state and is free of body forces and director couples, contact forces and director couples, and intrinsic director couples. Let $\mathbf{u}(t)$ be the displacement of the reference point and $\boldsymbol{\delta}_i(t)$ be the displacements of the directors relative to the reference configuration, so that

$$\mathbf{r}=\mathbf{R}+\mathbf{u}, \qquad \mathbf{d}_i=\mathbf{D}_i+\boldsymbol{\delta}_i, \tag{13a,b}$$

where $\mathbf{u}$ and $\boldsymbol{\delta}_i$ are considered to be small relative to $\mathbf{R}$ and $\mathbf{D}_i$, respectively. Neglecting quadratic terms in $\mathbf{u}$ and $\boldsymbol{\delta}_i$ the relevant kinematic variables may be summarized as:

$$\mathbf{u}=u^iD_i=u_i\mathbf{D}^i, \quad \boldsymbol{\delta}_i=\delta_i{}^j\mathbf{D}_j=\delta_{ij}\mathbf{D}^j, \tag{14a,b}$$

$$\mathbf{v}=\dot{\mathbf{u}}=\dot{u}^i\mathbf{D}_i=\dot{u}_i\mathbf{D}^i, \quad \dot{\mathbf{v}}=\ddot{\mathbf{u}}=\ddot{u}^i\mathbf{D}_i=\ddot{u}_i\mathbf{D}^i, \tag{14c,d}$$

$$\mathbf{w}_i=\dot{\boldsymbol{\delta}}_i=\dot{\delta}_i{}^j\mathbf{D}_j=\dot{\delta}_{ij}\mathbf{D}^j, \quad \dot{\mathbf{w}}_i=\ddot{\boldsymbol{\delta}}_i=\ddot{\delta}_i{}^j\mathbf{D}_j=\ddot{\delta}_{ij}\mathbf{D}^j, \tag{14e,f}$$

$$h_{ij}=\mathbf{D}_i\cdot\mathbf{D}_j+\mathbf{D}_j\cdot\boldsymbol{\delta}_i+\mathbf{D}_i\cdot\boldsymbol{\delta}_j=H_{ij}+\delta_{ij}+\delta_{ji}, \tag{14g}$$

$$\gamma_{ij}=\tfrac{1}{2}(\mathbf{D}_j\cdot\boldsymbol{\delta}_i+\mathbf{D}_i\cdot\boldsymbol{\delta}_j)=\tfrac{1}{2}(\delta_{ij}+\delta_{ji}), \tag{14h}$$

where the components $\delta_i{}^j$ and δ_{ij} of the displacements $\boldsymbol{\delta}_i$ should not be confused with the values $\delta_i{}^j$ and δ_{ij} of the Kronecker delta symbol.

Since the Cosserat point is in its natural state in the reference configuration all kinetic quantities are assumed small in the present configuration. Hence, neglecting quadratic terms of small quantities the kinetic quantities for the linear theory can be expressed by equations (7*a*)–(7*e*) with $\mathbf{d}_i$ replaced by $\mathbf{D}_i$. It follows that the component form of the linearized equations of motion become

$$\dot{m}=0, \qquad m(\ddot{u}^i+y^n\ddot{\delta}_n{}^{ij})=\mathbf{f}^i+\sum_{K=1}^{M}n_K{}^i, \tag{15a,b}$$

$$m(y^i\ddot{u}^j+y^{in}\ddot{\delta}_n{}^j)=\mathbf{l}^{ij}+\sum_{K=1}^{M}m_k{}^{ij}-k^{ij}, \quad k^{ij}=k^{ji}. \tag{15c,d}$$

Now we turn to a discussion of linearized constitutive equations of the form (12). Since the intrinsic director couple k^{ij} is assumed to vanish in the reference configuration we take k^{ij} to be linear in γ_{ij} in the present configuration. It follows that the strain energy function $\hat{\psi}$ must be a quardratic function of the strain γ_{ij} given by

$$\hat{\psi}=\tfrac{1}{2}C^{ijkl}\gamma_{ij}\gamma_{kl}, \tag{16}$$

where C^{ijkl} is a fourth-order tensor function of H_{ij} satisfying the symmetry restrictions

$$C^{ijkl}=C^{jikl}=C^{ijlk}=C^{klij}. \tag{17}$$

With the help of (12) and (16) we conclude that for a linear-elastic solid Cosserat point, k^{ij} is specified by the constitutive equation

$$k^{ij}=C^{ijkl}\gamma_{kl}. \tag{18}$$

In general, equation (18) is valid for an anisotropic Cosserat point. However, if the Cosserat point is isotropic in its reference configuration, the tensor C^{ijkl} may be expressed in the form

$$C^{ijkl}=c_1H^{ij}H^{kl}+c_2(H^{ik}H^{jl}+H^{il}H^{jk}), \tag{19}$$

where c_1 and c_2 are constitutive constants to be specified. Thus for an isotropic Cosserat point the strain energy function $\hat{\psi}$ and the intrinsic director couples k^{ij} take the forms:

$$\hat{\psi}=\tfrac{1}{2}[c_1H^{ij}H^{kl}\gamma_{ij}\gamma_{kl}+2c_2\gamma^{ij}\gamma_{ij}], \tag{20a}$$

$$k^{ij}=c_1(H^{kl}\gamma_{kl})H^{ij}+2c_2\gamma^{ij}, \tag{20b}$$

where $\gamma^{ij}=H^{ik}H^{jl}\gamma_{kl}$ are the contravariant components of the strain tensor.

Constitutive Equations for a Rectangular Parallelepiped

As an example of the use of the theory just described we model a rectangular parallelepiped as a Cosserat point. Let x_i be coordinates of a fixed rectangular Cartesian coordinate system with base vectors $\mathbf{e}_i$ and consider the rectangular parallelepiped which in its reference configuration occupies the region of space bounded by the six surfaces:

$$\partial\mathcal{R}_1: x_1=-\frac{L_1}{2}, \quad |x_2|\leqq\frac{L_2}{2}, \quad |x_3|\leqq\frac{L_3}{2}, \tag{21a}$$

$$\partial\mathcal{R}_2: x_1=\frac{L_1}{2}, \quad |x_2|\leqq\frac{L_2}{2}, \quad |x_3|\leqq\frac{L_3}{2}, \tag{21b}$$

$$\partial\mathcal{R}_3: x_2=-\frac{L_2}{2}, \quad |x_1|\leqq\frac{L_1}{2}, \quad |x_3|\leqq\frac{L_3}{2}, \tag{21c}$$

$$\partial\mathcal{R}_4: x_2=\frac{L_2}{2}, \quad |x_1|\leqq\frac{L_1}{2}, \quad |x_3|\leqq\frac{L_3}{2}, \tag{21d}$$

$$\partial\mathcal{R}_5: x_3=-\frac{L_3}{2}, \quad |x_1|\leqq\frac{L_1}{2}, \quad |x_2|\leqq\frac{L_2}{2}, \tag{21e}$$

$$\partial\mathcal{R}_6: x_3=\frac{L_3}{2}, \quad |x_1|\leqq\frac{L_1}{2}, \quad |x_2|\leqq\frac{L_2}{2}, \tag{21f}$$

where L_1, L_2, and L_3 are the lengths of the sides of the parallelepiped. Furthermore, let the body be composed of a linear-elastic material that is homogeneous, has a uniform density $\rho_0{}^*$, and is three-dimensionally isotropic. In this section, we model such a body as an isotropic Cosserat point.

For this body it is convenient to specify the reference values $\mathbf{D}_i$ of the directors in the forms

$$\mathbf{D}_1=L_1\mathbf{e}_1, \quad \mathbf{D}_2=L_2\mathbf{e}_2, \quad \mathbf{D}_3=L_3\mathbf{e}_3. \tag{22a,b,c}$$

The mass m, inertia coefficients y^i and y^{ij}, and the constitutive constants c_1 and c_2 in (20) may be identified by comparison with the three-dimensional description of the parallelepiped. Using the definitions (*A*8*a,b,c*) and (*A*15*a,b,c*) of the Appendix, we specify m, y^i, and y^{ij} by the equations

$$m=\rho_0{}^*L_1L_2L_3, \quad y^i=0, \tag{23a,b}$$

$$y^{11}=y^{22}=y^{33}=\frac{1}{12}, \quad \text{all others } y^{ij}=0. \tag{23c,d}$$

Equation (23*b*) states that the origin of the coordinate system is located at the center of mass of the body and (23*d*) states that the cooordinate directions are parallel to the principle axes of inertia of the body.

To identify the constants c_1 and c_2 it suffices to consider homogeneous deformation for which $G^{ij}=H^{ij}$, $\gamma_{ij}=\gamma_{ij}{}^*$ and use (*A*12) and (*A*21) to obtain

$$k^{ij}=(L_1L_2L_3)\left(\frac{E}{1+\nu}\right)\left[\left(\frac{\nu}{1-2\nu}\right)H^{ij}H^{mm}+H^{im}H^{jn}\right]\gamma_{mn}, \tag{24}$$

where for the linear theory the volume V in (*A*12*a*) may be replaced by its reference value $(L_1L_2L_3)$. Finally, comparing expressions (20*b*) and (24) we conclude that

$$c_1=\frac{E\nu L_1L_2L_3}{(1+\nu)(1-2\nu)}, \quad c_2=\frac{EL_1L_2L_3}{2(1+\nu)}. \tag{25a,b}$$

Downloaded 02 May 2010 to 171.66.16.54. Redistribution subject to ASME license or copyright; see http://www.asme.org/terms/Terms_Use.cfm

With this specification the theory of a Cosserat point predicts exact results for the static homogeneous deformation problems of simple tension and simple shear.

Numerical Solution of Continuum Problems

The theory of a Cosserat point has been developed to model the deformation of a body that is essentially a material point surrounded by some small volume. The development of this theory is motivated mainly by the expectation that it can be successfully used as a basis for formulating numerical solution procedures for continuum problems. This application of the theory is based on the notion that a finite contiuum may be divided into a number of distinct but connected parts, each of which is modeled as a Cosserat point. Within this context, each part of the continuum has its own equations of motion and constitutive equations. To determine the motion of the finite continuum as a whole it is necessary to couple the motions of the individual Cosserat points by making appropriate statements about contact forces and moments applied across the common boundary between any two connected Cosserat points.

In the companion paper [1] it is shown that the theory of a Cosserat point can indeed be successfully used to formulate the numerical solution of nonlinear one-dimensional continuum problems. Although it is expected that the theory can similarly be used to formulate numerical solution procedures for two-dimensional and three-dimensional problems, the necessary generalizations are not trivial and must be handled with care in future works.

Acknowledgments

The results reported here were obtained in the course of research supported by the Israeli Ministry of Absorption for Science under contract with the Technion Research and Development Foundation.

References

1 Rubin, M. B., "On the Numerical Solution of One-Dimensional Continuum Problems Using the Theory of a Cosserat Point," ASME JOURNAL OF APPLIED MECHANICS, Vol. 52, pp. 373-378.

2 Naghdi, P. M., "The Theory of Shells and Plates," *Flügge's Handbuch der Physik*, Vol. VI a/2, Trudesdell, C., ed., 1972, pp. 425-640.

3 Green, A. E., and Naghdi, P. M., "On Thermal Effects in the Theory of Shells," *Proc. Royal Society of London*, Series A, Vol. 365, 1979, pp. 161-190.

4 Green, A. E., Naghdi, P. M., and Wenner, M. L., "On the Theory of Rods, I. Derivations From the Three-Dimensional Equations," *Proc. Royal Society of London*, Series A, Vol. 337, 1974, pp. 451-483.

5 Green, A. E., Naghdi, P. M., and Wenner, M. L., "On the Theory of Rods, II. Developments by Direct Approach," *Proc. Royal Society of London*, Series A, Vol. 337, 1974, pp. 485-507.

6 Green, A. E., and Naghdi, P. M., "On Thermal Effects in the Theory of Rods," *Int. J. Solids Structures*, Vol., 15, 1979, pp. 829-853.

APPENDIX

In this Appendix we briefly review the three-dimensional purely mechanical theory of continuum mechanics referred to a set of convected coordinates. After introducing a kinematic approximation of the position vector as well as a number of definitions we derive the equations of motion of the theory of a Cosserat point directly from the three-dimensional equations. This demonstrates a one-to-one correspondence between kinematic and kinetic quantities in the theory of a Cosserat point with those in the three-dimensional theory. Finally, we exhibit the linearized forms of some of the basic equations.

Let material points of a three-dimensional body, embedded in a Eucledian three-space, be identified by a general convected coordinate system θ^i ($i = 1,2,3,$) and let $\mathbf{p}$ denote the position vector, relative to a fixed origin, of a typical particle at time t. Then,

$$\mathbf{p}=\mathbf{p}(\theta^1,\theta^2,\theta^3,t),\quad \mathbf{g}_i=\frac{\partial \mathbf{p}}{\partial \theta^i}, \tag{A1a,b}$$

$$g_{ij}=\mathbf{g}_i\cdot\mathbf{g}_j,\quad \mathbf{g}^i\cdot\mathbf{g}_j=\delta^i{}_j,\quad g^{ij}=\mathbf{g}^i\cdot\mathbf{g}^j, \tag{A1c,d,e}$$

$$g^{1/2}=[\mathbf{g}_1\mathbf{g}_2\mathbf{g}_3]=[\det g_{ij}]^{1/2}, \tag{A1f}$$

where $\mathbf{g}_i$ and $\mathbf{g}^i$ are the covariant and contravariant base vectors at time t, respectively, g_{ij} is the metric tensor, g^{ij} is its conjugate, and $\delta^i{}_j$ is the Kronecker symbol. The velocity vector $\mathbf{v}^*$ at time t is given by

$$\mathbf{v}^*=\frac{\partial \mathbf{p}}{\partial t}\,(\theta^i,t)=\dot{\mathbf{p}}\,(\theta^i,t), \tag{A2}$$

where a superposed dot denotes material time differentiation, holding θ^i fixed.

In the present configuration at time t the body occupies the region $\mathcal{R}$ bounded by the closed surface $\partial\mathcal{R}$ with sections $\partial\mathcal{R}_K$ ($K=1,2,\ldots,M$). With respect to the present configuration let: ρ^* be the mass density, $\mathbf{f}^*$ be the body force per unit mass, and $\mathbf{t}$ be the stress vector across a surface whose outward unit normal is ν^*. Now the integral balance laws may be written in the form [2]:

$$\frac{d}{dt}\int_{\mathcal{R}}\rho^* dv=0, \tag{A3a}$$

$$\frac{d}{dt}\int_{\mathcal{R}}\rho^*\mathbf{v}^* dv=\int_{\mathcal{R}}\rho^*\mathbf{f}^* dv+\sum_{K=1}^{M}\int_{\partial\mathcal{R}_R}\mathbf{t}\,da, \tag{A3b}$$

$$\frac{d}{dt}\int_{\mathcal{R}}\mathbf{p}\,x\,\rho^*\mathbf{v}^* dv=\int_{\mathcal{R}}\mathbf{p}\,x\,\rho^*\mathbf{f}^* dv+\sum_{K=1}^{M}\int_{\partial\mathcal{R}_K}\mathbf{p}\,x\,\mathbf{t}\,da, \tag{A3c}$$

where $dv = g^{1/2}d\theta^1 d\theta^2 d\theta^3$ and where equations (A3a,b,c) represent conservation of mass, balance of linear momentum, and balance of angular momentum, respectively. In addition, we define the mechanical power P^* through the equation

$$\int_{\mathcal{R}}P^* dv=\int_{\mathcal{R}}\rho^*\mathbf{f}^*\cdot\mathbf{v}^* dv+\sum_{K=1}^{M}\int_{\partial\mathcal{R}_K}\mathbf{t}\cdot\mathbf{v}^* da$$

$$-\frac{d}{dt}\int_{\mathcal{R}}\tfrac{1}{2}\rho^*\mathbf{v}^*\cdot\mathbf{v}^* dv\cdot \tag{A4}$$

With the help of normal continuity and boundedness assumptions it can be shown that the stress vector can be expressed in the form

$$\mathbf{t}=\mathbf{T}^i\nu_i^*/g^{1/2},\quad \mathbf{T}^i=g^{1/2}\tau^{ij}\mathbf{g}_j,\quad \nu^*=\nu^{*i}\mathbf{g}_i=\nu_i^*\mathbf{g}^i. \tag{A5a,b,c}$$

To derive equations of the forms (5) and (9) associated with the theory of a Cosserat point, we assume that the position vector $\mathbf{p}$ depends at most linearly on the coordinates θ^i. Hence, it admits the representation

$$\mathbf{p}(\theta^i,t)=\mathbf{r}(t)+\theta^i\mathbf{d}_i(t) \tag{A6}$$

where $\mathbf{r}$ and $\mathbf{d}_i$ are the same quantities introduced in the main text of the paper. In view of (A6), the three-dimensional velocity $\mathbf{v}^*$ may be represented in the form

$$\mathbf{v}^*=\mathbf{v}+\theta^i\mathbf{w}_i \tag{A7}$$

where $\mathbf{v}$ and $\mathbf{w}_i$ are defined by equations (2a) and (2b), respectively. Next, let us relate the quantities m, y^i, y^{ij}, $\mathbf{f}$, $\mathbf{n}_K$, $\mathbf{l}^i$, $\mathbf{m}_K{}^i$, $\mathbf{k}^i$, and P to associated three-dimensional quantities through the equations:

$$m=\int_{\mathcal{R}}\rho^* dv,\quad my^i=\int_{\mathcal{R}}\rho^*\theta^i dv, \tag{A8a,b}$$

$$my^{ij}=\int_{\mathcal{R}}\rho^*\theta^i\theta^j dv,\quad \mathbf{f}=\int_{\mathcal{R}}\rho^*\mathbf{f}^* dv, \tag{A8c,d}$$

Downloaded 02 May 2010 to 171.66.16.54. Redistribution subject to ASME license or copyright; see http://www.asme.org/terms/Terms_Use.cfm

$$\mathbf{n}_K = \int_{\partial\mathcal{R}_K} \mathbf{t}\,da, \quad \mathbf{l}^i = \int_{\mathcal{R}} \rho^*\mathbf{f}^*\theta^i\,dv, \tag{A8e,f}$$

$$\mathbf{m}_K{}^i = \int_{\partial\mathcal{R}_K} \mathbf{t}\theta^i\,da, \quad \mathbf{k}^i = \int_{\mathcal{R}} \mathbf{T}^i g^{-1/2}\,dv, \tag{A8g,h}$$

$$P = \int_{\mathcal{R}} P^*\,dv. \tag{A8i}$$

Now, substituting the representations (A6) and (A7) into equations (A3) and (A4), and using the definitions (A8), we can derive the equations of conservation of mass (5a), balance of linear momentum (5d), balance of angular momentum (5d), and the mechanical power expression (9).

In contrast to equations (5a,b,d) and (9), the director momentum equation (5c) cannot be obtained directly from the integral forms (A3) and (A4). However, it can be derived from the local form of the balance of linear momentum (A3b). With suitable continuity assumptions we can apply the Divergence Theorem and derive the local forms of equations (A3a,b)

$$\frac{\dot{}}{\rho^* g^{1/2}} = 0, \quad \rho^*\dot{\mathbf{v}}^* g^{1/2} = \rho^*\mathbf{f}^* g^{1/2} + \mathbf{T}^m{}_{,m}, \tag{A9a,b}$$

were a comma denotes partial differentiation with respect to θ^m. Multiplying (A9b) by θ^i we obtain

$$\rho^*\dot{\mathbf{v}}^*\theta^i g^{1/2} = \rho^*\mathbf{f}^*\theta^i g^{1/2} + (\theta^i\mathbf{T}^m)_{,m} - \mathbf{T}^i, \tag{A10}$$

which represents the first moment with respect to θ^i of (A9b). Integrating (A10) over the region $\mathcal{R}$ and again using the Divergence Theorem we derive the integral form

$$\frac{d}{dt}\int_{\mathcal{R}} \rho^*\mathbf{v}^*\theta^i\,dv = \int_{\mathcal{R}} \rho^*\mathbf{f}^*\theta^i\,dv + \sum_{K=1}^{M}\int_{\partial\mathcal{R}_K} \theta^i\mathbf{t}\,da - \int_{\mathcal{R}} \mathbf{T}^i g^{-1/2}\,dv, \tag{A11}$$

where use has been made of (A9a). Now, substituting the representation (A7) into (A11) and using the definitions (A8) we may derive the director momentum equation (5c).

The preceding discussion demonstrates the one-to-one relationship between the theory of a Cosserat point and the three-dimensional theory when the kinematic assumption (A6) is employed. Nonlinear constitutive equations for a Cosserat point were developed in the main text of this paper. In this regard it is interesting to note that for uniform deformation of a nonlinear elastic material there is a direct relationship between k^{ij} and the three-dimensional stress tensor τ^{ij} defined in (A5). In particular, for such a deformation the coordinates θ^i may be chosen so that the base vectors $\mathbf{g}_i$ (defined in (A1)) are equal to the directors $\mathbf{d}_i$ and τ^{ij} is independent of θ^i. Therefore, with the help of (7e), (A5), and (A8h) we conclude that

$$k^{ij} = V\tau^{ij}, \quad V = \int_{\mathcal{R}} dv, \tag{A12a,b}$$

where V is the volume of the Cosserat point in the present configuration. The relationship (A12a) is particularly useful when motivating constitutive equations for elastic Cosserat points.

Finally, we derive some expressions related to the linearized theory. The three-dimensional displacement vector $\mathbf{u}^*$ is defiend by the equation

$$\mathbf{u}^* = \mathbf{p} - \mathbf{P} \tag{A13}$$

where $\mathbf{P}$ is the value of $\mathbf{p}$ in the reference configuration. It follows from the representations (13) and (A6) that $\mathbf{u}^*$ is given by

$$\mathbf{u}^* = \mathbf{u} + \theta^i\bar{\delta}_i. \tag{A14}$$

With reference to the Cartesian coordinate system introduced in the text, we take

$$\theta^1 = \frac{x_1}{L_1}, \quad \theta^2 = \frac{x_2}{L_2}, \quad \theta^3 = \frac{x_3}{L_3}, \tag{A15a,b,c}$$

and express the displacements vector $\mathbf{u}^*$ in terms of its Cartesian components u_i^*, such that

$$\mathbf{u}^* = u_i^*\mathbf{e}_i, \quad u_i^* = \mathbf{u}\cdot\mathbf{e}_i + \theta^m\bar{\delta}_m\cdot\mathbf{e}_i. \tag{A16a,b}$$

For the special case when the reference values $\mathbf{D}_i$ of the directors $\mathbf{d}_i$ are given by (22) the displacements $\mathbf{u}$ and $\bar{\delta}_i$ may be expressed as

$$\mathbf{u} = u_i\mathbf{D}^i = \frac{u_1}{L_1}\mathbf{e}_1 + \frac{u_2}{L_2}\mathbf{e}_2 + \frac{u_3}{L_3}\mathbf{e}_3, \tag{A17a}$$

$$\bar{\delta}_i = \bar{\delta}_{ij}\mathbf{D}^j = \frac{\bar{\delta}_{i1}}{L_1}\mathbf{e}_1 + \frac{\bar{\delta}_{i2}}{L_2}\mathbf{e}_2 + \frac{\bar{\delta}_{i3}}{L_3}\mathbf{e}_3. \tag{A17b}$$

In the context of the linearized theory, the three-dimensional strain e_{ij}^*, referred to the base vectors $\mathbf{e}_i$, and γ_{ij}^*, referred to the reference values $\mathbf{G}_i$ of the base vectors $\mathbf{g}_i$, are determined by the relations

$$e_{ij}^* = \tfrac{1}{2}\left(\frac{\partial u_i^*}{\partial x_j} + \frac{\partial u_j^*}{\partial x_i}\right), \quad \gamma_{ij}^* = \frac{\partial x_m}{\partial\theta^i}\frac{\partial x_n}{\partial\theta^j}e_{mn}^*. \tag{A18a,b}$$

Similarly, the Cauchy stress t_{ij}, referred to the base vectors $\mathbf{e}_i$, and the stress τ^{ij} (defined in (A5)), referred to the base vectors $\mathbf{G}_i$ are related by the equation

$$\tau^{ij} = \frac{\partial\theta^i}{\partial x_m}\frac{\partial\theta^i}{\partial x_n}t_{mn}. \tag{A19}$$

Further, for a linear-elastic isotropic material the Cauchy stress t_{ij} is related to the strains e_{ij}^* through the constitutive equation

$$t_{ij} = \left(\frac{E}{1+\nu}\right)\left[\left(\frac{\nu}{1-2\nu}\right)\delta_{ij}\delta_{mn} + \delta_{im}\delta_{jn}\right]e_{mn}^*, \tag{A20}$$

where E is Young's modulus and ν is Poisson's ratio. Corresponding to (A20) the constitutive equation for τ^{ij} may be written in the form

$$\tau^{ij} = \left(\frac{E}{1+\nu}\right)\left[\left(\frac{\nu}{1-2\nu}\right)G^{ij}G^{mn} + G^{im}G^{jn}\right]\gamma_{mn}^*, \tag{A21}$$

where G^{ij} is the reference value of g^{ij}.

Downloaded 02 May 2010 to 171.66.16.54. Redistribution subject to ASME license or copyright; see http://www.asme.org/terms/Terms_Use.cfm

On the Numerical Solution of One-Dimensional Continuum Problems Using the Theory of a Cosserat Point

M. B. Rubin
Faculty of Mechanical Engineering,
Technion-Israel Institute of Technology,
Haifa, Israel
Assoc. Mem. ASME

The theory of a Cosserat point is specialized to describe the motion of a one-dimensional continuum. Attention is focused on two problems of an elastic bar. Vibration of a linear-elastic bar is considered in the first problem and static deformation of a nonlinear-elastic bar subjected to a uniform body force is considered in the second problem. A closed-form solution is derived for each problem by dividing the bar into two elements, each of which is modeled as a Cosserat point. The predictions of the two-element approximation are shown to be very accurate.

Introduction

Recently the theory of a Cosserat point was developed to describe the deformation of a continuum that is essentially a material point with some small volume [1]. The development of this theory parallels the developments of the theory of a Cosserat surface [2], which models a shell-like body, and that of the theory of a Cosserat curve [3, 4], which models a rod-like body.

In [1] equations of motion were developed for a Cosserat point that allow deformations in all three dimensions. More importantly, the discussion in [1] suggested that the theory of a Cosserat point can be used as a basis of numerical solution procedures for problems of continuum mechanics. Here, the theory is specialized to describe the motion of a one-dimensional continuum and details are provided to demonstrate how an approximate solution can be obtained by dividing the continuum into elements, each of which is modeled as a Cosserat point.

From the point of view of the theory of a Cosserat point, each element is modeled as a separate continuum, with its own constitutive equation. Furthermore, each element is subjected to its own body and contact forces. To obtain an approximate solution of a continuum problem, we couple the motion of each element to motion of its neighbors by using an integrated form of Cauchy's lemma, which states that the contact force applied by a given Cosserat point on its neighbor is equal in magnitude and opposite in direction to the contact force applied by the neighbor on the given Cosserat point.

In the following sections, we develop the basic equations of the specialized form of the theory of a Cosserat point for one-dimensional deformation of a bar. The general solution procedure is described for three types of boundary value problems and then both nonlinear and linear constitutive equations are developed for an elastic bar. As examples, we solve two problems: (1) vibration of a linear-elastic bar, and (2) static deformation of a nonlinear-elastic bar subjected to a body force. For both problems, we compare the solutions with exact solutions of the equations of the exact one-dimensional theory, recorded in the Appendix. The last section contains concluding remarks.

Basic Equations

In this section, we present equations of motion that describe the one-dimensional deformation of a rectangular cylindrical bar composed of a homogeneous elastic material. Let x_i^* $(i=1,2,3)$ be coordinates of a fixed right-handed Cartesian coordinate system with base vectors $\mathbf{e}_i$. In its reference configuration, the bar occupies the region of space R defined by

$$0 \le x^* \le L, \quad |x_2^*| \le \frac{L_2}{2}, \quad |x_3^*| \le \frac{L_3}{2} \qquad (1a,b,c)$$

where $x^* = x_1^*$, L is the length of the bar in its reference configuration, and L_2 and L_3 are the lengths of the lateral surfaces of the bar. For the one-dimensional formulation under consideration, we neglect deformation in the $\mathbf{e}_2$ and $\mathbf{e}_3$ directions. Furthermore, we assume that the lateral surfaces of the bar are free of contact forces and that the contact forces on the ends of the bar ($x^* = 0$, $x^* = L$) and the body forces applied to the bar are uniform in its cross section and only have components in the $\mathbf{e}_1$ direction.

Instead of solving partial differential equations of motion that are functions of one space variable and time, we obtain an approximate solution for the deformation of the bar by dividing it into N elements each of which is modeled as a Cosserat point [1]. In the present configuration at time t, the

Contributed by the Applied Mechanics Division for publication in the JOURNAL OF APPLIED MECHANICS.

Discussion on this paper should be addressed to the Editorial Department, ASME, United Engineering Center, 345 East 47th Street, New York, N.Y. 10017, and will be accepted until two months after final publication of the paper itself in the JOURNAL OF APPLIED MECHANICS. Manuscript received by ASME Applied Mechanics Division, November, 1983; final revision, April, 1984.

Copyright © 1985 by ASME
Downloaded 02 May 2010 to 171.66.16.54. Redistribution subject to ASME license or copyright; see http://www.asme.org/terms/Terms_Use.cfm

Ith element associated with the Ith Cosserat point occupies the region of space R_I bounded by the surface ∂R_I with six sections ∂R_{IK} $(K=1,2,\ldots,6)$ defined by

$$\partial R_{I1}: x^* = x_I(t),\ |x_2^*| \le \frac{L_2}{2},\ |x_3^*| \le \frac{L_3}{2}, \tag{2a}$$

$$\partial R_{I2}: x^* = x_{I+1}(t),\ |x_2^*| \le \frac{L_2}{2},\ |x_3^*| \le \frac{L_3}{2}, \tag{2b}$$

$$\partial R_{I3}: x_2^* = -\frac{L_2}{2},\ x_I \le x^* \le x_{I+1},\ |x_3^*| \le \frac{L_3}{2} \tag{2c}$$

$$\partial R_{I4}: x_2^* = \frac{L_2}{2},\ x_I \le x^* \le x_{I+1},\ |x_3^*| \le \frac{L_3}{2}, \tag{2d}$$

$$\partial R_{I5}: x_3^* = -\frac{L_3}{2},\ x_I \le x^* \le x_{I+1},\ |x_2^*| \le \frac{L_2}{2}, \tag{2e}$$

$$\partial R_{I6}: x_3^* = \frac{L_3}{2},\ x_I \le x^* \le x_{I+1},\ |x_2^*| \le \frac{L_2}{2}, \tag{2f}$$

where $x_I(t)$ $(I=1,2,\ldots,N+1)$ are functions of time to be determined.

Furthermore, the Cosserat point[1] [1] associated with the Ith element is defined by its locations $\mathbf{r}_I(t)$, relative to the origin of the fixed Cartesian coordinate system, and by three directors $\mathbf{d}_{Ii}(t)$. The position vector $\mathbf{r}_I$ and directors $\mathbf{d}_{Ii}$ are each a three-dimensional vector function of time only which in the reference configuration acquire the values $\mathbf{r}_I=\mathbf{R}_I$ and $\mathbf{d}_{Ii}=\mathbf{D}_{Ii}$. A motion of the Cosserat point is defined by

$$\mathbf{r}_I=\mathbf{r}_I(t),\ \mathbf{d}_{Ii}=\mathbf{d}_{Ii}(t),\ d_I^{1/2}=[\mathbf{d}_{I1},\mathbf{d}_{I2},\mathbf{d}_{I3}]>0,$$
$$(I=1,2,\ldots,N)\ (i=1,2,3) \tag{3a,b,c}$$

where the condition (3c) ensures that the directors form a right-handed set of linearly independent vectors.

The vector functions $\mathbf{r}_I$ and $\mathbf{d}_{Ii}$ in (3) are assumed to be sufficiently smooth in the sense that they are differentiable with respect to time as many times as required. Let $\mathbf{v}_I$ and $\mathbf{w}_{Ii}$, each a three-dimensional vector function of time, denote, respectively, the velocity of the material point and the director velocities at time t. Then

$$\mathbf{v}_I=\frac{d}{dt}(\mathbf{r}_I)=\dot{\mathbf{r}}_I,\ \mathbf{w}_{Ii}=\frac{d}{dt}(\mathbf{d}_{Ii})=\dot{\mathbf{d}}_{Ii}, \tag{4a,b}$$

where a superposed dot denotes time differentiation.

The conservation and balance laws for the Cosserat point associated with the Ith element may be written in the form

$$\dot{m}_I=0, \qquad m_I(\dot{\mathbf{v}}+y_I{}^i\dot{\mathbf{w}}_{Ii})=\mathbf{f}_I+\sum_{K=1}^{6}\mathbf{n}_{IK}, \tag{5a,b}$$

$$m_I(y_I{}^i\dot{\mathbf{v}}_I+y_I{}^{ij}\dot{\mathbf{w}}_j)=\mathbf{l}_I{}^i+\sum_{K=1}^{6}\mathbf{m}_{IK}{}^i-\mathbf{k}_I{}^i, \tag{5c}$$

$$\mathbf{d}_{Ii}\times\mathbf{k}_I{}^i=0, \tag{5d}$$
$$(I=1,2,\ldots,N)$$

In (5) as well as throughout the text, we use the usual summation convention over repeated lower case indices but not over repeated upper case indices.

The equations of motion (5) may be placed in a one-to-one correspondence with equations of the three-dimensional theory if the position vector $\mathbf{p}_I$ of material points within the Ith element is approximated to be a linear function of the convected coordinates $\theta_I{}^i$ associated with the element such that

$$\mathbf{p}_I=\mathbf{p}_I(\theta_I{}^i,t)=\mathbf{r}_I(t)+\theta_I{}^i\mathbf{d}_{Ii}(t). \tag{6}$$

For definiteness, we take $\theta_I{}^i$ to be unitless and specify the region of space R_I by

$$|\theta_I{}^1|\le\frac{1}{2},\ |\theta_I{}^2|\le\frac{1}{2},\ |\theta_I{}^3|\le\frac{1}{2}. \tag{7a,b,c}$$

To model one-dimensional deformation of the bar in the $\mathbf{e}_1$ direction, we need only consider a restricted theory of a Cosserat point that is characterized by equations of motion that are simpler than those in (5). In particular, in the present configuration, the position vector $\mathbf{r}_I$ and directors $\mathbf{d}_{Ii}$ may be represented by[2]

$$\mathbf{r}_I=\bar{x}_I(t)\mathbf{e}_1 \tag{8a}$$

$$\mathbf{d}_{I1}=\phi_I(t)\mathbf{e}_1,\ \mathbf{d}_{I2}=L_2\mathbf{e}_2,\ \mathbf{d}_{I3}=L_3\mathbf{e}_3, \tag{8b,c,d}$$

where $\bar{x}_I$ is the location of the reference point in the Cosserat point. ϕ_I is the length (in the $\mathbf{e}_1$ direction) of the Cosserat point, and L_2 and L_3 are constant lengths.

In the reference configuration x^* takes the value ξ and x_I take the values ξ_I. It follows from (2) and (6)–(8) that

$$x^*=\mathbf{p}_I\cdot\mathbf{e}_1=\bar{x}_I+\theta_I{}^1\phi_I \tag{9a}$$

$$\theta_I{}^1=\frac{2\xi-\xi_I-\xi_{I+1}}{2(\xi_{I+1}-\xi_I)} \quad \text{for} \quad \xi\epsilon[\xi_I,\xi_{I+1}] \tag{9b}$$

and that

$$x_I=\bar{x}_I-\frac{1}{2}\phi_I,\quad x_{I+1}=\bar{x}_I+\frac{1}{2}\phi_I \tag{10a,b}$$

$$\bar{x}_I=\frac{1}{2}(x_I+x_{I+1})=\bar{X}_I+\frac{1}{2}(u_I+u_{I+1}), \tag{10c}$$

$$\bar{X}_I=\frac{1}{2}(\xi_I+\xi_{I+1}) \tag{10d}$$

$$\phi_I=x_{I+1}-x_I=\Phi_I+(u_{I+1}-u_I), \tag{10e}$$

$$\Phi_I=(\xi_{I+1}-\xi_I) \tag{10f}$$

where $\bar{X}_I$ and Φ_I are the reference values of $\bar{x}_I$ and ϕ_I, respectively, and the displacement u_I of the end $x^*=x_I$ of the Ith element is defined by the equation

$$u_I=x_I-\xi_I. \tag{11}$$

For one-dimensional deformation we assume that the bar is loaded with a stress that is applied uniformly to each of the boundary surfaces ∂R_{I1} and ∂R_{I2}. It follows that for the restricted theory the contact forces $\mathbf{n}_{IK}$ and contact director couples $\mathbf{m}_{IK}{}^i$ are dependent quantities that are specified by

$$\mathbf{n}_{I1}=n_{I1}\mathbf{e}_1,\ \mathbf{n}_{I2}=n_{I2}\mathbf{e}_1,\quad \text{all other } \mathbf{n}_{IK}=0 \tag{12a,b,c}$$

$$\mathbf{m}_{I1}{}^1=-\frac{1}{2}n_{I1}\mathbf{e}_1,\ \mathbf{m}_{I2}{}^1=\frac{1}{2}n_{I2}\mathbf{e}_1,$$
$$\text{all other } \mathbf{m}_{IK}{}^i=0 \tag{12d,e,f}$$

where n_{I1} and n_{I2} are functions of time to be determined. Also, for the restricted theory we specify

$$\mathbf{f}_I=f_I\mathbf{e}_1,\ \mathbf{l}_I{}^1=l_I\mathbf{e}_1,\quad \text{all other } \mathbf{l}_I{}^i=0 \tag{13a,b,c}$$

$$\mathbf{k}_I{}^1=k_I\mathbf{e}_1,\quad \text{all other } \mathbf{k}_I{}^i=0 \tag{13d,e}$$

$$m_I=\rho_0^*\Phi_I L_2L_3,\quad y_I{}^i=0,\quad y^{ij}=\frac{1}{12}\delta^{ij}. \tag{13f,g,h}$$

where the function f_I and l_I must be specified, k_I must be specified by a constitutive equation, ρ_0^* is the uniform mass density of the bar in its reference configuration, and δ^{ij} is the

[1] Here we use the development [1] and merely introduce a subscript I to indicate quantities related to the Cosserat point that models the Ith element.

[2] Without loss in generality, we have taken the reference point of each Cosserat point to lie on the $\mathbf{e}_1$ axes so that the components of $\mathbf{r}_I$ in the $\mathbf{e}_2$ and $\mathbf{e}_3$ directions vanish.

Downloaded 02 May 2010 to 171.66.16.54. Redistribution subject to ASME license or copyright; see http://www.asme.org/terms/Terms_Use.cfm

Kronecker symbol. In (13*f*) we have used the condition that mass is conserved in each element (5*a*).

With the help of the restrictions (8), (12), and (13), we realize that (5*a*) and (5*d*) are satisfied, and that the balance laws (5*b*) and (5*c*) reduce to the two scalar equations

$$m_I\ddot{x}_i = f_I + n_{I1} + n_{I2}, \quad \frac{1}{12}m_I\ddot{\phi}_I = l_I - \frac{1}{2}n_{I1} + \frac{1}{2}n_{I2} - k_I. \tag{14a,b}$$

To complete the theory we must specify a constitutive equation for the intrinsic director couple k_i. In this paper, we consider an elastic material for which k_I is specified to be a function of the present length ϕ_I and reference length Φ_I of the director $\mathbf{d}_{I1}$ in the form

$$k_I = \hat{k}_I(\phi_I, \Phi_I). \tag{15}$$

We emphasize that the constitutive equation (15) for k_I depends only on the values of ϕ_I and ϕ_I associated with the Ith Cosserat point.

Solution Procedure

With reference to one-dimensional deformation of a bar, it is possible to formulate three basic types of boundary value problems: for problem *I*, we specify displacement at one end of the bar (say $x^* = x_1$) and specify force at the other end (say $x^* = x_{N+1}$); for problem *II*, we specify displacement at both ends of the bar; and for problem *III*, we specify force at both ends of the bar. The solution procedures used for these problems are quite similar so they will be discussed together except where the differences are significant.

In the preceding section, we exhibited equations of motion of the Cosserat point that model the Ith element of the bar. To obtain an approximate solution of a particular boundary value problem of the whole bar using the theory at a Cosserat point, we must couple the motion of each element to the motion of its neighbors. This coupling is accomplished by requiring the contact force applied by a given Cosserat point on its neighbor, across their common boundary surface, to be equal in magnitude and opposite in direction to the contact force applied by the neighbor on the given Cosserat point. Since $n_{I-1,2}$ is the force applied to the $(I-1)$th element by the Ith element and n_{I1} is the force applied to the Ith element by the $(I-1)$th element we may write the coupling equations in the form

$$n_{I-1,2} + n_{I1} = 0 \qquad I = 2,3, \ldots, N. \tag{16}$$

Equation (16) introduces coupling through kinetic variables. Additional kinematic coupling is implied in the kinematic relationships (10*c*,*e*) which relate the kinematic variables $\dot{x}_I$ and ϕ_I to the locations x_I and x_{I+1} of the boundaries of the Ith element.

For an arbitrary constitutive equation (15) and arbitrary values of the body force and body director couple the equations of motion (14) can be solved for the contact forces n_{I1} and n_{I2} to obtain

$$n_{I1} = -\frac{1}{2}f_I + l_I - k_I + \frac{1}{3}m_I\ddot{x}_I + \frac{1}{6}m_I\ddot{x}_{I+1}, \tag{17a}$$

$$n_{I2} = -\frac{1}{2}f_I - l_I + k_I + \frac{1}{6}m_I\ddot{x}_I + \frac{1}{3}m_I\ddot{x}_{I+1}, \tag{17b}$$

where we also have used the kinematic conditions (10). Substituting (17*a*,*b*) into the coupling equations (16) we obtain $N-1$ equations of the form

$$\frac{1}{6}m_{I-1}\ddot{x}_{I-1} + \frac{1}{3}(m_{I-1}+m_I)\ddot{x}_I + \frac{1}{6}m_I\ddot{x}_{I+1} = \frac{1}{2}(f_{I-1}+f_I) + (l_{I-1}-l_I) - (k_{I-1}-k_I) \qquad I = 2,3, \ldots, N, \tag{18}$$

to restrict the $N+1$ unknown x_I. The remaining two equations are specified by the boundary conditions and are different for each of the three problems described at the beginning of this section. These are discussed separately in the following.

Problem *I*: The boundary conditions for this problem are characterized by specifying the displacement (or position) of the end $x^* = x_1$ and the force at the end $x^* = x_{N+1}$. Therefore, we specify

$$x_1 = \bar{\chi}(t), \quad n_{N2} = \hat{\eta}(t). \tag{19a,b}$$

where $\bar{\chi}$ and $\hat{\eta}$ are specified functions of time only.
It follows from (17*b*) and (19*b*) that

$$\frac{1}{6}m_N\ddot{x}_N + \frac{1}{3}m_N\ddot{x}_{N+1} = \frac{1}{2}f_N + l_N - k_N + \hat{\eta}(t). \tag{20}$$

Once the body force f_I, body director couple l_I, and a constitutive equation for k_I are specified, the equations (18), (19*a*), and (20) may be solved for the $N+1$ unknown $x_I(t)$ subject to the initial conditions.

$$x_I(0) - \xi_I = u_I(0) = U_I, \quad \dot{x}_I(0) = \dot{u}_I(0) = V_I \qquad (I = 1,2, \ldots, N+1) \tag{21a,b}$$

where we have used (11) and where U_I and V_I are, respectively, the initial displacement and velocity of the boundary surface ∂R_{I1}. After $x_I(t)$ are known, the boundary forces n_{I1} and n_{I2} can be determined by the equations (17).

Problem *II*: The boundary conditions for this problem are characterized by specifying the displacement at both the ends $x^* = x_1$ and $x^* = x_{N+1}$. Therefore, we specify

$$x_1 = \bar{\chi}(t), \; x_{N+1} = \hat{\chi}(t). \tag{22a,b}$$

where $\bar{\chi}$ and $\hat{\chi}$ are specified functions of time only. Once the body force f_I, body director couple l_I, and a constitutive equation for k_I are specified, the equations (18) and (22*a*,*b*) may be solved for the $N+1$ unknown $x_I(t)$ subject to the initial conditions (21). Again, after $x_I(t)$ are known, the boundary forces n_{I1} and n_{I2} can be determined by the equations (17).

Problems *III*: The boundary conditions for this problem are characterized by specifying force at both the ends $x^* = x_1$ and $x^* = x_{N+1}$. Therefore, we specify

$$n_{11} = \bar{\eta}(t), \; n_{N2} = \hat{\eta}(t), \tag{23a,b}$$

where $\bar{\nu}$ and $\bar{\eta}$ are specified functions of time only. It follows from (17*a*) and (23*a*) that

$$\frac{1}{3}m_1\ddot{x}_1 + \frac{1}{6}m_1\ddot{x}_2 = \frac{1}{2}f_1 - l_1 + k_1 + \bar{\eta}(t). \tag{24}$$

Once the body force f_I, body director couple l_I, and a constitutive equation for k_I are specified, the equations (18), (20), and (24) may be solved for the $N+1$ unknown $x_I(t)$ subject to the initial conditions (21). Again, after $x_I(t)$ are known, the boundary forces n_{I1} and n_{I2} can be determined by equations (17).

In the following sections, we domonstrate the utility of the theory by solving two problems: a vibration problem for a linear-elastic material and a static deformation problem for a nonlinear-elastic material. Before discussing these problems in detail, it is convenient to specialize the foregoing equations by considering elements of equal reference length L_1 such that

$$\xi_I = (I-1)\frac{L}{N} = (I-1)L_1, \quad I = 1,2, \ldots, N+1, \tag{25a}$$

$$m_I = m = \rho_0^* L_1 L_2 L_3. \tag{25b}$$

For both example problems we divide the bar into two elements ($N=2$) and specify the boundary conditions by

$$u_1 = 0, \; n_{22} = 0, \tag{26a,b}$$

which state that the end $\xi = 0$ is fixed and the end $\xi = L$ is free

Downloaded 02 May 2010 to 171.66.16.54. Redistribution subject to ASME license or copyright; see http://www.asme.org/terms/Terms_Use.cfm

of contact force. It follows from (11), (25), and (26) that the equations of motion (18) and (20) reduce to

$$m\left(\frac{2}{3}\ddot{u}_2+\frac{1}{6}\ddot{u}_3\right)=\frac{1}{2}(f_1+f_2)+(l_1-l_2)-(k_1-k_2), \quad (27a)$$

$$m\left(\frac{1}{6}\ddot{u}_2+\frac{1}{3}\ddot{u}_3\right)=\frac{1}{2}f_2+l_2-k_2. \quad (27b)$$

Constitutive Equations

To specify a constitutive equation of the form (15) for the intrinsic director couple k_I which characterizes material response described by the constitutive equation (A4) it suffices to consider the static problem of simple tension where the end $\xi=0$ of the bar is fixed and the end $\xi=L$ is subjected to a constant force η. It follows from (17)-(20) that in the absence of accelerations, body force, and body director couple, we have

$$n_{I1}=-k_I=-\eta, \quad n_{I2}=k_I=\eta, \quad (I=1,2,\ldots,N) \quad (28a,b)$$

Thus the response of each element is the same. Using (9), (10), (25), and (A3) the displacement u^* associated with the Ith element may be represented in the form

$$u^*=x^*-\xi=[\bar{x}_I-\frac{1}{2}(\xi_I+\xi_{I+1})]+\left(\frac{2\xi-\xi_I-\xi_{I+1}}{2L_1}\right)(\phi_I-L_1). \quad (29)$$

By substituting (29) into (A4) and multiplying the result by the cross-sectional area L_2L_3, we can determine th force n_{I2} on the boundary ∂R_{I2} of the Ith element. Then, using (28) we obtain the nonlinear constitutive equation

$$k_I=\frac{EL_2L_3}{2}\left[\left(\frac{\phi_I}{L_1}\right)^2-1\right]. \quad (30)$$

Similarly, the linearized constitutive equation associated with (A5) may be obtained and written in the form

$$k_I=\frac{EL_2L_3}{L_1}(\phi_I-L_1)=\frac{EL_2L_3}{L_1}(u_{I+1}-u_I), \quad (31)$$

where we have used (10) and (25).

Vibration of a Linear-Elastic Bar

In this section we consider the problem of vibration of a uniform bar composed of a linear-elastic material. An approximate solution to the problem is obtained using the theory of a Cosserat point and the results are compared with those of the exact solution of equation (A2).

The two-element Cosserat solution is characterized by the equations of motion (27), the boundary conditions (26), and the linear constitutive equation (31). In the absence of body forces and body director couples, equations (27) may be written in the form[3]

$$\frac{2}{3}\ddot{u}_2+\frac{1}{6}\ddot{u}_3=\left(\frac{c}{L_1}\right)^2(-2u_2+u_3), \quad (32a)$$

$$\frac{1}{6}\ddot{u}_2+\frac{1}{3}\ddot{u}_3=\left(\frac{c}{L_1}\right)^2(u_2-u_3), \quad (32b)$$

where we have used (25) and $c=(E/\rho_0{}^*)^{1/2}$ is the bar wave speed. Using standard techniques, the two-degree-of-freedom system (32) can be solved for the two natural modes of vibration. The solutions associated with each of these modes may be summarized as follows:

$$\omega_1=\left[\frac{6}{7}(5-3\sqrt{2})\right]^{1/2}\left(\frac{c}{L_1}\right)=\left[\frac{24}{7}(5-3\sqrt{2})\right]^{1/2}\left(\frac{c}{L}\right), \quad (33a)$$

$$u_2=\frac{U_3}{\sqrt{2}}\cos\omega_1 t, \quad u_3=U_3\cos\omega_1 t, \quad (33b,c)$$

$$n_{11}=-\left(\frac{EL_2L_3}{L_1}\right)U_3\left(\frac{6\sqrt{2}-3}{7}\right)\cos\omega_1 t, \quad (33d)$$

$$n_{12}=-n_{21}=\left(\frac{EL_2L_3}{L_1}\right)U_3\left(\frac{12-3\sqrt{2}}{14}\right)\cos\omega_1 t \quad (33e)$$

and

$$\omega_2=\left[\frac{6}{7}(5+3\sqrt{2})\right]^{1/2}\left(\frac{c}{L_1}\right)=\left[\frac{24}{7}(5+3\sqrt{2})\right]^{1/2}\left(\frac{c}{L}\right), \quad (34a)$$

$$u_2=-\frac{U_3}{\sqrt{2}}\cos\omega_2 t, \quad u_3=U_3\cos\omega_2 t, \quad (34b,c)$$

$$n_{11}=\left(\frac{EL_2L_3}{L_1}\right)U_3\left(\frac{(6\sqrt{2}+3}{7}\right)\cos\omega_2 t, \quad (34d)$$

$$n_{12}=-n_{21}=\left(\frac{EL_2L_3}{L_1}\right)U_3\left(\frac{12+3\sqrt{2}}{14}\right)\cos\omega_2 t \quad (34e)$$

where ω_1 and ω_2 are the natural frequencies and U_3 is the initial value of the displacement u_3. Also, in (33) and (34) we have used equations (17) to determine the contact forces.

Now, in the absence of body force, equation (A2) can be solved using the linear constitutive equation (A5) and boundary conditions equivalent to (26) to obtain

$$u^*=(-1)^{m+1}U_3\sin k_m{}^*\xi\cos\omega_m{}^*t, \quad (35a)$$

$$\sigma=(-1)^{m+1}EU_3k_m{}^*\cos k_m{}^*\xi\cos\omega_m{}^*t, \quad (35b)$$

$$k_m{}^*=\frac{(2m-1)\pi}{2L}, \quad \omega_m{}^*=\frac{(2m-1)\pi c}{2L} \quad m=1,2,\ldots \text{ (no sum on } m) \quad (35c,d)$$

where $\omega_m{}^*$ is the natural frequency and $k_m{}^*$ is the wave number associated with the mth mode, and U_3 is the initial displacement of the end $\xi=L$ (note that $u^*(L,t)$ corresponds to $u_3(t)$ in the Cosserat theory).

Comparing the predictions (33) and (34) of the Cosserat theory with the first two modes ($m=1,2$) of the exact solution (35) we obtain

$$\frac{\omega_1}{\omega_1{}^*}=\frac{2}{\pi}\left[\frac{24}{7}(5-3\sqrt{2})\right]^{1/2}=1.0259, \quad \frac{u_2(0)}{u^*\left(\frac{L}{2},0\right)}=1, \quad (36a,b)$$

$$\frac{-n_{11}(0)}{L_2L_3\sigma(0,0)}=\frac{n_{12}(0)}{L_2L_3\sigma\left(\frac{L}{2},0\right)}=\frac{24\sqrt{2}-12}{7\pi}=0.9977 \quad (36c)$$

and

$$\frac{\omega_2}{\omega_2{}^*}=\frac{2}{3\pi}\left[\frac{24}{7}(5+3\sqrt{2})\right]^{1/2}=1.1946, \quad \frac{u_2(0)}{u^*\left(\frac{L}{2},0\right)}=1, \quad (37a,b)$$

$$\frac{-n_{11}(0)}{L_2L_3\sigma(0,0)}=\frac{n_{12}(0)}{L_2L_3\sigma\left(\frac{L}{2},0\right)}=\frac{8\sqrt{2}+4}{7\pi}=0.6964. \quad (37c)$$

[3] These equations for displacements are identical to those that are obtained using the Galerkin method and expanding the displacement in terms of triangular test functions that take the value of one at the Ith node and decay linearly to zero at the $(I-1)$th and $(I+1)$th nodes.

Downloaded 02 May 2010 to 171.66.16.54. Redistribution subject to ASME license or copyright; see http://www.asme.org/terms/Terms_Use.cfm

Table 1 Comparison of the two-element Cosserat approximation with the exact nonlinear solution

a	$u^*\left(\frac{L}{2}\right)\Big/L$	$u_2/u^*\left(\frac{L}{2}\right)$	$u^*(L)/L$	$u_3/u^*(L)$
−0.5	−0.2643	0.9459	−0.3333	0.9510
−0.4	−0.1872	0.9815	−0.2412	0.9807
−0.3	−0.1304	0.9911	−0.1700	0.9896
−0.2	−0.0820	0.9956	−0.1079	0.9944
−0.1	−0.0391	0.9983	−0.0518	0.9976
−0.01	−0.0038	0.9999	−0.0050	0.9998
0	0	1	0	1
0.01	0.0037	1.0001	0.0050	1.0002
0.1	0.0361	1.0012	0.0484	1.0019
1.0	0.2892	1.0046	0.3987	1.0106
10	1.4917	1.0056	2.1745	1.0231
100	5.6154	1.0051	8.4956	1.0258
∞	-	1.0048	∞	1.0245

The results (36) and (37) show that even for the simple two-element approximation the predictions of the theory of a Cosserat point compare very well with the exact results for the lowest mode. As to be expected, the two-element approximation does not predict the second mode accurately.[4] To predict the higher modes, we need only increase the number of elements.

Static Deformation of a Nonlinear Elastic Material

In this section, we consider the problem of static deformation of a uniform bar composed of a nonlinear-elastic material which is subjected to a uniform body force. As in the preceding section, we obtain an approximate solution to the problem using the theory of a Cosserat point and then compare the solution with the exact analytical solution of (*A*2).

The two-element Cosserat solution is characterized by the equations (27), the boundary conditions (26), and the nonlinear constitutive equation (30). Using the definitions in the Appendix of [1], it can be shown that the body force f_I and body director couple l_I associated with the three-dimensional body force f^* are determined by the formulas

$$f_I = \rho_0{}^* L_2 L_3 \int_{\xi_I}^{\xi_{I+1}} f^*(\xi)\, d\xi, \tag{38a}$$

$$l_I = \rho_0{}^* L_2 L_3 \int_{\xi_I}^{\xi_{I+1}} f^*(\xi)\left[\frac{2\xi - \xi_I - \xi_{I+1}}{2(\xi_{I+1} - \xi_I)}\right] d\xi. \tag{38b}$$

For our particular problem f^* is specified by the constant b and the formulas (38) yield

$$f_I = \frac{aEL_1L_2L_3}{L}, \quad l_I = 0, \quad a = \frac{\rho_0{}^* bL}{E}, \tag{39a,b,c}$$

where a is a constant that measures the ratio of weight to strength of the bar. Using (25) with $N=2$, and (39), the equilibrium equations associated with (27) may be solved for k_1 and k_2 to obtain

$$k_1 = \frac{1}{2}f_1 + f_2 = \frac{3}{4}aEL_2L_3, \quad k_2 = \frac{1}{2}f_2 = \frac{1}{4}aEL_2L_3 \tag{40a,b}$$

Substituting (30) into (40) we deduce that

$$\phi_1 = L_1\left(1+\frac{3}{2}a\right)^{1/2}, \quad \phi_2 = L_1\left(1+\frac{1}{2}a\right)^{1/2} \tag{41a,b}$$

where use has been made of the fact that ϕ_1 and ϕ_2 are positive quantities. Now, with the help of (10), (17), (25), (26), (39), and (41), the displacements and contact forces become[5]

$$u_2 = \left(\frac{L}{2}\right)\left[\left(1+\frac{3}{2}a\right)^{1/2} - 1\right], \tag{42a}$$

$$u_3 = \left(\frac{L}{2}\right)\left[\left(1+\frac{3}{2}a\right)^{1/2} + \left(1+\frac{1}{2}a\right)^{1/2} - 2\right], \tag{42b}$$

$$n_{11} = -aEL_2L_3, \quad n_{12} = -n_{21} = \frac{aEL_2L_3}{2}, \tag{42c,d}$$

In the absence of accelerations and for constant body force equation (*A*2) may be solved using the nonlinear constitutive equation (*A*4) and boundary conditions equivalent to (26) and the solution may be written in the form

$$x^* = \left(\frac{L}{3a}\right)\left[(1+2a)^{3/2} - \left\{1+2a\left(1-\frac{\xi}{L}\right)\right\}^{3/2}\right], \tag{43a}$$

$$u^* = \left(\frac{L}{3a}\right)\left[(1+2a)^{3/2} - \left\{1+2a\left(1-\frac{\xi}{L}\right)\right\}^{3/2} - \frac{3a\xi}{L}\right], \tag{43b}$$

$$\sigma = aE\left(1-\frac{\xi}{L}\right). \tag{43c}$$

Comparing the predictions (42) of the Cosserat theory with those of the exact solution (43) we obtain

$$\frac{u_2}{u^*\left(\frac{L}{2}\right)} = \left(\frac{3a}{2}\right)\left[\frac{\left(1+\frac{3}{2}a\right)^{1/2} - 1}{(1+2a)^{3/2} - (1+a)^{3/2} - \frac{3a}{2}}\right] \tag{44a}$$

$$\frac{u_3}{u^*(L)} = \left(\frac{3a}{2}\right)\left[\frac{\left(1+\frac{3}{2}a\right)^{1/2} + \left(1+\frac{1}{2}a\right)^{1/2} - 2}{(1+2a)^{3/2} - 1 - 3a}\right] \tag{44b}$$

$$\frac{-n_{11}}{\sigma(0)L_2L_3} = \frac{n_{12}}{\sigma\left(\frac{L}{2}\right)L_2L_3} = 1. \tag{44c}$$

The results (44) show that the two-element approximation produces exact values of the forces for the full range of values[6] a $\epsilon(-0.5, \infty)$. The values of the displacements $u^*(L/2)$, $u^*(L)$ and the normalized displacements (44*a*,*b*) are tabulated in Table 1 and the predictions are seen to be very good.

Conclusions

The theory of a Cosserat point [1] has been used to obtain

[4] The prediction of the mode shape is exact but the frequency is in error so the prediction of the forces are also in error.

[5] The displacements (42*a*,*b*) are identical to those that can be obtained using the Galerkin method described in footnote 3.

[6] The lower bound is determined by requiring the deformation gradient $\partial x^*/\partial\xi$ be non-negative.

Downloaded 02 May 2010 to 171.66.16.54. Redistribution subject to ASME license or copyright; see http://www.asme.org/terms/Terms_Use.cfm

an approximate solution of two one-dimensional problems. For each problem a uniform elastic bar that is fixed at one end and free of contact force at the other is considered. For the first problem vibrations of a linear-elastic bar is analyzed and for the second problem static deformation of a nonlinear-elastic bar subjected to a uniform body force is analyzed.

In each case a simple closed-form solution is developed by dividing the bar into two elements, each of which is modeled as a Cosserat point. The results of the first problem compared very well with exact values for the first mode of vibration of the bar. In particular, accurate values were predicted for the displacements and forces at the ends of each element as well as for the natural frequency of vibration.

The results of the second problem also compared very well with the exact solution. In particular, the predictions of the forces at the ends of each element were exact for the full range of deformation. The predictions of the displacements at the ends of each element were accurate to within 5 percent for the full admissible range of deformation (33 percent compression to infinite extension of the bar).

These results suggest that the theory of a Cosserat point can be used quite successfully as a basis of numerical solution procedures for both linear and nonlinear one-dimensional continuum problems. Although the predictions of the Cosserat theory were compared with those obtained using the Galerkin method (see footnotes 3 and 5), the comparison is not particularly illuminating because the differential operators for the one-dimensional problems considered are particularly simple. A complete comparison of numerical formulations based on the theory of a Cosserat point with other existing formulations should include two-dimensional and three-dimensional motions and is beyond the scope of the present work.

References

1 Rubin, M. B., "On the Theory of a Cosserat Point and its Application to the Numerical Solution of Continuum Problems," ASME JOURNAL OF APPLIED MECHANICS, Vol. 52, pp. 362-371.

2 Naghdi, P. M., "The Theory of Shells and Plates," Flügge's *Handbuch der Physik*, Vol. VI *a*/2, Truesdell, C., ed., 1972, pp. 425-640.

3 Green, A. E., Naghdi, P. M., and Wenner, M. L., "On the Theory of Rods, I. Derivations from the Three-Dimensional Equations," *Proc. Royal Society of London*, Series *A*, Vol. 337, 1974, pp. 451-483.

4 Green, A. E., Naghdi, P. M., and Wenner, M. L., "On the Theory of Rods, II. Developments by Direct Approach," *Proc. Royal Society of London*, Series *A*, Vol. 37, 1974, pp. 485-507.

APPENDIX

In the present configuration, at time t, a typical material point of a body is located by its position x_i^* $(i=1,2,3)$ with respect to the origin of a fixed Cartesian coordinate system. For one-dimensional deformation, a motion of the body is defined by

$$x_1^* = x^* = \hat{\chi}^*(\xi,t),\ x_2^* = X_2,\ x_3^* = X_3, \qquad (A1a,b,c)$$

where X_A $(A=1,2,3)$ are the coordinates of the same material point in the initial configuration $(t=0)$ and ξ is identified with X_1.

Let ρ_0^* be the mass density in the reference configuration, f^* be the component of body force per unit mass in the $\mathbf{e}_1$ direction, and σ be the (1,1) component of the Cauchy stress tensor. Then the balance of linear momentum for one-dimensional deformation may be written in the form

$$\rho_0^* \ddot{u}^* = \rho_0^* f^* + \frac{\partial \sigma}{\partial \xi}, \qquad (A2)$$

where the displacement u^* is defined by the equation

$$u^*(\xi,t) = x^*(\xi,t) - \xi \qquad (A3)$$

Here, we consider a nonlinear-elastic material that is characterized by the constitutive equation

$$\sigma = \frac{1}{2}E\left[\left(\frac{\partial x^*}{\partial \xi}\right)^2 - 1\right] = E\left[\frac{\partial u^*}{\partial \xi} + \frac{1}{2}\left(\frac{\partial u^*}{\partial \xi}\right)^2\right], \qquad (A4)$$

where E is Young's modulus. For the linear theory, the quadratic term in (A4) is neglected and the Cauchy stress is determined by the equation

$$\sigma = E\frac{\partial u^*}{\partial \xi}. \qquad (A5)$$

Downloaded 02 May 2010 to 171.66.16.54. Redistribution subject to ASME license or copyright; see http://www.asme.org/terms/Terms_Use.cfm

B. H. Eldiwany[1]
Mem. ASME

L. T. Wheeler
Mem. ASME

Department of Mechanical Engineering,
University of Houston,
Houston, Texas 77004

Groove Bottom Contours of Minimum Stress Concentration for Antiplane Shear Deformation

Results from free streamline hydrodynamics are exploited in order to solve optimization problems for antiplane shear deformation, in which the stress concentration is to be minimized. These problems pertain to the optimum shapes for grooves cut into a half-space. We obtain results, which from the standpoint of the hydrodynamics problem, complement those presently in the literature. The solution is given in an integral form which in general must be evaluated by numerical methods, but that reduces to elliptic integrals for the special case of a notch whose faces meet the half-space boundary at right angles.

1 Introduction

The analysis of stress concentration is a subject of continuing interest in the mechanics of elastic solids. The objective is to find the maximum stress under given conditions of loading and geometry and determine how the maximum can be reduced by variations in these conditions. The task of reducing stress concentration is normally approached by a trial method in which the shape of the solid is remodeled iteratively until the stress is brought to within acceptable levels. The idea that the stress concentration can be minimized by finding a shape that renders the stress uniform has been exploited in [1-4]. This leads to a free-boundary problem. Wheeler et al. [5] described the optimization problem of stress concentration for states of antiplane shear deformation and gave conditions under which it can be rigorously reduced to a free-boundary problem. Wheeler et al. also pointed out the equivalence between this free-boundary problem and two-dimensional free streamline problems of classical hydrodynamics.

Riabouchinsky [6, 7] solved the hydrodynamic problem of flow over two finite plates situated, one behind the other, at right angles to the stream, and gave the solution in terms of elliptic integrals.

The purpose of the present paper is to investigate the solution of the optimization problem of antiplane shear deformation for a half-space with a groove cut in its boundary. In particular, we determine the shape of the groove bottom that minimizes the stress concentration factor, and compare our results with more elementary groove shapes.

2 The Traction Boundary—Value Problem for Antiplane Shear Deformation

Let x_i $(i = 1, 2, 3)$ denote rectangular cartesian coordinates, and let D denote the plane domain formed by the intersection of the $x_1 - x_2$ plane with a cylinder R whose generators extend in the x_3-direction to $x_3 = \pm \infty$. Occupying R is an elastic medium whose response is governed by the linearized theory for homogeneous and isotropic solids.

For antiplane shear deformations parallel to the x_3-axis, the displacements have the form

$$u_1 = u_2 = 0,\ u_3 = u(x_1, x_2) \qquad \text{on } R \tag{2.1}$$

and the governing equations reduce to

$$\nabla^2 u = 0 \qquad \text{on } D \tag{2.2}$$

in the absence of body forces.

The nonvanishing stress components are

$$\tau_1 = \tau_{31} = \frac{\partial \phi}{\partial x_1},\ \tau_2 = \tau_{32} = \frac{\partial \phi}{\partial x_2} \qquad \text{on } D \tag{2.3}$$

where

$$\phi = \mu u, \tag{2.4}$$

μ being the shear modulus.

We assume that on the boundary of R the tractions are prescribed, and considering (2.1), these tractions reduce to a single component t, which is in the x_3 direction, but does not vary with x_3. Thus, we have

$$\frac{\partial \phi}{\partial n} = t \qquad \text{on } \partial D \tag{2.5}$$

where ∂D stands for the boundary of D. Accordingly, ϕ is the solution of the two-dimensional Neumann problem

$$\nabla^2 \phi = 0 \qquad \text{on } D, \qquad \frac{\partial \phi}{\partial n} = t \qquad \text{on } \partial D. \tag{2.6}$$

The stress function ϕ is determined to within a constant by (2.6), and the stresses are uniquely determined from (2.3). Clearly, the stresses do not depend on the elastic constants.

We introduce the complex stress functions $w(z)$ defined by

[1] Presently with Kalsi Engineering, Inc., Sugar Land, Texas 77478.

Contributed by the Applied Mechanics Division for presentation at the 1985 Joint ASME/ASCE Applied Mechanics, Fluids Engineering, and Bioengineering Conference, Albuquerque, N. Mex., June 24-26, 1985 of THE AMERICAN SOCIETY OF MECHANICAL ENGINEERS.

Discussion on this paper should be addressed to the Editorial Department, ASME, United Engineering Center, 345 East 47th Street, New york, N.Y. 10017, and will be accepted until two months after final publication of the paper itself in the JOURNAL OF APPLIED MECHANICS. Manuscript received by ASME Applied Mechanics Division, February, 1984; final revision, September, 1984. Paper No. 85-APM-18.

Copies will be available until February, 1986.

Copyright © 1985 by ASME
Downloaded 02 May 2010 to 171.66.16.54. Redistribution subject to ASME license or copyright; see http://www.asme.org/terms/Terms_Use.cfm

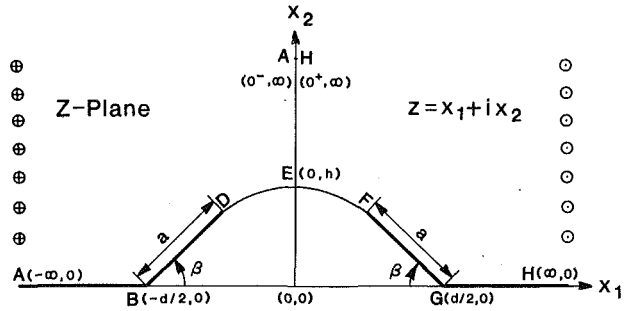


Fig. 1 The physical plane

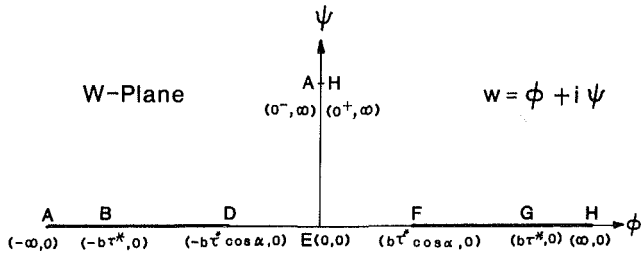


Fig. 2

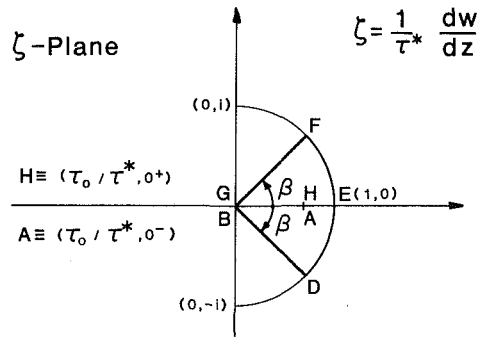


Fig. 3

$$w(z)=\phi+i\psi,\ z=x_1+ix_2,\ i=\sqrt{-1} \tag{2.7}$$

where ψ is the complex conjugate of ϕ, and is related to ϕ through the Cauchy-Riemann relations

$$\frac{\partial\phi}{\partial x_1}=\frac{\partial\psi}{\partial x_2},\ \frac{\partial\phi}{\partial x_2}=-\frac{\partial\psi}{\partial x_1}. \tag{2.8}$$

It follows that

$$\frac{dw}{dz}=\frac{\partial\phi}{\partial x_1}+i\frac{\partial\psi}{\partial x_1}=\tau_1-i\tau_2=\bar{\tau}, \tag{2.9}$$

where τ denotes the complex stress

$$\tau=\tau_1+i\,\tau_2=\tau\,e^{i\theta}. \tag{2.10}$$

Thus, the stress field can be determined by finding the complex stress function w.

Consider the domain D to be the half space $x_2 > 0$ with a groove cut through the plane $x_2 = 0$ (see Fig. 1). The loading consists of stresses applied at infinity,

$$\tau_1 \longrightarrow \tau_0, \quad \tau_2 \longrightarrow 0 \quad \text{as} \quad r \longrightarrow \infty, \tag{2.11}$$

while the boundary remains traction free.

Suppose that a curve C^* can be passed through points D and F such that the stress magnitude τ is a constant, τ^*, on C^*. According to a result of Wheeler et al. [5], such a profile is optimal in the sense that the stress concentration factor, K_0, is minimized.

The task undertaken here is to determine the shape of C^* for different β's and d's, with K_0 calculated for each configuration.

Let

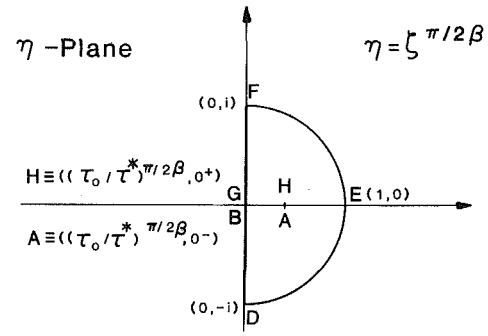


Fig. 4

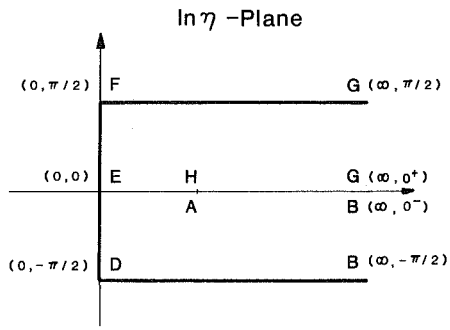


Fig. 5

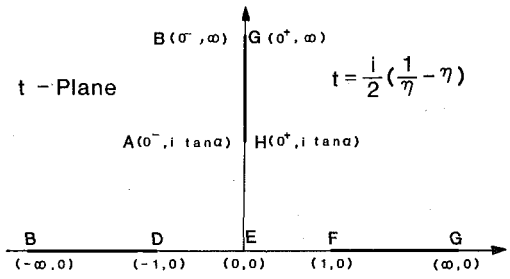


Fig. 6

$$\zeta=\frac{1}{\tau^*}\frac{dw}{dz}=\frac{1}{\tau^*}\left(\frac{\partial\phi}{\partial x_1}+i\frac{\partial\psi}{\partial x_1}\right)$$

$$=\frac{1}{\tau^*}(\tau_1-i\tau_2)=\frac{\tau}{\tau^*}e^{-i\theta}, \tag{2.12}$$

$$\theta=\tan^{-1}\frac{\tau_2}{\tau_1}. \tag{2.13}$$

Then ζ is the conjugate of the nondimensional complex stress τ/τ^*. The approach taken here is to exploit the conformal transformation which takes the ζ-plane into the w-plane. This task is accomplished with the aid of certain intermediate transformations, as follows

$$\eta=\zeta^{\frac{\pi}{2\beta}}=\left(\frac{\tau}{\tau^*}\right)^{\frac{\pi}{2\beta}}e^{-i\frac{\theta\pi}{2\beta}}, \tag{2.14}$$

$$\log\eta=\frac{\pi}{2\beta}\log\left(\frac{\tau}{\tau^*}\right)-i\frac{\theta\pi}{2\beta}, \tag{2.15}$$

$$t=\frac{i}{2}\left(\frac{1}{\eta}-\eta\right), \tag{2.16}$$

$$t=\frac{\left(\frac{w}{b}\right)\tan\alpha}{\left[\tau^{*2}-\left(\frac{w}{b}\right)^2\right]^{1/2}}, \tag{2.17}$$

Downloaded 02 May 2010 to 171.66.16.54. Redistribution subject to ASME license or copyright; see http://www.asme.org/terms/Terms_Use.cfm

$$\frac{w}{b} = \frac{\tau^* t}{[\tan^2\alpha + t^2]^{1/2}}. \tag{2.18}$$

The constant b fixes the width of the groove. The "physical" or z-plane is depicted in Fig. 1. The arbitrary complex constant in w has been chosen so that $\phi = 0$ at the midpoint E, and $\psi = 0$ on the stress-free boundary AB-$DEFGH$ (Fig. 2). The ζ-plane, shown in Fig. 3, is analogous to the hodograph plane of potential-flow theory. The circular sector of the ζ-plane is mapped into the semicircle of unit radius in the η-plane, Fig. 4, by the transformation (2.14). Consider next the function $\log \eta$. In the plane of this function the circular arcs, for which $\tau = \tau^*$, transform into portions of the imaginary axis, and the radial lines into lines parallel to the real axis. Then the Schwarz-Christoffel transformation (2.16) is used to transform the polygon in Fig. 5 into the upper half of the t-plane of Fig. 6. Evidently, the boundary of the semicircle of Fig. 4 is taken into the real axis of the t-plane. Finally the transformation (2.18) takes the upper half of the t-plane into the upper half of the w-plane with the indicated correspondence of the boundary points. In particular the points A and H, for which $\eta = (\tau/\tau^*)^{\pi/2\beta}$, go into $t = i \tan\alpha$, where the parameter α is determined by the relation

$$\left(\frac{\tau_0}{\tau^*}\right)^{\frac{\pi}{2\beta}} = \frac{1-\sin\alpha}{\cos\alpha}. \tag{2.19}$$

This gives the stress concentration factor K_0 as a function of the parameter α,

$$K_0 = \frac{\tau^*}{\tau_0} = \left(\frac{\cos\alpha}{1-\sin\alpha}\right)^{\frac{2\beta}{\pi}} = \left(\frac{1+\sin\alpha}{1-\sin\alpha}\right)^{\frac{\beta}{\pi}}. \tag{2.20}$$

Also note that on C^*, $\tau = \tau^*$ which gives

$$t = -\sin\frac{\pi\theta}{2\beta} \quad \text{on } C^*. \tag{2.21}$$

In principle w may be obtained as a function of z by means of (2.17) or (2.18), and the stress field thus found in the domain D.

3 The Determination of the Groove Profile

The parameter α and the angle β fix the groove shape. The following analysis gives the dimensions a and d of the groove as well as the cartesian coordinates of the optimum groove bottom, C^*.

For the calculation of a, it is desirable to replace dx_2 by

$$dx_2 = \left(\frac{dx_2}{dz}\right)\left(\frac{dz}{dw}\right)\left(\frac{dw}{dt}\right)dt. \tag{3.1}$$

Along FG, these derivatives have the values:

$$\frac{dx_2}{dz} = -e^{i\beta}\sin\beta, \tag{3.2}$$

$$\frac{dz}{dw} = \frac{e^{i\beta}}{\tau}, \tag{3.3}$$

$$\frac{dw}{dt} = \frac{b\,\tau^*\tan^2\alpha}{(\tan^2\alpha + t^2)^{3/2}}. \tag{3.4}$$

By integrating (3.1) between F and G, and using the substitution $t = \sec x$, we get

$$\frac{a}{b} = \int_0^{\pi/2}\left(\frac{\tau^*}{\tau}\right)\frac{\sin^2\alpha\cos\alpha\sin x\cos x}{(1-\sin^2\alpha\sin^2 x)^{3/2}}dx. \tag{3.5}$$

Using (2.15) and (2.16), it is easy to verify that

$$\frac{\tau}{\tau^*} = |\zeta| = |\eta|^{\frac{2\beta}{\pi}} = \left(\frac{1-\sin x}{\cos x}\right)^{\frac{2\beta}{\pi}} = \left(\frac{\cos x}{1+\sin x}\right)^{\frac{2\beta}{\pi}}. \tag{3.6}$$

Accordingly,

$$\frac{a}{b} = \int_0^{\pi/2}\left(\frac{1+\sin x}{\cos x}\right)^{\frac{2\beta}{\pi}}\frac{\sin^2\alpha\cos\alpha\sin x\cos x}{(1-\sin^2\alpha\sin^2 x)^{3/2}}dx. \tag{3.7}$$

Next, on C^*, $\psi = 0$, $d\phi/ds = \tau^*$, and $t = -\sin(\theta\pi/2\beta)$ as in (2.21), and if the arc length s is measured from point E, we may put $\phi = \tau^* s$. Substitution in (2.18) and differentiation yields

$$\frac{ds}{b} = -\frac{\pi}{2\beta}\frac{\tan\alpha\cos(\theta\pi/2\beta)}{[\tan^2\alpha + \sin^2(\theta\pi/2\beta)]^{3/2}}d\theta. \tag{3.8}$$

Then on integrating the expressions

$$dx_1 = \cos\theta\, ds, \tag{3.9}$$

$$dx_2 = \sin\theta\, ds, \tag{3.10}$$

we get the cartesian coordinates of the curve C^*, as follows:

$$\int_{-\left(\frac{d}{2} - a\cos\beta\right)}^{x_1}\frac{dx_1}{b} = -\frac{\pi}{2\beta}\int_\beta^\theta \frac{\sin^2\alpha\cos\alpha\cos\phi\cos\left(\frac{\phi\pi}{2\beta}\right)}{\left[1-\cos^2\alpha\cos^2\left(\frac{\phi\pi}{2\beta}\right)\right]^{3/2}}d\phi, \tag{3.11}$$

$$\int_{a\sin\beta}^{x_2}\frac{dx_2}{b} = -\frac{\pi}{2\beta}\int_\beta^\theta \frac{\sin^2\alpha\cos\alpha\sin\phi\cos\left(\frac{\phi\pi}{2\beta}\right)}{\left[1-\cos^2\alpha\cos^2\left(\frac{\phi\pi}{2\beta}\right)\right]^{3/2}}d\phi, \tag{3.12}$$

where $|\theta| \le \beta$, $|x_1| \le (d/2 - a\cos\beta)$, $h \ge x_2 \ge a\sin\beta$.

Divide (3.11) and (3.12) by a/b and use (3.7) followed by the change of variables $x = \pi\phi/2\beta$ and some simplification to arrive at

$$\frac{x_1}{a} = \cos\beta - \frac{d}{2a} + \frac{\int_\psi^{\pi/2}\frac{\cos\left(\frac{2\beta x}{\pi}\right)\cos x}{[1-\cos^2\alpha\cos^2 x]^{3/2}}dx}{\int_0^{\pi/2}\left(\frac{1+\sin x}{\cos x}\right)^{2\beta/\pi}\frac{\sin x\cos x}{[1-\sin^2\alpha\sin^2 x]^{3/2}}dx}, \tag{3.13}$$

$$\frac{x_2}{a} = \sin\beta + \frac{\int_\psi^{\pi/2}\frac{\sin\left(\frac{2\beta x}{\pi}\right)\cos x}{[1-\cos^2\alpha\cos^2 x]^{3/2}}dx}{\int_0^{\pi/2}\left(\frac{1+\sin x}{\cos x}\right)^{2\beta/\pi}\frac{\sin x\cos x}{[1-\sin^2\alpha\sin^2 x]^{3/2}}dx}, \quad -\pi/2 \le \psi \le \pi/2. \tag{3.14}$$

The total width, d, and the total depth, h, of the groove are given by the expressions

$$\frac{d}{2a} = \cos\beta + \frac{\int_0^{\pi/2}\frac{\cos\left(\frac{2\beta x}{\pi}\right)\cos x}{[1-\cos^2\alpha\cos^2 x]^{3/2}}dx}{\int_0^{\pi/2}\left(\frac{1+\sin x}{\cos x}\right)^{2\beta/\pi}\frac{\sin x\cos x}{[1-\sin^2\alpha\sin^2 x]^{3/2}}dx}, \tag{3.15}$$

Downloaded 02 May 2010 to 171.66.16.54. Redistribution subject to ASME license or copyright; see http://www.asme.org/terms/Terms_Use.cfm

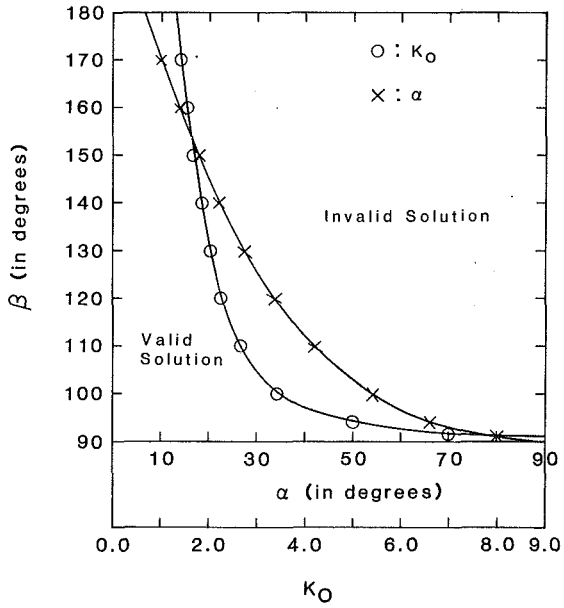


Fig. 7 Regions of validity of the solution

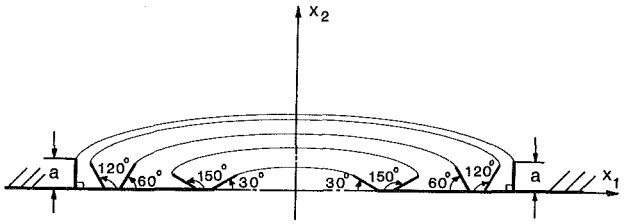


Fig. 8 The optimum grooves for $K = 1.3$

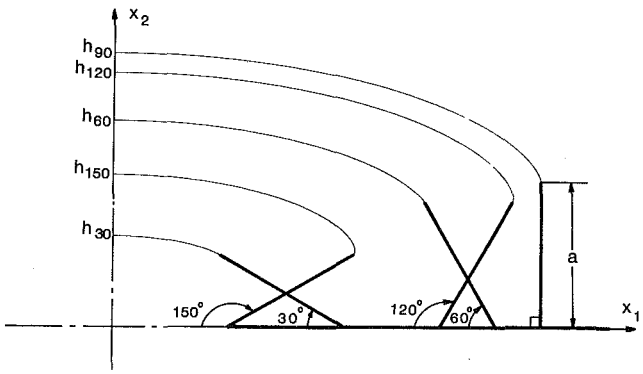


Fig. 9 The optimum grooves for $K = 1.5$

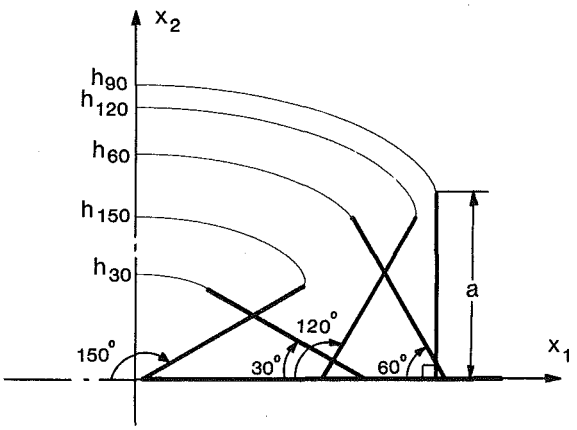


Fig. 10 The optimum grooves for $K = 1.7$

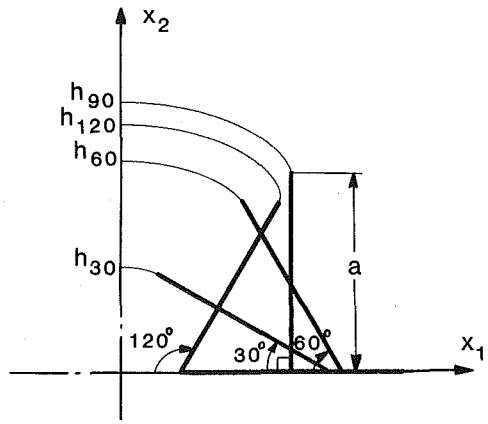


Fig. 11 The optimum grooves for $K = 2.0$

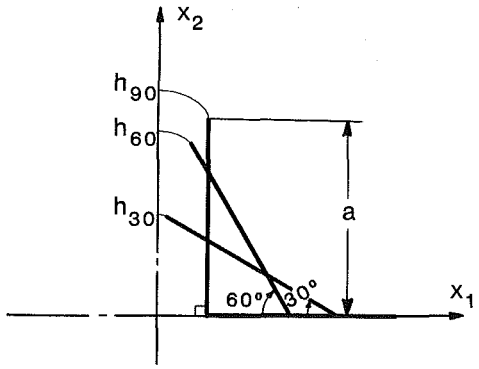


Fig. 12 The optimum grooves for $K = 3.0$

$$\frac{h}{2a} = \sin\beta + \frac{\displaystyle\int_0^{\pi/2} \frac{\sin\left(\frac{2\beta x}{\pi}\right)\cos x}{[1-\cos^2\alpha\cos^2 x]^{3/2}}\,dx}{\displaystyle\int_0^{\pi/2}\left(\frac{1+\sin x}{\cos x}\right)^{2\beta/\pi}\frac{\sin x\cos x}{[1-\sin^2\alpha\sin^2 x]^{3/2}}\,dx}, \tag{3.16}$$

Further simplification of the expression for x_1 may be obtained by substituting for d/a from (3.15). This yields

$$\frac{x_1}{a} = -\frac{\displaystyle\int_0^{\psi} \frac{\cos\left(\frac{2\beta x}{\pi}\right)\cos x}{[1-\cos^2\alpha\cos^2 x]^{3/2}}\,dx}{\displaystyle\int_0^{\pi/2}\left(\frac{1+\sin x}{\cos x}\right)^{2\beta/\pi}\frac{\sin x\cos x}{[1-\sin^2\alpha\sin^2 x]^{3/2}}\,dx}, \tag{3.17}$$

where $-\pi/2 \le \psi \le \pi/2$.

In the special case $\beta = \pi/2$, however, the integral forms simplify and give results in terms of standard elliptic integrals. These results are summarized as follows:

$$\frac{x_1}{b} = -\frac{\sin 2\theta}{2(\tan^2\alpha+\sin^2\theta)^{1/2}} - \sin^2\alpha\sec\alpha\,F\left(\cos\alpha, \frac{\pi}{2}-\theta\right) + \sec\alpha\,E\left(\cos\alpha, \frac{\pi}{2}-\theta\right) - \frac{d}{2b}, \tag{3.18}$$

$$\frac{x_2}{b} = \frac{\tan^2\alpha}{[\tan^2\alpha+\sin^2\alpha]^{1/2}} - \frac{\tan^2\alpha}{[\tan^2\alpha+1]^{1/2}} + \frac{a}{b}, \tag{3.19}$$

Downloaded 02 May 2010 to 171.66.16.54. Redistribution subject to ASME license or copyright; see http://www.asme.org/terms/Terms_Use.cfm

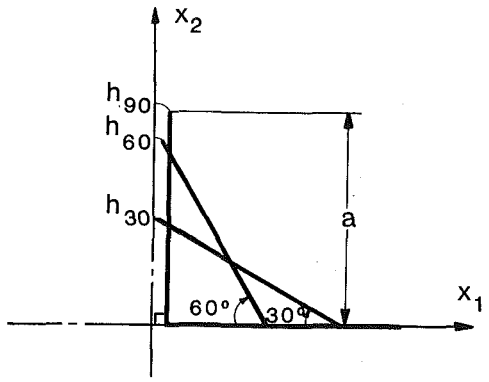


Fig. 13 The optimum grooves for $K = 5.0$

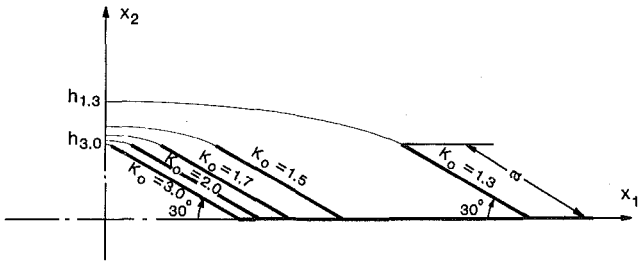


Fig. 14 The optimum grooves for $\beta = 30$ deg

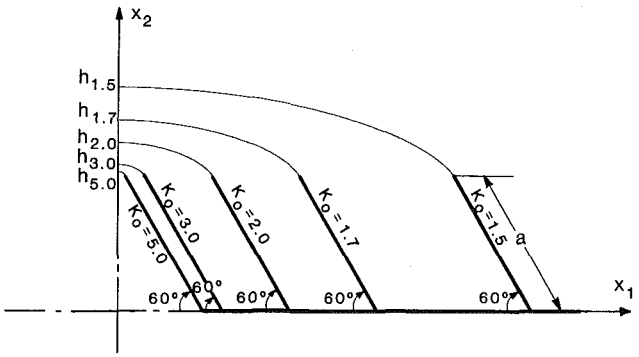


Fig. 15 The optimum grooves for $\beta = 60$ deg

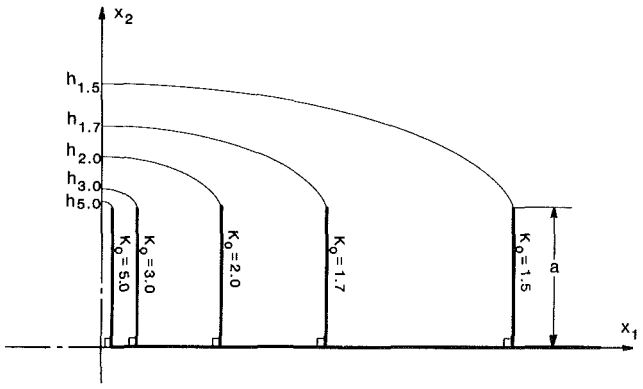


Fig. 16 The optimum grooves for $\beta = 90$ deg

$$\frac{d}{2b} = \sec\alpha[E' - \sin^2\alpha K'], \tag{3.20}$$

$$\frac{a}{2b} = \sec\alpha[\sin^2\alpha + E - \cos^2\alpha K], \tag{3.21}$$

$$\frac{h-a}{b} = \sec\alpha[\sin\alpha - \sin^2\alpha], \tag{3.22}$$

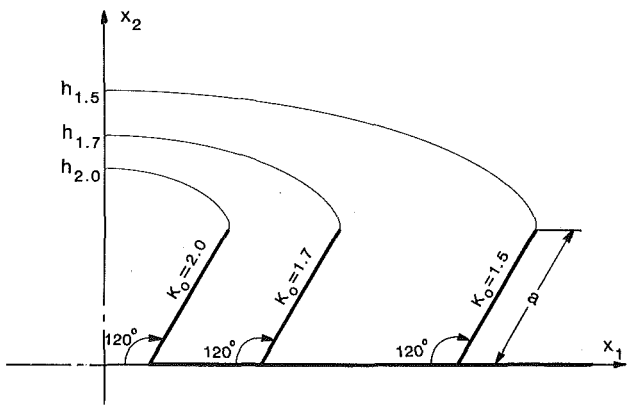


Fig. 17 The optimum grooves for $\beta = 120$ deg

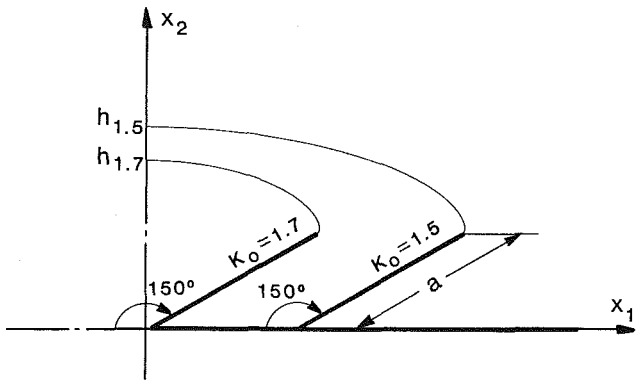


Fig. 18 The optimum grooves for $\beta = 150$ deg

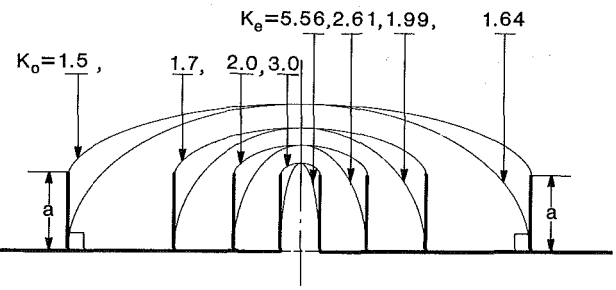


Fig. 19 The optimum grooves versus elliptic grooves

where $F(\cos\alpha, \pi/2 - \theta)$ and $E(\cos\alpha, \pi/2 - \theta)$ are Legendre's normal elliptic integrals of the first and second kind, K and E are Legendre's complete elliptic integrals of the first and second kind, and K' and E' are Legendre's complete complementary integrals of the first and second kind, respectively [8]. For details, see [9].

4 Numerical Results

Two independent parameters α and β are needed to determine the shape of the groove and the stress concentration factor, K_0. Since K_0 depends only on α and β [see (2.20)], we may by fixing α and changing β obtain various groove shapes for the same value of K_0.

On the other hand we may fix β and by varying α obtain a family of groove shapes as well as the corresponding stress concentration factors.

Three limiting cases can be discerned. The first is $\alpha = 0$, which gives $K_0 = 1$. This is equivalent to removing an infinite strip (x_2 = constant) from the boundary.

The second limiting case is for $\alpha = \pi/2$ which gives $K_0 = \infty$. This is equivalent to a surface crack where $d \to 0$ and $h > 0$ (see Fig. 1).

The third limiting case is associated with the onset of

Downloaded 02 May 2010 to 171.66.16.54. Redistribution subject to ASME license or copyright; see http://www.asme.org/terms/Terms_Use.cfm

Table 1 The optimum grooves versus elliptic grooves.

$d/2a$	h/a	K_0	K_{ellipse}
60.813	6.331636	1.10	1.104
16.184	3.541307	1.20	1.219
7.571	2.617476	1.30	1.346
2.956	1.888491	1.50	1.639
1.607	1.584345	1.70	1.986
0.849	1.364963	2.00	2.608
0.248	1.133551	3.00	5.563
72.750×10^{-3}	1.043307	5.00	15.440
16.360×10^{-3}	1.010260	10.00	62.753
3.973×10^{-3}	1.002520	20.00	253.308
1.755×10^{-3}	1.001116	30.00	571.411
9.849×10^{-4}	1.000627	40.00	1016.985
6.295×10^{-4}	1.000401	50.00	1590.086

physically unacceptable overlapping of the groove faces. This determines a range $\pi > \beta > \pi/2$ and $\pi/2 > \alpha > 0$ which places limits on the validity of the solutions as indicated by Fig. 7. Also in Fig. 7, K_0 is plotted versus β to give the upper bound of the optimum stress concentration factor. In the following results only the acceptable solutions are considered.

A representative set of β's are selected to plot the optimum grooves given in Figs. 8–18. We take β equal to 30, 60, 90, 120, and 150 deg. Also, the groove shapes are normalized with respect to the length, a, of the straight faces. Figure 8 gives the corresponding groove shapes for $K_0 = 1.30$. Because of the symmetry in the groove shapes about the x_2-axis, and for clarity, only the right half of the acceptable grooves are given in Figs. 9–18, where the scale is kept the same for the sake of comparison.

Figures 14–18 give five families of grooves for five different values of β, and in each family the groove shapes are plotted for a selection of values of K_0.

Further, Fig. 19 and Table 1 show a comparison between optimum grooves and elliptical grooves [10] with the stress concentration factors as indicated. Clearly the stress concentration factors for the two grooves diverge for sharper cuts, which emphasizes the importance of optimization for higher stress concentration factors.

Finally, it is worth mentioning that while antiplane shear deformation does not appear to be of major physical importance, it is reasonable to believe that the stresses arising in the groove problem presented here correspond approximately to those arising in the torsion of a circular shaft having a circumferential groove whose dimensions are small in comparison to the nominal shaft radius.

Acknowledgment

This work was completed while one of the authors (L. T. Wheeler) was supported by a Shell Companies Foundation grant to Professor M. M. Carroll of the University of California.

References

1 Durelli, A. J., and Murray, W. M., "Stress Distribution Around an Elliptical Discontinuity in any Two-Dimensional, Uniform, and Axial System of Combined Stress," *Exper. Stress Analysis Proc.*, Vol. 1, No. 1, 1943, pp. 19–31.

2 Mansfield, E. H., "Neutral Holes in Plane Sheet–Reinforced Holes Which are Elastically Equivalent to the Uncut Sheet," *Quart. J. Mech. Appl. Math.*, Vol. VI, 1953, pp. 370–378.

3 Neuber, H., "Zur Optimierung der Spannungskonzentration," *Continuum Mechanics and Related Problems of Analysis*, Nauka, Moscow, 1972, pp. 375–380.

4 Cherepanov, G. P., "Inverse Problems of the Plane Theory of Elasticity, *PMM*, Vol. 38, No. 6, 1974, pp. 963–979.

5 Wheeler, L. T., Tezduyar, T. E., and Eldiwany, B. H., "Profiles of Minimum Stress Concentration for Antiplane Deformation of an Elastic Solid, *J. Elasticity*, to appear, Summer, 1985.

6 Riabouchinsky, D., "On Steady Fluid Motions With Free Surfaces," *Proc. Lond. Math. Soc.*, Vol. 19, Series 2, 1920, pp. 206–215.

7 Riabouchinsky, D., "On Some Cases of Two-Dimensional Fluid Motions," *Proc. Lond. Math. Soc.*, Vol. 25, Series 2, 1925, pp. 185–194.

8 Byrd, P. F., and Friedman, M. D., *Handbook of Elliptic Integrals for Engineers and Scientists*, Springer-Verlag, 1971.

9 Eldiwany, B. H., "Shape Optimization for Minimal Stress Concentration," Ph.D. Thesis, Department of Mechanical Engineering, University of Houston, Houston, Texas, 1984.

10 Kochin, N. E., Kibel, I. A., and Roze, N. V., *Theoretical Hydrodynamics*, Wiley, New York, 1964, pp. 276–281.

Downloaded 02 May 2010 to 171.66.16.54. Redistribution subject to ASME license or copyright; see http://www.asme.org/terms/Terms_Use.cfm

Large Inextensional Deformation of Orthotropic Cantilevered Plates With Distributed Loads

P. Darmon
Graduate Student.
Student Mem. ASME

R. C. Benson
Asociate Professor.
Mem. ASME

Department of Mechanical Engineering,
University of Rochester,
Rochester, N.Y. 14627

The theory of large inextensional deformation of cantilevered plates, as recently put forth by Simmonds and Libai, is extended to include orthotropic plates and plates with distributed loading. The bending rigidities of the orthotropic plate are calculated in terms of known material constants, and as functions of the single curvilinear coordinate employed in the theory. The constitutive relationships are then reformulated and the equilibrium equations transformed accordingly. The distributed loading that enters into the local equilibrium equations of the Simmonds-Libai theory is, in this paper, carried through to the overall equilibrium equations.

Introduction

It is the purpose of this paper to modify the inextensible plate theory of Simmonds and Libai [1], to permit application to plates with orthotropic properties and distributed loading. The authors are motivated by the desire to efficiently model some of the delicate recording media used in modern communication machinery; specific examples of which include magnetic recording tape, and copier paper. They also see useful application in other areas such as collapsible space structures, and cloth. Their prime interest, however, is the modeling of paper. Paper is a mundane but important engineering material. Capable of very large deflection under very small load, it is difficult to handle with automatic machinery. Such flexibility also presents a problem of analysis, as the deflections are typically so large as to require a nonlinear theory.

There are a number of nonlinear theories and numerical solution schemes which might be brought to bear in the analysis of paper, but one stands out for its versatility: the theory of the elastica [2], the nonlinear model for inextensible beam bending. The advantage of the elastica is that it exploits the near-inextensible nature of paper, thus eliminating the need to expend a great amount of computational effort, via an all-purpose, nonlinear, numerical code, only to rediscover that a sheet does not stretch very much. The elastica is also one of the more tractable nonlinear theories. For many problems, closed form solutions may be obtained in the form of elliptic integrals. Articles by Benson [3] and Wang [4] are representative of some of the recent work using inextensible beam theory, with paper handling cited as an application.

The Simmonds-Libai theory is the analogous, nonlinear, inextensible plate theory (as opposed to beam theory), which handles not only planar bending, but also twisting out of the plane. The attraction of the Simmonds-Libai theory is that it explicitly, like the elastica, incorporates the feature of inextensibility into the nonlinear plate model. By exploiting the fact that an inextensible plate must deform into a developable surface [5], Simmonds and Libai are able to formulate a set of 13 first-order, ordinary, differential equations which depend on a single spatial variable. This coordinate passes perpendicularly through all generators of the developed surface. Later, Simmonds and Libai [6] derived an alternative set of equations, in terms of the angle of the generators, for quadrilateral and triangular plates. More recently Simmonds [7] has extended the analysis to include dynamical motion. Readers of the Simmonds-Libai papers should also consult reference [8] in which some minor corrections to reference [1] were made.

For many of the intended applications, and specifically paper, we find that the plates to be analyzed possess features that are not treated by Simmonds and Libai, or else have received restricted attention. The Simmonds-Libai theory does not incorporate the effects of orthotropism or carry distributed loading through to the final formulation. The former effect is critical to paper sheets that typically have principal stiffnesses in a ratio of about 2:1. For planar bending this poses no problem, but when the bending occurs along a turning set of generators (the fundamental kinematic feature of the Simmonds-Libai theory), then it is important to account for the variable stiffness. The importance of the latter effect can be illustrated by a heavy, skew-cantilevered plate that deflects under gravity but which carries no edge loading at all.

We wish then to extend the Simmonds-Libai theory to include orthotropic plates and plates with substantial

Contributed by the Applied Mechanics Division for presentation at the 1985 Joint ASME/ASCE Applied Mechanics, Fluids Engineering, and Bioengineering Conference, Albuquerque, N. Mex., June 24-26, 1985 of THE AMERICAN SOCIETY OF MECHANICAL ENGINEERS.

Discussion on this paper should be addressed to the Editorial Department, ASME, United Engineering Center, 345 East 47th Street, New York, N.Y. 10017, and will be accepted until two months after final publication of the paper itself in the JOURNAL OF APPLIED MECHANICS. Manuscript received by ASME Applied Mechanics Division, May 1, 1984; final revision, July, 1984. Paper No. 85-APM-7.

Copies will be available until February, 1986.

Copyright © 1985 by ASME
Downloaded 02 May 2010 to 171.66.16.54. Redistribution subject to ASME license or copyright; see http://www.asme.org/terms/Terms_Use.cfm

distributed loading. We will use the notations of [1] and refer to that paper extensively.

Geometry

In the Simmonds-Libai theory, the plate is bounded by four edges. One is a built-in straight edge, two are stress-free curved edges, and one is a straight edge that is acted upon at its center with a net force and a net torque, see Fig. 1. The origin of a material xyz-frame is located at the point of action of the load. The xy-plane, also called the "reference frame," coincides with the developed (undeformed) plate. The y-axis lies along the loaded edge, and the x-axis points toward the interior of the plate. The direction of the generators of the developed surface is given by the angle α.

Orthotropic Plate

The fundamental feature of the Simmonds-Libai plate theory is the casting of equations in terms of a coordinate arc, ξ, which is chosen to be always in the direction of principle curvature, κ_ξ. Perpendicular to ξ is the straight line generator, η, with $\kappa_\eta = 0$[1]. Despite the fact that ξ is not a material coordinate (changing with plate deformation), the moment/curvature ratio along this path is always constant for an isotropic plate:

$$\frac{M_\xi}{\kappa_\xi} = \frac{Eh^3}{12(1-\nu^2)} \equiv D. \tag{1}$$

Here E is Young's modulus, ν is Poisson's ratio, h is the plate thickness, and D is the flexural rigidity for an isotropic plate. In adapting the Simmonds-Libai theory to an orthotropic plate we must take into account the new phenomenon that the constitutive equations will exhibit a directional dependence as the ξ arc turns in the plate.

The constitutive equations for the orthotropic plate, as expressed in the material reference frame xy, are

$$M_x = D_x\kappa_x + D_{xy}\kappa_y, \tag{2}$$

$$M_y = D_{xy}\kappa_x + D_y\kappa_y, \tag{3}$$

$$M_{xy} = 2G_{xy}\kappa_{xy}, \tag{4}$$

where M_x, M_y, and M_{xy} denote the components of the second-order moment tensor, κ_x, κ_y, and κ_{xy} denote the components of the second-order curvature tensor. D_x, D_y, and D_{xy} are flexural rigidities, and G_{xy} is the torsional rigidity as defined by Ugural [9]. The constitutive equations in the $\xi\eta$-frame are formally equivalent to equations (2)–(4) with subscripts ξ and η replacing subscripts x and y, respectively. However, whereas D_x, D_y, D_{xy} and G_{xy} are constants, D_ξ, D_η, $D_{\xi\eta}$ and $G_{\xi\eta}$ are functions of ξ.

The transformation of flexural and torsional rigidities from the material xy-frame to the lines-of-curvature $\xi\eta$-frame is performed by a simple rotation. In indicial, tensor notation[2], this appears as:

$$D^*_{ijkl} = R_{ia}R_{jb}R_{kc}R_{ld}D_{abcd}, \tag{5}$$

where

$$\mathbf{R} = \begin{bmatrix} \cos\alpha & -\sin\alpha \\ \sin\alpha & \cos\alpha \end{bmatrix} \equiv \begin{bmatrix} c & -s \\ s & c \end{bmatrix}. \tag{6}$$

The components of equation (5) are identified with those of equations (2)–(4) as follows:

$$\begin{aligned} D_{1111} &= D_x,\ D_{2222} = D_y, \\ D_{1122} &= D_{2211} = D_{xy}, \\ D_{1212} &= D_{1221} = D_{2112} = D_{2121} = G_{xy}, \\ &\text{remaining eight } D_{ijkl} = 0. \end{aligned} \tag{7}$$

[1] Note: Simmonds and Libai used κ_I for our κ_ξ, and κ_{II} for our κ_η.
[2] Subscript range is 1,2.

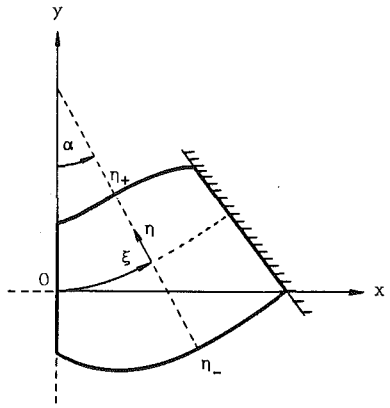


Fig. 1 Geometry

Similarly D^*_{ijkl} is identified with D_ξ, D_η, $D_{\xi\eta}$, and $G_{\xi\eta}$.

Since in the Simmonds-Libai plate theory $\kappa_\eta = \kappa_{\xi\eta} = 0$, it is sufficient merely to calculate $D_\xi = D^*_{1111}$ and $D_{\xi\eta} = D^*_{1122}$.

$$D_\xi = c^4D_x + 2c^2s^2(D_{xy} + 2G_{xy}) + s^4D_y, \tag{8}$$

$$D_{\xi\eta} = (c^4 + s^4)D_{xy} + c^2s^2(D_x + D_y - 4G_{xy}). \tag{9}$$

In subsequent calculations we will require the derivatives of these rigidities as they vary along the coordinate arc, ξ.

$$D'_\xi = -4csg[c^2D_x - (c^2 - s^2)(D_{xy} + 2G_{xy}) - s^2D_y], \tag{10}$$

$$D'_{\xi\eta} = -4csg\left[(c^2 - s^2)D_{xy} - \frac{1}{2}(c^2 - s^2)(D_x + D_y - 4G_{xy})\right]. \tag{11}$$

We are now able to reformulate the Simmonds-Libai equations, beginning with (36) of [1]. The constitutive equations now read as follows:

$$M_\xi = \frac{D_\xi k}{1 - \eta g}, \tag{12}$$

$$M_\eta = \frac{D_{\xi\eta} k}{1 - \eta g}, \tag{13}$$

$$H \equiv \frac{1}{2}(M_{\xi\eta} + M_{\eta\xi}) = 0. \tag{14}$$

The expressions for the stress components Q_ξ and Q_η, given by (40) and (41) of [1], now are:

$$Q_\xi = -\frac{D_\xi}{(1 - \eta g)^2}\left[\frac{D'_\xi}{D_\xi}k + k' + \frac{\eta k g'}{1 - \eta g}\right], \tag{15}$$

$$Q_\eta = -\frac{D_\xi k g}{(1 - \eta g)^2}, \tag{16}$$

and (42) of [1] remains unchanged.

Simmonds and Libai explain in the section "Equilibrium of the Fictitious Beam" of [1] that the assumption of inextensionality is in conflict with the local deformation needed to satisfy the stress-free condition on the two curved edges. To preserve inextensionality completely to the edges requires that loads be applied on the "stress-free" boundaries. The smallness of these edge loads is then a measure of the validity of the kinematical model. For the orthotropic plate the Simmonds and Libai equations (43)–(59) retain the same form and (60)[3]–(66) become:

$$\Delta Q = \frac{D_\xi}{(1 - \eta g)^2}\left[\left(\frac{D'_\xi}{D_\xi}k + k' + \frac{\eta k g'}{1 - \eta g}\right)\sin\theta + kg\cos\theta\right], \tag{17}$$

[3] The appearance of $k'g$ in equation (60) of [1], should be read as kg'.

Downloaded 02 May 2010 to 171.66.16.54. Redistribution subject to ASME license or copyright; see http://www.asme.org/terms/Terms_Use.cfm

$$\Delta M_t = -\mathbf{M}\cdot\mathbf{t} = -M_\eta \cos\theta = -\frac{D_{\xi\eta} k \cos\theta}{1-\eta g}, \tag{18}$$

$$\Delta M_x = -\mathbf{M}\cdot\mathbf{u} = M_\xi \sin\theta = \frac{D_\xi k \sin\theta}{1-\eta g}, \tag{19}$$

$$B_m = -\frac{D_\xi k \tan\theta}{1-\eta g}, \tag{20}$$

$$C = D_\xi \tan^2\theta + D_{\xi\eta}, \tag{21}$$

$$B_t = \frac{2D_\xi}{1-\eta g}\left[\left(\frac{D'_\xi}{D_\xi} + \frac{k'}{k} + \frac{\eta g'}{1-\eta g}\right)\tan\theta + g - \frac{1}{2}(1+\tan^2\theta)\beta'\right], \tag{22}$$

$$B_u = -\frac{2D_\xi \tan\theta}{1-\eta g}\left[\left(\frac{3}{2}\frac{D'_\xi}{D_\xi} + \frac{k'}{k} + \frac{\eta g'}{1-\eta g}\right)\tan\theta + g(2+\tan^2\theta) - \frac{3}{2}(1+\tan^2\theta)\beta' + \frac{D'_{\xi\eta}}{2D_\xi \tan\theta}\right]. \tag{23}$$

In the section "Overall Equilibrium" of [1], equations (67)–(77) remain unchanged. The first two components of the torque, T_t and T_u, are now given by (24) and (25). The third component, T_m (equation (80) of [1]), is also unchanged:

$$T_t = -D_\xi\left[\left(\frac{D'_\xi}{D_\xi}k + k'\right)L_1 + kg'L_2 - \frac{\eta k \tan\theta}{1-\eta g}\Big|_-^+\right], \tag{24}$$

$$T_u = -D_\xi k L_0. \tag{25}$$

Differentiating T_u gives the following expression:

$$T'_u = -D_\xi\left[\frac{D'_\xi}{D_\xi}kL_0 + k'L_0 + kg'L_1 - k\tan\theta\Big|_-^+\right]. \tag{26}$$

Finally the differential equations for the geodesic curvature g, and the normal curvature k, namely equations (83)–(84)[4] of [1], are replaced with equations (27) and (28).

$$g' = \left[\left(\frac{\eta\tan\theta}{1-\eta g}\Big|_-^+ - \frac{T_t}{D_\xi k}\right)L_0 - \left(\frac{gT_t - Pc_m}{D_\xi k} + \tan\theta\Big|_-^+\right)L_1\right]\Big/(L_0L_2 - L_1^2), \tag{27}$$

$$k' = \left\{\left[\left(\frac{gT_t - Pc_m}{D_\xi} + k\tan\theta\Big|_-^+\right)L_2 - \left(\frac{\eta k\tan\theta}{1-\eta g}\Big|_-^+ - \frac{T_t}{D_\xi}\right)L_1\right]\Big/(L_0L_2 - L_1^2)\right\} - \frac{D'_\xi}{D_\xi}k. \tag{28}$$

It is interesting to note in equation (27), that g' does not depend on D'_ξ. The rest of the equations of [1] remain unchanged.

Distributed Loads

Through the section titled "Overall Equilibrium," Simmonds and Libai [1] incorporate a distributed load $\mathbf{p}$, whereupon they restrict further derivation to the case $\mathbf{p}=0$. To retain this distributed load in the latter sections of the analysis requires that integrals be carried in the differential equations for the components of the torque, namely equations (74)–(76) of [1]. These equations now assume the form:

$$T'_t - gT_u - kT_m + l_m = 0, \tag{29}$$

$$T'_u + gT_t - Pc_m + Q_m = 0, \tag{30}$$

$$T'_m + kT_t + Pc_u - Q_u - l_t = 0. \tag{31}$$

where

$$\mathbf{l} = \int_{\eta-}^{\eta+} \eta(1-\eta g)\mathbf{p}\, d\eta, \tag{32}$$

$$\mathbf{q} = \int_{\eta-}^{\eta+} (1-\eta g)\mathbf{p}\, d\eta, \tag{33}$$

$$\mathbf{Q} = \int_0^\xi \mathbf{q}(t)\, dt. \tag{34}$$

The subscript t, u, and m in (29)–(31) designate vector components in the respective directions: increasing ξ, increasing η, and the binormal to ξ and η. With these changes, the differential equations for the geodesic and normal curvatures transform to:

$$g' = \left[\left(\frac{\eta\tan\theta}{1-\eta g}\Big|_-^+ - \frac{T_t}{Dk}\right)L_0 - \left(\frac{gT_t - Pc_m + Q_m}{Dk} + \tan\theta\Big|_-^+\right)L_1\right]\Big/(L_0L_2 - L_1^2), \tag{35}$$

$$k' = \left[\left(\frac{gT_t - Pc_m + Q_m}{D} + k\tan\theta\Big|_-^+\right)L_2 - \left(\frac{\eta k\tan\theta}{1-\eta g}\Big|_-^+ - \frac{T_t}{D}\right)L_1\right]\Big/(L_0L_2 - L_1^2). \tag{36}$$

The rest of the equations of [1] are unaffected by the distributed load.

If the load $\mathbf{p}$ is due to gravity, then $\mathbf{p}$ is a constant vector and the integrals for $\mathbf{l}$ and $\mathbf{q}$ can be calculated in closed form:

$$\mathbf{q} = \mathbf{p}(\eta_+ - \eta_-)\left[1 - \frac{1}{2}g(\eta_+ + \eta_-)\right], \tag{37}$$

$$\mathbf{l} = \mathbf{p}(\eta_+ - \eta_-)\left[\frac{1}{2}(\eta_+ + \eta_-) - \frac{1}{3}g(\eta_+^2 + \eta_+\eta_- + \eta_-^2)\right]. \tag{38}$$

Combination of Effects

Although the analyses of orthotropic plates and plates with distributed loading have been conducted separately, the two adaptations of the Simmonds-Libai theory can be easily merged. It is sufficient to consider the equations for orthotropic plates up to equation (26), then the equations for distributed loading (29)–(34). Finally the equations for the geodesic and normal curvatures are obtained by combining (27)–(28) with (35)–(36):

$$g' = \left[\left(\frac{\eta\tan\theta}{1-\eta g}\Big|_-^+ - \frac{T_t}{D_\xi k}\right)L_0 - \left(\frac{gT_t - Pc_m + Q_m}{D_\xi k} + \tan\theta\Big|_-^+\right)L_1\right]\Big/(L_0L_2 - L_1^2), \tag{39}$$

$$k' = \left\{\left[\left(\frac{gT_t - Pc_m + Q_m}{D_\xi} + k\tan\theta\Big|_-^+\right)L_2 - \left(\frac{\eta k\tan\theta}{1-\eta g}\Big|_-^+ - \frac{T_t}{D_\xi}\right)L_1\right]\Big/(L_0L_2 - L_1^2)\right\} - \frac{D'_\xi}{D_\xi}k. \tag{40}$$

Observations on Numerical Solution

Since the 1979 publication of the Simmonds-Libai theory,

[4] Any appearance of T_t, in equation (83)–(84) of [1], should be read as T_t/D.

Downloaded 02 May 2010 to 171.66.16.54. Redistribution subject to ASME license or copyright; see http://www.asme.org/terms/Terms_Use.cfm

[1], no solution or numerical results have appeared in print[5]. The present authors, however, can report that they have recently obtained convergence in their computer formulation of the Simmonds-Libai equations. In a subsequent paper they intend to present the results of their numerical study along with a comparison to experimental measurements made on thin steel plates. The computer program is presently being upgraded to include orthotropism and distributed loading as described here. For others interested in a numerical solution to the Simmonds-Libai equations, a few points deserve previewing here.

A boundary layer develops at the loaded edge of the plate when there is no applied bending moment. With zero normal curvature k, the derivative of the geodesic curvature, g', becomes infinite. See equations (27), (35), and (39). We find that this causes numerical sensitivity to the small changes in the initial value of g. We are presently examining ways to treat the boundary layer through alternative analytical or numerical techniques.

Of the various numerical techniques [10] that might be used for the integration of the differential equations, we found that "shooting" methods required far less time than a simultaneous, finite-difference, matrix approach. A fourth-order Runge-Kutta method lacked sufficient numerical stability for some of our trial problems. The Hamming predictor-corrector method, however, provided stable and accurate answers, and we recommend it to other analysts.

[5] See comment at end of reference [8].

Acknowledgment

The authors would like to thank the sponsor of this research, the Xerox Corporation. They also wish to thank Professor James G. Simmonds for helpful contributions to this work.

References

1 Simmonds, J. G., and Libai, A., "Exact Equations for the Inextensional Deformation of Cantilevered Plates," ASME JOURNAL OF APPLIED MECHANICS, Vol. 46, Sept. 1979, pp. 631–636.

2 Frish-Fray, *Flexible Bars*, Butterworth, Washington, 1962.

3 Benson, R. C., "The Deformation of a Thin, Incomplete, Elastic Ring in a Frictional Channel," ASME JOURNAL OF APPLIED MECHANICS, Vol. 48, Dec. 1981, pp. 895–899.

4 Wang, C. Y., "On Symmetric Buckling of a Finite Flat-Lying Heavy Sheet," ASME JOURNAL OF APPLIED MECHANICS, Vol. 51, June 1984, pp. 278–282.

5 Sokolnikoff, I. S., *Tensor Analysis Theory and Applications to Geometry and Mechanics of Continua*, 2nd Ed., Wiley, New York, 1964, pp. 165–166.

6 Simmonds, J. G., and Libai, A., "Alternate Exact Equations for the Inextensional Deformation of Arbitrary, Quadrilateral, and Triangular Plates," ASME JOURNAL OF APPLIED MECHANICS, Vol. 46, Dec. 1979, pp. 895–900.

7 Simmonds, J. G., "Exact Equations for the Large Inextensional Motion of Elastic Plates," ASME JOURNAL OF APPLIED MECHANICS, Vol. 48, Mar. 1981, pp. 109–112.

8 Libai, A., and Simmonds, J. G., *Nonlinear Elastic Shell Theory, Advances in Applied Mechanics*, Academic Press, New York, Vol. 23, 1983, pp. 335–337.

9 Ugural, A. C., *Stresses in Plates and Shells*, McGraw-Hill, New York, 1981, pp. 140–144.

10 Carnahan, B., Luther, H. A., and Wilkes, J. O., *Applied Numerical Methods*, Wiley, New York, 1969.

Downloaded 02 May 2010 to 171.66.16.54. Redistribution subject to ASME license or copyright; see http://www.asme.org/terms/Terms_Use.cfm

Dynamics and Stability of Coaxial Cylindrical Shells Conveying Viscous Fluid[1]

M. P. Paidoussis
Professor and Chairman.
Mem. ASME

A. K. Misra
Associate Professor.
Mem. ASME

S. P. Chan
Research Assistant.

Department of Mechanical Engineering,
McGill University,
817 Sherbrooke St. W.,
Montreal, Québec,
Canada H3A 2K6

In this paper the dynamics and stability characteristics of coaxial cylindrical shells containing incompressible, viscous fluid flow are examined in contrast to previous studies where the fluid has been considered to be inviscid. Specifically, upstream pressurization of the flow (to overcome frictional pressure drop) and skin friction on the shell surfaces are taken into account, generating time-mean normal and tangential loading on the shells. Shell motions are described by Flügge's thin shell equations, suitably modified to incorporate the time-mean stress resultants arising from viscous effects. The fluctuating fluid forces, coupled to shell vibration, are determined entirely by means of linearized potential flow theory and formulated with the aid of generalized-force Fourier-transform techniques. It is found that the effect of viscosity in the annular flow generally tends to destabilize the system, vis-à-vis inviscid flow, whereas viscous effects in the inner flow stabilize the system. These effects can be quantitatively very important, so that, generally, neglect of viscous effects cannot be justified.

1 Introduction

In a recent paper, the dynamics and stability of coaxial cylindrical shells conveying *inviscid* fluid have been examined quite extensively [1]. The rationale for neglecting viscous effects had been that they would principally induce steady-state, time-mean axial and radial loads on the shells, the effects of which, on their own, on the stability of the system are well understood [2–4]—rather than implying that viscous effects are unimportant.

In the case of tubular *beams* conveying fully developed turbulent flow, it has been shown [5–7] that viscous effects are negligible in the following sense: the terms in the equation of motion arising from pressure drop in the fluid are completely cancelled by those produced by surface traction forces on the beam due to fluid friction, so that the analysis may be conducted as if the fluid were effectively inviscid. Experiments involving very large pressure drops (4.52 MPa/m, or 200 psi/ft) have verified the accuracy of this analytical result [6]. However, this is not necessarily the case for cylindrical shells, and hence the viscous effects may not be eliminated a priori. The purpose of this paper is to study these effects in coaxial shells conveying fluid and to compare the results, insofar as the dynamics and stability of the system are concerned, with those previously obtained with inviscid fluid analysis.

There appeared to be two approaches possible, in principle at least. In the first, both steady and unsteady viscous effects would have been taken into account. This would involve the determination of the vibration-dependent viscous fluid field, which would necessitate the iterative solution of the Navier-Stokes equations by numerical means; for arbitrary (i.e., not prescribed) motions of the shells, this approach would entail very expensive, if at all feasible, numerical calculations. In the second approach, the shell-vibration-dependent fluid forces would be determined by means of inviscid, potential-flow theory, as was done previously [1], whereas the viscous forces would be determined separately in a time-averaged sense; the equations of motion of the shell would then contain the stress resultants arising from these mean viscosity-induced forces. The second approach, although recognized to be considerably less rigorous, was preferred for entirely practical reasons. It is expected to yield a reasonable first assessment of the importance of viscous effects in the problem at hand; the degree of its success will of course ultimately have to be determined by comparison with experiment.

Since an extensive literature review has already been presented in reference [1], repetition of the same here would be superfluous. Nevertheless, it might be worth reiterating that, quite apart from possible interest in this work as a fundamental problem in applied mechanics, there is considerable practical interest: coaxial shells containing flowing fluid in the annulus between them, and sometimes also in the inner shell, are frequently found as important structural elements in heat exchangers, certain designs of nuclear reactors, and large jet pumps, and are often involved in flow-induced vibration problems [8].

[1] This paper was presented at the 1984 ASME Symposium on Flow-Induced Vibrations, held in conjunction with the Winter Annual Meeting, New Orleans, La., December 10–14, 1984.

Contributed by the Applied Mechanics Division for publication in the JOURNAL OF APPLIED MECHANICS.

Discussion on this paper should be addressed to the Editorial Department, ASME, 345 East 47th Street, New York, N.Y. 10017, and will be accepted until two months after final publication of the paper itself in the JOURNAL OF APPLIED MECHANICS. Manuscript received by ASME Applied Mechanics Division, January, 1984; final revision, August, 1984.

Copyright © 1985 by ASME
Downloaded 02 May 2010 to 171.66.16.54. Redistribution subject to ASME license or copyright; see http://www.asme.org/terms/Terms_Use.cfm

2 Formulation of the Equations of Motion

2.1 System Definition and Assumptions. The system consists of two coaxial cylindrical shells of length L; at either end, each shell is clamped onto rigid tubes of the same radii and thicknesses, and sufficiently long for perturbations originating in the shells to be attenuated to negligible levels at both inlet and outlet of the rigid tubes—for analytical convenience. The shells are assumed to be thin, elastic and isotropic.

Generally, the system contains two flows: one in the inner shell and the other in the annular space; the fluid is presumed to be incompressible, and the flows fully-developed turbulent.[2] The static pressures of the two flows at the outlet of the flexible shells are taken to be equal and, for simplicity, also equal to that of the fluid surrounding the outer shell, which is stagnant; moreover, also for simplicity, the density of the outer fluid is considered to be much smaller than that of the flowing fluids (e.g., air versus water).

The shells are subjected to two sets of loads: the so-called *basic loads*, which are independent of shell displacements (and hence of time) and are entirely due to viscous effects, and the so-called *additional loads*, which are related to shell motions; as these latter will be arbitrarily small, the additional loads will be much smaller than the basic ones. The basic loads are responsible for prestressing the shells, and it is recognized that the associated stress resultants will do work in the course of arbitrary motions of the shells and will therefore appear explicitly in the equations of motion [2].

Damping of the shells, whether arising from internal dissipation in the shell material or from viscous flow, will not be taken into account. One reason for this is that no analytical means exists at present for formulating flow-induced damping forces on shells in flowing fluids; a second reason is that the principal effect of such forces is well understood, namely the damping of free motions of the system. However, the main reason is that the system, being inherently conservative, will lose stability by divergence, which is totally unaffected by damping; hence, as stability is the prime concern of this paper, neglect of dissipative effects may be justified.

2.2 The Equations of Motion. Consider a thin cylindrical shell, prestressed by the following basic loads:

(*i*) a constant axial force per unit area

$$\bar{p}_x = B, \tag{1}$$

(*ii*) an axially symmetric normal pressure

$$\bar{p}_r = -(Cx + D), \tag{2}$$

the functional forms of which will become obvious in Section 3. The associated axial and hoop stress resultants may be shown to be

$$\bar{N}_x = B(\tfrac{1}{2}L - x) - \nu a(\tfrac{1}{2}LC + D), \tag{3}$$

$$\bar{N}_\theta = -a(Cx + D), \tag{4}$$

respectively; a and L are the radius and length of the shell, respectively, and ν is Poisson's ratio. The small bending moments induced by $\bar{p}_x$ and $\bar{p}_r$ are neglected.

In addition to these stress resultants, there are those associated with motion (deformation) of the shell, which are coupled to the perturbations induced on the flowing fluid. The equilibrium of the shell, subject to the total stress system and to the appropriate compatibility conditions, yields the equations of motion. For the system under consideration here, involving two coaxial shells, they are found to be as follows:

$$\begin{aligned} &u_i'' + \tfrac{1}{2}(1-\nu_i)\ddot{u}_i + \tfrac{1}{2}(1+\nu_i)\dot{v}_i' + \nu_i w_i' \\ &\quad + k_i[\tfrac{1}{2}(1-\nu_i)\ddot{u}_i - w_i''' + \tfrac{1}{2}(1-\nu_i)\dot{w}_i'] \\ &\quad + q_{1i}u_i'' + q_{2i}(\dot{v}_i + w_i) + q_{3i}(\ddot{u}_i - w_i') \\ &\quad = \gamma_i(\partial^2 u_i/\partial t^2), \end{aligned} \tag{5}$$

$$\begin{aligned} &\tfrac{1}{2}(1+\nu_i)\dot{u}_i' + \ddot{v}_i + \tfrac{1}{2}(1-\nu_i)v_i'' + \dot{w}_i \\ &\quad + k_i\left[\frac{3}{2}(1-\nu_i)v_i'' - \tfrac{1}{2}(3-\nu_i)\dot{w}_i''\right] \\ &\quad + q_{1i}v_i'' + q_{3i}(\dot{v}_i + \dot{w}_i) = \gamma_i(\partial^2 v_i/\partial t^2), \end{aligned} \tag{6}$$

$$\begin{aligned} &\nu_i u_i' + \dot{v}_i + w_i + k_i[\tfrac{1}{2}(1-\nu_i)\dot{u}_i' - u_i''' \\ &\quad - \tfrac{1}{2}(3-\nu_i)\dot{v}_i'' + \nabla_i^4 w_i + 2\ddot{w}_i + w_i] \\ &\quad - q_{1i}w_i'' - q_{3i}(u_i' - \dot{v}_i + \ddot{w}_i) \\ &\quad = -\gamma_i[(\partial^2 w_i/\partial t^2) - (q_i/\rho_{si}h_i)], \end{aligned} \tag{7}$$

$$\begin{aligned} &u_o'' + \tfrac{1}{2}(1-\nu_o)\ddot{u}_o + \tfrac{1}{2}(1+\nu_o)\dot{v}_o' + \nu_o w_o' \\ &\quad + k_o[\tfrac{1}{2}(1-\nu_o)\ddot{u}_o - w_o''' + \tfrac{1}{2}(1-\nu_o)\dot{w}_o'] \\ &\quad + q_{1o}u_o'' + q_{2o}(\dot{v}_o + w_o) + q_{3o}(\ddot{u}_o - w_o') \\ &\quad = \gamma_o(\partial^2 u_o/\partial t^2), \end{aligned} \tag{8}$$

$$\begin{aligned} &\tfrac{1}{2}(1+\nu_o)\dot{u}_o' + \ddot{v}_o + \tfrac{1}{2}(1-\nu_o)v_o'' + \dot{w}_o \\ &\quad + k_o\left[\frac{3}{2}(1-\nu_o)v_o'' - \tfrac{1}{2}(3-\nu_o)\dot{w}_o''\right] \\ &\quad + q_{1o}v_o'' + q_{3o}(\ddot{v}_o + \dot{w}_o) = \gamma_o(\partial^2 v_o/\partial t^2), \end{aligned} \tag{9}$$

$$\begin{aligned} &\nu_o u_o' + \dot{v}_o + w_o + k_o[\tfrac{1}{2}(1-\nu_o)\dot{u}_o' - u_o''' \\ &\quad - \tfrac{1}{2}(3-\nu_o)\dot{v}_o'' + \nabla_o^4 w_o + 2\ddot{w}_o + w_o] \\ &\quad - q_{1o}w_o'' - q_{3o}(u_o' - \dot{v}_o + \ddot{w}_o) \\ &\quad = -\gamma_o[(\partial^2 w_o/\partial t^2) - (q_o/\rho_{so}h_o)], \end{aligned} \tag{10}$$

where u, v, w are the displacements of the middle surface of the shells, respectively in the axial, circumferential and radial directions, $(\,)' = a_i\partial(\,)/\partial x$, $(\,)' = a_o\partial(\,)/\partial x$, $(\dot{}) = \partial(\,)/\partial\theta$; the subscripts i and o refer to the inner and outer shells throughout (as in a_i and a_o for the radii), so that the rest of the quantities in the preceding equations may be defined without reference to the subscripts as follows:

$$k = \frac{1}{12}(h/a)^2, \quad \gamma = \rho_s a^2(1-\nu^2)/E,$$

$$\nabla^2 = a^2(\partial^2/\partial x^2) + (\partial^2/\partial\theta^2), \tag{11}$$

$$q_1 = [(1-\nu^2)/Eh]\bar{N}_x, \quad q_2 = [a(1-\nu^2)/Eh]\bar{p}_x,$$

$$q_3 = [a(1-\nu^2)/Eh]\bar{p}_r,$$

where h is the wall thickness, E Young's modulus, ρ_s density, and ν Poisson's ratio of the shells, and $\bar{N}_x$, $\bar{p}_x$, and $\bar{p}_r$ are as given by equations (1)–(3); moreover,

$$q_i = p_i\Big|_{r=a_i} - p_o\Big|_{r=a_i} \quad \text{and} \quad q_o = p_o\Big|_{r=a_o}, \tag{12}$$

where p_i and p_o represent the perturbation pressures exerted by the fluid on the shells in the course of arbitrary motions [1].

Equations (5)–(10), without the contributions of the basic loads, are Flügge's standard thin-shell equations [2]. Forms of the equations of motion, including the effect of the basic loads, albeit different ones (i.e., $\bar{p}_x = 0$ and $C = 0$ in equation (2), with constant axial end-loads and torques), have previously been derived [2–4]. For the basic loads given by equations (1) and (2), it was found necessary to derive the equations ab initio [9]. Although space limitations preclude the full presentation of this work, it may be useful to illustrate how the basic loads enter the equations of motion, by considering the contribution of the $\bar{N}_\theta$ term to the equilibrium condition of forces in the circumferential direction. If the total stress resultant is denoted by $\bar{\bar{N}}_\theta = \bar{N}_\theta + N_\theta$, where N_θ

[2] At the onset of instability, as determined by inviscid analysis [1], the Reynolds number is in the range 10^5 to 10^7, for the type of system to be analyzed here.

Downloaded 02 May 2010 to 171.66.16.54. Redistribution subject to ASME license or copyright; see http://www.asme.org/terms/Terms_Use.cfm

is the perturbation stress resultant, then the normal force in the circumferential direction acting on one side of a stretched element of the shell [2] is $\tilde{N}_\theta\ (1+\epsilon_\theta)\ dx$, where $\epsilon_\theta = (v^{\cdot}+w)/a$ is the circumferential strain; on the other side of the element there will be the same, augmented by $(\partial/\partial\theta)\ [\tilde{N}_\theta \times(1+\epsilon_\theta)\ dx]\ d\theta$; hence, the contribution of this term to equilibrium is

$$\frac{\partial}{\partial\theta}[\tilde{N}_\theta(1+\epsilon_\theta)\,dx]d\theta = N_\theta^{\cdot}dxd\theta + \tilde{N}_\theta(v^{\cdot\cdot}+w^{\cdot})\,dxd\theta,$$

to first order. The first term is the one normally appearing in the equilibrium equations of nonprestressed shells [2], while the second gives rise to the extra terms involving q_{3i} and q_{3o} in equations (6) and (9), where it is noted that $\tilde{N}_\theta = a\bar{p}_r$.

3 Mean Static Pressures and the Basic Loads

3.1 Derivation of the Basic Loads. The basic loads, defined in Section 2.1, will be determined while the shells are in their equilibrium configurations; they arise from pressurization of the fluid, necessary to overcome the viscous pressure drop in the confined flow passages, and the associated frictional forces on the shell walls.

For a flow velocity U and static pressure P, the time-mean Navier-Stokes equations are [10]

$$\frac{1}{\rho}\frac{\partial P}{\partial x} = -\frac{1}{r}\frac{d}{dr}(r\overline{u_x u_r}) + \frac{\eta}{r}\frac{d}{dr}\left(r\frac{dU}{dr}\right), \tag{13}$$

$$\frac{1}{\rho}\frac{\partial P}{\partial r} = -\frac{1}{r}\frac{d}{dr}(r\overline{u_r^2}) + \frac{1}{r}(\overline{u_\theta^2}), \tag{14}$$

$$0 = \frac{d}{dr}(\overline{u_r u_\theta}) + \frac{2}{r}(\overline{u_r u_\theta}), \tag{15}$$

where (x, θ, r) is the cylindrical polar coordinate system, (u_x, u_θ, u_r) the corresponding fluctuating velocity components of the turbulent flow, ρ the fluid density, and η the kinematic viscosity; $\overline{(\ )}$ represents the time-mean of $(\ )$.

Integrating equation (15), one has $\overline{u_r u_\theta} = C_1/r^2$, where C_1 is a constant. At $r = a$, clearly $\overline{u_r u_\theta} = 0$ on the shell wall. Hence, $C_1 = 0$ everywhere. Since all time-mean quantities are independent of x (except the pressure) for fully developed flow, then from equation (14) $\partial P/\partial r$ must be independent of x, implying that $\partial P/\partial x$ is independent of r; then, equations (13) and (14) may be integrated with respect to r, yielding

$$\frac{r^2}{2\rho}\frac{\partial P}{\partial x} = -r(\overline{u_x u_r}) + \eta r\frac{dU}{dr} + C_2(x), \tag{16}$$

$$\frac{P}{\rho} = -\overline{u_r^2} + \int_a^r \frac{1}{r}(\overline{u_\theta^2} - \overline{u_r^2})\,dr + C_3(x), \tag{17}$$

where C_2 and C_3 are functions of x to be determined from the boundary conditions.

Considering now the *flow in the inner shell*, for fully developed axisymmetric flow, $dU/dr = 0$ and $\overline{u_x u_r} = 0$ at $r = 0$; hence, $C_2(x) = 0$. At $r = a_i$, since $(\overline{u_x u_r}) = 0$, equation (16) takes the form

$$\frac{1}{\rho_i}\frac{\partial P_i}{\partial x} = \frac{2\eta_i}{a_i}\frac{dU_i}{dr}\bigg|_{r=a_i}. \tag{18}$$

The shear velocity, $U_{\tau i}$, is defined next by

$$U_{\tau i}^2 = -\eta_i\frac{dU_i}{dr}\bigg|_{r=a_i} = \frac{\tau_{wi}}{\rho_i}, \tag{19}$$

where τ_{wi} is the wall viscous force per unit surface area on the inner shell. Substituting (19) into (18) and integrating with respect to x yields

$$\frac{P_i}{\rho_i} = -\frac{2}{a_i}U_{\tau i}^2 x + C_4(r). \tag{20}$$

Comparing (20) with (17) leads to

$$C_3(x) = -\frac{2}{a_i}U_{\tau i}^2 x,$$

$$C_4(r) = -\overline{u_{ri}^2} + \int_{a_i}^r \frac{1}{r}(\overline{u_{\theta i}^2} - \overline{u_{ri}^2})\,dr + C_5, \tag{21}$$

where C_5 is a constant, which may easily be found to be $P_i\ (0, a_i)/\rho_i$, in which $P_i(0, a_i)$ is the pressure at $x = 0$, $r = a_i$. Hence, the static pressure in the inner fluid region may be written as

$$P_i(x,r) = -\frac{2\rho_i}{a_i}U_{\tau i}^2 x - \rho_i\overline{u_{ri}^2} + \rho_i\int_{a_i}^r \frac{1}{r}(\overline{u_{\theta i}^2} - \overline{u_{ri}^2})\,dr + P_i(0,a_i). \tag{22}$$

On the shell surface, this expression takes on the particularly simple form

$$P_i(x,a_i) = -\frac{2\rho_i}{a_i}U_{\tau i}^2 x + P_i(0,a_i). \tag{23}$$

Proceeding in a similar manner, as shown in Appendix 1, the *pressure in the annular region* is found to be

$$P_o(x,r) = -\left\{\frac{2a_o\rho_o}{a_o^2 - r_m^2}\right\}U_{\tau oo}^2 x - \rho_o\overline{u_{ro}^2} + \rho_o\int_{a_i}^r \frac{1}{r}(\overline{u_{\theta o}^2} - \overline{u_{ro}^2})\,dr + P_o(0,a_i), \tag{24}$$

where r_m is the radius at which U_o is a maximum (Appendix 1), and $U_{\tau oo}$ is the shear velocity of the annular flow on the outer shell, defined by

$$U_{\tau oo}^2 = -\eta_o\frac{dU_o}{dr}\bigg|_{r=a_o} \equiv \frac{\tau_{woo}}{\rho_o}; \tag{25}$$

a similar shear velocity on the inner shell is defined by

$$U_{\tau oi}^2 = \eta_o\frac{dU_o}{dr}\bigg|_{r=a_i} \equiv \frac{\tau_{woi}}{\rho_o}. \tag{26}$$

With the pressures in the inner and annular regions determined, it is now easy to obtain the basic loads on the shells.

On the inner shell, the radial basic load is $\tilde{p}_{ri} = P_i(x, a_i) - P_o(x, a_i)$ and, utilizing (24) evaluated at $r = a_i$ and (23), it may be expressed as

$$\tilde{p}_{ri} = \left\{-\frac{2\rho_i}{a_i}U_{\tau i}^2 + \left[\frac{2a_o}{a_o^2 - r_m^2}\right]\rho_o U_{\tau oo}^2\right\}x + P_i(0,a_i) - P_o(0,a_i), \tag{27}$$

where the fact that $\overline{u_{ro}^2}$ must vanish at the wall has been utilized. The axial basic load is $\tilde{p}_{xi} = \tau_{wi} + \tau_{woi}$. Hence, through equations (19) and (26), one obtains

$$\tilde{p}_{xi} = \rho_i U_{\tau i}^2 + \rho_o U_{\tau oi}^2. \tag{28}$$

On the outer shell, the radial basic load is given by $\tilde{p}_{ro} = P_o(x, a_o) - P_e$, where P_e is the uniform static pressure of the fluid surrounding the outer shell; hence, utilizing equation (24), one obtains

$$\tilde{p}_{ro} = -\left\{\frac{2a_o}{a_o^2 - r_m^2}\right\}\rho_o U_{\tau oo}^2 x + \rho_o\int_{a_i}^{a_o} \frac{1}{r}(\overline{u_{\theta o}^2} - \overline{u_{ro}^2})\,dr + P_o(0,a_i) - P_e. \tag{29}$$

The axial basic load is simply equal to τ_{woo}, or

$$\tilde{p}_{xo} = \rho_o U_{\tau oo}^2. \tag{30}$$

Downloaded 02 May 2010 to 171.66.16.54. Redistribution subject to ASME license or copyright; see http://www.asme.org/terms/Terms_Use.cfm

Examining now equations (27)–(30) it becomes clear how the particular forms of equations (1) and (2) arise, and what the values of the constants B, C and D must be for the basic loads on the inner and outer shells.

3.2 Evaluation of the Basic Loads. The basic loads, as expressed by equations (27)–(30), are fully determined, if such quantities as $U_{\tau i}$, r_m, $U_{\tau oo}$, etc., are known. Unfortunately, these quantities cannot be obtained analytically. However, they may be evaluated with the aid of empirical information of common usage in hydraulics [11] – with a high degree of precision for the quantities associated with the inner flow, and with a fair degree of confidence for those relating to the annular flow, as developed in Appendix 2.

As shown in that appendix, the integral term in equation (29) is quite small, and a reasonable engineering approximation would be to neglect it, as commonly done in hydraulics, where the pressure in the flow conduit is considered to be approximately independent of r. If that is done and, additionally, the inner, annular, and outer static pressures are set equal at $x = L$, then equations (23), (24), (27), and (29) may be written as

$$P_i(x) \simeq \frac{2\rho_i}{a_i} U_{\tau i}^2 (L-x) + P_e,$$

$$P_o(x) \simeq \left\{ \frac{2a_o\rho_o}{a_o^2 - r_m^2} \right\} U_{\tau oo}^2 (L-x) + P_e,$$

$$\tilde{p}_{ri} \simeq \frac{2\rho_i}{a_i} U_{\tau i}^2 (L-x) - \left\{ \frac{2a_o\rho_o}{a_o^2 - r_m^2} \right\} U_{\tau oo}^2 (L-x), \tag{31}$$

$$\tilde{p}_{ro} \simeq \left\{ \frac{2a_o\rho_o}{a_o^2 - r_m^2} \right\} U_{\tau oo}^2 (L-x).$$

Although equations (31) are not used in the calculations, but rather the more complex forms derived earlier, they are given here because they provide direct physical insight into the functional form of the quantities involved.

4 Perturbation Pressures and Solution of the Equations

Assuming that the basic loads do not deform the shell appreciably, the perturbation pressures may be taken to be superimposed on the mean pressure field and to be the same as those determined in [1] in which the fluid was taken to be inviscid, so that the shells were not prestressed by the mean flow. Moreover, the method of solution, based on Galerkin's method, is identical and will not be elaborated on.

The solution is expressed in the form

$$\begin{Bmatrix} u_i \\ v_i \\ w_i \\ u_o \\ v_o \\ w_o \end{Bmatrix} = \sum_{m=1}^{\infty} \begin{Bmatrix} A_{mn} & \cos n\theta\,(a_i \partial/\partial x) \\ B_{mn} & \sin n\theta \\ C_{mn} & \cos n\theta \\ D_{mn} & \cos n\theta\,(a_o \partial/\partial x) \\ E_{mn} & \sin n\theta \\ F_{mn} & \cos n\theta \end{Bmatrix} \phi_m(x) e^{i\Omega t}, \tag{32}$$

where n is the circumferential wave number and m the axial one; $\phi_m(x)$ are taken to be the eigenfunctions of a clamped-clamped beam [1].

The perturbation pressures are determined by Fourier-transform potential flow techniques, such as those developed by Dowell and Widnall [12]. The quantities q_i and q_o of equations (12) are found to be [1]

$$q_i = \sum_{m=1}^{\infty} Q_{mn}(\xi) \cos n\theta e^{i\Omega t},$$

$$q_o = \sum_{m=1}^{\infty} R_{mn}(\xi) \cos n\theta e^{i\Omega t}, \tag{33}$$

where

$$Q_{mn}(\xi) = \frac{\rho_i U_i^2 C_{mn}}{2\pi L^2} \int_{-\infty}^{\infty} \frac{(\kappa_i - \bar{\alpha})^2}{\bar{\alpha}} E_n(\bar{\alpha}, a_i) \phi_m^*(\bar{\alpha}) e^{-i\bar{\alpha}\xi} d\bar{\alpha}$$

$$- \frac{\rho_o U_o^2}{2\pi L^2} \left\{ C_{mn} \int_{-\infty}^{\infty} \frac{(\kappa_o - \bar{\alpha})^2}{\bar{\alpha}} F_n(\bar{\alpha}, a_i) \phi_m^*(\bar{\alpha}) e^{-i\bar{\alpha}\xi} d\bar{\alpha} \right.$$

$$\left. + F_{mn} \int_{-\infty}^{\infty} \frac{(\kappa_o - \bar{\alpha})^2}{\bar{\alpha}} G_n(\bar{\alpha}, a_i) \phi_m^*(\bar{\alpha}) e^{-i\bar{\alpha}\xi} d\bar{\alpha} \right\}, \tag{34}$$

$$R_{mn}(\xi) = \frac{\rho_o U_o^2}{2\pi L^2} \left\{ C_{mn} \int_{-\infty}^{\infty} \frac{(\kappa_o - \bar{\alpha})^2}{\bar{\alpha}} F_n(\bar{\alpha}, a_o) \phi_m^*(\bar{\alpha}) \right.$$

$$\left. \times e^{-i\bar{\alpha}\xi} d\bar{\alpha} + F_{mn} \int_{-\infty}^{\infty} \frac{(\kappa_o - \bar{\alpha})^2}{\bar{\alpha}} G_n(\bar{\alpha}, a_o) \phi_m^*(\alpha) e^{-i\bar{\alpha}\xi} d\bar{\alpha} \right\},$$

and

$$E_n(\bar{\alpha}, r) = \frac{I_n(\bar{\alpha} r)}{I_n'(\bar{\alpha} a_i)},$$

$$F_n(\bar{\alpha}, r) = \frac{I_n'(\bar{\alpha} a_o) K_n(\bar{\alpha} r) - I_n(\bar{\alpha} r) K_n'(\bar{\alpha} a_o)}{I_n'(\bar{\alpha} a_o) K_n'(\bar{\alpha} a_i) - I_n'(\bar{\alpha} a_i) K_n'(\bar{\alpha} a_o)}, \tag{35}$$

$$G_n(\bar{\alpha}, r) = \frac{I_n(\bar{\alpha} r) K_n'(\bar{\alpha} a_i) - I_n'(\bar{\alpha} a_i) K_n(\bar{\alpha} r)}{I_n'(\bar{\alpha} a_o) K_n'(\bar{\alpha} a_i) - I_n'(\bar{\alpha} a_i) K_n'(\bar{\alpha} a_o)}.$$

In the foregoing,

$$\xi = x/L, \quad \kappa_i = \Omega L/U_i, \quad \kappa_o = \Omega L/U_o, \quad \bar{\alpha} = \alpha L; \tag{36}$$

α is the Fourier transform variable and the asterisk denotes a transformed quantity; I_n and K_n are, respectively, the modified Bessel functions of the first and second kind, and $I_n'(z) = dI_n(z)/dz$; Ω is the radian frequency, which will be a function of m and n for any given physical system.

With all quantities defined, their substitution into the equations of motion leads to a homogeneous set of coupled equations, which may be transformed into a standard eigenvalue problem [1]. The equations are rendered dimensionless, but for brevity only the essential nondimensional quantities,

$$\bar{U}_i = U_i/\mathcal{U}_i, \quad \bar{U}_o = U_o/\mathcal{U}_o, \quad \bar{\Omega}_i = \Omega a_i/\mathcal{U}_i,$$
$$\bar{\Omega}_o = \Omega a_o/\mathcal{U}_o, \quad \beta_i = (\rho_i a_i)/(\rho_{si} h_i), \tag{37}$$
$$\mathcal{U}_i = \{E_i/[\rho_{si}(1-\nu_i^2)]\}^{1/2}, \quad \mathcal{U}_o = \{E_o/[\rho_{so}(1-\nu_o^2)]\}^{1/2},$$

are defined here.

5 Results

Numerical results were obtained for systems of coaxial steel shells with water as the internal and annular fluids. For purposes of comparison, the same geometric configurations as in the case of inviscid flow were studied [1], namely, the so-called "½-gap" and "1/10-gap" systems, where this designation means that the annular gap is either ½ or 1/10 the inner-shell radius. The relevant defining parameters for the ½-gap system are $a_o = 100$ mm, $h_i = h_o = h = 0.500$ mm, $\mathcal{U}_i = 5308$ m/s, $a_i/a_o = 2/3$, $L/a_o = 10$, $h/a_o = 5 \times 10^{-3}$, $\beta_i = 17.09$, $\nu_i = \nu_o = 0.30$. The 1/10-gap system differs only in that $a_i/a_o = 10/11$ and $\beta_i = 23.30$. Calculations were conducted with the series in equation (32) truncated at $m = 3$.

The effect of varying the internal or annular flow velocities on the dynamics of the system is investigated. The axial frictional force and the static pressure gradient are normally

Downloaded 02 May 2010 to 171.66.16.54. Redistribution subject to ASME license or copyright; see http://www.asme.org/terms/Terms_Use.cfm

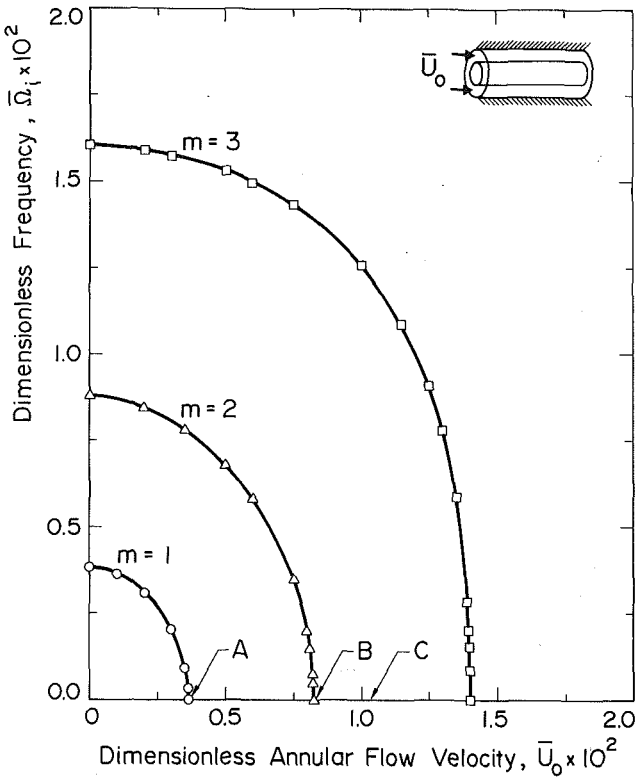


Fig. 1 The real dimensionless eigenfrequencies, $\bar{\Omega}_i$, of the 1/10-gap system with viscous annular flow and a stagnant inner fluid, as functions of the dimensionless annular flow velocity, $\bar{U}_o$, when the outer shell is rigid; $n = 3, m = 1, 2, 3$

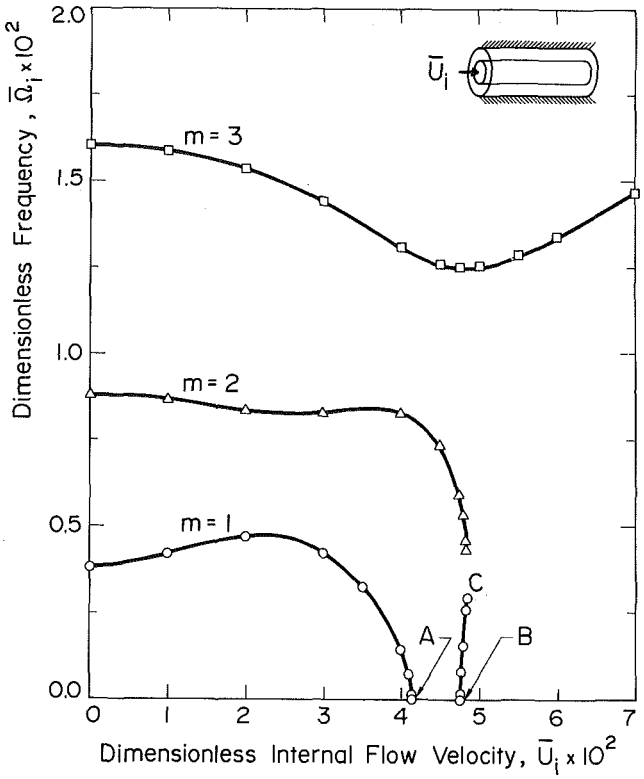


Fig. 2 The real dimensionless eigenfrequencies, $\bar{\Omega}_i$, of the 1/10-gap system with viscous inner flow and a stagnant annular fluid, as functions of the dimensionless inner flow velocity, $\bar{U}_i$, when the outer shell is rigid; $n = 3, m = 1, 2, 3$

adjusted at different flow velocities by the relationships described in Appendix 2, so that at $x=L$ the internal and annular static pressures be equal to that of the external stagnant fluid. In some cases, however, additional uniform pressurization was imposed on either the internal or annular flow regions.

Some calculations were conducted with the outer shell replaced by a rigid tube and will be considered first, before the system of two coaxial shells is investigated.

5.1 Systems With a Rigid Outer Tube. Typical results of the variation of the real dimensionless eigenfrequencies, $\bar{\Omega}_i$, with increasing dimensionless flow velocity in the annulus, $\bar{U}_o$, are shown in Fig. 1 (for $n = 3$, $m = 1, 2, 3$);[3] the internal fluid is stagnant and its static pressure is equal to that of the annular fluid at $x=L$. The system being conservative, the $\bar{\Omega}_i$ are real, up to the point of loss of stability by divergence, which is denoted by A in Fig. 1. Beyond A, the first ($m=1$) mode locus bifurcates and the eigenfrequencies become purely imaginary (hence, they cannot be shown in Fig. 1). The behavior of the second mode is similar. At point C, the loci of the first and second modes coalesce and the eigenfrequencies become complex; one of the two has a negative imaginary part, indicating that beyond C the system is subject to coupled-mode flutter. It should be noted that this flutter is here initiated with vanishingly small real frequency (point C in the figure), in contrast to the case of inviscid flow [1].

The question arises as to the physical significance of coupled-mode flutter, since it always occurs at a higher flow velocity than divergence; indeed, it may not materalize in practice. The reasons for pursuing calculations beyond the point of divergence, via this linear theory, are that (*i*) in the case of a single shell with internal flow, flutter was the only instability observed in practice, in some experiments at least, (albeit that in that case the divergence and coupled-mode flutter critical flow velocities were very close), and (*ii*) in cases of cylindrical beams in axial flow, a related problem, both divergence and coupled-mode flutter could be observed in the experiments [13, 14], and both were in good agreement with those predicted by linear theory.

Another point that could usefully be made here is that, if the sole interest of the analysis is the determination of the critical flow velocity for divergence, and not the variation of natural frequencies with flow and/or the value of flow velocity for coupled-mode flutter, then the analysis may be simplified drastically, by setting $\Omega=0$ in the complicated fluid-dynamic relationships (33)–(36).

Typical results for the case of a stagnant annular fluid and a flowing internal one are shown in Fig. 2. The dynamical behavior of the system is similar to that of Fig. 1, except that (*i*) loss of stability by divergence occurs at much higher flow velocity; (*ii*) the $\bar{\Omega}_i$'s tend to remain higher, or to rise with increasing $\bar{U}_i$, rather than monotonically dipping toward zero; (*iii*) coupled-mode flutter starts at point C, where first and second-mode eigenfrequencies are purely real, rather than imaginary, so that at its onset the frequency will be finite (cf. also reference [15]), in contrast to Fig. 1.

The results, in terms of stability are summarized in Table 1, where they are compared to those for inviscid flow. It is seen that viscous effects destabilize the system in the case of annular flow and stabilize it for inner flow. The explanation for this, as well as for items (*i*) and (*ii*) in the foregoing paragraph, may easily be grasped, in terms of the pressurization of the flowing fluid, required to overcome frictional pressure drop, and of the attendant differences in pressure on the two sides of the inner shell. Thus, in the case of inner flow, the pressure on the interior side of the flexible shell is higher than on the exterior (annulus) side for $0 \leq x <$

[3] The question arises as to why the calculations were conducted with $n = 3$. The reason is that, for the physical system considered, this was the critical value of n in the case of inviscid flow [1]; hence, these results may easily be compared with those for inviscid flow. The results for other $n > 1$ are entirely analogous to those shown in Fig. 1.

Downloaded 02 May 2010 to 171.66.16.54. Redistribution subject to ASME license or copyright; see http://www.asme.org/terms/Terms_Use.cfm

Table 1 Comparison of the dimensionless critical flow velocities, $\bar{U}_o$ and $\bar{U}_i$, for inviscid and viscous flows in the 1/10-gap system with a rigid outer shell ($n = 3$)

System	Critical flow velocities, $\bar{U}_i \times 10^2$ or $\bar{U}_o \times 10^2$			
	Divergence		Coupled-mode flutter	
	Inviscid	Viscous	Inviscid	Viscous
Annular flow only	1.36	0.36	1.85	1.04
Inner flow only	2.55	4.14	3.14	4.86

Table 2 Comparison of the dimensionless critical flow velocities, $\bar{U}_o$ and $\bar{U}_i$, for both shells flexible (inviscid and viscous flows), or only the inner one flexible (viscous flow), for the 1/10-gap system ($n = 3$)

System	Phenomenon	Critical flow velocities, $\bar{U}_i \times 10^2$ or $\bar{U}_o \times 10^2$		
		Inner shell flexible	Both shells flexible	
		Viscous	Viscous	Inviscid
Annular flow only	Divergence	0.36	0.36	0.96
	C-m flutter	1.04	1.31	1.36
Inner flow only	Divergence	4.14	4.14	2.55
	C-m flutter	4.86	4.82	3.13

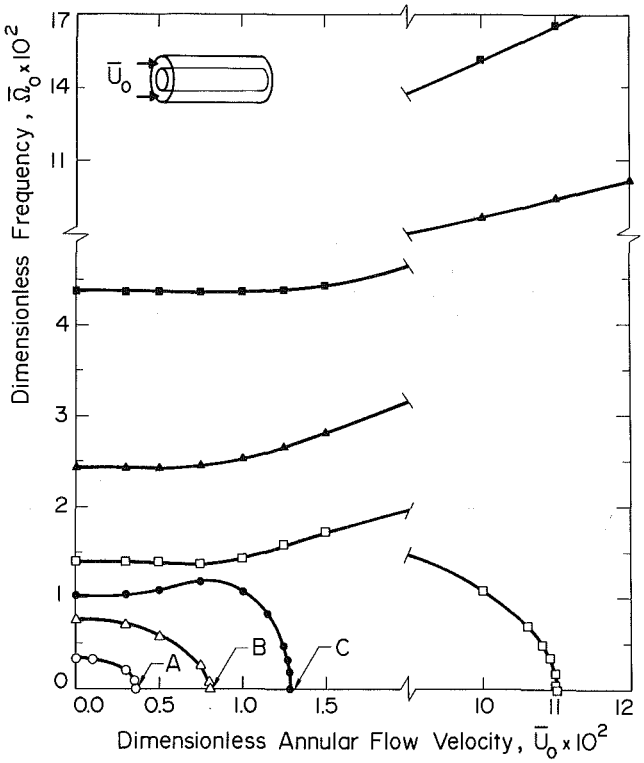


Fig. 3 The real dimensionless eigenfrequencies, $\bar{\Omega}_o$, of the 1/10-gap system of two coaxial (flexible) shells, with viscous annular flow and a stagnant inner fluid, as functions of $\bar{U}_o$; $n = 3$, $m = 1, 2, 3$. Open symbols: antiphase modes; closed symbols: in-phase modes; ○, ●: $m = 1$; △, ▲: $m = 2$; □, ■: $m = 3$.

L. Now, since internal pressurization tends to stabilize the system – at least in the shell modes ($n > 1$) and for constant pressurization [2] – it is clear that for viscous flow the system would be more stable than for inviscid flow, where this differential pressure is null. The situation for annular flow is exactly reversed, where now the overpressure is directed inward, tending to collapse the flexible inner shell, i.e., destabilizing the system.

The magnitude of these "pressurization" effects may appear surprising, so far as the results of Table 1 and Figs. 1 and 2 are concerned. However, for the physical system involved, it is found that the constant external pressure necessary to cause collapse of the flexible shell (in the absence of flow) is 36.3 kN/m^2; this compares to pressurization, in the case of annular flowing fluid (as in Fig. 1), of 146.4 kN/m^2 and zero, at $x = 0$ and L, respectively, with a linear variation in-between. Thus, the order of magnitude of the mean pressurization in the two cases is similar. Of course, for much shorter shells (here $L/a_o = 10$), this effect would be greatly diminished.

Here it should be reiterated that the inviscid results were obtained with the inner, annular, and outer pressures all equal (and constant along the length of the shell), so that in that case there are no "pressurization" effects whatsoever.

The shell may also buckle due to sufficiently high compressive load, and indeed the downstream part of the shell is subjected to such a load due to surface traction; however, the magnitude of this traction is two orders of magnitude lower than that needed to collapse the shell in this particular case; hence, it is of secondary importance here.

5.2 Systems With Both Shells Flexible. Typical results are shown in Fig. 3, for a system with annular flow and a stagnant inner fluid, similarly to Fig. 1. Here, for each m, there are two loci of frequencies: one for azimuthally in-phase motions of the two shells and the other for antiphase ones. It is the antiphase modes that are associated with the first loss of stability (cf. [1]).

In this case, the effect of mean pressurization is more complex. Thus, on the one hand, a higher annular pressure, vis-à-vis the inner one, would tend to destabilize the inner shell; on the other hand, the annular pressure being higher than the outer pressure would stabilize the outer shell. Hence, since motions of the two shells are coupled, the overall effect would be difficult to predict a priori and would clearly depend on the geometry and physical parameters of the system. The results, in terms of stability, for both shells flexible and for only the inner one flexible are compared in Table 2, where the former are also compared to the corresponding ones for inviscid flow. It is seen that the threshold of divergence for this particular system is unaffected by the flexibility of the outer shell, for both inner and annular flow, although in the latter case this cannot be considered to be a general conclusion (cf. [1]). Comparing viscous and inviscid-flow results, it is seen that once more viscous effects destabilize the system for annular flow and stabilize it for inner flow.

5.3 Effect of Additional Pressurization. In view of the importance of the pressurization effects obtained in the foregoing, it was decided to conduct calculations in which the original assumption that inner, annular, and outer static pressures be equal at $x = L$ is relaxed, so as to permit additional pressurization of one or the other fluids – imposed over and above that associated with the pressure drop.

Typical results are shown in Table 3, where an additional pressurization of 50 kN/m^2 (approximately one-half atmosphere) has been applied to either the inner or annular

Downloaded 02 May 2010 to 171.66.16.54. Redistribution subject to ASME license or copyright; see http://www.asme.org/terms/Terms_Use.cfm

Table 3 The effect of additional pressurization on stability of the 1/10-gap system of two coaxial shells ($n = 3$) with annular flow. The units for $P_i(L)$ and $P_o(L)$ are kN/m^2.

Flow and pressurization conditions		Critical flow velocities, $\bar{U}_o \times 10^2$	
Inner fluid	Annular fluid	Divergence	Coupled-mode flutter
Stagnant $P_i(L) = 0$	Flowing $P_o(L) = 0$	0.36	1.31
Stagnant $P_i(L) = 0$	Flowing $P_o(L) = 50$	0.21	1.30
Stagnant $P_i(L) = 50$	Flowing $P_o(L) = 50$	0.36	1.31

Table 4 The effect of annular gap width on the stability of two coaxial shells conveying fluid in the annulus and filled with stagnant fluid in the inner shell ($n = 3$) for both inviscid and viscous flows

System	Critical annular flow velocities, $\bar{U}_o \times 10^2$			
	Divergence		Coupled-mode flutter	
	Inviscid	Viscous	Inviscid	Viscous
1/10-gap	0.96	0.36	1.36	1.31
1/2-gap	2.06	0.85	2.62	2.39

fluid; the outer pressure has been kept constant at one atmosphere. It is seen that additional pressurization on the annular fluid causes a further reduction (by ~ 40 percent) of the critical flow velocity for divergence. If the inner fluid is pressurized to the same extent, this effect disappears, the results in the third line of the table becoming identical to those of the first line. These results reinforce the conclusions reached previously, as to the manner in which pressurization affects stability of the system.

5.4 Effect of Annular Width. In the foregoing, all calculations were conducted with an annular gap of 1/10 the inner shell radius. To investigate the effect of this parameter, calculations were also done with this gap being one-half the inner shell radius (and otherwise the same parameters as before). The results are summarized in Table 4. It is seen that, in both cases of inviscid and viscous flows, the system becomes unstable at lower flow velocities for smaller annular widths. One reason for this has already been exposed [1] and is associated with the fact that, as the annular gap is diminished, the unsteady fluid-dynamic forces are augmented by the corresponding increase in the virtual (added) mass of the annular fluid. An additional reason, in the case of viscous flow, is that the pressure drop in the annulus becomes higher in the narrower annulus, resulting in a larger destabilizing effect due to pressurization; although in this case, this effect is not as important as might have been expected.

6 Conclusion

The dynamics and stability of coaxial shells conveying fluid in either the inner shell or in the annulus in-between the two shells have been studied with the aid of viscous flow theory, and were then compared to the results previously obtained with inviscid flow theory. In this paper, the shells are clamped at both ends in all cases.

Two principal effects of the viscosity of the flow were taken into account: (*i*) the necessary upstream pressurization of the flow, to overcome frictional pressure drop; (*ii*) the surface tractions on the shells associated with skin friction. An effect *not* included is that of damping, which is undoubtedly very important insofar as the dynamics of the system are concerned: i.e., not only modal damping, but perhaps the natural frequencies themselves would be affected by viscous damping of shell motions, especially in very narrow annuli. However, the systems studied, being clamped at both ends and hence inherently conservative, will necessarily lose stability by divergence, which is independent of rate-dependent terms, including viscous damping; hence, the stability characteristics of the system, as obtained here, would remain unchanged by the inclusion of viscous damping.

It was shown that viscous flow may have a pronounced effect on the stability of the system, particularly in cases where the flow passages are narrow and the shells long, so that the pressure drop is high. Thus, if the flowing fluid is in the annular passage, pressurization of this fluid tends to collapse the inner shell while stabilizing the outer one; the net effect on stability depends on geometrical parameters and relative flexibility of the shells, but for the systems considered here, an overall destabilization of the system is produced, vis-à-vis the situation in inviscid flow. For similar reasons, viscous effects for flow in the inner shell tend to stabilize the system.

For systems with both internal and annular flow, the overall effect of viscosity will be a composite of the foregoing, and whether the system is stabilized or destabilized by viscous effects will clearly depend on the relative pressure drops in the inner and annular flow passages and hence on system geometry. Clearly, system stability will also depend on whether the two flows are concurrent or countercurrent.

The principal accomplishment of this work may be considered to be the finding that viscous effects, neglected in all previous studies (to the authors' knowledge) are by no means negligible and that further effort should be devoted to (*i*) refining the viscous-flow model proposed here and (*ii*) testing it experimentally.

Acknowledgments

The authors gratefully acknowledge the support given to this research by the Natural Sciences and Engineering Research Council of Canada, Le programme FCAC of Québec and McGill University.

References

1 Paidoussis, M. P., Chan, S. P., and Misra, A. K., "Dynamics and Stability of Coaxial Cylindrical Shells Containing Flowing Fluid," *Journal of Sound and Vibration*, Vol. 97, 1984, in press.

2 Flügge, W., *Stresses in Shells*, Springer-Verlag, Berlin, 1960.

3 Timoshenko, S., *Theory of Elastic Stability*, McGraw-Hill, New York, 1961.

4 Brush, D. O., and Almroth, B. O., *Buckling of Bars, Plates and Shells*, McGraw-Hill, New York, 1975.

5 Benjamin, T. B., "Dynamics of a System of Articulated Pipes Conveying Fluid; I. Theory," *Proceedings of the Royal Society (London)*, Series *A*, Vol. 261, 1961, pp. 457–486.

6 Gregory, R. W., and Paidoussis, M. P., "Unstable Oscillation of Tubular Cantilevers Conveying Fluid; I. Theory," *Proceedings of the Royal Society (London)*, Series *A*, Vol. 293, 1966, pp. 512–527.

Downloaded 02 May 2010 to 171.66.16.54. Redistribution subject to ASME license or copyright; see http://www.asme.org/terms/Terms_Use.cfm

7 Paidoussis, M. P., "Dynamics of Tubular Cantilevers Conveying Fluid," *Journal of Mechanical Engineering Science*, Vol. 12, 1970, pp. 85–103.

8 Paidoussis, M. P., "Flow-Induced Vibrations in Nuclear Reactors and Heat Exchangers: Practical Experiences and State of Knowledge," in *Practical Experiences With Flow-Induced Vibrations*, Naudascher, E., and Rockwell, D., eds., Springer-Verlag, Berlin, 1980, pp. 1–81.

9 Chan, S. P., "Dynamics and Stability of Two Coaxial Cylindrical Shells Conveying Fluid," M.Eng. thesis, McGill University, Montreal, Québec, Canada, 1983.

10 Laufer, J., "The Structure of Turbulence in Fully Developed Pipe Flow," NACA Tech. Note 2954, 1953.

11 Murdock, J. W., *Fluid Mechanics and its Applications*, Houghton Mifflin, Boston, 1976.

12 Dowell, E. H., and Widnall, S. E., "Generalized Aerodynamic Forces on an Oscillating Cylindrical Shell," *Quarterly of Applied Mathematics*, Vol. XXIV, 1966, pp. 1–17.

13 Paidoussis, M. P., "Dynamics of Flexible Slender Cylinders in Axial Flow. Part 2: Experiments," *Journal of Fluid Mechanics*, Vol. 26, 1966, pp. 737–751.

14 Paidoussis, M. P., Curling, L. R., and Gagnon, J. O., "Experiments on Fluidelastic Instability of Cylinder Clusters in Axial Flow," ASME *Journal of Fluids Engineering*, Vol. 104, 1982, pp. 342–347; and Discussion pp. 347–349.

15 Dugundji, J., Dowell, E. H., and Perkin, B., "Subsonic Flutter of Panels on Continuous Elastic Foundations," *AIAA Journal*, Vol. 1, 1963, pp. 1146–1154.

APPENDIX 1

The Annular Mean Pressure Field

Proceeding in the same manner as for the inner flow, it may be shown that $\overline{u_{ro}u_{\theta o}} = 0$ everywhere. Then, defining by r_m the radius where U_o is a maximum, one obtains,

$$dU_o/dr = 0 \quad \text{and} \quad \overline{u_{xo}u_{ro}} = 0, \quad \text{at} \quad r = r_m; \tag{A.1}$$

moreover, on the shell surfaces,

$$\overline{u_{xo}u_{ro}} = \overline{u_{ro}^2} = 0, \quad \text{at} \quad r = a_i \quad \text{and} \quad r = a_o. \tag{A.2}$$

Hence, proceeding in the way leading to equation (20), one obtains

$$C_2(x) = \frac{r_m^2}{2\rho_o}\frac{\partial P_o}{\partial x}, \quad \frac{1}{2\rho_o}\frac{\partial P_o}{\partial x}\left\{\frac{a_o^2 - r_m^2}{a_o}\right\} = -U_{\tau oo}^2, \tag{A.3}$$

and

$$\frac{P_o}{\rho_o} = -\left\{\frac{2a_o}{a_o^2 - r_m^2}\right\}U_{\tau oo}^2 x + C_4(r), \tag{A.4}$$

where $U_{\tau oo}^2$ is defined by equation (25).

Comparing equations (A.3) and (17), the functions $C_3(x)$ and $C_4(r)$ are defined, leading eventually to equation (24).

It is also necessary to relate $U_{\tau oo}^2$ and $U_{\tau oi}^2$ of equations (25) and (26). The second equation (A.3) has been obtained by applying the boundary equations (A.2) at $r = a_o$; if, instead, those at $r = a_i$ are applied, then

$$\frac{1}{2\rho_o}\frac{\partial P_o}{\partial x}\left\{\frac{r_m^2 - a_i^2}{a_i}\right\} = -U_{\tau oi}^2,$$

from which the following relationships are easily obtained:

$$U_{\tau oi}^2 = \frac{a_o}{a_i}\left\{\frac{r_m^2 - a_i^2}{a_o^2 - r_m^2}\right\}U_{\tau oo}^2, \quad \tau_{woi} = \frac{a_o}{a_i}\left\{\frac{r_m^2 - a_i^2}{a_o^2 - r_m^2}\right\}\tau_{woo}. \tag{A.5}$$

APPENDIX 2

Detailed Evaluation of the Basic Loads

In the expressions for the basic loads given by equations (27)–(30), the only unknown quantity relating to the inner flow is $U_{\tau i}$. It may be determined empirically from the well-known expression for pressure drop in a pipe,

$$\left|\frac{\partial P_i}{\partial x}\right| = \tfrac{1}{2}\frac{f_i \rho_i}{D_{hi}}U_i^2, \tag{A.6}$$

where f_i is the friction factor and D_{hi} is the hydraulic diameter (in this case equal to $2a_i$). Utilizing (19) and (18), the foregoing leads to

$$U_{\tau i}^2 = \frac{1}{8}f_i U_i^2. \tag{A.7}$$

The factor f_i depends on surface roughness and the Reynolds number. It may be obtained from the Moody diagram or the Colebrook equation [11], commonly used in hydraulics.

The unknown quantities in (27)–(30) associated with the annular flow are numerous and more difficult to evaluate. Firstly, r_m cannot be determined analytically and no definitive experimental data is available. It was decided to approximate it by its counterpart in the case of laminar flow,

$$r_m = \left\{\frac{a_o^2 - a_i^2}{2\ln(a_o/a_i)}\right\}^{1/2}, \tag{A.8}$$

obtained analytically. Next, concerning $U_{\tau oo}^2$, once more the empirical expression for pressure drop may be utilized,

$$\left|\frac{\partial P_o}{\partial x}\right| = \tfrac{1}{2}\frac{f_o \rho_o}{D_{ho}}U_o^2,$$

where in this case $D_{ho} = 2(a_o - a_i)$. Comparing with (A.3) leads directly to

$$U_{\tau oo}^2 = \frac{1}{8}\left\{\frac{a_o^2 - r_m^2}{a_o(a_o - a_i)}\right\}f_o U_o^2, \tag{A.9}$$

and through (A.5) $U_{\tau oi}^2$ may similarly be determined.

The last undetermined quantity is the integral

$$I = \int_{a_i}^{a_o}(1/r)\,(\overline{u_{\theta o}^2} - \overline{u_{ro}^2})\,dr$$

in equation (29). To the best of the authors' knowledge, experimental data on the fluctuating velocity components of turbulent annular flow is not available. As a compromise, the experimental results for turbulent flow in a circular pipe obtained by Laufer [10] were utilized, with r_m replacing the centerline ($r = 0$) of a circular pipe. Expressing Laufer's measurements in appropriate polynomial form, the following approximate expression was obtained:

$$\begin{aligned} I = &\left\{-0.786 + 0.560\left(\frac{r_m}{r_m - a_i}\right)\times\right. \\ &\left\{\left[0.904 + \frac{r_m}{r_m - a_i}\right]\ln\left(\frac{r_m}{a_i}\right)\right\} - 1\Big\}U_{\tau oi}^2 \\ &+\left\{0.786 - 0.560\left(\frac{r_m}{a_o - r_m}\right)\right. \\ &\left.\left\{\left[0.904 - \frac{r_m}{a_o - r_m}\right]\ln\left(\frac{a_o}{r_m}\right)\right\} + 1\right\}U_{\tau oo}^2. \end{aligned} \tag{A.10}$$

This is, at best, a gross approximation to the true value and its accuracy cannot readily be assessed. Fortunately, however, this integral turns out to be rather insignificant, as compared to the other terms of equation (29), which indirectly verifies the common engineering assumption that the static pressure in fully developed turbulent flow is approximately constant across a cross section of the flow conduit.

Downloaded 02 May 2010 to 171.66.16.54. Redistribution subject to ASME license or copyright; see http://www.asme.org/terms/Terms_Use.cfm

Free Vibration of Rectangular Plates Stiffened With Viscoelastic Beams

K. Ohtomi
Researcher,
Mechanical Engineering Laboratory,
Toshiba Research and
Development Center,
Kawasaki, Japan

This investigation treats the free vibration of a simply supported rectangular plate, stiffened with viscoelastic beams. Using a convenient method in which the effects of beams are expressed with Dirac delta functions, the equation of motion can be expressed by only one equation. The frequency equation is obtained by applying the Laplace transformation to the equation of motion. The effects of the volume and the number of beams on the frequency and the logarithmic decrement are clarified.

Introduction

The vibration of rectangular plates stiffened with beams has been investigated by many authors. Lin [1] studied the free vibration of plates stiffened with many stringers. The differential equation was solved for an individual plate and the solutions for an individual plate were coupled with the boundary conditions. Duffield and Willems [2] analyzed the parametric resonance of a plate using the energy method. Saito and Suzuki [3] performed an analytical evaluation of the viscoelastic beam effect on plate vibration characteristics.

In the work reported here, the free vibration of a simply supported rectangular plate, stiffened with viscoelastic beams, was studied analytically. The effects of the volume and the number of beams on the plate are clarified. The effects of the stiffened beams are expressed with Dirac delta functions and the equation of motion is derived. The beam material is also assumed to be linearly viscoelastic and has a complex modulus. The frequency equation is obtained by applying the Laplace transformation to the equation of motion. In numerical computations, the case for the plate aspect ratio 2 is treated. In this case, the effects of the volume and the number of beams are clarified. Moreover, the effects of Young's modulus and the loss factor on the plate are analyzed.

Equation of Motion

Consider the free vibration of a simply supported rectangular plate stiffened with viscoelastic beams, as shown in Fig. 1. This kind of problem has been analyzed using the energy method or the transfer matrix method. However, by increasing the number of beams, the analysis procedure has become complex. This paper proposes a convenient method in which the effects of beams are expressed with Dirac delta functions. Using this method, the equation of motion governing a plate stiffened with viscoelastic beams can be expressed by only one equation.

At the location where the beam is attached, $y = c_j$ ($j = 1, 2, \ldots, L$), discontinuities appear in the shearing force and bending moment. The discontinuity in shearing force caused by the jth beam is expressed as

$$F_j = E^*_{bj} I_j \frac{\partial^4 w}{\partial x^4} + \rho_{bj} A_j \frac{\partial^2 w}{\partial t^2} - \rho_{bj} I_j \frac{\partial^4 w}{\partial x^2 \partial t^2} \tag{1}$$

and the one of bending moment caused by the jth beam is expressed as

$$M_j = G^*_j J_{pj} \frac{\partial^3 w}{\partial x^2 \partial y} - \rho_{bj} I_{pj} \frac{\partial^3 w}{\partial y \partial t^2} \tag{2}$$

where E^*_{bj} is the complex Young's modulus for the jth beam, I_j is the secondary moment of inertia for the beam cross section, ρ_{bj} is the mass per unit volume, A_j is the cross-sectional area, G^*_j is the complex shear modulus, J_{pj} is the torsion constant, I_{pj} is the secondary polar moment of inertia, and t is time. Complex moduli, E^*_{bj} and G^*_j, can be written as

$$E^*_{bj} = E_{bj}(1 + i\eta_{Ej}), \quad G^*_j = G_j(1 + i\eta_{Gj}) \tag{3}$$

where E_{bj} and G_j are real parts of the complex moduli, E^*_{bj} and G^*_j, respectively, and η_{Ej} and η_{Gj} are the loss factors.

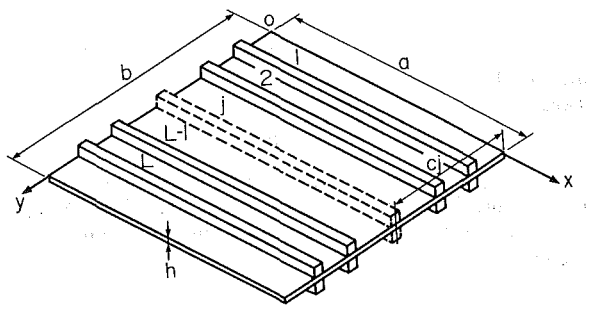


Fig. 1 Simply supported rectangular plate stiffened with viscoelastic beams

Contributed by the Applied Mechanics Division for publication in the JOURNAL OF APPLIED MECHANICS.
Discussion on this paper should be addressed to the Editorial Department, ASME, United Engineering Center, 345 East 47th Street, New York, N.Y. 10017, and will be accepted until two months after final publication of the paper itself in the JOURNAL OF APPLIED MECHANICS. Manuscript received by ASME Applied Mechanics Division, May, 1984; final revision, August, 1984.

Copyright © 1985 by ASME
Downloaded 02 May 2010 to 171.66.16.54. Redistribution subject to ASME license or copyright; see http://www.asme.org/terms/Terms_Use.cfm

The effects of F_j and M_j on the plate can be expressed with Dirac delta functions, as follows:

$$D\nabla^4 w+\rho h\frac{\partial^2 w}{\partial t^2}+\sum_{j=1}^{L}\left[\delta(y-c_j)F_j+\frac{\partial}{\partial y}\{\delta(y-c_j)M_j\}\right]=0 \tag{4}$$

where

$$D=\frac{Eh^3}{12(1-\nu^2)},\quad \nabla^4=\frac{\partial^4}{\partial x^4}+2\frac{\partial^4}{\partial x^2\partial y^2}+\frac{\partial^4}{\partial y^4}$$

In the preceding equation, E is the Young's modulus of the plate, ρ is the mass per unit volume, h is the thickness of the plate, and ν is the Poisson's ratio.

Analysis

For free vibration of a simply supported plate, equation (4) has a solution of the form

$$w(x,y,t)=h\sin\frac{m\pi x}{a}Y(y)e^{i\omega t} \tag{5}$$

where m is a positive integer, $i=(-1)^{1/2}$, Y is the complex mode function, and ω is the complex natural frequency. Substituting equation (5) into equation (4) and introducing the quantities

$$\begin{aligned}
&\Omega=\omega/(D/\rho hb^4)^{1/2},\quad \bar{y}=y/b,\quad \bar{c}_j=c_j/b,\\
&\alpha_{1j}=\rho_{bj}A_j/\rho bh,\quad \alpha_{2j}=(m\pi\gamma)^2\rho_{bj}I_j/\rho b^3h,\\
&\alpha_{3j}=\rho_{bj}I_{pi}/\rho b^3h,\quad \beta_1=(m\pi\gamma)^4,\\
&\beta_2=2(m\pi\gamma)^2,\quad \gamma=b/a,\\
&\bar{E}_j^*=\bar{E}_j(1+i\eta_{Ej}),\quad \bar{E}_j=(m\pi\gamma)^4E_{bj}I_j/Db,\\
&\bar{G}_j^*=\bar{G}_j(1+i\eta_{Gj}),\quad \bar{G}_j=(m\pi\gamma)^2G_jJ_{pj}/Db,\\
&\qquad j=1,2,\ldots,L
\end{aligned} \tag{6}$$

yields

$$\begin{aligned}
-\Omega^2\Big[&Y+\sum_{j=1}^{L}\delta(\bar{y}-\bar{c}_j)(\alpha_{1j}+\alpha_{2j})Y\\
&-\sum_{j=1}^{L}\{\delta(\bar{y}-\bar{c}_j)\alpha_{3j}Y'\}'\Big]\\
+\Big[&(\beta_1Y-\beta_2Y''+Y'''')+\sum_{j=1}^{L}\delta(\bar{y}-\bar{c}_j)\bar{E}_j^*Y\\
&-\sum_{j=1}^{L}\{\delta(\bar{y}-\bar{c}_j)\bar{G}_j^*Y'\}'\Big]=0
\end{aligned} \tag{7}$$

where $(\,)'$ denotes differentiation with respect to the dimensionless coordinate $\bar{y}$.

Boundary conditions at $y=0, b$ ($\bar{y}=0, 1$) are

$$Y(0)=Y(1)=Y''(0)=Y''(1)=0 \tag{8}$$

By applying the Laplace transformation to equation (7) and the first and the third equations in equation (8), solving for the transform Y and inverting the result, the solution is obtained as

$$\begin{aligned}
Y(\bar{y})=&\sum_{j=1}^{L}P_jY(\bar{c}_j)F_0(\bar{y}-\bar{c}_j)u(\bar{y}-\bar{c}_j)\\
&-\sum_{j=1}^{L}R_jY'(\bar{c}_j)F_1(\bar{y}-\bar{c}_j)u(\bar{y}-\bar{c}_j)\\
&-\beta_2Y'(0)F_0(\bar{y})+Y'''(0)F_0(\bar{y})+Y'(0)F_2(\bar{y})
\end{aligned} \tag{9}$$

where u is the unit step function and

$$\begin{aligned}
&P_j=\Omega^2(\alpha_{1j}+\alpha_{2j})-\bar{E}_j^*\\
&R_j=\Omega^2\alpha_{3j}-\bar{G}_j^*\\
&F_0(\bar{y})=\{(1/\bar{a})\sinh\bar{a}\bar{y}-(1/\bar{b})\sin\bar{b}\bar{y}\}/(\bar{a}^2+\bar{b}^2)\\
&F_i(\bar{y})=\frac{d^iF_0(\bar{y})}{d\bar{y}i},\quad i=1,2,3,4
\end{aligned}$$

with

$$\begin{aligned}
&\bar{a}^2=\{\beta_2+(\beta_2^2+4\beta_3)^{1/2}\}/2\\
&\bar{b}^2=\{-\beta_2+(\beta_2^2+4\beta_3)^{1/2}\}/2\\
&\beta_3=\Omega^2-\beta_1
\end{aligned}$$

Substituting equation (9) into the second and the fourth equation in equation (8) leads to the following equations:

$$\begin{aligned}
&\sum_{j=1}^{L}P_jY(\bar{c}_j)F_0(1-\bar{c}_j)-\sum_{j=1}^{L}R_jY'(\bar{c}_j)F_1(1-\bar{c}_j)\\
&\quad-\beta_2Y'(0)F_0(1)+Y'''(0)F_0(1)+Y'(0)F_2(1)=0
\end{aligned} \tag{10}$$

$$\begin{aligned}
&\sum_{j=1}^{L}P_jY(\bar{c}_j)F_2(1-\bar{c}_j)-\sum_{j=1}^{L}R_jY'(\bar{c}_j)F_3(1-\bar{c}_j)\\
&\quad-\beta_2Y'(0)F_2(1)+Y'''(0)F_2(1)+Y'(0)F_4(1)=0
\end{aligned} \tag{11}$$

Substituting $\bar{y}=\bar{c}_n$ into equation (9) and the derivative of equation (9) with respect to $\bar{y}$, the following equations are obtained:

$$\begin{aligned}
Y(\bar{c}_n)=&\sum_{j=1}^{n-1}P_jY(\bar{c}_j)F_0(\bar{c}_n-\bar{c}_j)\\
&-\sum_{j=1}^{n-1}R_jY'(\bar{c}_j)F_1(\bar{c}_n-\bar{c}_j)\\
&-\beta_2Y'(0)F_0(\bar{c}_n)+Y'''(0)F_0(\bar{c}_n)\\
&+Y'(0)F_2(\bar{c}_n)
\end{aligned} \tag{12}$$

$$\begin{aligned}
Y'(\bar{c}_n)=&\sum_{j=1}^{n-1}P_jY(\bar{c}_j)F_1(\bar{c}_n-\bar{c}_j)\\
&-\sum_{j=1}^{n-1}R_jY'(\bar{c}_j)F_2(\bar{c}_n-\bar{c}_j)\\
&-\beta_2Y'(0)F_1(\bar{c}_n)+Y'''(0)F_0(\bar{c}_n)\\
&+Y'(0)F_3(\bar{c}_n)\\
&\qquad n=1,2,\ldots,L
\end{aligned} \tag{13}$$

From equation (10) to equation (13), the frequency equation is obtained as

$$f(\omega)=\begin{vmatrix}\mathbf{e}^{(1,1)}&\mathbf{e}^{(1,2)}&\mathbf{e}^{(1,3)}\\ \mathbf{e}^{(2,1)}&\mathbf{e}^{(2,2)}&\mathbf{e}^{(2,3)}\\ \mathbf{e}^{(3,1)}&\mathbf{e}^{(3,2)}&\mathbf{e}^{(3,3)}\end{vmatrix}=0 \tag{14}$$

where $\mathbf{e}^{(1,1)}$, $\mathbf{e}^{(1,2)}$, $\mathbf{e}^{(2,1)}$, and $\mathbf{e}^{(2,2)}$ are $L\times L$ matrices, $\mathbf{e}^{(1,3)}$ and $\mathbf{e}^{(2,3)}$ are $L\times 2$ matrices, $\mathbf{e}^{(3,1)}$ and $\mathbf{e}^{(3,2)}$ are $2\times L$ matrices, and $\mathbf{e}^{(3,3)}$ is a 2×2 matrix. The details are shown in the Appendix.

Using the root of equation (14) and substituting equations (10)–(13) into equation (9), we determine the complex mode function $Y(\bar{y})$ as

Downloaded 02 May 2010 to 171.66.16.54. Redistribution subject to ASME license or copyright; see http://www.asme.org/terms/Terms_Use.cfm

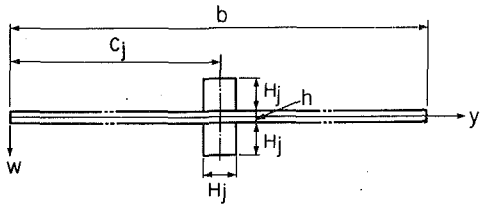


Fig. 2 Viscoelastic beams attached at $y = c_j = jb/(L+1)$

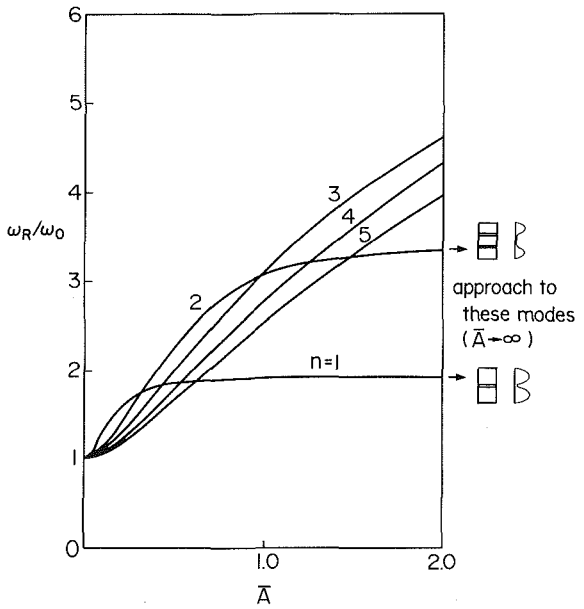


Fig. 3(a) Variation in natural frequency versus total volume of beams, $\gamma = 2$, $\omega_0 = 5\pi^2 (D/\rho h b^4)^{1/2}$

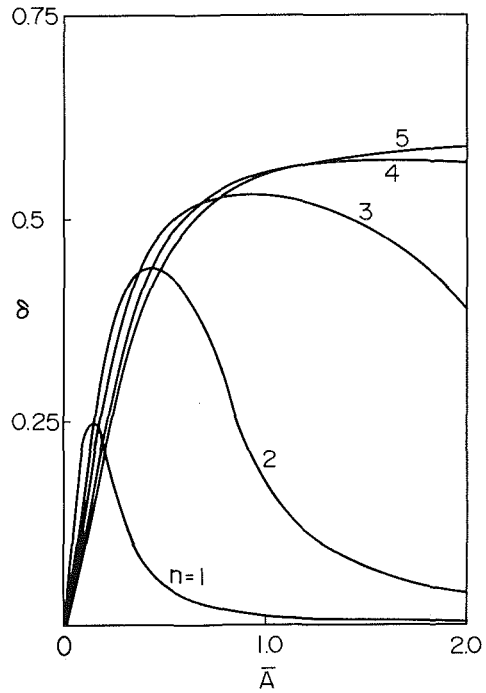


Fig. 3(b) Variation in logarithmic decrement versus total volume of beams, $\gamma = 2$

Fig. 3

$$Y(\bar{y}) = Y'''(0)\Big[\sum_{j=1}^{L} P_j \xi_j F_0(\bar{y}-\bar{c}_j)\,u(\bar{y}-\bar{c}_j)$$

$$-\sum_{j=1}^{L} R_j \xi_{L+j} F_1(\bar{y}-\bar{c}_j)\,u(\bar{y}-\bar{c}_j)$$

$$-\beta_2 \xi_{2L+1} F_0(\bar{y}) + F_0(\bar{y}) + \xi_{2L+1} F_2(\bar{y})\Big] \tag{15}$$

where

$$\xi_n = Y(\bar{c}_n)/Y'''(0)$$

$$\xi_{L+n} = Y'(\bar{c}_n)/Y'''(0)$$

$$\xi_{2L+1} = Y'(0)/Y'''(0), \quad n = 1, 2, \ldots, L$$

If $Y_p(\bar{y})$ and $Y_q(\bar{y})$ are taken as the complex mode functions of the pth and the qth modes, the following orthogonality relation exists between $Y_p(\bar{y})$ and $Y_q(\bar{y})$, which is proved by using equations (7) and (8):

$$\int_0^1 \Big[Y_p + \sum_{j=1}^{L} \delta(\bar{y}-\bar{c}_j)\,(\alpha_{1j}+\alpha_{2j})\,Y_p$$

$$-\sum_{j=1}^{L} \{\delta(\bar{y}-\bar{c}_j)\,\alpha_{3j} Y_p'\}'\Big] Y_q\, d\bar{y} = C_p \delta_{pq} \tag{16}$$

where C_p is a complex constant and δ_{pq} is Kronecker's delta. Equation (16) is a useful relation for treating forced vibrations.

Numerical Results

Numerical Condition. In numerical computations, the cases of a plate with viscoelastic beams, whose cross-sectional shape is square, are treated. The equal beams are attached to both sides of a plate at regular intervals, as shown in Fig. 1. Figure 2 shows the viscoelastic beam attached at $y = c_j = jb/(L+1)$. The influence of the upper side beam on a plate is the same as the influence of the lower side beam. From this, I, I_p, A, and J_p of the jth set of two beams can be expressed as

$$I_j = 2\left\{\frac{H_j^4}{12} + \frac{H_j^2 (H_j+h)^2}{4}\right\}$$

$$I_{pj} = I_j + \frac{H_j^4}{6}, \quad A_j = 2H_j^2$$

$$J_{pj} = 2 \cdot 0.1406 \cdot H_j^4 \text{ [4]}$$

Material properties and geometry for the plate and viscoelastic beams are given as

$h/b = 0.004$, $\nu = 1/3$, $m = 1$,

$\gamma = 2$ (aspect ratio),

$\rho_b/\rho = 0.5$, $(\rho_b = \rho_{bj})$ (density ratio),

$E_b/E = 0.1$ or < 0.5, $(E_b = E_{bj})$ (ridigity ratio),

$G = E_b/2(1+\nu)$, $(G = G_j)$,

$\eta = \eta_E = \eta_G = 0.2$ or < 0.5,

$(\eta_E = \eta_{Ej}, \eta_G = \eta_{GJ})$ (loss factor)

and the dimensionless total volume of the beams is expressed as

$$\bar{A} = a\sum_{j=1}^{L} A_j/abh = 2LH^2/bh \quad (H = H_j)$$

$$= 0.1 \text{ or } < 2$$

The lowest natural frequency ω_R (real part of the complex natural frequency ω) and logarithmic decrement δ of the plate for various parameters are shown as follows.

Downloaded 02 May 2010 to 171.66.16.54. Redistribution subject to ASME license or copyright; see http://www.asme.org/terms/Terms_Use.cfm

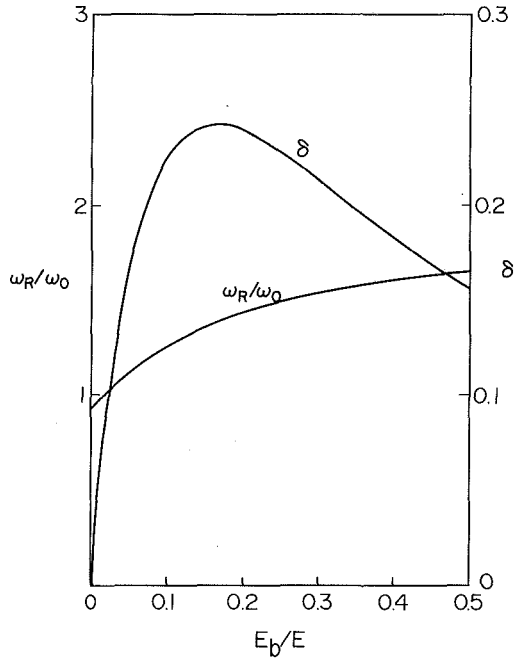


Fig. 4 Natural frequency and logarithmic decrement dependencies on Young's modulus of beams, $\gamma=2$, $L=1$, $\bar{A}=0.1$, $\omega_0=5\pi^2\,(D/\rho hb^4)^{1/2}$

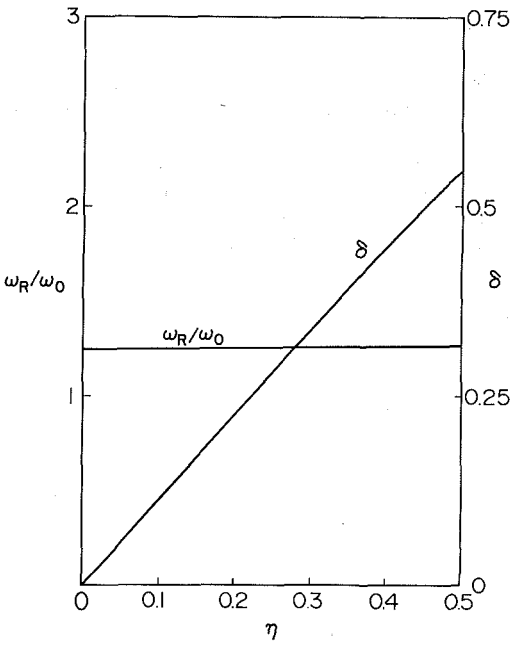


Fig. 5 Natural frequency and logarithmic decrement dependencies on loss factor of beams, $\gamma=2$, $\bar{A}=0.1$, $L=1$, $E_b/E=0.1$, $\omega_0=5\pi^2\,(D/\rho hb^4)^{1/2}$

Effect of Volume and Number of Beams

Variations in frequency ω_R and logarithmic decrement δ with dimensionless total volume of beams $\bar{A}$, when the number of beams $n = 1-5$, are shown in Figs. 3, in which ω_R is nondimensionalized by ω_0, that is the frequency of the plate without beams. The frequency for $n=1$ increases with increasing $\bar{A}$ and approaches the limiting value, which has the mode shown in Fig. 3(*a*). The graph for $n=1$ and the graph for $n=2$ cross at about $\bar{A}=0.3$. Similarly, the frequency for $n=2$ approaches the limiting value and the graph crosses the value for $n=3$ at about $\bar{A}=1$. Above the $A>1$ value, the frequency for $n=3$ is largest. Namely, by increasing $\bar{A}$, the optimum number of beams that gives the highest frequency and the frequency for the optimum number of beams increase. On the other hand, logarithmic decrements for $n=1$, 2, 3, and 4 have optimum points in the $\bar{A} < 2$ range. The reasons why the logarithmic decrement has an optimum can be explained as follows. When the volume of the beams is small, the damping effect on a plate is greater than the rigidity effect. As $\bar{A}$ increases, the rigidity effect becomes large. For $\bar{A} \to \infty$, the displacement and the rotation for a plate at the location of the beam is zero, i.e., the damping effect of the viscoelastic beam has vanished. Consequently, the logarithmic decrement has an optimum decrement at a certain value of $\bar{A}$. By increasing $\bar{A}$, the optimum number of beams that gives the highest value of δ and the logarithmic decrement for the optimum number of beams increase.

Effect of Young's Modulus for Beams. Figure 3(*b*), for $n=1$, shows that the logarithmic decrement has a maximum at about $\bar{A}=0.1$. Under this condition, varying the Young's modulus of the beams results in data shown in Fig. 4. Figure 4 shows that frequency increases with increasing $\bar{E}_b$, but the logarithmic decrement first increases and then decreases with increasing $\bar{E}_b$, i.e., an optimum point exists at a certain value of E_b. The reason for this is the same as the reason for the data in Fig. 3.

Loss Factor Effect. Figure 5 shows the results for varying loss factor η under the condition of $\bar{A}=0.1$ in Fig. 3. It can be seen, from Fig. 5, that the frequency is almost constant and the logarithmic decrement increases linearly with increasing η.

Conclusions

The problem of free vibration of a rectangular plate stiffened with viscoelastic beams has been studied analytically. The following conclusions have been reached.

(1) A convenient method for analyzing the vibration of a plate with viscoelastic beams has been developed.

(2) The effects of the volume and the number of beams on the frequency and the logarithmic decrement have been clarified. The results obtained show that the logarithmic decrement has an optimum at a certain volume of beams related to the number of beams.

(3) The effects of Young's modulus and the loss factor on the frequency and the logarithmic decrement have been roughly analyzed.

Acknowledgment

The author wishes to acknowledge the consistent guidance and encouragement of Professor Emeritus Hideo Saito of Tohoku University.

References

1 Lin, Y. K., "Free Vibration of Continuous Skin-Stringer Panels," ASME JOURNAL OF APPLIED MECHANICS, Vol. 27, 1960, pp. 669–676.

2 Duffield, R. C., and Willems, N., "Parametric Resonance of Stiffened Rectangular Plates," ASME JOURNAL OF APPLIED MECHANICS, Vol. 39, 1972, pp. 217–226.

3 Saito, H., and Suzuki, Y., "Vibration of Plate Stiffened With Viscoelastic Material," *Transactions of the Japan Society of Mechanical Engineers* (in Japanese), Vol. 43, 1977, pp. 114–119.

4 Timoshenko, S. P., and Goodier, J. N., *Theory of Elasticity*, McGraw-Hill, New York, 1970, pp. 309–313.

Downloaded 02 May 2010 to 171.66.16.54. Redistribution subject to ASME license or copyright; see http://www.asme.org/terms/Terms_Use.cfm

APPENDIX

Expressions of e

The elements of **e** are as follows.

$$e_{kn}^{(1,1)} = \begin{cases} 0 & k<n \\ -1 & k=n \\ P_n F_0(\bar{c}_k - \bar{c}_n) & k>n \end{cases}$$

$$e_{kn}^{(1,2)} = \begin{cases} 0 & k \leqq n \\ -R_n F_1(\bar{c}_k - \bar{c}_n) & k>n \end{cases}$$

$$e_{k1}^{(1,3)} = -\beta_2 F_0(\bar{c}_k) + F_2(\bar{c}_k)$$

$$e_{k2}^{(1,3)} = F_0(\bar{c}_k)$$

$$e_{kn}^{(2,1)} = \begin{cases} 0 & k \leqq n \\ P_n F_1(\bar{c}_k - \bar{c}_n) & k>n \end{cases}$$

$$e_{kn}^{(2,2)} = \begin{cases} 0 & k<n \\ -1 & k=n \\ -R_n F_2(\bar{c}_k - \bar{c}_n) & k>n \end{cases}$$

$$e_{k1}^{(2,3)} = -\beta_2 F_1(\bar{c}_k) + F_3(\bar{c}_k)$$

$$e_{k2}^{(2,3)} = F_1(\bar{c}_k)$$

$$e_{1n}^{(3,1)} = P_n F_0(1-\bar{c}_n)$$

$$e_{2n}^{(3,1)} = P_n F_2(1-\bar{c}_n)$$

$$e_{1n}^{(3,2)} = -R_n F_1(1-\bar{c}_n)$$

$$e_{2n}^{(3,2)} = -R_n F_3(1-\bar{c}_n)$$

$$e_{11}^{(3,3)} = -\beta_2 F_0(1) + F_2(1)$$

$$e_{12}^{(3,3)} = F_0(1)$$

$$e_{21}^{(3,3)} = -\beta_2 F_2(1) + F_4(1)$$

$$e_{22}^{(3,3)} = F_2(1)$$

$$k,n = 1, 2, \ldots, L$$

Downloaded 02 May 2010 to 171.66.16.54. Redistribution subject to ASME license or copyright; see http://www.asme.org/terms/Terms_Use.cfm

Buckling of Truncated Conical Shells Under Combined Axial Load, Pressure, and Heating

J. Tani
Professor,
Institute of High Speed Mechanics,
Tohoku University,
Sendai, Japan
Mem. ASME

On the basis of the Donnell-type shell equations with the effect of nonlinear prebuckling deformations taken into consideration, a theoretical analysis is performed on the buckling of clamped truncated conical shells under two loads combined out of uniform pressure, axial load, and uniform heating. The problem is solved by a finite difference method. It is found that the interaction curves of buckling loads are changed remarkably by the difference in the shape of conical shells. This is due to the large nonlinear prebuckling deformation and the difference in the buckling mode between two cases of single load.

Introduction

During the last two decades, a number of papers have been written on the buckling problem of conical shells under various types of loads. Without attempting to be exhaustive, we cite here only some articles that are most pertinent to this paper. The buckling of isotropic conical shells under single load, i.e., external pressure [1, 2], axial compression [3, 4], and uniform heating [5], has been studied theoretically for a wide range of the shell geometry with the effect of nonlinear prebuckling deflections taken into consideration. However, to the best of our knowledge, the effect of nonlinear prebuckling deflections on the buckling of conical shells under combined loading has not been examined theoretically yet, except for the conical shells under combined axial compression and internal pressure [3, 6].

In this paper, theoretical analyses are presented for the elastic buckling of clamped, truncated, thin conical shells under two loads combined out of uniform pressure, axial load, and uniform heating, with the effect of nonlinear prebuckling deflections taken into consideration. The material properties of the conical shell are assumed to be independent of temperature. Solutions are determined from the Donnell-type basic equations by means of a finite difference method. It is clarified that the interaction effects of two loads on the stability is of great importance for the shallow conical shell.

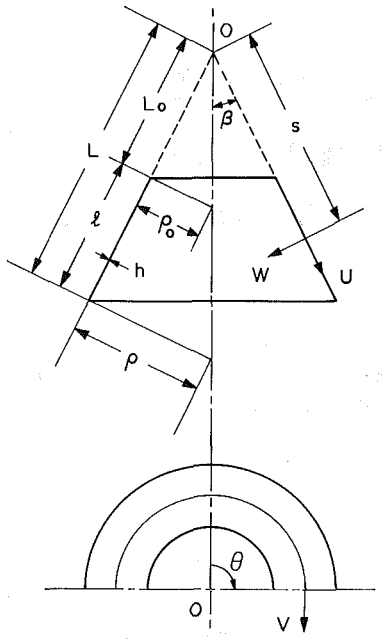


Fig. 1 Geometry of a conical shell and coordinate system

Mathematical Formulation

The configuration of conical shells and the coordinate system are taken as shown in Fig. 1. The truncated, thin, isotropic conical shell is considered to be subjected to two loads combined out of uniform pressure p, axial load P, and uniform heating. Assume that its temperature rise T above the unstrained state is constant throughout the wall and that its material properties, i.e., Young's modulus E, Poisson's ratio ν, and thermal expansion coefficient α are independent of temperature. Furthermore, the truncated conical shell is assumed to be perfectly clamped to the rigid end plates. The rigid plate at $x=1$ is immovable, while the one at $x=\gamma$ can only move in the axial direction. The displacement components along the middle surface are denoted by U, V, and W. Denoting by F the stress function for stress resultants N_s, N_θ and $N_{s\theta}$, the Donnell-type shell equations governing the finite deformation of the conical shell are given in nondimensional form as follows:

Contributed by the Applied Mechanics Division for publication in the JOURNAL OF APPLIED MECHANICS.
Discussion on this paper should be addressed to the Editorial Department, ASME, United Engineering Center, 345 East 47th Street, New York, N.Y. 10017, and will be accepted until two months after final publication of the paper itself in the JOURNAL OF APPLIED MECHANICS. Manuscript received by ASME Applied Mechanics Division, April, 1983; final revision, September, 1984.

Copyright © 1985 by ASME
Downloaded 02 May 2010 to 171.66.16.54. Redistribution subject to ASME license or copyright; see http://www.asme.org/terms/Terms_Use.cfm

$$\nabla^4 f = -\frac{12}{x}\left(Z + w_{,x} + \frac{1}{x}w_{,\phi\phi}\right)w_{,xx} + \frac{12}{x^2}\left(w_{,x\phi} - \frac{1}{x}w_{,\phi}\right)^2 \tag{1}$$

$$\nabla^4 w = \frac{1}{x}\left(f_{,x} + \frac{1}{x}f_{,\phi\phi}\right)w_{,xx} + \frac{1}{x}f_{,xx}\left(Z + w_{,x} + \frac{1}{x}w_{,\phi\phi}\right) - 2\left(\frac{1}{x}f\right)_{,x\phi}\left(\frac{1}{x}w\right)_{,x\phi} + Zk_p \tag{2}$$

$$w = w_{,x} = u = v = 0 \qquad \text{at} \quad x = 1 \tag{3}$$

$$\left.\begin{aligned} &w - u = 0,\ (w + u\cot^2\beta)_{,\phi} = 0 \\ &v = w_{,x} = 0 \\ &\int_0^{2\pi}\left\{x\left[\frac{1}{x}(xw_{,x})_{,x}\right]_{,x} + \frac{2-\nu}{x}w_{,x\phi\phi} - \frac{3-\nu}{x^2}w_{,\phi\phi} + \left(\frac{1}{x}f_{,\phi}\right)_{,x}w_{,\phi} - \left(f_{,x} + \frac{1}{x}f_{,\phi\phi}\right)(Z + w_{,x})\right\}d\theta \\ &= \pi\gamma^2 Zk_p + 2\pi Zk_a \end{aligned}\right\} \quad \text{at } x = \gamma \tag{4}$$

$$\left.\begin{aligned} &u_{,x} + \frac{1}{2Z}(w_{,x})^2 = \frac{1}{12Z}\left(\frac{1}{x}f_{,x} + \frac{1}{x^2}f_{,\phi\phi} - \nu f_{,xx} + k_t\right) \\ &v_{,\phi} + u - w + \frac{1}{2xZ}(w_{,\phi})^2 = \frac{x}{12Z}\left[f_{,xx} - \nu\left(\frac{1}{x}f_{,x} + \frac{1}{x^2}f_{,\phi\phi}\right) + k_t\right] \\ &u_{,\phi} + xv_{,x} - v + \frac{1}{Z}w_{,x}w_{,\phi} = -\frac{1+\nu}{6Z}\left(f_{,x} - \frac{1}{x}f\right)_{,\phi} \end{aligned}\right\} \tag{5}$$

where subscripts following a comma stand for partial differentiation, while

$$\phi = \theta\sin\beta, \quad \nabla^2 = \frac{\partial^2}{\partial x^2} + \frac{1}{x}\frac{\partial}{\partial x} + \frac{1}{x^2}\frac{\partial^2}{\partial\theta^2} \tag{6}$$

In these equations, the nondimensional quantities are related to the corresponding physical ones through the following relations

$$\left.\begin{aligned} &x = \frac{s}{L}, \quad (u,v) = \frac{\sqrt{1-\nu^2}}{h\cot\beta}(U,V), \quad w = \sqrt{1-\nu^2}\frac{W}{h} \\ &f = \frac{F}{D}, \quad \gamma = \frac{L_0}{L}, \quad Z = \frac{\sqrt{1-\nu^2}L}{h\tan\beta}, \quad k_p = \frac{pL^3\tan\beta}{D} \\ &k_t = 12\alpha T(1-\nu^2)\left(\frac{L}{h}\right)^2, \quad k_a = \frac{PL}{\pi D\sin 2\beta} \end{aligned}\right\} \tag{7}$$

in which γ, Z, and $D = Eh^3/12(1-\nu^2)$ are a truncation ratio, a shape factor, and the flexural rigidity of the conical shell, respectively, while k_p, k_t, and k_a are pressure, temperature, and axial load factors, respectively.

As only axisymmetric loads are considered in the analysis, the prebuckling deformation will be independent of the circumferential coordinate. When the deformation is axisymmetric, equations (1)–(5) reduce to the following form:

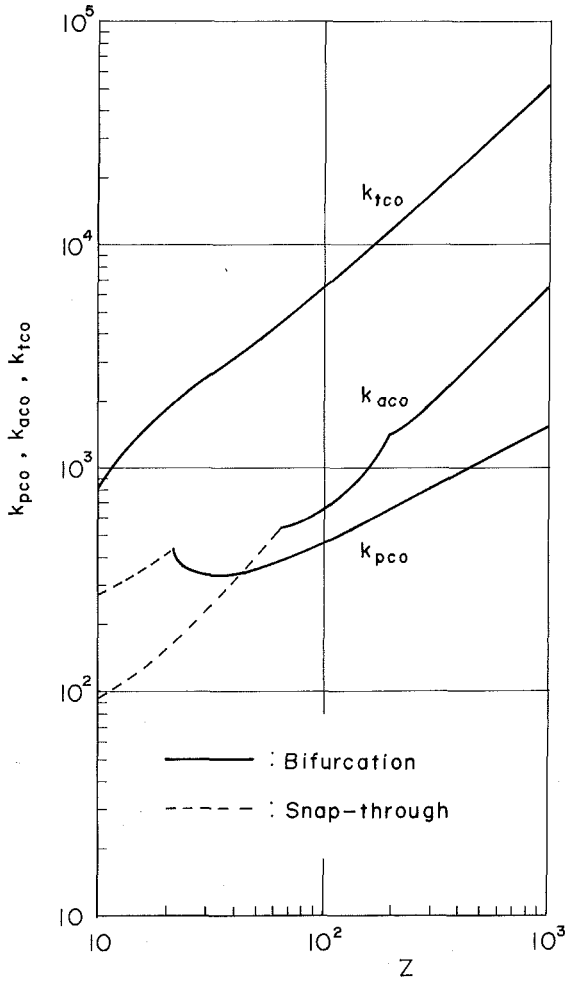


Fig. 2 Relations between buckling load coefficients k_{aco}, k_{pco}, k_{tco}, and shape factor Z: truncation ratio $\gamma = 0.5$

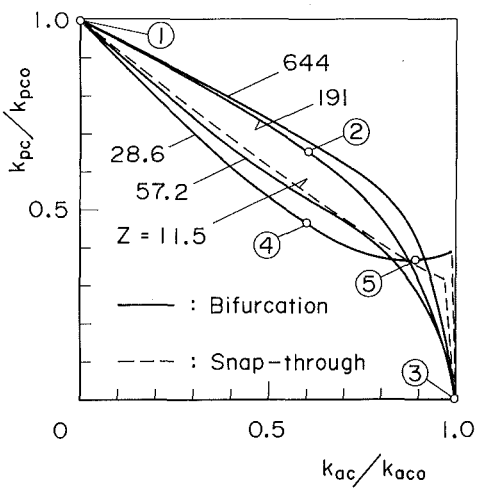


Fig. 3 Interaction curves for cones under combined uniform pressure and axial compression: $\gamma = 0.5$

Downloaded 02 May 2010 to 171.66.16.54. Redistribution subject to ASME license or copyright; see http://www.asme.org/terms/Terms_Use.cfm

Table 1 Buckling loads and wave numbers N_{co} of single loading cases: $\gamma = 0.5$

$\frac{l}{h}$	$\frac{\rho_0+\rho}{2h}$	Z	k_{aco}		k_{pco}		k_{tco}	
100	2500	11.5	0.101×10^{3}	(0)[a]	0.291×10^{3}	(0)	0.0987×10^{4}	(12)
100	1000	28.6	0.218	(0)	0.339	(7)	0.254	(12)
100	500	57.2	0.465	(0)	0.368	(8)	0.412	(23)
100	150	191	0.641	(7)	0.641	(9)	1.15	(29)
300	400	644	4.12	(12)	1.22	(12)	3.48	(48)

[a]Numerals in brackets indicate the buckling wave number.

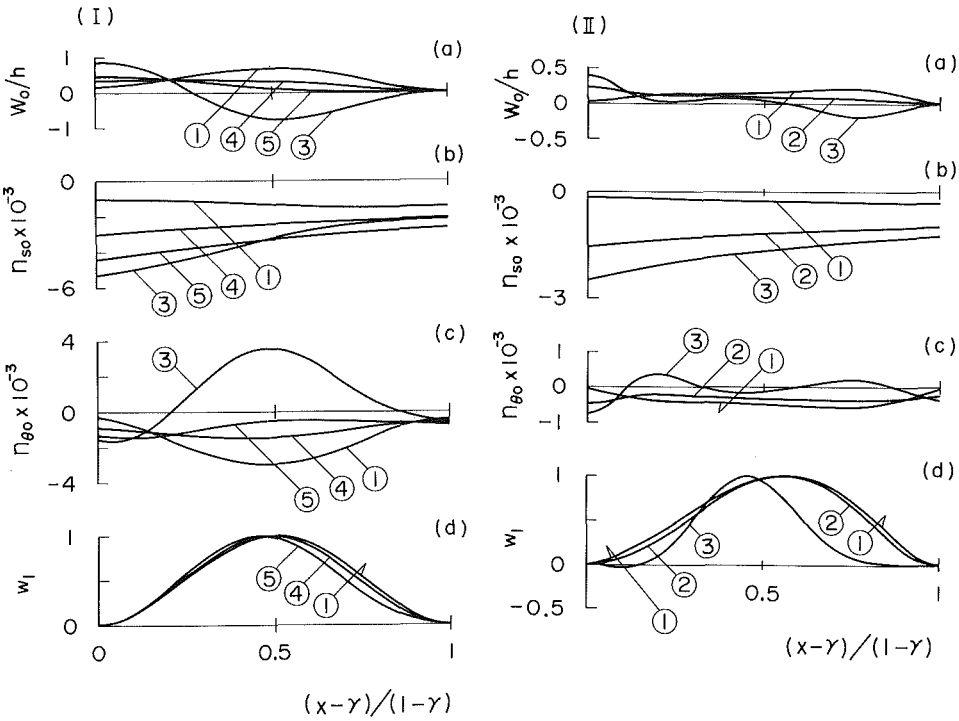


Fig. 4 (a) Prebuckling deflections, (b) and (c) prebuckling stress resultants, and (d) buckling deflections in the case (AP). (I) Z = 28.6, (II) Z = 191: γ = 0.5.

$$x\left[\frac{1}{x}(xg_0)_{,x}\right]_{,x} = -12\left(Z+\frac{1}{2}w_{0,x}\right)w_{0,x} \tag{8}$$

$$\frac{1}{x}\left\{x\left[\frac{1}{x}(xw_{0,x})_{,x}\right]_{,x}\right\}_{,x} = \frac{1}{x}[g_0(Z+w_{0,x})]_{,x} + Zk_p \tag{9}$$

$$xg_{0,x} - \nu g_0 + xk_t = 0, \quad w_0 = w_{0,x} = 0 \quad \text{at} \quad x = 1 \tag{10}$$

$$\left.\begin{aligned} &xg_{0,x} - \nu g_0 + xk_t = 0, \quad w_{0,x} = 0 \\ &x\left[\frac{1}{x}(xw_{0,x})_{,x}\right]_{,x} \\ &\quad = g_0(Z+w_{0,x}) + \frac{\gamma^2}{2}Zk_p + Zk_a \end{aligned}\right\} \text{at } x=\gamma \tag{11}$$

in which $g_0 = f_{0,x}$, and f_0 and w_0 refer to the axisymmetric behavior.

Immediately after bifurcation buckling, we may put

$$\left.\begin{aligned} &u = u_0(x) + u_1(x)\cos N\theta, \quad v = v_1(x)\sin N\theta \\ &w = w_0(x) + w_1(x)\cos N\theta, \quad f = f_0(x) + f_1(x)\cos N\theta \end{aligned}\right\} \tag{12}$$

where u_0 and N are the axisymmetric displacement and the number of circumferential waves, respectively, while u_1, v_1, w_1, and f_1 are infinitesimal incremental quantities.

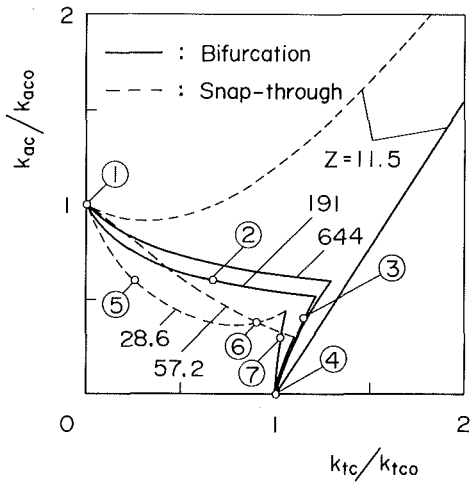


Fig. 5 Interaction curves for cones under combined axial load and uniform heating: γ = 0.5

The buckling equations are obtained by substituting equations (12) into equations (1)–(5), subtracting the prebuckling equations (8)–(11) from the resulting equations,

Downloaded 02 May 2010 to 171.66.16.54. Redistribution subject to ASME license or copyright; see http://www.asme.org/terms/Terms_Use.cfm

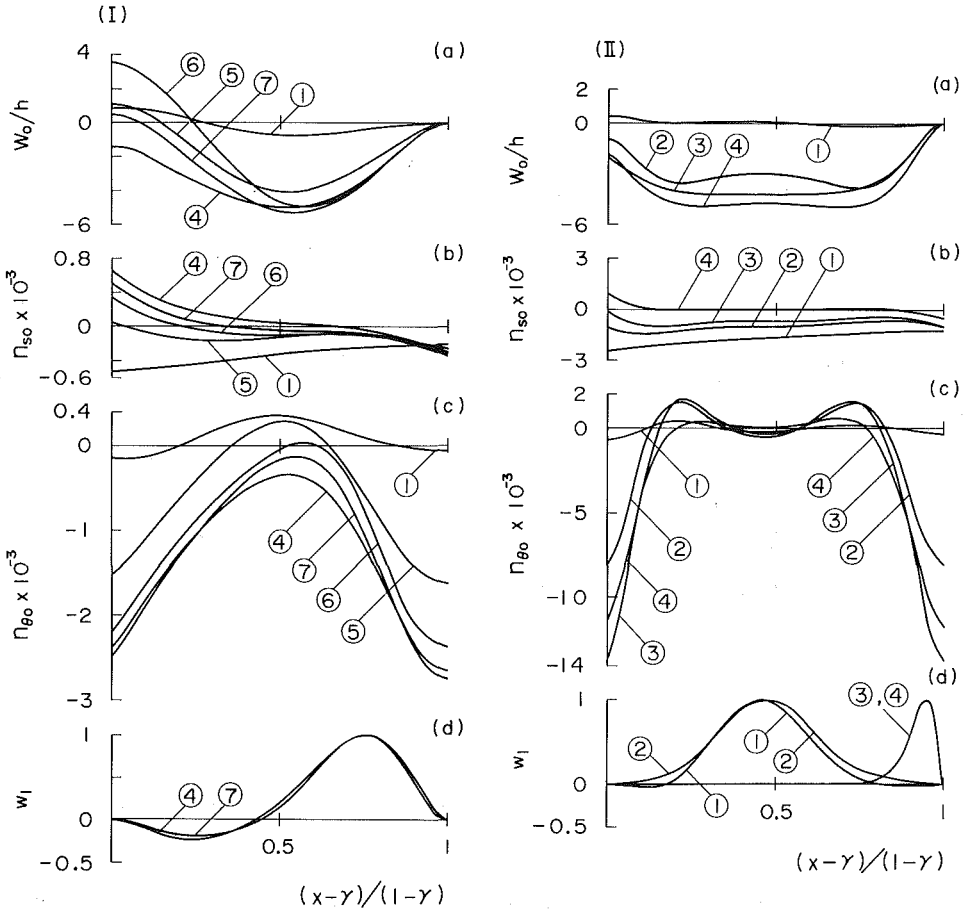


Fig. 6 (*a*) Prebuckling deflections, (*b*) and (*c*) prebuckling stress resultants, and (*d*) buckling deflections in the case (*AT*). (*I*) $Z = 28.6$, (*II*) $Z = 191$: $\gamma = 0.5$.

and linearizing with respect to the infinitesimal quantities. This leads to

$$\nabla_1^4 f_1 = -\frac{12}{x}\left[(Z+w_{0,x})w_{1,xx} + \left(w_{1,x}-\frac{n^2}{x}w_1\right)w_{0,xx}\right] \tag{13}$$

$$\nabla_1^4 w_1 = \frac{1}{x}\left[(Z+w_{0,x})f_{1,xx} + w_{0,xx}\left(f_{1,x}-\frac{n^2}{x}f_1\right) + w_{1,xx}g_0 + \left(w_{1,x}-\frac{n^2}{x}w_1\right)g_{0,x}\right] \tag{14}$$

$$\left.\begin{aligned} &w_1 = 0,\ w_{1,x} = 0, \\ &x^2 f_{1,xx} - \nu(x f_{1,x} - n^2 f_1) = 0 \\ &x^3 f_{1,xxx} - (1-\nu+2n^2+\nu n^2)x f_{1,x} \\ &\quad + 3n^2 f_1 = 0 \end{aligned}\right\} \quad \text{at } x=\gamma, 1 \tag{15}$$

where

$$n = \frac{N}{\sin\beta}, \quad \nabla_1^2 = \frac{d^2}{dx^2} + \frac{1}{x}\frac{d}{dx} - \frac{n^2}{x^2}$$

Numerical Procedures and Results

The details of the numerical procedures used in this study were described in reference [4] and will not be repeated here. The system of nonlinear differential equations (8)–(11) governing the axisymmetric prebuckling deformation is solved by Newton's method, in which the direct solution of the nonlinear system is replaced by the solution of a sequence of linear correctional equations. These equations and the eigenvalue problem posed by equations (13)–(15) are solved by means of the finite difference method and Potter's algorithm [7] with the modification suggested by Blum et al. [8]. Interactive calculations of Newton's method are done until the condition $|\delta y^{(m)}/y^{(m)}| \leq 10^{-4}$ is satisfied, where $\delta y^{(m)}$ and $y^{(m)}$ correspond to the values of correction term and solution of m iteration at each station, respectively. A mesh of 100 or 150 points on the interval of $(1-\gamma)$ is considered in the finite difference method.

When the values of ν, γ, β, and Z are given, the buckling determinant obtained from the aforementioned eigenvalue problem will be a function of k_a, k_p, k_t, and N. Hence, giving two values out of k_a, k_p, and k_t, and changing the value of N, we can determine the minimum value of one load factor not given in advance and corresponding value of N from the buckling determinant, which give the critical combination of loads (k_{ac}, k_{pc}, and k_{tc}) as well as the buckling wave number N_c. In the present study, putting one value out of k_a, k_p, and k_t equal to zero, we will determine the critical combination of two load factors.

Numerical calculations are carried out for the conical shells with the truncation ratio $\gamma = 0.5$ and various values of the shape factor Z. Poisson's ratio ν is assumed to be 0.3.

The Case of Single Load. The buckling load factors k_{aco}, k_{pco}, and k_{tco}, and the corresponding buckling wave number N_{co} of the conical shell under only one loading out of axial

Downloaded 02 May 2010 to 171.66.16.54. Redistribution subject to ASME license or copyright; see http://www.asme.org/terms/Terms_Use.cfm

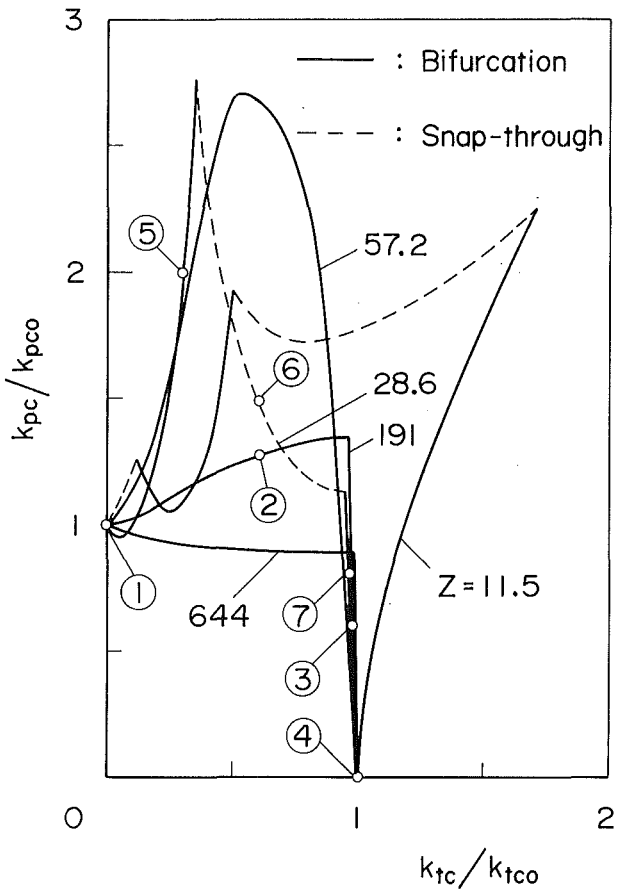


Fig. 7 Interaction curves for cones under combined uniform pressure and uniform heating: $\gamma = 0.5$

compression, external pressure, and uniform heating are determined for various values of Z. The variations of k_{aco}, k_{pco}, and k_{tco} with Z are shown in Fig. 2. This result is the same as those obtained previously by the author [2, 4, 5]. In this and following figures, solid and dashed lines correspond to the asymmetric buckling with bifurcation due to the existence of branching equilibrium states and the axisymmetric one with snap-through due to a limit point instability, respectively. The values of k_{aco}, k_{pco}, k_{tco}, and N_{co} in the typical cases are listed in Table 1. These cases will be used to examine the effect of combined loads. It is to be noted that the thermal buckling occurs with many circumferential waves.

The Case (*AP*) of Combined Axial Load and Uniform Pressure. Figure 3 presents interaction curves for various combinations of axial compression k_{ac} and uniform external pressure k_{pc}. From this figure it will be seen that for the shallow conical shell with $Z = 28.6$, the interaction curve of the combined critical loads shows a convex character as viewed from the origin and for the pressure ratio k_{pc}/k_{pco} ranging from 0.36 to 0.39, there exist three critical values of the axial compression k_{ac}. This is due to the nonlinear prebuckling deformation. Additional numerical results in which the aforementioned phenomenon appears more clearly are shown in the Appendix. Further, this phenomenon which was not found by Shiffner [3] and Esslinger, et al. [3] is the same as those obtained for circular cylindrical shells by Kodama, et al. [9] and Tennyson, et al. [10].

The axisymmetric prebuckling deflection W_0 and nondimensional stress resultants n_{so} $(=L^2N_{so}/D)$, $n_{\theta o}$ $(=L^2N_{\theta o}/D)$ as well as the buckling deflection W_1 at the points numbered in Fig. 3 are illustrated in Fig. 4. In these and following figures, 0 and 1 in the abscissae $(x-\gamma)/(1-\gamma)$ correspond to the small and large ends of the truncated conical shell, respectively. From the case (*I*) $Z = 28.6$ in Fig. 4, it can be seen that the prebuckling deflection and stress resultants of the bifurcation buckling differ very much from those of the snap-through one. From the case (*II*) $Z = 191$ in Fig. 4, it can be seen that the prebuckling deflection and stress resultants, and the buckling deflection change gradually with the variation of loading.

The Case (*AT*) of Combined Axial Load and Uniform Heating. Figure 5 presents interaction curves for various combinations of axial compression k_{ac} and uniform heating k_{tc}. The following observations can be made from this figure. The interaction curves of the combined critical loads in this case show a convex character as viewed from the origin, in general. The critical load (k_{ac} or k_{tc}) larger than those (k_{aco} or k_{tco}) in single loading cases can be realized by combining the axial compression and uniform heating. For the shallow conical shells with $Z = 11.5$ and 28.6, there exist three critical values of the axial compression k_{ac} in some ranges of k_{tc}. This is due to the large prebuckling deformation and the difference in the buckling mode between two cases of single loading as seen in the following figure.

The axisymmetric prebuckling states and the buckling deflection at the points numbered in Fig. 5 are illustrated in Fig. 6. It is at first to be noted in Fig. 6 that the conical shell under only uniform heating gives rise to the local buckling with many circumferential waves near the edge due to the large hoop compressive stress and that the cone under only axial compression gives rise to the axisymmetric snap-through or overall bifurcation buckling. It can be seen from Fig. 6 that the sudden fold of the interaction curves in Fig. 5 corresponds to the remarkable difference among the snap-through, overall bifurcation, and local bifurcation bucklings.

The Case (*PT*) of Combined Uniform Pressure and Heating. Figure 7 presents interaction curves for various combination of uniform external pressure k_{pc} and heating k_{tc}. From this figure it will be seen that for the shallow conical shell with $Z = 11.5$ and 28.6, and interaction curves of the combined critical loads show very complicate aspect and that the critical load (k_{pc} or k_{tc}) larger than those (k_{pco} or k_{tco}) in single loading cases can be realized for relatively shallow conical shells by combining the uniform external pressure and heating.

The axisymmetric prebuckling states and the buckling deflection at the points numbered in Fig. 7 are illustrated in Fig. 8. It can be seen from this figure that the sudden fold of the interaction curves in Fig. 7 corresponds to a remarkable difference in the buckling form, that is, the snap-through, overall bifurcation, and local bifurcation bucklings.

Conclusions

The buckling problem of truncated conical shells under two loads combined out of the axial load, uniform pressure, and heating is analyzed theoretically by the application of the finite difference method to the Donnell-type shell equations. The cone is considered to be perfectly clamped to the rigid end plates, but free from the restriction of the deformation in the axial direction. The following is concluded for the shallow conical shell.

1. The interaction curves of the critical loads combined the axial compression k_{ac} and uniform external pressure k_{pc} or uniform heating k_{tc} show a convex character as viewed from the origin and there exist three critical values of k_{ac} or k_{tc} in some ranges of k_{pc} or k_{pc} and k_{ac}, respectively.
2. The critical load (k_{ac}, k_{pc}, or k_{tc}) larger than those (k_{aco}, k_{pco}, or k_{tco}) in single loading cases can be realized by combining the uniform heating and external pressure or axial compression.
3. The aforementioned phenomenon is due to the

Downloaded 02 May 2010 to 171.66.16.54. Redistribution subject to ASME license or copyright; see http://www.asme.org/terms/Terms_Use.cfm

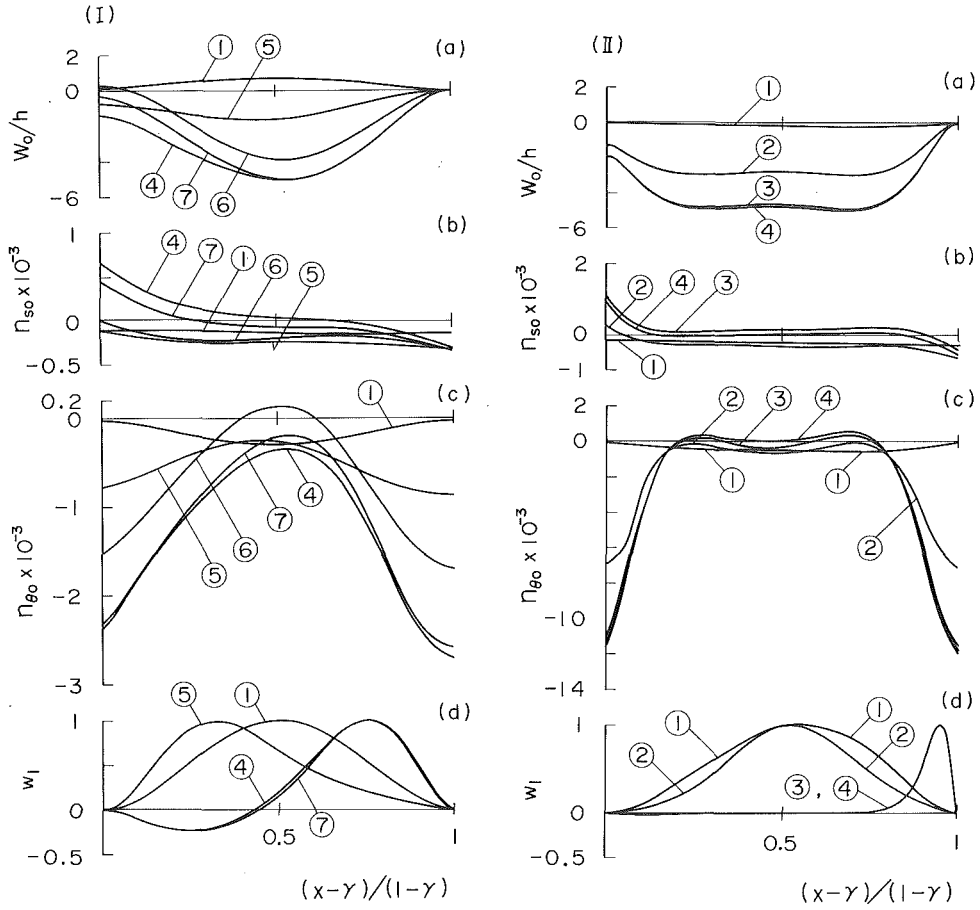


Fig. 8 (*a*) Prebuckling deflections, (*b*) and (*c*) prebuckling stress resultants, and (*d*) buckling deflections in the case (*PT*). (*I*) $Z = 28.6$, (*II*) $Z = 191$: $\gamma = 0.5$.

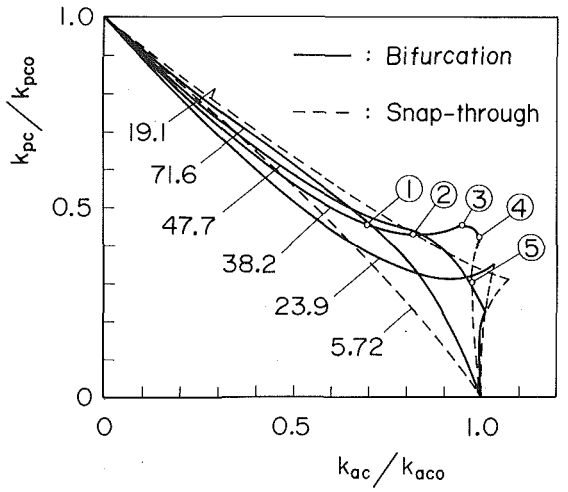


Fig. 9 Interaction curves for shallow cones under combined axial load and uniform pressure: $\gamma = 0.5$

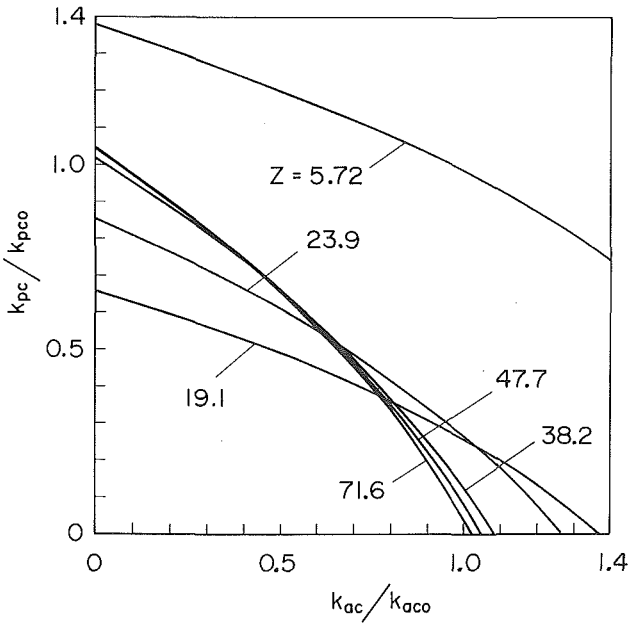


Fig. 10 Interaction curves for shallow cones by the membrane theory: $\gamma = 0.5$

nonlinear prebuckling deformation and the difference in the buckling mode between two cases of single loading.

References

1 Famili, J., "Asymmetric Buckling of Finitely Deformed Conical Shells," *AIAA Journal*, Vol. 3, 1965, pp. 1456–1461.

2 Tani, J., "Influence of Prebuckling Deformations on the Buckling of Truncated Conical Shells Under External Pressure," *Reports of the Institute of High Speed Mechanics*, Tohoku University, Japan, Vol. 28, 1973, pp. 149–164.

3 Schiffner, K., "Untersuckung des Stabilitätsverhaltens dünnwandiger Kegelschalen unter axialsymmetrischer Belastung mittels einer nichtlinearen Schalentheorie," *Sonderdruck aus dem Jahrbuch*, 1965 der WGLR, pp. 448–452.

4 Tani, J., "Influence of Prebuckling Deformations on the Buckling of Truncated Conical Shells Under Axial Compression," *Transactions of the Japan Society of Aeronautical and Space Science*, Vol. 16, 1973, pp. 232–245.

5 Tani, J., "Thermal Buckling of Truncated Conical Shells," *Reports of*

Downloaded 02 May 2010 to 171.66.16.54. Redistribution subject to ASME license or copyright; see http://www.asme.org/terms/Terms_Use.cfm

Table 2 Buckling loads and wave number N_{co} of shallow cones subjected to single load: $l/h = 100$, $\gamma = 0.5$

$\frac{\rho_0+\rho}{2h}$	Z	k_{aco}		k_{pco}	
5000	5.72	0.586×10^2	(0)[a]	0.219×10^3	(0)
1500	19.1	1.48	(0)	0.397	(0)
1200	23.9	1.84	(0)	0.363	(7)
750	38.2	3.04	(0)	0.337	(7)
600	47.7	3.78	(0)	0.351	(8)
400	71.6	5.60	(6)	0.403	(8)

[a]Numerals in brackets indicate N_{co}.

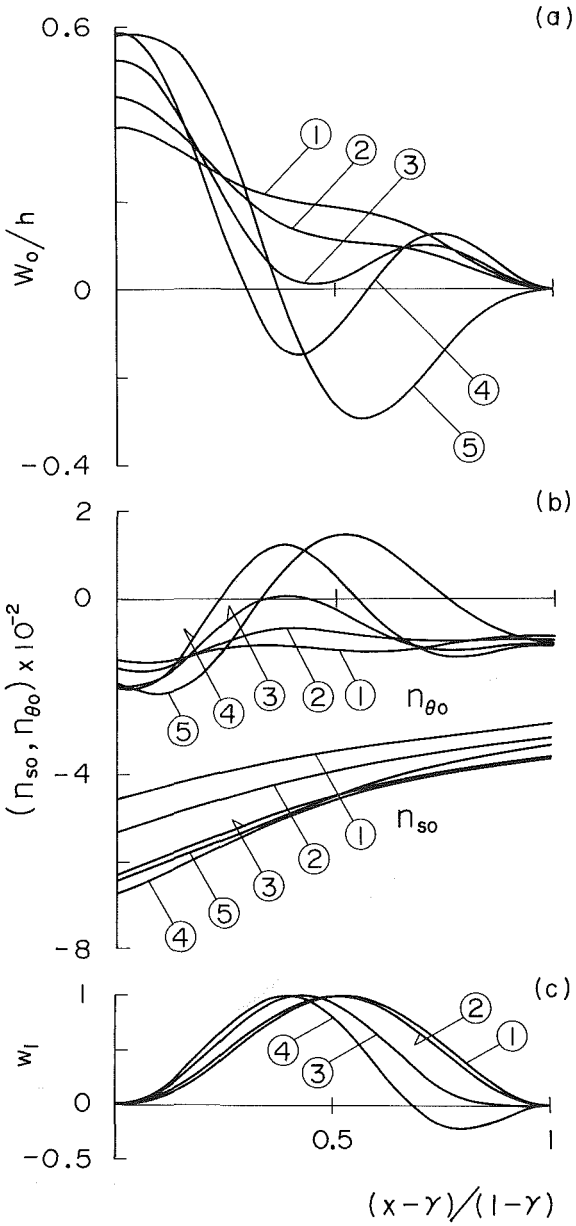


Fig. 11 (a) Prebuckling deflections, (b) prebuckling stress resultants, and (c) buckling deflections in the case (AP): $Z = 38.2$, $\gamma = 0.5$

the Institute of High Speed Mechanics, Tohoku University, Japan, Vol. 34, 1976, pp. 29-41.

6 Esslinger, M., and Cipriam, J., "Buckling of Thin Conical Shells Under Axial Loads With and Without Internal Pressure," *Buckling of Shells, Proceedings of a State-of-the-Art Colloquium*, Universitat Stuttgart, Germany, 1982, pp. 3.1-3.18.

7 Potters, M. L., "A Matrix Method for the Solution of a Second-Order Difference Equation in Two Variables," Report MR 19 Mathematich Centrum, Amsterdam, The Netherlands, 1955.

8 Blum, R. E., and Fulton, R. E., "A Modification of Potter's Method for Solving Eigenvalue Problems Involving Tridiagonal Matrices," *AIAA Journal*, Vol. 4, 1966, pp. 2231-2232.

9 Kodama, S., and Yamaki, N., "Buckling of Circular Cylindrical Shells Under Combined Pressure and Axial Loadings," *Transactions of the Japan Society of Mechanical Engineers* (in Japanese), Vol. 49, 1983, pp. 366-376.

10 Tennyson, R. C., Booton, M., and Chan, K. H., "Buckling of Short Cylinder under Combined Loading," ASME JOURNAL OF APPLIED MECHANICS, Vol. 45, 1978, pp. 574-578.

11 Plaut, R. H., "Stability of Shallow Arches Under Multiple Loads," *Journal of the Engineering Mechanics Division, ASCE*, Vol. 104, 1978, pp. 1015-1026.

12 Thompson, J. M. T., "On the Convection of a Cusp in Elastic Stability," *Journal of Mechanical Physics and Solids*, Vol. 31, 1983, pp. 205-222.

APPENDIX

To clarify thoroughly the effect of loading order in the case of combined axial load and uniform pressure, the detailed numerical results are shown for the range of the small values of Z with the buckling load factors k_{aco}, k_{pco}, and the corresponding buckling wave number N_{co} for the single load as indicated in Table 2. It is to be noted that there is noteworthy difference in the buckling forms of the axial compression and uniform external pressure; that is, the snap-through and bifurcation bucklings, except for the cases with $Z = 5.72$, 19.1, and 71.6.

Figures 9 and 10 show the interaction curves obtained by using the nonlinear bending theory and the membrane theory for the prebuckling state, respectively. In these figures, k_{aco} and k_{pco} have the values listed in Table 2 and obtained with the effect of the nonlinear prebuckling deflection taken into consideration. It can be seen from the comparison between these figures that the nonlinear prebuckling deflection is very much important for the shallow conical shells. The following observations also can be made from Fig. 9. There exist three states at one buckling pressure k_{pc} in the cases with $Z = 23.9$ or 38.2, respectively.

The axisymmetric prebuckling deflection W_0 and non-dimensional stress resultants n_{so}, $n_{\theta o}$ as well as the buckling deflection W_1 at the points numbered in Fig. 9 are illustrated in Fig. 11. It can be seen from this figure that the prebuckling deflection and stress resultants of the point (5) are very different from the others. It is to be noted that in this point the snap-through buckling occurs.

The complicated interaction curves like those obtained in the present study emerged also from the stability problem of shallow arches under multiple load [11, 12].

Downloaded 02 May 2010 to 171.66.16.54. Redistribution subject to ASME license or copyright; see http://www.asme.org/terms/Terms_Use.cfm

Pretwist and Shear Flexibility in the Vibrations of Turbine Blades

S. Krenk

O. Gunneskov

Risø National Laboratory,
Roskilde, Denmark DK-4000

A theory is developed for pretwisted beams with finite shear flexibility. The effect of pretwist is accounted for via the axial derivative of the St. Venant warping function. The shear flexibility relies on a decomposition of the shear stresses into torsion and shear contributions, and the normalized strain energy of the latter is expressed in terms of the shear flexibility tensor. An explicit approximation for the shear flexibility tensor is derived for cross sections of moderate wall thickness. A special Legendre transformation is used to obtain a consistent discretization, which is then cast in the form of a finite beam element. The accuracy of the method is illustrated by comparison with experimental results for a steam turbine blade, and the effects of pretwist and shear flexibility are discussed.

1 Introduction

Vibrations of turbine blades can often be modeled adquately by an appropriate beam theory, provided this beam theory includes provisions for special features such as blade pretwist, shear deformations, and forces induced by the displacements. This paper develops a theory for elastic beams that accounts for blade pretwist and shear deformations in considerable detail. Extensions necessary for the inclusion of induced loads are briefly indicated, while the full details are given in a subsequent paper.

Traditionally beam theories are developed by assuming that the distribution of the displacements or stresses over the cross sections are adequately described by a small number of shape functions, whereby the problem is reduced to a system of ordinary differential equations in the axial coordinate. Thus it is necessary to *assume* a suitable number of shape functions. In the absence of pretwist, i.e., for cylindrical beams, it is well established that a minimal set of shape functions for the axial deformations contains any linear function plus a warping function. The warping function is usually found from consideration of uniform torsion.

The presence of pretwist raises the question about the proper choice of warping function and the necessity of additional shape functions. These questions have been at least partially answered in recent works by Shield [1] and Krenk [2], who performed an asymptotic analysis of uniform torsion and extension of a beam with constant cross section and constant, small, rate of pretwist. Their results show that the leading coupling term consists of two parts: one due to axial strains created by mismatch of neighboring warped cross sections that are rotated by pretwist, and another term created by *local* rotations in the cross section, when the elastic center is not on the axis of pretwist. The latter term contains Poisson's ratio as a factor and can not be accomodated in beam theories where the transverse deformations are neglected. As a consequence, the St. Venant warping function for a similar beam without pretwist should be retained, and the axial strain created by mismatch should be included.

The effect of warping mismatch has already been included in special problems by Rosen [3] and Hodges [4], and a linear theory for general nonsymmetric pretwisted beams was developed by Krenk [5]. However none of these contributions include the effect of shear deformation, an effect that is important for higher vibration modes of turbine blades. An accurate evaluation of the shear flexibility requires additional shape functions for the shear stress distribution, and a clear distinction between the states of torsion and shear is achieved by orthogonality in elastic energy.

The two main objectives of the present paper are to introduce shear flexibility into a theory for pretwisted beams in a sufficiently general form to treat nonhomogeneous and nonsymmetric cross sections, and to recast the differential equations of this theory into discretized form, suitable for numerical calculations.

The first objective is accomplished by extending the family of orthogonal shape functions to include the shear stress distribution for an equivalent cantilever without pretwist. The result is a two-dimensional shear flexibility tensor associated with each cross section, the evaluation of which is closely related to the evaluation of the warping function.

The discretization also benefits from the shear flexibility, because it replaces the classical fourth-order differential equations for bending with second-order differential equations. However, if the generalized displacements are represented locally by polynomials, not all of the stress contributions in the equilibrium equations can have the same degree. This problem is overcome by use of a special Legendre transformation that introduces two new independent functions. Discretized representations are then introduced into the modified potential energy functional, and variations produce a system of linear equations. The equations associated with

Contributed by the Applied Mechanics Division for publication in the JOURNAL OF APPLIED MECHANICS.

Discussion on this paper should be addressed to the Editorial Department, ASME, United Engineering Center, 345 East 47th Street, New York, N.Y. 10017, and will be accepted until two months after final publications of the paper itself in the JOURNAL OF APPLIED MECHANICS. Manuscript received by ASME Applied Mechanics Division, June, 1984; Final revision, September, 1984.

Copyright © 1985 by ASME
Downloaded 02 May 2010 to 171.66.16.54. Redistribution subject to ASME license or copyright; see http://www.asme.org/terms/Terms_Use.cfm

the variations of the new independent variables are used to eliminate them locally, and thus the end result is simply a slightly modified stiffness matrix of a size determined by the original displacement formulation.

The accuracy of this method is illustrated by a vibration analysis of a steam turbine blade, and some typical features of pretwist and shear flexibility are discussed.

2 Beam Theory With Pretwist and Shear Flexibility

Let a beam be described in a cartesian $\{x_\alpha,z\}$ coordinate system with the z-axis as the axis of pretwist and $\alpha=1,2$. The use of two-dimensional tensor notation in the transverse planes leads to numerous simplifications in the following. The cross sections are assumed to remain undeformed in their own plane leading to transverse displacements in the form

$$u_\alpha(x_\nu,z)=\xi_\alpha(z)-e_{\alpha\beta}x_\beta\phi(z) \tag{2.1}$$

where $e_{\alpha\beta}$ is the permutation symbol. The axial displacement is assumed to be a linear function of x_ν plus a contribution from warping.

$$w(x_\nu,z)=\zeta(z)-x_\alpha\eta_\alpha(z)-\omega(x_\nu,z)\theta(z) \tag{2.2}$$

Note that the warping intensity $\theta(z)$ is not linked to the angle of twist $\phi(z)$ a priori. $\omega(x_\nu,z)$ is the St. Venant warping function of the cross section at z. In the presence of a counterclockwise rate of pretwist β the change of $\omega(x_\nu,z)$ with z is determined by the partial derivative [2]

$$\frac{\partial\omega}{\partial z}=-\beta x_\alpha e_{\alpha\beta}\omega_{,\beta}=\beta\,\psi(x_\nu,z) \tag{2.3}$$

The function $\psi(x_\nu,z)$ is introduced to display the dependence on β explicitly.

The material is assumed to be elastic with an axial modulus of elasticity E and shear modulus G. In the absence of transverse deformations the strain energy associated with a cross section is

$$U_i=\int_A \tfrac{1}{2}(E\epsilon^2+G\gamma_\alpha\gamma_\alpha)dA \tag{2.4}$$

where ϵ is the axial strain and γ_α is the shear strain vector.

The axial strain ϵ follows from (2.2) and (2.3), and within infinitesimal strain theory

$$\epsilon(x_\nu,z)=\zeta'(z)-x_\alpha\eta'_\alpha(z)-\omega(x_\nu,z)\theta'(z)-\beta\,\psi(x_\nu,z)\theta(z) \tag{2.5}$$

Before proceeding, it is important to define the shape function $\omega(x_\nu,z)$ precisely. The St. Venant problem of uniform torsion of a cylindrical beam defines a unique strain distribution $\tilde\gamma_\alpha(x_\nu)$ over the cross section. To obtain the associated axial displacement it is necessary to *assume* an axis of rotation, say $x_\alpha=a_\alpha$. In the present notation

$$\tilde\gamma_\alpha=-\omega_{,\alpha}-e_{\alpha\beta}(x_\beta-a_\beta) \tag{2.6}$$

and it is seen that a unique determination of $\omega(x_\nu)$ requires specification of a_α and an additive constant. Usually these constants are determined by the condition that $\omega(x_\nu)$ is orthogonal to the linear terms in (2.5) in energy sense, i.e., by the conditions

$$\int_A E\omega dA=0 \qquad \int_A Ex_\alpha\omega dA=0 \tag{2.7}$$

These conditions define the point a_α as a characteristic of the cross section [6, 7].

In the following, a_α will be called the shear center of the cross section. The reason for this terminology is that the shear stress distribution $G\tilde\gamma_\alpha$ from torsion must be supplemented with shear stress distributions $\bar\tau_\alpha$ corresponding to a resulting shear force, and their contributions to the strain energy become additive when the shear resultant acts through the point a_α. Indeed, the coupling term may be rewritten by use of (2.6) an the divergence theorem.

$$\int_A\tilde\gamma_\alpha\bar\tau_\alpha dA=-\int_A\omega\bar\tau_{\alpha,\alpha}dA+\int_A(x_\alpha-a_\alpha)e_{\alpha\beta}\bar\tau_\beta dA \tag{2.8}$$

When the problem of a cylindrical cantilever with transverse end load is used to determine the shear stress distribution, $\bar\tau_{\alpha,\alpha}/E$ is a linear function [8], and the first integral in the right side of (2.8) vanishes. Thus the coupling term is equal to the moment of the shear resultant around a_α, and vanishes for application at the shear center a_α. The characteristic point a_α may be determined either from the conditions (2.7) on the warping function ω, weighted with E, or from the conditon (2.8) concerning orthogonality of shear strains from torsion and shear, weighted with G. For homogeneous cross sections $\tilde\gamma_\alpha$, and thereby a_α, is independent of Poisson's ratio.

The present definition of the shear center relies entirely on orthogonality properties in the strain energy integral and is a restatement of the "least energy" definition of Trefftz [9]. It should not be confused with a widely used definition of the shear center as the point of application of a transverse force leading to vanishing *average* rotation. That center depends on Poisson's ratio in a manner the details of which have been presented by Koiter [10]. Indeed, in an energy-based approximate beam theory no suitable measure for average rotation seems to exist. Neither of these two common definitions of the shear center is directly related to the problem of a cantilever with constrained warping, as both rely on the *homogeneous* stress states of the two St. Venant problems.

The shear strain following from the displacement field (2.1) and (2.2) is

$$\begin{aligned}\gamma_\alpha(x_\nu,z) &= \tilde\gamma_\alpha(x_\nu)\theta(z)-e_{\alpha\beta}(x_\beta-a_\beta)(\phi'(z)-\theta(z))\\ &\quad+(\xi'_\alpha(z)-e_{\alpha\beta}a_\beta\phi'(z)-\eta_\alpha(z))\end{aligned} \tag{2.9}$$

where $\tilde\gamma_\alpha$ is the St. Venant solution (2.6). Each of the three terms on the right side is associated with a characteristic type of loading. The first term represents the St. Venant solution of a homogeneous torsion problem, the second term is a contribution from nonhomogeneous torsion, while the third term corresponds to a transverse force on the cross section. While the first term represents an exact solution to a problem of three-dimensional elasticity, the two last terms are approximations. The modification from nonhomogeneous torsion is accepted as part of the general torsion problem, while an improved representation of the contribution from the transverse force is desirable.

Notwithstanding the unsatisfactory distribution of the last term over the cross section, this part of the shear strain must be proportional to the shear force Q_β, thus implying a relation of the form

$$\xi'_\alpha-e_{\alpha\beta}a_\beta\phi'-\eta_\alpha=D_{\alpha\beta}Q_\beta/A \tag{2.10}$$

The shear flexibility tensor $D_{\alpha\beta}$ represents a measure of the shear flexibility $1/G$ incorporating the actual shear stress distribution over the cross section. Its determination is discussed briefly in the next section.

The strain energy is now found as the sum of three contributions: one from the axial strain ϵ in (2.5), one from the shear strain of general torsion represented by the first two terms of (2.9), and finally a contribution from the shear force determined directly from (2.10). In total

$$\begin{aligned}U_i &= \int_A \tfrac{1}{2}E(\zeta'-x_\alpha\eta'_\alpha-\omega\theta'-\beta\,\psi\theta)^2\\ &\quad+\tfrac{1}{2}G\,|\tilde\gamma_\alpha\theta-e_{\alpha\beta}(x_\beta-a_\beta)(\phi'-\theta)|^2dA+\tfrac{1}{2}A(\xi'_\alpha\\ &\quad-e_{\alpha\gamma}a_\gamma\phi'-\eta_\alpha)D^{-1}_{\alpha\beta}(\xi'_\beta-e_{\beta\delta}a_\delta\phi'-\eta_\beta)\end{aligned} \tag{2.11}$$

Upon carrying out the area integration the strain energy is expressed in terms of the cross section parameters of Table 1.

$$\begin{aligned}U_i &= \tfrac{1}{2}\{F(\zeta')^2+I_{\alpha\beta}\eta'_\alpha\eta'_\beta+I_{\omega\omega}(\theta')^2+\beta^2I_{\psi\psi}\theta^2\\ &\quad-2S_\alpha\zeta'\eta'_\alpha-2\beta S_\psi\zeta'\theta+2\beta I_{\alpha\psi}\eta'_\alpha\theta+2\beta I_{\omega\psi}\theta'\theta\end{aligned}$$

Downloaded 02 May 2010 to 171.66.16.54. Redistribution subject to ASME license or copyright; see http://www.asme.org/terms/Terms_Use.cfm

Table 1 Section parameters

$F = \int_A E\,dA$	$S_\alpha = \int_A x_\alpha E\,dA$	$I_{\alpha\beta} = \int_A x_\alpha x_\beta E\,dA$
$I_{\omega\omega} = \int_A \omega^2 E\,dA$	$S_\psi = \int_A \psi E\,dA$	$I_{\alpha\psi} = \int_A x_\alpha \psi E\,dA$
$I_{\omega\psi} = \int_A \omega\psi E\,dA$		$I_{\psi\psi} = \int_A \psi^2 E\,dA$
$I_R^2 = \int_A (x_\alpha - a_\alpha)(x_\alpha - a_\alpha) G\,dA$		$K = \int_A \tilde{\gamma}_\alpha \tilde{\gamma}_\alpha G\,dA$

Table 2 Generalized loads

$p_\alpha = \int_A q_\alpha\,dA$	$p = \int_A q\,dA$
$m_\alpha = -\int_A x_\alpha q\,dA$	$m = \int_A x_\alpha e_{\alpha\beta} q_\beta dA$
$b = -\int_A \omega q\,dA$	

Table 3 Generalized forces

$$N = \int_A \epsilon E\,dA = F\zeta' - S_\beta \eta_\beta' - \beta S_\psi \theta$$

$$M_\alpha = -\int_A x_\alpha \epsilon E\,dA = -S_\alpha \zeta' + I_{\alpha\beta}\eta_\beta' + \beta I_{\alpha\psi}\theta$$

$$B = -\int_A \omega\epsilon E\,dA = I_{\omega\omega}\theta' + \beta I_{\omega\psi}\theta$$

$$M_\theta = \int_A \frac{\partial}{\partial z}(\omega\epsilon E)\,dA = -\beta(-S_\psi\zeta' + I_{\beta\psi}\eta_\beta' + I_{\omega\psi}\theta' + \beta I_{\psi\psi}\theta) + (I_R^2 - K)(\phi' - \theta)$$

$$M = \int_A x_\alpha e_{\alpha\beta}\tau_\beta\,dA = K\phi' + (I_R^2 - K)(\phi' - \theta) + a_\alpha e_{\alpha\beta} Q_\beta$$

$$Q_\alpha = \int_A \tau_\alpha\,dA = A\,D_{\alpha\beta}^{-1}(\xi_\beta' - e_{\beta\gamma}a_\gamma\phi' - \eta_\beta)$$

$$+ (I_R^2 - K)(\phi' - \theta)^2 + K(\phi')^2 + A(\xi_\alpha' - e_{\alpha\gamma}a_\gamma\phi' - \eta_\alpha)D_{\alpha\beta}^{-1}(\xi_\beta' - e_{\beta\delta}a_\delta\phi' - \eta_\beta)\} \quad (2.12)$$

The external work on the cross section is

$$U_e = \int_A (q_\alpha u_\alpha + qw)\,dA = p_\alpha\xi_\alpha + p\zeta + m_\alpha\eta_\alpha + m\phi + b\theta \quad (2.13)$$

where the generalized loads are given in Table 2.

The equilibrium equations and boundary conditions follow from variations of the potential energy functional $U = \int_L (U_i - U_e)\,dz$. In terms of the generalized forces of Table 3 the equilibrium equations are

$$N' + p = 0 \quad (2.14)$$

$$M_\alpha' + Q_\alpha + m_\alpha = 0 \quad (2.15)$$

$$B' + M_\theta + b = 0 \quad (2.16)$$

$$M' + m = 0 \quad (2.17)$$

$$Q_\alpha' + p_\alpha = 0 \quad (2.18)$$

Suitable boundary conditions include all of the pairs (ζ,N), (η_α,M_α), (θ,B), (ϕ,M) and (ξ_α,Q_α).

Although the equilibrium equations closely resemble those of [5] for pretwisted beams without shear flexibility, it is important to note that in the present case Q_α is not a reaction determined from (2.15) but a generalized force with its own constitutive relation (2.10). Therefore all of the equilibrium equations are now of the second order in the generalized displacements. Before returning to this important point in connection with discretization of the equilibrium equations a few details are given regarding the determination of the shear flexibility tensor $D_{\alpha\beta}$.

3 The Shear Flexibility Tensor

The shear flexibility tensor $D_{\alpha\beta}$ appears in the present theory as a measure of the shear strain energy associated with a cross section exposed to pure shear. As for the shear center the problem becomes well defined by reference to an equivalent cylindrical cantilever with specified end load. In the shear problem the end load is a transverse force Q_α, and when the shear stress distribution is required to be independent of the axial coordinate it is unique [8]. Let this unique shear stress distribution be written in the form

$$\tau_\gamma(x_\nu) = \tau_\gamma^\beta(x_\nu) Q_\beta / A \quad (3.1)$$

where the shear stress distribution functions $\tau_\gamma^\beta(x_\nu)$ depend on the cross section geometry and material parameters. The shear strain energy of the cross section is

$$\frac{1}{2A} Q_\alpha D_{\alpha\beta} Q_\beta = \int_A \frac{1}{2G}\tau_\gamma\tau_\gamma dA \quad (3.2)$$

and substitution of (3.1) leads to

$$D_{\alpha\beta} = \frac{1}{A}\int_A \frac{1}{G}\tau_\gamma^\alpha\tau_\gamma^\beta dA \quad (3.3)$$

This definition of the shear flexibility consistently accounts for tensor properties and nonhomogeneous shear modulus $G(x_\nu)$.

In general the shear stress distribution functions $\tau_\gamma^\beta(x_\nu)$, and thereby $D_{\alpha\beta}$, depend on Poisson's ratio. In the present theory the condition of undeformable cross sections as expressed by (2.1) already severely restricts the ability to account for Poisson's ratio. It is therefore not possible to assess this influence completely. However, an investigation of the shear flexibility by Cowper [11] based on *mean* displacements of symmetric cross sections clearly indicates that the influence of Poisson's ratio is small compared with the influence of the geometry of the cross section.

The full boundary value problem for the shear stress distribution functions $\tau_\gamma^\beta(x_\nu)$ can only be solved in explicit form for a few simple shapes, and an approximate solution for cross sections of moderate wall thickness is therefore of considerable practical interest. The approximation is obtained by use of a local representation of the shear stress vector in terms of the lowest degree polynomial that can satisfy the local equilibrium and compatibility equations, when the wall curvature is neglected. For constant G this representation consists of a shear flow τ_t^β distributed uniformly over the wall thickness and a transverse component τ_n^β of parabolic variation along the wall normal n_γ

$$\tau_t^\beta = \tau_t^\beta(s), \qquad \tau_n^\beta = \tau_{n,0}^\beta(s)\{1 - (2n/d)^2\} \quad (3.4)$$

where d is the local wall thickness and (n,s) are coordinates oriented along the local normal and tangent, respectively.

The transverse component τ_n^β is determined by expressing the local coordinates (n,s) in terms of the global coordinates x_ν and substituting (3.4) into the equilibrium equation of the St. Venant shear problem. This gives

$$\tau_{n,0}^\beta = \frac{1}{8} d^2 A\,E\,n_\gamma J_{\gamma\beta} \quad (3.5)$$

$J_{\alpha\beta}$ is the inverse of the elastic moment tensor referred to the elastic center $c_\alpha = S_\alpha/F$, i.e.,

$$J_{\alpha\beta}^{-1} = I_{\alpha\beta} - F\,c_\alpha c_\beta \quad (3.6)$$

Substitution of this result into (3.3) gives the shear flexibility tensor as a line integral.

$$D_{\alpha\beta} = \int_C \frac{d}{AG}\left\{\tau_t^\alpha\tau_t^\beta + \frac{A^2 d^4 E^2}{120} n_\gamma J_{\gamma\alpha} n_\delta J_{\delta\beta}\right\} ds \quad (3.7)$$

The contribution from the transverse component is mostly of importance for flat, open sections such as airfoils. Typical values for $D_{\alpha\beta}$ are given in the example. In the particular case

Downloaded 02 May 2010 to 171.66.16.54. Redistribution subject to ASME license or copyright; see http://www.asme.org/terms/Terms_Use.cfm

of a homogeneous rectangle (3.7) gives $GD_{\alpha\beta}=6/5\delta_{\alpha\beta}$, and thus the inclusion of the transverse component produces the desired isotropy of the tensor $D_{\alpha\beta}$ as well as the expected numerical factor.

4 A Modified Energy Functional

A notable feature of the equilibrium equations (2.14)-(2.18) is the occurrence of the terms M_θ and Q_α without differentiation. They are a consequence of the explicit dependence of U_i upon θ and η_α. Indeed, it follows from (2.12) that

$$\frac{\partial U_i}{\partial \theta} = -M_\theta, \qquad \frac{\partial U_i}{\partial \eta_\alpha} = -Q_\alpha \tag{4.1}$$

If a discretized form of the equilibrium equations is developed directly from the potential energy by substitution of polynomial representations of the generalized displacements, terms such as $(\theta')^2$ and θ^2 will exhibit markedly different axial variation. This is undesirable and can be avoided by introducing M_θ and Q_α as independent functions. The procedure to be used is similar to the Legendre transformation method of removing the derivatives from a functional [12]. However, in the present case the derivatives are retained, while the explicit dependence on θ and η_α is removed.

The idea is to replace U_i from (2.12) with

$$H = U_i + \theta M_\theta + \eta_\alpha Q_\alpha \tag{4.2}$$

H is considered as a function of the derivatives ζ', η'_α, θ', ϕ', ξ'_α and the new variables M_θ and Q_α. The potential energy functional is then replaced by

$$\Phi = \int_L (H - \theta M_\theta - \eta_\alpha Q_\alpha - U_e)\, dz \tag{4.3}$$

It is immediately seen from (4.1) and (4.3) that variations of θ, θ' and $\eta_\alpha, \eta'_\alpha$ in Φ will introduce the independent new variables M_θ and Q_α in their proper positions in the equilibrium equations. Variations of M_θ and Q_α in Φ produce equations for θ and η_α instead of the equations for M_θ and Q_α in Table 3. The details of this procedure are given in the next section in connection with a specific discretization.

5 Discretization

The presence of shear flexibility leads to second-order differential equations in the generalized displacements in contrast to the fourth-order bending equations of classical beam theory. This permits the use of piecewise linear representation of the generalized displacements, and in connection with piecewise constant representation of the section properties, this leads to a simple discretization of Galerkin type. However, as already mentioned a fully displacement-based procedure would lead to lack of local compatibility between the individual terms in the equilibrium equations, and M_θ and Q_α are therefore introduced initially as independent, piecewise constant functions. In the following the discretized equations are derived in a finite element format.

Consider a beam element with end points a and b. The generalized displacements vary linearly between the end point values and are therefore completely determined by the vector

$$\mathbf{v} = \begin{Bmatrix} \mathbf{v}^a \\ \mathbf{v}^b \end{Bmatrix} \tag{5.1}$$

where $\mathbf{v}^a$ and $\mathbf{v}^b$ contain the end point values.

$$\mathbf{v}^a = \{\zeta, \eta_\alpha, \theta, \phi, \xi_\alpha\}^a \tag{5.2}$$

M_θ and Q_α are constant within the element.

The discretized equilibrium equations are determined from stationarity of Φ from (4.3). The first step consists in eliminating θ and η_α from H and then taking variations of Φ with respect to M_θ and Q_α. The elimination need not be done explicitly but can be accomplished by considering θ as a function of M_θ and η_α as a function of Q_α in H. It then follows from the chain rule that

$$\delta\Phi = \int_a^b \left\{ \left(\frac{\partial H}{\partial \theta}\frac{\partial \theta}{\partial M_\theta} + \frac{\partial H}{\partial M_\theta} - \theta \right) \delta M_\theta + \left(\frac{\partial H}{\partial \eta_\beta}\frac{\partial \eta_\beta}{\partial Q_\alpha} + \frac{\partial H}{\partial Q_\alpha} - \eta_\alpha \right) \delta Q_\alpha \right\} dz = 0 \tag{5.3}$$

The last two terms in each parenthesis cancel, leaving

$$\delta\Phi = \int_a^b \left\{ \left(\frac{\partial U_i}{\partial \theta} + M_\theta \right) \frac{\partial \theta}{\partial M_\theta}\delta M_\theta + \left(\frac{\partial U_i}{\partial \eta_\beta} + Q_\beta \right) \frac{\partial \eta_\beta}{\partial Q_\alpha}\delta Q_\alpha \right\} dz = 0 \tag{5.4}$$

In this form the parentheses are identical to those resulting from direct use of the potential energy, but the important point is that here the variational factors are independent *constants*. The integrations then become simple mean values, and the resulting equations can be read directly off Table 3.

$$\begin{aligned} M_\theta &= \frac{1}{l}\left\{ -\beta S_\psi, \beta I_{\beta\psi}, \beta I_{\omega\psi} - \frac{l}{2}(\beta^2 I_{\psi\psi} + I_{R^2} - K), \right. \\ &\quad \left. -(I_{R^2} - K), 0 \right\} \cdot \mathbf{v}^a + \frac{1}{l}\left\{ \beta S_\psi, -\beta I_{\beta\psi}, -\beta I_{\omega\psi} \right. \\ &\quad \left. -\frac{l}{2}(\beta^2 I_{\psi\psi} + I_{R^2} - K), I_{R^2} - K, 0 \right\} \cdot \mathbf{v}^b \end{aligned} \tag{5.5}$$

$$\begin{aligned} Q_\alpha &= \frac{A}{l} D^{-1}_{\alpha\beta}\left\{ 0, -\frac{l}{2}, 0, e_{\beta\gamma}a_\gamma, -1 \right\} \cdot \mathbf{v}^a \\ &\quad + \frac{A}{l} D^{-1}_{\alpha\beta}\left\{ 0, -\frac{l}{2}, 0, -e_{\beta\gamma}a_\gamma, 1 \right\} \cdot \mathbf{v}^b \end{aligned} \tag{5.6}$$

Note that direct use of the potential energy functional would have given a different representation of M_θ and Q_α.

The next step establishes the equilibrium equations by variations $\delta\mathbf{v}^a$ and $\delta\mathbf{v}^b$ in the functional Φ.

$$\begin{aligned} \delta\Phi &= \int_a^b \left\{ \frac{\partial H}{\partial \zeta'}\frac{1}{l}(\delta\zeta^b - \delta\zeta^a) - \frac{\partial U_e}{\partial \zeta}\frac{1}{l}\left((z - z_a)\delta\zeta^b \right. \right. \\ &\quad \left. + (z_b - z)\delta\zeta^a \right) + \frac{\partial H}{\partial \eta'_\alpha}\frac{1}{l}(\delta\eta^b_\alpha - \delta\eta^a_\alpha) - \left(Q_\alpha \right. \\ &\quad \left. \left. + \frac{\partial U_e}{\partial \eta_\alpha} \right) \frac{1}{l}\left((z - z_a)\delta\eta^b_\alpha + (z_b - z)\delta\eta^a_\alpha \right) + \text{etc.} \right\} dz \end{aligned} \tag{5.7}$$

The derivatives $\partial H/\partial\zeta'$, $\partial H/\partial\eta'_\alpha$, etc. are the generalized forces N, M_α, etc. from Table 3, where θ and η_α are to be considered as constants. Instead of eliminating θ and η_α the auxiliary variables M_θ and Q_α are eliminated by use of (5.5), (5.6) leading to a system of equations of the form

$$\begin{Bmatrix} \mathbf{K}^{aa} & \mathbf{K}^{ab} \\ \mathbf{K}^{ba} & \mathbf{K}^{bb} \end{Bmatrix} \begin{Bmatrix} \mathbf{v}^a \\ \mathbf{v}^b \end{Bmatrix} = \begin{Bmatrix} \mathbf{r}^a \\ \mathbf{r}^b \end{Bmatrix} \tag{5.8}$$

The $\mathbf{K}$ matrices constitute the element stiffness matrix, and the vectors $\mathbf{r}^a$ and $\mathbf{r}^b$ contain the contributions from this element to the generalized loads at the nodes a and b.

The integrations in (5.7) can be carried out by inspection. The stiffness submatrix $\mathbf{K}^{aa}$ is symmetric and given by

Downloaded 02 May 2010 to 171.66.16.54. Redistribution subject to ASME license or copyright; see http://www.asme.org/terms/Terms_Use.cfm

$$\mathbf{K}^{aa}=\frac{1}{l}\begin{Bmatrix} F & -S_\beta & \frac{\beta l}{2}S_\psi & 0 & 0 \\ & I_{\alpha\beta}+\frac{l^2}{4}AD^{-1}_{\alpha\beta} & -\frac{\beta l}{2}I_{\alpha\psi} & -\frac{l}{2}AD^{-1}_{\alpha\beta}e_{\beta\gamma}a_\gamma & \frac{l}{2}AD^{-1}_{\alpha\beta} \\ & & \dfrac{(I_{\omega\omega}-\beta l I_{\omega\psi})}{\left(\dfrac{+(\beta l/2)^2 I_{\psi\psi}}{+(l/2)^2(I_R{}^2-K)}\right)} & -\frac{l}{2}(I_R{}^2-K) & 0 \\ & & & \left(\dfrac{I_R{}^2+e_{\alpha\delta}a_\delta}{AD^{-1}_{\alpha\beta}e_{\beta\gamma}a_\gamma}\right) & \left(\dfrac{-AD^{-1}_{\alpha\beta}}{e_{\beta\gamma}a_\gamma}\right) \\ & & & & AD^{-1}_{\alpha\beta} \end{Bmatrix} \tag{5.9}$$

The submatrix $\mathbf{K}^{bb}$ follows from $\mathbf{K}^{aa}$ by replacing l with $(-l)$ in the terms within the braces in (5.9).

$$\mathbf{K}^{ab}=\frac{1}{l}\begin{Bmatrix} -F & S_\beta & \frac{\beta l}{2}S_\psi & 0 & 0 \\ S_\alpha & -I_{\alpha\beta}+\frac{l^2}{4}AD^{-1}_{\alpha\beta} & -\frac{\beta l}{2}I_{\alpha\psi} & \frac{l}{2}AD^{-1}_{\alpha\beta}e_{\beta\gamma}a_\gamma & -\frac{l}{2}AD^{-1}_{\alpha\beta} \\ -\frac{\beta l}{2}S_\psi & \frac{\beta l}{2}I_{\beta\psi} & \left(\dfrac{-I_{\omega\omega}+\left(\frac{\beta l}{2}\right)^2 I_{\psi\psi}}{+\frac{l^2}{4}(I_R{}^2-K)}\right) & -\frac{l}{2}(I_R{}^2-K) & 0 \\ 0 & -\frac{l}{2}AD^{-1}_{\beta\gamma}e_{\gamma\delta}a_\delta & \frac{l}{2}(I_R{}^2-K) & \left(\dfrac{-I_R{}^2-e_{\alpha\delta}a_\delta}{AD^{-1}_{\alpha\beta}e_{\beta\gamma}a_\gamma}\right) & \left(\dfrac{AD^{-1}_{\alpha\beta}}{e_{\beta\gamma}a_\gamma}\right) \\ 0 & \frac{l}{2}AD^{-1}_{\alpha\beta} & 0 & AD^{-1}_{\alpha\beta}e_{\beta\gamma}a_\gamma & -AD^{-1}_{\alpha\beta} \end{Bmatrix} \tag{5.10}$$

$\mathbf{K}^{ba}$ is the transpose of $\mathbf{K}^{ab}$. Note that the lower half of $\mathbf{K}^{ab}$ follows from the upper half by exchanging l with $(-l)$ in the terms inside the braces in (5.10).

Concentrated loads are applied directly to the nodes, while loads with linear distribution over the element are contained in the vectors

$$\mathbf{r}^a=\frac{l}{6}\begin{Bmatrix} 2p^a+p^b \\ 2m^a_\alpha+m^b_\alpha \\ 2b^a+b^b \\ 2m^a+m^b \\ 2p^a_\alpha+p^b_\alpha \end{Bmatrix},\quad \mathbf{r}^b=\frac{l}{6}\begin{Bmatrix} p^a+2p^b \\ m^a_\alpha+2m^b_\alpha \\ b^a+2b^b \\ m^a+2m^b \\ p^a_\alpha+2p^b_\alpha \end{Bmatrix} \tag{5.11}$$

For vibration analysis the mass matrix is also needed. It follows from the kinetic energy of the element.

$$\frac{1}{2}\{\dot{\mathbf{v}}^a,\dot{\mathbf{v}}^b\}\begin{Bmatrix}\mathbf{M}^{aa} & \mathbf{M}^{ab}\\ \mathbf{M}^{ba} & \mathbf{M}^{bb}\end{Bmatrix}\begin{Bmatrix}\dot{\mathbf{v}}^a\\ \dot{\mathbf{v}}^b\end{Bmatrix}$$

$$=\frac{1}{2}\int_a^b\int_A \rho(\dot{u}_\alpha\dot{u}_\alpha+\dot{w}^2)dA\,dz \tag{5.12}$$

By substitution of the displacement representation (2.1) and (2.2) with linear interpolation the following result is obtained.

$$\mathbf{M}^{aa}=\mathbf{M}^{bb}=2\mathbf{M}^{ab}=2\mathbf{M}^{ba}=$$

$$\frac{l}{3}\begin{Bmatrix} F^\rho & -S^\rho_\beta & -S^\rho_\omega & 0 & 0 \\ & I^\rho_{\alpha\beta} & I^\rho_{\alpha\omega} & 0 & 0 \\ & & I^\rho_{\omega\omega} & 0 & 0 \\ & & & I^\rho_{\gamma\gamma} & -e_{\alpha\beta}S^\rho_\beta \\ & & & & \delta_{\alpha\beta}F^\rho \end{Bmatrix} \tag{5.13}$$

The mass submatrices are symmetric, and the superscript ρ indicates weighting of the sectional parameters with the mass density ρ instead of the previously used modulus of elasticity.

6 Example

As an application of the present theory we consider vibrations of a clamped steam turbine blade from one of the last stages in a low pressure turbine. The total free length of the blade was 490 mm of which the foot contributed 19 mm.

Downloaded 02 May 2010 to 171.66.16.54. Redistribution subject to ASME license or copyright; see http://www.asme.org/terms/Terms_Use.cfm

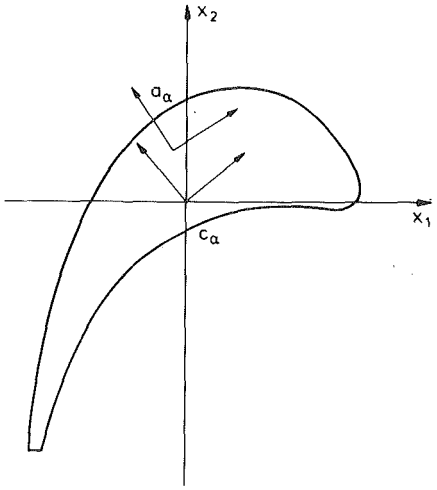


Fig. 1 Root cross section, $A = 4.88 \cdot 10^{-3}$ m^2, $I_{min} = 2.00 \cdot 10^{-7}$ m^4, and $I_{max} = 1.25 \cdot 10^{-6}$ m^4

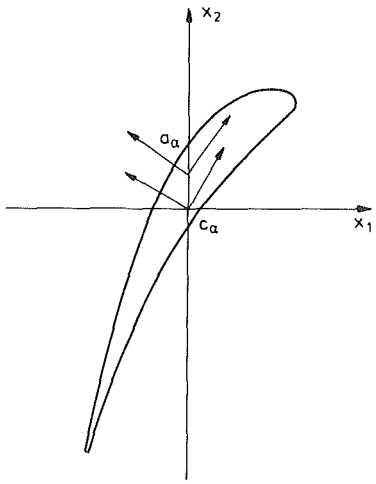


Fig. 2 Representative tip cross section, $A = 8.30 \cdot 10^{-4}$ m^2, $I_{min} = 1.41 \cdot 10^{-8}$ m^4, and $I_{max} = 4.92 \cdot 10^{-7}$ m^4

The blade had a considerable variation in cross section from the thick root section shown in Fig. 1 to rather thin sections near the tip. A representative section 150 mm from the tip is shown in Fig. 2. The total angle of pretwist was 28 deg, and the sections were stacked around the elastic center, i.e., $c_\alpha = 0$.

The blade was modeled by 11 elements, of which two were used for the foot. The cross-sectional parameters were calculated by a triangulation procedure using parabolic representations within narrow triangles and performing integrations by means of quadrature accurate for fourth-degree polynomials. A general description of this procedure for open and cellular cross sections is given in [13]. The combination of large thickness and camber of the root section makes direct use of centerline and thickness unsatisfactory, as it would lead to substantial errors in the area and the sectional moments.

The calculated and the experimentally determined eigenfrequencies are shown in Table 4. The agreement is considered to be good in view of the modeling detail, which has been chosen according to available data and is believed to be representative of practical applications. Calculations on different types of turbine blades confirm the degree of accuracy.

Two points deserve further notice: the effect of pretwist and the shear flexibility tensor. In the case of centered stacking, like here, the torsion-extension coupling via S_ψ is asymptotically exact [2]. As demonstrated by Hodges [4] this coupling term is simply related to the polar moment of inertia used in theories based on the "helical fiber" concept [14]. In fact

$$S_\psi = I_{\gamma\gamma} - \frac{E}{G} K \tag{6.1}$$

and thus the ratio $EK/GI_{\gamma\gamma}$ provides a measure of the error introduced in the torsion-extension coupling by the "helical fiber" assumption. For the cross sections of Figs. 1 and 2 this ratio is 0.22 and 0.06, respectively. This illustrates the conclusion from [5] that for open thin-walled sections with small camber and centered stacking the "helical fiber" assumption leads to a representative torsion-extension coupling in spite of its erroneous theoretical foundation.

Table 4 Eigenfrequencies in Hz

Mode no.	1	2	3	4
Calculated	143	385	599	789
Experimental	143	365	587	768

The elastic center and the principal axes of $I_{\alpha\beta}$ are shown in Figs. 1 and 2 together with the shear center and the principal axes of the shear flexibility tensor $D_{\alpha\beta}$. The difference in angle between the two sets of principal axes is 6.7 deg and 6.0 deg, respectively. However, more important than this minor difference in alignment of bending and shear is the magnitude of the shear flexibility coefficients, D_{max} and D_{min}. D_{max} is obtained for transverse shear, and the values are 2.22 and 6.41, respectively. D_{min} refers to chordwise shear with values of 1.47 and 1.17, respectively. Only the last of these coefficients is close to the classical value of 1.20 for a rectangle. The large value of the shear flexibility coefficient for transverse shear is due to the camber that induces shear stress components along the centerline with a very small contribution to the shear resultant.

7 Discussion

The theory for pretwisted beams has been extended to include transverse shear flexibility, described via a shear flexibility tensor to be evaluated by integration of the shear strain energy of each individual cross section. This flexibility may deviate considerably from that of a rectangle, often used in practice. Decomposition of normal and shear stresses in orthogonal contributions leads to a clear distinction between the axes of pretwist, elastic center and shear center.

In discretizing the equations inconsistencies resulting from adding functions and their derivatives were avoided by modification of the potential energy functional. The result is a representation in which the generalized forces are piecewise constant within each element. The simplicity of the representation is possible because the inclusion of shear flexibility has already reduced the equilibrium equations to second order. Calculations on various turbine blades, of which one is included as an example, show good accuracy of this simple beam element that retains the possibility of including large cross-sectional variability without the use of additional degrees of freedom.

The analysis has been confined to the linear theory of elasticity, although many applications will require inclusion of nonlinear effects from centrifugal forces. These effects can be introduced in the form of an additional stiffness matrix that is proportional to the generalized forces in the particular element. If the generalized forces are evaluated from the undeformed geometry, the discretized problem remains linear and can be treated directly by suitable modification of the stiffness matrix of the present paper. The details are given in [15].

Acknowledgment

The authors gratefully acknowledge the permission to use experimental results of Brown, Boveri & Cie., Baden, Switzerland.

Downloaded 02 May 2010 to 171.66.16.54. Redistribution subject to ASME license or copyright; see http://www.asme.org/terms/Terms_Use.cfm

References

1 Shield, R. T., "Extension and Torsion of Elastic Bars With Initial Twist," ASME JOURNAL OF APPLIED MECHANICS, Vol. 49, 1982, pp. 779–786.

2 Krenk, S., "The Torsion-Extension Coupling in Pretwisted Elastic Beams," *International Journal of Solids and Structures*, Vol. 19, 1983, pp. 67–72.

3 Rosen, A., "The Effect of Initial Twist on the Torsional Rigidity of Beams—Another Point of View," ASME JOURNAL OF APPLIED MECHANICS, Vol. 47, 1980, pp. 389–392.

4 Hodges, D. H., "Torsion of Pretwisted Elastic Beams due to Axial Loading," ASME JOURNAL OF APPLIED MECHANICS, Vol. 47, 1980, pp. 393–397.

5 Krenk, S., "A Linear Theory for Pretwisted Elastic Beams," ASME JOURNAL OF APPLIED MECHANICS, Vol. 50, 1983, pp. 137–142.

6 Wlassow, W. S., *Dünnwandige elastische Stäbe*, VEB Verlag für Bauwesen, Berlin, 1964.

7 Kollbrunner, C. F., and Hajdin, N., *Dünnvandige Stäbe*, Vol. 1, Springer Verlag, Berlin, 1972.

8 Love, A. E. H., *A Treatise on the Mathematical Theory of Elasticity*, Dover, New York, 1944.

9 Trefftz, E., "Über den Schubmittelpunkt in einem durch eine Einzellast gebogenen Balken," *Zeitschrift für Angewandte Mathematik und Mechanik*, Vol. 15, 1935, pp. 220–225.

10 Koiter, W. T., "The Flexural Centre or the Centre of Shear," *Journal of the Royal Aeronautical Society*, Vol. 58, 1954, pp. 64–65.

11 Cowper, G. R., "The Shear Coefficient in Timoshenko's Beam Theory," ASME JOURNAL OF APPLIED MECHANICS, Vol. 33, 1966, pp. 335–340.

12 Gelfand, I. M., and Fomin, S. V., *Calculus of Variations*, Prentice-Hall, Englewood Cliffs, N.J. 1963.

13 Krenk, S., and Gunneskov, O., "A Triangulation Procedure for Elastic Cross Sections of Moderate Wall Thickness," to appear.

14 Chu, Chen, "The Effect of Initial Twist on the Torsional Rigidity of Thin Prismatical Bars and Tubular Members," *Proceedings of the 1st U.S. National Congress on Applied Mechanics*, 1952, pp. 265–269.

15 Krenk, S. and Gunneskov, O., "Vibrations of Rotating Turbine Blades," to appear.

Downloaded 02 May 2010 to 171.66.16.54. Redistribution subject to ASME license or copyright; see http://www.asme.org/terms/Terms_Use.cfm

A Beam Theory for Anisotropic Materials

O. A. Bauchau
Assistant Professor,
Department of Mechanical Engineering,
Aeronautical Engineering and Mechanics,
Rensselaer Polytechnic Institute,
Troy, N.Y. 12181

Beam theory plays an important role in structural analysis. The basic assumption is that initially plane sections remain plane after deformation, neglecting out-of-plane warpings. Predictions based on these assumptions are accurate for slender, solid, cross-sectional beams made out of isotropic materials. The beam theory derived in this paper from variational principles is based on the sole kinematic assumption that each section is infinitely rigid in its own plane, but free to warp out of plane. After a short review of the Bernoulli and Saint-Venant approaches to beam theory, a set of orthonormal eigenwarpings is derived. Improved solutions can be obtained by expanding the axial displacements or axial stress distribution in series of eigenwarpings and using energy principles to derive the governing equations. The improved Saint-Venant approach leads to fast converging solutions and accurate results are obtained considering only a few eigenwarping terms.

1 Introduction

Timoshenko beam theory is well known by structural designers and is widely used as a first approximation in numerous structural applications. For solid cross-sectional beams made out of isotropic materials, this theory gives accurate predictions for aspect ratios $L/h \gtrsim 5$ (L is the span of the beam and h its height). Because it is based on the assumption that cross sections remain plane after deformation, the theory predicts a linear distribution of axial strains. However, additional axial strains are induced by warping incompatibilities generated either by specific loading or boundary conditions, or by the occurrence of nonuniform torsion or bending. According to Saint-Venant's Principle these additional strains tend to decay away from the perturbation that created them. The decay length δ is defined as the distance it takes for these strains to decay to a neglectible value. For solid cross-sectional beams made out of isotropic materials, this decay length is of the order of the height of the beam, i.e., $\delta \simeq h$. A physical meaning of the validity range of the theory is found by rewriting it as $L/\delta \gtrsim 5$, stating that the span of the beam must be large compared to the perturbed zone δ.

In the case of thin-walled box beams, it was recognized early that beam theory was only a poor approximation, because warping and shear lag effects are significant for those structures. Von Karman and Chien [1] gave a solution to this problem using a system of orthogonal states of stress. Argyris and Dunne [2] derived solutions for more general problems and showed the existence of fast converging series based on a similar system of orthogonal stress states.

More recently, with the increasing use of composite materials, Saint-Venant's principle has been investigated theoretically for anisotropic elasticity [3, 4]. The decay length δ was found to be proportional to $\sqrt{E/G}$ (E is the longitudinal Young's modulus and G the shear modulus). This means that for highly anisotropic materials the decay length can be much larger than for isotropic materials. Goetschel [5] calculated these decay length for different beams made out of composite materials. For a thin-walled rectangular cross-section δ is found to be $7h$, and for an I cross section $\delta = 15h$. Beam theory can still be applied if $L/\delta \gtrsim 5$, i.e., $L/h \gtrsim 35$ and 75, respectively. Needless to say, such a restriction makes beam theory inapplicable to practical structures.

The purpose of this paper is to derive a beam theory that can be used when only the geometric condition $L/h \gtrsim 5$ is satisfied.

2 Geometry Assumptions

Thin-walled box beams with closed cross sections will be considered (see Fig. 1). The contour of the section (denoted ζ) is a parametric function of the variable s, while the variable z

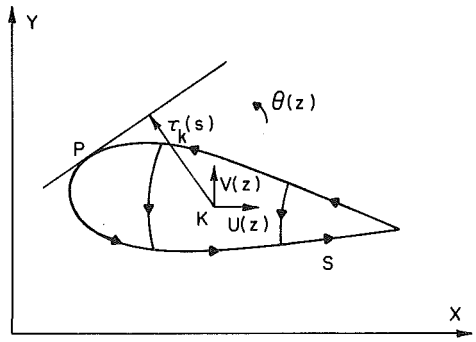


Fig. 1 Geometry of a typical cross section

Contributed by the Applied Mechanics Division for publication in the JOURNAL OF APPLIED MECHANICS.
Discussion on this paper should be addressed to the Editorial Department, ASME, United Engineering Center, 345 East 47th Street, New York, N.Y. 10017, and will be accepted until two months after final publication of the paper itself in the JOURNAL OF APPLIED MECHANICS. Manuscript received by ASME Applied Mechanics Division, April, 1984; final revision, August, 1984.

Copyright © 1985 by ASME
Downloaded 02 May 2010 to 171.66.16.54. Redistribution subject to ASME license or copyright; see http://www.asme.org/terms/Terms_Use.cfm

runs along the span of the beam. The basic assumption is that each section is infinitely rigid in its own plane, but free to warp out of plane. This assumption has two important implications: (*i*) the inplane displacements of the section are fully represented by three rigid body modes $u(z)$, $v(z)$, $\theta(z)$, respectively, the two translations and the rotation of the section, and (*ii*) any applied transverse load only induces membrane stresses in the structure, specifically an axial stress flow n, and a shear stress flow q. For thin walled beams these two stress flows are uniform across the thickness and the other stress components are assumed to be neglectible.

Finally, we must specify the stress-strain relations: the materials is either isotropic or curvilinear orthotropic with the axes of orthotropy parallel to the axis of the beam and the tangent to the cross-sectional curve, so that:

$$n = A_{nn}\epsilon \tag{1}$$

$$q = A_{qq}\gamma \tag{2}$$

A_{nn} and A_{qq} are the elastic coefficients (see Appendix *B*); ϵ is the axial strain, and γ the shear strain. They are related to the displacements by

$$\epsilon = \frac{\partial w}{\partial z} \tag{3}$$

$$\gamma = \frac{\partial w}{\partial s} + u'\frac{dx}{ds} + v'\frac{dy}{ds} + \theta'\tau_k \tag{4}$$

where w is the axial displacement, $\tau_k(s)$ is the distance from the center K to the tangent to the cross-sectional curve (see Fig. 1), and $(\,)'$ means derivative with respect to z.

3 The Bernoulli Solution

Bernoulli's beam theory is based on the additional assumption that cross sections remain plane after deformation, implying a linear axial displacement:

$$w(s,z) = Z(z) + (x-x_n)X(z) + (y-y_n)Y(z) \tag{5}$$

where $Z(z)$ is a uniform extension of the section, $X(z)$, $Y(z)$ are the rotations of the section, and x_n, y_n are the coordinates of the neutral axis.

It is convenient to derive the equations of the problem from energy principles; in this case we must minimize the total potential energy π,

$$\pi = \frac{1}{2}\int_0^L\int_\zeta (A_{nn}\epsilon^2 + A_{qq}\gamma^2)dsdz - \int_0^L (p_x u + p_y v + m\theta)dz \tag{6}$$

where p_x, p_y are the applied transverse loads per unit span in the x and y directions, respectively, and m is the applied torque per unit span.

Using the basic assumption (5) and the strain definitions (3) and (4) we find,

$$\epsilon = Z' + (x-x_n)X' + (y-y_n)Y' \tag{7}$$

$$\gamma = (X+u')\frac{dx}{ds} + (Y+v')\frac{dy}{ds} + \theta'\tau_k \tag{8}$$

The total potential energy (6) now becomes

$$\pi = \frac{1}{2}\int_0^L [SZ'^2 + I_{xx}X'^2 + I_{yy}Y'^2 + 2I_{xy}X'Y' + A_{xx}(X+u')^2 + A_{yy}(Y+v')^2 + 2A_{xy}(X+u')(Y+v') + I_p\theta'^2]dz - \int_0^L (p_x u + p_y v + m\theta)dz \tag{9}$$

where $S = \int_\zeta A_{nn}\,ds$ is the axial stiffness; $I_{xx} = \int_\zeta A_{nn}(x-x_n)^2 ds$ is the bending stiffness (similar definitions for I_{yy} and I_{xy}), $A_{xx} = \int_\zeta A_{qq}(dx/ds)^2$ is the shear stiffness (similar definitions for A_{yy} and A_{xy}), and $I_p = \int_\zeta A_{qq}\tau_k^2\,ds$ is the torsional stiffness.

The location of the shear center K was chosen to decouple bending and torsion by setting

$$\int_C A_{qq}\tau_k\frac{dx}{ds}ds = \int_C A_{qq}\tau_k\frac{dy}{ds}ds = 0 \tag{10}$$

This gives a pair of linear equations for the coordinates x_k, y_k of the shear center. The Bernoulli solution is obtained by minimizing (9) with respect to the functions X, Y, u, v, θ, Z

$$(I_{xx}X' + I_{xy}Y')'' = -p_x,$$

$$(I_{xy}X' + I_{yy}Y')'' = -p_y \tag{11a}$$

$$[A_{xx}(X+u') + A_{xy}(Y+v')]' = -p_x,$$

$$[A_{xy}(X+u') + A_{yy}(Y+v')]' = -p_y \tag{11b}$$

$$(I_p\theta')' = -m, \quad (SZ')' = 0 \tag{11c}$$

This solution takes into account shearing deformations (11.*b*), it is sometimes referred to as Timoshenko beam theory. The solution to equations (11) is summarized here with a subscript "*b*":

$$w_b = Z + (x-x_n)X + (y-y_n)Y, \quad u_b = u$$

$$n_b = A_{nn}[Z' + (x-x_n)X' + (y-y_n)Y'], \quad v_b = v \tag{12}$$

$$q_b = A_{qq}\left[(X+u')\frac{dx}{ds} + (Y+v')\frac{dy}{ds} + \theta'\tau_k\right], \quad \theta_b = \theta.$$

4 The Saint-Venant Solution

The absence of out-of-plane warpings in the Bernoulli approach results in poor accuracy of the solution. In a first attempt to correct this situation Saint-Venant's approach is considered now. The assumption here is that the axial stresses are linearly distributed, i.e.,

$$n(s,z) = A_{nn}[A(z) + (x-x_n)B(z) + (y-y_n)C(z)], \tag{13}$$

in place of equation (5).

The Reissener Principle [6] will be used here to derive the governing equations. With our notations the functional to be minimized reads:

$$\pi_R = \int_0^L\int_\zeta \left[(n\epsilon + q\gamma) - \frac{1}{2}\left(\frac{n^2}{A_{nn}} + \frac{q^2}{A_{qq}}\right)\right]dsdz - \int_0^L (p_x u + p_y v + m)\,dz \tag{14}$$

Using the basic assumption (13) and the strain definitions (3) and (4) it becomes

$$\pi_R = \int_0^L\int_\zeta \left\{A_{nn}[A + (x-x_n)B + (y-y_n)C]\frac{\partial w}{\partial z} + q\left(\frac{\partial w}{\partial z} + u'\frac{dx}{ds} + v'\frac{dy}{ds} + \theta'\tau_k\right) - \frac{1}{2}A_{nn}[A + (x-x_n)B + (y-y_n)C]^2 - \frac{1}{2}\frac{q^2}{A_{qq}}\right\}dsdz - \int_0^L (p_x u + p_y v + m\theta)dz \tag{15}$$

Minimizing first with respect to w and q the following differential system is found:

$$\frac{\partial q}{\partial s} = -A_{nn}[A' + (x-x_n)B' + (y-y_n)C']$$

$$\frac{\partial w}{\partial w} - \frac{q}{A_{qq}} = -u'\frac{dx}{dz} - v'\frac{dy}{dz} - \theta'\tau_k \tag{16}$$

The detailed integration of this system is described in Appendix *A*. The solution (*A*15) is then replaced in the Reissener functional, and the variations on the remaining function u, v, θ, A, B, C yield the complete solution:

Downloaded 02 May 2010 to 171.66.16.54. Redistribution subject to ASME license or copyright; see http://www.asme.org/terms/Terms_Use.cfm

$$X' = i_{xx}M_x + i_{xy}M_y, \quad Y' = i_{xy}M_x + i_{yy}M_y$$
$$u' = U_x T_x + U_y T_y - X, \quad v' = V_x T_x + V_y T_y - Y \qquad (17)$$
$$J\theta' = M_k, \quad SZ = N$$

where

$M_x = \int_\zeta n(x-x_n)\,ds$ is the bending moment (similar definition for M_y),

$T_x = \int_\zeta q \dfrac{dx}{ds}\,ds$ is the shear force (similar definition for T_y),

$M_k = \int_\zeta q\ \tau_k\ ds$ is the torque at the shear center K,

$N = \int_\zeta n\ ds$ is the axial force,

$J = \int_\zeta Q_t\ \tau_k ds$ is the torsional stiffness

i_{xx}, i_{yy}, i_{xy} is the inverse tensor of bending stiffnesses.

Here again the location of the shear center K has been chosen to decouple bending and torsion by setting

$$\int_\zeta Q_1 \tau_k ds = \int_\gamma Q_2 \tau_k ds = 0. \qquad (18)$$

This results in a pair of linear equations for the coordinates of the shear center x_k, y_k. The Saint-Venant solution is now summarized with a subscript "sv":

$$w_{sv} = Z + (x-x_n)X + (y-y_n)Y + W_x T_x + W_y T_y + W_t \frac{M_k}{J},$$

$$n_{sv} = A_{nn}\left\{\frac{N}{S} + [i_{xx}(x-x_n) + i_{xy}(y-y_n)]M_x + [i_{xy}(x-x_n) + i_{yy}(y-y_n)]M_y\right\},$$

$$q_{sv} = Q_x T_x + Q_y T_y + Q_t \frac{M_k}{J},$$
$$u_{sv} = u, \quad v_{sv} = v, \quad \theta_{sv} = \theta. \qquad (19)$$

where the different functions are solutions of the system (17) and W_x, W_y, W_t as well as Q_x, Q_y, Q_t are defined in Appendix A. It is interesting to note that this solution satisfies all the equations of the problem, except the stress strain relation (1).

5 Eigenwarpings

In the Bernoulli solution (12) all warpings are ignored, and the Saint-Venant solution (19) only considers specific warpings (W_x, W_y, W_t). In this section a set of orthonormal warpings is derived. They will be used later for a series expansion of the exact solution. Eigenwarpings are derived from the principle of minimum potential energy (6). An homogeneous problem is considered (i.e., no loading is applied) and a solution of the following form is assumed:

$$w(s,z) = W(s)F(z), \quad u'(z) = UF(z),$$
$$v'(z) = VF(z), \quad \theta'(z) = \Xi F(z) \qquad (20)$$

$F(z)$ and $W(s)$ are unknown functions of z and s, respectively, U, V, and Ξ are unknown parameters. These assumptions result in expressions for the strains where the variables are separated:

$$\epsilon = W(s)F'(z) \qquad (21)$$

$$\gamma = \left(\frac{dW}{ds} + U\frac{dx}{ds} + V\frac{dy}{ds} + \Xi\tau_k\right)F(z) = \Gamma(s)F(z) \qquad (22)$$

The energy principle (6) now reads:

$$\pi = \frac{1}{2}\int_0^L \int_\zeta (A_{nn}W^2F'^2 + A_{qq}\Gamma^2F^2)ds\ dz \qquad (23)$$

This functional can be first minimized with respect to F, to find

$$F'' - \mu^2 F = 0 \qquad (24)$$

where μ^2 is a yet unknown separation constant. Using this relation the energy principle becomes:

$$\pi = \frac{1}{2}\left[\int_0^L F^2 dz\right]\left[-\mu^2\int_\zeta A_{nn}W^2 ds + \int_\zeta A_{qq}\Gamma^2 ds\right] \qquad (25)$$

This functional is now minimized with respect to the function W and the parameters U, V, and Ξ. This leads to an eigenvalue problem for μ^2, that can be written in the form of a Rayleigh quotient

$$\mu_i^2 = \frac{\int_\zeta A_{qq}\left(\dfrac{dW_i}{ds} + U_i\dfrac{dx}{ds} + V_i\dfrac{dy}{ds} + \Xi_i\tau_k\right)^2 ds}{\int_\zeta A_{nn}W_i^2 ds} \qquad (26)$$

$W_i(s)$ are the eigenwarpings of the problem. A set of orthonormality relationships is associated with this problem:

$$\int_\zeta A_{nn}W_iW_j ds = \delta_{ij}, \quad \int_\zeta A_{qq}\Gamma_i\Gamma_j ds = \mu^2\delta_{ij} \qquad (27)$$

6 Improving the Bernoulli Solution

The Bernoulli solution will be improved by adding to the basic assumption (5), a series expansion in terms of eigenwarpings, and by correcting the other displacements components accordingly (see equation (20)):

$$w(s,z) = w_b + \sum_i w_i(s)F_i(z) \qquad (28.a)$$

$$u' = u'_b + \sum_i U_iF_i(z), \quad v' = v'_b + \sum_i V_iF_i(z),$$

$$\theta' = \theta'_b + \sum_i \Xi_iF_i(z) \qquad (28.b)$$

Note that arbitrary axial displacements can be represented with the preceding series expansion (28.a), so no assumption is made on axial displacements distribution. However, the assumption of infinite inplane rigidity of the section is required to express the inplane displacements (28.b) as functions of z only.

The strains corresponding to this displacement field can be used to evaluate the potential energy (6), and taking into account orthonormality relations (27) it reads:

$$\pi = \pi_b + \sum_i \int_0^L \left[\frac{1}{2}(F_i'^2 + \mu_i^2F_i^2) - d_i\right]dz \qquad (29)$$

where π_b is the potential energy for the Bernoulli solution (9), and

$$d_i = T_xU_i + T_yV_i + M_k\Xi_i \qquad (30)$$

Expression (29) shows the Bernoulli solution to be decoupled from the corrective terms F_i and the different corrective terms decoupled from each other. Minimizing π_b will render the Bernoulli solution (12) and minimizing the corrective terms with respect to F_i gives:

$$F_i'' - \mu_i^2F_i = -d_i \qquad (31)$$

This differential equation is solved readily and yields the

Downloaded 02 May 2010 to 171.66.16.54. Redistribution subject to ASME license or copyright; see http://www.asme.org/terms/Terms_Use.cfm

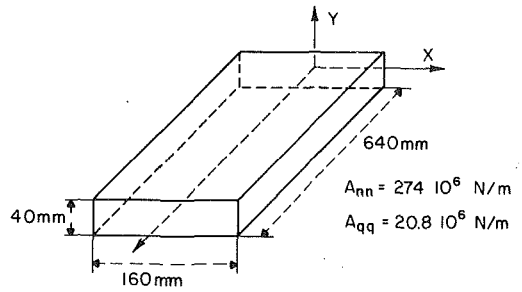


Fig. 2 The thin-walled, rectangular cross-sectional beam analyzed in the numerical example

solution of the problem as a series expansion of eigenwarpings:

$$w = w_b + \sum_i W_i F_i \quad u' = u_b' + \sum_i U_i F_i$$

$$n = n_b + \sum_i A_{nn} W_i F_i' \quad v = v_b + \sum_i V_i F_i \tag{32}$$

$$q = q_b + \sum_i A_{qq} \Gamma_i F_i \quad \theta' = \theta_b' + \sum_i \Xi_i F_i$$

When infinite series are used, equations (32) give the exact solution of the problem under the sole assumption of infinite inplane rigidity of the section.

7 Improving the Saint-Venant Solution

Following a similar procedure, the Saint-Venant solution is improved by adding to the basic assumption (13) a series expansion in terms of eigenwarpings.

$$n(s,z) = n_{sv} + \sum_i A_{nn} W_i(s) K_i(z) \tag{33}$$

The Reissener principle (14) is used here again to derive the solution. The system of two differential equations resulting from the variations on w and q is integrated as previously for the terms pertaining to the basic Saint-Venant solution (see Appendix A). The remaining terms of the system can be identified as the Euler equations of the functional (25) which are satisfied by all eigenwarpings. The complete solution to this system is then placed into the functional (15) which becomes

$$\pi_R = \pi_{Rsv} + \sum_i \int_0^L \left(-\frac{1}{2} \frac{K_i'^2}{\mu_i^2} - \frac{1}{2} K_i^2 + \frac{d_i'}{\mu_i^2} K_i \right) dz \tag{34}$$

where π_{Rsv} is the Reissner functional for the Saint-Venant solution (15). Here again the basic solution is decoupled from the corrective terms, as are the different corrective terms from each other. Minimization of π_{Rsv} will render the Saint-Venant solution (19) and minimization of the corrective terms with respect to K_i gives

$$K_i'' - \mu_i^2 K_i = -d_i' \tag{35}$$

The solution of this simple differential equation gives the solution of the problem as

$$w = w_{sv} + \sum_i \frac{W_i}{\mu_i^2} K_i' \quad u' = u_{sv}' + \sum_i \frac{U_i}{\mu_i^2} K_i'$$

$$n = n_{sv} + \sum_i A_{nn} W_i K_i \quad v' = v_{sv}' + \sum_i \frac{V_i}{\mu_i^2} K_i' \tag{36}$$

$$q = q_{sv} + \sum_i A_{qq} \frac{\Gamma_i}{\mu_i^2} K_i' \quad \theta' = \theta_{sv}' + \sum_i \frac{\Xi_i}{\mu_i^2} K_i'$$

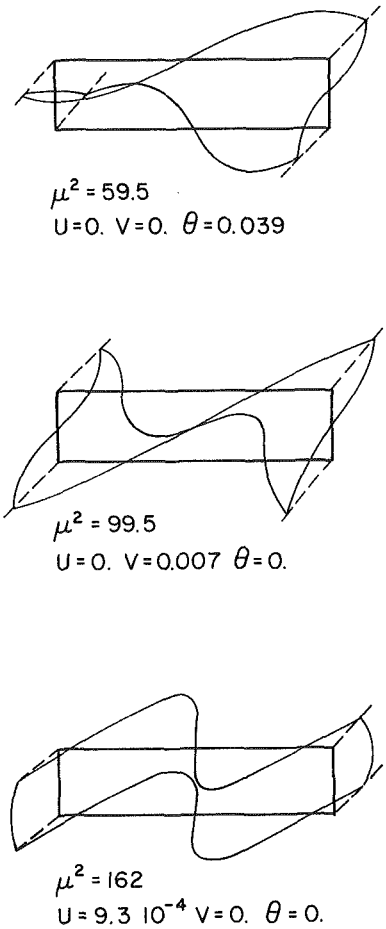


Fig. 3 A few eigenwarpings of the rectangular section

For infinite series, equation (36) give the exact solution to the problem, again under the assumption of infinite inplane rigidity of the section. Solution (32) is based on an assumed displacement approach and yield a lower bound of the strain energy if a truncated series expansion is used. On the other hand, solution (36) is based on an assumed equilibrating stress field yielding an upper bound of the strain energy for truncated series expansion.

8 Numerical Examples

A specific example is treated here, using the different approaches described in the previous sections. Figure 2 depicts the thin-walled, rectangular cross-sectional beam to be analyzed. The aspect ratio $L/h = 4$. The first step is to calculate the eigenwarpings W_i and the associated eigenvalues μ_i. The eigenvalue problem (26) can be solved using a finite element technique where the function W is discretized over the section. Then, a standard subspace iteration method allows the calculation of the eigenvalues and eigenwarpings. For this example, 36 nodal points were used to model the section and 24 eigenwarpings were extracted. The first few modes are shown in Fig. 3. If the beam is subjected to a uniform load p_o in the y direction, the differential equation (31) to be solved for the improved Bernoulli approach is

$$F_i'' - \mu_i^2 F_i = -p_0 V_i (L - z)$$

Boundary conditions at $z = 0 \quad F_i = 0$; at $z = L \; F_i' = 0$

This equation is readily integrated to give the final solution (32). In particular the tip deflection of the beam is found to be:

Downloaded 02 May 2010 to 171.66.16.54. Redistribution subject to ASME license or copyright; see http://www.asme.org/terms/Terms_Use.cfm

Table 1 Numerical results for the different approaches

	Tip deflection $\frac{V_{tip}}{p_0 L^4}$ [10^{-6}m]		Tip twist $\frac{\theta_{tip}}{m_0 L^4}$ [10^{-6}]	
	"Bernoulli"	"Saint-Venant"	"Bernoulli"	"Saint-Venant"
Euler	3.29	3.29		
Shear	0.734	1.57	91.70	143.3
	$\Delta = 19\%$		$\Delta = 44\%$	
1st term	0.446	−0.160	20.65	−9.90
2nd term	0.104	−0.0176	10.05	−2.10
3rd term	0.0283	−0.00311	3.57	−0.463
4th term	0.00229	−0.000186	0.722	−0.067
Total	4.604	4.677	126.7	130.
	$\Delta = 1.5\%$		$\Delta = 3\%$	

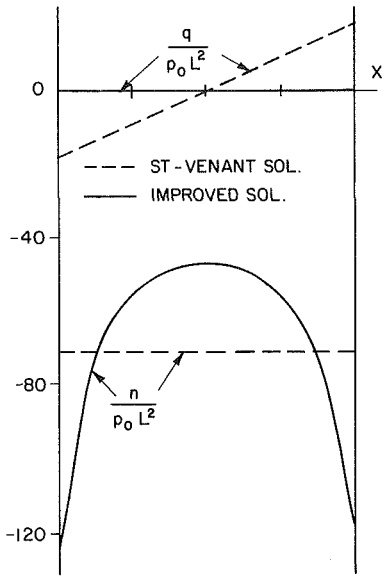


Fig. 4 Stress distributions in the upper skin of the beam (root section) under uniform transverse load p_0

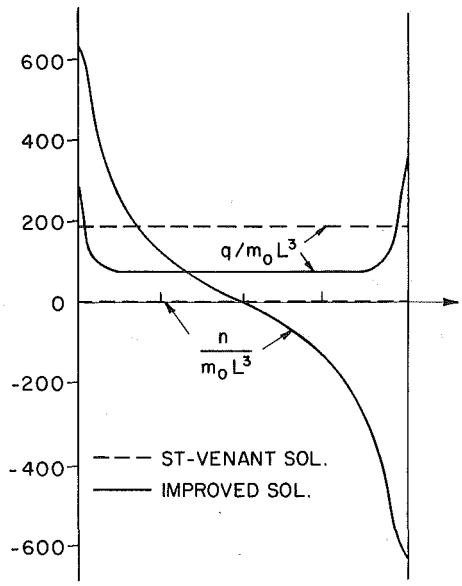


Fig. 5 Stress distributions in the upper skin of the beam (root section) under uniform torque m_0

$$\frac{v_{tip}}{P_0 L^4} = \frac{1}{8 I_{yy}} + \frac{1}{2 L^2 A_{yy}} + \sum_i \left(\frac{V_i}{\mu_i L}\right)^2 \left[\frac{1}{2} + \frac{1}{\mu_i^2 L^2} - \frac{1 + \mu_i L sh \mu_i L}{\mu_i^2 L^2 ch \mu_i L}\right] \tag{37}$$

The first term represents the bending deflection, the second term is the shearing deflection, and the summation represents the corrective deflections due to the different eigenwarping terms. Alternatively the improved Saint-Venant approach requires to solve equation (35),

$$K_i'' - \mu_i^2 K_i = p_0 V_i$$

Boundary conditions at $z = 0$ $K_i' = -p_0 L V_i$; at $z = L$ $K_i = 0$

From the general solution (36) the tip deflection is now

$$\frac{v_{tip}}{p_0 L^4} = \frac{1}{8 I_{yy}} + \frac{V_y}{2 L^2} + \sum_i \left(\frac{V_i}{\mu_i^2 L^2}\right)^2 \left[1 - \frac{1 + \mu_i L \mathrm{sh} \mu_i L}{\mathrm{ch} \mu_i L}\right] \tag{38}$$

Table 1 lists the numerical results for the two approaches. A comparison between the basic Bernoulli and Saint-Venant solutions shows a discrepancy of 20 percent. After adding three corrective terms this discrepancy is reduced to about 1 percent, showing that both solutions have converged. It is important to note the excellent convergence rate of the Saint-Venant approach in $(1/\mu_i L)^4$ versus $(1/\mu_i L)^2$ for the Bernoulli approach. Considering one term only in the improved Saint-Venant approach leads to a solution acceptable for engineering purposes. It should be noted here that according to (26), the eigenvalues μ_i are proportional to $\sqrt{A_{qq}/A_{nn}}$. Thus the magnitude of the corrective terms in the improved Saint-Venant approach is proportional to $(A_{nn}/A_{qq})^2$ resulting in large corrections for highly anisotropic materials.

If the beam is subjected to a uniform torque m_0, the tip twist $\theta_{tip}/m_0 L^4$ can be calculated in a similar fashion. The tip twist are $1/2 I_p L^2$ and $1/2 J L^2$ for the basic Bernoulli and Saint-Venant approaches, respectively. The corrective terms are identical to those in (37) and (38) except that V_i is replaced by Ξ_i. The results are summarized in Table 1 and show a 44 percent discrepancy for the basic solutions. The corrective terms reduce this discrepancy to about 3 percent. Again the Saint-Venant approach shows a better convergence rate; two corrective terms are necessary here to obtain an accurate solution.

It is also interesting to compute the stress distribution at the root of the beam. Figure 4 shows the distribution of axial stresses $n/p_0 L^2$ and shear stess $q/p_0 L^2$ in the upper face of the beam under a uniform loading p_0, using the improved Saint-Venant approach (36). Instead of the uniform axial stress predicted by the basic theory, a large shear lag effect is

Downloaded 02 May 2010 to 171.66.16.54. Redistribution subject to ASME license or copyright; see http://www.asme.org/terms/Terms_Use.cfm

observed. Figure 5 depicts the stress distributions when the loading is a uniformly distributed torque m_0. Here the uniform shear stress distribution predicted by the basic theory is significantly altered and large axial stresses are generated near the corners of the section.

9 Conclusion

Two approaches for an improved beam theory have been developed, consisting both of a series expansion of the exact solution in terms of eigenwarpings. The Saint-Venant approach shows an excellent convergence rate and for a specific example two terms of the series were shown to give accurate results.

Instead of solving the differential equations (31) or (35) exactly, a finite element approach is possible. The energy principles (29) or (34) can be used to derive the stiffness matrices for improved beam elements.

This theory is not limited to thin-walled box beams. In the case of solid cross sections, the concept of eigenwarpings can be extended as long as the basic assumption remains valid, i.e., as long as the section can be assumed infinitely rigid in its own plane. Once the eigenwarpings are found, the solutions (32) or (36) remain valid.

Acknowledgments

This research was supported by NASA and AFOSR under NASA Grant NGL 33-018-003, Dr. M. Greenfield and Dr. A. Amos are technical monitors, in the respective agencies.

References

1 Von Karman, Th., and Chien, W. Z., "Torsion With Variable Twist," *Journal of the Aeronautical Sciences*, Vol. 13, No. 10, Oct. 1946, pp. 503–510.

2 Argyris, J. H., and Dunne, P. C., "The General Theory of Cylindrical and Conical Tubes Under Torsion and Bending Loads," *J. of Royal Aero. Soc.*, Vol. 51, 1947, pp. 199–269; 757–784; 844–930.

3 Horgan, C. O., "On Saint-Venant's Principle in Plane Anisotropic Elasticity," *J. of Elasticity*, Vol. 2, 1972, pp. 169–180.

4 Choi, I., and Horgan, C. O., "Saint-Venant's Principle and End Effects in Anisotropic Elasticity," ASME JOURNAL OF APPLIED MECHANICS, Vol. 44, 1977, pp. 424–430.

5 Goetschel, D. B., and Hu, T. H., "Quantification of Saint-Venant's Principle for a General Prismatic Member," ASME JOURNAL OF APPLIED MECHANICS, to appear.

6 Reissener, E., "On a Variational Theorem in Elasticity," *J. of Math. and Phys.*, Vol. 29, No. 22, July 1950, pp. 90–95.

7 Tsai, S. W., and Hahn, H. T., *Introduction to Composite Materials*, Technonic, 1980.

APPENDIX A

In developing the Saint-Venant theory, the differential system (16) must be integrated. The solution for $w(s,z)$ consists of a linear part (identical to the Bernoulli solution) plus an additional warping function $g(s,z)$:

$$w(s,z)=Z(z)+(x-x_n)X(z)+(y-y_n)Y(z)+g(s,z) \quad (A1)$$

Considering at first the B' term only at the right-hand side of the system and introducing (A1) gives

$$\frac{\partial q}{\partial s}=-A_{nn}(x-x_n)B'$$

$$\frac{\partial}{\partial s}[g+(x-x_n)(u'+X)+(y-y_n)(v'+Y)+Z]$$

$$-\frac{q}{A_{qq}}=0 \quad (A2)$$

The following type of solution is expected:

$$q(s,z)=Q(s)B' \quad g(s,z)=W(s)B'$$
$$u'+X=UB', \quad v+Y=VB', \quad Z=aB', \quad (A3)$$

which reduce the system (A2) to:

$$\frac{dQ}{ds}=-A_{nn}(x-x_n)$$

$$\frac{d\rho}{ds}-\frac{Q}{A_{qq}}=0 \quad (A4)$$

where

$$\rho(s)=W(s)+U(x-x_n)+V(y-y_n)+a \quad (A5)$$

System (A4) can be integrated now since s is the only variable left. Alternatively it is readily verified that (A4) are the Euler equations of the following functional

$$\pi_1=\frac{1}{2}\int_\zeta A_{qq}\left(\frac{d\rho_1}{ds}\right)^2 ds-\int_\zeta A_{nn}(x-x_n)\rho_1 ds \quad (A6)$$

The solution ρ_1 minimizes π_1, then successively

$$Q_1(s)=A_{qq}\frac{d\rho_1}{ds} \quad (A7)$$

and

$$W_1(s)=\rho_1-U_1(x-x_n)-V_1(y-y_n)-a_1 \quad (A8)$$

Finally W_1 is enforced to be a warping by setting

$$\int_\zeta A_{nn}W_1 ds=\int_\zeta A_{nn}(x-x_n)W_1 ds$$

$$=\int_\zeta A_{nn}(y-y_n)W_1 ds=0 \quad (A9)$$

these three relations are used to calculate a_1, U_1, and V_1.

In a second step we consider only the C' term in (16). Following the same procedure as in the foregoing, the solution ρ_2 is found from minimizing

$$\pi_2=\frac{1}{2}\int_\zeta A_{qq}\left(\frac{d\rho_2}{ds}\right)^2 ds-\int_\zeta A_{nn}(y-y_n)\rho_2 ds \quad (A10)$$

$Q_2(s)$ and $W_2(s)$ then follow like in (A7) and (A8). In a last step, the θ' term in (16) is integrated. Following once again a similar procedure, the system now reduces to

$$\frac{dQ}{ds}=0$$

$$\frac{d\rho}{ds}-\frac{Q}{Aqq}=-\rho_k$$

The equation can be integrated directly or show to be equivalent to the minimization of

$$\pi_t=\frac{1}{2}\int_\zeta A_{qq}\left(\frac{d\rho_t}{ds}\right)^2 ds+\int_\zeta A_{qq}\tau_k\left(\frac{d\rho_t}{ds}\right)ds \quad (A12)$$

and finally

$$Q_t=A_{qq}\left(\frac{d\rho_t}{ds}+\tau_k\right) \quad (A13)$$

and

$$W_t=\rho_t-U_t(x-x_n)-V_t(y-y_n)-a_t$$

The complete solution of system (16) is obtained by adding the different contributions:

$$q(s,z)=Q_1B'+Q_2C'+Q_t\theta'$$
$$w(s,z)=Z(z)+(x-x_n)X(z)+(y-y_n)Y(z)$$
$$+W_1B'+W_2C'+W_t\theta'$$
$$u'=U_1B'+U_2C'+U_t\theta'-X$$
$$v=V_1B'+V_2C'+V_t\theta'-Y \quad (A15)$$

In later developments it will be convenient to use linear combinations of these solutions, for instance

Downloaded 02 May 2010 to 171.66.16.54. Redistribution subject to ASME license or copyright; see http://www.asme.org/terms/Terms_Use.cfm

$$Q_x = i_{xx}Q_1 + i_{xy}Q_2 \qquad (A16)$$

$$Q_y = i_{xy}Q_1 + i_{yy}Q_2 \qquad (A16)$$

W_x, W_y; U_x, U_y and V_x, V_y can be defined similarly.

APPENDIX B

The inplane stiffness of an orthotropic laminate can be written in matrix form as [7]:

$$\begin{bmatrix} n \\ n_t \\ q \end{bmatrix} = \begin{bmatrix} A_{11} & A_{12} & A_{16} \\ A_{21} & A_{22} & A_{26} \\ A_{61} & A_{62} & A_{66} \end{bmatrix} \begin{bmatrix} \epsilon \\ \epsilon_t \\ \lambda \end{bmatrix} \qquad (B1)$$

where n_t and ϵ_t are the stress and strain in the direction tangent to the cross-sectional curve. The assumption of infinite inplane rigidity of the cross section allows to set $n_t \simeq 0$ so that $B1$ reduces to:

$$\begin{bmatrix} n \\ q \end{bmatrix} = \begin{bmatrix} A_{nn} & A_{nq} \\ A_{nq} & A_{qq} \end{bmatrix} \begin{bmatrix} \epsilon \\ \lambda \end{bmatrix} \qquad (B2)$$

where

$$A_{nn} = A_{11} - A_{12}^2/A_{22}, \quad A_{qq} = A_{66} - A_{26}^2/A_{22},$$
$$A_{nq} = A_{16} - A_{12}A_{26}/A_{22} \qquad (B3)$$

when the material is isotropic, an orthotropic with the axes of orthotropy parallel to the axis of the beam and the tangent to the cross-sectional curve, we have $A_{16} = A_{26} = 0$, thus $A_{nq} = 0$ and equations (32) are decoupled as (1) and (2).

Downloaded 02 May 2010 to 171.66.16.54. Redistribution subject to ASME license or copyright; see http://www.asme.org/terms/Terms_Use.cfm

Theoretical Estimation of the Response of Helically Armored Cables to Tension, Torsion, and Bending

J. Lanteigne
Research Scientist,
Institut de Recherche d'Hydro-Québec,
1800 Montée Ste-Julie,
Varennes, Québec,
Canada J0L 2P0

This paper concerns the mechanical behavior of ACSR (aluminum conductor steel-reinforced) conductors under static-loading conditions, which may comprise any combination of tension, torsion, and bending. The model described is quite general and can be applied to other types of helically armored cables. A stiffness matrix is developed and relations are given for axial, torsional, and flexural rigidities and for coupling parameters. For small curvatures, the flexural rigidity is comparable to the upper limit accepted in current practice by ACSR users. As the curvature increases, however, frictional forces develop between the outer layers and sliding of wires may occur, with the result that the flexural rigidity decreases. The tension level also influences the flexural rigidity of the conductor. Actually the model does not consider the flexural rigidity of the system as a fixed entity but as directly influenced by local compressive forces and internal radial and tensile forces. The analysis can also apply to situations where a given number of initial constituent wires have failed and the load is transferred to neighboring wires, leaving the conductor unbalanced; it will be seen how internal arrangements manage to accommodate the local perturbation.

Introduction

Helically armored cables are used intensively in many applications such as electromechanical and communication links, suspension bridges, power transmission lines, etc. One such cable is illustrated schematically in Fig. 1. It consists of N layers of wires helically wrapped around a central core. The radius R_n of layer n is given by the distance from the cable centerline to the center of any constituent wire of that layer. The inclination of the wire to the cable centerline defines the lay angle α_n, a right-hand lay being considered positive; adjacent layers are always alternate. All wires of a specific layer have the same radius r_n, but can differ from one layer to another. The radius of the central core is defined as r_c. This configuration is quite general and may be characteristic of many types of cable. The work described here, however, was mainly devoted to ACSR conductors. ACSR conductors are composite structural elements. Usually the central core and the first inner layer consist of steel wire with the other layers made of cold-drawn aluminum wire. In-service conductors are always exposed to external loads: the axial tension is permanently exerted while transverse eolian vibrations induce tension variations and a dynamic curvature along the span. The dynamic curvature is maximum near the suspension clamps where, in addition, the conductor is subjected to a static curvature, due to the sag of the span, as well as the compressive forces exerted by the clamping devices. ACSR conductors are not usually self-equilibrating cables so that when they are subjected to an external tension, an internal torque induced tries to "unwind" the conductor [1]. As a result, any variation in the tension excites a torsional

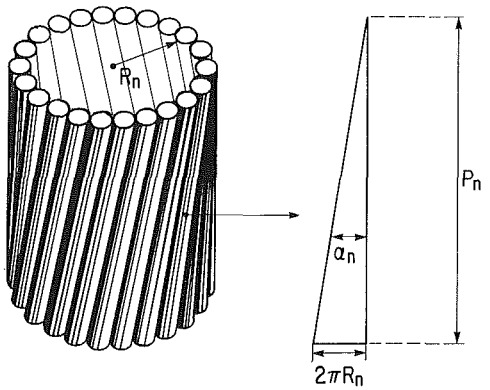


Fig. 1 Layer *n* of an ACSR conductor

Contributed by the Applied Mechanics Division for presentation at the 1985 Joint ASME/ASCE Applied Mechanics, Fluids Engineering, and Bioengineering Conference, Albuquerque N. Mex., June 24–26, 1985 of THE AMERICAN SOCIETY OF MECHANICAL ENGINEERS.

Discussion on this paper should be addressed to the Editorial Department, ASME, United Engineering Center, 345 East 47th Street, New York, N.Y. 10017, and will be accepted until two months after final publication of the paper itself in the JOURNAL OF APPLIED MECHANICS. Manuscript received by ASME Applied Mechanics Division, January, 1984; final revision, July, 1984. Paper No. 85-APM-13.

Copies will be available until February, 1986.

Copyright © 1985 by ASME
Downloaded 02 May 2010 to 171.66.16.54. Redistribution subject to ASME license or copyright; see http://www.asme.org/terms/Terms_Use.cfm

vibration mode, transmitting a torque to the support. Depending on the clamping force, the conductor can rotate in the support and cause fretting damage. In addition, the dynamic curvature produces a variation in the axial stress in the wires, whose level is largely dependent on the flexural rigidity of the conductor. Such reversed-bending cycles are frequently terminated by the fatigue failure of some constituent wires. For effective control of the life expectancy of conductors, a number of questions need to be clarified: What is the stress variation in a wire during a time cycle and how much does it decrease with the distance from the suspension clamp? How can the configuration of the conductor and its tension level be modified in order to significantly reduce the bending stress amplitude and how does interwire friction influence fatigue behavior? Such questions obviously cannot be solved if the flexural rigidity is not estimated correctly. Many investigators are aware that this parameter changes within the span of a conductor in free vibration, when the measurements are performed at different distances from the suspension clamp and at different moments during the time cycle [2]. This phenomenon is considered, by the present author, to be directly related to the influences of local compressive forces and internal radial and tensile forces on the flexural rigidity of the system. In the absence of external compression on the conductor, the flexural rigidity is likely to decrease as the curvature increases. This could be analyzed as follows: when the curvature increases, the wires of the outermost layer could slide against the wires of the subjacent layer and, as a result, would separate and begin to behave individually. The system is then mechanically equivalent to a conductor whose internal layers act together as a structural member, and whose outer layer, consisting of individual wires, is "disconnected" from the original conductor. Thus, a 50 percent drop in the flexural rigidity, as previously reported in the literature [3], is a common characteristic of ACSR conductors.

In the first part of the model described here, the stiffness matrix of a straight cable element subjected to tension, torsion, and bending is derived for small curvatures. The second part is devoted to the dominant factors affecting the flexural rigidity of the conductor, when it is subjected to large curvatures. It will be observed that the axial case or coupled axial torsion is one that can also be treated by this analysis, although it has already been considered in detail in relevant papers. McConnel and Zemke [1], for example, recently proposed a model to predict the coupled axial torsion properties of ACSR conductors, and arrived at good predictions as confirmed by experiments. Previously, however, Knapp [4] arrived at a more fundamental development of the same problem applied to helical armored cables. This derivation was quite general (the cross section of the cable could consist of many structural components) and could describe, for instance, the coupled axial torsion of a cable having a central elastic core. The author therefore considered the compressibility of the core, the variation of the lay angles, and the variation of the intrinsic radii of torsion and curvature of helical wires, due to axial loading. Costello [5] and Costello and Butson [6] have recently addressed the tension, torsion, and bending problem, assuming frictionless cables, but taking into consideration internal bending and twisting moments of individual wires.

Linear Analysis

1. Determination of Wire Axial Strain. The developed helix geometry of a typical wire i on layer n is shown in Fig. 1, for a single pitch length. As can be seen, the lay angle is given by $\tan \alpha_n = 2\pi R_n / P_n$, where P_n and R_n are the pitch length and the radius of layer n. A right-hand lay, as in Fig. 1, is defined positive. Consider now a conductor length l subjected to an axial elongation Δu and a rotation $\Delta\phi$ (defined positive when it is counterclockwise looking at the conductor cross section). As shown in Fig. 2, the wire axial strain is:

$$\epsilon_i = \frac{a' - a}{a} \tag{1}$$

Prime refers to the deformed state. The following geometrical relations are obtained from Fig. 2:

$$a = \frac{l}{\cos\alpha_n} \qquad a' = \frac{l + \Delta u}{\cos\alpha_n'}$$

$$\cos\alpha_n' = \frac{l + \Delta u}{\sqrt{(l+\Delta u)^2 + (l\tan\alpha_n + R_n\Delta\phi)^2}}$$

Combining these relations with equation (1), the axial strain of wire i becomes:

$$\epsilon_i = \sqrt{(1 + \Delta u/l)^2 \cos^2\alpha_n + (\sin\alpha_n + R_n\cos\alpha_n\Delta\phi/l)^2} - 1 \tag{2}$$

Equation (2) is linearized by neglecting second-order strain quantities in binomial expansions. This yields firstly,

$$(\epsilon_i + 1)^2 = 1 + 2\cos^2\alpha_n(\Delta u/l) + 2R_n\sin\alpha_n\cos\alpha_n(\Delta\phi/l)$$

Expanding further,

$$(\epsilon_i + 1)^2 = 1 + 2\epsilon_i$$

which gives

$$\epsilon_i = \cos^2\alpha_n(\Delta u/l) + R_n\sin\alpha_n\cos\alpha_n(\Delta\phi/l) \tag{3}$$

At this stage, a word should be said about the assumptions underlying equation (3) and the subsequent analysis. Since this model is designed mainly for ACSR conductors, it is assumed that the center core is rigid. Radial contraction due to deformation of the core under compressive stress developed by the wires is therefore neglected. Reduction of the lay radius R_n due to interwire contact is also neglected. Wire flattening is beyond the scope of this work, although radial force developed by the wires under tension is discussed later. The application of McConnel and Zemke [1] and Knapp [4] models to axial torsion problems in ACSR conductors leads to the same results, despite the fact that the latter author considered the variations of the lay angles and of the intrinsic radii of torsion and curvature of helical wires after cable deformation whereas the former did not. Therefore these variations are neglected here. It is also assumed that if curvatures are small,[1] plane sections of the conductor remain plane after elongation, torsion, and bending, an assumption that led to good theoretical predictions, in the simple case of coupled axial torsion, as confirmed by experiments [1, 4]. For cases in which conductor curvatures are considered, this assumption will result in high estimation of the flexural rigidity IE. All strain quantities should be small[2] and all constituents homogeneous, isotropic, and linear elastic. Since the position of a helical wire is described by its centroidal axis, some geometrical considerations are also necessary: The diameter of any constituent wire should be small compared to the pitch length of its layer and to the diameter of the conductor.

Conductor bending will now be introduced into the analysis. Consider a conductor length bent to a curvature $1/c = \partial\psi/\partial z$, in addition to the previous strains $\partial u/\partial z$ and $\partial\phi/\partial z$, as shown in Fig. 3. Following the path of a typical wire, and keeping in mind that frictional forces contribute to maintain the cross-section plane after bending, it is seen that between A and B, the wire undergoes an axial elongation component due to the curvature. At B the wire crosses the neutral axis and between B and C undergoes an axial compression component

[1] A realistic estimation of whether curvature is small or large is given later.

[2] Large nonlinear displacements that are generally treated by geometric stiffness matrices in addition to the linear stiffness matrix are not covered in this paper.

Downloaded 02 May 2010 to 171.66.16.54. Redistribution subject to ASME license or copyright; see http://www.asme.org/terms/Terms_Use.cfm

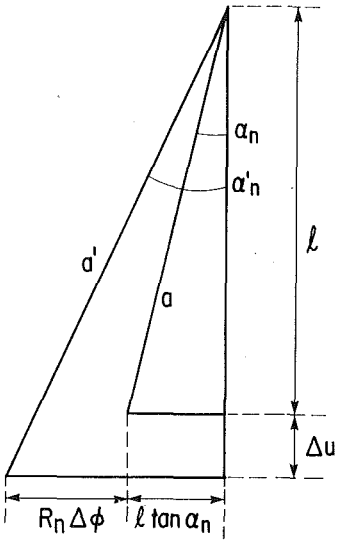


Fig. 2 Deformation of wire i of layer n

(a tension T giving rise to the cable axial strain $\partial u/\partial z$ is assumed permanently exerted, to avoid here the complex problem of strand buckling out of action). Next to be considered is the extension of the wire produced by the curvature at distance $y_i(z)$ from the neutral axis (see Fig. 3). Developing the wire over the small length dz, as in Fig. 2, equation (3) can be written:

$$\epsilon_i = \cos^2\alpha_n\,(\partial u/\partial z + y_i(z)\,\partial\psi/\partial z) + R_n \sin\alpha_n \cos\alpha_n (\partial\phi/\partial z) \quad (4)$$

where $y_i(z)\,\partial\psi/\partial z$ is the bending strain component. It is observed that the distance from the neutral axis $y_i(z)$ depends on the cross section z. Let us arbitrarily fix an origin $z = 0$ and find an expression for y_i at the section $z = 0$. As shown in Fig. 4, the mean distance from the conductor neutral axis to wire i is given by:

$$\bar{y}_i = R_n \sin\left(\frac{2\pi i}{K_n}\right) \quad (5)$$

where K_n is the number of wires in layer n. Moving from the cross section $z = 0$ to any cross section z, $y_i(z)$ varies according to:

$$\bar{y}_i(z) = R_n \sin\left(\frac{2\pi i}{K_n} + \frac{2\pi z}{P_n}\right)$$

or

$$\bar{y}_i(z) = R_n \sin\left(\frac{2\pi i}{K_n} + \frac{z\tan\alpha_n}{R_n}\right) \quad (6)$$

where z is the axial coordinate and P_n, the lay length of layer n. Substituting equation (6) into (4), the mean axial strain becomes:

$$\bar{\epsilon}_i(z) = \cos^2\alpha_n \frac{\partial u}{\partial z} + R_n \sin\alpha_n \cos\alpha_n \frac{\partial\phi}{\partial z}$$

$$+ R_n \cos^2\alpha_n \sin\left(\frac{2\pi i}{K_n} + \frac{z\tan\alpha_n}{R_n}\right)\frac{\partial\psi}{\partial z} \quad (7)$$

It should be noted that the axial strain due to curvature was determined at the centroid of wire i. Considering any location within the wire cross section, it is seen from Fig. 4 that the actual distance from this location to the conductor neutral axis is:

$$y_i(z) = \bar{y}_i(z) + \rho_i \sin\varphi_i \quad \text{where} \quad 0 < \rho < r_n, \quad 0 < \varphi < 2\pi \quad (8)$$

In equation (8) ρ_i and φ_i are the local polar coordinates of wire i. The general expression for the axial strain is therefore:

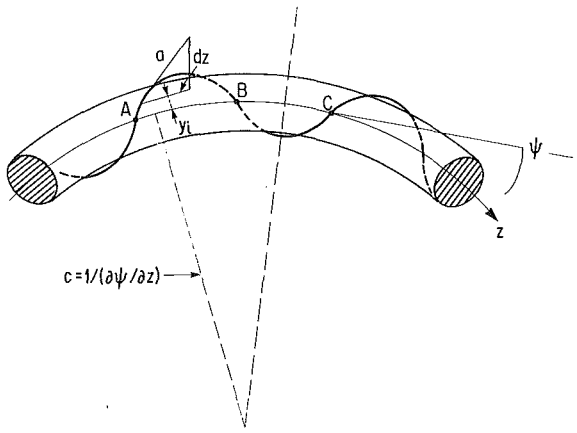


Fig. 3 A conductor length under uniform curvature $\partial\psi/\partial z$

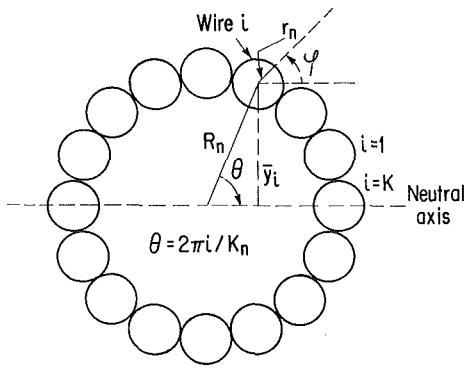


Fig. 4 Configuration of layer n (K_n wires) at cross section $z = 0$

$$\epsilon_i(z) = \cos^2\alpha_n \frac{\partial u}{\partial z} + R_n \sin\alpha_n \cos\alpha_n \frac{\partial\phi}{\partial z}$$

$$+ \left[R_n \sin\left(\frac{2\pi i}{K_n} + \frac{z\tan\alpha_n}{R_n}\right) + \rho_i \sin\varphi_i\right]\cos^2\alpha_n \frac{\partial\psi}{\partial z} \quad (9)$$

This equation expresses the axial strain of a wire in layer n of a conductor subjected to external strains $\partial u/\partial z$, $\partial\phi/\partial z$, and $\partial\psi/\partial z$ (axial deformation, rotational strain, and curvature). The axial force at the centroid of wire i is given as:

$$F_i(z) = A_n E_n \bar{\epsilon}_i(z) \quad (10)$$

where A_n and E_n are the cross section and Young's modulus of wires in layer n. It is seen, substituting equation (7) into equation (10), that the wire axial force can be expressed in terms of the three independent strain parameters:

$$F_i(z) = A_n E_n \left[\cos^2\alpha_n \frac{\partial u}{\partial z} + R_n \sin\alpha_n \cos\alpha_n \frac{\partial\phi}{\partial z}\right] + F_i^b(z) \quad (11)$$

where F_i^b is the wire axial force component due to cable bending. It can be expressed by:

$$F_i^b(z) = A_n E_n R_n \cos^2\alpha_n \sin\left(\frac{2\pi i}{K_n} + \frac{z\tan\alpha_n}{R_n}\right)\frac{\partial\psi}{\partial z} \quad (12)$$

The maximum value of F_i^b for a wire i in layer n occurs at the cross section z satisfying the condition

$$\frac{2\pi i}{K_n} + \frac{z\tan\alpha_n}{R_n} = \frac{\pi}{2}.$$

It is given by:

$$F_n^b = A_n E_n R_n \cos^2\alpha_n \frac{\partial\psi}{\partial z} \quad (13)$$

From equation (12), one sees that the following peculiarities become apparent:

Downloaded 02 May 2010 to 171.66.16.54. Redistribution subject to ASME license or copyright; see http://www.asme.org/terms/Terms_Use.cfm

$$\sum_{i=1}^{K_n} F_i^b \cos\alpha_n = 0.$$

(1) The projection of F_i^b onto the conductor axis, summed for all wires K_n of layer n, gives 0. Therefore, at any cross section, the curvature of the conductor will not produce a net conductor elongation.

$$\sum_{i=1}^{K_n} F_i^b \sin\alpha_n = 0.$$

(2) The cross-sectional component of F_i^b, summed for all wires K_n of layer n, gives 0. Therefore, at any cross section, the curvature of the conductor will not produce a net conductor rotation.

$$\int_0^{P_n} F_i^b dz = 0.$$

(3) Averaging F_i^b over the pitch length P_n gives 0, which is the local extension of the wire, when it is considered at section z_1, is compensated by the same amount of compression at $z_2 = z_1 + P_n/2$.

The first two statements are not valid however when some constituent wires are not carrying the external loads (simulating wire failures), since in that case

$$\sum_{i=1}^{K_n} \sin\left(\frac{2\pi i}{K_n}\right) \neq 0$$

2. Internal Strain Energy and External Potential Energy. A conductor length l is subjected to uniform elongation Δu, rotation angle $\Delta\phi$, and bending angle $\Delta\psi$. The deformed state of wire i can be described by equation (9) as:

$$\epsilon_i(z) = \cos^2\alpha_n \frac{\Delta u}{l} + R_n \sin\alpha_n \cos\alpha_n \frac{\Delta\phi}{l} + \left[R_n \sin\left(\frac{2\pi i}{K_n} + \frac{z\tan\alpha_n}{R_n}\right) + \rho_n \sin\varphi_n\right] \cos^2\alpha_n \frac{\Delta\psi}{l} \tag{14}$$

Let the displacements be changed by the amounts $\delta(\Delta u)$, $\delta(\Delta\phi)$, and $\delta(\Delta\psi)$.

The variation of internal strain energy is then given by:

$$\delta U_i = E_n \int\int\int_{v_n} \epsilon_i \delta\epsilon_i dv_n \tag{15}$$

where dv_n is the element of volume $\rho_n d\rho_n d\varphi_n dz/\cos\alpha_n$ of any wire in layer n, and $\delta\epsilon_i$, the increment of axial strain. Differentiating equation (14), substituting into equation (15), and integrating, an expression is obtained for the variation of the internal strain energy of wire i. Summing over all wires $i = 1$, K_n and all layers $n = 1, N$ yields:

$$\delta U = \sum_{n=1}^{N} \sum_{i=1}^{K_n} \delta U_i + \delta U_c \tag{16}$$

where δU_c is the contribution of the wire core. The full expression for equation (16) is:

$$\begin{aligned}\delta U = &\sum_{n=1}^{N} \sum_{i=1}^{K_n} A_n E_n \{\cos^3\alpha_n \Delta u + R_n \sin\alpha_n \cos^2\alpha_n \Delta\phi \\ &+ A_{in}\Delta\psi\}\delta\left(\frac{\Delta u}{l}\right) + \sum_{n=1}^{N} \sum_{i=1}^{K_n} A_n E_n \{R_n \sin\alpha_n \cos^2\alpha_n \Delta u \\ &+ R_n^2 \sin^2\alpha_n \cos\alpha_n \Delta\phi + A_{in} R_n \tan\alpha_n \Delta\psi\}\delta\left(\frac{\Delta\phi}{l}\right) \\ &+ \sum_{n=1}^{N} \sum_{i=1}^{K_n} A_n E_n \left\{A_{in}\Delta u + A_{in} R_n \tan\alpha_n \Delta\phi + \left(B_{in} + \frac{(R_n^2 + r_n^2/2)}{2}\cos^3\alpha_n\right)\Delta\psi\right\}\delta\left(\frac{\Delta\psi}{l}\right) + A_c E_c \Delta u \delta\left(\frac{\Delta u}{l}\right) \\ &+ J_c G_c \Delta\phi\delta\left(\frac{\Delta\phi}{l}\right) + I_c E_c \Delta\psi\delta\left(\frac{\Delta\psi}{l}\right)\end{aligned} \tag{17}$$

where A_c, E_c, G_c, I_c, and J_c are the wire core cross section, Young's modulus, shear modulus, planar, and polar moments of inertia, respectively. A_{in} and B_{in} are given by:

$$A_{in} = \frac{R_n{}^2 \cos^3\alpha_n}{l\tan\alpha_n}\left[\cos\left(\frac{2\pi i}{K_n}\right) - \cos\left(\frac{2\pi i}{K_n} + \frac{l\tan\alpha_n}{R_n}\right)\right]$$

$$B_{in} = \frac{R_n{}^3 \cos^3\alpha_n}{4l\tan\alpha_n}\left[\sin\left(\frac{4\pi i}{K_n}\right) - \sin\left(\frac{4\pi i}{K_n} + \frac{2l\tan\alpha_n}{R_n}\right)\right] \tag{18}$$

The variation in the internal strain energy expressed by equation (17) is produced by a variation in the external potential energy δV:

$$\delta V = T\delta(\Delta u) + \mathfrak{T}\delta(\Delta\phi) + \mathfrak{M}\delta(\Delta\psi) \tag{19}$$

where T, $\mathfrak{T}$, and $\mathfrak{M}$ are the applied tension, torque, and bending moment, respectively. Equating (19) and (17) according to the principle of stationary potential energy at equilibrium, and since Δu, $\Delta\phi$, and $\Delta\psi$ are independent coordinates, the following relation is obtained:

$$\begin{Bmatrix} T \\ \mathfrak{T} \\ \mathfrak{M} \end{Bmatrix} = \begin{bmatrix} (AE) & k_{T\mathfrak{T}} & k_{T\mathfrak{M}} \\ k_{T\mathfrak{T}} & (JG) & k_{\mathfrak{T}\mathfrak{M}} \\ k_{T\mathfrak{M}} & k_{\mathfrak{T}\mathfrak{M}} & (IE) \end{bmatrix} \begin{Bmatrix} \Delta u/l \\ \Delta\phi/l \\ \Delta\psi/l \end{Bmatrix} \tag{20}$$

where (AE), (JG), and (IE) are the effective axial, torsional, and flexural rigidities and $k_{T\mathfrak{T}}$, $k_{T\mathfrak{M}}$, and $k_{\mathfrak{T}\mathfrak{M}}$ are stiffness coefficients for coupled axial torsion, axial bending and torsion bending. They are given by:

$$\begin{aligned}(AE) &= \sum_{n=1}^{N} K_n A_n E_n \cos^3\alpha_n + A_c E_c \\ (JG) &= \sum_{n=1}^{N} K_n A_n E_n R_n^2 \sin^2\alpha_n \cos\alpha_n + J_c G_c \\ (IE) &= \sum_{n=1}^{N} K_n A_n E_n \left(\frac{r_n^2/2 + R_n^2}{2}\right)\cos^3\alpha_n + I_c E_c \\ &\quad + \sum_{n=1}^{N} \sum_{i=1}^{K_n} A_n E_n B_{in} \\ k_{T\mathfrak{T}} &= \sum_{n=1}^{N} K_n A_n E_n R_n \sin\alpha_n \cos^2\alpha_n \\ k_{T\mathfrak{M}} &= \sum_{n=1}^{N} \sum_{i=1}^{K_n} A_n E_n A_{in} \\ k_{\mathfrak{T}\mathfrak{M}} &= \sum_{n=1}^{N} \sum_{i=1}^{K_n} A_n E_n A_{in} R_n \tan\alpha_n\end{aligned} \tag{21}$$

The stiffness matrix given by equation (20) is found to be symmetric. This happens essentially for two reasons: first, the strain equation (2) was linearized prior to integration (15), and the contraction δR_n was neglected. Stiffness coefficients (21) are developed for the most general case where structural integrity needs not be preserved (e.g., one or several strands of the conductor may have failed). In such a case, the conductor is unbalanced, and coupling parameters $k_{T\mathfrak{M}}$ and $k_{\mathfrak{T}\mathfrak{M}}$ are necessary to describe the static state of equilibrium. If the

Downloaded 02 May 2010 to 171.66.16.54. Redistribution subject to ASME license or copyright; see http://www.asme.org/terms/Terms_Use.cfm

configuration of the conductor is symmetrical, the following expression is obtained for each layer:

$$\sum_{i=1}^{K_n} \cos\left(\frac{2\pi i}{K_n}\right) = 0$$

$$\sum_{i=1}^{K_n} \sin\left(\frac{4\pi i}{K_n}\right) = 0 \tag{22}$$

As a result,

$$\sum_{i=1}^{K_n} A_{in} = 0$$

$$\sum_{i=1}^{K_n} B_{in} = 0 \tag{23}$$

and the stiffness coefficients become:

$$k_{T\mathfrak{M}} = 0$$

$$k_{\mathfrak{J}\mathfrak{M}} = 0$$

$$(IE) = \sum_{n=1}^{N} K_n A_n E_n \frac{(r_n^2/2 + R_n^2)}{2} \cos^3\alpha_n + I_c E_c \tag{24}$$

The other coefficients remain unchanged.

The Influence of Internal Radial Forces and Curvature on the Effective Flexural Rigidity of the Conductor

In the preceding analysis it was assumed that interstrand friction could validate the assumption of plane cross sections of a flexed conductor. The real situation is much more complex however. In fact it has been observed that sometimes only the internal layers of a conductor length under bending act together while the outer strands could move individually [3]. This section will focus on the influence of the axial and radial forces of strands on the effective rigidity of a conductor under bending. The radial pressure exerted by a layer is maximum on the central wire core, which is subjected to the pressure of all layers, and minimum at the interface between the outer layer and the directly subjacent layer. As will be seen next, the cohesive forces are largest at the center and decrease toward the surface whereas when the conductor is bent, tensile forces develop in the strands that, contrary to radial forces, increase from the neutral axis to the outermost strand. For small curvatures, the layers behave very much as predicted by equation (21) but, as the curvature increases, a level is reached where the tensile forces built up are sufficient to overcome the interstrand frictional forces. From that level, wires start sliding. This occurs primarily at the outermost layer, where the bending stress is maximum and, as stated earlier, the radial forces are minimum. Upon further bending effort, sliding could also occur between subjacent layers causing a substantial decrease in the overall flexural rigidity of the system.

To illustrate this, let a frictionless conductor be subjected to a tension T and a curvature $\partial\psi/\partial z$ as shown in Fig. 5(a). Since in that case all wires are bent about their own axis, the distance from the neutral axis is given by $-r_n \le y \le r_n$ for a wire in layer n. Substituting equation (4) in equation (10), the wire axial force can be written:

$$F_n = F_n^T + F_n^b \tag{25}$$

where

$$F_n^b = A_n E_n y \cos^2\alpha_n \frac{\partial\psi}{\partial z} \tag{26}$$

No tensile force is developed on bending at the centroid of the wires ($F_n^b = 0$). If layer $n-1$ consists of wires of the same radius and material, the difference in axial force, when compared to equation (26), is only due to the lay angle.

Consider now that friction acts to maintain the cross section plane after bending as shown in Fig. 5(b). Let first the conductor be subjected to the tensile load T. The resulting axial forces of wires are obtained from equations (4) and (10):

$$F_n^T = A_n E_n \left[\cos^2\alpha_n \frac{\partial u}{\partial z} + R_n \sin\alpha_n \cos\alpha_n \frac{\partial\phi}{\partial z}\right] \tag{27}$$

It was previously assumed that cross sections of the conductor remained plane after elongation. In other words, at every interstrand contact point of two wires of adjacent layers, there should not exist a significant difference in axial displacement of a wire relatively to the other. Therefore it is reasonable to assume that friction plays a negligible role when there is no tendency for wires to displace one against another. It could be reasonable to assume further that frictional forces become apparent when significant difference in axial force is observed on two adjacent layers. Then let the conductor be bent to the curvature $\partial\psi/\partial z$. As developed earlier, the maximum tensile force built up at the centroid of a wire in layer n is given by equation (13):

$$F_n^b = A_n E_n R_n \cos^2\alpha_n \frac{\partial\psi}{\partial z} \tag{28}$$

Similarly in layer $n-1$ (counting layers from the inside):

$$F_{n-1}^b = A_{n-1} E_{n-1} R_{n-1} \cos^2\alpha_{n-1} \frac{\partial\psi}{\partial z} \tag{29}$$

If these layers consist of wires of the same radius and material, then:

$$F_n^b = F_{n-1}^b + AE \frac{\partial\psi}{\partial z} [R_n \cos^2\alpha_n - R_{n-1} \cos^2\alpha_{n-1}] \tag{30}$$

These tensile forces develop if a frictional force F_n^f, at interstrand contact point of two outermost wires of layers n and $n-1$, is added to already present force F_{n-1}^b of layer $n-1$ to build a tensile force $F_n^b = F_{n-1}^b + F_n^f$ on layer n (see Fig. 5(b)). Therefore according to equation (30), the frictional force may be estimated by:

$$F_n^f = F_n^b - F_{n-1}^b = AE \frac{\partial\psi}{\partial z} [R_n \cos^2\alpha_n - R_{n-1} \cos^2\alpha_{n-1}] \tag{31}$$

Interstrand frictional force cannot exceed the critical value fF_n^c where f is the friction coefficient and F_n^c, the radial force exerted against the conductor axis at locations where wire n crosses wires of the sublayer $n-1$. Therefore sliding may occur when the following is satisfied:

$$(F_n^b - F_{n-1}^b) \ge fF_n^c \tag{32}$$

The achievement of criterion equation (32) can be proposed to estimate the onset of slippage of wires of layer n against the core formed by inner layers. Once slippage occurs, displacement of the wire along its length proceeds from the compressed region (beneath the neutral axis) toward the tensioned region (above the neutral axis). If sufficient slippage is allowed (i.e., equation (32) is satisfied for inner layers), the axial force component F_n^b would first relax to the value F_{n-1}^b and then further to F_{n-2}^b, F_{n-3}^b and ideally to 0 as in Fig. 5(a).

To incorporate equation (32) to the present analysis, an expression for the radial force component F_n^c is required. This force, exerted at interstrand contact points, is induced by the conductor tension and is increased locally when the conductor is subjected to a bending moment. Hruska [7] has established the basis to estimate the radial force per unit length f_n^c produced by a wire of layer n on inner layers, while under uniform tension along its length. Hruska's analysis is summarized in the following, using in the example, the four-layer conductor of Fig. 6 subjected to tensile loading. The radial

Downloaded 02 May 2010 to 171.66.16.54. Redistribution subject to ASME license or copyright; see http://www.asme.org/terms/Terms_Use.cfm

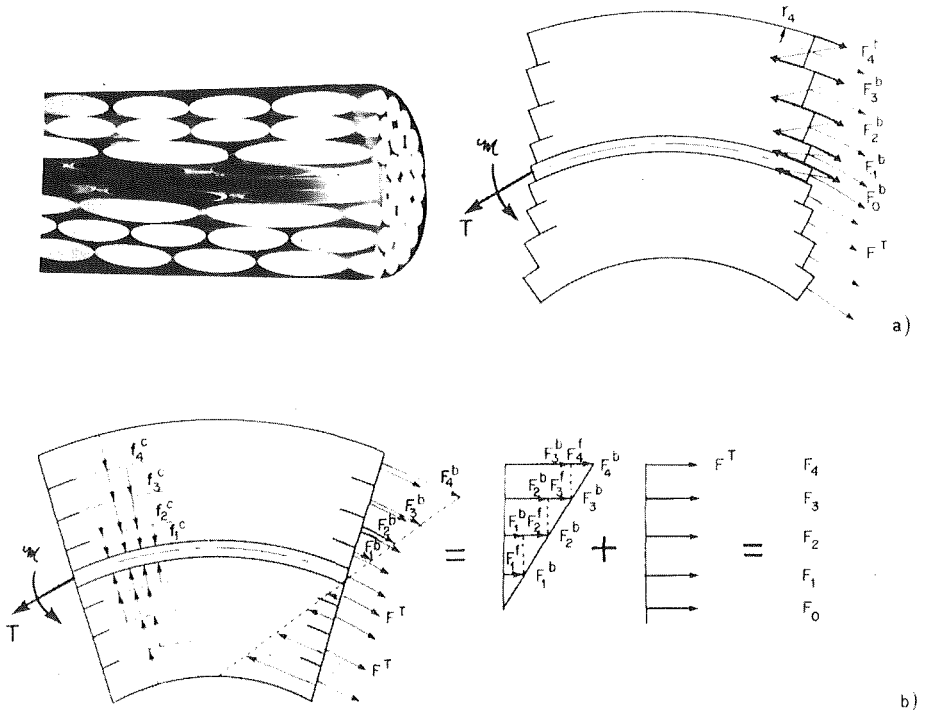


Fig. 5 Longitudinal section of the Bersimis 42/7 conductor and diagram of the loads assuming (*a*) frictionless wires and (*b*) the whole cable as a unit

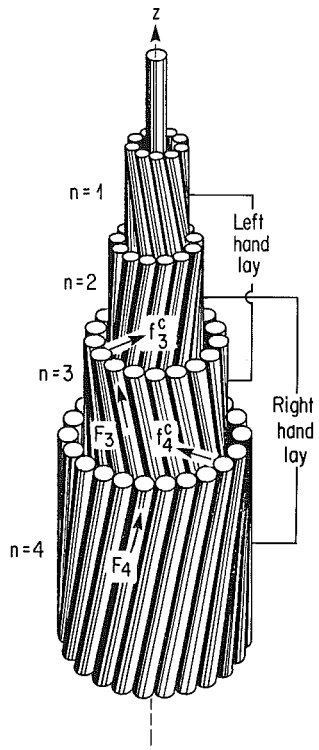


Fig. 6 Force components

force/length produced by any wire in layer 4 on layers 3, 2, 1 and on the core is given by $f_4^c = F_4/\rho$ where ρ is the radius of curvature of the wire which is equal to $R_4/\sin^2\alpha_4$ and F_4, the wire axial force, is given by equation (10). Hence:

$$f_4^c = \frac{F_4 \sin^2\alpha_4}{R_4}$$

A wire of layer 3 exerts a similar compression on inner layers, i.e., $F_3\sin^2\alpha_3/R_3$. Moreover, this wire must accept the compression produced by K_4 wires of layer 4 on K_3 wires of layer 3. This contribution is $f_4^{c*}K_4/K_3$. Then:

$$f_3^c = \left(\frac{F_4 \sin^2\alpha_4}{R_4}\right)\frac{K_4}{K_3} + \frac{F_3 \sin^2\alpha_3}{R_3}$$

Similar expressions for the radial force/length of wires of layers 2 and 1 are:

$$f_2^c = \left(\frac{F_4 \sin^2\alpha_4}{R_4}\right)\frac{K_4}{K_2} + \left(\frac{F_3 \sin^2\alpha_3}{R_3}\right)\frac{K_3}{K_2} + \frac{F_2 \sin^2\alpha_2}{R_2}$$

$$f_1^c = \left(\frac{F_4 \sin^2\alpha_4}{R_4}\right)\frac{K_4}{K_1} + \left(\frac{F_3 \sin^2\alpha_3}{R_3}\right)\frac{K_3}{K_1} + \left(\frac{F_2 \sin^2\alpha_2}{R_2}\right)\frac{K_2}{K_1} + \frac{F_1 \sin^2\alpha_1}{R_1}$$

The general expression is:

$$f_m^c = \sum_{n=m}^{N}\left(\frac{F_n \sin^2\alpha_n}{R_n}\right)\frac{K_n}{K_m} \tag{33}$$

These forces directly against the conductor axis are not uniformly distributed but are concentrated at contact points[3] where strands of the subjacent layer cross. Let us now derive an expression for the distance between two contact points along the length of a strand on layer n. From Fig. 2 it is seen that the length of the strand, projected onto the conductor axis, for a complete revolution around the axis, gives the lay length:

$$P_n = a\cos\alpha_n = 2\pi R_n / |\tan\alpha_n| \tag{34}$$

Therefore,

[3] "Contact points" are used here rather than "contact surfaces" since it is assumed that wire flattening was neglected. In reality, the contact surfaces are ellipses on which the maximum stress assumed is the yield stress of the material in compression [8]. The development of average contact stress on these surfaces is beyond the scope of this work, but has been treated by Phillips and Costello [9]. Strictly speaking, if flattening of the wires did not occur, contact stresses would be infinite. This singularity is avoided, however, by using radial forces directly against the axis at crossing strands instead of radial stresses.

Downloaded 02 May 2010 to 171.66.16.54. Redistribution subject to ASME license or copyright; see http://www.asme.org/terms/Terms_Use.cfm

Table 1 Geometrical parameters and mechanical properties of the Bersimis 42/7 ACSR conductor

Geometrical parameters of layers

layer	number of strands in layer	lay length	lay angle	lay radius	strand radius
n	K_n	P_n m (in)	α_n degrees	R_n mm (in)	r_n mm (in)
1	6	0.171 (6.75)	-5.33	2.540 (0.10)	1.270 (0.05)
2	8	0.258 (10.125)	8.44	6.096 (0.24)	2.286 (0.09)
3	14	0.299 (11.75)	-12.64	10.668 (0.42)	2.286 (0.09)
4	20	0.380 (15)	14.14	15.240 (0.60)	2.286 (0.09)

Core properties

r_c = 1.270 mm (0.05 in) radius
I_c = 2.043 * 10^{-12} m^4 (4.909 * 10^{-6} in^4) planar moment of inertia
J_c = 4.086 * 10^{-12} m^4 (9.817 * 10^{-6} in^4) polar moment of inertia
G_c = 76 900 MPa (11.15 * 10^6 psi) shear modulus
E_c = 200 000 MPa (29 * 10^6 psi) young's modulus

Elastic properties of constituents

E_1 = 200 000 MPa (29 * 10^6 psi) young's modulus of steel wires
E_2 = E_3=E_4= 69 000 MPa (10^7 psi) young's modulus of cold-drawn aluminum wires

Global characteristics

Overall diameter of the conductor: 35.05 mm (1.38 in)
Rated tensile strength: 154.57 kN (34 700 lb)

$$a = \frac{2\pi R_n}{|\sin\alpha_n|} \tag{35}$$

Over this length, the strand has touched all K_{n-1} strands of the sublayer $n-1$.

Then the distance d between two contact points in layer n is:

$$d = \frac{2\pi R_n}{K_{n-1}\,|\sin\alpha_n|} \tag{36}$$

For the particular case $n = 1$, $K_0 = 1$ will be used in equation (36) since the central core is a single wire. The radial compressive force/length is supported entirely at these contact points. Thus the net radial force exerted by a wire in layer m is given by:

$$F_m^c = f_m^c d \tag{37}$$

Inserting equations (33) and (36) into equation (37) gives:

$$F_m^c = \frac{2\pi R_m}{K_{m-1}\,|\sin\alpha_m|} \sum_{n=m}^{N} \left(F_n \frac{\sin^2\alpha_n}{R_n}\right) \frac{K_n}{K_m} \tag{38}$$

Using equations (13), (38), and (32), the condition for sliding of layer m becomes:

$$(A_m E_m R_m \cos^2\alpha_m - A_{m-1} E_{m-1} R_{m-1} \cos^2\alpha_{m-1}) \frac{\partial\psi}{\partial z} > \frac{2\pi R_m f}{K_{m-1}\,|\sin\alpha_m|} \sum_{n=m}^{N} \left(\frac{F_n \sin^2\alpha_n}{R_n}\right) \frac{K_n}{K_m} \tag{39}$$

This equation is not homogeneous since F_n (equation (10)) contains implicitly the curvature $\partial\psi/\partial z$. A numerical solution can be achieved however as will be seen in next section.

It should be noted here that this criterion is based on the maximum bending stress developed on layer m, which means that it applies specifically for the strand furthest from the neutral axis. It is therefore implicitly understood that if the situation favors sliding of the outermost strand of layer m against the outermost strand of layer $m-1$, then layer m will tend to behave as if it were disconnected from the system formed by sublayers 1, 2,. . ., $m-1$. The occurrence of sliding may then be associated to a net loss of flexural rigidity, assuming that wires sliding are bent about their own axis and that are no longer related to the conductor neutral axis. If equation (39) is satisfied in layers m, $m+1$, N, the expression for flexural rigidity, equation (24), gradually reduces to:

$$(IE) = \sum_{n=1}^{m-1} K_n A_n E_n \frac{(r_n^2/2 + R_n^2)}{2} \cos^3\alpha_n + I_c E_c + \sum_{n=m}^{N} K_n E_n I_n \tag{40}$$

where $I_n = \pi r_n^4/4$. This could represent a drastic reduction of flexural rigidity. Equation (40) presupposes that F_m^b, F_{m+1}^b, . . . , $F_N^b = 0$, which is not necessarily the case, as discussed before, since frictional forces resist such relaxations and still contribute to increase the bending stiffness. Therefore equation (40), for a given tension and curvature imposed to the conductor, must be considered as an ideal lower bound. It reaches a theoretical minimum value when all layers satisfy equation (39):

$$(IE) = \sum_{n=1}^{N} K_n E_n I_n + E_c I_c \tag{41}$$

which is actually the lower flexural rigidity commonly used.

Practical Applications

This discussion shows how the analysis presented here could be used practically to treat different situations. In all examples, the same typical ACSR conductor was used, namely the Bersimis 42/7 (42 EC aluminum strands, 6 steel strands and a steel wire core). The geometrical parameters and mechanical properties of this four-layer conductor and its constituents are given in Table 1.

Let us first consider that all strands carry the external load. In that case, it has been found that tension and torsion are coupled, while bending is dissociated from the first two external loads (refer to equations (21) and (24)). If the conductor is subjected to a tension T with both extremities fixed such that it cannot rotate ($\Delta\phi/l = 0$), equation (20) reduces to:

$$\begin{Bmatrix} T \\ \mathfrak{I} \\ 0 \end{Bmatrix} = \begin{bmatrix} (AE) & k_{T\mathfrak{I}} & 0 \\ k_{T\mathfrak{I}} & (JG) & 0 \\ 0 & 0 & (IE) \end{bmatrix} \begin{Bmatrix} \Delta u/l \\ 0 \\ \Delta\psi/l \end{Bmatrix} \tag{42}$$

The solution to this system is straightforward:

Downloaded 02 May 2010 to 171.66.16.54. Redistribution subject to ASME license or copyright; see http://www.asme.org/terms/Terms_Use.cfm

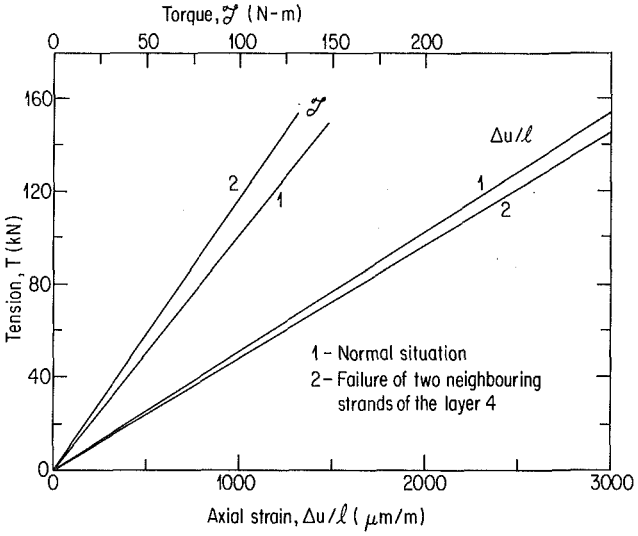


Fig. 7 Prediction of the linear response of the Bersimis conductor subjected to pure tension (both extremities fixed)

$$\Delta u/l = \frac{T}{(AE)}$$

$$\mathfrak{I} = \frac{k_{T\mathfrak{I}}T}{(AE)}$$

$$\Delta\psi/l = 0 \tag{43}$$

Using Table 1 and equation (21), the following stiffness coefficients are obtained:

$$(AE) = 5.118*10^7\text{N}$$

$$k_{T\mathfrak{I}} = 5.058*10^4\text{N-m}$$

The cable axial strain $\Delta u/l$ and induced torque $\mathfrak{I}$ are plotted in Fig. 7.

Consider now the same situation if wires 4 and 5 of layer 4 have failed. The cross section $z = 0$ of the conductor will appear as in Fig. 8. Equation (20) can now be written:

$$(AE)\Delta u/l + k_{T\mathfrak{M}}\Delta\psi/l = T$$

$$k_{T\mathfrak{I}}\Delta u/l + k_{\mathfrak{I}\mathfrak{M}}\Delta\psi/l = \mathfrak{I}$$

$$k_{T\mathfrak{M}}\Delta u/l + (IE)\Delta\psi/l = 0 \tag{44}$$

The solution of this system is:

$$\Delta\psi/l = -\frac{k_{T\mathfrak{M}}}{(AE)(IE) - k_{T\mathfrak{M}}^2}T$$

$$\Delta u/l = \frac{T}{(AE) - k_{T\mathfrak{M}}^2/(IE)}$$

$$\mathfrak{I} = \left[\frac{k_{T\mathfrak{I}}(IE) - k_{T\mathfrak{M}}k_{\mathfrak{I}\mathfrak{M}}}{(AE)(IE) - k_{T\mathfrak{M}}^2}\right]T \tag{45}$$

Stiffness coefficients are obtained from Table 1 and equation (21). It should be noted, however, that K_4 is reduced from 20 to 18. It is seen from equation (21) that to evaluate $k_{T\mathfrak{M}}$, $k_{\mathfrak{I}\mathfrak{M}}$, and (IE), the coefficients A_{in} and B_{in} of equation (18) have to be solved, coefficients that depend on l, the length of the conductor. Furthermore it is seen that if l is chosen such that $l = mP_4$, where m is an integer and P_4 the lay length of layer 4, then $A_{in} = 0$ and $B_{in} = 0$ (since $\tan\alpha_4 = 2\pi R_4/P_4$). Far from being curious, this result simply means that no net curvature appears at the conductor extremities, since the helical symmetry of the two broken strands will cancel such an effect when l is exactly equal to the pitch length or a multiple of same. The failure of these strands, on the other hand, will produce a "snaking" of the conductor between its extremities, the pitch of this snaking being governed by the

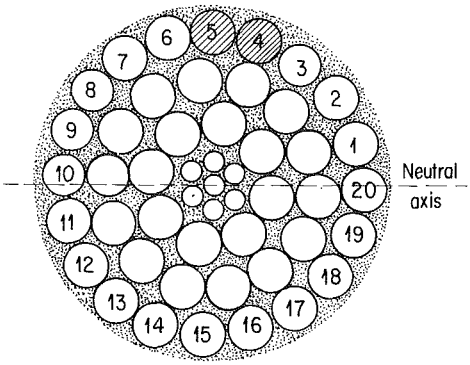


Fig. 8 Cross section $z = 0$ of the Bersimis 42/7 ACSR conductor illustrating numbering of layer 4 and failure of wires 4 and 5 of this layer

helical path of the strands along the conductor. It is seen, also from equation (18), that if l is large (i.e., many lay lengths), this snaking decreases, and eventually vanishes. The effect is most observed when l is small. Then consider the limits of A_{in} and B_{in} (equation (18)) as l reaches a very small value. This leads to indeterminate forms that can be solved by writing:

$$\lim_{l\to 0} A_{in} = \frac{\lim_{l\to 0}\dfrac{\partial}{\partial l}\left[\cos\left(\dfrac{2\pi i}{K_n}\right) - \cos\left(\dfrac{2\pi i}{K_n} + \dfrac{l\tan\alpha_n}{R_n}\right)\right]}{\lim_{l\to 0}\dfrac{\partial}{\partial l}\left[\dfrac{l\tan\alpha_n}{R_n^2\cos^3\alpha_n}\right]} \tag{46}$$

The result is

$$A_{in} = R_n\cos^3\alpha_n\sin\left(\frac{2\pi i}{K_n}\right) \tag{47}$$

Similarly

$$B_{in} = \frac{-R_n^2\cos^3\alpha_n}{2}\cos\left(\frac{2\pi i}{K_n}\right) \tag{48}$$

As can be seen, these coefficients now depend on the angle $2\pi i/K_n$ defined at the cross section $z = 0$. At any other cross section, the coefficients remain the same, but the neutral axis rotates, with the result that the snaking orbits around the conductor for a complete revolution over the distance P_n.

Referring to equations (21) and (47), the expression for $k_{T\mathfrak{M}}$ is now:

$$k_{T\mathfrak{M}} = \sum_{n=1}^{4}\sum_{i=1}^{K_n} A_nE_nA_{in} - A_4E_4A_{44} - A_4E_4A_{54}$$

in which the first term gives zero, i.e.,

$$k_{T\mathfrak{M}} = 0 - A_4E_4R_4\cos^3\alpha_4\left[\sin\left(\frac{2\pi*4}{20}\right) + \sin\left(\frac{2\pi*5}{20}\right)\right]$$

Using Table 1, $k_{T\mathfrak{M}} = -30713$ N-m. Similarly, the other coefficients are:

$$(AE) = 4.911*10^7\text{ N}$$

$$(IE) = 3.020*10^3\text{ N-m}^2$$

$$k_{\mathfrak{I}\mathfrak{M}} = -117.9\text{ N-m}^2$$

$$k_{T\mathfrak{I}} = 4.265*10^4\text{N-m}$$

The cable axial strain $\Delta u/l$ and torque $\mathfrak{I}$ are plotted in Fig. 7 and the curvature $\Delta\psi/l$ in Fig. 9 Note that if no strand had failed, the stiffness coefficients would have been:

$$(AE) = 5.118*10^7\text{ N}$$

$$(IE) = 3.480*10^3\text{ N-m}^2$$

$$k_{T\mathfrak{M}} = k_{\mathfrak{I}\mathfrak{M}} = 0$$

$$k_{T\mathfrak{I}} = 5.058*10^4\text{ N-m}$$

It is seen from Fig. 9 and equation (45) that at the maximum tension $T = 155$ kN, the curvature $\Delta\psi/l$ is

Downloaded 02 May 2010 to 171.66.16.54. Redistribution subject to ASME license or copyright; see http://www.asme.org/terms/Terms_Use.cfm

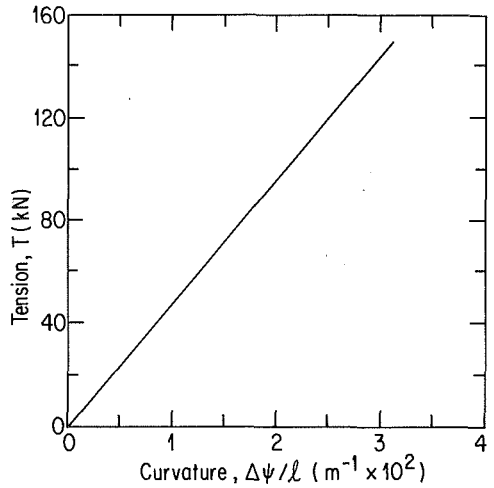


Fig. 9 Curvature induced by the failure of two neighboring strands of layer 4 of the Bersimis conductor as a function of applied tension ((*IE*) is assumed constant and maximum)

$3.22*10^{-2}m^{-1}$. According to equation (13), the axial stress component due to bending on wire 14 of layer 4, opposite to wires 4 and 5, is

$$\sigma^b = \frac{F^b}{A_4} = E_4 R_4 \cos^2\alpha_4 \Delta\psi/l \simeq 32 \text{ MPa}$$

which is a significant perturbation. If the broken strands had been opposite each other instead of side by side, this perturbation would have been minimized.

In the last example, the curvature may have been so large that, as explained earlier, the flexural rigidity was decreased. Consider now the conductor, without any strand failure, subjected to a tension T and curvature $\Delta\psi/l$. The question is, how does (IE) decrease as $\Delta\psi/l$ increases? Using equation (7) with $\Delta u/l = T/(AE)$, as estimated by equation (43), and $\Delta\phi/l = 0$, the axial strain is obtained for wires of any layer as a function of applied tension T and curvature $\Delta\psi/l$. Then equation (10) is used to calculate the axial force F_n of a wire of any layer and equation (13) to calculate the axial force component due to the curvature F_n^b. Then, substituting equation (10) into equation (38), four relations are found for the radial forces F_m^c exerted by a layer m on surrounded layers. The difference $(F_m^b - F_{m-1}^b)$, which is the frictional force developing between two adjacent layers, is obtained from equation (13). Finally, equation (39) gives four conditions to obtain wire sliding as a function of curvature and tension, using Table 1 to attribute suitable values to parameters, and selecting $f = 0.7$ as the coefficient of friction of aluminum-aluminum and aluminum-steel. Thus the sliding conditions are:

$$\text{Sliding of layer 4 on 3} \quad \text{if} \quad \frac{\Delta\psi}{l} \geq 4.790*10^{-7}T$$

$$\text{Sliding of layer 3 on 2} \quad \text{if} \quad \frac{\Delta\psi}{l} \geq 7.066*10^{-6}T$$

where $\Delta\psi/l$ is expressed in m^{-1} and T in N. The conditions for sliding of layers 2 and 1 are never satisfied, in fact, since the rate of increase of fF_2^c and fF_1^c with increasing curvature is large above the rate of increase $(F_3^b - F_2^b)$ and $(F_2^b - F_1^b)$. This is due to the high radial pressure exerted on the core. Using equation (40), the decrease of (IE) associated with the sliding of layers 4 and 3 can be obtained. Figure 10 illustrates the variation in (IE) as a function of curvature $\Delta\psi/l$ and radius of curvature $1/(\Delta\psi/l)$ for different tension levels T expressed in percentage of the rated strength. As mentioned in the preceding section, in practice (IE) in Fig. 10 would decrease smoothly rather than step by step, as shown, since the frictional forces would impede such drastic steps. For $T = 20$

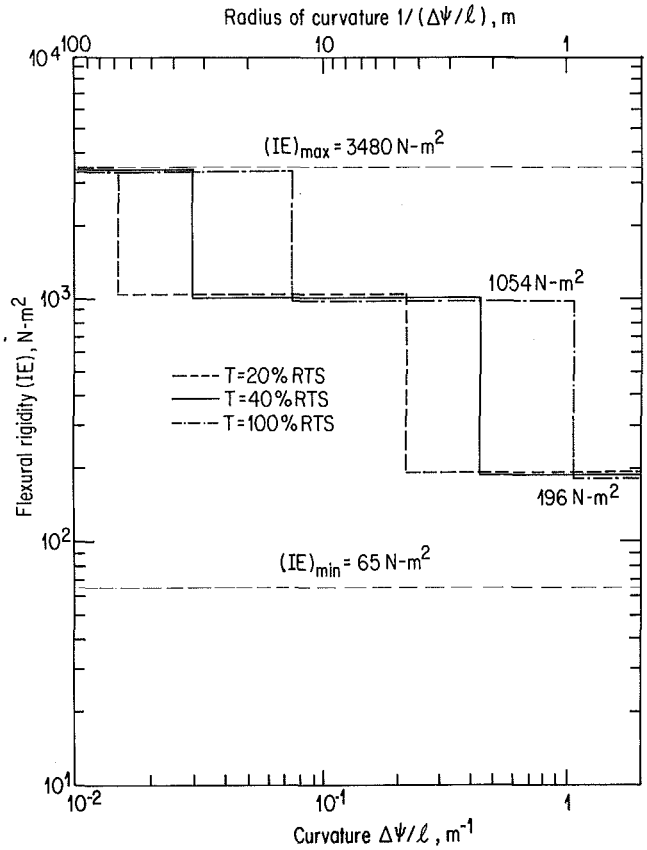


Fig. 10 Variation in the flexural rigidity (*IE*) of the Bersimis ACSR 42/7 conductor as a function of applied curvature and tension

percent RTS (30914 N), sliding occurs primarily between layers 4 and 3 at $\Delta\psi/l \geq 1.48*10^{-2}m^{-1}$ and between layers 3 and 2 at $\Delta\psi/l \geq 2.18*10^{-1}m^{-1}$; the corresponding bending stresses are:

$$\sigma_4^b = E_4 R_4 \cos^2\alpha_4 \Delta\psi/l \simeq 14.6 \text{ MPa}$$

and

$$\sigma_3^b = E_3 R_3 \cos^2\alpha_3 \Delta\psi/l \simeq 152.6 \text{ MPa}$$

Discussion

In the second part of this development, no mention has been made to the eventuality of frictional interactions between neighboring wires of the same layer. This frictional interaction is produced by the tangential force, which is the projection of the wire axial force onto the cable cross section, i.e., $F_n \sin\alpha_n$. The maximum frictional force resulting is $fF_n \sin\alpha_n$ and it is exerted along lines of contact of two wires within the same layer. This interaction was not considered for many reasons: Firstly this force is not concentrated at contact points like the component F_n^c, but distributed along lines of contact; secondly, the variation of tensile forces due to bending from one wire to its neighbor is less significant for two wires of the same layer than two wires of adjacent layers; finally, and above all, this force is not cumulated from one layer to the next inner one like F_n^c (equation (38)). Around the core of a cable under tension, the radial component F_n^c can be two orders of magnitude as large as the tangential component. Let for example the Bersimis conductor defined in Table 1 be subjected to the everyday tensile load 31 kN. Then each steel wire of layer 1 compresses the wire core at every contact point by the amount $F_1^c = 3.6$ kN while $F_1 \sin\alpha_1$ is only 60 N. Therefore it is believed that for most applications frictional interactions due to tangential forces can be neglected when compared to frictional interactions due to radial forces.

The present work was compared to some other models of

Downloaded 02 May 2010 to 171.66.16.54. Redistribution subject to ASME license or copyright; see http://www.asme.org/terms/Terms_Use.cfm

cable analysis. For the axial case, this work gives exactly the same results as those predicted by McConnell and Zemke [1]. Axial response of ACSR conductors Bersimis 42/7, Condor 54/7, and Drake 26/7 was investigated using the analysis of Knapp [4], a model taking into consideration bending and twisting moments of individual wires. Equations (20) and (21) compared with Knapp's development within 1 percent of error. The present work was also compared to the analysis of Costello [5], with the following example already solved by the author:

The configuration of a two-layer cable is the following:

$$r_c = 2.616 \text{ mm}, r_1 = 2.565 \text{ mm}, \quad K_1 = 6, R_1 = 5.181 \text{ mm}, \quad \alpha_1 = 7.49 \text{ deg}$$
$$r_2 = 2.438 \text{ mm}, \quad K_2 = 12, \quad R_2 = 10.184 \text{ mm}, \quad \alpha_2 = -14.49 \text{ deg}$$

The overall radius of the cable is 12.622 mm and it is assumed that these wires are steel wires, with $E = 2*10^5$ MPa. Then Costello arrived at (according to the nomenclature presented in this work):

$$T = 68.52 \frac{\Delta u}{l} - 0.0902 \frac{\Delta \phi}{l}$$

Equations (20) and (21) give:

$$T = 69.15 \frac{\Delta u}{l} - 0.0941 \frac{\Delta \phi}{l}$$

The axial rigidity is expressed here in Newtons while the axial torsion coupling parameter is expresed in N-m. It can be seen that agreement is quite good despite the fact that this cable is not at all similar to an ACSR. The negative coupling parameter comes from the fact that the outer layer is left lay. Here again minor discrepancies are due to the fact that the author has taken into account bending and shearing stresses of individual wires. Finally, this work was compared to the analysis of Costello for the bending problem: Since the author has considered frictionless cables, the present work should use equation (41) for flexural rigidity. When there is no strand failure, $k_{T\mathfrak{M}} = k_{3\mathfrak{M}} = 0$; then equation (20) reduces to:

$$\mathfrak{M} = (IE) \frac{\partial \psi}{\partial z}$$

For a given curvature, the bending moment $\mathfrak{M}$ compares with Costello's results within 2 percent of error. This error is attributed to the fact that the author has included the Poisson's ratio effect in his analysis.

It is worth discussing now the present use of flexural rigidity (IE). Many investigators believe that all layers of the conductor generally act together and consequently use the so-called $(IE)_{\max}$ commonly defined by:

$$(IE)_{\max} = \sum_{n=1}^{N} K_n E_n (I_n + A_n R_n^2/2) + I_c E_c$$

where $I_n = \pi r_n^4/4$. Apart from the coefficient $\cos^3 \alpha_n$, this formulation is similar to equation (24) obviously because current practice does not take the lay angles into consideration but assumes that the conductor consists of straight wires. Applying this formulation to Bersimis conductor yields $(IE)_{\max} = 3786$ N-m^2 while equation (24) gives $(IE) = 3480$ N-m^2, in which case the two values differ by 9 percent and sometimes by more than 10 percent. Other investigators would rather use $(IE)_{\min}$ which is exactly the same as that given by equation (41). For the Bersimis conductor, $(IE)_{\min} = 65$ N-m^2 with the ratio $(IE)_{\max}/(IE)_{\min} = 58$. Yet others believe that the real (IE) lies somewhere between these two limits and arbitrarily determine a value on an empirical basis.

From the present analysis, and as can be seen in Fig. 10, it is very unlikely that the lower limit will ever be reached, even for very large curvatures. It appears also that increasing the axial tension could increase the flexural rigidity whereas increasing the curvature would rather decrease it.

In this work an idealized situation was proposed, based on neglecting local compression exerted on the conductor by clamping devices at suspension points. This compression is likely to increase the parameter (IE), even if the important curvatures at these locations would rather produce the opposite trend.

Summary and Conclusions

The stiffness matrix of a conductor subjected to tension, torsion, and bending was derived. It is found that the coupling parameters, tension bending, and torsion bending, which are generally zero, must be taken into account when the conductor is perturbed by one or many strand failures. A strand failure of a conductor length in tension induces snaking between its extremities and a torque when extremities are clamped. Losses in axial, torsional, and flexural rigidities are also associated with strand failures. The behavior of the conductor for small curvatures was described considering plane cross sections of a curved conductor, which leads to the upper limit of the flexural rigidity $(IE)_{\max}$. For large curvatures, a threshold of sliding was proposed, expressed in the form of a criterion that gives a critical curvature, at a given tension level, at which sliding between two specific layers occurs. As a result, the flexural rigidity decreases since a layer sliding against inner layers is assumed to consist of wires bent about their own axis. It was found after the analysis that sliding of the first two inner layers (including steel layer) of the Bersimis conductor could not occur upon bending, because the radial compressive force component induced was such that tensile forces developing could not overcome the resulting frictional forces.

Acknowledgments

This work was supported in part by the Canadian Electrical Association. The author wishes to thank Mr. Ahmad Jamaleddine of IREQ, Lesley Régnier of Hydro-Québec, together with Professors Louis Cloutier and Alain Cardou of the Mechanical Engineering Department, University of Laval, for careful reading of the manuscript.

References

1 McConnell, K. G., and Zemke, W. P., "A Model to Predict the Coupled Axial Torsion Properties of ACSR Electrical Conductors," *Experimental Mechanics*, Vol. 22, No. 7, 1982, pp. 237–244.

2 Scanlan, R. H., and Swart, R. L., "Bending Stiffness and Strain in Stranded Cables," *IEEE* 68 CP 43-PWR, 1968.

3 Rawlins, C. B., *Transmission Line Reference Book, Wind-Induced Conductor Motion*, Chapter 2, Electrical Power Research Institute, California.

4 Knapp, R. H., "Derivation of a New Stiffness Matrix for Helically Armoured Cables Considering Tension and Torsion," *International Journal for Numerical Methods in Engineering*, Vol. 14, No. 4, 1979, pp. 515–529.

5 Costello, G. A., "Stresses in Multilayered Cables," *Journal of Energy Resources Technology*, Vol. 105, 1983, pp. 337–340.

6 Costello, G. A., and Butson, G. J., "Simplified Bending Theory for Wire Rope," *Journal of Engineering Mechanics Division*, ASCE, Vol. 108, No. EM2, Proc. Paper 16984, 1982, pp. 219–227.

7 Hruska, F. H., "Radial Forces in Wire Ropes," *Wire and Wire Products*, Vol. 27, No. 5, 1952, pp. 459–463.

8 Timoshenko, S., and Goodier, J. N., *Theory of Elasticity*, McGraw-Hill, 1951, pp. 372–382.

9 Phillips, J. W., and Costello, G. A., "Contact Stresses in Twisted Wire Cables," *Journal of the Engineering Mechanics Division*, ASCE, Vol. 99, Proc. Paper 9676, 1973, pp. 331–341.

Downloaded 02 May 2010 to 171.66.16.54. Redistribution subject to ASME license or copyright; see http://www.asme.org/terms/Terms_Use.cfm

S. B. Dong
Professor,
Mechanics and Structures Department,
University of California,
Los Angeles, Calif. 90024
Mem. ASME

K. H. Huang
Lecturer,
Department of Basic Sciences,
Tianjin University,
Tianjin, People's Republic of China

Edge Vibrations in Laminated Composite Plates

Plane strain edge vibrations or end modes in laminated composite plates are investigated by means of finite elements. This method is capable of modeling the behavior of any laminate construction whose properties are completely anisotropic within the plane. Two eigenvalue problems involving nonsymmetric matrices are derived. The form of each eigenvalue problem depends on the parameter chosen for the eigenvalue, i.e., either the frequency or the axial wave number. Orthogonality relations are discussed. Examples on two four-ply composite plates are given as illustrations. The analogy of the analysis procedure as the dynamic counterpart of the quantitative measure of Saint-Venant's principle is called to attention.

Introduction

The Rayleigh-Lamb frequency equation stands as a milestone in plane elasticity theory for natural vibrations of a homogeneous, isotropic plate [1, 2]. Although this result first appeared in 1889, one aspect of the behavior related to edge vibrations was not fully explained until some 60 years later when Mindlin and his co-workers provided all the details (see reference [3]). Edge vibrations or end modes pertain to standing waves with real frequencies ω_i's in which the motions are confined near the edge of a semi-infinite or finite plate. They involve axial wave numbers ξ's in their analytical wave form $\exp(-i\xi x)$ that are purely imaginary or complex. Recall that when ξ is real, the motions corresponds to harmonic or propagating waves.

Plane strain edge vibrations for an anisotropic plate were investigated by Kaul and Mindlin [4]. They were able to sketch the entire frequency spectra for a monoclinic crystal plate, which included the real, purely imaginary, and complex branches. The spectral data consisted of bounds, asymptotes, intersections, slopes, and curvatures, which were found from limit and otherwise special solutions of the governing equations and from roots of degenerate forms of the frequency equation. This ability for an approximate layout of the spectra is remarkable, considering the large number of elastic constants and other problem-related parameters that are involved.

Another interpretation of edge vibrations can be given. The problem of determining their frequencies and associated wave numbers may be regarded as the dynamic counterpart of a quantitative analysis of Saint-Venant's principle. Saint-Venant's principal has been invoked on a qualitative basis in elastostatic problems for a long time. It was placed on firm mathematical footing by Toupin [5] and Knowles [6] in the form of an upper bound estimate of the strain energy decay rates of systems of elastostatic self-equilibrated edge tractions as they progressed into the interior of an elastic body. Their energy decay rate inequality has the form:

$$V(x) \leq V(0) \cdot e^{-2i\xi x} \tag{1}$$

where ξ is in general complex with the imaginary part describing the characteristic inverse decay length, $V(0)$ is the total strain energy, and $V(x)$ represents the strain energy in the body beyond x. Because the imaginary part of complex ξ is of primary interest, it is useful to shift to the notation γ defined by $\gamma = i\xi$ so that equation (1) assumes the form:

$$V(x) \leq (0)e^{-2\gamma x} \tag{1a}$$

Due to the quadratic nature of strain energy, an immediate consequence is the pointwise estimates of displacements, strains, and stresses as:

$$\{u_i(x), \epsilon_{ij}(x), \sigma_{ij}(x)\} \leq \{U_i, K_{ij}, \bar{K}_{ij}\} \cdot e^{-\gamma x} \tag{2}$$

where U_i, K_{ij}, $\bar{K}_{ij}$ are constants. Horgan [7, 8] and Choi and Horgan [9, 10] applied this inequality relation to investigate the attenuation of elastostatic edge stresses in a plate with anisotropic and composite constructions under plane strain. They deduced characteristic equations from their boundary value problems, in which the eigenvalues are the inverse decay lengths and the associated eigenvectors represented the distributions of self-equilibrium edge tractions. The formulations in references [6–10] employed the Airy stress function, which does not lend itself readily to dynamic problems. Recently, this type of Saint-Venant analysis was reformulated using displacements as the primary dependent variables [11], with the objective toward a finite element capability for treating arbitrary laminated anisotropic plates under plane strain. In this paper, an extension based on this displacement formulation, which includes inertial effects, will be made to investigate edge vibrations in laminated anisotropic plates.

In this version of the finite element method, the

Contributed by the Applied Mechanics Division for presentation at the 1985 Joint ASME/ASCE Applied Mechanics, Fluids Engineering, and Bioengineering Conference, Albuquerque, N. Mex., June 24-26, 1985 of THE AMERICAN SOCIETY OF MECHANICAL ENGINEERS.

Discussion on this paper should be addressed to the Editorial Department, ASME, United Engineering Center, 345 East 47th Street, New York, N.Y. 10017, and will be accepted until two months after final publication of the paper itself in the JOURNAL OF APPLIED MECHANICS. Manuscript received by the ASME Applied Mechanics Division, February, 1983; final revision, August, 1984. Paper No. 85-APM-16.

Copies will be available until February, 1986.

Copyright © 1985 by ASME
Downloaded 02 May 2010 to 171.66.16.54. Redistribution subject to ASME license or copyright; see http://www.asme.org/terms/Terms_Use.cfm

discretization occurs in the plate's thickness direction with subdivision into mathematical laminas. Each lamina has constant thickness and may be assigned any planar anisotropic elastic properties and density. Within each lamina, the displacement interpolations over the thickness are by quadratic polynomials. This form of finite element modeling was previously applied to the analysis of plane propagating waves in laminated composite plates [12–14], which corresponds to ξ real in equation (1) or γ purely imaginary. Thus, the analysis herein essentially complements these earlier studies to explore the imaginary and complex regions of the frequency spectra. The formulation herein will lead to two classes of eigenvalue problems depending on the choice of γ or ω as the eigenvalue parameter. Both eigenvalue problems involve real nonsymmetric matrices in contrast to those in references [12–14] with only real symmetric matrices participating.

All the edge vibration data constitute a complete set of eigendata, which can be useful in a number of ways. First, the eigenvalue analysis is capable of yielding as many eigenvectors as needed. This information together with an eigenvector expansion theorem provides modal synthesis capabilities for many boundary value problems. For example, the problem of the reflection of a wave impinging on a free edge can be solved. The traction-free edge conditions are not satisfied by the incident and reflected waves alone. The residual from the difference of these two waves can be synthesized from the set of edge vibration eigenvectors. Due to completeness of the eigenvectors, this modal representation can be carried out to any required degree of accuracy. As another possible application, edge vibrations can be used for the experimental characterization of dynamic material properties because their relatively high edge vibration amplitudes can be measured with reasonable ease. This approach, although apparently feasible, remains to be developed and completely worked out for dynamic characterization of composite materials.

Formulation of Governing Equations

Consider a semi-infinite plate composed of perfectly bonded layers with possibly distinct mechanical properties and thickness. Let (x,y) be rectangular cartesian coordinates with the plate occupying the region $x \geq 0$ and let t denote time. Confining our attention to planar motions in the $x-y$ plane, let $u=u(x,y,t)$, $v=v(x,y,t)$, and $\{\epsilon\}^T=\{\epsilon_{xx}, \epsilon_{yy}, \gamma_{xy}\}$ denote the displacements and nonvanishing strain components, respectively, which are related by:

$$\epsilon_{xx}=u_{,x};\ \epsilon_{yy}=v_{,y};\ \gamma_{xy}=u_{,y}+v_{,x} \tag{3}$$

The constitutive relation for each layer's material will be sufficiently general to accommodate monoclinic properties with the material's only plane of symmetry coinciding with the $x-y$ plane. Let $\{\sigma\}^T = \{\sigma_{xx}, \sigma_{yy}, \sigma_{xy}\}$ represent the stresses so that the constitutive relation for the kth layer has the form:

$$\{\sigma\}=[\mathbf{C}^{(k)}]\{\xi\} \tag{4}$$

where

$$[\mathbf{C}^{(k)}]=\begin{bmatrix} C_{11}^{(k)} & C_{12}^{(k)} & C_{16}^{(k)} \\ C_{12}^{(k)} & C_{22}^{(k)} & C_{26}^{(k)} \\ C_{16}^{(k)} & C_{26}^{(k)} & C_{66}^{(k)} \end{bmatrix} \tag{5}$$

In our finite element derivation, the governing equations will be formulated by Hamilton's principle operating on the Lagrangian functional L, i.e., $\delta L=0$. For plane strain, L has the form:

$$L=\sum_{k=1} L_k=\sum_{k=1}\frac{1}{2}\left[\left\{\int \rho_k\{\dot{\mathbf{u}}\}^T\{\dot{\mathbf{u}}\}^T dy\right\}dx - \frac{1}{2}\left\{\int\{\epsilon\}^T[\mathbf{C}^{(k)}]\{\epsilon\}dy\right\}dx\right] \tag{6}$$

The first integral in equation (6) represents the kinetic energy with a superior dot indicating time differentiation and the second is the strain energy.

The finite element discretization subdivides the plate into mathematical laminas in the y-direction. A lamina differs from a plate laminate in that it is possible for a number of laminas modeling the physical behavior in a laminate. In each lamina, the displacement field has the form:

$$\begin{aligned} u(x,y,t)&=n_1(y)\cdot u_b(x,t)+n_2(y)\cdot u_m(x,t)+n_3(y)\cdot u_f(x,t) \\ v(x,y,t)&=n_1(y)\cdot v_b(x,t)+n_2(y)\cdot v_m(x,t)+n_3(y)\cdot v_f(x,t) \end{aligned} \tag{7}$$

where generalized displacements u_b, v_b; u_m, v_m; u_f, v_f are taken at the back, mid, and front nodal surfaces of the lamina. At this point, these displacements are regarded as undetermined functions of x and t. The interpolation polynomials n_i are quadratic functions given by:

$$n_1=1-3\zeta+2\zeta^2;\quad n_2=4\zeta-4\zeta^2;\quad n_3=2\zeta^2-\zeta \tag{8}$$

with the normalized measure ζ defined by:

$$\zeta=(y-y_b)/(y_f-y_b)$$

where y_b, y_f are thickness coordinates of the bounding surfaces of the lamina.

Appropriate space and time differentiations can be carried out on the displacement form (7). Substituting these derivatives into the elemental Lagrangian L_k and carrying the integration over the lamina's thickness yields

$$L_k=\frac{1}{2}\int\Big[-\{\mathbf{q}'\}^T[\mathbf{k}_1]\{\mathbf{q}'\}-\{\mathbf{q}'\}^T[\mathbf{k}_2]\{\mathbf{q}\} \tag{9}$$

$$-\{\mathbf{q}\}^T[\mathbf{k}_2]^T\{\mathbf{q}'\}-\{\mathbf{q}\}^T[\mathbf{k}_3]\{\mathbf{q}\}+\{\dot{\mathbf{q}}\}^T[\mathbf{m}]\{\dot{\mathbf{q}}\}\Big]dx \tag{10}$$

where $[\mathbf{k}_1]$, $[\mathbf{k}_2]$, $[\mathbf{k}_3]$ are three stiffness related matrices and $[\mathbf{m}]$ is the consistent mass matrices. The array $\{\mathbf{q}\}$ represents the lamina's ordered set of generalized coordinates defined by:

$$\{\mathbf{q}\}^T=[u_b,v_b,u_m,v_m,u_f,v_f] \tag{11}$$

In equation (10), a prime denotes differentiation with respect to x. It is noted that $[\mathbf{k}_1]$, $[\mathbf{k}_3]$, and $[\mathbf{m}]$ are symmetric while $[\mathbf{k}_2]$ is not. The elements of the stiffness related matrices $[\mathbf{k}_i]$ are listed in the Appendix of reference [11] and those for $[\mathbf{m}]$ may be found in reference [13].

The Lagrangian for the complete plate is found by summing the contributions from all laminas. Variation of L gives:

$$[\mathbf{K}_1]\{\mathbf{Q}''\}+[\mathbf{K}_2^*]\{\mathbf{Q}'\}-[\mathbf{K}_3]\{\mathbf{Q}\}-[\mathbf{M}]\{\ddot{\mathbf{Q}}\}=0 \tag{12}$$

where $\{\mathbf{Q}\}$ is an ordered array of the generalized displacements for the plate. Plate matrices $[\mathbf{K}_1]$, $[\mathbf{K}_2^*]$, $[\mathbf{K}_3]$, and $[\mathbf{M}]$ are obtained by superposition of the element matrices and $[\mathbf{K}_2^*]$ defined by

$$[\mathbf{K}_2^*]=[\mathbf{K}_2]-[\mathbf{K}_2]^T \tag{13}$$

which makes it skew-symmetric. Equation (12) represents a system of second-order partial differential equations. For natural vibrations, the motion is simple harmonic in time, i.e., $e^{i\omega t}$. The x-dependence of the solution will be taken as $e^{-\gamma x}$, and this choice is guided by the theorems of Toupin and Knowles for the elastostatic case. Therefore, the displacement vector $\{\mathbf{Q}\}$ may be written as:

$$\{\mathbf{Q}\}=\{\mathbf{Q}_0\}e^{-i\omega t-\gamma x} \tag{14}$$

where $\{\mathbf{Q}_0\}$ represents the nodal amplitudes. Substituting this solution form into equation (12) yields:

Downloaded 02 May 2010 to 171.66.16.54. Redistribution subject to ASME license or copyright; see http://www.asme.org/terms/Terms_Use.cfm

$$\gamma^2[\mathbf{K}_1]\{\mathbf{Q}_0\} - \gamma[\mathbf{K}_1^*]\{\mathbf{Q}_0\} - [\mathbf{K}_3]\{\mathbf{Q}_0\} + \omega^2[\mathbf{M}]\{\mathbf{Q}_0\} = 0 \tag{15}$$

Equation (15) is a two-parameter algebraic eigensystem with either γ or ω serving as the eigenvalue parameter. If ω is given, then what will be called eigenvalue problem *I* (EVP *I*) is obtained:

$$\left[\gamma^2[\mathbf{K}_1] - \gamma[\mathbf{K}_2^*] - [[\mathbf{K}_3] - \omega^2[\mathbf{M}]]\right]\{\mathbf{Q}_0\} = 0 \tag{16}$$

with γ appearing to the first and second powers. This equation is very similar to that derived in reference [11], with the difference being the inclusion of the inertial effects as $\omega^2[\mathbf{M}]$. The roots of this equation may be real, purely imaginary, or complex. The real and complex roots represent the edge vibrations, while the purely imaginary roots are associated with propagating waves by recalling that $\gamma = i\xi$. On the other hand, if γ is specified (usually as real), then eigenvalue problem *II* (EVP *II*) is obtained:

$$[\mathbf{K}(\gamma)]\{\mathbf{Q}_0\} = \omega^2[\mathbf{M}]\{\mathbf{Q}_0\} \tag{17}$$

where

$$[\mathbf{K}(\gamma)] = -\gamma^2[\mathbf{K}_1] + \gamma[\mathbf{K}_2^*] + [\mathbf{K}_3] \tag{18}$$

EVP *II*, because $[\mathbf{K}(\gamma)]$ is nonsymmetric, admits both real and complex roots. At this point, only real roots are of interest because of their obvious physical significance. Some remarks will be made in the concluding section of this paper regarding the role of the complex roots for ω^2. Both eigenvalue problems (16) and (17) are solved by a very efficient Block-Stodola iteration technique [15].

When $\omega^2 = 0$ in equation (16), the analysis reduces to the elastostatic case. This case was discussed in reference [11] in connection with the attenuation of self-equilibrated edge effects in laminated plates in the context of Saint-Venant's principle. Therefore, equation (16) represents the dynamic counterpart of Saint-Venant's principle for the determination of the decay rates into the plate's interior of self-equilibrated edge vibrations.

Orthogonality

Orthogonality relationships will first be discussed for EVP *I*, i.e., equation (16). The orthogonality relationships for EVP *II* will be seen as part of those equations for EVP *I*. For our purpose, it is useful to reduce quadratic eigenvalue problem (16) to a first-order system using the substitution:

$$\{\mathbf{Q}_1\} = -\gamma\{\mathbf{Q}_0\} \tag{19}$$

Insertion of equation (19) into equation (16) gives:

$$-\gamma[\mathbf{K}_1]\{\mathbf{Q}_1\} + [\mathbf{K}_2^*]\{\mathbf{Q}_1\} - [\mathbf{K}_3^*]\{\mathbf{Q}_0\} = 0 \tag{20}$$

where $[\mathbf{K}_3^*] = [\mathbf{K}_3^*(\omega)]$ is the symmetric matrix given by

$$[\mathbf{K}_3^*] = [\mathbf{K}_3] - \omega^2[\mathbf{M}] \tag{21}$$

Reconstituting equations (19) and (20) as a first-order eigenvalue problem yields:

$$[\mathbf{A}]\{\bar{\mathbf{Q}}\} = \gamma[\mathbf{B}]\{\bar{\mathbf{Q}}\} \tag{22}$$

where

$$\{\bar{\mathbf{Q}}\} = \begin{bmatrix} \{\mathbf{Q}_0\} \\ \{\mathbf{Q}_1\} \end{bmatrix} = \begin{bmatrix} \{\mathbf{Q}_0\} \\ -\gamma\{\mathbf{Q}_0\} \end{bmatrix} \tag{23}$$

and the nonsymmetric [**A**] matrix and symmetric [**B**] matrix are defined as

$$[\mathbf{A}] = \begin{bmatrix} [0] & -[\mathbf{I}] \\ -[\mathbf{K}_3^*] & [\mathbf{K}_2^*] \end{bmatrix}; \quad [\mathbf{B}] = \begin{bmatrix} [\mathbf{I}] & [0] \\ [0] & [\mathbf{K}_1] \end{bmatrix} \tag{24}$$

The problem posed by equation (22) is regarded as the one employing right-handed generalized coordinates. Its solution is given by a transformation to right normal coordinates $\{\mathbf{x}\}$ in the form:

$$\{\bar{\mathbf{Q}}\} = [\bar{\phi}]\{\mathbf{x}\} \tag{25}$$

where the right-handed eigenvectors $[\bar{\phi}]$ can be partitioned and further simplified as follows:

$$[\bar{\phi}] = \begin{bmatrix} [\phi_0] \\ [\phi_1] \end{bmatrix} = \begin{bmatrix} [\phi_0] \\ -[\phi_0][\gamma] \end{bmatrix} \tag{26}$$

with $[\phi_0]$, $[\phi_1]$ as the eigenvectors of the coordinates $\{\mathbf{Q}_0\}$, $\{\mathbf{Q}_1\}$, respectively, and $[\gamma]$ as the diagonal matrix of the corresponding eigenvalues. The transpose of equation (22) is the adjoint problem:

$$[\mathbf{A}]^T\{\bar{\mathbf{L}}\} = [\mathbf{B}]\{\bar{\mathbf{L}}\} \tag{27}$$

where $\{\bar{L}\}$ is the vector of left generalized coordinates in the form:

$$\{\bar{\mathbf{L}}\} = \begin{bmatrix} \{\mathbf{L}_0\} \\ \{\mathbf{L}_1\} \end{bmatrix} \tag{28}$$

with $\{\mathbf{L}_1\}$ defined as

$$\{\mathbf{L}_1\} = -\gamma\{\mathbf{L}_0\} \tag{29}$$

The solution to equation (27) consists of a transformation to left normal coordinates $\{y\}$ with left-handed eigenvectors $[\bar{\Psi}]$ in the form

$$\{\bar{\mathbf{L}}\} = [\bar{\Psi}]\{\mathbf{y}\} \tag{30}$$

with $[\bar{\Psi}]$ appearing in partitioned form as:

$$[\bar{\Psi}] = \begin{bmatrix} [\psi_0] \\ [\psi_1] \end{bmatrix} \tag{31}$$

From the first equation in the partitioned form of adjoint problem (27) and with the aid of equation (29), eigenvectors $[\psi_0]$ and $[\psi_1]$ can be shown to be related as follows:

$$-[\mathbf{K}_3^*][\psi_1] = [\psi_0][\gamma] \tag{32}$$

The right and left-handed eigenvectors obey the orthogonality relations:

$$[\bar{\psi}]^T[\mathbf{B}][\bar{\phi}] = [\mathbf{I}] \tag{33}$$

$$[\bar{\psi}]^T[\mathbf{A}][\bar{\phi}] = [\text{diag}] \tag{34}$$

where [diag] denotes a diagonal matrix. In terms of eigenvectors $[\psi_0]$, $[\psi_1]$, $[\phi_0]$, $[\phi_1]$, equations (33) and (34) take the form:

$$[\psi_0]^T[\phi_0] + [\psi_1]^T[\mathbf{K}_1][\phi_1] = [\mathbf{I}] \tag{33a}$$

$$-[\psi_0]^T[\phi_1] - [\psi_1]^T[\mathbf{K}_3^*][\phi_0] + [\psi_1]^T[\mathbf{K}_2^*][\phi_1] = [\text{diag}] \tag{34a}$$

Using (26) and (32), the preceding pair of orthogonality relationships can be expressed exclusively in terms of $[\psi_0]$ and $[\phi_0]$:

$$[\psi_0]^T[\phi_0] + [\gamma][\psi_0]^T[\mathbf{K}_3^*]^{-1}[\mathbf{K}_1][\phi_0][\gamma] = [\mathbf{I}] \tag{33b}$$

$$[\gamma][\gamma_0]^T[\phi_0] + [\psi_0]^T[\phi_0][\gamma] - [\gamma][\psi_0]^T[\mathbf{K}_3^*]^{-1}[\mathbf{K}_2^*][\psi_0][\gamma] = [\text{diag}] \tag{34b}$$

The orthogonality relationships for EVP *II* is easily seen as those given by equations (33) and (34). In EVP *II* given by equation (17), [**K**] is nonsymmetric and [**M**] is symmetric corresponding to [**A**] and [**B**], respectively. Let the transformations to right and left normal coordinates with right and left-handed eigenvectors be denoted by

$$\{\mathbf{Q}_0\} = [\phi_0]\{\mathbf{x}\}; \qquad \{\mathbf{L}_0\} = [\psi_0]\{\mathbf{y}\} \tag{35}$$

The orthogonality relationships are

$$[\psi_0]^T[\mathbf{B}][\phi_0] = [\mathbf{I}] \tag{36}$$

$$[\psi_0]^T[\mathbf{A}][\phi_0] = [\text{diag}] \tag{37}$$

A dual expansion theorem can be derived which relies on these orthogonality relations. Such an expansion theorem for the elastostatic case was discussed in reference [11], and that result can be straightforwardly generalized to the steady-state dynamic case by inclusion of the mass matrix.

Downloaded 02 May 2010 to 171.66.16.54. Redistribution subject to ASME license or copyright; see http://www.asme.org/terms/Terms_Use.cfm

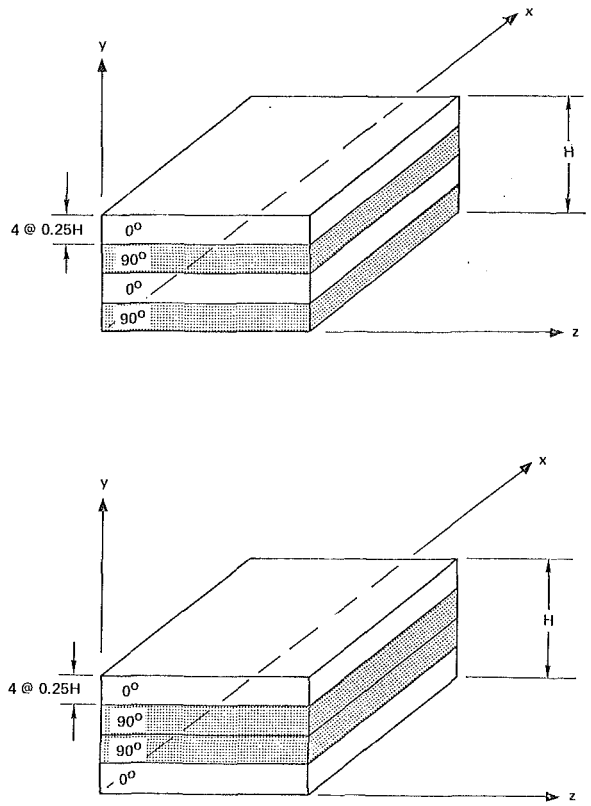


Fig. 1 Two laminated composite plates

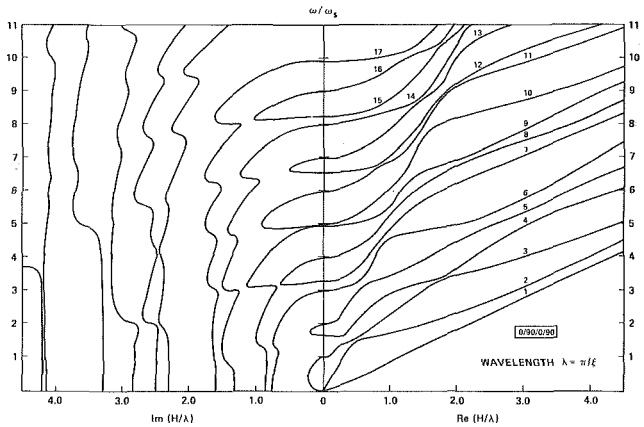


Fig. 2 Real and imaginary frequency spectra for [0/90/0/90] plate

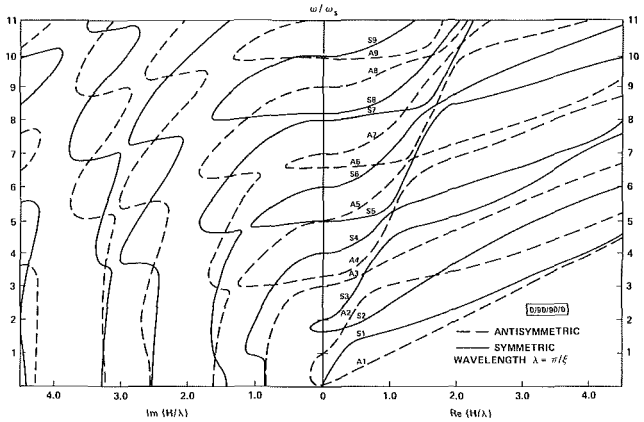


Fig. 3 Real and imaginary frequency spectra for [0/90/90/0] plate

Examples

A computer code was formulated to carry out the numerical analysis. Verification of this code was by means of the problem of the homogeneous, isotropic plate for which analytical results are contained in the Rayleigh-Lamb frequency equation. The modeling capability using quadratic displacement interpolations in the thickness direction has been amply demonstrated in related problems [11-14], and there is no need to dwell on this aspect of the numerical approach. Essentially, it was only necessary to assure that the computer program is grammatically correct. Comparison of the numerical data for edge vibrations involving both imaginary and complex wave numbers showed excellent agreement in the frequencies with those extracted from the Rayleigh-Lamb frequency equation. Some partial results are documented in reference [15] as an illustration of the Block-Stodola iteration technique and they revealed four and five decimal place accuracies. Inasmuch as no new information is contained in this example, which was intended only for computer program verification, we will forego presentation of any of the numerical results here.

The edge vibrations in two four-ply laminated composite plates, both of unit thickness, were investigated. One possessed a stacking sequence of [0/90/0/90] and the other was a [0/90/90/0] lay-up as shown in Fig. 1. The elastic properties for each ply relative to their natural elastic axes are:

$$E_L = 20.2\times 10^6_{\text{psi}};\quad E_T = 2.2\times 10^6_{\text{psi}}$$

$$G_{LT} = G_{TT} = 0.85\times 10^6_{\text{psi}};\quad \nu_{LT} = \nu_{TT} = 0.21 \qquad (38)$$

The density ρ was taken as unity. These plates are the same as those used in the examples of reference [11]. The corresponding elastic moduli with the fiber axis parallel (0 deg) the transverse (90 deg) to the x-axis, are, respectively:

$$[C]_{0\,\text{deg}} = \begin{bmatrix} 21289.29 & 592.01 & - \\ - & 2318.64 & - \\ - & - & 850.00 \end{bmatrix}_{\text{ksi}};$$

$$[C]_{90\,\text{deg}} = \begin{bmatrix} 2318.64 & 500.45 & - \\ - & 2318.64 & - \\ - & - & 850.00 \end{bmatrix}_{\text{ksi}} \qquad (39)$$

For each of the two configurations, 40 equal-thickness elements (81 nodal surfaces and 162 degrees of freedom) were employed in the model for the entire plate. This model will be more than adequate to capture the modal patterns for all vibration data reported herein. For the [0/90/90/0] lay-up, half of the model was used, and the vibrations symmetric and antisymmetric with respect to the middle surface were studied separately.

The frequency spectra for these two plates are plotted in Figs. 2 and 3 for real and purely imaginary wave numbers. The real wave number data were presented only for completeness; they are based on the formulation given in reference [12]. All frequencies were normalized with respect to the frequency of the lowest thickness-shear vibration at infinitely long wave length. This frequency is the same for both plates and is given by

$$\omega_s = 2896.4/\sqrt{\rho}\ (\text{rad/sec}) = 460.98/\sqrt{\rho}\ \text{Hz} \qquad (40)$$

As can be seen from these plots, the frequency branches are highly intricate. The difference in the spectral behavior

Downloaded 02 May 2010 to 171.66.16.54. Redistribution subject to ASME license or copyright; see http://www.asme.org/terms/Terms_Use.cfm

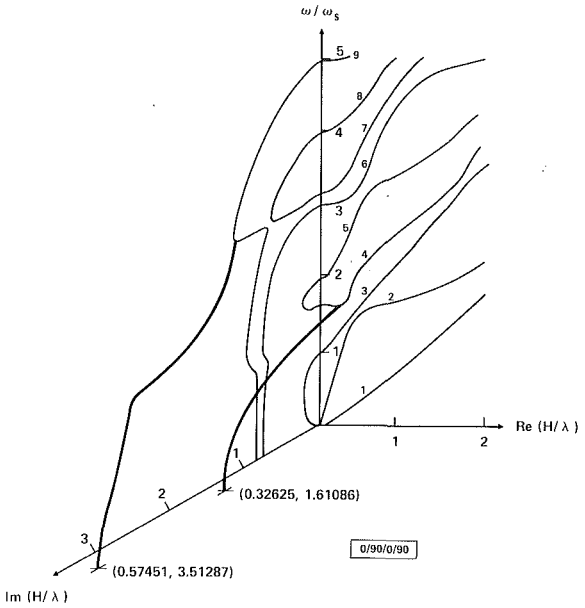


Fig. 4 Complex frequency spectra for [0/90/0/90] plate

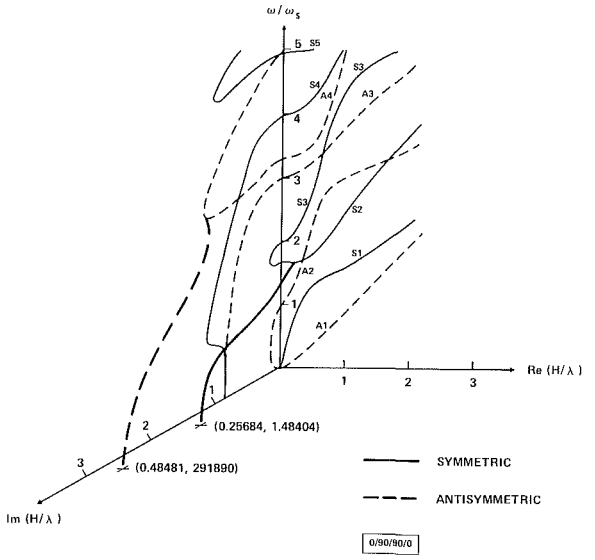


Fig. 5 Complex frequency spectra for [0/90/90/0] plate

between these plates can be seen by comparisons of Figs. 2 and 3. On Figs. 4 and 5 are shown some three-dimensional plots of selected branches of the frequency spectra involving complex wave numbers. These complex branches intersect both the real and purely imaginary branches when they join with them in the real and the purely imaginary wave number planes. This algebraic characteristic is similar to that seen in homogeneous, isotropic plates, which has been explained by Mindlin and Onoe [16].

Although not shown here, the computer code also provides modal stress patterns for each of the displacement modal patterns. Both displacement and stress modal patterns are similar to those of the elastostatic case reported in reference [11] in a general way. Therefore, no plots of them need to be given here and the reader referred to reference [11] for examples of them. There are only slight differences due to the presence of inertia.

Concluding Remarks

A finite element analysis for plane strain edge vibrations or end modes in laminated composite plates has been presented. This method is capable of treating any laminate construction whose properties are planar anisotropic. The analysis procedure may be considered as the dynamic counterpart of the quantitative analysis of Saint-Venant's principle. The governing differential equations appear in terms of the nodal displacements. Two eigenvalue problems can be obtained, one with frequency ω and the other with wave number γ as the eigenvalue parameter. If the wave number is adopted as the eigenvalue parameter and real values assigned to the frequency, the eigensystem is quadratic in γ and the solution yields a set of characteristic inverse decay lengths and their corresponding displacement modal patterns over the plate thickness (right eigenvectors). The adjoint problem gives the same eigenvalues and the left eigenvectors. If the frequency is chosen as the eigenvalue parameter with real values assigned to γ, then a nonsymmetric eigenvalue problem results whose solution contains the frequencies and the corresponding displacement modal patterns in the thickness direction. These frequencies can be real, imaginary, or complex. For natural edge vibrations, only real frequencies are of physical significance. Orthogonality relations are discussed for these eigenvalue problems. The numerical examples dealt with two four-ply composite plates and illustrate the intricate layout of the frequency spectra for these plates. This method is effective for finding both frequencies and their associated inverse decay lengths (imaginary and complex wave numbers). The eigenvectors are the displacement modal patterns. Stress modal patterns can be determined from the displacement modal patterns. From such plots, all the interlaminar effects for a given laminate construction can be observed. See reference [11] for examples of such for the elastostatic case of the two four-ply plates considered herein.

These eigendata are also useful in a boundary value problem to satisfy a stress-free edge condition. When a steady-state incident wave impinges on a free surface, a reflected wave alone will not be sufficient to meet stress free edge conditions. It is necessary to augment a set of self-equilibrated edge vibrations obtained by means of a dual expansion theorem, which when superposed with the reflected wave, gives a stress system that cancels those due to the incident wave.

A note on imaginary and complex frequencies should be added. The notion of assigning a value to either the frequency or wave number and solving the resulting eigenvalue problem is equivalent to carrying out an integral transform at a discrete value of the transform parameter. For example, when the wave number ξ is assigned a real value, the resulting eigendata represent the numerical information in the Fourier transform plane for that value. Similarly, when ξ is purely imaginary value, then the eigendata represent numerical information in the Laplace transform plane. Similar interpretations may be ascribed to the frequency ω. They will represent either Laplace or Fourier transform data at a particular value of the assigned value for ω. Thus, frequencies that are imaginary or complex, although devoid of physical meaning do have mathematical significance as part of the total package of numerical transform data. Moreover, the real and imaginary axes of both ξ and ω in this problem constitute a four-dimensional space in which all spectral branches are continuous. Illustrations in a subspace of three dimensions were shown in Figs. 4 and 5. The accompanying data for all the points in the spectra are the numerical integral transform data. It is not unreasonable to speculate that when computers become even more powerful and efficient algorithms are devised, it will be feasible to synthesize the dynamic response in a composite plate for any transient loading and for any system of boundary conditions on an edge or edges from the complete set of eigendata for a given plate.

Downloaded 02 May 2010 to 171.66.16.54. Redistribution subject to ASME license or copyright; see http://www.asme.org/terms/Terms_Use.cfm

References

1 Lord Rayleigh, "On the Free Vibrations of an Infinite Plate of Homogeneous Isotropic Elastic Matter," *Proceedings of the London Mathematical Society*, Vol. 20, 1888–1889, pp. 225–234.

2 Lamb, H., "On Waves in an Elastic Plate," *Proceedings, Royal Society*, London, Series *A*, Vol. 93, 1917, pp. 114–128.

3 Mindlin, R. D., "Waves and Vibrations in Isotropic Elastic Plates," *Proceedings of the First Symposium on Naval Structural Mechanics*, Pergamon Press, 1960, pp. 199–232.

4 Kaul, R. K., and Mindlin, R. D., "Frequency Spectrum of a Monoclinic Crystal Plate," *Journal of the Acoustical Society of America*, Vol. 34, Dec. 1962, pp. 1902–1910.

5 Toupin, R. A., "Saint-Venant's Principle," *Archive for Rational Mechanics and Analysis*, Vol. 18, 1965, pp. 83–96.

6 Knowles, J. K., "On Saint-Venant's Principle in the Two-Dimensional Linear Theory of Elasticity," *Archive for Rational Mechanics and Analysis*, Vol. 21, 1966, pp. 1–22.

7 Horgan, C. O., "On Saint-Venant's Principle in Plane Anisotropic Elasticity," *Journal of Elasticity*, Vol. 2, 1972, pp. 169–180.

8 Horgan, C. O., "Some Remarks on Saint-Venant's Principle for Transversely Isotropic Composites," *Journal of Elasticity*, Vol. 2, 1972, pp. 335–339.

9 Choi, I., and Horgan, C. O., "Saint-Venant's Principle and End Effects in Anisotropic Elasticity," ASME JOURNAL OF APPLIED MECHANICS, Vol. 44, No. 3, 1977, pp. 424–430.

10 Choi, I., and Horgan, C. O., "Saint Venant End Effects for Plane Deformation of Sandwich Strips," *International Journal of Solids and Structures*, Vol. 14, No. 3, 1978, pp. 187–195.

11 Dong, S. B., and Goetschel, D. B., "Edge Effects in Laminated Composite Plates," ASME JOURNAL OF APPLIED MECHANICS, Vol. 49, 1982, pp. 129–135.

12 Dong, S. B., and Nelson, R. B., "On Natural Vibrations and Waves in Laminated Orthotropic Plates," ASME JOURNAL OF APPLIED MECHANICS, Vol. 39, 1972, pp. 739–745.

13 Nelson, R. B., and Dong, S. B., "High Frequency Vibrations and Waves in Laminated Orthotropic Plates," *Journal of Sound and Vibration*, Vol. 30, 1973, pp. 33–44.

14 Dong, S. B., and Pauley, K. E., "Plane Waves in Anisotropic Plates," *ASCE Journal of the Engineering Mechanics Division*, Vol. 104, No. EM4, 1978, pp. 801–817.

15 Dong, S. B., "A Block-Stodola Eigensolution Technique for Large Algebraic Systems With Nonsymmetrical Matrices," *International Journal for Numerical Methods in Engineering*, Vol. 11, 1977, pp. 247–267.

16 Mindlin, R. D., and Onoe, M., "Mathematical Theory of Vibrations of Elastic Plates," *Proceedings of the Eleventh Annual Symposium on Frequency Control*, U.S. Army Signal Engineering Laboratories, Fort Monmouth, N.J., 1957, pp. 17–40.

Downloaded 02 May 2010 to 171.66.16.54. Redistribution subject to ASME license or copyright; see http://www.asme.org/terms/Terms_Use.cfm

Dynamic Rate Effects on Timoshenko Beam Response

T. J. Ross
Senior Research
Structural Engineer,
Civil Engineering Research Division,
Air Force Weapons Laboratory,
Albuquerque, N. Mex. 87117

The problem of a viscoelastic Timoshenko beam subjected to a transversely applied step-loading is solved using the Laplace transform method. It is established that the support shear force is amplified more than the support bending moment for a fixed-end beam when strain rate influences are accounted for implicitly in the viscoelastic constitutive formulation.

Introduction

Under the rapid rates of loading and strain that occur in impulsive pressure tests on beams, the material strengths and elastic properties of reinforcing steel and concrete are greater than they are under static load tests. An accurate assessment of these rate effects on beam response would allow for effective procedures in the design of modern structures to sustain loads that are imposed over very short durations. In particular, it is beneficial to know the rate-dependent behavior of the beam internal forces – the shear and bending moment – to be able to relate them to beam capacity to ensure safety against failure under impulsive pressure situations. Figure 1 illustrates the problem. A beam is excited by a rapidly applied transverse surface pressure (Fig. 1(*a*)), $q(x, t)$, and subsequently experiences transverse motion (Fig. 1(*b*)). If internal rate-dependent forces exceed beam capacity (or strength), a failure will be initiated (Fig. 1(*c*)). This paper focuses on two types of failure at a beam support – direct shear and bending – and the relative likelihood of their occurrence under rapid loading.

To assess the influence of rate effects on beam response, two approaches are outlined and compared. The first approach (Ross, 1983) models strain rate effects by using viscoelastic constitutive relationships in the Timoshenko beam equations of motion. The viscoelastic relation used is that of a Voigt (also called Kelvin) solid in shear, and is schematically shown along with the stress-strain characteristics in Fig. 2. This approach, although intuitively plausible, has limitations because the viscous parameter (shown in the figure as η) is not constant over a large range of strain rates. The second approach, based on load rate, employs the results of a normal mode analysis (Ross and Wong, 1985) and alters the beam material properties to account for rate influence.

This study concludes with the finding that the strain rate effects tend to amplify the support shear force more than the support bending moment in the early transient response regime of a beam subjected to a rapidly applied transverse loading. The time to shear failure at the support is significantly decreased when strain rate effects are considered. When assessing the analytic influence of external load rate on beam response, it is found that support shear failures are more sensitive to rate effects on beam strength than rate effects on beam stiffness.

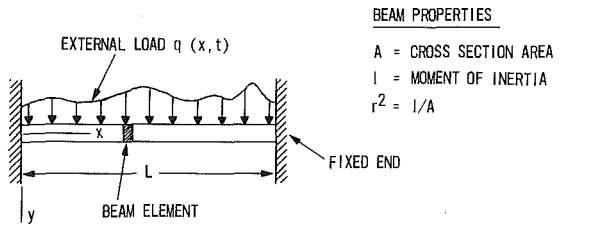


Fig. 1(*a*) Beam geometry

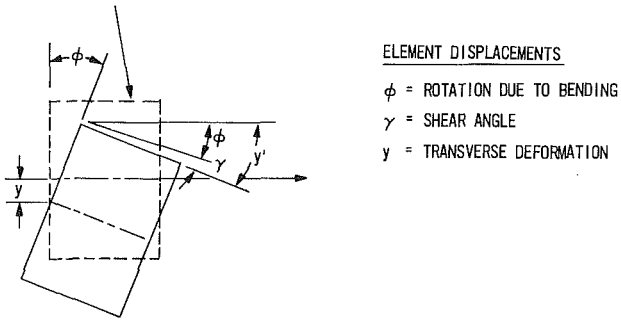


Fig. 1(*b*) Beam displacements

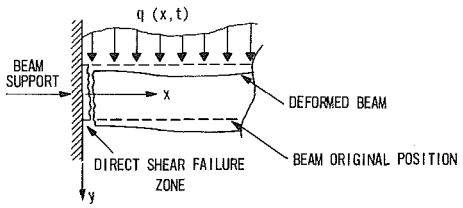


Fig. 1 (*c*) Beam support failure

Fig. 1 Beam excited by a rapidly applied transverse pressure

Contributed by the Applied Mechanics Division for presentation at the 1985 Joint ASME/ASCE Applied Mechanics, Fluids Engineering, and Bioengineering Conference, Albuquerque, N. Mex., June 24-26, 1985 of THE AMERICAN SOCIETY OF MECHANICAL ENGINEERS.

Discussion on this paper should be addressed to the Editorial Department, ASME, United Engineering Center, 345 East 47th Street, New York, N.Y., 10017, and will be accepted until two months after final publication of the paper itself in the JOURNAL OF APPLIED MECHANICS. Manuscript received by ASME Applied Mechanics Division, January, 1984; final revision, September, 1984. Paper No. 85-APM-21.

Copies will be available until February 1986.

Copyright © 1985 by ASME
Downloaded 02 May 2010 to 171.66.16.54. Redistribution subject to ASME license or copyright; see http://www.asme.org/terms/Terms_Use.cfm

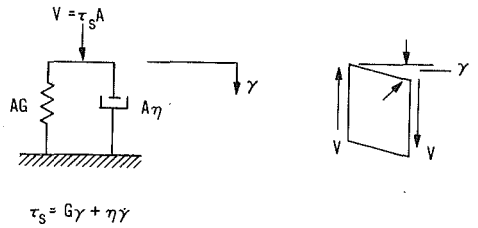


Fig. 2(a) Voigt solid in shear

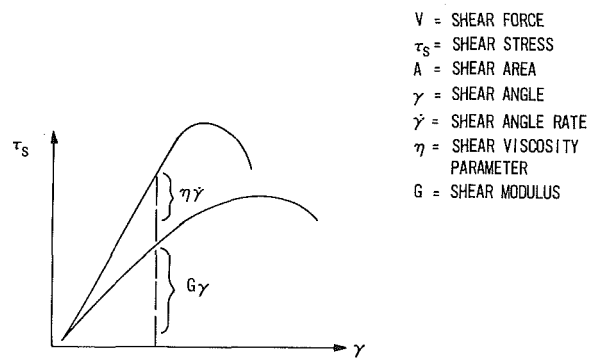


Fig. 2(b) Stress-strain relation in shear

Fig. 2 Linear viscoelastic model

Strain Rate Influence

No previous study or analysis has been found on the forced or free vibration of a Timoshenko beam with linear viscoelastic constitutive properties. In developing the viscoelastic Timoshenko beam, it is assumed that the proportionality parameter for the strain rate terms is a constant during the time domain of interest. Since the analytic time span of interest in impulsive loading is a very short time (generally less than 0.2 msec), this assumption should be acceptable. Certainly strain rate is a function of the response history and, when the strain rate changes, so too should the viscous proportionality constant. However, the general trends showing strain rate influence on shear and moment should be apparent even with the assumption of a constant rate parameter. Moreover, it is also assumed that the rate effects in shear and moment are linearly related by the same constant, β, as is the relationship between Young's modulus E and the shear modulus G (i.e., $G=E/\beta$). In particular, if α' is the viscous coefficient for a compressive strain rate, then $\eta=\alpha'/\beta$ is the viscous coefficient for a shear-strain rate. This should be valid for the linear-elastic case.

For the Timoshenko beam, the viscoelastic constitutive relations for the bending moment M and the shear force V are

$$\begin{aligned} M &= -I\{E\phi' + \alpha'\dot{\phi}'\} = -Ar^2\beta\{G\phi' + \eta\dot{\phi}'\} \\ V &= k'A\{G(y'-\phi) + \eta(\dot{y}'-\dot{\phi})\} \end{aligned} \tag{1}$$

where I, A, r, and k' are the moment of inertia, cross-sectional area, radius of gyration, and the shear deformation coefficient of the beam, respectively. The dependent variables ϕ and y are the angle of rotation due to bending and the transverse deflection of the beam, respectively (see Fig. 1(*b*)). The symbols (˙) and ($'$) over a dependent variable denote differentiation with respect to time, d/dt, and distance along the beam axis, d/dx, respectively. The terms $\dot{\phi}$, $\dot{\phi}'$, and $\dot{y}'$ are generalized strain rate terms. Equations (1) contain an elastic part and a viscous part for both shear and moment. Since strain rate is always a non-negative quantity, these equations show that the viscoelastic stiffness is always greater than or equal to the elastic stiffness. This condition is seen in rate application tests for both concrete and steel. Hence, the viscous term accounts for an increase in stiffness due to rate effects.

The equations of motion for a viscoelastic Timoshenko beam are

$$\begin{aligned} k'AG(y'-\phi) + k'A\eta(\dot{y}'-\dot{\phi}) + Ar^2\beta(G\phi'' + \eta\dot{\phi}'') = 0 \\ k'AG(y''-\phi') + kA\eta(\dot{y}''-\dot{\phi}') - \rho A\ddot{y} = -q \end{aligned} \tag{2}$$

where ρ is the beam density, q is the applied transverse distributed load on the beam which can be a generalized function of space and time, $q(x,t)$, and the symbols (¨) and ($''$) are the respective derivatives, d^2/dt^2 and d^2/dx^2. To make equations (2) mathematically tractable, the rotary inertia term has been neglected. This makes the first of equations (2) approximate. But considering the fact that the effects due to shear deformations are three to four times as large as the effects due to rotary inertia (Timoshenko, et al., 1974), it is felt that the approximation is valid in order for a solution to be obtained. In fact, Mindlin (1951) found that the transverse shear deformation accounted almost entirely for the discrepancy between the simpler Bernoulli-Euler theory and the exact three-dimensional theory.

The solution to equations (2), along with the boundary conditions (for this case assumed to be those for a fixed-fixed beam) and initial conditions (assumed to be homogeneous), is quite difficult. A convergent series solution for small time (i.e., a nondimensionalized time parameter such as Gt/η being less than 1) is not possible because of the poor coupling between the two equations. For example, second derivatives in space or time on ϕ appear only in the first of equations (2) and second derivatives on y appear only in the second of equations (2).

A self-similar solution (for a semi-infinite beam) is difficult for inhomogeneous equations, unless the loading term is an implicit function of space and time and can be expressed in terms of the similarity variable. A separation of variables technique is also difficult since the equations are clearly not separable because of the strain rate terms. The method of characteristics is a possible technique if one can show that the equations are hyperbolic. Colton (1973) shows the elastic version of these equations to be hyperbolic. This is cumbersome to do for these equations and, even if the equations are hyperbolic, the solution procedure becomes lengthy. To reduce the simultaneous third-order equations to a system of first-order equations and then to transform the independent variables to the characteristic coordinates would require the analytic evaluation of a determinant of rank six. The characteristics also would not be straight lines, resulting in the evaluation of simultaneous ordinary differential equations with variable coefficients.

The theory finally adopted as a solution technique was the Laplace transform method in both space and time coordinates; that is, a double Laplace transformation with a subsequent double inversion. Anderson (1971) successfully employed this technique in this analysis of an elastic Timoshenko beam under forced motions. He pointed out that the advantage of the transform method is that a series solution can be obtained by using the theory of residues. Here, the inversions in space and time are obtained by summing the residues about the poles of the resulting characteristic equations in the Laplacian domain. This residue principle replaces the usual integration associated with the orthogonality condition when solving the equations in normal modes.

Laplace Transform Method

Since orthogonality is not valid (i.e., a harmonic solution is not possible) for the Timoshenko beam with viscoelastic properties, a Laplace transform method is used in conjunction with an asymptotic approximation in time. This approximation was adopted because of the complex form of the resulting Laplacian expression and the difficulty in the

Downloaded 02 May 2010 to 171.66.16.54. Redistribution subject to ASME license or copyright; see http://www.asme.org/terms/Terms_Use.cfm

subsequent inversion process. The asymptotic nature of the solution is acceptable, however, since the focus of this paper is on very small times after the initial impulsive pressure loading. A fixed-end beam under the influence of a step-loading is studied.

The Laplace transform method transforms the dependent variables, y and ϕ, using

$$\bar{y}(x,s)=\int_0^\infty e^{-st}y(x,t)dt$$
$$\bar{\bar{y}}(p,s)=\int_0^\infty e^{-px}\bar{y}(x,s)dx \tag{3}$$

with similar linear operators applying to ϕ, i.e., $\bar{\phi}(x,s)$ and $\bar{\bar{\phi}}(p,s)$. A single bar above a variable indicates a transform in time and a double bar designates a double transform in both time and space. The parameters p and s are the Laplacian variables for space (x) and time (t), respectively.

Viscoelastic Solution. To satisfy the conditions of transformation in time and space, all initial conditions must be specified at a single time (usually $t=0$) and all boundary conditions must be specified at a single location (usually at $x=0$ or $x=L$, where L is the beam length). This condition is satisfied for the time domain using four homogeneous initial conditions. So we have $\bar{y}(p,0)=\dot{\bar{y}}(p,0)=\bar{\phi}=(p,0)=\dot{\bar{\phi}}(p,0)=0$. For the space domain, only two boundary conditions at $x=0$ are known a priori: a zero displacement and a zero slope corresponding to a fixed-end condition. The other two boundary conditions are unknown, but can be found in terms of the support shear force, $V(0,t)$, and the support bending moment, $M(0,t)$. The four transformed boundary conditions are found by taking the time Laplace transform of both equations (1) and the homogeneous boundary conditions for displacement and rotation. This results in

$$\bar{y}(0,s)=0 \qquad \bar{y}'(0,s)=\frac{-\bar{V}(0,s)}{\zeta}+\bar{\phi}(0,s)$$
$$\bar{\phi}(0,s)=0 \qquad \bar{\phi}'(0,s)=\frac{\bar{M}(0,s)k'}{r^2\beta\zeta} \tag{4}$$

where $\zeta=k'A(G+\eta s)$ and $\bar{V}(0,s)$, $\bar{M}(0,s)$ are the time Laplace transforms of the support shear force and support bending moment, respectively. The quantities $\bar{V}$ and $\bar{M}$ appear as unknown variables in equations (4), but can be evaluated with the use of boundary conditions at $x=L$, as will be shown.

Transforming equations (2) first in time and then in space results in the following simultaneous linear algebraic equations in the Laplace variables $\bar{\bar{y}}$ and $\bar{\bar{\phi}}$:

$$p\bar{\bar{y}}+\left(\frac{r^2\beta}{k'}p^2-1\right)\bar{\bar{\phi}}=\frac{\bar{M}(0,s)}{\zeta}$$
$$\left(\frac{\rho As^2}{\zeta}-p^2\right)\bar{\bar{y}}+p\bar{\bar{\phi}}=\frac{-\bar{\bar{q}}+\bar{V}(0,s)}{\zeta} \tag{5}$$

where $\bar{\bar{q}}\equiv\bar{\bar{q}}(p,s)$ is the double Laplace transform of the external loading, $q(x,t)$. Solution to equations (5) gives

$$\bar{\bar{y}}(p,s)=\left\{\frac{pk'\bar{M}}{r^2\beta\zeta}+\left(\frac{k'}{r^2\beta\zeta}-\frac{p^2}{\zeta}\right)(-\bar{\bar{q}}+\bar{V})\right\}\Big/D(p)$$
$$\bar{\bar{\phi}}(p,s)=\left\{\frac{k'}{r^2\beta\zeta}\left(p^2-\frac{\rho As^2}{\zeta}\right)\bar{M}+\frac{pk'}{r^2\beta\zeta}(-\bar{\bar{q}}+\bar{V})\right\}\Big/D(p) \tag{6a}$$

where $\bar{V}$ and $\bar{M}$ are shorthand versions of $\bar{V}(0,s)$ and $\bar{M}(0,s)$ and where

$$D(p)=p^4-\frac{\rho As^2}{\zeta}p^2+\frac{k'\rho As^2}{r^2\beta\zeta}=(p^2-p_1^2)(p^2-p_2^2) \tag{6b}$$

The roots of $D(p)$ are given as

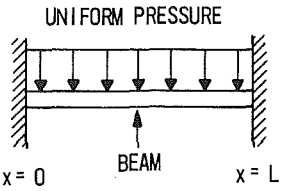


Fig. 3(a) Uniform pressure distribution in space

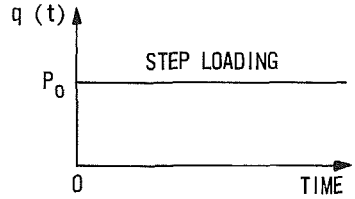


Fig. 3(b) Step function in time

Fig. 3 Beam load function

$$\begin{matrix}p_1(s)\\p_2(s)\end{matrix}=\left\{\frac{\rho As^2}{2\zeta}\pm\frac{\rho As^2}{2\zeta}\left\{1-\frac{4k'\zeta}{r^2\beta\rho As^2}\right\}^{1/2}\right\}^{1/2} \tag{7}$$

The inversion of equations (6a) is accomplished in two sequential steps: the fist inversion is in "p" and the second is in "s." Inverting first with respect to p is accomplished using the inversion theorem or the residue theorem

$$\bar{y}(x,s)=\frac{1}{2\pi j}\int_{g-j\infty}^{g+j\infty}e^{px}\bar{\bar{y}}(p,s)dp$$
$$=\Sigma\text{ residues of }e^{px}\bar{\bar{y}}(p,s)\text{ at }\pm p_1\text{ and }\pm p_2 \tag{8}$$

where j is the complex number $(-1)^{1/2}$ and "g" is chosen so that all the singular points of $\bar{\bar{y}}(p,s)$ lie to the left of "g" on the real line in the complex p plane. A similar operation is also accomplished for $\bar{\bar{\phi}}(x,s)$.

Anderson (1971) has shown that the residue theorem results in

$$L_p^{-1}\frac{p^{n-1}}{D(p)}=G_n(x,s) \tag{9}$$

and

$$G_n(x,s)=\frac{1}{(p_1^2-p_2^2)}\frac{d^{n-1}}{dx^{n-1}}\left\{\frac{\sinh p_1x}{p_1}-\frac{\sinh p_2x}{p_2}\right\}$$

where L_p^{-1} is a symbol denoting the inversion operator in the variable p and $(n-1)$ is the power of p in equations (6). Hence, equations (9) are used to invert all terms on the right-hand sides of equations (6a) except those terms associated with the distributed load $q(x,t)$. For terms involving $\bar{\bar{q}}(p,s)$, the convolution theorem is used in the inversion process. Applying this theorem to the pertinent terms in equations (6a) results in

$$A_0(x,s)=-L_p^{-1}\left\{\frac{k'}{r^2\beta\zeta}-\frac{p^2}{\zeta}\right\}\frac{\bar{\bar{q}}(p,s)}{D(p)} \tag{10}$$
$$=-\int_0^x\bar{q}(x-u,s)\left\{\frac{k'}{r^2\beta\zeta}G_1(u,s)-\frac{G_3(u,s)}{\zeta}\right\}du$$

and similarly

$$B_0(x,s)=-L_p^{-1}\left\{\frac{pk'}{r^2\beta\zeta}\right\}\frac{\bar{\bar{q}}(p,s)}{D(p)}$$
$$=-\int_0^x\bar{q}(x-u,s)\left\{\frac{k'}{r^2\beta\zeta}G_2(u,s)\right\}du \tag{11}$$

where u is a variable of integration.

For this analysis, a simple step function in time and a uniformly distributed pressure in space (see Fig. 3) is an adequate load function to show the relationship between shear

Downloaded 02 May 2010 to 171.66.16.54. Redistribution subject to ASME license or copyright; see http://www.asme.org/terms/Terms_Use.cfm

and moment. The load function and its double Laplace transform are given by

$$q(x,t) = P_0 H(t)\{H(x)-H(x-L)\} \tag{12}$$
$$\bar{\bar{q}}(p,s) = \frac{P_0}{s}\{1-e^{-Lp}\}$$

where $H(u)$ is the unit step function and P_0 is the peak load (see Fig. 3)

Finally, using the results from equations (9–12) produces

$$\begin{aligned}\bar{y}(x,s) &= A_0(x,s)+A_3(x,s)\bar{V}+A_4(x,s)\bar{M}\\ \bar{\phi}(x,s) &= B_0(x,s)+B_3(x,s)\bar{V}+B_4(x,s)\bar{M}\end{aligned} \tag{13}$$

where

$$\begin{aligned}A_3(x,s) &= k'G_1(x,s)/r^2\beta\zeta - G_3(x,s)/\zeta\\ A_4(x,s) &= k'G_2(x,s)/r^2\beta\zeta\\ B_3(x,s) &= A_4(x,s)\\ B_4(x,s) &= k'G_3(x,s)/r^2\beta\zeta - k'\rho A s^2 G_1(x,s)/r^2\beta\zeta\end{aligned}$$

The two unknown constants $\bar{V}$ and $\bar{M}$ are determined by evaluating equation (13) and the boundary conditions $\bar{y}(L,s)=\bar{\phi}(L,s)=0$ at the other end of the beam, $x=L$. Solving simultaneously for $\bar{V}$ and $\bar{M}$ results in

$$\bar{V}(0,s)=\frac{B_0A_4-A_0B_4}{A_3B_4-A_4B_3} \qquad \bar{M}(0,s)=\frac{A_0B_3-B_0A_3}{A_3B_4-A_4B_3} \tag{14}$$

where

$$A_i=A_i(L,s) \quad i=0,3,4$$
$$B_i=B_i(L,s) \quad i=0,3,4$$

Since the focus of this paper is to show that early time rate effects enhance the shear more than the bending moment, a pertinent quantity of interest here is the ratio $V(0,t)/M(0,t)$ abbreviated as V/M. This ratio is obtained once $\bar{V}$ and $\bar{M}$ are inverted in the variable s. However, the expressions in equations (14) are very complicated, involving products of hyperbolic functions. Since the interest is in achieving a solution for a small time beyond $t=0$, it is possible to use an asymptotic approximation on s, thereby simplifying equations (14) prior to inversion. If the Laplace variable s is allowed to grow very large (corresponding to a small time), the roots given in equation (7) and the expressions in equations (14) are simplified to

$$\begin{aligned}p_1^2(s) &= \frac{\rho s}{k'\eta}\\ p_2^2(s) &= 0\end{aligned} \tag{15}$$

and

$$\begin{aligned}\bar{V}(0,s) &= \frac{P_0\sinh p_1L}{sp_1(\cosh p_1L-1)}\\ \bar{M}(0,s) &= \frac{P_0r^2\beta}{sk'(\cosh p_1L-1)}\end{aligned} \tag{16}$$

The inversion of equations (16) is now accomplished using the theory of residues. In both equations (16) all singularities occur at the pole $s=0$. However, because both equations (16) involve hyperbolic functions, the order of the poles is unknown. This is overcome by replacing the hyperbolic functions by their Maclaurin expansions, which results in

$$\begin{aligned}\bar{V}(0,s) &= \frac{P_0}{s^2}\left\{\frac{a_0+a_1s+a_2s^2+\ldots}{b_0+b_1s+b_2s^2+\ldots}\right\}\\ \bar{M}(0,s) &= \frac{P_0r^2\beta}{k's^2}\left\{\frac{1}{b_0+b_1s+b_2s^2+\ldots}\right\}\end{aligned} \tag{17}$$

where

$$a_0 = L \qquad b_0 = \rho L^2/2k'\eta$$
$$a_1 = \rho L^3/6k'\eta \qquad b_1 = \rho^2L^4/24k'^2\eta^2$$

and so forth, for higher order terms of the series.

The denominators in equations (17) identify the poles as being of second order. Using the residue theorem, the inversions are found as

$$\begin{aligned}V(0,t) &= \lim_{s\to0}\frac{d}{ds}\left\{\frac{s^2P_0e^{st}}{s^2}\left[\frac{a_0+a_1s+\ldots}{b_0+b_1s+\ldots}\right]\right\}\\ &= P_0\left\{\frac{a_0t+a_1-a_0b_1/b_0}{b_0}\right\}\end{aligned} \tag{18}$$

$$\begin{aligned}M(0,t) &= \lim_{s\to0}\frac{d}{ds}\left\{\frac{s^2P_0r^2\beta e^{st}}{k's^2}\left[\frac{1}{b_0+b_1s+\ldots}\right]\right\}\\ &= \frac{P_0r^2\beta}{k'}\left\{\frac{t-b_1/b_0}{b_0}\right\}\end{aligned} \tag{19}$$

The ratio of shear to moment at the support ($x=0$), including rate effects (denoted by a subscript z), is obtained as

$$\left\{\frac{V(0,t)}{M(0,t)}\right\}_z=\frac{k'L}{r^2\beta}\left\{\frac{t+\dfrac{\rho L^2}{12k'\eta}}{t-\dfrac{\rho L^2}{12k'\eta}}\right\} \tag{20}$$

Elastic Solution. In an effort to determine whether shearing forces are enhanced more than bending moments by the presence of rate effects, equation (20) must be compared to the same ratio determined for a fixed-end Timoshenko beam without rate effects. Proceeding is the same manner as before, equations (2) are simplified when rate effects are ignored. These equations become

$$\begin{aligned}y' - \phi + \frac{r^2\beta}{k'}\phi'' &= 0\\ y'' - \phi' &= \frac{\rho\ddot{y}}{k'G}=\frac{-q}{k'AG}\end{aligned} \tag{21}$$

As before, using the boundary conditions for a fixed-end beam and the homogeneous initial conditions, equation (3)-(14) remain exactly the same except for the following change:

$$\zeta=k'AG \tag{22}$$

This change then results in a change of the roots after an asymptotic approximation on s ($s\to\infty$), and equations (15) change as follows

$$\begin{aligned}p_1^2(s) &= \frac{\rho s^2}{k'G}\\ p_2^2(s) &= 0\end{aligned} \tag{23}$$

Again proceeding as before, equation (16) remains unchanged and, after Maclaurin expansions are performed on the hyperbolic functions, equations (17) become

$$\begin{aligned}\bar{V}(0,s) &= \frac{P_0}{s^3}\left\{\frac{a_0+a_1s^2+a_2s^4+\ldots}{b_0+b_1s^2+b_2s^4+\ldots}\right\}\\ \bar{M}(0,s) &= \frac{P_0r^2\beta}{k's^3}\left\{\frac{1}{b_0+b_1s^2+b_2s^4+\ldots}\right\}\end{aligned} \tag{24}$$

where

$$a_0 = L \qquad b_0 = \rho L^2/2k'G$$
$$a_1 = \rho L^3/6k'G \qquad b_1 = \rho^2L^4/24k'^2G^2$$

and so forth for the higher order terms.

The poles at $s=0$ in equations (24) are now identified as being of order three. Now, using the residue theorem for the inversion, equations (18) and (19) become

Downloaded 02 May 2010 to 171.66.16.54. Redistribution subject to ASME license or copyright; see http://www.asme.org/terms/Terms_Use.cfm

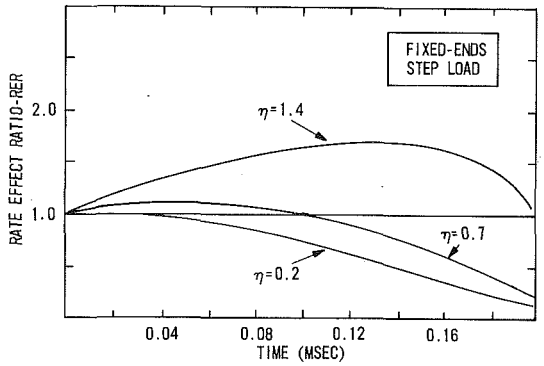


Fig. 4 Rate effect ratio (*RER*) versus time for example beam

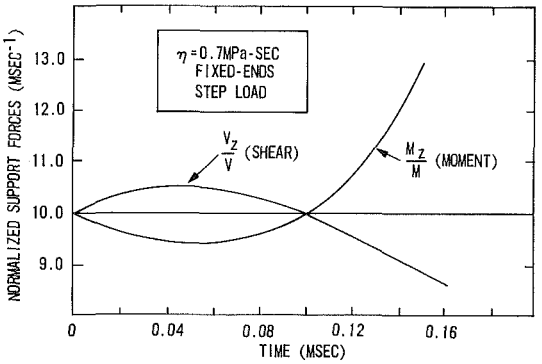


Fig. 5 Normalized support forces versus time for example beam for a constant viscosity parameter, $\eta = 0.7$ MPa-sec

$$V(0,t) = \frac{1}{2}\lim_{s\to 0}\frac{d^2}{ds^2}\left\{\frac{s^3P_0e^{st}}{s^3}\left[\frac{a_0+a_1s^2+\ldots}{b_0+b_1s^2+\ldots}\right]\right\} = \frac{P_0}{2}\left\{\frac{a_0t^2+2a_1-2a_0b_1/b_0}{b_0}\right\} \quad (25)$$

$$M(0,t) = \frac{1}{2}\lim_{s\to 0}\frac{d^2}{ds^2}\left\{\frac{s^3P_0r^2\beta e^{st}}{k's^3}\left[\frac{1}{b_0+b_1s^2+\ldots}\right]\right\} = \frac{P_0r^2\beta}{2k'}\left\{\frac{t^2-2b_1/b_0}{b_0}\right\} \quad (26)$$

Substituting for the appropriate constants in equations (25) and (26), the shear-to-moment ratio at the support, neglecting rate effects, becomes

$$\left\{\frac{V(0,t)}{M(0,t)}\right\} = \frac{k'L}{r^2\beta}\left\{\frac{t^2+\dfrac{\rho L^2}{6k'G}}{t^2-\dfrac{\rho L^2}{6k'G}}\right\} \quad (27)$$

Strain Rate Effects on Shear and Moment. The purpose for obtaining the solution of the viscoelastic Timoshenko beam is to show that, in early time after the beam is subjected to a rapidly applied load, rate effects have a more pronounced effect on shear than bending moment. This situation would indicate the dominance of shear over bending moment under impulsive load conditions. This dominance of shear over moment is manifested if the following ratio is greater than 1:

$$RER = \left|\frac{\left(\dfrac{V}{M}\right)_z}{\left(\dfrac{V}{M}\right)}\right| \geq 1 \quad (28)$$

where *RER* is the "rate effect ratio" and the numerator and denominator of equation (28) are given by equations (20) and (27), respectively.

Table 1 Example reinforced concrete beam properties

Length(L)	=	1.14 m (44.75 in)
Thickness(h)	=	0.18 m (7.25 in)
Area(A)	=	0.18 m^2 (7.25 in^2)
Beam density(ρ)	=	2400 kg/m^3 (150 pcf)
Shear modulus(G)	=	13,800 MPa (2 × 10^6 psi)
Elastic modulus(E)	=	33,100 MPa (4.8 × 10^6 psi)
Poisson's ratio(ν)	=	0.20
Shear deformation coefficient(k')	=	0.822
Direct shear capacity(V_u)	=	6140 kg (13500 lb)

Obviously, before the value of $(V/M)_z$ can be computed, an estimate for the shear viscosity parameter, η, must be available. Bazant and Byung (1982) provide an excellent bibliography on basic data regarding the dynamic properties of concrete and steel as a function of strain rate. Information on rate effects on elastic and strength properties of concrete is also given in Watstein and Boresi (1953). Figures 6 and 7 show the enhancement of the modulus of elasticity (denoted the modulus enhancement) and the uniaxial compressive strength of concrete (denoted the strength enhancement) as a function of strain rate and loading rate, respectively.

Since these data are for samples in uniaxial compression, the slope of the curve represents a measure of the viscosity coefficient for compression, α'. As discussed, the shear viscosity is computed from the relation $\alpha' = \eta\beta$. It can be shown that the viscoelastic constitutive relationship for shear displayed in Fig. 2(*a*) can be rewritten in a form that expresses the viscosity parameter as a function of the dynamic enhancement of the elastic shear modulus. This relation is given as

$$\eta = \frac{\alpha'}{\beta} = \frac{G\gamma}{\dot{\gamma}}(\Psi - 1) \quad (29)$$

where γ is the shear angle at the centroid of the Timoshenko beam, Ψ is the modulus enhancement factor, shown in Fig. 6(*a*), and $\dot{\gamma}$ is the shear strain rate. The data used to construct Figs. 6(*a*) and 7(*a*) correspond to measured values of the secant modulus through a uniaxial strain of 0.001. The expression in equation (29) is valid when $\gamma = 0.001$ and $\dot{\gamma}$ takes the value of the uniaxial strain rate. For example, at a strain rate of 5/sec and an elastic modulus enhancement factor, Ψ, of approximately 1.25, the viscosity parameter is about $\eta = 0.70$ MPa-sec. Since the analysis described in this paper relies on a discrete value of η, selected values of this coefficient are valid only over a short range of strain rates and load rates. This limitation presents no barrier at this point since the *RER* computed by equation (28) is valid only for a small interval of time beyond $t = 0$.

Figure 4 shows a plot of the absolute value of the *RER* versus time for an example beam with the properties shown in Table 1. The time scale has been truncated at about 0.2 msec. This is about the time at which the denominator in equation (28) becomes nonanalytic. This time is equivalent to the time it takes a shear wave to travel a distance of about 40 percent of the beam length and is taken to be the maximum time over which equation (28) is valid. The curves shown in Fig. 4 correspond to three different values of the shear viscosity parameter. Generally, the smaller the shear viscosity parameter, the shorter is the time during which the *RER* is greater than one. This is intuitive because the asymptotic approximation used to derive the *RER* is based on the Laplace variable "s" approaching infinity. In the time domain this corresponds to a solution near $t = 0$. Since the Laplacian parameter s appears as a product ηs, the lower the value η, the higher the value s required to let ηs get large. Hence, a small shear viscosity parameter corresponds to a much shorter time where the *RER* exceeds one.

When the *RER* in Fig. 4 drops below a value of one, a condition arises where the normalized support bending

Downloaded 02 May 2010 to 171.66.16.54. Redistribution subject to ASME license or copyright; see http://www.asme.org/terms/Terms_Use.cfm

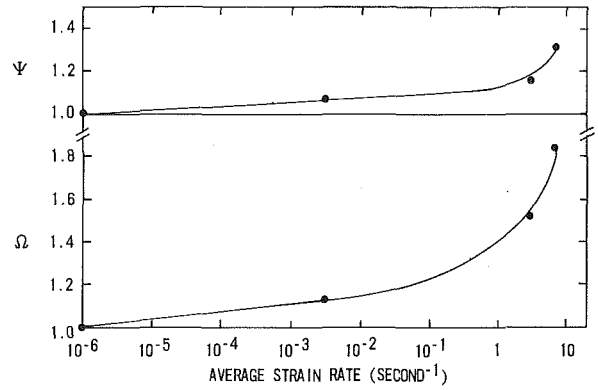


Fig. 6 Enhancement factors for 45 MPa concrete versus strain rate for (*a*) elastic modulus, ψ, and (*b*) strength, Ω (adapted from Watstein and Boresi, 1953)

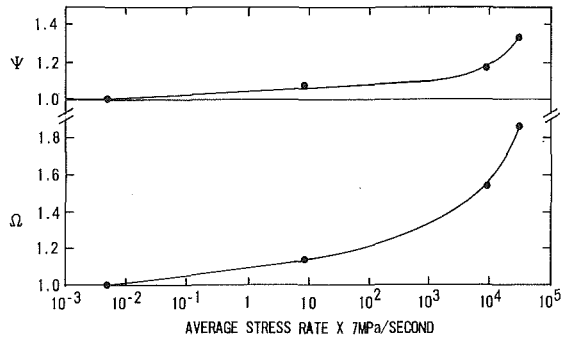


Fig. 7 Enhancement factors for 45 MPa concrete versus load rate (stress rate) for (*a*) elastic modulus, Ψ, and (*b*) strength, Ω (adapted from *Watstein and Boresi, 1953*)

moment begins to dominate the normalized support shear force. This phenomenon is shown more clearly in Fig. 5, which shows normalized plots of shear and moment versus time for a single value of the shear viscosity parameter. The normalized shear, denoted as V_z/V in the figure, is the ratio of equation (18) to equation (25) and the normalized moment, denoted as M_z/M in the figure, is the ratio of equation (19) to equation (26). Again, the subscript "z" refers to a quantity that considers the strain rate effect. Figure 5 also displays the fact that the support shear is enhanced more than the support bending moment in early time when strain rate effects are considered. However, as can be seen in the figure, the bending moment does begin to have a significant effect after the early influence of the shear. This happens at later time, however, and it has already been discussed that the asymptotic nature of the solution provides for acceptable results only in the very early time domain.

The plots in Figs. 4 and 5 clearly show the major result of the strain rate portion of this paper. Strain rate effects have a more pronounced effect on shear than on bending moment during an early time in the loading history comparable to the times of interest in this study.

Information on the behavior of the support shear $V(0,t)$ shows another feature of the effect of strain rate. It is interesting to evaluate the magnitude of the support shear force by comparing it to the ultimate shear capacity of the beam in a direct shear mode, denoted as V_u (see this mode in Fig. 1(*c*) and a value for the example beam in Table 1). In particular, when the normalized quantity V/V_u exceeds the parameter Ω, called the strength enhancement factor, the beam is defined to have failed in direct shear at the support. When strength enhancement due to rate effects is ignored, the value of Ω is taken to be unity, as seen in Figs. 6(*b*) and 7(*b*) for very small strain rates and load rates, respectively.

Figures 8(*a*) and 8(*b*) show plots of the time parameter t', defined as the time the ratio V/V_u reaches unity, versus peak pressure P_0 from a step loading. These plots are computed by normalizing equations (18) and (25) with respect to ΩV_u and then plotting the behavior of t' for different values of P_0. In each plot, one curve is for an elastic beam without rate effects ($\eta = 0$), and the other is for a viscoelastic beam with $\eta = 1.4$ MPa-sec (strain rate = 1.5/sec). In Fig. 8(*a*), V_u is not enhanced for rate effects ($\Omega = 1$), whereas in Fig. 8(*b*) V_u is enhanced by a factor of $\Omega = 1.5$, which corresponds to a strain rate of 1.5/sec as seen from the curve in Fig. 6(*b*). As shown in Fig. 8(*a*) and (*b*), the viscoelastic curve is always lower than the elastic curve, indicating that the support shear force will reach its failure level ($V = \Omega V_u$) sooner when considering elastic rate effects than when rate effects are not considered. In addition, the parameter t' increases when the influence of rate effects on the strength capacity V_u is included through the use of a strength enhancement factor. The information provided in Figs. 4, 5, and 8 is qualitative owing to the approximations involved in Laplace solution procedure.

Load Rate Influence

It is simpler to include load rate effects than strain rate effects in the elastic analysis, because the elastic Timoshenko beam equations remain unaltered when load rates are considered. The same two factors that are associated with strain rate effects are also associated with load rate effects. The first is the modulus enhancement factor, which accounts for increased stiffness due to load rate, and the second is the strength enhancement factor, which accounts for increased material strength due to load rate. Both these factors for load rate are approximations to the true enhancements due to rate influences. The use of load rate as an indicator of the true rate of response (stress rate) is not precise. Nevertheless, its use can be justified when one considers that most available test data on dynamic material properties are based on average load rate. Furthermore, the load rate is probably an upper bound to the true rate of response during the first quarter-cycle of vibration (generally the response period for impulsive loads).

By assuming load rate to be equivalent to stress rate, enhancement factors for both elastic and strength properties can be obtained from the curves shown in Fig. 7. When these enhancement factors are used to increase the elastic modulus of the beam and to increase the beam strength capacity, curves analogous to those shown in Figs. 8(*a*) and (*b*) can be developed to show load rate influence on the parameter t'. Figures 9(*a*) and (*b*) show the separate influence of the strength enhancement factor $\Omega = 1.6$ and the elastic modulus enhancement factor $\Psi = 1.2$, respectively, on the normalized support shear for a load rate of approximately 70,000 MPa/sec (the associated strain rate is approximately 4/sec). In Fig. 9(*a*), the effect of the strength enhancement factor is to reduce V/V_u by the quantity $1/\Omega$. In Fig. 9(*b*), the effect of the elastic modulus enhancement factor is to alter the frequency content of the beam, making it slightly stiffer and, hence, quicker to respond.

A result reached in this section on load rate is the same as that drawn in the section on strain rate. The parameter t' increases as the strength enhancement factor increases (Fig. 9(*a*)) and it decreases as the elastic modulus enhancement factor increases (Fig. 9(*b*)). On the basis of this limited study on load rate effects, it is concluded that the major influences on t' come from strength enhancement. The effect of modulus enhancement on time to failure is very small. The results from the analysis including strain rate (see preceding section) show a larger decrease in time to failure due to viscoelastic enhancement, and also show that the support shear force is influenced more than the support bending moment. Thus, the effect of viscous or elastic modulus enhancement is to amplify the dominance of shear force over

Downloaded 02 May 2010 to 171.66.16.54. Redistribution subject to ASME license or copyright; see http://www.asme.org/terms/Terms_Use.cfm

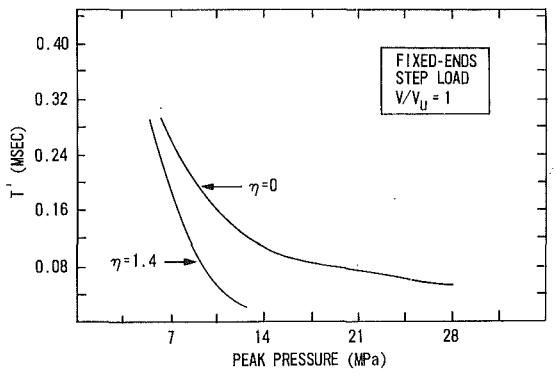


Fig. 8(*a*) Ω = 1.0

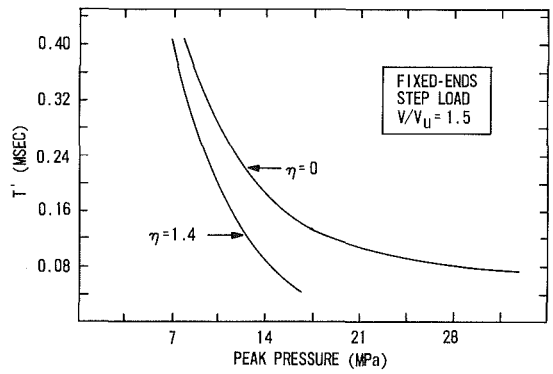


Fig. 8(*b*) Ω = 1.5

Fig. 8 Strain rate effects on shear failure time, t', for example beam

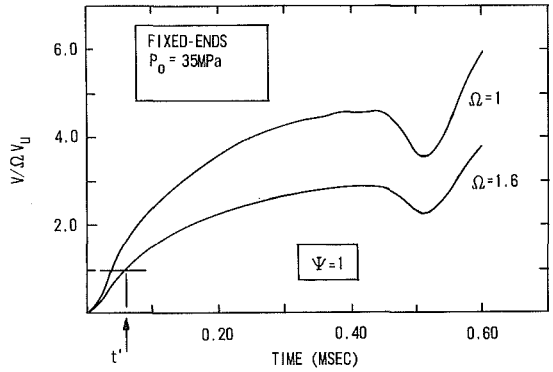


Fig. 9(*a*)

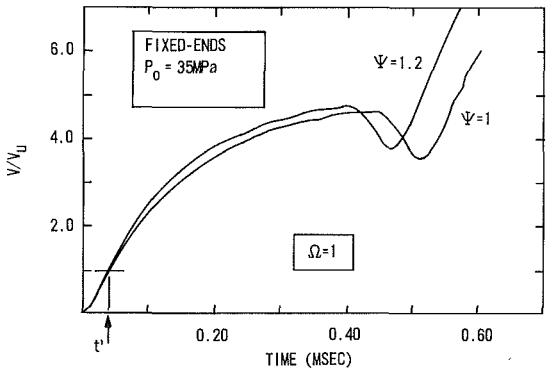


Fig. 9(*b*)

Fig. 9 Effects on normalized support shear of example beam for a load rate of 70,000 MPa/sec due to a (*a*) strength enhancement, and (*b*) elastic modulus (stiffness) enhancement

bending moment for the early time after a rapid loading is applied on the beam.

Conclusions

The elastic Timoshenko beam equations are extended to account for viscoelastic material properties in order to model strain rate effects. Results from a Laplace solution show that strain rate amplifies shear more than bending moment in the early transient response regime of a beam subjected to a uniformly distributed, transverse step-loading (see Figs. 4 and 5). In particular, the time to failure in a direct shear mode at the support is significantly decreased when strain rate effects are included in the Timoshenko model (see Fig. 8). The simplified modeling of load rate by using the elastic Timoshenko beam equations indicates that both material strengths and elastic moduli are enhanced under rapidly applied load conditions. Analysis shows that predictions for failure in a direct shear mode are much more sensitive to load rate effects on strength than on elastic moduli (see Fig. 9).

When comparing the analytic influences of strain rate to those of load rate on the predicted failure in a direct shear mode at a beam support, a few interesting conclusions arise. First, the parameter t' (the time at which the support shear force exceeds the direct shear capacity of a beam) increases as the strength of the beam increases under a rate influence (see Figs. 8 and 9(*a*)) and it decreases as the stiffness (elastic modulus) of the beam increases under a rate influence (Figs. 8 and 9(*b*)). This conclusion was verified by both strain rate and load rate analyses. Second, the analysis including strain rate showed a larger decrease in time to failure due to stiffness (elastic modulus) enhancement than did the analysis including load rate (Figs. 8(*a*), (*b*), and 9(*b*)). Third, the effect of strain rate and load rate is to amplify the dominance of the support shear force over the support bending moment for a rapidly loaded beam (Figs. 4 and 5).

Acknowledgment

This work was partially supported by the US Air Force Office of Scientific Research under Task 2302Y2 and is gratefully acknowledged.

References

1 Anderson, G. M., 1971, "Timoshenko Beam Dynamics," ASME JOURNAL OF APPLIED MECHANICS, Vol. 38, pp. 591–594.

2 Bazant, Z. P., and Byung, H. O., 1982, "Strain Rate Effect in Rapid Triaxial Loading of Concrete," ASCE, *Journal of the Engineering Mechanics Division*, Vol. 108, EM5, pp. 764–782.

3 Colton, J. D., 1973, "Multiple Fracture of Beams and Plates Under Localized Impulsive Loading," Ph.D dissertation, Stanford University, Stanford, Calif.

4 Mindlin, R. D., 1951, "Influence of Rotary Inertia and Shear on Flexural Motions of Isotropic Elastic Plates," ASME JOURNAL OF APPLIED MECHANICS, Vol. 18, pp. 31–38.

5 Ross, T. J., 1983, "Direct Shear Failure in Reinforced Concrete Beams Under Impulsive Loading," Ph.D Disseration, Stanford University, Stanford, Calif.

6 Ross, T. J., and Wong, F. S., 1985, "Timoshenko Beams With Rotational End Constraints," ASCE *Journal of Engineering Mechanics*, Vol. 111, EM3.

7 Timoshenko, S., Young, D. A., and Weaver, W., 1974, *Vibration Problems in Engineering*, 4th Ed., Wiley, New York, pp. 432–435.

8 Watstein, D., and Boresi, A. P., 1953, "The Effect of Loading Rate on the Compressive Strength and Elastic Properties of Plain Concrete," *Journal of the American Concrete Institute*, Vol. 24, p. 729.

Downloaded 02 May 2010 to 171.66.16.54. Redistribution subject to ASME license or copyright; see http://www.asme.org/terms/Terms_Use.cfm

Period-Doubling Bifurcations and Modulated Motions in Forced Mechanical Systems[1]

S. Tousi
Graduate Assistant.

A. K. Bajaj
Assistant Professor.
Associate Mem. ASME

School of Mechanical Engineering,
Purdue University,
West Lafayette, Ind. 47907

Weakly nonlinear and harmonically forced two-degree-of-freedom mechanical systems with cubic nonlinearities and exhibiting internal resonance are studied for their steady-state solutions. Using the method of averaging, the system is transformed into a four-dimensional autonomous system in amplitude and phase variables. It is shown that for low damping the constant solutions of the averaged equations are unstable over some interval in detuning. The transition in stability is due to the Hopf bifurcation and the averaged system performs limit cycle motions near the critical value of detuning. The bifurcated periodic solutions are constructed via a numerical algorithm and their stability is analyzed using Floquet theory. It is seen that the periodic branch connects two Hopf points in the steady-state response curves. For sufficiently small damping, the averaged equations, therefore, have stable limit cycles where the constant solutions are unstable. Reduction in damping results in destabilization of these periodic solutions with one Floquet multiplier leaving the inside of the unit circle through -1. This leads to period-doubling bifurcations in the averaged equations. There is, thus, an interval in detuning parameter over which the constant and the periodic solutions are unstable and the period-doubled solutions are stable. For small enough damping there are cascades of period-doubling bifurcations that ultimately lead to chaotic motions. Some of these sequences seem to be compatible with the Feigenbaum Universality Constant.

Introduction

Weakly nonlinear multidegrees-of-freedom mechanical systems under periodic excitations have been studied extensively for their steady-state periodic solutions [1]. For systems having "internal resonance" [1, 2], the response curves can be particularly complicated with many branches. These branches represent either stable or unstable periodic motions. The transition from stable to unstable motions is usually of two types. The first type is associated with the familiar jump phenomenon and it occurs at a turning point. In the regions associated with the second kind of instability the system equations perform amplitude-modulated motions. This was observed, among others, by Miles [3] in forced oscillations of a spherical pendulum and by Sethna [4] in a two-degrees-of-freedom system with quadratic nonlinearities.

Sethna and Bajaj [5] showed that the second kind of instability occurs due to the Hopf bifurcation [6] in the averaged equations. They used a perturbation approach in conjunction with an integral manifold theorem [7] in the method of averaging [7] to show that for detuning near transition points the averaged system has a limit cycle and therefore the original nonlinear system performs amplitude modulated motions.

Autonomous dynamical systems dependent on a parameter have been the subject of extensive research for quite some time. It is well known that constant solutions can become unstable by a saddle-node or Hopf bifurcation giving rise to a new branch of constant or limit cycle solutions, respectively [8, 9]. It is also easy to envisage a situation in which a limit cycle, which depends on some parameter, becomes unstable and bifurcates into more complicated solutions. A limit cycle can become unstable and undergo either a saddle-node (tangent) bifurcation, a flip (period-doubling) bifurcation, or a bifurcation into a two-torus [8, 9]. In some systems the process of period-doubling bifurcations may take place repeatedly culminating ultimately in "chaotic" motions [9, 10].

The cascades of period-doubling bifurcations and the resulting periodic and chaotic motions have been the subject of intensive research in the last 8–10 years. These have been found to occur in various dynamical systems ranging from one-dimensional noninvertible maps [11, 12] to chemical reactions [13], nonlinear forced oscillators [14–17], and truncated models of Navier-Stokes equations [18].

In the present work we study small, forced nonlinear motions in a two-degrees-of-freedom system that exhibits internal resonance and has cubic nonlinearities. The method of averaging is used and the system is reduced to a system of

[1] This work was supported by funds from the National Science Foundation under Grant MEA-8117086.

Contributed by the Applied Mechanics Division for publication in the JOURNAL OF APPLIED MECHANICS.

Discussion on this paper should be addressed to the Editorial Department, ASME, United Engineering Center, 345 East 47th Street, New York, N.Y. 10017, and will be accepted until two months after final publication of the paper itself in the JOURNAL OF APPLIED MECHANICS. Manuscript received by ASME Applied Mechanics Division, June, 1984; final revision, September, 1984.

Copyright © 1985 by ASME
Downloaded 02 May 2010 to 171.66.16.54. Redistribution subject to ASME license or copyright; see http://www.asme.org/terms/Terms_Use.cfm

four first-order autonomous equations in amplitude and phase variables. The averaged system depends essentially on two parameters, the excitation frequency and the damping. It is studied for its constant solutions. They are, for some range of parameters, unstable due to a complex conjugate pair of eigenvalues crossing the imaginary axis. The Hopf-bifurcating limit cycle solutions of the averaged equations are constructed numerically using a scheme derived by Chua and Lin [19]. This technique, which is efficient for generating stable as well as unstable periodic solutions, can be used to continue the limit cycles for values of parameters far from the bifurcation points.

The stability of periodic solutions of the averaged equations is analyzed via Floquet theory [7]. Saddle-node as well as period-doubling bifurcations are observed in various parameter ranges. For small enough damping cascades of period-doubling bifurcations leading to chaotic motions are found and these results are presented in some detail.

Equations of Motion and the Averaged Equations

Consider nonlinear two-degrees-of-freedom mechanical systems with time-independent constraints and performing nonlinear motions in the neighborhood of a stable static equilibrium configuration. We assume that the nonlinearities arise only from restoring forces and that the dissipative forces acting on the system are linear and the external excitation forces harmonic. In addition, the restoring forces are odd in generalized coordinates.

Let q_1 and q_2 be the principal coordinates for the undamped linearized system. Also, ω_1 and ω_2 are the undamped natural frequencies with $\omega_1 \leq \omega_2$. The nonlinear equations of motion can then be written as

$$\ddot{q}_i + \omega^2_{(i)} q_i = -c_{ij}\dot{q}_j - A_{ijkl}q_j q_k q_l + R_i \cos \nu t + 0(||\mathbf{q}||^4), \qquad i = 1,2, \tag{1}$$

where $c_{ij} = c_{ji}$ arise from the Rayleigh dissipation function, where A_{ijkl} are symmetric with respect to permutations in i, j, k, l, and where a dot represents derivative with respect to time. In (1), the usual summation convention has been adopted.

To make it explicit that we are interested in small nonlinear motions, we introduce a scaling parameter ϵ, $0 < \epsilon << 1$. We also scale the damping and the external excitation. Thus,

$$q_i = \epsilon^{1/2}\zeta_i, c_{ij} = \epsilon D_{ij}, R_i = \epsilon^{3/2}P_i, i, j = 1,2. \tag{2}$$

For simplicity we set $P_2 = 0$ so that the second normal mode only gets excited through its nonlinear coupling with the first mode.

Interesting resonance and instability phenomena are expected [1, 2] when the excitation frequency ν is in the neighborhood of the lower natural frequency ω_1 and when the frequencies ω_1 and ω_2 are close to small rational ratios. The two possible cases are $\omega_2/\omega_1 \approx 1$ and $\omega_2/\omega_1 \approx 3$. In the present work we concentrate on the latter case. To make the foregoing explicit, let

$$\epsilon\Gamma = (\nu^2 - \omega_1^2), \quad 9\epsilon\Gamma = (9\nu^2 - \omega_2^2), \tag{3}$$

where Γ is some "detuning" parameter.

We employ the method of averaging [7] to obtain steady-state solutions of (1). To transform equation (1) into a "standard form," the followng polar transformation is introduced

$$\zeta_i = A_i(t)\cos(s_i \nu t + \Psi_i(t)),$$
$$\dot{\zeta}_i = -s_i \nu A_i(t)\sin(s_i \nu t + \Psi_i(t)), \qquad i = 1,2, \tag{4}$$

where $s_1 = 1$ and $s_2 = 3$. Now, substituting (2)–(4) in (1) and following the method of averaging, we get the averaged equations in new variables a_i, ψ_i, $i = 1,2$. These variables are such that

$$A_i = a_i + 0(\epsilon), \Psi_i = \psi_i + 0(\epsilon), \qquad i = 1,2.$$

Averaged equations in the normalized form are given by

$$\begin{aligned} b_1' &= -\delta b_1 + 3A_2 b_1^2 b_2 \sin(3\psi_1 - \psi_2)/2 - \sin\psi_1 \\ &= G_1(b_1, b_2, \psi_1, \psi_2, \gamma), \\ b_2' &= -\delta b_2 - A_2 b_1^3 \sin(3\psi_1 - \psi_2)/6 \\ &= G_2(b_1, b_2, \psi_1, \psi_2, \gamma), \end{aligned} \tag{5}$$

$$\begin{aligned} \psi_1' &= -\gamma + 3A_1 b_1^2/2 + 3A_2 b_1 b_2 \cos(3\psi_1 - \psi_2)/2 \\ &\quad + 3A_3 b_2^2 - \cos\psi_1/b_1 = G_3(b_1, b_2, \psi_1, \psi_2, \gamma), \\ \psi_2' &= -3\gamma + A_2 b_1^3 \cos(3\psi_1 - \psi_2)/6b_2 + A_3 b_1^2 + b_2^2/2 \\ &= G_4(b_1, b_2, \psi_1, \psi_2, \gamma), \end{aligned} \tag{6}$$

where the normalized variables are defined by

$$A_1 = A_{1111}/A_{2222}, A_2 = A_{1112}/A_{2222}, \quad A_3 = A_{1122}/A_{2222},$$
$$D = D_{11} = D_{22}, \qquad a_1 = (2P_1/A_{2222})^{1/3} b_1,$$
$$a_2 = (2P_1/A_{2222})^{1/3} b_2, \qquad \epsilon t = 2\nu(2/P_1^2 A_{2222})^{1/3}\tau,$$
$$\gamma = \Gamma(2/P_1^2 A_{2222})^{1/3}, \qquad \delta = \nu D(2/P_1^2 A_{2222})^{1/3}.$$

Equations (5) critically depend on two external parameters. The parameter δ represents ratio of damping in the system to the strength of external excitation. Detuning γ represents the deviation of square of the excitation frequency ν from square of the first natural frequency ω_1.

The averaging theorem [7] and the theorem on integral manifolds [7] relate the solutions of the averaged system (5) to the solutions of the coupled oscillators (1). Constant solutions of (5) correspond to $2\pi/\nu$-periodic solutions to (1). Periodic solutions to (5) correspond to amplitude modulated motions of the oscillators. For a geometric interpretation see [5].

In the next section we analyze equation (5) for their constant solutions.

Steady-State Periodic Solutions and Their Stability

Let $\mathbf{x} = (b_1, b_2, \psi_1, \psi_2)^T$ be a four-vector. We can write the system (5) as

$$\mathbf{x}' = \mathbf{G}(\mathbf{x}, \gamma). \tag{7}$$

Here we have shown the dependence only on detuning γ because in subsequent discussions and results it will play a prominent role. Let $\mathbf{x}^0(\gamma)$ be a constant solution to (7) for some value of the parameters. It satisfies

$$\mathbf{G}(\mathbf{x}^0(\gamma), \gamma) = 0. \tag{8}$$

The four equations in (8) can be manipulated to eliminate the phase variables ψ_1^0 and ψ_2^0 and the resulting equations in the amplitudes b_1^0 and b_2^0 take the form

$$b_1^{02} - \delta^2(b_1^{02} + 9b_2^{02})^2 - (-\gamma b_1^{02} + 3A_1 b_1^{04}/2 + 3A_3 b_1^{02} b_2^{02} - 9b_2^{02}(-6\gamma + b_2^{02} + 2A_3 b_1^{02})/2)^2 = 0,$$
$$A_2^2 b_1^{06} - 36\delta^2 b_2^{02} - 9b_2^{02}(-6\gamma + b_2^{02} + 2A_3 b_1^{02})^2 = 0.$$

Solutions to these nonlinear algebraic equations determine the steady-state periodic response. We obtain the response curves as a function of the detuning γ for various values of the damping coefficient δ and a specific set of values for the nonlinear parameters A_1, A_2, and A_3.

The nonlinear parameters chosen for numerical results are:

$$A_1 = 0.66, A_2 = 1.00, A_3 = 1.00.$$

Stability of the Steady-State Solutions. The stability of a constant solution $\mathbf{x}^0$ of equation (7) is determined by the eigenvalues of Jacobian matrix $\mathbf{A} = \partial\mathbf{G}/\partial\mathbf{x}$ $(\mathbf{x}^0(\gamma))$. For a solution $\mathbf{x}^0$ to be stable, the eigenvalues of matrix $\mathbf{A}$ must have negative real parts.

The stability of constant solutions is, in general, a continuous function of the system parameters. As a parameter is varied, it may happen that the corresponding constant

Downloaded 02 May 2010 to 171.66.16.54. Redistribution subject to ASME license or copyright; see http://www.asme.org/terms/Terms_Use.cfm

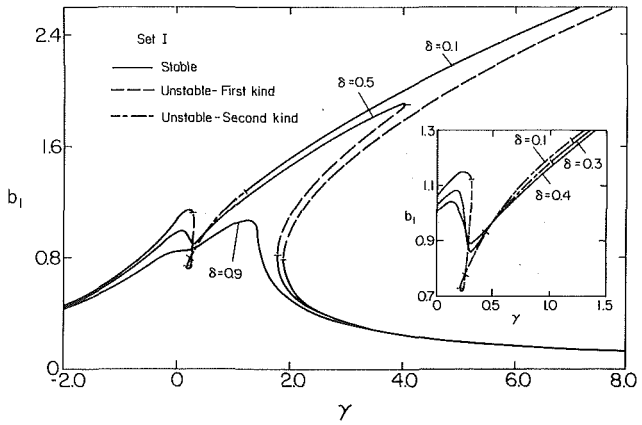


Fig. 1 Steady State solutions b_1^0 versus detuning γ

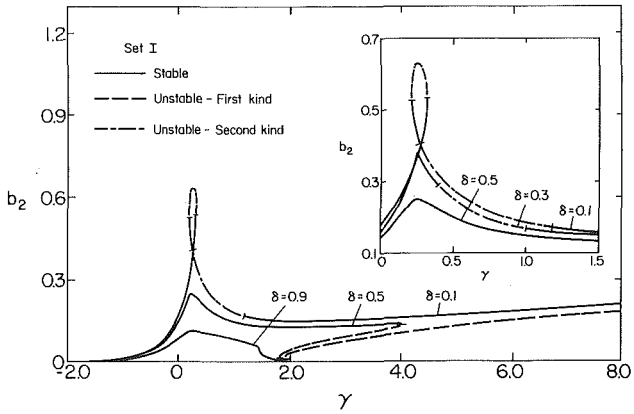


Fig. 2 Steady State solutions b_2^0 versus detuning γ

solution undergoes change in stability. Following the arguments given by Sethna and Bajaj [5], it can be easily shown that, for $\delta \neq 0$, there are only two possible ways in which a stable solution becomes unstable as some system parameter is varied. In the first case one real eigenvalue passes from the left to the right half of the complex plane through the origin. This corresponds, under some nondegeneracy conditions [9], to a turning point in the response curves and gives rise to the "jump" phenomenon. We identify such a change in stability as "transition of the first kind."

The second case occurs when a constant solution becomes unstable with a complex pair of eigenvalues crossing the imaginary axis into the right half of the complex plane. We call such a stability transition "transition of the second kind." This corresponds to the extensively studied problem of the Hopf bifurcation [6] and based on the Hopf bifurcation theorem we expect the averaged equations (7) to exhibit limit cycle oscillations near these parameter values. This topic will be studied further in the next section.

We now present some response curves for the specific parameter set mentioned earlier.

Response Curves. Response curves as a function of the detuning parameter γ for various values of damping δ are shown in Figs. 1 and 2. Since response curves for weakly nonlinear two-degrees-of-freedom systems have been extensively studied in the literature (e.g., see Nayfeh and Mook [2]), we mostly describe only their less well known and more interesting features.

Response curves for both b_1 and b_2 are bent forward and have multivalued regions with the usual jump and hysteresis phenomena for moderate to large positive values of detuning γ. The amplitude of the first mode is many times that of the second mode in this region. As damping is increased the maximum response amplitude decreases and for large enough δ ($\simeq 0.9$), the multivalued regions cease to exit.

The response curves are much more interesting for smaller values of detuning γ. There is a second multivalued region near $\gamma \simeq 0.0$. It disappears quickly as damping is increased. For mode b_1, the amplitude of response is small in this region. For the second mode, however, the maximum amplitude occurs in this region irrespective of the damping present. We conclude therefore that for the secondary mode, b_2, the maximum response occurs when the primary linear mode is in near resonance with the external excitation whereas for the primary mode the maximum response occurs far away from resonance at a frequency larger than the linear natural frequency.

Near $\gamma \simeq 0.0$, there is an interval over which the response is unstable with transition of the second kind. For example, in case of $\delta = 0.1$, as the detuning is decreased from some large enough value, the upper solution branch becomes unstable at $\gamma \simeq 1.18$ by the Hopf bifurcation. This instability persists till $\gamma \simeq 0.26$ when the branch again stabilizes by the same process. For γ between 0.31 and 1.18 there is no stable constant solution. We can, on physical grounds, expect the averaged system to execute some time-dependent but bounded steady-state motions. As damping δ is increased, the extent of such regions decreases and the upper branch completely stabilizes for damping beyond $\delta \simeq 0.4$.

As already mentioned in the Introduction, the previously discussed behavior in the averaged equations was observed, among others, by Miles [3] and Sethna [4]. It was analyzed analytically by Sethna and Bajaj [5] who showed that, at least, near the transition points (e.g., for $\delta = 0.1$, $\gamma \simeq 0.26$ and 1.18), the averaged system has a limit cycle and the original oscillators execute amplitude modulated motions. Study of motions in these regions is of major interest in this work and it forms the subject of sections that follow.

Periodic Solutions of the Averaged Equations

In the last section we showed that, for small damping, constant solutions can become unstable by the transition of the second kind. Let γ_{cr} be, for some δ, such a point of stability transition. Then, the Hopf bifurcation theorem [6] under some technical conditions, guarantees the existence of a limit cycle solution of the averaged system near $\gamma = \gamma_{cr}$, $\mathbf{x} = \mathbf{x}^0$ (γ_{cr}). The amplitude of the limit cycle is of the order of $|\gamma - \gamma_{cr}|^{1/2}$ and its period is close to $2\pi/\omega_0$, where ω_0 is the imaginary part of the critical eigenvalue of Jacobian matrix $\mathbf{A}$. Furthermore, the limit cycle is stable or unstable depending on whether it is supercritical or subcritical.

The Hopf bifurcation theorem provides answers only near the critical values of the parameter. We are interested in the global nature of the bifurcated solution in that we want to find the response curves for the whole range of parameter γ over which the steady state solutions are unstable. The perturbation solution is, therefore, of little help and a numerical technique for finding and constructing periodic solutions is implemented.

A conventional technique for finding limit cycle solutions of an autonomous system is to numerically integrate it for a sufficiently long interval in time until all the transients have decayed. This procedure is not satisfactory for weakly damped systems. In addition, it cannot be used to detect unstable periodic solutions. We employ an algorithm given by Chua and Lin [19] that overcomes both these difficulties. This algorithm transforms a set of ordinary differential equations into a set of nonlinear algebric equations which are solved numerically by the Newton-Raphson iteration technique. Readers should consult reference [19] for details.

The iteration scheme of Chua and Lin requires reasonably good initial guess of a point on the periodic solution and its

Downloaded 02 May 2010 to 171.66.16.54. Redistribution subject to ASME license or copyright; see http://www.asme.org/terms/Terms_Use.cfm

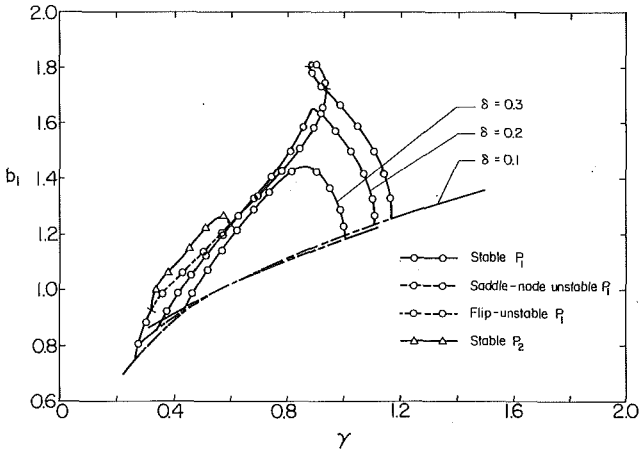


Fig. 3 Amplitude b_1 of the periodic solutions versus detuning γ; δ = 0.1, 0.2, 0.3

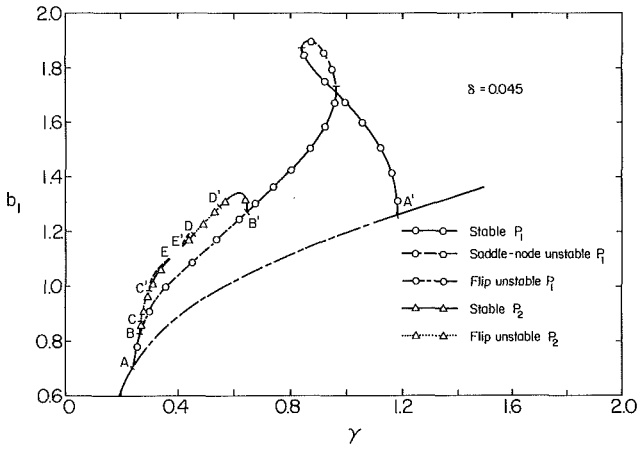


Fig. 4 Amplitude b_1 of the periodic solutions versus detuning γ; δ = 0.045

time period in order for it to converge rapidly. For values of the parameter γ close to γ_{cr}, the Hopf bifurcation theory provides a good starting point. Thus, for the periodic solution corresponding to γ near γ_{cr}, $\mathbf{x}^0$ (γ_{cr}) and $2\pi/\omega_0$ can be taken as an initial guess. Once a periodic orbit and its period are determined for a specific value of γ, they can be used to start the iterations for constructing the solution for a nearby parameter value. The increments in γ have, clearly, to be small enough to assure convergence of the iteration process.

Stability of Periodic Solutions. As is well known (e.g., see Hale [7]), the stability of a T-periodic solution $\mathbf{x}^*(\tau)$, $\mathbf{x}^*(\tau) = \mathbf{x}^*(\tau + T)$, of equations (7) is determined by the Floquet multipliers of the linearized equations

$$\mathbf{y}' = \mathbf{A}(\tau)\mathbf{y} \tag{10}$$

where

$$\mathbf{A}(\tau) = \frac{\partial \mathbf{G}}{\partial \mathbf{x}}(\mathbf{x}^*(\tau))$$

is a T-periodic variational matrix. Let $\mathbf{Y}(\tau)$ be the matrix solution satisfying

$$\mathbf{Y}' = \mathbf{A}(\tau)\mathbf{Y}, \mathbf{Y}(0) = \mathbf{I}. \tag{11}$$

The Floquet multipliers are then the eigenvalues of the monodromy matrix $\mathbf{Y}(T)$. Since the averaged system is autonomous, one of the multipliers is always $+1$. If the remaining three multipliers lie inside the unit circle, the periodic solution $\mathbf{x}^*(\tau)$ is stable (Note that system (7) is four-dimensional). If even one of the multipliers is outside the unit circle, the periodic solution $\mathbf{x}^*(\tau)$ is unstable. Of the three multipliers other than $+1$, either all are real or one is real and the other two are a complex conjugate pair.

The stability of a periodic solution may change as the parameter γ is varied. As γ is changed, a given stable periodic solution can become unstable in three possible ways. In case (*i*), one of the Floquet multipliers leaves the unit circle through $+1$ while the other two remain inside the unit circle (note that the fourth multiplier is always $+1$). This corresponds to a turning point in the periodic solution response curve and is called a tangent or a saddle-node bifurcation. In case (*ii*), one of the multipliers goes out of the unit circle through -1. This is known as flip (or period-doubling) bifurcation and the periodic solution of the averaged system bifurcates into a stable periodic solution of twice the period. Finally, it is also possible that a complex conjugate pair leaves the unit circle (case (*iii*)). The bifurcated solution is then expected to be doubly periodic (motion on a two-torus). This case was never encountered in all our computations. For a theoretical discussion of these bifurcations in autonomous systems the reader should consult Iooss and Joseph [8] and Guckenheimer and Holmes [9].

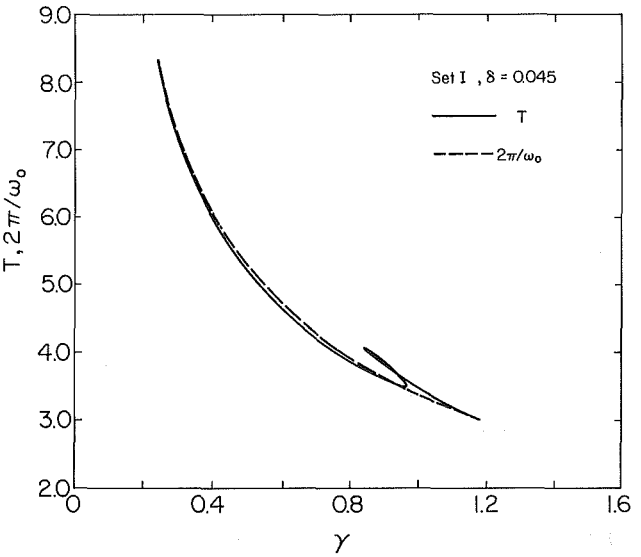


Fig. 5 Time period, T, of periodic solutions and growth period $2\pi/\omega_0$ of steady state solutions versus γ

The monodromy matrix $\mathbf{Y}(T)$ and the Floquet multipliers can only be determined numerically. Since the period solution $\mathbf{x}^*(\tau)$ also is known numerically only, it is computationally more convenient to integrate the equations (7) and (11) simultaneously with initial conditions $\mathbf{x}(0) = \mathbf{x}^0$ and $\mathbf{Y}(0) = \mathbf{I}$. As a check on the computations, one can verify that at least one Floquet multiplier is $+1$.

We now present some numerical results of the periodic solutions created by the Hopf bifurcation of steady state solutions of the averaged system.

Numerical Results. Response curves displaying amplitude of the first mode b_1 as a function of detuning parameter γ are shown in Figs. 3 and 4.

For $\delta = 0.3$ and 0.2 a unique branch of periodic solutions originates from the left Hopf point and shrinks on to the right Hopf point. These solutions are all stable over the whole interval in γ. As damping δ is decreased, the periodic solution can become unstable in two possible ways. There are both the turning points and the period-doubling bifurcations present in the response curves. This is evident from the cases of $\delta = 0.1$ and 0.045. Despite turning points and flip bifurcations, the periodic branch always connects the two points of Hopf bifurcation. Thus, only one of the possibilities of the global

Downloaded 02 May 2010 to 171.66.16.54. Redistribution subject to ASME license or copyright; see http://www.asme.org/terms/Terms_Use.cfm

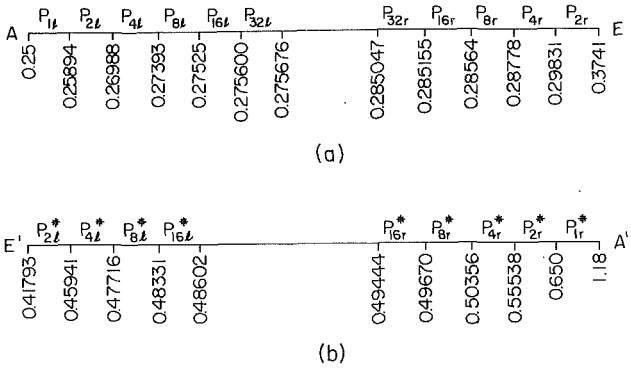


Fig. 6 Bifurcation points for the period-doubling sequences for δ = 0.045

Hopf bifurcation theorem of Alexander and Yorke [20] is realized in the system under study.

For $\delta = 0.1$ the periodic response becomes unstable at $\gamma \simeq 0.32$ and 0.6 due to flip bifurcations. New stable periodic branches with period twice that of the unstable solution originate at these points. Similar behavior can be seen in Fig. 4 for $\delta = 0.045$. We will discuss these period-doubling bifurcations in much more detail in the next section.

The time period, T, of the periodic solutions is found to vary monotonically except when there is a loop (two turning points) present in the response. Figure 5 shows this for $\delta = 0.045$. Computations show that T and $2\pi/\omega_0$ are very close to each other. Here ω_0 is the imaginary part of the complex eigenvalues corresponding to the unstable steady state solution for the same value of γ. If this surprising observation is a general property of such mechanical systems, we may use it to get good initial guess for the time periods of periodic solutions away from the bifurcation points.

Interpretation of the Periodic Solutions. A periodic solution of (7) is a closed curve in the four-dimensional state space $\mathbf{x} = (b_1, b_2, \psi_1, \psi_2)^T$ and it forms an infinitely long cylindrical surface with the time axis. We can write these solutions as a periodic function in some variable θ with period 2π,

$$b_i = b_i^*(\theta), \quad \psi_i = \psi_i^*(\theta), \quad i = 1,2. \tag{12}$$

Based on the integral manifold theorem [7], if the linear variational equation (10) has three Floquet multipliers away from the unit circle, the integral manifold S of the system in standard form is a surface periodic in t with period $2\pi/\nu$, periodic in θ with period 2π, lies close to the cylindrical surface and coincides with the cylinder as $\epsilon \to 0$. We can, therefore, write

$$A_i = A_i(\theta,t,\epsilon), \Psi_i = \Psi_i(\theta,t,\epsilon), \quad i = 1,2 \tag{13}$$

where A_i and Ψ_i are doubly periodic functions in t with period $2\pi/\nu$ and in θ with period 2π. The solution to the original coupled oscillators is then given by

$$\zeta_1(t,\theta,\epsilon) = A_1(t,\theta,\epsilon)\cos(\nu t + \Psi_1(t,\theta,\epsilon)),$$
$$\zeta_2(t,\theta,\epsilon) = A_2(t,\theta,\epsilon)\cos(3\nu t + \Psi_2(t,\theta,\epsilon)). \tag{14}$$

Thus, the motion of the coupled oscillators for a parameter value at which the averaged system has a limit cycle is amplitude modulated with basic frequency ν. The period of the amplitude modulations is determined by the period of the limit cycle of the averaged system and for small ϵ it is large compared to $2\pi/\nu$. The modulations are, therefore, very slow when measured in natural time t.

Period-Doubling Bifurcations in the Averaged Equations

It was noted in the last section that for small damping some

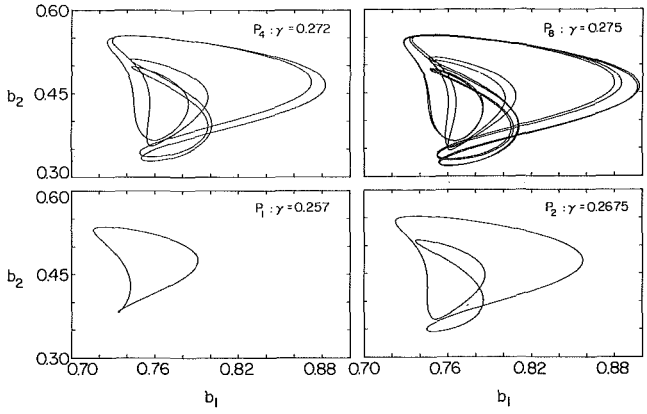


Fig. 7(a) Phase plots for some stable solutions in a period-doubling sequence

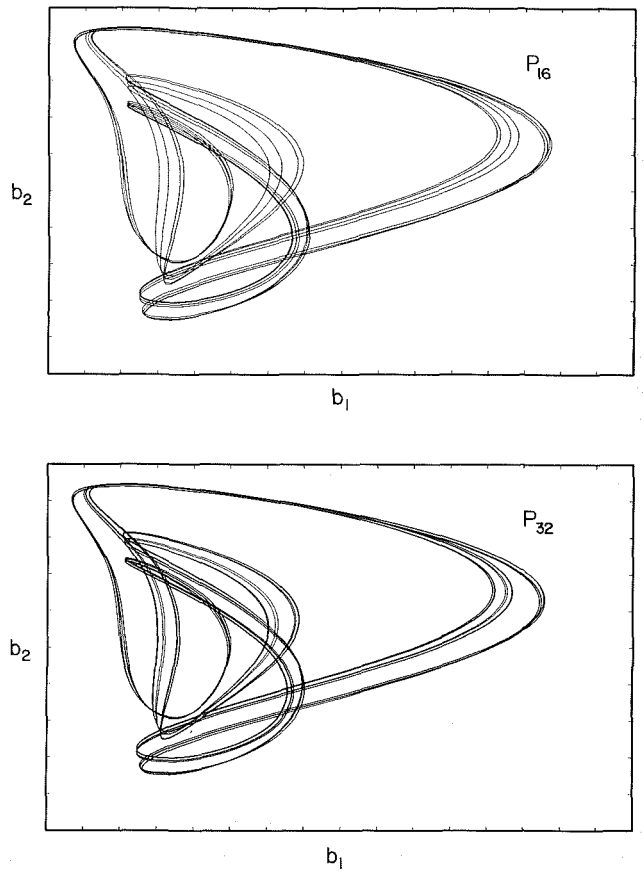


Fig. 7(b) Phase plots for P_{16} solution at γ = 0.276 and P_{32} solution at γ = 0.27565.

Fig. 7

portion of the Hopf-bifurcated periodic branch of the averaged equations becomes unstable by flip bifurcation and a new stable periodic solution with twice the period is created. For moderately low values of damping (e.g., $\delta = 0.1$, Fig. 3) the period-doubled branch is stable over the whole interval of its existence (γ : 0.32 − 0.60). Further decrease in δ results in destabilization of this stable branch by tangent and/or flip bifurcations and this process may ultimately lead to an infinite sequence of such bifurcations.

For $\delta = 0.045$ (Fig. 4) the averaged system has four apparently infinite sequences of period-doubling bifurcations. The Hopf-bifurcated periodic branch loses stability at B ($\gamma \simeq 0.2589$) and at B' ($\gamma \simeq 0.65$). This gives rise to two branches BE and $B'E'$ of period-doubled solutions. Each of these branches itself contains two period-doubling bifurcations

Downloaded 02 May 2010 to 171.66.16.54. Redistribution subject to ASME license or copyright; see http://www.asme.org/terms/Terms_Use.cfm

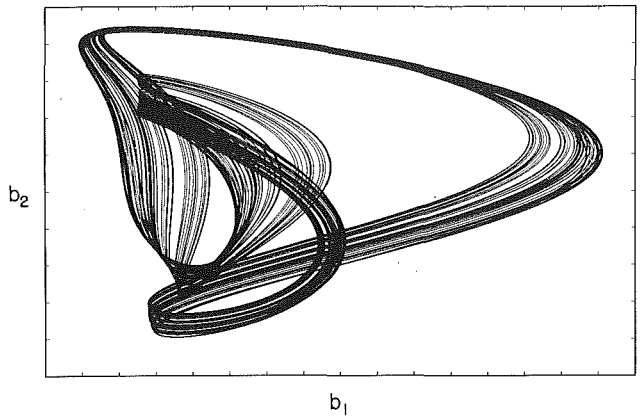


Fig. 8 Irregular (chaotic) motion at $\gamma = 0.28$

Table 1(*a*) Feigenbaum series for the periodic orbits P_i

i	δ_{ir}	δ_{il}
1	–	1.731261
2	7.197531	2.701235
4	4.920561	3.068182
8	4.412371	3.771429
16	4.490741	4.605263

Table 1(*b*) Feigenbaum series for the periodic orbits P_i^*

i	δ_{ir}^*	δ_{il}^*
1	5.601353	–
2	1.825936	2.336901
4	7.553936	2.886179
8	3.035398	2.269373

(points C, C' and D, D') and the process continues. We have not been able to continue the solutions far enough beyond the turning points E and E' and therefore it is difficult to say that the points E and E' are connected by the period-doubled solutions. The four infinite sequences are therefore $A\ B\ C\ \ldots$; $EC'\ \ldots$; $E'\ D\ \ldots$; and $A'\ B'\ D'\ \ldots$

We refer to the sequences originating at A ($\gamma \simeq 0.24$) by P_i and those originating at A' ($\gamma \simeq 1.18$) by P_i^*. Integer i represents the specific stable periodic branch and it takes values 1, 2, 4, 8, . . .

Figure 6 gives the critical values of detuning parameter γ for the four period-doubling sequences. It also shows the particular solution that is stable in a given interval. P_{il} branch, for example, originates at $\gamma \simeq 0.24$. As γ is increased P_{1l} becomes unstable due to flip bifurcation at $\gamma \simeq 0.25894$. The P_{2l} solution goes through period-doubling bifurcation at $\gamma \simeq 0.26988$. Continuing in this manner we have been able to trace solutions up to P_{32l}. Starting from the other side near the turning point $E(\gamma \simeq 0.3741)$, period-doubling bifurcations occur at $\gamma \simeq 0.29831$, 0.28778, 0.28564 etc. This gives the sequence P_{2r}, P_{4r}, ... Phase plane projections on to the $b_1 - b_2$ plane for all periodic solutions starting from P_{1l} and up to P_{32l} are shown in Fig. 7(*a*,*b*). Note that each new solution winds twice as many times around as the periodic orbit from which it is generated.

Within the interval (0.275 676 – 0.28 5047) there is no stable periodic solution of period less than $64T$. For $\gamma = 0.28$, a point approximately halfway between the end points, equations (7) were integrated numerically for a long time (100 times the largest period in P_{32}) and the corresponding phase-plane projection is shown in Fig. 8. The motion is clearly bounded. It does not, however, seem to approach any periodic orbit and most likely represents some irregular but bounded motion.

The behavior of the other two period-doubling sequences is similar. Here we have traced the solutions up to P_{16}. In the interval (0.48602 – 0.49444) there is no stable periodic solution of period less than $32T$. The results of time integration of the averaged equations for $\gamma = 0.49$ again show that the motion does not seem to settle to a periodic solution even though it remains bounded.

Compatibility of Results with Feigenbaum Universality Constant

As mentioned in the Introduction, period-doubling bifurcations leading to irregular or "chaotic" motions have recently been found to occur in many dynamical systems. Eckmann [21] has suggested it to be one of three possible scenarios leading to turbulence. It is known as the Feigenbaum scenario. We discuss briefly the work of Feigenbaum [11] and the compatibility of our results with Feigenbaum series.

In all the four sequences of period-doubling bifurcations, each new solution is stable over an interval smaller than the interval of stability of the preceding member of the sequence. This observation leads to the Feigenbaum Universality Constant which states that there should be a limit in the sequence of period-doubling bifurcations of stable orbits beyond which the system behaves in a chaotic manner.

Feigenbaum analyzed noninvertible one-dimensional maps $x_{n+1} = F_\lambda(x_n)$ dependent on a parameter λ. He showed that the family F_λ has an infinite sequence of period-doubling bifurcations of stable periodic orbits at parameter values λ_1 (period 1-2), λ_2 (period 2-4),----, λ_{j+1} (period $2^j - 2^{j+1}$) with the limit $\lambda_\infty = \lim_{j\to\infty} \lambda_j$. At a $\lambda \geq \lambda_\infty$, F_λ has an aperiodic solution. There is a universal number δ (called Feigenbaum Universality Constant) given by

$$\delta = \lim_{n\to\infty} \delta_n = \lim_{n\to\infty} \frac{\lambda_n - \lambda_{n-1}}{\lambda_{n+1} - \lambda_n} = 4.66920.$$

The remarkable fact is that this constant δ is independent of the exact nature of the function F_λ and holds for all nonlinear transformations satisfying some very mild conditions. Though this number is derived for only one-dimensional maps many higher dimensional systems, exhibiting period-doubling bifurcations leading to chaos, have been found to possess this property. This includes, among others, the parametrically forced pendulum [15], a periodically forced piecewise linear oscillator [16], eight and nine-mode transactions of the Navier-Stokes equations [18], and some problems of mode interaction in plasma dynamics [22].

We have already discussed the four sequences of period-doubling bifurcations that appear in the averaged equations. These sequences are very likely to be infinite (see [23] for more complicated possibilities). Becauase of numerical errors indicated earlier we could obtain only a limited number of terms. These are shown in Table 1. The sequences corresponding to the orbits P_i do seem to converge to $\delta \approx 4.66$. . and are thus compatible with Feigenbaum Constant. The sequences for P_i^* seem to oscillate and more numerical analysis is needed before any firm statement can be made.

We have, thus, seen that the averaged equations can, for low enough damping, go to chaotic or irregular motions preceded by a sequence of period-doubling bifurcations. These periodic solutions, as described earlier, clearly imply amplitude modulated motions for the original system of coupled oscillators. We can, however, only speculate on the relationship between chaotic motions of the averaged system and the motions of the coupled oscillators and further study is needed.

Downloaded 02 May 2010 to 171.66.16.54. Redistribution subject to ASME license or copyright; see http://www.asme.org/terms/Terms_Use.cfm

Acknowledgment

The authors would like to thank the reviewers for constructive suggestions.

References

1 Sethna, P. R., "Coupling in Certain Classes of Weakly Nonlinear Vibrating Systems,' *Nonlinear Differential Equations and Nonlinear Mechanics*, LaSalle, J. P., and Lefschetz, S., eds., Academic Press, New York, 1963, pp. 58–70.

2 Nayfeh, A. H., and Mook, D. T., *Nonlinear Oscillations*, Wiley Interscience, New York, 1979.

3 Miles, J. W., "Stability of Forced Oscillations of a Spherical Pendulum," *Q. Appl. Math.*, Vol. 20, 1962, pp. 21–32.

4 Sethna, P. R., "Vibrations of Dynamical Systems With Quadratic Nonlinearities," ASME JOURNAL OF APPLIED MECHANICS, Vol. 32, 1965, pp. 576–582.

5 Sethna, P. R., and Bajaj, A. K., "Bifurcations in Dynamical Systems With Internal Resonance," ASME JOURNAL OF APPLIED MECHANICS, Vol. 45, 1978, pp. 895–902.

6 Marsden, J. E., and McCracken, M. *Hopf Bifurcations and Its Applications*, Springer-Verlag, New York, 1976.

7 Hale, J. K., *Oscillations in Nonlinear Systems*, McGraw-Hill, New York, 1963.

8 Iooss, G., and Joseph, D. D., *Elementary Stability and Bifurcation Theory*, Springer-Verlag, New York, 1980.

9 Guckenheimer, J., and Holmes, P., *Nonlinear Oscillations, Dynamical Systems, and Bifurcations of Vector Fields*, Springer-Verlag, New York, 1983.

10 Lichtenberg, A. J., and Lieberman, M. A., *Regular and Stochastic Motion*, Springer-Verlag, New York, 1982.

11 Feigenbaum, M. J., "The Universal Metric Properties of Nonlinear Transformations," *J. Stat. Phys.*, Vol. 21, No. 6, 1979, pp. 669–706.

12 Collet, P., and Eckmann, J. P., *Iterated Maps on the Interval as Dynamical Systems*, Birkhauser, Boston, 1980.

13 Jorgensen, D. V., and Aris, R., "On the Dynamics of a Stirred Tank With Consecutive Reactions," *Chem. Eng. Sci.*, Vol. 38, No. 1, 1983, pp. 45–53.

14 Tomita, K., "Chaotic Response of Nonlinear Oscillators," *Phys. Reports*, Vol. 86, No. 3, 1982, pp. 113–167.

15 McLaughlin, J. B., "Period-Doubling Bifurcations and Chaotic Motion for a Parametrically Forced Pendulum," *J. Stat. Phys.*, Vol. 24, No. 2, 1981, pp. 375–388.

16 Shaw, S. W., and Holmes, P. J., "A Periodically Forced Piecewise Linear Oscillator," *J. Sound and Vibration*, Vol. 90, No. 1, 1983, pp. 129–155.

17 Thompson, J. M. T., Bokaian, A. R., and Ghaffari, R., "Subharmonic Resonances and Chaotic Motions of a Bilinear Oscillator," *IMA J. Appl. Math.*, Vol. 31, 1983, pp. 207–234.

18 Franceschini, V., "Two Models of Trunicated Navier-Stokes Equations on a Two-Dimensional Torus," *Phys. Fluids*, Vol. 26, No. 2, 1983, pp. 433–447.

19 Chua, L. O., and Lin, P. M., "Computer-Aided Analysis of Electronic Circuits," Prentice-Hall, Englewood Cliffs, N. J., 1975.

20 Alexander, J. C., and Yorke, J. A., "Global Bifurcations of Periodic Orbits," *AM. J. Math.*, Vol. 100, No. 2, 1978, pp. 263–292.

21 Eckmann, J. P., "Roads to Turbulence in Dissipative Dynamical Systems," *Rev. Mod. Phys.*, Vol. 53, No. 4, Part I, 1981, pp. 6434–654.

22 Ott, Edward, "Strange Attractors and Chaotic Motions of Dynamical Systems," *Rev. Mod. Phys.*, Vol. 53, No. 4, Part I, 1981, pp. 655–672.

23 Holmes, P., and Whitley, D., "Bifurcations of One-and Two-Dimensional Maps," *Phil. Trans. Royal Soc. Lond.*, Series *A*, Vol. 311, 1984, pp. 43–102.

Downloaded 02 May 2010 to 171.66.16.54. Redistribution subject to ASME license or copyright; see http://www.asme.org/terms/Terms_Use.cfm

The Dynamics of a Harmonically Excited System Having Rigid Amplitude Constraints

Part 1: Subharmonic Motions and Local Bifurcations[1]

S. W. Shaw
Department of Mechanical Engineering,
Michigan State University,
East Lansing, Mich. 48824
Assoc. Mem. ASME

A simple model for the response of mechanical systems having two-sided amplitude constraints is considered. The model consists of a piecewise-linear single degree-of-freedom oscillator subjected to harmonic excitation. Encounters with the constraints are modeled using a simple impact rule employing a coefficient of restitution, and excursions between the constraints are assumed to be governed by a linear equation of motion. Symmetric double-impact motions, both harmonic and subharmonic, are studied by means of a mapping that relates conditions at subsequent impacts. Stability and bifurcation analyses are carried out for these motions and regions are found in which no stable symmetric motions exist. The possible motions that can occur in such regions are discussed in the following paper, Part 2.

1 Introduction and Model

The responses of mechanical systems having amplitude constraints when subjected to periodic excitation are inherently nonlinear. Systems having one and two-sided constraints have been considered in earlier works using traditional methods such as Galerkin, averaging, Fourier, numerical, and perturbation methods [1–5]. More recently the author has analyzed systems having one-sided constraints using bifurcation theory and other tools of modern dynamical systems theory [6–8]. Experimental work has verified the validity and usefulness of these analyses [9–11]. Motions of systems with two-sided constraints have been studied in the context of the so-called impact-damper by several authors, see [12–14] and the references cited therein. Also, Holmes [15] has analyzed the repeated impacts of a ball bouncing on a sinusoidally vibrating table under the influence of gravity and describes phenomena similar to those discussed in the following. In this paper and in Part 2, a system having two-sided constraints is considered.

A single degree-of-freedom system having symmetrically placed rigid stops and subjected to periodic excitation is shown in Fig. 1. For small forcing amplitudes the system will undergo simple oscillations and behave as a linear system. As the amplitude is increased, the mass eventually begins to hit the stops and the motion becomes nonlinear. The equation governing motions between the stops is

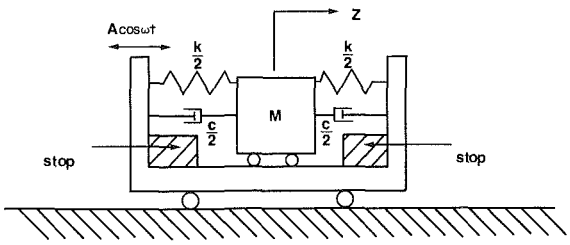


Fig. 1 The physical model

$$mz'' + cz' + kz = A\Omega^2 m\cos(\Omega\tau); |z| < z_0 \qquad (1)$$

where $(\ )'$ refers to a time derivative $d/d\tau$. Whenever $|z| = z_0$ a simple impact rule [16] is applied

$$z'(\tau^+) = -rz'(\tau^-) \quad \text{with} \quad (\tau^+ - \tau^-) \to 0 \qquad (2)$$

where r is a coefficient of restitution having a value between zero and unity. Rescaling equation (1) by letting $t = \sqrt{k/m}\,\tau$ and $x = z/z_0$ the nondimensional equation at motion is obtained

$$\ddot{x} + 2\alpha\dot{x} + x = \beta\cos(\omega t), \quad |x| < 1, \qquad (3)$$

where $(\dot{\ }) = d/dt$, and $2\alpha = c/\sqrt{mk}$, $\omega = \Omega\sqrt{m/k}$, and $\beta = A/z_0$ $(\Omega^2/k/m)$ are the dimensionless damping constant, forcing frequency, and forcing amplitude, respectively. Impacts occur at $|x| = 1$ whereupon

[1] Work supported in part by NSF.
Contributed by the Applied Mechanics Division for presentation at the 1985 Joint ASME/ASCE Applied Mechanics, Fluids Engineering, and Bioengineering Conference, Albuquerque, N. Mex., June 24–26, 1985 of THE AMERICAN SOCIETY OF MECHANICAL ENGINEERS.
Discussed on this paper should be addressed to the Editorial Department, ASME United Engineering Center, 345 East 47th Street, New York, N.Y. 10017, and will be accepted until two months after final publication of the paper itself in the JOURNAL OF APPLIED MECHANICS. Manuscript received by ASME Applied Mechanics Division, March 1984; final revision, June, 1984. Paper No. 85-APM-14.
Copies will be available until February, 1985.

Copyright © 1985 by ASME
Downloaded 02 May 2010 to 171.66.16.54. Redistribution subject to ASME license or copyright; see http://www.asme.org/terms/Terms_Use.cfm

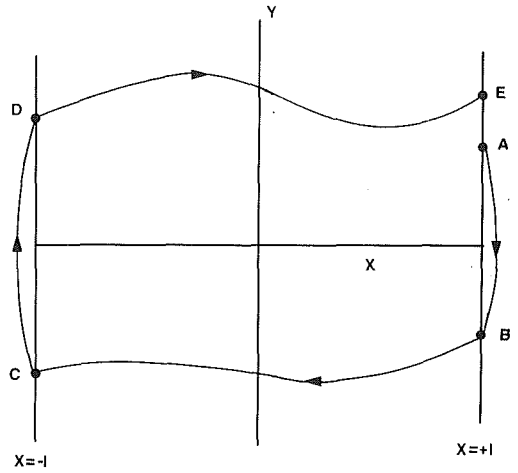


Fig. 2 Double-impact motion in projected phase plane (x, y)

$$\dot{x}(t^+) = -r\dot{x}(t^-) \quad \text{with} \quad (t^+ - t^-) \to 0. \tag{4}$$

Equations (3) and (4) completely determine the dynamics of the mass m. Since both α and r provide energy loss mechanisms, α is taken to be zero for convenience in the following. The procedures for α nonzero are exactly the same, but the computations are more lengthy.

2 Methods of Analysis

When written in first-order form equation (3) becomes (for $\alpha = 0$)

$$\begin{aligned} \dot{x} &= y \\ \dot{y} &= -x + \cos(\omega t) \\ \dot{t} &= 1, \quad |x| < 1. \end{aligned} \tag{5}$$

The three variables (x,y,t) are needed to specify the state of the system. In this three-dimensional phase space, solutions are restricted to $|x| \leq 1$.

Referring to Fig. 2, the motion is followed in the projected phase space (x,y), i.e., the usual phase plane. From point A to B and from C to D the impact rule (4) is used. From B to C and from D to E the linear equation of motion (5), with the appropriate initial conditions, governs the motion. In this manner it is seen that the time and velocity at the starting point A (the mass arriving at the $x = +1$ stop with positive velocity) uniquely determine the time and velocity at the next similar encounter, point E. In principle, we may write:

$$t_E = t_E(t_A, y_A) \tag{6a}$$

$$y_E = y_E(t_A, y_A). \tag{6b}$$

In this way each excursion from $x = +1$ to $x = -1$ and back is reduced to a simple recursion relation. This recursion relation arises naturally from the equations of motion (3) and (4) and is used in the sequel to study the motions of m. The idea of studying dynamical systems using recursion relations, or maps, has its foundations in the works of Poincaré [17]. Thus, the mapping given by equations (10) will be referred to, as is common, as the *Poincaré Map* for this system. By considering the phase space (x,y,t) with $|x| \leq 1$ it is seen that this method determines how points with $x = +1$ and $y > 0$ are mapped back to $x = +1$, $y > 0$ under the governing equations of motion. This is now formalized. Defining the *Poincaré Section* as

$$\Sigma = \{(x,y,t) \mid x = +1, y > 0\}, \tag{7}$$

the Poincaré Map $\mathbf{P}$ is a rule that takes points in Σ into themselves:

$$\mathbf{P} = \Sigma \to \Sigma \text{ or } (t_{i+1}, y_{i+1}) = \mathbf{P}(t_i, y_i) \tag{8}$$

where the points (t_i, y_i) are in Σ. The set of points Σ correspond to those states in which the mass m is just coming into contact with the constraint at $+1$. For example, points A and E in Fig. 2 are in Σ. The mapping $\mathbf{P}$ is equivalent to equation (6) for those points in Σ that result in excursions like the one shown in Fig. 2. It should be noted that some points in Σ may be mapped back to Σ without an encounter at $x = -1$. Also, some points in Σ may be mapped onto $|x| = 1$, $y = 0$ in which case discontinuities in $\mathbf{P}$ may arise (see [6–8]).

Periodic motions of the mass m may be studied using $\mathbf{P}$ as follows. Each iterate of $\mathbf{P}$ corresponds to an encounter with the constraint at $x = +1$ and relates the conditions (time and velocity) at the previous impact to those of the subsequent one. A motion that repeats after k impacts at $x = +1$ must satisfy the following condition:

$$\left(\bar{t} + \frac{2\pi n}{\omega}, \bar{y}\right) = \mathbf{P}^k(\bar{t}, \bar{y}) \tag{9}$$

where $\mathbf{P}^k$ indicates that $\mathbf{P}$ has been applied k times (i.e., defining $\mathbf{P}^{j+1}(.) = \mathbf{P}(\mathbf{P}^j(.))$, $\mathbf{P}^0(.) = (.)$ is sufficient to define $\mathbf{P}^k(.)$). Condition (9) corresponds to a *2k impact motion of period n* in which the mass m repeats its motion after k impacts at $x = +1$ and $x = -1$ each during which n cycles of the forcing pass. Such a motion is commonly referred to as a subharmonic of order n. The point $(\bar{t}, \bar{y})$ is referred to as a periodic point of $\mathbf{P}$.

Such a periodic motion may be stable or unstable. The stability of interest here is local stability and indicates whether or not motions near the periodic one (in the phase space) are attracted or repelled by the periodic motion [18–21]. Considering a small perturbation near the periodic point and linearizing one obtains

$$(\xi_{i+1}, \eta_{i+1}) = \underline{D\mathbf{P}}^k(\xi_i, \eta_i) \tag{10}$$

where (ξ, η) is the perturbation and $\underline{D\mathbf{P}}^k$ is the first derivative of $\mathbf{P}^k$ evaluated at the periodic point. Single impact periodic orbits are of interest here and $\underline{D\mathbf{P}}^1 = \underline{D\mathbf{P}}$ is given by

$$\underline{D\mathbf{P}} = \underline{D\mathbf{P}}(\bar{t}, \bar{y}) = \begin{bmatrix} \dfrac{\partial t_E}{\partial t_A} & \dfrac{\partial t_E}{\partial y_A} \\ \dfrac{\partial y_E}{\partial t_A} & \dfrac{\partial y_E}{\partial y_A} \end{bmatrix}_{(\bar{t},\bar{y})} \tag{11}$$

$$\triangleq \left[\frac{\partial(t_E, y_E)}{\partial(t_A, y_A)}\right]_{(\bar{t},\bar{y})}.$$

If both eigenvalues of $\underline{D\mathbf{P}}$ have modulus less than one then $(\bar{t}, \bar{y})$ is stable. If any eigenvalue(s) has modulus greater than one then $(\bar{t}, \bar{y})$ is unstable (see [6, 18–21]). As system parameters are varied the periodic orbit changes continuously as do its associated eigenvalues, λ_1 and λ_2. *Local bifurcations* occur as eigenvalues pass through the unit circle in the complex plane [18], i.e., when $|\lambda_i| = 1$, $i = 1$ or 2. As will be seen in the following, $\underline{D\mathbf{P}}$ has a determinant with magnitude less than one for the motions of interest and thus only $\lambda_i = \pm 1$ bifurcations are possible. No Hopf bifurcations occur in which λ_1 and λ_2 escape the unit circle as a complete conjugate pair [18]. At $\lambda_i = -1$ period doubling or flip, bifurcations, occur in this system and they are discussed in Part 2 of this paper. Bifurcations corresponding to $\lambda_i = +1$ also occur and a detailed discussion of them follows in Section 4 of this paper.

It should be stressed that $\mathbf{P}$ is not known in closed form. The transcendental nature of the solution for the times of impact at points C and E (Fig. 2) prevent an explicit expression for $\mathbf{P}$ from being obtained (as in [6–8]). However, expressions for certain periodic points and their stability can be determined explicitly as is now shown.

Downloaded 02 May 2010 to 171.66.16.54. Redistribution subject to ASME license or copyright; see http://www.asme.org/terms/Terms_Use.cfm

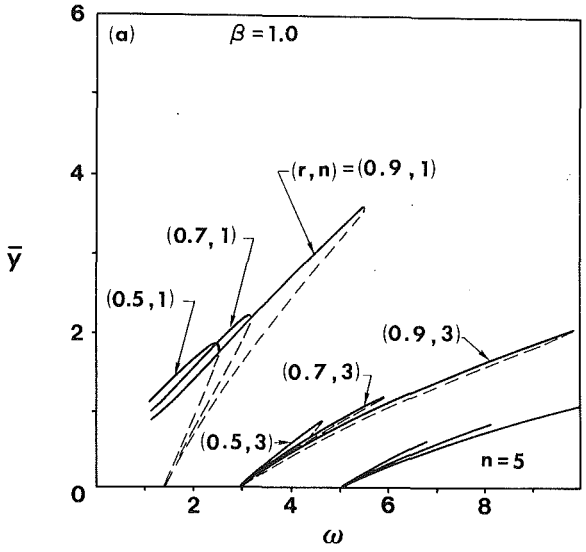


Fig. 3(a)

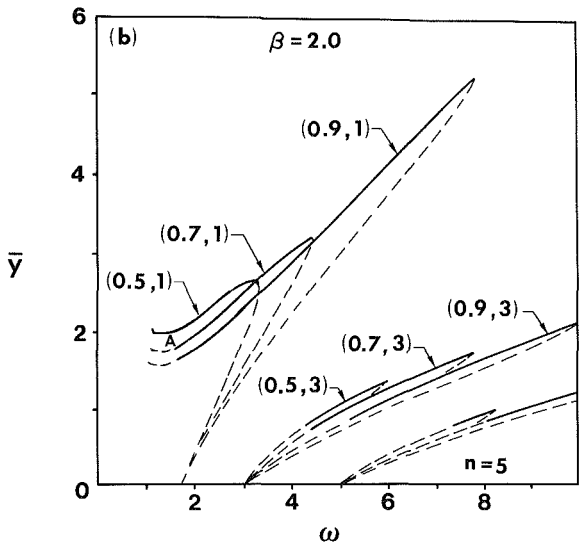


Fig. 3(b)

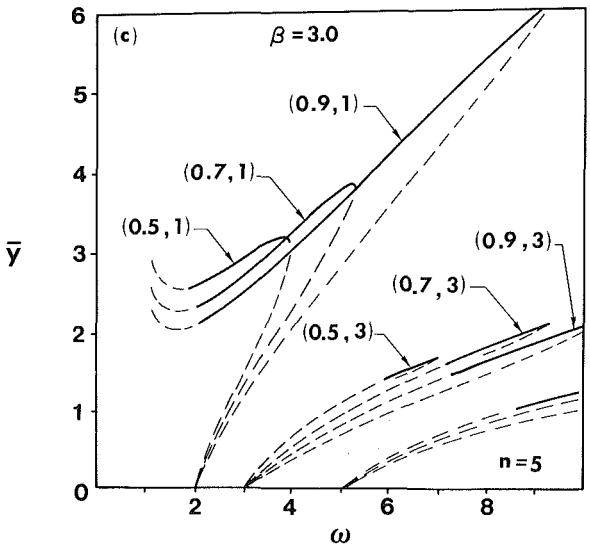


Fig. 3(c)

Fig. 3 Frequency response curves: (a) $\beta = 1.0$, (b) $\beta = 2.0$, and (c) $\beta = 3.0$. Stable motions are shown by solid lines, unstable motions by dashed lines.

3 Symmetric Double Impact Motions

The symmetry of this system allows certain periodic motions to be determined explicitly. These motions are symmetric and take excursions of length $\pi n/\omega$ in time between the stops. Only odd subharmonics (n odd) will occur due to the symmetry. An analysis similar to those found in [12, 13], which exploits the linearity of the equation of motion between the stops, is used to find the time $\bar{t}$ (i.e., forcing phase) and the velocity of the mass $\bar{y}$ at each impact at $x = +1$ for such a motion; in other words the periodic point $(\bar{t},\bar{y})$ of the mapping **P**. The resulting expression for $\bar{t}$ is:

$$\bar{t} = \frac{1}{\omega}\left\{\arctan\left(\frac{\omega s(1+r)}{-(1+c)(1-r)}\right) + \arccos\left(\frac{-(1+c)(1-r)}{W}\right)\right\} \tag{12}$$

where $W = \pm|\gamma|[(\omega s(1+r))^2 + ((1+c)(1-r))^2]^{1/2}$, $s = \sin(\pi n/\omega)$, and $c = \cos(\pi n/\omega)$. By considering the inverse cosine involved in equation (12) it is seen that two solutions for $\bar{t}$ exist. The expression for $\bar{y}$ is:

$$\bar{y} = -\frac{2\gamma\omega\bar{s}}{(1-r)}, \quad \text{where} \quad \bar{s} = \sin(\omega\bar{t}) \tag{13}$$

and there are two corresponding solutions for $\bar{y}$. One should note than an additional condition must be added to insure that the motions corresponding to the periodic point $(\bar{t},\bar{y})$ do not penetrate either constraint (see [6–8, 12, 21]).

$$|x(t; +1, \bar{t}, \bar{y})| < 1 \quad \text{for} \quad \bar{t} < t < \bar{t} + \frac{\pi n}{\omega}. \tag{14}$$

A mathematical orbit given by a $(\bar{t},\bar{y})$ that violates this condition is referred to as a *penetrating orbit* [21]. Certainly $\bar{y} < 0$ correspond to such motions.

Frequency response curves for this impacting system are conveniently shown as velocity at impact $(\bar{y})$ versus forcing frequency (ω), since on a periodic orbit, $\bar{y}$ is known explicitly (equation (13)). In Fig. 3 sample response curves are shown for various values of β (forcing amplitude) and r (coefficient of restitution). On these curves the type of motion is indicated: dashed portions represent nonpenetrating unstable motions, and solid portions correspond to nonpenetrating stable motions. No examples of penetrating orbits with $\bar{y} > 0$ were found. The motions apparently disappear at the boundaries $\omega = 1$ and $\bar{y} = 0$ (see Fig. 3), mathematical solutions for $\omega < 1$ or $\bar{y} < 0$ correspond to nonphysical penetrating orbits. Those of physical interest are the stable motions. Note that the resonance peaks are "bent over" as expected since the stops act in a manner similar to a hardening spring. The determination of the stability of these nonpenetrating orbits is now discussed.

4 Stability and Local Bifurcations

As described in Section 2, the stability of the periodic points $(\bar{t},\bar{y})$ is determined by the eigenvalues of the first derivative of the return map, $\underline{DP}$, evaluated at $(\bar{t},\bar{y})$. Using the chain rule and the notation defined in equation (11) one obtains

$$\underline{DP} = \left[\frac{\partial(t_E, y_E)}{\partial(t_A, y_A)}\right] = \left[\frac{\partial(t_E, y_E)}{\partial(t_D, y_D)}\right]\left[\frac{\partial(t_D, y_D)}{\partial(t_C, y_C)}\right] \left[\frac{\partial(t_C, y_C)}{\partial(t_B, y_B)}\right]\left[\frac{\partial(t_B, y_B)}{\partial(t_A, y_A)}\right]. \tag{15}$$

The four components on the right-hand side of equation (15) can be determined in closed form. Two of these matrices are determined directly from the impact rule (4) while the other two exploit the piecewise-linear nature of the problem and require implicit differentiation. A similar analysis is described

Downloaded 02 May 2010 to 171.66.16.54. Redistribution subject to ASME license or copyright; see http://www.asme.org/terms/Terms_Use.cfm

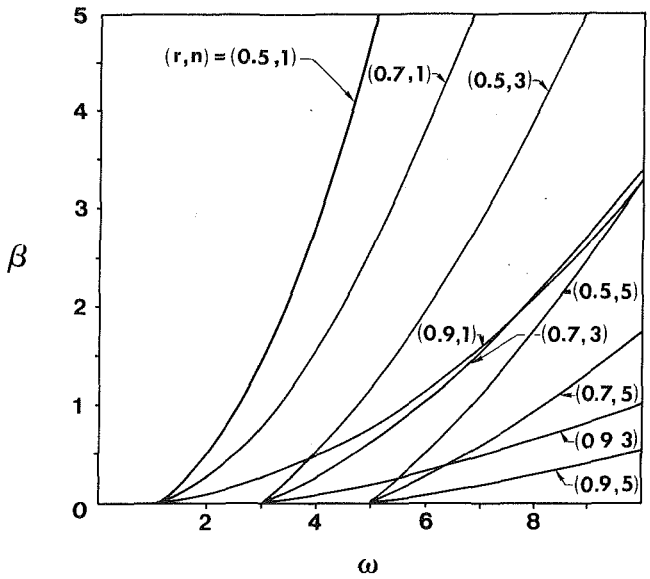


Fig. 4 Saddle-node bifurcation values

in more detail in [6]. The resulting matrix $\underline{DP}$, when evaluated on the periodic motion has determinant and trace

$$\bar{D} = r^4 \tag{16}$$

and

$$\bar{T} = \text{trace}(\underline{\bar{DP}}) = -\left(\frac{r}{\bar{y}}\right)^4 \left[s^2\left(2\left(\frac{\bar{y}}{r}\right)^2 - \bar{M}^2\right) + 4\left(\frac{\bar{y}}{r}\right)^2 \bar{M}sc - 2\left(\frac{\bar{y}}{r}\right)^2 c^2\right], \tag{17}$$

respectively, where $\bar{M} = (\beta c - 1)(1 + r)$, $\bar{c} = \cos(\omega \bar{t})$, and $\bar{s}, \bar{y}$, and c have been defined in the foregoing. The eigenvalues of $\underline{\bar{DP}}$ are determined via the expression

$$\lambda_{1,2} = \frac{1}{2}(\bar{T} \pm \sqrt{\bar{T}^2 - 4\bar{D}}) \tag{18}$$

and are thus known explicitly. In Section 2, the stability conditions were stated. Bifurcations occur when $|\lambda_i| = 1$ and since $\bar{D} = r^4 < 1$ it is seen that only $\lambda_i = \pm 1$ bifurcations are possible. No Hopf bifurcations to doubly periodic motions occur. Although no simple expressions for the eigenvalues exist, they are known explicitly nonetheless.

Stability boundaries in the (r, β, ω) parameter space are determined in two ways. The most direct method is to use a numerical root-solving technique to determine discrete parameter values for which $|\lambda_i| = 1$. However, for $\lambda_i = +1$ saddle-node bifurcations, a knowledge of what occurs at the bifurcation points allows a more indirect, yet simple, analysis to be done as is now described. At a saddle-node bifurcation two orbits of like period and number of impacts, one a stable node and the other a saddle, coalesce and annihilate one another. In this system the periodic points $(\bar{t}, \bar{y})$ are known explicitly and this annihilation occurs precisely at the point where the two branches of the arccosine function merge, i.e., when the magnitude of its argument becomes unity. From equation (12) it is seen that this condition may be written as

$$(1 + c)(1 - r) = |W| \tag{19a}$$

which is equivalent to

$$\beta = \frac{|1 - \omega^2|(1 + c)(1 - r)}{[(1 + c)^2(1 - r)^2 + \omega^2 s^2 (1 + r)^2]^{1/2}}. \tag{19b}$$

This condition coincides with the $\lambda = +1$ condition for $\underline{\bar{DP}}$. Saddle-node bifurcation curves given by (19*b*) are shown in (β, ω) space for several values of r and n in Fig. 4. Only results for $\bar{y} > 0$ are shown. The resonance curves of Fig. 3 exhibit saddle-node bifurcations corresponding to the points where the commonly-referred-to "jump" phenomena occurs as ω is increased. These points lie on the corresponding curves of Fig. 4.

Examination of Fig. 3 shows that some of these symmetric orbits have a change in stability that cannot be explained by the saddle-node bifurcation. These changes in stability do correspond to an eigenvalue passing through $+1$, however, and thus some degeneracy must occur at such points.

As a single system parameter is changed and an eigenvalue passes through $+1$, there are three possible bifurcations that are generally possible. To analyze these cases it is convenient to first reduce the dimension of the system using the methods of center manifold theory [22]. Behavior near the periodic point $(\bar{t}, \bar{y})$ in phase space and near the bifurcation point in parameter space is of interest here. Using local variables near $(\bar{t}, \bar{y})$ the mapping **P** is expanded about $(\bar{t}, \bar{y})$ in a Taylor series to obtain a local nonlinear mapping which, when written with its linear part in *normal form* [18], is

$$\begin{bmatrix} u \\ v \end{bmatrix} \to \begin{bmatrix} \lambda_1 & 0 \\ 0 & \lambda_2 \end{bmatrix} \begin{bmatrix} u \\ v \end{bmatrix} + \begin{bmatrix} F(u,v) \\ G(u,v) \end{bmatrix} \tag{20}$$

where (u, v) are the local variables associated with the eigenvalues λ_1 and λ_2, and F and G are of second or higher order in u and v. At the bifurcation point $\lambda_1 = \bar{D}$ and $\lambda_2 = 1$ and from equation (39) it is clearly seen that there is linear contraction in the u direction but that behavior in the v direction depends on nonlinear terms. A local center manifold [22] given by a function

$$u = h(v) \tag{21}$$

exists on which the local behavior may be reduced to that of the one-dimensional mapping given by

$$w \to \lambda_2 w + G(h(w), w) \quad \text{or} \quad w \to f_\mu(w) \tag{22}$$

where w is the coordinate tangent to $h(v)$ and μ represents the parameter being varied. A functional equation for $h(v)$ is found by combining equations (20) and (21) with $\lambda_2 = 1$, $\lambda_1 = \bar{D}$:

$$h(v + G(h(v), v)) - \bar{D}h(v) - F(h(v), v) = 0. \tag{23}$$

Expanding h, F, and G in Taylor series about the origin yields

$$h(v) = \left(\frac{\frac{1}{2}F_{vv}}{1 - \bar{D}}\right) v^2 + 0(|v|^3) \tag{24}$$

where subscripts denote partial derivatives. The local dynamics at the bifurcation point are thus governed by the mapping

$$w_{n+1} = w_n + \frac{1}{2}G_{vv}w_n^2 + \left[\frac{1}{6}G_{vvv} + \frac{1}{2}G_{uv}F_{vv}/(1 - \bar{D})\right] w_n^3 + 0(|w_n|^4). \tag{25}$$

Note that the coefficient of each term depends on the parameters, r, ω, β, and n. In this analysis only one of r, β, or ω is allowed to vary and the parameter being varied is denoted by μ (as in equation (22)). Equation (25) represents a Taylor series expansion of the mapping $w_{n+1} = f_\mu(w_n)$ given by equation (22). This one-dimensional mapping is used to discuss the three types of bifurcations that can occur when λ_i passes through $+1$.

The mapping $f_\mu(w)$ given by (25) has a fixed point at $w = 0$ corresponding to the symmetric period n double impact

Downloaded 02 May 2010 to 171.66.16.54. Redistribution subject to ASME license or copyright; see http://www.asme.org/terms/Terms_Use.cfm

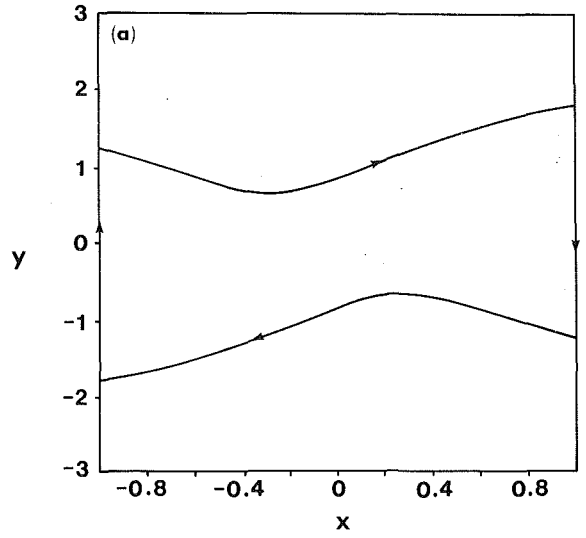


Fig. 5(*a*) Stable symmetric period-one double-impact motion $\omega = 1.6$

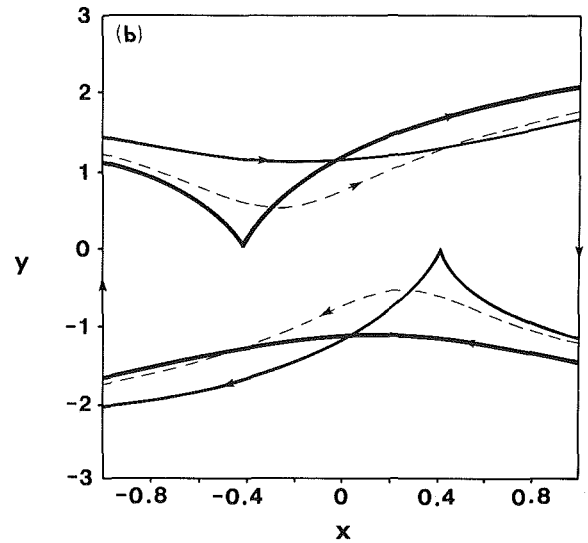


Fig. 5(*b*) Unstable symmetric period-one double-impact (dashed) motion, pair of antisymmetric stable period-one double-impact motions (solid), $\omega = 1.45$

Fig. 5 Pitchfork bifurcation shown in projected phase plane (x, y) $r = 0.7$, $\beta = 2.0$

motion of the system. It is assumed that the bifurcation point is at $\mu = 0$ in what follows, i.e., that

$$\frac{\partial f}{\partial w}\bigg|_{w=0,\mu=0} \triangleq \frac{\partial f}{\partial w}\bigg|_{*} = +1 \tag{26}$$

so that $\lambda_2 = +1$ and $\lambda_1 = \bar{D}$ when $\mu = 0$. A *saddle-node* bifurcation occurs if

$$\frac{\partial^2 f}{\partial w^2}\bigg|_{*} \neq 0 \tag{27a}$$

and

$$\frac{\partial f}{\partial \mu}\bigg|_{*} \neq 0 \tag{27b}$$

are satisfied. If condition (27*b*) fails then a *transcritical bifurcation* occurs (under an additional nondegeneracy condition), such bifurcations do not appear to occur here. If condition (27*a*) fails, a *pitchfork bifurcation* occurs (also under an additional nondegeneracy condition). In this bifurcation the symmetric double impact orbit will change

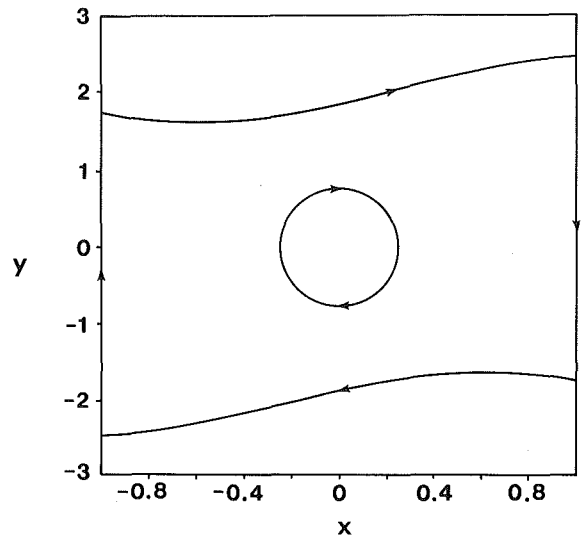


Fig. 6 Coexistence on linear and nonlinear motions, $r = 0.7$, $\beta = 2$, $\omega = 3.0$

stability and a pair of antisymmetric double impact orbits are born. From (27*a*) and (25) it is seen that a necessary condition for a pitchfork bifurcation to occur is that

$$G_{vv} = 0. \tag{28}$$

In what follows, condition (28) will be checked at the $\lambda = +1$ points. Condition (27*b*) will be satisfied if stability boundaries in the parameter are crossed transversally.

The calculation of G_{vv} is lengthy, but straightforward. It requires computation of all six terms of the second derivative of the mapping $\underline{D^2 P}$ evaluated on the symmetric double-impact motion and at the bifurcation point. All $\lambda = +1$ bifurcation points in Fig. 3 that were not saddle-nodes given by equation (19*b*) were found to satisfy condition (28). Thus pitchfork bifurcations occur at these points. Third-order terms involving $\underline{D^3 P}$ are required to determine if these bifurcations are sub or supercritical [18]. They were indirectly determined to be supercritical by use of a digital stimulation as is now briefly described.

The mapping **P** relating conditions at subsequent impacts is not known explicitly. It is easily iterated using a digital computer, however. The explicit solutions of the linear equation (5) are used between impacts and the impact times are solved using the Newton Raphson method. The impact rule (4) is then applied, which serves to set new initial conditions. In this manner the dynamics of the system can be studied. Note that this is not a numerical solution of a differential equation in the ordinary sense since the only approximations are in the impact times. These can be computed to high precision. Here the simulation is used only to verify the preceding analysis and to plot a few representative motions. In the following paper (Part 2) it is used much more extensively.

In Fig. 5 a supercritical pitchfork bifurcation is demonstrated. In Fig. 5(*a*) a stable period-one double-impact symmetric orbit is shown in the phase plane (x,y) and in Fig. 5(*b*) this orbit has become unstable and the two stable antisymmetric orbits born in the bifurcation are also shown. This bifurcation corresponds to point A shown in Fig. 3(*b*). It should be noted that the initial conditions for the symmetric orbit are known explicitly by equations (12) and (13) but that those in the antisymmetric ones are not known and these orbits are found after the transient motion dies out.

The digital simulation is the means by which penetrating orbits are determined also. Thus, it is used along with equations (12) and (13) in the construction of Fig. 3.

Downloaded 02 May 2010 to 171.66.16.54. Redistribution subject to ASME license or copyright; see http://www.asme.org/terms/Terms_Use.cfm

5 Conclusions

An analysis of the symmetric double impact motions, both harmonic and subharmonic, is presented. The motions and their stability are determined analytically and local bifurcations are considered. The frequency response curves shown in Fig. 3 indicate that there exist regions in parameter space for which there exist no stable symmetric orbits having two impacts. Local bifurcation analysis gives information about what motions exist near the stability boundaries, but in general these regions have been left unexplored. Part 2 gives a detailed account of what types of motions are possible in such regions.

Forced vibrations of systems having two-sided amplitude constraints have several potential applications. The response of such mechanical systems, including linkages, gears, and fasteners with looseness or "play" may be modeled using an oscillator like that considered here. Also, the motions of railcar wheels [23] and many nonlinear control systems [24] have been studied using piecewise-linear models. Impacting systems have been used as a model for the generation of noise in machinery [25, 26]. Also, motions of impact print hammers can be modeled using a system with periodic forcing and amplitude constraints [27].

It should be noted that the case of small clearances corresponds to *large* β in which no nonpenetrating stable double-impact orbits exist except at higher frequencies. This is so since the individual excursion times between stops is small and the total time on a periodic motion must sum to $2\pi n/\omega$. Also when β is *small*, or equivalently the stops are far apart, the simple linear response may coexist with the nonlinear motions. For small damping, i.e., $\alpha << 1$, this linear steady-state response is given (to leading order) by

$$x_{\text{lin}}(t) = \gamma\cos(\omega t) + 0(\alpha). \tag{29}$$

From this it is found that such motions exist if

$$|\gamma| < x_0 = 1 \quad \text{(nondimensionalized)} \tag{30a}$$

or equivalently, for $\omega > 1$

$$\sqrt{\beta+1} < \omega. \tag{30b}$$

For small β these motions can play an important part in the dynamics. In Fig. 6 the coexistence of stable linear and nonlinear motions is shown. (In fact the linear motion shown is merely neutrally stable as shown since $\alpha = 0$, but for $0 < \alpha << 1$ it will be stable and look essentially the same.)

The validity of the model presented here for applications to more complex systems is expected to be good. A simple single-degree of freedom piecewise linear model was shown to capture much of the behavior of a beam having a one-sided amplitude constraint as described in [9, 10]. Similar success is anticipated for systems having two-sided constraints.

References

1 Maezawa, S., and Furukawa, S., "Superharmonic Resonance in Piecewise Linear Systems," *Bulletin of the Japanese Society of Mechanical Engineering*, Vol. 16, 1973, pp. 931–941.

2 Maezawa, S., "Steady Forced Vibrations of Unsymmetrical Piecewise Linear Systems," *Bulletin of the Japanese Society of Mechanical Engineers*, Vol. 4, 1961, pp. 201–229.

3 Bogoliubov, N. N., and Mitropolsky, Y. A., *Asymptotic Methods in the Theory of Nonlinear Oscillations*, Gordon and Breach, New York, 1961.

4 Klotter, K., "Steady State Vibrations in Systems having Arbitrary Restoring and Damping Forces," *Symposium of Nonlinear Circuit Analysis, Polytechnic Institute of Brooklyn*, 1953, pp. 234–257.

5 Watanabe, T., "Forced Vibrations of Continuous System With Nonlinear Boundary Condition," ASME *Journal of Mechanical Design*, Vol. 100, 1978, pp. 487–491.

6 Shaw, S. W., and Holmes, P. J., "A Periodically Forced Piecewise Linear Oscillator," *Journal of Sound and Vibration*, Vol. 90, 1983, pp. 129–155.

7 Shaw, S. W., and Holmes, P. J., "A Periodically Forced Impact Oscillator With Large Dissipation," ASME JOURNAL OF APPLIED MECHANICS, Vol. 50, 1983, pp. 849–857.

8 Shaw, S. W., and Holmes, P. J., "Periodically Forced Linear Oscillator With Impacts: Chaos and Long Period Motions," *Physical Review Letters*, Vol. 51, 1983, pp. 623–626.

9 Moon, F. C., and Shaw, S. W., "Chaotic Vibrations of a Beam With Nonlinear Boundary Conditions," *International Journal of Nonlinear Mechanics*, Vol. 18, No. 6, 1983, pp. 465–477.

10 Shaw, S. W., "Forced Vibrations of a Beam with One-sided Amplitude Constraint: Theory and Experiment," *Journal of Sound and Vibration*, to appear.

11 Robinson, F. N. H., "An Experimental Study of the Catastrophic Behavior of a Nonlinear Differential Equation," preprint, Clarendon Laboratory, Oxford, U.K., 1982.

12 Nigh, M. M., and Shabana, A. A., "Effect of an Impact Damper on a Multidegree of Freedom System," *Journal of Sound and Vibration*, Vol. 89, 1983, pp. 541–557.

13 Masri, S. F., "Theory of the Dynamic Vibration Neutralizer With Motion-Limiting Stops," ASME JOURNAL OF APPLIED MECHANICS, Vol. 39, 1972, pp. 563–568.

14 Veluswami, M. A., and Crossley, F. R. E., "Multiple Impacts of a Ball Between Two Plates, Part 2: Mathematical Modelling," ASME *Journal of Engineering for Industry*, Vol. 97, 1975, pp. 828–835.

15 Holmes, P. J., "The Dynamics of Repeated Impacts With a Sinusoidally Vibrating Table," *Journal of Sound and Vibration*, Vol. 82, 1982, pp. 173–189.

16 Greenwood, D. T., *Principles of Dynamics*, Prentice-Hall, Englewood Cliffs, N.J., 1965.

17 Poincare, H., *Les Methodes Nouvelles de la Mecanique Celeste*, 3 Vols., Gauthier-Villars, Paris, 1899.

18 Guckenheimer, J., and Holmes, P., *Nonlinear Oscillations, Dynamical Systems, and Bifurcations of Vector Fields*, Springer-Verlag, New York, 1983.

19 Hsu, C. S., Yee, H. C., and Cheng, W. H., "Determination of Global Regions of Asymptotic Stability for Difference Dynamical Systems," ASME JOURNAL OF APPLIED MECHANICS, Vol. 44, 1977, pp. 147–153.

20 Masri, S. F., and Caughey, T. K., "On the Stability of the Impact Damper," ASME JOURNAL OF APPLIED MECHANICS, Vol. 33, 1966, pp. 586–592.

21 Senator, M., "Existence and Stability of Periodic Motions of a Harmonically Forced Impacting System," *Journal of the Acoustical Society of America*, Vol. 47, 1970, pp. 1390–1397.

22 Carr, J., *Applications of Centre Manifold Theory*, Springer-Verlag, New York, 1981.

23 Beaman, J. J., and Hedrick, J. K., "Freight Car Harmonic Response—A Simplified Nonlinear Method," *Nonlinear System Analysis and Synthesis, Vol. 2 - Techniques and Applications*, Ramnath, R. V., Hedrick, J. K., and Paynter, H. M., American Society of Mechanical Engineers, New York, 1979.

24 Minorsky, N., *Theory of Nonlinear Control Systems*, McGraw-Hill, New York, 1969.

25 Wood, L. A., and Byrne, K. P., "Analysis of a Random Repeated Impact Process," *Journal of Sound and Vibration*, Vol. 78, 1981, pp. 329–345.

26 Wood, L. A., and Byrne, K. P., "Experimental Investigation of a Random Repeated Impact Process," *Journal of Sound and Vibration*, Vol. 85, 1982, pp. 53–69.

27 Hendriks, F., "Bounce and Chaotic Motion in Impact Print Hammers," *IBM Journal of Research and Development*, Vol. 27, 1983, pp. 273–280.

Downloaded 02 May 2010 to 171.66.16.54. Redistribution subject to ASME license or copyright; see http://www.asme.org/terms/Terms_Use.cfm

The Dynamics of a Harmonically Excited System Having Rigid Amplitude Constraints

Part 2: Chaotic Motions and Global Bifurcations[1]

S. W. Shaw
Department of Mechanical Engineering,
Michigan State University,
East Lansing, Mich. 48824
Assoc. Mem. ASME

The simple model described in [1] was shown to exhibit nonlinear behavior such as subharmonic responses. In this paper parameter regions are examined in which no simple stable motions exist. In such regions complicated bifurcation sequences are encountered which result in long period and chaotic motions. These motions are irregular, bounded responses to periodic excitation and have not been previously considered in systems having two-sided amplitude constraints.

1 Introduction

In the preceding article [1], a simple oscillator was introduced as a model to study the response of systems having rigid two-sided amplitude constraints. The system was analyzed using a mapping **P** which relates conditions at subsequent impacts at one restraint. Defining a surface of section Σ in the phase space corresponding to such impacts the dynamics are studied using the mapping

$$\mathbf{P}: \Sigma \rightarrow \Sigma. \tag{1}$$

Points in Σ represent the velocity of the mass and the time at impact. The types of motions of interest here are those that hit both constraints. Periodic motions that do so contain an even number of impacts equal to $2k$, k each at each constraint. In the following, a periodic motion with $2k$ impacts corresponds to a point $(\bar{\imath},\bar{y})$ in Σ for which $\mathbf{P}^k(\bar{\imath},\bar{y}) = (\bar{\imath} + 2\pi n/\omega,\ \bar{y})$: a *k-cycle* point of **P**. Several $2k$ impact periodic motions may exist at one set of parameter values and may even have different periods. Note that after each $2k$ impacts, the forcing phase is exactly the same on such a motion.

The existence and stability of symmetric two-impact motions were found explicitly in [1]. Also, local bifurcations at the points of change in stability were considered, thus giving some information about the existence of other types of motions, such as pairs of antisymmetric orbits. Digital simulations were described and used to plot some typical motions. It was found that there existed open sets of parameter values for which no symmetric double-impact motions were stable. In this paper these regions are explored more fully using the digital simulation together with some methods of modern dynamical systems theory. In particular, *global bifurcations* that give rise to extremely complex motions will be discussed. The reader is referred to the works of Holmes [3] and Shaw and Holmes [4] for similar treatments of impacting systems.

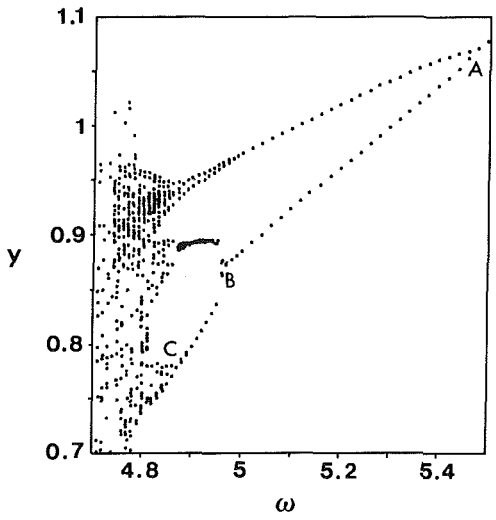


Fig. 1 Frequency response, $\beta = 2.0$, $r = 0.7$, $4.7 \leq \omega \leq 5.5$

In Fig. 1 results from the simulation are shown for $r = 0.7$, $\beta = 2.0$, and ω varying in the range (4.7, 5.5). Impact velocities at $x = +1$ are shown versus ω. This range corresponds roughly to a region in parameter space where the double-impact period-one motion no longer exists and the double-impact

[1] Work supported in part by NSF.
Contributed by the Applied Mechanics Division for presentation at the 1985 Joint ASME/ASCE Applied Mechanics, Bioengineering, and Fluids Engineering Conference, Albuquerque, N. Mex., June 24-26, 1985 of THE AMERICAN SOCIETY OF MECHANICAL ENGINEERS.
Discussion on this paper should be addressed to the Editorial Department, ASME, United Engineering Center, 345 East 47th Street, New York, N.Y. 10017, and will be accepted until two months after final publication of the paper itself in the JOURNAL OF APPLIED MECHANICS. Manuscript received by ASME Applied Mechanics Division, March, 1984; final revision, June, 1984. Paper No. 85-APM-15.
Copies will be available until February, 1986.

Copyright © 1985 by ASME
Downloaded 02 May 2010 to 171.66.16.54. Redistribution subject to ASME license or copyright; see http://www.asme.org/terms/Terms_Use.cfm

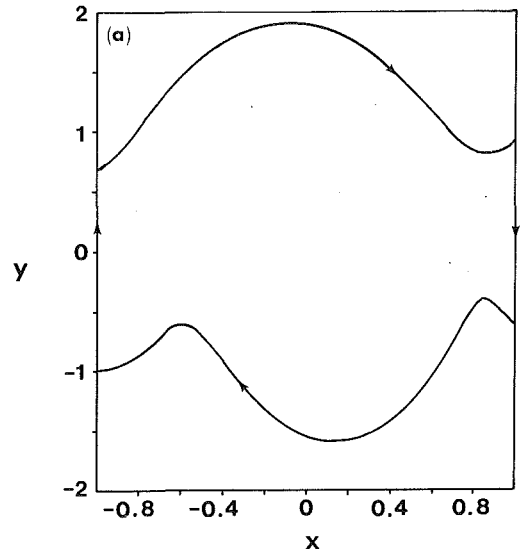


Fig. 2(*a*) Unsymmetric period 3, two impact, $\omega = 5.00$

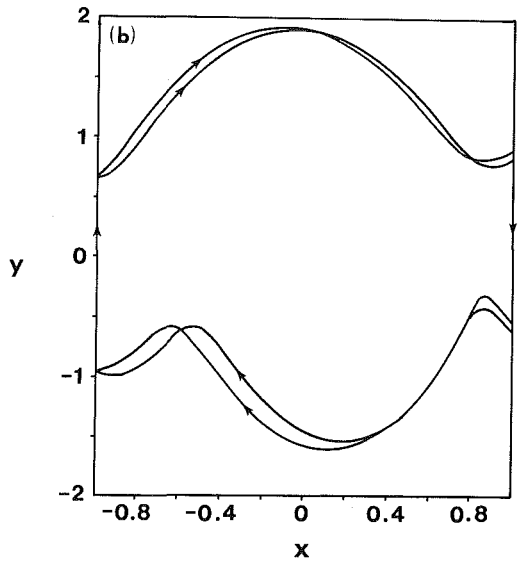


Fig. 2(*b*) Period 6, four impact, $\omega = 4.90$

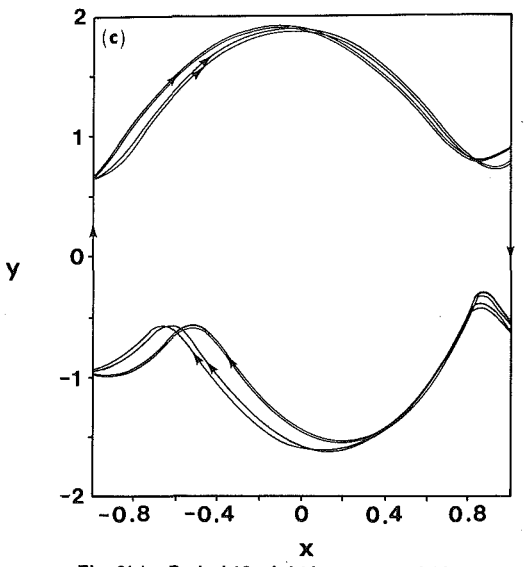


Fig. 2(*c*) Period 12, eight impact, $\omega = 4.86$

Fig. 2 Period doublings shown in projected phase plane (x,y), $\beta = 2.0$, $r = 0.7$

period-three motion is unstable (see Fig. 3(*b*) in [1]). Following the steady-state motion as ω decreases from 5.5., it is seen that a supercritical pitchfork bifurcation occurs near $\omega = 5.5$ which results in the creation of a pair of antisymmetric double-impact period-three motions; see point A in Fig. 1. These motions then each undergo a succession of period doubling or flip bifurcations, which eventually result in apparently nonperiodic, or *chaotic* motions. In such flip bifurcations an eigenvalue of $\overline{DP}^k$, for a $2k$ impact motion of period n (a k-cycle point of **P**), passes through -1 and out of the unit circle [5]. The motions becomes unstable in this process and a new motion of period $2n$ containing $4k$ impacts emerges (a $2k$-cycle point of **P**). In this example these new motions are stable; the period-doubling bifurcations are supercritical. Period-doubling cascades are typical behavior for nonlinear systems [6]. While well understood for certain classes of one-dimensional maps [7], the overall bifurcation sequences for higher dimensional systems are still unclear [8].

It should be noted that a period-nine motion having six impacts coexists with the motions indicated in Fig. 1 over a large portion of the frequency range shown. This motion, *not* shown in Fig. 1, exists in $4.6 \lesssim \omega \lesssim 5.4$. Also, the structure in the region shown in Fig. 1 exists in other (perhaps all) similar ranges of ω below the points where period n (odd) symmetric orbits undergo pitchfork bifurcations.

Points B and C in Fig. 1 show period doublings from a double-impact period-three motion to a four-impact period-six motion and then to a period-twelve motion with eight impacts, respectively. Representative orbits are shown in Fig. 2. The bifurcations at points A and B look similar as shown in Fig. 1, but are in fact very different. At point A *two* new orbits, each having period three and two impacts, appear as the symmetric orbit becomes unstable, hence the two branches shown. At point B one of these unsymmetric motions becomes unstable and *one* new orbit appears having period six and four impacts. The two impacts at $x = +1$ on this motion have different velocities and thus at point B two new branches appear, both corresponding to a different impact at $x = +1$ *on the same motion*.

The period doubling sequence takes the period-three motion through periods 3.2, 3.2^1, 3.2^2, 3.2^3, ... as ω is decreased. In fact such period doublings typically accumulate geometrically at a universal rate [7] as parameters are varied. Thus a stable motion of period 3.2^n for any $n \geq 0$ exists over the relatively narrow frequency range shown in Fig. 1. The bifurcations creating these (and infinitely many more) motions are part of the creation of a very complex set of orbits for this system. Such motions are considered in Sections 2 and 3.

The vector field described by the equation of motion is $2\pi/\omega$ periodic in the variable t. For this reason only the *phase* of the forcing term need be considered. Defining the phase variable $\phi = t \bmod (2\pi/\omega)$ one can replace t with ϕ in the section Σ and the associated mapping **P**. Doing so transforms the periodic point $(\bar{t},\bar{y})$ of **P** into a *fixed point* of $\mathbf{P}^k$: $\mathbf{P}^k(\bar{\phi},\bar{y}) = (\bar{\phi},\bar{y})$. This is convenient for describing orbits in Σ. Note that some information is lost in this process since the period of the motion associated with $(\bar{\phi},\bar{y})$ is not known in this formulation. The motions shown in Fig. 2 are represented in Fig. 3 as points in Σ. Note that a $2k$ impact periodic motion is represented by k points in Σ.

2 Horseshoes – Existence and Implications

Motions shown in the region from $\omega = 4.7$ to $\omega \simeq 4.85$ in Fig. 1 appear quite irregular and in fact many seem nonperiodic. Even if there does exist an asymptotically stable simple periodic motion at a particular set of parameter values, the transient dynamics are very irregular. In this region the period-three double-impact motion exists but is unstable.

Downloaded 02 May 2010 to 171.66.16.54. Redistribution subject to ASME license or copyright; see http://www.asme.org/terms/Terms_Use.cfm

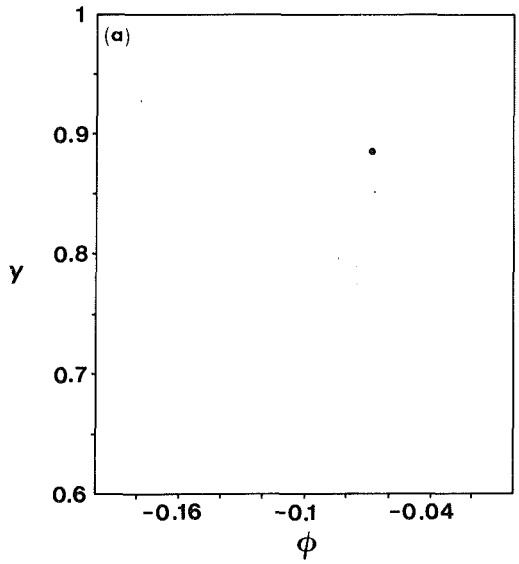


Fig. 3(a)

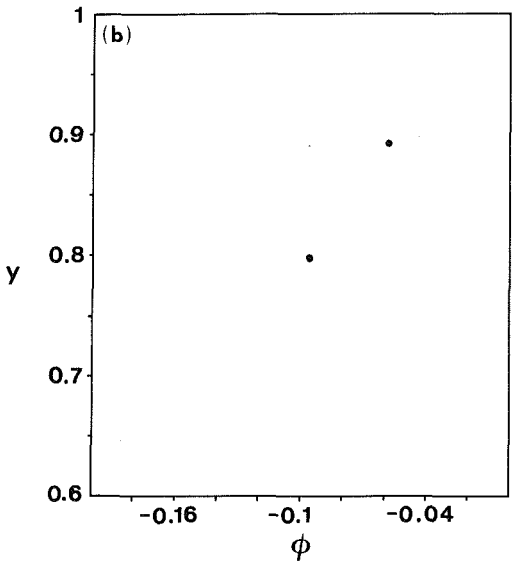


Fig. 3(b)

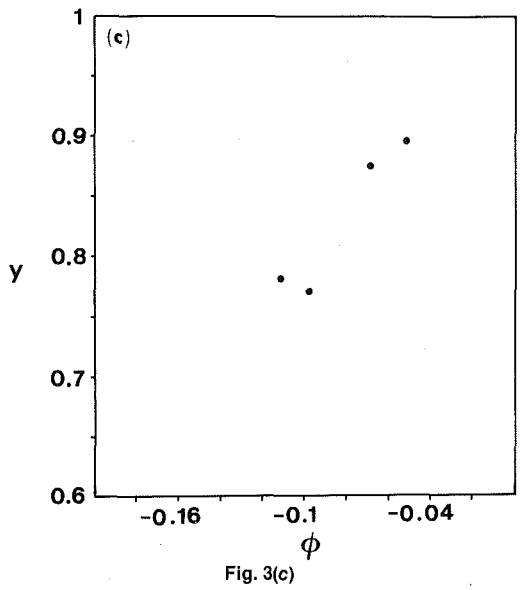


Fig. 3(c)

Fig. 3 Motions shown in Σ, same parameter values as in Fig. 2.

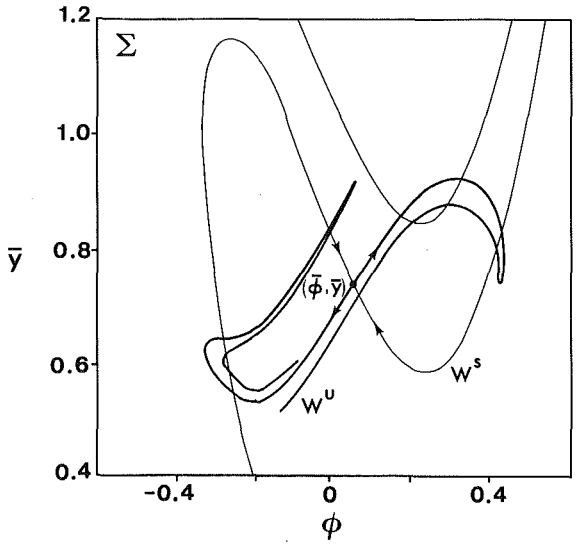


Fig. 4 Stable mainfold W^s (light line) and unstable manifold W^u (heavy line), $\beta = 2.0$, $r = 0.7$, $\omega = 4.5$

There also exist those motions created in the pitchfork, flip, and other bifurcations as ω was decreased from 5.5, most (perhaps all) of which are also unstable. This set of unstable motions form part of a larger set of points which are invariant under **P**, as described in the following.

The location and stability of the period-three symmetric orbit is known explicitly, in Σ it is represented by $(\bar{\phi},\bar{y})$. The stable (W^s) and unstable (W^u) manifolds of $(\bar{\phi},\bar{y})$ are defined as those sets of points in Σ which are, respectively, forward and backward asymptotic to $(\bar{\phi},\bar{y})$ under iterates of **P**:

$$W^s = \{(\phi,y)\epsilon\Sigma \mid \mathbf{P}^n(\phi,y) \to (\bar{\phi},\bar{y}) \quad \text{as } n \to +\infty\}$$
$$W^u = \{(\phi,y)\epsilon\Sigma \mid \mathbf{P}^n(\phi,y) \to (\bar{\phi},\bar{y}) \quad \text{as } n \to -\infty\}. \tag{2}$$

Portions of these sets are easily generated using the digital simulation as follows. Points very near $(\bar{\phi},\bar{y})$ are mapped forward in time to generate points on W^u and time is run backward and the impact rule inverted in order to generate points on W^s. Examination of these sets indicates a mechanism by which the preceding irregular motions arise in this system.

In Fig. 4, W^s and W^u are shown for $r = 0.7$, $\beta = 2.0$, and $\omega = 4.5$. Note that they intersect transversally. Such intersections imply (from the Smale-Birkoff Homoclinic Theorem, see [5] for more details) that there exists a complicated invariant set, a *Smale horseshoe*, for some iterate (perhaps of high number) of **P**. The implications of the existence of this set are more fully discussed in the following.

In Fig. 5 a close-up of the region of interest is shown. Points of interest are labeled by letters and the images of these points under a single iterate of **P** are indicated by the primed points. Regions of Σ are defined as follows: $H_1 = adli$, $H_2 = jkcb$, $V_1 = ahgb$, and $V_2 = cdef$ (see Fig. 5). The digital simulation indicates that

$$\mathbf{P}(H_i) = V_i \quad i = 1,2 \tag{3}$$

and thus a topological horseshoe exists at these parameter values. The horseshoe arises in a global bifurcation as parameters are varied (see [3]).

The set of points bounded by segments of W^s between a and d and between b and c and by segments of W^u between a and b and between c and d is defined as Q. The set of points that never leave Q as **P** is iterated is the *invariant set* of **P** on Q, Λ_Q. This set is determined by considering the intersection of all images (forward and backward) of **P** acting on Q:

Downloaded 02 May 2010 to 171.66.16.54. Redistribution subject to ASME license or copyright; see http://www.asme.org/terms/Terms_Use.cfm

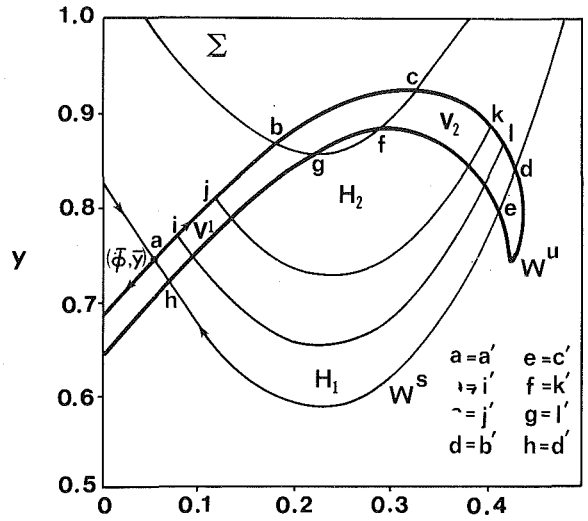


Fig. 5 Region of interest from Fig. 4

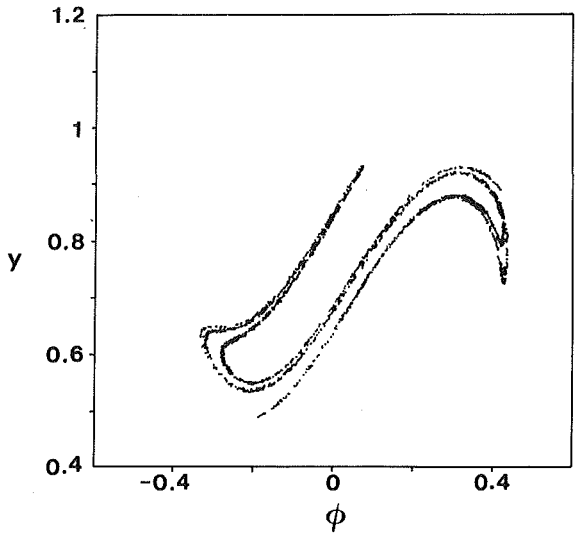


Fig. 6 Orbit in Σ, 3000 points, $\beta = 2.0$, $r = 0.7$, $\omega = 4.5$

$$\Lambda_Q = \bigcap_{m=-\infty}^{\infty} \mathbf{P}^m(Q) \tag{4}$$

This set is a cantor set (cf. [9]) and contains the following:

(*i*) a countable infinity of unstable periodic orbits including those of arbitrarily long periods,
(*ii*) an uncountable infinity of unstable, bounded, nonperiodic orbits, and
(*iii*) a dense orbit.

The dynamics of **P** restricted to Λ_Q can be described using symbol sequences (cf. [5]). A point $(\phi,y)\,\epsilon\Lambda_Q$ is characterized by a symbol sequence defined as

$$a(\phi,y) = \{a_j(\phi,y)\}_{j=-\infty}^{\infty}$$

where

$$a_j(\phi,y) = \begin{cases} 1 \text{ if } \mathbf{P}^j\ (\phi,y)\epsilon V_1 \\ 2 \text{ if } \mathbf{P}^j\ (\phi,y)\epsilon V_2. \end{cases} \tag{5}$$

Each point in Λ_Q has a corresponding symbol sequence. It has not been proven that Λ_Q is *hyperbolic* [5] for the present example and thus many points in Λ_Q may correspond to the same sequence. However, every possible doubly infinite sequence containing two symbols (1 and 2 here) is represented by at least one point in Λ_Q. It is *assumed* that Λ_Q *is* hyperbolic in this case (without rigorous justification) for what follows. This implies that there is a one-to-one correspondence between the symbol sequences and the orbits in Λ_Q. The periodic orbits are easily enumerated by arrangements of the two symbols. The nonperiodic orbits are uncountable since Λ_Q forms an uncountable set and the periodic orbits form a countable one. A dense orbit is constructed by joining together all possible finite symbol sequences. Each iterate of **P** of a point $(\phi,y)\,\epsilon\Lambda_Q$ corresponds to a *shift* of the associated symbol sequence (ϕ,y) defined by the shift operator σ where

$$\sigma(a) = b \text{ with } b_i = a_{i+1}. \tag{6}$$

The foregoing implies that there exist motions that visit the regions V_1 and V_2 in *any prescribed order*.

While the invariant set Λ_Q is itself of great mathematical interest, it does not dictate the overall dynamics of the system. This is so since almost all points in Q are eventually mapped out of Q under some iterate of **P**. The manner in which points enter and leave Q can be highly irregular but an experiment or digital simulation has very little (if any) chance of actually following an orbit in Λ_Q since they are all unstable (under the hyperbolicity assumption). Thus *transient chaos* is expected, but the motion may be asymptotic to a stable simple periodic orbit outside of Q. If no such stable motions exist however, then a collection of sets such as Λ_Q which exist in Σ can in fact dominate the motion.

3 Chaotic Motions and Strange Attracting Sets

The existence of an *attracting set* for the mapping **P** is easily established. The attracting set is defined as the intersection of all forward images of a region R for which $\mathbf{P}(R) \subset R$;

$$A = \bigcap_{n\geq 0} \mathbf{P}^n(R). \tag{7}$$

Taking $R = \{(\phi,y)\epsilon\Sigma \mid 0 < y \leq L\}$ with L large enough one can show that $\mathbf{P}(R) \subset R$ easily in a manner similar to that found in [4]. The set A might be a fixed point or it might be a finite set of points corresponding to a multiple impact periodic motion. It can also contain horseshoes as previously demonstrated, in which case it is referred to as a *strange attracting set*.

A digital simulation for the parameter values $\beta = 2.0$, $r = 0.7$, and $\omega = 4.5$ is shown in Fig. 6. The motion is shown as points in Σ with $\phi = t \bmod (2\pi/\omega)$ 3000 points are shown. While the collection of points certainly exhibits some structure, they are mapped within that structure in an irregular yet deterministic manner. Note that the points appear to lie on a set of curves that resembles the unstable manifold of Fig. 4. In fact, in some systems it can be proven that the attracting set is equal to the closure of the unstable manifold, $\overline{W^u}$ [10]. This may well be true in this case also.

The question arises as to whether or not orbits such as the one in Fig. 6 are truly "chaotic" or, does **P** possess a "strange attractor"? The mathematical model has an attracting set and orbits are asymptotic to that set. As parameters are varied in two-dimensional maps (such as **P**) saddle-node bifurcations are known to occur which result in the creation of extremely long period stable periodic motions [8]. These orbits each undergo period-doubling sequences of their own and thus stable periodic motions of arbitrarily long period (i.e. impact numbers) exist over certain parameter ranges. However, the basins of attraction of those motions can be so thin as to render them unobservable by digital simulations [11]. There is no way of knowing whether orbits such as the one shown in Fig. 6 are actually representative of stable (long period) periodic motions as suggested by Newhouse [12] or whether

Downloaded 02 May 2010 to 171.66.16.54. Redistribution subject to ASME license or copyright; see http://www.asme.org/terms/Terms_Use.cfm

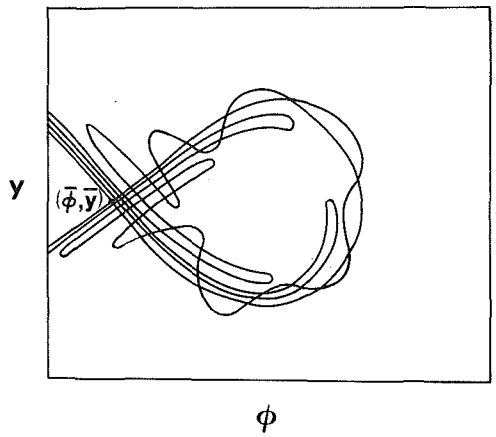


Fig. 7 A homoclinic tangle

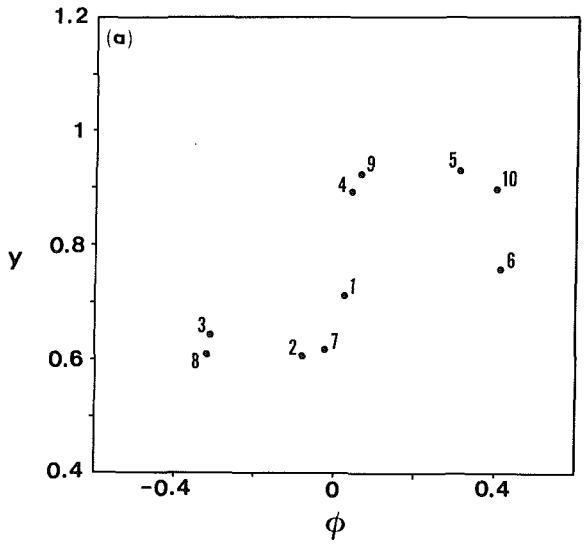


Fig. 8(a) $(\phi,y)_0 = (0.0500, 0.743)$

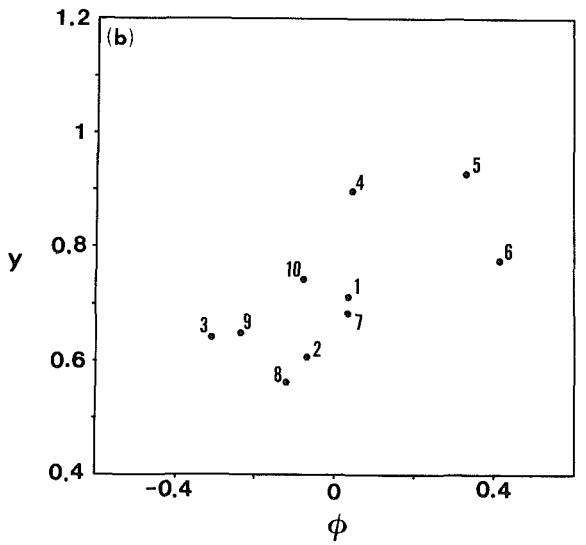


Fig. 8(b) $(\phi,y)_0 = (0.0501, 0.743)$

Fig. 8 Sensitive dependence on initial conditions

they are nonperiodic, i.e, chaotic. However, from an engineering viewpoint it hardly matters since in such parameter ranges precise quantitative experimental results cannot be expected to concur with those from a mathematical model. Nonetheless, the model should provide a reasonable guide to the overall behavior of such systems including the description of low-impact-number stable subharmonics and of regions where transient *or* steady-state chaotic motions may be expected to occur [13, 14].

Motions such as the "chaotic" one in the foregoing can be thought of as follows. The unstable and stable manifolds fold back-and-forth on themselves [5] in a homoclinic tangle as shown in Fig. 7. If W^u is equal to the attracting set then motions will approach this set. Motions on W^u stay on W^u but separate exponentially fast. Thus the motion is restricted to an infinitely folded-over sheet on which motions diverge from each other. The resulting motions are like that of Fig. 6. Figure 8 shows the first few iterates under **P** of two nearby points started near $(\bar{\phi},\bar{y})$. The points are initially separated by only $\Delta\phi = 10^{-5}$. Note how quickly they diverge. Such *sensitive dependence on initial conditions* [15] is characteristic of chaotic motions.

Examination of the frequency response curves in [1] shows that as ω is increased the so-called "jump" phenomena can occur in which a motion suddenly disappears at a particular frequency and a new motion for the system of significantly different magnitude becomes apparent. These jumps are associated with saddle-node bifurcations. In this oscillator the system may jump from a simple symmetric motion onto a chaotic one as ω is increased. An example of this situation is for $\beta = 2.0$, $r = 0.7$, and ω varying near 4.5 where the period-one double-impact motion undergoes a saddle-node bifurcation. As ω is decreased below $\omega = 4.5$, the chaotic motions coexist with the larger amplitude simple symmetric motion. They eventually disappear at some ω ($\simeq 3$) in a manner that is not presently understood. Discontinuities in the mapping **P** corresponding to degenerate impacts that just "kiss" the constraint may play an important role in these transitions (see [4, 16, 17]).

4 Conclusions

In this, the second of a two-part paper, complicated motions were shown to exist in the model over some open sets of parameter values. The imposition of amplitude constraints as a passive control device may result in undesirable system responses. Not only are subharmonic resonances introduced [1], but irregular or chaotic motions can also occur. Systems with amplitude restraining stops have been studied in the context of nonlinear vibration absorbers by several authors, see the works of Masri and coworkers and the references cited therein [18–20]. Statistical considerations of chaotic motions such as the one shown in Fig. 6 may yield more efficient designs for such impact dampers.

Another important application where the simple model studied here may be of use is in the dynamics of heat exchanger tubes in nuclear reactors [21]. Such tubes are designed to have clearances at support points to allow for thermal expansion. When fluid flows past these tubes vortex shedding occurs and the tubes are excited. The response of such systems is very complicated [21] and the wearing of these tubes is a major problem in the nuclear industry. Fluid flow past panels and beams can result in chaotic motions [22] and thus chaotic motions may provide an appropriate tool in the study of tube wear.

Experimental results on the chaotic behavior of systems with two-sided amplitude constraints has not appeared in the literature. However, preliminary experiments on a cantilever beam with tip constraints do indicate that such motions do in fact occur [23]. Analytical and experimental studies of systems with one-sided constraints is more extensive and does include chaotic responses [4, 13, 16, 17, 24]. Workers in many areas are becoming aware of the richness of nonlinear phenomena. The system considered here provides another example of a class of systems in which such behavior can be important.

Downloaded 02 May 2010 to 171.66.16.54. Redistribution subject to ASME license or copyright; see http://www.asme.org/terms/Terms_Use.cfm

Acknowledgment

The author is grateful to Professor Phil Holmes of Cornell for reading and providing helpful comments on this work.

References

1 Shaw, S. W., "The Dynamics of a Harmonically Excited System Having Rigid Amplitude Constraints, Part 1: Subharmonic Motions and Local Bifurcations," ASME JOURNAL OF APPLIED MECHANICS, Vol. 52, 1985.

2 Greenwood, D. T., *Principles of Dynamics*, Prentice Hall, Englewood Cliffs, N.J., 1965.

3 Holmes, P. J., "The Dynamics of Repeated Impacts with a Sinusoidally Vibrating Table," *Journal of Sound and Vibration*, Vol. 84, 1982, pp. 173–189.

4 Shaw, S. W., and Holmes, P. J., "A Periodically Forced Piecewise Linear Oscillator," *Journal of Sound and Vibration*, Vol. 90, 1983, pp. 129–155.

5 Guckenheimer, J., and Holmes, P., *Nonlinear Oscillations, Dynamical Systems, and Bifurcations of Vector Fields*, Springer-Verlag, New York, 1983.

6 Feigenbaum, M., "Quantitative Universality for a Class of Nonlinear Transformations," *Journal of Statistical Physics*, Vol. 19, 1979, pp. 25–52.

7 Collet, P., and Eckman, J. P., *Iterated Maps on the Interval as Dynamical Systems*, Birkhauser, Boston, 1980.

8 Holmes, P., and Whitley, D., "Bifurcations of One and Two-Dimensional Maps," *Proceedings of the Royal Society London*, to appear, 1984.

9 Chillingworth, D. R. J., *Differential Topology With a View to Applications*, Pitman Press, London, 1976.

10 Holmes, P., and Whitley, D., "On the Attracting Set of Duffing's Equation; 1: Analytical Methods for Small Force and Damping," *Proceedings, Year of Concentration in Partial Differential Equations and Dynamical Systems, University of Houston, Texas*, 1983.

11 Greenspan, B., and Holmes, P., "Homoclinic Orbits, Subharmonics, and Global Bifurcations in Forced Oscillations," *Nonlinear Dynamics and Turbulence*, Barenblatt, G., Iooss, B., and Joseph, D. D., eds., Pitman Press, London, 1983.

12 Newhouse, S. E., "Lectures on Dynamical Systems," *CIME Lectures, Dynamical Systems, Bressanone, Italy, June 1978*, Birkhauser, Boston, 1980, pp. 1–114.

13 Shaw, S. W., "Forced Vibrations of a Beam having One-Sided Amplitude Constraint: Theory and Experiment," *J. of Sound and Vibration*, to appear.

14 Moon, F. C., and Holmes, P. J., "A Magnetoelastic Strange Attractor," *Journal of Sound and Vibration*, Vol. 65, 1979, pp. 275–296.

15 Guckenheimer, J., "Sensitive Dependence on Initial Conditions for One-Dimensional Maps," *Communications in Mathematical Physics*, Vol. 70, 1979, pp. 133–160.

16 Shaw, S. W., and Holmes, P. J., "A Periodically Forced Impact Oscillator With Large Dissipation," ASME JOURNAL OF APPLIED MECHANICS, Vol. 50, 1983, pp. 849–857.

17 Shaw, S. W., and Holmes, P. J., "Periodically Forced Linear Oscillator With Impacts; Chaos and Long Period Motions," *Physical Review Letters*, Vol. 51, 1983, pp. 623–626.

18 Masri, S. F., and Caughey, T. K., "On the Stability of the Impact Damper," ASME JOURNAL OF APPLIED MECHANICS, Vol. 33, 1966, pp. 586–592.

19 Masri, S. F., "General Motion of Impact Dampers," *Journal of the Acoustical Society of America*, Vol. 47, No. 1, Part 2, 1970, pp. 229–237.

20 Masri, S. F., "Periodic Excitation of Multiple-Unit Impact Dampers," *Journal of the Engineering Mechanics Division, ASCE*, Vol. 96, No. E6, 1970, pp. 1195–1207.

21 Rogers, R. J., and Pick, R. J., "On the Dynamic Spatial Response of a Heat Exchanger Tube with Intermittent Baffle Contacts," *Nuclear Engineering and Design*, Vol. 36, 1976, pp. 81–90.

22 Dowell, E. H., "Flutter of a Buckled Plate as an Example of Chaotic Motion of a Deterministic Autonomous System," *J. of Sound and Vibration*, Vol. 85, 1982, pp. 333–344.

23 Moon, F. C., personal communication.

24 Masri, S. F., Mariamy, Y. A., and Anderson, J. C., "Dynamic Response of a Beam with a Geometric Nonlinearity," ASME JOURNAL OF APPLIED MECHANICS, Vol. 48, 1981, pp. 404–410.

Downloaded 02 May 2010 to 171.66.16.54. Redistribution subject to ASME license or copyright; see http://www.asme.org/terms/Terms_Use.cfm

C. Wampler

K. Buffinton
Assoc. Mem. ASME

Department of Mechanical Engineering,
Stanford University,
Stanford, Calif. 94305

J. Shu-hui
Department of Engineering Mechanics,
Tsinghua University,
Beijing, China

Formulation of Equations of Motion for Systems Subject to Constraints

A method for constructing equations of motion governing constrained systems is presented. The method, which is particularly useful when equations of motion have already been formulated, and new equations of motion, reflecting the presence of additional constraints are needed, allow the new equations to be written as a recombination of terms comprising the original equations. An explicit form in which the new dynamical equations may be cast for the purpose of numerical integration is developed, along with special cases that demonstrate how the procedure may be simplified in two commonly occurring situations. An illustrative example from the field of robotics is presented, and several areas of application are identified.

Introduction

Until recently, the only ways to formulate equations of motion for systems subject to constraints were either to introduce the constraints as kinematical equations at an early stage of the analysis or to increase the number of equations through the introduction of unknown forces. The appropriateness of the latter approach is questionable unless the constraint forces themselves are of interest, and the former approach tends to unnecessarily complicate the development of the equations of motion. Moreover, it can occur that, after equations of motion have been formulated, additional constraints are introduced. For example, this situation arises when design objectives change, when a system's topology changes during its motion, or when a system is replaced with a simpler one as a means of checking a numerical simulation. In such situations, premature introduction of constraints deprives one of the opportunity to make maximum use of expressions developed in connection with the unconstrained system. Kamman and Huston [1] and Singh and Likins [2] present alternate schemes, based on Kane's method [3, 4], which are applicable to the numerical generation of equations of motion for constrained systems. The present paper, which also makes use of Kane's method, provides a general statement of how dynamical equations governing constrained systems can be generated, either numerically or literally, directly from expressions comprising the equations governing the systems without constraints.

The sequel begins with a brief review of Kane's method. This is followed immediately by a statement and proof of a procedure for developing Kane's equations for systems subject to additional constraints. Elaborative comments are offered regarding the forms in which both the constraint equations and the constrained equations of motion may be cast. Two special cases are treated next, and an illustrative example follows. Finally, a discussion of applications and a summary are presented.

Kane's Equations of Motion

A detailed discussion of Kane's method is available in [4]. However, some fundamental definitions are reviewed here for the sake of completeness and to establish a point of departure for the presentation of an alternate method for developing Kane's equations of motion for systems subjected to additional constraints.

For a system of N particles P_i of mass m_i $(i=1, \ldots, N)$, let $\mathbf{a}_i$ denote the inertial acceleration of particle P_i, and let $\mathbf{f}_i$ be the sum of forces acting on that particle. Define the inertia force of P_i as

$$\mathbf{f}_i^* \triangleq -m_i\mathbf{a}_i. \tag{1}$$

The equations of motion can be written by using D'Alembert's Principle as

$$\mathbf{f}_i + \mathbf{f}_i^* = \mathbf{0} \quad (i=1, \ldots, N), \tag{2}$$

or in matrix notation,

$$\underline{\mathbf{F}} + \underline{\mathbf{F}}^* = \underline{\mathbf{0}} \tag{3}$$

where

$$\underline{\mathbf{F}} \triangleq [\mathbf{f}_1 \ \ldots \ \mathbf{f}_N]^T, \quad \underline{\mathbf{F}}^* \triangleq [\mathbf{f}_1^* \ \ldots \ \mathbf{f}_N^*]^T \tag{4}$$

and an underscore signifies a matrix. Assuming the system possesses n degrees of freedom, one can introduce an $n \times 1$ column matrix $\underline{u} \triangleq [u_1 \ \ldots \ u_n]^T$, called the *generalized speed matrix* [4, 5], whose elements are independent linear combinations of the time-derivatives of the generalized coordinates chosen to describe the system. The matrix of particle velocities, $\underline{v} \triangleq [\mathbf{v}_1 \ \ldots \ \mathbf{v}_N]^T$, then can be expressed as

$$\underline{\mathbf{v}} = \underline{\mathbf{v}}_p \underline{u} + \underline{v}_t \tag{5}$$

where the elements of the $N \times n$ and $N \times 1$ matrices $\underline{\mathbf{v}}_p$ and $\underline{\mathbf{v}}_t$ are vector functions of the generalized coordinates and time.

Contributed by the Applied Mechanics Division for publication in the JOURNAL OF APPLIED MECHANICS.

Discussion on this paper should be addressed to the Editorial Department, ASME, United Engineering Center, 345 East 47th Street, New York, N.Y. 10017, and will be accepted until two months after final publication of the paper itself in the JOURNAL OF APPLIED MECHANICS. Manuscript received by ASME Applied Mechanics Division, March, 1984; final revision, July, 1984.

Copyright © 1985 by ASME
Downloaded 02 May 2010 to 171.66.16.54. Redistribution subject to ASME license or copyright; see http://www.asme.org/terms/Terms_Use.cfm

The matrix $\underline{\mathbf{v}}_p$, which is simply the coefficient of the generalized speed matrix $\underline{u}$, is called the *partial velocity matrix*. After dot-multiplying equation (3) by $\underline{\mathbf{v}}_p^T$ to obtain

$$\underline{\mathbf{v}}_p^T \bullet (\underline{\mathbf{F}} + \underline{\mathbf{F}}^*) = \underline{0} \tag{6}$$

and defining a *generalized active force matrix* $\underline{F}$ and a *generalized inertia force matrix* $\underline{F}^*$ as

$$\underline{F} \triangleq \underline{\mathbf{v}}_p^T \bullet \underline{\mathbf{F}}, \quad \underline{F}^* \triangleq \underline{\mathbf{v}}_p^T \bullet \underline{\mathbf{F}}^* \tag{7}$$

so that $\underline{F}$ and $\underline{F}^*$ are $n \times 1$ column matrices, one arrives at

$$\underline{F} + \underline{F}^* = \underline{0}. \tag{8}$$

This is the matrix form of Kane's dynamical equations, which, as proved in [4], applies to both holonomic and simple nonholonomic systems.

There are two features of the foregoing procedure that deserve to be highlighted. The first is that it eliminates "nonworking" forces in such a way that they may be neglected from an analysis at the outset. This can be seen by considering that the generally large number of nonworking forces, such as those acting between particles of a rigid body, which may be present in the $3N$ scalar equations represented by equation (3), are eliminated by the dot-product operations of equation (6). Since no evidence of these forces remains in the resulting n scalar equations represented by equation (8), they need never be introduced explicitly. The second feature is that the procedure allows the use of generalized speeds. This permits the selection of dependent variables as not only individual time-derivatives of the generalized coordinates, but convenient linear combinations of them as well. This enables one to express equation (5), and hence equation (8), in the simplest possible forms.

Kane's Equations With Constraints

If a system described by equation (8) is subjected to m independent constraints such that the number of degrees of freedom decreases from n to $n-m$, the generalized speed matrix $\underline{u}$ must be replaced by a new generalized speed matrix $\underline{\tilde{u}} \triangleq [\tilde{u}_1 \ \ldots \ \tilde{u}_{n-m}]^T$. The equations of motion for the system then can be generated by considering the problem as a completely new one. Alternatively, as a consequence of the following theorem, one can make use of many of the expressions that were generated in forming equation (8).

Theorem. If an n degree-of-freedom system of N particles P_i $(i=1, \ldots, N)$ possessing a partial velocity matrix $\underline{\mathbf{v}}_p$, a generalized active force matrix $\underline{F}$, and a generalized inertia force matrix $\underline{F}^*$, each associated with the generalized speed matrix $\underline{u}$, is subjected to additional forces $\tilde{\mathbf{f}}_i$, acting on $P_i (i=1, \ldots, N)$, and m additional linearly independent constraints which are such that

$$\underline{u} = \underline{\alpha}\underline{\tilde{u}} + \underline{\beta} \tag{9}$$

where $\underline{\tilde{u}}$ is an $(n-m) \times 1$ matrix of new independent generalized speeds, and the $n \times (n-m)$ matrix $\underline{\alpha}$ and the $n \times 1$ matrix $\underline{\beta}$ are functions of the generalized coordinates and time, then the generalized active and generalized inertia force matrices $\underline{\tilde{F}}$ and $\underline{\tilde{F}}^*$ associated with $\underline{\tilde{u}}$ are

$$\underline{\tilde{F}} = \underline{\alpha}^T (\underline{F} + \underline{\mathbf{v}}_p^T \bullet \underline{\tilde{\mathbf{F}}}), \quad \underline{\tilde{F}}^* = \underline{\alpha}^T \underline{F}^* \tag{10}$$

where $\underline{\tilde{\mathbf{F}}} \triangleq [\tilde{\mathbf{f}}_1 \ \ldots \ \tilde{\mathbf{f}}_N]^T$; the new equations of motion are

$$\underline{\alpha}^T (\underline{F} + \underline{F}^* + \underline{\mathbf{v}}_p^T \bullet \underline{\tilde{\mathbf{F}}}) = \underline{0}. \tag{11}$$

Proof. Replacing $\underline{u}$ in equation (5) with the right-hand member of equation (9), one obtains

$$\underline{\mathbf{v}} = \underline{\tilde{\mathbf{v}}}_p \underline{\tilde{u}} + \underline{\tilde{\mathbf{v}}}_t \tag{12}$$

where

$$\underline{\tilde{\mathbf{v}}}_p = \underline{\mathbf{v}}_p \underline{\alpha}, \quad \underline{\tilde{\mathbf{v}}}_t = \underline{\mathbf{v}}_p \underline{\beta} + \underline{\mathbf{v}}_t. \tag{13}$$

Since the $\tilde{u}_i$ $(i=1, \ldots, n-m)$ are independent, $\underline{\tilde{\mathbf{v}}}_p$ is the partial velocity matrix for the additionally constrained system. The new generalized active force matrix and generalized inertia force matrix are

$$\underline{\tilde{F}} \triangleq \underline{\tilde{\mathbf{v}}}_p^T \bullet (\underline{\mathbf{F}} + \underline{\tilde{\mathbf{F}}}), \quad \underline{\tilde{F}}^* \triangleq \underline{\tilde{\mathbf{v}}}_p^T \bullet \underline{\mathbf{F}}^*. \tag{14}$$

Equations (14) lead directly to equations (10) when $\underline{\tilde{\mathbf{v}}}_p$ is expressed as in the first of equations (13) and use is made of equations (7). Substituting from equations (10) into Kane's equations of motion for the new system, that is, into

$$\underline{\tilde{F}} + \underline{\tilde{F}}^* = \underline{0}, \tag{15}$$

one obtains equation (11).

Note that any nonworking forces among $\underline{\tilde{\mathbf{F}}}$ can, as always, be omitted from an analysis at the outset. Additionally, for generality, the theorem is stated in terms of a system of particles, so it applies to the special case of systems containing rigid bodies. In this context, one can take advantage of methods, detailed in [4], which involve use of the angular velocity of a body to facilitate construction of expressions for generalized active and inertia forces. Also as shown in [4], $\underline{F}$ and $\underline{F}^*$ may be obtained by using potential and kinetic energy functions. In taking such an approach, Passerello and Huston [6] devised a method for constructing generalized inertia forces for nonholonomic systems, which lead them to a quantity equivalent to $\underline{\tilde{F}}^*$; however, they did not extend their procedure to the construction of generalized active forces.

Constraint Equations

Before proceeding with a more explicit form of equation (11), it is useful to examine how constraints come to be expressed in the form of equation (9). This examination is divided into two portions. The first deals primarily with theoretical issues underlying the form of the constraint equations. The second, as well as the remainder of this paper, addresses operational concerns one must confront when developing equations for constrained systems.

Begin the theoretical development by considering a system described by n generalized speeds and subject to s simple nonholonomic constraints, or holonomic constraints differentiated with respect to time, of the form

$$\hat{\underline{A}}\underline{u} + \hat{\underline{B}} = \underline{0} \tag{16}$$

where the $s \times n$ matrix $\hat{\underline{A}}$ and the $s \times 1$ matrix $\hat{\underline{B}}$ are continuous functions of the generalized coordinates and time. While the number of independent constraints in general can be time-dependent, assume that at some instant there are $m (m \leq s; m \leq n)$. The number of degrees of freedom for the new system is then $\nu \triangleq n-m$ and the solution to equation (16) for $\underline{u}$ falls into one of two categories. If $\hat{\underline{B}}$ does not lie in the column space of $\hat{\underline{A}}$ (i.e., if $\hat{\underline{B}}$ cannot be formed by a linear combination of the columns of $\hat{\underline{A}}$), the constraints are "inconsistent," the problem is ill-posed, and no solution can be found for $\underline{u}$. If $\hat{\underline{B}}$ does lie in the column space of $\hat{\underline{A}}$, at least one solution exists for $\underline{u}$. Let $\underline{W}_1$ be a $n \times \nu$ matrix with linearly independent columns that form a basis for the null space of $\hat{\underline{A}}$, that is,

$$\hat{\underline{A}}\underline{W}_1 = \underline{0}, \tag{17}$$

and let $\underline{W}_2$ be a $n \times m$ matrix whose columns complete a basis for the vector space $\Re^n$. A well known result from linear algebra is then that the general solution to equation (16) is

$$\underline{u} = \underline{W}_1 \underline{z} - \underline{W}_2 \underline{y} \tag{18}$$

where $\underline{y}$ is an $m \times 1$ matrix of unique scalars such that

$$\hat{\underline{B}} = \hat{\underline{A}}\underline{W}_2 \underline{y}, \tag{19}$$

and $\underline{z}$ is a $\nu \times 1$ matrix of independent quantities describing the constrained system. The $\nu \times 1$ matrix $\underline{\tilde{u}}$ of generalized speeds for the constrained system may be defined, therefore, as

$$\underline{\tilde{u}} \triangleq \underline{z}. \tag{20}$$

Downloaded 02 May 2010 to 171.66.16.54. Redistribution subject to ASME license or copyright; see http://www.asme.org/terms/Terms_Use.cfm

By substituting from equation (20) into equation (18), one obtains an equation of the form of equation (9) with

$$\underline{\alpha} = \underline{W}_1, \quad \underline{\beta} = -\underline{W}_2 \underline{y}. \tag{21}$$

The preceding general development demonstrates that it is always possible to produce an equation of the form of equation (9) for a system subjected to constraints in the form of equation (16). However, it does not indicate an operational procedure for producing equations (21). The matrices $\underline{W}_1$ and $\underline{W}_2$ are not unique, and several approaches for constructing them can be envisioned. The problem is equivalent to that of constructing a generalized inverse of $\underline{\hat{A}}$, of which the Moore-Penrose generalized inverse is a particular example [7]. Singular value decomposition, used in [2], and the "zero eigenvalue" technique, presented in [1], are two methods of arriving at this inverse. Although these methods are numerically well conditioned, they are computationally expensive, and since they are iterative procedures, preclude a symbolic formulation of the equations of motion. Other simpler methods exist, one of which is described in the following.

For a physically realizable constrained system, an independent set of constraint equations is often readily identifiable. Assume m have been identified so that a system that originally had n degrees of freedom is reduced to one having only $\nu \triangleq n-m$. Equation (16) then can be written containing no dependent equations as

$$\underline{A}\underline{u} + \underline{B} = \underline{0} \tag{22}$$

where $\underline{A}$ is an $m \times n$ matrix and $\underline{B}$ is an $m \times 1$ matrix. The matrix $\tilde{\underline{u}}$ may now be defined as

$$\tilde{\underline{u}} \triangleq \underline{C}\underline{u} + \underline{D}, \tag{23}$$

where the $\nu \times n$ matrix $\underline{C}$ and the $\nu \times 1$ matrix $\underline{D}$ are functions of the generalized coordinates and time. This definition is arbitrary, so long as $\underline{C}$ is such that the composite system of equations

$$\begin{bmatrix} \underline{A} \\ \underline{C} \end{bmatrix} \underline{u} + \begin{bmatrix} \underline{B} \\ \underline{D} \end{bmatrix} = \begin{bmatrix} \underline{0} \\ \underline{I} \end{bmatrix} \tilde{\underline{u}}, \tag{24}$$

where $\underline{0}$ is the $m \times \nu$ zero matrix and $\underline{I}$ is the $\nu \times \nu$ identity matrix, can be solved uniquely for $\underline{u}$; or, equivalently, that the $n \times n$ composite matrix

$$\underline{E} \triangleq \begin{bmatrix} \underline{A} \\ \underline{C} \end{bmatrix} \tag{25}$$

is invertible. Solving equation (24) for $\underline{u}$ yields an equation of the form of equation (9) with

$$\underline{\alpha} = \underline{E}^{-1} \begin{bmatrix} \underline{0} \\ \underline{I} \end{bmatrix}, \quad \underline{\beta} = -\underline{E}^{-1} \begin{bmatrix} \underline{B} \\ \underline{D} \end{bmatrix}. \tag{26}$$

These expressions for $\underline{\alpha}$ and $\underline{\beta}$ are equivalent to those of equations (21) in that they satisfy the relations

$$\underline{A}\underline{\alpha} = \underline{0}, \quad \underline{A}\underline{\beta} = -\underline{B}. \tag{27}$$

In practice, the relationship between $\tilde{\underline{u}}$ and $\underline{u}$ is often chosen without regard to the invertibility of $\underline{E}$, but so as to render the elements of $\tilde{\underline{u}}$ physically meaningful. This can be adequate, but difficulties arise if at some time during the system's motion it approaches a configuration for which $\underline{E}$ is singular. Should this occur, $\tilde{\underline{u}}$ must be redefined, at least temporarily.

Explicit Equations of Motion

To numerically integrate the equations of motion, it is helpful to have $\dot{\tilde{\underline{u}}}$ appear explicitly. To achieve this, consider the following. It can be shown that there exist unique matrices $\underline{M}$ and $\underline{N}$ such that

$$\underline{F} + \underline{F}^* + \underline{\mathbf{v}}_P^T \cdot \tilde{\underline{\mathbf{F}}} = \underline{M}\dot{\underline{u}} + \underline{N} \tag{28}$$

where the $n \times n$ matrix $\underline{M}$ is a function of the generalized coordinates and time, and the $n \times 1$ matrix $\underline{N}$ is a function of the generalized coordinates, $\underline{u}$, and time. Differentiating equation (24), and solving for $\dot{\underline{u}}$, one finds with the aid of the first of equations (26) that

$$\dot{\underline{u}} = \underline{\alpha}\dot{\tilde{\underline{u}}} + \underline{\delta} \tag{29}$$

where

$$\underline{\delta} \triangleq -\underline{E}^{-1} \begin{bmatrix} \dot{\underline{A}}\underline{u} + \dot{\underline{B}} \\ \dot{\underline{C}}\underline{u} + \dot{\underline{D}} \end{bmatrix}. \tag{30}$$

Substituting from equations (28) and (29) into equation (11), one arrives at the equations of motion, explicit in $\dot{\tilde{\underline{u}}}$,

$$\underline{\alpha}^T \underline{M}\underline{\alpha}\dot{\tilde{\underline{u}}} + \underline{\alpha}^T (\underline{M}\underline{\delta} + \underline{N}) = \underline{0}. \tag{31}$$

Thus, to obtain explicit equations of motion for a constrained system, identify the matrices $\underline{M}$ and $\underline{N}$ for the unconstrained system, and the matrices $\underline{\alpha}$ and $\underline{\delta}$ from the constraint equations, and then substitute into equation (31).

Special Cases

***(1)* Selection of $\tilde{\underline{u}}$ as a subset of $\underline{u}$.** In many cases an analyst will find it convenient to select $\tilde{\underline{u}}$ to be comprised of some subset of the elements of $\underline{u}$. Suppose that the first ν elements of $\underline{u}$. Suppose that the first ν elements of $\underline{u}$ are chosen. One may then write the matrices $\underline{C}$ and $\underline{D}$ of equation (23) as

$$\underline{C} = [\underline{I}^{\nu\nu} \quad \underline{0}^{\nu m}], \quad \underline{D} = \underline{0}, \tag{32}$$

and, after subdividing $\underline{A}$, the matrix $\underline{E}$ of equation (25) as

$$\underline{E} = \begin{bmatrix} \underline{A}_1^{m\nu} & \underline{A}_2^{mm} \\ \underline{I}^{\nu\nu} & \underline{0}^{\nu m} \end{bmatrix} \tag{33}$$

where $\underline{I}$ and $\underline{0}$ represent identity and zero matrices. (The convention adopted here is that two matrix superscripts indicate the dimensions of a rectangular matrix and a single superscript indicates the dimension of a column matrix.) Next, solve for $\underline{\alpha}$, $\underline{\beta}$, and $\underline{\delta}$ as given in equations (26) and (30), respectively, to obtain

$$\underline{\alpha} = \begin{bmatrix} \underline{I}^{\nu\nu} \\ \underline{\alpha}_1^{m\nu} \end{bmatrix}, \quad \underline{\beta} = \begin{bmatrix} \underline{0}^{\nu} \\ \underline{\beta}_1^{m} \end{bmatrix}, \quad \underline{\delta} = \begin{bmatrix} \underline{0}^{\nu} \\ \underline{\delta}_1^{m} \end{bmatrix} \tag{34}$$

where

$$\underline{\alpha}_1 \triangleq -\underline{A}_2^{-1}\underline{A}_1, \quad \underline{\beta}_1 \triangleq -\underline{A}_2^{-1}\underline{B}, \tag{35}$$

and

$$\underline{\delta}_1 \triangleq -\underline{A}_2^{-1}(\dot{\underline{A}}\underline{u} + \dot{\underline{B}}). \tag{36}$$

Finally, after partitioning $\underline{M}$ and $\underline{N}$ of equation (28) so that

$$\underline{M} = \begin{bmatrix} \underline{M}_{11}^{\nu\nu} & \underline{M}_{12}^{\nu m} \\ \underline{M}_{21}^{m\nu} & \underline{M}_{22}^{mm} \end{bmatrix}, \quad \underline{N} = \begin{bmatrix} \underline{N}_1^{\nu} \\ \underline{N}_2^{m} \end{bmatrix}, \tag{37}$$

substitute the expressions of equation (34) into equation (31) to obtain

$$(\underline{M}_{11} + \underline{M}_{12}\underline{\alpha}_1 + \underline{\alpha}_1^T\underline{M}_{21} + \underline{\alpha}_1^T\underline{M}_{22}\underline{\alpha}_1)\dot{\tilde{\underline{u}}} + \underline{N}_1 + \underline{\alpha}_1^T\underline{N}_2 + (\underline{M}_{12} + \underline{\alpha}_1^T\underline{M}_{22})\underline{\delta}_1 = \underline{0}. \tag{38}$$

The principal benefits of choosing $\tilde{\underline{u}}$ in this way are that it permits working with matrices of lower dimensions and with a familiar set of generalized speeds. The inversion of the $n \times n$ matrix $\underline{E}$ is reduced to the simpler task of inverting the $m \times m$ matrix $\underline{A}_2$. Since the elements of $\underline{A}$ are functions of the generalized coordinates and time, a potential liability is that any one set of generalized speeds may not yield a submatrix $\underline{A}_2$ which is nonsingular for all configurations and times of interest. Whenever necessary, one can circumvent this

Downloaded 02 May 2010 to 171.66.16.54. Redistribution subject to ASME license or copyright; see http://www.asme.org/terms/Terms_Use.cfm

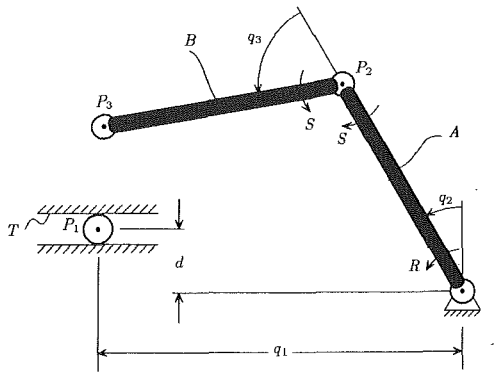


Fig. 1 Unconstrained system

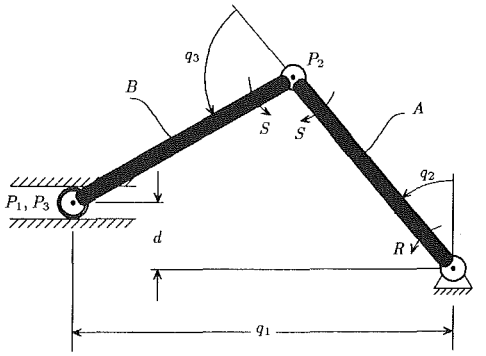


Fig. 2 Constrained system

problem by reordering the elements of the original generalized speed matrix $\underline{u}$ while retaining the form of $\underline{C}$ given in equation (32). This amounts to redefining $\tilde{\underline{u}}$ while still taking advantage of the procedure for matrix substructuring outlined in the foregoing. Since the m rows of $\underline{A}$ are independent, at least m of its n columns must also be independent; thus, by a suitable reordering of the generalized speeds, one can always produce an $\underline{A}_2$ which is invertible.

(2) **Prescribing the Last m Generalized Speeds as Functions of the Generalized Coordinates and Time.** In certain instances, it is desirable to prescribe some of the generalized speeds as functions of the generalized coordinates and time. Without loss of generality, one may assume that the last m speeds are so prescribed. The constraint equations are then

$$[\underline{0}^{mv} \quad \underline{I}^{mm}]\underline{u} + \underline{B} = \underline{0}. \tag{39}$$

Choosing $\tilde{\underline{u}}$ to be comprised of the first v elements of $\underline{u}$ as in special case *(I)*, one has

$$\underline{\alpha} = \begin{bmatrix} \underline{I}^{vv} \\ \underline{0}^{mv} \end{bmatrix}, \quad \underline{\beta} = \begin{bmatrix} \underline{0} \\ -\underline{B} \end{bmatrix}, \quad \underline{\delta} = \begin{bmatrix} \underline{0} \\ -\dot{\underline{B}} \end{bmatrix}, \tag{40}$$

and the dynamical equations of motion are

$$\underline{M}_{11}\dot{\tilde{\underline{u}}} + \underline{N}_1 - \underline{M}_{12}\dot{\underline{B}} = \underline{0}. \tag{41}$$

Example

To illustrate the foregoing procedures, consider the planar mechanism shown in Fig. 1. The system consists of two subsystems, the first of which is composed solely of a particle P_1 of mass M which slides in a frictionless track T so that its position may be described by the single generalized coordinate q_1. The second subsystem consists of two rigid massless links A and B, each of length L, and two particles P_2 and P_3, each of mass m, assembled as shown. The configuration of the assembly is described by the two angles q_2 and q_3. Motors (not shown) exert a torque R on A and a torque S between A and B. This system possesses several physically realizable counterparts. For example, one may regard the linkage as a simplified model of a robot manipulator and the particle P_1 as a load that the robot is intended to grasp and move.

To develop the equations of motion for the system without, as yet, any additional constraints, begin by noting that, since the number of degrees of freedom for the system is three, the generalized speed matrix $\underline{u}$ has three elements which may be defined conveniently as

$$u_1 \triangleq \dot{q}_1, \quad u_2 \triangleq \dot{q}_2, \quad u_3 \triangleq \dot{q}_3. \tag{42}$$

The generalized active force matrix can then be shown to be

$$\underline{F} = \begin{bmatrix} 0 \\ R + mgL(2s_2 + s_{23}) \\ S + mgLs_{23} \end{bmatrix} \tag{43}$$

while the generalized force matrix is

$$\underline{F}^* = \begin{bmatrix} -M\dot{u}_1 \\ -mL^2\{(3+2c_3)\dot{u}_2 + (1+c_3)\dot{u}_3 + s_3[u_2^2 - (u_2+u_3)^2]\} \\ -mL^2[(1+c_3)\dot{u}_2 + \dot{u}_3 + s_3u_2^2] \end{bmatrix} \tag{44}$$

where g is the acceleration of gravity, $s_i \triangleq \sin q_i$ and $c_i \triangleq \cos q_i$ $(i=2,3)$, and $s_{23} \triangleq \sin(q_2+q_3)$. The resulting equations of motion, obtained by substituting from equations (43) and (44) into equation (8), are

$$\left.\begin{aligned} -M\dot{u}_1 &= 0 \\ R + mgL(2s_2 + s_{23}) - mL^2\{(3+2c_3)\dot{u}_2 & \\ + (1+c_3)\dot{u}_3 + s_3[u_2^2 - (u_2+u_3)^2]\} &= 0 \\ S + mgLs_{23} - mL^2[(1+c_3)\dot{u}_2 + \dot{u}_3 + s_3u_2^2] &= 0. \end{aligned}\right\} \tag{45}$$

These equations govern the motion of the system so long as the robot and the load do not interact, that is, until P_3 makes contact with P_1.

Consider next the system's topology depicted in Fig. 2. The only modification that has been made is that P_3 is now constrained to be coincident with P_1. This introduces two scalar constraint equations so that the number of degrees of freedom of the constrained sytsem is $3-2=1$. The constraints are holonomic; that is, any two of q_1, q_2, q_3 can be expressed as functions of the remaining one. However, because the constraint equations cannot be solved easily, it is convenient to work with their time-derivatives and to apply the previously stated theorem. The differentiated constraint equations, obtained by equating the velocities of P_3 and P_1, can be expressed in the form of equation (22) with

$$\underline{A} = \begin{bmatrix} s_2 & Ls_3 & Ls_3 \\ c_2 & -L(1+c_3) & -Lc_3 \end{bmatrix}, \quad \underline{B} = \begin{bmatrix} 0 \\ 0 \end{bmatrix}. \tag{46}$$

Since the system retains only one degree of freedom, the generalized speed matrix for the constrained system $\tilde{\underline{u}}$ contains only a single element. To take advantage of the procedures outlined in special case *(I)*, this element may be taken to be equal to u_1. The corresponding form of equation (32) is then

$$\underline{C} = [1 \quad 0 \quad 0], \quad D = 0. \tag{47}$$

Identifying the appropriate parts of equations (46) and (47) and performing the operations indicated in equations (35) and (36), one obtains

$$\underline{\alpha}_1 = -\frac{1}{Ls_3}\begin{bmatrix} -s_{23} \\ s_2 + s_{23} \end{bmatrix}, \quad \underline{\beta}_1 = \begin{bmatrix} 0 \\ 0 \end{bmatrix}, \tag{48}$$

and

Downloaded 02 May 2010 to 171.66.16.54. Redistribution subject to ASME license or copyright; see http://www.asme.org/terms/Terms_Use.cfm

$$\underline{\delta}_1 = -\frac{1}{Ls_3}\begin{bmatrix} -c_{23}u_2 & -Lu_3 & -Lu_3 \\ (c_2+c_{23})u_2 & L(1+c_3)u_3 & L(1+c_3)u_3 \end{bmatrix}\underline{u} \tag{49}$$

where $c_{23} \triangleq \cos(q_2+q_3)$. Since no new working forces have been introduced, use of equations (28) and (37) to identify the necessity submatrices of $\underline{M}$ and $\underline{N}$ directly from equations (43) and (44) is appropriate and yields

$$M_{11} = -M, \quad \underline{M}_{12} = [0 \quad 0], \quad \underline{M}_{21} = \begin{bmatrix} 0 \\ 0 \end{bmatrix}, \tag{50}$$

$$\underline{M}_{22} = -mL^2\begin{bmatrix} 3+2c_3 & 1+c_3 \\ 1+c_3 & 1 \end{bmatrix}, \tag{51}$$

and

$$\underline{N}_2 = \begin{bmatrix} N_1 = 0, \\ R+mgL(2s_2+s_{23})-mL^2s_3[u_2^2-(u_2+u_3)^2] \\ S+mgLs_{23}-mL^2s_3u_2^2 \end{bmatrix}. \tag{52}$$

The equation governing the motion of the constrained system is obtained by substituting from equations (48)–(52) into equation (38) and can be written as

$$-[M+\frac{m}{s_3^2}(s_2^2+2s_3c_2s_{23})]\dot{\tilde{u}}_1$$

$$-\frac{1}{Ls_3}\{s_2S+s_{23}(S-R)-mgLs_2s_{23}-mL^2s_3[s_2u_2^2$$

$$+s_{23}(u_2+u_3)^2]\}-\frac{m}{s_3^2}\{[s_2c_2-s_3(c_3-2c_2c_{23})]u_1u_2$$

$$+Ls_{23}(2-c_3^2)(u_2+u_3)u_3\}=0. \tag{53}$$

It should be realized that although this procedure yields the single dynamical equation for the constrained system, the equation can be solved only when supplemented by expressions relating $\underline{u}$ and $\underline{\tilde{u}}_1$, as in equation (9), and $\underline{u}$ and the $\dot{q}_i$ $(i=1,2,3)$, as in equation (42). Also note that equations (46) and (47) do not give rise to an invertible relationship between $\underline{u}$ and $\tilde{u}_1$ for certain values of q_2 and q_3. In particular, the values $q_3=0$ with $q_2=\pm\cos^{-1}(d/2L)$, where d is defined in Figs. 1 and 2, lead to singular relationships. If motion near these configurations is of interest, one can either reorder the elements of $\underline{u}$ whenever a singular configuration is approached, or seek a definition of $\tilde{u}_1$ which leads to an invertible relationship for all configurations. A choice of $\tilde{u}_1$ which is satisfactory for all configurations, but which was avoided at the outset for the sake of clarity of illustration, is

$$\tilde{u}_1 = s_3u_1 - Ls_2(u_2+u_3) \quad 0<|d|<2L. \tag{54}$$

Applications

While the procedures set forth in the foregoing are applicable to any dynamical system subject to constraints that may be cast as simple nonholonomic, there are three particular areas of application that deserve special mention. The first arises in connection with systems whose topologies change during motion. The "robot" in the example just presented is a system of this type. To simulate its motion throughout its range of operation, the governing dynamical equations both for the original and modified system topologies must be available. As has been shown, the method of this paper provides a clear and convenient way of obtaining the equations for the modified system.

A second area of application involves problems such that the early introduction of constraints unnecessarily encumbers the formulating of dynamical equations. This can be the case

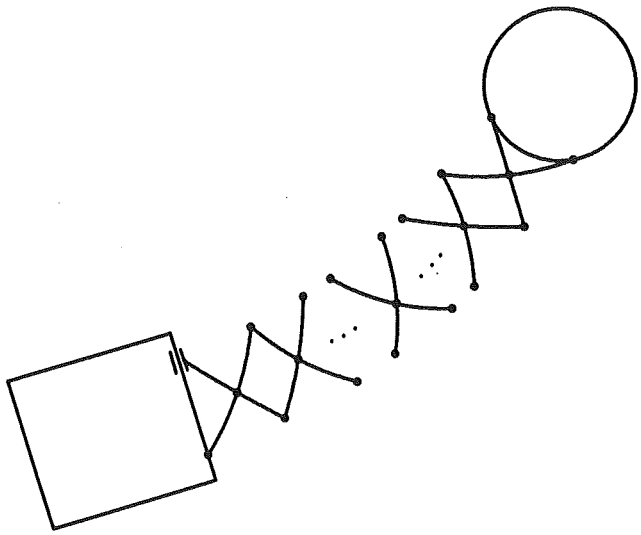


Fig. 3 Spacecraft with a deployable elastic linkage

in any complex problem but is particularly true for systems that have a repetitive structure. In these situations the dynamical equations sometimes can be easily derived for a generic element of the structure and then combined recursively, via the method under consideration, to obtain the equations governing the motion of the complete structure. In [8] this technique is used to generate the equations of motion for a spacecraft consisting of two rigid bodies connected by a flexible linkage (See Fig. 3.). The equations are obtained by first developing the dynamical equations for a typical link, regarded as detached from the others, and by then introducing constraints reflecting the connections between links in the assembled mechanism.

Finally, the methods at hand are relevant to the introduction of fictitious constraints for the purpose of checking dynamical equations. For a simple example illustrating this idea, consider again the unconstrained system of Fig. 1. Assume that a computer program has been written to numerically integrate the governing dynamical equations [See equation (45).]. Also assume that the program calculates the system's total mechanical energy (the sum of potential energy plus kinetic energy) at each time-step of the integration. When the torques R and S are equal to zero, the total energy must remain constant throughout any motion for the equations to be valid. Suppose a sign error is made in formulating the generalized inertial force matrix $\underline{F}^*$ of equation (44), so that the erroneous expression for $\underline{F}^*$ is given by

$$\underline{F}^* = \begin{bmatrix} -M\dot{u}_1 \\ -mL^2\{(3-2c_3)\dot{u}_2+(1+c_3)\dot{u}_3+s_3[u_2^2-(u_2+u_3)^2]\} \\ -mL^2[(1+c_3)\dot{u}_2+\dot{u}_3+s_3u_2^2] \end{bmatrix} \tag{55}$$

[Equation (55) differs from equation (44) in the sign contained within the coefficient of $\dot{u}_2$ in F_2^*.] When the dynamical equations obtained by substituting from equations (43) and (55) into equation (8) are integrated numerically, the total energy is not constant, thus indicating the error. Now, to localize the error, one can utilize fictitious constraints in conjunction with the energy integral of the constrained system. In particular, consider the constraint $q_3=0$. By referring to the procedures of special case (*2*), one can show that this constraint is easily incorporated into the computer program for the unconstrained system simply by deleting all terms arising from F_3 and F_3^* and by setting q_3 and u_3 equal to zero. When the resulting equations are integrated

Downloaded 02 May 2010 to 171.66.16.54. Redistribution subject to ASME license or copyright; see http://www.asme.org/terms/Terms_Use.cfm

numerically, the energy integral will not be constant. Since F_3, F_3^*, and all terms consisting of products containing q_3 or u_3 do not contribute to the constrained equations of motion, one can conclude that the error is in one of the remaining expressions. Note that if the constraint $q_2 = 0$, rather than $q_3 = 0$, is imposed, the corresponding energy integral would be constant, thus identifying expressions which are error free.

This example is only a limited illustration of the use of fictitious constraints to check dynamical equations. More broadly, fictitious constraints can provide valuable checks for any system which, when properly constrained, is transformed into one possessing energy or momentum integrals, known responses, or known governing equations. As demonstrated, constraints of the type presented in special case (*2*) are particularly useful because the constrained equations involve only a subset of the terms comprising the unconstrained equations, thus helping to single out terms in error.

Summary

A method facilitating the generation of equations of motion for systems subject to constraints has been presented. Applicable to both holonomic and simple nonholonomic systems, the method is based on Kane's dynamical equations and retains all of their inherent advantages, most notably the elimination of nonworking forces. The method is simple to apply, either by hand or when the requisite operations are relegated to a computer. Among the potential applications of the method are the analysis of systems whose topologies may change, the analysis of systems with a repeating structure, and the debugging of computer simulations of mechanical systems.

References

1 Kamman, J. W., and Huston, R. L., "Multibody System Dynamics With Constraints: The 'Closed-Loop' Problem," Office of Naval Research, Technical Paper ONR-UC-MIE-080181-12, Aug. 1, 1981.

2 Singh, R. P., and Likins, P. W., "Singular Value Decomposition for Constrained Dynamical Systems," Paper in the process of review for ASME JOURNAL OF APPLIED MECHANICS.

3 Kane, T. R., "Dynamics of Nonholonomic Systems," ASME JOURNAL OF APPLIED MECHANICS, Vol. 83, 1961, pp. 574–578.

4 Kane, T. R., *Dynamics*, 3rd Ed., Stanford University, Stanford, Calif., 1972.

5 Kane, T. R., and Wang, C. F., "On the Derivation of Equations of Motion," *Journal of the Society for Industrial and Applied Mathematics*, Vol. 13, 1965, pp. 487–492.

6 Passerello, C. E., and Huston, R. L., "Another Look at Nonholonomic Systems," ASME JOURNAL OF APPLIED MECHANICS, Vol. 40, No. 1, 1973, pp. 101–104.

7 Ben-Israel, A., and Greville, T. N. E., *Generalized Inverses: Theory and Applications*, John Wiley & Sons, New York, 1974.

8 Djerassi, S., "Deployment of an Elastic Linkage from a Spacecraft," Doctoral Dissertation, Stanford University, submitted, 1984.

Downloaded 02 May 2010 to 171.66.16.54. Redistribution subject to ASME license or copyright; see http://www.asme.org/terms/Terms_Use.cfm

M. S. Bhat
Lecturer.

S. K. Shrivastava
Associate Professor.

Department of Aerospace Engineering,
Indian Institute of Science,
Bangalore 560012, India

Dissipativeness and Stability of a Class of Distributed Parameter Systems

Input-output stability of linear-distributed parameter systems of arbitrary order and type in the presence of a distributed controller is analyzed by extending the concept of dissipativeness, with certain modifications, to such systems. The approach is applicable to systems with homogeneous or homogenizable boundary conditions. It also helps in generating a Liapunov functional to assess asymptotic stability of the system.

1 Introduction

For designing a controller for a physical system, it is generally necessary to ascertain its stability. Liapunov method is widely used to study internal stability. The bounded input-bounded output criterion gives external stability. For lumped parameter systems both have been used extensively. For distributed parameter systems described by partial differential equations, literature on input-output stability is rather limited. Employing semigroup-theoretic approach/functional (operator) method, the input-output stability criteria are obtained in the frequency domain by Zames [1], Chen and Tsay [2], Desoer and Wang [3] et al., and in the time domain by Willems [4], Wang [5], and Cook [6] et al. A system with space-dependent coefficients is considered by Jumarie [7]. These analyses deal with a restricted class of systems, and are not easy to apply to engineering problems.

In this paper, input-output stability of distributed parameter systems is analyzed through the concept of dissipativeness. The study follows closely the work of Hill and Moylan [8, 9] on lumped parameter systems. To extend the concept to distributed parameter systems, certain modifications are introduced. It is noted that storage functional can be used as a suitable Liapunov like functional. A bound on the possible range of storage functional is obtained. Using input-output relations and state space descriptions, a theorem on dissipativeness of the system is derived. Thus, the method also helps in generating a Liapunov functional that can be used to assess the internal stability of the system [10].

The modified concept is applied to a linear distributed parameter system of arbitrary order and type with an interior distributed control and homogeneous boundary conditions. The problems faced in its extension to systems with boundary control are briefly discussed. An illustration is included to show application of the approach.

Contributed by the Applied Mechanics Division for publication in the JOURNAL OF APPLIED MECHANICS.

Discussion on this paper should be addressed to the Editorial Department, ASME, United Engineering Center, 345 East 47th St., New York, N.Y. 10017, and will be accepted until two months after final publication of the paper itself in the JOURNAL OF APPLIED MECHANICS. Manuscript received by ASME Applied Mechanics Division, May, 1982; final revision, August, 1984.

2 System Definition

The state and output for a broad class of distributed parameter systems are governed by the following linear autonomous vector partial differential equations:[1]

$$\mathbf{y}_t(\mathbf{x},t) = \mathbf{A}(\mathbf{x},D)\,\mathbf{y}(\mathbf{x},t) + \mathbf{B}(\mathbf{x},t)\,\mathbf{u}(\mathbf{x},t), \tag{1}$$

$$\mathbf{z}(\mathbf{x},t) = \mathbf{C}(\mathbf{x})\mathbf{y}(\mathbf{x},t) + \mathbf{E}(\mathbf{x})\mathbf{u}(\mathbf{x},t), \tag{2}$$

where $\mathbf{y}(.,.) \in \mathbf{H}^k(Q)$ is an n-dimensional state vector (see the Appendix for definition of spaces). $\mathbf{y}_t(\mathbf{x}, t)$ (i.e., $\partial \mathbf{y}(\mathbf{x}, t)/\partial t$) is assumed to be an element of $\mathbf{H}^0(Q)$. $\mathbf{A}(\mathbf{x}, D)$ is a matrix of continuous closed linear autonomous kth order spatial differential operator from $\mathbf{H}^k(Q)$ to $\mathbf{H}^0(Q)$ with continuous injection. This is given by the formal expression

$$\mathbf{A}(\mathbf{x},D) = \sum_{j=0}^{k} \mathbf{a}_j(\mathbf{x}) D^j; \quad D^j = \partial^j/\partial \mathbf{x}^j,$$

where $\mathbf{a}(\mathbf{x}) \in C^\infty(\Omega)$ is such that $\mathbf{A}(\mathbf{x}, D)$ has nontrivial essential spectrum bounded from below and it is invertible. Physically this implies that the system cannot translate without consumption of energy.

The p-dimensional control function $\mathbf{u}(\mathbf{x}, t)$ is defined on the space of admissible controls $\mathbf{U}_{ad}(Q) \subset \mathbf{L}_2(\mathbf{x}, t; \mathbf{U})$, with compact support in Q. The space of controls $\mathbf{U}$ is assumed to be the subset of the product space $\mathbf{U}^0(Q) = \Sigma_{i=0}^{p} H^0(Q)_i$. $U^0(Q)$ is a p-dimensional Hilbert product space. By associating suitable measure, $\mathbf{U}$ can be made as a whole of $\mathbf{U}^0(Q)$. Matrix $\mathbf{B}(\mathbf{x}, t)$ is sufficiently smooth, uniformly bounded operator from $\mathbf{U}(Q)$ to $\mathbf{H}^0(Q)$ with continuous injection. $\mathbf{L}_2(\mathbf{x}, t; \mathbf{U})$ is the product space of vector valued functions with domain in $\mathbf{U}$ which are Lebesgue measurable and bounded with respect to $\mathbf{L}_2$-norm.

The matrix operators $\mathbf{C}(\mathbf{x})$ and $\mathbf{E}(\mathbf{x})$ are bounded and continuous. Under these assumptions, the r-dimensional output vector $\mathbf{z}(.,.) \in Z_0(Q)$ is continuous and smooth, where $\mathbf{Z}_0(Q)$ is a r-dimensional Hilbert product space.

The associated initial and boundary conditions are specified by the following:

[1] Bold letter indicates a vector quantity.

Copyright © 1985 by ASME
Downloaded 02 May 2010 to 171.66.16.54. Redistribution subject to ASME license or copyright; see http://www.asme.org/terms/Terms_Use.cfm

$$\mathbf{y}(\mathbf{x},0)=\mathbf{y}_0(\mathbf{x});\mathbf{x}\in\Omega;\mathbf{y}_0\in\mathbf{H}^0(\Omega),\|y_0\|<\infty, \tag{3}$$

$$\mathbf{A}_b(\mathbf{s},D)\mathbf{y}(\mathbf{s},t)=\mathbf{b}(\mathbf{s})\mathbf{u}(\mathbf{s},t);(\mathbf{s},t)\in\partial Q,$$

$$\mathbf{y}\in\mathbf{H}^{k-1/2}(\partial Q),D^j\mathbf{y}\in\mathbf{H}^{k-j-1/2}(\partial Q),$$

$$0\le j\le k-1,\mathbf{v}\in\mathbf{V}_{ad}(\partial Q), \tag{4}$$

where $\mathbf{A}_b(\mathbf{s}, D)$ is a matrix of spatial differential operator of order $\gamma \le k-1$ with coefficient function $\nu(\mathbf{s})$ which is Holder continuous and measurable on $\partial\Omega$. $D^j = \partial/\partial \mathbf{s}^j$ is the normal derivative taken toward exterior of $\partial\Omega$. $\mathbf{A}_b(\mathbf{s}, D^j)$ is jth order boundary differential operator: $\mathbf{H}^{k-1/2}(\partial Q) \rightarrow \mathbf{H}^{k-j-1/2}(\partial Q)$; ($\theta_j \triangleq k-j-1/2$). $\mathbf{A}_b$ is kept fairly general so as to encompass Dirichlet, Neumann, or mixed boundary conditions. It is assumed that the linear operator $\mathbf{A}(\mathbf{x}, D)$ with the linear boundary operator $\mathbf{A}_b(\mathbf{s}, D)$ generates analytic semigroup. The q-dimensional boundary control $\mathbf{v}(\mathbf{s}, t)$ belongs to the nonempty set of admissible control $\mathbf{V}_{ad}(\partial Q) \subset \mathbf{V}(\partial Q) = \mathbf{H}^0(T; \Sigma_{j=0}^{\gamma} H^{k-j-1/2}(\partial\Omega)_j)$. The matrix operator $\mathbf{b}(\mathbf{s})$ is a bounded mapping from $\mathbf{V}_{ad}(\partial Q)$ into $H^{\theta}(\partial Q)$ ($\theta = \theta_\gamma$) with continuous injection: $\psi \rightarrow \int_{\partial Q} \psi\, \mathbf{b}\, \mathbf{v}\, d\mathbf{s}\, dt$ is a continuous linear form $\psi \in H^0(\partial Q)$.

It is assumed that the system defined by equations (1)–(4) is well posed, i.e., the solution $\mathbf{y}$ depends continuously on initial and boundary data, and the control variables $\mathbf{u}$, $\mathbf{v}$ influence $\mathbf{y}$ continuously. In the sequel, conditions for boundedness of the output vector $\mathbf{z}$ with bounded input functions $\mathbf{u}$ and $\mathbf{v}$ are derived for a subclass of the general system via the concept of dissipativeness.

3 Dissipativeness of a System With Interior Control and Homogeneous Boundary Conditions

The notion of dissipativeness is used for the systems for which the supply rate (input power) and storage function (storage energy), defined in an abstract sense, can be found satisfying the condition that the energy is always dissipated (cf: Willems [11]). For a lumped parameter system, Hill and Moylan [8, 9] establish the relationship between dissipativeness and input-output stability. Moylan [12] employs passivity criteria to determine input-output stability. In the case of a distributed parameter system, the later concept may not be applicable, as the sign definiteness of the input energy (product of output and input functions over Q) cannot be determined readily. However, the concept of dissipativeness can be extended to certain classes of distributed parameter systems.

First, a system with homogeneous boundary conditions controlled by interior distributed controller alone is discussed. With $\mathbf{y} \in \mathbf{H}_0^k(Q)$, the system is governed by the equations (1) and (2), initial condition (3), and boundary condition:

$$\mathbf{A}_b(\mathbf{s},D)\mathbf{y}(\mathbf{s},t)=\mathbf{0};\quad D^j\mathbf{y}\in\mathbf{H}^{k-j-1/2}(\partial Q);$$

$$0\le j\le\gamma\le k-1. \tag{5}$$

To facilitate the analysis, certain assumptions are made:

1. The operators $\mathbf{A}(\mathbf{x}, D)$ and $\mathbf{C}(\mathbf{x})$ are symmetric or symmetrizable through appropriate transformation. By symmetrizability it is understood that there exists a symmetric matrix operator $\mathbf{I}$: $\mathfrak{D}(\mathbf{I}) \rightarrow \mathbf{R}(\mathbf{I})$ in $\mathbf{H}^0$ such that $\mathbf{I}\,\mathbf{A}$ is symmetric; $\mathfrak{D}(\mathbf{I}\,\mathbf{A}) = \mathfrak{D}(\mathbf{A}) \cap \mathbf{R}(\mathbf{I})$. The method to get $\mathbf{I}$ (integrating function/operator) is similar to that used for obtaining Greens function [13] for differential operators. Existence of a positive-definite symmetrizer for $\mathbf{C}$ is established by Taussky [14].

2. $\mathbf{A}(\mathbf{x}, D)$ can be split as $\mathbf{A}(\mathbf{x}, D) = \mathbf{L} + \mathbf{L}_0$ where $\mathbf{L}$ is a positive-definite operator in $\mathbf{H}^0$ and $\mathfrak{D}(\mathbf{L}_0) \subset \mathfrak{D}(\mathbf{L})$. Also $\mathbf{L}^{-1}\mathbf{L}_0$ is uniformly continuous in the energy space $\mathbf{H}^{\alpha}$; $2\alpha = k_1$, where k_1 is the order of $\mathbf{L}$.

3. The matrix operator Ψ_I defined by

$$\psi_I = \begin{vmatrix} \mathbf{P} & \mathbf{S} \\ \mathbf{S}' & \mathbf{R} \end{vmatrix} \tag{6}$$

is negative semidefinite, where $\mathbf{P}(\mathbf{x})$, $\mathbf{S}(\mathbf{x})$ and $\mathbf{R}(\mathbf{x})$ will be used later to define the supply rate.

4. The time derivative of stored energy density functional Λ_I, to be defined, exists and is unique along the trajectory given by equations (1)–(3), and (5).

5. The distributed parameter system is completely controllable [15, 16].

6. The distributed parameter system is observable [15].

7. $\mathbf{Y}_s(Q) \subset \mathbf{H}^k(Q)$ is the space spanned by $\mathbf{y}$ when $\mathbf{u}$ spans $\mathbf{U}_{ad}(Q)$: $\mathbf{Y}_s(Q) = L_2[T; \mathbf{Y}_s(\Omega)]$.

The "supply rate" to the distributed parameter system over the domain Ω can be written as:

$$W(t)=\int_\Omega(\mathbf{z}'\mathbf{P}\,\mathbf{z}+2\,\mathbf{z}'\mathbf{S}\,\mathbf{u}+\mathbf{u}'\mathbf{R}\,\mathbf{u})\,d\mathbf{x}=\int_\Omega W_I d\mathbf{x}, \tag{7}$$

where $\mathbf{P}(\mathbf{x})$, $\mathbf{S}(\mathbf{x})$, and $\mathbf{R}(\mathbf{x})$ are uniformly continuous smooth real valued functions having compact support in Ω, and $\mathbf{P}(\mathbf{x})$ and $\mathbf{R}(\mathbf{x})$ are symmetric and invertible. W_I is the supply rate density functional. To establish dissipativeness of a system, it is necessary that

$$W(t)\le 0 \qquad \text{for all } \mathbf{u}(\mathbf{x},t). \tag{8}$$

The useful energy that can be drawn from the system after time t_f is equal to the energy storable using minimal control effort, i.e.

$$\Lambda_I(\mathbf{y}) = -\underset{\mathbf{u}}{Inf}\int_0^{t_f} W\,dt. \tag{9}$$

The "stored energy density" functional can be written as

$$\tilde{\Lambda}_I = \underset{\mathbf{u}}{Inf}\, W_I. \tag{10}$$

The functional $\Lambda_I(.)$ is related to the nonzero initial state $\mathbf{y}_0(\mathbf{x})$. One can assume that the state $\mathbf{y}_0(\mathbf{x})$ is reached from $\mathbf{y}(\mathbf{x}, t_0) = 0$ defined at some previous time t_0, by employing the admissible control variables over the extended time domain. The "required supply" to achieve the initial state $\mathbf{y}_0$ is then defined by:

$$\Lambda_r = \underset{\mathbf{u}\in\mathbf{U}_{ad}(Q_0)}{Inf.}\int_{t_0}^{0}\int_\Omega W(\mathbf{x},t)\,d\mathbf{x}\,dt, Q_0=\Omega\chi[t_0,0] \tag{11}$$

It is the least amount of energy required to excite the system from the null state to the initial state $\mathbf{y}_0$. On the other hand, the available storage functional $\Lambda_I(.)$ is the maximum amount of energy that one can extract from the system, with $\mathbf{y}_0$ as the initial value of the state.

With these, the dissipativeness of the distributed parameter system can be defined as follows:

Definition: The distributed parameter system governed by equations (1)–(3) and (5) with the supply rate density functional $W_I(\mathbf{z}, \mathbf{u})$ is dissipative if for all $\mathbf{u} \in \mathbf{U}_{ad}(Q)$ and for all $t \le 0$, the following inequality holds:

$$\Lambda=\int_Q W_I(\mathbf{z},\mathbf{u})\,d\mathbf{x}\,dt\ge 0. \tag{12}$$

The integral is taken along the state trajectory. According to the curl condition in the multivariable calculus, the path integral is independent of the route chosen due to symmetry of Ψ_I.

Certain characteristics of dissipative systems are given by the following:

Lemma 1. For a dissipative system,

Downloaded 02 May 2010 to 171.66.16.54. Redistribution subject to ASME license or copyright; see http://www.asme.org/terms/Terms_Use.cfm

(*a*) $\Lambda_l < \infty$ for any state $\mathbf{y}(\mathbf{x},t_0)$ null controllable at t_0, and
(*b*) $\Lambda_r > -\infty$ for any state $\mathbf{y}(\mathbf{x},t)$ which is completely controllable.

Lemma 2. For a dissipative system,

(*a*) $\Lambda_l(0) = \Lambda_r(0) = 0$, and
(*b*) $\Lambda_l(\mathbf{y}_0) = \Lambda_r(\mathbf{y}_0)$ for any $\mathbf{y}_0(.) \epsilon \mathbf{Y}_s(\Omega), \mathbf{x} \epsilon \Omega$. (13)

Corollary: For a dissipative and completely controllable system,

$$0 \le \Lambda_l \le \Lambda_r < \infty \tag{14}$$

Proof: From the definition of controllability (which covers null controllability also), Lemma 1 can be proved with the understanding that a linear homogeneous system specified here require finite energy in finite time to steer it to the target. For Lemma 2, condition (*a*) is obvious, since no energy need to be supplied nor can be extracted from the system at the null state. For a dissipative system,

$$\int_{t_0}^{t_f}\int_\Omega W_l d\mathbf{x}\, dt \ge 0, \quad \text{or} \quad \int_{t_0}^{0}\int_\Omega W_l d\mathbf{x} dt + \int_0^{t_f}\int_\Omega W_l d\mathbf{x}\, dt \ge 0,$$

for all $\mathbf{u} \epsilon \mathbf{U}_{ad}(Q_1)$, $Q_1 = Q \cup Q_0$.
Therefore,

$$\underset{\mathbf{u} \epsilon \mathbf{U}_{ad}(Q_1)}{Inf}\left[\int_{t_0}^{0}\int_\Omega W_l d\mathbf{x}\, dt + \int_0^{t_f}\int_\Omega W_l d\mathbf{x} dt\right] \ge 0.$$

Using the definitions of Λ_r and Λ_l (equations (11) and (9)) in this inequality, condition (*b*) follows. Proof of the corollary is straightforward.

Let $\Lambda(.)$ be an arbitrary storage functional (need not be Λ_l or Λ_r) such that $\Lambda(.) = 0$ at $\mathbf{y} = \mathbf{0}$, i.e.,

$$\Lambda = \int_0^{t_f}\int_\Omega W_l d\mathbf{x}\, dt.$$

It denotes integral effect of storage over the domain Ω. Dissipativeness of the system requires that

$$\Lambda(\mathbf{y}_0) + \int_0^{t_f}\int_\Omega W_l d\mathbf{x}\, dt \ge \Lambda(\mathbf{y}(\mathbf{x},t_f)), \tag{15}$$

for all $t_f \ge 0$, and all $\mathbf{u} \epsilon \mathbf{U}_{ad}(Q)$. Thus, for a dissipative system having stored energy $\Lambda(\mathbf{y}_0)$, the remaining stored energy at a later instant t_f will be less at least by the energy extracted during the interval $[0, t_f]$. This leads to the following Theorem.

Theorem 1. The distributed parameter system is dissipative, if **f** there exists a storage functional $\Lambda(\mathbf{y})$ such that

$$0 \le \Lambda(\mathbf{y}) < \infty \quad \text{for all } \mathbf{u} \epsilon \mathbf{U}_{ad}(Q). \tag{16}$$

Proof: Since Λ_r and Λ_l are also storage functionals, they satisfy (16) by virtue of the Corollary (14). To prove the converse, let $\Lambda(\mathbf{y})$ exist. Then from (15)

$$\Lambda(\mathbf{y}_0) + \int_Q W_l d\mathbf{x}\, dt \ge \Lambda(\mathbf{y}(\mathbf{x},t_f).). \tag{17}$$

Setting $\mathbf{y}_0 = \mathbf{0}$ and observing that the required storage at t_f (i.e., $\Lambda(\mathbf{y}(\mathbf{x}, t_f))$ is positive-semidefinite, it follows that $\int_Q W_l\, d\mathbf{x} dt \ge 0$. Thus the system is dissipative.

The following theorem limits the range of possible storage functionals.

Theorem 2. If Λ is an arbitrary storage functional for a dissipative system, it satisfies the following inequality:

$$0 \le \Lambda_l < \Lambda < \Lambda_r < \infty \quad \text{for all } \mathbf{y} \epsilon \mathbf{Y}_s(Q_1), t \epsilon [t_0, t_f]. \tag{18}$$

Proof: Let the system be completely controllable. From equation (15)

$$\int_{t_0}^{t_1}\int_\Omega W_l d\mathbf{x}\, dt \ge \Lambda(\mathbf{y}(\mathbf{x},t_1)), t_1 \epsilon [t_0, t_f]$$

for all $\mathbf{y}(., t_1) \epsilon \mathbf{Y}_s(\Omega)$ (hence true for all $\mathbf{u} \epsilon \mathbf{U}_{ad}$). Then

$$\underset{\mathbf{u} \epsilon \mathbf{U}_{ad}(Q_1)}{Inf}\int_{t_0}^{t_1}\int_\Omega W_l d\mathbf{x}\, dt = \Lambda_r(\mathbf{y}(t_1)) \ge \Lambda(\mathbf{y}(t_1)),$$

where $\Lambda_r(\mathbf{y}(t_1))$ is the required supply to achieve $\mathbf{y}(\mathbf{x}, t_1)$ from the null state. This is true for all $t_1 \epsilon [0, t_f]$, resulting in the upper bound. To prove the lower bound, only complete null controllability is required, that is, for any $t = t_1$, $t_1 \epsilon [0, t_f]$, one should be able to reach $\mathbf{y}(\mathbf{x}, t_f) = 0$. Then from equation (15),

$$\Lambda(y(t_1)) \ge -\int_{t_1}^{t_f}\int_\Omega W_l d\mathbf{x}\, dt \ge \Lambda_l(\mathbf{y}(t_1)), \quad \text{for all } t_1 \epsilon [0, t_f].$$

Theorem 2 is important, permitting one to use any arbitrary positive-semidefinite functionals over the domain Ω, similar to the supply rate functional, as a storage functional, as long as it satisfies the inequality (18). Then the dissipativeness can be defined via $\Lambda(\mathbf{y})$.

The preceding analysis of the dissipativeness is based on the input-output relations. In the present case, along with input-output description, the state space description is also known. As such, it is desirable to study the dissipativeness based on state space and input-output relations equations (1, 2). The following theorem can be stated.

Theorem 3. The necessary and sufficient conditions for the distributed parameter system described by (1)–(3) and (5) to be dissipative with respect to the supply rate $W(t)$ are:

$$\Lambda_l \text{ is positive-definite; } \Lambda_l(\mathbf{0}) = 0 \tag{19}$$

$$(\nabla_y \tilde{\Lambda}_l(\mathbf{y}))' A y = -l'(\mathbf{y}) l(\mathbf{y}) + \mathbf{y}' \mathbf{P}_l \mathbf{y} \tag{20}$$

$$1/2\, \mathbf{B}'(\nabla_y \tilde{\Lambda}_l(\mathbf{y})) = \mathbf{S}_l' \mathbf{y} - (\mathbf{G}(\mathbf{y}))' l \tag{21}$$

$$\mathbf{R}_l = \mathbf{G}'\mathbf{G} \tag{22}$$

where

$$\mathbf{P}_l = \mathbf{C}'\mathbf{P}\,\mathbf{C}, \quad \mathbf{S}_l = \mathbf{C}'(\mathbf{P}\,\mathbf{E} + \mathbf{S}),$$
$$\mathbf{R}_l = \mathbf{R} + \mathbf{E}'\mathbf{S} + \mathbf{S}'\mathbf{E} + \mathbf{E}'\mathbf{P}\,\mathbf{E} \tag{23}$$

and ∇_y is a functional gradient operator with respect to $\mathbf{y} \epsilon \mathbf{H}_0^k(Q)$.

If some l and $\mathbf{G}$ can be found such that these conditions are satisfied, the system is said to be dissipative.

Proof: The theorem can be proved on the same lines as in the case of lumped parameter systems [8]. Extension to the distributed parameter system is made possible by the use of Kalman-Yakubovitch lemma [17].

For sufficiency of the conditions (19)–(22) define the total supply as

$$\Lambda = \int_Q (\mathbf{z}'\mathbf{P}\,\mathbf{z} + 2\,\mathbf{z}'\mathbf{S}\,\mathbf{u} + \mathbf{u}\,\mathbf{R}\,\mathbf{u})\, d\mathbf{x}\, dt. \tag{24}$$

Using equation (1) and equations (20)–(22), and simplifying,

$$\Lambda = \int_Q [(\nabla_y \tilde{\Lambda}_l)'(\mathbf{A}\,\mathbf{y} + \mathbf{B}\,\mathbf{u}) + l'l + 2l'\mathbf{G}\mathbf{u} + \mathbf{u}'\mathbf{G}'\mathbf{G}\,\mathbf{u}] d\mathbf{x}\, dt.$$

Employing (1) and the generalized Green's theorem, one gets

$$\Lambda = \int_Q [\partial\, \tilde{\Lambda}_l/\partial\, t + (l + \mathbf{G}\,\mathbf{u})'(l + \mathbf{G}\,\mathbf{u}) d\mathbf{x}\, dt$$

$$= \Lambda_l|_{t=t_f} + \int_Q (l + \mathbf{G}\,\mathbf{u})'(l + \mathbf{G}\,\mathbf{u}) d\mathbf{x}\, dt. \tag{25}$$

From (19) $\Lambda_l|_{t=t_f}$ is positive-definite. The second term being quadratic is also positive-definite. Therefore Λ is positive-definite and the system is dissipative.

Downloaded 02 May 2010 to 171.66.16.54. Redistribution subject to ASME license or copyright; see http://www.asme.org/terms/Terms_Use.cfm

To prove the necessity, it is assumed that the state vector $\mathbf{y} \in \mathbf{H}_0^k(Q)$ is steady state holdable by $\mathbf{w}(\mathbf{x})$, where $\mathbf{w} \in \mathbf{U}_{ad}(\Omega)$ is an interior distributed control function of the steady state equation corresponding to equations (1)–(3) and (5) for which a solution exists in a weak sense. With this and Assumption 5, one can apply the maximum principle to equations (12) and (9) to get

$$\partial \tilde{\Lambda}_I / \partial t \leq W_I(\mathbf{z},u). \tag{26}$$

Introduction of a slack variable (or dissipative function) 'd'

$$d(\mathbf{y},\mathbf{u}) = (I + \mathbf{G}\,\mathbf{u})'(I + \mathbf{G}\,\mathbf{u})$$

into equation (26) yields,

$W_I - \partial \tilde{\Lambda}_I / \partial t = d(\mathbf{y},\mathbf{u})$, or

$$\mathbf{z}'\mathbf{P}\,\mathbf{z} + 2\mathbf{z}'\mathbf{S}\,\mathbf{u} + \mathbf{u}'\mathbf{R}\,\mathbf{u} - (\nabla_y \tilde{\Lambda}_I)\mathbf{y}_t = (I + \mathbf{G}\,\mathbf{u})'(I + \mathbf{G}\,\mathbf{u}).$$

Using Green's formula and equation (2) and equating the powers of $\mathbf{u}$, one gets (20)–(22) for dissipativeness.

4 Relation Between Dissipativeness and Stability

The state equation (1) can be posed in a weak sense as

$$<\partial \mathbf{y}/\partial\, t, \xi> = <\mathbf{A}\,\mathbf{y}, \xi> + <\mathbf{B}\,\mathbf{u}, \xi>, \quad \text{for all } \xi \in \mathbf{H}_0^k(Q).$$

From the assumptions made earlier it can be shown that the operator $\mathbf{A}(\mathbf{x}, D)$ is one-to-one and bounded. Also a bounded inverse of $\mathbf{A}(\mathbf{x}, D)$ exists. This follows from either closed graph theorem or spectral theory (a regular point of $\mathbf{A}(\mathbf{x}, D)$ lies in the resolvant set of $\mathbf{A}$) [18]. $\mathbf{B}(\mathbf{x}, t)$, $C(x)$, and $\mathbf{E}(\mathbf{x})$ have been assumed to be bounded linear mappings. By choosing $\xi(\mathbf{x}, t) = \mathbf{y}(\mathbf{x}, t)$, it is noted that for a dissipative system the following inequality holds (cf. Lions [19] and Willems [20]).

$$\|\mathbf{y}(\mathbf{x},t_f)\|_{L_2(\Omega)} + \int_0^{t_f} <\mathbf{A}\,\mathbf{y},\mathbf{y}>_{L_2(\Omega)} dt \leq M[\|\mathbf{B}\,\mathbf{u}\|^2_{L_2(Q)} + \|\mathbf{y}_0\|^2_{L_2(\Omega)}]$$

where M is a finite positive constant. Hence for a bounded input $\mathbf{u}$ and bounded initial condition, the state remains bounded at any arbitrary time t_f. If Γ is a bounded map from input $\mathbf{u} \in \mathbf{U}_{ad}(Q)$ to $\mathbf{z} \in Z_0(Q)$ and if graph of Γ is closed, then according to the closed graph theorem, the output vector $\mathbf{z}$ is bounded in L_2-norm. This leads to the following Lemmas.

Lemma 4. If a linear distributed parameter system (equations (1)–(3)) with homogeneous boundary condition (5) is dissipative with respect to the supply rate $W(t)$ (7) and if the spectrum of $\mathbf{A}(\mathbf{x}, D)$ does not contain any null elements and $\mathbf{P}_I$ is negative-semidefinite, the system is bounded input bounded output (BIBO) stable.

Lemma 5. If a linear-distributed parameter system (1) with homogeneous boundary conditions (5) is dissipative with respect to $W(t)$ and if $\mathbf{P}_I$ is a negative-definite symmetric matrix, the system $\mathbf{y}_t = \mathbf{A}\,\mathbf{y}$ is asymptotically stable.

Lemma 6. If a linear-distributed parameter system with homogeneous boundary condition is asymptotically stable, then it is BIBO stable also. Under the assumptions, made earlier, the converse is also true.

These Lemmas are not hard to prove. Lemma 4 follows from the discussions preceding it. Lemma 5 can be proved by either Liapunov theorem or semigroup theory. Lemma 6 is easy to prove, if one uses the property that for a linear homogeneous distributed parameter system, under suitable conditions, $\mathbf{A}(\mathbf{x}, D)$ can be treated as infinitesimal generator of semigroups, and the Liapunov theorem can be redefined in terms of these semigroups. [21, Chapter 5]. Then using the procedure by Brogan [22] it can be shown that the system is BIBO stable. If the system is BIBO stable, then $\|\mathbf{z}\| \leq \alpha \|\mathbf{u}\|$ where $\|.\|$ is taken in L_2-sense, for simplicity. Then it follows that

$$\|z\|^2 \leq \alpha^2 \|\mathbf{u}\|^2 \quad \text{or} \quad [\mathbf{z},\mathbf{u}] \begin{vmatrix} -I & 0 \\ 0 & \alpha^2 I \end{vmatrix} \begin{vmatrix} \mathbf{z} \\ \mathbf{u} \end{vmatrix} \geq 0, I = \text{identity}.$$

Thus $\mathbf{P}_I = -\mathbf{I}$, and the system is asymptotically stable from Lemma 5.

5 Extension to Systems with Hybrid Distributed Control

Extension of the theorem and Lemmas derived in the foregoing to the general case of a linear distributed parameter system with arbitrary boundary conditions employing hybrid (interior and boundary) distributed controller is not easy. The supply rate for this problem can be written as

$$W(t) = \int_\Omega (\mathbf{z}'\mathbf{P}\,\mathbf{z} + 2\,\mathbf{z}'\mathbf{S}\,\mathbf{u} + \mathbf{u}'\mathbf{R}\,\mathbf{u})\,d\mathbf{x} + \int_{\partial\Omega} (\mathbf{y}'(s,t)\mathbf{p}\,\mathbf{y}'(s,t) + 2\,\mathbf{y}'(\mathbf{s},t)\mathbf{s}_0\mathbf{v} + \mathbf{v}'\mathbf{r}\,\mathbf{v})\,d\mathbf{s} = \int_\Omega W_I d\mathbf{x} + \int_{\partial\Omega} W_b d\mathbf{s} \tag{27}$$

To establish dissipativeness, it is required to find the change in the supply rate with time. This in turn demands an a priori knowledge of $\mathbf{y}_t(\mathbf{x}, t)$ and $\mathbf{y}_t(\mathbf{s}, t)$. The former is available from the state equation (1). However, $\mathbf{y}_t(\mathbf{s}, t)$ cannot be defined as it requires $(k+1)$th order of smoothness of $\mathbf{y}(\mathbf{x}, t)$ in Ω for using the trace theorem. Hence dissipativeness of a general nonhomogeneous distributed parameter system remains an open problem.

For a restricted class of nonhomogeneous problems, it is possible to apply the earlier analysis by homogenizing the boundary data through an appropriate transformation.

Consider a general distributed parameter system controlled by the hybrid-distributed controller (equations (1)–(4)). Define a pseudo state vector $\eta \in \mathbf{H}_0^k(Q)$ such that

$$\mathbf{A}_b(\mathbf{s},D)\,\eta(\mathbf{s},t) = 0 \qquad \text{on} \quad \partial Q. \tag{28}$$

Then $\mathbf{y}(\mathbf{x}, t)$ is an extension of the function $\eta(\mathbf{x}, t)$ on $\bar{Q}$, where

$$\mathbf{y}(\mathbf{x},t) = \eta(\mathbf{x},t) + \mathbf{g}(\mathbf{x},t); \mathbf{g},\mathbf{y} \in \mathbf{H}^k(Q), \eta \in \mathbf{H}_0^k(Q) \tag{29}$$

Substituting (29) in the boundary condition (4), one gets

$$\mathbf{A}_b(\mathbf{s},D)\,\mathbf{g}(\mathbf{s},t) = \mathbf{b}(\mathbf{s},t)\,\mathbf{v}(\mathbf{s},t) \tag{30}$$

Consider a domain $\mathfrak{D}(\mathbf{A}_b) \in \mathbf{H}^\theta(\partial Q)$. This is a Hilbert space $\mathbf{H}_A^{k-1}(\tilde{Q})$ where $\tilde{Q} = \tilde{\Omega}\,X\,T$ and $\tilde{\Omega}$ is a $(m-1)$ dimensional Euclidean domain. $\mathbf{A}_b(\mathbf{s}, D)$ is an autonomous spatial differential operator of the order at most $(k-1)$ defined on $\tilde{Q}$. The boundary condition for equation (30) can be obtained from the compatibility conditions between the initial and boundary data defined on $\tilde{\Omega}$. Thus

$$\mathbf{B}\,\mathbf{y}(\mathbf{s},t) = \mathbf{A}_b(\mathbf{s},D)\,\mathbf{y}_0(s), \tag{31}$$

where $\mathbf{B}$ is the boundary differential operator determined using Cauchy-Kowalovskaya theorem.

If $\mathbf{A}_b(\mathbf{s}, D)$ is a closed convex, symmetrizable, positive-definite bounded below operator with a bounded inverse, a solution to equation (30) exists, and it is possible to homogenize the problem using the pseudo state vector $\eta(\mathbf{x}, t)$. It may also be noted that if $A_b(\mathbf{s}, D)$ is self-adjoint, positive-definite, then the solution to equation (30) is unique.

For the system satisfying the preceding conditions, one gets a nonhomogeneous differential equations in $\eta(\mathbf{x}, t)$ with homogeneous boundary conditions. To this system, the theorem derived in Sections 3 and 4 for dissipativeness, and the stability analysis are applicable.

Downloaded 02 May 2010 to 171.66.16.54. Redistribution subject to ASME license or copyright; see http://www.asme.org/terms/Terms_Use.cfm

6 Illustration

Control of a Vibrating String. Consider planar vibration of a string under an interior distributed control. It is governed by

$$\rho\, w_{tt}(x,t) + \rho\, a_1 w_t(x,t) + \rho\, a_0 w(x,t) + EID^2 w(x,t) = u(x,t); (x,t) \in Q, \tag{32}$$

with initial and homogeneous boundary conditions

$$w(x,0) = w_0(x), w_t(x,0) = w_1(x), x \in (0,1);$$

$$w(0,t) = w(1,t) = 0, \tag{33}$$

where $Q = (0, 1) \chi [0, t_f]$; the final time t_f is fixed; $w \in H^2(Q)$; and $u \in U_{ad}(Q) \subset H^0(Q)$. The terms $a_1 w_t$ and $a_0 w$ represent linear damping and restoring forces, respectively. Equation (32) can be written as

$$\mathbf{y}_t = \mathbf{A}\,\mathbf{y} + \mathbf{B}\,u \tag{34}$$

where

$$\mathbf{A} = \begin{vmatrix} 0 & 1 \\ -a^2 D^2 - a_0 & -a_1 \end{vmatrix}, \quad \mathbf{B} = \begin{vmatrix} 0 \\ 1/\rho \end{vmatrix}, \quad \mathbf{y} = \begin{vmatrix} y \\ y_t \end{vmatrix} = \begin{vmatrix} w \\ w_t \end{vmatrix}, \quad a^2 = \frac{EI}{\rho}$$

The output state can be expressed as

$$z(x,t) = \alpha\, y_1(x,t) + \beta\, y_2(x,t) \tag{35}$$

The terms P, S, and R in the supply rate (equation (33)) are selected as $P = -1$, $S = 1$, $R = c^2$ (such a system is called finite gain system [8]). Assumption 3 requires that $c \geq 1$. From Theorem 3 (equations (22), (21), and (20)) one gets the conditions for dissipativeness as

$$a_0 - \pi^2 a^2 - 1/2\, a_1 \leq \alpha < 0, \quad \beta \geq 0, \quad \alpha \geq -\beta^2, \tag{36}$$

with the arbitrary functions G and l given by

$$G = c, \quad l = \beta(a_1 y_2 - a_0 y_1) + \alpha\, y_2/c. \tag{37}$$

The corresponding storage density function is

$$\tilde{\Lambda} = |\alpha|\rho(a_0 y_1^2 + y_2^2 + a^2 (D y_1)^2 + \beta(a_1 y_2^2 - a_0 y_1 y_2) \tag{38}$$

For the dissipative dynamical system satisfying condition (36) one can check that $\tilde{\Lambda}$ is positive-definite and the system is asymptotically stable. For the system satisfying $\alpha \geq -\beta^2$, with negative definite P_I, the system is input-output stable.

7 Conclusion

The concept of dissipativeness and its relationship with input-output stability is extended to a class of distributed parameter systems. The homogeneous boundary value problem in presence of an interior distributed control is analyzed without much difficulty. However, the general nonhomogeneous boundary value problem employing interior and boundary control remains unsolved. It is shown that under certain conditions it may be possible to homogenize the boundary value problem and apply the earlier results. Finally, a simple illustration of vibrating string with interior control demonstrates the approach.

In analyzing the dissipativeness one also gets a quadratic functional which can be used as a Liapunov functional. This is valuable because it is generally not easy to find a Liapunov functional for a distributed parameter input-output system. The present analysis, therefore, helps in analyzing both the internal and external stability of the system.

Linear systems of arbitrary order and type are considered here with certain realistic assumptions. Hence the analysis is applicable to a wide range of physical systems.

References

1 Zames, G., "On the Input-Output Stability of Time-Varying Nonlinear Feedback Systems, Part I and II," *IEEE Trans. Auto. Control*, Vol. *AC*-11, 1966, pp. 228–238; 465–476.

2 Chen, C. F., and Tsay, Y. T., "A General Frequency Stability Criterion for Multi-Input Multi-Output Lumped and Distributed Parameter Systems," *Int. J. Control*, Vol. 23, 1976, pp. 341–359.

3 Desoer, C. A., and Wang, Y.-T., "On the Generalized Nyquist Stability Criterion," *IEEE Trans. Auto. Control*, Vol. AC-25, 1980, pp. 187–196.

4 Willems, J. C., "The Generation of Liapunov Functions for Input-Output Stable Systems," *SIAM J. Control*, Vol. 9, 1971, pp. 105–134.

5 Wang, P. K. C., "Stability for a Mixed Distributed and Lumped Parameter Control Systems," *Int. J. Control*, Vol. 6, 1967, pp. 65–73.

6 Cook, P. A., "Circle Criteria for Stability in Hilbert Spaces," *SIAM J. Control*, Vol. 13, 1975, pp. 593–610.

7 Jamarie, G., "A Practical Criterion for the Input-Output Stability of Distributed Parameter Systems," With Space Dependent Coefficients," *Int. J. Control*, Vol. 21, 1975, pp. 285–292.

8 Hill, D., and Moylan, P. J., "The Stability of Nonlinear Dissipative Systems," *IEEE Trans. Auto. Control*, Vol. AC-21, 1976, pp. 708–711.

9 Hill, D., and Moylan, P. J., "Dissipative Dynamical Systems: Basic Input-Output and State Properties," *J. of the Franklin Institute*, Vol. 309, 1980, pp. 327–357.

10 Bhat, M. Seetharama, "Stability and Control of Distributed Parameter Systems," Ph.D. thesis, Indian Institute of Science, Bangalore, India, 1982.

11 Willems, J. C., "Dissipative Dynamical Systems, Part I: General Theory, Part II: Linear Systems With Quadratic Supply Rate," *Archive for Rational Mechanics and Analysis*, Vol. 45, 1972, pp. 321–393.

12 Moylan, P. J., "Implications of Passivity in a Class of Nonlinear Systems," *IEEE Trans. Auto. Control*, Vol. *AC*-19, 1974, pp. 373–381.

13 Carrier, G. F., and Pearson, C. E., *Partial Differential Equations*, Academic Press, New York, 1976, Chapter 9.

14 Taussky, O., "Positive Definite Matrices and Their Role in the Study of Characteristic Root of General Matrices," *Advances in Mathematics*, Vol. 2, 1968, pp. 175–186.

15 Wang, P. K. C., "Control of Distributed Parameter Systems," *Advances in Control Systems, Theory and Applications*, Leondes, C. T., Ed., Academic Press, New York, Vol. 1, 1964, pp. 75–172.

16 Russell, D. L., "Controllability and Stabilizability Theory for Linear Partial Differential Equations: Recent Progress and Open Questions," *SIAM Review*, Vol. 20, 1978, pp. 639–739.

17 Lefschetz, S., *Stability of Nonlinear Control Systems*, Academic Press, New York, 1965, pp. 114–118.

18 Kryszig, E., *Introductory Functional Analysis With Applications*, Wiley, New York, 1978.

19 Lions, J. L., *Equations Differentielles Operationnels et Probleme Aux Limits*, Springer-Verlag, Berlin, 1961.

20 Willems, J. C., "Survey of Stability of Distributed, Parameter Systems, Control of Distributed Parameter Systems," *Joint Automatic Control Conference*, 1969, Boulder, Colo., 1969, pp. 63–102.

21 Buis, G. R., Vogt, W. G., and Eisen, M. M., "Liapunov Stability for Partial Differential Equations, *NASA CR*-1100, 1968.

22 Brogan, W. L., *Modern Control Theory*, Quantum, New York, 1974, Chapter 14.

23 Adams, R. A., *Sobolev Spaces*, Academic Press, New York, 1975.

24 Lions, J. L., and Magenes, E., *Nonhomogeneous Boundary Value Problems and Applications*, Vol. II, Springer-Verlag, Berlin, 1972, Chapter 4.

APPENDIX

All the spaces are defined on a real field. Ω is an open-bounded subset of the Euclidean space R^m with Lipschitz boundary $\partial\Omega$. The vectors $\mathbf{x}$ and $\mathbf{s}$ denote variable points in Ω and $\partial\Omega$, respectively. The time variable $t \in T = [0, t_f]$, $t_f \leq \infty$, where t_f is the final time. $Q = \Omega \chi T$, $\partial Q = \partial\Omega \chi T$ and $\bar{Q} = \bar{\Omega} \chi T$ define the product spaces.

The Sobolev space $W^{k,2}(\Omega)$ is the space of functions in $L_2(\Omega)$ with partial derivatives of the order less than or equal to k in $L_2(\Omega)$. This is a Hilbert space with usual L_2-norm in the variable up to order k, inclusive [23]. To deal with an n-dimensional vector-valued function with its components on space $H^k(\Omega)_i$, $(i = 1, 2, \ldots, n)$, a product space is defined as $\mathbf{H}^k(\Omega) \triangleq \Sigma_{i=1}^n (H^k(\Omega)_i)$ with the inner product

$$<\mathbf{a},\mathbf{b}> = \sum_{i=1}^{n} <a_i, b_i>_{H^k(\Omega)_i}, \mathbf{a},\mathbf{b} \in \mathbf{H}^k(\Omega).$$

The product space on the domain $\partial\Omega$ can be written in a similar manner.

Downloaded 02 May 2010 to 171.66.16.54. Redistribution subject to ASME license or copyright; see http://www.asme.org/terms/Terms_Use.cfm

Generally, the definition of such product spaces on Q and ∂Q is not simple. The state vector $\mathbf{y}(\mathbf{x}, t)$ having continuous spatial derivative up to kth order may be treated as an element of the space of functions $\mathbf{H}^k(Q)$,

$$\mathbf{H}^k(Q) = \mathbf{H}^0(T;\mathbf{H}^k(\Omega)) = \left\{ \mathbf{y}(\mathbf{x},t); T \to \mathbf{H}^k(\Omega) \,\middle|\, \|\mathbf{y}\|_{\mathbf{H}^k(Q)} = \left(\int_0^{t_f} \|\mathbf{y}(t)\|^2_{\mathbf{H}^k(\Omega)} dt \right)^{1/2}, T = [0, t_f], t_f < \infty \right\} \quad (39)$$

$$\mathbf{L}_2(Q) = \mathbf{H}^0(Q) = \left\{ \boldsymbol{\phi}(\mathbf{x},t): T \to L_2(\Omega) \,\middle|\, \|\boldsymbol{\phi}\|_{L_2(T;L_2(\Omega))} = \left(\int_0^{t_f} \|\boldsymbol{\phi}(t)\|^2_{\mathbf{L}_2(\Omega)} dt \right)^{1/2}; \quad T = [0, t_f], t_f < \infty \right\} \quad (40)$$

If $\mathbf{y}(\mathbf{s}, t)$ and its normal derivatives of order at most k-1 on the boundary $\partial\Omega$ are zero, then $\mathbf{y} \in \mathbf{H}_0^k(Q)$. ($\mathbf{H}_0^k(Q)$ is the space of functions having compact support in Q). The space of functions defined on ∂Q requires Sobolev space (Hilbert space $\mathbf{H}^\theta(\partial Q)$, with L_2-norm) of nonintegral and even nonpositive order (Adams [23, Chapter 7]). The fractional-order Sobolev spaces in Ω can be constructed directly in terms of Fourier transform of tempered distributions. For $j < \theta < j+1$, $H^\theta(\Omega)$ can be defined using interpolation method as a space between $H^j(\Omega)$ and $H^{j+1}(\Omega)$. Noting that $H^\theta(\Omega)$ is of local type (Lions and Magenes [24, p. 31]), $H^\theta(\partial\Omega)$ can be written in terms of local coordinates. Similarly $H^\theta(\partial\Omega)$ can be constructed. If $\mathbf{y} \in \mathbf{H}^k(Q)$, then $\mathbf{y} \in \mathbf{H}^{k-1/2}(\partial Q)$, $(\mathbf{s}, t) \in \partial Q$, $D^j\mathbf{y} \in H^{k-j-1/2}(\partial Q)$, $\theta_j = k-j-1/2$ [24]. Using the trace theorem, $\mathbf{y}(\mathbf{s}, t)$ can be obtained from the given $\mathbf{y}(\mathbf{x}, t)$. The norm in space X, i.e., $H^\theta(\partial\Omega)$, $H^\theta(\partial Q)$, etc. are written as $\|.\|_X$.

Downloaded 02 May 2010 to 171.66.16.54. Redistribution subject to ASME license or copyright; see http://www.asme.org/terms/Terms_Use.cfm

Journal of Applied Mechanics

Brief Notes

A Brief Note is a short paper that presents a specific solution of technical interest in mechanics but which does not necessarily contain new general methods or results. A Brief Note should not exceed 1500 words *or equivalent* (a typical one-column figure or table is equivalent to 250 words; a one line equation to 30 words). Brief Notes will be subject to the usual review procedures prior to publication. After approval such Notes will be published as soon as possible. The Notes should be submitted to the Technical Editor of the JOURNAL OF APPLIED MECHANICS. Discussions on the Brief Notes should be addressed to the Editorial Department, ASME, United Engineering Center, 345 East 47th Street, New York, N. Y. 10017, or to the Technical Editor of the JOURNAL OF APPLIED MECHANICS. Discussions on Brief Notes appearing in this issue will be accepted until two months after publication. Readers who need more time to prepare a Discussion should request an extension of the deadline from the Editorial Department.

Influence of Fiber Inertia on the Stress Intensity Around a Subsurface Elastic Fiber

R. L. Ryan[1] and S. Mall[2]

Introduction

In a recent study [1] we determined the stress intensity at the ends of a subsurface elastic fiber produced by the interaction of longitudinal waves with the fiber. In that study the inertia of the fiber was considered negligible compared to that of the matrix. Here, the analysis of reference [1] is modified to include the inertia of the fiber. It is shown that the effect of fiber inertia is to produce high magnifications in the stress intensity at certain (resonant) frequencies.

Analysis

The geometry of the fiber with elastic modulus E^* and density ρ^* is shown in Fig. 1. In reference [1] it was shown that if the fiber is subjected to an input wave of the form

$$u_0 = 2ik_L\phi_0 \cos k_L x e^{-i\omega t}, v_0 = 0 \tag{1}$$

where ϕ_0 is a constant and k_L is the longitudinal wave number, then the normalized shear stress along the fiber $\tau(x)$ is related to the horizontal component u of the scattered field by a C.P.V. integral of the form

$$\left(\frac{\partial u}{\partial x}\right)_{y=0} = 2/\pi \int_\epsilon^1 \tau(s)[P_1(s,x;k_L) + P_2(s,x;k_L)]ds, \epsilon < x < 1, \tag{2}$$

where the kernels $P_{1,2}$ are given by equations (6) and (7) of [1]. Furthermore, $\tau(x)$ satisfies the equilibrium conditions

$$\frac{\partial u^*}{\partial x} = -\beta \int_\epsilon^x \tau(s)ds, \epsilon < x < 1 \tag{3}$$

and

$$\int_\epsilon^1 \tau(s)ds = 0, \tag{4}$$

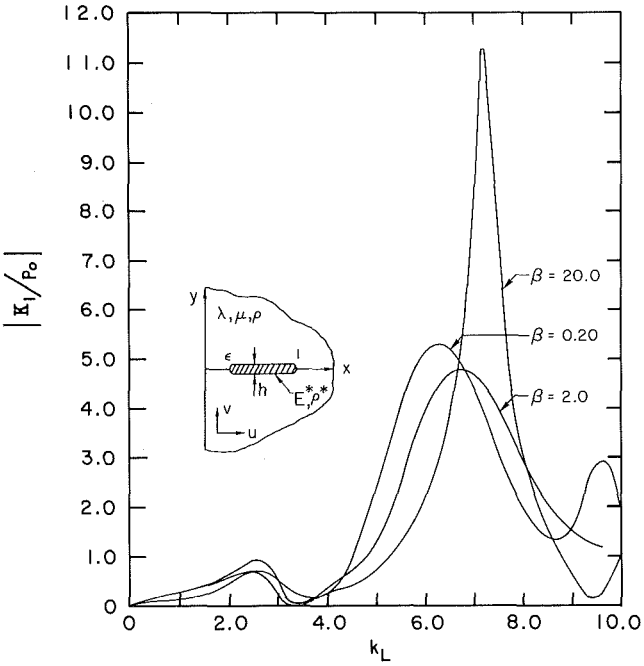


Fig. 1 Stress intensity $|K_1/p_0|$ versus wave number k_L, $\epsilon = 0$, $p_0 = \mu k_L{}^2\phi_0$

where

$$u^* = u + u_0 \tag{5}$$

is the horizontal displacement of the fiber and $\beta = 2\mu/E^*h$.

To account for the inertia of the fiber we replace equations (3) and (4) by

$$\frac{\partial u^*}{\partial x} = -\beta Q(x) + \beta Q(1)\sin[ck_L(x-\epsilon)]/\sin[ck_L(1-\epsilon)] \tag{6}$$

$$\int_\epsilon^1 \tau(s)ds = -(1-\epsilon)u^*[(1+\epsilon)/2]c^2k_L^2/\beta, \tag{7}$$

where $c = \sqrt{(\lambda+2\mu)\rho^*/E^*\rho}$ and

$$Q(x) = \int_\epsilon^x \tau(s)\sin[ck_L(s-x)]ds. \tag{8}$$

[1] Department of Mechanical Engineering, University of Maine, Orono, Me 04469.
[2] Department of Engineering Mechanics, University of Missouri, Rolla, MO.65401.

Manuscript received by ASME Applied Mechanics Division, May, 1984; final revision october, 1984.

Copyright © 1985 by ASME
Downloaded 02 May 2010 to 171.66.16.54. Redistribution subject to ASME license or copyright; see http://www.asme.org/terms/Terms_Use.cfm

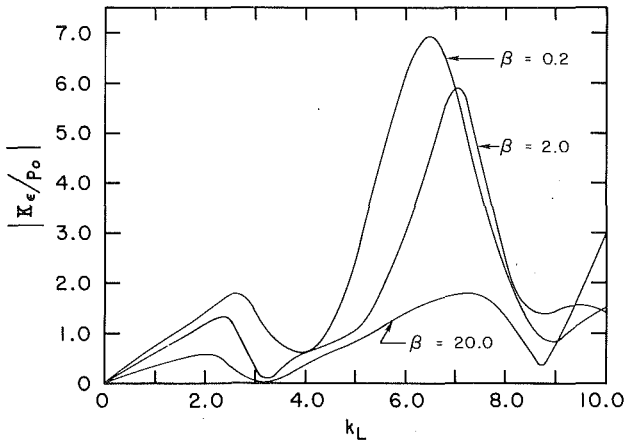


Fig. 2 Stress intensity $|K_\epsilon/p_0|$ versus wave number k_L, $\epsilon = 0.1$

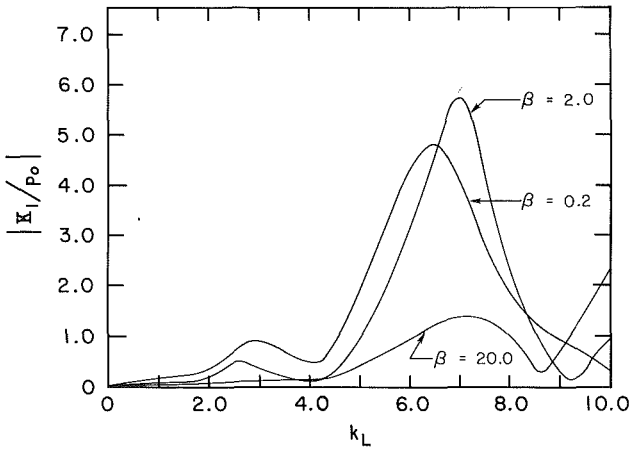


Fig. 3 Stress intensity $|K_1/p_0|$ versus wave number k_L, $\epsilon = 0.1$

Equation (6) follows from the solution of the equation of fiber motion

$$\frac{\partial^2 u^*}{\partial x^2} + c^2 k_L^2 u^* = -\beta\tau(x), \epsilon < x < 1,$$

which satisfies the condition of no axial force transfer from the fiber to the matrix, i.e., $\partial u^*/\partial x = 0$ at $x = \epsilon$ and $x = 1$. (For a verification of this condition see reference [2].) Next, combining (6) and (7) with (5) and (2) yields

$$-\frac{\partial u_0}{\partial x} = 2/\pi \int_\epsilon^1 \tau(s)\{P_1(s,x;k_L) + P_2(s,x;k_L) + \beta P_3(s,x,ck_L)\}ds, \epsilon < x < 1 \quad (9)$$

$$\int_\epsilon^1 \tau(s)[1 + (1-\epsilon)ck_L R(s;ck_L)]ds = 0, \quad (10)$$

where

$$P_3(s,x,ck_L) = \cos[ck_L(s-x)]H(x-s) - \sin[ck_L(x-\epsilon)]\cos[ck_L(1-s)]/\sin[ck_L(1-\epsilon)], \quad (11)$$

$$R(s;ck_L) = \sin[ck_L(2s-1-\epsilon)/2]H(1+\epsilon-2s) - \cos[ck_L(1-s)]/2\sin[ck_L(1-\epsilon)/2], \quad (12)$$

and $H(\bullet)$ is the unit step function.

Equations (9) and (10) may be solved by the Lobatto-Chebyshev technique as described in [1]; from the solution the stress intensities at the ends of the fiber $x = (\epsilon, 1)$ may be computed from the formula

$$(K_\epsilon, K_1) = \pm\sqrt{2(1-\epsilon)}i\mu k_L^2 \phi_0(\mp 1 + \nu/2)h(\mp 1). \quad (13)$$

In (13) $\nu = 2(1+\epsilon)/(1-\epsilon)$, and $h(\mp 1)$ are the end point values of a function $h(t)$ related to $\tau(s)$ through the transformations

$$h(t) = f(s), -2\pi i k_L^2 \phi_0 sf(s) = \sqrt{(s-\epsilon)(1-s)}\,\tau(s), 2s = (1-\epsilon)t + 1 + \epsilon. \quad (14)$$

It is noted that for the case of a surface-broaching fiber ($\epsilon = 0$) $\tau(0) = 0$, so that $K_\epsilon = 0$.

Results and Conclusions

Figures 1-3 depict the normalized stress intensities as a function of wave number for selected values of ϵ and β. The curves correspond to the case $\lambda = 2\mu$ ($\nu = 1/3$) and $c = 1$. Recalling that $c = \sqrt{(\lambda+2\mu)\rho^*/E^*\rho}$ and $\beta = 2\mu/E^*h$, and since $E = 8\mu/3$ when $\lambda = 2\mu$, it follows that $\rho^*/\rho = 2/3\beta h$ and $E^*/E = 3/4\beta h$. Thus if h is assumed of order 10^{-2}, say, then the curves corresponding to $\beta = 0.2$ represent density and stiffness ratios of order 10^2 (relatively rigid) while those corresponding to $\beta = 20$ represent ratios of order 1 (relatively elastic).

The major peaks in the curves are a result of a sharp interaction between the fiber and matrix, produced mainly by the inertia force of the fiber. This may be easily verified by noting that the frequencies at which the peaks occur fall close to the frequencies of the maximum inertia force in the fiber, namely $k_n^* = ck_{Ln} = n\pi/(1-\epsilon)$, $n = 2, 4, 6, \ldots$. It should be noted that here the stress intensity represents both a measure of the tendency of the fiber to split the matrix and a measure of debonding between the fiber and the matrix. Thus, if the bond strength is greater than the tensile strength of the matrix, then splitting of the matrix is likely to occur near the resonant frequencies indicated. Finally, it is noted that either splitting or debonding is most likely to occur in the case of a relatively elastic fiber at the surface. Evidently, the inertia force is greatest for this case.

References

1 Ryan, R. L., and Mall, S., "Scattering of an Elastic Wave by a Subsurface Elastic Fiber," ASME JOURNAL OF APPLIED MECHANICS, Vol. 51, 1984, pp. 199-202.

2 Muki, R., and Sternberg, E., "On the Diffusion of Load from a Transverse Tension-Bar Into a Semi-Infinite Elastic Sheet," ASME JOURNAL OF APPLIED MECHANICS, Vol. 35, 1968, pp. 737-746.

Circumferential Part-Through Cracks in Cylindrical Shells Under Tension

J. A. Alabi[1] and J. L. Sanders, Jr.[2]

An analytical expression for the maximum stress intensity factor associated with circumferential part-through cracks in cylindrical shells is presented. The cracked cylinder problem has been analyzed (Alabi, 1984) by using the line-spring model developed by Rice and Levy (1972). The analysis is applicable to complete circular cylinders containing sufficiently long cracks and is supplementary to similar investigations carried out for short cracks (Delale and Erdogan, 1982, Brooks, 1981).

Let the cylinder that contains a part-through crack extending over a circumferential angle of 2α be subjected to uniform axial tension σ far away from the crack. Then the normalized stress intensity factor, K/K_0 is given by

[1]Graduate Student, and Professor of Structural Mechanics, Fellow ASME, respectively, Division of Applied Sciences, Harvard University, Cambridge, Mass. 02138.

Manuscript received by ASME Applied Mechanics Division, October, 1984.

Downloaded 02 May 2010 to 171.66.16.54. Redistribution subject to ASME license or copyright; see http://www.asme.org/terms/Terms_Use.cfm

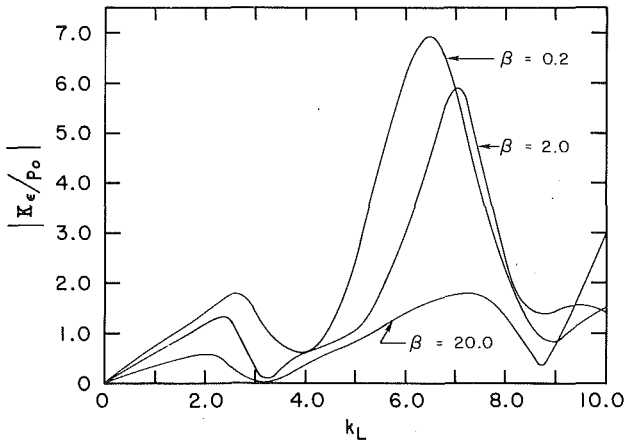


Fig. 2 Stress intensity $|K_\epsilon/p_0|$ versus wave number k_L, $\epsilon = 0.1$

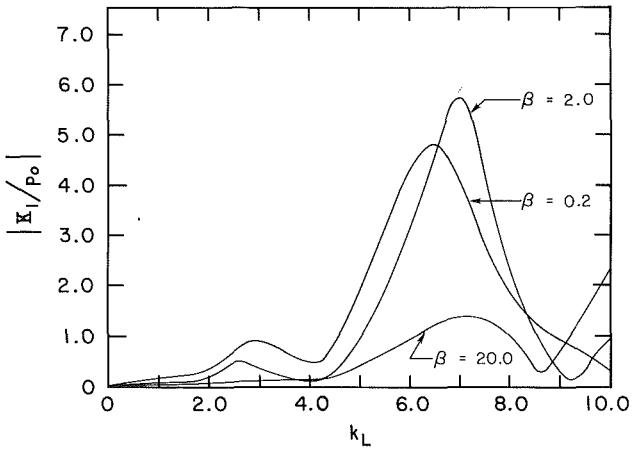


Fig. 3 Stress intensity $|K_1/p_0|$ versus wave number k_L, $\epsilon = 0.1$

Equation (6) follows from the solution of the equation of fiber motion

$$\frac{\partial^2 u^*}{\partial x^2} + c^2 k_L^2 u^* = -\beta\tau(x), \epsilon < x < 1,$$

which satisfies the condition of no axial force transfer from the fiber to the matrix, i.e., $\partial u^*/\partial x = 0$ at $x = \epsilon$ and $x = 1$. (For a verification of this condition see reference [2].) Next, combining (6) and (7) with (5) and (2) yields

$$-\frac{\partial u_0}{\partial x} = 2/\pi \int_\epsilon^1 \tau(s)\{P_1(s,x;k_L) + P_2(s,x;k_L) + \beta P_3(s,x,ck_L)\}ds, \epsilon < x < 1 \quad (9)$$

$$\int_\epsilon^1 \tau(s)[1 + (1-\epsilon)ck_L R(s;ck_L)]ds = 0, \quad (10)$$

where

$$P_3(s,x,ck_L) = \cos[ck_L(s-x)]H(x-s) - \sin[ck_L(x-\epsilon)]\cos[ck_L(1-s)]/\sin[ck_L(1-\epsilon)], \quad (11)$$

$$R(s;ck_L) = \sin[ck_L(2s-1-\epsilon)/2]H(1+\epsilon-2s) - \cos[ck_L(1-s)]/2\sin[ck_L(1-\epsilon)/2], \quad (12)$$

and $H(\bullet)$ is the unit step function.

Equations (9) and (10) may be solved by the Lobatto-Chebyshev technique as described in [1]; from the solution the stress intensities at the ends of the fiber $x = (\epsilon, 1)$ may be computed from the formula

$$(K_\epsilon, K_1) = \pm\sqrt{2(1-\epsilon)}i\mu k_L^2 \phi_0(\mp 1 + \nu/2)h(\mp 1). \quad (13)$$

In (13) $\nu = 2(1+\epsilon)/(1-\epsilon)$, and $h(\mp 1)$ are the end point values of a function $h(t)$ related to $\tau(s)$ through the transformations

$$h(t) = f(s), -2\pi i k_L^2 \phi_0 s f(s) = \sqrt{(s-\epsilon)(1-s)}\,\tau(s), 2s = (1-\epsilon)t + 1 + \epsilon. \quad (14)$$

It is noted that for the case of a surface-broaching fiber ($\epsilon = 0$) $\tau(0) = 0$, so that $K_\epsilon = 0$.

Results and Conclusions

Figures 1-3 depict the normalized stress intensities as a function of wave number for selected values of ϵ and β. The curves correspond to the case $\lambda = 2\mu$ ($\nu = 1/3$) and $c = 1$. Recalling that $c = \sqrt{(\lambda+2\mu)\rho^*/E^*\rho}$ and $\beta = 2\mu/E^*h$, and since $E = 8\mu/3$ when $\lambda = 2\mu$, it follows that $\rho^*/\rho = 2/3\beta h$ and $E^*/E = 3/4\beta h$. Thus if h is assumed of order 10^{-2}, say, then the curves corresponding to $\beta = 0.2$ represent density and stiffness ratios of order 10^2 (relatively rigid) while those corresponding to $\beta = 20$ represent ratios of order 1 (relatively elastic).

The major peaks in the curves are a result of a sharp interaction between the fiber and matrix, produced mainly by the inertia force of the fiber. This may be easily verified by noting that the frequencies at which the peaks occur fall close to the frequencies of the maximum inertia force in the fiber, namely $k_n^* = ck_{Ln} = n\pi/(1-\epsilon)$, $n = 2, 4, 6, \ldots$. It should be noted that here the stress intensity represents both a measure of the tendency of the fiber to split the matrix and a measure of debonding between the fiber and the matrix. Thus, if the bond strength is greater than the tensile strength of the matrix, then splitting of the matrix is likely to occur near the resonant frequencies indicated. Finally, it is noted that either splitting or debonding is most likely to occur in the case of a relatively elastic fiber at the surface. Evidently, the inertia force is greatest for this case.

References

1 Ryan, R. L., and Mall, S., "Scattering of an Elastic Wave by a Subsurface Elastic Fiber," ASME JOURNAL OF APPLIED MECHANICS, Vol. 51, 1984, pp. 199-202.

2 Muki, R., and Sternberg, E., "On the Diffusion of Load from a Transverse Tension-Bar Into a Semi-Infinite Elastic Sheet," ASME JOURNAL OF APPLIED MECHANICS, Vol. 35, 1968, pp. 737-746.

Circumferential Part-Through Cracks in Cylindrical Shells Under Tension

J. A. Alabi[1] and J. L. Sanders, Jr.[2]

An analytical expression for the maximum stress intensity factor associated with circumferential part-through cracks in cylindrical shells is presented. The cracked cylinder problem has been analyzed (Alabi, 1984) by using the line-spring model developed by Rice and Levy (1972). The analysis is applicable to complete circular cylinders containing sufficiently long cracks and is supplementary to similar investigations carried out for short cracks (Delale and Erdogan, 1982, Brooks, 1981).

Let the cylinder that contains a part-through crack extending over a circumferential angle of 2α be subjected to uniform axial tension σ far away from the crack. Then the normalized stress intensity factor, K/K_0 is given by

[1]Graduate Student, and Professor of Structural Mechanics, Fellow ASME, respectively, Division of Applied Sciences, Harvard University, Cambridge, Mass. 02138.

Manuscript received by ASME Applied Mechanics Division, October, 1984.

Copyright © 1985 by ASME
Downloaded 02 May 2010 to 171.66.16.54. Redistribution subject to ASME license or copyright; see http://www.asme.org/terms/Terms_Use.cfm

$$\frac{K}{K_0} = 1 - \frac{c_{12}}{\sqrt{24(1-\nu^2)}\left(1+\frac{c_{22}}{\sqrt{2}}\right)}\left(\frac{f_M}{f_N}\right) \quad (1)$$

where $K_0 \equiv \sigma h^{1/2} f_N(a_0/h)$ is the stress intensity factor for the corresponding plane strain problem, a_0 is the maximum depth of the crack, and f_N and f_M are dimensionless functions obtained from the elasticity solution to the single edge-notched specimen in plane strain. The functions f_N and f_M are the same as g_t and $6g_b$, respectively, given in equation (18) of Delale and Erdogan (1982). Here c_{11}, c_{12}, and c_{22} are compliances defined by the relations

$$\begin{aligned} c_{11} &= \epsilon\sqrt{12}(1-\nu^2)^{3/2}\alpha_{tt} \\ c_{12} &= 6\epsilon(1-\nu^2)\alpha_{tb} \\ c_{22} &= 3\sqrt{12}\epsilon(1-\nu^2)^{1/2}\alpha_{bb} \end{aligned} \quad (2)$$

where α_{tt}, α_{tb}, and α_{bb} are given in Delale and Erdogan (1981). ϵ is a small parameter given by

$$\epsilon^2 = (h/R)[12(1-\nu^2)]^{-1/2} \quad (3)$$

h and R are, respectively, the shell thickness and radius and ν is Poisson's ratio.

In connection with the formula for K/K_0 (equation (1)), the following remarks are in order. The formula is valid irrespective of whether the crack is on the inside or outside of the cylinder surface. K/K_0 does not depend on the value of c_{11}. The formula involves only two dimensionless parameters viz the ratios of shell thickness to radius, h/R, and maximum crack depth to shell thickness, a_0/h. A third parameter, the ratio of crack length to shell thickness, has not been taken into account in deriving the result because its effect is only of the second order according to the analysis carried out in Alabi (1984) which is based on first-order thin shell theory. This implies that the maximum stress intensity factor along the front of a long crack depends on the maximum depth of the crack only and is insensitive to the length or shape of the crack, provided the position of maximum depth is not too close to the crack tips, i.e., $|\theta| = \alpha$. It also implies that there is negligible difference between the stress intensity factor at the deepest part of a long crack, and that associated with an axisymmetric crack whose depth equals the maximum depth of the long crack. These results apply provided the profile of the long crack is sufficiently smooth.

A feature of the investigation of Delale and Erdogan (1982) is that the effects of transverse shear is included in their analysis. However, the close agreement between their results and those presented in Alabi (1984) for long cracks seems to indicate that such effects do not significantly affect fracture strength except perhaps for very short cracks, i.e., when $\alpha = 0(\epsilon^2)$.

Acknowledgment

Support of the Office of Naval Research under Contract N00014-81-K-0668 and the Division of Applied Sciences, Harvard University, is gratefully acknowledged.

References

Alabi, J. A., 1984, "Circumferential Cracks in Cylindrical Shells," Ph.D. Thesis, Division of Applied Sciences, Harvard University.

Brooks, G. N., 1981, "Plastic Boundary Layers and Part-Through Cracks in Shells," Ph.D. Thesis, Department of Mechanical Engineering, Stanford University.

Delale, F., and Erdogan, F., 1982, "Application of the Line-Spring Model to a Cylindrical Shell Containing a Circumferential or Axial Part-Through Crack," ASME Journal of Applied Mechanics, Vol. 49, pp. 97-102.

Delale, F., and Erodgan, F., 1981, "Line-Spring Model for Surface Cracks in a Reissner Plate," *Int. J. Engng. Sci.*, Vol. 19, pp. 1331-1340.

Rice, J. R., and Levy, N., 1972, "The Part-Through Crack in an Elastic Plate," ASME Journal of Applied Mechanics, Vol. 39, pp. 185-194.

Moduluation-Function Technique in Nonuniform Mechanical Systems

Y. Frostig[1] and G. Rosenhouse[1]

This note demonstrates the advantages of the modulation-function technique, proposed here as means of finding efficient solutions for second-order structural systems, the inhomogeneity of which may also vary quickly. The problems dealt with, include buckling of columns, longitudinal vibration of rods, and the dynamic response of time-varying SDF's. The basic formulas are presented and numerical examples are worked out for buckling.

1 Introduction

Literature on dynamic and stability analysis of second-order inhomogeneous structural systems falls into two categories, the first covering specifically cases of slow space and time variation of the properties and the second—continuous cases with arbitrary variation, using known solutions of the corresponding differential equations or numerical methods. The most widely used technique in the first category is the JWKB approximation [1-5], which was originally developed by physicists for use in quantum mechanics. However, since the approximation is restricted to cases of slow variation, it has a pronounced disadvantage in structural analysis. The perturbation technique [6] is another popular method in the same context and has the same limitations as the JWKB.

If the variation of the system's parameters is given by explicit expressions [7-10], an exact solution is obtainable. Alternatively, variational calculus, the Galerkin method, and its analogues [11], or numerical methods such as finite differences or finite elements [12] may be used. Still another method is based on subdivision of the inhomogeneous element and approximation of the subelements by functions for which a closed-form solution is known [13-15].

A general solution was realized by recourse to amplitude—and angle—or phase modulation [16-17]. The analysis yields at first both the formal result and an indication as to whether the solution is exact or not, but provides no clue as to the magnitude of the error entailed by the approximation. In the sequel, we show how the initial solution is to be corrected, and formulate conditions for convergence.

A second-order inhomogeneous system (examples of which are presented in the following) may be defined by the differential equation:

$$Ly(x) = 0, L = \frac{d^2}{dx^2} + \frac{E_2(x)}{E_1(x)}\frac{d}{dx} + \frac{\lambda^2 A(x)}{E_1(x)}, E_1(x) \neq 0 \quad (1)$$

where $E_1(x)$, $E_2(x)$, $A(x)$ are functions incorporating the mechanical properties of the system, λ is unknown eigenvalue, $y(x)$ is the dependent variable of the problem, and x is its independent variable. Adopting the following series form for the solution,

$$y(x) = y_0(x) + y_1(x) + y_2(x) + \ldots + y_n(x), \quad (2)$$

the explicit solution is obtained by assuming the solution for $y_0(x)$, and then $\{y_i(x): i \neq 0\}$ are derived by means of successive approximations.

[1]Lecturer and Senior Lecturer, respectively, Faculty of Civil Engineering, Technion, Israel Institute of Technology, Haifa, Israel.

Manuscript received by ASME Applied Mechanics Division, June, 1982; final revision, May, 1984.

Downloaded 02 May 2010 to 171.66.16.54. Redistribution subject to ASME license or copyright; see http://www.asme.org/terms/Terms_Use.cfm

$$\frac{K}{K_0} = 1 - \frac{c_{12}}{\sqrt{24(1-\nu^2)}\left(1+\frac{c_{22}}{\sqrt{2}}\right)}\left(\frac{f_M}{f_N}\right) \quad (1)$$

where $K_0 \equiv \sigma h^{1/2} f_N(a_0/h)$ is the stress intensity factor for the corresponding plane strain problem, a_0 is the maximum depth of the crack, and f_N and f_M are dimensionless functions obtained from the elasticity solution to the single edge-notched specimen in plane strain. The functions f_N and f_M are the same as g_t and $6g_b$, respectively, given in equation (18) of Delale and Erdogan (1982). Here c_{11}, c_{12}, and c_{22} are compliances defined by the relations

$$\begin{aligned} c_{11} &= \epsilon\sqrt{12}(1-\nu^2)^{3/2}\alpha_{tt} \\ c_{12} &= 6\epsilon(1-\nu^2)\alpha_{tb} \\ c_{22} &= 3\sqrt{12}\epsilon(1-\nu^2)^{1/2}\alpha_{bb} \end{aligned} \quad (2)$$

where α_{tt}, α_{tb}, and α_{bb} are given in Delale and Erdogan (1981). ϵ is a small parameter given by

$$\epsilon^2 = (h/R)[12(1-\nu^2)]^{-1/2} \quad (3)$$

h and R are, respectively, the shell thickness and radius and ν is Poisson's ratio.

In connection with the formula for K/K_0 (equation (1)), the following remarks are in order. The formula is valid irrespective of whether the crack is on the inside or outside of the cylinder surface. K/K_0 does not depend on the value of c_{11}. The formula involves only two dimensionless parameters viz the ratios of shell thickness to radius, h/R, and maximum crack depth to shell thickness, a_0/h. A third parameter, the ratio of crack length to shell thickness, has not been taken into account in deriving the result because its effect is only of the second order according to the analysis carried out in Alabi (1984) which is based on first-order thin shell theory. This implies that the maximum stress intensity factor along the front of a long crack depends on the maximum depth of the crack only and is insensitive to the length or shape of the crack, provided the position of maximum depth is not too close to the crack tips, i.e., $|\theta| = \alpha$. It also implies that there is negligible difference between the stress intensity factor at the deepest part of a long crack, and that associated with an axisymmetric crack whose depth equals the maximum depth of the long crack. These results apply provided the profile of the long crack is sufficiently smooth.

A feature of the investigation of Delale and Erdogan (1982) is that the effects of transverse shear is included in their analysis. However, the close agreement between their results and those presented in Alabi (1984) for long cracks seems to indicate that such effects do not significantly affect fracture strength except perhaps for very short cracks, i.e., when $\alpha = 0(\epsilon^2)$.

Acknowledgment

Support of the Office of Naval Research under Contract N00014-81-K-0668 and the Division of Applied Sciences, Harvard University, is gratefully acknowledged.

References

Alabi, J. A., 1984, "Circumferential Cracks in Cylindrical Shells," Ph.D. Thesis, Division of Applied Sciences, Harvard University.

Brooks, G. N., 1981, "Plastic Boundary Layers and Part-Through Cracks in Shells," Ph.D. Thesis, Department of Mechanical Engineering, Stanford University.

Delale, F., and Erdogan, F., 1982, "Application of the Line-Spring Model to a Cylindrical Shell Containing a Circumferential or Axial Part-Through Crack," ASME Journal of Applied Mechanics, Vol. 49, pp. 97-102.

Delale, F., and Erodgan, F., 1981, "Line-Spring Model for Surface Cracks in a Reissner Plate," *Int. J. Engng. Sci.*, Vol. 19, pp. 1331-1340.

Rice, J. R., and Levy, N., 1972, "The Part-Through Crack in an Elastic Plate," ASME Journal of Applied Mechanics, Vol. 39, pp. 185-194.

Moduluation-Function Technique in Nonuniform Mechanical Systems

Y. Frostig[1] and G. Rosenhouse[1]

This note demonstrates the advantages of the modulation-function technique, proposed here as means of finding efficient solutions for second-order structural systems, the inhomogeneity of which may also vary quickly. The problems dealt with, include buckling of columns, longitudinal vibration of rods, and the dynamic response of time-varying SDF's. The basic formulas are presented and numerical examples are worked out for buckling.

1 Introduction

Literature on dynamic and stability analysis of second-order inhomogeneous structural systems falls into two categories, the first covering specifically cases of slow space and time variation of the properties and the second—continuous cases with arbitrary variation, using known solutions of the corresponding differential equations or numerical methods. The most widely used technique in the first category is the JWKB approximation [1-5], which was originally developed by physicists for use in quantum mechanics. However, since the approximation is restricted to cases of slow variation, it has a pronounced disadvantage in structural analysis. The perturbation technique [6] is another popular method in the same context and has the same limitations as the JWKB.

If the variation of the system's parameters is given by explicit expressions [7-10], an exact solution is obtainable. Alternatively, variational calculus, the Galerkin method, and its analogues [11], or numerical methods such as finite differences or finite elements [12] may be used. Still another method is based on subdivision of the inhomogeneous element and approximation of the subelements by functions for which a closed-form solution is known [13-15].

A general solution was realized by recourse to amplitude—and angle—or phase modulation [16-17]. The analysis yields at first both the formal result and an indication as to whether the solution is exact or not, but provides no clue as to the magnitude of the error entailed by the approximation. In the sequel, we show how the initial solution is to be corrected, and formulate conditions for convergence.

A second-order inhomogeneous system (examples of which are presented in the following) may be defined by the differential equation:

$$Ly(x) = 0, L = \frac{d^2}{dx^2} + \frac{E_2(x)}{E_1(x)}\frac{d}{dx} + \frac{\lambda^2 A(x)}{E_1(x)}, E_1(x) \neq 0 \quad (1)$$

where $E_1(x)$, $E_2(x)$, $A(x)$ are functions incorporating the mechanical properties of the system, λ is unknown eigenvalue, $y(x)$ is the dependent variable of the problem, and x is its independent variable. Adopting the following series form for the solution,

$$y(x) = y_0(x) + y_1(x) + y_2(x) + \ldots + y_n(x), \quad (2)$$

the explicit solution is obtained by assuming the solution for $y_0(x)$, and then $\{y_i(x): i \neq 0\}$ are derived by means of successive approximations.

[1]Lecturer and Senior Lecturer, respectively, Faculty of Civil Engineering, Technion, Israel Institute of Technology, Haifa, Israel.

Manuscript received by ASME Applied Mechanics Division, June, 1982; final revision, May, 1984.

Copyright © 1985 by ASME
Downloaded 02 May 2010 to 171.66.16.54. Redistribution subject to ASME license or copyright; see http://www.asme.org/terms/Terms_Use.cfm

2 Fundamental Solution $y_0(x)$

We try a solution of the form [16]:

$$y_0(x) = Q(x)e^{i\alpha(x)} \tag{3}$$

Substituting equation (3) into the left-hand side of (1), we have

$$\left\{Q'' + \frac{E_2}{E_1}Q' + \left(\lambda^2\frac{A}{E_1} - \alpha'^2\right)Q\right\}e^{i\alpha(x)} + i\left\{2Q'\alpha' + \alpha''Q + \frac{E_2}{E_1}\alpha'Q\right\}e^{i\alpha(x)}. \tag{4}$$

Next we assume:

$$Q'' + \frac{E_2}{E_1}Q' + \left(\lambda^2\frac{A}{E_1} - \alpha'^2\right)Q = 0,$$

$$2Q'\alpha' + \alpha''Q + \frac{E_2}{E_1}\alpha'Q = 0 \tag{5a}$$

or, for the last equation

$$Q^2\alpha' = C^*\exp\left[-\int\frac{E_2}{E_1}dx\right] \quad C^* = \text{const.} \tag{5b}$$

which, in turn, substituted in (5*a*), yields the phase equation:

$$Q\left\{\frac{3}{4}\frac{\alpha''}{\alpha'^2} - \frac{1}{2}\frac{\alpha'''}{\alpha'} - \alpha'^2 + \left[\frac{\lambda^2 A}{E_1} - \frac{1}{2}\left(\frac{E_2}{E_1}\right)' - \frac{1}{4}\left(\frac{E_2}{E_1}\right)^2\right]\right\} = 0. \tag{6}$$

For those cases where equation (6) does not yield an exact solution, we adopt the approximation

$$\alpha' = \pm\left\{\alpha_0^2\frac{\lambda^2 A}{E_1} + \beta_0^2\left(\frac{E_2}{E_1}\right)' + \gamma_0^2\left(\frac{E_2}{E_1}\right)^2\right\}^{1/2} = \pm a_0 a'(x) \tag{7}$$

The unknown constant coefficients, α_0, β_0, γ_0 will be calculated by an approaching-steps method explained later on. When or if $a'(x)$ equals the term in square brackets in equation (6), then the method coincides with JWKB. However, JWKB breaks down if these terms equal zero. This possibility does not occur if the proposed method is used, due to the use of three unknowns: α_0, β_0, γ_0. Using the result obtained for α', the amplitude function, Q, is derived from equation (5*b*). The general form of the solution is reproduced from [16], namely:

$$y_0(x) = Q(x)[B_1e^{i\alpha(x)} + B_2e^{-i\alpha(x)}] = Q(x)[C_1\cos\alpha(x) + C_2\sin\alpha x)] \tag{8}$$

Substituting equation (8) in (1)—or alternatively after α has been calculated, Q from equation (5*b*), in (5*a*) yield:

$$(E_{10} + \Delta E_{10})y_0'' + (E_{20} + \Delta E_{20})y_0' + [(\lambda^2 A)_0 + \Delta(\lambda^2 A)_0]y_0 = \Delta = \Delta_0 e^{i\alpha} \tag{9}$$

where

$$E_{10} + \Delta E_{10} = 1, \frac{E_2}{E_1} = E_{20} + \Delta E_{20}, \frac{\lambda^2 A}{E_1} = (\lambda^2 A)_0 + \Delta(\lambda^2 A)_0.$$

$$\Delta_0 = Q'' + \frac{E_2}{E_1}Q' + \left(\lambda^2\frac{A}{E} - \alpha'^2\right)Q.$$

When Δ_0 is zero, the solution for y_0 is the exact for y; when $\Delta_0 \neq 0$, the solution is an approximate one.

Moreover, y_0 is the exact solution of the fundamental differential equation:

$$L_0y_0 = 0, L_0 = \left[\frac{d^2}{dx^2} + \frac{E_{20}}{E_{10}}\frac{d}{dx} + \left(\frac{\lambda^2 A}{E_{10}}\right)_0\right], E_{10} \neq 0 \tag{10a}$$

Finally, we may define Δ as follows:

$$\Delta = \Delta E_{10}y_0'' + \Delta E_{20}y_0' + \Delta(\lambda^2 A)_0 y_0 = \Delta L y_0 = (L - L_0)y, \tag{10b}$$

with L and L_0 denoting the differential operators as defined in equation (1) and (10*a*). Consequently, Δ may be characterized as the free term of the differential equation for y_0, the contribution of which is represented by the particular solution of the latter, in turn obtainable by the Lagrange method of parameter variation. Denoting the free term by $\Phi(\xi)$, we have [17]:

$$y_{0p}(x) = Q(x)\int_0^x \Phi(\xi)\left\{\frac{\sin[\alpha(x) - \alpha(\xi)]}{Q(\xi)\alpha'(\xi)}\right\}d\xi \tag{11}$$

3 Refinement of Solution

Generally speaking, equation (1) may be characterized as follows:

$$(E_{10} + \Delta E_{10})\sum_{k=0}^{n} y_k'' + (E_{20} + \Delta E_{20})\sum_{k=0}^{n} y_k' + [(\lambda^2 A)_0 + \Delta(\lambda^2 A)_0]\sum_{k=0}^{n} y_k = 0 \tag{12}$$

which also may be replaced by the following set of equations:

$$\begin{aligned}
&E_{10}y_0'' + E_{20}y_0' + (\lambda^2 A)_o y_0 = 0\\
&E_{10}y_1'' + E_{20}y_1' + (\lambda^2 A)_0 y_1 = -[\Delta E_{10}y_0'' + \Delta E_{20}y_0' + \Delta(\lambda^2 A)_0 y_0] = -(L - L_0)y_0 = -\delta_0\\
&E_{10}y_2'' + E_{20}y_2' + (\lambda^2 A)_0 y_2 = -[\Delta E_1 y_1 + \Delta E_2 y_1' + (\lambda^2 A)_0 y_1] = -\delta_1\\
&E_{10}y_n'' + E_{20}y_n' + (\lambda^2 A)_0 y_n = -[\Delta E_1 y_{n-1}'' + \Delta E_2 y_{n-1}' + (\lambda^2 A)_0 y_{n-1}] = -\delta_{n=1}
\end{aligned} \tag{13}$$

Equations (13) are solved by gradual approximation beginning with the fundamental equation (for y_0) and ending with the $(n+1)'$th equation (for y_n). It should be pointed out that the homogeneous solution at all intermediate stages is the same as the fundamental solution, y_0, so that the higher order corrections, δ, need only be related to the particular solution at each stage. The general solution, which consists of two parts, follows equation (8). Omitting the constant coefficients C_1, C_2 we have

$$y^{(i)} = Q\begin{bmatrix}\sin\alpha\\ \cos\alpha\end{bmatrix} + y_1^{(i)} + y_2^{(i)} + \ldots + y_n^{(i)}; i = 1,2 \tag{14}$$

or

$$\begin{Bmatrix} y^{(2)}(x)\\ y^{(1)}(x)\end{Bmatrix} = Q(x)\begin{bmatrix}\sin\alpha(x)\\ \cos\alpha(x)\end{bmatrix} - \frac{1}{a_0}\int_0^x K(x,\xi_1)\begin{bmatrix}\sin\alpha(\xi_1)\\ \cos\alpha(\xi_1)\end{bmatrix}d\xi_1 + \frac{1}{a_0^2}\int_0^x\int_0^{\xi_2} K(x,\xi_2)K(\xi_2,\xi_1)\begin{bmatrix}\sin\alpha(\xi_1)\\ \cos\alpha(\xi_1)\end{bmatrix}d\xi_1 d\xi_2 + \ldots + \frac{(-1)^n}{a_0^n}\int_0^x\int_0^{\xi_n}\ldots\int_0^{\xi_2} K(x,\xi_n)$$

Downloaded 02 May 2010 to 171.66.16.54. Redistribution subject to ASME license or copyright; see http://www.asme.org/terms/Terms_Use.cfm

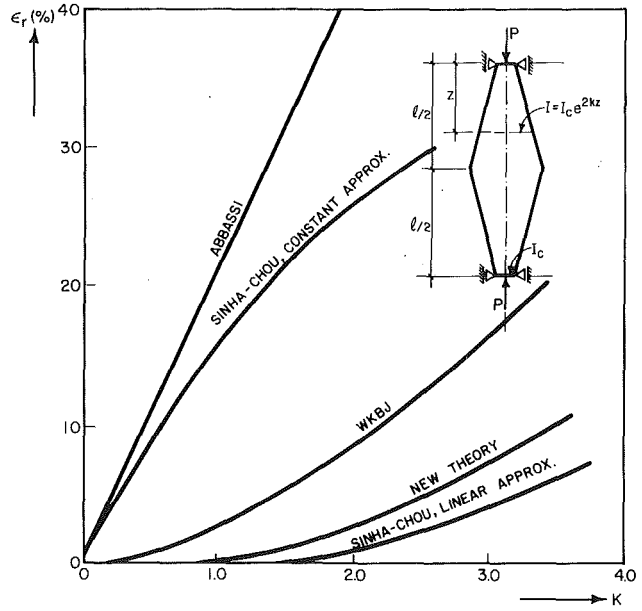


Fig. 1 Relative errors of respective methods

$$K(\xi_n,\xi_{n-1}) \ldots K(\xi_2,\xi_1) \begin{bmatrix} \sin\alpha(\xi_1) \\ \cos\alpha(\xi_1) \end{bmatrix} d\xi_1 d\xi_2 \ldots d\xi_n$$

and

$$K(x,\xi) = \frac{\Delta_{0\alpha}(\xi)}{a'(\xi)} \sin[\alpha(x) - \alpha(\xi)]. \tag{15}$$

The convergence condition for the general solution derives from the requirement that each of the solutions y_i be bounded.

The convergence condition, using the Schwarz inequality rule, reads

$$\begin{bmatrix} y_1^{(2)^2} \\ y_1^{(1)^2} \end{bmatrix}^{1/2}$$

$$\leq \frac{1}{a_0} \left[\int_0^l K^2(x,\xi_1) d\xi_1\right]^{1/2} \left[\int_0^l \begin{bmatrix} \sin^2\alpha(\xi_1) \\ \cos^2\alpha(\xi_1) \end{bmatrix} d\xi_1\right]^{1/2} \tag{16}$$

Finally, the general form of the convergence condition is:

$$R = \left[\int_0^l \left(\frac{\Delta_\alpha}{a'}\right)^2 d\xi\right]^{1/2}$$

and

$$[y_n^{(i)^2}]^{1/2} < \frac{R^n l^n}{a_0^n}; \quad i = 1,2$$

or

$$\begin{Bmatrix} y^{(2)}(x) \\ y^{(1)}(x) \end{Bmatrix} < Q(x) \left[\begin{Bmatrix} \sin(x) \\ \cos(x) \end{Bmatrix} + \frac{Rl}{a_0} + \left(\frac{Rl}{a_0}\right)^2 \right.$$

$$\left. + \left(\frac{Rl}{a_0}\right)^3 + \ldots + \left(\frac{Rl}{a_0}\right)^n \right] \tag{17}$$

The foregoing series, with positive (or absolute terms), converges for $Rl/a_1 < 1$. Hence, the convergence condition yields:

$$[R^2] = \int_0^l \left[\frac{\Delta_{0\alpha}(\xi_1)}{a'(\xi_1)}\right] d\xi_1 < \frac{a_0}{l} \tag{18}$$

The unknowns here, α_0, β_0, γ_0 are obtainable through minimization of R, applying the following equation

$$\frac{\partial(R^2)}{\partial\xi_0} = \int_0^l \frac{\partial}{\partial\xi_0} \left\{\left[\frac{\Delta_{0\alpha}(\xi_1,\alpha_0,\beta_0,\gamma_0)}{a'(\xi_1,\alpha_0,\beta_0,\gamma_0)}\right]^2\right\} d\xi_1 = 0;$$

$$\xi_0 = \alpha_0,\beta_0,\gamma_0 \tag{19}$$

The solution is more exact, the larger the number of unknowns. The solution will diverge if R, after minimization, is greater than α_0/l. Where $Q(x) \to \infty$ or $\alpha'(x) - 0$, the solution does not converge and the location is called a "transition point." In this region a trigonometric solution may be resorted to, with the range of the solution ϵ and α_0 as parameters obtainable from (19); when condition (17) is satisfied, this solution converges to the exact value in the vicinity of the transition region. If the fundamental solution, y_0, belongs to a differential equation with constant coefficients, equation (19) yields the same solution as the method of least square error (Actually, since $Q(x) = 1$, $\Delta^2_{0\alpha}$ is the square error).

4 Stability of Straight Rods With Varying Cross Section

4.1 Solution by Suggested Method Versus Those of Sinha-Chou [15] and Abbassi [3, 4]. The axial buckling force of a column with axial variation of the cross section was calculated in [3, 4, 15]. The procedure consists of solving the equation:

$$y'' + n^2\phi(x)y(x) = 0, 0 \leq x \leq l, \tag{20}$$

where n^2 is proportional to the buckling force, l is the length of the rod and $y(x)$ is its lateral displacement. Equation (1) was solved by Sinha and Chou [15] by replacing $\phi(x)$ with ultraspherical polynomials $\phi(x)$, which yielded a new equation with a known solution, namely:

$$y''(x) + n^2\Phi(x)y(x) = 0 \tag{21}$$

The series of $\Phi(x)$ contained either one constant term, or alternatively one constant and one linear function of x. The solution is given by trigonometric functions if $\Phi(x)$ is constant, and by Airy functions if it is linear.

Abbassi's solution for equation (1) in his first article [3] reads

$$y_0(x) = A\cos[\int n\phi^{1/2}(x)dx] + B\sin[\int n\phi^{1/2}(x)dx], \tag{22}$$

it was improved in the second article [4] by addition of an amplitude function, yielding an identical solution to the JWKB method [2, 5].

$$y(x) = \phi^{-1/4}(x)y_0(x) \tag{23}$$

Using equation (7), we have for the suggested solution:

$$\alpha'(x) = \alpha_0\phi^{1/2}(x) \tag{24}$$

Consequently, equation (5) yields

$$Q(x) = \phi^{-1/4}(x) \tag{25}$$

which in turn yields the function of the buckling line:

$$y(x) = \phi^{-1/4}(x)\{C_1\cos[\alpha_0 a(x)] + C_2\sin[\alpha_0 a(x)]\} \tag{26}$$

where

$$\alpha_0 a(x) = \alpha(x) = \alpha_0 \int \Phi^{1/2}(x)dx,$$

with the constant α_0 obtainable from equation (19). For $\alpha_0 = n$ equation (26) reduces to (23).

As an illustration, we consider the lower buckling force of a freely supported column with exponentially varying cross section (Fig. 1 reproduced from Sinha and Chou [15]). The equation of the buckling line is

$$y'' + n^2 e^{-2kx} y = 0, \quad k > 0, n^2 = \frac{P}{E_0 I_c} \tag{27}$$

Downloaded 02 May 2010 to 171.66.16.54. Redistribution subject to ASME license or copyright; see http://www.asme.org/terms/Terms_Use.cfm

and the boundary conditions are:

$$y'(x) = 0 : x = 0.5l$$

$$y(x) = 0 : x = 0$$

Substitution of the preceding boundary conditions in (26) yields the following transcendental equation:

$$\sin\left[\frac{\alpha_0}{k}\left(1-e^{-\frac{k}{2}}\right)\right] + \frac{2\alpha_0}{k}e^{-\frac{k}{2}}\cos\left[\frac{\alpha_0}{k}\left(1-e^{-\frac{k}{2}}\right)\right] = 0. \tag{28}$$

The parameter n, which represents the buckling force, is obtained by substitution of $\phi(x)$ from equation (24) in (19) as follows:

$$n^2 = {\alpha_0}^2 - \frac{k^3}{4} \cdot \frac{1}{1-e^{-k}} \tag{29}$$

The suggested method was compared with the following alternatives: (*a*) The solution presented by Sinha and Chou [15], with $\phi(\xi)$ expanded in ultraspherical polynomials within the interval $[0;l/2]$, and only the first term taken into account:

$$\phi(\xi) \simeq A_0 = e^{-\frac{k}{2}}\Lambda_\lambda\left(\frac{k}{2}\right),$$

$$\Lambda_\lambda(x) = \Gamma(\lambda+1)I_\lambda(x)\left(\frac{x}{2}\right)^{-2}$$

and I_λ is a modified Bessel function of the first kind. The result is:

$$n^2 = \frac{P}{EI_c} = \frac{\pi^2}{n^2}\,\frac{e^{\frac{k}{2}}}{\Lambda_\lambda\left(\frac{k}{2}\right)}. \tag{30}$$

(*b*) Same as (*a*), with a linear approximation. In this case:

$$\phi(\xi) \simeq A_1 + B_1\xi, A_1 = e^{-\frac{k}{2}}\left[\Lambda_\lambda\left(\frac{k}{2}\right) + \frac{k}{2}\Lambda_{\lambda+1}\left(\frac{k}{2}\right)\right],$$

$$B_1 = -2ke^{-\frac{2}{k}}\Lambda_{\lambda+1}\left(\frac{k}{2}\right).$$

The solution results from the characteristic equation:

$$J_{1/3}(w_0)J_{2/3}(w_{1/2}) + J_{-1/3}(w_0)J_{-2/3}(w_{1/2}) = 0, \tag{31}$$

where

$$z_0 = A_1{B_1}^{-2/3}; w_0 = \frac{2}{3}nz_0^{3/2}; z_{1/2} = \left(\frac{1}{2}A_1 + B_1\right)B^{-2/3};$$

$$w_{1/2} = \frac{2}{3}nz_{1/2}^{3/2}.$$

(*c*) Abbassi's approximation [3]:

$$n^2 = \frac{P}{EI_c} = \frac{1}{4}\,\frac{\pi^2}{l^2}\,\frac{k^2}{(1-e^{-k/2})^2}.$$

(*d*) The classical JWKB technique [4], which yields the characteristic equation:

$$\tan\left[\frac{n}{k}\left(1-e^{-\frac{k}{2}}\right)\right] = -2\frac{n}{k}e^{-\frac{k}{2}} \tag{32}$$

(*e*) The exact solution, derived from the transcendental equation:

$$J_0\left(\frac{n}{k}\right)Y_1\left(\frac{n}{k}e^{-\frac{k}{2}}\right) - J_1\left(\frac{n}{k}e^{-\frac{k}{2}}\right)Y_0\left(\frac{n}{k}\right) = 0, \tag{33}$$

whose roots are given in [18]. Note: the last three methods are also mentioned in the paper of Sinha and Chou.

Figure 1 shows, for the respective methods, the absolute error of the solution defined by Sinha and Chou as follows:

$$\epsilon_r = \frac{P_{\text{approx.}} - P_e}{P_{\text{approx.}}}\,100(\%) \tag{34}$$

P_e and P_{approx} denoting the exact and approximate buckling forces respectively. It is seen that, in spite of the general character of the suggested method, it is satisfactory for the specific case; the result is close to that of the linear approximation, which is rather more complicated. It should be mentioned here that instead of equation (31) which replaces the exact solution in equation (33) the proposed solution recommends equation (29), which is simpler.

5 Conclusions

Comparison of the suggested method with others indicates that it is suitable for any one dimensional inhomogeneous system which satisfies Dirichlet's conditions of convergence.

Refinement of the technique makes for better accuracy and yields the convergence condition.

The advantages of the suggested method are:

1. It permits analytic approximation of the inhomogeneity contribution. (In many cases, even the exact solution is obtainable).

2. The error is relatively small and may be reduced further through minimization.

3. In most cases the analysis is not cumbersome and the time requirement is moderate.

Where the problem reduces to the case of constant coefficients - $a' = 1$, $Q = 1$ - the suggested method is identical with minimization of the error squared.

The proposed method has a certain advantage over variational techniques since here the boundary conditions restriction is not necessary at the initial stages of analysis.

For transition points or regions where Q diverges to infinity, the suggested method may not suffice and a trigonometric solution is required, with the solution region (ϵ) and the coefficient of the trigonometric function (a_0) as parameters.

References

1 Froman, N., and Froman, P. O., *JWKB Approximation, Contributions to the Theory*, 1st ed. North-Holland, Amsterdam, 1965.

2 Pipes, L. A., "Analysis of Linear Time-Varying Circuits by the Brillouin-Wentzel-Kramer Method," *Trans. AIEE Communication and Electronics*, No. 11, 1954, pp. 93-96.

3 Abbassi, N. M., "Buckling of Struts of Variable Bending Rigidity," ASME JOURNAL OF APPLIED MECHANICS, Vol. 25, No. 4, 1958, pp. 537-540.

4 Abbassi, N. M., "The Second Approximation of Buckling Loads of Tapered Struts," ASME JOURNAL OF APPLIED MECHANICS, Vol. 27, No. 1, 1960, pp. 211-212.

5 Pipes, L. A., "Four Methods for the Analysis of Time Variable Circuits," *IRE Transactions—Circuit Theory*, 1955, pp. 4-12.

6 Nayfeh, A. H., *Perturbation Methods*, Wiley-Interscience, New York, 1973.

7 Datta, A. N., "Longitudinal Propagation of Elastic Disturbance for Linear Variation of Elastic Parameters," *Indian Journal of Theoretical Physics*, Vol. 4, 1956, pp. 43-60.

8 Sur, S. P., "A Note on the Longitudinal Propagation of Elastic Disturbance in a Thin Inhomogeneous Elastic Rod," *Indian Journal of Theoretical Physics*, Vol. 9, 1961, pp. 61-67.

9 Lindholm, U. S., and Doshi, K. D., "Wave Propagation in an Elastic Non-homogeneous Bar of Finite Length," ASME JOURNAL OF APPLIED MECHANICS, Vol. 32, 1965, pp. 135-142.

10 Francis, P. H., "Note on the Propagation of Elastic Waves in a Non-homogeneous Rod of Finite Length," ASME JOURNAL OF APPLIED MECHANICS, Vol. 34, 1967, pp. 227-228.

11 Kantorovich, L. V., and Krylov, V. I., *Approximate Methods of Higher Analysis* (translated by Curtis, D. B.), Interscience, Noordhoff, 1964.

12 Collatz, L., *The Numerical Treatment of Differential Equations*, 2nd Printing, 3rd Ed. Springer-Verlag, Berlin, 1966.

Downloaded 02 May 2010 to 171.66.16.54. Redistribution subject to ASME license or copyright; see http://www.asme.org/terms/Terms_Use.cfm

13 Solodov, A. V., *Linear Automatic Control Systems With Varying Parameters*, Blackie & Son, London, 1966.
14 Sinha, S. C., and Chou, C. C., "An Approximate Analysis of Transient Response of Time-Dependent Linear System by Use of Orthogonal Polynomials," *Journal of Sound and Vibration*, Vol. 49, No. 3, 1976, pp. 309-326.
15 Sinha, S. C., and Chou, C. C., "Approximate Eigenvalues for System With Variable Parameters," ASME JOURNAL OF APPLIED MECHANICS, Vol. 46, 1979, pp. 203-205.
16 Rosenhouse, G., "Transmission of Plane Sound Waves in Elastic Nonhomogeneous Media—General Solution," *Int. Journal of Eng. Science*, Vol. 11, No. 11-B, 1973, pp. 1197-1220.
17 Rosenhouse, G., "Transmission of Plane Sound Waves in Elastic Nonuniform Structures Due to Distribution of Acoustic Sources," *Acustica*, Vol. 39, No. 1, 1977, pp. 47-51. (See also Vol. 41, No. 1, 1978, p. 51)
18 Hung, C., and Tai, T. W., "An Aging Spring," *Studies in Applied Mathematics*, Vol. XLIX, No. 2, 1970, pp. 183-184.

A Note on Numerical Analysis of Dynamic Coupled Thermoelasticity

W. K. Liu[1] and H.-G. Chang[1]

A method of computation for dynamic coupled thermoelasticity is developed. This approach has the advantage of applying an implicit algorithm to the elasticity equation and an unconditionally stable explicit algorithm to the heat conduction equation. As a result, the coupled *matrix equations are "symmetric" and "profiled." In addition, unconditional stability is sought.*

Unconditionally Stable Implicit-Explicit Algorithms for Dynamic Coupled Thermoelasticity

The traditional numerical approach to the analysis of coupled thermal-structural problems can be characterized by two steps:

1. The temperature field is calculated by solving the transient heat conduction equation.
2. Based on the computed temperature field and the mechanical loadings, the dynamic response of the structure is evaluated.

This uncoupled solution procedure is valid, if the characteristic time of the thermal disturbance is much greater than the characteristic time of the structural disturbance. It turns out that for many usual engineering problems, the preceding criterion is quite valid. However, in areas such as pulsed lasers, high-energy particle accelerators and fast-burst nuclear reactors, coupled theories of thermoelasticity have to be used because the characteristic times of structural and thermal disturbances are of comparable magnitude.

Due to the mathematical difficulty of the coupled field theories and the geometrical complexity of most engineering applications, numerical techniques are the effective methods in obtaining solutions to such problems (see e.g. [1, 2] and references therein). In [1] an unconditionally stable implicit-explicit method is described. In [2] the time integration of the resulting semidiscrete equations is carried out by using the implicit-explicit methods developed by Hughes and the author [3], however, the resulting coupled equations are "non-symmetric."

In this paper, we introduce an unconditionally stable implicit-explicit method for the analysis of coupled thermal stress waves. The mechanical displacement and temperature are independent variables. The resulting *coupled* matrix equations are symmetric and yet maintain the computational efficiency of the traditional *uncoupled* thermal-structural analysis procedures. In addition, the procedure becomes more versatile by including a common data base for transferring the temperature field computed from a thermal analysis processor to a structural analysis processor for determining displacements and stress. Many existing implicit computer codes could easily be modified to accommodate this family of time integration procedures which can handle the analyses for *both* coupled and uncoupled dynamic thermoelasticity problems.

The coupled matrix equations are [1]:

$$\mathbf{M}_s\mathbf{a}_{n+1} + \mathbf{K}_s\mathbf{d}_{n+1} - \mathbf{R}\theta_{n+1} = \mathbf{f}_{n+1} \tag{1}$$

and

$$\mathbf{M}_\theta\omega_{n+1} + \mathbf{K}_\theta\theta_{n+1} + \theta_0\mathbf{R}^T\mathbf{v}_{n+1} = \mathbf{r}_{n+1} \tag{2}$$

where $\mathbf{M}_s$, $\mathbf{K}_s$, $\mathbf{M}_\theta$, $\mathbf{K}_\theta$ are positive and symmetric matrices, $\mathbf{f}$ and $\mathbf{r}$ are structural and thermal load vectors; $\mathbf{R}$ is the coupling matrix; n is the time step number, $\mathbf{d}$, $\mathbf{v}$, and $\mathbf{a}$ represent the structural displacement, velocity, and acceleration vectors, respectively, and θ and ω represent the structural temperature and time rate of change of the structural temperature respectively.

The unconditionally stable algorithms can be shown to be:

(*a*) Solve for θ_{n+1}, which is governed by

$$\mathbf{M}_\theta\omega_{n+1} + \mathbf{K}^*_\theta\theta_{n+1} = \mathbf{r}^*_{n+1} \tag{3}$$

(*b*) Solve for $\mathbf{a}_{n+1}$, which is governed by

$$(\mathbf{M}_s + \beta\Delta t^2\mathbf{K}_s)\,\mathbf{a}_{n+1} = \mathbf{f}^*_{n+1} + \mathbf{R}\theta_{n+1} \tag{4}$$

(*c*) Update $\mathbf{d}_{n+1}$ and $\mathbf{v}_{n+1}$ via

$$\mathbf{d}_{n+1} = \tilde{\mathbf{d}}_{n+1} + \beta\Delta t^2\mathbf{a}_{n+1} \tag{5}$$

$$\mathbf{v}_{n+1} = \tilde{\mathbf{v}}_{n+1} + \gamma\Delta t\mathbf{a}_{n+1} \tag{6}$$

In equations (3)-(6), $\mathbf{K}^*_\theta$, $\mathbf{r}^*$, and $\mathbf{f}^*$ are defined as follows:

$$\mathbf{K}^*_\theta = \mathbf{K}_\theta + \gamma\Delta t\theta_0\mathbf{R}^T\mathbf{M}_s^{-1}\mathbf{R} \tag{7}$$

which is a *symmetric* and *banded* matrix if $\mathbf{M}_s$ is a lumped matrix.

$$\mathbf{r}^*_{n+1} = \mathbf{r}_{n+1} - \theta_0\mathbf{R}^T\mathbf{v}^*_{n+1} + \gamma\Delta t\theta_0\mathbf{R}^T\mathbf{M}_s^{-1}\mathbf{R}\tilde{\theta}_{n+1} \tag{8a}$$

where

$$\tilde{\theta}_{n+1} = \theta_n + \frac{1}{2}\Delta t\omega_n \tag{8b}$$

$$\mathbf{v}^*_{n+1} = \tilde{\mathbf{v}}_{n+1} + \gamma\Delta t\mathbf{a}^*_{n+1} \tag{9}$$

$$\tilde{\mathbf{v}}_{n+1} = \mathbf{v}_n + (1-\gamma)\,\Delta t\mathbf{a}_n \tag{10}$$

$$\mathbf{a}^*_{n+1} = (\mathbf{M}_s + \beta\Delta t^2\mathbf{K}_s)^{-1}\mathbf{f}^*_{n+1} \tag{11}$$

$$\mathbf{f}^*_{n+1} = \mathbf{f}_{n+1} - \mathbf{K}_s\tilde{\mathbf{d}}_{n+1} + \mathbf{R}\tilde{\theta}_{n+1} \tag{12}$$

and

$$\tilde{\mathbf{d}}_{n+1} = \mathbf{d}_n + \Delta t\mathbf{v}_n + \left(\frac{1}{2} - \beta\right)\Delta t^2\mathbf{a}_n \tag{13}$$

It should be emphasized that both equations (3) and (4) are *symmetric* and *banded* and the implicit-explicit methods developed in [3] can be applied to equation (4) whereas any other implicit or explicit methods can be used to integrate equation (3). This is in contrast to the algorithm proposed in [1] in which $\mathbf{K}^*_\theta$ is a *full* matrix. If the coupling matrix, $\mathbf{R}$, is set to zero only in equation (3), the traditional uncoupled thermal-structural analysis is achieved. In the analysis of thermal-structural problems in which the effect of finite thermal propagation speeds is important, we proposed to employ the recently developed modified unconditionally

[1]Department of Mechanical and Nuclear Engineering, Northwestern University, Evanston, Ill. 60201. Mem. and Student Mem. ASME, respectively.

Manuscript received by ASME Applied Mechanics Division, June, 1984; final revision, November, 1984.

Downloaded 02 May 2010 to 171.66.16.54. Redistribution subject to ASME license or copyright; see http://www.asme.org/terms/Terms_Use.cfm

13 Solodov, A. V., *Linear Automatic Control Systems With Varying Parameters*, Blackie & Son, London, 1966.
14 Sinha, S. C., and Chou, C. C., "An Approximate Analysis of Transient Response of Time-Dependent Linear System by Use of Orthogonal Polynomials," *Journal of Sound and Vibration*, Vol. 49, No. 3, 1976, pp. 309-326.
15 Sinha, S. C., and Chou, C. C., "Approximate Eigenvalues for System With Variable Parameters," ASME JOURNAL OF APPLIED MECHANICS, Vol. 46, 1979, pp. 203-205.
16 Rosenhouse, G., "Transmission of Plane Sound Waves in Elastic Nonhomogeneous Media—General Solution," *Int. Journal of Eng. Science*, Vol. 11, No. 11-B, 1973, pp. 1197-1220.
17 Rosenhouse, G., "Transmission of Plane Sound Waves in Elastic Nonuniform Structures Due to Distribution of Acoustic Sources," *Acustica*, Vol. 39, No. 1, 1977, pp. 47-51. (See also Vol. 41, No. 1, 1978, p. 51)
18 Hung, C., and Tai, T. W., "An Aging Spring," *Studies in Applied Mathematics*, Vol. XLIX, No. 2, 1970, pp. 183-184.

A Note on Numerical Analysis of Dynamic Coupled Thermoelasticity

W. K. Liu[1] and H.-G. Chang[1]

A method of computation for dynamic coupled thermoelasticity is developed. This approach has the advantage of applying an implicit algorithm to the elasticity equation and an unconditionally stable explicit algorithm to the heat conduction equation. As a result, the coupled *matrix equations are "symmetric" and "profiled." In addition, unconditional stability is sought.*

Unconditionally Stable Implicit-Explicit Algorithms for Dynamic Coupled Thermoelasticity

The traditional numerical approach to the analysis of coupled thermal-structural problems can be characterized by two steps:

1. The temperature field is calculated by solving the transient heat conduction equation.
2. Based on the computed temperature field and the mechanical loadings, the dynamic response of the structure is evaluated.

This uncoupled solution procedure is valid, if the characteristic time of the thermal disturbance is much greater than the characteristic time of the structural disturbance. It turns out that for many usual engineering problems, the preceding criterion is quite valid. However, in areas such as pulsed lasers, high-energy particle accelerators and fast-burst nuclear reactors, coupled theories of thermoelasticity have to be used because the characteristic times of structural and thermal disturbances are of comparable magnitude.

Due to the mathematical difficulty of the coupled field theories and the geometrical complexity of most engineering applications, numerical techniques are the effective methods in obtaining solutions to such problems (see e.g. [1, 2] and references therein). In [1] an unconditionally stable implicit-explicit method is described. In [2] the time integration of the resulting semidiscrete equations is carried out by using the implicit-explicit methods developed by Hughes and the author [3], however, the resulting coupled equations are "non-symmetric."

In this paper, we introduce an unconditionally stable implicit-explicit method for the analysis of coupled thermal stress waves. The mechanical displacement and temperature are independent variables. The resulting *coupled* matrix equations are symmetric and yet maintain the computational efficiency of the traditional *uncoupled* thermal-structural analysis procedures. In addition, the procedure becomes more versatile by including a common data base for transferring the temperature field computed from a thermal analysis processor to a structural analysis processor for determining displacements and stress. Many existing implicit computer codes could easily be modified to accommodate this family of time integration procedures which can handle the analyses for *both* coupled and uncoupled dynamic thermoelasticity problems.

The coupled matrix equations are [1]:

$$\mathbf{M}_s\mathbf{a}_{n+1} + \mathbf{K}_s\mathbf{d}_{n+1} - \mathbf{R}\theta_{n+1} = \mathbf{f}_{n+1} \tag{1}$$

and

$$\mathbf{M}_\theta\omega_{n+1} + \mathbf{K}_\theta\theta_{n+1} + \theta_0\mathbf{R}^T\mathbf{v}_{n+1} = \mathbf{r}_{n+1} \tag{2}$$

where $\mathbf{M}_s$, $\mathbf{K}_s$, $\mathbf{M}_\theta$, $\mathbf{K}_\theta$ are positive and symmetric matrices, $\mathbf{f}$ and $\mathbf{r}$ are structural and thermal load vectors; $\mathbf{R}$ is the coupling matrix; n is the time step number, $\mathbf{d}$, $\mathbf{v}$, and $\mathbf{a}$ represent the structural displacement, velocity, and acceleration vectors, respectively, and θ and ω represent the structural temperature and time rate of change of the structural temperature respectively.

The unconditionally stable algorithms can be shown to be:

(*a*) Solve for θ_{n+1}, which is governed by

$$\mathbf{M}_\theta\omega_{n+1} + \mathbf{K}^*_\theta\theta_{n+1} = \mathbf{r}^*_{n+1} \tag{3}$$

(*b*) Solve for $\mathbf{a}_{n+1}$, which is governed by

$$(\mathbf{M}_s + \beta\Delta t^2\mathbf{K}_s)\,\mathbf{a}_{n+1} = \mathbf{f}^*_{n+1} + \mathbf{R}\theta_{n+1} \tag{4}$$

(*c*) Update $\mathbf{d}_{n+1}$ and $\mathbf{v}_{n+1}$ via

$$\mathbf{d}_{n+1} = \tilde{\mathbf{d}}_{n+1} + \beta\Delta t^2\mathbf{a}_{n+1} \tag{5}$$

$$\mathbf{v}_{n+1} = \tilde{\mathbf{v}}_{n+1} + \gamma\Delta t\mathbf{a}_{n+1} \tag{6}$$

In equations (3)-(6), $\mathbf{K}^*_\theta$, $\mathbf{r}^*$, and $\mathbf{f}^*$ are defined as follows:

$$\mathbf{K}^*_\theta = \mathbf{K}_\theta + \gamma\Delta t\theta_0\mathbf{R}^T\mathbf{M}_s^{-1}\mathbf{R} \tag{7}$$

which is a *symmetric* and *banded* matrix if $\mathbf{M}_s$ is a lumped matrix.

$$\mathbf{r}^*_{n+1} = \mathbf{r}_{n+1} - \theta_0\mathbf{R}^T\mathbf{v}^*_{n+1} + \gamma\Delta t\theta_0\mathbf{R}^T\mathbf{M}_s^{-1}\mathbf{R}\tilde{\theta}_{n+1} \tag{8a}$$

where

$$\tilde{\theta}_{n+1} = \theta_n + \frac{1}{2}\Delta t\omega_n \tag{8b}$$

$$\mathbf{v}^*_{n+1} = \tilde{\mathbf{v}}_{n+1} + \gamma\Delta t\mathbf{a}^*_{n+1} \tag{9}$$

$$\tilde{\mathbf{v}}_{n+1} = \mathbf{v}_n + (1-\gamma)\,\Delta t\mathbf{a}_n \tag{10}$$

$$\mathbf{a}^*_{n+1} = (\mathbf{M}_s + \beta\Delta t^2\mathbf{K}_s)^{-1}\mathbf{f}^*_{n+1} \tag{11}$$

$$\mathbf{f}^*_{n+1} = \mathbf{f}_{n+1} - \mathbf{K}_s\tilde{\mathbf{d}}_{n+1} + \mathbf{R}\tilde{\theta}_{n+1} \tag{12}$$

and

$$\tilde{\mathbf{d}}_{n+1} = \mathbf{d}_n + \Delta t\mathbf{v}_n + \left(\frac{1}{2} - \beta\right)\Delta t^2\mathbf{a}_n \tag{13}$$

It should be emphasized that both equations (3) and (4) are *symmetric* and *banded* and the implicit-explicit methods developed in [3] can be applied to equation (4) whereas any other implicit or explicit methods can be used to integrate equation (3). This is in contrast to the algorithm proposed in [1] in which $\mathbf{K}^*_\theta$ is a *full* matrix. If the coupling matrix, $\mathbf{R}$, is set to zero only in equation (3), the traditional uncoupled thermal-structural analysis is achieved. In the analysis of thermal-structural problems in which the effect of finite thermal propagation speeds is important, we proposed to employ the recently developed modified unconditionally

[1]Department of Mechanical and Nuclear Engineering, Northwestern University, Evanston, Ill. 60201. Mem. and Student Mem. ASME, respectively.

Manuscript received by ASME Applied Mechanics Division, June, 1984; final revision, November, 1984.

Copyright © 1985 by ASME
Downloaded 02 May 2010 to 171.66.16.54. Redistribution subject to ASME license or copyright; see http://www.asme.org/terms/Terms_Use.cfm

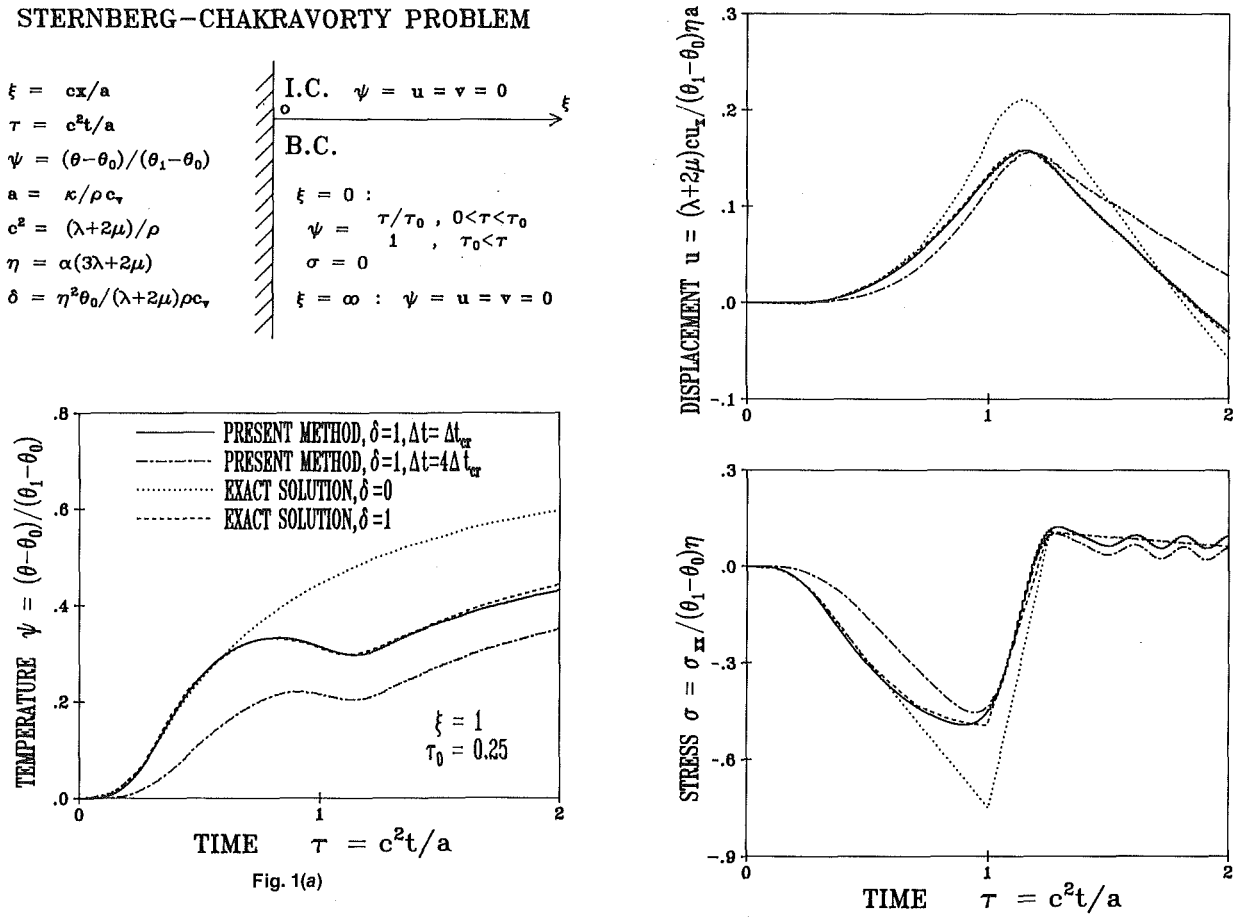


Fig. 1(a)

Fig. 1(b)

stable explicit Rational Runge Kutta (RRK) method [4] for the time integration of equation (3):

$$\mathbf{M}_\theta \omega_1 + \mathbf{K}^*_\theta \theta_n = \mathbf{r}^*_{n+1} \tag{14}$$

$$\mathbf{M}_\theta \omega_2 + \mathbf{K}^*_\theta \left(\theta_n + \frac{1}{2}\Delta t \omega_1\right) = \mathbf{r}^*_{n+1} \tag{15}$$

$$\mathbf{b} = 2\omega_1 - \omega_2 \tag{16}$$

$$\mathbf{e} = 2(\omega_1^T \mathbf{b})\omega_1 - (\omega_1^T \omega_1)\mathbf{b} \tag{17}$$

and

$$\theta_{n+1} = \theta_n + \Delta t \mathbf{e}/(\mathbf{b}^T \mathbf{b}) \tag{18}$$

The step-by-step second-order accurate time integration (γ = ½ and β = ¼) is to proceed over the time interval [0, T]. The solution procedures are as follows:

1. Initialization. Set $n = 0$ and define all the initial data.

2. Form and factorize the effective stiffness matrix, $\mathbf{M}_s + \beta\Delta t^2 \mathbf{K}_s$.

3. Time step loop.

4. Define, in terms, $\tilde{\mathbf{d}}_{n+1}$, $\tilde{\mathbf{v}}_{n+1}$, $\mathbf{f}^*_{n+1}$, $\mathbf{a}^*_{n+1}$, $\mathbf{v}^*_{n+1}$, $\tilde{\theta}_{n+1}$ and $\mathbf{r}^*_{n+1}$ according to equations (13), (10), (12), (11), (9), (8*b*) and (8*a*), respectively.

5. Solve for θ_{n+1} according to equations (14)–(18).

6. Forward reduction and backsubstitution for $\mathbf{a}_{n+1}$ according to equation (4) in which $\mathbf{f}^*_{n+1}$ has already been computed in step 4.

7. Determine, in terms, $\mathbf{d}_{n+1}$ and $\mathbf{v}_{n+1}$ from equations (5) and (6), respectively.

8. If $(n+1)\,\Delta t \geq T$ stop; otherwise replace n by $n+1$ and go to 3.

Remarks

(*a*) In the solutions for θ_{n+1} and $\mathbf{a}_{n+1}$, there is only one function evaluation per time step for the internal force vector of the structure (i.e., $\mathbf{f}^*_{n+1}$). See equations (3) and (4).

(*b*) Only one forward-reduction and one backsubstitution for the *symmetric* and *banded* effective stiffness matrix, $\mathbf{M}_s + \beta\Delta t^2 \mathbf{K}_s$, are required per time step.

(*c*) The *explicit* solution for θ_{n+1} (which is unconditionally stable, see [4]) can be computed efficiently in a similar way as the procedure outlined in remark (*c*) of reference [1] except no forward-reduction and backsubstitution for the effective stiffness matrix is required. Instead, two trivial inner dot products have to be evaluated. It should also be noted that the RRK method given in [1] is a *component by component* algorithm; whereas, the present one (see [4]) is a *vectorized* one.

(*d*) If a physical situation dictates that $\mathbf{M}_\theta$ can be ignored, equation (3) is replaced by $\mathbf{K}^*_\theta \theta_{n+1} = \mathbf{r}^*_{n+1}$. This can be computed efficiently by Gaussian elimination procedures (see e.g., [3–6]) since $\mathbf{K}^*_\theta$ is symmetric and "profiled."

(*e*) The mixed time implicit-explicit methods developed in [5, 6] for the structural and thermal problems can be applied directly to equations (3) and (4) efficiently without engendering any difficulty.

(*f*) The *explicit* expression for $\mathbf{K}_\theta$ is given in [7].

(*g*) In reference [2], the authors applied the implicit-explicit algorithms directly to the coupled field equations which resulted in a nonsymmetric but banded effective

Downloaded 02 May 2010 to 171.66.16.54. Redistribution subject to ASME license or copyright; see http://www.asme.org/terms/Terms_Use.cfm

stiffness. In the present formulation, equations (3) and (4) are both symmetric and with much smaller averaged bandwidths.

Numerical Example

The statement of the Sternberg-Chakravorty problem (see reference [8] for details) is depicted in Fig. 1(*a*). The normalized temperature, displacement and stress are compared with the exact solutions given in [8]. The comparisons are shown in Fig. 1(*a*) and Fig. 1(*b*). δ is the thermomechanical coupling parameter. If δ is set to one, the problem is a fully coupled problem; whereas if δ is set to zero, the problem is an uncoupled one. As may be seen from the figures, there is no sign of numerical instability. The numerical solutions agree well with those given in [8] even though we run at a time step which is four times the critical thermal time step (Δt_{cr}). The problem is also run at $\Delta t = 8\Delta t_{cr}$ for 2000 time steps, the numerical solutions (not shown here) are stable, however, the accuracy deteriorates. Nevertheless, this shows that the present method is unconditionally stable.

Acknowledgment

The support of this research by NSF Grant CEE-8211862 is gratefully acknowledged.

References

1 Liu, W. K., and Zhang, Y. F., "Unconditionally Stable Implicit-Explicit Algorithms for Coupled Thermal Stress Waves," *Computers and Structures*, Vol. 17, 1983, pp. 371-374.

2 Prevost, J. H., and Tao, D., "Finite Element Analysis of Dynamic Coupled Thermoelasticity Problems with Relaxation Times," ASME Paper 83-WA/APM-9.

3 Hughes, T. J. R., and Liu, W. K., "Implicit-Explicit Finite Element for Transient Analysis," ASME JOURNAL OF APPLIED MECHANICS, Vol. 45, 1978, pp. 371-378.

4 Liu, W. K., Belytschko, T., and Zhang, Y. F., "Partitioned Rational Runge Kutta for Parabolic Systems," *International Journal for Numerical Methods in Engineering*, Vol. 20, 1984, pp. 1581-1597.

5 Liu, W. K., "Development of Mixed Time Partition Procedures for Thermal Analysis of Structure," *International Journal for Numerical Methods in Engineering*, Vol. 19, 1983, pp. 125-140.

6 Liu, W. K., and Belytschko, T., "Mixed-Time Implicit-Explicit Finite Elements for Transient Analysis," *Journal of Computers and Structures*, Vol. 15, 1982, pp. 445-450.

7 Liu, W. K., and Belytschko, T., "Efficient Linear and Nonlinear Heat Conduction with a Quadrilateral Element," *International Journal for Numerical Methods in Engineering*, Vol. 20, 1984, pp. 931-948.

8 Nickell, R. E., and Sackman, J. L., "Approximate Solutions in Linear Coupled Thermoelasticity," ASME JOURNAL OF APPLIED MECHANICS, Vol. 35, 1968, pp. 255-266.

Deformation of a Wedged Elastic Sheet due to Pressure

C. Y. Wang[1]

Introduction

Consider a thin elastic sheet pressurized on one side and constrained on the other side by two intersecting rigid plates (Fig. 1). As pressure is increased, the sheet tends to conform to the rigid boundary. This situation occurs in the pressure molding of thin sheet material. We assume the surfaces of contact are well lubricated such that relative frictional resistance can be neglected in comparison to pressure forces. It is desired determine the forces and moments developed by this process.

[1] Michigan State University, East Lansing, Mich., 48824. Mem. ASME

Manuscript received by ASME Applied Mechanics Division, April 1984; final revision, October, 1984.

Formulation

We only need to study the segment of elastic sheet that is not in contact with the rigid boundary. Let Cartesian axes (x', y') be situated at one of the points of separation as shown. Let s' be the arc length from origin and θ be the local angle of inclination. A local moment balance gives

$$dm = -py'ds'\sin\theta + (G' - px')ds'\cos\theta \tag{1}$$

where p is the pressure and G' is the concentrated reactive force at the origin. If the sheet is thin, the moment m is proportional to the local curvature

$$m = EI\frac{d\theta}{ds}. \tag{2}$$

Here EI is the flexural rigidity. Since a natural length scale is absent, we normalize all lengths by $(EI)^{1/3}p^{-1/3}$ and all forces by $(EI)^{1/3}p^{2/3}$ and drop primes. The governing equations become

$$\frac{d^2\theta}{ds^2} = -y\sin\theta + (G-x)\cos\theta \tag{3}$$

$$\frac{dx}{ds} = \cos\theta, \quad \frac{dy}{ds} = \sin\theta \tag{4}$$

$$x(0) = y(0) = \theta(0) = \frac{d\theta}{ds}(0) = 0 \tag{5}$$

Let the arc length of the separated segment be: $2l$. Due to symmetry it is sufficient to consider the half $0 \le s \le l$. The boundary conditions at the symmetry point are

$$\theta(l) = \alpha, \quad \frac{d^2\theta}{ds^2}(l) = 0 \tag{6}$$

Here $(\pi - 2\alpha)$ is the given inclusion angle between the two plates. The unknowns are θ, x, y, G and l.

The maximum moment normalized by $(EI^{2/3}p^{1/3})$ occurs at l:

$$M = \frac{d\theta}{ds}(l) \tag{7}$$

It can be shown the normalized maximum compressive force, also occurring at l, is equal to the normalized distance d to the corner.

$$H = d = \frac{y(l)}{\cos\alpha} \tag{8}$$

The lateral distance c to the corner is equal to the normalized reactive force G.

$$G = c = x(l) + y(l)\tan\alpha \tag{9}$$

The Small α Perturbation

Let $\alpha \equiv \epsilon^3 << 1$. A careful analysis of the gauge functions shows the proper perturbation series for the unknowns are

$$s = \epsilon t \tag{10}$$

$$\theta = \epsilon^3\theta_0(t) + \epsilon^9\theta_1(t) + 0(\epsilon^{15}) \tag{11}$$

$$x = \epsilon x_0(t) + \epsilon^7 x_1(t) + 0(\epsilon^{13}),$$

$$y = \epsilon^4 y_0(t) + \epsilon^{10} y_1(t) + 0(\epsilon^{16}) \tag{12}$$

$$l = \epsilon l_0 + \epsilon^7 l_1 + 0(\epsilon^{13}),$$

$$G = \epsilon G_0 + \epsilon^7 G_1 + 0(\epsilon^{13}) \tag{13}$$

The governing equations yield the leading orders

$$\frac{d^2\theta_0}{dt^2} = G_0 - x_0, \quad \frac{dx_0}{dt} = 1, \frac{dy_0}{dt} = \theta_0 \tag{14}$$

$$\theta_0(0) = \theta_0'(0) = x_0(0) = y_0(0) = 0 \tag{15}$$

$$\theta_0(l_0) = 1, \quad \theta_0''(l_0) = 0 \tag{16}$$

Downloaded 02 May 2010 to 171.66.16.54. Redistribution subject to ASME license or copyright; see http://www.asme.org/terms/Terms_Use.cfm

stiffness. In the present formulation, equations (3) and (4) are both symmetric and with much smaller averaged bandwidths.

Numerical Example

The statement of the Sternberg-Chakravorty problem (see reference [8] for details) is depicted in Fig. 1(*a*). The normalized temperature, displacement and stress are compared with the exact solutions given in [8]. The comparisons are shown in Fig. 1(*a*) and Fig. 1(*b*). δ is the thermomechanical coupling parameter. If δ is set to one, the problem is a fully coupled problem; whereas if δ is set to zero, the problem is an uncoupled one. As may be seen from the figures, there is no sign of numerical instability. The numerical solutions agree well with those given in [8] even though we run at a time step which is four times the critical thermal time step (Δt_{cr}). The problem is also run at $\Delta t = 8\Delta t_{cr}$ for 2000 time steps, the numerical solutions (not shown here) are stable, however, the accuracy deteriorates. Nevertheless, this shows that the present method is unconditionally stable.

Acknowledgment

The support of this research by NSF Grant CEE-8211862 is gratefully acknowledged.

References

1 Liu, W. K., and Zhang, Y. F., "Unconditionally Stable Implicit-Explicit Algorithms for Coupled Thermal Stress Waves," *Computers and Structures*, Vol. 17, 1983, pp. 371-374.

2 Prevost, J. H., and Tao, D., "Finite Element Analysis of Dynamic Coupled Thermoelasticity Problems with Relaxation Times," ASME Paper 83-WA/APM-9.

3 Hughes, T. J. R., and Liu, W. K., "Implicit-Explicit Finite Element for Transient Analysis," ASME JOURNAL OF APPLIED MECHANICS, Vol. 45, 1978, pp. 371-378.

4 Liu, W. K., Belytschko, T., and Zhang, Y. F., "Partitioned Rational Runge Kutta for Parabolic Systems," *International Journal for Numerical Methods in Engineering*, Vol. 20, 1984, pp. 1581-1597.

5 Liu, W. K., "Development of Mixed Time Partition Procedures for Thermal Analysis of Structure," *International Journal for Numerical Methods in Engineering*, Vol. 19, 1983, pp. 125-140.

6 Liu, W. K., and Belytschko, T., "Mixed-Time Implicit-Explicit Finite Elements for Transient Analysis," *Journal of Computers and Structures*, Vol. 15, 1982, pp. 445-450.

7 Liu, W. K., and Belytschko, T., "Efficient Linear and Nonlinear Heat Conduction with a Quadrilateral Element," *International Journal for Numerical Methods in Engineering*, Vol. 20, 1984, pp. 931-948.

8 Nickell, R. E., and Sackman, J. L., "Approximate Solutions in Linear Coupled Thermoelasticity," ASME JOURNAL OF APPLIED MECHANICS, Vol. 35, 1968, pp. 255-266.

Deformation of a Wedged Elastic Sheet due to Pressure

C. Y. Wang[1]

Introduction

Consider a thin elastic sheet pressurized on one side and constrained on the other side by two intersecting rigid plates (Fig. 1). As pressure is increased, the sheet tends to conform to the rigid boundary. This situation occurs in the pressure molding of thin sheet material. We assume the surfaces of contact are well lubricated such that relative frictional resistance can be neglected in comparison to pressure forces. It is desired determine the forces and moments developed by this process.

[1] Michigan State University, East Lansing, Mich., 48824. Mem. ASME

Manuscript received by ASME Applied Mechanics Division, April 1984; final revision, October, 1984.

Formulation

We only need to study the segment of elastic sheet that is not in contact with the rigid boundary. Let Cartesian axes (x', y') be situated at one of the points of separation as shown. Let s' be the arc length from origin and θ be the local angle of inclination. A local moment balance gives

$$dm = -py'ds'\sin\theta + (G' - px')ds'\cos\theta \tag{1}$$

where p is the pressure and G' is the concentrated reactive force at the origin. If the sheet is thin, the moment m is proportional to the local curvature

$$m = EI\frac{d\theta}{ds}. \tag{2}$$

Here EI is the flexural rigidity. Since a natural length scale is absent, we normalize all lengths by $(EI)^{1/3}p^{-1/3}$ and all forces by $(EI)^{1/3}p^{2/3}$ and drop primes. The governing equations become

$$\frac{d^2\theta}{ds^2} = -y\sin\theta + (G-x)\cos\theta \tag{3}$$

$$\frac{dx}{ds} = \cos\theta, \quad \frac{dy}{ds} = \sin\theta \tag{4}$$

$$x(0) = y(0) = \theta(0) = \frac{d\theta}{ds}(0) = 0 \tag{5}$$

Let the arc length of the separated segment be: $2l$. Due to symmetry it is sufficient to consider the half $0 \le s \le l$. The boundary conditions at the symmetry point are

$$\theta(l) = \alpha, \quad \frac{d^2\theta}{ds^2}(l) = 0 \tag{6}$$

Here $(\pi - 2\alpha)$ is the given inclusion angle between the two plates. The unknowns are θ, x, y, G and l.

The maximum moment normalized by $(EI^{2/3}p^{1/3})$ occurs at l:

$$M = \frac{d\theta}{ds}(l) \tag{7}$$

It can be shown the normalized maximum compressive force, also occurring at l, is equal to the normalized distance d to the corner.

$$H = d = \frac{y(l)}{\cos\alpha} \tag{8}$$

The lateral distance c to the corner is equal to the normalized reactive force G.

$$G = c = x(l) + y(l)\tan\alpha \tag{9}$$

The Small α Perturbation

Let $\alpha \equiv \epsilon^3 << 1$. A careful analysis of the gauge functions shows the proper perturbation series for the unknowns are

$$s = \epsilon t \tag{10}$$

$$\theta = \epsilon^3\theta_0(t) + \epsilon^9\theta_1(t) + 0(\epsilon^{15}) \tag{11}$$

$$x = \epsilon x_0(t) + \epsilon^7 x_1(t) + 0(\epsilon^{13}),$$

$$y = \epsilon^4 y_0(t) + \epsilon^{10} y_1(t) + 0(\epsilon^{16}) \tag{12}$$

$$l = \epsilon l_0 + \epsilon^7 l_1 + 0(\epsilon^{13}),$$

$$G = \epsilon G_0 + \epsilon^7 G_1 + 0(\epsilon^{13}) \tag{13}$$

The governing equations yield the leading orders

$$\frac{d^2\theta_0}{dt^2} = G_0 - x_0, \quad \frac{dx_0}{dt} = 1, \frac{dy_0}{dt} = \theta_0 \tag{14}$$

$$\theta_0(0) = \theta_0'(0) = x_0(0) = y_0(0) = 0 \tag{15}$$

$$\theta_0(l_0) = 1, \quad \theta_0''(l_0) = 0 \tag{16}$$

Copyright © 1985 by ASME
Downloaded 02 May 2010 to 171.66.16.54. Redistribution subject to ASME license or copyright; see http://www.asme.org/terms/Terms_Use.cfm

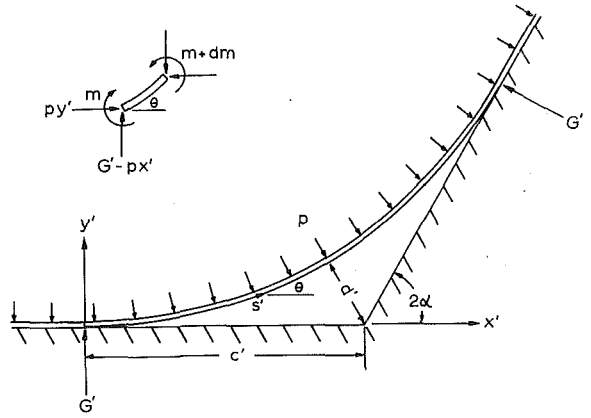


Fig. 1 The coordinate system

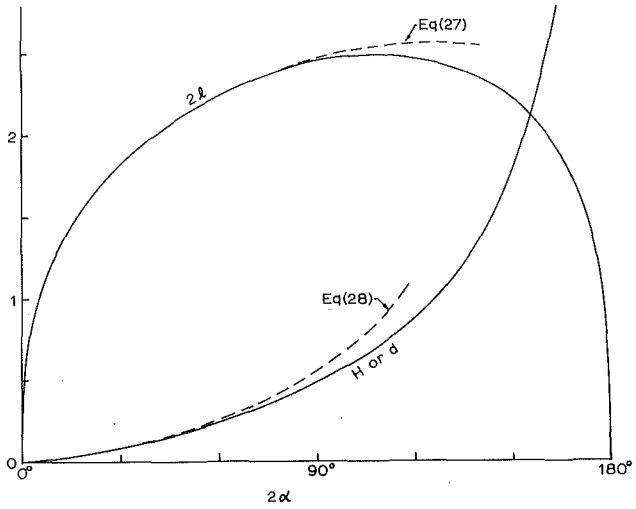


Fig. 2 The free length $2l$, maximum axial compression H, and distance d as a function of α. The inclusion angle of the plates is $(\pi - 2\alpha)$. Dashed lines are approximations.

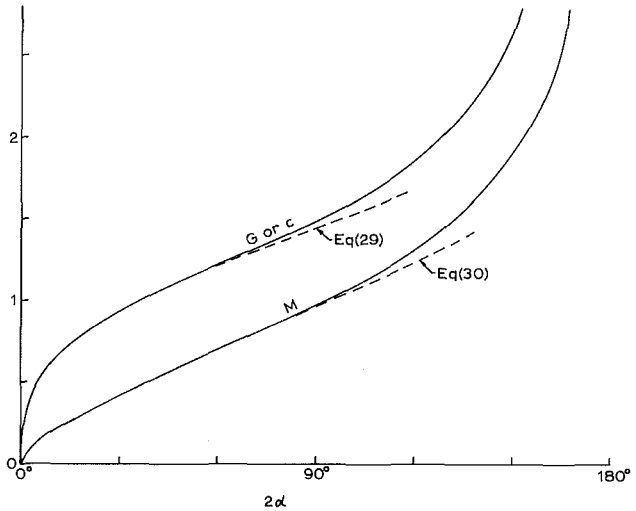


Fig. 3 The maximum moment M, point force G, and distance c as a function of α. Dashed lines are approximations.

The solution is

$$\theta_0 = \frac{3^{\frac{1}{3}}}{6} t^2 - \frac{t^3}{6} \tag{17}$$

$$x_0 = t,\ y_0 = \frac{3^{\frac{1}{3}}}{6} t^3 - \frac{t^4}{24} \tag{18}$$

$$G_0 = l_0 = 3^{\frac{1}{3}} \tag{19}$$

The first-order equations are more difficult

$$\frac{d^2\theta_1}{dt^2} = -y_0\theta_0 - \frac{1}{2}(G_0 - x_0)\theta_0^2 + G_1 - x_1 \tag{20}$$

$$\frac{dx_1}{dt^2} = -\frac{1}{2}\theta_0^2,\ \frac{dy_1}{dt} = \theta_1 - \frac{1}{6}\theta_0^3 \tag{21}$$

$$\theta_1(0) = \theta_0'(0) = x_1(0) = y_1(0) \tag{22}$$

$$\theta_1(l_0) + l_1\theta_0'(l_0) = 0,\ \theta_1''(l_0) + l_1\theta_0'''(l_0) = 0 \tag{23}$$

Equation (23) is obtained from a Taylor expansion about l_0. The first-order solution is

$$x_1 = -\frac{3^{\frac{2}{3}}}{40} t^5 + \frac{3^{\frac{1}{3}}}{72} t^6 - \frac{1}{504} t^7 \tag{24}$$

$$\theta_1 = \frac{3^{\frac{1}{3}}}{14} t^2 - \frac{1}{80} t^6 + \frac{3^{\frac{2}{3}}}{280} t^7 - \frac{3^{\frac{1}{3}}}{896} t^8 + \frac{1}{8064} t^9 \tag{25}$$

$$G_1 = \frac{3^{\frac{1}{3}}}{7},\ l_1 = -\frac{4}{35} 3^{\frac{1}{3}} \tag{26}$$

Thus,

$$2l = 2 \cdot 3^{\frac{1}{3}} \alpha^{\frac{1}{3}} - \frac{8}{35} 3^{\frac{1}{3}} \alpha^{\frac{7}{3}} + 0\left(\alpha^{\frac{13}{3}}\right) \tag{27}$$

$$H = d = \frac{3^{\frac{4}{3}}}{8\cos\alpha} \alpha^{\frac{4}{3}} + 0\left(\alpha^{\frac{10}{3}}\right) \tag{28}$$

$$G = c = 3^{\frac{1}{3}} \alpha^{\frac{1}{3}} + \frac{3^{\frac{1}{3}}}{7} \alpha^{\frac{7}{3}} + 0\left(\alpha^{\frac{13}{3}}\right) \tag{29}$$

$$M = \frac{3^{\frac{2}{3}}}{2} \alpha^{\frac{2}{3}} + \frac{65 \cdot 3^{\frac{2}{3}}}{896} \alpha^{\frac{8}{3}} + 0\left(\alpha^{\frac{14}{3}}\right) \tag{30}$$

Numerical Results and Discussion

For large α the problem was solved numerically. Choose any G. Equations (3)–(5) were integrated as an initial value problem until $\theta'' = 0$. Then we obtained inversely the angle α and all the other pertinent parameters. The fifth-order Runge-Kutta Fehlberg algorithm was used with accuracy adjusted by the step size.

Figure 2 shows the results. The normalized free length $2l$ reaches a maximum of 2.49 at $2\alpha \sim 110$ deg while the normalized compressive force H (and distance d) increases monotonically with increased α. Our approximate solutions compare surprisingly well for $\alpha < 90$ deg. Figure 3 shows the behavior of point force G (equal to distance c) and maximum moment M as a function of α. The forces and moment approach infinity as 2α approaches 180 deg, or when the inclusion angle approaches zero. Figures 2 and 3 are useful in the design of pressure molds.

If α is fixed, the shape of the elastic sheet remain similar as pressure is increased. If the variation of EI with pressure is negligible, the dimensions of the sheet decrease as $(p)^{-1/3}$, the forces increase as $(p)^{2/3}$ and the moments increase as $(p)^{1/3}$. Similarity solutions of elastica problems have been studied by Flaherty, Keller and Rubinow [1] in the case of collapsed flexible tubes by Wang [2] in the case of folding a non-pressurized elastic sheet.

Downloaded 02 May 2010 to 171.66.16.54. Redistribution subject to ASME license or copyright; see http://www.asme.org/terms/Terms_Use.cfm

References

1 Flaherty, J. E., Keller, J. B., and Rubinow, S. I., "Post Buckling Behavior of Elastic Tubes and Rings With Opposite Sides in Contact," *SIAM J. Appl. Math.*, Vol. 23, 1972, pp. 446-455.

2 Wang, C. Y., "Folding of Elastica—Similarity Solutions," ASME JOURNAL OF APPLIED MECHANICS, Vol. 48, 1981, pp. 199-200.

Instability Characteristics of the Asymptotic Suction Profile

I. H. Herron[1], C. H. Von Kerczek[2], and J. Tozzi[2]

1 Introduction

Interest in the stability characteristics of the asymptotic suction profile has reemerged recently for both theoretical and practical reasons. It is one of the simplest solutions of the boundary layer equations and, at the same time, satisfies the Navier-Stokes equations so that it has great theoretical usefulness. From a more practical viewpoint, suction-stabilized boundary layers offer the possibility of low drag fuel efficiency for airplanes or other vehicles.

For these reasons it is desirable to have a complete understanding of the stability characteristics of the asymptotic suction profile. For the asymptotic theory one can refer to the paper by Hughes and Reid (1965); and more recently by Lakin and Reid (1982).

Our intention here is to present detailed stability characteristics of the asymptotic suction profile which we obtained in the course of a wider investigation and which do not seem to be available in the fluid mechanics literature. Although the critical Reynolds number is over 50,000, we found that it was not too difficult to compute accurate stability characteristics.

The technique of solution involves expansion of the terms in the differential equation in Chebyshev polynomials (Orszag, 1971) along with the use of a transformation of the semi-infinite interval into a bounded interval (Grosch and Orszag, 1977).

2 Basic Profile and Stability Equation

The basic profiles studied is a quasiparallel flow

$$\mathbf{U}(y) = (1 - e^{-y})\,\hat{i} - \frac{1}{R}\,\hat{j} \tag{1}$$

where $R = U^*L^*/\nu_*$ is the Reynolds number and $L^* = \nu_*/|V_*|$ is the length scale, V_* is the (constant) suction velocity, and U^* is the free stream velocity.

The disturbance stream function is assumed to be of the form $\phi(y)e^{i\alpha(x-ct)}$ and the linearized disturbance equations reduce to a modified Orr-Sommerfeld equation

$$(D^2-\alpha^2)^2\phi + D(D^2-\alpha^2)\phi - i\alpha R\{(U-c)(D^2-\alpha^2)\phi - U''\phi\} = 0 \tag{2}$$

The appropriate boundary conditions are

$$\phi(0) = \phi'(0) = 0 \tag{3}$$

and $\phi, \phi' \to 0$ as $y \to +\infty$.

The semi-infinite interval $y \in [0, \infty)$ is transformed by the fractional linear transformation

$$\eta = \frac{y-L}{y+L}. \tag{4}$$

[1]Department of Mathematics, Howard University, Washington, D.C. 20059.

[2]Department of Mechanical Engineering, Catholic University, Washington, D.C. 20064. C. H. Von Kerczek, Mem. ASME.

Manuscript received by ASME Applied Mechanics Divison, July, 1984.

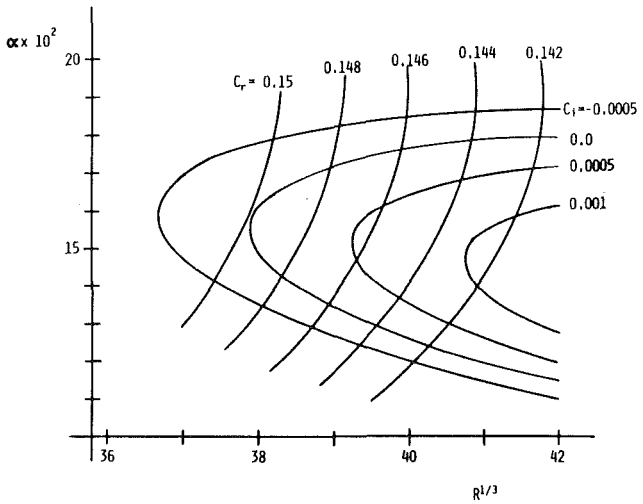


Fig. 1 Curves of phase velocity C_r and growth rate C_i of disturbances to the asymptotic suction flow plotted for wavenumber α and the cube root, $R^{1/3}$, of Reynolds number

The resulting bounded interval $\eta \in [-1, 1)$ is well suited to the use of Chebyshev polynomials and one expands all variables as

$$f(y) = \sum_{n=0}^{\infty} a_n T_n(y). \tag{5}$$

No boundary conditions were explicitly assumed at $y = \infty$ ($\eta = 1$), resulting in the conditions that ϕ and ϕ' are bounded as $y \to \infty$. Several values of L were examined and we found no difference to eight digits between taking $L = 0.7$ and $L = 2.0$. Therefore we simply used $L = 1.4$ for all the results shown in this Note.

The series (5) was truncated at $N = 60$ for most cases we considered although acceptable results even for $R \sim 50000$ were obtained with N as low as 36. For $R = 500$ extremely accurate results, were obtained with $N = 30$. An independent check of some of these results was also made using an initial value method and we could get agreement in the values of the eigenvalues to at least eight significant figures with the Chebyshev results.

Our calculations agree with results of Hocking (1975)

$$R_{\text{crit}} = 54370, \alpha_{\text{crit}} = 0.1555,$$

$$\alpha_{\text{crit}} C_{r_{\text{crit}}} = \omega_{\text{crit}} = 0.023303.$$

Neutral curves based on asymptotic methods are given by Lakin and Reid (1982). Our neutral curve agrees with theirs to the accuracy that the graph can be read. Indicative of this accuracy is that our critical point data given in the foregoing differs from Lakin and Reid's critical point data by less than one-tenth of a percent. In this Note, we also give data on the disturbance growth rate and phase velocity as a function of wave number and Reynolds number.

Figure 1 summarizes the numerical results and should be useful for quick estimates of the stability characteristics of the asymptotic suction profile.

References

Grosch, C. E., and S. A. Orszag, 1977, "Numerical Solution of Problems in Unbounded Regions: Coordinate Transforms," *J. Comp. Physics*, Vol. 25, pp. 273-296.

Hocking, L. M., 1975, "Non-linear Instability of the Asymptotic Suction Velocity Profile," *Q. J. Mech. Appl. Math*, Vol. XXVIII, Part 3, pp. 341-353.

Hughes, T. H., and W. H. Reid, 1965, "On the Stability of the Asymptotic Suction Boundary Layer Profile," *J. Fluid Mech.*, Vol. 23, No. 4, pp. 715-735.

Lakin, W. D., and W. H. Reid, 1982, "Asymptatic Analysis of the Orr-Sommerfeld Problem for Boundary Layer Flows," *Q. J. Mech. Appl. Math*, Vol. XXXV, Part 1, pp. 69-89.

Orszag, S. A., 1971, "Accurate Solution of the Orr-Sommerfeld Stability Equation," *J. Fluid Mech.*, Vol. 50, pp. 689-703.

Downloaded 02 May 2010 to 171.66.16.54. Redistribution subject to ASME license or copyright; see http://www.asme.org/terms/Terms_Use.cfm

References

1 Flaherty, J. E., Keller, J. B., and Rubinow, S. I., "Post Buckling Behavior of Elastic Tubes and Rings With Opposite Sides in Contact," *SIAM J. Appl. Math.*, Vol. 23, 1972, pp. 446-455.

2 Wang, C. Y., "Folding of Elastica—Similarity Solutions," ASME JOURNAL OF APPLIED MECHANICS, Vol. 48, 1981, pp. 199-200.

Instability Characteristics of the Asymptotic Suction Profile

I. H. Herron[1], C. H. Von Kerczek[2], and J. Tozzi[2]

1 Introduction

Interest in the stability characteristics of the asymptotic suction profile has reemerged recently for both theoretical and practical reasons. It is one of the simplest solutions of the boundary layer equations and, at the same time, satisfies the Navier-Stokes equations so that it has great theoretical usefulness. From a more practical viewpoint, suction-stabilized boundary layers offer the possibility of low drag fuel efficiency for airplanes or other vehicles.

For these reasons it is desirable to have a complete understanding of the stability characteristics of the asymptotic suction profile. For the asymptotic theory one can refer to the paper by Hughes and Reid (1965); and more recently by Lakin and Reid (1982).

Our intention here is to present detailed stability characteristics of the asymptotic suction profile which we obtained in the course of a wider investigation and which do not seem to be available in the fluid mechanics literature. Although the critical Reynolds number is over 50,000, we found that it was not too difficult to compute accurate stability characteristics.

The technique of solution involves expansion of the terms in the differential equation in Chebyshev polynomials (Orszag, 1971) along with the use of a transformation of the semi-infinite interval into a bounded interval (Grosch and Orszag, 1977).

2 Basic Profile and Stability Equation

The basic profiles studied is a quasiparallel flow

$$\mathbf{U}(y) = (1 - e^{-y})\,\hat{i} - \frac{1}{R}\,\hat{j} \tag{1}$$

where $R = U^*L^*/\nu_*$ is the Reynolds number and $L^* = \nu_*/|V_*|$ is the length scale, V_* is the (constant) suction velocity, and U^* is the free stream velocity.

The disturbance stream function is assumed to be of the form $\phi(y)e^{i\alpha(x-ct)}$ and the linearized disturbance equations reduce to a modified Orr-Sommerfeld equation

$$(D^2-\alpha^2)^2\phi + D(D^2-\alpha^2)\phi - i\alpha R\{(U-c)(D^2-\alpha^2)\phi - U''\phi\} = 0 \tag{2}$$

The appropriate boundary conditions are

$$\phi(0) = \phi'(0) = 0 \tag{3}$$

and $\phi, \phi' \to 0$ as $y \to +\infty$.

The semi-infinite interval $y \in [0, \infty)$ is transformed by the fractional linear transformation

$$\eta = \frac{y-L}{y+L}. \tag{4}$$

[1]Department of Mathematics, Howard University, Washington, D.C. 20059.

[2]Department of Mechanical Engineering, Catholic University, Washington, D.C. 20064. C. H. Von Kerczek, Mem. ASME.

Manuscript received by ASME Applied Mechanics Divison, July, 1984.

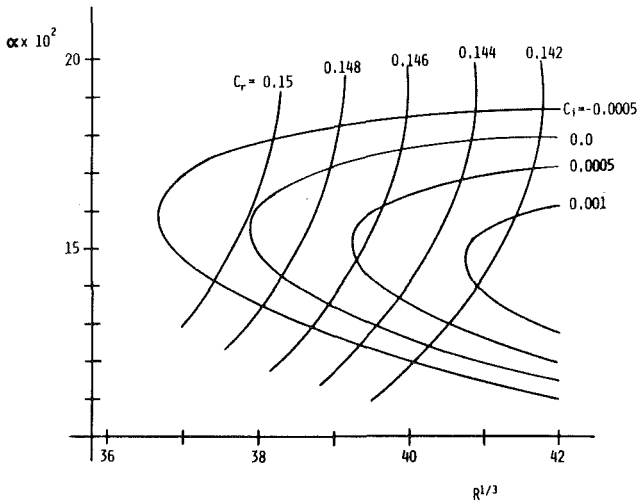


Fig. 1 Curves of phase velocity C_r and growth rate C_i of disturbances to the asymptotic suction flow plotted for wavenumber α and the cube root, $R^{1/3}$, of Reynolds number

The resulting bounded interval $\eta \in [-1, 1)$ is well suited to the use of Chebyshev polynomials and one expands all variables as

$$f(y) = \sum_{n=0}^{\infty} a_n T_n(y). \tag{5}$$

No boundary conditions were explicitly assumed at $y = \infty$ ($\eta = 1$), resulting in the conditions that ϕ and ϕ' are bounded as $y \to \infty$. Several values of L were examined and we found no difference to eight digits between taking $L = 0.7$ and $L = 2.0$. Therefore we simply used $L = 1.4$ for all the results shown in this Note.

The series (5) was truncated at $N = 60$ for most cases we considered although acceptable results even for $R \sim 50000$ were obtained with N as low as 36. For $R = 500$ extremely accurate results, were obtained with $N = 30$. An independent check of some of these results was also made using an initial value method and we could get agreement in the values of the eigenvalues to at least eight significant figures with the Chebyshev results.

Our calculations agree with results of Hocking (1975)

$$R_{\text{crit}} = 54370, \alpha_{\text{crit}} = 0.1555,$$

$$\alpha_{\text{crit}} C_{r_{\text{crit}}} = \omega_{\text{crit}} = 0.023303.$$

Neutral curves based on asymptotic methods are given by Lakin and Reid (1982). Our neutral curve agrees with theirs to the accuracy that the graph can be read. Indicative of this accuracy is that our critical point data given in the foregoing differs from Lakin and Reid's critical point data by less than one-tenth of a percent. In this Note, we also give data on the disturbance growth rate and phase velocity as a function of wave number and Reynolds number.

Figure 1 summarizes the numerical results and should be useful for quick estimates of the stability characteristics of the asymptotic suction profile.

References

Grosch, C. E., and S. A. Orszag, 1977, "Numerical Solution of Problems in Unbounded Regions: Coordinate Transforms," *J. Comp. Physics*, Vol. 25, pp. 273-296.

Hocking, L. M., 1975, "Non-linear Instability of the Asymptotic Suction Velocity Profile," *Q. J. Mech. Appl. Math*, Vol. XXVIII, Part 3, pp. 341-353.

Hughes, T. H., and W. H. Reid, 1965, "On the Stability of the Asymptotic Suction Boundary Layer Profile," *J. Fluid Mech.*, Vol. 23, No. 4, pp. 715-735.

Lakin, W. D., and W. H. Reid, 1982, "Asymptatic Analysis of the Orr-Sommerfeld Problem for Boundary Layer Flows," *Q. J. Mech. Appl. Math*, Vol. XXXV, Part 1, pp. 69-89.

Orszag, S. A., 1971, "Accurate Solution of the Orr-Sommerfeld Stability Equation," *J. Fluid Mech.*, Vol. 50, pp. 689-703.

Copyright © 1985 by ASME

Downloaded 02 May 2010 to 171.66.16.54. Redistribution subject to ASME license or copyright; see http://www.asme.org/terms/Terms_Use.cfm

Wave Motion in Liquid Films on Rotating Plates

A. T. Kirkpatrick[1], M. A. El-Masri[2], and J. F. Louis[2]

Background

This Note is concerned with wave motion in liquid film flow on plates rotating about an axis coincident with an edge of the plate. Using a control volume formulation of the mass and momentum conservation equations, the effects of the centrifugal and coriolis forces on wave inception and speed will be determined, and compared to results obtained for the related case of inclined film flow.

In many of the theories developed for the inclined channel problem, the viscous stress terms are modeled by empirical hydraulic friction terms. At high Froude numbers (Fr > 2) large-amplitude waves form. Jeffries [1] obtained a stability criterion for the onset of progressive waves using the nonlinear shallow water wave equations with an added frictional resistance term to account for wall shear stress and flow turbulence. Dressler [2] obtained discontinuous periodic solutions for large-amplitude wave motion. Dressler and Brock [3] investigated the dependence of the stability of the flow on the form of the resistance term used to model the flow. Lighthill and Whitham [4] used a kinematic wave analysis to predict the motion of large-amplitude waves with vertical fronts. A profile equation for steady film flow on rotating plates was derived by El-Masri and Louis [5] as part of a study of high-temperature gas turbine blade water cooling channels.

Wave Profile Equation

In a coordinate system moving at speed c, the wave speed, a mass and force balance is applied to a small element of fluid of unit width and length dR, where $dR << R$, as shown in Fig. 1.

The continuity equation is

$$vh = (c-u)h = B = \text{constant}, \tag{1}$$

where u is the average flow velocity, c-u is the average flow velocity in the wave coordinate system, and h is the film thickness. The control volume momentum equation in the streamwise direction is:

$$\Sigma F = \int \rho \mathbf{v} \cdot (\mathbf{v} \cdot \mathbf{n}) dA, \tag{2}$$

where $\mathbf{n}$ is an outward normal unit vector and dA is an element of area on the control surface. Upon substitution of the shear stress τ_w, centrifugal force, $\omega^2 R$, and the pressure difference due to the coriolis force, $g_c = 2\omega u$:

$$-\tau_w dR + \rho h g_r dR + 1/2 \rho g_c h^2 - 1/2 \rho (g_c + dg_c)(h+dh)^2 = -\rho v^2 h + \rho (v+dv)^2 (h+dh)^2. \tag{3}$$

Using equation (1), neglecting second-order terms, and modeling the shear stress, τ_ω, with a friction factor relationship: $\tau_\omega = f \rho u^2$, the equation for the profile of the flow can be written:

$$\frac{dh}{dR} = \frac{-fu^2 + hg_r}{hg_c - \omega h(u-c) - (u-c)^2}. \tag{4}$$

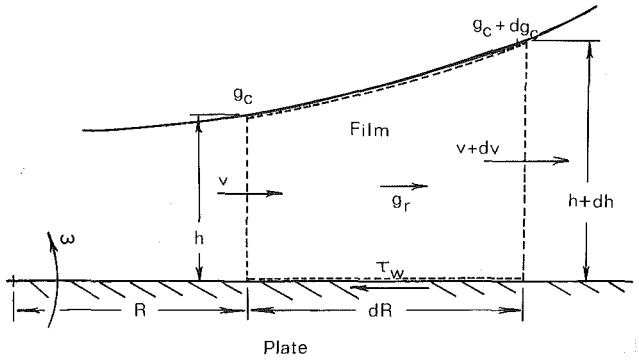


Fig. 1 Differential liquid film element on rotating plate

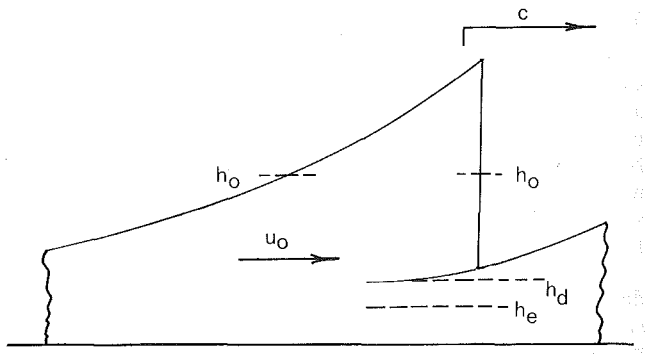


Fig. 2 Liquid film wave model

The two terms in the numerator of equation (4) represent the friction and centrifugal forces. When these two forces balance, dh/dR is zero, and the film has a locally constant thickness, defined as the normal thickness, h_n, where

$$h_n = fu^2/g_r. \tag{5}$$

The film thickness where the denominator of equation (5) is zero is defined as the critical thickness, h_o, where

$$h_0 = [B^2/\omega(u_0 + c)]^{1/3}. \tag{6}$$

We can use equations (1) and (6) to eliminate B and then solve for the nondimensional wavespeed c/u_0:

$$c^2 - (2u_0 + h_0\omega)c + (u_0^2 - u_0 h_0 \omega) = 0. \tag{7}$$

The solution for $c > u_0$ of the preceding equation is

$$c/u_0 = 1 + \omega h_0/2u_0 + 1/2[(\omega h_0/u_0)^2 + 8\omega h_0/u_0]^{1/2}. \tag{8}$$

The term $\omega h_0/u_0$ is the rotational Froude number, Fr, since

$$\mathrm{Fr}^2 = u_0^2/g_c h_0 = u_0/2\omega h_0. \tag{9}$$

so equation (8) becomes

$$c/u_0 = 1 + (1 + (1 + 16\mathrm{Fr}^2)^{1/2})/4\mathrm{Fr}^2. \tag{10}$$

The rotating channel and inclined plane ($c/u_0 = 1 + \mathrm{Fr}^{-1}$ [2]) wavespeeds are plotted versus Froude number in Fig. 3. The rotating wavespeeds are slightly greater than the inclined wavespeeds, with the difference becoming negligible at Froude numbers above 10.

Upon substitution of equations (5) and (6) into the profile equation, we obtain

$$\frac{dh}{dR} = \frac{g_r}{\omega(c+u_0)} \frac{h^3 - h_n^3}{h^3 - h_0^3}. \tag{11}$$

Inspection of the profile equation reveals that no continuous periodic solutions exist since the solution is of logarithmic form. Discontinuous periodic solutions can be constructed by periodically piecing together the above wave profile, as first proposed by Dressler [2].

As shown in Fig. 2, there are two points along the wave

[1]Associate Professor, Department of Mechanical Engineering, Colorado State University, Fort Collins, Colo. 80523. Assoc. Mem. ASME
[2]Associate Professor, Assoc. Mem. ASME, and Professor, respectively, Department of Mechanical Engineering, Massachusetts Institute of Technology, Cambridge, Mass. 02139.
Manuscript received by ASME Applied Mechanics Division, November, 1983.

Copyright © 1985 by ASME
Downloaded 02 May 2010 to 171.66.16.54. Redistribution subject to ASME license or copyright; see http://www.asme.org/terms/Terms_Use.cfm

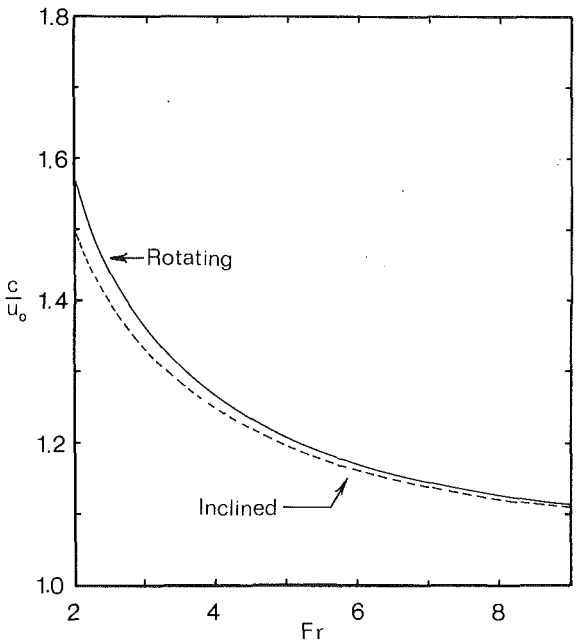


Fig. 3 Wavespeed for rotating and inclined liquid films

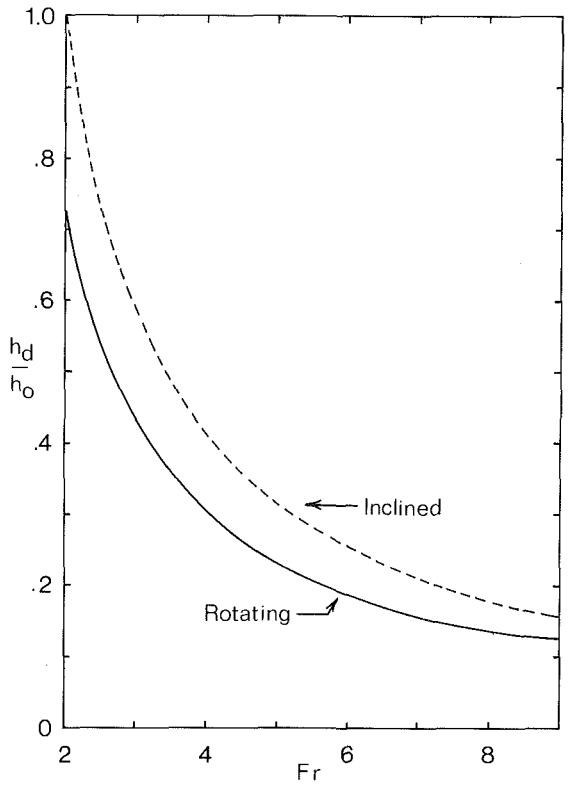


Fig. 4 Minimum thicknesses for rotating and inclined liquid films

where the film thickness is equal to the critical thickness. Along the back of the wave, at the critical thickness, the pressure and momentum terms balance by definition. However, since there are only four forces acting, the friction and centrifugal terms are also balance at the critical thickness, so

$$h_n = h_0, \tag{12}$$

i.e., h_0 is one root of the cubic in the numerator of equation (11).

Equations (12) and (5) can be used to express the Froude number in terms of the friction factor and force ratio at the critical thickness, h_0:

$$\mathrm{Fr}^2 = u_0/2\omega h_0 = \frac{1}{f} g_r/g_c. \tag{13}$$

Factoring out h_0 from the numerator and denominator of equation (11) yields:

$$\frac{dh}{dR} = \frac{g_r}{\omega(c+u_0)}\left[\frac{h^2 + \left(h_0 - \dfrac{fc^2}{g_r}\right)h + (fB^2/h_0 g_r)}{h^2 + hh_0 + h_0{}^2}\right]. \tag{14}$$

Using equations (1), (5), and (10), the quadratic numerator can be expressed in terms of c/u_0, and subsequently in terms of Fr:

$$\frac{dh}{dR} = \frac{g_r}{\omega(c+u_0)}$$

$$\left[\frac{h^2 - ((c/u_0)^2 - 1)h_0 h + (c/u_0 - 1)^2 h_0{}^2}{h^2 + hh_0 + h_0{}^2}\right] \tag{15}$$

$$= \frac{g_r}{\omega(c+u_0)}\left[\frac{(h-h_d)(h-h_e)}{h^2 + hh_0 + h_0{}^2}\right], \tag{16}$$

where

$$\frac{h_{d,e}}{h_0} = \tfrac{1}{2}(c/u_0 - 1)[(c/u_0 + 1) \pm ((c/u_0 + 3)(c/u_0 - 1))^{1/2}] \tag{17}$$

$$= \tfrac{1}{8}(F+G)\left[(F+G+4) \pm \frac{2}{\sqrt{2}}(G(F+G+4))^{1/2}\right], \tag{18}$$

and

$$F = \mathrm{Fr}^{-2}/2; G = (1 + 16\mathrm{Fr}^2)^{1/2}\mathrm{Fr}^{-2}/2. \tag{19}$$

The normal root h_d is formed with the positive sign and the term h_e is found with the negative sign. Note that $h_d > h_e$ since the term under the square root is positive for $c > u_0$. The term h_d represents the asymptotic minimum thickness of the wave, and the term h_e is an unattained minimum thickness.

For comparison, the inclined plane minimum thickness [2] is

$$\frac{h_{d,e}}{h_0} = [(1 + 2\mathrm{Fr}) \pm (1 + 4\mathrm{Fr})^{1/2}]\mathrm{Fr}^{-2}/2. \tag{20}$$

For the same Froude number, the rotating film is predicted to have a smaller minimum thickness relative to an inclined film.

Condition for Wave Motion

In order to have wave motion as modeled in the preceding section, the slope of the liquid film must be positive, i.e., $dh/dR > 0$ at $h = h_0$. Using equation (15) we have

$$h^2 - ((c/u_0)^2 - 1)h_0 h + (c/u_0 - 1)^2 h_0{}^2 > 0. \tag{21}$$

This implies

$$c/u_0 < \frac{3}{2} \text{ and } \mathrm{Fr} > \sqrt{5}. \tag{22}$$

The corresponding condition for inclined flow, $\mathrm{Fr} > 2$, was obtained by Lighthill [4] using a kinematic wave analysis. Upon substitution of equation (13), we can restate equation (22):

$$f\, g_c/g_r < 1/5 \tag{23}$$

The corresponding inclined plane wave motion criterion obtained by Dressler [2] and Jeffries [1], has a factor of 1/4. This implies that the critical Froude number for rotating film flow is larger than the critical Froude number for inclined film flow by the factor $(5/4)^{1/2}$.

Summary and Conclusions

A hydraulic analysis of film flow on a rotating plate yields

Downloaded 02 May 2010 to 171.66.16.54. Redistribution subject to ASME license or copyright; see http://www.asme.org/terms/Terms_Use.cfm

the nondimensional wavespeed as a function of the rotational Froude number. For the same Froude number, the rotational wavespeed is slightly greater than the equivalent inclined film wavespeed. A stability condition for wave motion has also been obtained. The stability condition indicates that the critical Froude number for rotating films is larger than that for inclined films.

References

1 Jeffries, H., "The Flow of Water in an Inclined Channel of Rectangular Section," *Phil. Mag.*, Vol. 49, No. 293, May 1925, pp. 793-807.

2 Dressler, R. F., "Mathematical Solution of the Problem of Roll Waves in Inclined Open Channels," *Communications on Pure and Applied Mathematics*, Vol. 2, No. 2, 1949, pp. 149-174.

3 Dressler, R. F., and Pohle, F. V., "Resistance Effects on Hydraulic Instability," *Communications on Pure and Applied Mathematics*, Vol. 6, 1953, pp. 93-96.

4 Lighthill, M. J., and Whitham, G. B., "On Kinematic Waves," *Proc. Roy. Society*, Series A, Vol. 299, May 1955, pp. 281-345.

5 El-Masri, M. A., and Louis, J. F., "On the Design of High Temperature Gas Turbine Blade Cooling Channels," ASME *Journal of Engineering for Power*, Vol. 100, No. 4, Oct. 1978, pp. 586-591.

On the Size of the Cohesive Zone at the Crack Tip[1]

N. C. Huang[2]

Introduction

In fracture mechanics of linearly elastic materials, the crack is usually treated as a line vacancy. The stresses near the crack tip can always posses an inverse square-root singularity. Since infinite stress is physically impossible, theories have been proposed directed at the removal of the stress singularity at the crack tip. The most significant theories include Irwin's concept of plastic deformation [1] and Barenblatt's concept of a cohesive zone [2]. Barenblatt considered that fracture was the breakage of lattice bonds. As the extension of the lattice at the crack tip reaches a certain limit, the crack propagates. Prior to the crack initiation, the material can be regarded as a continuum. After the crack initiation, the bonding force disappears. Between these two stages, there exists a transition in which the material is no longer a continuum and yet there is still lattice bonding between molecules or atoms. The region of this transition is referred to as a cohesive zone and the lattice bond in the cohesive zone is called the cohesive force. Barenblatt studied the problem of steady growth of a crack under an opening mode deformation. His problem can be formulated by a nonlinear integral equation where the kernel function in the integral involves the nonlinear relation between the cohesive force and the crack opening displacement. Barenblatt pointed out that a closed-form solution of the nonlinear integral equation was extremely difficult. Furthermore, the exact expression for the cohesive force in the actual material is not known. To avoid the difficulty of solving the associated nonlinear integral equation and dealing with the uncertain expression of cohesive forces, Barenblatt analyzed the problem approximately with the following assumptions: (1) The size of the cohesive zone is small in comparison with the length of the initial crack. (2) In the opening mode growth of an equilibrium crack, the shape of the deformed semi-infinite crack surface is independent of the applied load. His first assumption was made based on an argument of rapid decrease of the magnitude of the cohesive force with increasing crack-opening displacement. Willis [3] proved that if Barenblatt's first assumption holds, then the maximum crack-opening displacement at the interface of the initial crack and the cohesive zone is of the same order of magnitude as the size of the cohesive zone.

When the crack-opening displacement is sufficiently large, the cohesive force decreases with increasing crack-opening displacement. It is clear that the size of the cohesive zone depends on the cut-off value of the crack-opening displacement or the cut-off value of the cohesive force. Obviously the ratio of the size of the cohesive zone to the length of the initial crack depends on the size of the initial crack. In this paper we attempt to find the relation between the size of the cohesive zone and factors such as the cut-off value of the cohesive force and the length of the initial crack.

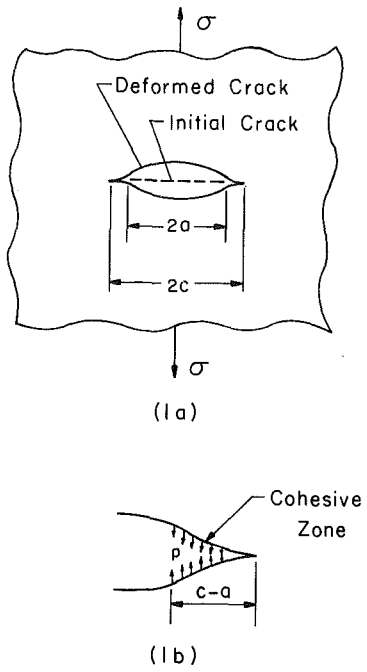


Fig. 1 Geometry of the problem

Basic Equations

Let us consider an infinitely large linearly elastic solid containing a finite crack of length $2a$ subjected to a remote tensile stress σ in the direction perpendicular to the crack as shown in Fig. 1(a). A cohesive zone of length c-a exists in the front of each crack tip as shown in Fig. 1(b). Let us set the origin $x=0$ at the center of the crack. The distributed cohesive forces per unit length acting on the boundary of the cohesive zone are denoted by $p(x)$.

In the following we adopt the plane-strain formulation for our analysis. The stress intensity factor for the opening model deformation at the tip of the cohesive zone due to the remote tensile stress σ is

$$K_\sigma = \sigma(\pi c)^{1/2} \tag{1}$$

The stress intensity factor introduced by the cohesive force $p(x)$ in the cohesive zone is found to be [3]

$$K_p = -2\left(\frac{c}{\pi}\right)^{1/2} \int_a^c \frac{p(x)}{(c^2-x^2)^{1/2}}\, dx. \tag{2}$$

According to Barenblatt, the stress singularity at the crack tip is removed through the action of the cohesive force. Thus

[1]This work has been supported by the Department of Transportation, Urban Mass Transportation Administration under contgract IN-06-0009 titled Cold Weather Transit Technology Program.

[2]Professor, Department of Aerospace and Mechanical Engineering, University of Notre Dame, Notre Dame, Ind. 46556. Mem. ASME.

Manuscript received by ASME Applied Mechanics Division March 1984; final revision, September, 1984.

Downloaded 02 May 2010 to 171.66.16.54. Redistribution subject to ASME license or copyright; see http://www.asme.org/terms/Terms_Use.cfm

the nondimensional wavespeed as a function of the rotational Froude number. For the same Froude number, the rotational wavespeed is slightly greater than the equivalent inclined film wavespeed. A stability condition for wave motion has also been obtained. The stability condition indicates that the critical Froude number for rotating films is larger than that for inclined films.

References

1 Jeffries, H., "The Flow of Water in an Inclined Channel of Rectangular Section," *Phil. Mag.*, Vol. 49, No. 293, May 1925, pp. 793-807.

2 Dressler, R. F., "Mathematical Solution of the Problem of Roll Waves in Inclined Open Channels," *Communications on Pure and Applied Mathematics*, Vol. 2, No. 2, 1949, pp. 149-174.

3 Dressler, R. F., and Pohle, F. V., "Resistance Effects on Hydraulic Instability," *Communications on Pure and Applied Mathematics*, Vol. 6, 1953, pp. 93-96.

4 Lighthill, M. J., and Whitham, G. B., "On Kinematic Waves," *Proc. Roy. Society*, Series A, Vol. 299, May 1955, pp. 281-345.

5 El-Masri, M. A., and Louis, J. F., "On the Design of High Temperature Gas Turbine Blade Cooling Channels," ASME *Journal of Engineering for Power*, Vol. 100, No. 4, Oct. 1978, pp. 586-591.

On the Size of the Cohesive Zone at the Crack Tip[1]

N. C. Huang[2]

Introduction

In fracture mechanics of linearly elastic materials, the crack is usually treated as a line vacancy. The stresses near the crack tip can always posses an inverse square-root singularity. Since infinite stress is physically impossible, theories have been proposed directed at the removal of the stress singularity at the crack tip. The most significant theories include Irwin's concept of plastic deformation [1] and Barenblatt's concept of a cohesive zone [2]. Barenblatt considered that fracture was the breakage of lattice bonds. As the extension of the lattice at the crack tip reaches a certain limit, the crack propagates. Prior to the crack initiation, the material can be regarded as a continuum. After the crack initiation, the bonding force disappears. Between these two stages, there exists a transition in which the material is no longer a continuum and yet there is still lattice bonding between molecules or atoms. The region of this transition is referred to as a cohesive zone and the lattice bond in the cohesive zone is called the cohesive force. Barenblatt studied the problem of steady growth of a crack under an opening mode deformation. His problem can be formulated by a nonlinear integral equation where the kernel function in the integral involves the nonlinear relation between the cohesive force and the crack opening displacement. Barenblatt pointed out that a closed-form solution of the nonlinear integral equation was extremely difficult. Furthermore, the exact expression for the cohesive force in the actual material is not known. To avoid the difficulty of solving the associated nonlinear integral equation and dealing with the uncertain expression of cohesive forces, Barenblatt analyzed the problem approximately with the following assumptions: (1) The size of the cohesive zone is small in comparison with the length of the initial crack. (2) In the opening mode growth of an equilibrium crack, the shape of the deformed semi-infinite crack surface is independent of the applied load. His first assumption was made based on an argument of rapid decrease of the magnitude of the cohesive force with increasing crack-opening displacement. Willis [3] proved that if Barenblatt's first assumption holds, then the maximum crack-opening displacement at the interface of the initial crack and the cohesive zone is of the same order of magnitude as the size of the cohesive zone.

When the crack-opening displacement is sufficiently large, the cohesive force decreases with increasing crack-opening displacement. It is clear that the size of the cohesive zone depends on the cut-off value of the crack-opening displacement or the cut-off value of the cohesive force. Obviously the ratio of the size of the cohesive zone to the length of the initial crack depends on the size of the initial crack. In this paper we attempt to find the relation between the size of the cohesive zone and factors such as the cut-off value of the cohesive force and the length of the initial crack.

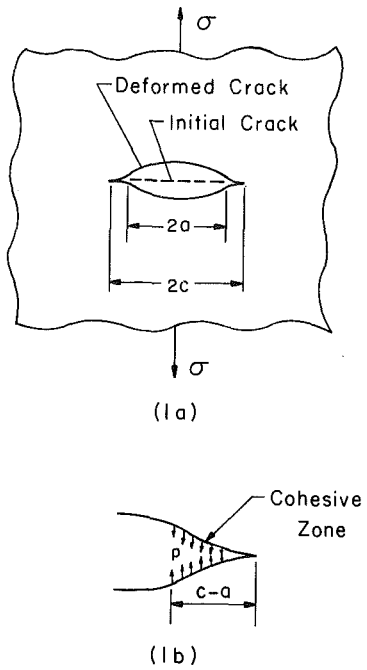


Fig. 1 Geometry of the problem

Basic Equations

Let us consider an infinitely large linearly elastic solid containing a finite crack of length $2a$ subjected to a remote tensile stress σ in the direction perpendicular to the crack as shown in Fig. 1(a). A cohesive zone of length c-a exists in the front of each crack tip as shown in Fig. 1(b). Let us set the origin $x=0$ at the center of the crack. The distributed cohesive forces per unit length acting on the boundary of the cohesive zone are denoted by $p(x)$.

In the following we adopt the plane-strain formulation for our analysis. The stress intensity factor for the opening model deformation at the tip of the cohesive zone due to the remote tensile stress σ is

$$K_\sigma = \sigma(\pi c)^{1/2} \tag{1}$$

The stress intensity factor introduced by the cohesive force $p(x)$ in the cohesive zone is found to be [3]

$$K_p = -2\left(\frac{c}{\pi}\right)^{1/2} \int_a^c \frac{p(x)}{(c^2-x^2)^{1/2}}\, dx. \tag{2}$$

According to Barenblatt, the stress singularity at the crack tip is removed through the action of the cohesive force. Thus

[1]This work has been supported by the Department of Transportation, Urban Mass Transportation Administration under contgract IN-06-0009 titled Cold Weather Transit Technology Program.

[2]Professor, Department of Aerospace and Mechanical Engineering, University of Notre Dame, Notre Dame, Ind. 46556. Mem. ASME.

Manuscript received by ASME Applied Mechanics Division March 1984; final revision, September, 1984.

Copyright © 1985 by ASME
Downloaded 02 May 2010 to 171.66.16.54. Redistribution subject to ASME license or copyright; see http://www.asme.org/terms/Terms_Use.cfm

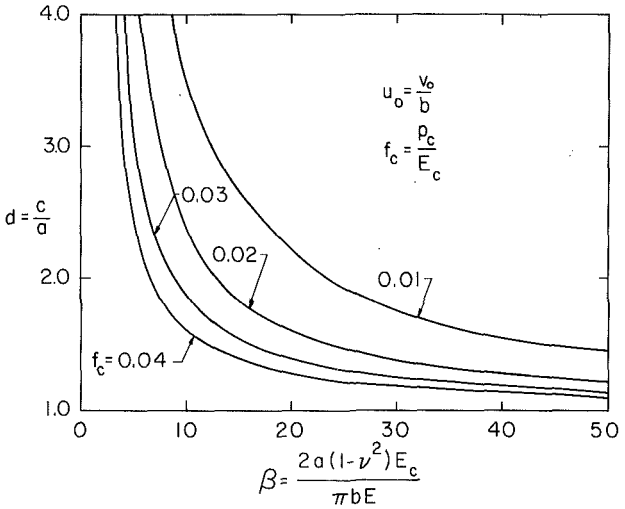


Fig. 2 d versus β curves for $m = 8$, $u_0 = 2$, and different values of f_c

$$K_\sigma + K_p = 0, \tag{3}$$

which leads to

$$\sigma = \frac{2}{\pi}\int_a^c \frac{p(x)}{(c^2-x^2)^{1/2}}dx. \tag{4}$$

Let E be the modulus of elasticity of the material and ν Poisson's ratio. The crack-opening displacement in the cohesive zone under the action of the remote stress and the cohesive force can be found by means of the weight funciton technique [4]. It is

$$v(x) = \frac{2\sigma(1-\nu^2)}{E}\left[(c^2-x^2)^{1/2} - \frac{1}{\pi\sigma}\int_a^c p(t) ln\left|\frac{(c^2-t^2)^{1/2}+(c^2-x^2)^{1/2}}{(c^2-t^2)^{1/2}-(c^2-x^2)^{1/2}}\right|\right]dt. \tag{5}$$

Equations (4) and (5) can be combined as

$$v(x) = \frac{2(1-\nu^2)}{\pi E}\int_a^c p(t)\left[2\left(\frac{c^2-x^2}{c^2-t^2}\right)^{1/2} - ln\left|\frac{(c^2-t^2)^{1/2}+(c^2-x^2)^{1/2}}{(c^2-t^2)^{1/2}-(c^2-x^2)^{1/2}}\right|\right]dt. \tag{6}$$

In our study, we assumed that the relation between the cohesive forces $p(x)$ and the crack-opening displacement $v(x)$ in the cohesive zone can be derived from a potential similar to what exists between the interatomic force and the separation between atoms. Let v_0 be the displacement required for transforming the continuum to the cohesive zone, b the half length of lattice and E_c the initial modulus of the cohesive zone. We then have the p-v relation as

$$p = \frac{E_c}{m-2}\left[\left(1+\frac{v+v_0}{b}\right)^{-2} - \left(1+\frac{v+v_0}{b}\right)^{-m}\right], \tag{7}$$

where m is a material constant. The first term in equation (7) corresponds to the intermolecular attraction while the second term corresponds to the intermolecular repulsion. Note that when $v=0$, we have the cohesive force for transforming the continuum to the cohesive zone as

$$p_0 = \frac{E_c}{m-2}\left[\left(1+\frac{v_0}{b}\right)^{-2} - \left(1+\frac{v_0}{b}\right)^{-m}\right]. \tag{8}$$

Crack-opening displacement in the cohesive zone initiates as $p > p_0$.

By substituting equation (7) into equation (6), we obtain a nonlinear singular integral equation for $v(x)$. It can be solved numerically by an iterative process. The size of the cohesive zone c-a is determined by the condition that $p(a)$ is equal to the critical value of the cohesive force p_a for complete breakage of the lattice bond.

Let us introduce the following dimensionless quantities:

$$d = c/a, \xi = x/a, \tau = t/a, \beta = \frac{2a(1-\nu^2)E_c}{\pi bE}, u = v/b, \tag{9}$$

$$u_0 = v_0/b, f = p/E_c, f_0 = p_0/E_c, f_a = p_a/E_c, f_c = p_c/E_c.$$

Equations (6), (7) and (8) can be expressed in dimensionless form as

$$u(\xi) = \beta\int_1^d f(\tau)g(\xi,\tau)d\tau, \tag{10}$$

$$f = \frac{1}{m-2}[(1+u+u_0)^{-2} - (1+u+u_0)^{-m}], \tag{11}$$

$$f_0 = \frac{1}{m-2}[(1+u_0)^{-2} - (1+u_0)^{-m}], \tag{12}$$

where

$$g(\xi,\tau) = 2\frac{\alpha(\xi)}{\alpha(\tau)} - ln\left|\frac{\alpha(\tau)+\alpha(\xi)}{\alpha(\tau)-\alpha(\xi)}\right| \tag{13}$$

and

$$\alpha(\xi) = (d^2-\xi^2)^{1/2}. \tag{14}$$

After $u(\xi)$ is determined, the cohesive zone size parameter d is determined by the condition that

$$f(1) = f_a. \tag{15}$$

Note that in equation (11) the maximum value of f is found at

$$u = \bar{u} = \left(\frac{m}{2}\right)^{\frac{1}{m-2}} - u_0 - 1. \tag{16}$$

For $u > \bar{u}$, $df/du < 0$ and for $u < \bar{u}$, $df/du > 0$. If the continuum-cohesive zone transition is governed by the critical lattice bond, than $df/du > 0$ at $u = 0$. Obviously, at $f = f_a$, $df/du < 0$, Hence, there eixsts a maximum value of f in the $f(\xi)$ distribution curve in the cohesive zone. On the other hand, if the continuum-cohesive zone transition is governed by the critical lattice extension, then $\bar{u}$ may be negative and f decreases monotonically with increasing u for $u > 0$. In this case, $f(\xi)$ increase monotonically with ξ in the cohesive zone and the size of the cohesive zone decreases with u_a, where u_a is the value of u at $f = f_a$. Thus the size of the cohesive zone can be made arbitrarily small if u_a is chosen to be arbitrarily close to zero. In the following, consider only the case for which the continuum-cohesive zone transition is governed by the critical lattice bond. From equation (16), it is seen that in order to have $\bar{u} > 0$,

$$u_0 < \left(\frac{m}{2}\right)^{\frac{1}{m-2}} - 1. \tag{17}$$

Numerical Results

Our nonlinear singular integral equation is solved numerically by the method of a three-point Lagrange interpolation discretization associated with Newton's iterative process. Dugdale's solution [5] is employed as the initial try $u(\xi)$. In our numerical computation, we select $m = 8$ for which $\bar{u}$ is found to be 0.2599. In Fig. 2, we plot the cohesive zone size parameter d versus β for different values of f_c. It is seen that, for given β, the value of d decreases with increasing f_c. For given f_c, the value of d decreases with increasing β. When β is sufficiently large, the value of d is small and the size of the cohesive zone can be smaller than the size of the original crack. However, when β is sufficiently small, the value of d can be large in comparison with the size of the original crack.

Downloaded 02 May 2010 to 171.66.16.54. Redistribution subject to ASME license or copyright; see http://www.asme.org/terms/Terms_Use.cfm

The order of magnitude of β for a realistic material is approximately $10^3 - 10^4$ and hence Barenblatt's assumption of small size of cohesive zone is legitimate.

References

1 Irwin, G. R., "Fracture," *Handbuch der Physik*, S. Flügge, ed., Vol. 4, 1958, pp. 551-590.

2 Barenblatt, G. I., "The Mathematical Theory of Equilibrium Crack in Brittle Fracture," *Advances in Applied Mechanics*, Vol. 7, 1962, pp. 55-129.

3 Rice, J. R., "Mathematical Analysis in the Mechanics of Fracture," *Fracture*, Liebowitz, H., ed., Vol. 2, 1968, pp. 196-311.

4 Bueckner, H. F., "A Novel Principle for the Computation of Stress Intensity Factors," *ZAMM*, Vol. 50, 1970, pp. 529-546.

5 Dugdale, D. S., "Yielding of Steel Sheets Containing Slits," *Journal of Mechanics and Physics of Solids*, Vol. 8, 1960, pp. 100-108.

Centrifugal Instability of Turbulent Wall Jets Along Strongly Concave Surfaces

N. Fujisawa[1], R. Kobayashi[2], and H. Shirai[3]

Introduction

The purpose of this Note is to present a theoretical consideration for Taylor-Görtler centrifugal instability of turbulent wall jets along strongly concave surfaces, as a result of which longitudinal vortices are expected to occur as secondary flow in the wall jets. While the onset of the longitudinal vortices in laminar flows becomes a beginning of laminar-turbulent transition, the centrifugal instability in turbulent flows gives certainly some influences upon transfer phenomena. Tani [1] first found experimentally the longitudinal vortices appearing in turbulent boundary layers along concave walls. For the case of turbulent wall jets (Fig. 1), we predicted theoretically [2] that the centrifugal instability occurs at the critical value $b/R = 0.31$ of the curvature parameter, where R is the radius of curvature on the wall and b the half-width of the wall jet. We found in an experiment done thereafter [3], as shown in Fig. 2, that the intensity of turbulence in the turbulent wall jets rather decreases first as the curvature parameter b/R is increased from zero (flat wall), which comes from the effect on the turbulent field, and that a further increase of b/R beyond about 0.17 results in a remarkable increase of the turbulence intensity in the wall jet. (The deviation from the first tendency of decreasing turbulence intensity is observed to start from b/R of about 0.1.) This increase of the turbulence was explained in relation to the Taylor-Görtler centrifugal instability.

We consider that one of the reasons for the difference of the critical theoretical value $(b/R)cr = 0.31$ from the experimental value 0.1 comes from data of Reynolds stress used in the numerical calculation, in which a distribution of the Reynolds stress across the wall jet was based on the data measured for a case of flat wall. Because our recent systematic experiment on the effect of curvature [4] showed an observable decrease of the Reynolds stress with increasing curvature parameter in a range of $b/R = 0$ to 0.1, we again treat the instability problem in consideration to the variation of the Reynolds stress due to the curvature parameter.

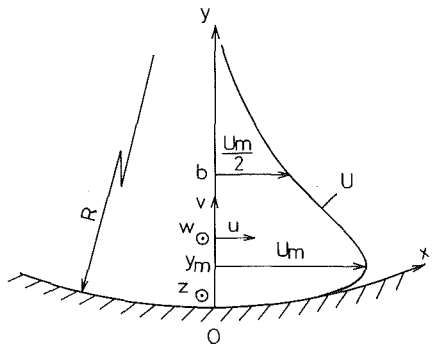


Fig. 1 Wall jet and coordinate system

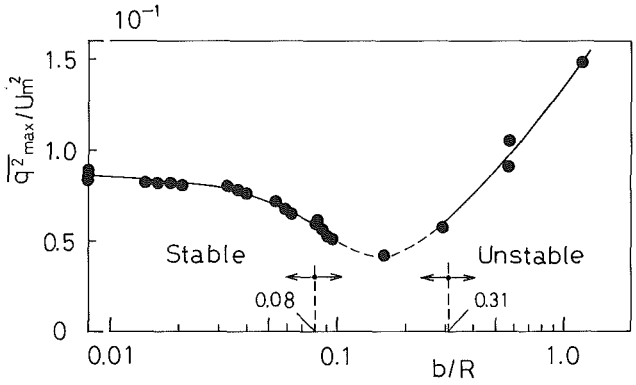


Fig. 2 Variations of maximum turbulence energy $\overline{q^2}$ max/Um^2 with curvature b/R [Re = (6 ~ 9) × 10^4]

Basic Equations

The present coordinate system is adopted as shown in Fig. 1. A two-dimensional incompressible wall jet is directed to the x-axis having a constant radius R of curvature, which is assumed much larger than the half-width b of the wall jet. The shear stress τ in the turbulent wall jet is related to the velocity field with the eddy-viscosity concept. We now suppose that the velocity components u,v,w are slightly perturbed with the type of longitudinal vortices, which are expressed as follows:

$$u = U(y) + \hat{u}(y)e^{\gamma t}\cos\alpha z, \qquad v = \hat{v}(y)e^{\gamma t}\cos\alpha z, \quad w = \hat{w}(y)e^{\gamma t}\sin\alpha z \tag{1}$$

where α is the wavenumber, γ the growth rate of the disturbances, and t the time. Detail formulations of basic equations for the present problem are the same as the ones given in reference [2]. We finally obtained a set of perturbation equations governing the linear stability problem in the neutral state ($\gamma = 0$),

$$M\bar{u}'' + M'\bar{u}' - \sigma^2 M\bar{u} = \bar{U}'\bar{v}, \tag{2}$$

$$M\bar{v}^{(4)} + 2M'\bar{v}''' + (M'' - 2\sigma^2 M)\bar{v}'' - 2\sigma^2 M'\bar{v}' + \sigma^2(M'' + \sigma^2 M)\bar{v} = -2\sigma^2 G^2 \bar{U}\bar{u}, \tag{3}$$

$$\bar{v}' + \sigma\bar{w} = 0, \tag{4}$$

where the primes denote differentiation with respect to η (= y/b). The principle of exchange of stability is used. This has not been proven, but nevertheless is usually assumed based on experimental indications, for Görtler instability. The dimensionless expressions are defined as $\bar{U} = U/Um$, $\bar{u} = \hat{u}/Um$, $\bar{v} = \hat{v}b/\nu$, $\bar{w} = \hat{w}b/\nu$, $\sigma = \alpha b$, $G = Re\sqrt{b/R}$, $Re = Umb/\nu$ and $M = 1 + \epsilon/\nu$ with the kinetic viscosity ν of the fluid and the eddy-viscosity ϵ. Using the definition $\tau_R = \rho\epsilon(dU/dy)$ for the Reynolds stress τ_R. $M(\eta)$ is also written as the relation $M = 1 + Re\tau_R/(\rho Um^2\bar{U}')$, where ρ is the density of the fluid. The boundary conditions are $\bar{u} = \bar{v} = \bar{w} = 0$ at the surface ($\eta = 0$) and also at a point far from the surface ($\eta \to \infty$).

[1]Research Assistant, Department of Mechanical Engineering, Gunma University, Kiryu, Japan.

[2]Professor, Institute of High Speed Mechanics, Tohoku University, Sendai, Japan.

[3]Professor, Department of Mechanical Engineering, Gunma University, Kiryu, Japan.

Manuscript received by ASME Applied Mechanics Division, June, 1984.

Downloaded 02 May 2010 to 171.66.16.54. Redistribution subject to ASME license or copyright; see http://www.asme.org/terms/Terms_Use.cfm

The order of magnitude of β for a realistic material is approximately $10^3 - 10^4$ and hence Barenblatt's assumption of small size of cohesive zone is legitimate.

References

1 Irwin, G. R., "Fracture," *Handbuch der Physik*, S. Flügge, ed., Vol. 4, 1958, pp. 551-590.

2 Barenblatt, G. I., "The Mathematical Theory of Equilibrium Crack in Brittle Fracture," *Advances in Applied Mechanics*, Vol. 7, 1962, pp. 55-129.

3 Rice, J. R., "Mathematical Analysis in the Mechanics of Fracture," *Fracture*, Liebowitz, H., ed., Vol. 2, 1968, pp. 196-311.

4 Bueckner, H. F., "A Novel Principle for the Computation of Stress Intensity Factors," *ZAMM*, Vol. 50, 1970, pp. 529-546.

5 Dugdale, D. S., "Yielding of Steel Sheets Containing Slits," *Journal of Mechanics and Physics of Solids*, Vol. 8, 1960, pp. 100-108.

Centrifugal Instability of Turbulent Wall Jets Along Strongly Concave Surfaces

N. Fujisawa[1], R. Kobayashi[2], and H. Shirai[3]

Introduction

The purpose of this Note is to present a theoretical consideration for Taylor-Görtler centrifugal instability of turbulent wall jets along strongly concave surfaces, as a result of which longitudinal vortices are expected to occur as secondary flow in the wall jets. While the onset of the longitudinal vortices in laminar flows becomes a beginning of laminar-turbulent transition, the centrifugal instability in turbulent flows gives certainly some influences upon transfer phenomena. Tani [1] first found experimentally the longitudinal vortices appearing in turbulent boundary layers along concave walls. For the case of turbulent wall jets (Fig. 1), we predicted theoretically [2] that the centrifugal instability occurs at the critical value $b/R = 0.31$ of the curvature parameter, where R is the radius of curvature on the wall and b the half-width of the wall jet. We found in an experiment done thereafter [3], as shown in Fig. 2, that the intensity of turbulence in the turbulent wall jets rather decreases first as the curvature parameter b/R is increased from zero (flat wall), which comes from the effect on the turbulent field, and that a further increase of b/R beyond about 0.17 results in a remarkable increase of the turbulence intensity in the wall jet. (The deviation from the first tendency of decreasing turbulence intensity is observed to start from b/R of about 0.1.) This increase of the turbulence was explained in relation to the Taylor-Görtler centrifugal instability.

We consider that one of the reasons for the difference of the critical theoretical value $(b/R)cr = 0.31$ from the experimental value 0.1 comes from data of Reynolds stress used in the numerical calculation, in which a distribution of the Reynolds stress across the wall jet was based on the data measured for a case of flat wall. Because our recent systematic experiment on the effect of curvature [4] showed an observable decrease of the Reynolds stress with increasing curvature parameter in a range of $b/R = 0$ to 0.1, we again treat the instability problem in consideration to the variation of the Reynolds stress due to the curvature parameter.

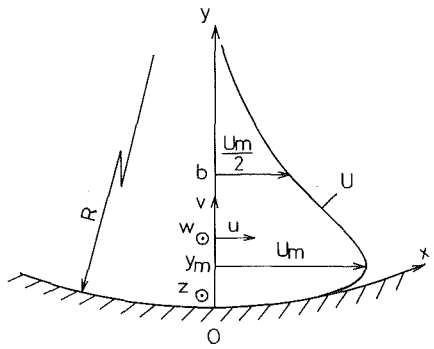


Fig. 1 Wall jet and coordinate system

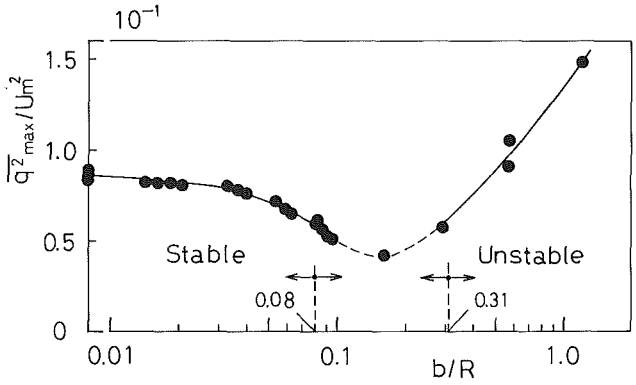


Fig. 2 Variations of maximum turbulence energy $\overline{q^2}$ max/Um^2 with curvature b/R [Re = (6 ~ 9) × 10^4]

Basic Equations

The present coordinate system is adopted as shown in Fig. 1. A two-dimensional incompressible wall jet is directed to the x-axis having a constant radius R of curvature, which is assumed much larger than the half-width b of the wall jet. The shear stress τ in the turbulent wall jet is related to the velocity field with the eddy-viscosity concept. We now suppose that the velocity components u,v,w are slightly perturbed with the type of longitudinal vortices, which are expressed as follows:

$$u = U(y) + \hat{u}(y)e^{\gamma t}\cos\alpha z, \qquad v = \hat{v}(y)e^{\gamma t}\cos\alpha z, \quad w = \hat{w}(y)e^{\gamma t}\sin\alpha z \tag{1}$$

where α is the wavenumber, γ the growth rate of the disturbances, and t the time. Detail formulations of basic equations for the present problem are the same as the ones given in reference [2]. We finally obtained a set of perturbation equations governing the linear stability problem in the neutral state ($\gamma = 0$),

$$M\bar{u}'' + M'\bar{u}' - \sigma^2 M\bar{u} = \bar{U}'\bar{v}, \tag{2}$$

$$M\bar{v}^{(4)} + 2M'\bar{v}''' + (M'' - 2\sigma^2 M)\bar{v}'' - 2\sigma^2 M'\bar{v}' + \sigma^2(M'' + \sigma^2 M)\bar{v} = -2\sigma^2 G^2 \bar{U}\bar{u}, \tag{3}$$

$$\bar{v}' + \sigma\bar{w} = 0, \tag{4}$$

where the primes denote differentiation with respect to η (= y/b). The principle of exchange of stability is used. This has not been proven, but nevertheless is usually assumed based on experimental indications, for Görtler instability. The dimensionless expressions are defined as $\bar{U} = U/Um$, $\bar{u} = \hat{u}/Um$, $\bar{v} = \hat{v}b/\nu$, $\bar{w} = \hat{w}b/\nu$, $\sigma = \alpha b$, $G = Re\sqrt{b/R}$, $Re = Umb/\nu$ and $M = 1 + \epsilon/\nu$ with the kinetic viscosity ν of the fluid and the eddy-viscosity ϵ. Using the definition $\tau_R = \rho\epsilon(dU/dy)$ for the Reynolds stress τ_R. $M(\eta)$ is also written as the relation $M = 1 + Re\tau_R/(\rho Um^2\bar{U}')$, where ρ is the density of the fluid. The boundary conditions are $\bar{u} = \bar{v} = \bar{w} = 0$ at the surface ($\eta = 0$) and also at a point far from the surface ($\eta \to \infty$).

[1]Research Assistant, Department of Mechanical Engineering, Gunma University, Kiryu, Japan.

[2]Professor, Institute of High Speed Mechanics, Tohoku University, Sendai, Japan.

[3]Professor, Department of Mechanical Engineering, Gunma University, Kiryu, Japan.

Manuscript received by ASME Applied Mechanics Division, June, 1984.

Copyright © 1985 by ASME

Downloaded 02 May 2010 to 171.66.16.54. Redistribution subject to ASME license or copyright; see http://www.asme.org/terms/Terms_Use.cfm

Numerical Calculations

The present instability problem is now reduced to find the Görtler parameter G as eigenvalue in the set of perturbation equations (2) to (4) with the numerical parameters σ (the wave number) and Re (the Reynolds number). Experimental results measured in reference [4] were used for the distributions of the velocity $U(y)$ and the Reynolds stress $\tau_R(y)$ across the wall jet in the equations. The experiment for the turbulent wall jets along mildly concave surfaces showed that the velocity profile $\bar{U}(\eta)$ is in agreement with the one of the plane wall jet, while the magnitude $\tau_R/\rho Um^2$ of the Reynolds stress decreases as the curvature is increased. In the present numerical calculations, the distributions of the Reynolds stress were formulated as a function of the curvature b/R, in which the following empirical relation for the maximum Reynolds stress $\tau_{R,\max}$ is used in a range of $b/R = 0$ to 0.1:

$$\tau_{R,\max}/\rho Um^2 = 0.012\,(1 - 5.8\,b/R) \tag{5}$$

The numerical technique for solving the equations (2) to (4) is the same as the one in reference [2].

Results and Discussions

The results of the present numerical calculations showed that the Görtler parameter $G\,(= Re\sqrt{b/R})$ in the neutral state increases with increasing Reynolds number as a function $G \sim Re^n$ with $n = 1.00$ to 1.05 in the calculated range of $Re = 3 \times 10^4$ to 10^6. It can, therefore, be said that the curvature b/R rather than the Görtler parameter G plays an important role in the present instability problem. The numerical results give the critical condition $(b/R)\text{cr} = 0.08$. As seen in Fig. 2, the critical value of 0.08 is apparently much closer to the experimental one 0.1 than the previous theoretical value 0.31. Therefore, the critical curvature obtained from the experiment is in close agreement with the one from the stability theory, when the effect of curvature on the Reynolds stress is included.

References

1 Tani, I., "Production of Longitudinal Vortices in the Boundary Layer Along a Concave Wall," *Journal of Geophysical Research*, Vol. 67, 1962, pp. 3075–3080.

2 Kobayashi, R., and Fujisawa, N., "Taylor-Görtler Instability of Turbulent Wall Jets Along Concave Surfaces, ASME Journal of Applied Mechanics, Vol. 47, 1980, pp. 671–672; Reports of the Institute of High Speed Mechanics, Tohoku University, Vol. 43, 1981, pp. 1–19.

3 Kobayashi, R., and Fujisawa, N., "Turbulence Measurements in Wall Jets Along Strongly Concave Surfaces," *Acta Mechanica*, Vol. 47, 1983, pp. 39–52.

4 Kobayashi, R., and Fujisawa, N., "Curvature Effects on Two-Dimensional Turbulent Wall Jets Along Concave Surfaces," *Bulletin of the JSME*, Vol. 26, 1983, pp. 2074–2080.

On Nonlinear Oscillation of Moving String

K. R. Korde[1]

1 Introduction

The problem of nonlinear oscillation of axially moving string has been extensively studied e.g., [1–3]. Mote [1] used the method of characteristics and demonstrated the importance of nonlinear consideration over the usual linearity assumptions, even for small-amplitude oscillations. In other investigations [2, 3] the authors have used the method of harmonic balance and the Galerkin method, respectively, and obtained the approximate analytical form of period-tension relationship, which did not appear in [1]. Recently Burton [4], and Burton and Hamdan [5], have discussed "Time Transformation Method" for nonlinear oscillation problems. The technique appears to be very elegant for the purpose of evaluation of periodic time of oscillation. In the present Note, we use the time transformation method and ontain the period-amplitude-tension relationship for the problem of axially moving string. Ames [6, p. 466] has considered the nonlinear oscillation of moving thread line. Of the three cases he considers, two are amenable for solutions by the present method. Approximate form of periodic time in each case is also obtained. It may be mentioned that in the present Note only the fundamental mode is being analyzed.

2 Outline of Time Transformation Method [4, 5]

We find the transformation between the time t and a "new time" T such that in the T domain the motion is simple harmonic. The time transformation is determined by first rewriting the governing differential equation in the T domain and then solving for the derivative $F(T) \equiv dT/dt$ of the transformation, with $T(0) = 0$. Once $F(T)$ has been found, the period τ is obtained by performing the integration from 0 to 2τ in T,

$$\tau = \int_0^{2\pi} \frac{dT}{F(T)} \tag{1}$$

3 Axially Moving String:

Referring to [1], the equation governing the nonlinear oscillation of a moving string is

$$W_{tt} + 2\beta W_{xt} - (1 - \beta^2) W_{xx} = K W_x^2 W_{xx} \tag{2}$$

with

$$K = \frac{3}{2\alpha^2}$$

with boundary conditions

$$W(0,t) = W(1,t) = 0$$

where

x is nondimensional axial coordinate,
t is nondimensional time,
β is nondimensional axial velocity,
α is nondimensional initial tension, and
$W(x,t)$ is the nondimensional transverse displacement of string.

On applying time transformation technique as described in Section 2,

we write

$$W_t = F\ W_T, \quad W_{tt} = F^2 W_{TT} + FF' W_T,$$
$$W_{xt} = F\ W_{xT},$$

where prime denotes the differentiation with respect to T. Equation (2) then becomes

$$F^2 W_{TT} + FF' W_T + 2\beta F\ W_{xT} - (1 - \beta^2) W_{xx} = K\ W_x^2 W_{xx} \tag{3}$$

We choose $W(x,T) = A \sin \pi x \operatorname{Cos} T$ in (3) and obtain

$$F^2 A \operatorname{Sin}\pi x \operatorname{Cos} T + FF' A \operatorname{Sin}\pi x \operatorname{Sin} T + 2\beta FA\pi \operatorname{Cos}\pi x \operatorname{Sin} T + (1 - \beta^2)(-A\pi^2 \operatorname{Sin}\pi x \operatorname{Cos} T) = \frac{K\ A^3 \pi^4}{4} [\operatorname{Sin}\pi x + \operatorname{Sin} 3\pi x] \operatorname{Cos}^3 T$$

To eliminate the spatial part in this equation, we make use of

[1]Department of Mathematics, V. Regional College of Engineering, Nagpur, India 440011.

Manuscript received by ASME Applied Mechanics Division, March, 1984; final revision, November, 1984.

Downloaded 02 May 2010 to 171.66.16.54. Redistribution subject to ASME license or copyright; see http://www.asme.org/terms/Terms_Use.cfm

Numerical Calculations

The present instability problem is now reduced to find the Görtler parameter G as eigenvalue in the set of perturbation equations (2) to (4) with the numerical parameters σ (the wave number) and Re (the Reynolds number). Experimental results measured in reference [4] were used for the distributions of the velocity $U(y)$ and the Reynolds stress $\tau_R(y)$ across the wall jet in the equations. The experiment for the turbulent wall jets along mildly concave surfaces showed that the velocity profile $\bar{U}(\eta)$ is in agreement with the one of the plane wall jet, while the magnitude $\tau_R/\rho Um^2$ of the Reynolds stress decreases as the curvature is increased. In the present numerical calculations, the distributions of the Reynolds stress were formulated as a function of the curvature b/R, in which the following empirical relation for the maximum Reynolds stress $\tau_{R,\max}$ is used in a range of $b/R = 0$ to 0.1:

$$\tau_{R,\max}/\rho Um^2 = 0.012\,(1 - 5.8\,b/R) \tag{5}$$

The numerical technique for solving the equations (2) to (4) is the same as the one in reference [2].

Results and Discussions

The results of the present numerical calculations showed that the Görtler parameter $G\,(= Re\sqrt{b/R})$ in the neutral state increases with increasing Reynolds number as a function $G \sim Re^n$ with $n = 1.00$ to 1.05 in the calculated range of $Re = 3 \times 10^4$ to 10^6. It can, therefore, be said that the curvature b/R rather than the Görtler parameter G plays an important role in the present instability problem. The numerical results give the critical condition $(b/R)\text{cr} = 0.08$. As seen in Fig. 2, the critical value of 0.08 is apparently much closer to the experimental one 0.1 than the previous theoretical value 0.31. Therefore, the critical curvature obtained from the experiment is in close agreement with the one from the stability theory, when the effect of curvature on the Reynolds stress is included.

References

1 Tani, I., "Production of Longitudinal Vortices in the Boundary Layer Along a Concave Wall," *Journal of Geophysical Research*, Vol. 67, 1962, pp. 3075–3080.

2 Kobayashi, R., and Fujisawa, N., "Taylor-Görtler Instability of Turbulent Wall Jets Along Concave Surfaces, ASME Journal of Applied Mechanics, Vol. 47, 1980, pp. 671–672; Reports of the Institute of High Speed Mechanics, Tohoku University, Vol. 43, 1981, pp. 1–19.

3 Kobayashi, R., and Fujisawa, N., "Turbulence Measurements in Wall Jets Along Strongly Concave Surfaces," *Acta Mechanica*, Vol. 47, 1983, pp. 39–52.

4 Kobayashi, R., and Fujisawa, N., "Curvature Effects on Two-Dimensional Turbulent Wall Jets Along Concave Surfaces," *Bulletin of the JSME*, Vol. 26, 1983, pp. 2074–2080.

On Nonlinear Oscillation of Moving String

K. R. Korde[1]

1 Introduction

The problem of nonlinear oscillation of axially moving string has been extensively studied e.g., [1–3]. Mote [1] used the method of characteristics and demonstrated the importance of nonlinear consideration over the usual linearity assumptions, even for small-amplitude oscillations. In other investigations [2, 3] the authors have used the method of harmonic balance and the Galerkin method, respectively, and obtained the approximate analytical form of period-tension relationship, which did not appear in [1]. Recently Burton [4], and Burton and Hamdan [5], have discussed "Time Transformation Method" for nonlinear oscillation problems. The technique appears to be very elegant for the purpose of evaluation of periodic time of oscillation. In the present Note, we use the time transformation method and ontain the period-amplitude-tension relationship for the problem of axially moving string. Ames [6, p. 466] has considered the nonlinear oscillation of moving thread line. Of the three cases he considers, two are amenable for solutions by the present method. Approximate form of periodic time in each case is also obtained. It may be mentioned that in the present Note only the fundamental mode is being analyzed.

2 Outline of Time Transformation Method [4, 5]

We find the transformation between the time t and a "new time" T such that in the T domain the motion is simple harmonic. The time transformation is determined by first rewriting the governing differential equation in the T domain and then solving for the derivative $F(T) \equiv dT/dt$ of the transformation, with $T(0) = 0$. Once $F(T)$ has been found, the period τ is obtained by performing the integration from 0 to 2τ in T,

$$\tau = \int_0^{2\pi} \frac{dT}{F(T)} \tag{1}$$

3 Axially Moving String:

Referring to [1], the equation governing the nonlinear oscillation of a moving string is

$$W_{tt} + 2\beta W_{xt} - (1 - \beta^2) W_{xx} = K W_x^2 W_{xx} \tag{2}$$

with

$$K = \frac{3}{2\alpha^2}$$

with boundary conditions

$$W(0,t) = W(1,t) = 0$$

where

x is nondimensional axial coordinate,
t is nondimensional time,
β is nondimensional axial velocity,
α is nondimensional initial tension, and
$W(x,t)$ is the nondimensional transverse displacement of string.

On applying time transformation technique as described in Section 2,

we write

$$W_t = F\ W_T, \quad W_{tt} = F^2 W_{TT} + FF' W_T,$$
$$W_{xt} = F\ W_{xT},$$

where prime denotes the differentiation with respect to T. Equation (2) then becomes

$$F^2 W_{TT} + FF' W_T + 2\beta F\ W_{xT} - (1 - \beta^2) W_{xx} = K\ W_x^2 W_{xx} \tag{3}$$

We choose $W(x,T) = A \sin \pi x \cos T$ in (3) and obtain

$$F^2 A \operatorname{Sin}\pi x \operatorname{Cos} T + FF' A \operatorname{Sin}\pi x \operatorname{Sin} T + 2\beta FA\pi \operatorname{Cos}\pi x \operatorname{Sin} T + (1 - \beta^2)(-A\pi^2 \operatorname{Sin}\pi x \operatorname{Cos} T) = \frac{K\ A^3 \pi^4}{4} [\operatorname{Sin}\pi x + \operatorname{Sin} 3\pi x] \operatorname{Cos}^3 T$$

To eliminate the spatial part in this equation, we make use of

[1]Department of Mathematics, V. Regional College of Engineering, Nagpur, India 440011.

Manuscript received by ASME Applied Mechanics Division, March, 1984; final revision, November, 1984.

Copyright © 1985 by ASME
Downloaded 02 May 2010 to 171.66.16.54. Redistribution subject to ASME license or copyright; see http://www.asme.org/terms/Terms_Use.cfm

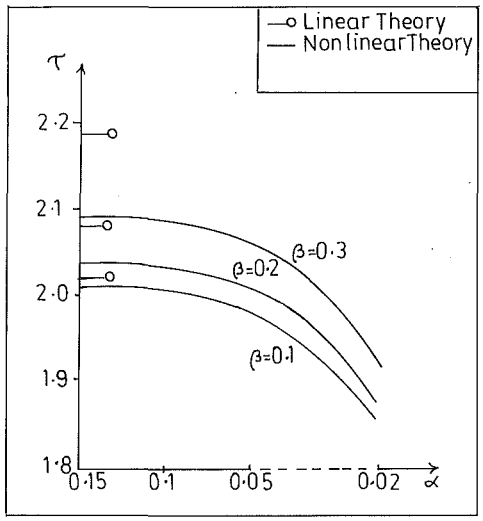


Figure - 1
Period of oscillation as a function of non dimensional tension α, Eq^n (6)

Fig. 1 Period of oscillation as a function of nondimensional tension α equation (6)

the well-known method of harmonic balance, i.e., compare the coefficient of sin πx and obtain

$$FF'\mathrm{Sin}T+F^2\mathrm{Cos}T=p\mathrm{Cos}^3T+q\mathrm{Cos}T \tag{4}$$

where $p=K\ A^2\pi^4/4$, $q=(1-\beta^2)\pi^2$

Substituting $F^2 = V$ in (4), it becomes

$$\frac{dV}{dT}+\frac{2\mathrm{Cos}T}{\mathrm{Sin}T}v=\frac{2(p\mathrm{Cos}^3T+g\mathrm{Cos}T)}{\mathrm{Sin}T}$$

This equation on integration yields

$$V\mathrm{Sin}^2T=2\int_0^T(p\mathrm{Cos}^3y+q\mathrm{Cos}\ y)\mathrm{Sin}\ y\ dy$$

or

$$F^2 = V=\frac{p}{2}(1+\mathrm{Cos}^2T)+q$$

or

$$F = \left(q+\frac{3p}{4}\right)^{1/2}(1+R\mathrm{Cos}2T)^{1/2} \tag{5}$$

where $R=p/4q+3p$, so that $R<1/3$

Hence from equation (1), the periodic time of oscillation

$$\tau = \int_0^{2\pi}\frac{dT}{F(T)}=\left(q+\frac{3p}{4}\right)^{-1/2}\int_0^{2\pi}(1+R\mathrm{Cos}2T)^{-1/2}dT$$

$$= \frac{4\pi}{(4q+3p)}\left[1+\frac{3}{16}R^2+0(R^4)\right]$$

or

$$\tau = \frac{4\pi}{(4q+3p)^{1/2}}\left[1+\frac{3p^2}{16(4q+3p)^2}\right] \tag{6}$$

To plot the period-tension relationship, we choose $A=0.005$ in (6). The graphs agree closely with those obtained in [1, 3]. The linear fundamental period $\tau_L = 2/(1-\beta^2)$ is also shown in the graph. Figure 1 indicates the reduction of period as predicted by Mote [1]. It can be seen that the leading factor in equation (6), i.e., the term $4\pi/(4q+3p)^{1/2}$, is identical to the formula obtained by Bapat and Srinivasan ([2], equation (9)). The additional factor in equation (6), i.e., the term $[1+3/16R^2+0(R^4)]$, therefore represents a correction to the previous result, to the extent that it deviates from unity.

4 Nonlinear Case I [6, p. 466]

The nonlinear equation governing the transverse oscillation of a moving thread line is taken in the form

$$\frac{\alpha^2}{4}W_{xx}+\alpha W_{xt}+W_{tt}=W_{xx}(1+W_x^2)^{-1/2} \tag{7}$$

with the boundary conditions

$$W(0,t)=W(1,t)=0$$

Equation (7) is approximated as

$$\left(\frac{\alpha^2}{4}-1\right)W_{xx}+\alpha W_{xt}+W_{tt}+\frac{1}{2}W_x^2W_{xx}=0$$

Applying the time transformation technique, the period is given by (6),

where $$p=-\frac{A^2\pi^4}{8},q=\pi^2\left(1-\frac{\alpha^2}{4}\right)$$

5 Nonlinear Case II [6, p. 466]

In this case the governing equation is taken in the form

$$\frac{\alpha^2}{4}V^2W_{xx}+\alpha V\ W_{xt}+W_{tt}=\frac{W_{xx}}{1+W_x^2} \tag{8}$$

where $V=(1+W_x^2)^{-1/2}$ on substituting V into (8) and assuming $W_x^2<1$, we obtain

$$\left(\frac{\alpha^2}{4}-1\right)(1-W_x^2)+\alpha W_{xt}\left(1-\frac{1}{2}W_x^2\right)+W_{tt}=0$$

with the same boundary conditions as in Case I. The period is given by (6)

where

$$p=\left(\frac{\alpha^2}{4}-1\right)\frac{A^2\pi^4}{4},q=\pi^2\left(1-\frac{\alpha^2}{4}\right)$$

Acknowledgments

The author is thankful to Dr. S. G. Ghangrekar, Department of Mathematics, V. Regional College of Engineering, Nagpur, India for his guidance and valuable suggestions, and to one of the reviewers for some helpful suggestions.

References

1 Mote, C. D., Jr., "On Nonlinear Oscillation of an Axially Moving String," ASME Journal of Applied Mechanics, Vol. 88, 1966, pp. 463-464.

2 Bapat, V. A., and Srinivasan, P., "Nonlinear Transverse Oscillations in Traveling String by the Method of Harmonic Balance," ASME Journal of Applied Mechanics, Vol. 89, 1967, pp. 775-777.

3 Ghangrekar, S. G., "On Nonlinear Oscillation of Moving String," Labdev J. of Sci. and Tech: Physical Sciences, Vol. 13-A (1975), pp. 255-257.

4 Burton, T. D., "Nonlinear Oscillator Limit Cycle Analysis Using a Time Transformation Approach," *Int. J. Nonlinear Mechanics*, Vol. 17, No. 1, 1982, pp. 7-19.

5 Burton, T. D., and Hamdan, M. N., "Analysis of Nonlinear Autonomous Conservative Oscillators by a Time Transformation Method," *Journal of Sound and Vibration*, Vol. 87, No. 4, 1983, pp. 543-554.

6 Ames, W. F., *Nonlinear Partial Differential Equations in Engineering*," Academic Press, New York, 1965.

Thermally Induced Roof Noise

C. H. Ellen[1], C. V. Tu[1], and W. Y. D., Yuen[1]

1 Introduction

It is well-known that the heating and cooling of sheet metal

[1]Research Manager, Engineering and Physics, Research Officer, and Senior Research Officer, respectively, Research and Technology Centre of John Lysaght (Australia) Limited, Port Kembla, Australia, NSW 2505.

Manuscript received by ASME Applied Mechanics Division, November, 1984.

Downloaded 02 May 2010 to 171.66.16.54. Redistribution subject to ASME license or copyright; see http://www.asme.org/terms/Terms_Use.cfm

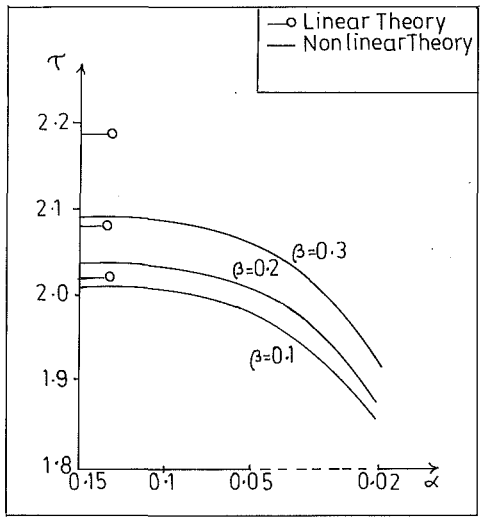


Figure - 1
Period of oscillation as a function of non dimensional tension α, Eq^n (6)

Fig. 1 Period of oscillation as a function of nondimensional tension α equation (6)

the well-known method of harmonic balance, i.e., compare the coefficient of sin πx and obtain

$$FF' \mathrm{Sin}T + F^2 \mathrm{Cos}T = p\mathrm{Cos}^3 T + q\mathrm{Cos}T \tag{4}$$

where $p = K\ A^2\pi^4/4$, $q = (1-\beta^2)\pi^2$

Substituting $F^2 = V$ in (4), it becomes

$$\frac{dV}{dT} + \frac{2\mathrm{Cos}T}{\mathrm{Sin}T} v = \frac{2(p\mathrm{Cos}^3 T + g\mathrm{Cos}T)}{\mathrm{Sin}T}$$

This equation on integration yields

$$V\mathrm{Sin}^2 T = 2\int_0^T (p\mathrm{Cos}^3 y + q\mathrm{Cos}\ y)\mathrm{Sin}\ y\ dy$$

or

$$F^2 = V = \frac{p}{2}(1+\mathrm{Cos}^2 T) + q$$

or

$$F = \left(q + \frac{3p}{4}\right)^{1/2} (1 + R\mathrm{Cos}2T)^{1/2} \tag{5}$$

where $R = p/4q + 3p$, so that $R < 1/3$

Hence from equation (1), the periodic time of oscillation

$$\tau = \int_0^{2\pi} \frac{dT}{F(T)} = \left(q + \frac{3p}{4}\right)^{-1/2} \int_0^{2\pi} (1 + R\mathrm{Cos}2T)^{-1/2} dT$$

$$= \frac{4\pi}{(4q+3p)} \left[1 + \frac{3}{16} R^2 + 0(R^4)\right]$$

or

$$\tau = \frac{4\pi}{(4q+3p)^{1/2}} \left[1 + \frac{3p^2}{16(4q+3p)^2}\right] \tag{6}$$

To plot the period-tension relationship, we choose $A = 0.005$ in (6). The graphs agree closely with those obtained in [1, 3]. The linear fundamental period $\tau_L = 2/(1-\beta^2)$ is also shown in the graph. Figure 1 indicates the reduction of period as predicted by Mote [1]. It can be seen that the leading factor in equation (6), i.e., the term $4\pi/(4q+3p)^{1/2}$, is identical to the formula obtained by Bapat and Srinivasan ([2], equation (9)). The additional factor in equation (6), i.e., the term $[1 + 3/16R^2 + 0(R^4)]$, therefore represents a correction to the previous result, to the extent that it deviates from unity.

4 Nonlinear Case I [6, p. 466]

The nonlinear equation governing the transverse oscillation of a moving thread line is taken in the form

$$\frac{\alpha^2}{4} W_{xx} + \alpha W_{xt} + W_{tt} = W_{xx}(1 + W_x^2)^{-1/2} \tag{7}$$

with the boundary conditions

$$W(0,t) = W(1,t) = 0$$

Equation (7) is approximated as

$$\left(\frac{\alpha^2}{4} - 1\right) W_{xx} + \alpha W_{xt} + W_{tt} + \frac{1}{2} W_x^2 W_{xx} = 0$$

Applying the time transformation technique, the period is given by (6),

where $$p = -\frac{A^2\pi^4}{8}, q = \pi^2\left(1 - \frac{\alpha^2}{4}\right)$$

5 Nonlinear Case II [6, p. 466]

In this case the governing equation is taken in the form

$$\frac{\alpha^2}{4} V^2 W_{xx} + \alpha V\ W_{xt} + W_{tt} = \frac{W_{xx}}{1 + W_x^2} \tag{8}$$

where $V = (1 + W_x^2)^{-1/2}$ on substituting V into (8) and assuming $W_x^2 < 1$, we obtain

$$\left(\frac{\alpha^2}{4} - 1\right)(1 - W_x^2) + \alpha W_{xt}\left(1 - \frac{1}{2} W_x^2\right) + W_{tt} = 0$$

with the same boundary conditions as in Case I. The period is given by (6)

where

$$p = \left(\frac{\alpha^2}{4} - 1\right)\frac{A^2\pi^4}{4}, q = \pi^2\left(1 - \frac{\alpha^2}{4}\right)$$

Acknowledgments

The author is thankful to Dr. S. G. Ghangrekar, Department of Mathematics, V. Regional College of Engineering, Nagpur, India for his guidance and valuable suggestions, and to one of the reviewers for some helpful suggestions.

References

1 Mote, C. D., Jr., "On Nonlinear Oscillation of an Axially Moving String," ASME Journal of Applied Mechanics, Vol. 88, 1966, pp. 463-464.

2 Bapat, V. A., and Srinivasan, P., "Nonlinear Transverse Oscillations in Traveling String by the Method of Harmonic Balance," ASME Journal of Applied Mechanics, Vol. 89, 1967, pp. 775-777.

3 Ghangrekar, S. G., "On Nonlinear Oscillation of Moving String," Labdev J. of Sci. and Tech: Physical Sciences, Vol. 13-A (1975), pp. 255-257.

4 Burton, T. D., "Nonlinear Oscillator Limit Cycle Analysis Using a Time Transformation Approach," *Int. J. Nonlinear Mechanics*, Vol. 17, No. 1, 1982, pp. 7-19.

5 Burton, T. D., and Hamdan, M. N., "Analysis of Nonlinear Autonomous Conservative Oscillators by a Time Transformation Method," *Journal of Sound and Vibration*, Vol. 87, No. 4, 1983, pp. 543-554.

6 Ames, W. F., *Nonlinear Partial Differential Equations in Engineering*," Academic Press, New York, 1965.

Thermally Induced Roof Noise

C. H. Ellen[1], C. V. Tu[1], and W. Y. D., Yuen[1]

1 Introduction

It is well-known that the heating and cooling of sheet metal

[1]Research Manager, Engineering and Physics, Research Officer, and Senior Research Officer, respectively, Research and Technology Centre of John Lysaght (Australia) Limited, Port Kembla, Australia, NSW 2505.

Manuscript received by ASME Applied Mechanics Division, November, 1984.

Copyright © 1985 by ASME
Downloaded 02 May 2010 to 171.66.16.54. Redistribution subject to ASME license or copyright; see http://www.asme.org/terms/Terms_Use.cfm

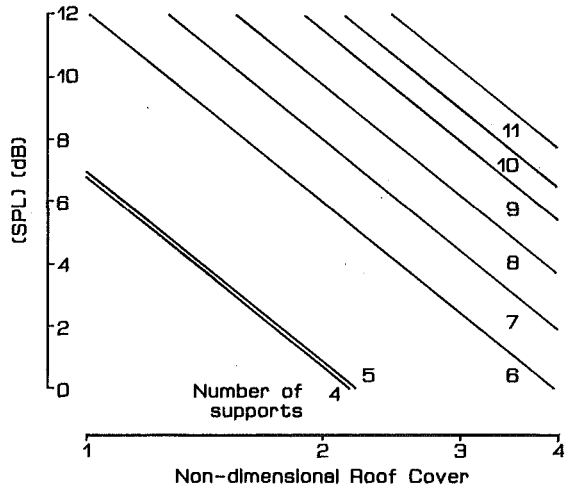


Fig. 1 The effect on the noise level of changing the number of battens supporting a roof

cladding on roofs and walls often cause noise. Although certain roofs appear to be more noisy than others, there seems to be no previous analysis of the phenomena involved that might provide roof noise design criteria.

It is possible to explain thermally induced roof noise on the basis of slip/stick behavior at the cladding supports. Modern roofing is typically supplied in long sheet lengths which are fastened to supporting battens, or purlins, at a number of intermediate positions along their length. When the thermal balance of the sheeting is disturbed by cloud shadows interrupting the solar energy input or by wind gusts altering the cooling rate, temperature changes are induced in the roof sheeting. These changes would cause small length changes in the sheeting if it were not restrained by the fasteners. The main restraining effect, against expansion or contraction of the sheeting, is due to frictional forces between the sheeting and battens caused by the fasteners pressing the sheeting against the battens. Thus, temperature changes induce thermal stresses that build up until one of the friction forces at a fastener exceeds the static frictional limit. When this occurs the roof slips locally, the roof deflection pattern changes, and the thermal forces are redistributed, possibly overloading another fastener frictional force and causing a further slip. Although the mechanism is essentially a dynamic one, a quasistatic analysis may be made, i.e., the temperature rise sufficient to take fastener frictional forces to their static limit is calculated, the change in deflection pattern determined when the frictional force is changed to the lower dynamic limit, and the sound energy estimated from a piston motion formula. It is only through this slip/stick feature that changes on an acoustic time scale are introduced to a system that is, otherwise, changing at a much slower rate.

2 Theory

With a roof in equilibrium, it is obvious that a temperature rise will cause changes in the in-plane forces but that the frictional forces at each support will remain unchanged except at the end supports. Therefore no slips will be initiated until the temperature rise is sufficient to cause the frictional force at the outermost supports to exceed the limiting static value. The displacement due to the resulting slip will equal $\Delta Fs/(Ehr)$ where ΔF is the frictional force change per unit width of roof, s is the span of the outer panel that has slipped, E is the elastic modulus of the roof material, h is the thickness of the roof sheeting, and r is the ratio of the roof profile integral length to surface cover.

Consider, for simplicity, that the roof structure is symmetrical, with equal spans between supports and equal fastener effects, and, therefore, that the displacement occurs at both ends simultaneously. Furthermore, it is then possible to show that, once a sufficiently large temperature rise has occurred, the roof slip pattern becomes cyclical with a sequence of slip cascades, each penetrating inward to one less support than the cascade before until only the outer two supports slip after which the next cascade involves slips at all supports, except the center support, if there is an even number of supports, or the center two supports if there is an odd number of supports. Therefore, to complete a cycle on a roof with N supports there are $N/2-1$ (N even), or $(N-3)/2$ (N odd), slip cascades and each cascade has associated with it a displacement of the roof at each outer support of $\Delta Fs/(Ehr)$. Since, at the end of a cycle, the roof is in the same state as it was originally, it is possible to equate the sum of the end slip displacements to the total outward movement derived on the basis of the thermal expansion of the roof, $(N-1)s\alpha\Delta T_c$, where α is the coefficient of thermal expansion and ΔT_c is the cycle temperature increment, in order to obtain an expression for the temperature rise associated with a cycle of roof thermal slip cascades. Since a noise burst is associated with each slip cascade, the rate, R, of noise bursts (cascades per unit temperature change) is given by

$$R=\{(N-1)/2\}\alpha Ehr/\Delta F, \qquad \text{where} \quad \Delta F=F_s-F_d, \qquad (1)$$

ie the difference between the static and dynamic frictional forces at each fastener.

An expression for the temperature change necessary to cause a roof to change from cycling during heating to cycling during cooling (or vice versa) may be obtained from reasoning similar to that employed in the derivation of equation (1). For a roof with N supports , $N/2-1$ (N even), or $(N-1)/2$(N odd), fastener forces must be reversed on each side of the mid-span position by the temperature reversal before cycling in the opposite direction is set up. Each fastener force is, therefore, changed by an average of F_s+F_d and, therefore, the force on the innermost spans changes by $(N/2-1)(F_s+F_d)$(N even) or on the innermost span by $\{(N-1)/2\}(F_s+F_d)$(N odd). It can be shown, from a detailed analysis of the slip sequence, that the innermost fastener will not slip during this load reversal phase and, thus, if the change of strain on the innermost span is equated to the thermal strain associated with the heating to cooling temperature change, ΔT_{HC}, then

$$\Delta T_{HC}=\begin{cases}(N/2-1)(F_s+F_d)/(\alpha Ehr) & \text{for } N \text{ even}\\ \{(N-1)/2\}(F_s+F_d)/(\alpha Ehr) & \text{for } N \text{ odd.}\end{cases} \qquad (2)$$

The change in the average value of the transverse displacement of a roof panel caused by a change, ΔF, in the compressive force, F, which is applied at an eccentric distance f from the neutral plane of the panel with flexural rigidity EI per unit width, is given by $\Delta Fsf/(12EI)$, if F is small. The radiated sound power may be related to this displacement and a time scale associated with the fundamental frequency of the panel, $\{EI/(ms^4)\}^{1/2}$ where m is its mass per unit area, to give an expression for the relative sound pressure level, in dB, as

$$SPL=20\log\{\Delta Ff/(ms)\}+\text{constant}. \qquad (3)$$

Although equation (3) has been derived for a single span it may be shown that the functional form of a multispan roof is the same. The numerical difference, depending on the number of spans, may be found by solving the problem in more detail. In the interest of brevity the results only will be quoted herein. For roofs of the same type and distance between battens, but having an increasing number of spans the SPL, determined by equation (3), should be adjusted by 0, −9, 1, −1, 2, 2, 3, 3, 3, and 4 dB for $N=2$ to 11, respectively.

Because of the characteristics of the acoustic problem, only

Downloaded 02 May 2010 to 171.66.16.54. Redistribution subject to ASME license or copyright; see http://www.asme.org/terms/Terms_Use.cfm

the broad features of the noise level *changes* can be predicted by equation (3). Even these predictions may be distorted by other features of the roof which have not been included in the acoustic description. Such features might include the ceiling transmission loss, acoustic absorption within the roof space due to mineral wool thermal insulation, and the resonances of the roof space and the receiving area or rooms below it.

3 Applications of the Theory

The theory presented in Section 2 leads to a description of the slip characteristics of roofing which is subject to temperature changes as might be caused by natural heating and cooling effects on the exterior of a building. Questions often arise as to ways in which the thermally induced noise may be reduced. These may be addressed by examining the parameter dependence in equation (1), which relates to the rate of noise bursts; in equation (2) which gives the temperature change necessary to change from slip "cycling" in one direction to "cycling" in the other (expansion to contraction or vice versa), and in equation (3), which gives an estimate of the level of the impulsive noise created during a slip cascade. It should be noted that, in these expressions, $F_s - F_d$ and $F_s + F_d$, are, respectively, the difference and sum of the actual frictional forces per unit width caused by the fastener attachment at each batten. Thus, for example, if roof sheeting is fixed by fasteners at each rib, these quantities will be twice as large as they would be for a roof that is fastened on every second rib (a 6 dB increase in noise levels).

From the derived expressions it can be seen that the difference in static and dynamic frictional forces is important in determining the rate of noise bursts and their associated noise levels. The inverse relationship simply reflects that fact that the more frequent the slipping the smaller the energy build-up and subsequent release as noise. The static and dynamic coefficients of friction between metal sheeting and dry timber battens are typically 0.3 and 0.2, respectively, but would rise to 0.5 and 0.25 if the timber were damp or resinous. Therefore, in otherwise identical roofs, the rate of noise bursts for damp timber battens is predicted to be just under half that for dry timber battens; the noise level, on the other hand, is predicted to be 8 dB higher. This, as was indicated at the end of the previous paragraph, would be slightly worse than the effect caused by doubling the number of fasteners along each batten. It is also of interest to note that the interval between noise bursts caused by temperature reversal effects would be increased by 50 percent if timber battens were damp.

The deeper the profile, the larger the values of r and f, and, therefore, the rate and level of noise bursts. The noise levels are predicted to reduce as the span increases although the rate of noise bursts and the interval characterizing reversal effects remain unaltered. For a roof with a given cover, a reduction in the number of battens and, therefore, an increase in each span will decrease the noise level due to (*i*) the rediction in N (for $N>4$; see value given after equation (3)) and, (*ii*) the increase in s (which gives a 6 dB reduction for each doubling of s): the combined effects are illustrated in Fig. 1.

It is of interest to note that if typical values are substituted into equation (2),a 5°C temperature difference is predicted to be necessary before noise bursts occur. With a temperature cooling rate of 1/3°C/s, typical of cooling rates caused by cloud shadows on sunny days, a 15 s delay would occur before noise is heard: this is of the same magnitude as that often observed.

A number of detailed experiments was conducted to test the validity of the theoretical predictions. Although space requirements preclude a description of these, it is worth recording that the experimental findings were in agreement with the theory. In addition, a number of remedial treatments based on the theory has now been carried out to roofs that were considered to be excessively noisy. In all cases the treatments were successful.

Acknowledgment

The authors wish to thank the management of John Lysaght (Australia) Limited for permission to publish this paper.

Unsteady Nonsimilar Laminar Incompressible Boundary-Layer Flow Over a Yawed Infinite Circular Cylinder

R. Vasantha[1] and G. Nath[1]

Introduction

The accurate prediction of flow field over a yawed infinite circular cylinder finds application in the design of aeroplane wings. The steady nonsimilar flow over a yawed infinite circular cylinder has been studied by several investigators [1-3] in the past. However, in most practical situations, the flow may be unsteady. The unsteady flow over a yawed infinite circular cylinder has not been considered in the literature except in the stagnation region [4].

The aim of this Note is to present the results for an unsteady incompressible nonsimilar flow over a yawed infinite circular cylinder when the free stream velocity varies arbitrarily with time. The governing partial differential equations with three independent variables have been solved numerically using an implicit finite-difference scheme in combination with the quasilinearization technique [5]. The results have been compared with those available in the literature.

Governing Equations

The unsteady laminar incompressible boundary-layer flow over a yawed infinite circular cylinder is considered. It is assumed that the chordwise external velocity varies both with streamwise coordinate and time, whereas spanwise velocity varies only with time, and cylinder surface is assumed to be at a constant, given temperature. The boundary layer equations governing the flow can be expressed as

$$u_x + u_y = 0 \tag{1a}$$

$$u_t + uu_x + vu_y = (u_e)_t + u_e(u_e)_x + \nu u_{yy} \tag{1b}$$

$$w_t + uw_x + vw_y = (w_e)_t + \nu w_{yy} \tag{1c}$$

$$T_t + uT_x + vT_y = (k/\rho c_p)T_{yy} + (\nu/c_p)(u_y^2 + w_y^2) \tag{1d}$$

We apply the following transformations

$$\left.\begin{aligned} &\xi = \rho\mu\int_0^x u_s dx,\ \eta = u_s(2\xi)^{-1/2}y \\ &t^* = U_\infty R^{-1}t,\ \psi(x,y,t) = (2\xi)^{1/2}\varphi(t^*)f(\xi,\eta,t^*) \end{aligned}\right\} \tag{2a}$$

$$\left.\begin{aligned} &u = \psi_y,\ v = -\psi_x \\ &u = u_e F(\xi,\eta,t^*),\ f' = F,\ w = w_e S(\xi,\eta,t^*) \\ &v = -\mu u_s \varphi(t^*)(2\xi)^{1/2}[f_g + (f/2\xi)] \\ &u_e = u_s(x)\varphi(t^*),\ w_e = w_\infty \varphi(t^*) \end{aligned}\right\} \tag{2b}$$

[1]Research Scholar, and Professor, respectively, Department of Applied Mathematics, Indian Institute of Science, Bangalore-560012, India.

Manuscript received by the Applied Mechanics Division, May, 1984; Final revision, November, 1984.

Downloaded 02 May 2010 to 171.66.16.54. Redistribution subject to ASME license or copyright; see http://www.asme.org/terms/Terms_Use.cfm

the broad features of the noise level *changes* can be predicted by equation (3). Even these predictions may be distorted by other features of the roof which have not been included in the acoustic description. Such features might include the ceiling transmission loss, acoustic absorption within the roof space due to mineral wool thermal insulation, and the resonances of the roof space and the receiving area or rooms below it.

3 Applications of the Theory

The theory presented in Section 2 leads to a description of the slip characteristics of roofing which is subject to temperature changes as might be caused by natural heating and cooling effects on the exterior of a building. Questions often arise as to ways in which the thermally induced noise may be reduced. These may be addressed by examining the parameter dependence in equation (1), which relates to the rate of noise bursts; in equation (2) which gives the temperature change necessary to change from slip "cycling" in one direction to "cycling" in the other (expansion to contraction or vice versa), and in equation (3), which gives an estimate of the level of the impulsive noise created during a slip cascade. It should be noted that, in these expressions, $F_s - F_d$ and $F_s + F_d$, are, respectively, the difference and sum of the actual frictional forces per unit width caused by the fastener attachment at each batten. Thus, for example, if roof sheeting is fixed by fasteners at each rib, these quantities will be twice as large as they would be for a roof that is fastened on every second rib (a 6 dB increase in noise levels).

From the derived expressions it can be seen that the difference in static and dynamic frictional forces is important in determining the rate of noise bursts and their associated noise levels. The inverse relationship simply reflects that fact that the more frequent the slipping the smaller the energy build-up and subsequent release as noise. The static and dynamic coefficients of friction between metal sheeting and dry timber battens are typically 0.3 and 0.2, respectively, but would rise to 0.5 and 0.25 if the timber were damp or resinous. Therefore, in otherwise identical roofs, the rate of noise bursts for damp timber battens is predicted to be just under half that for dry timber battens; the noise level, on the other hand, is predicted to be 8 dB higher. This, as was indicated at the end of the previous paragraph, would be slightly worse than the effect caused by doubling the number of fasteners along each batten. It is also of interest to note that the interval between noise bursts caused by temperature reversal effects would be increased by 50 percent if timber battens were damp.

The deeper the profile, the larger the values of r and f, and, therefore, the rate and level of noise bursts. The noise levels are predicted to reduce as the span increases although the rate of noise bursts and the interval characterizing reversal effects remain unaltered. For a roof with a given cover, a reduction in the number of battens and, therefore, an increase in each span will decrease the noise level due to (*i*) the rediction in N (for $N>4$; see value given after equation (3)) and, (*ii*) the increase in s (which gives a 6 dB reduction for each doubling of s): the combined effects are illustrated in Fig. 1.

It is of interest to note that if typical values are substituted into equation (2),a 5°C temperature difference is predicted to be necessary before noise bursts occur. With a temperature cooling rate of 1/3°C/s, typical of cooling rates caused by cloud shadows on sunny days, a 15 s delay would occur before noise is heard: this is of the same magnitude as that often observed.

A number of detailed experiments was conducted to test the validity of the theoretical predictions. Although space requirements preclude a description of these, it is worth recording that the experimental findings were in agreement with the theory. In addition, a number of remedial treatments based on the theory has now been carried out to roofs that were considered to be excessively noisy. In all cases the treatments were successful.

Acknowledgment

The authors wish to thank the management of John Lysaght (Australia) Limited for permission to publish this paper.

Unsteady Nonsimilar Laminar Incompressible Boundary-Layer Flow Over a Yawed Infinite Circular Cylinder

R. Vasantha[1] and G. Nath[1]

Introduction

The accurate prediction of flow field over a yawed infinite circular cylinder finds application in the design of aeroplane wings. The steady nonsimilar flow over a yawed infinite circular cylinder has been studied by several investigators [1-3] in the past. However, in most practical situations, the flow may be unsteady. The unsteady flow over a yawed infinite circular cylinder has not been considered in the literature except in the stagnation region [4].

The aim of this Note is to present the results for an unsteady incompressible nonsimilar flow over a yawed infinite circular cylinder when the free stream velocity varies arbitrarily with time. The governing partial differential equations with three independent variables have been solved numerically using an implicit finite-difference scheme in combination with the quasilinearization technique [5]. The results have been compared with those available in the literature.

Governing Equations

The unsteady laminar incompressible boundary-layer flow over a yawed infinite circular cylinder is considered. It is assumed that the chordwise external velocity varies both with streamwise coordinate and time, whereas spanwise velocity varies only with time, and cylinder surface is assumed to be at a constant, given temperature. The boundary layer equations governing the flow can be expressed as

$$u_x + u_y = 0 \tag{1a}$$

$$u_t + uu_x + vu_y = (u_e)_t + u_e(u_e)_x + \nu u_{yy} \tag{1b}$$

$$w_t + uw_x + vw_y = (w_e)_t + \nu w_{yy} \tag{1c}$$

$$T_t + uT_x + vT_y = (k/\rho c_p)T_{yy} + (\nu/c_p)(u_y^2 + w_y^2) \tag{1d}$$

We apply the following transformations

$$\left.\begin{aligned} &\xi = \rho\mu\int_0^x u_s dx,\ \eta = u_s(2\xi)^{-1/2}y \\ &t^* = U_\infty R^{-1}t,\ \psi(x,y,t) = (2\xi)^{1/2}\varphi(t^*)f(\xi,\eta,t^*) \end{aligned}\right\} \tag{2a}$$

$$\left.\begin{aligned} &u = \psi_y,\ v = -\psi_x \\ &u = u_e F(\xi,\eta,t^*),\ f' = F,\ w = w_e S(\xi,\eta,t^*) \\ &v = -\mu u_s \varphi(t^*)(2\xi)^{1/2}[f_g + (f/2\xi)] \\ &u_e = u_s(x)\varphi(t^*),\ w_e = w_\infty \varphi(t^*) \end{aligned}\right\} \tag{2b}$$

[1]Research Scholar, and Professor, respectively, Department of Applied Mathematics, Indian Institute of Science, Bangalore-560012, India.

Manuscript received by the Applied Mechanics Division, May, 1984; Final revision, November, 1984.

Copyright © 1985 by ASME
Downloaded 02 May 2010 to 171.66.16.54. Redistribution subject to ASME license or copyright; see http://www.asme.org/terms/Terms_Use.cfm

$$u_\infty = U_\infty \cos\theta,\ w_\infty = U_\infty \sin\theta$$
$$(T - T_w)/(T_\infty - T_w) = g(\xi, \eta, t^*) \qquad (2c)$$

to set of equations (1) and we find that equation (1*a*) is satisfied identically and equations (1*b*)–(1*d*) reduce to

$$F'' + \varphi f F + \beta\varphi(1 - F^2) + \alpha\varphi_t^* \varphi^{-1}(1 - F) - \alpha F_t^* = 2\xi\varphi(FF_\xi - F' f_\xi) \qquad (3a)$$

$$S'' + \varphi f S' + \alpha\varphi^{-1}\varphi_t^*(1 - S) - \alpha S_t^* = 2\xi\varphi(FS_\xi - S' f_\xi) \qquad (3b)$$

$$Pr^{-1} g'' + \varphi f g' + 2\varphi^2 E[\cos^2\theta (u_s/u_\infty)^2 F'^2 + \sin^2\theta S'^2] - \alpha g_t^* = 2\xi\varphi(Fg_\xi - g' f_\xi) \qquad (3c)$$

where

$$\alpha = 2\xi U_\infty/(\rho\mu R u_s^2),\ \beta = (2\xi/u_s)(du_s/d\xi)$$
$$E = U_\infty^2/[2c_p(T_\infty - T_w)] \qquad (4)$$

The boundary conditions are

$$F(\xi, 0, t^*) = S(\xi, 0, t^*) = g(\xi, 0, t^*) = 0$$
$$F(\xi, \infty, t^*) = S(\xi, \infty, t^*) = g(\xi, \infty, t^*) = 1 \qquad (5)$$

The initial conditions at $t^* = 0$ are given by the set of equations (3) by putting $\varphi = 1$, $\varphi_t^* = S_t^* = g_t^* = 0$ in them. For a yawed infinite circular cylinder

$$u_s = 2u_\infty \sin\bar{x},\ \bar{x} = x/R,\ w_\infty = \text{constant}$$
$$\xi = 2\rho\mu U_\infty R(1 - \cos\bar{x}),\ \alpha = [\cos\theta(1 + \cos\bar{x})]^{-1} \qquad (6)$$
$$\beta = 2\cos\bar{x}/(1 + \cos\bar{x})$$

Here x and z are the dimensional chordwise and spanwise directions, respectively; y is the distance normal to the surface; u, v, and w are the dimensional velocity components in the x, y, and z directions, respectively; t and t^* are the dimensional and dimensionless times, respectively; ξ and η are transformed coordinates; and f are the dimensional and dimensionless stream functions, respectively; F and S are the dimensionless velocity components in the x and z directions, respectively; T and g are the dimensional and dimensionless temperatures, respectively; F_w' and S_w' are the skin-friction parameters in the x and z directions, respectively; g_w' is the heat-transfer parameter; E is the viscous dissipation parameter; k, ρ, ν and c_p denote, respectively, the thermal conductivity, density, kinematic viscosity, and specific heat at a constant pressure; R is the radius of the yawed circular cylinder; Pr and θ are, respectively, the Prandtl number and yaw angle; $\bar{x}$ is the dimensionless distance; U_∞ is the resultant free stream velocity; α is dimensionless function of $\bar{x}$; and β is the dimensionless pressure gradient parameter. φ is an arbitrary function of t^* representing the nature of unsteadiness in the free-stream velocity which has continuous first derivative for $t^* \geq 0$. The prime denotes derivatives with respect to η and the subscripts t, t^*, x, y, and ξ denote derivatives with respect to t, t^*, x, y, and ξ, respectively. The subscripts e, s, w and ∞ denote condition at the edge of the boundary layer, steady condition, condition at the wall and free-stream condition, respectively.

Results and Discussion

The set of equations (3) under boundary conditions (5) and initial conditions has been solved numerically using an implicit finite-difference scheme with quasilinearization technique [5]. The unsteady free stream velocity distributions considered here are given by

$$\varphi(t^*) = 1 + \epsilon t^{*2},\ \varphi(t^*) = (1 + \epsilon_1 \cos(\omega^* t^*))/(1 + \epsilon_1) \qquad (7)$$

where $\epsilon = 0.25$, $\epsilon_1 = 0.1$ and $\omega^* = 5.6$. Here ϵ and ϵ_1 are constants and ω^* is the frequency parameter. Here the governing partial differential equations have been converted to difference equations. The central difference formula has been used in the η-direction and the backward difference formula in the ξ and t^* directions. Consequently, the derivatives can be expressed as

$$F'' = (F_{m,n,p+1} - F_{m,n,p} + F_{m,n,p-1})/(\Delta\eta)^2$$
$$F' = (F_{m,n,p+1} - F_{m,n,p-1})/(2\Delta\eta)$$
$$F_\xi = (F_{m,n,p} - F_{m,n-1,p})/\Delta\xi \qquad (8)$$
$$F_t^* = (F_{m,n,p} - F_{m-1,n,p})/\Delta t^*$$

Here m denotes mth discretization of t^*, n denotes nth discretization of ξ and p denotes pth discretization of η. $\Delta\eta$, $\Delta\xi$ and Δt^* are the step sizes in the η, ξ, and t^* directions, respectively.

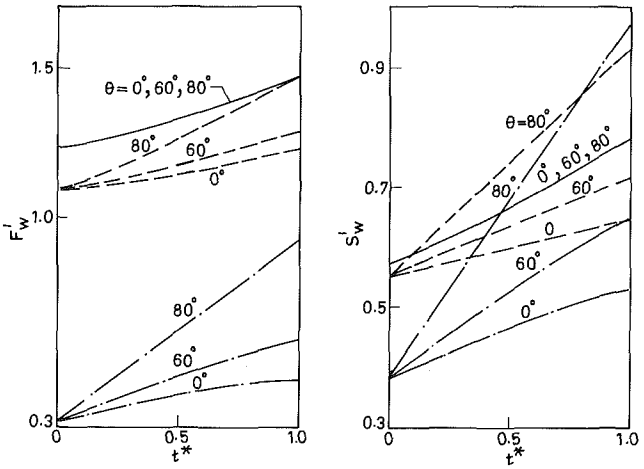


Fig. 1 Effect of θ on skin-friction parameters for $\varphi(t^*) = 1 + \epsilon t^{*2}$, $\epsilon = 0.25$, $E = 0.01$; $Pr = 0.72$. ——, $\bar{x} = 0$; - - - -, $\bar{x} = 1.0$; —·—, $\bar{x} = 1.8$.

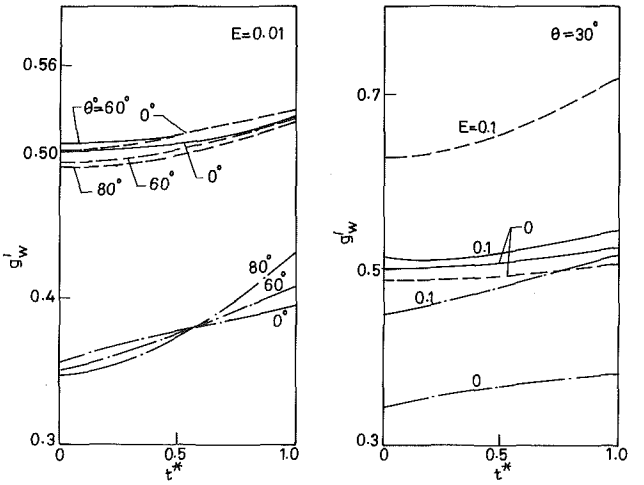


Fig. 2 Effect of θ and E on heat transfer parameter for $\varphi(t^*) = 1 + \epsilon t^{*2}$, $\epsilon = 0.25$, $Pr = 0.72$. ——, $\bar{x} = 0$; - - - -, $\bar{x} = 1.0$; —·—, $\bar{x} = 1.8$.

Downloaded 02 May 2010 to 171.66.16.54. Redistribution subject to ASME license or copyright; see http://www.asme.org/terms/Terms_Use.cfm

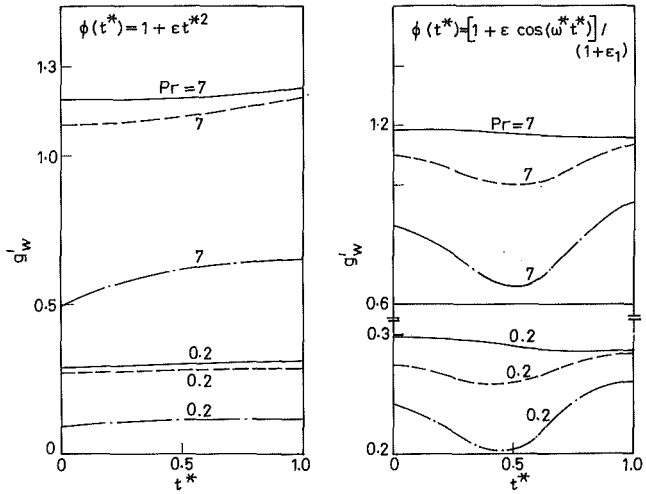


Fig. 3 Effect of Pr on heat-transfer parameter for $\varphi(t^*) = 1 + \epsilon t^{*2}$ and $\varphi(t^*) = (1 + \epsilon_1 \cos(\omega^* t^*))/(1 + \epsilon_1)$, $\epsilon = 0.25$, $\epsilon_1 = 0.1$, $\omega^* = 5.6$; $E = 0.01$, $\theta = 30$ deg. ——, $\bar{x} = 0$; - - - -, $\bar{x} = 1.5$; —·—, $\bar{x} = 1.865$.

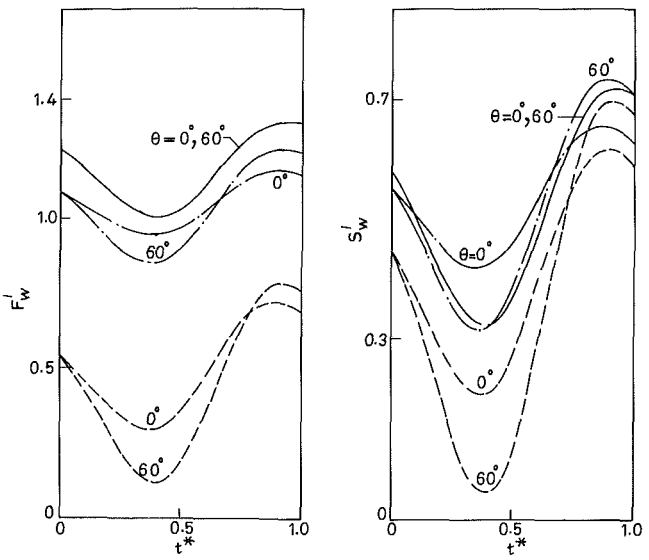


Fig. 4 Effect of θ on skin-friction parameters for $\varphi(t^*) = (1 + \epsilon_1 \cos(\omega^* t^*))/(1 + \epsilon_1)$, $\epsilon_1 = 0.1$; $\omega^* = 5.6$; $E = 0.01$, $Pr = 0.72$. ——, $\bar{x} = 0$; —·—, $\bar{x} = 1.0$; - - - -, $\bar{x} = 1.7$.

To access the accuracy of the method, we have compared the skin-friction and heat-transfer results (F'_w, g'_w) for the steady-state case ($t^* = 0$) for $\theta = 0$ (i.e., for unyawed cylinder) with those of Terrill [6] and Venkatachala and Nath [7] who have used difference-differential and finite-difference methods, respectively, and they are found to be in excellent agreement. Also, the velocity profiles (F, S) for yawed cylinder ($\theta > 0$) have been compared with those of Chiu and Lienhard [3] who used the series solution method. The results are found to be in fairly good agreement. We have also compared our skin-friction results (F'_w, S'_w) for unsteady flow over the yawed circular cylinder when $\bar{x} = 0$ with those of Stock [4] and found them in excellent agreement. However, to reduce the number of figures, the comparison is not presented here.

The effects of time (t^*), yaw angle (θ), dissipation parameter (E) and Prandtl number (Pr) on skin-friction (F'_w, S'_w) and heat-transfer (g'_w) are shown in Figs. 1–4. The effect of θ on F'_w and S'_w is found to be more pronounced for nonsimilar ($\bar{x} > 0$) case than for similar case ($\bar{x} = 0$). In fact, for $\bar{x} = 0$ the effect of θ on F'_w and S'_w is found to be very small and hence is not possible to distinguish it in the figures. As t^* increases skin-friction parameters (F'_w, S'_w) increase (Fig. 1). Also heat-transfer parameter (g'_w) increases as t^* increases for all θ, E and Pr (Figs. 2 and 3). The reason for this behavior is that as t^* increases the momentum and thermal boundary-layer thickness decrease. Hence, the skin-friction (F'_w, S'_w) and heat-transfer (g'_w) increase. As Pr increases g'_w increases (Fig. 3), because thermal boundary layer thickness decreases as Pr increases which results in higher temperature gradient at the wall and hence higher heat transfer.

The effects of t^*, Pr, E, and θ on heat-transfer (g'_w) and skin friction (F'_w, S'_w) for the oscillatory free-stream velocity $\varphi(t^*) = (1 + \epsilon_1 \cos(\omega^* t^*))/(1 + \epsilon_1)$ have been studied. However, only the effect of Pr on g'_w and the effect of θ on F'_w and S'_w are shown in Figs. 3 and 4. The skin-friction and heat-transfer parameters respond significantly to the fluctuations in the external velocity.

Conclusions

Both the skin friction and heat transfer show a strong dependence on the free stream velocity distribution. The yaw angle affects both the skin friction and heat transfer, but the viscous dissipation and Prandtl number affect only the heat transfer.

References

1 Sears, W. R., "The Boundary Layer of Yawed Cylinders," *Journal of the Aeronautical Sciences*, Vol. 15, No. 4, Apr. 1948, pp. 49–52.

2 Cooke, J. C., "The Boundary Layer of a Class of Infinite Yawed Cylinders," *Proceedings of the Cambridge Philosophical Society*, Vol. 46, 1950, pp. 645–648.

3 Chiu, W. S., and Lienhard, J. H., "On Real Fluid Flow Over Yawed Circular Cylinders," *Journal of Basic Engineering*, Vol. 89, No. 4, Dec. 1967, pp. 851–857.

4 Stock, H. W., "Similar Solutions of Unsteady, Laminar Boundary Layers on Swept Cylinders," *AIAA Journal*, Vol. 19, No. 6, June 1981, pp. 817–819.

5 Inouge, K., and Tate, A., "Finite Difference Version of Quasilinearization Applied to Boundary-Layer Equations," *AIAA Journal*, Vol. 12, No. 4, Apr. 1974, pp. 558–560.

6 Terrill, R. M., "Laminar Boundary-Layer Flow Near Separation With or Without Suction," *Philosophical Transactions of the Royal Society of London*, Series *A*, Vol. 253, No. 1022, Sept. 1960, pp. 55–100.

7 Venkatachala, B. J., and Nath, G., "Nonsimilar Laminar Incompressible Boundary Layers With Vectored Mass Transfer," *Proceedings of Indian Academy of Sciences (Eng. Sci.)*, Vol. 3, Part 2, July 1980, pp. 129–142.

Downloaded 02 May 2010 to 171.66.16.54. Redistribution subject to ASME license or copyright; see http://www.asme.org/terms/Terms_Use.cfm

Journal of Applied Mechanics

Discussion

On Laminar Thin-Film Flow Along a Vertical Wall[1]

H. I. Andersson[2]. The paper by Roy (1984) presents an interesting extension of the momentum integral analysis by Hassan (1967), taking into account the joint existence of a developing boundary layer along the wall, and the external accelerating inviscid flow. We wish to mention, however, that the dimensionless parameter α and the dimensionless length scale η used in the paper, conveniently can be related to more common film flow quantities by:

$$\frac{h_0}{h_\infty} = \alpha^{-1/3}; \quad \frac{x}{h_\infty Q/\nu} = \frac{1}{6}\alpha^{2/3}(\eta^2 - 1) \qquad (1)$$

where h_∞ denotes the downstream asymptotic film thickness and $Q \equiv u_0 h_0$ denotes the volumetric flow rate. Thus, the three cases considered numerically by Roy (1984), i.e., $\alpha = 0.2$, 0.6, and 1.0 correspond to $h_0/h_\infty = 1.71$, 1.19, and 1.0, respectively.

For the fully viscous flow region, Hassan (1967) and Roy (1984) derived the same momentum integral equation. While Roy integrated this differential equation numerically by a Runge-Kutta method, Hassan tried to solve it analytically, but did not succeed in obtaining a proper solution. An analytic solution to this equation has, however, been published in a recent paper by Andersson (1984).

One may question the deviations between the two sets of solutions displayed by Roy, obtained for cubic and parabolic velocity profiles, respectively. It may, however, easily be verified that both approaches tend to the same exact Navier-Stokes solution in the downstream asymptotic limit. Accordingly, the discrepancies between the two approaches seem astonishing.

Roy concludes that the cubic profile is superior to the parabolic one. If, however, the cubic profile used by Hassan and Roy in the fully viscous region is scaled against the characteristic velocity Q/h_∞, the resulting dimensionless profile depends on the local value $h(x)/h_\infty$, only. Andersson (1984) demonstrated that if $h(x)/h_\infty > (8/3)^{1/3}$, then this profile exhibits a maximum velocity below the film surface. Furthermore, if $h(x)/h_\infty > 16^{1/3}$, a flow reversal occurs at the free surface. Accordingly, Roy's conclusion is questionable, at least for values of h_0/h_∞ greater than 2.5.

Finally, it should be mentioned that a quite different approach to the vertical film flow problem will be presented in a forthcoming paper by Andersson and Ytrehus (1985). For the particular case with zero entrance velocity at the top of the wall, an exact reference solution for the developing flow in the entrance region is made available, against which approximate solutions may be tested for accuracy.

References

Andersson, H. I., 1984, "On Integral Method Predictions of Laminar Film Flow," *Chemical Engineering Science*, Vol. 39, pp. 1005–1010.

Andersson, H. I., and Ytrehus, T., 1985, "Falkner-Skan Solution for Gravity Driven Film Flow," submitted to ASME JOURNAL OF APPLIED MECHANICS.

Hassan, N. A., 1967, "Laminar Flow Along a Vertical Wall," ASME JOURNAL OF APPLIED MECHANICS, Vol. 34, pp. 535–537.

Roy, T. R., 1984, "On Laminar Thin-Film Flow Along a Vertical Wall," ASME JOURNAL OF APPLIED MECHANICS, Vol. 51, pp. 691–692.

Author's Closure

The remarks made in the discussion by Dr. Andersson are anomalous and incorrect. The dimensionless parameter α, which has been defined in the paper as $\alpha = 3\nu u_0/gh_0^2$ cannot be simultaneously equated to $(h_\infty/h_0)^3$ as mentioned by the discusser. The value of the dimensionless downstream asymptotic film thickness h_∞/h_0 is to be determined only through the solution of our equation (15). Its values for the three demonstrated cases, i.e., for $\alpha = 0.2$, 0.6, and 1.0 are presented in the table, and these results are clearly different from those calculated by the discusser.

Again, the velocity profile (13) in our paper may be written in the form

$$u = Q/\delta[(1/5)(3\beta^3 + 12)y/\delta - (3/2)\beta^3(y/\delta)^2 + (4/5)(\beta^3 - 1)(y/\delta)^3]$$

where $Q = u_0 h_0$ and $\beta^3 = g\delta^3/3\nu u_0 h_0$. Since $\beta^3 = (\delta/h_0)^{1/8}\alpha$, the condition $\partial^2 u/\partial y^2]_{y=\delta} \gtrless 0$ for this profile means $\alpha \lessgtr 3(\delta/h_0)^{3/8}$. This relation holds true for the aforementioned solution of equation (15). Furthermore, the maximum values of $3(\delta/h_0)^{3/8}$, corresponding to the dimensionless film thickness δ^* at the beginning of the fully viscous flow, are given in the accompanying table for $\alpha = 0.2$, 0.6, and 1.0. The relation, $\alpha \lessgtr 3(\delta/h_0)^{3/8}$, may be verified readily from these results.

	Approximate values of		
α	h_∞/h_0	h_0/h_∞	$3(\delta^*)^{3/8}$
0.2	0.7165	1.3957	0.1531
0.6	0.9175	1.0899	0.3885
1.0	1.0440	0.9579	0.5538

[1] By T. R. Roy, and published in the September 1984 issue of the ASME JOURNAL OF APPLIED MECHANICS, Vol. 51, pp. 691–692.

[2] Senior Lecturer, Institute of Applied Mechanics, The Norwegian Institute of Technology, N-7034 Trondheim-NTH, Norway.

Copyright © 1985 by ASME
Downloaded 02 May 2010 to 171.66.16.54. Redistribution subject to ASME license or copyright; see http://www.asme.org/terms/Terms_Use.cfm

Journal of Applied Mechanics

Book Reviews

Fracture Mechanics Methodology. Edited by G. C. Sih and L. Faria. Martinus Nijhoff, The Netherlands, 1984. 177 Pages. Price: $45.00.

REVIEWED BY C. H. POPELAR[1]

This book is one in the series on Engineering Application of Fracture Mechanics. The book is a product of lectures prepared for a short course on Fracture Mechanics Methodology in Lisbon from June 1–June 4, 1981. While the main emphasis of the book is the application of fracture mechanics to aircraft structures, many of the principles are applicable to other flawed members. The treatment is essentially confined to linear-elastic fracture mechanics. The fracture mechanics methodology expounded in the first two chapters (constituting over one-half of the book) is based on the strain energy density approach. The remaining chapters deal with the conventional linear-elastic fracture mechanics approach based on a critical stress intensity factor. Each of the book's five chapters is written by a different author.

In Chapter 1, R. Bodaliance treats the subject of fatigue-life predictions in metals and composites using the strain energy density approach. It is demonstrated that good agreement can be obtained between predicted and measured crack growth in metals under mixed-mode loading by integrating cycle by cycle the fatigue crack growth rate as a function of the range of the strain energy density factor deduced from constant amplitude Mode *I* tests. The fatigue life of composites is shown to correlate with a parameter based on the strain energy density modeling microcracks in the laminate matrix.

Chapter 2 by G. C. Sih contains the fundamental hypotheses and the theoretical development of the strain energy density approach. A more logical progression for those unfamiliar with this approach would have this chapter as the first one. The relationship between the strain energy density factor and the stress intensity factors of the three crack tip modes of deformation is established for small scale yielding. With such a relation the critical value of the strain energy density factor can be obtained when the Mode *I* fracture toughness is known. Several examples of the application of the approach within the confines of linear-elastic fracture mechanics are given. The use of the strain energy density in predicting ductile and fatigue crack growth is discussed. The chapter concludes with a comparison of the virtues of the strain energy density approach relative to alternative approaches to ductile fracture such as: the Irwin plastic zone correction, *J*-integral, critical strain, crack opening displacement, and resistance curve.

In Chapter 3 O. Orringer treats failures due to damage modes other than a sharp crack. This chapter contains several case studies of failures in railroad systems. Failure analysis based on spectral analysis of service load data is developed. Life prediction of structural components using linear damage rules and conventional fatigue crack growth methods are discussed.

Chapter 4 by C. M. Branco reviews the flaw acceptance method; i.e., ascertaining whether or not a detected flaw is acceptable for safe performance of a component. The British Standard PD6493 (1980) approach for determining acceptable defect levels is presented. While specifically developed for welded joints, its application to aircraft structures for stress levels below the yield strength is discussed. When significant inelastic behavior exists, the method tends to be overly conservative and an inelastic approach is required.

In Chapter 5, L. Faria reviews briefly the probabilistic approach for assessing the reliability of a structural design.

Whenever chapters of a book are authored by different individuals, there is the risk of inconsistent notation. This book is no exception. For example, *S* has been used in the first two chapters to denote the strain energy density factor whereas it denotes stress in the next two chapters and the factor of safety in the final chapter. To the authors credit, they have been careful to note the different meanings attributed to *S*. Aside from this irritant the book is well written. It is interspersed with application of fracture mechanics to the investigation of real failures. This book should be of interest to those concerned with the evaluation of the structural integrity of components.

Incompressible Flow. By Ronald L. Panton. Wiley, New York, 1984. 780 Pages. Price $44.95.

REVIEWED BY S. A. BERGER[2]

This advanced treatment of the fundamentals of fluid dynamics is designed as a text for graduate students in

[1] Professor, Department of Engineering Mechanics, The Ohio State University, Columbus, Ohio 43210.

[2] Professor, Department of Mechanical Engineering, University of California, Berkeley, Calif. 94720.

Copyright © 1985 by ASME
Downloaded 02 May 2010 to 171.66.16.54. Redistribution subject to ASME license or copyright; see http://www.asme.org/terms/Terms_Use.cfm

mechanical, aerospace and civil engineering, physics, and applied mathematics, as well as a reference for professionals working in those fields. Contrary to what is suggested by the title, the book begins with a very general discussion of compressible viscous flow, so that the reader may better understand the incompressible case. Then within the context of incompressible flows, the full Reynolds number spectrum of flows is discussed, from high to vanishingly small Reynolds number. Thus extensive treatments are given *both* of boundary layers and inviscid flows. The book concludes with chapters on stability and turbulence.

Throughout is evidenced a conscious attempt to strike an even balance between the physical, mathematical, and practical engineering aspects of the subject. Particularly noteworthy to the engineering community is the heavy emphasis placed on dimensional analysis.

This is a *superb* book. I know of no book, certainly none in English, that comes close to covering as many topics or covers them as well or as comprehensively. Throughout, the discussion is very clear, and lucid, and well organized. Subtle issues concerning the basic equations and concepts are raised and addressed with great insight. Excellent physical interpretations, including molecular considerations, are given of the basic equations and each of the solutions in the book. Brief but interesting historical background and comments are also provided and enliven the text. The text is replete with uncommonly treated problems, problems that greatly enhance the theory but which are at best only mentioned in passing in other texts. Most books in this field tend to be "recipe" books; the others often are unfathomable even to the better student. This book is neither.

The treatment of mathematical preliminaries and background is particularly noteworthy and sets this book apart from others. In the text itself or in appendices there is an excellent survey of the mathematics necessary to fully understand the fluid mechanics material. This includes an early discussion of vector and tensor calculus, probably the two subjects students or readers in general are most weak in and which are most useful in understanding the material that follows. The text acknowledges the crucial and increasingly more important role numerical methods are playing in fluid mechanics by discussing such methods in detail. Finally, and again unlike any other book in the field, there is an excellent extensive treatment of asymptotic methods, including singular perturbation theory, critical to fully comprehending a topic such as boundary layer theory.

The book would be a suitable text for at least a year-long sequence of courses in fluid mechanics, and in fact there is probably enough material, with some supplementation, for courses spanning even a longer time span.

Again, this is a superb book, encyclopedic in scope, lucid in its presentation, showing throughout the efforts and talents of a brilliant teacher. It should make an excellent text, and in view of its virtues an ideal book for self-study.

Flexible Shells, Theory and Applications. Edited by E. L. Axelrad and F. A. Emmerling. Springer-Verlag, New York, 1984. 282 Pages. Price $23.00.

REVIEWED BY R. C. BENSON[3]

One of the most interesting developing fields in applied mechanics research, at least to this reviewer, is that of flexible shells. Contrasted with stiff, load-bearing shells, flexible shells not only permit large displacements, but are actually designed for that purpose. The wind-up tape measure is a commonplace example of a flexible shell. When extended, the tape measure resists bending due to its shallow cross-curvature, nevertheless, it may be collapsed without damage for storage. Historically, stiff shell applications have motivated much of the research in shell theory, and one need only look at modern aircraft to see evidence of the successes that have been achieved. By comparison, the body of literature appropriate to flexible shells is much sparser, even taking into account those works that are germane to shells both stiff and flexible. The challenge of analysis lies in the necessity of abandoning many of the kinematic assumptions that make small-deflection shell theories tractable.

The editors of *Flexible Shells* are to be commended for identifying the title subject as one meriting dedicated study, and for producing a book that is sure to become an important reference ion the field. The 17 technical papers which comprise *Flexible Shells* are drawn from the European Mechanics Colloquium 165. The purpose of the colloquium, as stated in the preface of the book, was to discuss:

"1. The formulations of the nonlinear shell theory, different in the generality of kinematic hypothesis, and in the choice of dependent variables.
2. The specialization of the shell theory for the class of shells and the respective elastic stress states assuring flexibility.
3. Possibilities to deal with the complications of the buckling analysis of flexible shells, caused by the precritical perturbations of their shape and stress state.
4. Methods of solution appropriate for the nonlinear flexible-shell problems.
5. Applications of the theory."

This précis suffices to describe the book as well as the colloquium, and the reader will find about equal attention to each topic. This, of course, is an aggressively broad list, and one should not expect that this or any single book could provide a comprehensive exposition. Where *Flexible Shells* succeeds, rather, is in providing an overview to the subject. The respective articles touch on modern developments in nonlinear shell theory, methods of analysis, and numerical solution techniques (often in regimes of multiple equilbria). There is also a nice mix of retrospection and speculation throughout the book which helps to establish the present state of knowledge in the field.

As each of the technical papers is by a different set of authors, the reader must adjust to a diversity of style. It is no impediment, however, and the editors have done a good job in organizing *Flexible Shells* so that there is a natural flow from the general to the specific. There are also a number of recurring concepts, such as Axelrad's "semimembrane theory", which help tie the book together. This is a nice addition to the flexible shell literature – argueably the first focal reference. Researchers in the field of flexible shells may not find all of their questions answered here, but there will not be a better place to start the literature search.

Elastic Stability of Circular Cylindrical Shells. By N. Yamaki. Elsevier, The Netherlands, 1984. 550 Pages. Price $57.75.

REVIEWED BY G. J. SIMITSES[4]

This book treats the subject of stability, collapse, and postbuckling behavior of elastic, isotropic, thin circular

[3] Associate Professor, Department of Mechanical Engineering, University of Rochester, Rochester, N.Y. 14627.

[4] Professor, School of Engineering Science and Mechanics, Georgia Institute of Technology, Atlanta, Ga. 30332.

Copyright © 1985 by ASME
Downloaded 02 May 2010 to 171.66.16.54. Redistribution subject to ASME license or copyright; see http://www.asme.org/terms/Terms_Use.cfm

cylindrical shells supported in various ways and subjected to static fundamental loads, which are applied individually or in combination. The theoretically defined supports consist of two types of transverse conditions: simply supported and clamped, and all possible combinations of in-plane conditions. The fundamental loads are uniform axial compression, uniform lateral, or hydrostatic pressure (of constant-directional behavior during deformation) and torsion.

The presented theoretical results are based mainly on Donnell-type of equations. Moreover, regardless of the linearity or nonlinearity of the governing equations (classical buckling or postbuckling behavior) the principally employed solution scheme utilizes the Galerkin procedure. The theoretical results include buckling loads and postbuckling behavior of geometries that are free of initial geometric imperfections. Furthermore, the effect of prebuckling deformation and initial geometric imperfections on the critical loads are investigated and presented for all cases of individual application of the fundamental loads.

Experimental results are also presented for all cases of individually applied loads and these results as well as those obtained by other experimentalists serve as a basis for comparison of the theoretical predictions.

As stated by the author in the Preface this book presents a comprehensive treatise on the elastic stability of circular cylindrical shells, which represents the sum of the past 17 years of research conducted at the Institute of High Speed Mechanics, Tohoku University." As also stated "no attempt is made to give a complete bibliography. . . ."

A book cannot be all things to all people. The generalist will find the coverage a bit restrictive in geometry (circular cylindrical thin shells) in construction (isotropic), in material behavior (linearly elastic), and even in solution schemes used. On the other hand, the specialist will find the book very thorough, informative, and accurate in its treatment of elastic buckling and postbuckling of isotropic, circular, cylindrical thin shells.

The book is recommended to all interested in the subject, and it will be very helpful to those who deal with shell stability of other geometries and construction.

Measuring Techniques in Gas-Liquid Two-Phase Flows. Edited by J. M. Delhaye and G. Cognet. Springer-Verlag, New York, 1984. 746 pages.

REVIEWD BY R. DIPIPPO[5]

This book contains 34 papers dealing with recently developed measuring techniques for use with two-phase, liquid-vapor flows. No coverage is given to flows containing solids. The papers were originally presented at a IUTAM symposium held in Nancy, France during July 1983. Before publication, each paper was scrutinized by at least three people selected from an impressive list of researchers in the field.

The papers are grouped according to topic as follows: Optical Imaging; Optical Scattering; Optical and Acoustical Attenuation; Neutron Physics; Tagging Techniques; Local Probes, Technology and Signal Analysis; Flowmeters; and Electrochemical Methods. Although it is not uncommon for books of this sort to lack an index, this one does have a short, "analytical" index of 68 entries that includes the major topics in the book which runs to 746 pages.

The following list of specific techniques will give an idea of the breadth of coverage: photography, holography, spark cameras, activable photochromic dyes, laser Doppler anemometry, laser Raman spectroscopy, gamma-ray, X-ray, and ultraviolet absorption, fast neutron scattering, nuclear magnetic resonance, orifice plates, Pitot tubes, true mass flowmeters, and vortex flowmeters.

The book was produced directly from camera-ready copy, and as such, the formats differ somewhat from paper to paper. However, it is exceptionally readable and includes hundreds of clearly-drawn figures and superb photographs. Some of the color plates could be described as spectacular, e.g., a liquid-gas interface being pierced by a 40 μm single-fiber laser probe.

While not for the casual reader, this collection of current papers will serve as a valuable reference for those doing experimental work in two-phase, liquid-vapor flows.

[5]Professor, Mechanical Engineering Department, Southeastern Massachusetts University, No. Dartmouth, Mass. 02747.

Copyright © 1985 by ASME
Downloaded 02 May 2010 to 171.66.16.54. Redistribution subject to ASME license or copyright; see http://www.asme.org/terms/Terms_Use.cfm